

Complexes of N_4 Substituted
Thiosemicarbazones with Applications in
Medicine and Catalysis



Inaugural Dissertation
for the attainment of the
Doctoral Degree

University of Cologne
Department of Chemistry
Research Group of Prof. Dr. Klein

Submitted by
Alexander Haseloer
From Cologne

Cologne, 2021

Referees:

Prof. Dr. Axel Klein

Prof. Dr. Hans-Günther Schmalz

Prof. Dr. Ulrich Schatzschneider

Chair:

Prof. Dr. Bernd Neumaier

Date of Examination:

04.11.2021

“And once the storm is over, you won’t remember how you made it through, how you managed to survive. You won’t even be sure, whether the storm is really over. But one thing is certain. When you come out of the storm, you won’t be the same person who walked in. That’s what this storm’s all about.”

そしてその砂嵐が終わったとき、どうやってそいつをくぐり抜けて生きのびることができたのか、君にはよく理解できないはずだ。いやほんとうにそいつが去ってしまったのかどうかもたしかじゃないはずだ。でもひとつだけはっきりしていることがある。その嵐から出てきた君は、そこに足を踏み入れたときの君じゃないっていうことだ。そう、それが砂嵐というものの意味なんだ。

– Haruki Murakami, Kafka on the Shore

Acknowledgements

First of all, I want to give my thanks to Prof. Dr. Axel Klein for providing me with the opportunity to work in his group and giving me the freedom to work on topics on my own. His willingness to discuss these topics and giving me guidance provided a lot of help over the years.

I also want to express my deep gratitude to Prof. Dr. Hans-Günther Schmalz for his willingness to review my thesis, and Prof. Dr. Bernd Neumaier for the chairmanship of the examination, as well as his guidance on the field of nuclear medicine and fruitful discussions.

Thanks to Astrid Baum and Mathias Neihls for measuring EI-MS and HR-ESI-MS respectively, Daniela Naumann for measuring high-field NMR, and Dirk Pullem for the elemental analysis. I also want to show my gratitude to Silke Kremer, Dr. Jörg Neudörfl, and Dr. Ingo Pantenburg from the XRD platform for their help in the determination of the crystal structures, and Dr. Daniel Werner and the group of Prof. Wickleder for the opportunity to travel to the PETRA III radiation source at DESY to measure crystals with synchrotron radiation. I would also like to thank Ines Schmidt, Max Reimer, Dr. Selina Olthof, and Prof. Dr. Klaus Meerholz for measuring UPS. Thanks to Dr. Gerald Hörner for his extensive DFT calculations. Thanks to Christian Tobek for measuring DTA-TG and powder XRD.

I want to give my thanks to Dr. Tamara Lützenkirchen, and Prof. Dr. Ines Neundorff for their help with synthesis and analysis the peptide structures, and Dr. Markus Zegke for his inspiration on actinide chemistry as well as synthesis of uranium complexes. I am very grateful for the interesting discussions and their immense influence on this thesis.

I am also very grateful for the research group of Prof. Dr. Axel Klein. Thanks to Sascha Schäfer, Lukas Kletsch, Rose Jordan, Leo Payen, Joshua Friedel, Johannes Hohnsen, Maryam Niazi, Antony Eric Tobeckukwu, Dr. Simon Schmitz, and Tobias Greven for sweetening my work and everyday life. Of course, I also do not forget the former members of the research group that were part of interesting discussions, Dr. Kathrin Stirnat, Dr. Alexander Krest, Dr. Natalia Arefyeva, Dr. Simon Garbe, Dr. Aaron Sandleben, Dr. Nicolas Vogt, Dr. René von der Stück, and Dr. Maren Krause. Furthermore, I want to thank the other research groups of the department as well.

I want to express my gratitude for the interns who worked with me in the last years. Chronologically they are Lukas Münzer, Nora Gildemeister, Joss Pepe Strache,

Andre Thesing, Luca Denkler, Jennifer Klug, Caroline Hoffmann, Christina Wartmann, Andre Santos, Uxue Agirre, Nils Siefert, Tobias Probst, Tobias Greven, Vladimir Stojandinovic, Finn Dicke and Johannes Hohnsen. I also want to acknowledge the people who wrote their thesis under my supervision Juri Petri, Laura Waslawiak, Rose Jordan, and Tobias Greven. Furthermore, I want to thank the interns who worked with me in collaboration with Dr. Markus Zegke Yusuf Bulut, Dennis Grödler, and Daniel Streub and with Prof. Dr. Martin Prechtl Manuel Camora. Their work and expertise on specific topics helped me a lot.

Thanks to friends and colleageaues from the german young chemists network (JCF), the youth organization of the Wöhler Vereinigung für Anorganische Chemie JuWöV. Especially I want to thank Silvia Freese and Thorben Jaik as well as the whole team of the planned Frühjahrssymposium 2020, and the whole fantastic people living the organization. I also want to thank the Verband für angestellte Akademiker und Führungskräfte in der chemischen Industrie (VAA) and the Cologne Crocodiles for making the work as a PhD student more varied.

I want to thank Christina Jäger and Jens Lefarth especially for their friendship and time over the last ten years.

Finally, I want to express my deepest gratitude to my family for their support in the years leading to this thesis.

Thank you.

Abstract

The presented work is based on the *N4* derivatization of thiosemicarbazones and the influence within medical and catalytical applications. A total of 48 thiosemicarbazones were synthesized and characterized. Chapter 2.1 gives an insight into the electrochemical characteristics of the synthesized ligands and the comparison shows the influence of the substitution patterns. As expected, all thiosemicarbazones get reduced on the imine moiety and oxidized at the sulphur atom during the first electrochemical processes.

To further understand the influence of the substitutions on the metal centre, Ir(III) complexes were synthesized in the chapter 2.2. Herein, the complexes bear several coligand combinations of which the hydride coligand acts as a sensor for the electron density at the metal centre. The influence of a *N2* substitution on a metal centre appears is neglectable. Decomposition in DCM yielded oxalate bridged dinuclear iridium complexes which could be determined by single crystal XRD.

2-Pyridinyl thiosemicarbazones were used to coordinate nickel group metals. A series of Pt(II) chloro complexes were synthesized, characterized, and conjugated to peptides by solid phase peptide synthesis. Antiproliferation studies showed that no toxicity arises from the peptide conjugate and the corresponding complexes.

Since the complex [Pt(dpyTSCLp-sC18)Cl] was instable under HPLC conditions the chlorido coligand was exchanged for NCS^- and CN^- . The resulting complexes of the nickel group were investigated by NMR, CV and (SEC-)UV/Vis. The coligands did not follow any trend, yet the complex [Pt(dpyTSCLp-sC18)CN] showed high stability under HPLC conditions, was stable in aqueous media, and was not toxic.

Tetradentate thiosemicarbazone complexes of Ni(II), Cu(II), Pd(II) and Pt(II) were synthesized and characterized in Chapter 2.7. The complexes showed high similarity in their electrochemical and photophysical properties, due to mainly ligand centred frontier orbitals with low contributions of the metal ions.

Additionally, the functionalities of the ligands and complexes could be tuned to gain access to cation specific fluorophores, highly active C-C coupling catalysts. Also, the first U(IV) complexes of thiosemicarbazones could be synthesized and characterized in this work.

Content

1. Introduction	1
1.1. Introduction to thiosemicarbazones	1
1.2. Synthesis of thiosemicarbazones	2
1.3. Coordination chemistry of thiosemicarbazones	3
1.4. Medical application of thiosemicarbazones.....	5
1.5. Nuclear medicine.....	7
1.5.1. Nuclear diagnostics	7
1.5.2. Nuclear therapy	9
1.6. Complex-peptide conjugates in nuclear medicine	12
1.7. Thiosemicarbazones in catalysis.....	13
1.8. Complex-peptide conjugates in catalysis	14
1.9. Application in fluorescence microscopy.....	16
1.10. Aim of the thesis.....	19
2. Results and discussion.....	21
2.1. Synthesis of thiosemicarbazones	21
2.1.1. NMR spectroscopy of thiosemicarbazones	22
2.1.2. SC-XRD determination of the thiosemicarbazones	28
2.1.3. Electrochemical analysis of the thiosemicarbazones.....	32
2.2. Iridium complexes of benzylic thiosemicarbazones.....	35
2.2.1. Analysis of the ligands	35
2.2.1.1. ¹ H NMR spectroscopy.....	35
2.2.1.2. Electrochemical analysis.....	36
2.2.2. General remarks on the synthesis of the iridium complexes.....	38
2.2.2.1. UV/Vis absorption spectroscopy of the iridium complexes	40
2.2.2.2. X-Ray structures of Ir(III) thiosemicarbazones	43
2.2.2.3. Hydride NMR shifts of iridium complexes.....	45
2.2.2.4. Electrochemical analyses of the iridium complexes.....	46
2.2.3. Formation of $[\{\text{Ir}(\text{PPh}_3)_2\text{Cl}_2\}_2(\mu^2\text{-oxalato-}\kappa^4\text{O}^1,\text{O}^2:\text{O}^{1'},\text{O}^{2'})]$	49
2.3. Platinum complexes of the TSCmB and TSCLp series.....	55
2.3.1. The α -N heterocyclic TSCmB ligands.....	55
2.3.1.1. NMR spectroscopy.....	55
2.3.1.2. Electrochemical analysis.....	57
2.3.2. Chlorido platinum complexes with TSCmB ligands	58
2.3.2.1. Crystal structure and Hirshfeld analysis of $[\text{Pt}(\text{apyTSCmB})\text{Cl}]$	59

2.3.3.	Synthesis of the TSCLp series	64
2.3.4.	Comparison of Pt(II) thiosemicarbazones	66
2.3.4.1.	UV/Vis spectroscopy.....	67
2.3.4.2.	NMR spectroscopy.....	67
2.3.4.3.	Electrochemical analysis of the platinum complexes.....	69
2.3.4.1.	Further attempted syntheses to form TSCLp	72
2.4.	Solid phase peptide synthesis as approach for the synthesis of new platinum peptide conjugates	74
2.4.1.	Peptide synthesis.....	74
2.4.2.	[Pt(dpyTSCL-sC18)Cl] – synthesis and characterization	75
2.4.3.	Antiproliferation	78
2.5.	Synthesis and characteristics of platinum cyanido complexes	80
2.5.1.	Synthesis of [Pt(dpyTSCmB)CN]	80
2.5.2.	Electrochemical analysis of [Pt(dpyTSCmB)CN]	81
2.5.3.	Crystal structure and Hirshfeld analysis of [Pt(dpyTSCmB)CN].....	82
2.5.4.	NMR spectroscopy.....	87
2.5.5.	Translation to HdpyTSCL-sC18.....	87
2.5.6.	Antiproliferation	89
2.6.	Further d ⁸ ion complexes of the α-N heterocyclic TSCmB family	93
2.6.1.	Synthesis of [M(pyTSCmB)X] complexes	93
2.6.2.	UV/Vis spectroscopy.....	94
2.6.1.	Crystal structures of Pd(II) and Ni(II) complexes	96
2.6.2.	Electrochemical analyses of the series.....	98
2.6.3.	Spectroelectrochemical UV/Vis spectroscopy	100
2.7.	Tetradentate O ^{^-} N ^{^-} N ^{^-} S TSC ligands containing a pending pyridyl phenolate group.....	102
2.7.1.	Synthesis of H ₂ hphfpyTSCmB	102
2.7.1.1.	Analysis by NMR for 6-substituted pyridine TSCmB.....	104
2.7.2.	Synthesis of [M(hphfpyTSCmB)] for M=Ni, Cu, Pd, Pt.....	105
2.7.2.1.	NMR spectroscopy of d ⁸ complexes.....	106
2.7.2.2.	EPR of [Cu(hphfpyTSCmB)]	106
2.7.2.3.	UV/Vis spectra and TD-DFT for [M(hphfpyTSCmB)].....	107
2.7.2.4.	IR spectroscopy	114
2.7.2.5.	Electrochemical analysis of [M(hphfpyTSCmB)].....	115
2.7.2.6.	Spectroelectrochemical analysis	117
2.7.3.	Attempted synthesis of H ₂ hphfpyTSCLp.....	121
2.8.	Prostate-specific membrane antigens directed thiosemicarbazones.....	123
2.8.1.	Attempted syntheses for N-free TSCL derivatives	125

2.8.2.	LuG as primary amine source	127
2.9.	Synthesis and complexes of fluorescent thiosemicarbazones.....	128
2.9.1.	Synthesis of acridinyl thiosemicarbazones.....	128
2.9.2.	Fluorescence spectroscopy	132
2.9.2.1.	Fluorescence of 4-formyl acridone.....	132
2.9.2.2.	Fluorescence quenching of HfactTSClp.....	132
2.9.2.3.	Influence of transition metal ions on the fluorescence of HfactTSClp	134
2.9.3.	Synthesis of 9-substituted acridines and phenazines	136
2.10.	TSC Pd(II) complexes for C–C cross coupling reactions.....	138
2.10.1.	Attempted syntheses of biotinylated thiosemicarbazones.....	138
2.10.2.	Synthesis of Pd(II) complexes as catalysts.....	142
2.10.3.	Catalytic properties of the [Pd(PPh ₃)(TSC)Cl] structures.....	144
2.10.3.1.	<i>Sonogashira-Hagihara</i> coupling	144
2.10.3.2.	<i>Suzuki-Miyaura</i> coupling	145
2.11.	U(IV) thiosemicarbazones	148
2.11.1.	U(IV) complexes of benzylic thiosemicarbazones	148
2.11.1.1.	Synthesis of U(IV) complexes	148
2.11.1.2.	Crystal structure analysis.....	149
2.11.1.3.	UV/Vis spectroscopy.....	150
2.11.1.4.	Electrochemical analysis.....	151
2.11.1.5.	Thermoanalytic behaviour	153
2.11.2.	Synthesis of pentafluorobenzylic thiosemicarbazones	154
2.11.2.1.	NMR analysis	154
2.11.2.2.	Mass spectroscopy	156
2.11.2.3.	Hirshfeld surface analysis	157
2.11.2.4.	Electrochemical analysis.....	158
2.12.	Bisthiosemicarbazones	160
2.12.1.	Synthesis of 4-substituted pyridinyl bisthiosemicarbazones	160
2.12.2.	UV/Vis spectroscopy.....	162
2.12.3.	Electrochemical analysis.....	163
3.	Conclusion.....	166
4.	Outlook.....	170
5.	Experimental Part.....	175
5.1.	Materials.....	175
5.2.	Equipment and analytical methods.....	176

5.3.	Synthesis of thiosemicarbazides	180
5.3.1.	Synthesis of ITCmB	180
5.3.2.	Synthesis of <i>N</i> 4-1-phenylethyl thiosemicarbazide	180
5.3.3.	Synthesis of <i>N</i> 2-methyl <i>N</i> 4-phenylethyl thiosemicarbazide	181
5.3.4.	Synthesis of 1-isothiocyanatoadamantane	181
5.3.5.	Synthesis of <i>N</i> 4-adamantyl thiosemicarbazide	182
5.3.6.	Synthesis of <i>N</i> 2-methyl <i>N</i> 4-adamantyl thiosemicarbazide	182
5.3.7.	Synthesis of 3-morpholinopropane-1-isothiocyanate.....	183
5.3.8.	Synthesis of <i>N</i> 4-propylmorpholino thiosemicarbazide	183
5.3.9.	Synthesis of tert-butyl (4-aminophenyl)carbamate	184
5.3.10.	Synthesis of tert-butyl (4-isothiocyanatophenyl)carbamate	184
5.3.11.	tert-butyl (4-(thiosemicarbazide)phenyl)carbamate	185
5.3.12.	Synthesis of di-tert-butyl <i>L</i> -glutamate	185
5.3.13.	Synthesis of H-Lys(Cbz)-OH	186
5.3.14.	Synthesis of Boc-Lys(Cbz)-OH.....	187
5.3.15.	Synthesis of Boc-Lys(Cbz)-OtBu.....	187
5.3.16.	Synthesis of Boc-Lys-OtBu	188
5.3.17.	Synthesis of tert-butyl <i>N</i> ² -(tert-butoxycarbonyl)- <i>N</i> ⁶ -thioxomethylidene- <i>L</i> -lysinate (ITCLp) 189	
5.3.18.	Synthesis of tert-butyl <i>N</i> ² -(tert-butoxycarbonyl)- <i>N</i> ⁶ -(hydrazinecarbonothioyl)- <i>L</i> -lysinate (TSCLp) 190	
5.3.19.	Synthesis of Fmoc-Lys(Cbz)-OH	190
5.3.20.	Synthesis of Fmoc-Lys(Cbz)-OtBu	191
5.3.21.	Synthesis of Fmoc-Lys(Alloc)-OtBu.....	192
5.3.22.	Synthesis of Fmoc-Lys-OtBu	192
5.3.23.	Synthesis of Lys(Cbz)-OtBu	193
5.3.24.	Synthesis of tBuO-Glu(OtBu)-u-Lys(Cbz)-OtBu.....	194
5.3.25.	Synthesis of tBuO-Glu(OtBu)-u-Lys-OtBu	195
5.4.	Synthesis of ketones.....	195
5.4.1.	Synthesis of 2-formyl 6-bromo pyridine.....	195
5.4.2.	Synthesis of 2-acetyl 6-bromo pyridine.....	196
5.4.3.	Synthesis of (2-hydroxyphenyl)boronic acid	196
5.4.4.	Synthesis of 2-formyl 6-(2-methoxyphenyl) pyridine.....	197
5.4.5.	Synthesis of 2-formyl 6-(2-hydroxyphenyl) pyridine by cross coupling	198
5.4.6.	Synthesis of 6-Phenyl 2-formylpyridine	198
5.4.7.	Synthesis of 6-(2-cyanophenyl) picolinaldehyde.....	199
5.4.8.	Synthesis of 1-(6-phenyl-pyridin-2-yl)ethan-1-one	200

5.4.9.	Synthesis of 2-(methoxymethyl) aniline.....	200
5.4.10.	General Procedure for the synthesis of acridines	201
5.4.10.1.	Synthesis of 4-ethyl acridine	202
5.4.10.2.	Synthesis of methyl acridone-4-carboxylate	202
5.4.10.3.	Synthesis of methyl acridine-4-carboxylate	203
5.4.10.4.	Synthesis of 4-(methoxymethyl)-4-acridine	203
5.4.11.	Synthesis of 4-(bromomethyl)acridine.....	204
5.4.12.	Synthesis of acridine-4-carbaldehyde	205
5.4.13.	Synthesis of biotin derivatives.....	206
5.4.13.1.	N-Boc norbiotin amine	206
5.4.13.2.	Norbiotin amine	206
5.4.13.3.	Synthesis of biotin NHS	207
5.4.14.	Synthesis of 4-hydroxypyridine 2,6-dicarboxylic acid (Chelidamic acid).....	208
5.4.15.	Synthesis of (4-chloropyridine-2,6-diyl)bis(pyrrolidine-1-ylmethanone).....	209
5.4.16.	Synthesis of 4-chloro-2,6-diacetylpyridine.....	210
5.5.	Synthesis of thiosemicarbazones	211
5.5.1.	Synthesis of fluorinated thiosemicarbazones	211
5.5.1.1.	Synthesis of HFbzTSC.....	211
5.5.1.4.	Synthesis of HFbzTSCAd	212
5.5.1.5.	Synthesis of HFbzTSCmB	212
5.5.1.6.	Synthesis of HFbz(m)TSCmB.....	212
5.5.2.	Synthesis of the Thiosemicarbazones from TSCmB	213
5.5.2.1.	Synthesis of HfpyTSCmB.....	213
5.5.2.2.	Synthesis of H6-BrfpyTSCmB	213
5.5.2.3.	Synthesis of H6-phfpyTSCmB	214
5.5.2.4.	Synthesis of HmphfpyTSC.....	214
5.5.2.5.	Synthesis of Hm(tBu)phfpyTSC.....	215
5.5.2.6.	Synthesis of H ₂ hphfpyTSC.....	215
5.5.2.7.	Synthesis of HmphfpyTSCmB	216
5.5.2.8.	Synthesis of H ₂ hphfpyTSCmB	216
5.5.2.9.	Synthesis of H ₂ hphfpyTSCmB by deprotection	217
5.5.2.10.	Synthesis of HcphfpyTSCmB.....	217
5.5.2.11.	Synthesis of HapyTSCmB	218
5.5.2.12.	Synthesis of H6-BrapyTSCmB	218
5.5.2.13.	Synthesis of H6-phapyTSCmB.....	219
5.5.2.14.	Synthesis of HdpyTSCmB.....	219

5.5.2.15.	Synthesis of H ₂ bzTSCmB	220
5.5.2.16.	Synthesis of H ₂ aphTSCmB.....	220
5.5.2.17.	Synthesis of H ₂ bphTSCmB	221
5.5.2.18.	Synthesis of H ₂ tetTSCmB	221
5.5.2.19.	Synthesis of H ₂ vanTSCmB.....	221
5.5.2.20.	Synthesis of H ₂ 4-NO ₂ aphTSCmB.....	222
5.5.2.22.	Synthesis of HpyxTSCmB	223
5.5.3.	Synthesis of Thiosemicarbazones from (m)TSCmB	223
5.5.3.1.	H ₂ bz(m)TSCmB.....	223
5.5.3.2.	H ₂ aph(m)TSCmB.....	224
5.5.3.3.	H ₂ tet(m)TSCmB.....	224
5.5.3.4.	H ₂ van(m)TSCmB.....	224
5.5.3.5.	H ₂ 4-NO ₂ aph(m)TSCmB.....	225
5.5.4.	Synthesis of Thiosemicarbazones from TSCLp	225
5.5.4.1.	Synthesis of HfpyTSCLp	225
5.5.4.2.	Synthesis of HapyTSCLp.....	225
5.5.4.3.	Synthesis of HdpyTSCLp.....	226
5.5.4.4.	Synthesis of thiosemicarbazone from acridine-4-carbaldehyde.....	227
5.5.4.5.	Synthesis of HbzTSCLp.....	228
5.5.4.6.	Synthesis of HSalTSCLp.....	228
5.5.4.7.	Synthesis of HmphfpyTSCLp	228
5.5.4.8.	Synthesis of HdpyTSCLBoc.....	229
5.5.4.9.	Synthesis of HdpyTSCL-sC18.....	230
5.5.5.	Synthesis from other thiosemicarbazides	230
5.5.5.1.	Synthesis of HfpyTSCpm	230
5.5.5.2.	Synthesis of HapyTSCpm	231
5.5.5.3.	Synthesis of H ₂ bzTSCbap	232
5.5.5.4.	Synthesis of H ₂ bzTSCap.....	232
5.6.	Synthesis of Bisthiosemicarbazones.....	233
5.6.1.	Synthesis of (2 <i>E</i> , 2' <i>E</i>)-2,2'-((4-chloropyridine-2,6-diyl)bis(ethan-1-yl-1-ylidene))bis(<i>N</i> -(1-phenylethyl)hydrazine-1-carbothioamid).....	233
5.6.2.	Synthesis of (2 <i>E</i> , 2' <i>E</i>)-2,2'-((4-chloropyridine-2,6-diyl)bis(ethan-1-yl-1-ylidene))bis(<i>N</i> -(1-phenylethyl)hydrazine-1-carbothioamid).....	234
5.6.3.	Synthesis of (2 <i>E</i> ,2' <i>E</i>)-2,2'-((4-chloropyridine-2,6-diyl)bis(ethan-1-yl-1-ylidene))bis(<i>N</i> -((3 <i>s</i> ,5 <i>s</i> ,7 <i>s</i>)-adamantan-1-yl)-hydrazine-1-carbothioamid	234
5.7.	Metal precursor synthesis.....	235
5.7.1.	Synthesis of [Pd(PPh ₃) ₂ Cl ₂].....	235

5.7.2.	Synthesis of $[\text{Ru}(p\text{-Cymene})\text{Cl}_2]_2$	235
5.7.3.	Synthesis of $\text{PPh}_3\text{-}d_{15}$	236
5.7.4.	Synthesis of $[\text{Ir}(\text{PPh}_3)_3\text{Cl}]$	Fehler! Textmarke nicht definiert.
5.7.5.	Synthesis of $[\text{Ir}(\text{PPh}_3\text{-}d_{15})_3\text{Cl}]$	236
5.7.6.	Synthesis of $[\text{Ir}(\text{PCy}_3)_3\text{Cl}]$	236
5.7.7.	Synthesis of $[\text{Ir}(\text{AsPh}_3)_3\text{Cl}]$	237
5.7.8.	Synthesis of $[\text{Re}(\text{CO})_5\text{Br}]$	237
5.7.9.	Synthesis of $(\text{NEt}_4)_2\text{fac-}[\text{Re}(\text{CO})_3\text{Br}_3]$	238
5.8.	Synthesis of complexes	239
5.8.1.	Synthesis of $[\text{Pd}(\text{PPh}_3)(\text{HbzTSC})\text{Cl}]$	239
5.8.2.	Synthesis of $[\text{Pd}(\text{PPh}_3)(\text{bzTSCmB})\text{Cl}]$	239
5.8.3.	Synthesis of $[\text{Pd}(\text{PPh}_3)(\text{bzTSClp})]$	240
5.8.4.	Synthesis of $[\text{Pd}(\text{PPh}_3)(\text{HbzTSCbap})\text{Cl}]$	240
5.8.5.	Synthesis of Ir(III) complexes.....	241
5.8.5.1.	Iridium complexes of $\text{H}_2\text{bzTSCmB}$	241
5.8.5.2.	Iridium complexes of $\text{H}_2\text{bz(m)TSCmB}$	242
5.8.5.3.	Iridium complexes of $\text{H}_2\text{aphTSCmB}$	242
5.8.5.4.	Iridium complexes of $\text{H}_2\text{aph(m)TSCmB}$	244
5.8.5.5.	Iridium complexes of $\text{H}_2\text{bphTSCmB}$	245
5.8.6.	Synthesis of $[\text{Pt}(\text{fpyTSCmB})\text{Cl}]$	245
5.8.7.	Synthesis of $[\text{Pt}(\text{fpyTSClp})\text{Cl}]$	246
5.8.8.	Synthesis of $[\text{Pt}(6\text{-phfpyTSCmB})\text{Cl}]$	246
5.8.9.	Synthesis of $[\text{Ni}(\text{hphfpyTSCmB})]$	246
5.8.10.	Synthesis of $[\text{Pd}(\text{hphfpyTSCmB})]$	247
5.8.11.	Synthesis of $[\text{Pt}(\text{hphfpyTSCmB})]$	247
5.8.12.	Synthesis of $[\text{Cu}(\text{hphfpyTSCmB})]$	247
5.8.13.	Synthesis of $[\text{Cu}(\text{tBu})\text{hphfpyTSC}]$	248
5.8.14.	Synthesis of $[\text{Cu}(\text{tBu})\text{hphfpyTSCmB}]$	248
5.8.15.	Synthesis of $[\text{Ni}(\text{apyTSCmB})\text{Cl}]$	248
5.8.16.	Synthesis of $[\text{Ni}(\text{apyTSCmB})(\text{NCS})]$	249
5.8.17.	Synthesis of $[\text{Pd}(\text{apyTSCmB})\text{Cl}]$	249
5.8.18.	Synthesis of $[\text{Pt}(\text{apyTSCmB})\text{Cl}]$	249
5.8.19.	Synthesis of $[\text{Pt}(\text{apyTSClp})\text{Cl}]$	250
5.8.20.	Synthesis of $[\text{Pt}(6\text{-BrapyTSCmB})\text{Cl}]$	250
5.8.21.	Synthesis of $[\text{Pt}(6\text{-PhapyTSCmB})\text{Cl}]$	251
5.8.22.	Synthesis of $[\text{Pd}(\text{dpyTSCmB})\text{Cl}]$	251

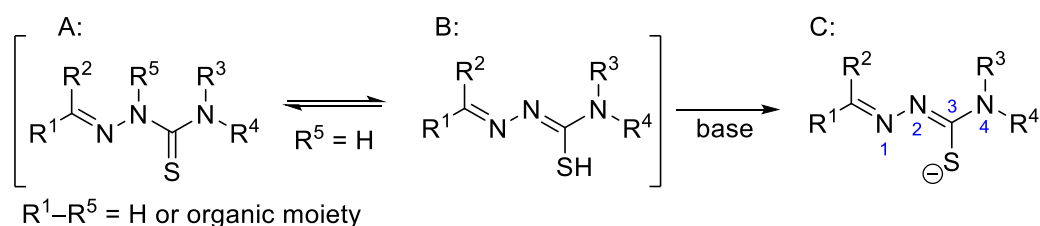
5.8.23.	Synthesis of [Pt(dpyTSCmB)Cl]	251
5.8.24.	Synthesis of [Pt(dpyTSCLp)Cl]	252
5.8.25.	Synthesis of [Pt(dpyTSCL-sC18)Cl]	252
5.8.26.	Synthesis of U(IV) Complexes	252
5.8.26.1.	Synthesis of [U(bzTSC) ₄]	252
5.8.26.2.	Synthesis of [U(bzTSCm) ₄]	253
5.8.26.3.	Synthesis of [U(bzTSCdm) ₄]	254
5.8.27.	Co-Ligand exchange reactions	254
6.	Literature	257
7.	Appendix	285
7.1.	NMR spectra of thiosemicarbazides and their precursors	285
7.2.	NMR spectra of the synthesized ketones and their precursors	328
7.2.1.	Acridine synthesis	335
7.3.	NMR spectra of biotin derivatives	342
7.4.	NMR spectra of thiosemicarbazones	343
7.5.	NMR spectra of metal precursor	404
7.6.	NMR spectra of complexes	405
7.7.	NMR of catalysis crude mixtures	435
7.8.	Mass spectra	436
7.9.	Cyclic voltammograms	462
7.9.1.	Ligands	462
7.9.2.	Complexes	467
7.10.	Spectroelectrochemical UV/Vis spectra	476
7.10.1.	Ligands	476
7.10.2.	Complexes	480
7.11.	Crystal data	490
7.11.1.	HfpyTSCmB	490
7.11.2.	HapyTSCmB	492
7.11.3.	HdpyTSCmB	494
7.11.4.	HbphTSCmB	496
7.11.5.	HFbzTSC	499
7.11.6.	HFbzTSCm	501
7.11.7.	HFbzTSCdm	503
7.11.8.	HFbzTSCAd	505
7.11.9.	HFbzTSCmB	508
7.11.10.	HFbz(m)TSCmB	511

7.11.11.	HmphfpyTSC · ½ Et ₂ O	514
7.11.12.	H ₂ hphfpyTSCmB.....	518
7.11.13.	[Ni(apyTSCmB)Cl].....	522
7.11.14.	[Ni(apyTSCmB)NCS]	523
7.11.15.	[Pd(apyTSCmB)Cl]	525
7.11.16.	[Pd(dpyTSCmB)Cl]·HCl.....	529
7.11.17.	[Pt(apyTSCmB)Cl].....	532
7.11.18.	[Pt(dpyTSCmB)CN].....	534
7.11.19.	[{Ir(PPh ₃) ₂ Cl ₂ } ₂ (μ ² -oxalato-κ ⁴ O ¹ ,O ² :O ^{1'} ,O ^{2'})].	538
7.11.20.	[Ir(PPh ₃) ₂ (bzTSCmB)Cl].....	542
7.11.21.	[Ir(PPh ₃) ₂ (bphTSCmB)Cl] · MeCN	544
7.12.	TD-DFT calculated transitions for [M(hphfpyTSCmB)]	548
7.13.	Erklärung.....	551
7.14.	Curriculum vitae	552
8.	Publications	553
8.1.	Articles.....	553
8.2.	Conference presentations.....	554

1. Introduction

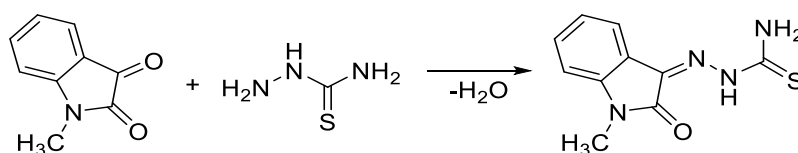
1.1. Introduction to thiosemicarbazones

Thiosemicarbazides are hydrazine derived *N,S*-donor thioureas and show a characteristic thion-thiol tautomerism (Scheme 1.1 A and B).¹⁻³ Condensation of thiosemicarbazides with carbonyl groups leads to thiosemicarbazones (TSC) which enhances the tautomerism and leads to more acidic hydrazone protons.⁴⁻⁶ Treating these compounds with bases lead to a deprotonation of the hydrazone moiety and the tautomerism vanishes yielding solely thiolates (Scheme 1.1 C).



Scheme 1.1 General structure of thiosemicarbazones. A: thione, B: thiol and C: thiolate. At C, the numbering scheme for the thiosemicarbazone atoms according to IUPAC is noted in blue.

Thiosemicarbazones were first mentioned in the early 1950s as auxiliary agents for identification of aldehydes and ketones.^{7, 8} In the subsequent decade the application of TSCs in medicine was discovered, with metisazone, the condensation product of isatin and thiosemicarbazide used as first TSC-containing pharmaceutical for smallpox (Scheme 1.2).⁹⁻¹¹



Scheme 1.2 Condensation reaction of isatin and thiosemicarbazide to form metisazone.

The prevailing mode of action of the TSC in their medical applications seems to be the complexation of metal ions. By condensation of carbonyls containing further functionalities, the abilities of TSCs to act as ligand can be modified or extended (Chart 1.1). E.g., benzylic carbonyls give either a further sterically hindrance for *N*[^]*S* coordinated complexes¹²⁻¹⁶ or undergo C–H activation yielding *C*[^]*N*[^]*S* donor systems (Chart 1.1 A).¹⁷⁻²⁰ The introduction of a pyridine ring through a suitable carbonyl supplies a further *N*-donor to the system and allows *N*[^]*N*[^]*S* tridentate binding with two five-ring chelates (Chart 1.1 B). Further heterocyclic groups such as pyrazoles (Chart 1.1 C),²¹⁻²⁴ allow the modification of this *N*[^]*N*[^]*S* motive. In addition, other structural motifs were investigated such as *O*[^]*N*[^]*S* systems derived from salicylic aldehyde or from the previously shown isatin (Chart 1.1 D).²⁵⁻²⁷ By obtaining acetyl

derivatives from triphenyl phosphines, P[^]N[^]S derivatives (Chart 1.1 E) were also be achieved.²⁸⁻³¹

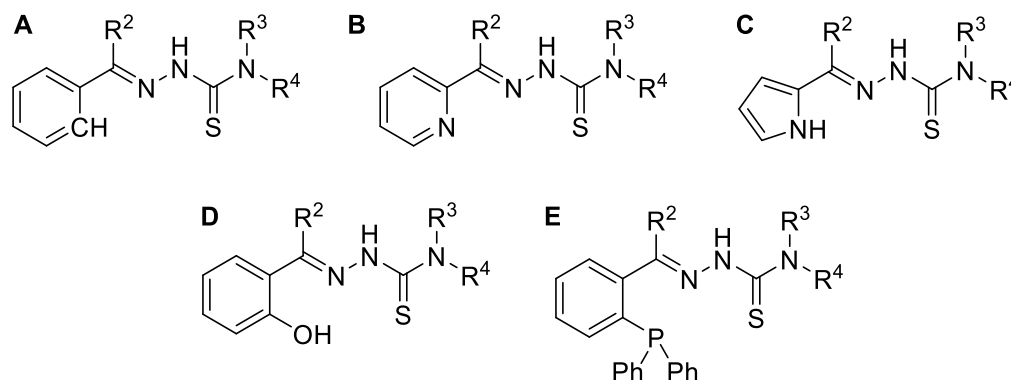
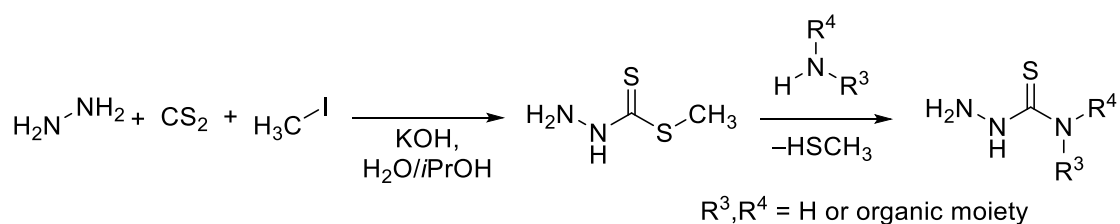


Chart 1.1 Structural motifs of thiosemicarbazones with possible C^NS, N^NS, O^NS and P^NS binding sites.

The great possibility of derivatization leads to the ability of thiosemicarbazones to form complexes with almost any transition metal ion as neutral or anionic ligands.³²⁻³⁵ Furthermore, due to the tuneable ligand structures these complexes can have various coordination spheres allowing access to a manifold of interesting properties for catalytical,³⁶⁻⁴⁰ analytical⁴¹⁻⁴⁴ and medical applications.^{11, 45-52}

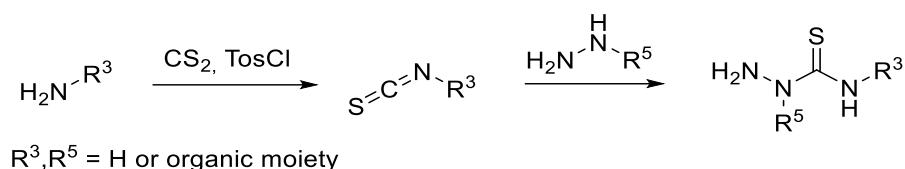
1.2. Synthesis of thiosemicarbazones

To synthesize thiosemicarbazones, two methods have been widely used. Method A starts by building up the hydrazine functionality. The corresponding intermediate product is a carbothioamide which is reported to react with primary and secondary amines to form thiosemicarbazones with mono or disubstituted N₄ positions (Scheme 1.3).⁵³⁻⁵⁶



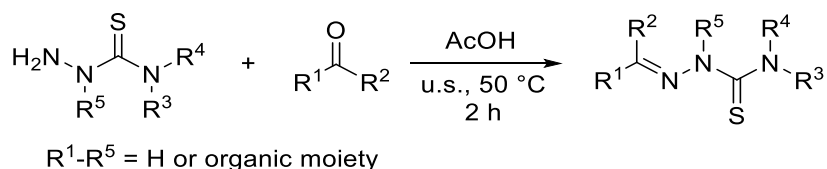
Scheme 1.3 Synthesis of thiosemicarbazides via methylhydrazine carbothioamide. (Method A)

Unfortunately, method A starts with a considerably unpleasant reaction and the by-products of this synthesis, various methylated sulphur compounds, are undesirable. The alternative method B starts with an amine which is first converted into the corresponding isothiocyanate and then reacted with hydrazines to the thiosemicarbazides (Scheme 1.4).⁵⁷⁻⁶⁰ This method yields a mono-substituted N₄ position but it is able to change the formerly secondary amine N₂ into a tertiary when using hydrazine related compounds.⁶¹⁻⁶³



Scheme 1.4 Synthesis of thiosemicarbazides via isothiocyanates. (Method B)

Both reactions yield thiosemicarbazides which belong to a larger family of hydrazides. They can undergo a condensation reaction with carbonyls. This reaction has been widely studied by *Carradori et al.* who established a reaction protocol using glacial acetic acid as a catalyst in a microwave with very high yields. The drawback is the small reaction vessel used in microwave assisted synthesis. An ultrasonic assisted synthesis (Scheme 1.5) with similar reagents showed slightly lower conversion, but the reaction can be run on sizeable quantities which are only limited by the size of the ultrasonic bath.⁶⁴



Scheme 1.5 Synthesis of thiosemicarbazones by ultrasonic assisted condensation reaction.

1.3. Coordination chemistry of thiosemicarbazones

As previously mentioned thiosemicarbazones have different structural motifs from which a variety of structures can be derived. The favoured chelate binding mode occurs by M^1S (Chart 1.2 A). Upon coordination, frequently deprotonation at the $N2H$ function occurs, but the resulting complexes are best described as thiolate-coordinated in keeping with the tautomeric equilibrium of the TSC and the resonance of the deprotonated species. Both thione (Chart 1.2 A) and thiolate (Chart 1.2 B) complexes were reported. The thiolate function can also bridge between two metals (Chart 1.2 C). Monodentate binding of thiolates can be found if only one coordination site is available at the metal (Chart 1.2 D).

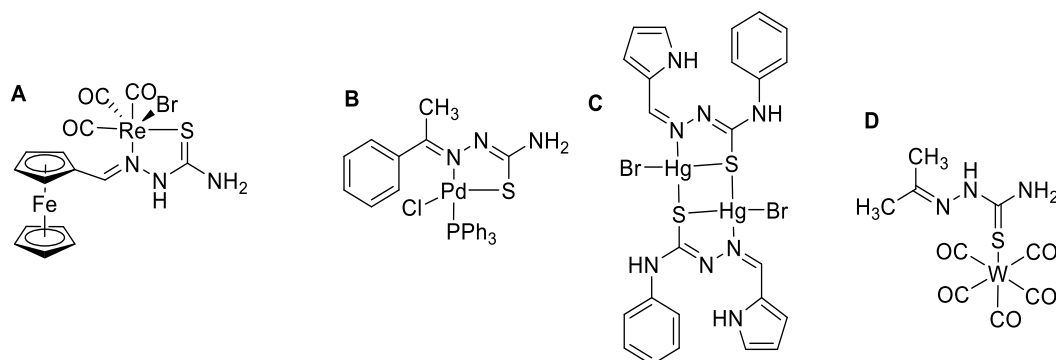


Chart 1.2 Coordination motifs of thiosemicarbazones.^{13, 65-67}

As mentioned above, extension of the TSCs by adding additional donor groups either as carbonyls or on the *N4* substituents greatly enhances the coordination abilities of these molecules. Thus tri-, tetra-, and pentadentate TSC ligands (Chart 1.3 A-C) have been designed and used in coordination chemistry.

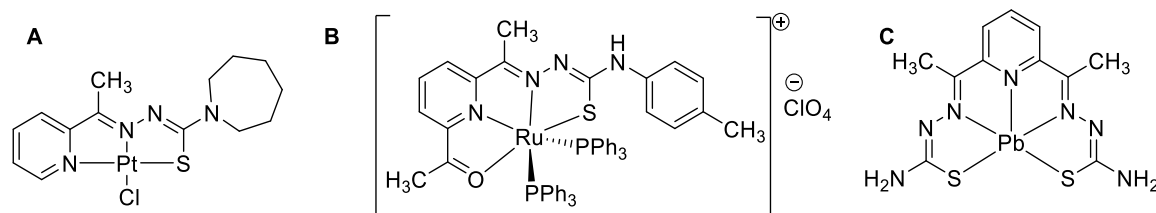
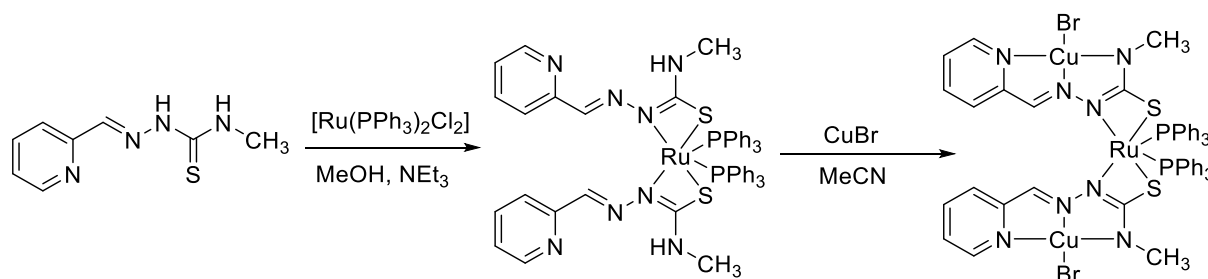


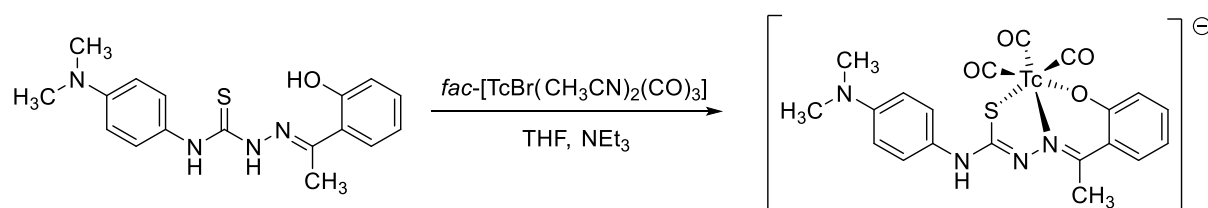
Chart 1.2 Coordination motifs of tri-, tetra- and pentadentate thiosemicarbazone complexes.⁶⁸⁻⁷⁰

The complexes shown in Chart 1.2 and Chart 1.3 are the standard coordination modes by $M1^{\wedge}S$ and additional donors. Over time there has been many “non-classical” coordination patterns of thiosemicarbazones. Ruthenium for example can bind to the thiosemicarbazone at *N2* and the thiolate forming four membered rings. Additionally, these ruthenium complexes are able to bind further metal ions by the *N1* and *N4* position.⁷¹ The group of Lobana used similar Ru(II) species to form Cu(II)/Ru(II) heterobimetallic complexes by oxidative addition of a Cu(I) halide (Scheme 1.6).⁷²



Scheme 1.6 Formation of a Cu(II)-Ru(II)-Cu(II) trinuclear heterobimetallic complex by addition of CuBr to a ruthenium TSC.

The previously in Chart 1.3 and Scheme 1.6 described complexes are all bearing co-planar oriented thiosemicarbazones despite their different coordination polyhedra. In octahedral complexes like Chart 1.3 B, the ligand coordinates meridional. Structurally demanding metal ion fragments, e.g. $fac-[Re(CO)_3]^+$ or $fac-[Tc(CO)_3]^+$, however are capable of twisting the ligand into a facial coordination (Scheme 1.7).



Scheme 1.7 Synthesis of a Tc(I) thiosemicarbazone complex.⁷³

As TSC molecules allow a wealth of substitution patterns on both the *N1* and the *N4* site, a plethora of structures can be obtained to adopt the coordination requirements of various metals in various oxidation states. Since TSCs provide rather the rather soft donor atoms N and S for coordination, many complexes of metals in the centre of the periodic table are reported (Figure 1.1). Remarkable exceptions from the HSAB rules are TSC complexes of Al(III)⁷⁴ or the lanthanides.⁷⁵

Group	1	2	3	4	5	6	7	8	9	10	11	12	13	14	15	16	17	18
1	1 H																	2 He
2	3 Li	4 Be											5 B	6 C	7 N	8 O	9 F	10 Ne
3	11 Na	12 Mg											13 Al	14 Si	15 P	16 S	17 Cl	18 Ar
4	19 K	20 Ca	21 Sc	22 Ti	23 V	24 Cr	25 Mn	26 Fe	27 Co	28 Ni	29 Cu	30 Zn	31 Ga	32 Ge	33 As	34 Se	35 Br	36 Kr
5	37 Rb	38 Sr	39 Y	40 Zr	41 Nb	42 Mo	43 Tc	44 Ru	45 Rh	46 Pd	47 Ag	48 Cd	49 In	50 Sn	51 Sb	52 Te	53 I	54 Xe
6	55 Cs	56 Ba	57 La	* 72 Hf	73 Ta	74 W	75 Re	76 Os	77 Ir	78 Pt	79 Au	80 Hg	81 Tl	82 Pb	83 Bi	84 Po	85 At	86 Rn
7	87 Fr	88 Ra	89 Ac	* 104 Rf	105 Db	106 Sg	107 Bh	108 Hs	109 Mt	110 Ds	111 Rg	112 Cn	113 Nh	114 Fl	115 Mc	116 Lv	117 Ts	118 Og
				* 58 Ce	59 Pr	60 Nd	61 Pm	62 Sm	63 Eu	64 Gd	65 Tb	66 Dy	67 Ho	68 Er	69 Tm	70 Yb	71 Lu	
				* 90 Th	91 Pa	92 U	93 Np	94 Pu	95 Am	96 Cm	97 Bk	98 Cf	99 Es	100 Fm	101 Md	102 No	103 Lr	

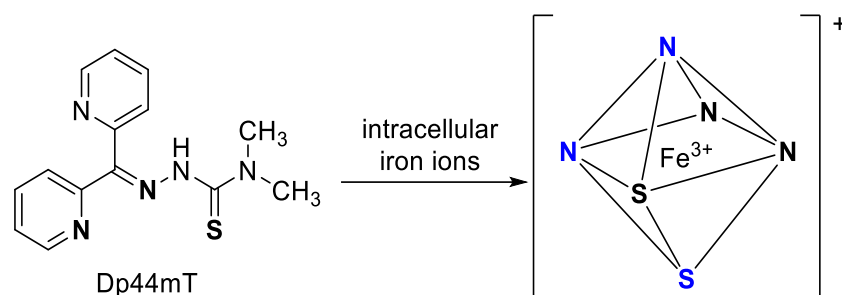
Figure 1.1 The periodic table of elements. The elements of which thiosemicarbazone complexes are known are highlighted.

1.4. Medical application of thiosemicarbazones

As mentioned before, metisazone (Scheme 1.2) was a breakthrough pharmaceutical against smallpox and stood at the beginning of the application of thiosemicarbazones in medicine. Since then, a huge number of further TSCs has been tested for their biological properties and anti-bacterial, anti-fungal and anti-cancer activities were found. As metal coordination is accepted as the prevailing mode of TSC in biological systems, also TSC metal complexes were studied for their biological activities.⁷⁶⁻⁷⁸

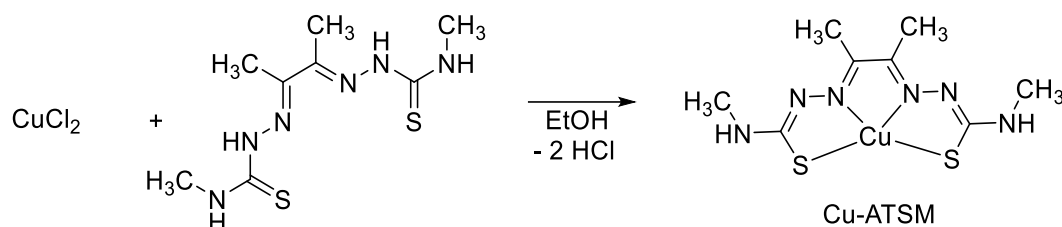
One of the most interesting findings was the 2-di(pyridin-2-yl)methylene)-*N4*-dimethyl thiosemicarbazone (Dp44mT),^{79, 80} that inhibits topoisomerase II α causing selective cytotoxicity in the breast cancer cell line MDA-MB-231 in comparison with “healthy” mammary epithelial cells MCF-12A.⁸¹ Another mode of inhibition is the coordination of iron. Two Dp44mT molecules can octahedrally coordinate Fe(III) ions (Scheme 1.8).⁸²⁻⁸⁴ These Fe(III) complexes are reduced by nicotinamide adenine

dinucleotide (NADH) to the corresponding Fe(II) species, which are able to generate reactive oxygen species (ROS) and even undergo *Fenton*-type chemistry.^{82, 85-87}



Scheme 1.8 Dp44mT with the chelating atoms in bold and the proposed octahedral monocationic Fe(III) complex with the two meridional Dp44mT chelating atoms in different colours.

Another important TSC complex, frequently used in medical imaging, is the so-called Cu-ATSM (Scheme 1.9).^{51, 88-94} 1,2-Dimethyl-1,2-ethanediyldene-bis-*N*(4-methyl thiosemicarbazone) (ATSM) is a tetradentate dianionic planar ligand which can form very stable complexes with transition metals like Cu(II) (Scheme 1.9).^{51, 92, 95} Cu-ATSM has the remarkable ability to accumulate in hypoxic tumour cells. Tumour hypoxia is a major obstacle for imaging since the tumour's low metabolism makes it hard for pharmaceuticals to get into the cell.⁹⁶⁻⁹⁹ Cu-ATSM can get into the cell forming ROS inside which eventually leads to apoptosis (programmed cell death).¹⁰⁰



Scheme 1.9 Synthesis of Cu-ATSM.

More important is the use of Cu-ATSM in nuclear medicine.^{88, 93, 94} Isotopically labelled ⁶⁴Cu-ATSM is chemically identical to the non-radioactive counterpart, but physically ⁶⁴Cu is a positron emitter with a half-life of 12.7 h.⁹¹ This positron has a mean energy of 0.28 MeV (max. 0.65 MeV)⁸⁹ making ⁶⁴Cu it a promising isotope for positron emission tomography (PET) since it has a mean range of 0.7 mm (max. 2.2 mm) until it annihilates and emits the 511 keV photons used in this imaging method.¹⁰¹⁻¹⁰³

1.5. Nuclear medicine

1.5.1. Nuclear diagnostics

In nuclear medicine ionizing radiation of radioactive isotopes is used to detect and treat diseases.¹⁰⁴⁻¹⁰⁷ These isotopes can be incorporated by ligands or just the isotope itself. One good example for this is $^{82}\text{RbCl}$ ($t_{1/2} = 6.3$ h) which allows detection of heart muscle blood flow due to its resemblance to potassium chloride. Another used labelled compound is $^{15}\text{O}_2$ ($t_{1/2} = 2.03$ min) as a steady-state inhalation method to measure regional cerebral blood flow and regional cerebral metabolic rate of oxygen.¹⁰⁸⁻¹¹⁴ Some methods use biologically similar structures to detect a change in the metabolism. The most prominent examples from this category are [^{18}F]-fluorodesoxyglucose ([^{18}F]-FDG) and [^{18}F]-fluoroethyl tyrosine ([^{18}F]-FET). With this, tumour cells can be recognized by using higher metabolism of tumour cells which thus have a higher uptake of sugar and amino acids, compared to inflammatory regions which only have a higher uptake of sugar.¹¹⁵⁻¹²¹ This leads to the differentiation of tumours and inflammatory regions as shown in Figure 1.2.¹²²⁻¹²⁴

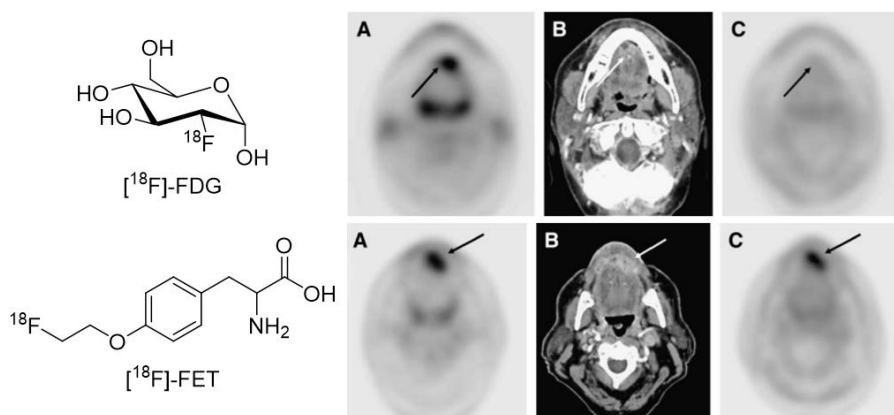


Figure 1.2 left: chemical structures of [^{18}F]-fluorodesoxyglucose (^{18}F -FDG) and [^{18}F]-fluoroethyl tyrosine (^{18}F -FET). Right: A: ^{18}F -FDG-PET scan. B: CT scan. C: ^{18}F -FET-PET scan. The upper row shows a 50-year-old man with chronic inflammatory tissue. The lower row shows a 72-year old man with squamous cell carcinoma (SCC).¹²⁵

In nuclear medicine particles emitted by various isotopes can be used to visualize certain biological abnormalities which are unable to be detected by computed tomography.^{126, 127} The first uses of ionizing radiation in imaging techniques were discovered by *George de Hevesy* in 1935 when he evaluated the distribution of ^{31}P in plants.^{128, 129} In the following years developments of bigger amounts as well as new isotopes led to the discovery of more sophisticated procedures and the whole field of nuclear medicine.

Invented in the late 50's by *Hal Anger* the Anger-camera or gamma camera is able to detect two dimensional pictures of radiation intensities in the human body.¹³⁰⁻¹³²

For the first time, physicians were able to gain biological information out of the living human body. A more sophisticated method is called single photon emission computed tomography (SPECT).¹³³ It works by combining several gamma cameras to give a three-dimensional radiation density map of the body.¹³⁴⁻¹³⁶ This pushed the spatial resolution to good accuracies.^{137, 138} The most common isotopes for gamma camera and SPECT are ^{99m}Tc, ¹¹¹In, ¹²³I and ²⁰¹Tl.¹²⁰ The ¹²³I labelled iodobenzamide (IBZM) (Figure 1.3) is used to help differentiate between *Parkinson's* from other neurodegenerative diseases.^{139, 140}

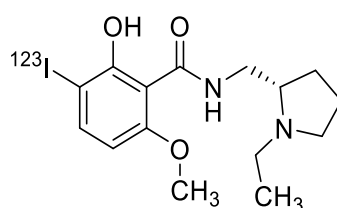


Figure 1.3 Iodine-123 labelled iodobenzamide (IBZM).

These isotopes are mostly produced in nuclear reactors by neutron activation or by working up spent nuclear fuel.¹⁴¹⁻¹⁴⁴ Beginning in the early 1930's nuclear physicists began bombarding everything with radiation and constructed new ways how to accelerate particles. One of these new methods is the cyclotron, a schematic representation is depicted in Figure 1.4.¹⁴⁵ A cyclotron accelerates light particles like protons, deuterium ions or helium cores up to 100 MeV and by irradiating gases, liquids and solids, creation of new isotopes takes place. These isotopes are usually neutron deficient and tend to decay rather in a β^+ than β^- fashion. Thus, giving the rise to the production of positron emitting particles.¹⁴⁶

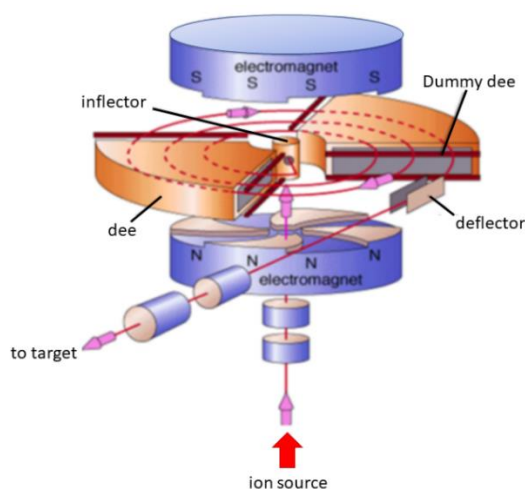
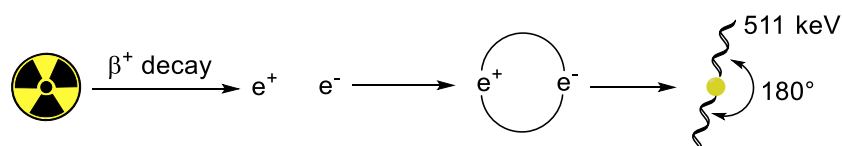


Figure 1.4 Schematic representation of a cyclotron. The ion source is typically a hydrogen plasma source yielding hydride ions in the gas phase. The ion beam is deflected into the dee by an inflector. The deflector is a stripping foil yielding the positively charged hydrogen ions which are focused on a target.¹⁴⁷ In this graphic the electromagnets are smaller than in reality. Typically, they need to be as big as the dee electrodes to ensure a homogenous magnetic field.

A β^+ decaying nuclide emits a positron and an antineutrino. Due to the broad continuous distribution of the energy of the emitted particles in β decays, *Enrico Fermi*, *Wolfgang Pauli*, *Niels Bohr* and others were suggesting various ideas how this was compatible with the conservation of energy which subsequently led to the discovery of neutrinos.¹⁴⁸⁻¹⁵² The emission energies are thus given as maximal energies of the positrons. Positrons are the antiparticles of electrons and when they hit each other they form a metastable exotic atom, the positronium.¹⁵³ Due to the spins of the positron ($S = \pm 1/2$) and the electron ($S = \pm 1/2$) the positronium can either form a 1S_0 singlet state of the positronium with antiparallel spins or a 3S_1 triplet state with parallel spins. The singlet state decays into two photons with an energy of 511 keV, the rest mass of an electron. The schematic of this process is shown in Scheme 1.10. The triplet state on the other hand decays in odd number of photons. Their half-life times are 0.1244 ns and 142 ns respectively.^{154, 155}



Scheme 1.10 A positron is emitted by a radioactive source and forms with an electron from surrounding tissue a positronium. A positronium is an unstable exotic atom which decays by annihilation of the matter-antimatter pair. The emitted photons have an energy of 511 keV and are emitted in a 180° angle to each other.

These 511 keV photons are the starting point of the positron emission tomography (PET). PET measures the photons from the positronium decay and only if they coincidentally reach two detectors 180° apart it counts as a decay.¹⁵⁶ Despite the decay probabilities the biggest influence on the accuracy is the decay energy of the positron.¹⁵⁷⁻¹⁶⁰ A high energy positron travels further in the tissue before it forms a positronium and annihilates.^{157, 161, 162} Therefore, the combination of highly biologically selective and low energy positrons is favourable. Isotopes which are common in this imaging method are ^{11}C ($t_{1/2} = 20.38$ min), ^{15}O ($t_{1/2} = 2.03$ min) and ^{18}F ($t_{1/2} = 109.728$ min). But also various metal isotopes have been investigated in the last decades like ^{62}Cu ($t_{1/2} = 9.74$ min) and ^{68}Ga ($t_{1/2} = 67.63$ min).¹²⁰

1.5.2. Nuclear therapy

Other types of decay result in the emission of electrons or alpha particles. These decay products are used in radiotherapy due to the ionization of tissue. Alpha particles are helium-4 nuclei. The particles are only emitted by nuclei with a proton number of 60 in non-extreme neutron deficient regions. An exception to the previous sentence is boron-8 which is the lightest isotope to undergo an alpha decay.

Super heavy isotopes decay mostly in alpha fashion and the emission energies are characteristic and sharp for every isotope. For nuclear medical purposes isotopes like ^{213}Bi ($t_{1/2} = 45.59$ min), ^{223}Ra ($t_{1/2} = 11.43$ d) and ^{225}Ac ($t_{1/2} = 10.0$ d) are used as alpha emitters.¹⁶³⁻¹⁶⁵ The energy of these alpha particles is in range of 6 MeV, but due to their size the penetration depth is much lower than those of positrons or electrons with similar energy leading to a higher energy transfer and higher damage.¹⁶⁶

Neutron rich isotopes decay by transformation of a neutron into an electron, a proton, and an electron neutrino (β^- decay). Similar to the β^+ decay, the decay energies are given as maximal energies, because the resulting electron, neutrino, and daughter isotope result in an energy distribution. The electrons themselves can ionize the tissue and can cause apoptosis in surrounding cells due to DNA damage.¹⁶⁷ Neutron deficient nuclei may have a second decay pathway besides β^+ which is electron capture.^{168, 169} In this decay path an electron from the inner shells may fall into the core causing a proton to be transformed into a neutron and electron neutrinos,^{170, 171} leading to a vacancy in the inner shells.¹⁷² This vacancy is filled by electrons from upper shells and the energy is emitted as X-rays. Those so-called X-rays are able to ionize the outer shells of the atom in a *Auger-Meitner*, *Coster-Kronig* or super *Coster-Kronig* fashion resulting in the emission of several electrons (put together as AE or *Auger* electrons).¹⁷³⁻¹⁷⁵ The last way electrons may be emitted is internal conversion.¹⁷⁶ Here a nucleus changes its energy state from a metastable to a ground state resulting in the emission of a gamma photon which itself can ionize the outer shells resulting in the emission of conversion electrons (CE or IC-electrons). The energies of the electrons are highest for the β^- decay which is in the range of several kilo electronvolts to several mega electronvolts. Auger and CE electrons are in the range of kilo electronvolts down to a few hundred electron volts. An Overview of the composition and energy of some AE and CE emitting nuclides is given in Table 1.1.

Table 1.1 Properties of Auger emitting radionuclides.¹⁷⁷

Auger electrons (AEs)					Conversion electrons (CE)		
Isotope	Half life	AEs/decay	Energy/decay (keV)	Energy/AE (keV)	CE electrons /decay	Energy/decay (keV)	Energy/CE electron (keV)
^{67}Ga	78 h	5.0	6.6	1.3	0.3	14.1	29.7
$^{99\text{m}}\text{Tc}$	6 h	4.4	0.9	0.2	1.1	15.2	13.8
^{111}In	67 h	7.4	6.9	0.9	0.2	27.9	176.1
^{123}I	13 h	13.7	7.2	0.5	0.2	21.0	222.6
$^{193\text{m}}\text{Pt}$	4.3 d	27.4	10.9	0.4	3.0	126.8	42.4
$^{195\text{m}}\text{Pt}$	4.0 d	36.6	23.1	0.6	2.8	161.4	58.1
^{197}Hg	64.1 h	23.2	16.1	0.7	0.8	54.1	67.0
^{201}Tl	73 h	20.9	14.8	0.7	0.9	29.9	32.9

Electron emitting isotopes which are currently used are ^{111}In , ^{161}Tb , ^{177}Lu and ^{188}Re .¹⁷⁸⁻¹⁸¹ Platinum isotopes ^{191}Pt , $^{193\text{m}}\text{Pt}$ and $^{195\text{m}}\text{Pt}$ are also applicable electron emitters, yet their non-carrier added production on the cyclotron is only possible at high energies utilizing alpha particles in a reaction like $^{192}\text{Os}(\alpha, n)^{195\text{m}}\text{Pt}$. However, what differs the platinum isotopes from the others are the amount and energies of the emitted particles. $^{195\text{m}}\text{Pt}$ emits on average 36.6 *Auger* electrons, mean energy 0.6 keV, and 2.8 Internal conversion electrons with an average energy of 58.1 keV. ^{188}Re is one of the most used isotopes in radiotherapy and the electrons from the decay is 2.12 MeV, 3500-fold the energy of the *Auger* electrons.^{182, 183} The penetration depth of the electrons correlates with a linear energy transfer of around 4–26 keV/ μm for Auger electrons and 0.1–1 keV/ μm for beta electrons resulting in a much more defined radiated space for the platinum isotopes of only several hundred nanometers.¹⁸⁴ The effect of the energy and LET in combination is illustrated in Figure 1.5.

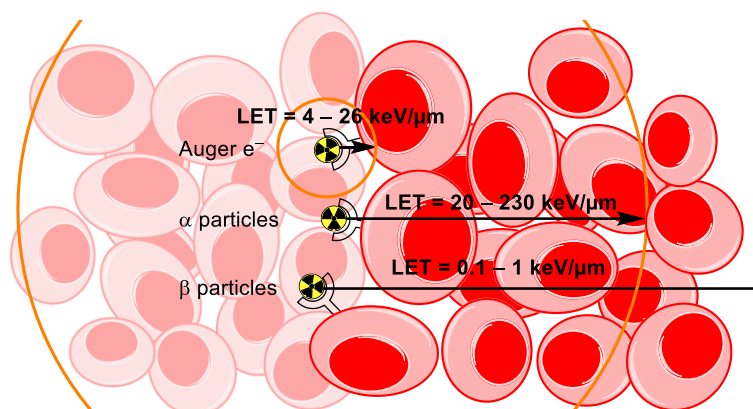


Figure 1.5 Pathways of decay particles and their linear energy transfer (LET) values in keV/ μm . Mean distance for Auger electrons $>0.5 \mu\text{m}$ and for α particles 50 – 100 μm . β particles are off the scale with around 2 – 10 mm.¹⁸⁴

The emitted electrons or alpha particles cause damage to DNA, disrupt the membrane and generate ROS.¹⁸⁵ These damages disrupt the cell and can lead to apoptosis.¹⁸⁶ With a longer treatment with radioactive substances a tumour can be therefore destroyed.¹⁸⁷⁻¹⁸⁹

Proton, neutron, and cluster emissions as well as spontaneous fission and other decay pathways have up to date no use in nuclear medicine due to their rareness or high instability of their mother nuclides.

1.6. Complex-peptide conjugates in nuclear medicine

The peptide receptor radionuclide therapy uses a different approach to the previously mentioned examples.¹⁹⁰ To get a high bioselectivity a peptide is designed to fit into the binding moiety of a receptor which is overexpressed on tumour surfaces.¹⁹¹ To select the best peptide for this therapeutically approach, a general understanding of the cancer cells' metabolism and genetic alterations must be developed. The higher growth rate of tumour cells might indicate to the overexpression of growth hormone receptors. Since somatostatin and its binding side to the receptor has been the target of various scientific studies various peptide substrates could be identified, which are applicable as biological vectors.^{192, 193}

A good example is octreotide, which was recently approved by the U.S. Food and Drug Administration (FDA) and the European Medicines Agency (EMA). Octreotide is a cyclic eight amino acid variant of the somatostatin.¹⁹⁴ It has the same binding sequence of somatostatin consisting of Thr-Lys-Trp-Phe as well as a binding position for ethylenediaminetetraacetic acid (EDTA) related chelators. The following chelators are bigger than EDTA but consist of the same features of tertiary amines and carboxylates. Diethylenetriaminepentaacetic acid (DTPA, structure shown in Figure 1.6) and 1,4,7,10-tetraazacyclododecane-1,4,7,10-tetraacetic acid (DOTA) and others are currently used in combination with octreotide and form complexes with the coordination numbers 6 and 8 respectively.^{195, 196} Radioactive isotopes like ⁶⁸Ga, ⁹⁰Y and ¹¹¹In have been chelated with these ligands and used in SPECT and PET.¹⁹⁷⁻²⁰⁰

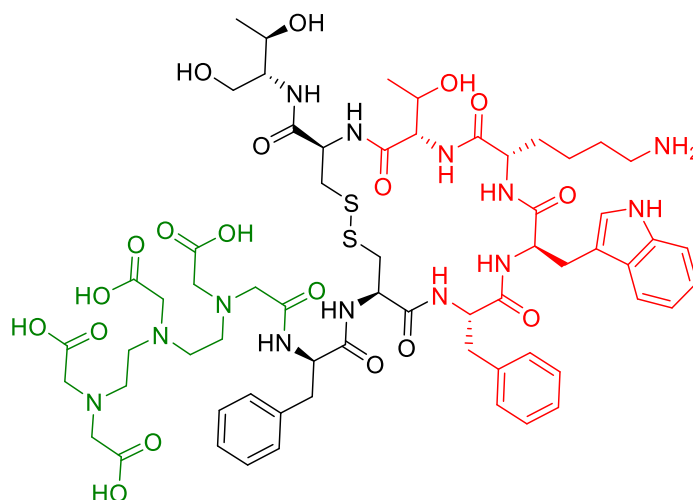


Figure 1.6 Molecular structure of Octreotide with conjugated DTPA (green). The binding site is coloured in red.¹⁹⁴

The combination of a highly bioselective binding site from a peptide and the chelating agents in combination with radioactive isotopes forms a high potential for

sensitive imaging tools like PET and SPECT as well as therapy depending on the isotope.

In Chart 1.4 the molecular structures of SOM-230 (Chart 1.4 A) and DOTA-TOC (Chart 1.4 B), the functional ligand of the ^{177}Lu drug Lutathera, are presented. SOM-230 is an advancement regarding the selectivity of octreotide, it's affinity to SSTR1 and SSTR5 is 30-40 times higher and the terminal elimination half life time which is around 10 times higher than octreotide.²⁰¹ Those remarkable features have been investigated intensively over the last years and led to various clinical trials showing a great potential as future radiopharmaceutical.²⁰²⁻²⁰⁶ DOTA-TOC on the other hand is more closely related to octreotide since it has only a tyrosine instead of phenyl alanine in position 3. Also it includes DOTA as chelating agent which fits perfectly for bigger cations like Ga(III), Y(III), In(III), or in case of Lutathera Lu(III).²⁰⁷⁻²¹² Lutathera is the first certified pharmaceutical for peptide receptor radionuclide therapy (PRRT).²¹³

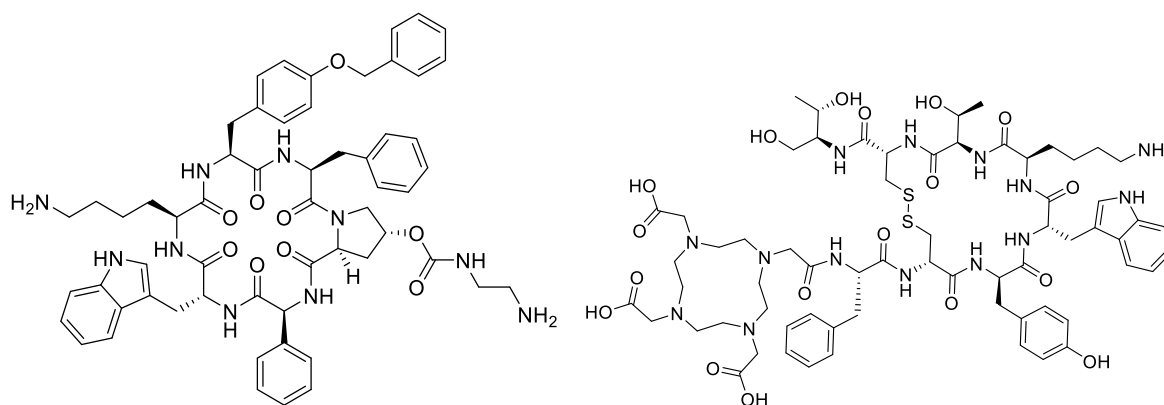
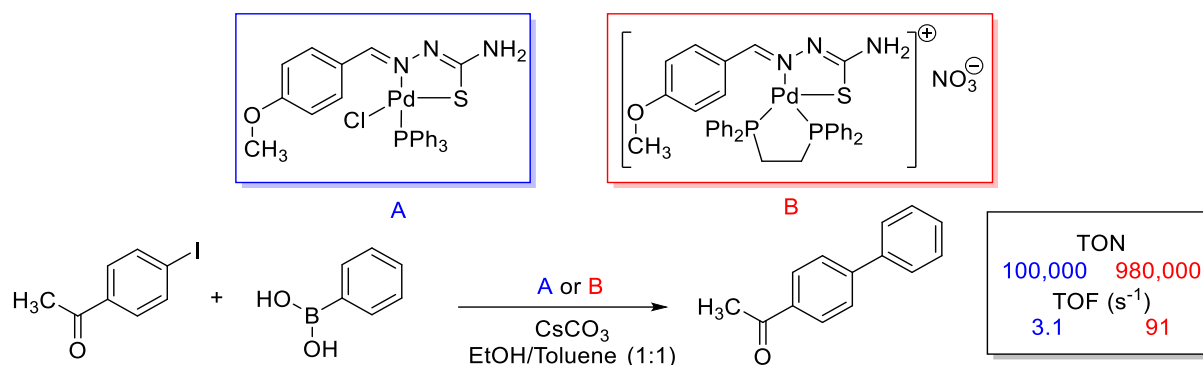


Chart 1.4 Molecular structures of octreotide derived structures SOM-230 (left) and DOTA-TOC (right).

1.7. Thiosemicarbazones in catalysis

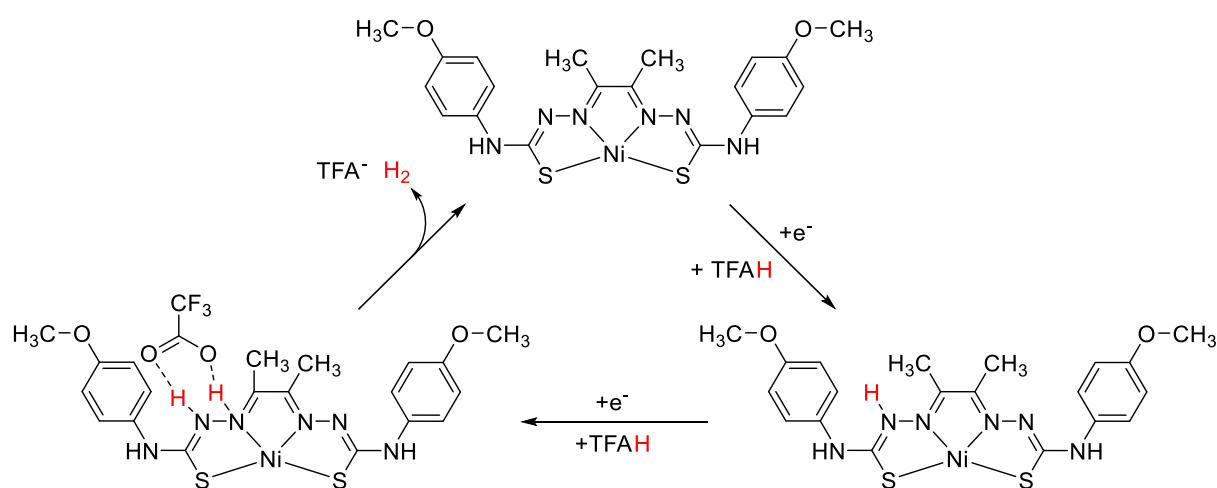
The complexes of TSC related compounds have been tested in several reactions as catalysts in reductions,^{40, 214-216} oxidations,^{84, 217-220} cross coupling reactions²²¹⁻²²⁴ and many more.^{20, 96, 215, 225-230}

The research group of *Bhattacharya* has reported several neutral and cationic palladium thiosemicarbazone complexes with phosphine coligands. These are capable of catalysing C–C coupling reactions under *Suzuki-Miyaura*, *Heck* and *Sonogashira* conditions with good to excellent turn over numbers (TON) and turn over frequencies (TOF). The almost 60-fold increased TOF of the *Suzuki* reaction in the last ten years is a very good example of his effort in designing new thiosemicarbazone based structures for catalysis. A comparison of two catalysts is illustrated in Scheme 1.11.^{231, 232}



Scheme 1.11 Suzuki reaction catalysed by palladium thiosemicarbazone complexes.^{231, 232}

A very different type of reaction was investigated by *Vincent Artero* and *Maylis Orio* and is shown in Scheme 1.12. They investigated the electrochemical hydrogen evolution of Ni(II) and Co(II) complexes bearing a tetradentate bithiosemicarbazone. Both complexes show extensive catalytic hydrogen evolution with maximum turn over frequencies of 3080 s⁻¹ and 1170 s⁻¹, respectively. These reactions show the ability of the thiosemicarbazone backbone to take part in a catalytic cycle by stabilizing the radical intermediate species.^{233, 234} By switching the electro catalytical system to a photoredox system, the *Orio* et al. also investigated other reduction methods. Using [Ir(ppy)₂(bpy)]PF₆ or [Ru(bpy)₃]Cl₂ as photosensitizers they were able to get decent activity in a photoinduced hydrogen evolution reaction.²³⁵ The mechanism was recently analysed by DFT calculations and is considered to be a mechanism involving 2 protons and 2 electrons as shown in Scheme 1.12.²³⁶



Scheme 1.12 Electrochemical hydrogen evolution reaction catalysed by a nickel bithiosemicarbazone, Proposed mechanism.²³⁶

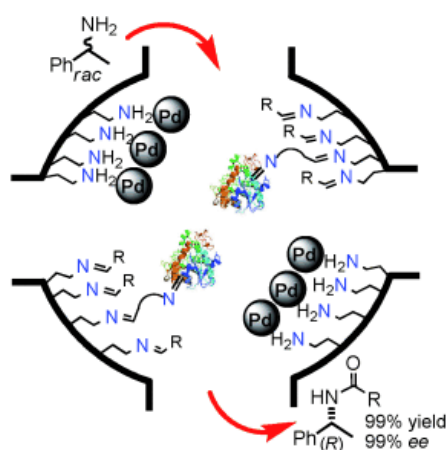
1.8. Complex-peptide conjugates in catalysis

The rise of artificial metalloenzymes have been awarded with the Nobel prize in chemistry in 2018 to *George P. Smith*, *Gregory P. Winter* and *Frances H. Arnold*.^{237, 238} *Arnold* has been awarded with the prize for her contribution to the artificial evolution

of enzymes. Their work was only able to be performed due to the technological evolution of computers and calculating models.^{239, 240}

However, over time the structural information of peptides has grown, and by utilizing polymerase chain reaction (PCR) they got designable.^{241, 242} By this method a wild type peptide can be structurally changed to perform better in the initial enzymatic reaction or even form bonds which are not in the nature of biological systems like C–Si.^{243, 244}

In recent years, the research group of *Jan-Erling Bäckvall* started to build nanoscale reaction vessels consisting of mesoporous silica in which peptides and palladium nanoparticles are bound (Scheme 1.13). Using nanoparticles of palladium under 2 nm in diameter allows the racemization of primary amines which then can be used by *Candida Antarctica* lipase B in proximity of an ester to generate pure enantiomers of the corresponding amide.²⁴⁵



Scheme 1.13 Artificial metalloenzyme by *Bäckvall* et al. used for the racemisation and amidation of racemic mixtures of primary amines.²⁴⁵

Thomas Ward and his group started to extend the scope of known catalysts to gain a peptide controlled second coordination sphere.²⁴⁶ His research group used common catalysts like ruthenium-based *Grubbs* catalysts or iridium metallocenes and added a biotin moiety to the backbone of the ligand, an example is shown in Figure 1.7.^{247, 248} Biotin itself is known for its strong bond to streptavidin. Streptavidin is a protein which is produced by *Streptomyces avidinii* and consists of four subunits.²⁴⁹ Each of the subunits has a very high molar affinity to biotin of around $K_a = 10^{14}$ – 10^{15} M^{-1} .^{250, 251} This protein can be tuned in artificial evolution to change the substrate scope of the catalyst.²⁵² For example, wildtype streptavidin can perform a reaction for one enantiomer whereas the change of a single amino acid in the second coordination sphere of the catalyst may result in the same reaction being yielding only the other enantiomer.²⁵³

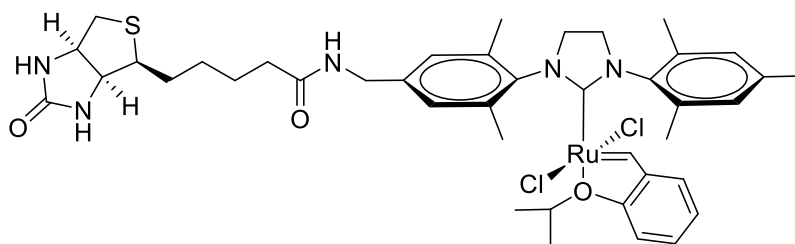


Figure 1.7 Structure of a biotinylated Grubbs catalyst which performs metathesis reactions on cell surfaces.²⁴⁷

These two examples show the potential of artificial metalloenzymes and the possibilities which are hiding in a biologically assisted catalysis. The improvement of these methods is depending on the ability to change the structure and functionality of the protein. Smaller proteins can be selectively synthesized, whereas bigger proteins need to be derivatised by a process called artificial or selective evolution. This method helps to generate a big variety of mutant forms of which the better performing types are selected for further mutations.²⁵⁴⁻²⁵⁶

In combination with the previously described methods, thiosemicarbazones should be able to carry a catalytically active metal ion in its binding pocket while still being able to bear the ability to be linked to biotin derived structures. These structures would implement the plethora of catalytical applications of thiosemicarbazone complexes with the substrate selectivity of artificial metalloenzymes.

1.9. Application in fluorescence microscopy

The absorption of a photon with an energy matching the HOMO-LUMO gap of a molecule, an electron can be excited from the S_0 ground state to an excited singlet state (S_1, S_2, \dots). Typically, the excitation is to a higher vibronic state of the S_x excited states, which differ by a few kcal/mol (Figure 1.8 green arrows). By vibrational relaxation (VR) these higher states relax to the ground state. Internal conversion (IC) results in the transformation of a S_{x+1} to a vibronic S_x state, keeping the multiplicity. From the S_1 ground state the molecule can emit energy in form of a photon to relax into the S_0 state. This process is called fluorescence (Figure 1.8 blue arrows). According to *Kasha's rule*, a photon emission only occurs from the lowest excited state of a given multiplicity ($S_{x>0}$) into the electronic ground state (S_0).^{257, 258} Since the initial absorbed energy is dissipated by IC the emission energies are lower than the excitation energies leading to a higher wavelength of the emitted light (*Stokes shift*).^{259, 260}

Furthermore, a process like IC is intersystem crossing (ISC). Herein, the relaxation of an excited singlet state occurs with an additional spin change to a triplet state (T_x).²⁶¹ The multiplicity change is regarded as a spin forbidden process, yet spin-orbit

coupling leads to an overlap of the singlet and triplet wavefunctions.²⁶² A radiative relaxation from the triplet to the singlet state is called phosphorescence (Figure 1.8 red arrows).

Due to the spin forbidden processes the ISC as well as the phosphorescence are slower processes in comparison to the processes without change of the multiplicity (IC and fluorescence).²⁶²

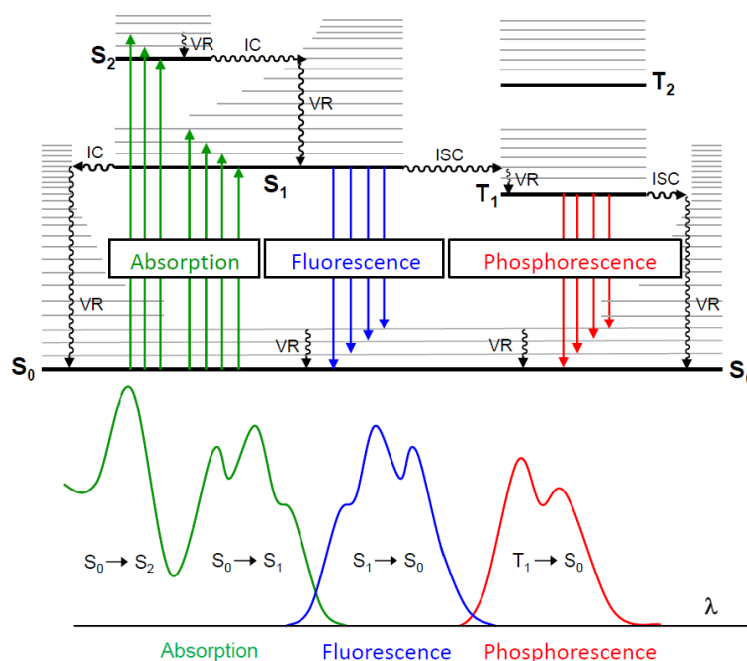


Figure 1.8 Jablonski-diagram depicting photophysical transitions, (IC = internal conversion, ISC = Intersystem crossing, VR = vibrational relaxation). Reproduced from literature.²⁶³

Besides artificial evolution and the impact of that on modern biochemical understandings a further Nobel prize was awarded, that impacted the research dramatically. In 2014 *Eric Betzig, William Moerner and Stefan Hell* received the Nobel prize for fluorescence microscopy.²⁶⁴ By implementing fluorescent probes into cellular tissue they were able to highlight several parts of the cell which were beyond the diffraction resolution of typical light microscopes.²⁶⁵⁻²⁶⁷ Typical examples for these probes are the green fluorescent protein (GFP)^{268, 269} and acridine orange (Figure 1.9).²⁷⁰⁻²⁷²

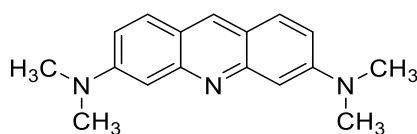


Figure 1.9 Molecular structure of acridine orange. N₃,N₃,N₆,N₆-tetramethyl acridine 3,6-diamine.

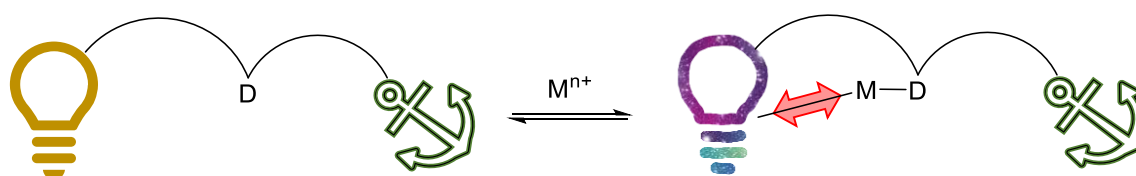
The GFP are a group of proteins are a group of proteins known since 1962 for their name giving green fluorescence.²⁷³ GFP derived structures are used in

biotechnological approaches for example in the localization of diacylglycerol²⁷⁴ or protein solubility.²⁷⁵ With a two photon excitation approach resolutions of around 54 nm could be achieved.²⁷⁶

On the other hand, the acridine derivative acridine orange is a more responsive luminophore. It is typically used in the detection of RNA and DNA and via intercalation it emits photons of different energies, with a 526 nm emission (green) for DNA and 650 nm emission (red) for RNA.^{277, 278} Also, the nitrogen donor of the acridine body can interact with various acceptors like solvents and metal ions and by that influence the luminescence.²⁷⁹

Additionally, some acridine derivatives showed a cation specific fluorescence.²⁸⁰⁻²⁸² This is possible because acridine has a nitrogen donor atom. When it coordinates to an atom, it influences the electronic structure of the fluorophore thus creating different ligand based fluorescent colours.

Combining acridine with an anchoring moiety, a system that can change its fluorescence properties at the surface of cells regarding the surrounding metal ions is possible. Additionally, it can be used to get a better understanding of the stability of the metal ions on the cell surface as a function of the fluorescence deviation. The idea can be illustrated as done in Scheme 1.14. The anchoring function may be introduced by a corresponding thiosemicarbazide, in this case the acridine needs to bear a carbonyl moiety.



Scheme 1.14 Representation of a cation specific fluorescence system attached to an anchoring system.

1.10. Aim of the thesis

This thesis is aimed to explore the various substitution patterns of the thiosemicarbazone molecules for several purposes:

- Introduction of further coordinating sites at the imine position $M1$ through suitable carbonyl compounds: The extension from bidentate $N^{\wedge}S$, to tridentate $C^{\wedge}N^{\wedge}S$, $O^{\wedge}N^{\wedge}S$, or $N^{\wedge}N^{\wedge}S$, or tetradentate $O^{\wedge}N^{\wedge}N^{\wedge}S$ (Figure 1.10).

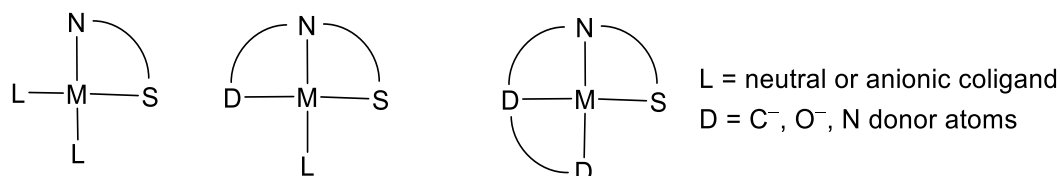


Figure 1.10 Structural motifs of thiosemicarbazone donors for complexes with the coordination number 4.

- Introduction of an amino acid residue at $N4$ to allow bioconjugation (Figure 1.11).

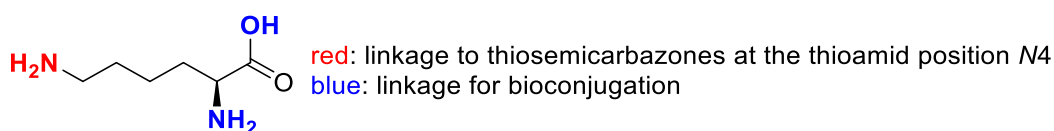


Figure 1.11 L-lysine as building block for bioconjugated thiosemicarbazones.

- Introduction of chromophores into the TSC scaffold as luminescent probes or photon-harvesting (Figure 1.12).

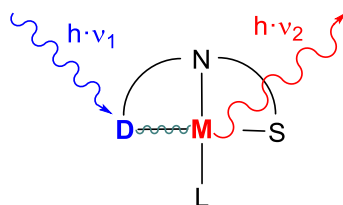


Figure 1.12 Schematic representation of photon-harvesting by a donor system (D). The absorbed energy is transferred to the metal centre (green) to the metal centre (M) which may emit light of another wavelength or undergo photo redox catalysis.

- Introduction of interesting metals such as Ni, Cu, Pd, Re, or Pt for nuclear-medical purposes. (Figure 1.13)

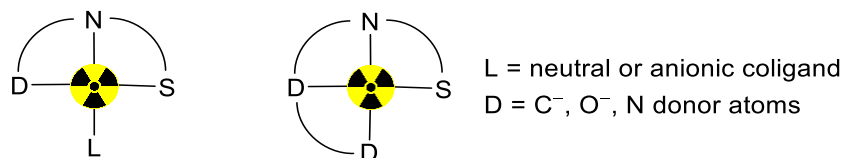
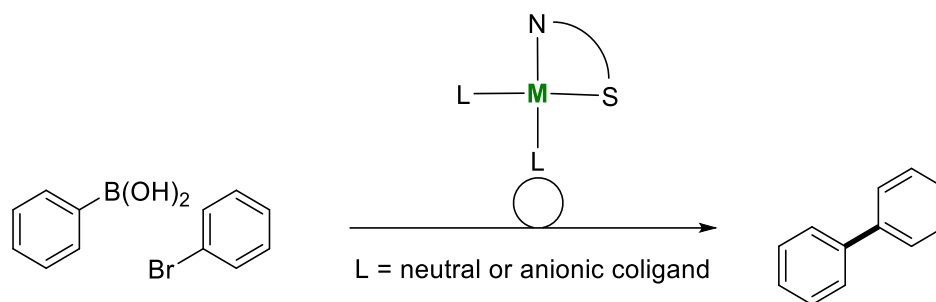


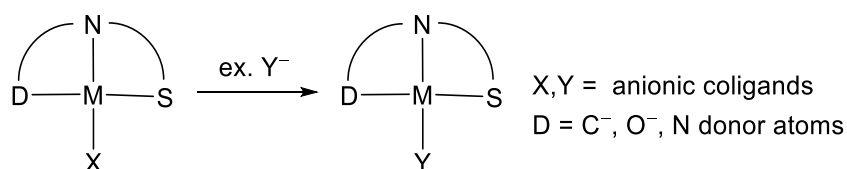
Figure 1.13 Possible binding motifs of radioactive nuclei in thiosemicarbazones.

- Introduction of catalytically interesting metals such as Cu, Pd, or Ir. (Scheme 1.15)



Scheme 1.15 Possible *Suzuki* catalysis employing a bidentate thiosemicarbazone as catalyst.

- Ligand exchange reactions and their influence on the complexes. (Scheme 1.16)



Scheme 1.16 Schematic representation of a coligand exchange by excess of a new anion.

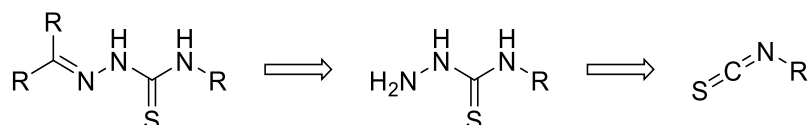
- Combinations thereof.

The new ligands and complexes were synthesized and analysed using CHNS combustion analysis together with nuclear magnetic resonance (NMR) spectroscopy, electron ionization mass spectroscopy (EI-MS) or high-resolution electron spray mass spectroscopy (HR-ESI-MS) and infrared spectroscopy (IR). Single crystal X-ray diffraction (SC-XRD) will allow to study the molecular and crystal structures. Further detailed characterization using electron paramagnetic resonance (EPR), ultraviolet and visible absorption spectroscopy (UV/Vis) and the investigation of the redox behaviour using cyclic voltammetry (CV) and combined methods like spectroelectrochemical UV/Vis (SEC-UV/Vis) and spectroelectrochemical EPR (SEC-EPR) will help to explore the electronic states of the molecules. DFT calculations, photoelectronic spectroscopy (PES), high pressure liquid chromatography (HPLC) on selected samples will complete the studies.

2. Results and discussion

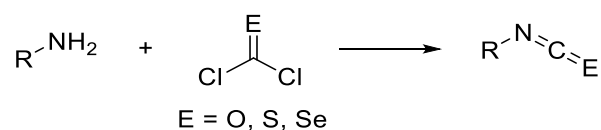
2.1. Synthesis of thiosemicarbazones

Thiosemicarbazones are synthesized by the condensation reaction of a thiosemicarbazide and a carbonyl group. The thiosemicarbazide itself is synthesized by the electrophilic addition of a hydrazine to an isothiocyanate. The retrosynthetic approach is shown in Scheme 2.1.



Scheme 2.1 Retrosynthetic approach for the synthesis of thiosemicarbazones.

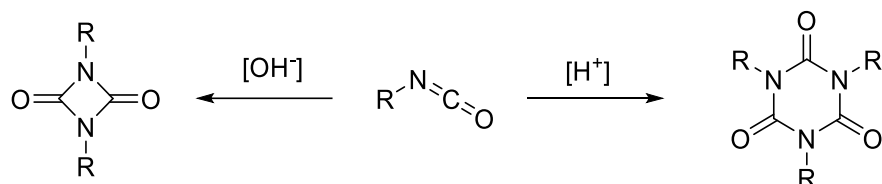
The isothiocyanates can be generated by either addition of thiophosgene to a primary amine or by the reaction between tosyl chloride and a dithioate. Here, semicarbazones can be generated, the oxygen derivatives of thiosemicarbazones. Selenocyanates and their selenosemicarbazones can be derived from this route as well as shown in Scheme 2.2.



Scheme 2.2 Addition of phosgenes to primary amines to generate isochalcogenocyanates.

The big difference between these structures is their stability. Isothiocyanates are drastically more stable and less reactive than isocyanates. This is given by the fact that isocyanates tend to form dimeric urethdiones under basic conditions or trimeric 1,3,5-triazine-2,4,6-triones under acidic conditions, shown in Scheme 2.3. The corresponding oligomerization reactions for the heavier analogues are not known. The selenocompounds on the other hand decompose by giving of elemental selenium.²⁸³⁻

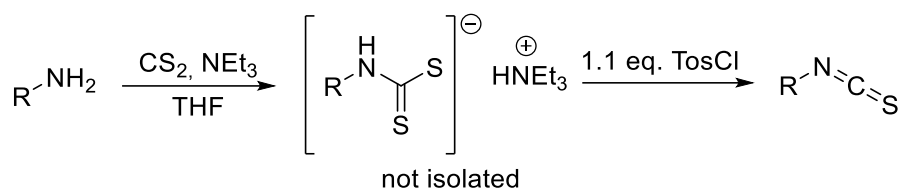
285



Scheme 2.3 Typical oligomerization reactions of isocyanates under basic and acidic conditions.

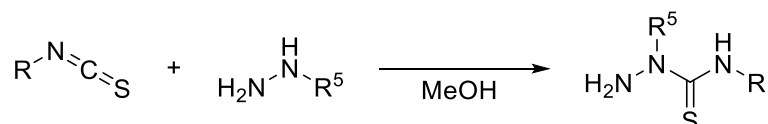
The synthesis of isothiocyanates with tosyl chloride starts with the addition of carbon disulphide to a primary amine yielding the corresponding dithiocarbamate triethylammonium salt. This salt reacts with tosyl chloride to the isothiocyanate. The reaction mechanism is supposed to be a reagent-promoted decomposition resulting

in the formation of hydrogen sulphide as byproduct.⁵⁷ In Scheme 2.4 the reaction is illustrated.



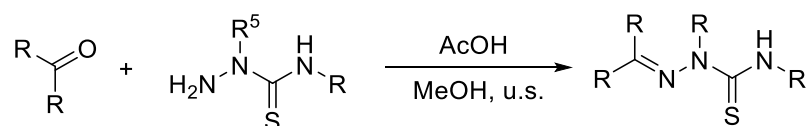
Scheme 2.4 Synthesis of isothiocyanates by reagent-mediated decomposition of an *in situ* formed dithiocarbamate.

The addition of amines to isothiocyanates leads to the formation of thioureas and thiosemicarbazides can be synthesized by treating isothiocyanates with hydrazine (Scheme 2.5).⁵³ Since the nature of the hydrazine addition is a nucleophilic attack of the hydrazine on the carbon of the isothiocyanate, the use of methyl hydrazine leads to the formation of *N*2 substituted thiosemicarbazides. By using hydrazine derivatives like methylhydrazine, the corresponding *N*2 substituted substance is obtained. This reaction is regioselective yielding predominantly the *N*2 substituted derivative.⁶²



Scheme 2.5 Nucleophilic addition of a hydrazine to isothiocyanates yielding thiosemicarbazides.

The condensation reaction with carbonyls has been investigated by *Carradori et al.* The group investigated the different synthetic methods to perform the condensation reaction, showing that microwave assisted synthesis gave the highest yields and a reflux reaction was the lowest yielding variant.⁶⁴ They also reported the ultrasonic assisted synthesis to yield the thiosemicarbazones (Scheme 2.6) having high yields in a short reaction time as well as the possibility to use bigger vessels than microwave assisted synthesis.



Scheme 2.6 Glacial acetic acid catalysed condensation reaction between a carbonyl and a thiosemicarbazide yielding thiosemicarbazones.

2.1.1. NMR spectroscopy of thiosemicarbazones

When synthesizing the methyl benzyl derivatives, ¹H NMR spectroscopy was a useful tool, especially for the detection of hydrazides and the proton at the chiral carbon. Shown in Figure 2.1, starting at the isothiocyanate, the proton signal splits into a quartet at 5.22 ppm. The region is otherwise empty which allows a good

indication of the reaction with hydrazine in which the proton signal shifts to 5.55 ppm and splits into a quintet due to the NH proton to which it couples. Additionally, the hydrazine -NH₂ moiety is detectable as a broad singlet at 4.55 ppm. By condensation with dipyridyl ketone, the signal at 4.55 ppm vanishes and the quintet is also ever so slightly affected by the reaction and shifts to 5.75 ppm. Even when coordinating metal ions this is very handy since it shifts drastically to 4.65 ppm when the protoligand reacts with tetrachloroplatinate and in ¹H, ¹H COSY NMR spectroscopy it helps identifying the methyl group of the sidechain as well as the secondary amine.

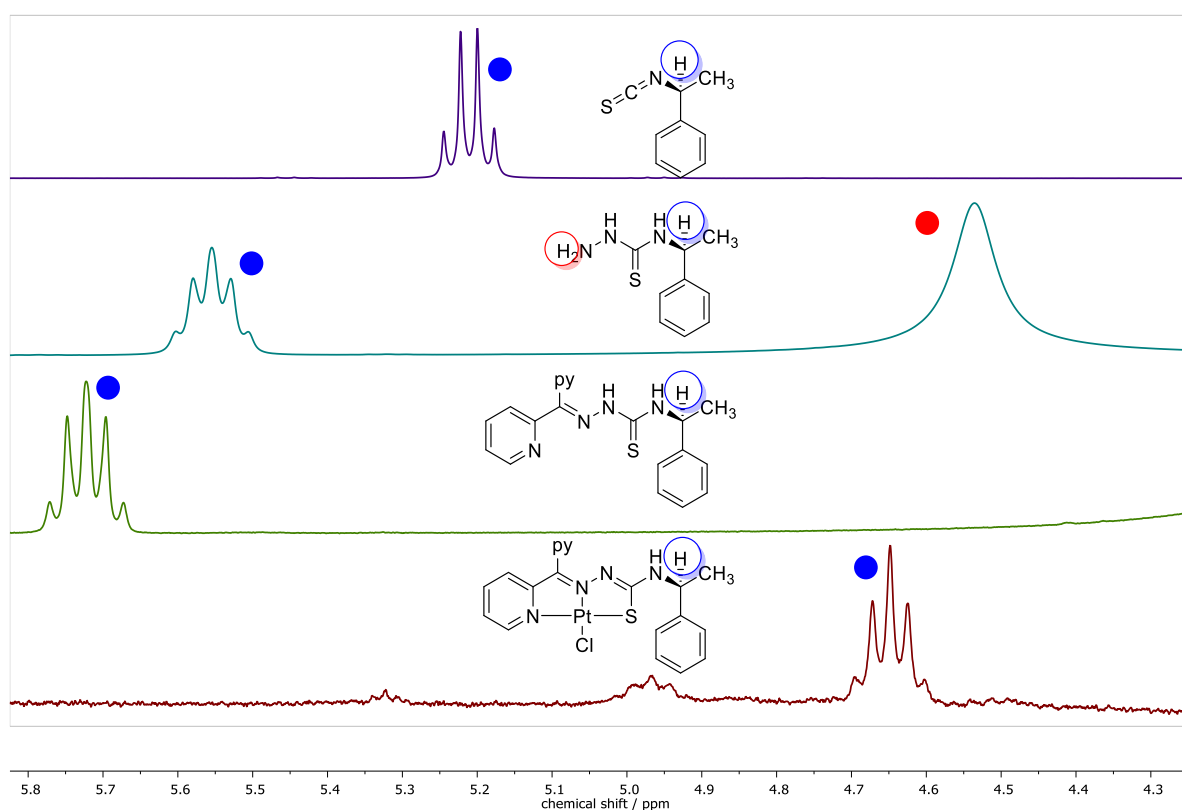


Figure 2.1 Excerpts of the ¹H NMR spectra of ITCmB, TSCmB, HdpyTSCmB and [Pt(dpyTSCmB)Cl]. All measured in DMSO-*d*₆ at 300 MHz.

During this thesis, 7 new thiosemicarbazides and 6 new carbonyls were synthesized. Furthermore 48 thiosemicarbazones resulted from the syntheses procedures mentioned above. The following figures shows the synthesized precursors and ligands. The precursors are divided into the synthesized thiosemicarbazides (Chart 2.1) and carbonyls (Chart 2.2). The Thiosemicarbazones are divided based on their donor system. In Chart 2.3 depicts O^N^S, Chart 2.4 C^N^S, Chart 2.5 N^N^S, Chart 2.6 O^N^N^S and Chart 2.7 S^N^N^N^S systems. Chart 2.8 shows the structures derived from pentafluorobenzaldehyde; the yields are given for the condensation reaction as well as the total synthesis yield. Further details on yields and reaction conditions are given in the Experimental Section.

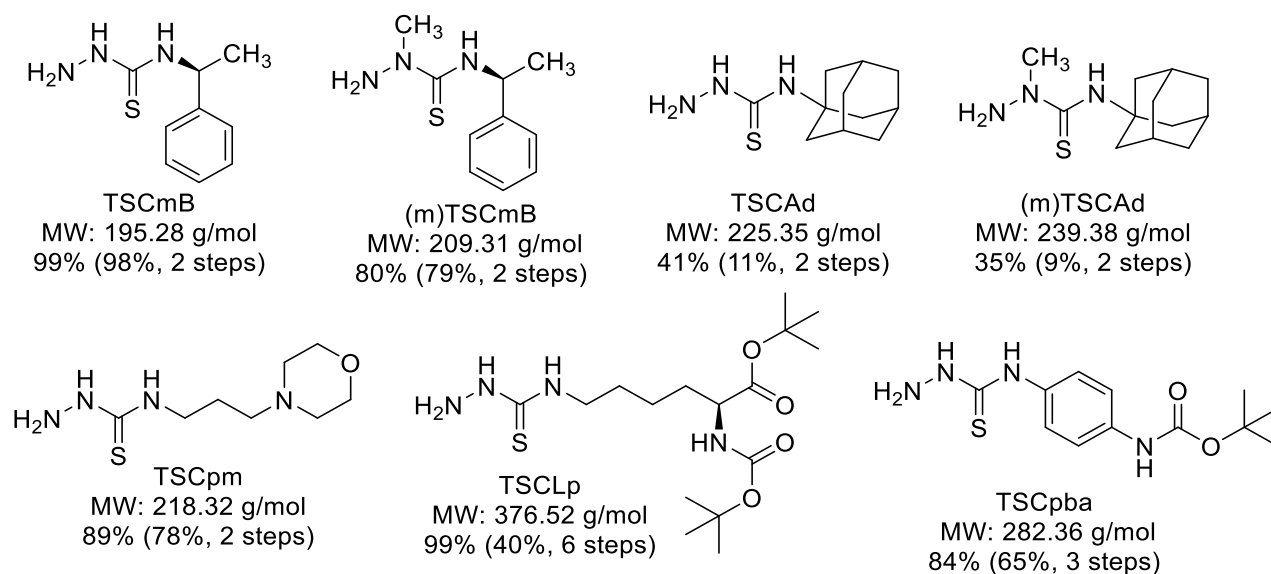


Chart 2.1 Molecular structures of synthesized thiosemicarbazides, abbreviations, and synthesis yields.

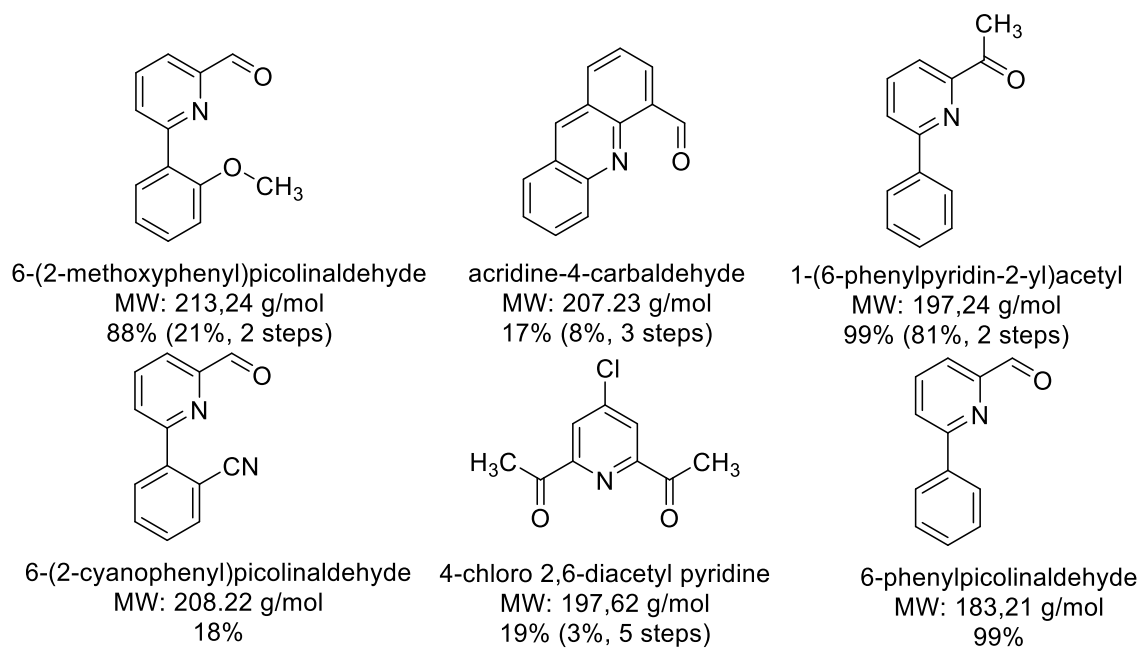


Chart 2.2 Molecular structures of synthesized carbonyls, abbreviations, and synthesis yields.

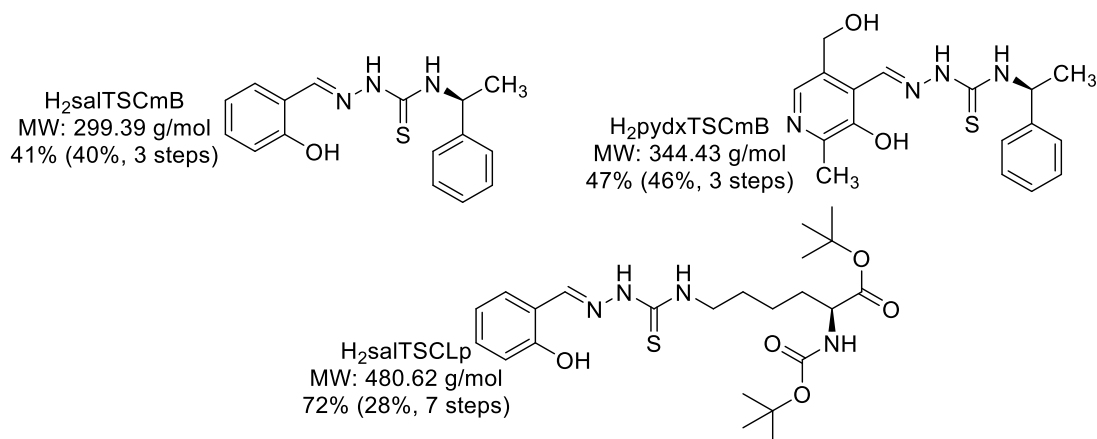


Chart 2.3 Molecular structures of synthesized salicylic derived thiosemicarbazones as tridentate dianionic $\text{O}^-\text{N}^-\text{S}$ donors, abbreviations, and synthesis yields.

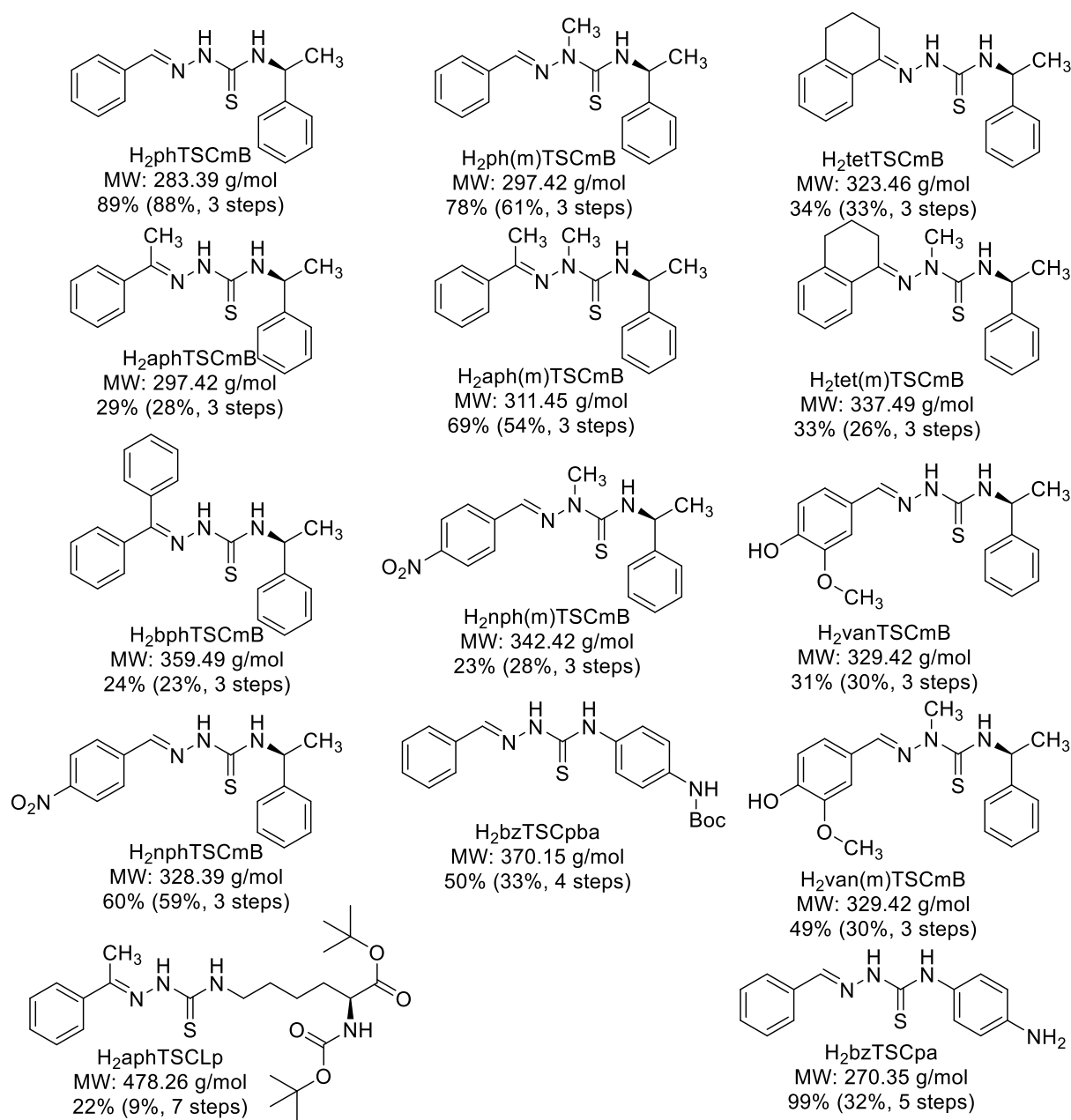


Chart 2.4 Molecular structures of synthesized benzyl derived thiosemicarbazones as bidentate monoanionic N^-S or tridentate dianionic $\text{C}^-\text{N}^-\text{S}$ donors, abbreviations, and synthesis yields.

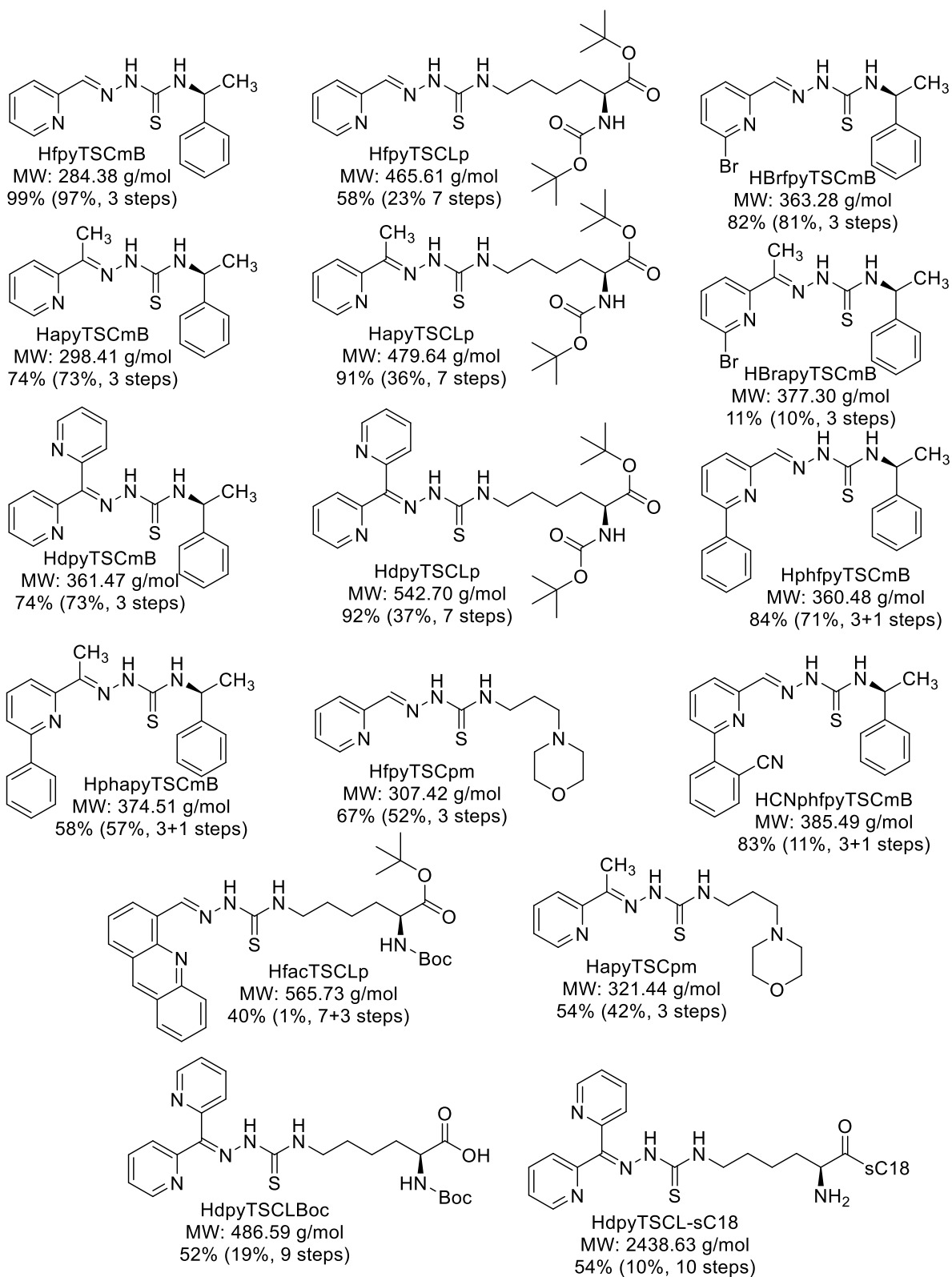


Chart 2.5 Molecular structures of synthesized pyridine derived thiosemicarbazones as tridentate monoanionic N⁻N⁻S donors, abbreviations, and synthesis yields.

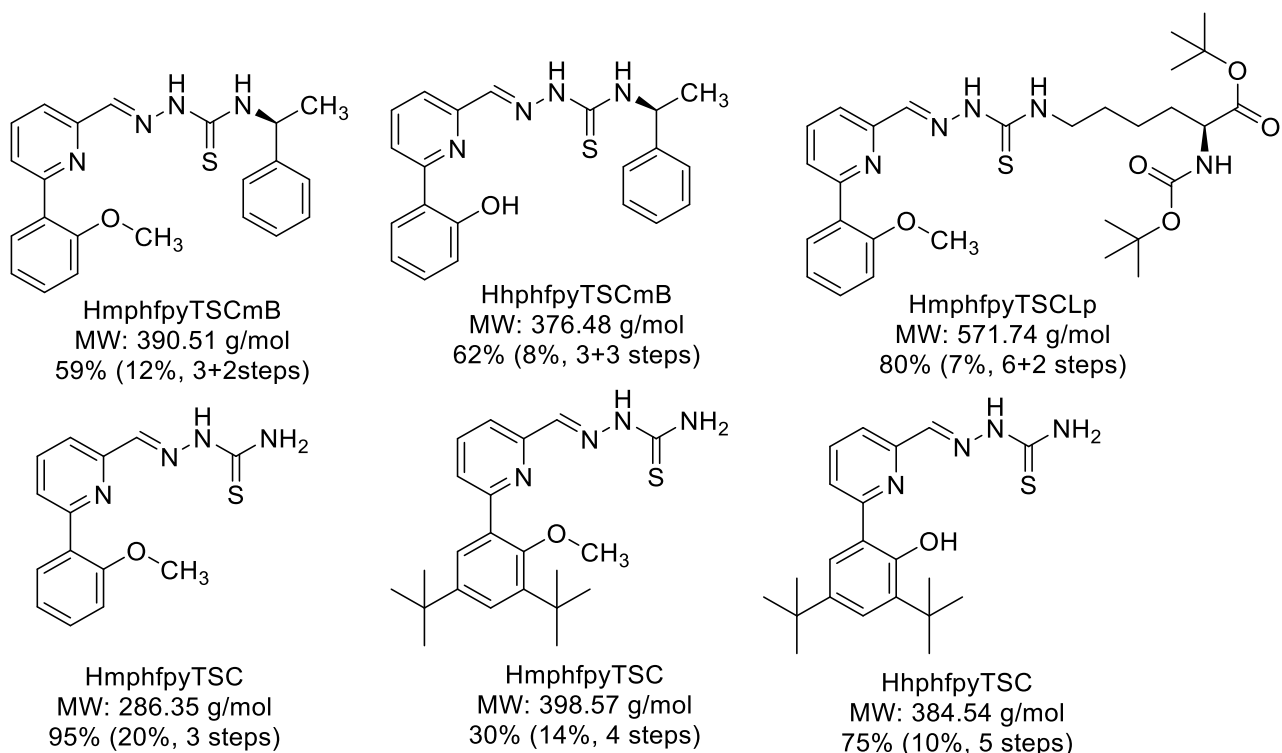


Chart 2.6 Molecular structures of synthesized 6-(2-phenol) pyridine derived thiosemicarbazones as tetradentate monoanionic or dianionic O⁻N⁻N⁻S donors, abbreviations, and synthesis yields.

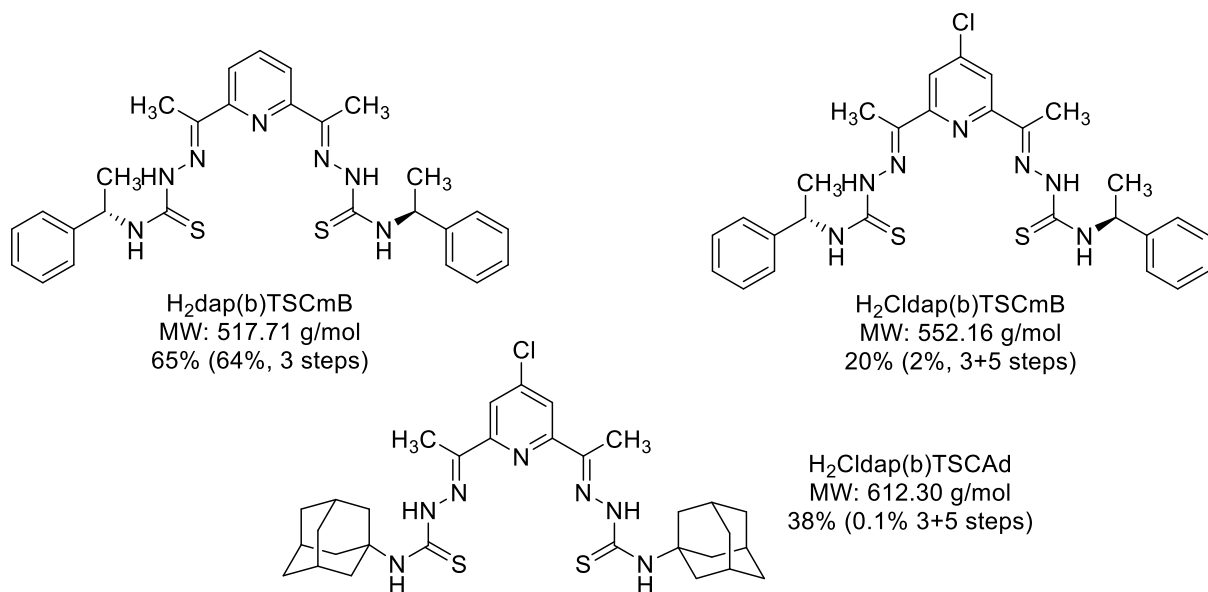


Chart 2.7 Molecular structures of synthesized diacetyl pyridine derived bis thiosemicarbazones as pentadentate dianionic S⁻N⁻N⁻N⁻S donors, abbreviations, and synthesis yields.

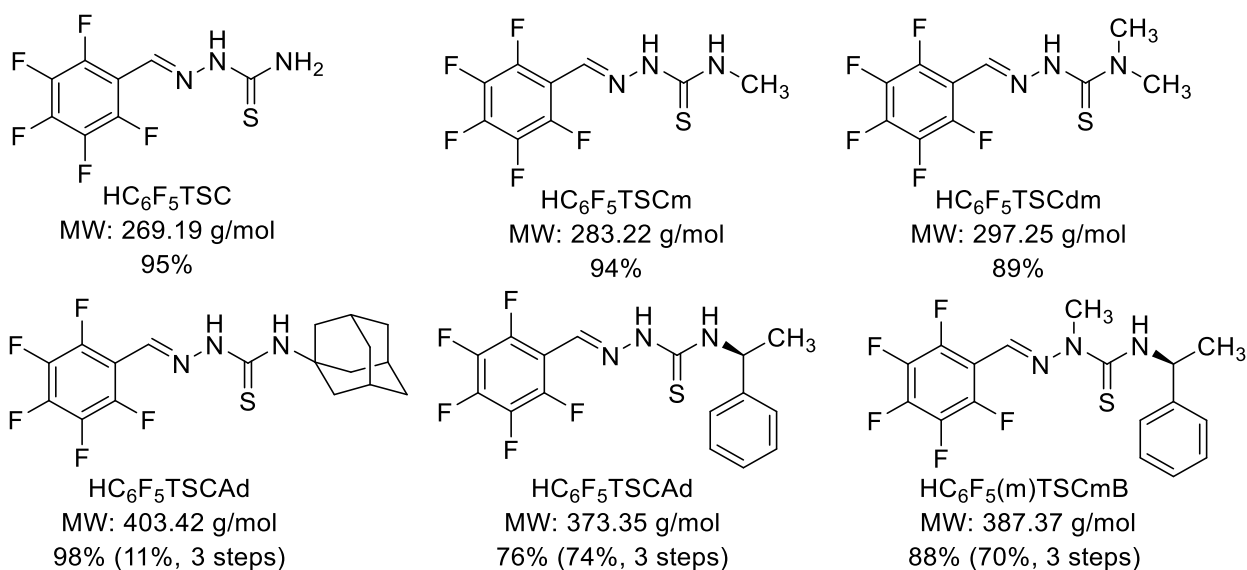


Chart 2.8 Molecular structures of synthesized thiosemicarbazones derived from pentafluorobenzaldehyde, abbreviations, and synthesis yields.

2.1.2.SC-XRD determination of the thiosemicarbazones

Twelve TSCs formed measurable crystals suitable for single crystal X-ray diffraction (SC-XRD).

When examining the pyridine derived structures, it is noticeable that the imine motif is an *E* isomer comparing the pyridine with the hydrazone motif. Since the bond at the *N4* amine to the methyl benzyl motif is a single bond, it is able to rotate and thus showing the only major difference in the organic structure.

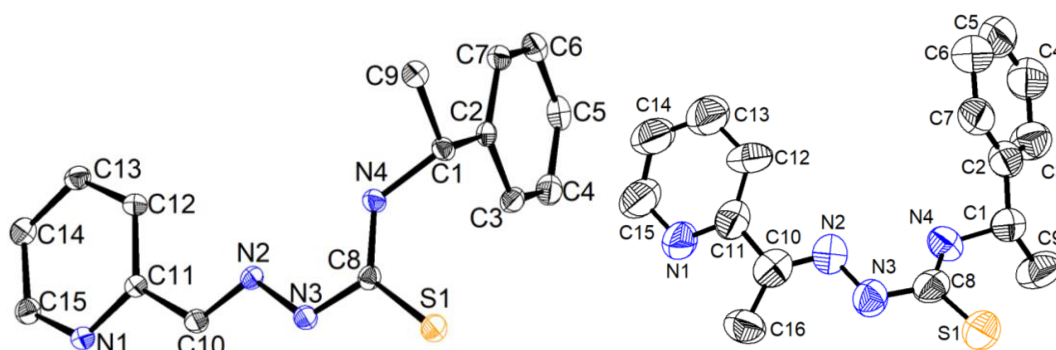


Figure 2.2 Molecular structures of HfpyTSCmB and HapyTSCmB. Atoms are shown with 50% probability. Hydrogen atoms are omitted for clarity.

The dipyridyl and diphenyl derivatives are very similar to their smaller analogues (Figure 2.3). Additionally, the solved crystal of HdpyTSCmB has a MeOH molecule co-crystallized. As for the formyl and acetyl pyridyl structures the chiral TSCmB ligands all crystallize in the orthorhombic space group $P2_12_12_1$, one of the *Sohnke* space groups, in which only chiral molecules can crystallize showing that only this enantiomer is formed. Also, all structures show

one axis in the cell being a lot longer than the others which explains their macroscopic needle like appearance.

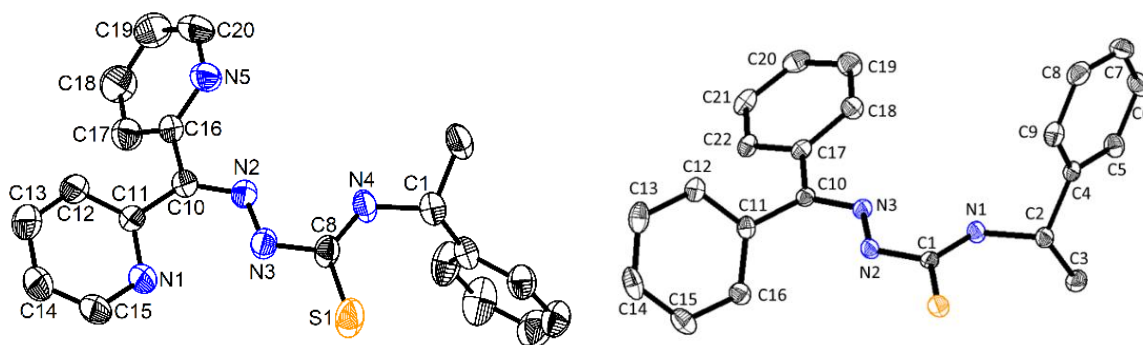


Figure 2.3 Molecular structure of HdpyTSCmB · MeOH and HbphTSCmB. Atoms are shown with 50% probability. Hydrogen atoms are omitted for clarity.

The 6-derivatized picolinaldehyde thiosemicarbazones HmphfpyTSC and H₂hphfpyTSCmB could also be crystallized (Figure 2.4). HmphfpyTSC showed a similar structure compared to the previously described molecules. The interaction between the pyridine ring and the hydrazone proton are comparable with HdpyTSCmB. Additional intermolecular interactions of the primary amine *N*4 and imine and thione groups of neighbouring molecules can be detected in the crystal structure. The methoxyphenyl ring exhibits a torsion angle of 40° towards the pyridine. Interestingly, the imine bond crystallized as *Z* tautomer, despite the previous formylpyridine structure exhibiting a *E* tautomerism. H₂hphfpyTSCmB on the other hand, has an almost coplanar hydroxyphenyl ring with a torsion angle of only 0.14°. This structural change may be due to correlations between the hydroxyl proton and the pyridine ring. In addition to this, the *N*4 position is also pointing towards the pyridine ring.

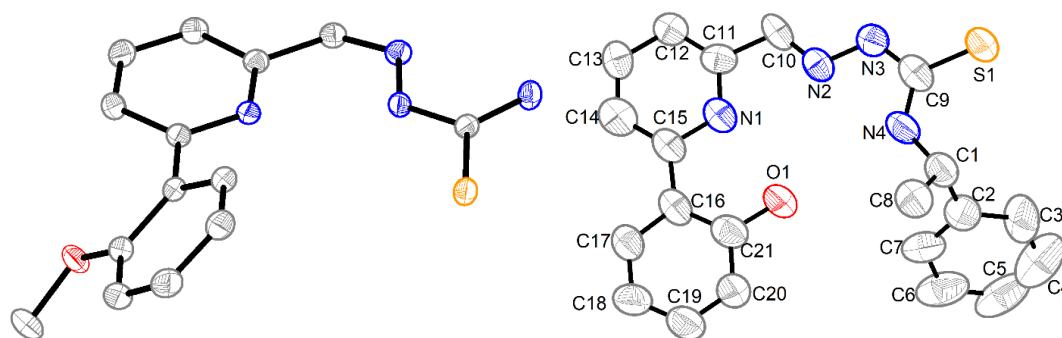


Figure 2.4 Molecular structure of HmphfpyTSC · ½ Et₂O (left) and H₂hphfpyTSCmB (right). Atoms are shown with 50% probability. Hydrogen atoms are omitted for clarity.

The pentafluorobenzaldehyde derived ligands HFbzTSC, HFbzTSCm and HFbzTSCdm all crystallized rapidly from their corresponding reaction mixture owed to the fact the reaction proceeds much faster with electron poor carbonyls as it is expectable for a condensation. They

crystallize in the $P\bar{1}$ space group and their structures are almost the same when leaving out the methyl substitution at *N4*. HFbzTSCAd crystallized in the monoclinic space group $P2_1/n$ and the chiral derivatives HFbzTSCmB and HFbz(m)TSCmB both crystallized in the monoclinic space group $P2_1$, which is a *Sohnke* group.

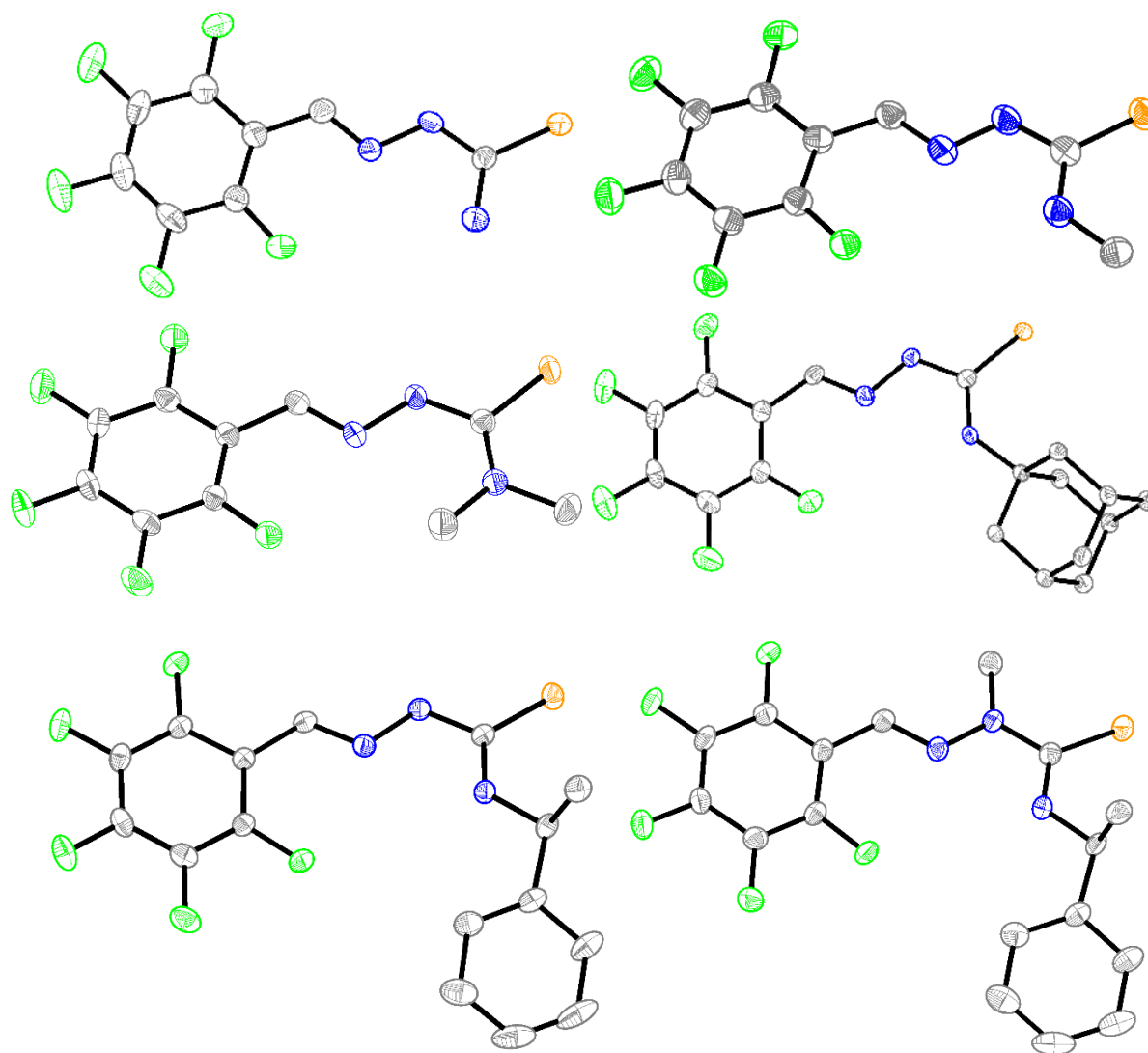


Figure 2.5 Molecular structures of HFbzTSC, HFbzTSCm, HFbzTSCdm, HFbzTSCAd, HFbzTSCmB, and HFbz(m)TSCmB. Atoms are shown with 50% probability. Hydrogen atoms are omitted for clarity.

When comparing the overall structure of the crystalline structures, a common similarity seems to be the interaction of a proton at *N4* with the imine *N1*. This yields a structure in which the carbon sulphur bond is turned away from the typical binding pocket. This leads also to the *Z* configuration of the *N4* substitution groups towards the thione.

Table 2.1 Crystallographic data for HfpyTSCmB, HmphfpyTSC, H₂hphfpyTSCmB, HapyTSCmB, HdpyTSCmB, HbphTSCmB, HFbzTSC, HFbzTSCm, HFbzTSCdm, HFbzTSCAd, HFbzTSCmB, HFbz(m)TSCmB, and HFbzTSCAd. ^acrystallized with ½ Et₂O. ^bcrystallized with MeOH.

Ligand	HfpyTSCmB	HmphfpyTSC ^a	H ₂ hphfpyTSCmB	HapyTSCmB	HdpyTSCmB ^b	HbphTSCmB	HFbzTSC	HFbzTSCm	HFbzTSCdm	HFbzTSCAd	HFbzTSCmB	HFbz(m)TSCmB
Empirical formula	C ₁₅ H ₁₄ N ₄ S	C ₁₆ H ₁₄ N ₄ O _{1.25} S	C ₂₂ H ₂₀ N ₄ OS	C ₁₆ H ₁₈ N ₄ S	C ₂₁ H ₁₇ N ₅ OS	C ₂₂ H ₂₀ N ₃ S	C ₈ H ₄ N ₃ F ₅ S	C ₉ H ₆ N ₃ F ₅ S	C ₁₀ H ₇ N ₃ F ₅ S	C ₁₈ H ₁₈ F ₅ N ₃ S	C ₁₆ H ₁₂ F ₅ N ₃ S	C ₁₇ H ₁₄ F ₅ N ₃ S
Formula weight	284.38	314.38	376.49	298.41	387.46	358.47	269.20	283.23	297.25	403.42	373-35	387.38
Temperature/K	293(2)	100 (1)	100(1)	293 (2)	293(2)	100(2)	150(1)	150(2)	150(2)	100(1)	100(1)	100(1)
Crystal System	orthogonal	monoclinic	monoclinic	monoclinic	orthogonal	orthogonal	triclinic	triclinic	triclinic	Monoclinic	Monoclinic	Monoclinic
Space group	<i>P</i> 2 ₁ 2 ₁ 2 ₁	<i>P</i> 2 ₁ / <i>n</i>	<i>P</i> 2 ₁	<i>P</i> 2 ₁	<i>P</i> 2 ₁ 2 ₁ 2 ₁	<i>P</i> 2 ₁ 2 ₁ 2 ₁	<i>P</i> $\bar{1}$	<i>P</i> $\bar{1}$	<i>P</i> $\bar{1}$	<i>P</i> 2 ₁ / <i>n</i>	<i>P</i> 2 ₁	<i>P</i> 2 ₁
Unit cell dimensions												
a / Å	9.994(2)	8.1645(2)	9.970(8)	8.7895(6)	7.7512(4)	9.9733(2)	5.9566(11)	6.0774(5)	7.8799(5)	6.4544(4)	8.8084(3)	8.0354(5)
b / Å	26.463(5)	16.6339(5)	7.3255(7)	7.9268(4)	13.4952(11)	10.3024(2)	6.4362(11)	7.8697(6)	8.5657(5)	11.0220(8)	6.0050(2)	5.9755(3)
c / Å	5.3980(11)	23.1166(7)	26.683(3)	23.0863(19)	19.6265(11)	18.4119(4)	13.043(2)	11.6226(10)	9.3890(6)	24.3140(17)	15.0956(6)	17.6790(11)
α / °	90	90	90	90	90	90	86.552(6)	99.071(7)	85.627(4)	90	90	90
β / °	90	99.6940(10)	91.814(6)	95.750(6)	90	90	88.830(6)	103.804(6)	67.820(4)	95.126(3)	93.200(2)	97.368(4)
γ / °	90	90	90	90	90	90	79.256(5)	91.774(7)	78.128(4)	90	90	90
Volume / Å³	1427.6(5)	3094.58(15)	1947.8(16)	1600.39(19)	2053.0(2)	1891.80(7)	490.35(15)	531.71(8)	574.28(6)	1722.8(2)	797.23(5)	841.86(9)
Z	16	8	4	8	4	4	2	2	2	4	2	2
Calc. Density	2.316	1.3495	1.2837	1.2384	1.254	1.259	1.8231	1.7689	1.7189	1.5553	1,5552	1.5281
F (000)	944	1318.4	795.5	632.7	808	756.0	268.5	284.5	300.5	833.0	382.2	398.2
Measured Reflexes	16989	90052	57157	36405	37979	25974	9448	6166	10614	36449	25397	26231
unique Reflexes	3961	6081	7558	6509	4394	3720	2294	2797	2031	3381	3067	3226
R_{int}	0.0390	0.0617	0.2721	0.2299	0.0910	0.0679	0.1260	0.0532	0.0427	0.0262	0.0448	0.0788
R1/wR2 [I_o>2σ(I_o)]	0.0406 / 0.1124	0.0417 / 0.1212	0.1057 / 0.2420	0.0726 / 0.1659	0.0676 / 0.1614	0.0247 / 0.0656	0.0745 / 0.1433	0.0434 / 0.1070	0.0314 / 0.0760	0.0452 / 0.1254	0.0205 / 0.0524	0.0336 / 0.0792
R1/wR2 [all data]	0.0447 / 0.1173	0.0464 / 0.1260	0.1889 / 0.3196	0.2229 / 0.2388	0.0926 / 0.1729	0.0268 / 0.0660	0.01492 / 0.1739	0.0597 / 0.1246	0.0414 / 0.0808	0.0491 / 0.1283	0.0216 / 0.0525	0.0361 / 0.0802
GOOF²	0.741	1.046	1.131	0.803	1.102	1.105	1.053	1.052	1.067	1.083	1.082	1.046
Largest peak/hole /e Å⁻³	0.337 / -0.478	0.49 / -0.82	1.02 / -0.57	0.57 / -0.63	0.360 / -0.192	0.18 / -0.25	0.88 / -0.82	0.36 / -0.45	0.25 / -0.23	0.43 / -0.43	0.18 / -0.17	0.39 / -0.27

The bond lengths of the C=N-NH-(C=S) backbone remain very similar, as they are listed in Table 2.2. The imine bond length stays at around 1.28 Å and is the shortest of all these. The hydrazone stays at around 1.37 Å which is ranging among other nitrogen-nitrogen single bonds. And the >C=S system stays at 1.68 Å which resembles carbon sulphur double bonds indicating all structures to crystallize in their thione form.

Table 2.2 Bond lengths of the >C=N-N-C(S)- backbone in HfpyTSCmB, HapyTSCmB, HdpyTSCmB, HbphTSCmB, HFbzTSC, HFbzTSCm, HFbzTSCdm, HmphfpyTSC, H₂hphfpyTSCmB, HFbzTSCAd, HFbzTSCmB, and HFbz(m)TSCmB determined by single crystal XRD.

Bond	HfpyTSCmB	HapyTSCmB	HdpyTSCmB	HbphTSCmB	HFbzTSC	HFbzTSCm	HFbzTSCdm
>C=N-	1.2843(2)	1.3382(1)	1.2925(1)	1.295(2)	1.280(9)	1.2817(1)	1.273(3)
=N-NH-	1.3718(2)	1.4173(1)	1.3720(1)	1.369(2)	1.363(9)	1.3656(1)	1.359(2)
-NH-(C=S)	1.3677(2)	1.4036(1)	1.3675(1)	1.369(2)	1.355(9)	1.3560(1)	1.363(3)
>C=S	1.6804(3)	1.6629(1)	1.6809(1)	1.682(2)	1.697(8)	1.6831(2)	1.695(2)
	HmphfpyTSC	H₂hphfpyTSCmB			HFbzTSCAd	HFbzTSCmB	HFbz(m)TSCmB
>C=N-	1.290(3)	1.26(1)			1.280(3)	1.283(2)	1.286(3)
=N-NH-	1.372(2)	1.39(1)			1.366(3)	1.368(2)	1.366(2)
-NH-(C=S)	1.359(3)	1.33(1)			1.369(3)	1.361(2)	1.392(3)
>C=S	1.689(2)	1.67(1)			1.689(2)	1.680(1)	1.676(2)

The synthesis and characterization of thiosemicarbazone containing compounds proved to be a straightforward task with the build data set. To gain a better understanding of the influence of the changing side groups the electrochemical parameters were determined.

2.1.3. Electrochemical analysis of the thiosemicarbazones

Although the crystal structures do not vary much, the electrochemical analyses of the molecules showed some interesting differences. The overview of the cyclic voltammetric analyses of 30 ligands is shown in Figure 2.6, with the cyclic voltammetry (CV) of H₂hphfpyTSCmB as an example. The cyclic voltammograms can be found in the appendix Chapter 7.9.1. Figures 7.354 to 7.367. The attachment of electron withdrawing groups like C₆F₅, pyridine or the salicylic moiety increases the reduction potential in comparison to the benzylic derivatives. An explanation for this behaviour describes the first reduction as imine centred and thus a stronger electron withdrawing aryl would lead to an increase the reduction potential.

Also, among all thiosemicarbazones measured in this thesis, the 6-hydroxyphenyl pyridine derived thiosemicarbazones are the easiest to reduce and oxidize.

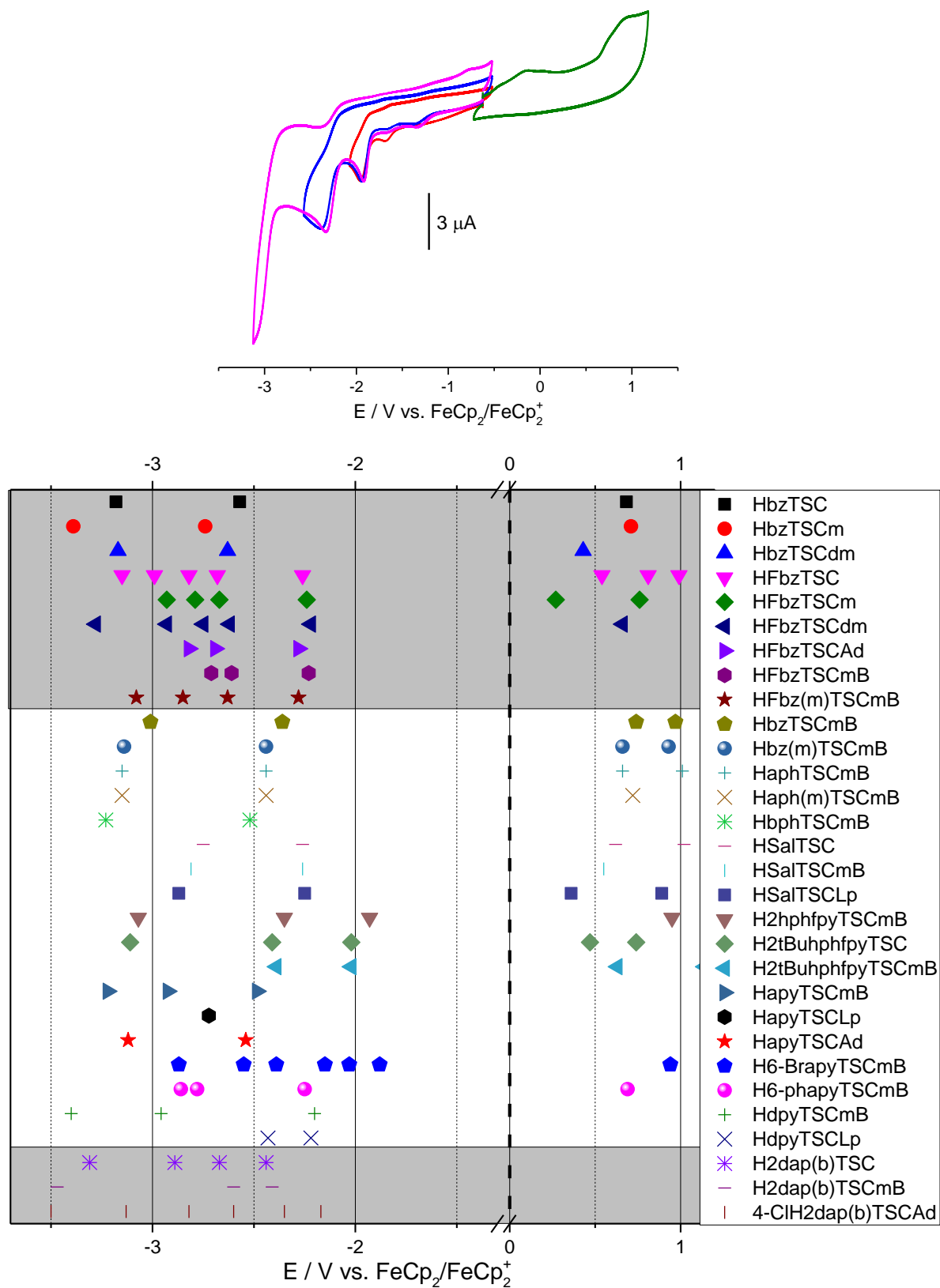


Figure 2.6 Upper: Cyclic voltammogram of H₂hphfpyTSCmB in 0.1 M nBu₄NPF₆/MeCN at a scan rate of 100 mV/s. Lower: Overview of the redox potentials of 30 different ligands. Measured in 0.1 M nBu₄NPF₆ in either MeCN (no background) or THF (grey background) at 100 mV/s scan rate. The break from 0.0 V to -1.3 V is highlighted by a black dashed line.

Diacetyl pyridine derived systems showed to need higher potentials to get oxidized since there was no detectable oxidation wave. The reductions are cathodically shifted which may indicate a more stable radical anion in comparison to monothiosemicarbazones due to a higher conjugation in the pyridyl imine backbone.

The small benzaldehyde thiosemicarbazones with no, monomethyl, and dimethyl derivatization at *N4* have two reductions and one oxidation. The oxidation occurs at 0.4 V to 0.7 V and are among the lowest observed oxidation potentials. The dimethyl substitution influence results in the lowest oxidation potential in that series indicating a considerably lower energy for the HOMO. The methyl benzyl derivatization shows similar electrochemical behaviour compared to the monomethyl derivative. The methylated hydrazone moiety shifts the oxidation and reduction slightly cathodically.

Perfluorination of the phenyl ring rises the potential for the imine reduction by about 0.4 V whilst reducing the potential for the oxidation slightly. This derivatization influences the imine moiety as expected, a lower electron density at the nitrogen donor should lead to a lower donor capability and thus more unstable complexes.

The oxidation is mainly on the sulphur atom. Here, the HOMO for the ligands is based, whereas the LUMO is based on the imine and arene. Here, the reduction occurs typically for thiosemicarbazones.

To get a further insight into the electronic structure of the ligand system further reactions have been performed, which are presented in the following chapter.

2.2. Iridium complexes of benzylic thiosemicarbazones

2.2.1. Analysis of the ligands

As mentioned in the previous chapter, a large variety of ligands has been synthesized. To get a better insight into the ligand structure and how the derivatization effects the electronic properties, a group of similar ligands have been selected to check for their characteristics. These ligands are depicted in Chart 2.9. They only differ in terms of methylation at the imine and hydrazone moieties.

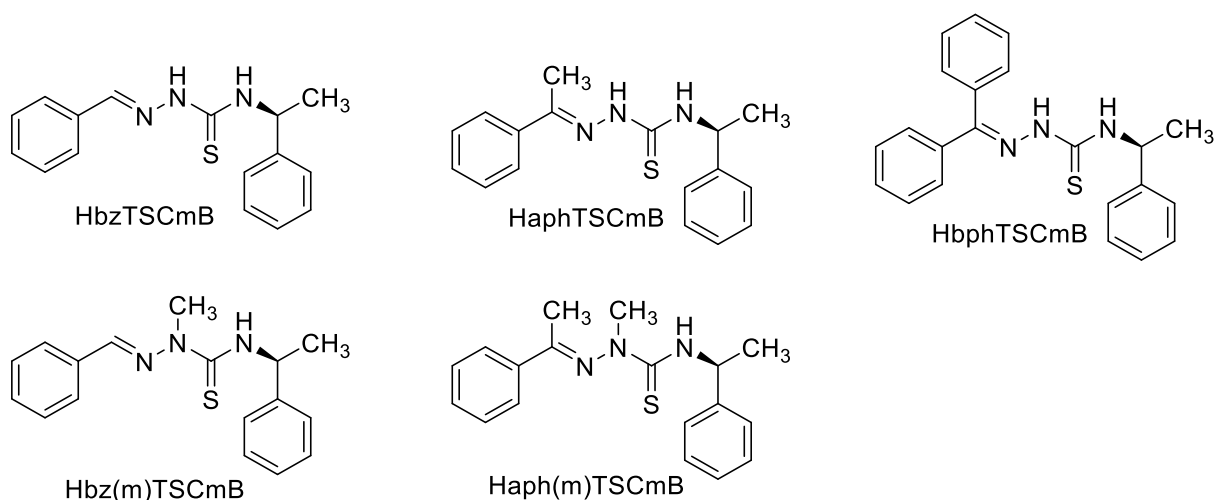


Chart 2.9 Selected thiosemicarbazones for further investigation regarding their electronic structure.

All ligands could be isolated from the condensation reaction, which is described thoroughly in chapter 2.1.1, yielding HbzTSCmB, Hbz(m)TSCmB, HaphTSCmB, Haph(m)TSCmB, HbphTSCmB in pure form. Hbph(m)TSCmB could not be obtained by this reaction. They were analysed by their NMR, MS, and electrochemical behaviour prior.

2.2.1.1. ^1H NMR spectroscopy

By measuring ^1H NMR spectra of all compounds in $\text{DMSO}-d_6$ the chemical shifts of the hydrazone, secondary amine, and imine protons can be visualized and compared to visualize the influence of the substitution.

Whilst the substitution at the imine influences the hydrazones immensely leading to a deshielding for the benzylic imine compared to the acetophenone derivative. The substitution of the hydrazone leads to a shielding at the secondary amine. The lowest chemical shift for the secondary amine is thus achieved by a substitution of the imine and the hydrazone in $\text{H}_2\text{aph(m)TSCmB}$.

Table 2.3 Chemical shifts for the substitution pattern of H₂bzTSCmB, H₂bz(m)TSCmB, H₂aphTSCmB, H₂aph(m)TSCmB and H₂bphTSCmB. All shifts extracted from spectra recorded in DMSO-*d*₆ at 300 MHz. Chemical Shifts are given in ppm.

	-(C- R)=N	=N-(N- R)-(C=S)	(C=S)-NH-	NH-(C- H)<
H ₂ bzTSCmB	8.10	11.55	8.60	5.73
H ₂ bz(m)TSCmB	7.33	3.44	8.35	5.44
H ₂ aphTSCmB	2.33	10.33	8.52	5.72
H ₂ aph(m)TSCmB	2.34	3.43	7.96	5.66
H ₂ bphTSCmB	mult.	8.62	8.98	5.71

2.2.1.2. Electrochemical analysis

As seen in the previous chapter, the methylated hydrazones the redox potentials are very similar. A further insight into the electrochemical behaviour can be gained by measuring UV/Vis spectra during the redox processes as shown in Figure 2.7. Comparing HbzTSCmB, Hbz(m)TSCmB, HaphTSCmB, and Haph(m)TSCmB in their neutral and radical anionic form helps to understand the behaviour of the ligands.

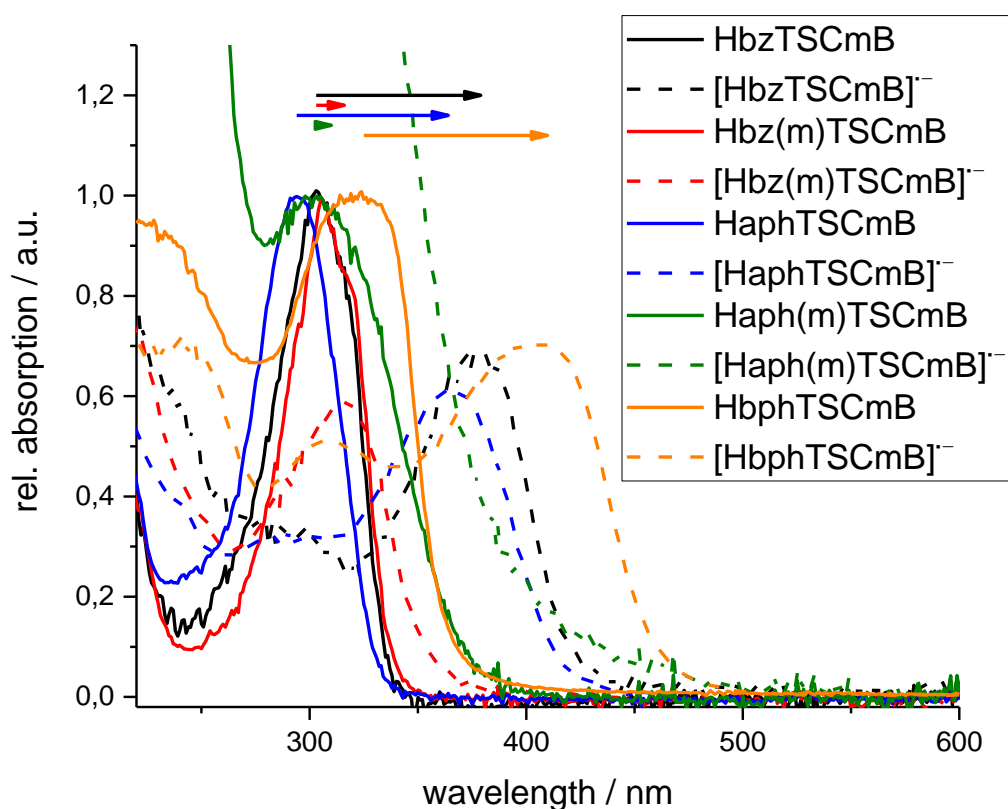
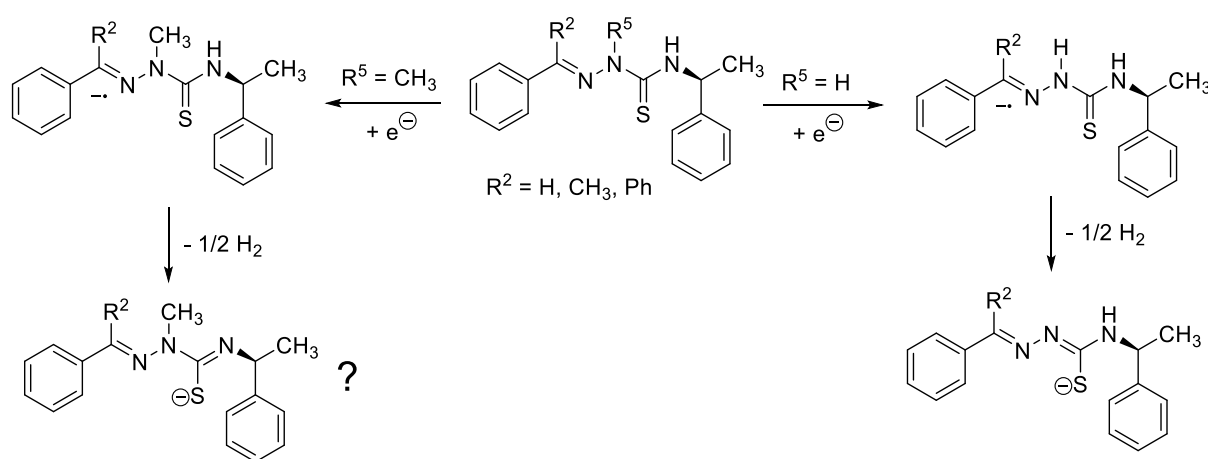


Figure 2.7 Normalized UV/Vis spectra of HbzTSCmB, Hbz(m)TSCmB, HaphTSCmB, Haph(m)TSCmB, and HbphTSCmB in their neutral (solid lines) and radical anionic form generated by electrochemical reduction (dashed lines). Arrows express the shift of the absorption maxima. All spectra recorded in 0.1 M Bu₄NPF₆ MeCN solution.

All ligands exhibit a similar π - π^* transition at roughly 300 nm in their neutral state. Upon reduction a radical anionic species can be generated and whilst the methylated species have shifts of roughly 10 nm the unmethylated species shift about 100 nm.

A reason for this behaviour might be that the unmethylated species express a further chemical process – the cleavage of the acidic proton- and thus increasing the π -system of the ligand. The methylated species is unable to express this bonding scheme and thus is the absorption maxima do not shift that large. Both reductions possibly occur at the imine moiety. These EC mechanisms are depicted in Scheme 2.7.



Scheme 2.7 Possible EC Mechanisms for the reduction of benzylic TSCs with $R^5 \neq \text{H}$ on the left and $R^5 = \text{H}$ on the right.

The HOMO and LUMO orbitals of the ligand series were calculated using the DFT functional B3LYP at def2-TZVP level and shown in Chart 2.10. The orbitals of the ligands are mostly identical which may help to understand their similar electrochemical behaviour. The HOMOs are mostly located at the sulphur-atom. The methylhydrazones seem to have a higher electron density at the hydrazone bridge compared to the unmethylated derivatives. The LUMO on the other hand is mostly located on the benzylimine structure leading to the measured similarity in the reduction.

Chart 2.10 HOMO and LUMO of HbzTSCmB, Hbz(m)TSCmB, HaphTSCmB, and Haph(m)TSCmB calculated with the B3LYP functional at def2-TZVP level. Iso-surface level of all calculated orbitals is 0.06.

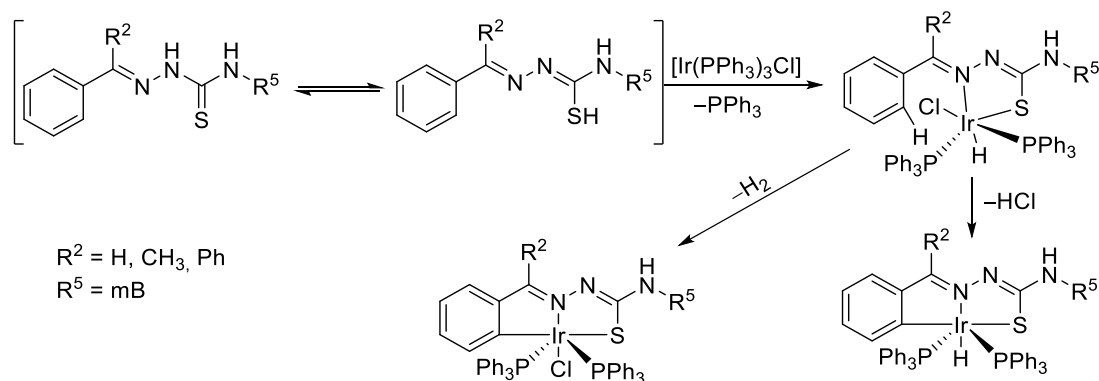
	HbzTSCmB	Hbz(m)TSCmB	HaphTSCmB	Haph(m)TSCmB
LUMO				
HOMO				

Haph(m)TSCmB has another feature shown in the calculated geometry. It is indicated that that Haph(m)TSCmB should have a steric hindrance towards planarity resulting from the two methyl functions. The other calculated geometries show planar ligands. Nevertheless, the HOMO and LUMO composition remains very similar.

2.2.2. General remarks on the synthesis of the iridium complexes

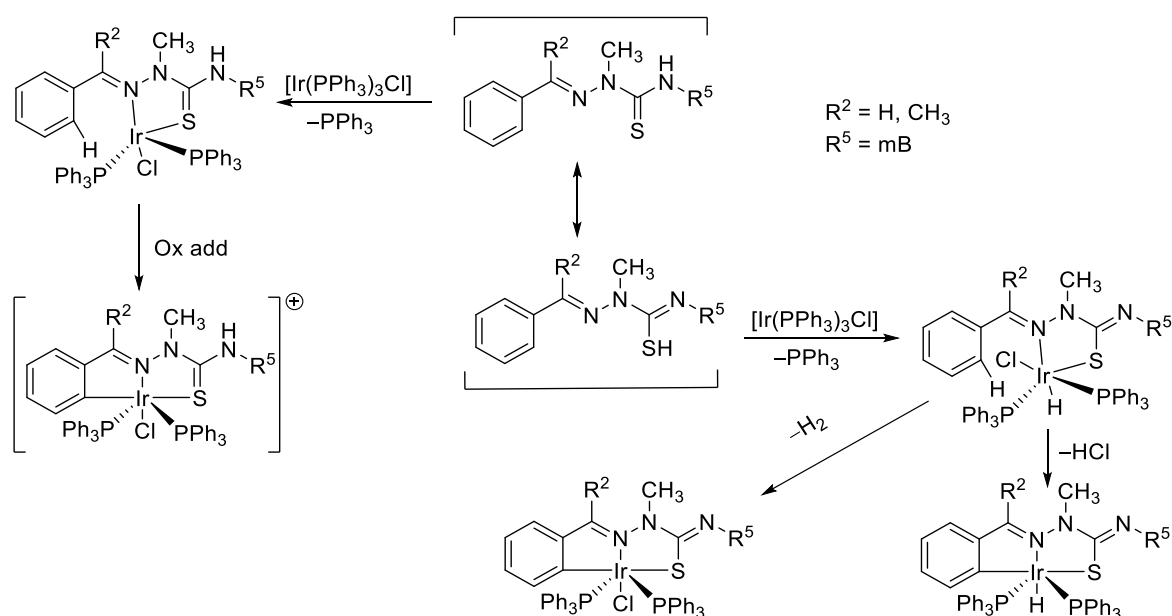
Bhattacharya et al. described the synthesis of hydrido and chlorido complexes of Ir(III) phosphine thiosemicarbazones. Hydrides are negatively charged hydrogen ions which express in ^1H NMR spectroscopy a negative chemical shift. In the iridium complexes the hydride is in *trans* position to the hydrazone function thus a change in the electronic structure of the backbone results in a shift for the hydride. Also, the phosphines are not innocent in this procedure. They not only couple to the hydrides, but their electronegativity has an influence on the electron density at the iridium and thus at the hydride. Comparing different chalcogen related donors and different thiosemicarbazone structures would result in a better picture of the electronic structures of the complexes.

The synthesis of the Ir(III) complexes was performed according to *Bhattacharya et al.*²⁸⁶ As shown in Scheme 2.8, the mechanism is supposed to start by an oxidative addition of the Ir(I) complex $[\text{Ir}(\text{PPh}_3)_3\text{Cl}]$ into the S–H bond forming the initial Ir(III) hydrido chlorido species. This reactive intermediate activates the neighbouring C–H bond of the arene leading to the cleavage of either H_2 , forming the corresponding chloride complex, or by cleavage of HCl , forming the hydride species. Both complexes form during the reaction and can be separated by chromatographic methods.



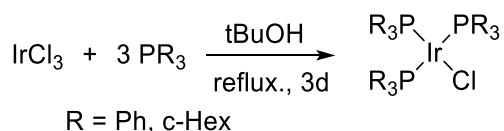
Scheme 2.8 Synthesis of hydrido and chloride species of Ir(III) thiosemicarbazone complexes using HbzTSCmB, HaphTSCmB and HbphTSCmB as ligands.

The synthesis of the Ir(III) complexes using the *N*2 methylated ligands, Hbz(m)TSCmB and Haph(m)TSCmB, was also performed as described previously. Yet the mechanism may differ. In Scheme 2.9 the mechanistic possibilities of an iridium coordination are illustrated. If there is a similar thion-thiol tautomerism between *N*4 and the thione the oxidative addition into the S–H bond remains possible (right pathway). The left path of the mechanistic ideas would form a neutral complex that has an oxidative C–H activation to form the complexes. The following experiments should help to determine which route takes place for the *N*2 substituted systems.



Scheme 2.9 Synthesis of hydrido and chloride species of Ir(III) thiosemicarbazone complexes using Hbz(m)TSCmB and Haph(m)TSCmB. Possible reaction outcomes based on oxidative addition into S–H bond or coordination to a neutral *N*⁴S backbone is depicted.

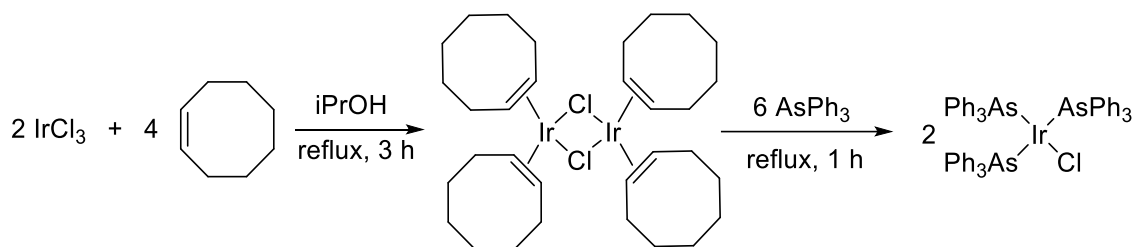
Since the initial Ir(I) phosphine complex needed to be synthesized prior according to literature, also the pnictogen donors were twitched a bit. The synthesis for the precursor, which is shown in Scheme 2.10, was performed with triphenyl phosphine, perdeuterated triphenyl phosphine (PPh₃-*d*₁₅) and tricyclohexyl phosphine as well.



Scheme 2.10 Synthesis of Ir(I) phosphine complexes as precursors for the complexation.

Tris triphenyl arsine iridium(I) chloride could be generated by synthesizing the very reactive cyclooctene derivative before the addition of AsPh₃. The reaction scheme is depicted in Scheme 2.11. Arsine is similar to phosphines, but due to higher electronegativity it should be able to lower the electron density of the iridium in the complex and thus shift the hydride to higher fields. Also, the phosphine atoms couple

to the hydride and split its NMR signal into a triplet whereas the arsine does not couple to the hydrides and the NMR signal stays as a singlet.



Scheme 2.11 One pot synthesis Ir(I) arsine complexes as precursors for the complexation using the Ir(I) cyclooctene as intermediate.

The *Tolman* cone angle of arsines are comparable to the phosphines.^{287, 288} The electronic influence of PCy₃, PPh₃ and AsPh₃ differs a lot. *Roodt* tested a series of phosphines, arsines and stilbenes and showed that the CO stretching frequencies for [Ni(E)CO] and [RhCl(CO)₂(E)] complexes is lowest for PCy₃ ($\nu_{\text{Ni}} = 2056.4 \text{ cm}^{-1}$; $\nu_{\text{Rh}} = 1943 \text{ cm}^{-1}$) followed by AsPh₃ ($\nu_{\text{Ni}} = 2067.9 \text{ cm}^{-1}$; $\nu_{\text{Rh}} = 1975 \text{ cm}^{-1}$) and is highest among the previously mentioned with PPh₃ ($\nu_{\text{Ni}} = 2068.9 \text{ cm}^{-1}$; $\nu_{\text{Rh}} = 1979 \text{ cm}^{-1}$).²⁸⁹ The lower the frequency of the CO-stretching mode, the higher the electron density at the metal centre. This could also mean that the herein synthesized iridium complexes bearing hydrides should exhibit different ¹H NMR shifts for the hydride depending on the pnictogen donor.²⁹⁰⁻²⁹²

2.2.2.1. UV/Vis absorption spectroscopy of the iridium complexes

UV/Vis absorption spectroscopy was used to investigate a possible change of the HOMO-LUMO band gap due to the changing of the coligands. The UV/Vis spectra of the complex series with HbzTSCmB are depicted in Figure 2.8. The hydrides have a more intense MLCT at about 450 nm, whereas the chlorides have less intense, blue shifted MLCT but higher ligand centred transitions. The deuterated phenyl phosphines do not seem to shift the absorption maxima energy wise, but the intensity and the sharpness of the signals increase slightly. This may be caused by the higher energy of vibrational modes of C–D compared to C–H bonds.

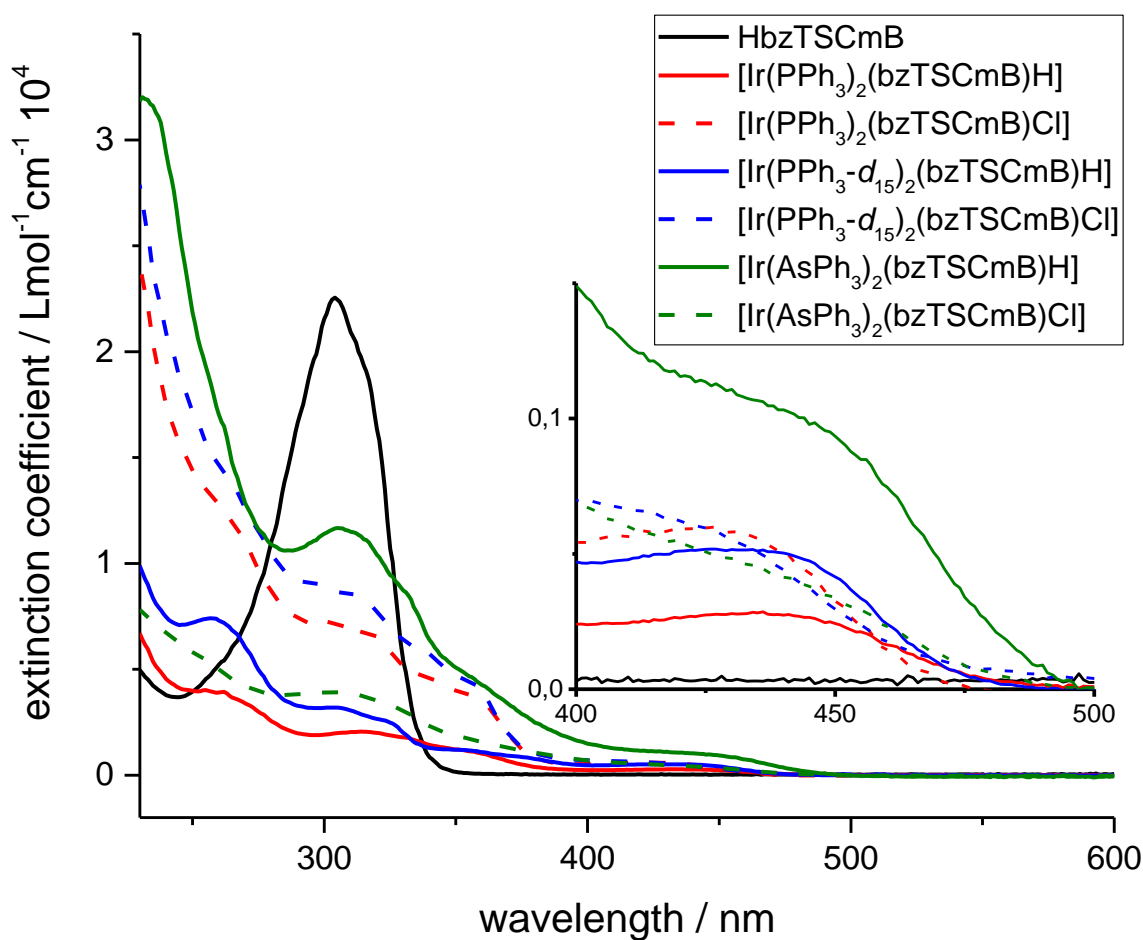


Figure 2.8 UV/Vis absorption spectra of HbzTSCmB and the iridium complexes resulting from the reaction with $[\text{Ir}(\text{PPh}_3)_3\text{Cl}]$ (red), $[\text{Ir}(\text{PPh}_3\text{-}d_{15})_3\text{Cl}]$ (blue) and $[\text{Ir}(\text{AsPh}_3)_3\text{Cl}]$ (green). All Spectra recorded in MeCN solutions.

Triphenyl arsine shows the lower energy absorptions compared to the triphenyl phosphine derivatives. This shows that the HOMO-LUMO gap of the MLCT transitions is influenced by the electronegativity of the pnictogen donor. Interestingly, while the MLCT band seems of the hydrides and chlorides seem to fit the bands of the phosphine derivatives, the higher energy region seems exchanged. While the band structure seems like the phosphines the extinction coefficient of the hydrides is far more intense.

Comparing the bzTSCmB^- to the aphTSCmB^- derivatives, the absorptions are blue shifted but show very similar characteristics. This series is shown in Figure 2.9. Also, the hydrides show lower extinction coefficients for the MLCT compared to chlorides. Also, the deuterated species has a higher absorption at the low energy UV range.

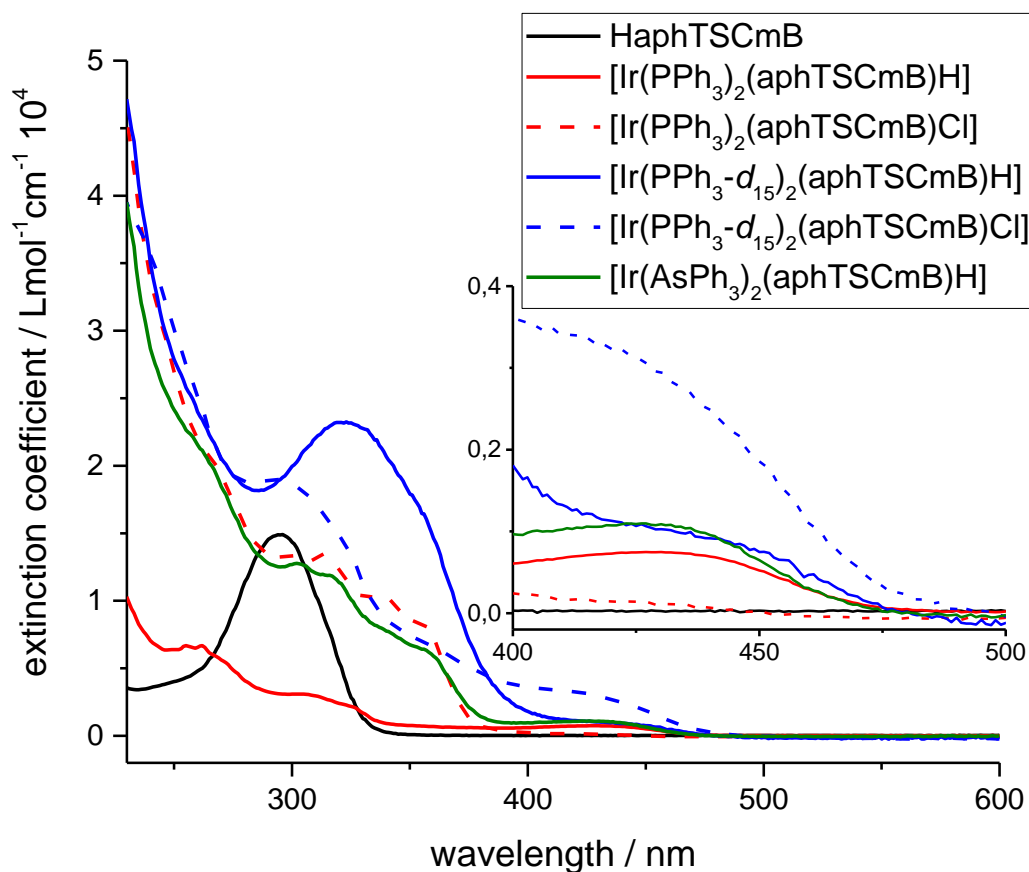


Figure 2.10 UV/Vis absorption spectra of HaphTSCmB and the iridium complexes resulting from the reaction with $[\text{Ir}(\text{PPh}_3)_3\text{Cl}]$ (red), $[\text{Ir}(\text{PPh}_3\text{-}d_{15})_3\text{Cl}]$ (blue) and $[\text{Ir}(\text{AsPh}_3)_3\text{Cl}]$ (green). All Spectra recorded in MeCN solutions.

Additionally, the hydrides could be used as sensors for the electron density at the metal centre. Since the pnictogen donors can couple to the hydride, the phosphine derivatives should form triplets and switching to arsine, they are supposed to be singlets since arsine has no nuclear spin in its stable configuration. In the ^1H NMR the hydrides will shift according to the Ir(III) centre resulting in a shielding for higher electron densities. In result, the derivatization at the hydrazone should cause a shift in the hydride signal. But this theoretical result was not detected.

In addition to the benzaldehyde and acetophenone derivatives, the iridium complexes of HbphTSCmB were also investigated (Scheme 2.8). $[\text{Ir}(\text{PPh}_3)_2(\text{bphTSCmB})\text{H}]$ has a similar absorption spectrum compared to the previously described structures. The UV/Vis spectrum exhibits an absorption maxima for the MLCT transition at 460 nm (Figure 2.11). The spectra, recorded in DCM shows a weak luminescence in solution at ambient conditions. A 0-0 transition is identifiable at the intersection of the fluorescence and absorption spectra at 496 nm (2.499 eV).

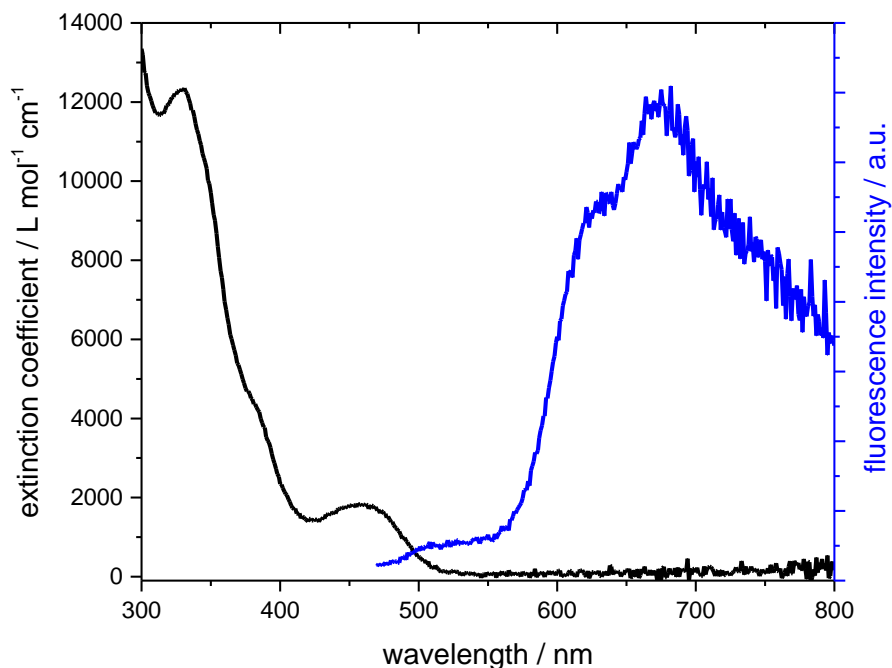


Figure 2.11 Absorption (black) and fluorescence (blue, $\lambda_{\text{ex}} = 460$ nm) spectra of $[\text{Ir}(\text{PPh}_3)_2(\text{bphTSCmB})\text{H}]$. Both spectra recorded at ambient conditions in CH_2Cl_2 and the same concentration.

2.2.2.2. X-Ray structures of Ir(III) thiosemicarbazones

By evaporation of MeCN from a concentrated solutions of $[\text{Ir}(\text{PPh}_3)_2(\text{bzTSCmB})\text{Cl}]$ and $[\text{Ir}(\text{PPh}_3)_2(\text{bphTSCmB})\text{Cl}]$, single crystals suitable for x-ray diffraction could be isolated. The structures (Figure 2.12) show octahedrally coordinated Ir(III) with a dianionic thiosemicarbazone coordinating $\text{C}^{\wedge}\text{N}^{\wedge}\text{S}$ in an equatorial fashion. The octahedral geometry is completed by a chloride coligand in the TSC plane and two triphenyl phosphines in trans position towards each other.

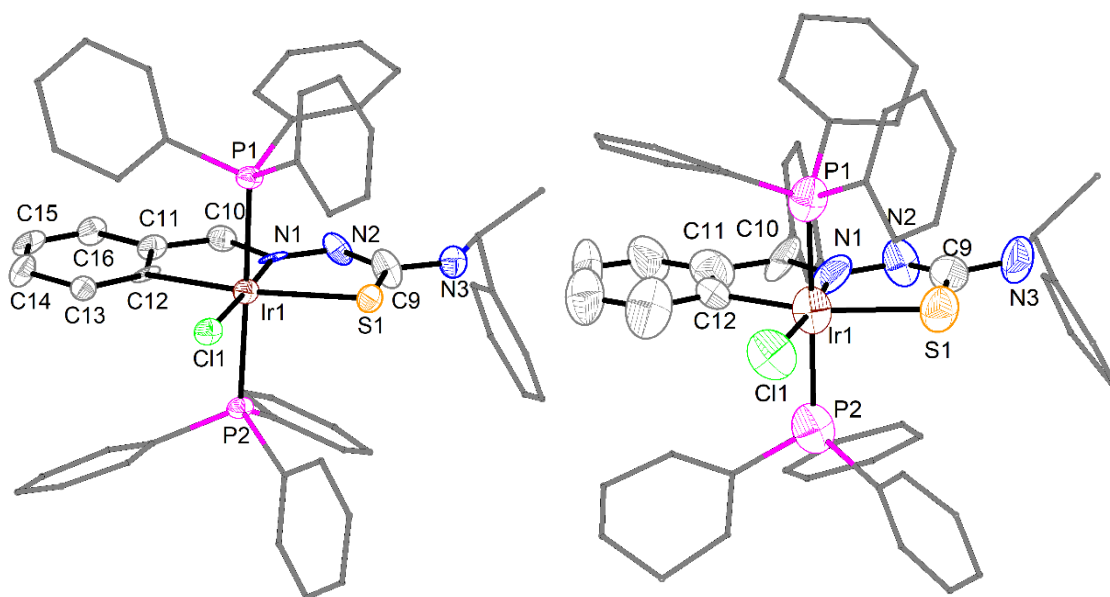


Figure 2.12 Molecular structure of $[\text{Ir}(\text{PPh}_3)_2(\text{bzTSCmB})\text{Cl}]$ (left) and $[\text{Ir}(\text{PPh}_3)_2(\text{bphTSCmB})\text{Cl}]$. Thermal ellipsoids are shown at 50% probability. Hydrogen atoms are omitted for clarity.

Table 2.4 Crystal data and structure refinement for [Ir(PPh₃)₂(bzTSCmB)Cl] and [Ir(PPh₃)₂(bphTSCmB)Cl].

	[Ir(PPh ₃) ₂ (bzTSCmB)Cl]	[Ir(PPh ₃) ₂ (bphTSCmB)Cl]
Empirical formula	C ₅₂ H ₄₅ ClIrN ₃ P ₂ S (1033.64 g/mol)	C ₁₂₀ H ₁₀₃ Cl ₂ Ir ₂ N ₈ P ₄ S ₂ (2300.40 g/mol)
Temperature/K	100.15	100.15
Crystal system	triclinic	monoclinic
Space group	P1	P2 ₁
a/Å	9.7457(6)	18.5194(17)
b/Å	11.8391(8)	12.5871(8)
c/Å	19.3725(16)	24.119(2)
α/°	75.172(5)	90
β/°	87.674(5)	102.739(7)
γ/°	88.402(4)	90
Volume/Å ³	2158.6(3)	5483.9(8)
Z	2	2
ρ _{calc} /g/cm ³	1.5902	1.393
μ/mm ⁻¹	8.023	2.621
F(000)	1032.0	2318.0
Radiation/Å	CuKα (λ = 1.54178)	MoKα (λ = 0.71073)
2θ range for data collection/°	4.7 to 145.3	3.462 to 53.908
Index ranges	-12 ≤ h ≤ 12, -14 ≤ k ≤ 14, -23 ≤ l ≤ 23	-22 ≤ h ≤ 23, -16 ≤ k ≤ 15, -30 ≤ l ≤ 30
Reflections collected	82657	40533
Independent reflections	16015 [R _{int} = 0.0935, R _{sigma} = 0.0715]	21417 [R _{int} = 0.1638, R _{sigma} = 0.3155]
Data/restraints/parameters	16015/3/1084	21417/9/1248
Goodness-of-fit on F ²	1.038	0.823
Final R indexes [I ₀ > 2σ _{I₀}]	R ₁ = 0.0612, wR ₂ = 0.1604	R ₁ = 0.0737, wR ₂ = 0.1451
Final R indexes [all data]	R ₁ = 0.0675, wR ₂ = 0.1635	R ₁ = 0.2391, wR ₂ = 0.2139
Largest diff. peak/hole / e Å ⁻³	4.11/-3.19	1.31/-1.59
Flack parameter	0.043(13)	0.18(2)

Interestingly, the chiral N₄ substitution introduced to the ligand in the synthesis remains unchanged and both structures show an almost ecliptical PPh₃ configuration.

Due to the bad crystallographic solution of [Ir(PPh₃)₂(bphTSCmB)Cl], it is not possible to discuss the bond lengths and angles in detail, but the structural parameters of the compound are comparable to the crystal structures published by *Bhattacharya et al.*²⁸⁶ In Table 2.5 the bonding distances of the iridium centre to the donor atoms for [Ir(PPh₃)₂(bzTSCmB)Cl], [Ir(PPh₃)₂(bphTSCmB)Cl] and *Bhattacharya's* tolualdehyde thiosemicarbazone based [Ir(PPh₃)₂(tolTSC)Cl] are given. The comparison shows a good comparability to the reported structure. The only major difference is the ordering of the triphenyl phosphines. The reported structure shows a more inclined angle of the phosphorus donors compared to the herein synthesized structures. Also, the dihedral angle of the triphenyl phosphines is less ecliptic.

Table 2.5 Bonding distances and angles in [Ir(PPh₃)₂(bzTSCmB)Cl], [Ir(PPh₃)₂(bphTSCmB)Cl] and the reported structure [Ir(PPh₃)₂(tolTSC)Cl] (CCDC: 761130).²⁸⁶

	[Ir(PPh ₃) ₂ (bzTSCmB)Cl]	[Ir(PPh ₃) ₂ (bphTSCmB)Cl]	[Ir(PPh ₃) ₂ (tolTSC)Cl]
Ir-Cl	2.400(2) Å	2.40(1) Å	2.389(3) Å
Ir-N1	2.039(8) Å	2.02(2) Å	2.006(7) Å
Ir-S	2.433(2) Å	2.41(1) Å	2.433(3) Å
Ir-C12	2.087(9) Å	1.96(3) Å	2.013(9) Å
Ir-P	2.343(2) Å / 2.354(3) Å	2.37 (1) Å / 2.36 (1) Å	2.346(3) Å / 2.367(3) Å
P-Ir-P	173.16(9)°	172.6(4)°	169.53(1)°
PPh ₃ dihedral angle	4.0(6)°	4(2)°	14.6(5)°

The comparison helps to validate the structures since the following measurements, especially NMR and mass spectroscopy, showed some difficulties. Nevertheless, the data provided in the following chapters will help to understand the electronic structure of thiosemicarbazones as ligands.

2.2.2.3. Hydride NMR shifts of iridium complexes

The synthesized hydrides are detectable in the NMR spectra at negative values as shown in Figure 2.13. Comparing the hydride shifts of the acetophenone derivatives, the shift of the hydride is at -14.34 ppm for the normal TSC. The methylation leads to a slight deshielding of the hydride to -14.22 ppm and exchanging the pnictogen donor to arsine leads to a shift to -15.58 ppm for the normal and -15.60 ppm for the methylated derivative. The benzaldehyde derivatives show similar behaviour, yet the hydrides are already more shielded than the acetophenone derivatives. These shifts are extremely similar which indicates only tiny differences in the electron density in the ground state.

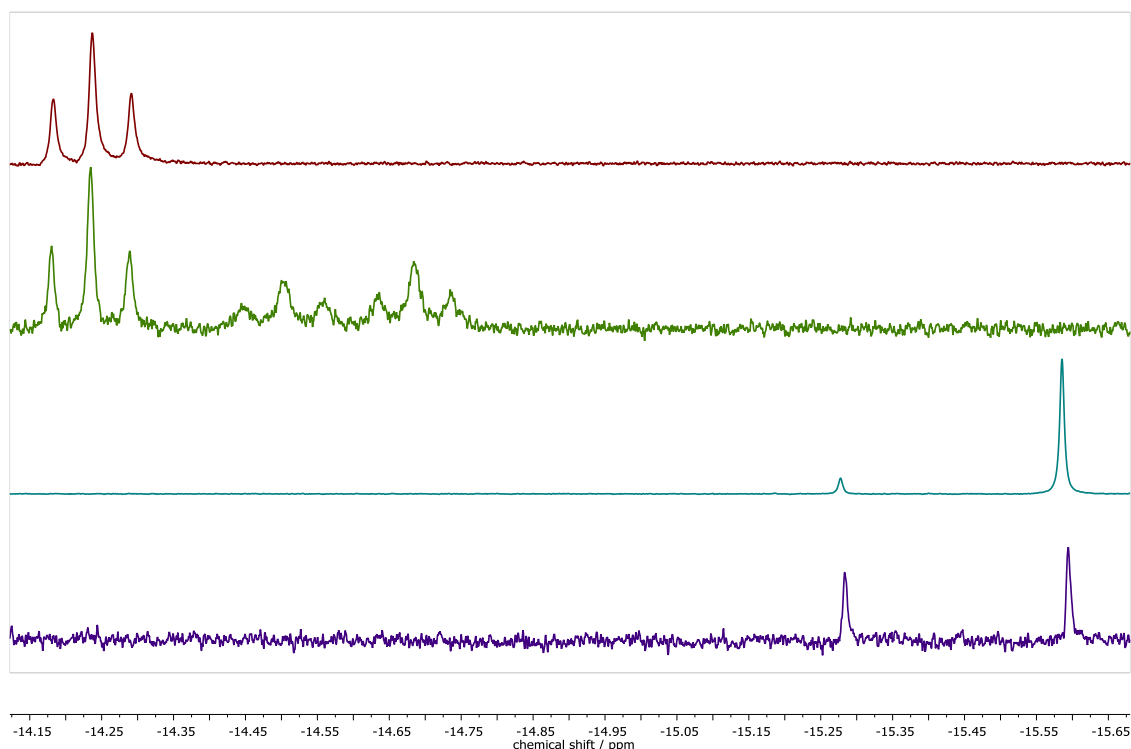


Figure 2.13 ^1H NMR Spectra of $[\text{Ir}(\text{PPh}_3)_2(\text{aphTSCmB})(\text{H})]$, $[\text{Ir}(\text{PPh}_3)_2(\text{aph(m)TSCmB})(\text{H})]$, $[\text{Ir}(\text{AsPh}_3)_2(\text{aphTSCmB})(\text{H})]$, and $[\text{Ir}(\text{AsPh}_3)_2(\text{aph(m)TSCmB})(\text{H})]$. All measured in $\text{DMSO}-d_6$ at 300 MHz.

Thus, the results indicate that the electron density at the Ir(III) centre can be comparatively described as being higher for AsPh_3 than PPh_3 and benzaldehyde over acetophenone. The methylation does not affect the electron density in the complex.

The deuteration of the triphenyl phosphine has no influence on the hydride shift, as expected, but the aromatic region is much more structured. The spectrum is shown in Figure 2.14. On top of this, the methylated species show something very interesting. As previously stated, it is unclear whether the *N4* amine is deprotonated at all. The ^1H NMR of $[\text{Ir}(\text{PPh}_3\text{-}d_{15})_2(\text{bz}(\text{m})\text{TSCmB})(\text{Cl})]$ solved this question. The proton at the chiral carbon atom of the methylbenzyl moiety shifts to 6.13 ppm and splits into a quartet ($J = 7.2$ Hz). The proton thus couples only to the doublet at 1.61 ppm ($J = 7.3$ Hz) showing the deprotonation of *N4*.

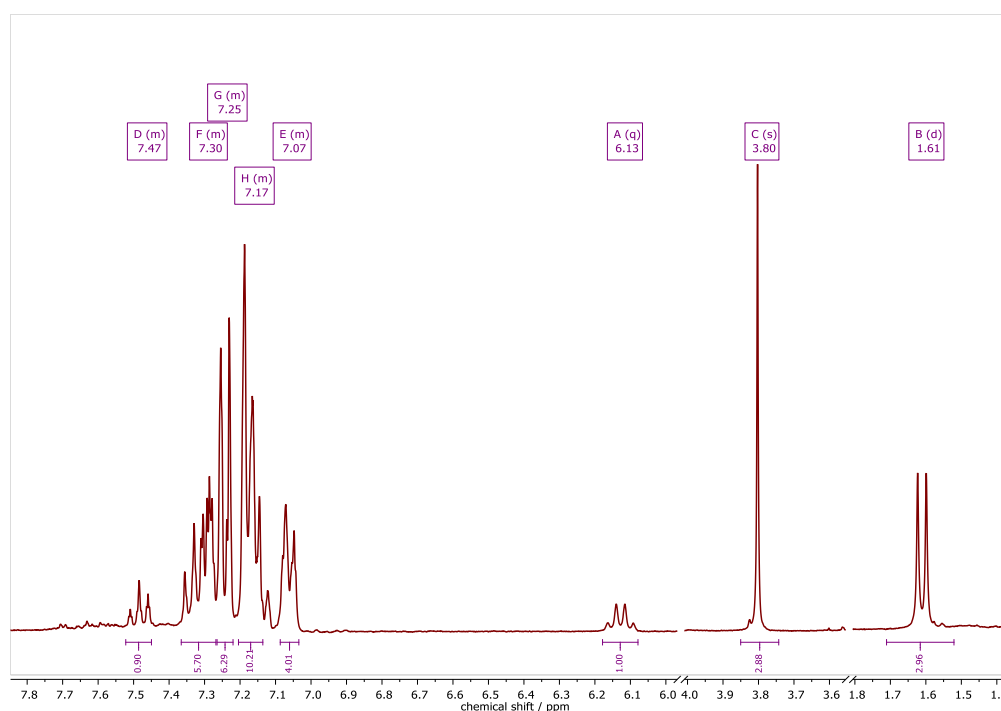


Figure 2.14 ^1H NMR of $[\text{Ir}(\text{PPh}_3\text{-}d_{15})_2(\text{bz}(\text{m})\text{TSCmB})(\text{Cl})]$ in $\text{DMSO-}d_6$ at 300 MHz.

2.2.2.4. Electrochemical analyses of the iridium complexes

Redox potentials were measured using cyclic voltammetry and for a better comparison, the peak potentials of the complexes were illustrated in Figure 2.15. Generally, the reduction is just slightly affected by the anionic coligand whereas the oxidation is at lower potentials for the hydrides compared to their chloride relatives. The introduction of a methyl function at *N2* shows only minor effects in the electrochemical analyses of the compounds.

The substitution with arsine as donors is more interesting, at least for the oxidation. The oxidation of the arsine compounds is at higher potentials. If the first oxidation is the process $\text{Ir}(\text{III})$ to $\text{Ir}(\text{IV})$, it indicates a lower electron density at the metal, which hints at the higher electron withdrawing effect of the triphenyl arsine groups. This is in line with the electronegativity scale of *Allred* and *Rochow*.²⁹³ Which

is interesting since other electronegativity scales depicted higher electronegativities for phosphorous than arsenic.²⁹⁴ A numerical example is the oxidation of $[\text{Ir}(\text{PPh}_3)_2(\text{bzTSCmB})(\text{H})]$ at 0.2 V compared to the potential of 0.35 V for the first oxidation at $[\text{Ir}(\text{AsPh}_3)_2(\text{bzTSCmB})(\text{H})]$.

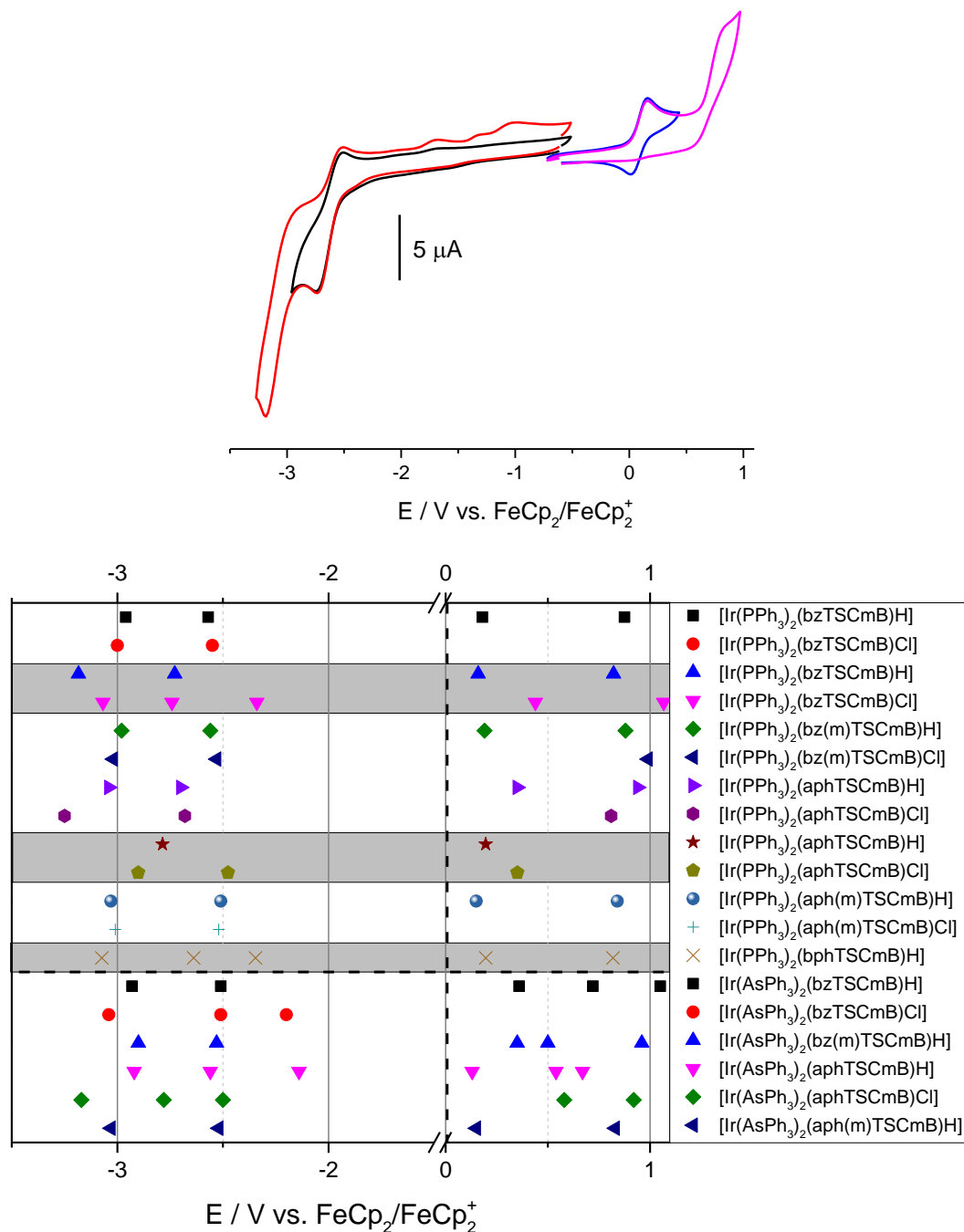


Figure 2.15 Upper: Cyclic voltammogram of $[\text{Ir}(\text{PPh}_3)_2(\text{bzTSCmB})(\text{H})]$ in 0.1 M $\text{nBu}_4\text{NPF}_6/\text{THF}$ at a scan rate of 100 mV/s. Lower: Overview of 19 the redox potentials of Ir(III) complexes determined by cyclic voltammetry measured in 0.1 M nBu_4NPF_6 in either MeCN (no background) or THF (grey background) at 100 mV/s scan rate. The break from 0.0 V to -1.5 V is highlighted by a black dashed line.

To gain better insight into the influence of the derivatization SEC-UV/Vis were measured of a good batch of complexes. Comparing the chloride and hydride as coligands, the SEC-UV/Vis, shown in Figure 2.16, revealed that the electrochemical

processes stay similar. Upon oxidation the main MLCT band decreases and the absorption structure at higher energies gets more defined. The reduction shows the formation of a broad band at 440 nm which has a fine structure for the hydride coligand. All in all, it seems that both redox processes are metal centred and the influence of the anionic coligand is neglectable.

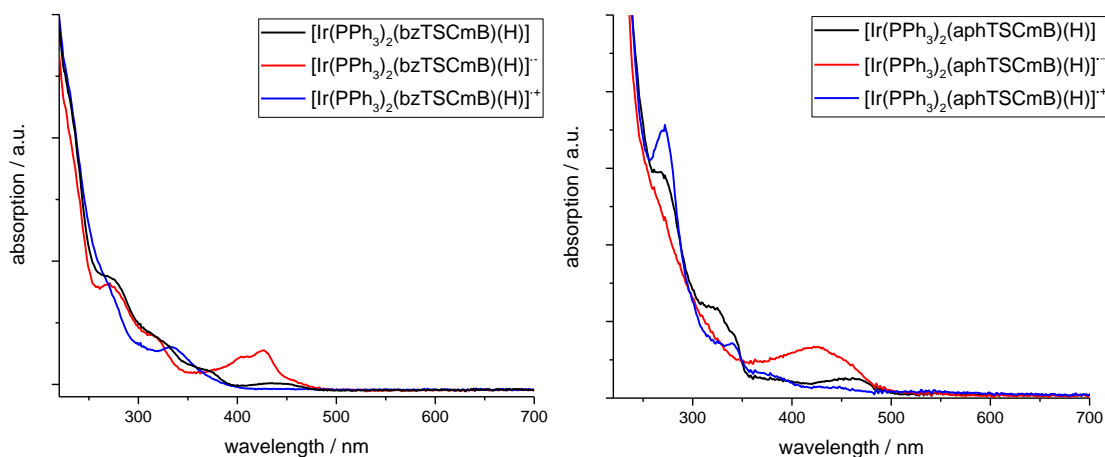


Figure 2.16 Spectroelectrochemical UV/Vis of $[\text{Ir}(\text{PPh}_3)_2(\text{bzTSCmB})(\text{H})]$ (left) and $[\text{Ir}(\text{PPh}_3)_2(\text{bzTSCmB})(\text{Cl})]$ (right) in 0.1 M Bu_4NPF_6 MeCN solution. The neutral form is in black, the spectra of the radical anionic species are in red, and the radical cationic species is in blue.

Comparing two different pnictogen donor systems the influence seems to be more vivid. The spectra are shown in Figure 2.17. During the oxidation, the hydride complex $[\text{Ir}(\text{PPh}_3)_2(\text{aphTSCmB})(\text{H})]$ forms a broad absorption at roughly 520 nm whereas the arsenic derivative seems to fall apart and only shows a broad ramp like spectrum for the radical cationic species. The reduction on the other hand seems to be identical for the derivatives showing the same intense absorption at around 420 nm as described previously.

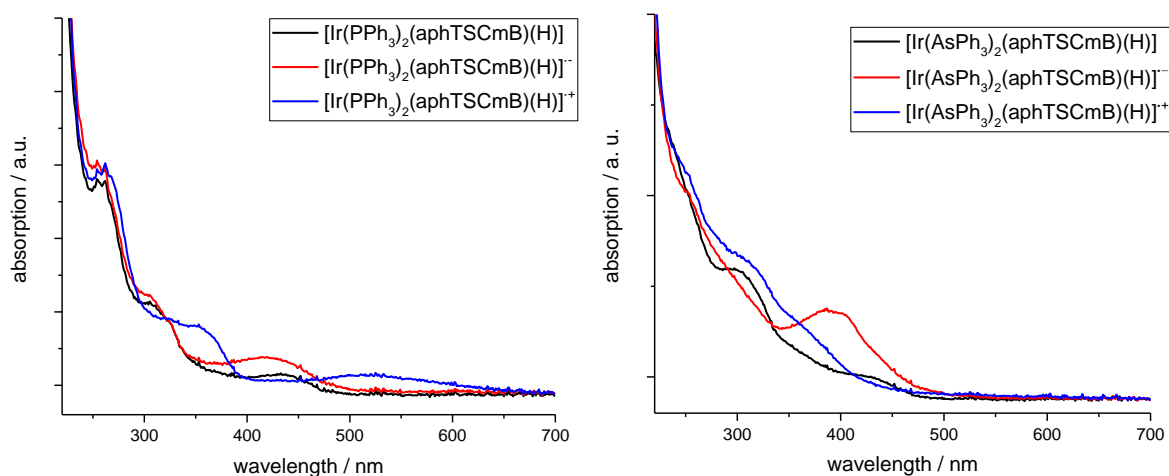


Figure 2.17 Spectroelectrochemical UV/Vis of $[\text{Ir}(\text{PPh}_3)_2(\text{aphTSCmB})(\text{H})]$ (left) and $[\text{Ir}(\text{AsPh}_3)_2(\text{aphTSCmB})(\text{H})]$ (right) in 0.1 M Bu_4NPF_6 MeCN solution. The neutral form is in black, the spectra of the radical anionic species are in red, and the radical cationic species is in blue.

In conclusion of this topic, we can see the influence of the derivatization of the ligand backbone very clear. The thione-thiol tautomerism is directed regarding the acidity of the corresponding amine. The C(S)-N2 bonding situation has little to no influence on the electron density on the metal centre yet the electrochemistry is influenced. Also, the methylation hinders the aromatization in the backbone yielding less red shifted absorptions in the radical anionic species.

2.2.3. Formation of $[\{\text{Ir}(\text{PPh}_3)_2\text{Cl}_2\}_2(\mu^2\text{-oxalato-}\kappa^4 \text{O}^1, \text{O}^2: \text{O}^{1'}, \text{O}^{2'})]$

Upon recrystallization of several previously synthesized Ir(III) complexes from DCM $[\{\text{Ir}(\text{PPh}_3)_2\text{Cl}_2\}_2(\mu^2\text{-oxalato-}\kappa^4 \text{O}^1, \text{O}^2: \text{O}^{1'}, \text{O}^{2'})]$ could be isolated whilst in others like $[\text{Ir}(\text{PPh}_3)_2(\text{aphTSCmB})(\text{H})]$ the structure remains stable over several weeks as detected by ^1H and $^{31}\text{P}\{^1\text{H}\}$ NMR. The recrystallization was performed under air and in transparent glass at room temperature over several days.

In Figure 2.18 is the molecular structure of the complex depicted. The triphenylphosphines exhibit a highly disordered state, which can be explained by their ability to freely rotate.

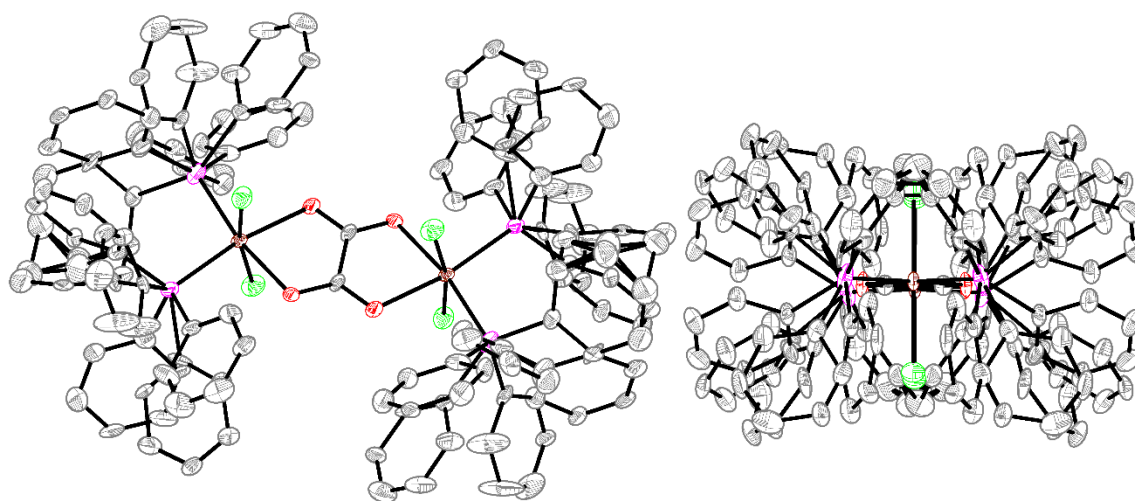


Figure 2.18 Molecular structure of $[\{\text{Ir}(\text{PPh}_3)_2\text{Cl}_2\}_2(\mu^2\text{-oxalato-}\kappa^4 \text{O}^1, \text{O}^2: \text{O}^{1'}, \text{O}^{2'})]$. Thermal ellipsoids are at 50%. The crystal was isolated from the recrystallization attempt of $[\text{Ir}(\text{PPh}_3)_2(\text{bzTSCmB})(\text{Cl})]$. Right: Structure along the Ir–Ir axis.

In Figure 2.19 is the crystal packing along the crystallographic b-axis depicted. Here another factor for the disorder of the triphenyl phosphines becomes obvious. The structure is overall in a layered modification in which the triphenyl phosphines intertwine and by small rotations the crystal structure will not yield a satisfying solution.

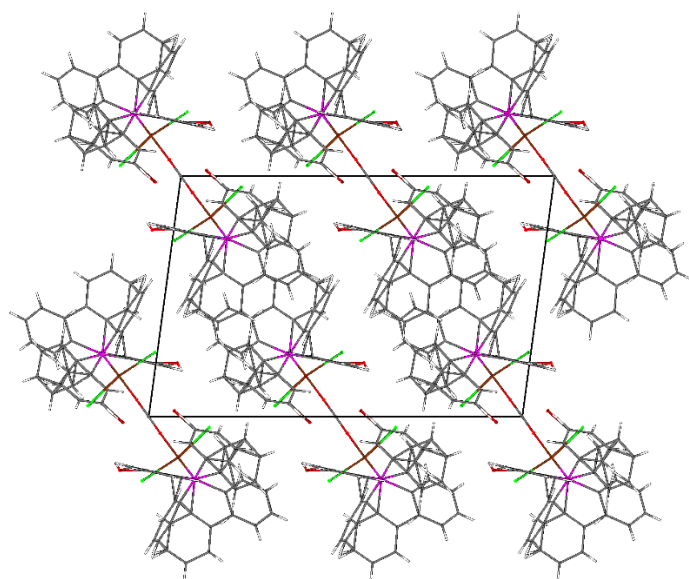


Figure 2.19 Unit cell of $[\{\text{Ir}(\text{PPh}_3)_2\text{Cl}_2\}_2(\mu^2\text{-oxalato-}\kappa^4\text{O}^1,\text{O}^2:\text{O}^1',\text{O}^2')]$ along the crystallographic b-axis.

Nevertheless, it is interesting to have a look at the “core” of the complex, shown in Figure 2.20. The iridium oxalate plane is highly symmetrical with every C–O bond being 1.254(1) Å. The Ir–O and Ir–P bonds are 2.134(1) Å and 2.291(1) Å, respectively. The chelate angle is 78.10(1)° and the P–Ir–P angle is 98.82(1)°. The sterically demanding triphenyl phosphines push the chlorine atoms towards the centre showing a Cl–Ir–Cl angle of 169.35(1)°. They are a little bit asymmetrical towards the plane yielding Cl–Ir–O angles of 86.69(1)° and 85.05(1)°. The Cl–Ir bond is 2.346(1) Å and the distance between the chlorine atoms across the oxalate is 5.093(1) Å.

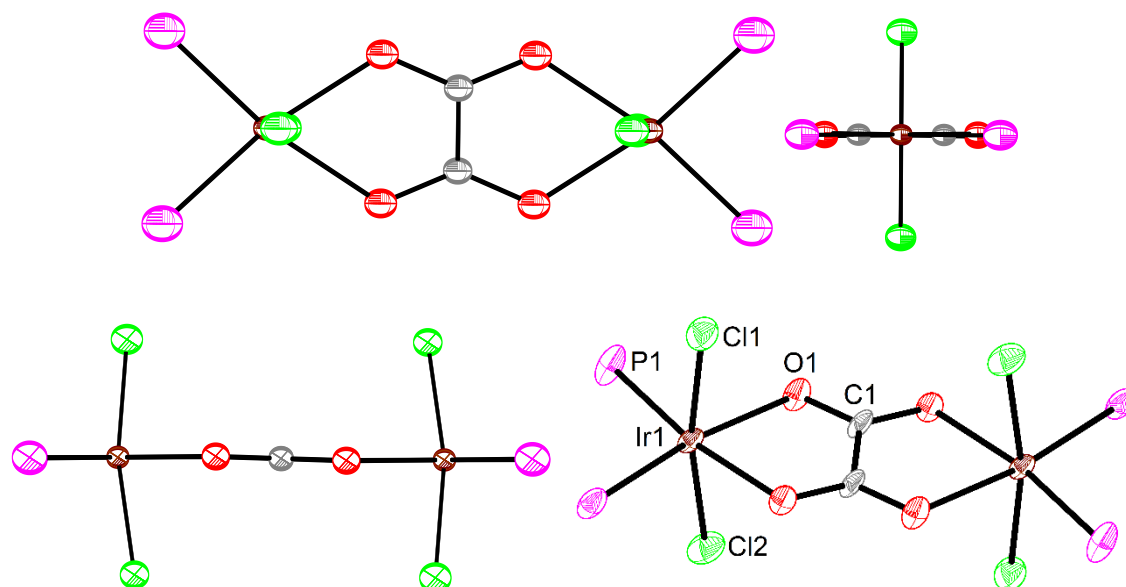


Figure 2.20 Different views on the central iridium oxalate moiety of $[\{\text{Ir}(\text{PPh}_3)_2\text{Cl}_2\}_2(\mu^2\text{-oxalato-}\kappa^4\text{O}^1,\text{O}^2:\text{O}^1',\text{O}^2')]$ with numbering. Thermal ellipsoids are at 50% probability. PPh_3 moieties are omitted for clarity.

A similar motif was isolated by *Crutchley* et al. They investigated an iridium complex by NMR and after several weeks they analysed the crystals from the NMR tube and found $[\text{Ir}(\text{PhPy})_2(\text{oxalate})]$.²⁹⁵ They suggested the formation of singlet oxygen which then reacted with the former ligand of the initial complex yielding the formation of oxalate. The complex could also be isolated by the deliberate reaction with oxalate. This reaction also works with oxamide yielding the corresponding μ^2 -oxamidato- κ^4 O,N:N',O' derivative.²⁹⁶ Similar mononuclear complexes were yielded by the reaction with carboxylates by the group of *Shiu*.²⁹⁷

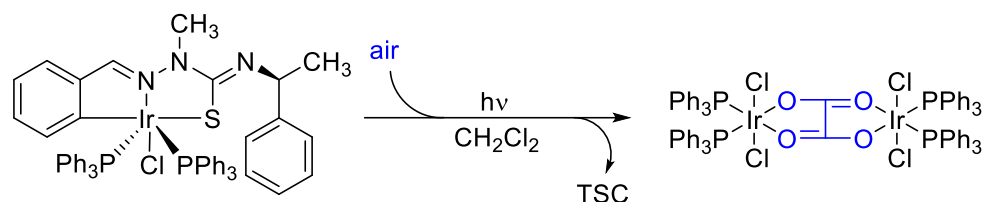
The reported complex from *Crutchley* can be compared with the herein isolated triphenylphosphine structure. It must be considered that *Crutchley's* complex consists of carbanionic donors in *trans* position to the oxalate oxygen, which has an influence on the Ir–O distance in the crystal structure. The distance is with 2.191(1) Å and 2.194(1) Å about 3% larger than the triphenyl derivative. The *trans* effect of the carbanions may cause this elongation. The C–C bond in the oxalate backbone is with 1.545(1) Å also about 3% larger than the triphenylphosphine structure with 1.495(1) Å.

The crystallographic data are given in Table 2.6. as mentioned, the distortion of the triphenyl phosphines yields bad refinement parameters for the structure.

Table 2.6 Crystallographic data of $[\{\text{Ir}(\text{PPh}_3)_2\text{Cl}_2\}_2(\mu^2\text{-oxalato-}\kappa^4\text{ O}^1,\text{O}^2:\text{O}^1',\text{O}^2')]$.

	$[\{\text{Ir}(\text{PPh}_3)_2\text{Cl}_2\}_2(\mu^2\text{-oxalato-}\kappa^4\text{ O}^1,\text{O}^2:\text{O}^1',\text{O}^2')]$
<i>Empirical formula</i>	C ₆₀ Cl ₄ Ir ₂ O ₄ P ₄ (1077.76 g/mol)
<i>Temperature/K</i>	100.0 K
<i>Crystal system</i>	monoclinic
<i>Space group</i>	C2/m
<i>a</i>	a = 20.404(9) Å
<i>b</i>	b = 12.969(5) Å β = 97.631(14)°
<i>c</i>	c = 13.271(6) Å
<i>Volume / Z</i>	3481(3) Å ³ / 4
<i>ρ_{calc}</i>	1.679 g/cm ³
<i>μ</i>	4.124 mm ⁻¹
<i>F(000)</i>	1732.0
<i>Radiation</i>	Mo Kα (λ = 0.71073 Å)
<i>2θ range for data collection/°</i>	4.028 to 51.334
<i>Index ranges</i>	24 ≤ h ≤ 24, -15 ≤ k ≤ 15, -15 ≤ l ≤ 15
<i>Reflections collected</i>	47285
<i>Independent reflections</i>	3324 [R _{int} = 0.1399, R _{sigma} = 0.0562]
<i>Data/restraints/parameters</i>	3324/15/375
<i>Goodness-of-fit on F²</i>	1.075
<i>Final R indexes [I_o > 2σ_{I_o}]</i>	R ₁ = 0.0463, wR ₂ = 0.1077
<i>Final R indexes [all data]</i>	R ₁ = 0.0571, wR ₂ = 0.1129
<i>Largest diff. peak/hole / e Å⁻³</i>	1.86/-2.16

Due to the conditions of the method, it is considerable that by photo redox reaction the thiosemicarbazone ligand is cleaved and CO_2 gets reduced to $\text{C}_2\text{O}_4^{2-}$. This explanation is viable since there are lots of iridium complexes known that are capable of reducing CO_2 at room temperature and atmospheric pressure.^{298, 299} Otherwise, it is also possible that the iridium centre produces singlet oxygen which reacts with the organic structures in solution forming oxalate. An exemplified reaction is shown in Scheme 2.12. It is unclear which pathway the reaction took.



Scheme 2.12 Unexpected formation of oxalate by Ir(III) thiosemicarbazones. Exemplified with $[\text{Ir}(\text{PPh}_3)_2(\text{bz}(\text{m})\text{TSCmB})\text{Cl}]$.

From several crystallization attempts IR-spectra were recorded. All of them showed characteristic frequencies for a μ^2 -oxalato- κ^4 unit indicating that the formation is not just a bad crystal structure. The IR spectra of the compounds, depicted in Figure 2.21, show strong bands at roughly 1000 cm^{-1} which is in the region typically for thiones indicating a possible decomposition in which the ligand stays intact.

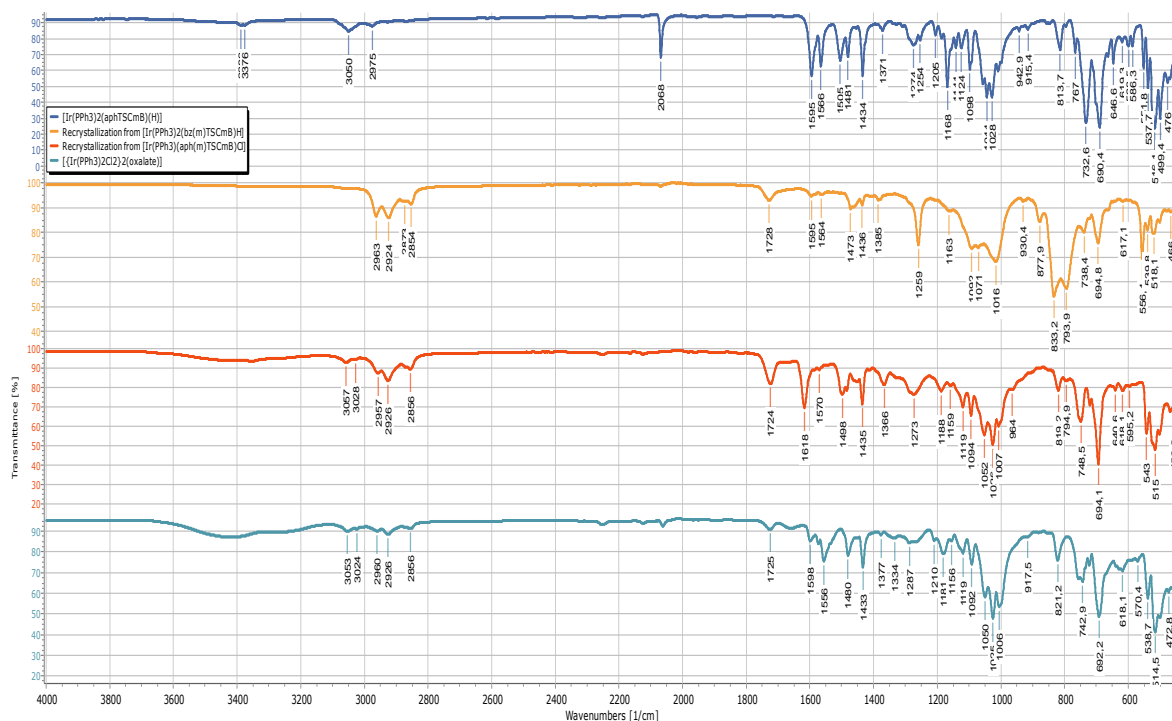


Figure 2.21 Stacked IR spectra of $[\text{Ir}(\text{PPh}_3)_2(\text{aphTSCmB})\text{H}]$ (blue trace), $[\text{Ir}(\text{PPh}_3)_2(\text{bz}(\text{m})\text{TSCmB})\text{H}]$ (yellow trace) and $[\text{Ir}(\text{PPh}_3)_2(\text{aph}(\text{m})\text{TSCmB})\text{Cl}]$ (red trace), as well as crystals of the oxalate species (turquoise trace). All spectra recorded from solids after “recrystallization” from DCM.

The region between 1350 cm⁻¹ and 1800 cm⁻¹ is depicted in the following Figure 2.22. This region is of special interest, since μ^2 -oxalato- κ^4 O¹,O²:O^{1'},O^{2'} containing structures show absorptions here.^{300, 301} It is possible that the band at 1724 cm⁻¹, result from asymmetric stretching frequencies of the C–O bonds. This may indicate that the crystal structure was not just a lucky crystal, but the whole structure turned into the corresponding oxalate. Additionally, the previously undetermined composition of [Ir(PPh₃)₂(aph(m)TSCmB)Cl] after the recrystallization process exhibits the oxalate frequency – so it is probably also the oxalate bridged dinuclear complex.

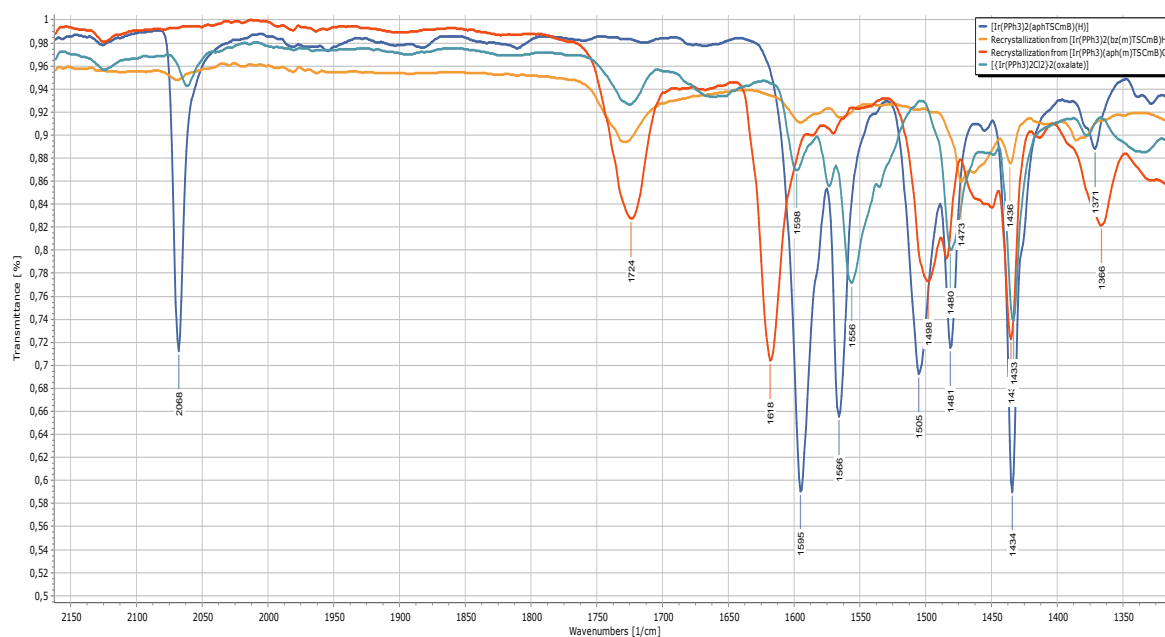


Figure 2.22 Superimposed excerpt of the IR spectra of [Ir(PPh₃)₂(aphTSCmB)](H) (blue trace), [Ir(PPh₃)₂(bz(m)TSCmB)](H) (yellow trace) and [Ir(PPh₃)₂(aph(m)TSCmB)Cl] (red trace). Crystals from the oxalate bridged species are in turquoise. All spectra recorded from solids after “recrystallization” from DCM.

When comparing the ¹H NMR spectra of the initial complex [Ir(PPh₃)₂(aphTSCmB)](H) with its corresponding ligand HaphTSCmB and the oxalate bridged structure, as done in Figure 2.23, it becomes obvious that the ligand is in no form detectable. This may indicate that it is not cleaved but in one way or another destroyed.

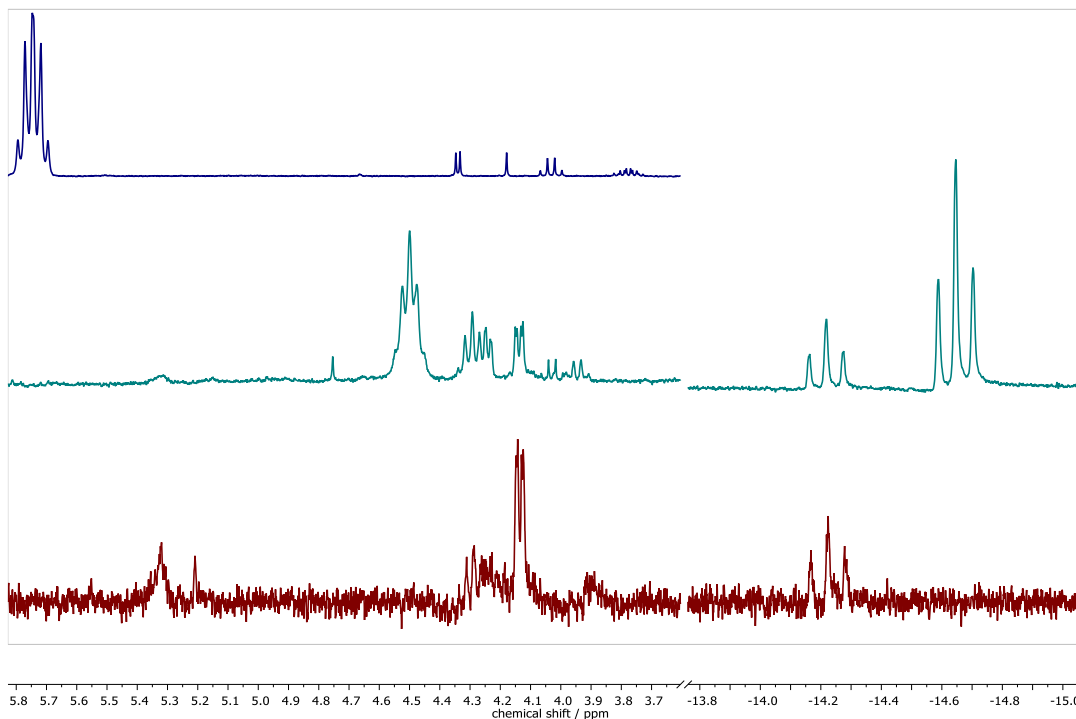


Figure 2.23 ¹H NMR spectra of HaphTSCmB (top), [Ir(PPh₃)₂(aphTSCmB)(H)] before (middle) and after “recrystallization” (bottom). All spectra recorded in DMSO-*d*₆ at 300 MHz.

2.3. Platinum complexes of the TSCmB and TSCLp series

2.3.1. The α -N heterocyclic TSCmB ligands

The previously synthesized TSCmB was used to gain access to tridentate monoanionic α -N heterocyclic TSCmB ligands by condensation with formyl pyridine, acetylpyridine and di-2-pyridyl ketone. The resulting ligands are HfpyTSCmB, HapyTSCmB and HdpyTSCmB, respectively. Their structures are shown in Chart 2.11.

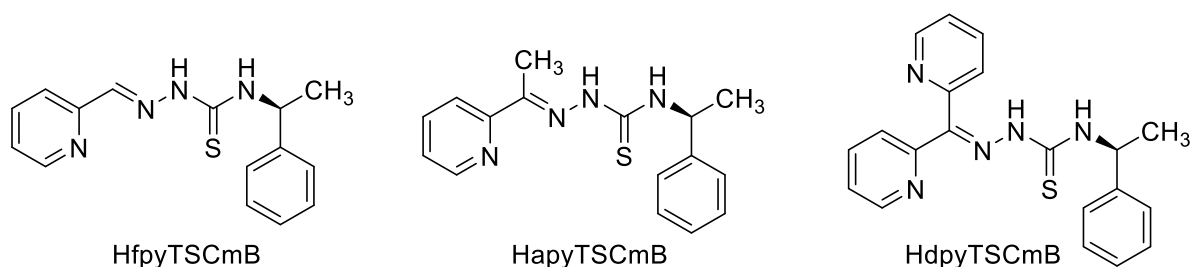


Chart 2.11 Molecular structures of pyridyl derived N^2N^2S donor systems.

As already stated in chapter 2.1, the three ligands could be investigated by SC-XRD revealing the highly similar geometries of the structures. Additionally, they were extensively analysed by NMR spectroscopy. In particular HdpyTSCmB, has been investigated with $^1H,^1H$ -TOCSY and $^1H,^1H$ -NOESY NMR showing the correlations within the molecule.

2.3.1.1. NMR spectroscopy

Starting with the $^1H,^1H$ -TOCSY NMR (Figure 2.24) the $N4$ substitution is good observable with the correlation from the methyl (1.55 ppm) the proton at the chiral carbon atom (5.7 ppm) to the secondary amine proton (9.1 ppm). The phenyl ring of the side chain forms a multiplett at 7.2 ppm with does not correlate to the other signals here. Additionally TOCSY allows to see the correlation at the two pyridine rings independently. Figure 2.24 shows the correlation of the pyridine rings. Both rings share signals, but they can be clearly assigned using the correlation spectra.

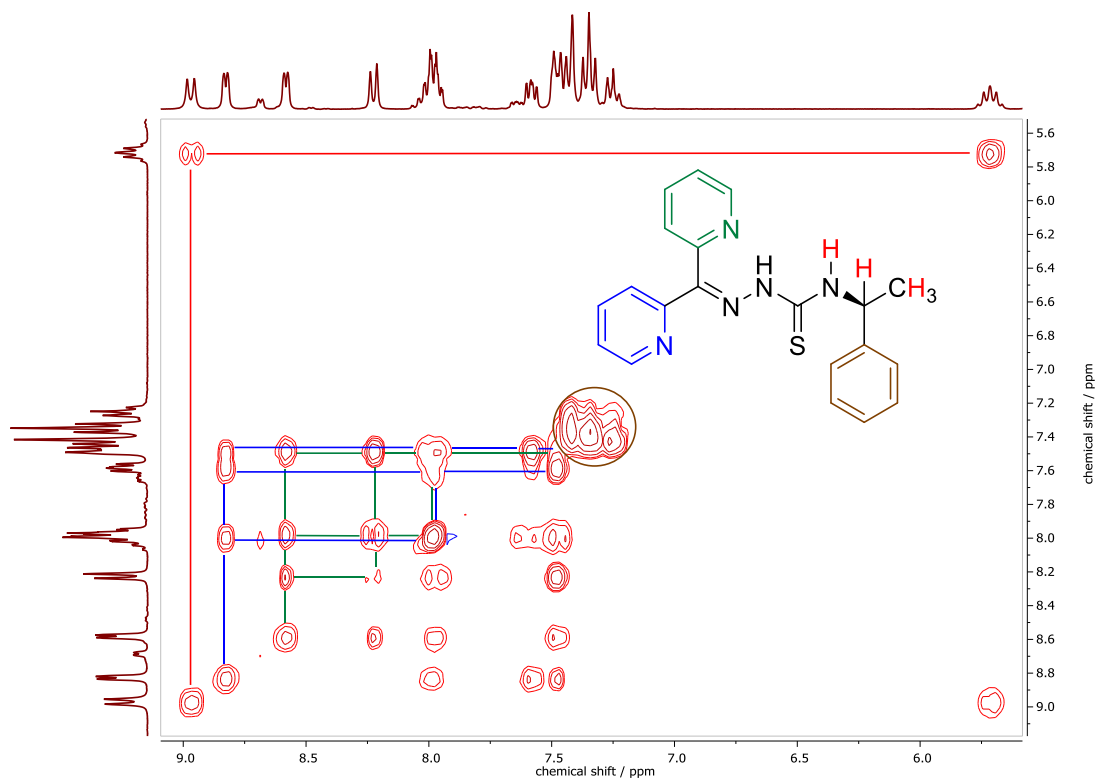


Figure 2.24 $^1\text{H},^1\text{H}$ TOCSY NMR spectrum of HdpyTSCmB in $\text{DMSO-}d_6$. Correlations of the pyridine rings are given in blue and green; the phenyl ring is given in bronze and the correlation between the amine to the chiral position is given in red.

The $^1\text{H},^1\text{H}$ NOESY spectroscopy shows the geometry of the molecule in solution (Figure 2.25). Here, the protons of the phenyl ring of the side group correlates to the amine as well as the protons of the methyl group and the chiral carbon. This is expected from the crystal structure.

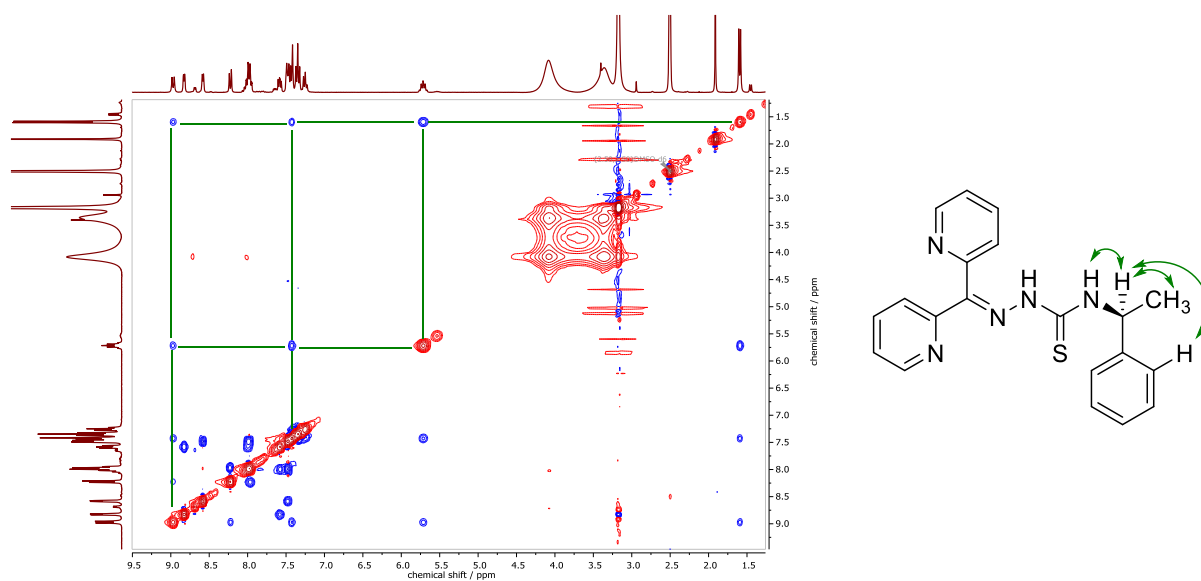


Figure 2.25 $^1\text{H},^1\text{H}$ NOESY NMR spectrum of HdpyTSCmB in $\text{DMSO-}d_6$. With NOESY correlations of the chiral side group in green

2.3.1.2. Electrochemical analysis

As shown in Chapter 2.1.4 Figure 2.5, the unsubstituted pyridine derived ligands are the easiest to reduce with an average reduction potential at about -1.5 V vs. ferrocene/ferrocenium. The neutral ligands exhibit a strong absorption at about 300 nm, which resembles a π - π^* transition. During the first reduction the intense absorption of the ligand decreases while another band at 400 nm emerges (Figure 2.26).

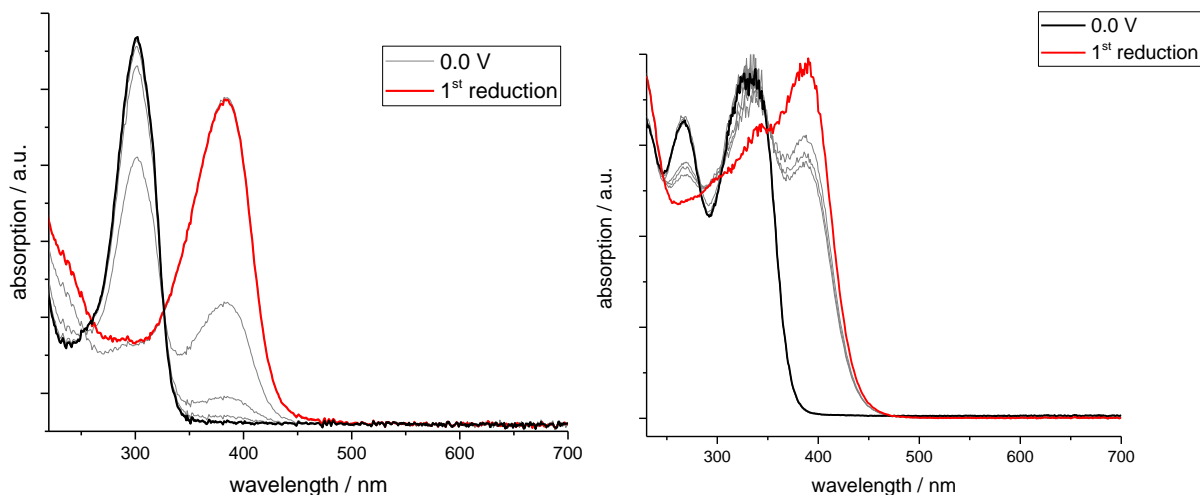
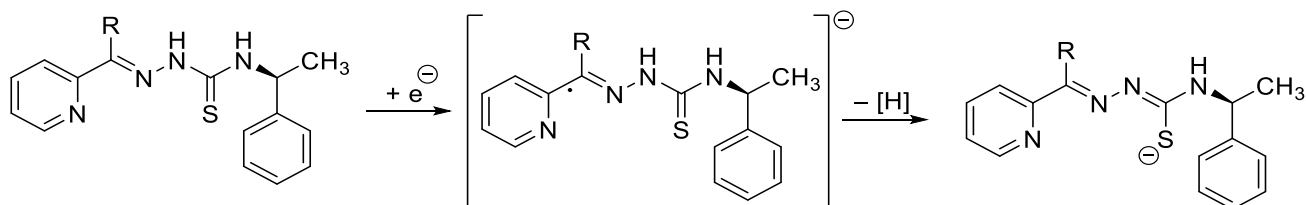


Figure 2.26 Spectroelectrochemical UV/Vis spectroscopy during the reduction of HapyTSMb (left) and HdpyTSCmB (right). Measurements were performed in 0.1 M Bu₄NPF₆ MeCN solution and 0.1 V increments.

These values are similar to the values determined for the benzylic thiosemicarbazones derivatives presented in the previous chapter. Thus, it can be concluded that the electrochemical process would be similarly to the unmethylated structures described previously. A possible EC-mechanism which would result in a bigger conjugated π -system and thus a shift to lower transition energies is shown in Scheme 2.13.



Scheme 2.13 Suggested EC-mechanism during the first reduction of pyridine derived TSC.

The UV/Vis upon oxidation, as shown in Figure 2.27, results in a shift to lower energies as well, but for HapyTSCmB and HdpyTSCmB it shifts to 370 nm. The high similarity in the shift may result from a similar electronic structure of the electrochemically resulted structure – of course with a different charge.

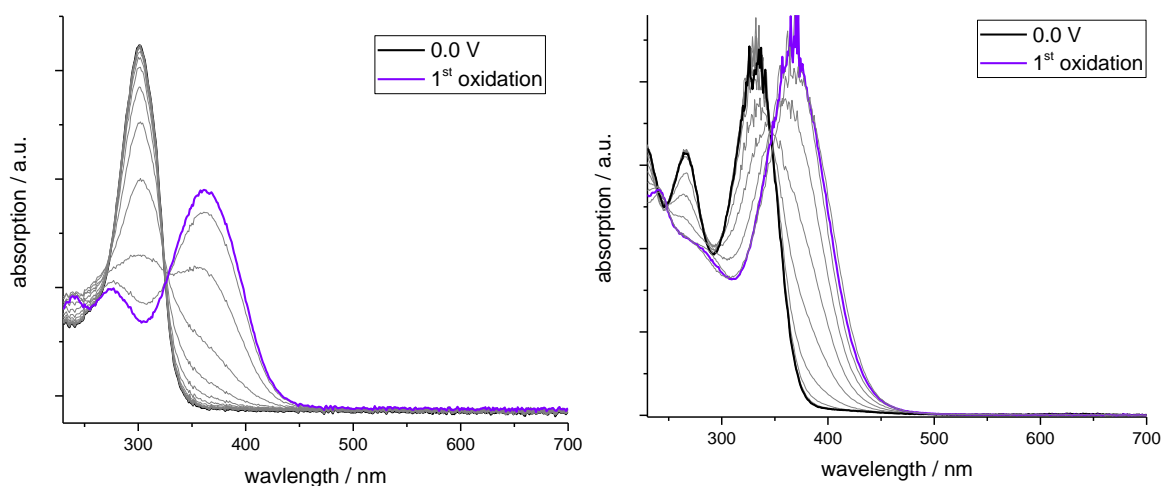


Figure 2.27 Spectroelectrochemical UV/Vis spectroscopy during the oxidation of HapyTSCmB (left) and HdpyTSCmB (right). Measurements were performed in 0.1 M Bu₄NPF₆ MeCN solution and 0.1 V increments.

2.3.2. Chlorido platinum complexes with TSCmB ligands

The previously synthesized ligands were reacted with the Pt(II) precursor K₂[PtCl₄] to gain the corresponding platinum chlorido complexes, which are shown in Chart 2.12. The reaction was carried out in water MeCN (1:1) mixtures with equimolar amounts of the reagents. Reactions with *cis*-[Pt(NH₃)₂Cl₂] and *cis*-[Pt(MeCN)₂Cl₂] as precursors yielded the same complexes in lower yields. Using HdpyTSCmB as ligand, K₂[PtCl₄] yielded on average 80% of the complex [Pt(dpyTSCmB)Cl], which is considerably higher than the yields of cisplatin at 70% and *cis*-[Pt(MeCN)₂Cl₂] at 65%.

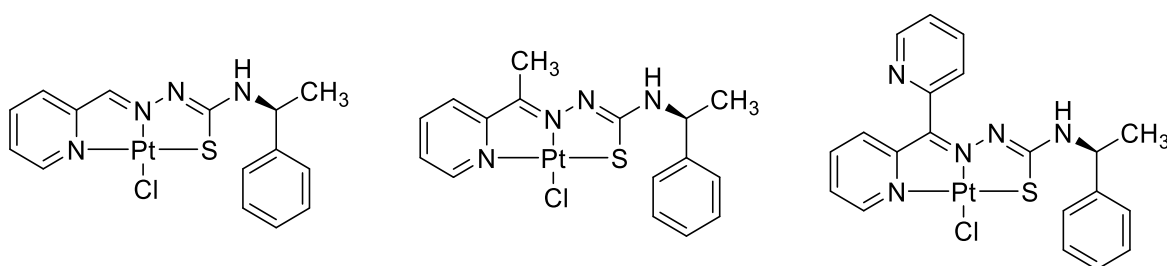


Chart 2.12 Molecular structures of HfpyTSCmB, HapyTSCmB and HdpyTSCmB.

For the dipyridyl derived HdpyTSCmB it was also tested whether an excess of Pt(II) yields a diplatinated complex as shown in Figure 2.28. A similar complex with Pd(II) centres has been reported by *Bakir* and *Lawrence* in 2017.³⁰² Despite using an excess K₂[PtCl₄], there were no findings suggesting the formation of such a complex in our syntheses.

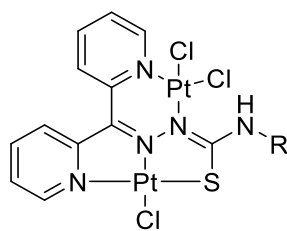


Figure 2.28 Molecular structure of a dipyridyl ketone derived thiosemicarbazone.

2.3.2.1. Crystal structure and Hirshfeld analysis of [Pt(apyTSCmB)Cl]

The molecular structure of [Pt(apyTSCmB)Cl] is shown in Figure 2.29 and the crystallographic parameters are given in Table 2.7. The coordination sphere at the Pt(II) centre appears to be distorted square planar.

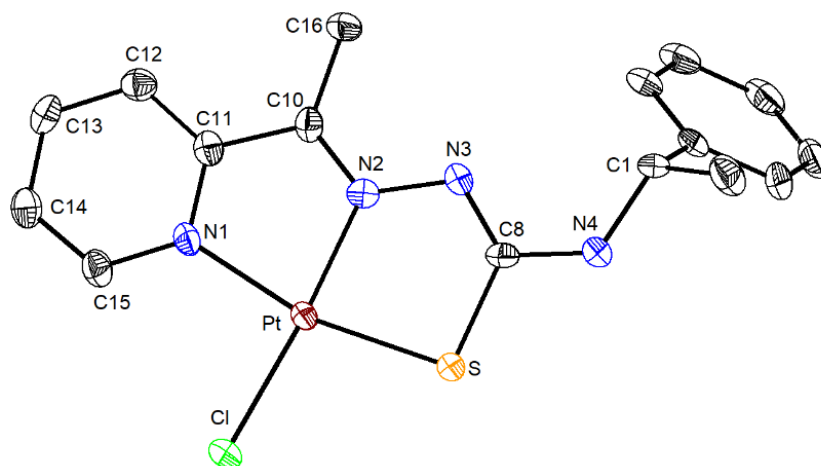


Figure 2.29 Molecular structure of [Pt(apyTSCmB)Cl]. Atoms are shown at 50% probability and hydrogen atoms were omitted for clarity.

The Pt(II) centre is coordinated by the N²N¹S donor structure of a monoanionic thiosemicarbazone and the distorted square planar coordination sphere is complete by a chloride coligand. The structure crystallizes in the orthorhombic space group $P2_12_12_1$, a space group which is attributed to the *Sohnke* groups. *Sohnke* groups are a type of non-enantiogenic groups in which only one type of chiral molecules is able to crystallize. Given the molecular structure of [Pt(apyTSCmB)Cl] it is clearly visible that the overall chirality is still the same of the bought methylbenzyl amine.

Table 2.7 Crystallographic data of [Pt(apyTSCmB)Cl].

	[Pt(apyTSCmB)Cl]
Empirical formula / Formula weight	C ₁₆ H ₁₆ ClN ₃ PtS (526.93 g/mol)
Temperature	100.0 K
Crystal system / Space group	orthorhombic P2 ₁ 2 ₁ 2 ₁
a/Å	7.2536(10)
b/Å	10.2592(14)
c/Å	46.004(6)
Volume/Å ³ / Z	3423.4(8) / 8
ρ_{calc} /cm ³	2.0446
μ /mm ⁻¹	17.934
F(000)	1983.1
Radiation	Cu K α (λ = 1.54178)
2 θ range for data collection/°	7.68 to 144.82
Index ranges	-8 ≤ h ≤ 8, -12 ≤ k ≤ 12, -56 ≤ l ≤ 54
Reflections collected	35614
Independent reflections	6735 [R _{int} = 0.0502, R _{sigma} = 0.0378]
Data/restraints/parameters	6735/0/419
Goodness-of-fit on F ²	1.198
Final R indexes [I ₀ > 2 σ (I)]	R ₁ = 0.0251, wR ₂ = 0.0624
Final R indexes [all data]	R ₁ = 0.0262, wR ₂ = 0.0624
Largest diff. peak/hole / e Å ⁻³	1.12/-1.50
Flack parameter	0.153(12)

The packing of the crystal, depicted in Figure 2.30, shows a slight stacking along the crystallographic a-axis. Herein, the central ring structures overlap quite well with a pyridine ring being close to the (Pt-N-N-C-S) five membered rings of the next molecule.

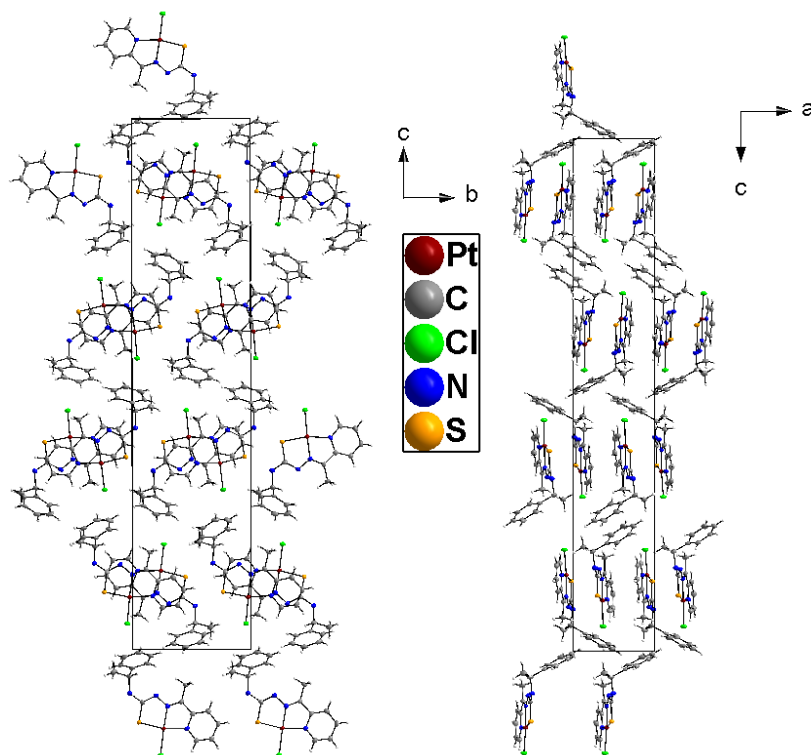


Figure 2.31 Crystal structure of [Pt(apyTSCmB)Cl] along the crystallographic a-axis (left) and b-axis (right).

Hirshfeld analysis of the molecule, shown in Figure 2.32, revealed further intermolecular interactions with the strong ones at the thiolate. The rest of the Hirshfeld surface seems to be very homogenous.

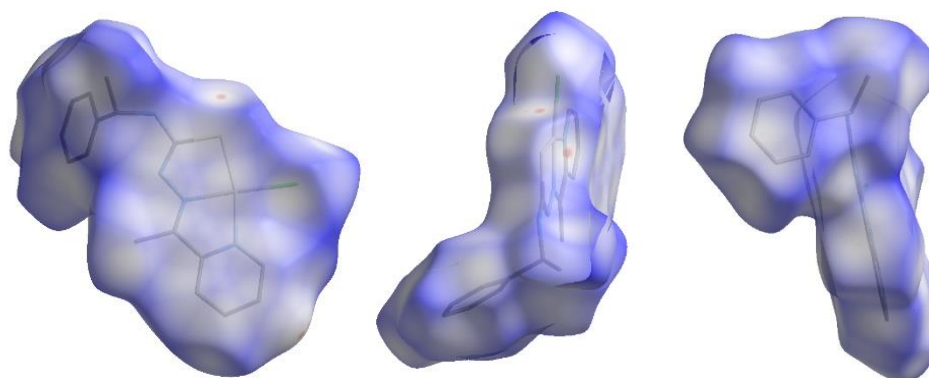


Figure 2.32 Hirshfeld surface of [Pt(apyTSCmB)Cl] showing only the promolecule along the crystallographic a-, b- and c-axis.

For a closer look into the thiolate interactions the neighbouring molecules are generated, as done in Figure 2.33. This reveals an interaction between the thiolate and the methyl moieties of the *N4* derivatized sidechains as well as the neighbouring pyridines. Also, weak interactions of two benzyl moieties and one methyl group to the chloride coligand lead to small contributions in the Hirshfeld surface.

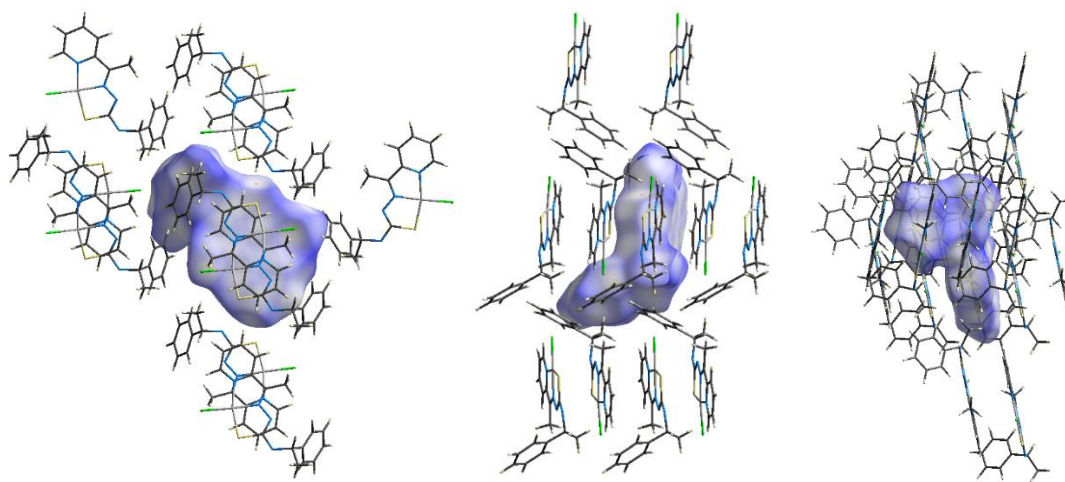


Figure 2.33 Hirshfeld surface of [Pt(apyTSCmB)Cl] including the surrounding molecules shown along the crystallographic a-, b- and c-axis.

A more detailed description of the interactions is generated by the fingerprint plots, which are shown in Figure 2.34. The shortest distances are between hydrogen and hydrogen, but the distances to sulphur, chlorine and carbon stays short as well. The interaction of the thiolate is quite intense even though the thiolate is just an edge of the surface compared to the thorn like extension of the coligand.

The main contributors of close hydrogen-hydrogen contacts are interactions between the aryl moieties of the structures, smaller contributions are due to close contacts between the acetyl and benzyl structures. The carbon carbon interactions are smaller due to the high hydrogen content. The combination suggests weak hydrogen- π interactions throughout the crystal combining acetyl-benzyl and pyridine-benzyl interactions with benzyl as π donor. Further benzyl-benzyl hydrogen interactions lead to a fixation of the rotatable group.

The mentioned thiolate interactions with hydrogen also play big role in the overall Hirshfeld surface being the biggest contributor for sulphur with only minor contributions to other atoms.

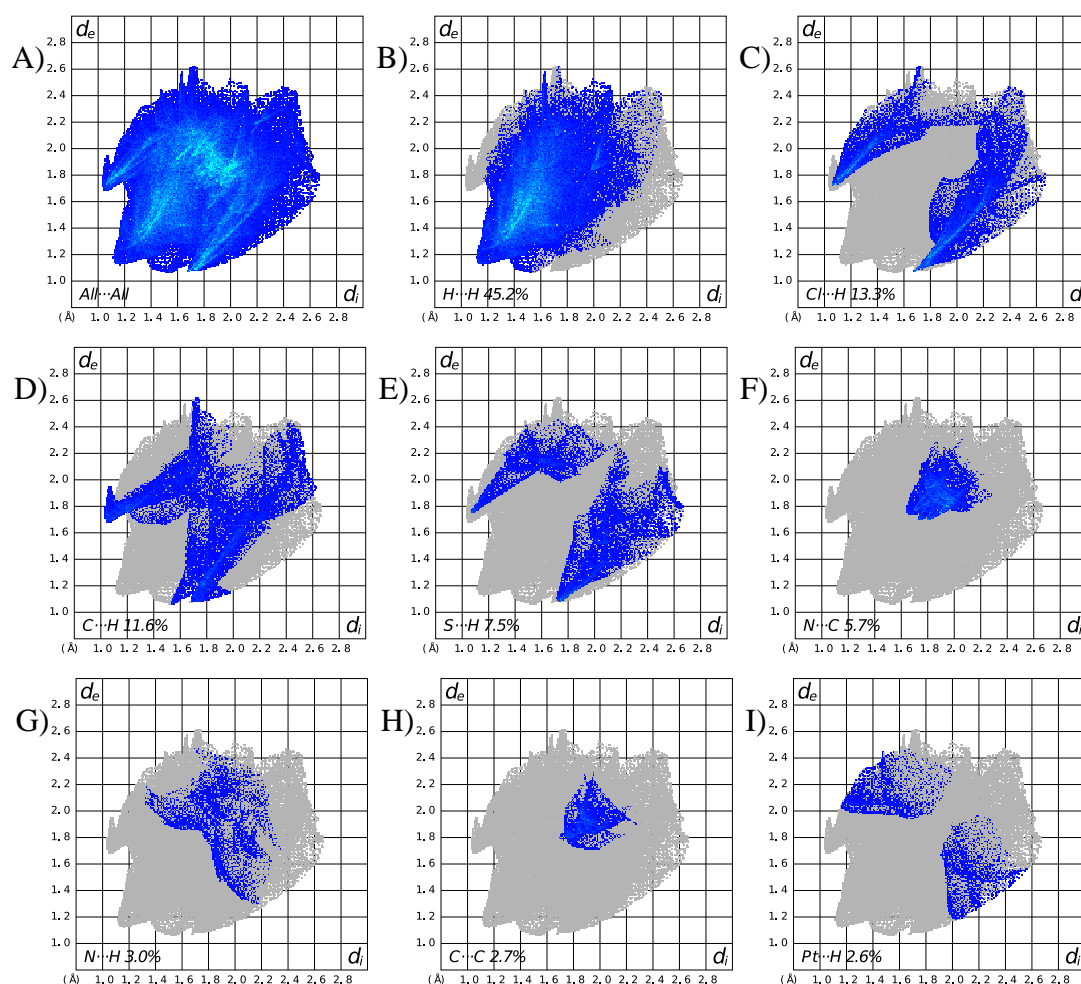


Figure 2.34 Fingerprint plots of [Pt(apYTSCmB)Cl]. A) showing the unfiltered fingerprint plot. B)-I) element combinations with close contacts were highlighted. Combinations without close contacts and contributions below 2.5% to the Hirshfeld surface were omitted. B) H...H, C) Cl...H/H...Cl, D) C...H/H...C E) S...H/H...S, F) N...C/C...N G) N...H/H...N, H) C...C, I) Pt...H/H...Pt.

The coordination sphere of the platinum centre was also investigated by Hirshfeld surface analysis as shown in Figure 2.35. The square planar coordination mode is very well represented by the intense red fields in the d_{norm} representation. But the z-

axis of the platinum centre reveals a slight interaction indicated by a light blue to white colour.

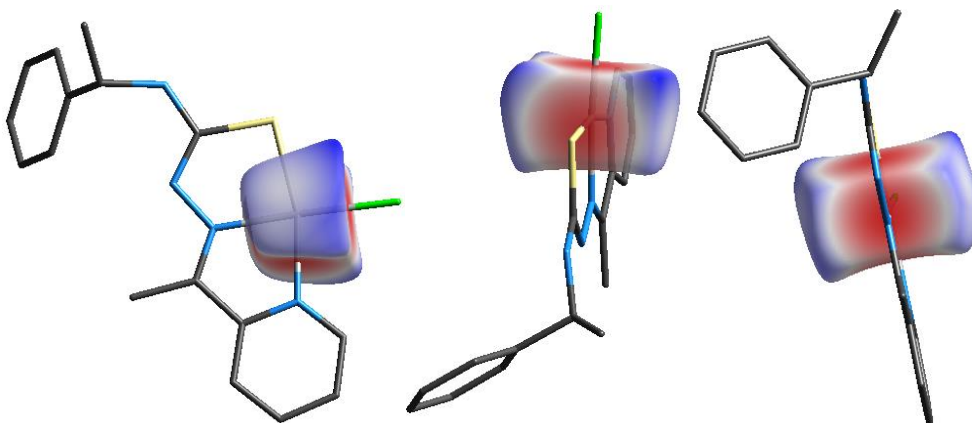


Figure 2.35 Hirshfeld surface of the platinum centre in [Pt(apyTSCmB)Cl] along the crystallographic a-, b- and c-axis.

The fingerprint plots, depicted in Figure 2.36, help to understand the more distant interactions. The deep blue colour of the Hirshfeld surface is the platinum-hydrogen interaction to the nearest methyl bridge as well as a further pyridine moiety. The closer contact in the z-axis is due to the interaction with a pyridine ring and its carbon atoms at roughly 3.5 Å.

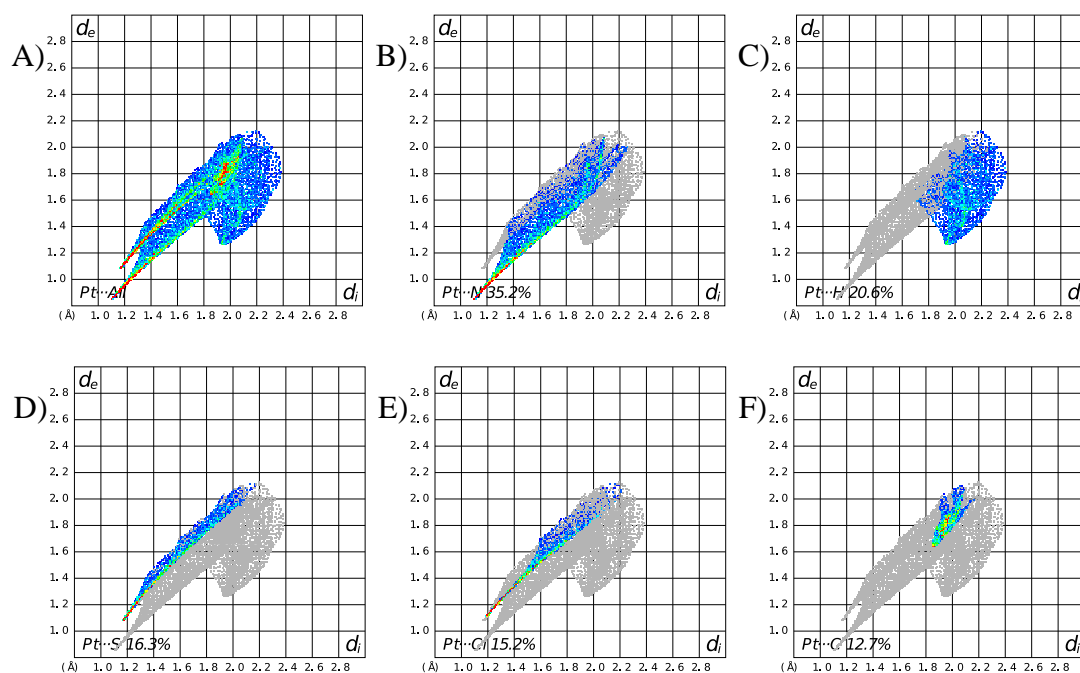
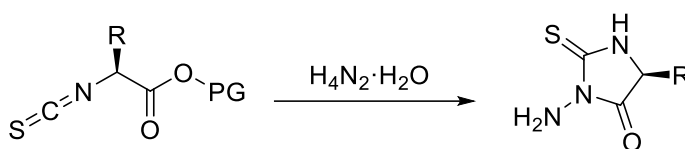


Figure 2.36 Fingerprint plots of the Pt(II) coordination sphere in [Pt(apyTSCmB)Cl]. A) showing the unfiltered fingerprint plot. B)-F) element combinations with close contacts were highlighted. Combinations without close contacts were omitted. B) Pt...N/N...Pt, C) Pt...H/H...Pt, D) Pt...S/S...Pt E) Pt...Cl/Cl...Pt, F) Pt...C/C...Pt.

2.3.3.Synthesis of the TSCLp series

As mentioned in the introduction, platinum isotopes are upcoming new nuclei with uses in nuclear medicine. But to use these isotopes in a human body, the complexes need to be characterized carefully. Since the amino acids and later the peptides are hard to calculate and characterize with wet chemical and electrochemical analytical methods. A smaller suitable model complex should be synthesized, and the previously mentioned TSCmB series seems like a good choice since it is a small chiral moiety without functional groups that may distort measurements.

On the other hand, the synthesis of amino acid derivatives was fiddly. The derivatization at the alpha amino acid was subject of earlier thesis of the work group.³⁰³ If the protection group of the acid function was not correctly chosen, the addition of hydrazine yielded thiohydantoin of the amino acids. The cyclization shown in Scheme 2.14 underwent with methylated carboxylic acids.

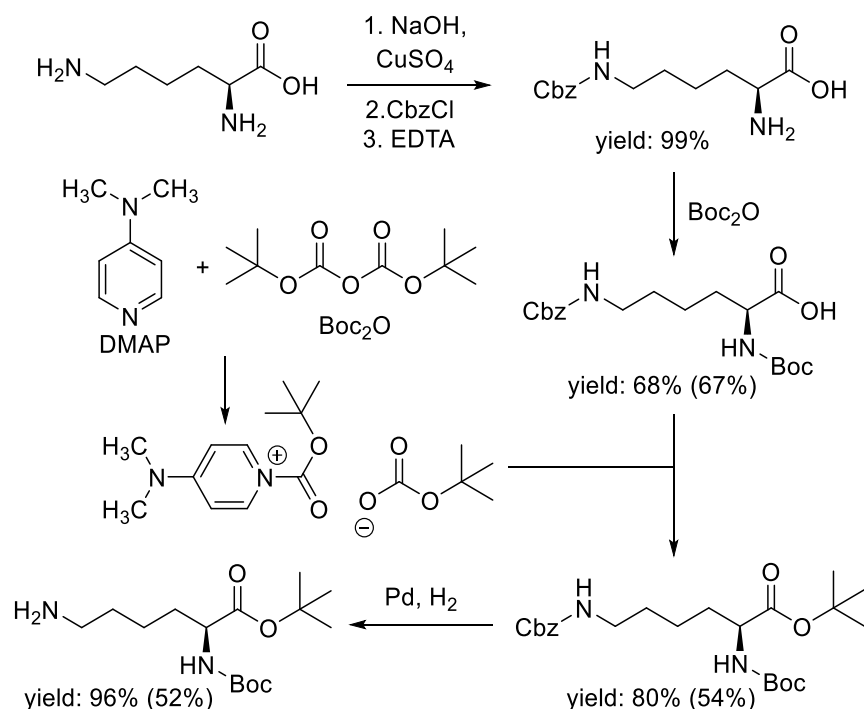


Scheme 2.14 Cyclization of a primary isothiocyanate amino acid with hydrazine.

These *N*₂,*N*₄ substituted thiosemicarbazides are not suitable for the radionuclide peptide approach since both amino acid functionalization are blocked. Lysine on the other hand has a terminal primary amine in its side chain. Turning this into a thiosemicarbazide would allow the amino acid to be part of a peptide chain not just an endpoint.

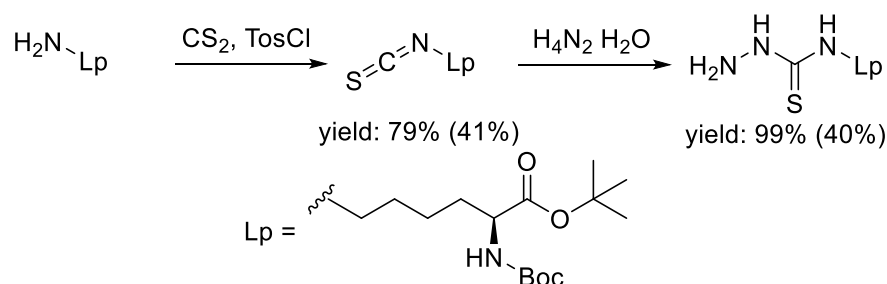
The synthesis of those thiosemicarbazides were performed by starting from lysine hydrochloride and synthesizing *N*α-Boc-L-lysine tertbutyl ester. This leaves the amino acid group free for the functionalization into an isothiocyanate and later a thiosemicarbazone.

The protected lysine is synthesized over 4 steps, starting with the benzyloxy carbonyl (Cbz) protection of the terminal amino acid. This is possible since the procedure starts by coordinating Cu(II) to the amino acid group making it more inert than the terminal amine. After a decomplexation with EDTA, the amine is protected with Boc₂O and finally the carboxyl group is protected with a tert-butyl group. The last protection is performed by an activated ester. After every group is protected the benzylic function is removed under reductive hydrogenation with 5% Pd/C leaving the desired amino acid. The reaction pathway is shown in Scheme 2.15.



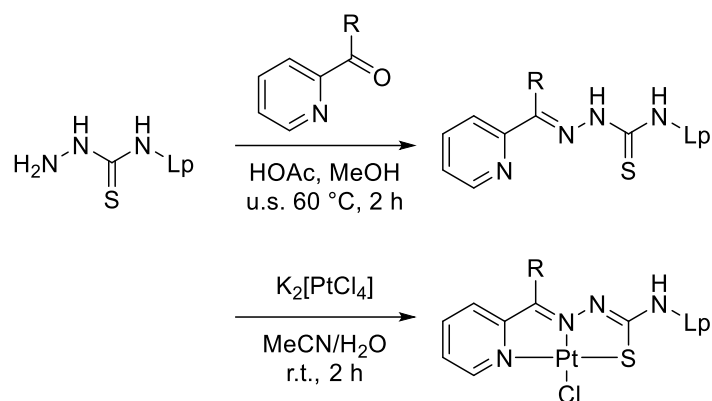
Scheme 2.15 Synthesis of the protected lysine with a free primary amine. Yields are given for every reaction step and total reaction yield in brackets.

The primary amine could be turned into a thiosemicarbazide as described in the previous chapters. Scheme 2.16 shows the reaction pathways from the amine to the protected lysine thiosemicarbazide with the yields of the reaction and the total synthesis yield. The thiosemicarbazide can be isolated in good yields of 40% over 6 steps.



Scheme 2.16 Synthesis of a thiosemicarbazide from protected lysine TSCLp. Total reaction yields are given in brackets.

From these thiosemicarbazides, the corresponding lysine derived thiosemicarbazones can be synthesized. The method used was the same as previously described, an ultra-sonic assisted condensation. The resulted ligands react with platinum sources to form their corresponding complexes as shown in Scheme 2.17. These complexes were tested comparatively with the model system TSCmB which was described previously.



Scheme 2.17 Synthesis route for the TSCLp derived thiosemicarbazones and their chlorido platinum complexes.

2.3.4. Comparison of Pt(II) thiosemicarbazones

As mentioned, the TSCLp and TSCmB series yielded 6 ligands used for platinum complexes which are named as shown in Chart 2.13.

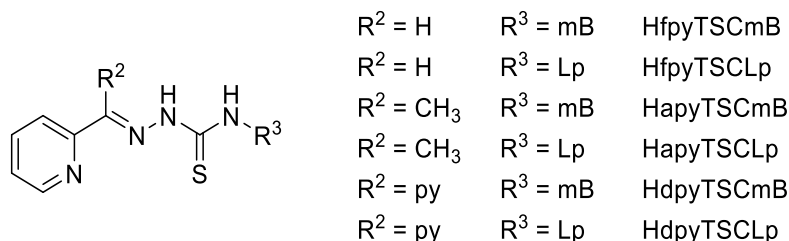
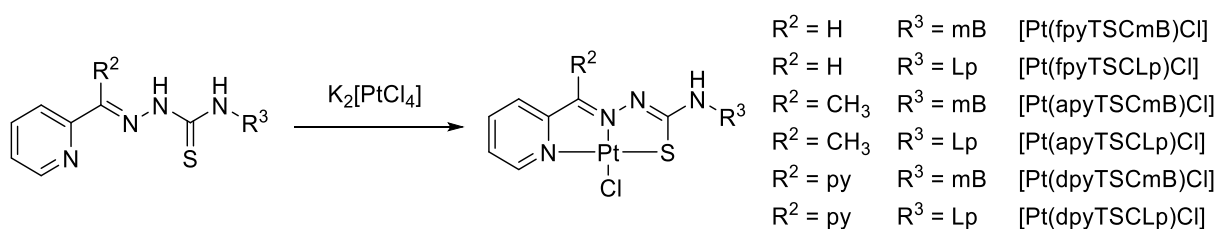


Chart 2.13 Naming Scheme for pyridine based thiosemicarbazones.

The reaction with a Pt(II) source like $\text{K}_2[\text{PtCl}_4]$ or $\text{PtCl}_2(\text{MeCN})_2$ yielding the corresponding platinum complex with a chlorido coligand bound tridentate to a deprotonated thiosemicarbazone. The reaction and naming scheme of the complexes is depicted in Scheme 2.18.



Scheme 2.18 Synthesis of Platinum complexes and their naming scheme.

Those complexes were analysed by various methods and their characteristics were compared using UV/Vis (chapter 2.3.4.1), NMR spectroscopy (chapter 2.3.4.2) and their electrochemical features as well as DFT calculations were compared (chapter 2.3.4.3).

2.3.4.1. UV/Vis spectroscopy

These structures were compared regarding their optical and electrochemical features. In Figure 2.37 the UV/vis spectra of HapyTSClP and [Pt(apyTSClP)Cl] measured in MeCN are shown. It has similar features comparable to the other ligand – complex systems. The ligands usually have a strong absorption between 300 and 400 nm corresponding to a $\pi-\pi^*$ transition. The $\pi-\pi^*$ transitions consist of 3 bands which are bathochromic shifted. The strong and broad band at 550 nm is the MLCT transition which gives the complexes their red colour. In Table 2.8, an overview of the absorption properties of the ligands and their corresponding chloro Pt(II) complexes is listed.

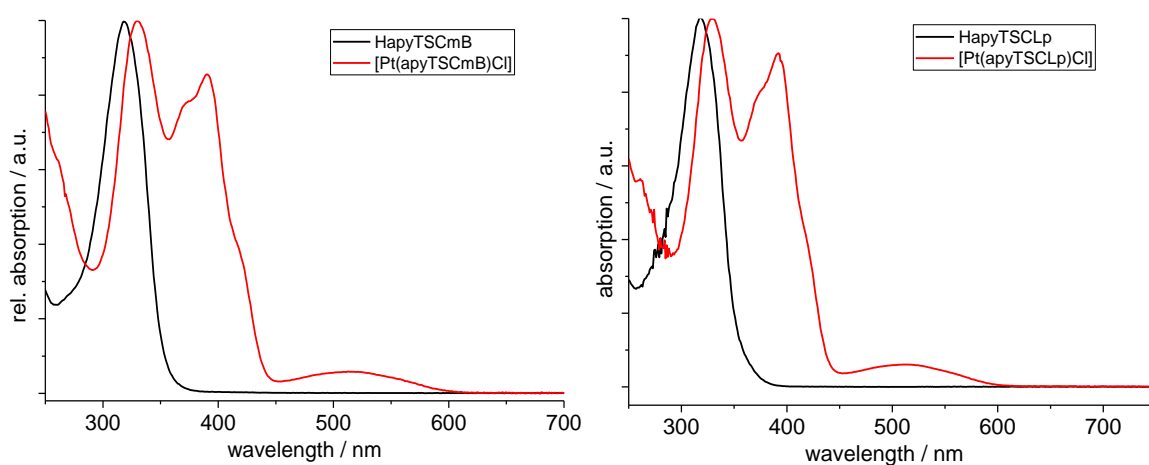


Figure 2.37 left: UV-vis absorption spectra of HapyTSCmB (black) and [Pt(apyTSCmB)Cl] (red), right: HapyTSClP (black) and [Pt(apyTSClP)Cl] (red) all spectra recorded in MeCN.

Table 2.8 UV-vis absorption data of selected TSC protoligands and Pt complexes.^a

protoligand	HfpyTSCmB	HfpyTSClP	HapyTSCmB	HapyTSClP	HdpyTSCmB	HdpyTSClP
1	316 [14505]	299 [15928]	319 [25604]	318 [25610]	275 [13171]	272 [17444]
2					339 [17809]	351 [15498]
complexes	[Pt(fpyTSCmB)Cl]	[Pt(fpyTSClP)Cl]	[Pt(apyTSCmB)Cl]	[Pt(apyTSClP)Cl]	[Pt(dpyTSCmB)Cl]	[Pt(dpyTSClP)Cl]
1	244 [14892]	247 [13518]	330 [18465]	329 [18347]	277 [24199]	268 [17685]
2	307 [13720]	290 [13451]	372 [12423]	372 [12847]	391 [20223]	324 [15802]
3	380 [16064]	379 [12463]	391 [16342]	391 [16366]	526 [1492]	403 [19747]
4	511 [983]	512 [676]	418 [7743]	419 [7695]		533 [1624]
5			515 [1463]	515 [1440]		

^aMeasured in MeCN, wavelengths λ in nm, extinction coefficients in brackets [L/(mol·cm)].

2.3.4.2. NMR spectroscopy

The structures could be characterized by ESI(+)-MS and ¹H NMR. The protected lysine derivatives were also soluble enough to perform ¹⁹⁵Pt,¹H HMBC NMR experiments. For [Pt(apyTSClP)Cl] ³J_{Pt,H} and ⁴J_{Pt,H} couplings are visible (Figure 2.38). Other platinum complexes exhibit a similar shift for ¹⁹⁵Pt of around –3100 ppm.³⁰⁴ homoleptic bis thiosemicarbazone complexes of platinum, e.g. [Pt(L)₂], exhibit a shift of around –3300 ppm and –3600 ppm, depending on their isomerism.^{305, 306}

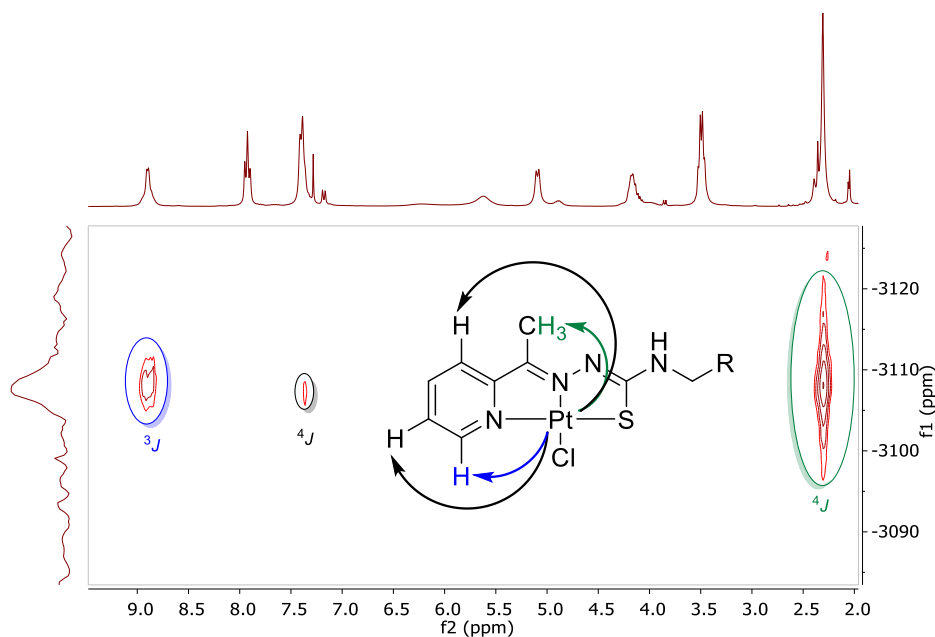
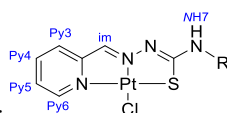


Figure 2.38 $^{195}\text{Pt}, ^1\text{H}$ HMBC NMR of $[\text{Pt}(\text{apyTSClP})\text{Cl}]$ in $\text{DMSO-}d_6$. The coupling is indicated with coloured arrows.

Comparing the six complexes in their ^1H NMR spectra the influence of the $N4$ substituents on the pyridine imine function is considerably small. The only expected deviation shows the $N4$ proton. For the methyl benzyl moiety, the shift is above 8.7 ppm whereas the lysine derivatives exhibit a shift of about 7 ppm. Furthermore, the influence of the imine functionalization is detectable. The $N4$ proton shifts about 0.3 ppm when comparing the methyl and pyridinyl derivatives. The formyl structure exhibits a shift in the middle of both. Similarity is the behaviour of the proton at the position Py4. As shown in Figure 2.38, here is a strong $^3J_{\text{Pt,H}}$ coupling, and it seems to be influenced by the imine functionality as shown in Table 2.9.

Table 2.9 Selected NMR data of Pt TSC complexes.^a

	$[\text{Pt}(\text{fpyTSC-R})\text{Cl}]$		$[\text{Pt}(\text{apyTSC-R})\text{Cl}]$		$[\text{Pt}(\text{dpyTSC-R})\text{Cl}]$	
R	mB	Lp	mB	Lp	mB	Lp
Py3	7.25 (dd)	8.30 (d)	7.68 (d)	7.78 (d)	7.45 (d)	7.85 (d)
Py4	8.13 (t)	8.15 (t)	8.16 (t)	7.90 (t)	8.06 (t)	8.08 (td)
Py5	7.70 (t)	7.71 (t)	7.74 (d)	7.69 (t)	7.70 (t)	7.53 (m)
Py6	8.70 (d)	8.72 (d)	8.76 (d)	8.88 (d)	8.84 (d)	8.90 (d)
	$^3J_{\text{Pt,H}} = 27 \text{ Hz}$	$^3J_{\text{Pt,H}} = 24 \text{ Hz}$	$^3J_{\text{Pt,H}} = 16 \text{ Hz}$	$^3J_{\text{Pt,H}} = 14 \text{ Hz}$	$^3J_{\text{Pt,H}} = 27 \text{ Hz}$	$^3J_{\text{Pt,H}} = 31 \text{ Hz}$
H _{im}	8.35 (s)	8.40 (s)				
	$^3J_{\text{Pt,H}} = 12 \text{ Hz}$	$^3J_{\text{Pt,H}} = 12 \text{ Hz}$				
CH _{3im}			2.26 (s)	2.30 (s)		
Py'3					7.36 (d)	7.43 (d)
Py'4					7.97 (t)	7.98 (td)
Py'5					7.60 (dd)	7.73 (td)
Py'6					8.72 (d)	8.75 (d)
NH7	8.87 (d)	7.08 (d)	8.76 (d)	7.07 (d)	9.02 (d)	7.06 (d)



^a Chemical shifts in ppm, nomenclature:

2.3.4.3. Electrochemical analysis of the platinum complexes

The electrochemical behaviour of the platinum complexes was measured with cyclic voltammetry. In Figure 2.39, the CV for [Pt(fpyTSCmB)Cl] and [Pt(apyTSCmB)Cl] are shown. Here it can be seen that the general structure of the waves remains similar. The first reduction is reversible while the other processes are irreversible.

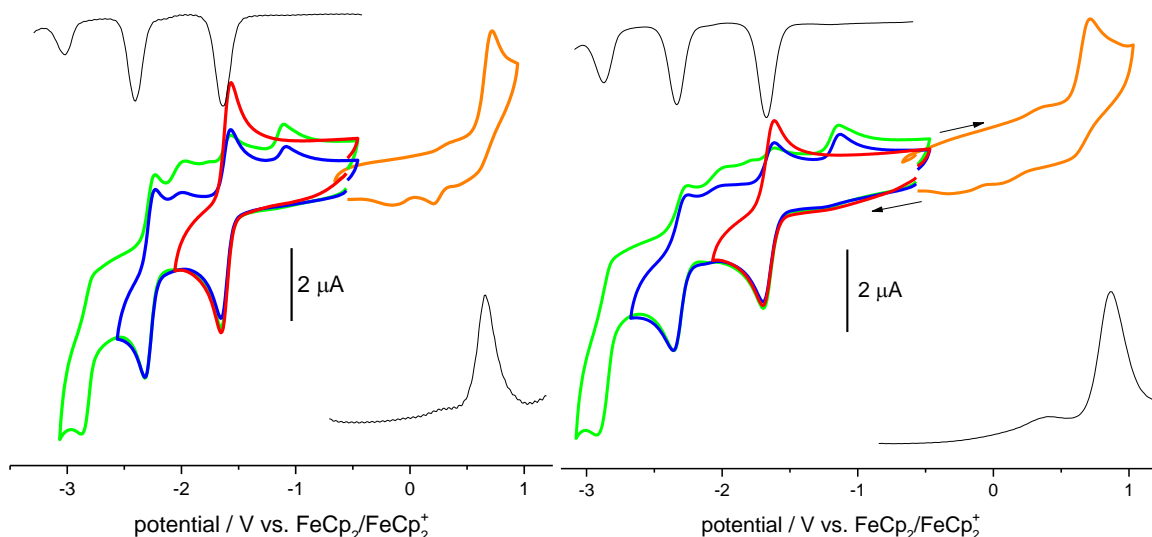


Figure 2.39 Cyclic voltammograms of [Pt(apyTSCmB)Cl] (left) [Pt(fpyTSCmB)Cl] (right) in 0.1 M nBu₄NPF₆/MeCN solution at 100 mV/s scan rate. Square wave measurements in black.

By comparing the electrochemical data for reductions and oxidations it becomes clear that the substitution at the *N4* position does not affect the electrochemical behaviour of the complex whereas the R² position, which is determined by the initial carbonyl used in the condensation reaction, has a big influence on the potentials. The data from the cyclic voltammetry is listed in Table 2.10. The data show that the aldehyde derived fpyTSC structures are reduced most easily but are hardest to be oxidized. The acetylpyridine derived apyTSC series have the lowest reduction potential and are the easiest structures to be oxidized.

Table 2.10 Electrochemical data for the platinum complexes [Pt(fpyTSCmB)Cl], [Pt(fpyTSClp)Cl], [Pt(apyTSCmB)Cl], [Pt(apyTSClp)Cl], [Pt(dpyTSCmB)Cl] and [Pt(dpyTSClp)Cl].^a

	<i>E</i> _{pa} Ox	<i>E</i> _{1/2} Red1	<i>E</i> _{1/2} Red2	<i>E</i> _{pc} Red3	Δ <i>E</i> (Red1-Red2)
[Pt(fpyTSCmB)Cl]	0.82	-1.50	-2.19	-2.83	0.69
[Pt(fpyTSClp)Cl]	0.81	-1.50	-2.20	-2.86	0.70
[Pt(apyTSCmB)Cl]	0.71	-1.60	-2.25	-2.90	0.65
[Pt(apyTSClp)Cl]	0.72	-1.65	-2.30	-2.92	0.65
[Pt(dpyTSCmB)Cl]	0.74	-1.51	-2.08	-2.90	0.57
[Pt(dpyTSClp)Cl]	0.74	-1.50	-2.10	-	0.60

^aMeasured in 0.1 M Bu₄NPF₆/MeCN at 100 mV/s. Potentials *E* in V, referenced to the redox pair FeCp₂⁺/FeCp₂.

Performing spectroelectrochemical analyses, we were able to detect the first reduction at the pyridine imine moiety (Figure 2.40). This is visible in the SEC-UV/Vis measurements of [Pt(dpyTSCmB)Cl] during the first reduction where the former $\pi-\pi^*$ transition at 380 nm decreases and a new, very intense band can be detected at 480 nm. By measuring SEC-EPR from a glassy frozen solution a narrow signal with g_{\perp} and g_{\parallel} values at 2.0066 and 2.0079 could be detected. The second reduction shows, during SEC-UV/Vis, broad absorption at 600 nm and even more red shifted. This may indicate the reduction at a metal centre.

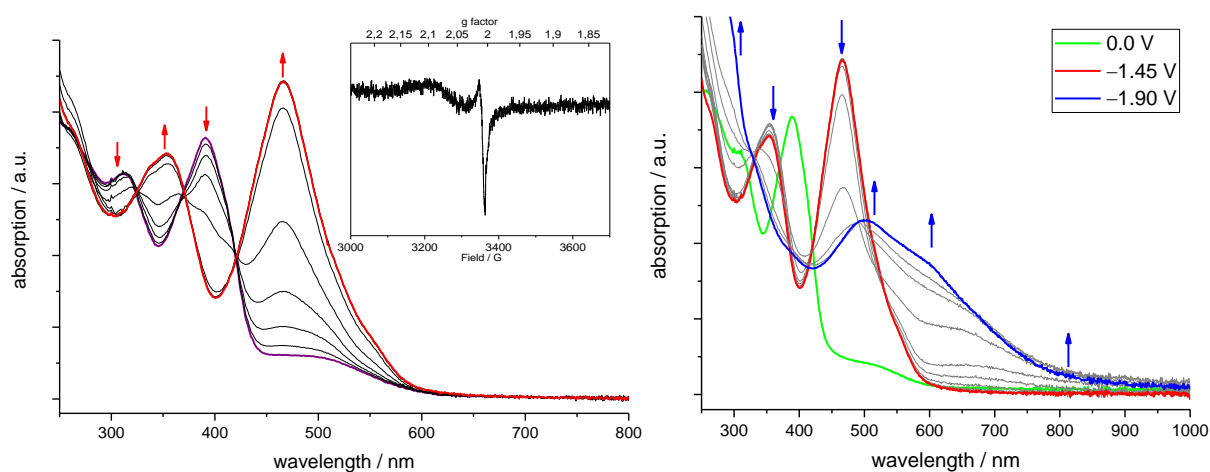


Figure 2.40 Spectroelectrochemical UV/Vis measurements of [Pt(dpyTSCmB)Cl] recorded during the first cathodic reduction (left) and second cathodic reduction (right) with 50 mV increments in 0.1 M nBu₄PF₆ MeCN solution. Left insert: Spectroelectrochemical EPR measurement of [Pt(dpyTSCmB)Cl]. Reduction was performed at room temperature in 0.1 M Bu₄NPF₆ MeCN solution, recorded at 110 K.

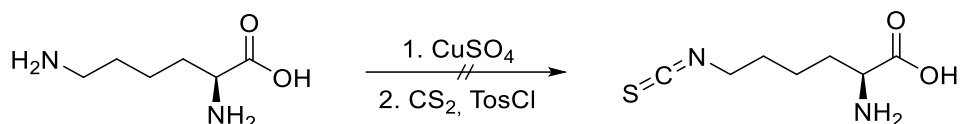
Calculation on the [Pt(TSCmB)Cl] series supported the previous claims (Chart 2.14). For all structures, the LUMO is located on the pyridine imine structure of the ligand whilst the HOMO is located on the metal centre and the sulphur. The geometry of the structures is in line with the previously presented crystal structures and the distances only express minor deviations.

Chart 2.14 Calculated frontier orbitals (LUMO+2, LUMO+1, LUMO, HOMO, HOMO-1, HOMO-2) for [Pt(fpyTSCmB)Cl], [Pt(apyTSCmB)Cl] and [Pt(dpyTSCmB)Cl] ordered by their relative energy level. All calculations were performed at B3LYP def2-TZVP level for C, H, N, S, Cl and LANL2DZ with ecp60 Hay&Watt for Pt. Isosurface level at 0.06.

Orbital	[Pt(fpyTSCmB)Cl]	[Pt(apyTSCmB)Cl]	[Pt(dpyTSCmB)Cl]
LUMO+2			
LUMO+1			
LUMO			
HOMO			
HOMO-1			
HOMO-2			

2.3.4.1. Further attempted syntheses to form TSCLp

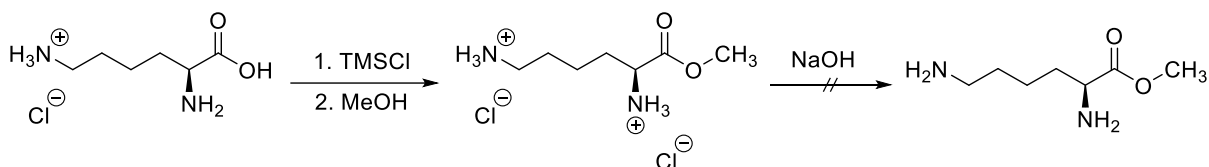
Further synthetic approaches were performed to find a shorter synthesis route of the TSCLp building block. By using the former protection of the amino acid with CuSO_4 , it was also tried to gain access to the isothiocyanate by this method. The reaction scheme is shown in Scheme 2.19.



Scheme 2.19 Attempted synthesis of lysine isothiocyanate.

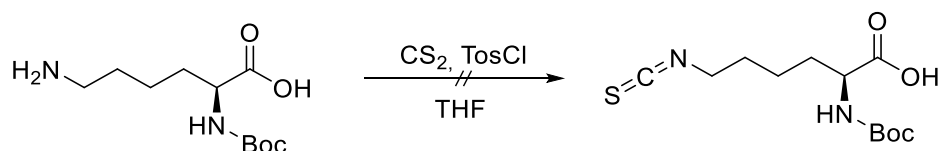
Over the course of the reaction, a black precipitate formed. Due to an equilibrium of carbon disulphide in aqueous solution with the formation of hydrogen sulphide it is assumed that the formed solid is CuS .

Another idea was to convert the carboxyl function to an ester to understand the reaction preference with both amines. The reaction idea is illustrated in Scheme 2.20. Applying the reaction conditions by *Sha et al.* the methyl ester of lysine could be formed, yet the reaction yielded the diammonium dichloride salt.³⁰⁷ Conversion to the free amines with sodium hydroxide failed, as no product could be isolated purely.



Scheme 2.20 Attempted synthesis of methyl lysinate.

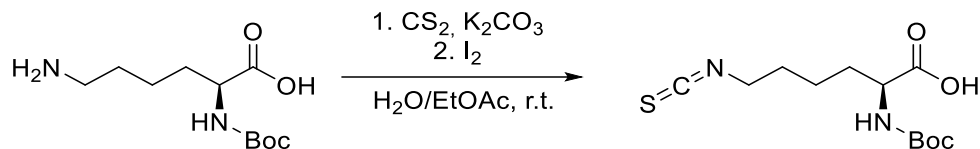
Ultimately, we started from the commercially available $\text{N}\alpha$ Boc protected lysine. According to our standard procedure we tried the addition of CS_2 and degradation with TosCl , as shown in Scheme 2.21. The reaction failed due to the bad solubility of the lysine derivative in THF.



Scheme 2.21 Attempted synthesis of Boc-lysine isothiocyanate.

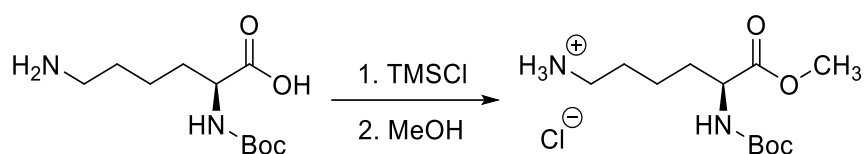
An alternate reaction for the formation of isothiocyanates in more polar solvents was performed. *Hu et al.* converted aliphatic and aromatic amines with carbon

disulphide and potassium carbonate into their dithiocarbamic acid potassium salts and *Patel* published a mild method using iodine to decompose dithiocarbamic acid salts into the corresponding isothiocyanates in a water/ethyl acetate mixture.^{308, 309} In Scheme 2.22, the supposed reaction is depicted.



Scheme 2.22 Attempted synthesis of lysine isothiocyanate in aqueous solution.

To increase the solubility in THF, it was tested whether a transformation of the carboxyl moiety into a methyl ester was feasible, so again the method by *Sha* was used on this molecule, but the reaction yielded an inseparable mixture of reagent and product in a 10:1 ratio. The attempted synthetic route is shown in Scheme 2.23. Giving the price of the protected lysine, the route was discarded.



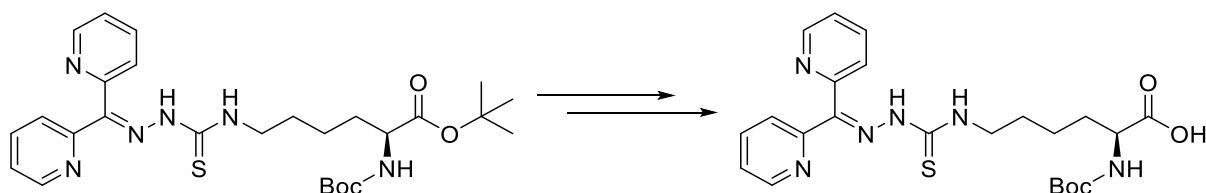
Scheme 2.23 Attempted synthesis of methyl-Boc lysate.

By this time, the previously described method, which takes the longest time, was the most cost efficient and reproduceable, thus it was the main method of synthesizing all structures of the TSCLp family.

2.4. Solid phase peptide synthesis as approach for the synthesis of new platinum peptide conjugates

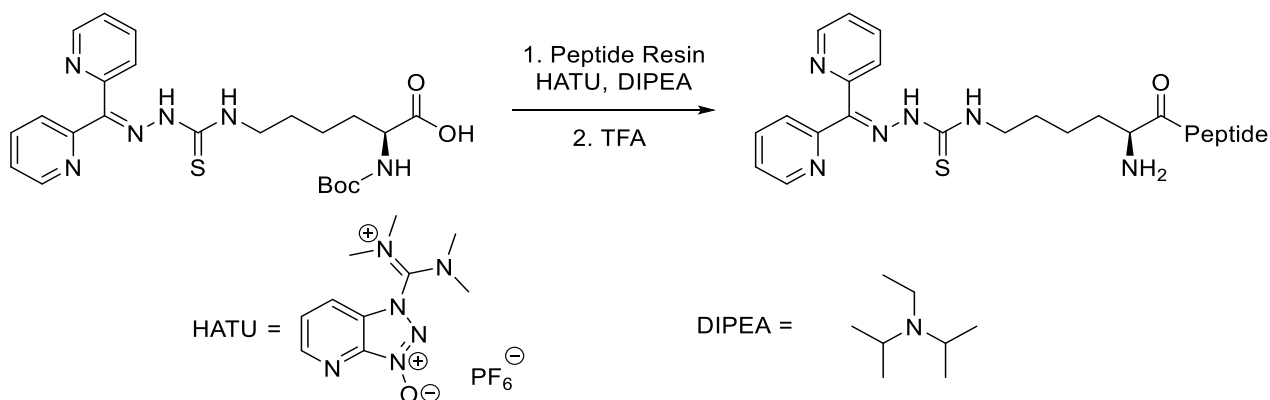
2.4.1. Peptide synthesis

To have the TSCLp series used in a *Merrifield* type of solid phase peptide synthesis, it must have a change to the protecting groups. By deprotecting the amino acid, a new fashion of protecting groups can be introduced (Scheme 2.24). The previously attached protecting groups are both detached by stirring the ligand in concentrated hydrochloric acid at ambient temperature. Afterwards, with di-*tert*-butyl carbonate the amine fraction can be protected with a Boc group again, leaving the carboxyl function unprotected and useable in the solid phase peptide synthesis.



Scheme 2.24 Change of protection groups to suit SPPS.

The peptide synthesis was performed by *Tamara Lützenburg* from the group of *Prof. Dr. Ines Neundorff*, at the Institute of Biochemistry of the University of Cologne. The amino acid derivative was coupled terminally to sC18 on a resin, using hexafluorophosphate azabenzotriazole tetramethyl uronium (HATU) and *N,N*-diisopropylethylamine (DIPEA) as coupling agents (Scheme 2.25). sC18 is a cell penetrating peptide, which is very common in the workgroup of *Ines Neundorff*.³¹⁰⁻³¹³ Its sequence is Gly-Leu-Arg-Lys-Arg-Leu-Arg-Lys-Phe-Arg-Asn-Lys-Ile-Lys-Glu-Lys. The coupled product was cleaved from the resin using trifluoroacetic acid which also deprotects the amino group of the derived amino acid.



Scheme 2.25 Addition of HdpyTSCL to the peptide during SPPS. Chemical structures of HATU and DIPEA are shown.

The synthesis was verified by HPLC-ESI-MS (Figure 2.41) in which the peaks resembling the HdpyTSCL-sC18 adduct could be identified. The successful synthesis yielded a 1 M solution in demineralized water. The following complexation was also performed in water and verified by UV/vis and HPLC-ESI-MS.

The ESI-MS shows characteristics which are seen in all the following. The peptide and the peptide complex are detected as cations with various charges.

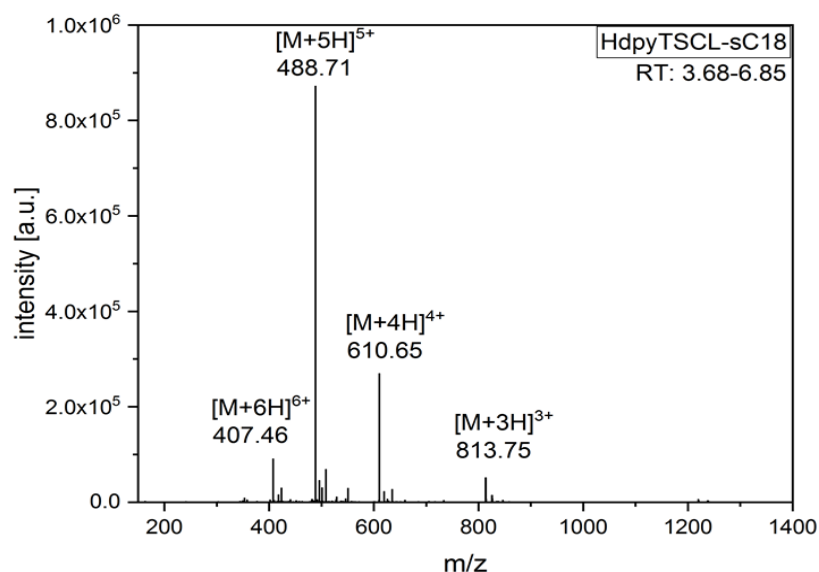
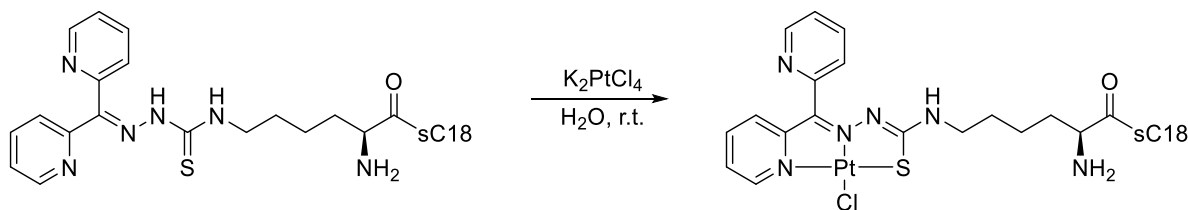


Figure 2.41 HPLC-ESI-MS of HdpyTSCL-sC18. The structure is detectable as various cations as shown in the figure.

2.4.2. [Pt(dpyTSCL-sC18)Cl] – synthesis and characterization

The complexation reaction works like the TSCmB derivatives (Scheme 2.26). By mixing two aqueous solutions of the ligand and a Pt(II) precursor like K_2PtCl_4 an immediate colour change occurs which indicates a successful coordination of platinum.



Scheme 2.26 Formation of [Pt(dpyTSCLp-sC18)Cl] by reaction of HdpyTSCL-sC18 with K_2PtCl_4 .

The UV/vis spectra for the ligand and the Pt complex were measured in water and the spectra showed the previously described characteristics of the ligand and complex spectra (Figure 2.42). The MLCT is bluer shifted compared to the previously measured spectra with a maximum at 477 nm. This maximum is due to the high polarity of the solvent in the procedure.

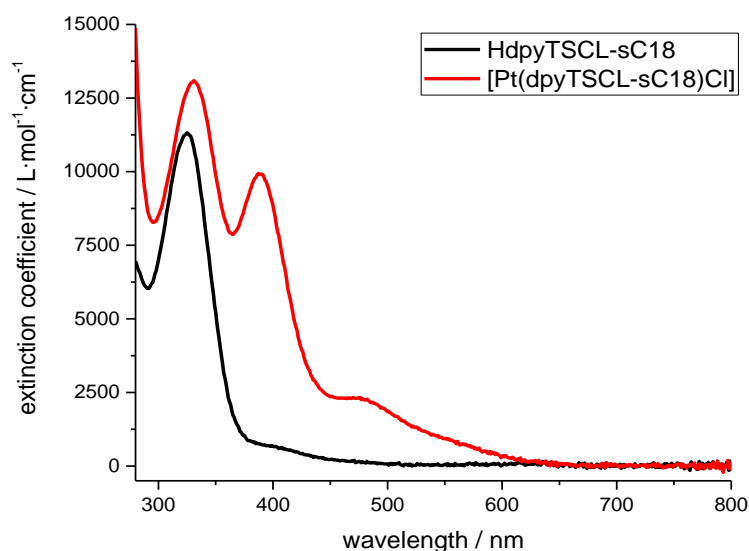


Figure 2.42 UV/vis absorption spectra of HdpvTSCL-sC18 and [Pt(dpyTSCL-sC18)Cl] in demineralized water.

To get an idea of the coordination sphere around the platinum, a solvatochromic study of the corresponding TSCLp complex was performed. Plotting the maxima of the MLCT against the $E_T(30)$ value of the solvent in which it was measured, a linear fit could be performed which shows that the peptide complex in water fits the trend suggesting a similar coordination fashion compared to the smaller derivatives (Figure 2.43).

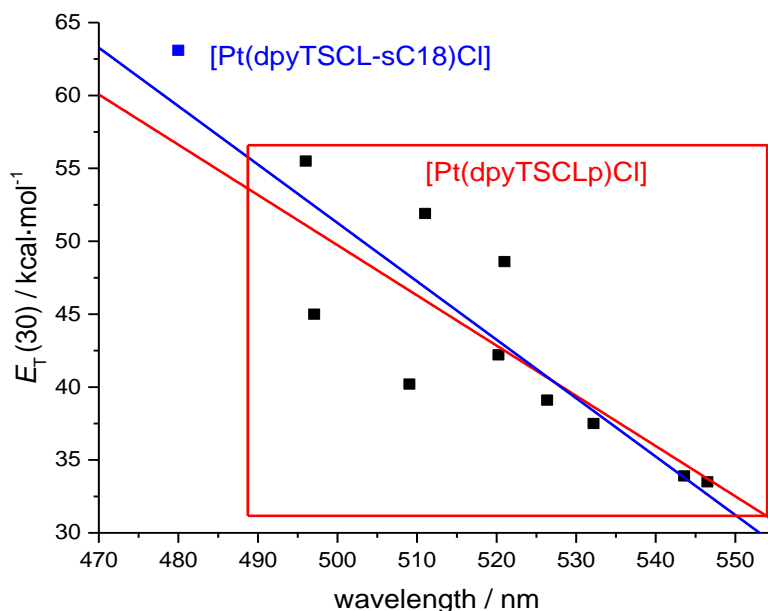


Figure 2.43 Correlation of the long-wavelength MLCT absorption maxima of [Pt(dpyTSCLp)Cl] and [Pt(dpyTSCL-sC18)Cl] with the Reichardt $E_T(30)$ values for the solvent polarity. Linear fits for [Pt(dpyTSCLp)Cl] (red) and including the conjugate [Pt(dpyTSCL-sC18)Cl] (blue).

The hydrolysis stability could also be measured using UV/vis spectra (Figure 2.44). Over 72 h a vial containing the peptide complex was measured every 30 minutes. The differences were below 3% regarding the MLCT indicating a rather high complex hydrolysis stability.

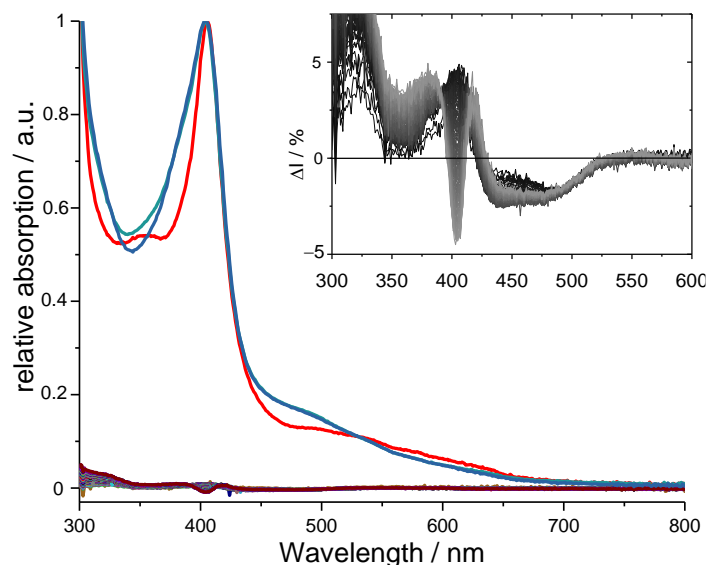


Figure 2.44 UV-vis absorption spectra [Pt(dpyTSCL-sC18)CN] in FBS (red at $t = 0$ h, blue at $t = 72$ h). The insert shows the difference spectra for 72 h measured every 30 min (black to grey).

The analysis by HPLC shows three distinct bands (Figure 2.45 A). The product signal has a retention time of around 5 minutes and could be identified by ESI-MS (Figure 2.45 C). At 5.62 minutes a second band appears which resembles the dehalided complex as minor product (Figure 2.45 D). The big signal at around 1 – 2 minutes has a mass corresponding to a trimer of the dehalided peptide complex (Figure 2.45 B).

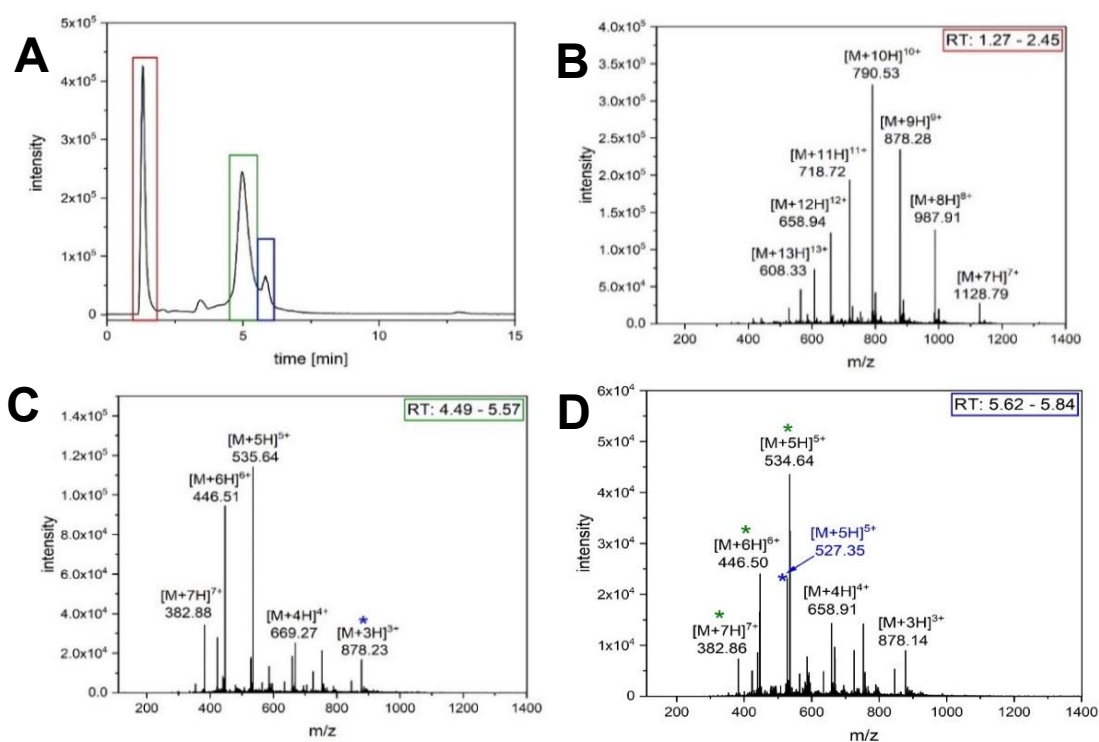


Figure 2.45 HPLC analysis (left) and ESI-MS(+) analysis (right) of [Pt(dpyTSCL-sC18)Cl] after desalting. Detected masses for $[M+nH]^{n+}$ are labelled in blue, the calculated mass for [Pt(dpyTSCL-sC18)Cl] is 2666.40 (found: 2666.26). Detected masses for $[M-C1+nH]^{(n+1)+}$ are labelled in black representing the complex [Pt(dpyTSCL-sC18)]⁺ without coordinated chloride. For $[M-C1]^+$ 2631.43 were calculated, 2630.47 were found.

2.4.3. Antiproliferation

Despite the occurring impurities from dehalidation and trimerization the complexes were further tested for stability and toxicology. The molecules were tested against human colour cell line HT-29 and human breast cancer cell line of the Michigan Cancer Foundation-7 (MCF-7). The compounds were tested in concentrations from 1 μM to 25 μM (Figure 2.46).

Looking at the model complex system, it shows a moderate inhabitation rate. HdpyTSCmB itself seems to be more toxic than the platinum complexes in general. Especially in the case of MCF-7, here the IC_{50} value is below 1 μM since the cell viability is 35% at this concentration. $[\text{Pt}(\text{dpyTSCmB})\text{Cl}]$ on the other hand has a comparable high IC_{50} value of $>25 \mu\text{M}$ against MCF-7. Against HT-29, the IC_{50} values for the ligand are higher and around 5 μM and the platinum complex is at around 25 μM .

The changes in the IC_{50} values might result from the mode of action. As described in chapter 1.4, the ligand may coordinate metal ions inside of the cells and then cause trouble by doing some redox chemistry. The platinum complex itself might be non-toxic, but a demetallation or metal exchange may form more toxic compounds. Thus, the stability of the complexes might be of importance in reducing the toxicity.

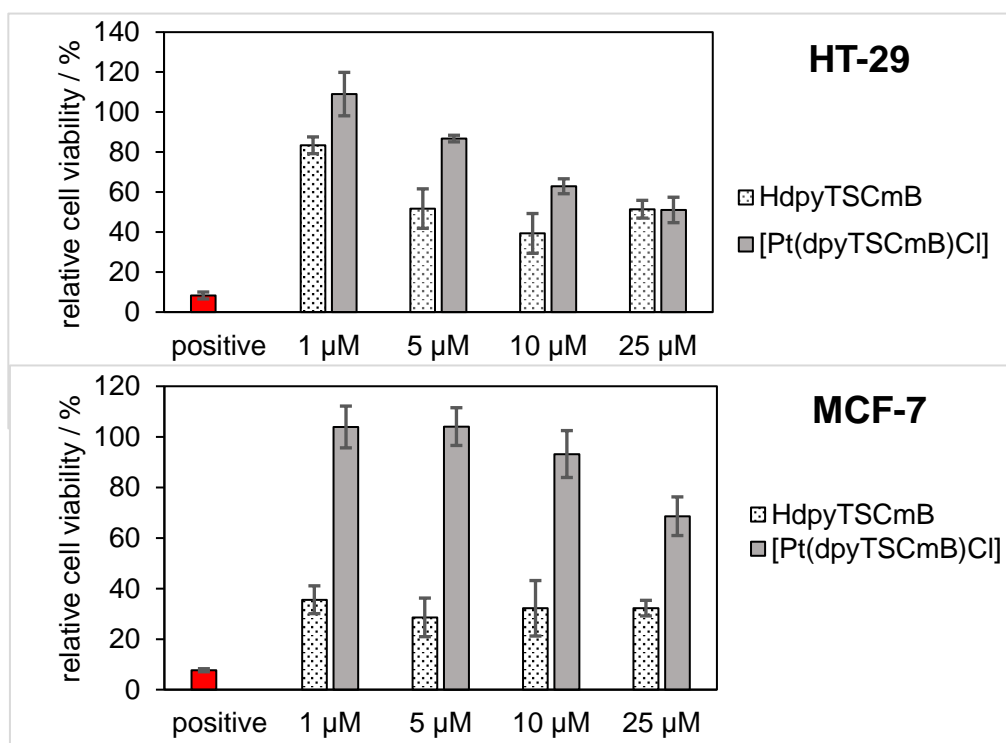


Figure 2.46 Anti-proliferative activity of HdpyTSCmB and $[\text{Pt}(\text{dpyTSCmB})\text{Cl}]$ at different concentrations against HT-29 (upper) and MCF-7 (lower) cells after incubation for 72 h. Cells treated with 70% EtOH served as a positive control. Data were normalised to untreated cells (100 % viability). Shown are mean \pm SD values of two independent experiments, each performed in triplicate.

Regarding the peptide conjugates, the toxicity is drastically lower and for HT-29 the toxicity just starts to be measurable for [Pt(dpyTSCL-sC18)Cl] but still the IC₅₀ value is above 25 μM. For MCF-7, there is no detectable cytotoxicity (Figure 2.47).

The high IC₅₀ values are of favour for nuclear medical applications. A high IC₅₀ means that the low concentrations of the substances which are applied in diagnosis or therapy are of no harm due to the chemical toxicity and thus the application only must deal with the harm of the radioactive isotopes.

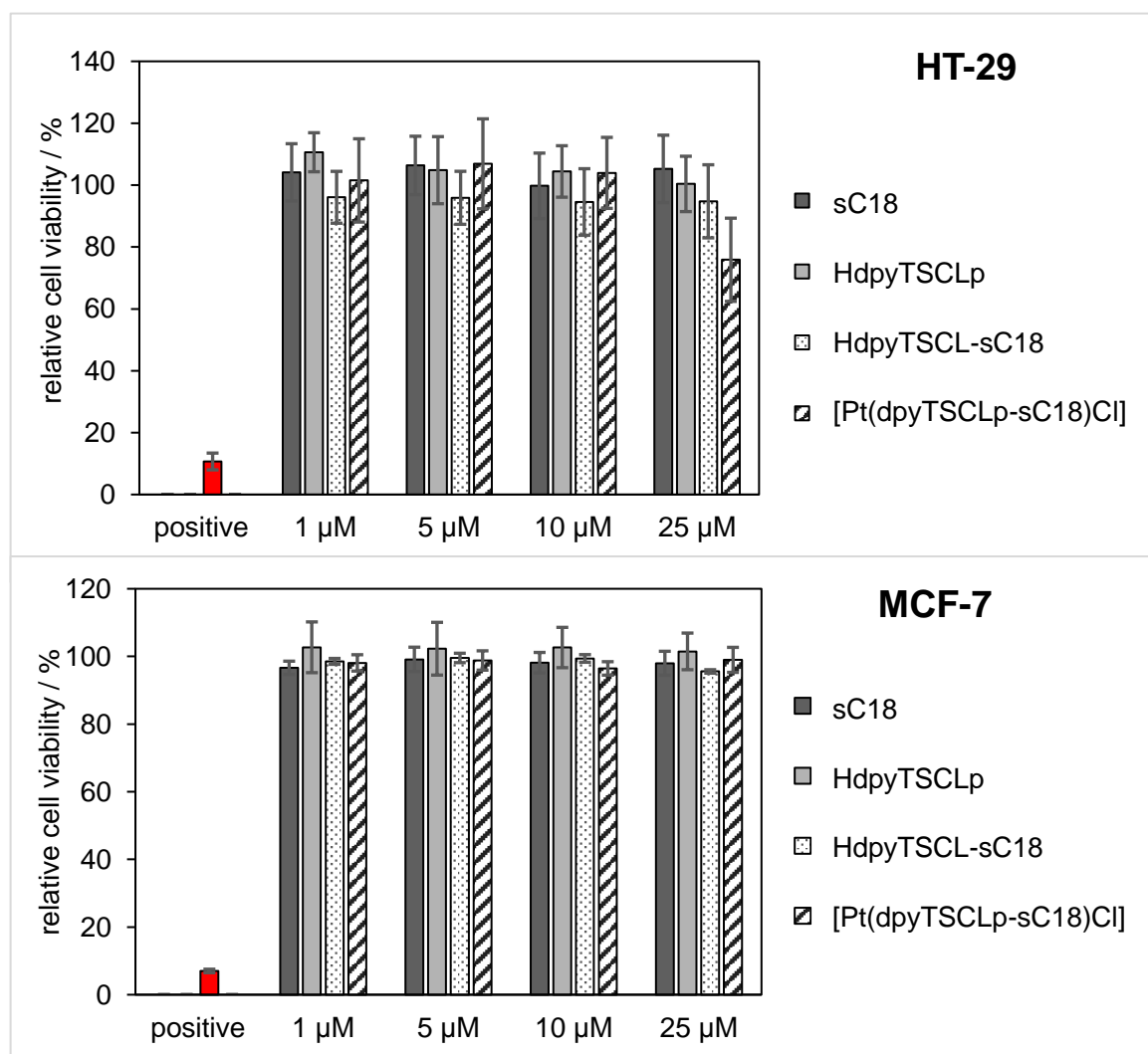


Figure 2.47 Anti-proliferative activity of sC18, HdpyTSCLp, HdpyTSCL-sC18 and [Pt(dpyTSCLp-sC18)Cl] at different concentrations against HT-29 (upper) and MCF-7(lower) cells after incubation for 72 h. Cells treated with 70% EtOH served as a positive control. Data were normalised to untreated cells (100 % viability). Shown are mean ± SD values of two independent experiments, each performed in triplicate.

2.5. Synthesis and characteristics of platinum cyanido complexes

2.5.1. Synthesis of [Pt(dpyTSCmB)CN]

The previously mentioned chloride complexes showed instability which was detectable in HPLC (Figure 2.45 A) and UV/Vis (Figure 2.42). This was probably due to a small complex instability leading to the dehalided species and trimerization of the peptides. By enforcing the HOMO-LUMO band gap, the complex stability might increase and thus the side products and the overall purity of the peptide conjugate would increase. The spectrochemical series of ligands by Shimura et al. is shown in Figure 2.48.³¹⁴

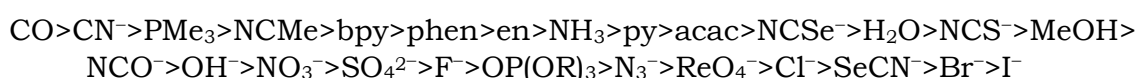
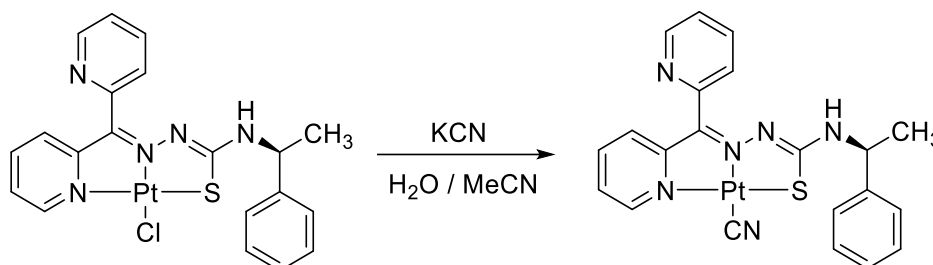


Figure 2.48 Spectrochemical series of ligands from Y. Shimura.³¹⁴ The series is the result of many octahedral d^6 metal complexes like Co^{3+} , Rh^{3+} and Pt^{4+} . Abbreviations: bpy = 2,2'-bipyridine; phen = 1,10'-phenanthroline; en = ethylenediamine; py = pyridine; acac = acetylacetonate. Cyanates are shown with their bonding atom in the first place.

Looking at the spectrochemical series it becomes clear that chloride as coligand is comparably weak. Considering other factors like charge, size, manageability as well as HSAB, cyanide ions are a good choice for ligand exchange, being among the highest possible ligand field splitting coligands. Cyanides can be introduced in various ways, for example they can be part of the starting system with a cyanide salt or by exchanging the coligand by treating a previously formed complex with KCN, AgCN or similar salts.³¹⁵⁻³¹⁷

Starting with [Pt(dpyTSCmB)Cl], it was treated with potassium cyanide to generate [Pt(dpyTSCmB)CN] (Scheme 2.27). Upon addition the solution turned from a dark red colour to a bright red solution and the product could be isolated by column chromatography. The UV/Vis showed a shift of around 20 nm corresponding to 0.1 eV indicating an increasing ligand field splitting (Figure 2.49)



Scheme 2.27 Synthesis of [Pt(dpyTSCmB)CN] by ligand exchange.

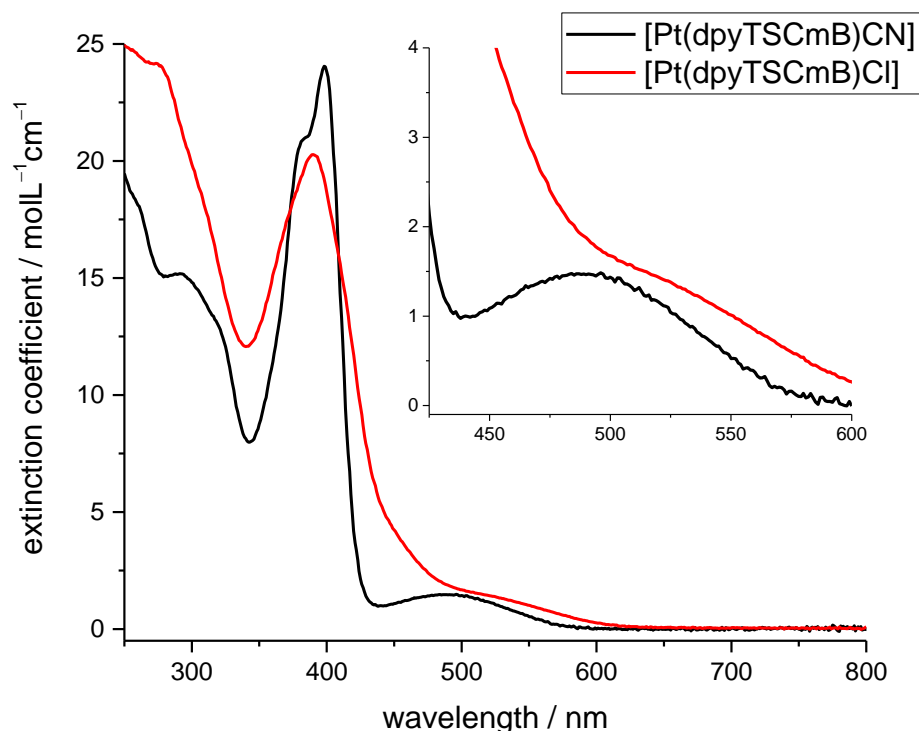


Figure 2.49 UV/vis spectra of [Pt(dpyTSCmB)Cl] (red) and [Pt(dpyTSCmB)CN] (black). Both spectra were recorded in MeCN.

2.5.2. Electrochemical analysis of [Pt(dpyTSCmB)CN]

This effect is also visible in cyclic voltammetry (Table 2.11). Here, the oxidation potential is shifted to significantly higher potentials whereas the reduction stayed almost the same yielding in a difference of 0.23 V.

Table 2.11 Electrochemical data of [Pt(dpyTSCmB)Cl] and [Pt(dpyTSCmB)CN]. Both recorded in 0.1 M Bu₄NPF₆ MeCN solution at 100 mV/s.

	[Pt(dpyTSCmB)Cl]	[Pt(dpyTSCmB)CN]
<i>Ox</i>	0.68 V	0.97 V
<i>Red1</i>	-1.50 V	-1.44 V
<i>Red2</i>	-2.12 V	-2.03 V
<i>Diff</i>	2.18 V	2.41 V

Spectroelectrochemical UV/Vis experiments gave access to an interesting property of the first reduction. Like the previously described complexes a band at roughly 480 nm emerges upon reducing the complex whilst the prominent π - π^* band diminishes. But in addition to the common property the reduced cyanido complex exhibits a further new broad band at 630 nm, as presented in Figure 2.50. This may be either an influence of the cyanide coligand on the reduced backbone or a reduced cyanide coligand that coordinates to a further metal centre. The second reduction seems to indicate a similar process like the initial chlorido complex which also expressed a broad absorption at 600 nm upon the second reduction as shown in Figure 2.40.

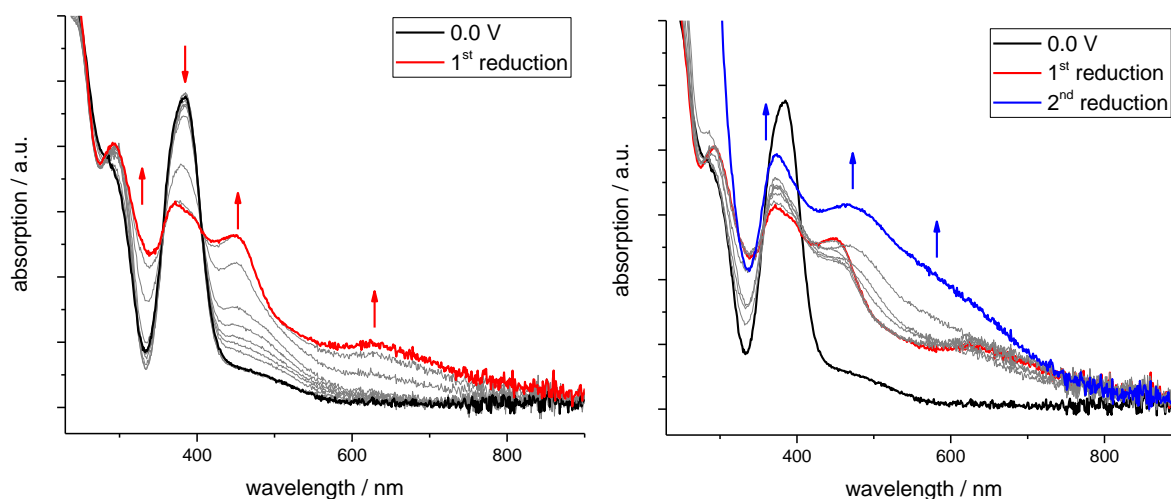


Figure 2.50 UV/vis spectra of [Pt(dpyTSCmB)CN] during the first reduction (left) and second reduction (right). Spectra were recorded in 0.1 M Bu₄NPF₆ MeCN solution.

The oxidation of [Pt(dpyTSCmB)CN] leads to a hypsochromic shift of the π - π^* transition and the MLCT band vanishes completely, as depicted in Figure 2.51. This may indicate an oxidation of the Pt(II) centre.

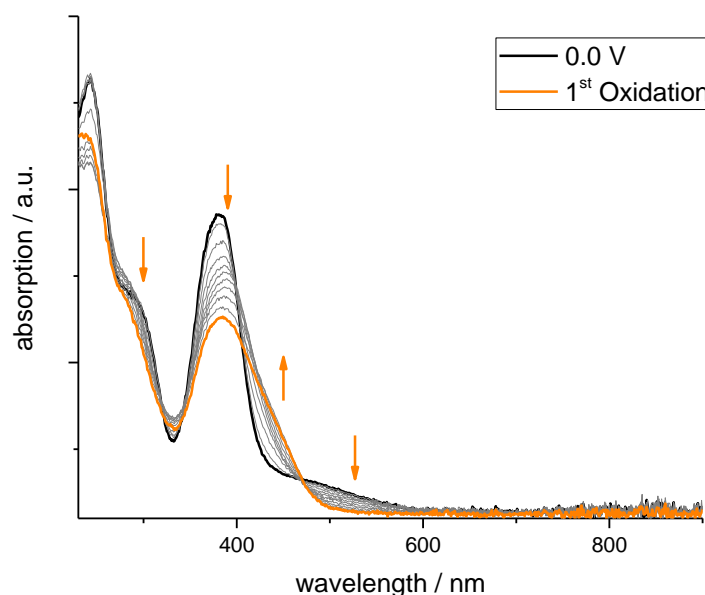


Figure 2.51 UV/vis spectra of [Pt(dpyTSCmB)CN] during the oxidation. Spectra were recorded in 0.1 M Bu₄NPF₆ MeCN solution.

2.5.3. Crystal structure and Hirshfeld analysis of [Pt(dpyTSCmB)CN]

Additionally, a suitable single crystal of the cyanido complex was obtained by slow evaporation of MeCN. It crystallized in $P2_1$ and the ORTEP representation is shown in Figure 2.52 and the crystallographic data are given in Table 2.12.

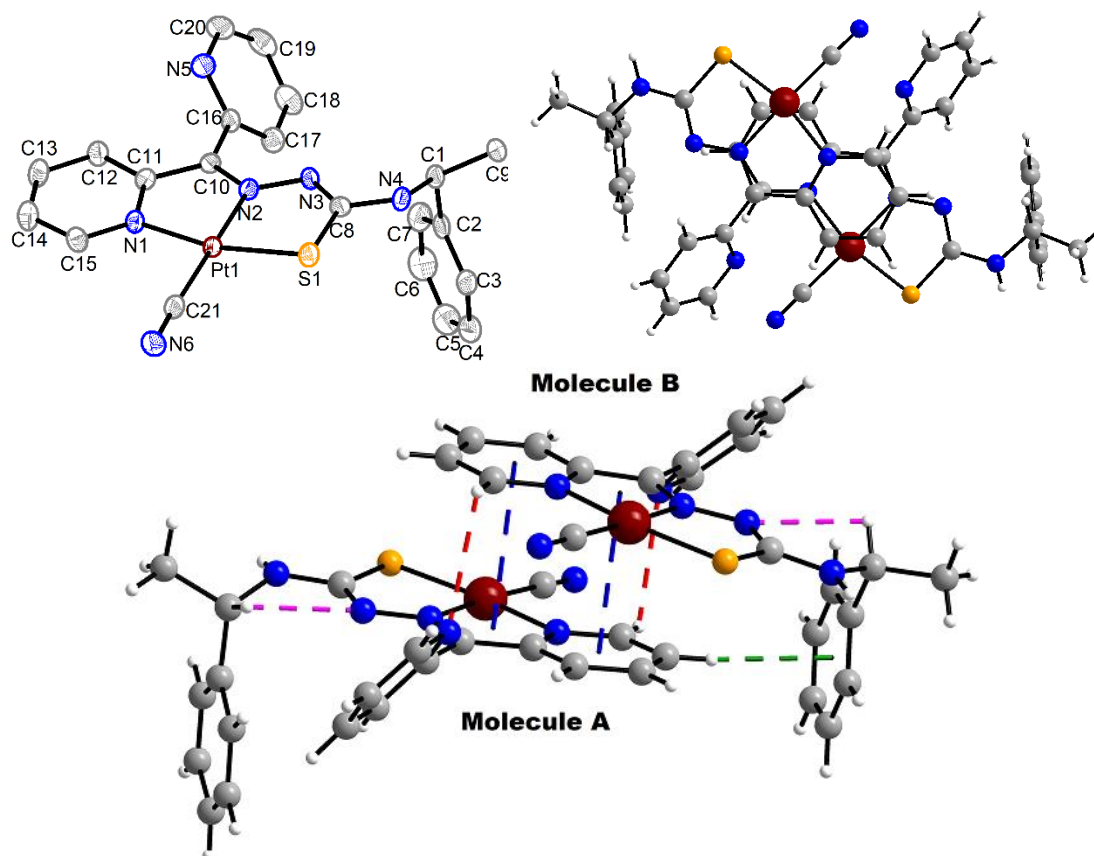


Figure 2.52. Molecular structure of [Pt(dpyTSCmB)CN]. (A): one out of two independent molecules. Atoms are shown with 50% probability. H atoms are omitted for clarity. B and C: Stacking and further intermolecular interactions between the two independent molecules in the crystal: **blue** = π - π : 3.6493(1) and 3.5155(1) Å; **pink** = N3 \cdots HC1: 2.425(4) and 2.503(4) Å; **red** = N5 \cdots HC15: 2.787(6) and 2.907(6) Å; **green** = π -HC14: 2.505(4) Å.

Table 2.12 Crystallographic data for [Pt(dpyTSCmB)CN].

	[Pt(dpyTSCmB)CN]
<i>Empirical formula / Formula weight</i>	C ₂₁ H ₁₈ N ₆ PtS / 581.56 g/mol
<i>Crystal system / Space group</i>	Monoclinic / P2 ₁
<i>Unit Cell Dimensions</i>	a = 7.6316(3) Å b = 14.3698(6) Å / β = 94.3320(10) c = 18.6158(7) Å
<i>Volume / Z</i>	2035.66(14) Å ³ / 4
<i>ρ_{calc}</i>	1.8975 g/cm ³
<i>F(000)</i>	1106.5
<i>Reflections collected</i>	52088
<i>Independent reflections</i>	7847 [R _{int} = 0.0429, R _{sigma} = 0.0318]
<i>Data/restraints/parameters</i>	7847/1/532
<i>Goodness-of-fit on F²</i>	1.034
<i>Final R indexes [I_o > 2σI_o]</i>	R ₁ = 0.0195, wR ₂ = 0.0492
<i>Final R indexes [all data]</i>	R ₁ = 0.0196, wR ₂ = 0.0493
<i>Largest diff. peak/hole</i>	1.01/-1.10 e Å ⁻³
<i>Flack parameter</i>	0.091(7)

As part of the crystal packing, the coordinating pyridine ring overlaps with the pyridine-hydrazone-platinum chelate of a neighbouring molecule and the non-coordinating pyridine is tilted towards the respected neighbour. A mean distance of

about 3.6 Å between the rings do not indicate an interaction and the distance from the nitrogen donor of the non-coordinating pyridine to the proton at C15 is roughly 2.9 Å here would be at least some energy gain. Also, on the side of intramolecular interactions the distance between the proton at C1 and N3 is only 2.5 Å. Here is a significant energy gain which should lock the molecule in place.

The interactions can be further described by Hirshfeld analysis. The Hirshfeld surface shows further interactions which are especially contributed to nitrogen interactions of the cyanide coligand as well as the hydrogen of the *N*4 secondary amine (Figure 2.53).

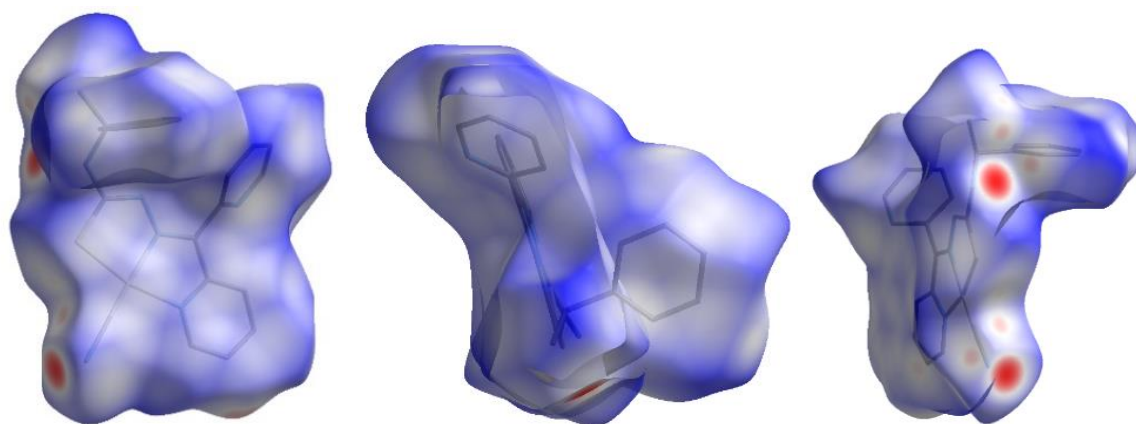


Figure 2.53 Hirshfeld surface of [Pt(dpyTSCmB)CN] showing only the promolecule along the crystallographic a-, b- and c-axis.

Looking at the crystal packing with the Hirshfeld surface included the strong interaction becomes very clear (Figure 2.54). The nitrogen of the cyanide coligand interacts with the amine of a neighbouring complex. At the cyanide there is also the carbon atom highlighted. This interaction can be contributed to the proximity of the methyl sidechain.

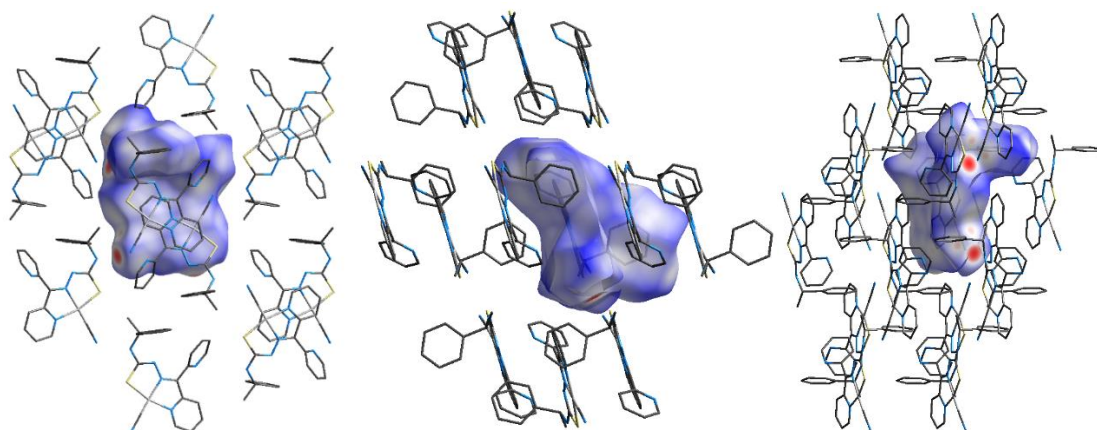


Figure 2.54 Hirshfeld surface of [Pt(dpyTSCmB)CN] including the surrounding molecules shown along the crystallographic a-, b- and c-axis.

Using fingerprint plots, we can visualize the interactions at the surface. The H...H and C...H/H...C interactions represent the π - π interactions described previously. A part of the longer interactions is from the cyanide carbon to the hydrogen atoms at the methyl sidechain of the N4 functionalization as well as an interaction of the coordinating pyridine with a benzyl π system at about 2.7 Å. Furthermore, the N...H/H...N have a big contribution to the overall Hirshfeld surface having the shortest intermolecular distances.

The contributions of the thiolate to the surface are mostly from the π - π interactions between the thiolate and neighbouring pyridine in case of the S...C/C...S contacts, but also the interactivity of the methylene group with the cyanide coligand leads to a proximity between the sulphur and the hydrogens as well as the π - π stacking brings the hydrogen atoms of the pyridine closer to the sulphur.

The platinum centre is also engaging in the π - π stacking represented by the fingerprint plot of Pt...N/N...Pt, Pt...C/C...Pt and Pt...H/H...Pt interactions. Due to the crystal packing the distances of platinum and the nitrogen donor of the neighbouring pyridine is closest among these.

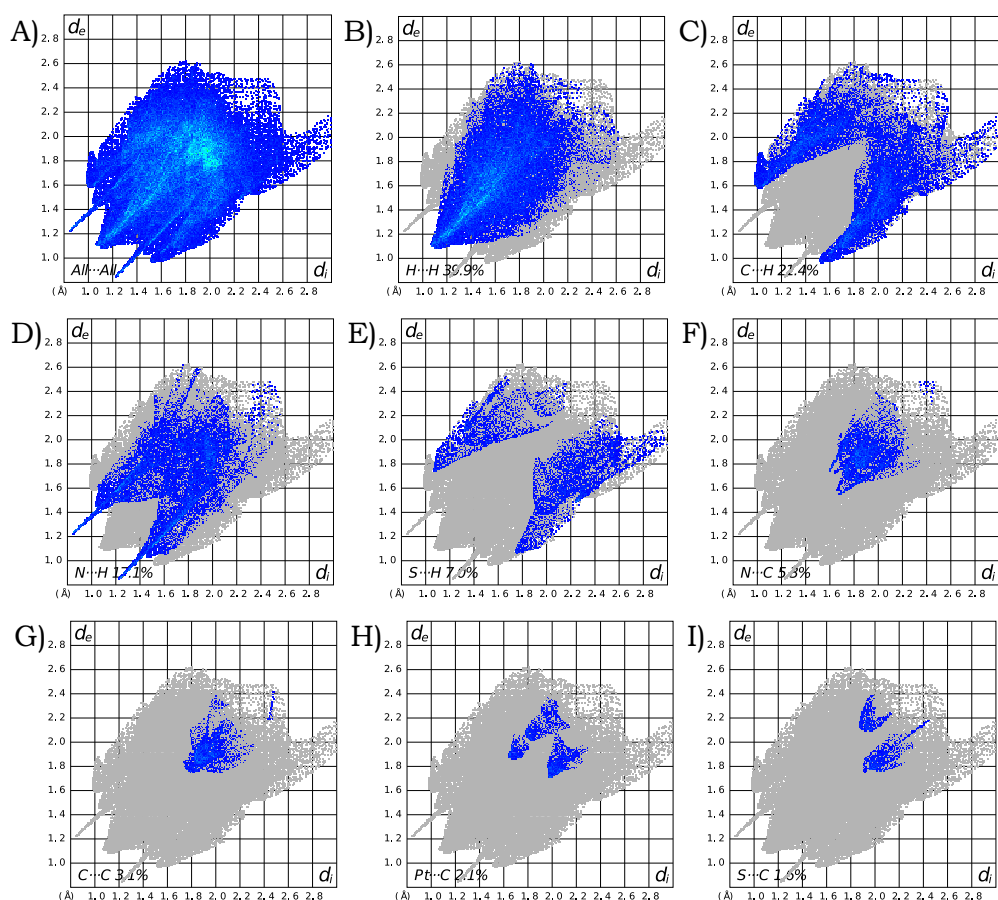


Figure 2.55 Fingerprint plots of [Pt(dpyTSCmB)CN]. A) showing the unfiltered fingerprint plot. B)-I) element combinations with close contacts were highlighted. Combinations without close contacts or below 1.5% were omitted. B) H...H, C) C...H/H...C, D) N...H/H...N E) S...H/H...S, F) N...C/C...N G) C...C, H) Pt...C/C...Pt, I) S...C/C...S.

Looking at the platinum coordination sphere the major contributors are nitrogen and carbon (Figure 2.56 and Figure 2.57. This is in part due to the coordination of the thiosemicarbazone and cyanide but also the close pyridine rings of other complexes play a big role as it can be seen by the difference of the interactions of Pt···C Pt···N to the Pt···S fingerprint plots. The part above d_i 2 Å is dominated by the interaction with the intermolecular pyridines.

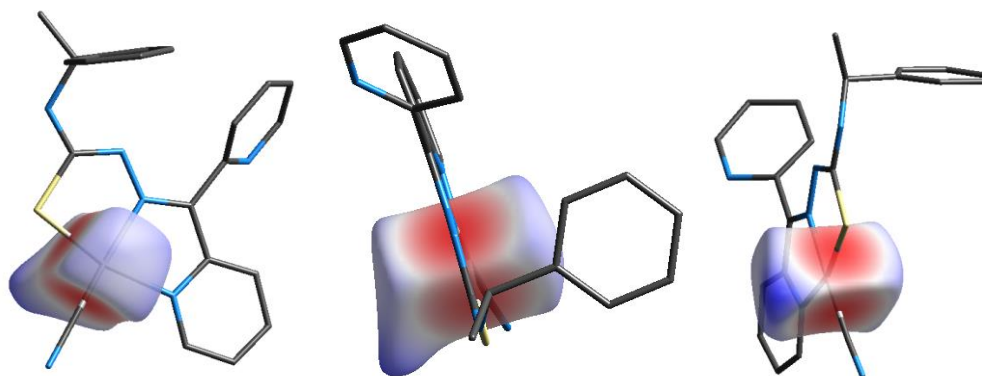


Figure 2.56 Hirshfeld surface of the platinum centre in [Pt(dpyTSCmB)CN] along the crystallographic a-, b- and c-axis.

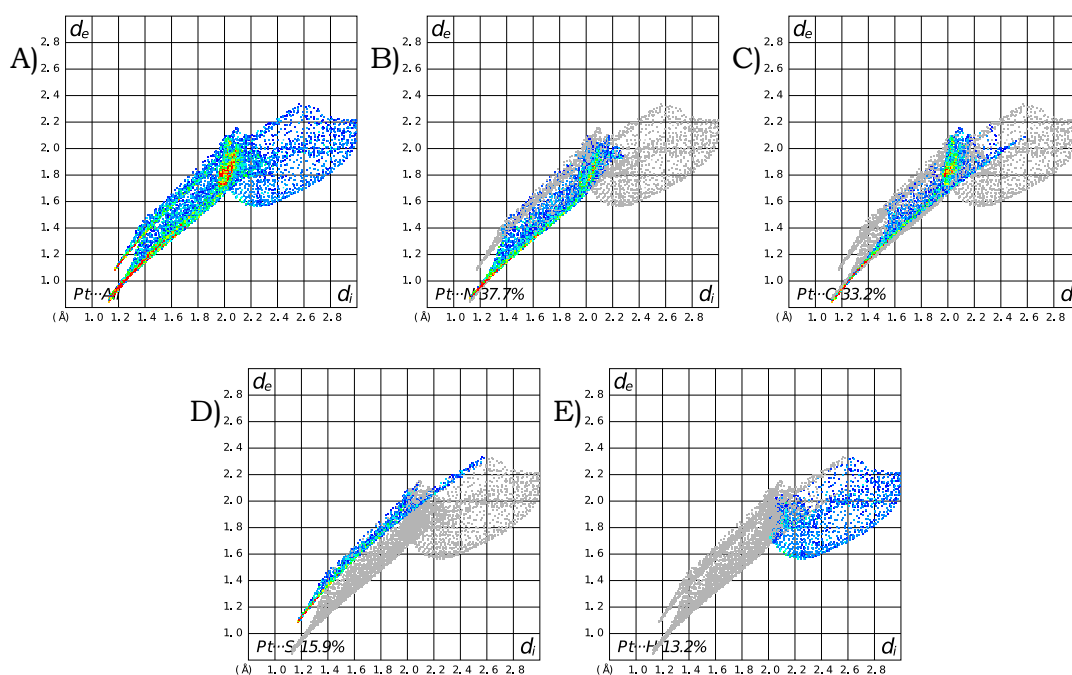


Figure 2.57 Fingerprint plots of the Pt(II) coordination sphere in [Pt(dpyTSCmB)CN]. A) showing the unfiltered fingerprint plot. B)-E) element combinations with close contacts were highlighted. Combinations without close contacts were omitted. B) Pt···N/N···Pt, C) Pt···C/C···Pt, D) Pt···S/S···Pt E) Pt···H/H···Pt.

2.5.4. NMR spectroscopy

The influence of the strong cyanide ligand is noticeable in the complete structure. On the one hand, the platinum NMR shifts from around -3100 ppm to -3248 ppm. On the other hand, the strong trans-effect induced by the cyanide raises the electron density in the hydrazone moiety. This turns N3 into a hydrogen donor which itself is now able to form a hydrogen bond to the proton at C1. By this interaction, the geometrical structure is fixed and the former interaction of the protons at C1 and N4 is hindered. This can also be detected in the ^1H NMR of the molecule (Figure 2.58).

The proton at the C1 position was prior to the ligand exchange a quintet at the same region, but after the exchange it became a quartet due to its only coupling to the neighbouring methyl function. The amine now forms a broad singlet instead of a doublet. The pyridine rings on the other hand are non-shifted.

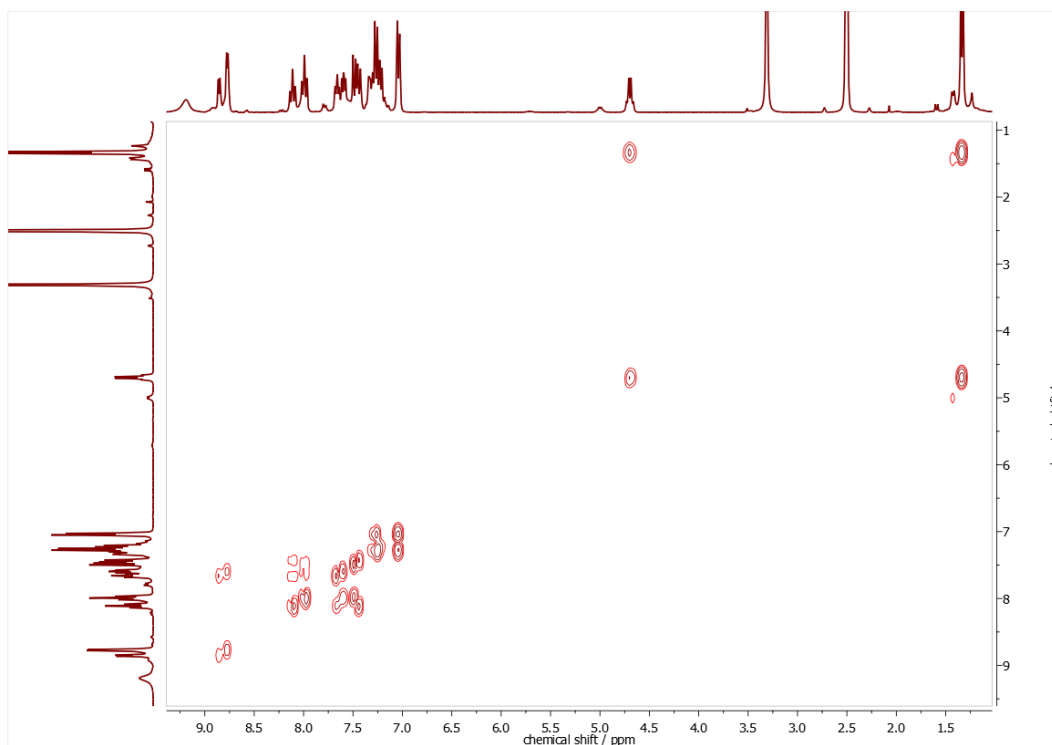


Figure 2.58 ^1H , ^1H COSY spectra of $[\text{Pt}(\text{dpyTSCmB})\text{CN}]$ in $\text{DMSO-}d_6$.

2.5.5. Translation to HdpyTSCL-sC18

Since the model complex could be fully characterized, the peptide complex was the next step. Starting from the peptide platinum chlorido complex and adding potassium cyanide leads to the formation of several products, whereas the treatment of a slightly acidic peptide solution with KCN and subsequent treating the solution with K_2PtCl_4 leads to the formation of $[\text{Pt}(\text{dpyTSCL-sC18})\text{CN}]$ (Scheme 2.28). The formation of the

complex could also be detected in UV/Vis spectroscopy with a MLCT at about 480 nm (Figure 2.59). When using 1 equivalent of KCN a mixture of 1 to 4 chloride to cyanide is observed, whilst using 1.5 equivalents of KCN yields the pure complex. The product is pure on HPLC and shows no signs of degradation or trimerization thus underlining the previously stated stability (Figure 2.60).

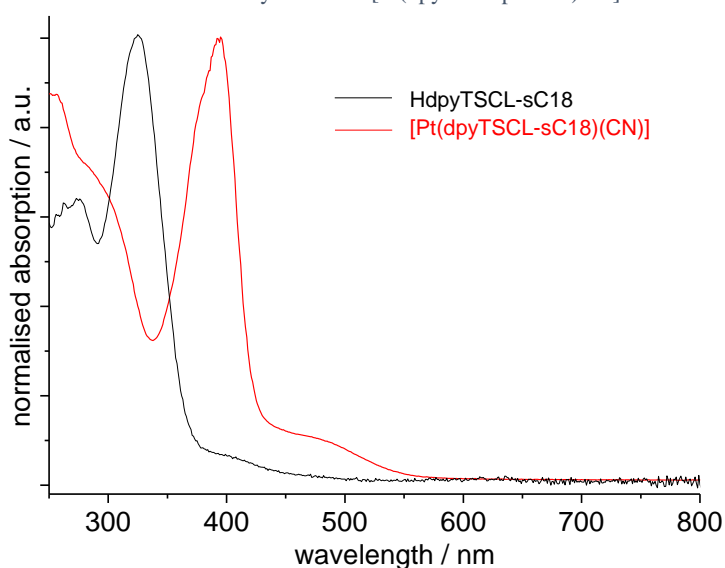
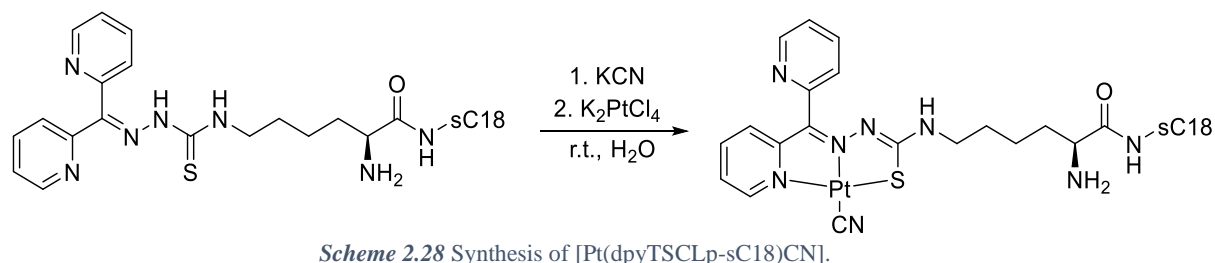


Figure 2.59 UV/Vis spectroscopy of HdpyTSCL-sC18 and [Pt(dpyTSCLp-sC18)CN] in demineralized water.

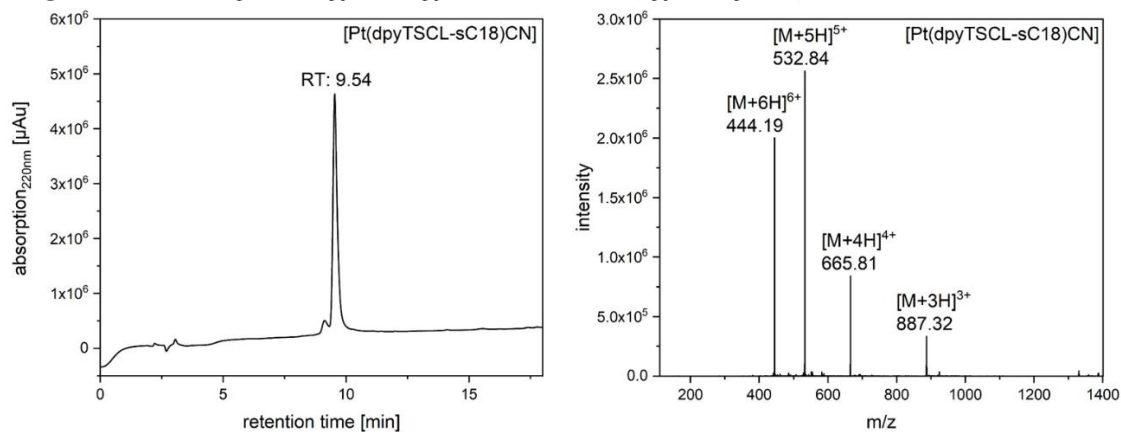


Figure 2.60 HPLC analysis and ESI-MS(+) analysis of [Pt(dpyTSCL-sC18)CN] conjugate after desalting. The sample was recorded using a linear gradient from 10-60% MeCN in H₂O (incl. 0.1% trifluoroacetic acid) within 15 min. The identified molecular ions agree well with the calculated molecular weight (calculated: 2657.44 g/mol; experimental: 2659.13 g/mol).

A possible explanation of these pathways and resulting products is the initial acidity of the solution. When adding KCN first to the slightly acidic peptide solution, a portion of the ions may form hydrogen cyanide. K₂PtCl₄ may form the corresponding

chloride complex and it may react with HCN to form the cyanido complex and hydrogen chloride. Here the formation of hydrogen chloride may promote the reaction. On the other hand, adding the K_2PtCl_4 first already lowers the pH due to higher chloride concentration and the formation of HCN is lower.

Tested for its hydrolysis stability, the cyanido complex showed a good stability over 72 h (Figure 2.61).

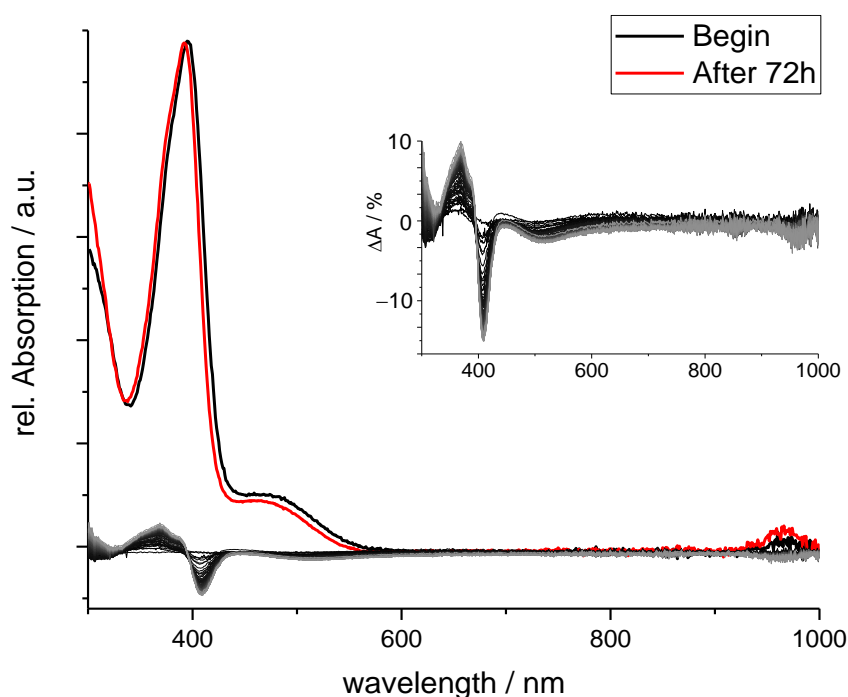


Figure 2.61 UV-vis absorption spectra [Pt(dpyTSCL-sC18)CN] in FBS (Black at $t = 0$ h, red at $t = 72$ h). The insert shows the difference spectra for 72 h measured every 30 min (black to grey).

2.5.6. Antiproliferation

Next, we investigated the anti-proliferative activity of the Pt(II) cyanido complexes in comparison to the previously described chloro derivatives (Figures 2.43 and 2.44). In current literature the compound Dp44mT (di-2-pyridylketone-4,4,-dimethyl-3-thiosemicarbazone) is quite common and since it is structurally very similar to HdpyTSCmB a control experiment was conducted (Figure 2.62).³¹⁸⁻³²⁴ For the tests two different cancer cell lines, namely breast adenocarcinoma MCF-7 (Michigan Cancer Foundation 7) and colorectal carcinoma HT-29 cells were chosen, since those have been already used in former experiments, thus allowing for comparing the activity of our novel compounds with recent results from our own studies and literature.³²⁵⁻³³⁰ HEK-293 (embryonic kidney) cells were used as non-cancerous control cell line.

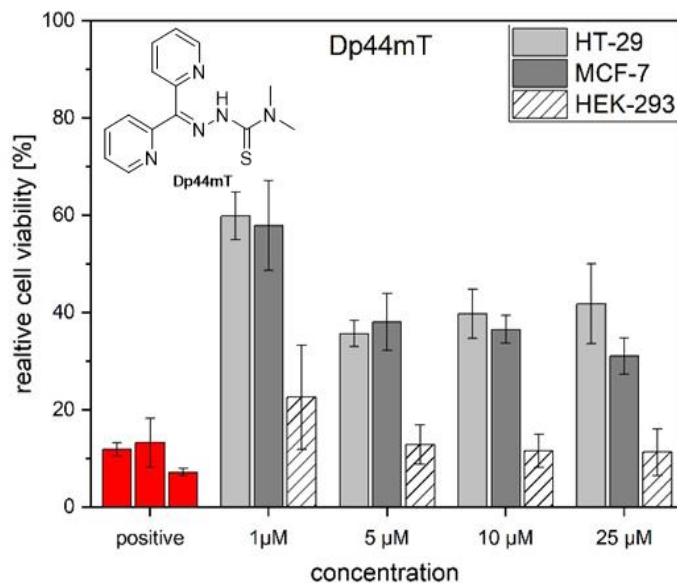


Figure 2.62 Anti-proliferative activity of Dp44mT (di-2-pyridylketone-4,4,-dimethyl-3-thiosemicarbazone) at different concentrations against MCF-7, HT-29 and HEK-293 cells after incubation for 72 h. Cells treated with 70 % EtOH served as a positive control. Data were normalised to untreated cells (100 % viability). Shown are mean \pm SD values of two independent experiments, each performed in triplicate.

HdpyTSCmB exhibited quite strong anti-proliferative activity against HT-29 cells, while MCF-7 cells were less harmed (Figure 2.63 A, B). However, also HEK-293 cells were strongly affected (Figure 2.63 C) letting assume only less selectivity of this compound. Overall, the activity was in the range of Dp44mT^{80, 331-333} and DpC (di-2-pyridylketone-4-cyclohexyl-4-methyl-3-thiosemicarbazone).^{319, 320, 334} Notably, the Pt complexes [Pt(dpyTSCmB)Cl] and [Pt(dpyTSCmB)CN] exhibited reduced activity compared with the ligand alone. Only at high concentrations of 10-25 μ M markedly reduced cell viability was observed. Thereby it seemed that the CN complex was more active against HT-29 cells, while the Cl derivative demonstrated higher activity against HEK cells. Interestingly, there was no difference detectable when incubating the complexes with MCF-7 cells. Recently, it was hypothesised that TSC molecules coordinate in the cell to redox-active metals such as Fe or Cu, and that these formed complexes would lead to the production of reactive oxygen species, damaging the cell.^{76, 320, 322-324, 331-333, 335-337} In fact, this would explain also our observation of higher activity of the free ligands compared with the Pt complexes. Obviously, Pt(II) is only a poor substitute to these redox-active metals that are known to quickly react with H₂O₂ forming hydroxyl radicals in Fenton-type reactions.^{80, 322-324, 331-333, 336} Considering that we have measured high electrochemical stability for both Pt model complexes [Pt(dpyTSCmB)Cl] and [Pt(dpyTSCmB)CN], particularly against reduction, would further substantiate our assumption.

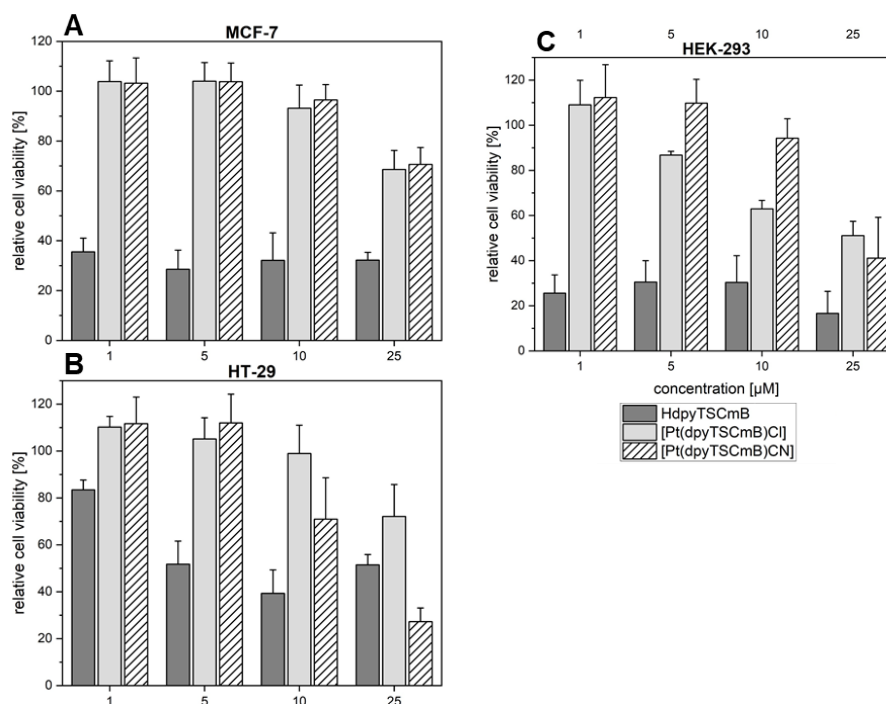


Figure 2.63 Anti-proliferative activity of HdpTSCmB, [Pt(dpyTSCmB)Cl] and [Pt(dpyTSCmB)CN] against MCF-7 (A), HT-29 (B) and HEK-293 (C) cells after incubating them for 72 h with different concentrations of the compounds. Cells treated ³³³with 70% EtOH served as a positive control. Data were normalised to untreated cells (100% viability). Shown are mean ± SD values of three independent experiments, each performed in triplicate.

Interestingly, no significant decrease in cell viability was determined after incubating all other compounds for 72 h with the three cell lines (Figure 2.64). For sC18 this agreed to already published results demonstrates again that sC18 is well-tolerated.³³⁸⁻³⁴⁰ For the other tested substances including the HdpTSCmB-sC18 ligand and the complex [Pt(dpyTSCmB-sC18)Cl], it is more surprising. However, since *Neundorff et al.* have already demonstrated that sC18 is a highly efficient carrier for various cargos, also including metal complexes,^{311, 325-327, 338-341} the possibility of the conjugate to enter the cell is quite high. The results let rather concluded that there might be a dramatic influence of the linker structure that bridges the TSC with the carrier molecule (in this case sC18). This hypothesis is probably proven by the observation that there is no detectable activity of HdpTSCmB being structurally highly divers to recently reported toxic binuclear Pt(II)Cl complexes containing triazole-bridged bithiosemicarbazone ligands.³⁴² Generally, the potency of such metal complexes is often dependent on specific properties like DNA intercalation. For sC18 conjugates it is already known that they are mainly taken up by endocytotic pathways, restricting efficient cytosolic release, and thus, transfer of the cargo to its final target.^{338, 339} One way to overcome this limitation is to include specific proteolytic cleavage sites within the ligand to peptide structure, e.g. for cathepsin B. This protease is abundant in the lysosomes and may induce enhanced endosomal release.³⁴¹

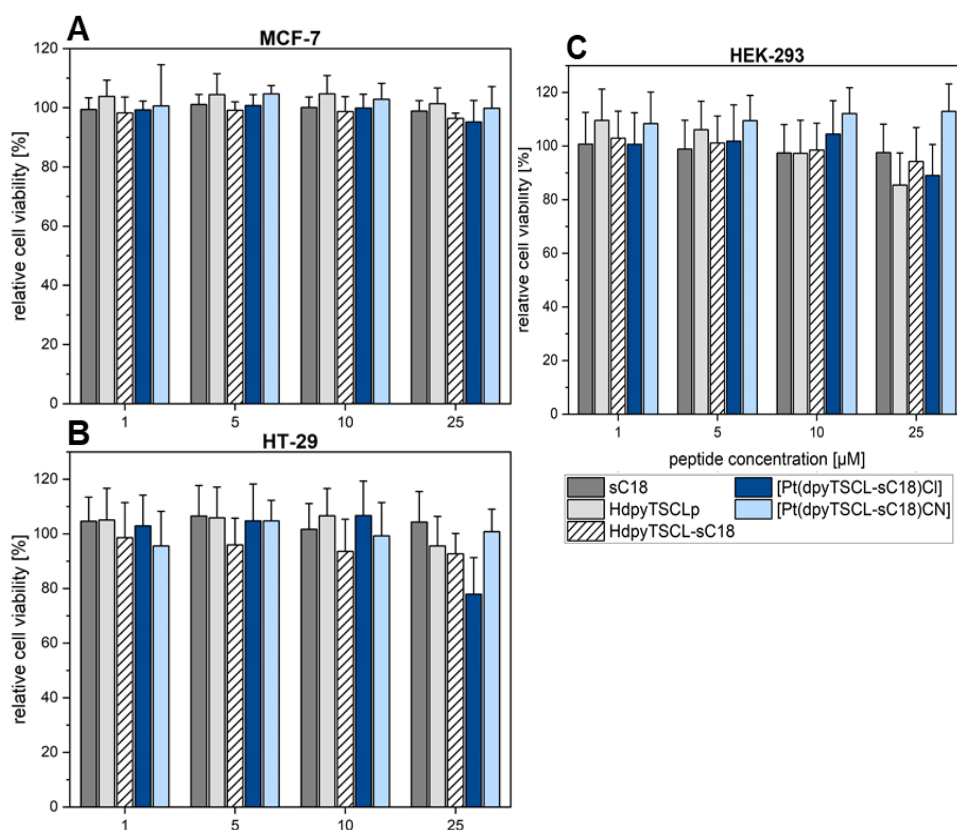


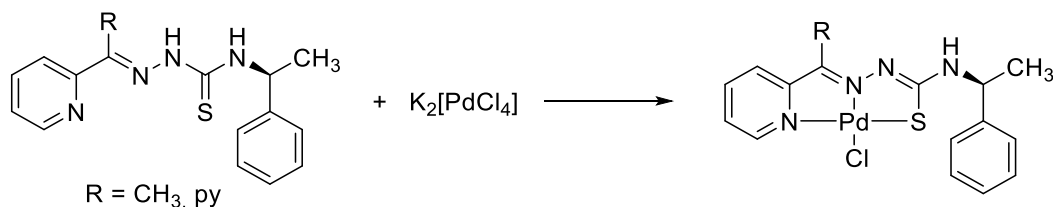
Figure 2.64 Anti-proliferative activity of sC18, HdpyTSCLp, HdpyTSCL-sC18, [Pt(dpyTSCL-sC18)Cl], and [Pt(dpyTSCL-sC18)CN] against MCF-7 (A), HT-29 (B) and HEK-293 (C). Cells treated with 70% EtOH served as a positive control. Data were normalised to untreated cells (100% viability). Shown are mean \pm SD values of three independent experiments, each performed in triplicate.

On the other side, the good tolerability of the novel Pt(II) conjugates paves the way for future studies, in which we will use these and related Pt-TSC-peptide conjugates for late-stage radiolabelling with Pt radionuclides, such as ^{189}Pt , ^{191}Pt , $^{193\text{m}}\text{Pt}$, and $^{195\text{m}}\text{Pt}$ that are very interesting candidates for Auger-electron radionuclide therapy.³⁴³⁻³⁴⁶ The advantage of this method is the emission of low energy electrons which are able to ionise material in a very confined space, thus reducing radiation damage to healthy cells.^{347, 348} Tagged by a ligand containing biological information, the radionuclide can be transported to a desired location or cell, thus focussing the decay and cell damage in a certain area (targeted radiotherapy). The facile, rapid, and stable binding of Pt(II) from a simple source such as K_2PtCl_4 together with the observed high stability and virtual non-toxicity make our systems very suitable for late-stage labelling.

2.6. Further d⁸ ion complexes of the α -N heterocyclic TSCmB family

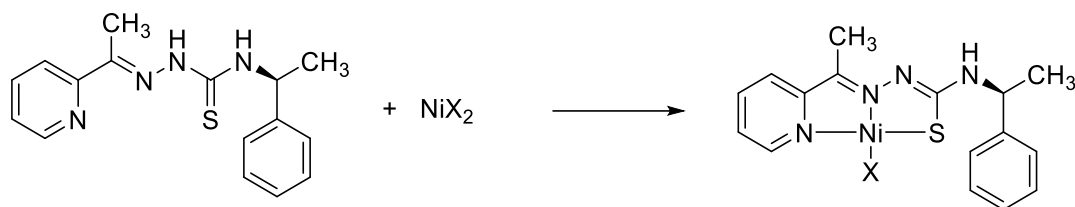
2.6.1. Synthesis of [M(pyTSCmB)X] complexes

Furthermore, the complexes [Pd(apyTSCmB)Cl] and [Pd(dpyTSCmB)Cl]·HCl could be isolated by reacting HapyTSCmB and HdpyTSCmB with K₂[PdCl₄] (Scheme 2.29).



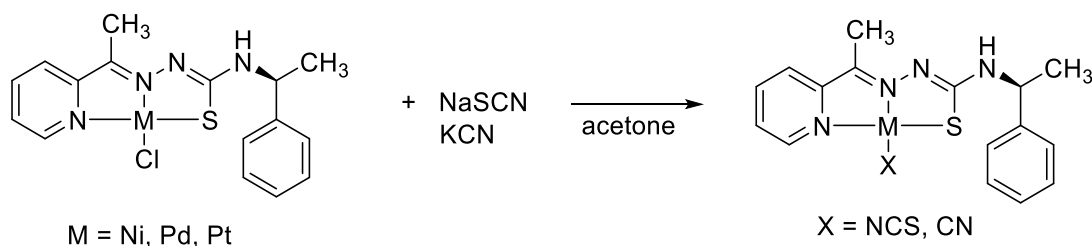
Scheme 2.29 Synthesis of [Pd(apyTSCmB)Cl] and [Pd(dpyTSCmB)Cl].

For Ni(II) complexes, the chlorido and thiocyanate could be isolated from the respective metal salt (Scheme 2.30). Whilst the chlorido species showed a broadening in the ¹H-NMR due to the paramagnetic influence of a not totally planar metal centre, the thiocyanate is strong enough to force the nickel centre to a square planar coordination sphere exhibiting sharp NMR signals due to diamagnetism. The thiocyanato coligand is coordinated by the nitrogen donor leaving a double bond to carbon and from carbon to sulphur.



Scheme 2.30 Synthesis of [Ni(apyTSCmB)X] with X = Cl, NCS.

A ligand exchange could be performed using the [M(apyTSCmB)Cl] derivatives and sodium thiocyanate in acetone (Scheme 2.31). The mixtures were refluxed for several hours upon a colour shift was observable and the complexes could be isolated. The cyanido coligand was introduced for all ligands by reacting the chlorido complexes with KCN in acetone.



Scheme 2.31 Synthesis of [Pd(apyTSCmB)(NCS)] and [Pt(apyTSCmB)(NCS)] by ligand exchange.

2.6.2. UV/Vis spectroscopy

UV/Vis spectroscopy of $[M(\text{apyTSCmB})X]$ showed the formation of the complexes with their respective blueshift of the MLCT upon ligand exchange (Figure 2.65).

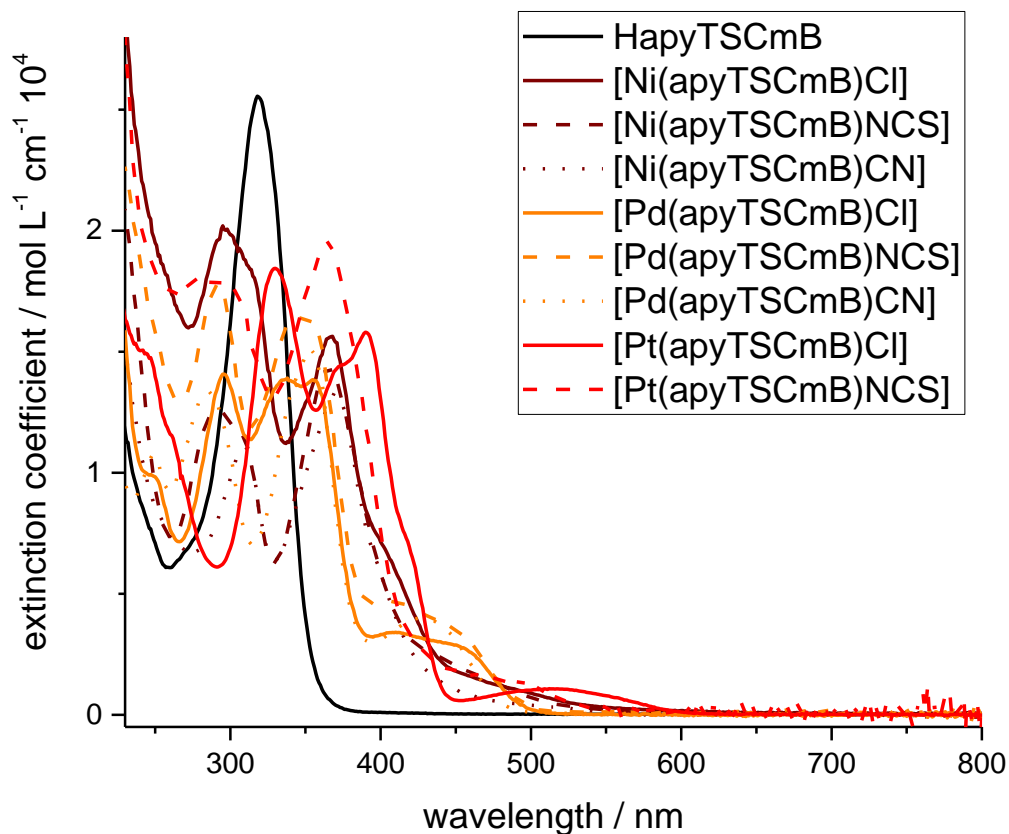


Figure 2.65 UV/Vis absorption spectra of HapyTSCmB, $[M(\text{apyTSCmB})X]$ ($M=\text{Ni, Pd, Pt}$; $X=\text{Cl, NCS, CN}$). All spectra recorded in MeCN.

The spectra unveiled colour of the complexes a bit more. The palladium complexes are all yellow-coloured solids. The absorption of these complexes exhibits the highest energies for the MLCT transition in the series. The nickel and platinum species are at lower energies with $[\text{Pt}(\text{apyTSCmB})\text{Cl}]$ being the lowest at roughly 520 nm. The ligand exchange to stronger coligands lead to a shift of the MLCT whilst the other transitions stay similar among the corresponding metal ion series.

Additionally, a series of $[\text{Pt}(\text{dpyTSCmB})X]$ complexes showed a very interesting shift of the MLCT band. As expected, the band shifts from 504 nm for the chlorido derivative to the cyanido with 475 nm (Figure 2.66). This shift results from a higher stabilization of the HOMO yielding a bigger HOMO-LUMO gap and thus the stronger coligands shift the MLCT to higher energies.

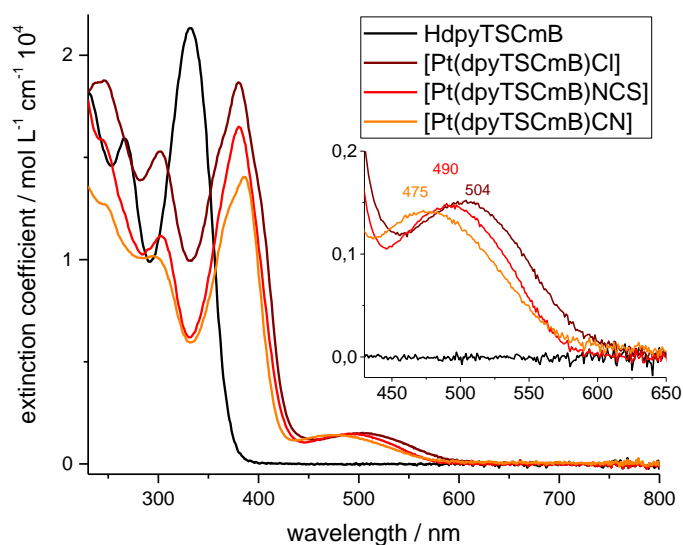
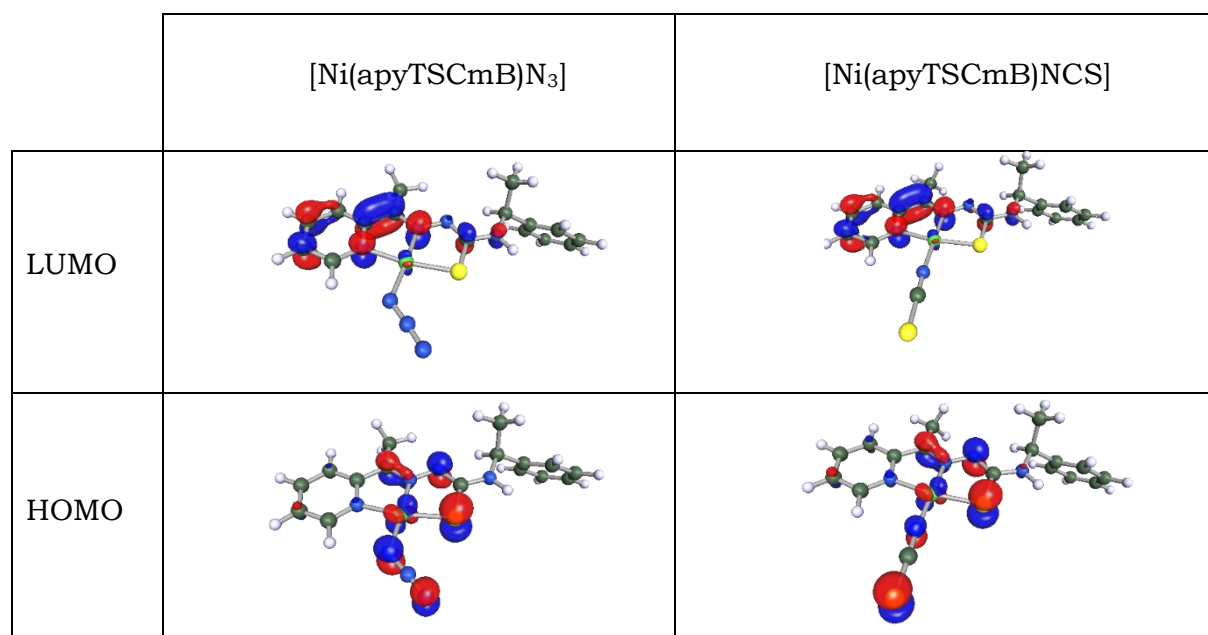


Figure 2.66 UV/Vis absorption spectra of HapyTSCmB, [Pt(dpyTSCmB)X] (X=Cl, NCS, CN). All spectra recorded in MeCN.

Furthermore, since the electronic structure of the thiocyanate coligand is very similar to the structure of the corresponding azido coligand, a reaction like the iClick reaction reported by *Schatzschneider* can be imagined.³⁴⁹ The DFT calculations showed a high comparability between the structures, yet the reactions with alkynes failed to produce similar heterocyclic structures.

The previously mentioned DFT calculations showed that the general orbital distribution is similar, yet the azide is angled (Chart 2.15). Furthermore, the terminal nitrogen carries a formal negative charge in the *Lewis* representation, which may indicate a higher tendency to react in a nucleophilic sense.

Chart 2.15 HOMO and LUMO of [Ni(apyTSCmB)N₃] and [Ni(apyTSCmB)(NCS)]. Calculations were performed on def2-TZVP level with B3LYP functional using $\epsilon = 20.7$ and a refractive index of 1.3 in COSMO to resemble acetone. Isosurface level at 0.06.



2.6.1. Crystal structures of Pd(II) and Ni(II) complexes

Slow evaporation yielded measurable single crystals of [Pd(apyTSCmB)Cl] and [Pd(dpyTSCmB)Cl] (Figure 2.64). Both structures show the expected similarity in the coordination geometry and the values can be compared with the platinum species.

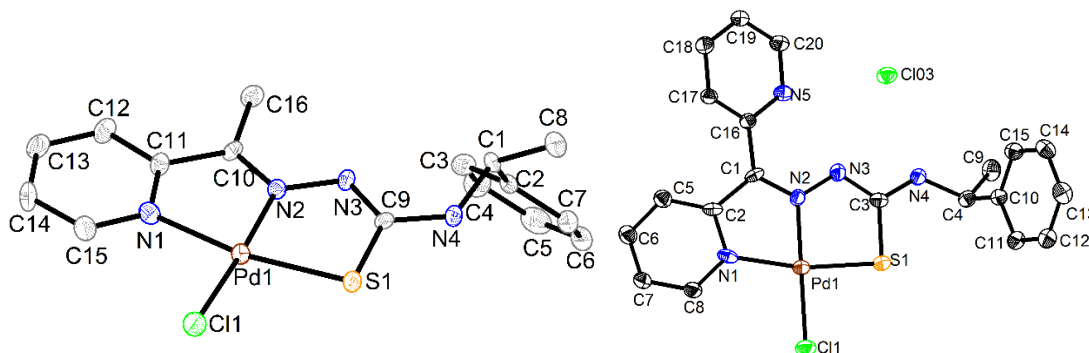


Figure 2.67 Molecular structure of [Pd(apyTSCmB)Cl] (left) and [Pd(dpyTSCmB)Cl]·HCl (right). Atoms are shown with 50% probability. Hydrogen atoms are omitted for clarity.

Table 2.13 Crystallographic data of [Pd(apyTSCmB)Cl], [Pd(dpyTSCmB)Cl]·HCl and [Pt(apyTSCmB)Cl].

	[Pd(apyTSCmB)Cl]	[Pd(dpyTSCmB)Cl]·HCl	[Pt(apyTSCmB)Cl]
Empirical formula	C ₁₆ H ₁₆ ClN ₄ PdS (440.28 g/mol)	C ₂₀ H ₁₈ Cl ₂ N ₅ PdS (537.75 g/mol)	C ₁₆ H ₁₆ ClN ₄ PtS (512.92 g/mol)
Temperature	100(2) K	100(2) K	100(2) K
Radiation source	Synchrotron (0.47686 Å)	Mo Kα (0.70926 Å)	Cu Kα (1.5406 Å)
Crystal system/ Space group	Orthorhombic / P2 ₁ 2 ₁ 2 ₁	Orthorhombic / P2 ₁ 2 ₁ 2 ₁	Orthorhombic / P2 ₁ 2 ₁ 2 ₁
Unit cell parameters	a = 7.2260(14) Å, b = 10.272(2) Å, c = 45.882(9) Å	a = 7.5680(15) Å, b = 11.766(2) Å, c = 23.397(5) Å	a = 7.2536(10) Å, b = 10.2592(14) Å, c = 46.003(6) Å
Volume / Z	3405.6(12) Å ³ / 8	2083.4(7) Å ³ / 4	3423.4(8) Å ³ / 8
ρ _{calc}	1.717 g/cm ³	1.714 g/cm ³	1.990 g/cm ³
μ	1.373 mm ⁻¹	1.265 mm ⁻¹	17.895 mm ⁻¹
F(000)	1762.7	1076.0	1952
Reflections collected	46718	81969	35614
Independent reflections	13084 [R _{int} = 0.0437]	8263 [R _{int} = 0.2091]	6735 [R _{int} = 0.0502]
Data/restraints/parameters	13084/0/189	8263/0/264	6735 / 0 / 419
Goodness-of-fit on F ²	1.352	1.083	1.190
Final R indices [I ₀ > 2σ _{I₀}]	R ₁ = 0.0692, wR ₂ = 0.1780	R ₁ = 0.0665, wR ₂ = 0.1526	R ₁ = 0.0249, wR ₂ = 0.0621
Final R indexes [all data]	R ₁ = 0.0761, wR ₂ = 0.1810	R ₁ = 0.1015, wR ₂ = 0.1685	R ₁ = 0.0261, wR ₂ = 0.0621
Largest diff. peak/hole / e Å ⁻³	1.76/-6.02	2.15/-0.91	1.004 and -1.225

Nickel on the other hand was able to yield crystals suitable for X-ray diffractometry of the chloride and the thiocyanate co ligands. The chlorido species was measured with MoKα wavelength and the thiocyanate crystal were measured at the DESY PETRA III beamline, but the data retrieved from this measurement were still considerably bad, yet the structure could be solved (Figure 2.68 right). In the structures, the Ni(II) centres are square planar. The thiocyanate is coordinated by the

nitrogen atom leading to an isoelectric coligand compared to azides. The thiosemicarbazone is also in the thiolate form.

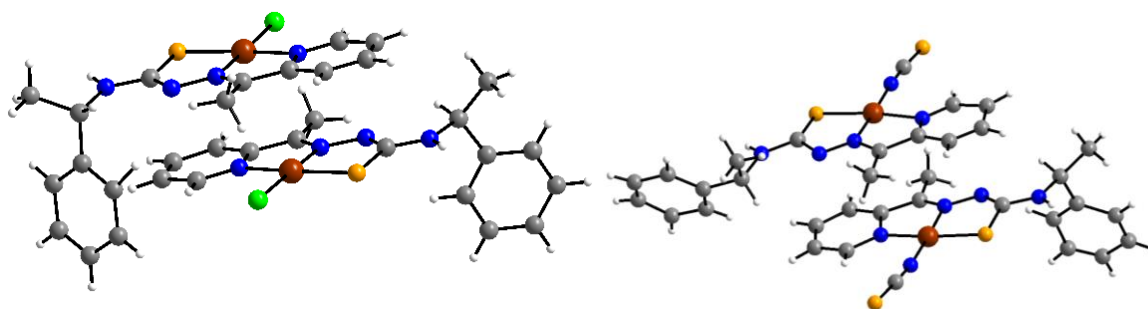


Figure 2.68 Ball-stick representation of the molecular structure of Ni(apyTSCmB)Cl] (left) [Ni(apyTSCmB)NCS] (right).

Table 2.14 Crystallographic data of [Ni(apyTSCmB)Cl] and [Ni(apyTSCmB)NCS].

	[Ni(apyTSCmB)Cl]	[Ni(apyTSCmB)NCS]
Empirical formula/Formula weight	C ₁₆ H ₁₇ ClN ₄ NiS (391.55 g/mol)	C ₁₇ H ₁₇ N ₅ NiS ₂ (414.17 g/mol)
Temperature	100 K	100 K
Radiation source	Mo K α (0.70926 Å)	Synchrotron (0.47686 Å)
Crystal system/Space group	orthorhombic P2 ₁ 2 ₁ 2 ₁	monoclinic P2 ₁
Cell Parameters	a = 9.8842(11) Å b = 14.8587(18) Å β = 90.045(6) $^\circ$ c = 22.153(3) Å	a = 8.6010(17) Å b = 7.2160(14) Å β = 95.59(3) $^\circ$ c = 28.833(6) Å
Volume / Z	3252.5(7) Å ³ / 8	1781.0(6) Å ³ / 4
ρ_{calc}	1.5986 g/cm ³	1.5445 g/cm ³
μ	1.488 mm ⁻¹	1.333 mm ⁻¹
F(000)	1621.4	858.6
2 θ range for data collection/ $^\circ$	4.52 to 52.82	2.84 to 47.06
Index ranges	-11 \leq h \leq 12, -18 \leq k \leq 18, -27 \leq l \leq 27	-9 \leq h \leq 8, -8 \leq k \leq 6, -32 \leq l \leq 24
Reflections collected	59120	6836
Independent reflections	6687 [R _{int} = 0.4166, R _{sigma} = 0.1949]	4251 [R _{int} = 0.0728, R _{sigma} = 0.1185]
Data/restraints/parameters	6687/0/426	4251/1/206
Goodness-of-fit on F ²	0.997	1.035
Final R indexes [I _o > 2 σ (I _o)]	R ₁ = 0.0957, wR ₂ = 0.1668	R ₁ = 0.1682, wR ₂ = 0.3908
Final R indexes [all data]	R ₁ = 0.1535, wR ₂ = 0.1891	R ₁ = 0.1936, wR ₂ = 0.4062
Largest diff. peak/hole / e Å ⁻³	3.09/-1.87	4.29/-2.54
Flack parameter	0.02(4)	0.30(12)

When comparing the crystal structures of [Ni(apyTSCmB)Cl], [Ni(apyTSCmB)NCS], [Pd(apyTSCmB)Cl], and [Pt(apyTSCmB)Cl] they appear to be very similar (Table 2.15). The Ni(II) chloride species exhibit slightly different bonding distances and angles due to the smaller *Van der Waals* radius of the metal ion. Ni(II) has an ion radius of 78 pm whilst Pd(II) is at 86 pm and Pt(II) at 85 pm. As to be expected, the thiocyanate coligand shortens the Ni-X bond distance by 15% compared to the chloride species.

Table 2.15 Bond distances and bond angles of the metal centres in [Ni(apyTSCmB)NCS], [Ni(apyTSCmB)Cl] [Pd(apyTSCmB)Cl] and [Pt(apyTSCmB)Cl].

	[Ni(apyTSCmB)Cl]	[Ni(apyTSCmB)NCS]	[Pd(apyTSCmB)Cl]	[Pt(apyTSCmB)Cl]
M-X	2.171(1) Å	1.851(1) Å	2.307(1) Å	2.317(2) Å
M-N_{py}	1.921(1) Å	1.949(1) Å	2.055(4) Å	2.055(6) Å
M-N_{hy}	1.838(1) Å	1.817(1) Å	1.957(4) Å	1.966(5) Å
M-S	2.150(1) Å	2.143(1) Å	2.255(1) Å	2.262(2) Å
X-M-N_{py}	97.41(1)°	96.93(1)°	97.99(13)°	97.35(18)°
N_{py}-M-N_{hy}	83.40(1)°	84.97(1)°	80.76(17)°	80.20(20)°
N_{hy}-M-S	86.36(1)°	85.78(1)°	85.01(13)°	85.75(17)°
S-M-X	92.80(1)°	92.34(1)°	96.26(5)°	96.75(6)°
Sum Angle	359.97°	360.02°	360.02°	360.06°

2.6.2. Electrochemical analyses of the series

Cyclic voltammetry was used to investigate the influence of the coligand on the redox processes. All 11 complexes were measured using the same conditions and their peak potentials are graphically displayed in Figure 2.69. The palladium complex series seem to have the highest oxidation and lowest reduction potentials compared to nickel and platinum. The nickel species have the lowest band gap comparing the acetylpyridine ligands. The platinum series with the dipyriddy ligand on the other hand has lower band gap. The values for the first oxidation and first reduction are listed in Table 2.16.

Comparing the coligands within their metal ion range it becomes clear that there is no absolute trend detectable. The reduction potential for the nickel seems to increase with the increasing ligand strength, but the palladium species express no such trend for the reduction but the oxidation. This trend is not observable for the other complexes.

As shown in Table 2.16, the electrochemical bandgap of the cyanide complexes is the highest among their series for the platinum and palladium species but the lowest for the nickel complex. And whilst the nickel thiocyanato complex has the biggest difference for the nickel complexes, [Pt(dpyTSCmB)(NCS)] expresses the lowest band gap of all measured complexes.

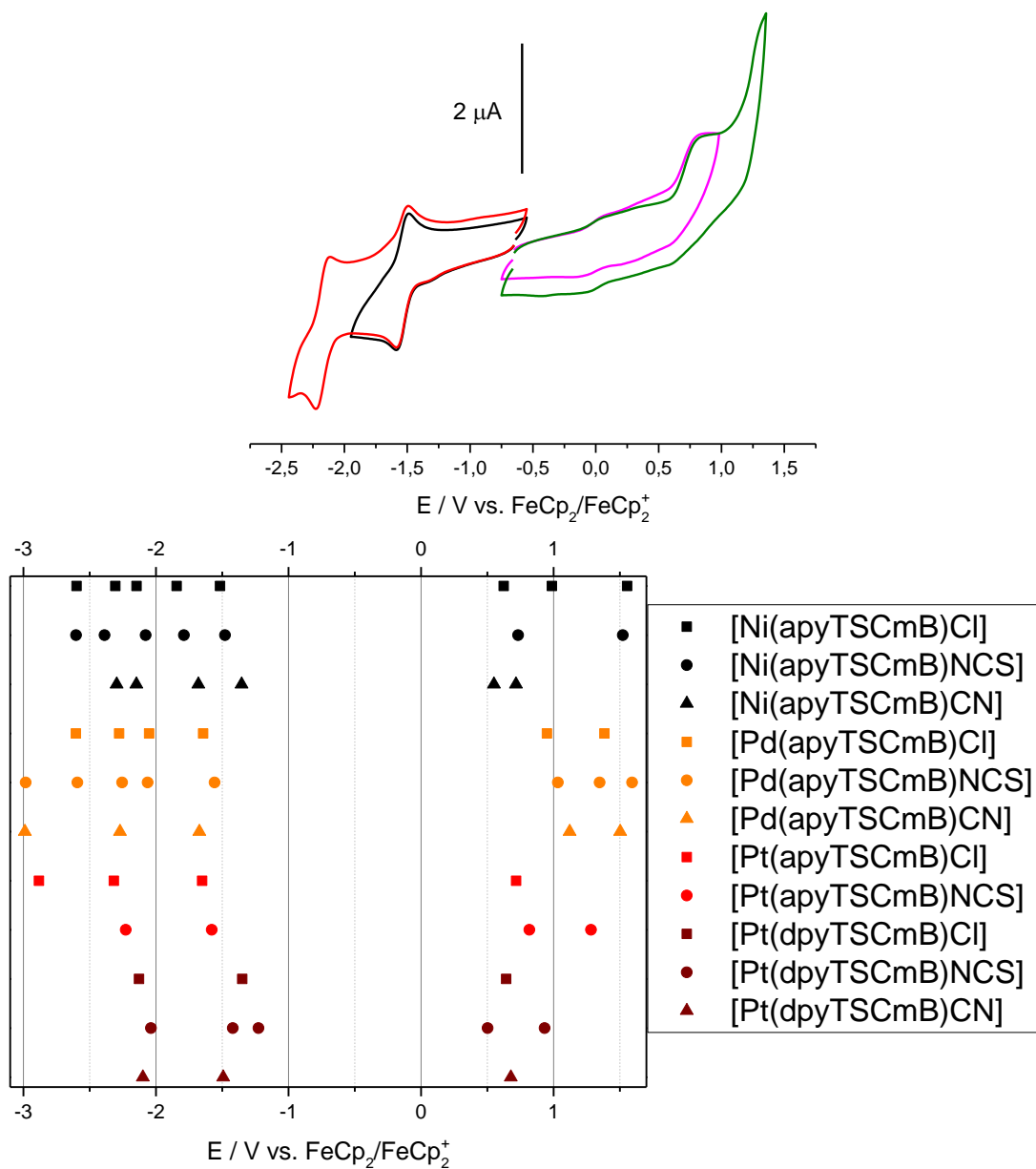


Figure 2.69 Upper: Cyclic voltammogram of [Pt(apyTSCmB)NCS]. Square wave measurements in black. Lower: Peak potentials from cyclic voltammetry of the different complexes. Chlorido complexes are depicted as squares, thiocyanato as circles, and cyanido complexes as triangles. Nickel complexes are in black, palladium in orange and platinum complexes with apyTSCmB⁻ red and dpyTSCmB⁻ wine-red. All cyclic voltammograms were recorded in 0.1 M nBu₄PF₆/MeCN at a scan rate of 100 mV/s.

Table 2.16 Peak potentials of the first oxidation and first reduction from cyclic voltammetry and the calculated electrochemical HOMO-LUMO gap Δ .^a

X	[Ni(apyTSCmB)X]			[Pd(apyTSCmB)X]			[Pt(apyTSCmB)X]		[Pt(dpyTSCmB)X]		
	Cl	NCS	CN	Cl	NCS	CN	Cl	NCS	Cl	NCS	CN
E _{Ox}	0.62	0.73	0.55	0.95	1.03	1.12	0.77	0.82	0.64	0.50	0.68
E _{Red}	-1.52	-1.48	-1.35	-1.64	-1.56	-1.67	-1.66	-1.58	-1.35	-1.23	-1.49
Δ	2.14	2.21	1.90	2.59	2.59	2.79	2.43	2.40	1.99	1.73	2.17

^aMeasured in 0.1 M Bu₄NPF₆/MeCN at 100 mV/s. Potentials E in V, referenced to the redox pair FeCp₂/FeCp₂⁺.

2.6.3. Spectroelectrochemical UV/Vis spectroscopy

Comparing the two palladium complexes [Pd(apvTSCmB)Cl] and [Pd(apvTSCmB)NCS] in SEC-UV/Vis measurements, depicted in Figure 2.70, it is clearly visible that the first reduction occurs on the pyridyl imine site with a new band arising at about 450 nm. This indicates that the first reduction is still the same process whereas the first oxidation differs. For the chloro complex the absorption bands decrease the thiocyanate showed a new band at 400 nm, whilst the $\pi-\pi^*$ only show a small hypochromic shift. The oxidation of the thiocyanate may cause this behaviour explaining the difference.

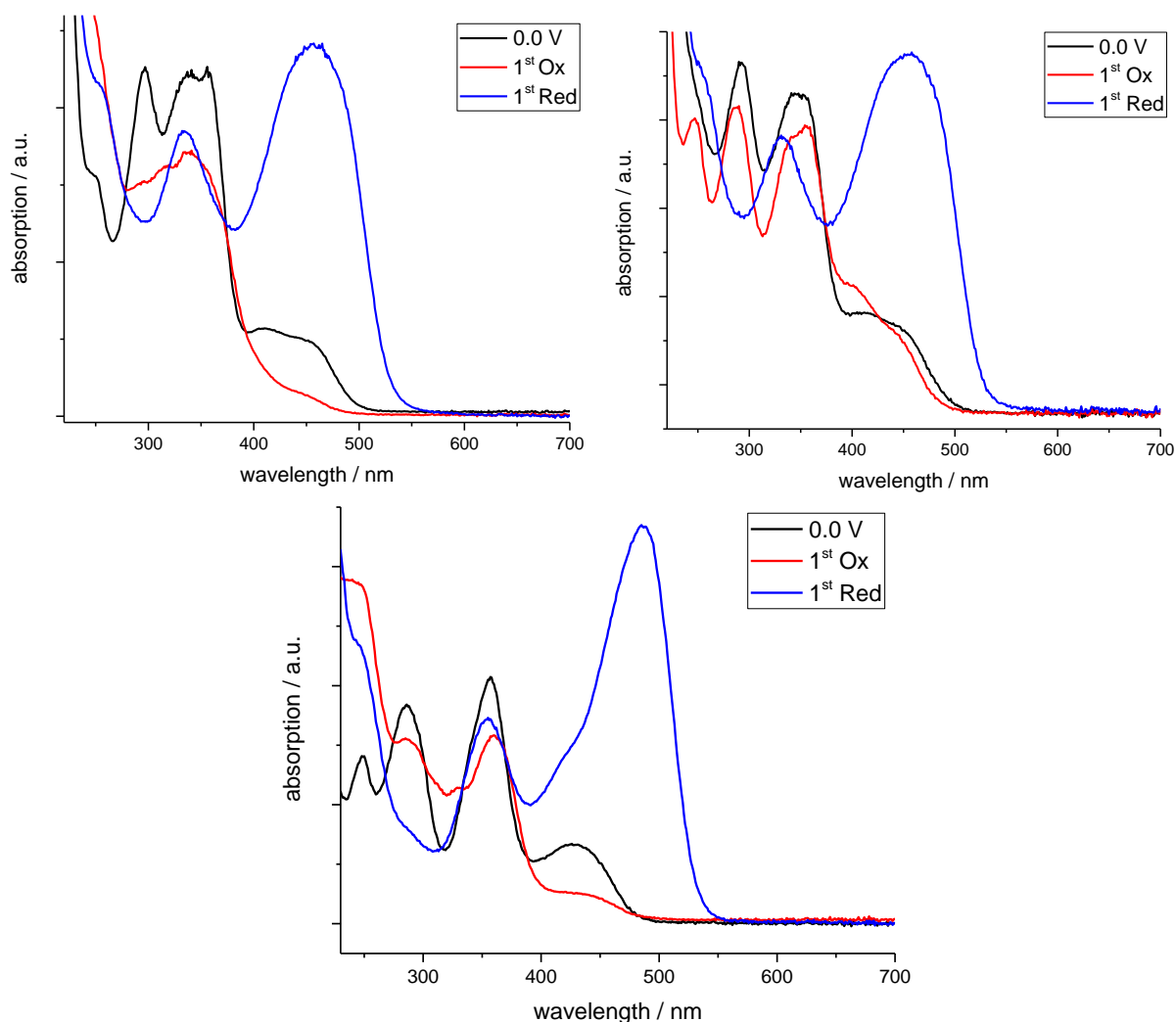


Figure 2.70 UV/Vis spectra of the neutral complexes (black), after the first oxidation (red) and after the first reduction (blue) of [Pd(apvTSCmB)Cl] (upper left), [Pd(apvTSCmB)NCS] (upper right) and [Pd(apvTSCmB)CN] (lower middle). All spectra recorded in MeCN.

Measuring the SEC-UV/Vis spectra of [Ni(apvTSCmB)X] it is clearly visible that the first reduction still occurs at the pyridyl imine moiety with a new band at 450 nm as shown in Figure 2.71. The oxidation on the other hand shows a completely different

band structure. A possible Ni(III) species may lead to a further chemical process dissociating the complex as no bands corresponding to MLCT are observable.

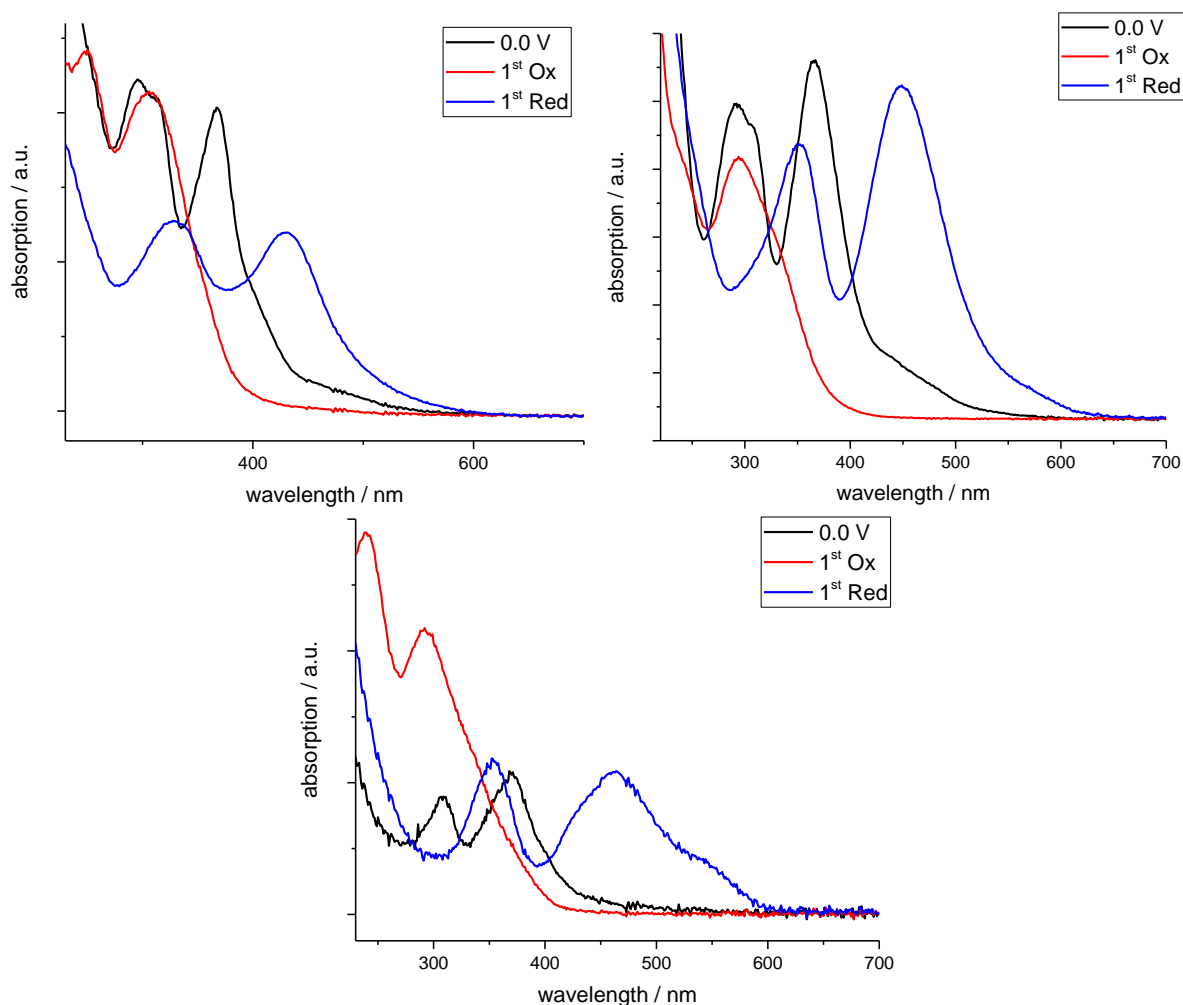


Figure 2.71 UV/Vis spectra of the neutral complex (black), after the first oxidation (red) and after the first reduction (blue) of [Ni(apYTSCmB)Cl] (upper left), [Ni(apYTSCmB)NCS] (upper right) and [Ni(apYTSCmB)CN] (lower middle). All spectra recorded in MeCN.

Concluding the electronic effect of the ligand exchange with the Chapter 2.6 and the already shown measurements for the platinum analogues in Chapters 2.3.4.3. and 2.5.2, it seems that the overall effect is harder to describe than expected. The band gap cannot be described simply like increasing the ligand strength leads to increased HOMO-LUMO bandgap. But the cyanide ligand seems to be strong enough to change the first reduction. The induced higher electron density at the metal centre is likely to change the distribution of the SOMO of the generated radical anion.

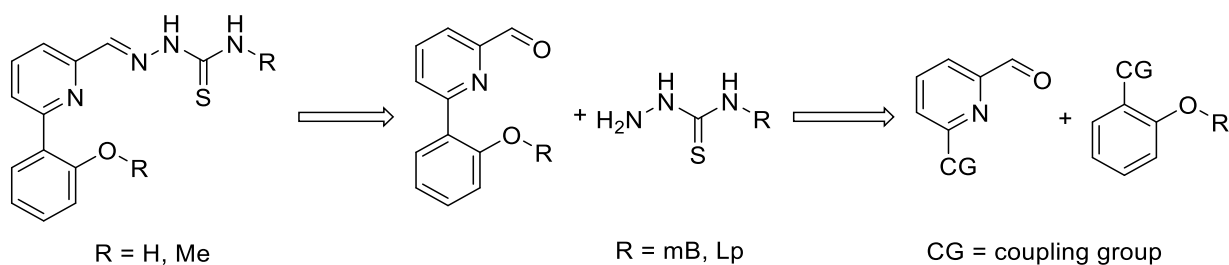
2.7. Tetradentate O^NN^S TSC ligands containing a pending pyridyl phenolate group

2.7.1. Synthesis of H₂hphfpyTSCmB

The previously synthesized complexes containing of a tridentate thiosemicarbazone and a halido coligand had the flaw that the coligand is just hemi stable. This can be observed in the HPLC purification of the peptide conjugates. In this not only the intact complex is detected but also the dehalido species could be measured in reasonable amounts.

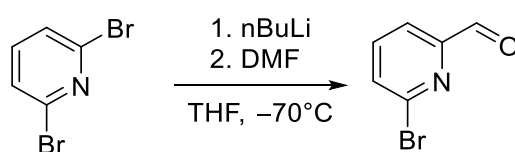
To increase the stability means lowering the amount of a “dehalided” species. That problem can be tackled by either changing the halido coligand to a stronger coligand as done in Chapter 2.6 or by changing the ligand backbone.

By adding an alcoholate moiety in the space of the former coligand a tetradentate dianionic species can be generated (Scheme 2.32). Using phenolates the conjugation between the phenol and the pyridine may enhance the planarity and thus forming a rigid cage around the centre ion. Primarily d⁸ systems like the nickel group would favour such a coordination sphere which would suit the use as ligand system in the platinum peptide conjugate system previously described. But also, further ligands that favour a coplanar tetradentate moiety would be suitable.



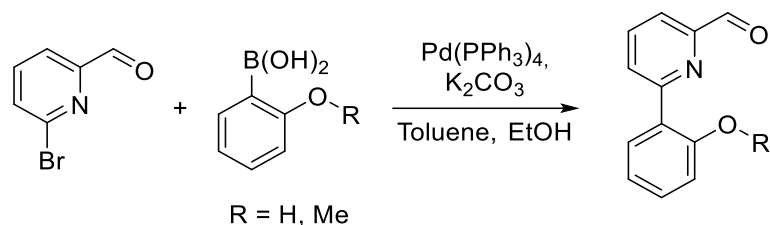
Scheme 2.32 Retrosynthetic approach for the synthesis of tetradentate thiosemicarbazones.

The synthesis route starts with the pyridine carbonyl. The cheapest road for the synthesis of a 2-carbonyl pyridine with a coupling group in position 6 was the synthesis of 6-bromopicolinaldehyde from 2,6-dibromo pyridine with DMF (Scheme 2.33)



Scheme 2.33 Synthesis of 6-bromopicolinaldehyde.

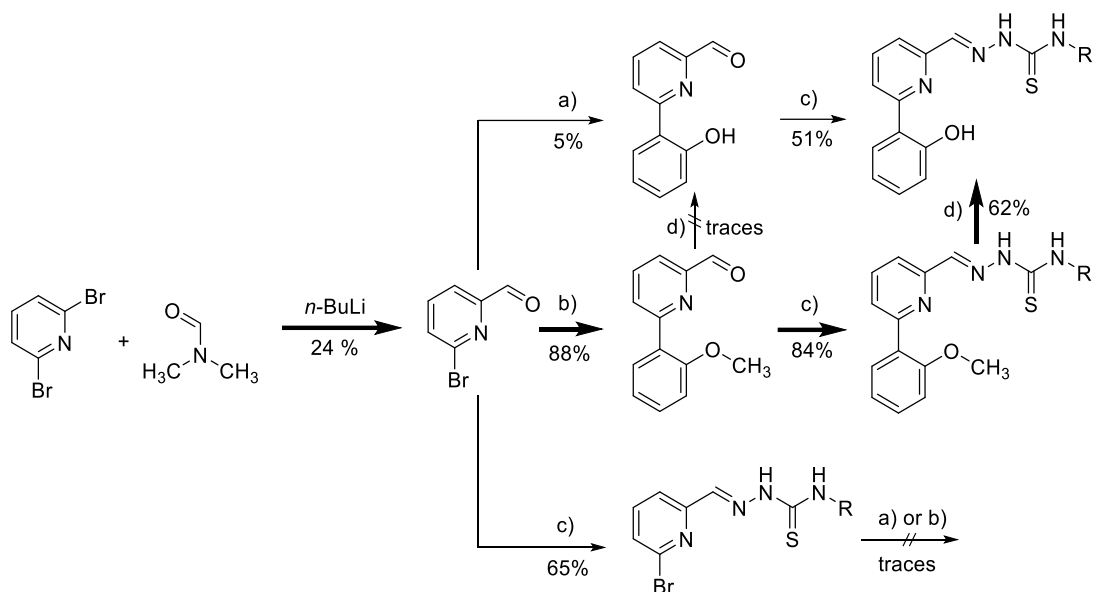
This molecule also defines the coupling group of the phenol. *Suzuki* type reactions can perform the C–C coupling between boronic acids and bromo arenes. Using (2-hydroxyphenyl)boronic acid and (2-methoxyphenyl)boronic acid can yield the deprotected and protected phenol derivative of the desired carbonyl (Scheme 2.34).



Scheme 2.34 Synthesis of 6-phenylpicolinaldehyde.

These carbonyls can be used in the standard condensation reaction for thiosemicarbazones yielding the tetradentate in a protected and a deprotected form. The methoxy derivative itself might also be a suitable ligand for metal ions like Cu(I), but for the topic of the nickel group complexes the alcoholates are favorable. Methoxyphenyl can be deprotected by using boron tribromide.

2,6-Dibromopyridine was reacted with *n*-BuLi and DMF giving 6-bromo-2-pyridinecarbaldehyde in 24% yield (Scheme 2.35). Subsequent *Suzuki* coupling using 2-methoxyphenyl boronic acid gave 6-(2-methoxyphenyl)picolinaldehyde in 88% (Scheme 2.35, a). In the same way, we tried 6-(2-hydroxyphenyl)picolinaldehyde but obtained only 5% yield (b). Both were converted into the thiosemicarbazones (TSC) through reaction with (*S*)-*N*4- α -methylbenzyl thiosemicarbazide in 84% or 51% yield, respectively (c). The protecting methoxy group was successfully converted to the hydroxy function using BBr₃ (d). Alternatively, we also tested a route in which the 2-formyl-6-bromo-pyridine was reacted with the thiosemicarbazide (Scheme 2.35, bottom, c). However, the final *Suzuki* reactions (a and b) did not work with this substrate, and we received only traces of the hydroxy and methoxy products. The overall yield of the “methoxy route” (upper reaction sequence) was 18 times higher than the direct route (middle reaction sequence) which gave only 2.5% overall yield for the protoligand (ligand prior to deprotonation) H₂hphfpyTSCmB.



Scheme 2.35 Synthesis routes and their yields starting from 2,6-dibromo pyridine. Conditions: a) (2-hydroxyphenyl) boronic acid, b) (2-methoxyphenyl) boronic acid both with Pd(PPh₃)₄, K₂CO₃ in boiling toluene/EtOH for 20 h; c) N4 methyl benzyl thiosemicarbazide in MeOH, glacial acetic acid at 60 °C in ultrasonic bath for 2 h; d) BBr₃ in DCM at ambient temperature for 4 h.

The ligand could be characterized using NMR techniques in CDCl₃ as well as ESI(+)-MS. Comparing the NMR data with the other formyl pyridine thiosemicarbazones, the influence of the 6 position on the backbone might become understandable.

2.7.1.1. Analysis by NMR for 6-substituted pyridine TSCmB

The highly deshielded singlet signals at 14.60 ppm and 9.35 ppm correspond to the hydroxyl and hydrazone protons. The amine forms a doublet at 7.98 ppm due to the correlation with the chiral carbon atom and the proton there has a quintet at 5.71 ppm. The imine proton is a singlet at 7.81 ppm.

For comparison, the ¹H NMR spectra of the 2-formyl pyridine, 2-formyl 6-bromo pyridine, 2-formyl 6-phenyl pyridine, 2-formyl 6-(2-methoxyphenyl) pyridine and 2-formyl 6-(2-hydroxyphenyl) pyridine derivatives in CDCl₃ are plotted in Figure 2.72. Especially with a focus on the hydrazone and the secondary amine.

The shifts for the chiral proton signal exhibits almost no shift. A slight shift for the hydroxyphenyl derivative is observable. The hydrazone gets deshielded drastically going from bromopyridine to hydroxyphenyl pyridine whereas the secondary amine shifts to lower fields.

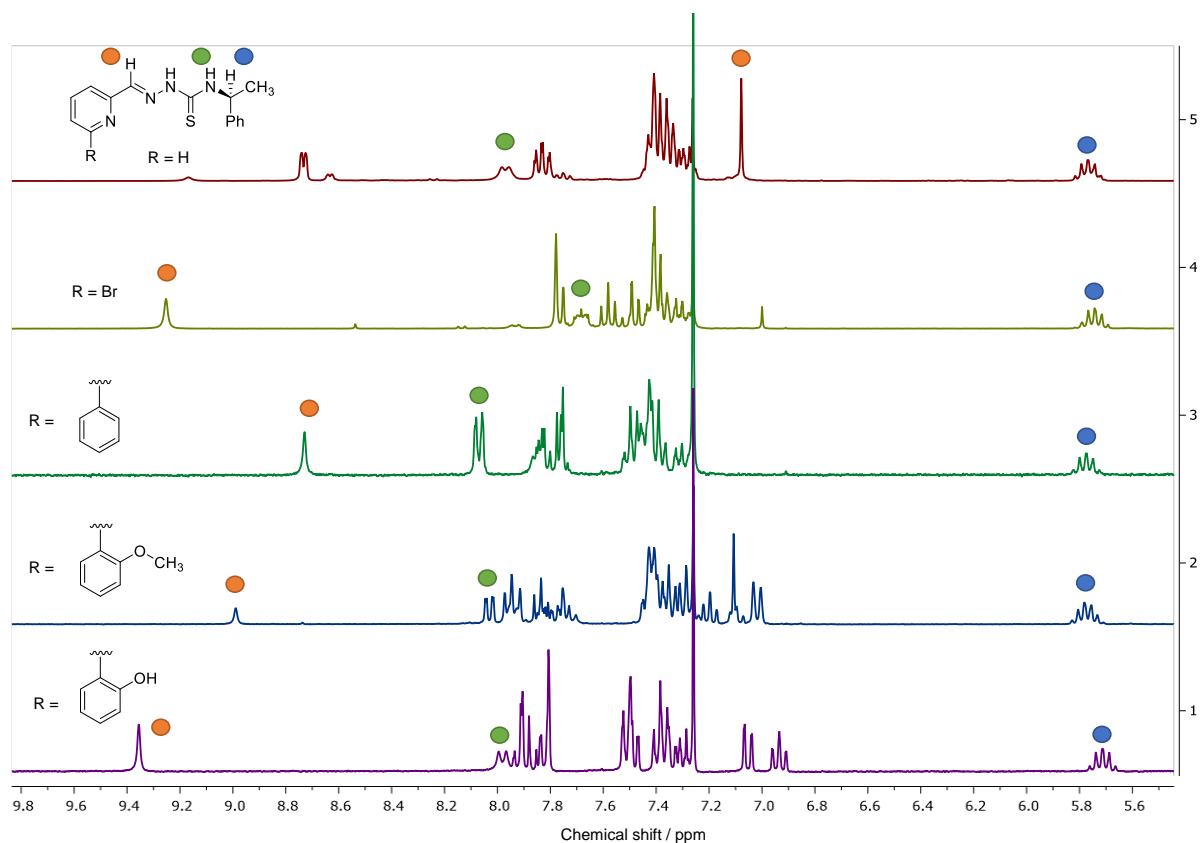
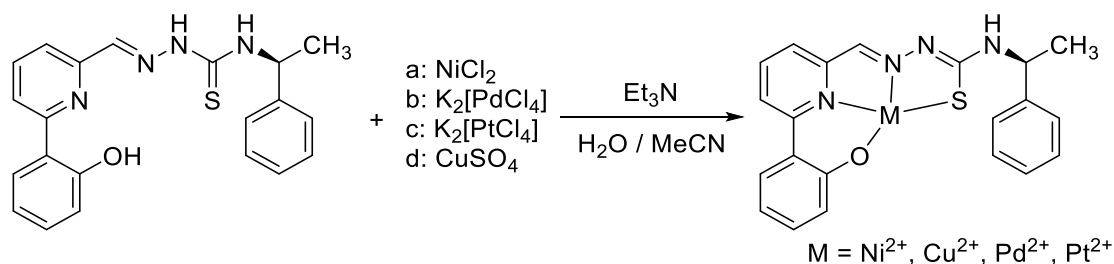


Figure 2.72 ^1H NMR spectra of 2-formyl pyridine, 2-formyl 6-bromo pyridine, 2-formyl 6-phenyl pyridine, 2-formyl 6-(2-methoxyphenyl) pyridine and 2-formyl 6-(2-hydroxyphenyl) pyridine thiosemicarbazones in CDCl_3 at 300 MHz.

2.7.2.Synthesis of $[\text{M}(\text{hphfpyTSCmB})]$ for $\text{M}=\text{Ni}, \text{Cu}, \text{Pd}, \text{Pt}$

The complexes were obtained through mixing of equimolar amounts of 6-(2-hydroxyphenyl)-2-formyl-pyridine N4-methylbenzyl TSC dissolved in MeCN with aqueous solutions of NiCl_2 , K_2PdCl_4 , or K_2PtCl_4 in the presence of NEt_3 as base (Scheme 2.36) The basic conditions assist the double deprotonation during the complexation of the metal ions. The coordination sphere is resembling a distorted square planar structure with a planar dianionic $\text{O}^-\text{N}^-\text{N}^-\text{S}$ ligand system. All complexes were isolated by column chromatography with ethyl acetate as eluent. The complexes exhibit the same retardation factor on TLC plates with around $R_f = 0.8$ compared to the ligand with $R_f = 0.9$. All complexes are strongly coloured and thus easily recognizable as intense red or brown bands on the silica column.



Scheme 2.36 Synthesis of complexes of $\text{H}_2\text{hphfpyTSCmB}$.

2.7.2.1. NMR spectroscopy of d⁸ complexes

The complex formation could also be shown with NMR spectroscopy (Figure 2.73). The NMR spectra of the metal complexes appear to be very similar. The phenolate protons are shifted to higher fields for the platinum species and exhibit a little coupling to the metal centre but overall, all characteristics remain similar. The similarity of the spectra underlines the formation of structurally similar complexes.

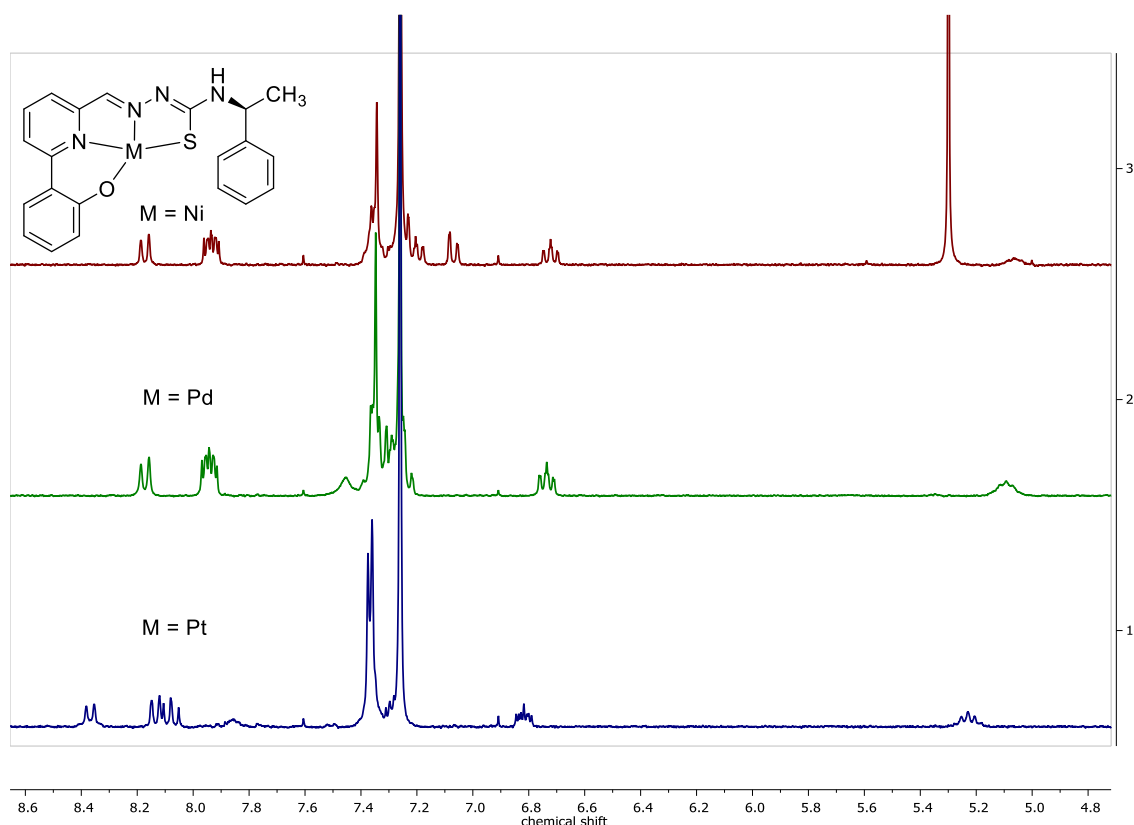


Figure 2.73 ¹H NMR spectra of [M(hphfpyTSCmB)] (M = Ni, Pd, Pt) in CDCl₃ at 300 MHz.

A nice feature of the *N4* substitution is again noticeable. The proton at the chiral carbon atom is shifting upon complexation since the neighbouring thioamide group changes to the thiolate function and this becomes visible in the NMR due to the shift of the quintet from 5.7 ppm to 5.2 ppm.

2.7.2.2. EPR of [Cu(hphfpyTSCmB)]

Since Cu(II) is a d⁹ ion, it exhibits a S = 1/2 ground state and thus EPR is a feasible method to get some insight into the surrounding structure of the unpaired electron. The EPR spectra of [Cu(hphfpyTSCmB)] in MeCN at ambient temperature is shown in Figure 2.74.

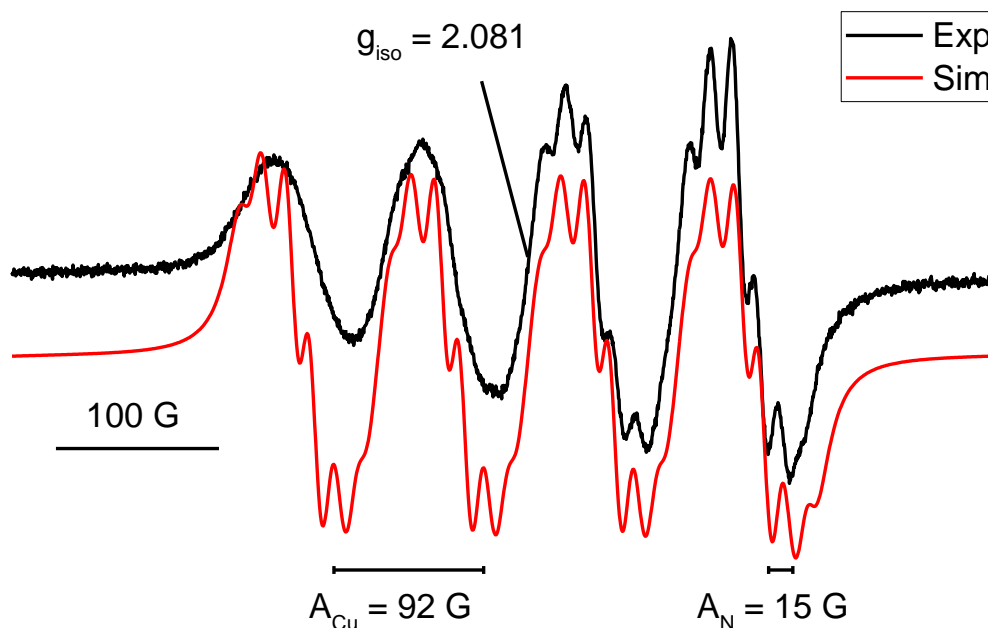


Figure 2.74 X-Band EPR spectrum of [Cu(hphfpyTSCmB)] in MeCN solution at ambient temperature and 9.873084 GHz. The simulation was performed with a Lorentzian fit with the following parameters: $g_{\text{iso}} = 2.081$, $A_{\text{Cu}} = 92$ G, $2 \times A_{\text{N}} = 15$ G, $A_{\text{H}} = 11$ G, linewidth 12.8 G. Experimental spectrum in black, simulated spectrum in red.

The isotropic EPR spectrum shows 4 major lines with a $g_{\text{iso}} = 2.081$, as expected for $I = 3/2$ nuclei like ^{63}Cu and ^{65}Cu with a spin of $S = 1/2$. Hyperfine coupling to two nitrogen atoms with $A_{\text{N}} = 15$ G and one hydrogen atom with $A_{\text{H}} = 11$ G completes the hyperfine coupling. This simulation fits to the general structure of the supposed [Cu(hphfpyTSCmB)] with pyridine and hydrazone donors as well as one hydrogen defining the spin Hamiltonian.

2.7.2.3. UV/Vis spectra and TD-DFT for [M(hphfpyTSCmB)]

UV/vis spectroscopy of the ligand and the platinum complex show some interesting features (Figure 2.75). The MLCT is at around 530 nm followed by three transitions at higher energies. The fourth band seems to resemble a sharper band of the $\pi\text{-}\pi^*$ transition in the ligand and due to the added restraints by the complexation it got narrower. Also, two intense high energy transitions are detectable.

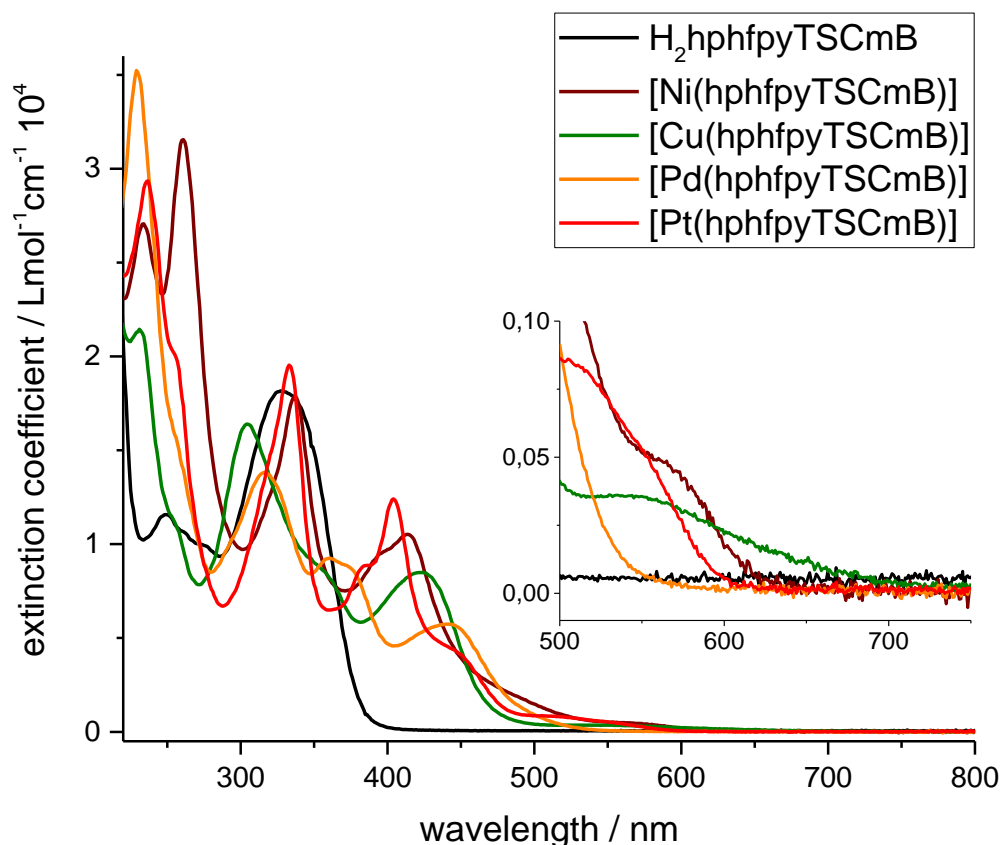


Figure 2.75 UV/Vis spectra of $H_2hphfpyTSCmB$ and the corresponding $[M(hphfpyTSCmB)]$ metal complexes ($M = Ni, Pd, Pt, Cu$). All spectra recorded in MeCN.

The absorption of the other complexes of the nickel group shows similar characteristics. The nickel complex $[Ni(hphfpyTSCmB)]$ MLCT absorbs at a bit higher wavelength compared to the platinum complex, but the characteristic bands are very similar in intensity and energy. The palladium complex on the other hand has remarkably lower MLCT transitions. Also, the other bands are drastically shifted for the palladium species. This phenomena was already described 50 years ago by *Sonogashira* and *Hagihara* and can be explained by the influence of the unoccupied $(n+1)p$ orbitals on the molecular orbitals of the occupied nd orbitals and the donating orbitals of the ligand.³⁵⁰ This contribution leads to the similarity of the nickel and the platinum species whereas it is different for palladium.

$[Cu(hphfpyTSCmB)]$ exhibits four absorption bands (Figure 2.75 green). Two bands at 305 nm and 328 nm as well as the band at 423 nm are in line with the nickel and platinum derivatives. At 552 nm is a band which can be assigned to a MLCT but compared with the d^8 homologues this band is much broader. This can be caused by a weak $d-d$ transition which is submerged under the MLCT. The broadening may also be the reason for the different colour in comparison to the dark red nickel complex ($\lambda_{max} = 592$ nm).

Quantum chemical calculations performed by *G. Hömer* predict the square planar coordination sphere for the nickel group complexes. Comparing the tetradentate platinum species with the tridentate of complex [Pt(fpyTSCmB)Cl] helps understanding the influence of the phenolate structure. The alcoholate is a harder base than chloride but due to the phenyl ring the conjugation helps distributing the electron density over more atoms.

The calculations also suggest a slightly less distorted square planar geometry for the tetracoordinated platinum complexes with $N^{\wedge}Pt^{\wedge}S$ angle of 164.9° compared to 166.6° .

Comparing the energies and orbital densities of the LUMO shows only little deviation between the three complexes (Figure 2.76). And the LUMO is located mainly on the pyridine-thiosemicarbazone unit with a small density on the metal, with the smallest contribution of palladium. These similarities in the orbital structures and energy levels suggest just small differentiations in their electrochemical behaviour.

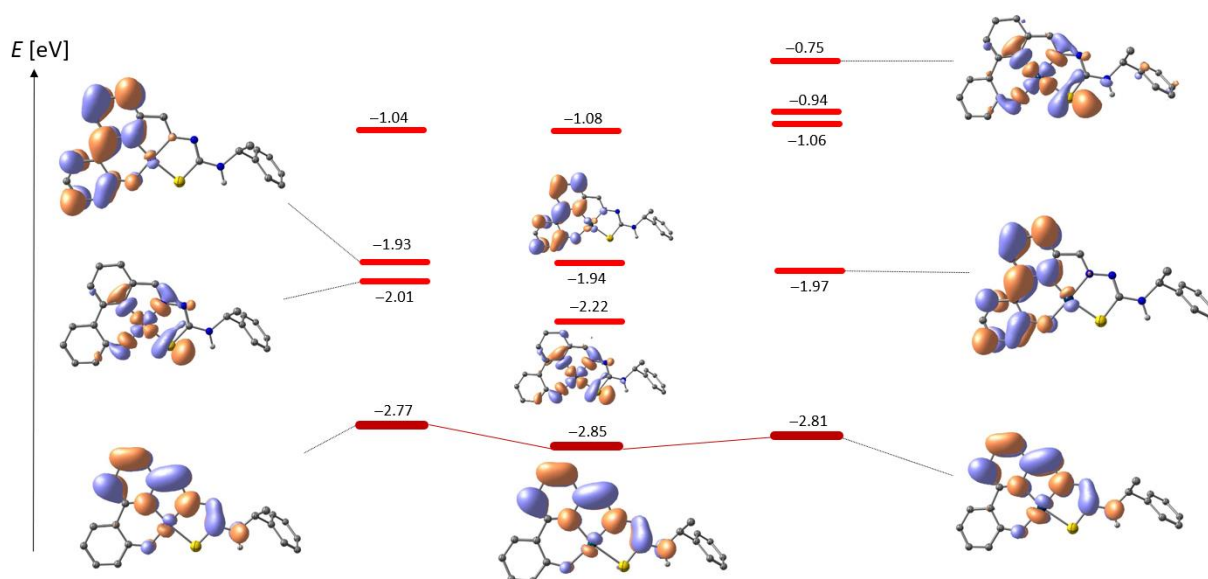


Figure 2.76 DFT calculated unoccupied molecular orbitals for [Ni(hphfpyTSCmB)] (left), [Pd(hphfpyTSCmB)] (middle) and [Pt(hphfpyTSCmB)] (right). The LUMO is highlighted in dark red. Orbital energies are given in eV. Calculations were performed at TPSSh level with def2-TZVP basis set for H,C,N,O,S and LANL2DZ for the metal ions.

The comparison of HOMOs is very similar to the LUMO comparison (Figure 2.77). The HOMO density has a high contribution of the phenolate and thiolate moieties. The metal ions' contribution is very small but for the palladium complex its minimal. The overall similarity of nickel and platinum complexes is also visible in the lower orbitals with the exception of the nonbonding d_{z^2} orbital at platinum, which should be due to relativistic effects.

This can be interpreted as the weakest donor-metal interaction for palladium or lowest covalency. Since the HOMO is in all cases an antibonding donor-metal interaction, it translated to the weakest interaction and the lowest HOMO for palladium. This also means that whilst the nickel and platinum complex should be similar ionizable, the palladium complex should be the hardest to ionize. The calculated energies can be compared to photoelectron spectroscopic measurements with a methodological offset of around 0.7 eV.

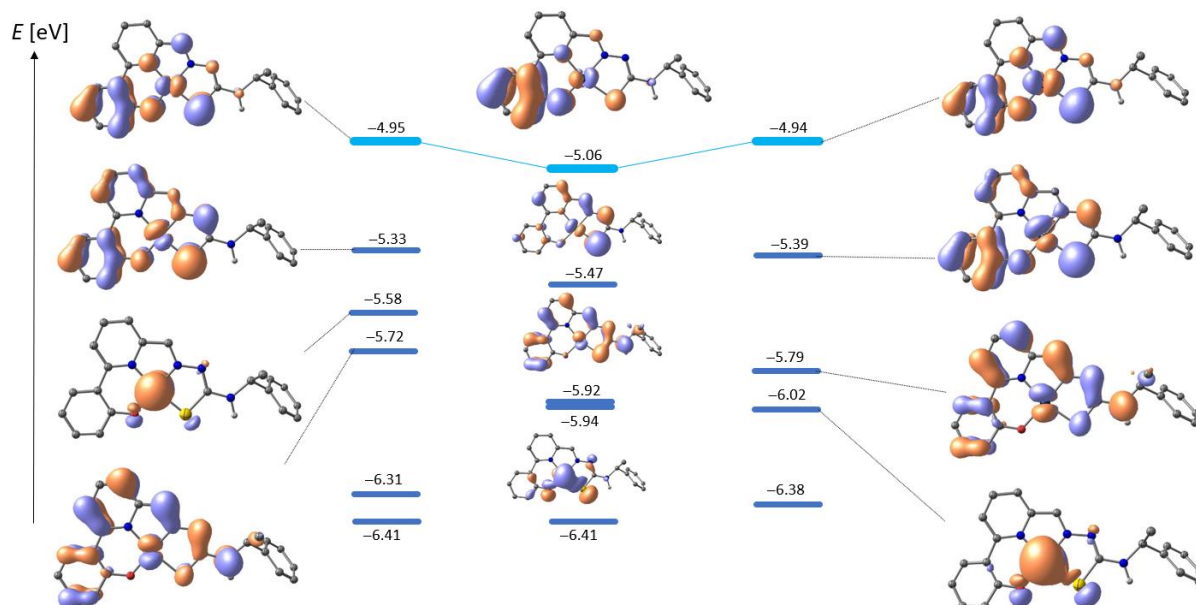


Figure 2.77 DFT calculated occupied molecular orbitals for [Ni(hphfpyTSCmB)] (left), [Pd(hphfpyTSCmB)](middle) and [Pt(hphfpyTSCmB)] (right). The HOMO is highlighted in light blue. Orbital energies are given in eV. Calculations were performed at TPSSh level with def2-TZVP basis set for H,C,N,O,S and LANL2DZ for the metal ions.

The calculations also gave absolute energies for the HOMO and LUMO. The absolute HOMO energy can be determined with ultraviolet photoelectron spectroscopy (UPS). The UPS measurements of the triadic complexes are shown in Figure 2.78. These measurements were taken to determine the workfunction Wf and the ionization energy I_E (the same as the binding energy in the highest occupied molecular orbital (HOMO)) of the materials. Therefore, only the regions of interest of the UPS measurements are highlighted in the right part of Figure 2.78.

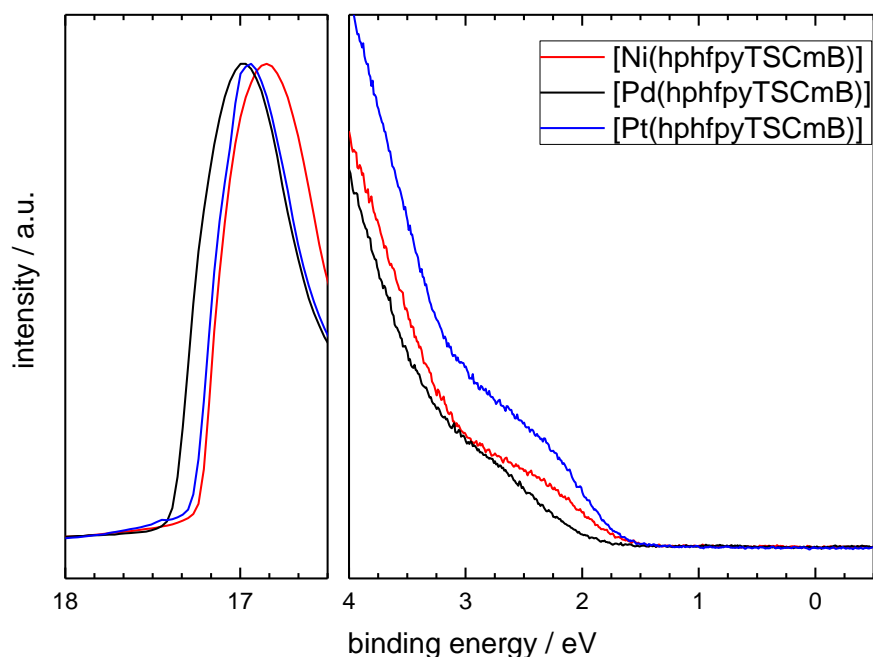


Figure 2.78 The three UPS measurements of the different materials are shown. On the left side the high binding energy cut-off (HBEC) and on the right side the HOMO region is highlighted. The workfunction and the ionization energy are determined by the HBEC and the HOMO region, respectively.

To calculate the workfunction out of a given UPS spectrum the high binding energy cut-off (HBEC), the energy of the excitation source $h\nu$ and the Fermi level E_F need to be known. Then the workfunction is calculated by the difference of the energy of the excitation source and the difference of the HBEC and the Fermi level.

$$Wf = h\nu - (HBEC - E_F)$$

Further, the ionization energy is calculated by the addition of the Wf and the difference of the HOMO onset and the Fermi level.

$$I_E = Wf + (onset - E_F)$$

The values for the HBEC and the HOMO onset are determined by using a linear fit of the cut off and the background and of the HOMO onset and the background, respectively.

Table 2.17 Calculated values for workfunction and HOMO level (ionization energy) for the three complexes. Measured data from UPS and calculated values from DFT at TPSSh level with def2-TZVP (C,H,N,S) and LANL2DZ (metals).

[M(hphfpyTSCmB)]	Ni	Pd	Pt
Workfunction / eV	3.99	3.84	3.94
Ionization energy / eV	5.66	5.76	5.61
Calculated HOMO energy / eV	5.65	5.76	5.64

The calculated and measured values of the HOMO energy suggest a good approximation for the calculation. LUMO energies can be determined with inverse photoelectric spectroscopy (IPES), yet the used electron beam of 20 eV reduced the complexes and no value could be determined.

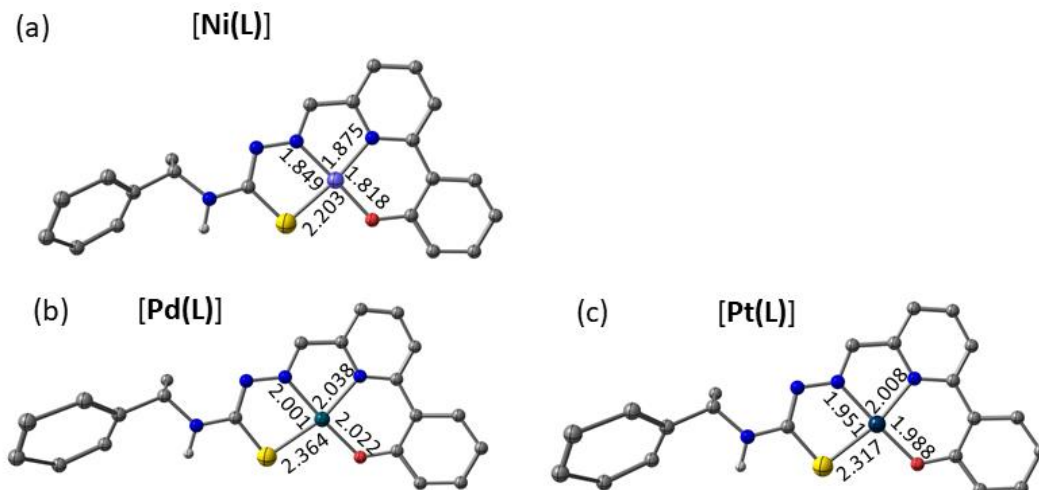


Figure 2.79 Calculated molecular structures of $[M(\text{hphfpyTSCmB})]$ ($M = \text{Ni(a), Pd(b), Pt(c)}$) and the distances from the metal centre to the donor atoms.

The optical spectra of $[M(\text{hphfpyTSCmB})]$ were modelled with TD-DFT methods using the TPSSh hybrid functional, the experimental transition energy and intensity could be satisfyingly matched for all complexes in this study. The calculated spectrum for $[\text{Ni}(\text{hphfpyTSCmB})]$ is shown in Figure 2.75, selected transitions are given in Table 2.18 and a full list of transitions are given in the appendix in Table 7.77, 7.78 and 7.79 and the calculated spectra for $M = \text{Pd}$ and Pt are depicted in Figures 7.481 and 7.482. Accordingly, the leading vis bands in the experimental spectrum $[\text{Ni}(\text{hphfpyTSCmB})]$ at $\lambda = 413$ and 560 nm can be attributed to intense LLCT transitions calculated at $\lambda = 420$ and 540 nm (an additional weak band toward the NIR is predicted for all complexes). Difference densities of these transitions indicate substantial CT character with the diimine unit acting as the acceptor. Ni(II) generally features prominently as an electron source in all transitions in the visible range, giving mixed ILCT/MLCT character. By contrast, the broad near UV transition envelope from $280\text{--}360$ nm is identified as a convolute of numerous individual transitions of varying character; nevertheless, the dominating transitions possess sharply decreased metal character and utilise donor orbitals located rather on the TSC moiety, rendering the transition(s) ILCT like. Similar conclusions and assignments hold for all complexes. However, the metal contribution to the leading transitions decreases along the series $\text{Pt} > \text{Ni} > \text{Pd}$.

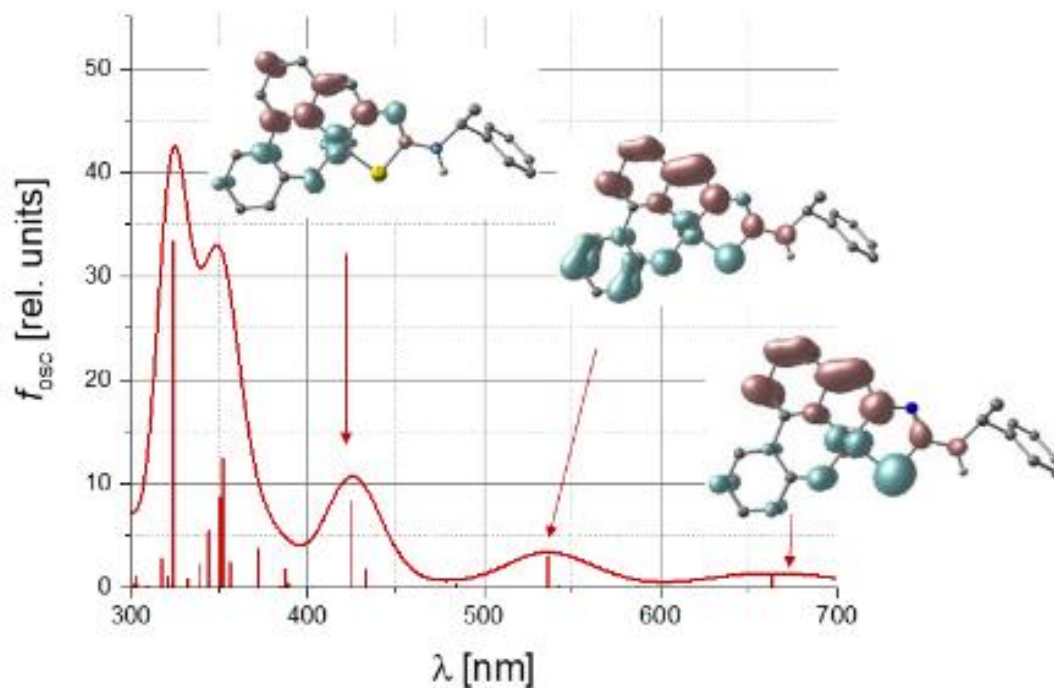


Figure 2.80 Calculated UV/Vis spectra for [Ni(hphfpyTSCmB)] with transitions HOMO-3→LUMO, HOMO-1→LUMO and HOMO→LUMO highlighted.

Table 2.18 Selected TD-DFT calculated absorptions of [Ni(L)]; character denotes leading orbital contributions.

transition	ν / cm^{-1}	λ / nm	f_{osc}	character
[Ni(hphfpyTSCmB)]				
5	15083.7	663	0.012	H → L (87 %)
11	18639.2	536.5	0.029	H-1 → L (82 %)
16	23089.4	433.1	0.017	H → L+2 (67 %)
20	23561.6	424.4	0.082	H-3 → L (48 %)
[Pd(hphfpyTSCmB)]				
3	16087.5	621.6	0.021	H → L (96 %)
5	19081.4	524.1	0.014	H-1 → L (82 %)
14	23475.9	426	0.039	H → L+2 (67 %)
18	24714	404.6	0.09	H-2 → L (40 %) // H-1 → L+2 (35 %)
24	26619	375.7	0.034	H-3 → L+1 (63 %)
[Pt(hphfpyTSCmB)]				
2	15092.2	662.6	0.015	H → L (92 %)
5	18968.9	527.2	0.034	H-1 → L (87 %)
12	24392.1	410	0.151	H-2 → L (46 %)
18	28003.1	357.1	0.046	H-5 → L (40 %)

2.7.2.4. IR spectroscopy

To validate the calculated structures, their calculated IR spectra were compared to the measured IR spectra (Figure 2.81). Deviations occur due to the difference in solvation. The experimental data were collected from solid structures whereas the calculations were performed as MeCN solutions. The intense bands in the region between 1000 cm^{-1} and 2000 cm^{-1} show a good comparison for the complexes. The high energy absorptions at 3000 cm^{-1} still fit well but deviate more.

Since the calculations were performed, the frequencies can be assigned to the vibrational modes. The intense band at 760 cm^{-1} corresponds to an out of plane vibration of the C–H bonds in pyridine and phenylide moieties. The frequencies at $1000 - 1100\text{ cm}^{-1}$ correspond to stretching and deformation vibrations of the methyl benzyl moiety followed by a strong band corresponding to a stretching vibration of the hydrazone nitrogen atoms at 1100 cm^{-1} . A deformation vibration of imine and amine is responsible for the band at 1250 cm^{-1} and the stretching vibration of the hydroxide group leads to the absorption at 1400 cm^{-1} . The most intense band at 1700 cm^{-1} consist of various vibrational modes throughout the molecule, among others are stretching frequencies of the thiourea moiety and in plane deformation vibrations of the phenylide C–H bonds. The high energy frequencies consist of stretching vibrations at the CH_3 and the N4 phenyl group, phenylide and the latest band consists of the stretching vibration of amine.

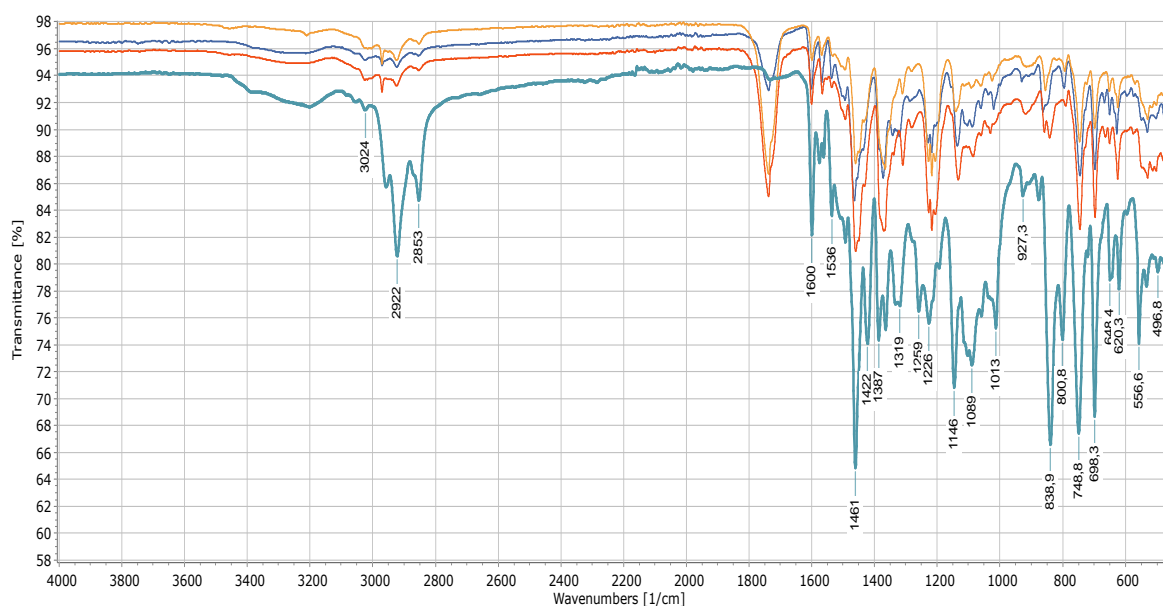


Figure 2.81 IR Spectra of $[\text{M}(\text{hphfyTSCmB})]$ $\text{M} = \text{Ni}$ (blue), Pd (yellow), Pt (orange), Cu (turquoise). All spectra recorded from solid samples.

The copper complex absorbs very similar to the other complexes above 2800 cm^{-1} . Also, the bands at 1600 cm^{-1} , 1461 cm^{-1} , 1146 cm^{-1} , 748 cm^{-1} and 698 cm^{-1} are visible in all spectra. The major difference between the copper structure and the others is the missing absorption at 1700 cm^{-1} .

2.7.2.5. Electrochemical analysis of [M(hphfyTSCmB)]

The cyclic voltammograms of the three nickel group complexes show a high similarity in comparison to the ligand (Figure 2.82). All structures show three one-electron reduction waves and one one-electron oxidation wave in the range of -3.2 V to $+0.94$. It appears that the first three reductions are based of the ligand's electrochemical behaviour. The first reduction on the other hand seems to be stabilized in a way that leads to a reversibility for all complexes.

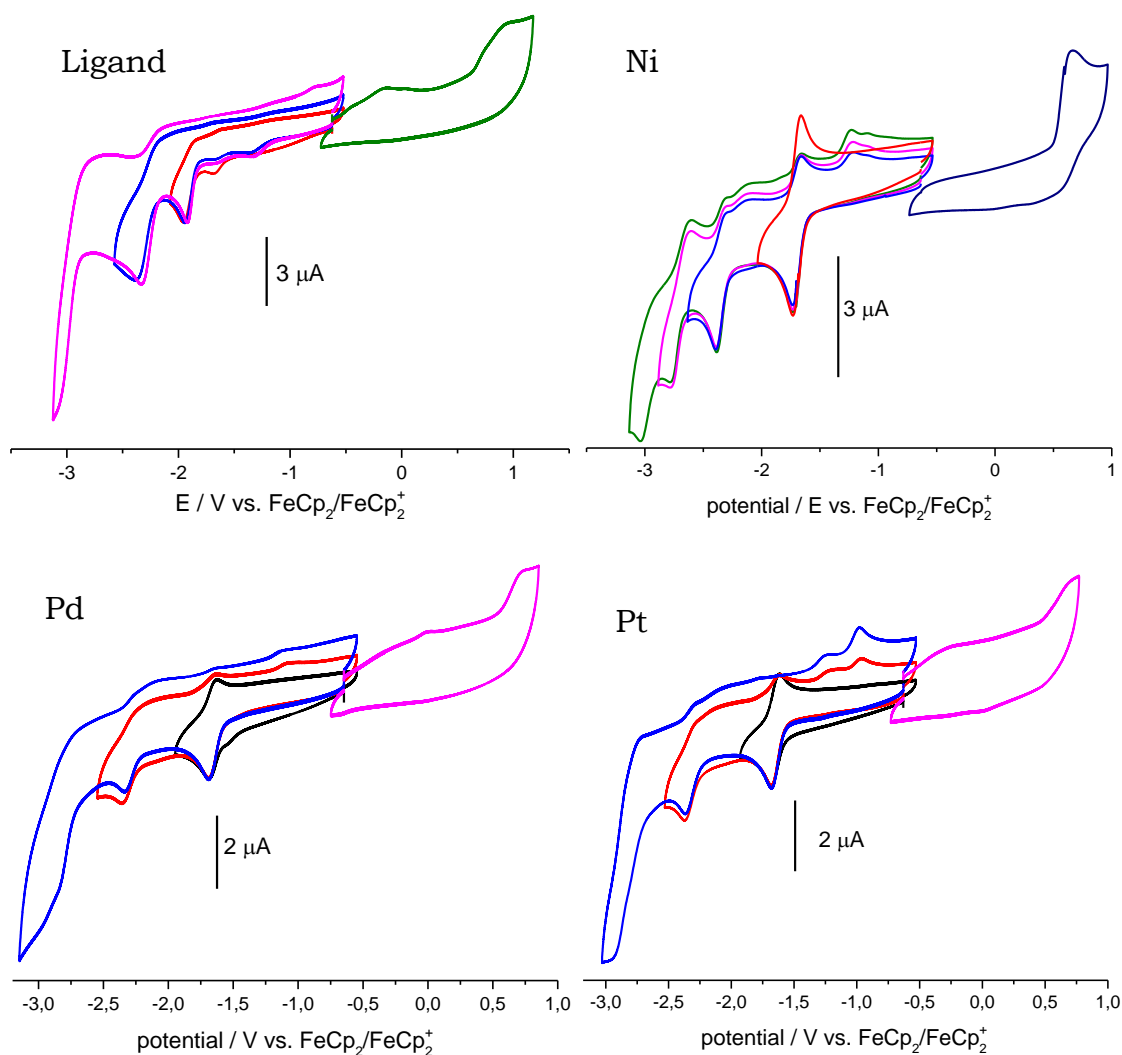


Figure 2.82 Cyclic voltammograms of [Ni(hphfyTSCmB)] (left) and [Pd(hphfyTSCmB)] (right) in 0.1 M Bu_4NPF_6 / MeCN at a feed rate of 100 mV/s.

It is noted that the Ni(II) compound proved to be hardest to reduce, in agreement with the computed LUMO energies. With respect to the protoligands, reduction potentials of the complexes are shifted anodically by 0.4 to 0.6 V pointing to a substantial stabilization of the LUMOs upon complexation. In fact, the cyclic voltammograms of the protoligand showed three irreversible reduction waves in the range from -1.9 to -3.2 V. For the complexes the first reduction gains markedly in reversibility and the three waves were shifted anodically by about 0.25 V.

For the protoligand one irreversible oxidation was observed at 0.94 V. The oxidation potentials recorded in the complex series are shifted cathodically by about 0.3 V when compared with the protoligand. With a view to the HOMOs depicted in Figure 2.73, the first oxidation can be associated with a phenolate/phenoxy redox couple.

Electrochemical analysis of [Cu(hphfpyTSCmB)] showed a difference to the d^8 homologues (Figure 2.83). The first reduction is at -1.3 V, shifted anodically, but the second reduction is at -2.6 V, shifted cathodically. A third reduction was not detected. Also, the oxidation occurs at 0.54 V, 150 mV lower than the oxidations of the other complexes. The calculations for the d^8 -series showed a significant electron density sitting at the metal centre at the HOMO. The lower oxidation potential may be caused by an oxidation of the metal centre (Cu(II)->Cu(III)). The second irreversible oxidation is at 0.86 V and may have a similar origin as the oxidation of the nickel group complexes.

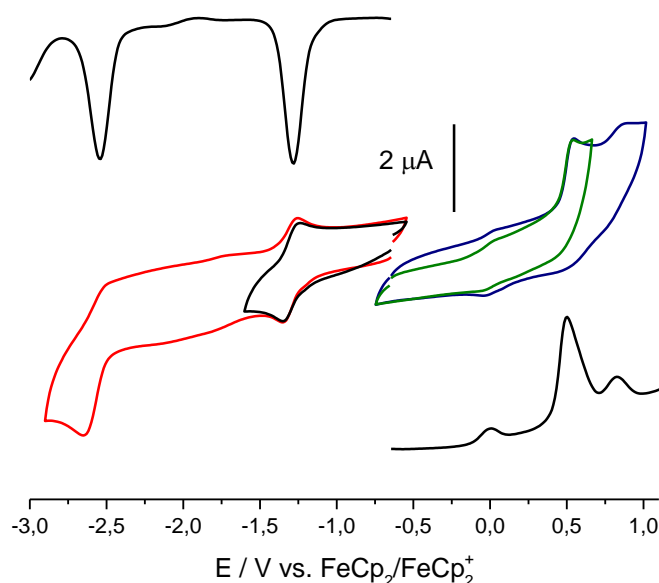


Figure 2.83 Cyclic voltammogram of [Cu(hphfpyTSCmB)] in 0.1 M $n\text{Bu}_4\text{PF}_6/\text{MeCN}$. Scan rate at 100 mV/s. Square wave measurements in black.

Table 2.19 Selected electrochemical data of the protoligand H₂hphfpyTSCmB and the complexes [M(hphfpyTSCmB)] (M = Ni, Pd, Pt).^a

	$E_{1/2}$ – Red2	$E_{1/2}$ – Red1	$E_{1/2}$ – Ox
H ₂ hphfpyTSCmB	-2.36 irr	-1.94 irr	0.94 irr
[Ni(hphfpyTSCmB)]	-2.37	-1.70	0.66 irr
[Pd(hphfpyTSCmB)]	-2.34	-1.66	0.72
[Pt(hphfpyTSCmB)]	-2.36	-1.65	0.69
[Cu(hphfpyTSCmB)]	-2.65	-1.30	0.54

^a From Cyclic voltammetry, electrochemical potentials in V, half-wave potentials $E_{1/2}$ and partially reversible redox waves, anodic (E_{pa}) or cathodic (E_{pc}) peak potentials for irreversible (irr) waves; measured in 0.1 M Bu₄NPF₆/MeCN at a scan rate of 100 mV/s.

2.7.2.6. Spectroelectrochemical analysis

To gain further insight into the electrochemical processes, the ligand as well as the nickel group complexes were measured in spectroelectrochemical UV/Vis absorption spectroscopy. Looking at the oxidation processes the ligand spectra show the rise of a new band at 410 nm while the main absorption bands at 340 nm and 270 nm decrease (Figure 2.84 left). During the second oxidation the newly formed band at 410 nm decreases (Figure 2.84 right).

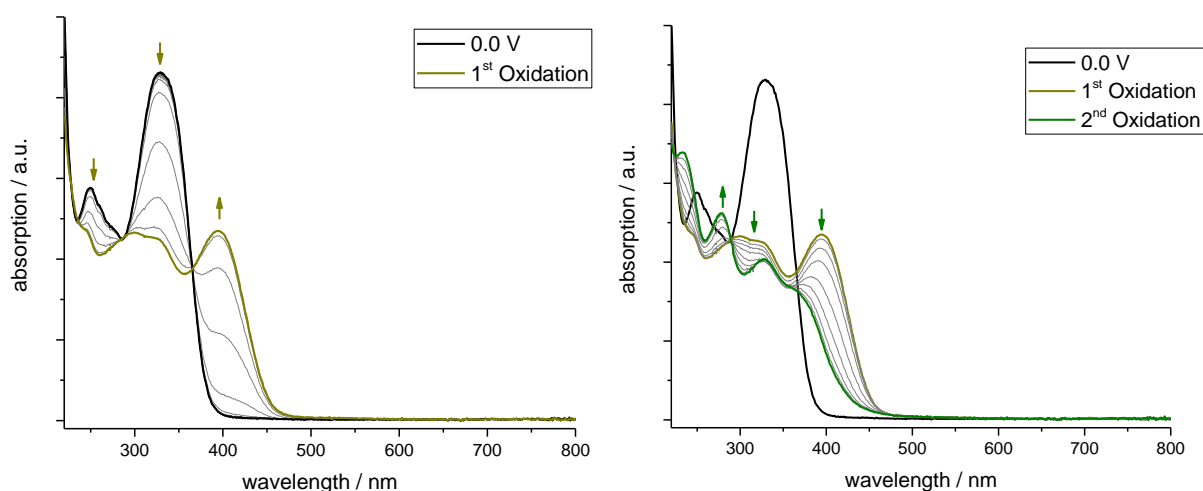


Figure 2.84 Spectroelectrochemical UV/Vis measurements measured during the first (left) and second (right) oxidation in H₂hphfpyTSCmB. All measurements performed in 0.1 M nBu₄NPF₆/MeCN solution with 0.1 V increments.

The UV/Vis spectra recorded during the first and second oxidation of the complexes are quite similar (Figure 2.85). The first reduction leads to a decrease in the low energy transitions. The high similarity could also be predicted by DFT calculations. Bands ranging between 300 nm and 500 nm, akin to those in Figure 2.80 were previously assigned to the oxidation of the phenolate group forming a coordinated phenoxy radical.³⁵¹⁻³⁵⁴ The second oxidation shows broad ramp like transitions starting at around 600 nm for all complexes. This leads also to a radical cation at the phenol moiety which is able to recombine and thus lead to an irreversibility of the first oxidation.

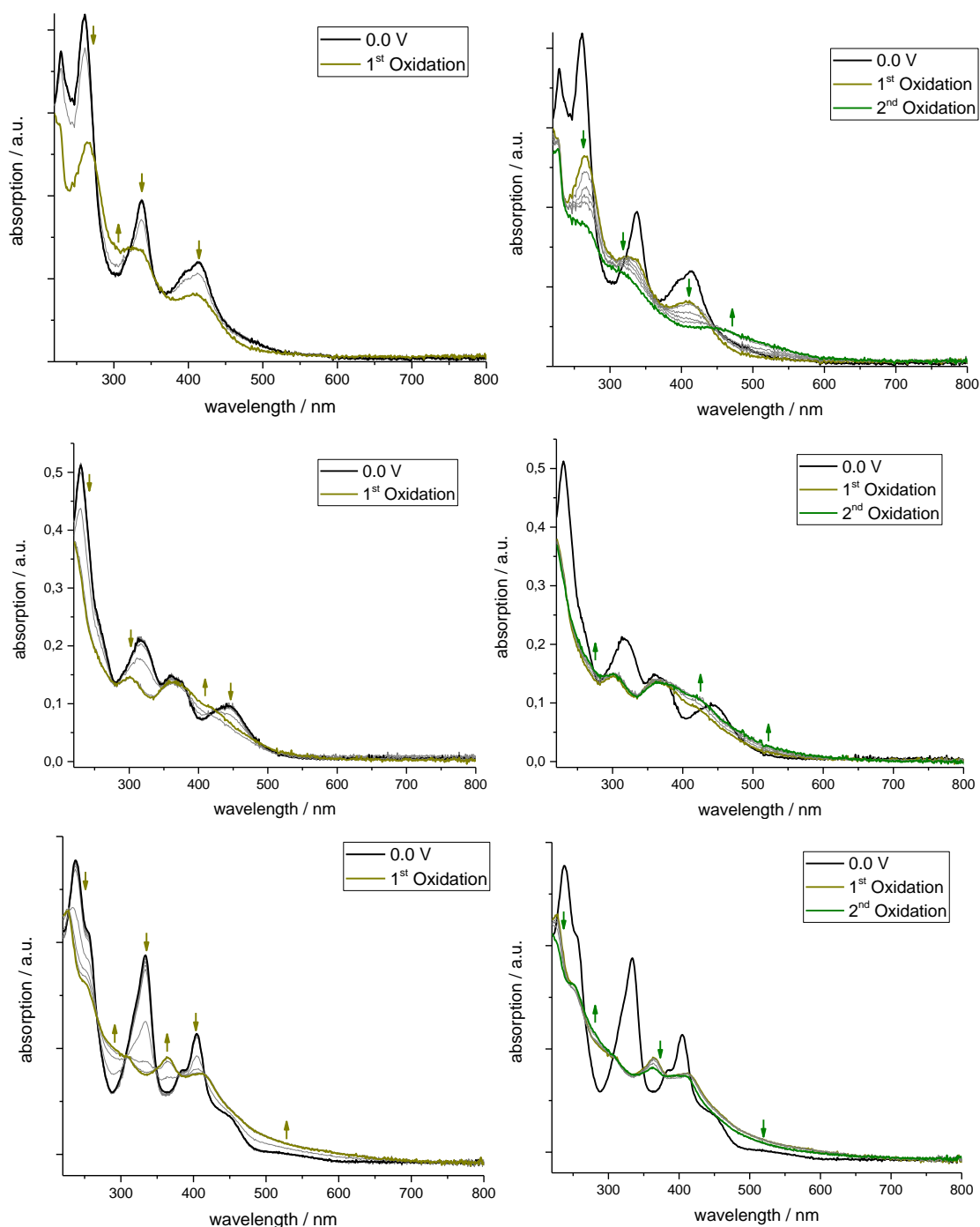


Figure 2.85 Spectroelectrochemical UV/Vis measurements measured during the first (left) and second (right) oxidation in [Ni(hphfpyTSCmB)] (first column), [Pd(hphfpyTSCmB)] (second column) and [Pt(hphfpyTSCmB)] (third column). All measurements performed in 0.1 M nBu₄NPF₆ MeCN solution with 0.1 V increments.

The first reduction at the ligand seems to show similar properties to the reductions of smaller analogues like HfpyTSCmB (Figure 2.86). The main absorption band decreases while a new intense band at 440 nm emerges. A second reduction leads to a shift of the new band to 420 nm. These transitions are assigned to π - π^* transitions in the TSC pyridine-imine moiety.

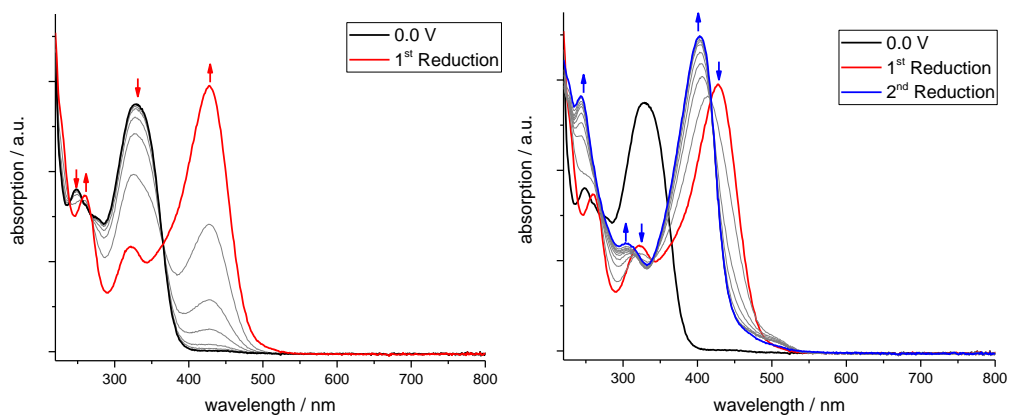


Figure 2.86 Spectroelectrochemical UV/Vis measurements measured during the first (left) and second (right) reduction in $H_2hphfyTSCmB$. All measurements performed in 0.1 M nBu_4NPF_6 MeCN solution with 0.1 V increments.

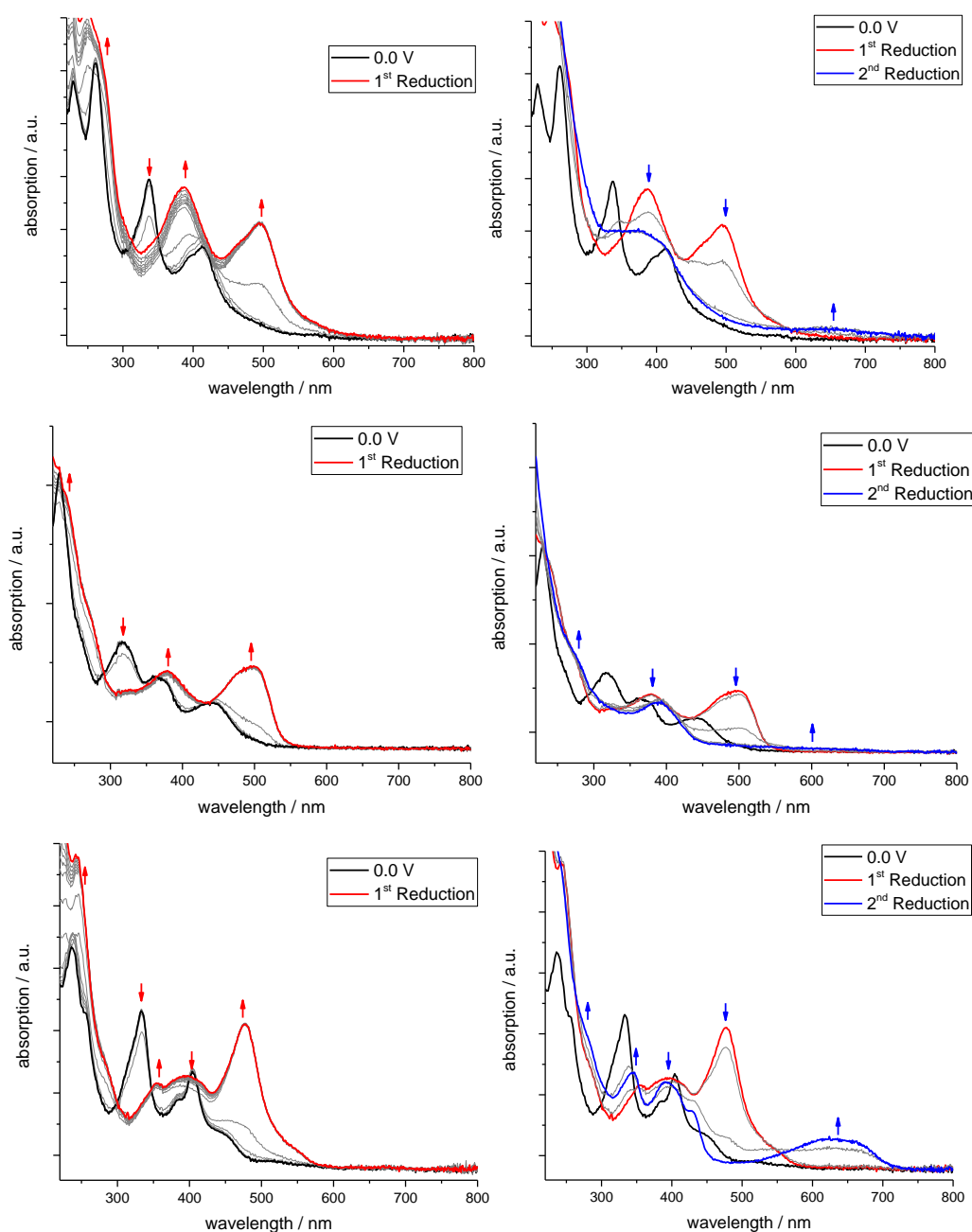


Figure 2.87 spectroelectrochemical UV/Vis measurements measured during the first (left) and second (right) reduction in $[Ni(hphfyTSCmB)]$ (first column), $[Pd(hphfyTSCmB)]$ (second column) and $[Pt(hphfyTSCmB)]$ (third column). All measurements performed in 0.1 M nBu_4NPF_6 MeCN solution with 0.1 V increments.

As for the reduction of the complexes of the nickel group, they are again very similar (Figure 2.87). Despite their differences in the starting UV/Vis spectra the first reduction shows a decrease in the π - π transition at about 300 nm and the formation of 2 new bands at about 400 nm and 500 nm. The second reduction decreases those bands again and new long wave bands at >600 nm can be detected. Interestingly in case for palladium the band is extremely weak and for platinum it is quite intense. The first reduction can be attributed to the reduction of the pyridine-imine acceptor system as for previously described complexes.

For the Cu(II) analogue the measurement yielded a similar band structure to the $[\text{M}(\text{hphfpyTSCmB})]^-$ (Figure 2.88). A strong band at 480 nm arises whilst the former π - π^* transition decreases. Also, as for the d^8 series upon second reduction the new band decreases again.

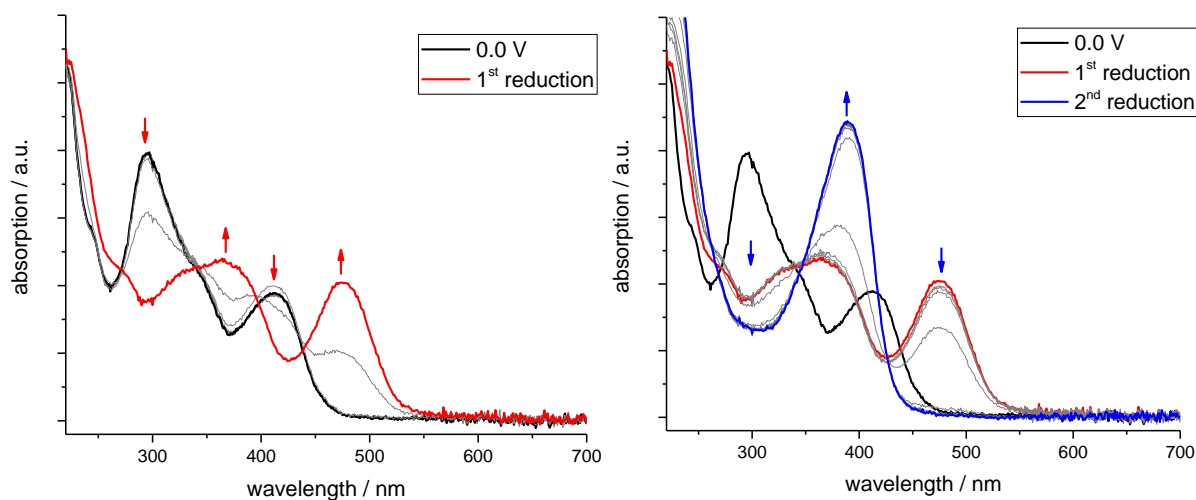


Figure 2.88 Spectroelectrochemical UV/Vis measurements measured during the first (left) and second (right) reduction of $[\text{Cu}(\text{hphfpyTSCmB})]$. All measurements performed in 0.1 M $n\text{Bu}_4\text{NPF}_6$ MeCN solution with 0.1 V increments.

Figure 2.89 shows the UV/Vis spectra during the oxidation of $[\text{Cu}(\text{hphfpyTSCmB})]$. The first oxidation process shows the formation of a broad band at 500 nm while the former π - π^* transitions decrease. This may be resulting from the formation of Cu(III).

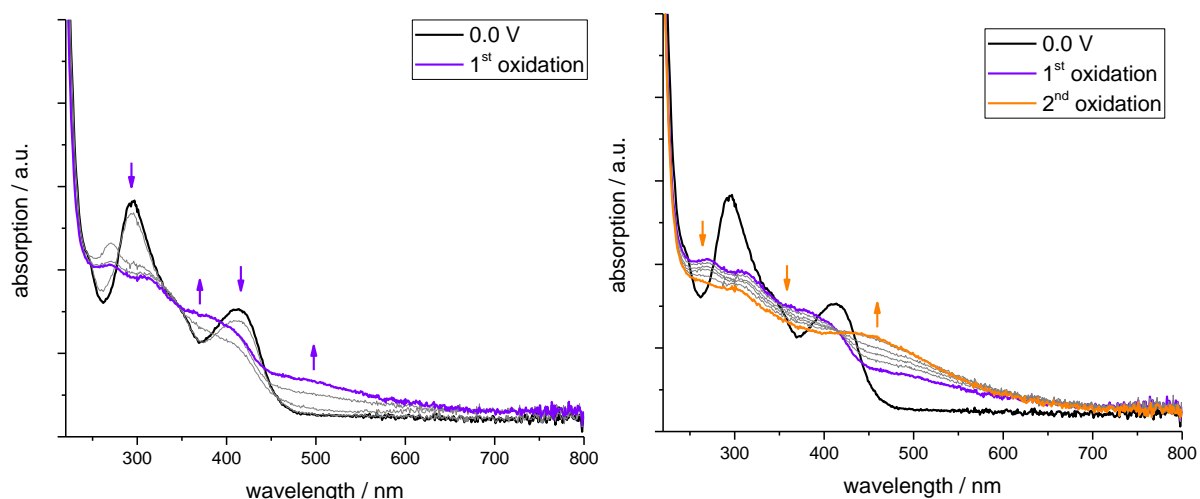
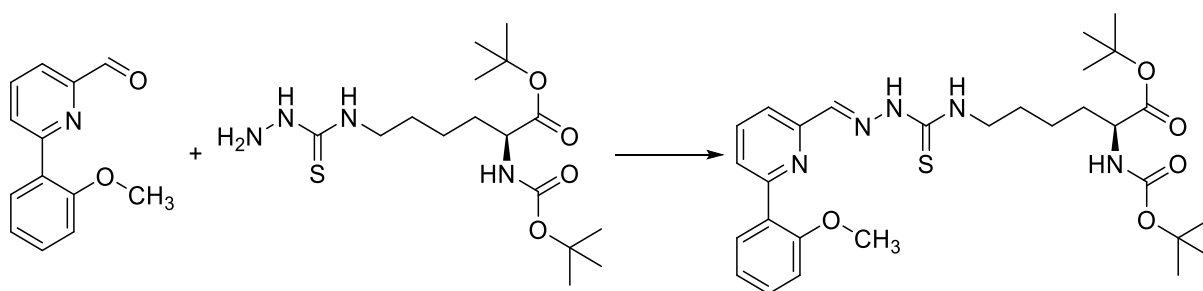


Figure 2.89 Spectroelectrochemical UV/Vis measurements measured during the first (left) and second (right) oxidation of [Cu(hphfyTSCmB)]. All measurements performed in 0.1 M nBu₄NPF₆ MeCN solution with 0.1 V increments.

In general, for the described complexes the influence of the metal in electrochemical analysis seems to be neglectable for the nickel triade. The Cu(II) derivative on the other hand shows some characteristics which rely heavily on metal centred processes. The complexes all seem to be very stable, and the irreversible oxidation is more part of the recombination of a generated organic radical cation than the loss of the coordinated metal.

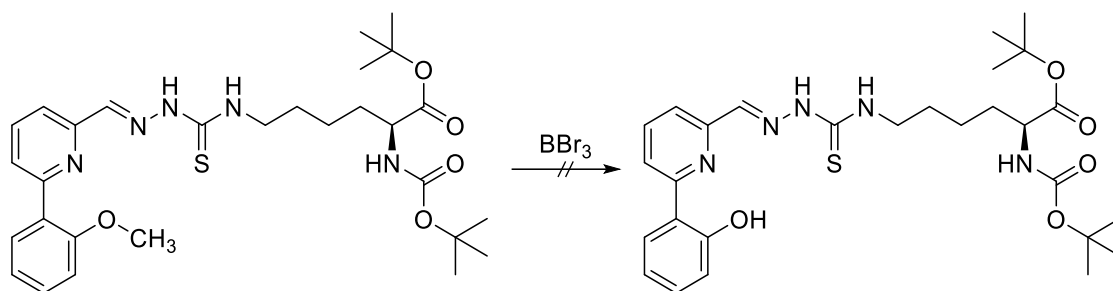
2.7.3. Attempted synthesis of H₂hphfyTSCLp

Since these complexes show interesting characteristics, the lysine derivatives were synthesized and characterized. The synthesis itself started with the condensation of the earlier mentioned synthesized 6-(2-methoxyphenyl)2-formyl pyridine and the also earlier mentioned protected lysine derivative of thiosemicarbazide (Scheme 2.37)



Scheme 2.37 Synthesis of the HmphfyTSCLp.

The structure could be isolated and characterized with extensive NMR experiments including H,N correlation spectra. Following the previously described methods it may be possible to achieve a deprotection using BBr₃ (Scheme 2.38). Unfortunately, the deprotection yielded a mixture of various products and reagents.



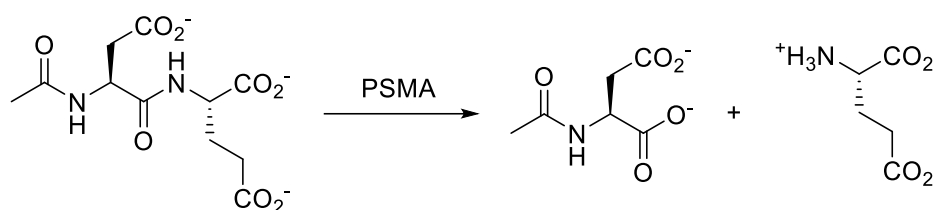
Scheme 2.38 Attempted deprotection of the HmphfpyTSCLp using BBr_3 .

It is also possible that the *tert*-butyl and Boc moieties get cleaved upon treatment with BBr_3 . The partial deprotection could also be observed in NMR of the crude mixture as a decrease of the *tert*-butyl groups' intensities and large excess of BBr_3 did not complete that step. Treating the crude product with Boc_2O and trying to isolate the Boc protected species as described in Chapter 2.4 Scheme 2.24 was unfruitful as well.

These results show that the addition of a carbonyl with the possibility to generate tetradentate dianionic complexes is possible, but the deprotection needs to be further investigated. The combination of SPPS applicable moieties with the previously described tetradentate complexes may be a powerful combination.

2.8. Prostate-specific membrane antigens directed thiosemicarbazones

The successful synthesis of the lysine derived thiosemicarbazone can be seen as a potential enabling technology for the synthesis of more sophisticated biological structures. For example, lysine-urea-glutamic acid (LuG) structures are used in the diagnostics of certain cancer types due to the overexpression of the prostate-specific membrane antigens (PSMA). PSMA is a class II membrane glycoprotein and catalyses the hydrolysis of N-acetylaspartylglutamate to glutamate and N-acetyl aspartate as shown in Scheme 2.39.



Scheme 2.39 Enzymatic process of PSMA.

PSMA is a highly expressed enzyme found in the prostate at a rate of 100 times higher than other tissues. In cancerous prostate tissue it is even higher with up to 12-fold increase in comparison to the non-cancerous tissue. This specific overexpression is very suitable as target for nuclear medical imaging molecules.³⁵⁵

A common structural motif for nuclear medical targeting is lysine ureido glutamic acids (LuG). These structures can be modified at the terminal amino function of the lysine group. The glutamic acid cannot be derivatized as it is the reactive partner of PSMA as shown in Scheme 2.39. Several isotopes of nuclear medical interest were already attached to LuG, for example ¹⁸F by *Neumaier* et al. and ^{99m}Tc by *Alberto* et al. for potential application in PET or SPECT respectively.^{355, 356} Also the group of *Kratchowil* have attached ²²⁵Ac as potential alpha therapy nuclide to a DOTA binding pocket at the derivative PSMA-617 (Chart 2.16).³⁵⁷ Since modified lysines were the topic of the prior chapter, we intend to form TSC-LuG derivatives.

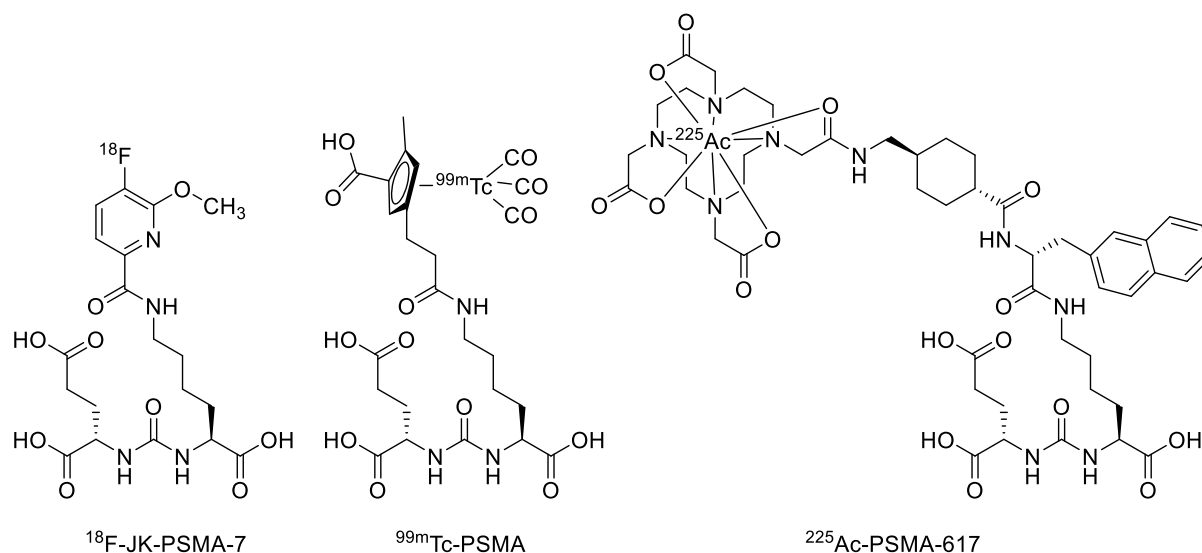
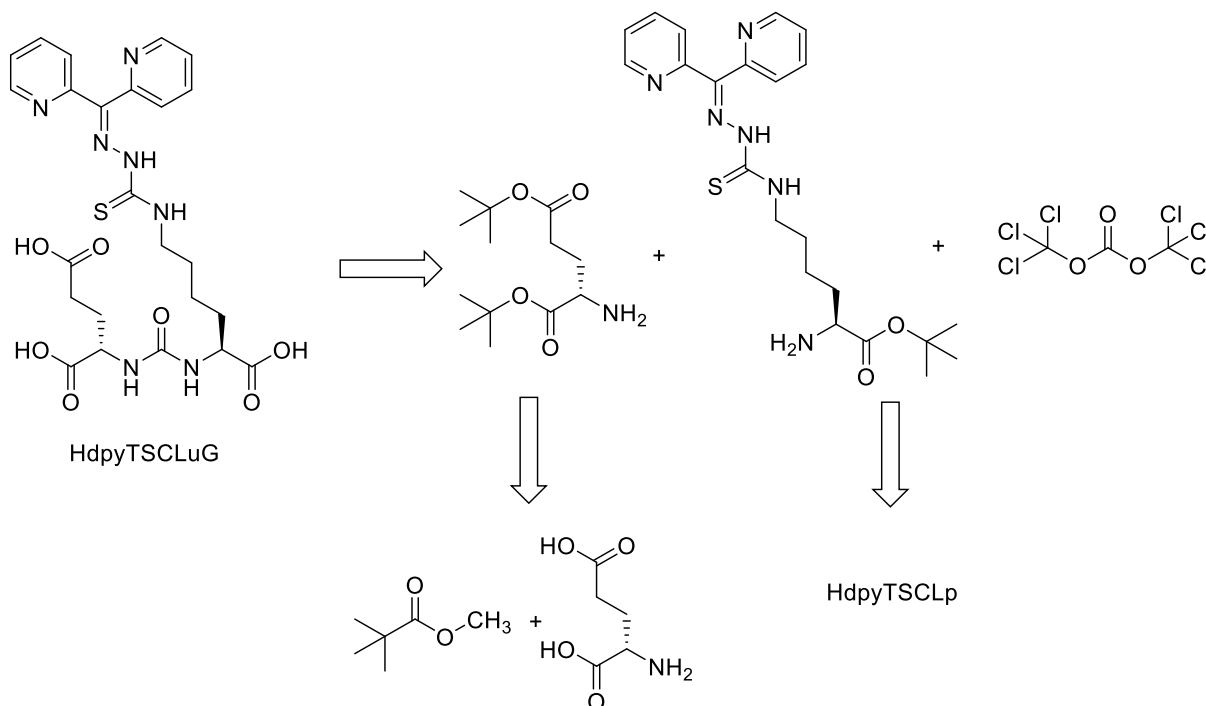


Chart 2.16 Molecular structures of ^{18}F -JK-PSMA-7, a $^{99\text{m}}\text{Tc}$ -PSMA by Alberto and ^{225}Ac -PSMA-617.³⁵⁵⁻³⁵⁷

One way to get to LuG thiosemicarbazones would be by starting from the protected lysine thiosemicarbazone. The TSCLp structure would be deprotected completely in the first step and a subsequent selective C-term protection would give the moiety needed for the coupling to glutamic acid with triphosgene (Scheme 2.40).



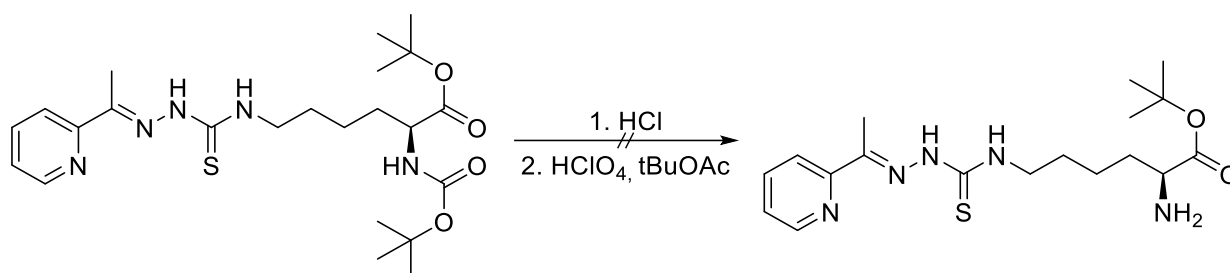
Scheme 2.40 Retrosynthetic approach of HdpyTSCLuG using triphosgene and N-terminus free lysine.

Another possibility would be to start with a different protection scheme, which would allow a late deprotection of the amine. A possible motif would be Fmoc-Lys(TSC)-OtBu. Here, the Fmoc could be cleaved under basic conditions, leaving the rest of the molecule potentially unharmed.

It would be also plausible to use LuG as primary amine source in the synthesis of thiosemicarbazides. The reaction with CS₂/TosCl may be able to yield isothiocyanates, but side reactions may occur due to the high reactivity of the compound and the manifold of reactive positions in the LuG structure.

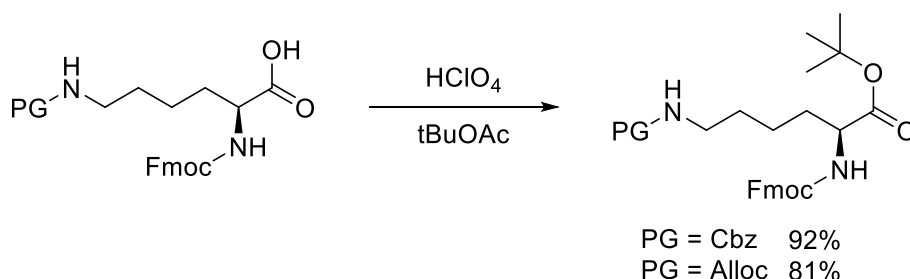
2.8.1. Attempted syntheses for N-free TSCL derivatives

To gain excess to N-terminus unprotected lysine derived thiosemicarbazones several attempts were tried. As in the reactions to gain excess to the C-terminus unprotected lysine derivatives for SPPS described in chapter 2.4., the protected thiosemicarbazone was deprotected using HCl as shown in Scheme 2.41. Subsequently, it was tried to perform a transesterification on the unprotected lysine using tert-butyl acetate (tBuOAc) and perchloric acid, yet the desired product could not be identified in the process.



Scheme 2.41 Attempted synthesis of N-terminus unprotected lysine using HapyTSCLp.

Several attempts were performed starting from the previously synthesized TSCLp series, but all failed. Afterwards we tried to establish a different protecting group the alpha-amine, which could be cleaved without harming the tert-butyl function. Fmoc would be suitable for this job. Lysine derivatives with Cbz-N^ε and Alloc-N^ε protection was synthesized by transesterification in good yields, as shown in Scheme 2.42.

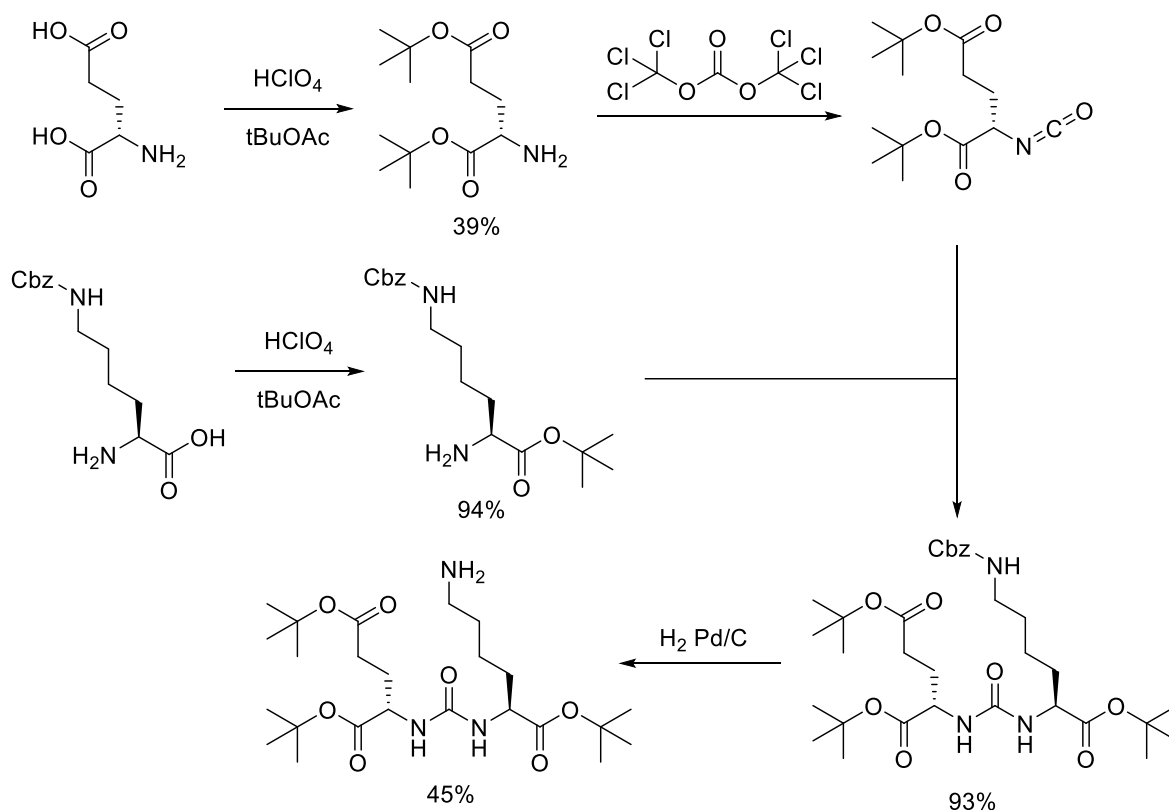


Scheme 2.42 Transesterification of different lysines using tBuOAc.

With extensive NMR spectroscopy the products could be analysed, and every hydrogen and carbon atom could be assigned to their corresponding signal as shown in Figure 2.90 for Fmoc-Lys(Alloc)-OtBu.

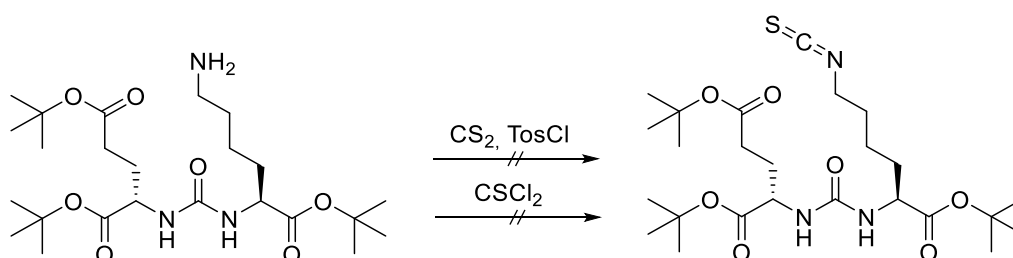
2.8.2. LuG as primary amine source

To synthesize the LuG pharmacophore, glutamic acid was protected using the previously described transesterification with tBuOAc and perchloric acid. Afterwards, treating the substance with triphosgene yields the isocyanate which was used without further purification. The addition of the previously synthesized Lys(Cbz)-OtBu yield the protected LuG. The synthesis is depicted in Scheme 2.44.



Scheme 2.44 Synthesis of tri-tBu protected LuG from glutamic acid and HLys(Cbz)-OH.

The primary amine of LuG could be isolated in good yields. The reactions towards the corresponding isothiocyanate did not yield the corresponding product yet (Scheme 2.45). A problem could be that the slightly acidic conditions of the conversion steps may cause a partial deprotection causing the side product to be troublesome in isolation, or side reactions involving a cyclization of the isothiocyanate with a carboxylate may also occur.



Scheme 2.45 Synthesis of TSCLuG from the protected LuG amine.

2.9. Synthesis and complexes of fluorescent thiosemicarbazones

2.9.1. Synthesis of acridinyl thiosemicarbazones

Extended π systems like phenanthrene, anthracene, pyrene, acridine and phenazine are prominent fluorescence emitters and the addition of their moieties as functional groups can lead to interesting properties for fluorescence microscopy (Chart 2.17). To conjugate those structures to the thiosemicarbazone they need to be functionalized with a carbonyl group and to obtain feasible structures they should carry only one carbonyl group.

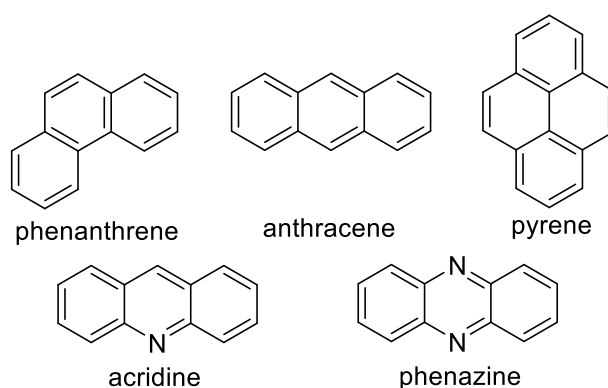


Chart 2.17 Molecular structures of common fluorophores.

Acridine and phenazine structures have an additional nitrogen donor which could bind to metal ions. Thus, generating the asymmetrical carbonyl functionalized derivatives of these molecules would be able to form N^2S donor systems when they are condensed to thiosemicarbazides. These structures could be useful to investigate the photophysical behaviour of the luminescent ligand and the deviation of the emission maxima in the presence of metal ions.

The resulting shift of the emission maxima is probably partly due to the *Lewis* acidity of the metal ions. *Fukuzumi* et al. investigated the correlation between the emission shift and the *Lewis* acidity and found that the stronger the acid is, the more bathochromic shifted the emission gets.³⁵⁸ The system he used for his investigations were acridones, oxidized acridines (Figure 2.91), which also coordinate through a central nitrogen atom and the influence of the coordination on the π -system is considerably high. Therefore, the potential of using acridines for the design of a fluorescent peptide marker that shows shifts in its fluorescence depending on its surrounding medium is thought to be promising.

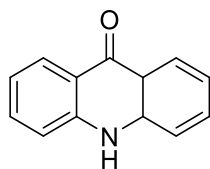
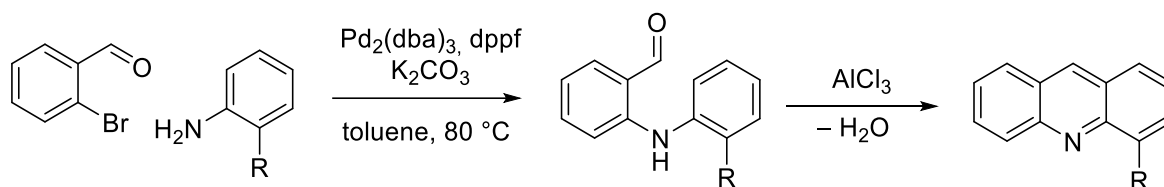


Figure 2.91 Molecular structures of acridone.

To achieve a N^NS binding pocket, we chose to synthesize 4-substituted acridines. For this method we chose a general synthetic route published by Xu et al. in 2015 (Scheme 2.46).³⁵⁹ The synthesis caught our interest due to its published versatility and low cost reagents. The reaction itself is a two-step cyclisation from 2-bromo benzaldehyde and an *ortho* substituted aniline. The first step is a Pd(0) catalysed *Buchwald-Hartwig* type reaction and subsequently followed by an intramolecular *Friedel-Crafts* acylation followed by a condensation to regain aromaticity. The reaction is performed as a one-pot synthesis.



Scheme 2.46 Synthesis of 4-substituted acridine derivatives as published by Xu.³⁵⁹

Considering the objective to introduce a carbonyl group in 4-position, we tried 2-ethyl aniline, methyl anthranilate as well as 2-(methoxymethyl)aniline. Using the previously described synthesis, the corresponding acridines could be isolated in moderate to good yields (Chart 2.18). In some cases, another fluorescent product could be isolated and identified as the corresponding acridone. Using 2-(hydroxymethyl)aniline, no product formation could be observed.

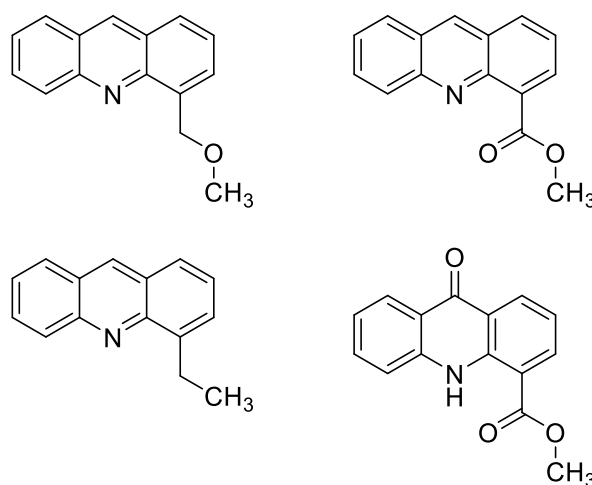
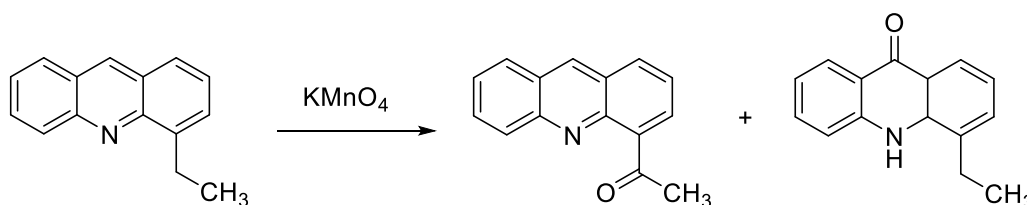


Chart 2.18 Molecular structures of the yielded acridines by the procedure described by Xu et al. 4-(methoxymethyl) acridine, 4-(methyl carboxylate) acridine, 4-ethyl acridine and 4-(methyl carboxylate) acridone.

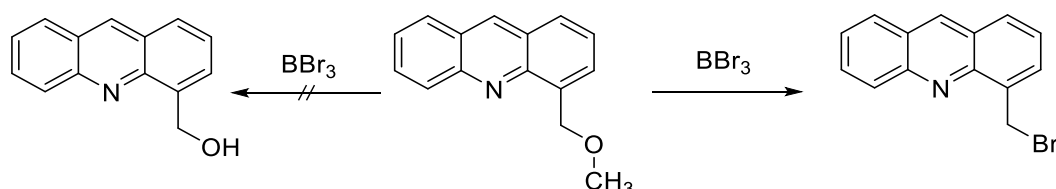
4-Ethyl acridine could be obtained in a good yield of 88%. A subsequent oxidation using the literature known oxidation for benzylic moieties with FeCl_3 and KMnO_4 was attempted (Scheme 2.47).³⁶⁰ With 10 equivalents of potassium permanganate and 6 equivalents of iron chloride an inseparable mixture was obtained, in which possibly an unidentified Fe(III) complex formed since after the workup procedure the NMR showed strong paramagnetic shifted signals.



Scheme 2.47 Attempted oxidation of 4-ethyl acridine with potassium permanganate.

With dispense of the iron chloride a mixture of 4-acetyl acridine and 4-ethyl acridone was detected in NMR spectroscopy but were inseparable by column chromatographic purification.

4-(methoxymethyl) acridine could be isolated in bad yields of around 16%. Nevertheless, we tried to deprotect the alcohol function with boron tribromide and oxidize the free alcohol with manganese dioxide. Surprisingly, the deprotection failed and instead of the alcohol we obtained 4-(methylbromide) acridine with a yield of 55% (Scheme 2.48).

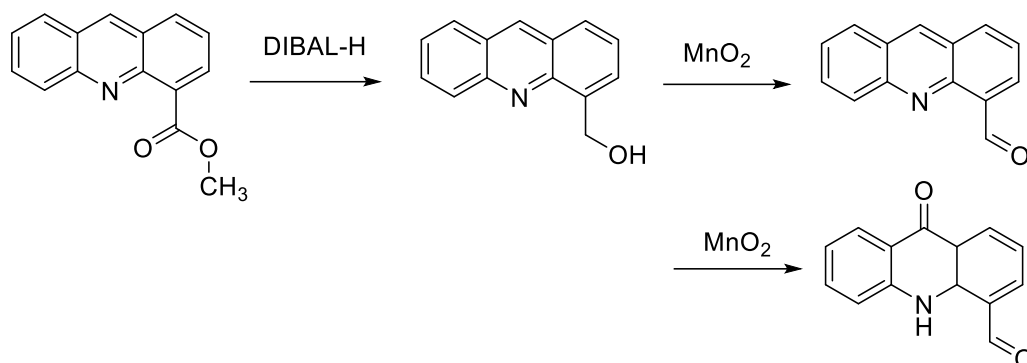


Scheme 2.48 Synthesis of 4-(methylbromide) acridine by attempted deprotection of 4-(methoxymethyl) acridine with BBr_3 .

The acridine synthesis with methyl anthranilate produced under normal conditions the acridone derivative. Extending the reaction time of the second step from 18 h to 72 h, the acridine could be isolated in modest yields. The problem may be occurred due to the strong electron withdrawing effect of the methyl carboxylate hindering the condensation.

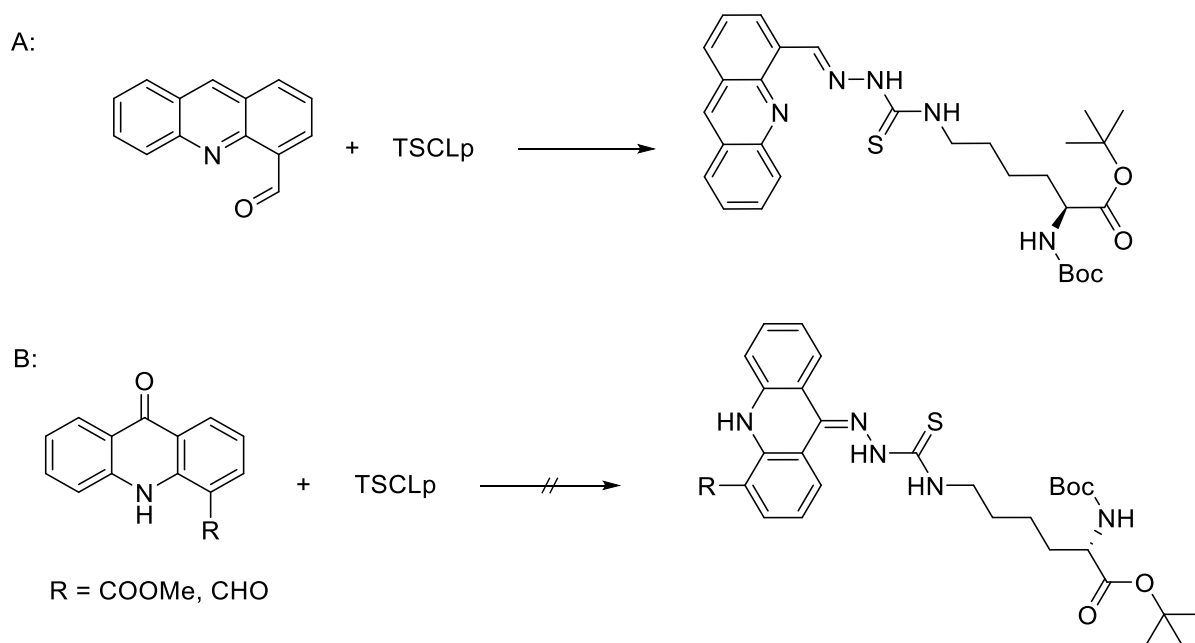
The yielded acridine was used to gain the formyl derivative. DIBAL-H is known to reduce methyl carboxylates to aldehydes.³⁶¹ The acridine derivative however was reduced to its alcohol. The alcohol could be oxidized with manganese dioxide to the carbaldehyde, yielding the desired 4-formyl acridine (Scheme 2.49). A problem in this reaction might be that the oxidation does not yield the acridine but oxidizes the

mixture further to the acridone making this reaction prone to failure. Both products could be isolated in different reaction attempts.



Scheme 2.49 Reduction of methyl carboxylate acridine to 4-(hydroxymethyl) acridine and subsequent oxidation to 4-formyl acridine and 4-formyl acridone.

Using 4-methylcarboxyl acridone as well as 4-formyl acridone, thiosemicarbazone synthesis was attempted. The acridones could possibly in react at their carbonyl position yielding fluorescent structures, yet no condensation product could be observed (Scheme 2.50 B). With 4-formyl acridine the corresponding thiosemicarbazone HfactSCLp could be isolated (Scheme 2.50 A).



Scheme 2.50 Attempted syntheses of thiosemicarbazones from 4-formyl acridine and acridones.

2.9.2. Fluorescence spectroscopy

2.9.2.1. Fluorescence of 4-formyl acridone

The 4-formyl acridone is a strong fluorophore emitting at 445 nm despite several different excitation wavelength (Figure 2.92). The emission occurs from the lowest excited singlet state and the different excitation maxima may be due to excitations into higher lying vibrational modes. These higher vibrational modes relax into the lowest singlet state before emitting photons at 445 nm.

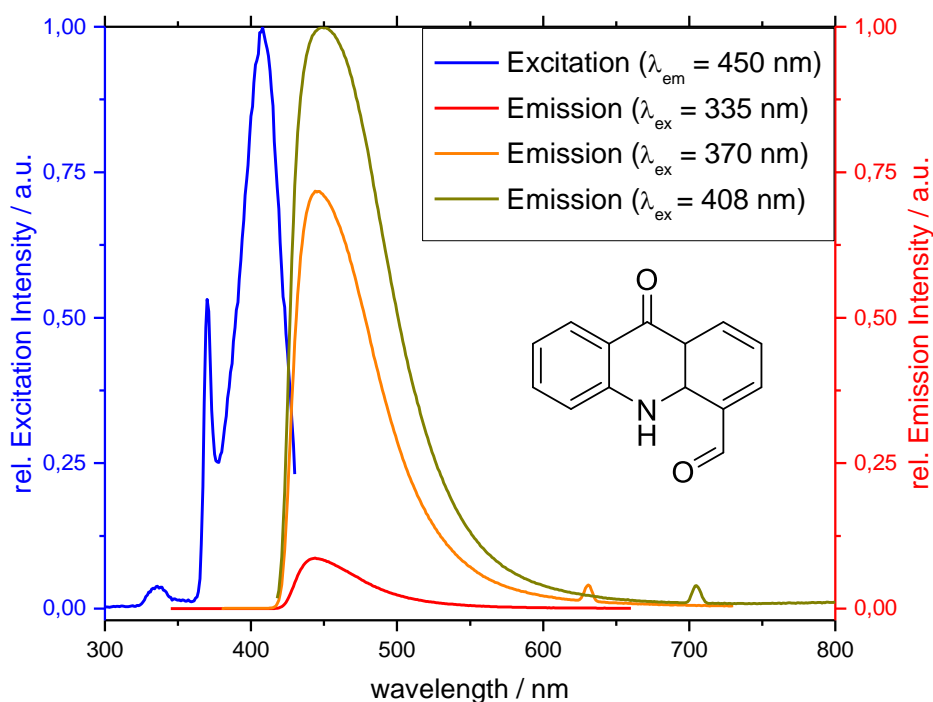


Figure 2.92 Excitation ($\lambda_{ex} = 450$ nm) (blue) and emission (red) spectra of 4-formyl acridone in MeCN. Emissions recorded with incident radiation of 335 nm 370 nm and 408 nm.

Further studies need to be conducted to synthesize the acridone derived TSCs, which could also function as fluorescent sensor. Yet the highly fluorescent character of the acridone moiety is a promising characteristic for the fluorescence of HfactSCLp and the corresponding complexes.

2.9.2.2. Fluorescence quenching of HfactSCLp

The acridine derivative HfactSCLp was investigated for its photoluminescent properties in MeCN. Since in the following experiments the metal salts were predissolved in water, the quenching capabilities of water in the mixture was also investigated. The excitation spectrum showed the highest intensity at a wavelength of 450 nm, which we therefore used in the following measurements as well. The pure ligand emitted strong at 490 nm and 560 nm and addition of 2.5% of water yielded a loss of around 10% in intensity (Figure 2.93).

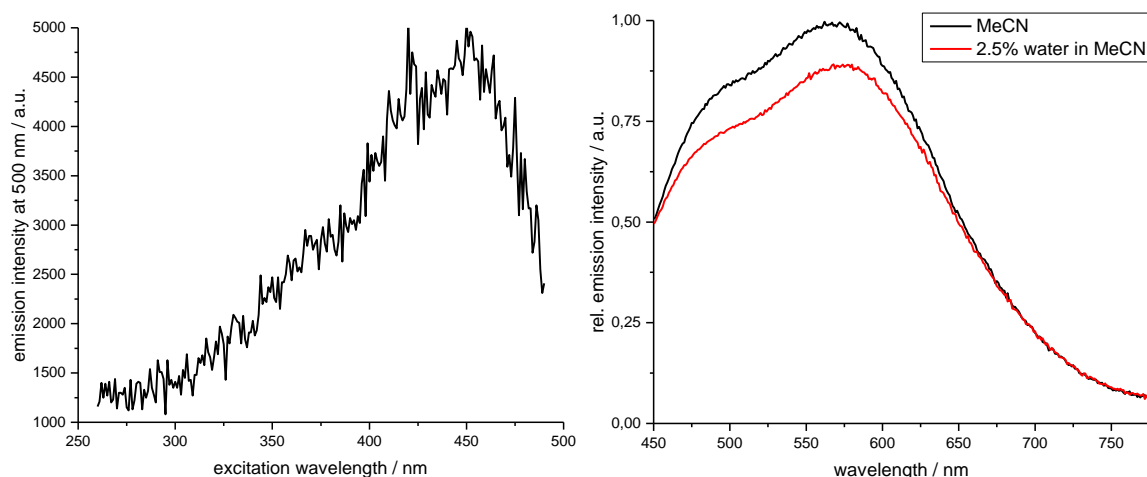


Figure 2.93 left: Excitation spectra of HfacTSCLp in MeCN; Emission intensity at 500 nm. Right: Emission spectra of HfacTSCLp after incident radiation of 450 nm, in pure MeCN (black) and with 2.5% water (red).

Since the measured shift can also be partly due to a deprotonation of the thiosemicarbazone moiety, a titration with aqueous sodium hydroxide was performed. Interestingly there is no shift in the wavelength, but a strong decrease of the intensity (Figure 2.94). Since the overall titration volume is less than 30 μL , the reduction by water quenching is neglectable. Up to 0.25 eq. NaOH the loss in intensity is around 28% and addition up to 5 eq. yielded a loss of 48%. This leads to the possible explanation that the resulting thiolate might exhibit no fluorescence, or it is at least less fluorescent than the thion (Scheme 2.51).

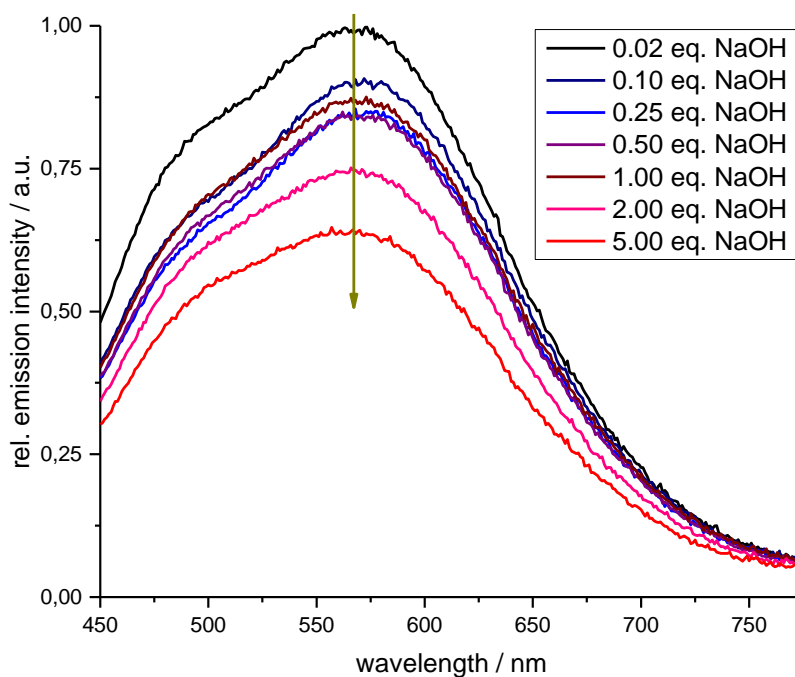
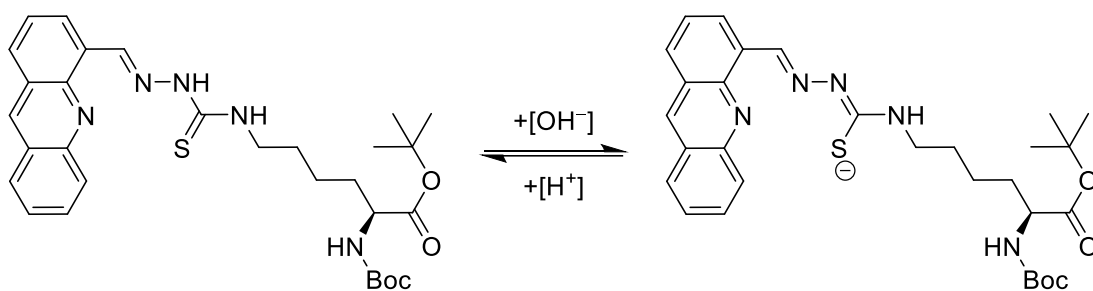


Figure 2.94 Titration of HfacTSCLp monitored by emission spectroscopy with an excitation wavelength of 450 nm up to 5 eq. of aqueous sodium hydroxide solution. Dark yellow arrow indicates the influence of the *Brønsted* base on the luminescence.



Scheme 2.51 Proposed acid-base reaction of HfactTSCLp and factTSCLp⁻.

2.9.2.3. Influence of transition metal ions on the fluorescence of HfactTSCLp

By these spectra we know the behaviour of HfactTSCLp in the spectra according to water quenching and *Brønsted* base reaction. For biological application we chose to proceed with metal salts of the most common trace elements in the human body, iron, cobalt, nickel, copper, and zinc in addition to platinum as one of the more important metals for biological investigations during this thesis. Also, we used the chloride salts since chloride might help to form mononuclear complexes as weak coligands but will not sufficiently hinder the coordination by a second thiosemicarbazone ligand, if feasible. All ions induced shifts primarily “choosing” one of the previously mentioned maxima of the free ligand. Where iron, cobalt and copper increased the intensity at 490 nm whilst decreasing the intensity at the band at 580 nm, nickel and platinum had the band at 580 nm increased thus glowing redder compared to the other tested ions. Zinc was a special case since it promoted the band at 490 nm, it also increased the band at 580 nm and creating an almost white fluorescence (Figure 2.95). A Photograph of the luminescent solutions under an UV lamp is shown in Figure 2.96. A summary of the fluorescence measurements is given in Table 2.20.

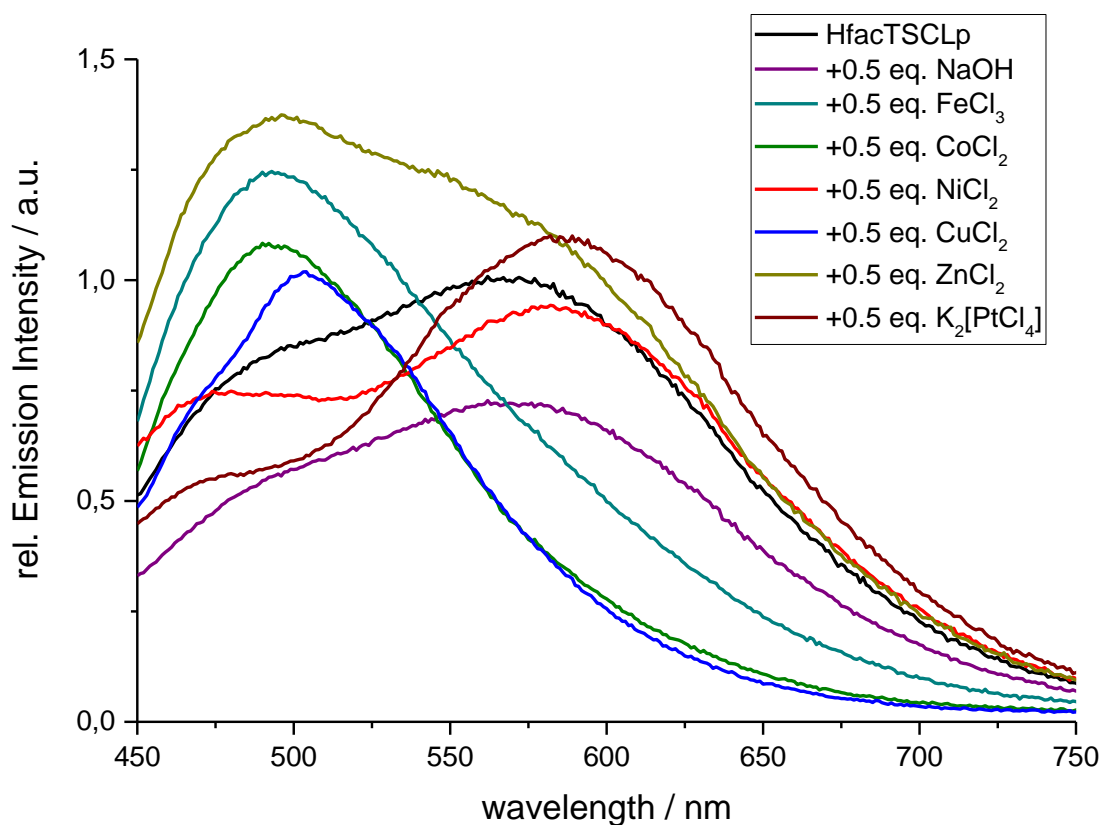


Figure 2.95 Emission spectra of HfactSCLp (black) after addition of NaOH (purple), FeCl₃ (dark cyan), CoCl₂ (olive), NiCl₂ (red), CuCl₂ (blue), ZnCl₂ (dark yellow), and K₂[PtCl₄] (wine red) in MeCN with an excitation wavelength of 450 nm.

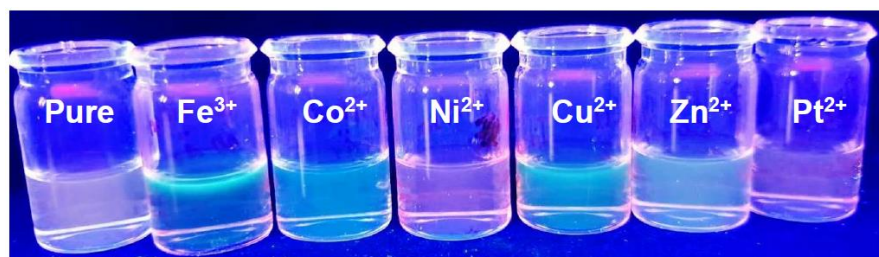


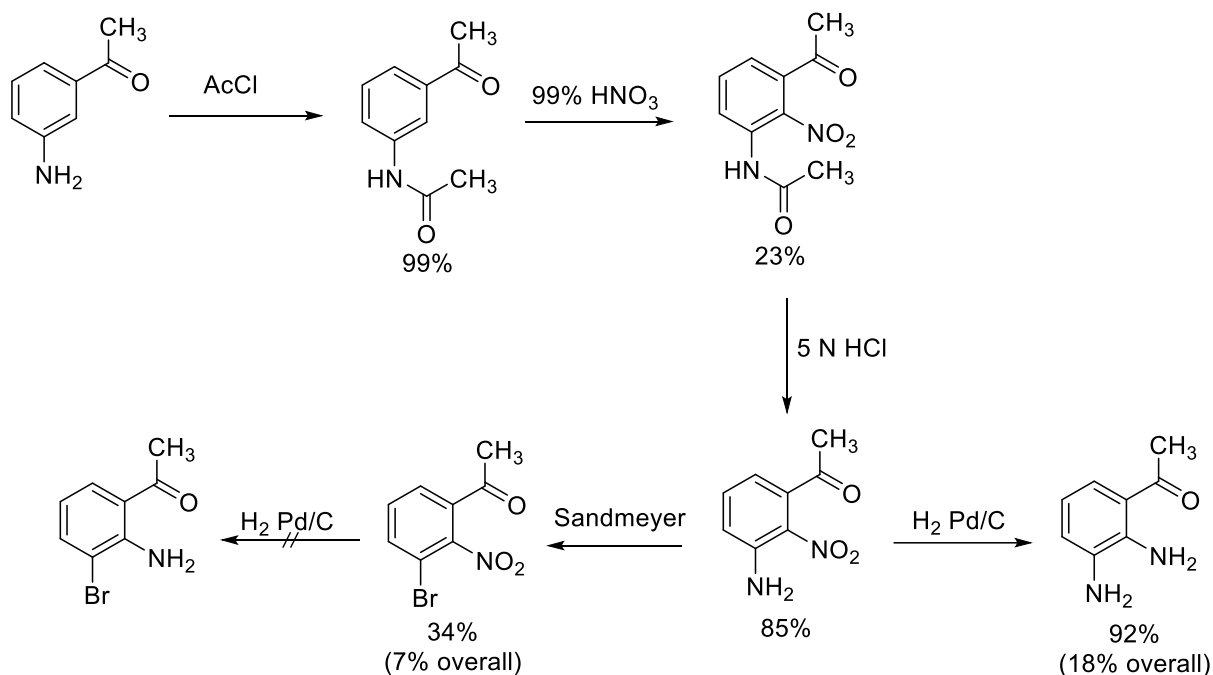
Figure 2.96 Reaction mixtures of the fluorescence measurements under a UV-lamp ($\lambda = 366$ nm).

Table 2.20 Wavelengths and emission intensities of HfactSCLp and its metal titrations. All values were measured at 0.5 eq. metal salt concentration, in MeCN and an excitation wavelength of 450 nm. If no maxima were detected, the emission wavelength of the ligand was used to determine the relative intensity.

Metal Salt	$\lambda_{\max,1}$ / nm	rel. intensity	$\lambda_{\max,2}$ / nm	rel. intensity
None	497	1.00	567	0.84
NaOH	497	0.57	567	0.72
FeCl ₃	493	1.25		0.71
CoCl ₂	492	1.08		0.46
NiCl ₂	471	0.74	581	0.94
CuCl ₂	505	1.02		0.47
ZnCl ₂	496	1.37	565	1.17
K ₂ [PtCl ₄]	474	0.55	588	1.10

2.9.3. Synthesis of 9-substituted acridines and phenazines

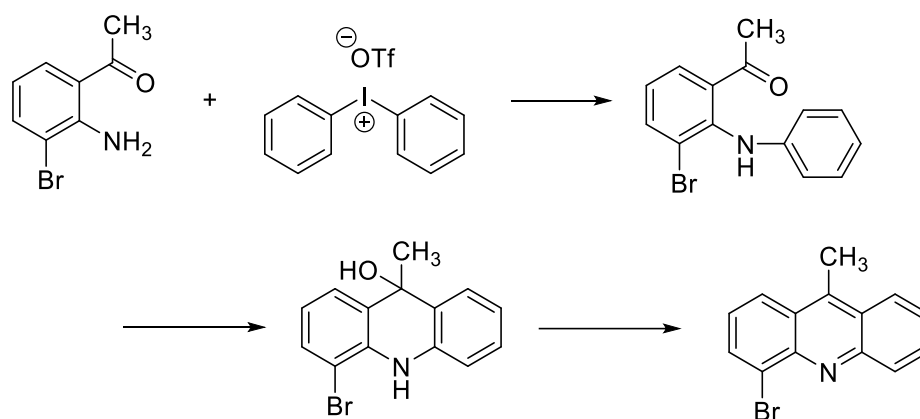
Since this method gave only poor yields, we decided to change the synthetic route. Starting from 3-amino acetophenone we tried to synthesis 2,3-diamino acetophenone and 2-amino 3-bromo acetophenone with the same starting reagent (Scheme 2.52). By protecting the amino moiety of the starting reagent, nitration with fuming nitric acid and subsequent deprotection 3-amino 2-nitro acetophenone could be synthesized. This was a handy molecule since we can either perform a *Sandmeyer* reaction and afterwards a hydrogenation to get 2-amino 3-bromo acetophenone or direct hydrogenation would lead to 2,3-diamino acetophenone.



Scheme 2.52 Synthetic route for 2,3-diamino acetophenone and 2-amino 3-bromo acetophenone.

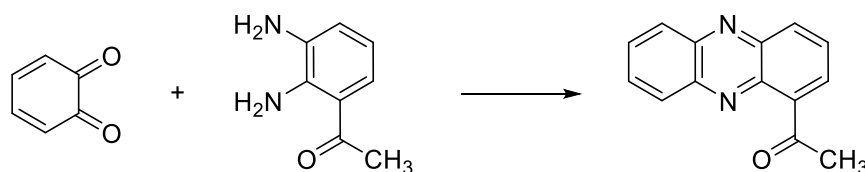
While the reaction to 2,3-diamino acetophenone was considerably easy and yielded the pure compound, the hydrogenation after the bromination by *Sandmeyer* did not yield the desired product in a pure form. A problem might be that several positions are prone to be attacked under these conditions.

According to a reaction by *Pang* et al., the 2-amino 3-bromo acetophenone would be used in a reaction with diphenyl iodonium triflate. In this reaction the iodonium salt phenylates the amino moiety and a subsequent intramolecular *Friedel-Crafts* acylation followed by a condensation yields the 4-substituted 9-methyl acridine (Scheme 2.53). 9-methyl acridine as backbone would be very promising, since it would hinder the oxidation to acridone thus making the ligand and its complexes a lot more redox stable.



Scheme 2.53 Reaction of 2-amino 3-bromo acetophenone with diphenyl iodonium triflate yielding 9-methyl acridine.

The 2,3 diamino acetophenone was used in a more direct reaction to synthesize a fluorophore. The double condensation with 1,2-benzoquinone would yield asymmetric phenazines (Scheme 2.54). But in the end, this reaction yields an inseparable slush with a lot of side products of which no fluorescence is noticeable on a TLC.



Scheme 2.54 Double condensation of 2,3-diamino acetophenone with 1,2-benzoquinone to their corresponding phenazine.

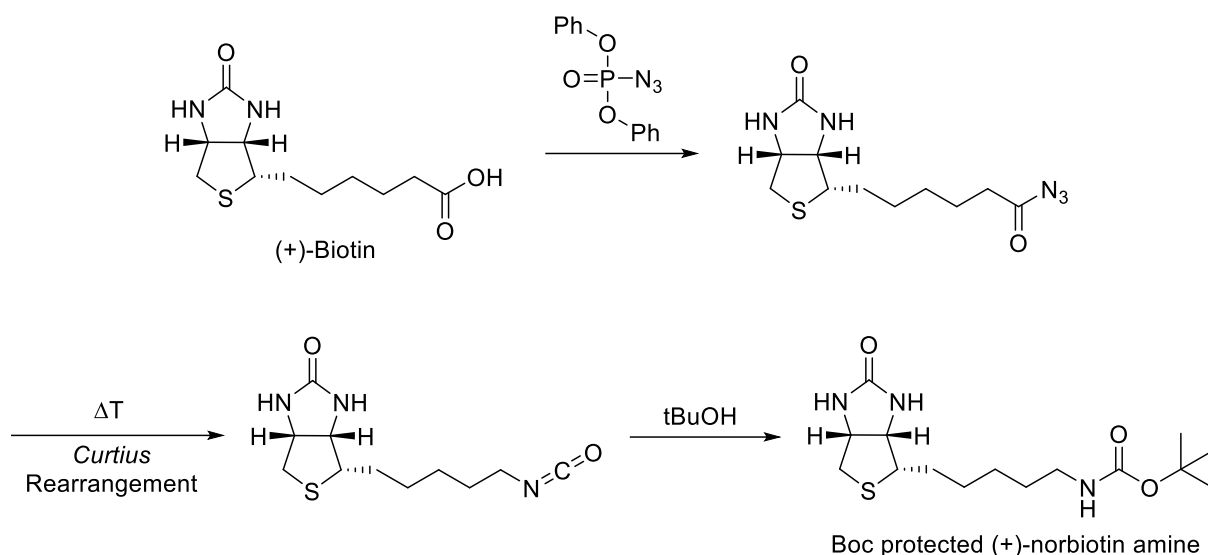
2.10. TSC Pd(II) complexes for C–C cross coupling reactions

As already mentioned in the introduction, Pd(II) complexes with bidentate benzyl derived thiosemicarbazones are remarkably good catalysts for several C–C cross coupling reactions. The group of *Bhattacharya* published several complexes and used them in catalysis based upon the bidentate system. Overall, the cationic species are more active catalysts for the reactions hence the evolution towards bidentate bisphosphine ligands. The purification of the cationic species proved to be difficult which is why we stuck with the neutral triphenylphosphine derivatives.

As typical for the thiosemicarbazone chemistry, the N4 side group was only a minor target for derivatization in the group of *Bhattacharya* which is why we try to test the chiral moieties we already used in the pharmaceutical part of this thesis. The aim is to combine the affinity of bioactive moieties with the efficient palladium catalysts for C-C coupling to gain access to new artificial metalloenzymes. Furthermore, we also want to attach biotin for a more sophisticated approach to the field of metalloenzymes.

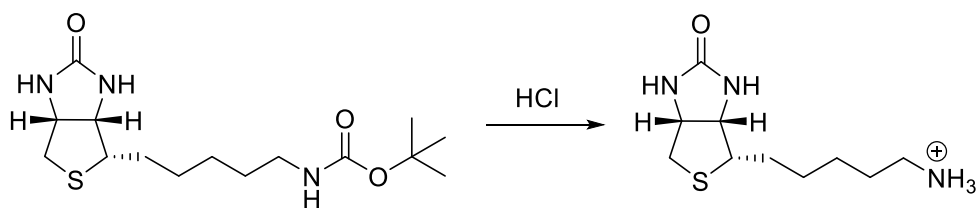
2.10.1. Attempted syntheses of biotinylated thiosemicarbazones

The first approach we tested to form thiosemicarbazones out of biotin was by turning biotin to norbiotin amine and then using the developed methods to form the isothiocyanate. Starting from (+)-biotin it was converted to the norbiotin amine in a cascade reaction (Scheme 2.55). The first step involves the synthesis of an acyl azide by reacting the biotin with diphenyl phosphoryl azide. This compound allows the direct synthesis of acyl azides from carboxyl functions instead of acyl chlorides. The synthesized acyl azides decomposes at increased temperature by a *Curtius* rearrangement to the corresponding isocyanate. As previously stated, isocyanates are more reactive than their sulphur homologues and will react with alcohols like *tert*-butanol to the carbamate which is in this case the Boc protected amine. This reaction is performed in one step since all ingredients are dissolved in *tert*-butanol and heated to reflux.



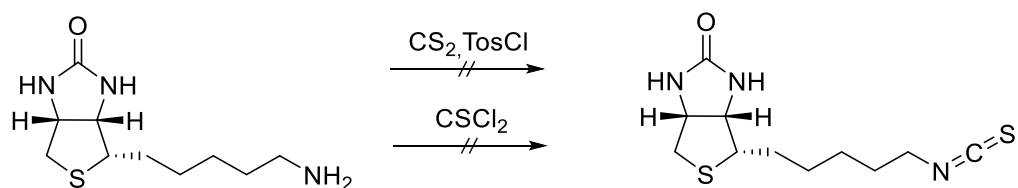
Scheme 2.55 Mechanistic steps for the one pot synthesis of Boc-protected norbiotin amine.

The Boc group can be cleaved with HCl to generate the ammonium salts, as shown in Scheme 2.56.



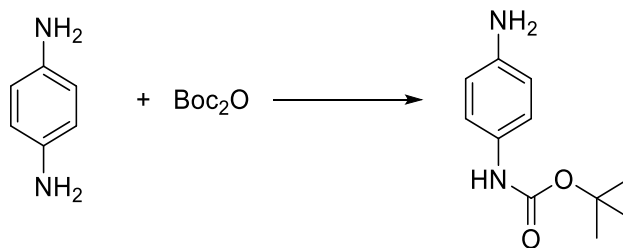
Scheme 2.56 Boc deprotection of norbiotin amine using in situ generated HCl.

Subsequent reactions with the previously noted CS_2 , TosCl method as well as thiophosgene failed to yield norbiotin isothiocyanate. The tested reactions are given in Scheme 259.



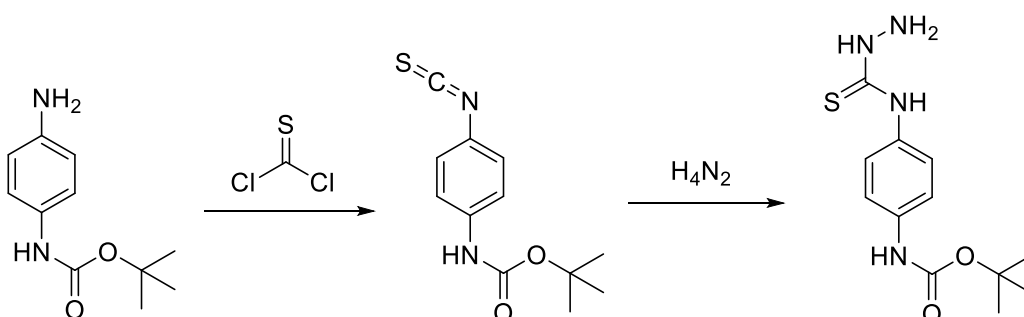
Scheme 2.57 Attempted syntheses for norbiotin isothiocyanate.

The next method tried to synthesise a bridge consisting of phenylene diamine, which can form an amide bond with biotin as well as forming an isothiocyanate from one of the amines. Starting from phenylene diamine, one of the amines could be protected using a stoichiometric amount of Boc_2O , as shown in Scheme 2.58.



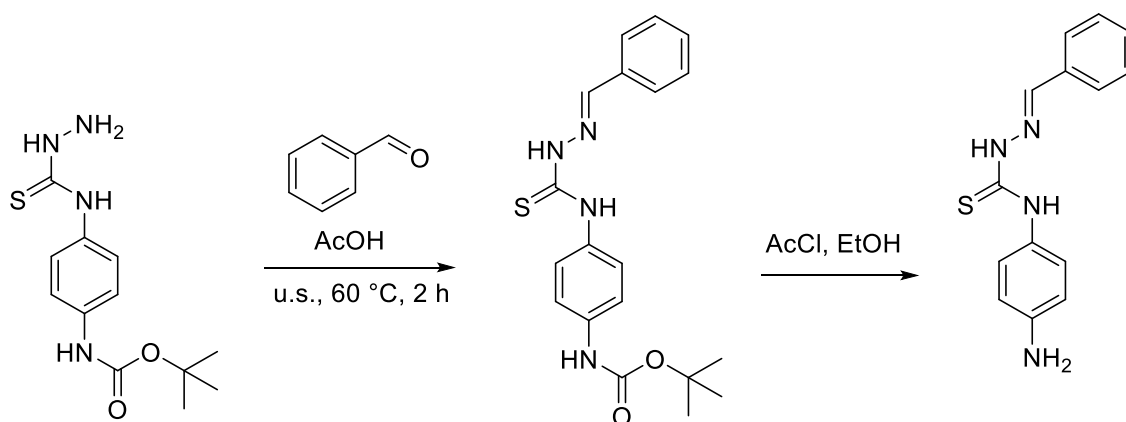
Scheme 2.60 Stoichiometrically selective Boc-protection of phenylenediamine.

The isothiocyanate was generated using thiophosgene yielding a brown solid in excellent yields. Despite the reaction also yielded 2 equivalents of muriatic acid, the concentration was too low to deprotect the amine. The reaction with hydrazine hydrate yielded the thiosemicarbazide in good yields. Both reactions are depicted in Scheme 2.59.



Scheme 2.59 Isothiocyanate route for the synthesis of TSCpBa with thiophosgene as thione source.

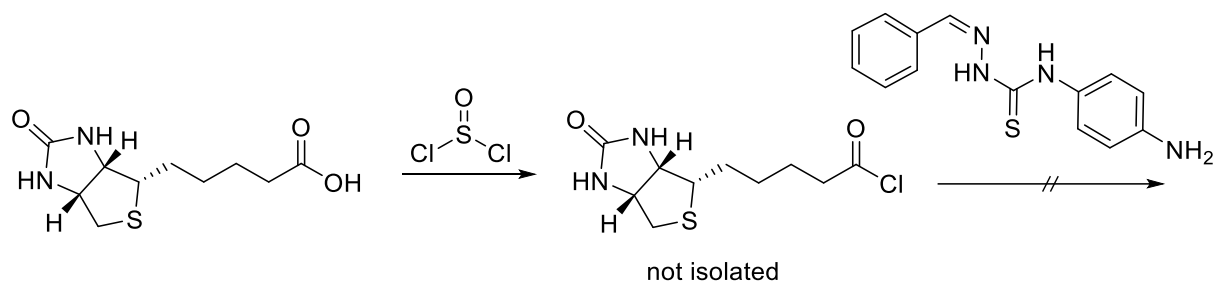
Since the hydrazide moiety may react with coupling agents, the condensation reaction with benzaldehyde was performed prior to the deprotection and coupling tests. The Boc protecting group was cleaved by a mixture of acyl chloride and EtOH, which generates ethyl acetate and hydrogen chloride *in situ* which then cleaves the protection group (Scheme 2.60).



Scheme 2.60 Synthesis of HbzTSCpBa and the deprotection with in situ generated HCl.

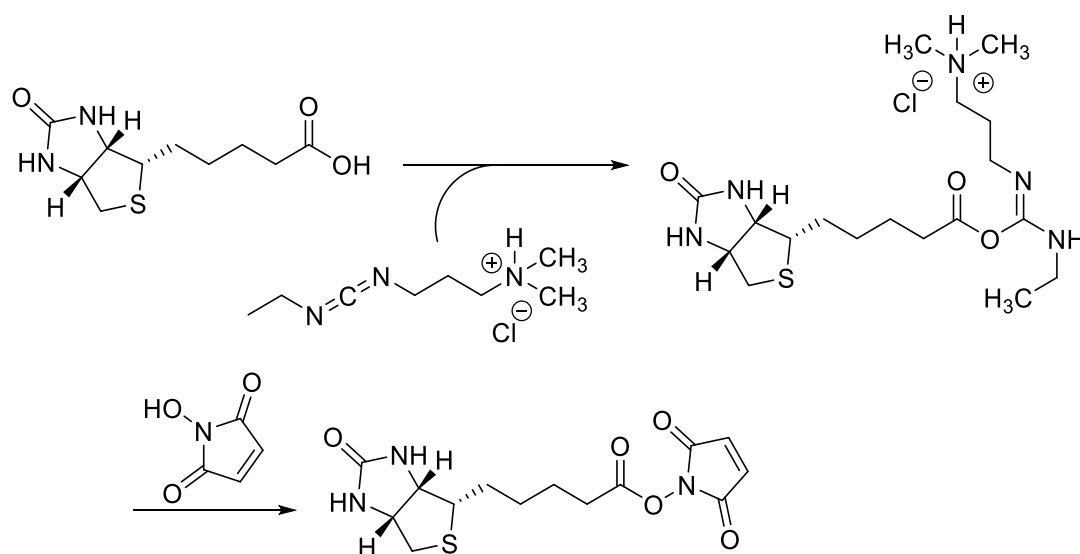
The amine was used in reactions with the goal to attach biotin by an amide coupling. Biotin should react with thionyl chloride to yield the acid chloride and

excess thionyl chloride could be removed under reduced pressure. The deprotected ligand was added to the reaction, but the reaction yielded a conglomerate of reagents and products which we were unable to separate (Scheme 2.61).



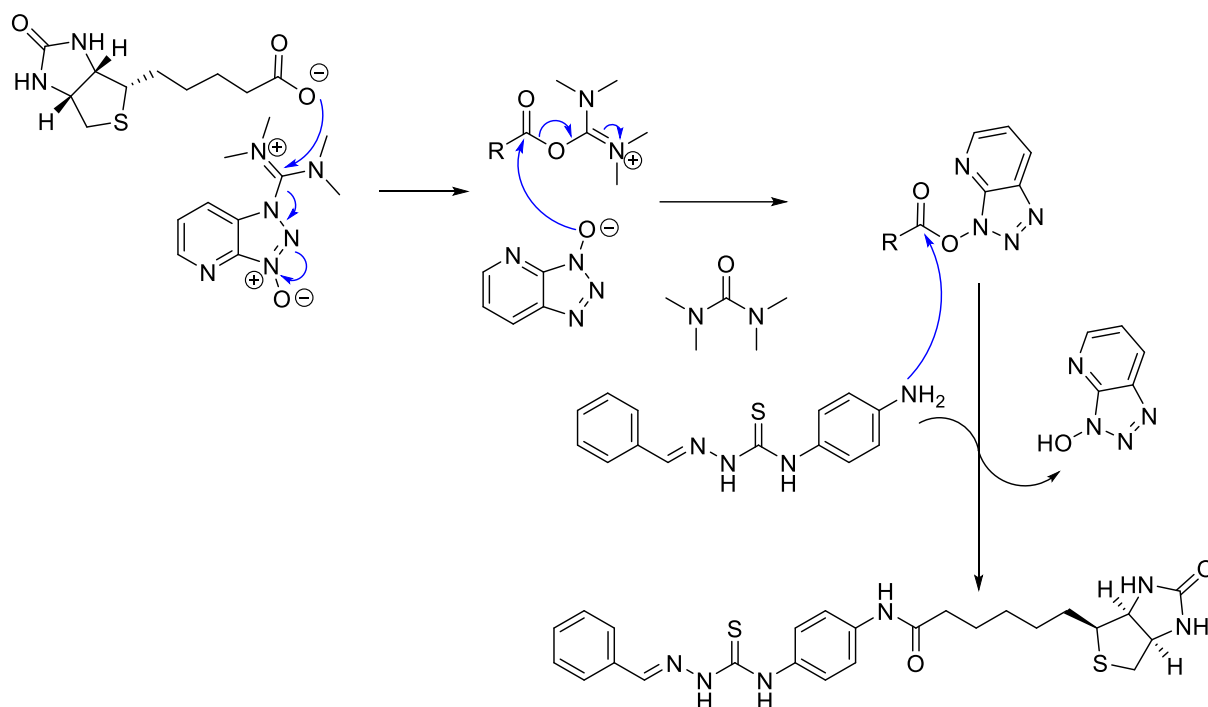
Scheme 2.61 Attempted amide coupling with biotin chloride and HbzTSCpap.

The second attempt was by generating a succinimide ester. These NHS esters are known to have a high tendency to react with amines. This was performed in a one pot reaction with EDC and *N*-hydroxy succinimide (NHS). The reaction, shown in Scheme 2.62, yielded the biotin-NHS adduct which could be used in a further coupling procedure with the thiosemicarbazone.



Scheme 2.62 Synthesis of biotin-NHS with EDC·HCl.

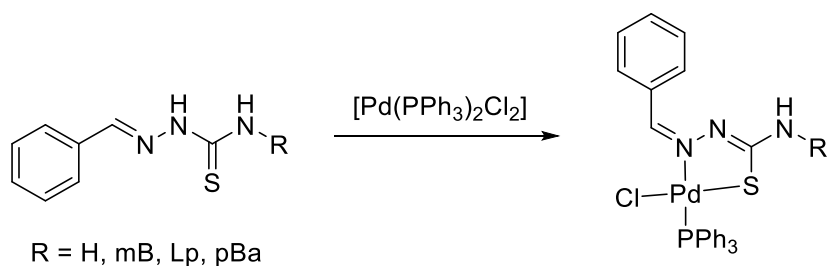
But this pathway was unfruitful as well since the coupling did not yield any biotinylated product. The last possibility in coupling biotin directly to the TSC was performed by using a strong amidation agent like hexafluorophosphate azabenzotriazole tetramethyl uronium (HATU). HATU was already used alongside *Hünig's* base (*N,N*-diisopropylethylamine, DIPEA) to couple TSCL to the peptide resin in the solid phase peptide synthesis. But also, this third possibility, whose mechanism is shown in Scheme 2.63, failed to yield a biotin-thiosemicarbazone structure. Further possibilities need to be tested.



Scheme 2.63 Attempted Synthesis and suggested mechanism of the amide coupling between biotin and HbzTSCpap using HATU and DIPEA.

2.10.2. Synthesis of Pd(II) complexes as catalysts

Nevertheless, we were able to generate HbzTSCmB, HbzTSClp and HbzTSCpBa as well as HbzTSC, a ligand tested by *Bhattacharya*. The four ligands were reacted with $[\text{Pd}(\text{PPh}_3)_2\text{Cl}_2]$ to generate the corresponding catalysts. The synthesis is schematically depicted in Scheme 2.64.



Scheme 2.64 Complexation of the benzylic thiosemicarbazones with $[\text{Pd}(\text{PPh}_3)_2\text{Cl}_2]$.

The UV/Vis spectra of the complexes were measured and is shown in Figure 2.97 and whilst the small derivatives showed very similar absorption characteristics, the lysine moiety seemed to cause a difference. The MLCT band is way more intense for this derivative.

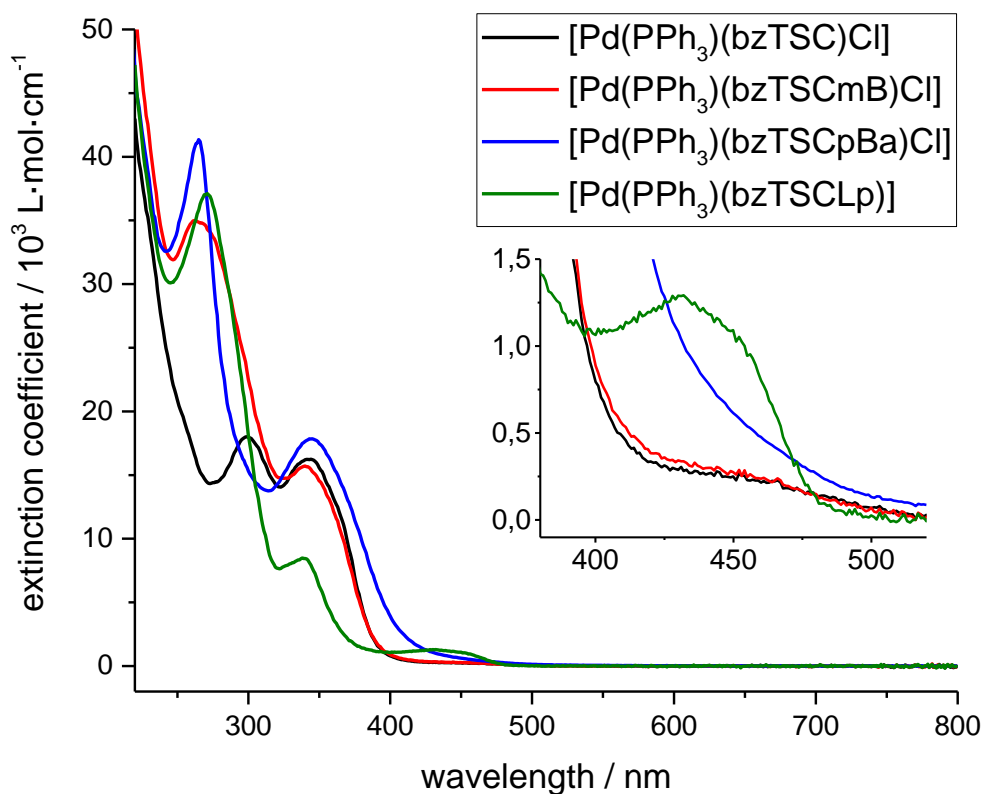


Figure 2.97 UV/Vis spectra of $[\text{Pd}(\text{PPh}_3)(\text{bzTSC})\text{Cl}]$, $[\text{Pd}(\text{PPh}_3)(\text{bzTSCmB})\text{Cl}]$, $[\text{Pd}(\text{PPh}_3)(\text{bzTSCpBa})\text{Cl}]$ and $[\text{Pd}(\text{PPh}_3)(\text{bzTSClp})]$ in MeCN.

Also, in cyclic voltammetry, shown in Figure 2.98, the small analogues seem to have very similar redox behaviour, except for the oxidation which occurs at lower potentials for *N4* derivatized structures, but lysine seems to be a different coordination compound. Maybe it is a cyclometallated species, but we were unable to confirm the cyclisation. Just the difference in analysis gives a clue to a “different” species. A possible, yet unverified, structure is shown in Figure 2.98.

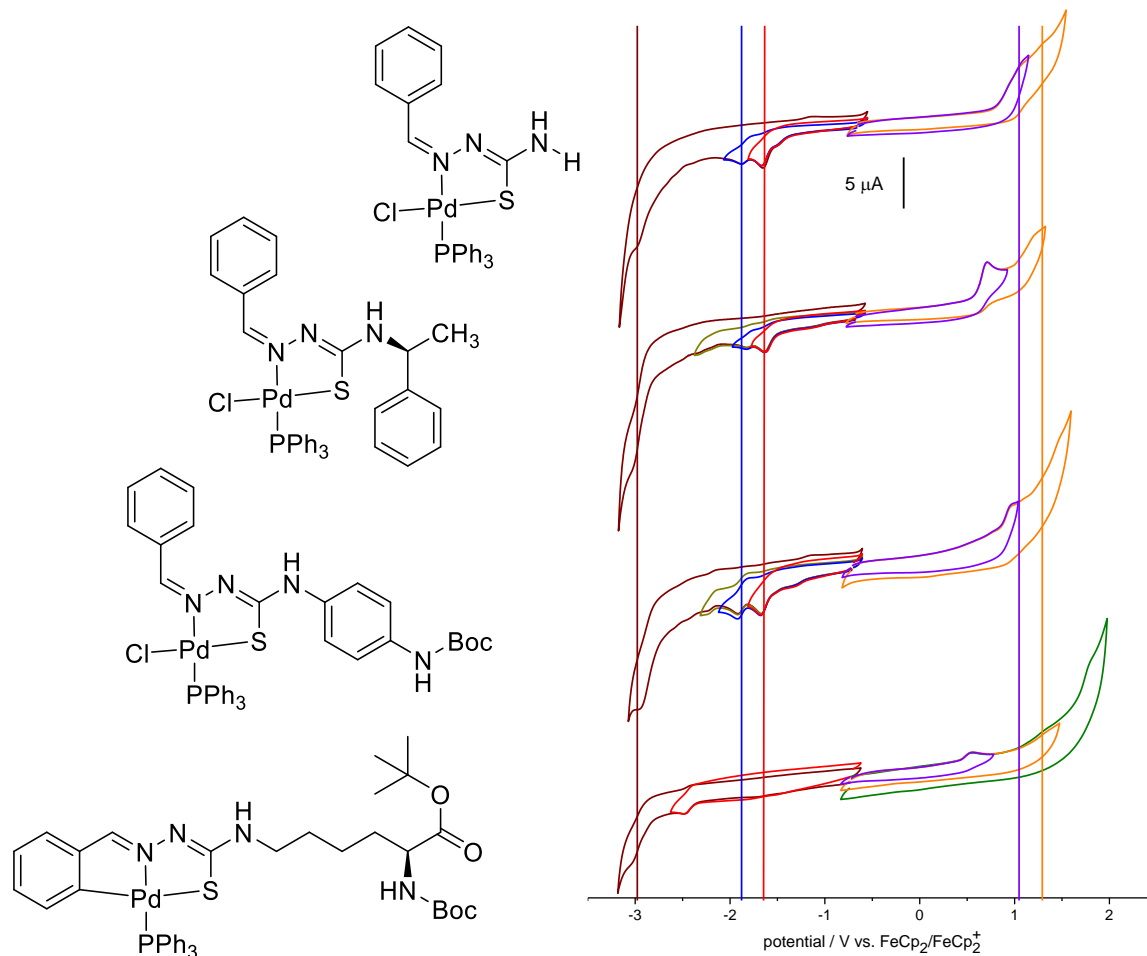


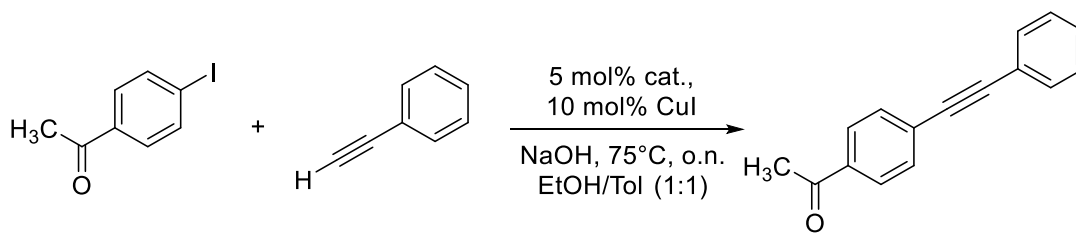
Figure 2.98 Cyclic voltammograms of [Pd(PPh₃)(bzTSC)Cl], [Pd(PPh₃)(bzTSCmB)Cl], [Pd(PPh₃)(bzTSCpBa)Cl] and [Pd(PPh₃)(bzTSClp)Cl] in 0.1 M NBu₄PF₆ MeCN solution with a feed rate of 100 mV/s.

2.10.3. Catalytic properties of the [Pd(PPh₃)(TSC)Cl] structures

2.10.3.1. Sonogashira-Hagihara coupling

The complexes were tested in catalytic reactions testing their properties in the formation of C–C bonds. The reactions were under *Sonogashira-Hagihara* or *Suzuki-Miyaura* conditions. The catalytic yields and their turnover numbers (TON) were determined by the shifts in the ¹H-NMR of the acetyl group.

The *Sonogashira-Hagihara* coupling was carried out with a catalyst loading of 0.5 mol% and 10 mol% CuI as cocatalyst. Herein 4-iodoacetophenone and phenylacetylene were reacted to form 1-(4-phenylethynyl)phenyl)ethanone. The test system is shown in Scheme 2.65.



Scheme 2.65 Sonogashira-Hagihara system for catalyst testing.

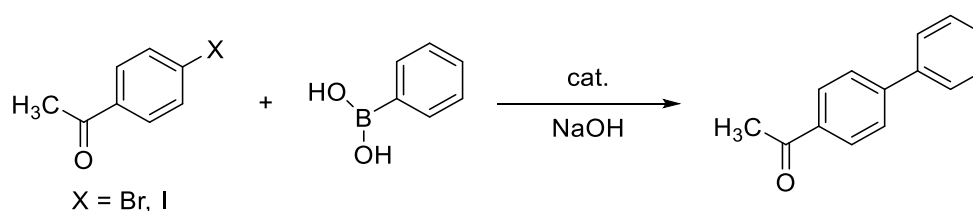
In the NMR spectra of the reaction the product could be identified, and the turnover numbers calculated by comparing the integrals of the phenyl moieties in the product and reagent at 7.42-7.30 ppm and 7.59-7.50 ppm, respectively. The results from this catalytic trials are shown in Table 2.21.

Table 2.21 TON of the catalysts under standard *Sonogashira-Hagihara* conditions.

Catalyst	TON
[Pd(bzTSC)(PPh ₃)Cl]	108
[Pd(bzTSCmB)(PPh ₃)Cl]	54
[Pd(bzTSCLp)(PPh ₃)Cl]	82

2.10.3.2. Suzuki-Miyaura coupling

The *Suzuki-Miyaura* coupling of 4-haloacetophenone and phenylboronic acid, shown in Scheme 2.66, was subject to a more in-depth investigation. Testing [Pd(bzTSC)(PPh₃)Cl], [Pd(bzTSCmB)(PPh₃)Cl], [Pd(bzTSCLp)(PPh₃)Cl] and [Pd(bzTSCpBa)(PPh₃)Cl] in various amounts with changing substrates and temperatures. The progress of the reaction could be detected by ¹H-NMR (Figure 2.99). The results of the catalysis trials are given in Table 2.22.



Scheme 2.66 Suzuki-Miyaura reaction for catalyst testing.

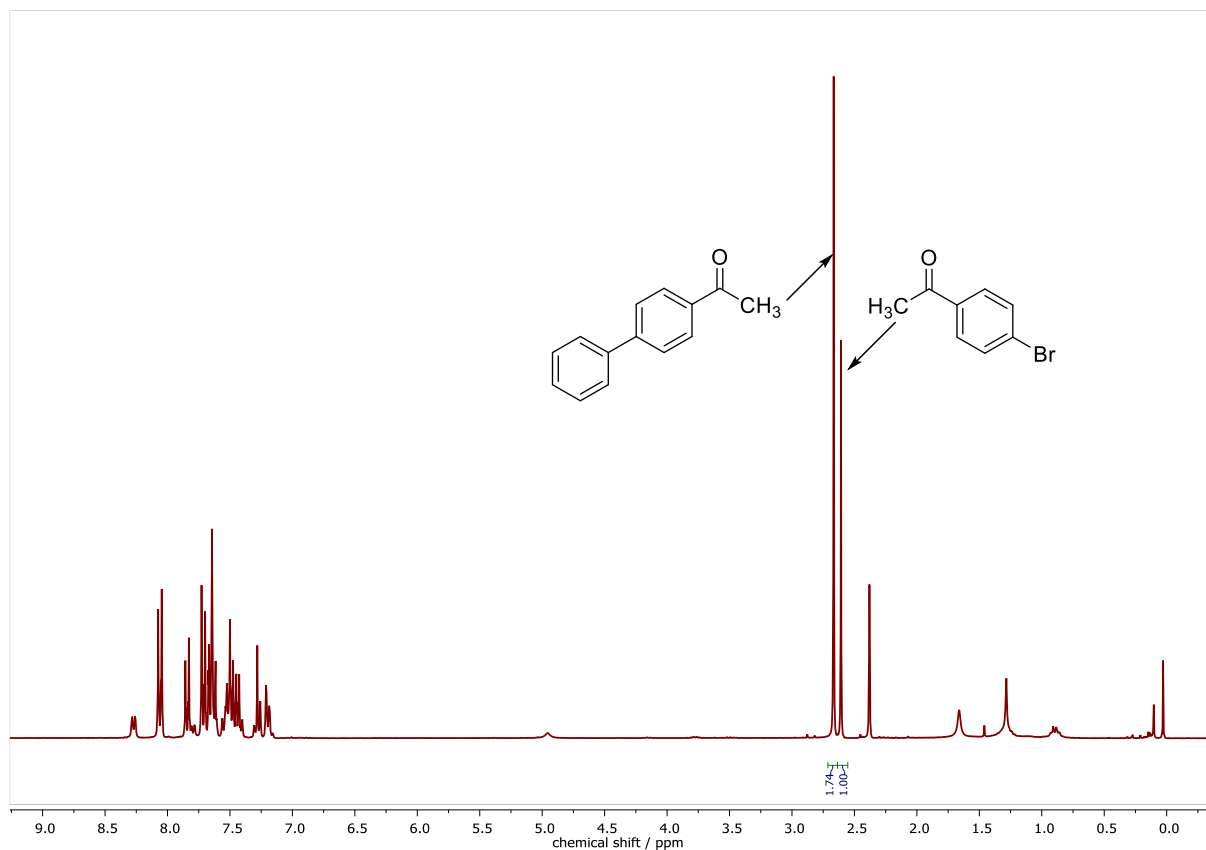


Figure 2.99 Typical ^1H NMR spectrum of the Suzuki reaction without full conversion. Conditions used are entry 12 of table 2.21. The spectrum was measured at 300 MHz in CDCl_3 . Integrals indicating a conversion of 63.5%.

Table 2.22 Results of the catalyst test runs.

Entry	Cat [mol%]	Cat	X	R-B(OH) ₂	Solvent	T [°C]	TON
1	0.001	H	I	Phenyl	EtOH/Tol (1:1)	95	61000
2	0.001	mB	I	Phenyl	EtOH/Tol (1:1)	95	2200
3	0.001	Lp	I	Phenyl	EtOH/Tol (1:1)	95	18000
4	0.001	pBa	I	Phenyl	EtOH/Tol (1:1)	25	750
5	0.001	pBa	I	Phenyl	EtOH/Tol (1:1)	95	12300
6	0.001	pBa	Br	Phenyl	EtOH/Tol (1:1)	25	4700
7	0.001	pBa	Br	Phenyl	EtOH/Tol (1:1)	95	63400
8	0.001	pBa	Br	Naphthyl	EtOH/Tol (1:1)	95	480
9	1	pBa	Br	Phenyl	H ₂ O	95	100
10	0.122	pBa	Br	Phenyl	H ₂ O	95	850
11	0.1	pBa	Br	Phenyl	H ₂ O	95	1000
12	0.01	pBa	Br	Phenyl	H ₂ O	95	10000

As shown in Table 2.22, the highest activities were found for entries 1 and 7. But also, entry 12 is quite interesting since the complex shows considerable high activity in water. Overall, the temperature dependence of this reaction is obvious. Going from 25 °C to 95 °C increases the TON by a 16-fold (entries 4 and 5) and by 13-fold (entries 6 and 8). The TON at ambient temperature is in a good range for more complex couplings, especially considering the possible use in metalloenzymes where too high temperatures may destroy the cavity.

Also, we were able to determine the activity of the complex in the reaction with the conditions of entry 4, which showed to be a nice linear fit, depicted in Figure 2.100. Yet the fit also shows that the reaction is considerably slow, and the reaction would take about 60 hours to run to completion.

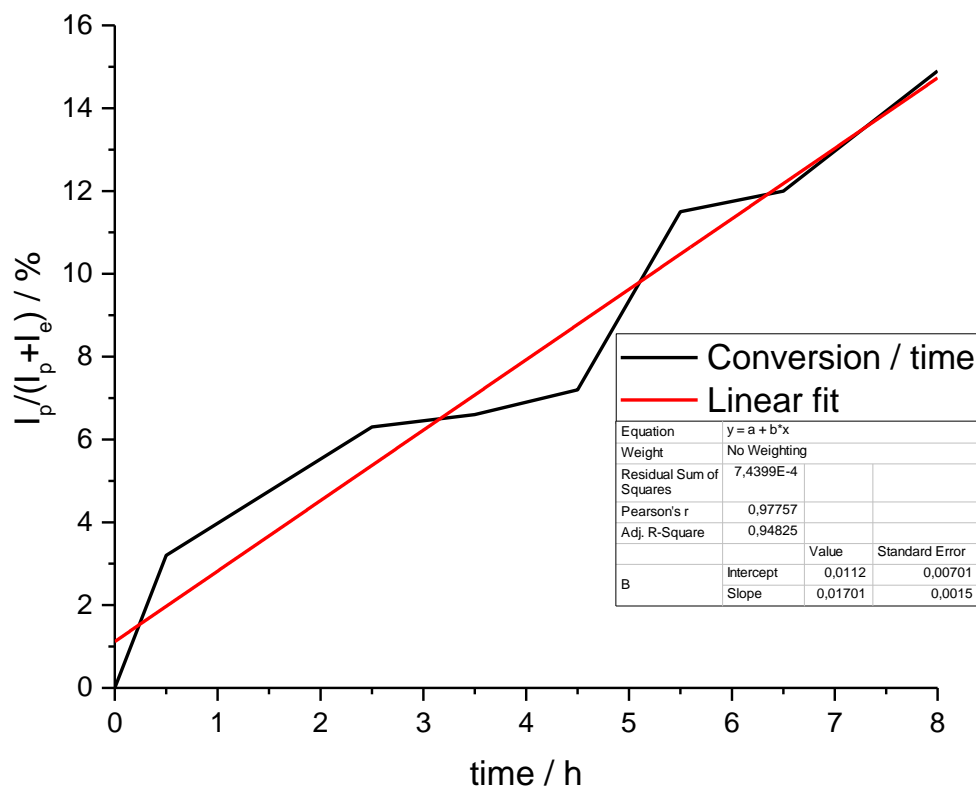


Figure 2.100 Determined curve for the kinetics (conversion/time) of the cross-coupling reaction under *Suzuki-Miyaura* conditions in EtOH/toluene (1:1) with catalyst [Pd(PPh₃)(TSCpBa)Cl] with a linear fit (red). (I_p NMR intensity of product, I_e NMR intensity of reagent).

Considering the palladium thiosemicarbazone catalysts we were able to get the amino acid derivative, which is possibly a cyclometallated – yet catalytically active - species, but not a biotinylated species. All complexes showed high activities in the *Suzuki* coupling of standard reagents which looks promising and should be further investigated considering the substrate scope as well as further coupling tests of biotin.

2.11. U(IV) thiosemicarbazones

2.11.1. U(IV) complexes of benzylic thiosemicarbazones

2.11.1.1. Synthesis of U(IV) complexes

Another complex system based on phenyl thiosemicarbazones was synthesized in collaboration with *Dr. Markus Zegke* of the group of *Prof. Dr. Matthias Wickleder*. Using the thiosemicarbazones shown in Chart 2.19. In yields of 85-97% and characterized by ^1H , ^{13}C NMR and EI-MS.

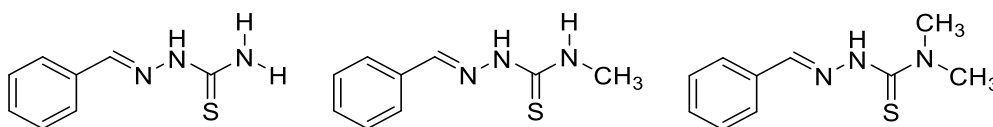
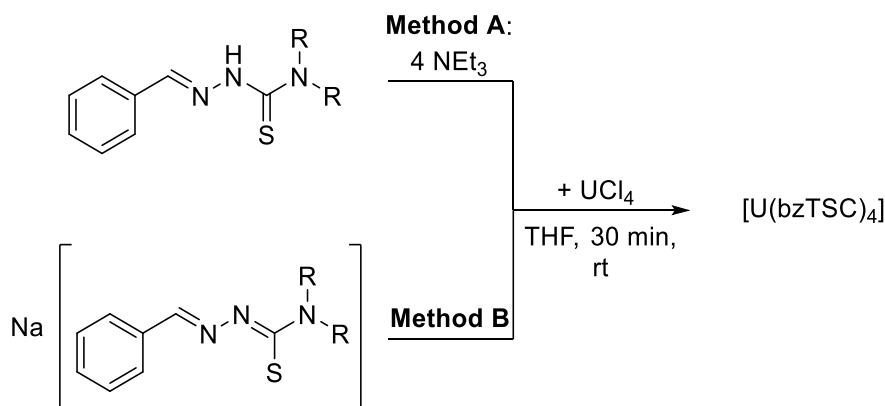


Chart 2.19 Molecular structures of HbzTSC, HbzTSCm and HbzTSCdm.

The uranium complexes were synthesized by two methods. The first was the mixing of the uranium salt with the ligand in presence of a base. The method B used first deprotonating the ligands with sodium ethoxide and subsequent reaction with UCl_4 , as depicted in Scheme 2.67, crystalline compounds can be isolated that were the corresponding $[\text{U}(\text{TSC})_4]$ complexes. The complexes could be isolated in yields of 26-63% for method A and 31-59% for method B, and they were analysed by ^1H -NMR and IR spectroscopy.



Scheme 2.67 Reaction of thiosemicarbazones with U(IV).

The resulting structures $[\text{U}(\text{bzTSC})_4]$, $[\text{U}(\text{bzTSCm})_4]$, and $[\text{U}(\text{bzTSCdm})_4]$ were investigated thoroughly in regards of their crystal structure, electrochemical and thermal behaviour.

2.11.1.2. Crystal structure analysis

In all cases, the U(IV) coordinates four thiosemicarbazones by the sulphur and a nitrogen atom. The obtained crystal structures unveiled a thiolate-N2 coordination for the unmethylated and monomethylated thiosemicarbazones bearing four membered rings, whereas the demethylated thiosemicarbazone coordinates by the N1 position instead of the N2 resulting in a five membered ring. The crystal structures are depicted in Figure 2.101 and the crystallographic data are reported in Table 2.22.

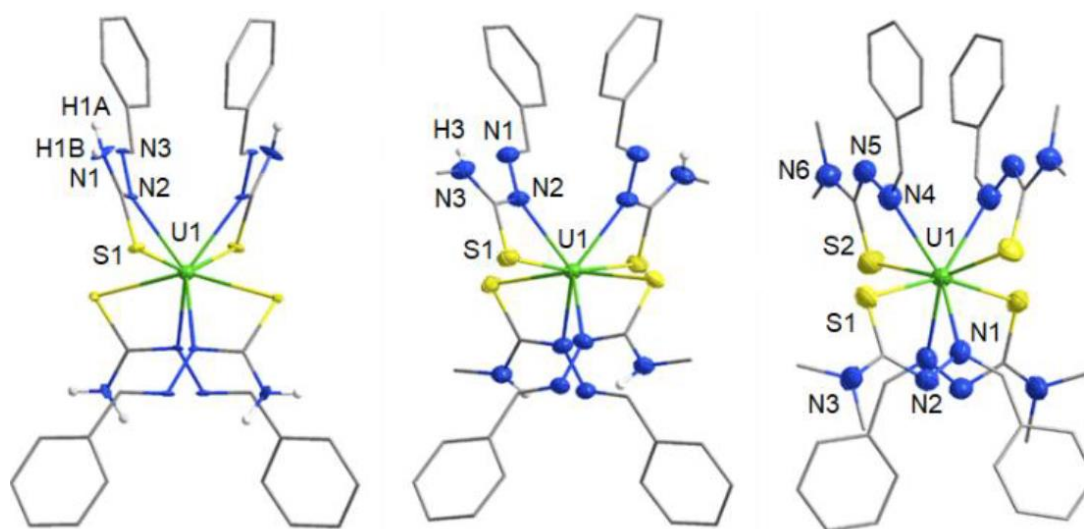


Figure 2.101 Crystal structures of [U(bzTSC)₄], [U(bzTSCm)₄] and [U(bzTSCdm)₄]. All hydrogen atoms except NH are omitted for clarity. Thermal ellipsoids are drawn at 50% probability for the heteronuclei.

Table 2.22 Crystallographic data for [U(bzTSC)₄], [U(bzTSCm)₄] and [U(bzTSCdm)₄].

	[U(bzTSC) ₄].4THF	[U(bzTSCm) ₄]	[U(bzTSCdm) ₄]
Chemical Formula	UC ₄₈ H ₆₄ N ₁₂ O ₄ S ₄	UC ₃₆ H ₄₀ N ₁₂ S ₄	UC ₄₀ H ₅₂ N ₁₂ S ₄
Molar Mass	1239.38 $\frac{\text{g}}{\text{mol}}$	1007.07 $\frac{\text{g}}{\text{mol}}$	1063.17 $\frac{\text{g}}{\text{mol}}$
Temperature	100 (2) K	100 (2) K	100 (2) K
Wavelength	$\lambda_{\text{Cu-K}\alpha} = 1.54178 \text{ \AA}$	$\lambda_{\text{Cu-K}\alpha} = 1.54178 \text{ \AA}$	$\lambda_{\text{Cu-K}\alpha} = 1.54178 \text{ \AA}$
Crystal System	tetragonal	tetragonal	monoclinic
Space Group	<i>I</i> ₄ /a (88)	<i>I</i> ₄ /a (88)	<i>C</i> 2/c (15)
Lattice Parameters	a = 17.1729 (7) \AA $\alpha = 90^\circ$ b = 17.1729 (7) \AA $\beta = 90^\circ$ c = 18.3410 (11) \AA $\gamma = 90^\circ$	a = 17.5361 (6) \AA $\alpha = 90^\circ$ b = 17.5361 (6) \AA $\beta = 90^\circ$ c = 12.9149 (7) \AA $\gamma = 90^\circ$	a = 22.6126 (6) \AA $\alpha = 90^\circ$ b = 14.4659 (3) \AA $\beta = 129.4^\circ$ c = 17.6453 (4) \AA $\gamma = 90^\circ$
Cell Volume	5408.9(5) \AA^3	3971.5(3) \AA^3	4456.8(4) \AA^3
Formula Unit	4	4	4
F(000)	2464	1984	2128
Measurement Range	$3.52^\circ < h < 72.00^\circ$ $-21 < h < 21$ $-21 < k < 20$ $-22 < l < 22$	$4.25^\circ < h < 72.09^\circ$ $-16 < h < 21$ $-21 < k < 20$ $-15 < l < 15$	$3.97^\circ < h < 72.11^\circ$ $-27 < h < 27$ $-17 < k < 17$ $-21 < l < 21$
Number of Reflections	2660	1964	4388
Observed Reflections	2632	1831	3788
Goodness-of-fit	1.115	1.145	1.056
R ₁ [<i>I</i> ₀ > 2 σ _{<i>I</i>}]all data	R ₁ = 0.0512, R ₁ = 0.0516	R ₁ = 0.0245, R ₁ = 0.0264	R ₁ = 0.0705, R ₁ = 0.0415
wR ₂ [<i>I</i> ₀ > 2 σ _{<i>I</i>}]all data	wR ₂ = 0.1542, wR ₂ = 0.1544	wR ₂ = 0.0704, wR ₂ = 0.0714	wR ₂ = 0.1056, wR ₂ = 0.1107
$\Delta\rho_{\text{max}}$, $\Delta\rho_{\text{min}}$	2.464 e \AA^{-3} , -1.094 e \AA^{-3}	0.701 e \AA^{-3} , -0.411 e \AA^{-3}	3.721 e \AA^{-3} , -0.935 e \AA^{-3}
CCDC Number	2043819	2043820	2043821

The bonding distances around the uranium centre as well as the S-U-N angle is given in Table 2.23. The comparison shows that switching from the four membered rings to the five membered cycle increases the bonding angle and decreases the thiolate-uranium bond, indicating a relaxation in the coordination sphere around the metal centre.

Table 2.23 Selected bond distances and angles for [U(bzTSC)₄], [U(bzTSCm)₄] and [U(bzTSCdm)₄].

	[U(bzTSC) ₄].4THF	[U(bzTSCm) ₄]	[U(bzTSCdm) ₄]
U-S	2.8289(1) Å	2.8319(1) Å	2.739(1) Å
U-N	2.4982(1) Å	2.464(3) Å	2.535(1) Å
S-U-N	57.769(1)°	57.53(8)°	67.02(1)°

The crystal structure of [U(bzTSC)₄] was determined to contain additional THF molecules in close contact to the amine moieties of the thiosemicarbazone ligands, as shown on the Hirshfeld surface in Figure 2.102. The methylated structures did not contain THF in their crystal structure, yet THF was chosen for further analyses in solution to get a better comparison of the complexes.

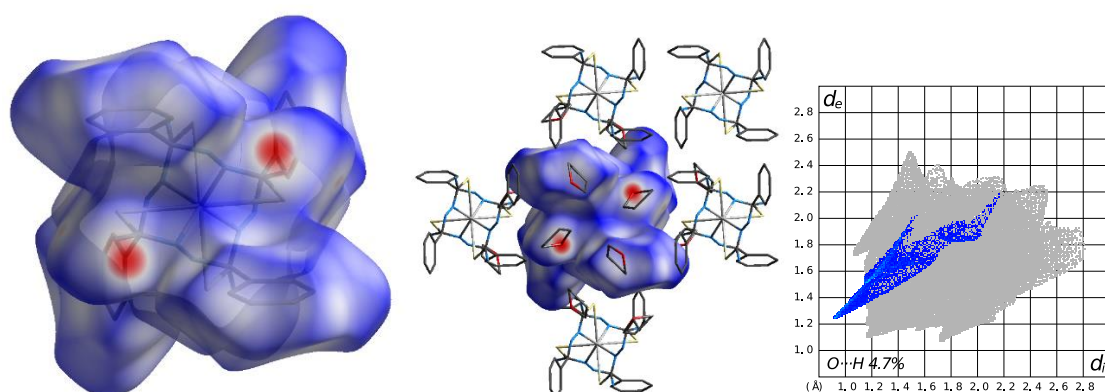


Figure 2.102 Hirshfeld surface of [U(bzTSC)₄] (left) and addition of the closest molecules surrounding the promolecule (middle). Viewed along the crystallographic c-axis. Fingerprint plot filtered for the O...H/H...O interaction (right).

The complexes were air stable and were characterized by UV/vis, NMR and SC-XRD. Also, cyclic voltammetry and spectroelectrochemical UV/vis experiments were performed to analyse the redox chemistry of the complexes.

2.11.1.3. UV/Vis spectroscopy

The UV/Vis spectra of HbzTSC and the corresponding uranium complex [U(bzTSC)₄] is shown in Figure 2.103. The spectra show little deviation considering the wavelength of the absorption maxima. This may be since the phenyl ring is a major chromophore, but it is almost untouched by the coordination, yet there are 4 times as many chromophores hence the higher absorption. Also, a slight broadening

is visible. Further bands which would relate to charge transfer interactions are not detectable for either of the U(IV) structures.

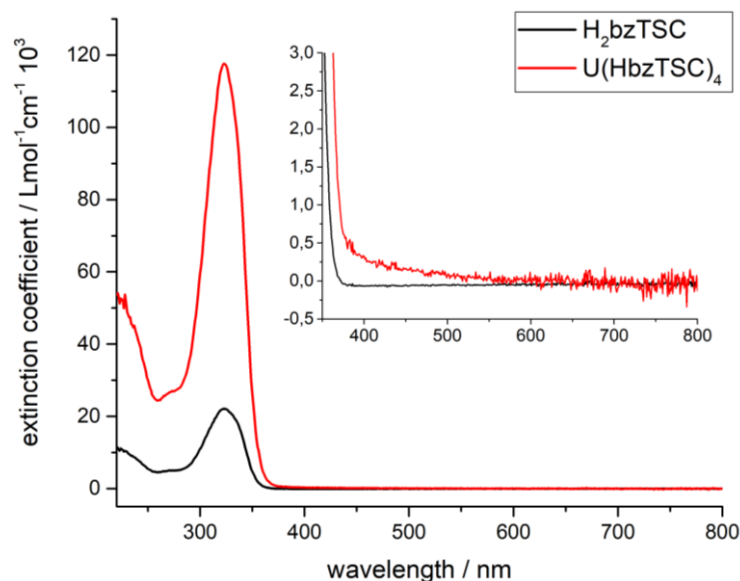


Figure 2.103 UV/Vis spectra of HbzTSC and $[U(bzTSC)_4]$ recorded in THF.

2.11.1.4. Electrochemical analysis

Cyclic voltammetry of the ligand shows one irreversible oxidation at 0.67 V as well as two irreversible reductions at -2.57 V and -3.17 V in addition to a reversible reduction at -2.84 V. The complex on the other hand, shows an irreversible oxidation at 0.48 V and one irreversible reduction at -2.53 V. Both voltammograms are depicted in Figure 2.104.

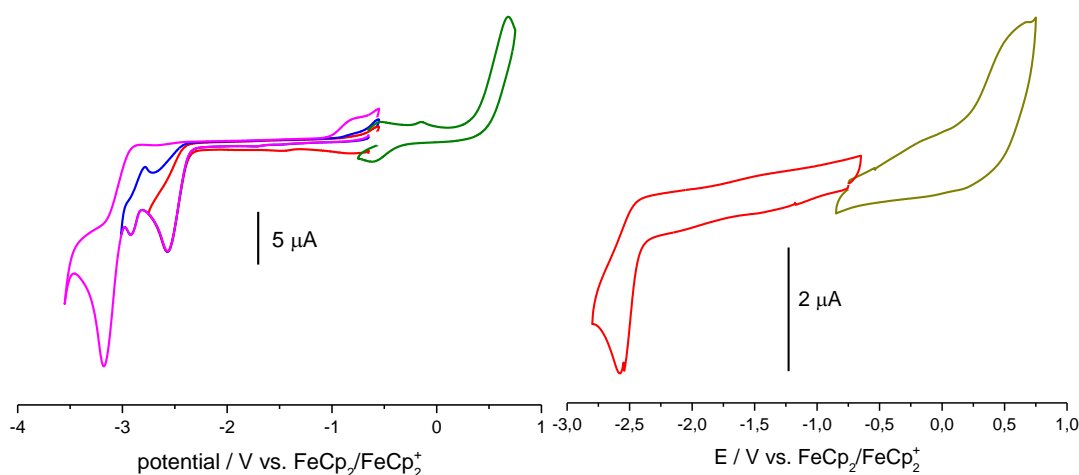


Figure 2.104 Cyclic Voltammograms of HbzTSC (left) and $[U(bzTSC)_4]$ (right) measured in 0.1 M nBu_4NPF_6/THF solution at a scan rate of 100 mV/s. Referenced against the $FeCp_2/FeCp_2^+$ redox pair.

Comparing the oxidation and redox processes the SEC-UV-vis experiments showed a high similarity between the ligand and the complex. Both structures show a bathochromic and hypochromic shift as well as the formation of a second band at

around 350 nm during the oxidation. In the reduction, the intense band at 320 nm decreases whereas another band at 400 nm emerges (Figure 2.105).

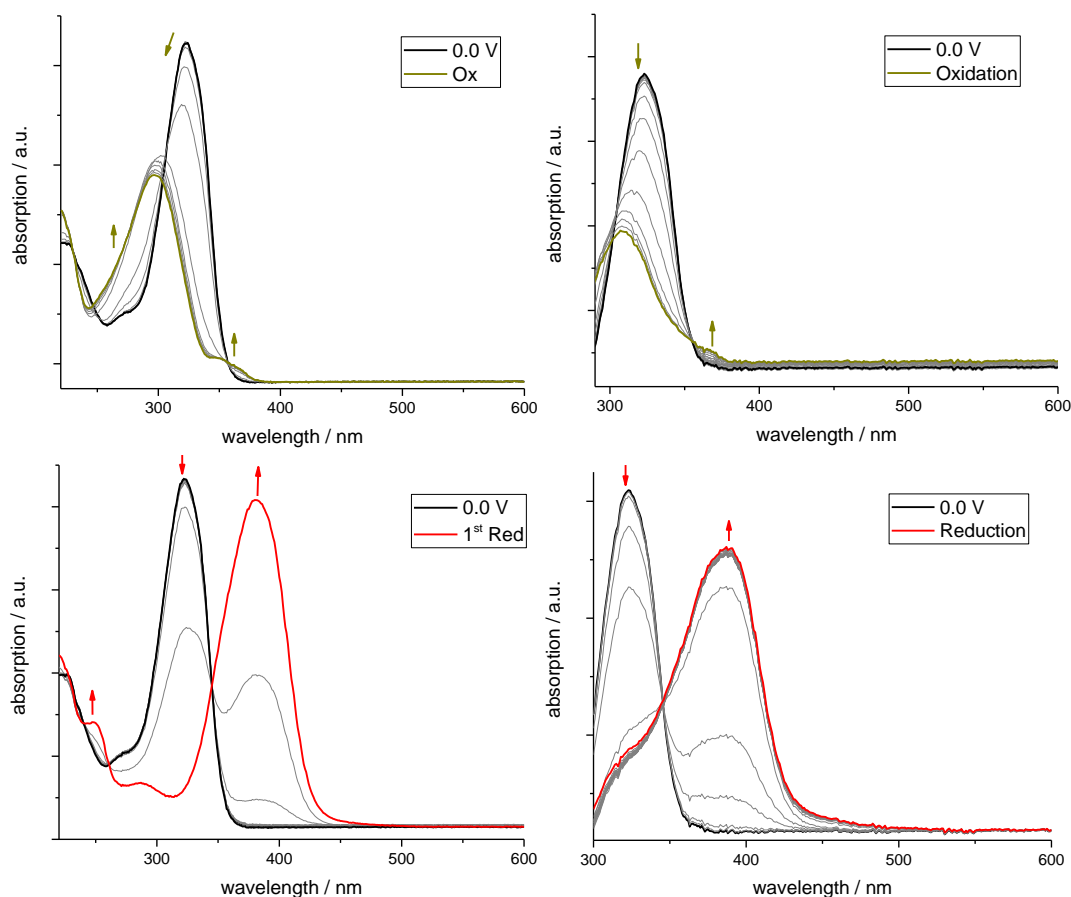


Figure 2.105 UV/Vis absorption spectra of HbzTSC (left) and $[U(bzTSC)_4]$ in 0.1 M nBu_4NPF_6/THF solution recorded during the oxidation (upper row) and first reduction (lower row) in 0.1 V increments.

For the ligand, further reduction processes could be detected (Figure 2.106). In the second reduction further shifts occur indicating a stable intermediate whereas the third reduction shows the degradation of the ligand.

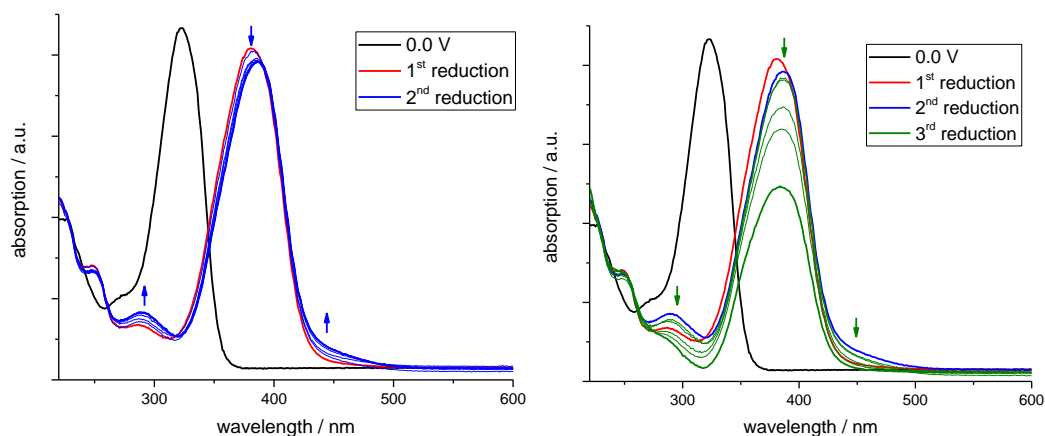


Figure 2.106 UV/Vis absorption spectra of HbzTSC in 0.1 M nBu_4NPF_6/THF solution recorded during the second (right) and third reduction (left) in 0.1 V increments.

2.11.1.5. Thermoanalytic behaviour

Since U(IV) chalcogenides are of special interest in material science due to their interesting semiconducting properties, a group of those are U(IV) sulphides, namely US_2 , $US(S_2)$ and U_2S_3 , which are investigated intensively as bulk material. Since the herein reported compounds contain U–S bonds their use as single source precursors can be considered. Similarly, ZnS and SnS films could be generated by CVD of a thiosemicarbazone precursor.^{362, 363}

TGA/DSC of the compounds however show the formation of a different compound. In Figure 2.107, the TGA/DSC of $[U(bzTSC)_4]$ is depicted. Over 160 °C $[U(bzTSC)_4]$ decomposes leaving about 35% of residual mass. A small drop in the TGA is already detectable at 55 °C. This could be the co-crystallized THF evaporating. The other uranium structures showed similar thermal decomposition.

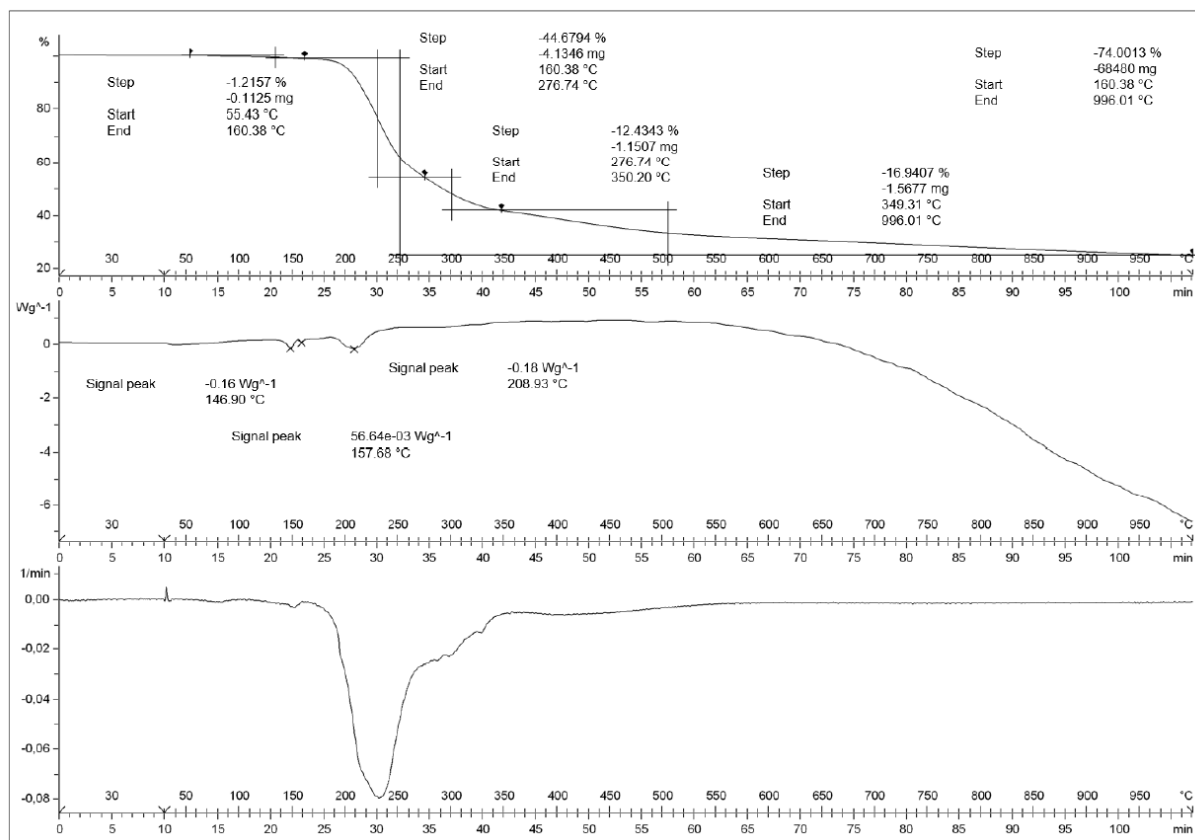


Figure 2.107 TGA/DSC and first derivative of TGA of $[U(bzTSC)_4] \cdot 4THF$. Temp. program: hold 30 °C for 10 min. and heat with 10 K·min⁻¹; argon flux: 30 ml·min⁻¹.

The experiments for the other structures are similar. Powder-XRD after the thermal treatment of the compounds showed the formation of $UO_{1.96}$ for all of them, as shown in Figure 2.108. Considering the low to zero amount of oxygen in the starting material, one could think of the oxygen originating from the corundum crucibles used in the TGA/DSC measurements, but that was not further investigated.

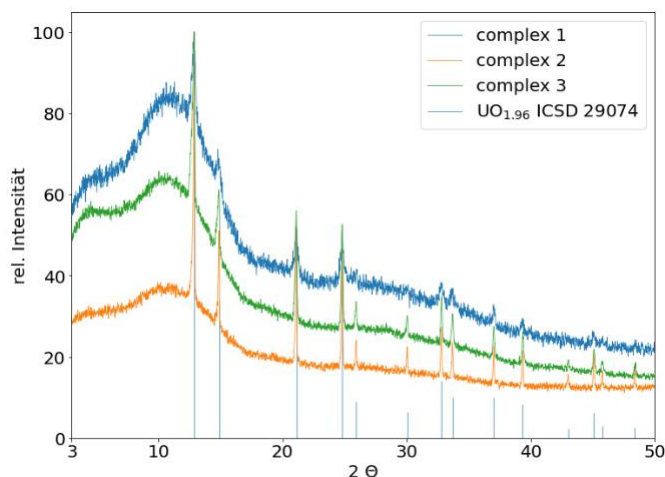
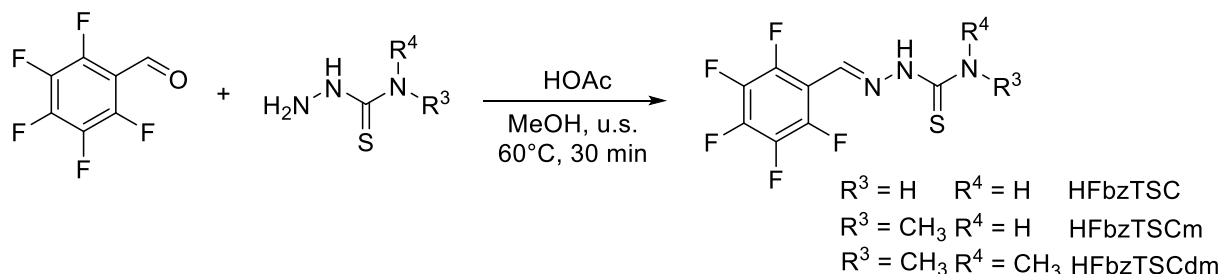


Figure 2.108 PXRD pattern of [U(bzTSC)₄] (blue), [U(bzTSCm)₄] (orange), and [U(bzTSCdm)₄] (green), after TGA/DSC compared with UO_{1.96} (ICSD 29074).

2.11.2. Synthesis of pentafluorobenzylc thiosemicarbazones

To increase the volatility of these complexes to advance further into the field of chemical vapor deposition, we started using pentafluorobenzaldehyde as carbonyl source. Upon reaction with the three thiosemicarbazides the corresponding thiosemicarbazones were isolated in good yields (Scheme 2.68). The reaction proceeds faster than the non-fluorinated derivatives due to the higher polarization at the carbonyl.



Scheme 2.68 Synthesis of HFbzTSC, HFbzTSCm and HFbzTSCdm from pentafluorobenzaldehyde and the corresponding thiosemicarbazide.

2.11.2.1. NMR analysis

The three ligands could be characterized by ¹H, ¹³C and ¹⁹F NMR and due to the small number of atoms they can all be easily assigned. Starting with ¹H NMR (Figure 2.109), we have three positions with protons which can be detected. The imine proton stays a singlet at 8.2 ppm, which is in line with previous findings reported in this thesis. The hydrazone proton stays acidic for all structures at 11.8 ppm for the mono- and unmethylated species. The demethylated ligand expresses the hydrazone proton at 11.4 ppm as a broad signal. This shows that the proton may be more easily cleaved in comparison to the other two ligands and resulting in a broadening. The thioamide

protons for the unmethylated splits into two distinct signals at 8.5 and 7.5 ppm due to the formation of rotamers. The introduction of one methyl group leads to the expression of a broader signal at 8.2 ppm, which unfortunately overlaps with the imine proton. Nevertheless, the methyl group expresses a doublet at 3.0 ppm with a COSY detectable coupling to the amine. The dimethylated species has no signal for the thioamide section but the two methyl groups can be detected as a singlet corresponding to 6 protons at 3.3 ppm.

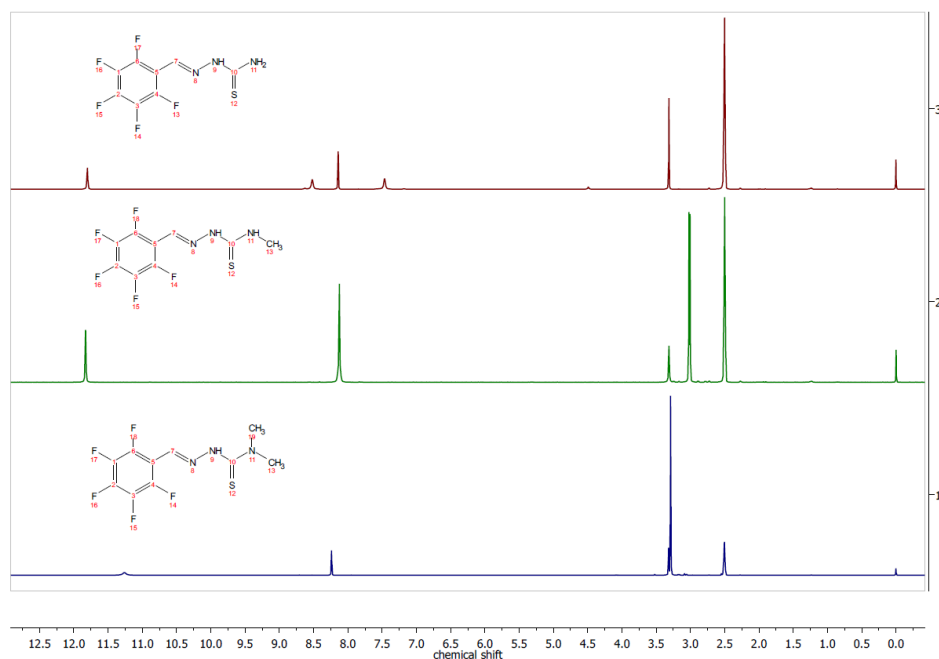


Figure 2.109 ^1H NMR spectra of HFbzTSC, HFbzTSCm and HFbzTSCdm in $\text{DMSO-}d_6$ at 300 MHz.

$^{13}\text{C}\{^1\text{H}\}$ DEPTQ experiments are straight forward. The detectable ^{13}C signals could be assigned – starting from high field – to the thione, imine and the methyl groups (Figure 2.110). The fluorinated phenyl rings do not express signals in this method due to a lack of neighbouring protons.

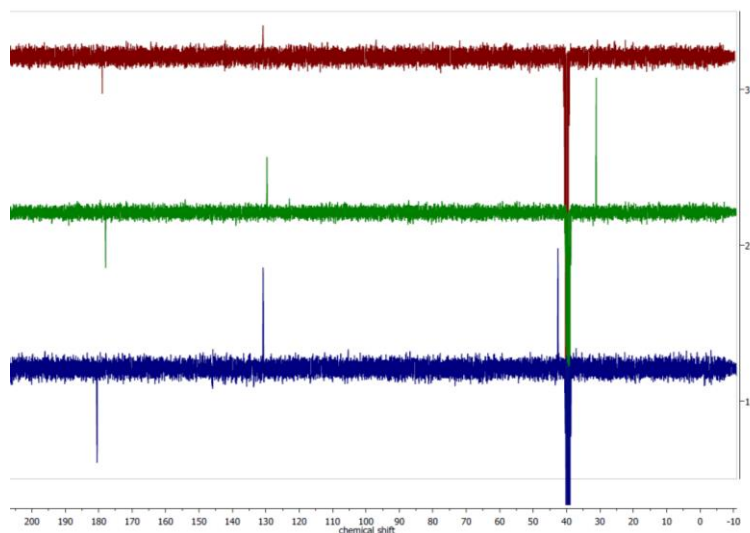


Figure 2.110 $^{13}\text{C}\{^1\text{H}\}$ DEPTQ spectra of HFbzTSC, HFbzTSCm and HFbzTSCdm in $\text{DMSO-}d_6$ at 75 MHz.

The ^{19}F NMR shows a doublet at -140 ppm resembling the ortho fluorine atoms, at -150 ppm triplets are assignable to para fluorine and at -160 ppm are the two fluorine atoms resembling those in meta position (Figure 2.111). The spectra indicate that all the samples are pure.

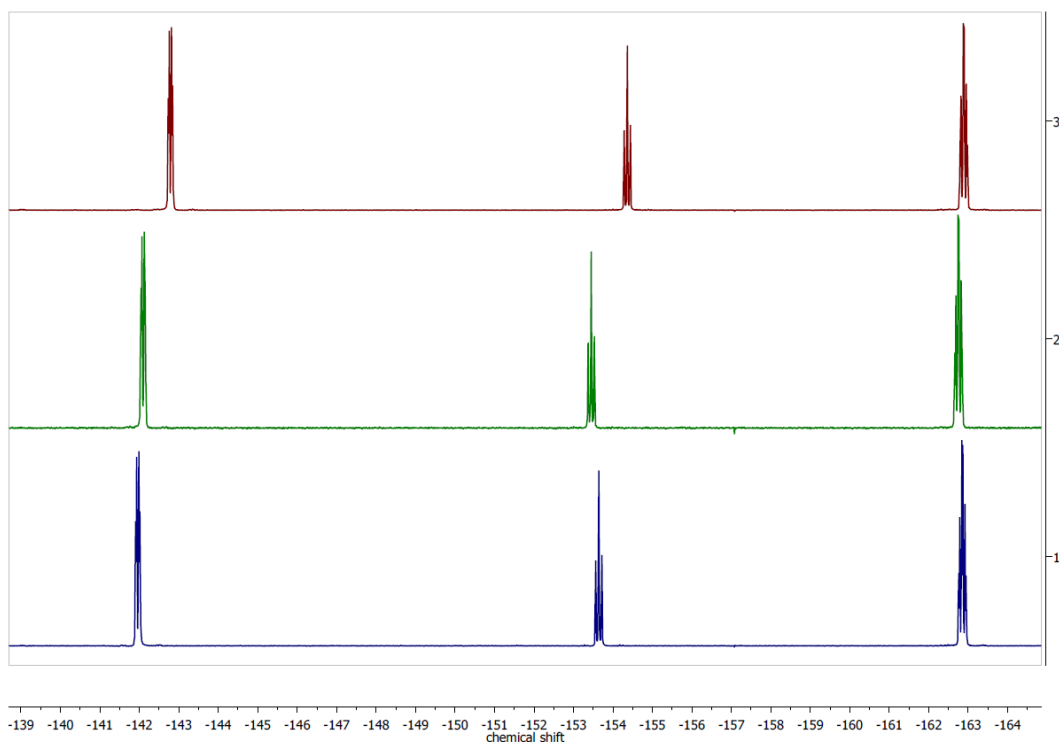


Figure 2.111 ^{19}F NMR spectra of HFbzTSC, HFbzTSCm and HFbzTSCdm in $\text{DMSO-}d_6$ at 282 MHz.

2.11.2.2. Mass spectroscopy

All three ligands were analysed by EI-MS. The advantage of EI-MS with these ligands is that the ion flow regarding the sample temperature helps to understand which molecule has the highest tendency to evaporate.

All ligands are detectable by their molecular peaks, and the thiourea fragment after the hydrazone splitted of. As an example, in Figure 2.112 the EI-MS of HFbzTSCdm is shown. The molecule ion is at 297 m/z. Additionally, the peaks at 194 m/z and 104 m/z resemble the arylimine and thiourea residues after ionization.

The unmethylated HFbzTSC evaporates at about 135 °C. The methylated structures evaporate much earlier. A single methylation yields a start of the ion beam at 112 °C and the double methylated starts at 105 °C. This can be a steric effect or the loss of interactions in the solid.

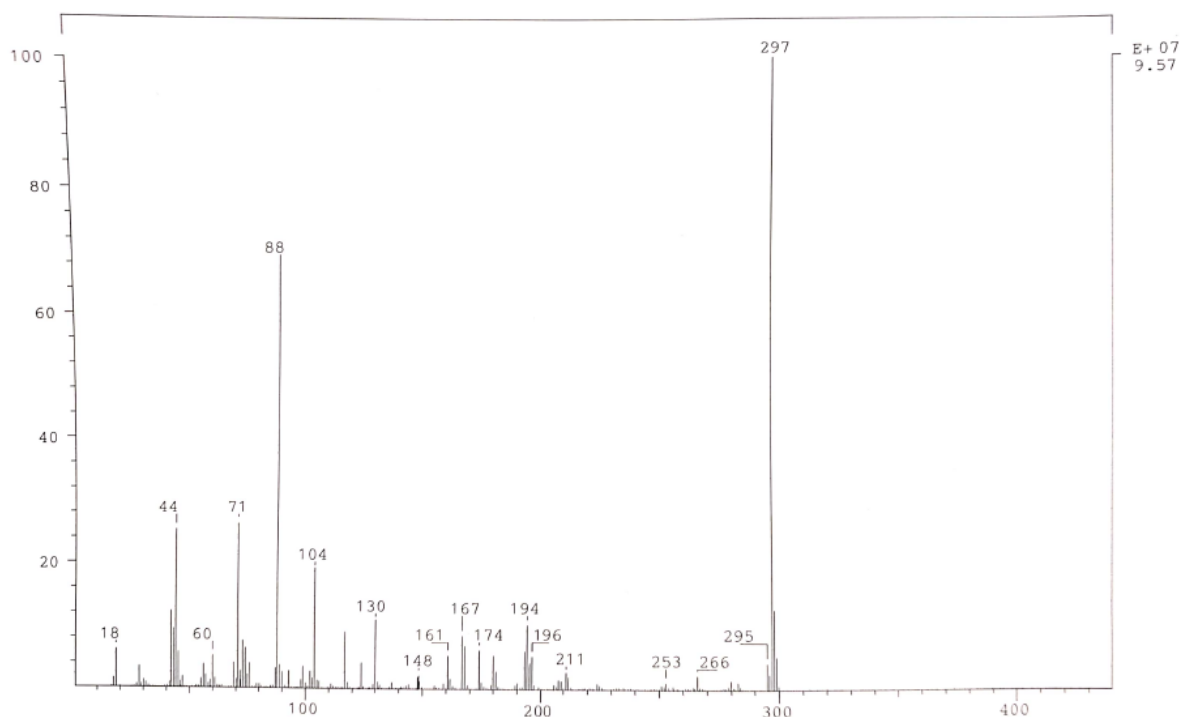


Figure 2.112 EI-MS spectra of HFbzTSCdm at 70 eV.

To further evaluate the idea of loss of interaction being responsible for the shift in evaporation temperature, *Hirshfeld* surface analysis was performed in the crystal structures of the ligands.

2.11.2.3. Hirshfeld surface analysis

As mentioned in Chapter 2.1.3 crystal structures of HFbzTSC, HFbzTSCm and HFbzTSCdm could be gained by X-ray diffractometry. In that chapter the intramolecular bond distances and angles were discussed and, in this chapter, the intermolecular distances and interactions will be described.

In Figure 2.113, the *Hirshfeld* surfaces of the three ligands are depicted. For all structures, a big contribution to close distances results from the interaction between the thione sulphur and the imine and hydrazone proton.

But it is also observable that the amine interactions decrease with more advanced methylation. The unmethylated derivative shows further close contacts from the amine protons to the sulphur.

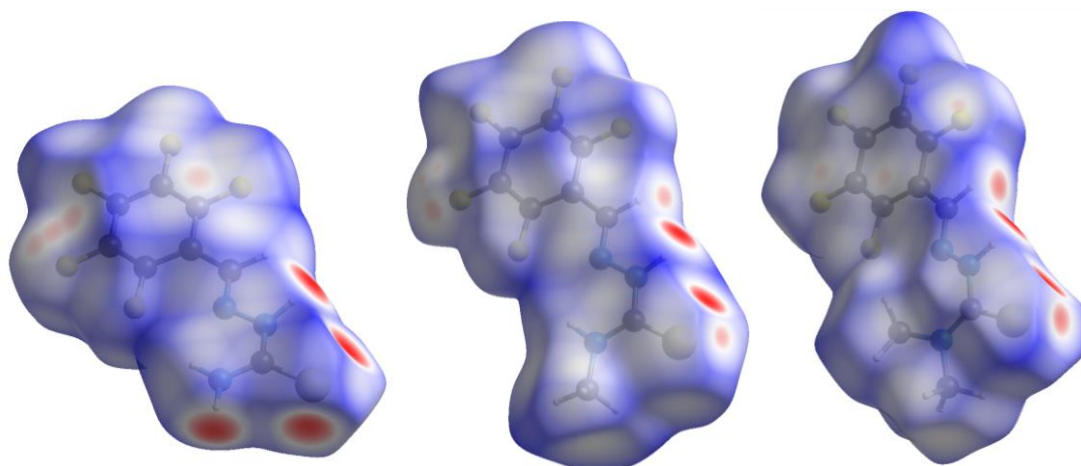


Figure 2.113 Hirshfeld surface analysis of HFbzTSC (left), HFbzTSCm (middle) and HFbzTSCdm (right).

Comparing the fingerprint plots of the structures, which are depicted in Figure 2.114, the loss of the amine sulphur interaction is also easily visible. Furthermore, the S...H interaction decreases with advancing methylation.

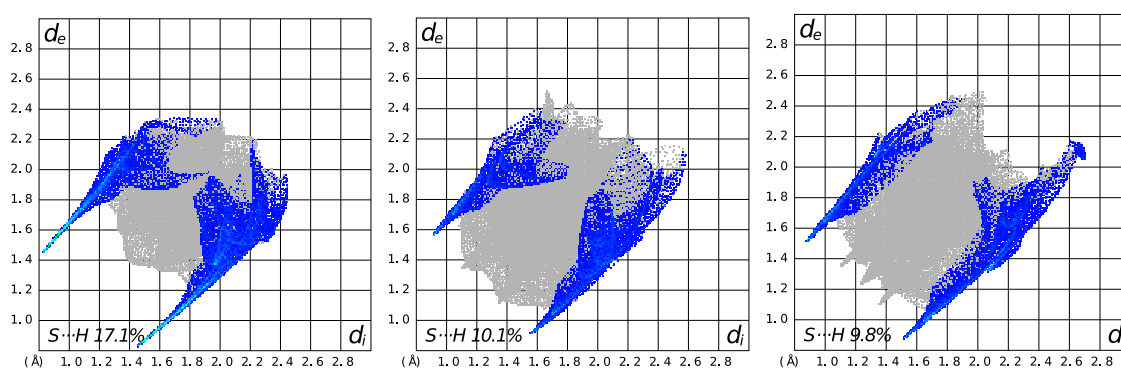


Figure 2.114 Fingerprint plots of HFbzTSC (left), HFbzTSCm (middle) and HFbzTSCdm (right) filtered for S...H/ H...S interactions.

The findings from the *Hirshfeld* surface analyses may indicate that the loss of intermolecular interactions result in lower evaporation temperatures, which is beneficial for the use of these ligands and their complexes in CVD.

2.11.2.4. Electrochemical analysis

The introduction of 5 fluorine atoms to the aryl should lead to an anodic shift of the reduction due to a lower electron density at the arylimine moiety, where, as pointed out multiple times in this work, the reduction should take place.

By comparing the cyclic voltammograms of HFbzTSC with its already mentioned nonfluorinated derivative HbzTSC, the reduction shifts from -2.55 V to -2.25 V

(Figure 2.115). This shift to higher potentials should result from the fluorination. Furthermore, the oxidation shifts cathodically.

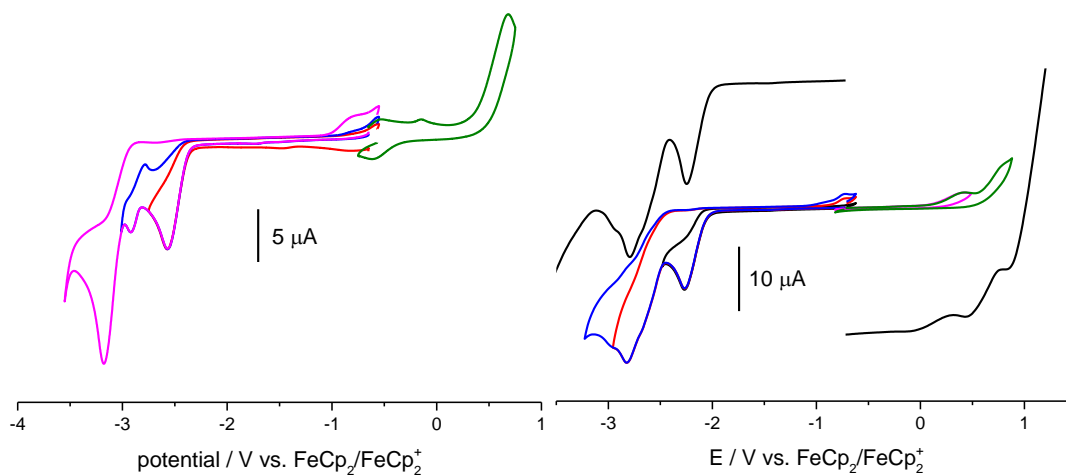


Figure 2.115 Cyclic Voltammograms of HbzTSC (left) and HFbzTSC(right) measured in 0.1 M nBu₄NPF₆/THF solution at a scan rate of 100 mV/s. Referenced against the FeCp₂/FeCp₂⁺ redox pair.

2.12. Bisthiosemicarbazones

Currently this thesis consists of asymmetric bi-, tri- and tetradentate ligands based on mono-carbonyl aryl systems, but pentadentate bithiosemicarbazones were synthesized to attach these structures as potent chelating agents to magnetic nanoparticles. These structures could be used to purify water from heavy metal waste since the ions are bound to the pentadentate ligand and the magnetic nanoparticle allows a simple work up procedure.³⁶⁴

Markus Schütz from the work group of Prof. *Mathur*, established a surface modification for these nanoparticles consisting of an azide derived catechol. Which leads to the desire to get alkyne structures of potent ligands. Such a desired structure would be 4-(but-1-yne) 2,6-diacetyl pyridine (Figure 2.116)

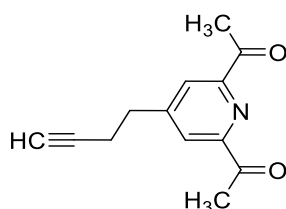
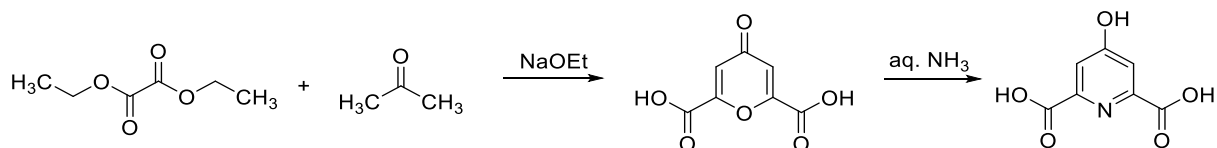


Figure 2.116 Structure motif of a desired 2,6-carbonyl pyridine with a substitution in the *para*-position for further functionalization.

2.12.1. Synthesis of 4-substituted pyridinyl bithiosemicarbazones

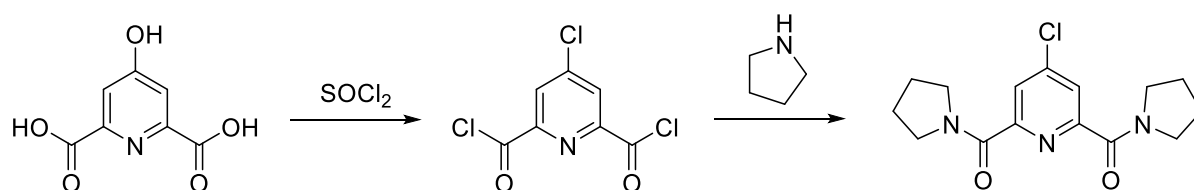
This structure would be synthesized from a 4-halido pyridine by C–C cross coupling. The direct halogenation in ortho position of a 2,6-diacetyl pyridine is yet to be discovered, so the reaction is quite a journey starting from diethyl oxalate and acetone. These compounds react with sodium ethoxide to chelidonic acid and a second step consisting of a condensation reaction with aqueous ammonia yields chelidamic acid (Scheme 2.71).³⁶⁵ This route was chosen since chelidamic acid is quite expensive whilst diethyl oxalate, acetone, ammonia, ethanol, and sodium are very cheap which allows for quite big amounts to be synthesized, even though the two steps yielded only 30%.



Scheme 2.69 Synthesis of chelidamic acid from diethyl oxalate and acetone.

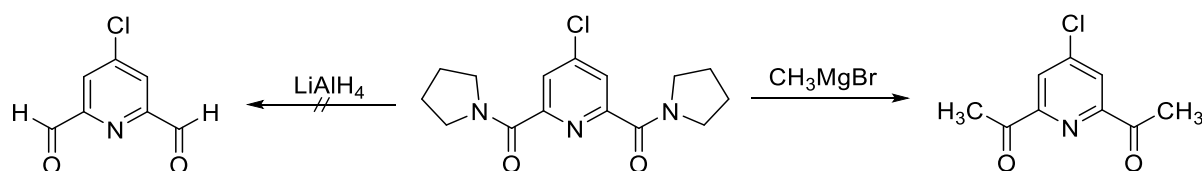
Chelidamic acid was further treated with excess thionyl chloride to convert the hydroxyl groups into chlorides.^{366, 367} After evaporation of thionyl chloride excess as

well as side products, a solution of pyrrolidine in dichloromethane was slowly added to the mixture to convert substitute the acyl chlorides into amides yielding (4-chloropyridine-2,6-diyl)bis(pyrrolidin-1-ylmethanone) in 55% (Scheme 2.72).



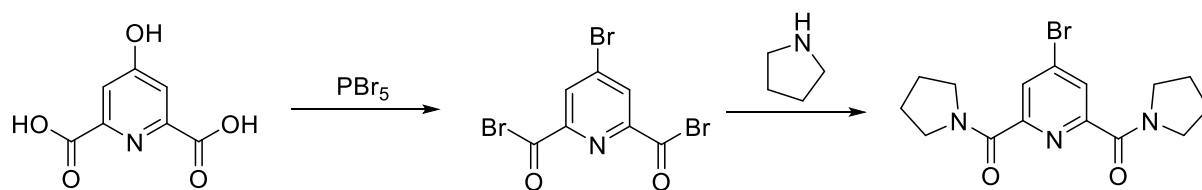
Scheme 2.70 Synthesis of 4-chloro 2,6-dipyrrolidin-1-yl-methanone pyridine.

This diamide can be treated with *Grignard* reagents to synthesize the carbonyl functions. Methyl magnesium bromide leads to 4-chloro 2,6-diacetyl pyridine with a yield of 19%, according to literature known procedure.³⁶⁸ In the same publication, the group of *Ivchenko* also described a reduction with lithium aluminium hydride to the 2,6-diformyl pyridine, yet this reaction failed (Scheme 2.73).



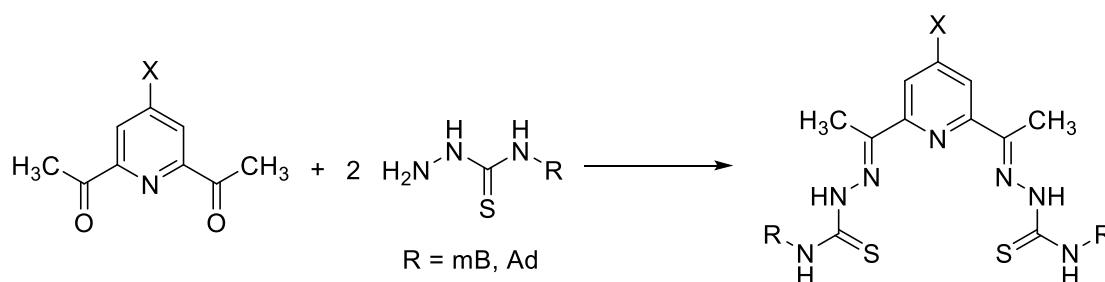
Scheme 2.71 Attempted derivatization with chemical reduction and *Grignard* reagents.

With the diacetyl pyridine as well as the thiosemicarbazone derivative *Suzuki* couplings with but-3-yn-1-ylboronic acid was attempted yet no one was successful, leading to the idea that the chloride might be too inert for the reaction. From chelidamic acid it is also published to convert the structure to the bromide species with PBr_5 and stabilizing the compound with pyrrolidine like before (Scheme 2.74), yet this reaction was not reproduceable.



Scheme 2.72 Attempted synthesis of 4-bromo 2,6-dipyrrolidin-1-yl-methanone pyridine.

Even though the coupling to the alkyne bearing boronic acid failed, pentadentate thiosemicarbazones were synthesized from 2,6-diacetyl pyridine and 4-chloro 2,6-diacetyl pyridine (Scheme 2.75).



Scheme 2.73 Condensation reaction of 2,6-diacetyl pyridines with thiosemicarbazides yielding bithiosemicarbazones.

The synthesized ligands were investigated using NMR and UV/Vis spectroscopy as well as electrochemical analyses were performed.

2.12.2. UV/Vis spectroscopy

The synthesized ligands, H₂dap(b)TSCmB, H₂Cldap(b)TSCmB and H₂Cldap(b)TSCAd were compared with the literature known, N⁴ unsubstituted H₂dap(b)TSC. In their UV/Vis spectra in THF, shown in Figure 2.117, all molecules showed very similar absorption properties.

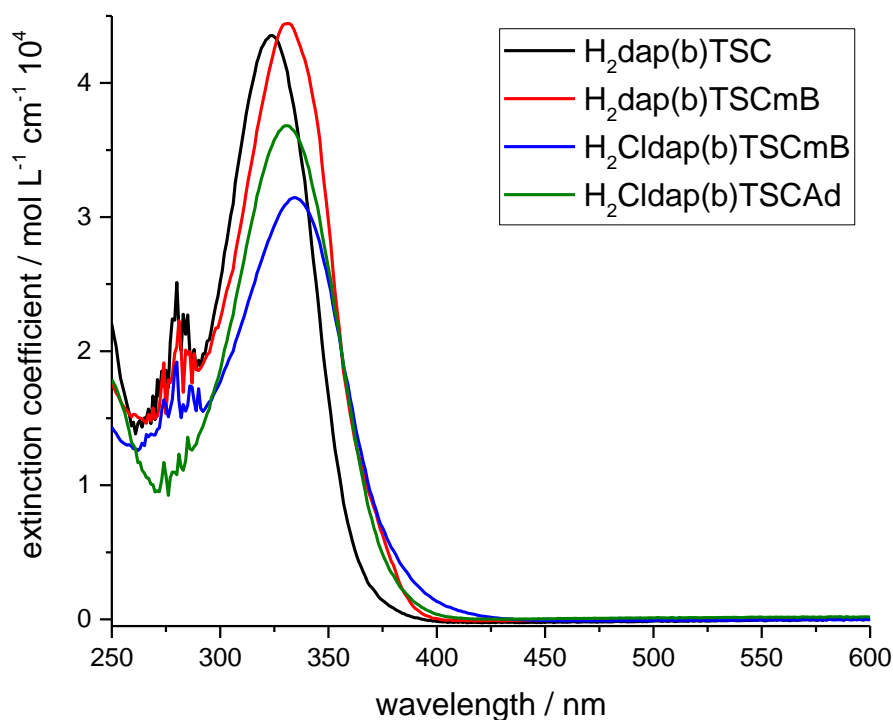


Figure 2.117 UV/Vis spectra of H₂dap(b)TSC, H₂dap(b)TSCmB, H₂Cldap (b)TSCmB and H₂Cldap(b)TSCAd. All spectra were recorded in THF.

All ligands show their expected π - π^* transition at about 330 nm. The shift from the substitutions is extremely small. The literature known H₂dap(b)TSC has a maximum at 324 nm, this shifts yet so slightly to 331 nm for H₂dap(b)TSCmB and 334 nm for H₂Cldap(b)TSC. H₂Cldap(b)TSCAd has its maximum at 330 nm.

2.12.3. Electrochemical analysis

The cyclic voltammograms of the pentadentate ligands showed an interesting property. The CV of H₂dap(b)TSCmB is depicted in Figure 2.118. The square wave measurement resolves the reduction processes a bit better, showing a “doublet” wave for the processes. This may indicate that the pyridine imine structures get reduced separately not simultaneously.

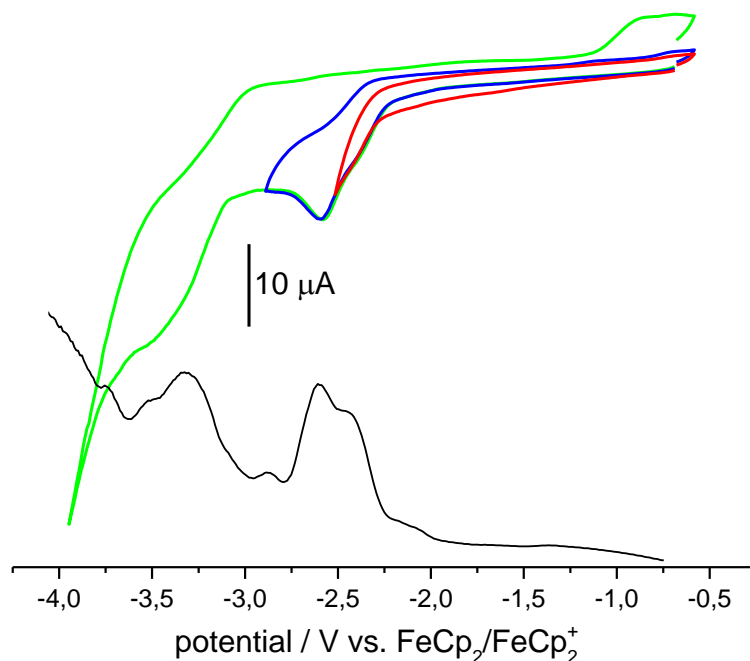


Figure 2.118 Cyclic voltammogram of H₂dap(b)TSCmB in 0.1 M nBu₄PF₆ THF solution with a scan rate of 100 mV/s.

To have a better understanding of this “doublet” wave, spectroelectrochemical UV/Vis spectroscopy was performed (Figure 2.119). As already stated in multiple chapters prior, the first reduction of the ligands results in an EC mechanism shifting the absorption maxima in during the SEC measurement. This also occurs for the first reduction of the ligand.

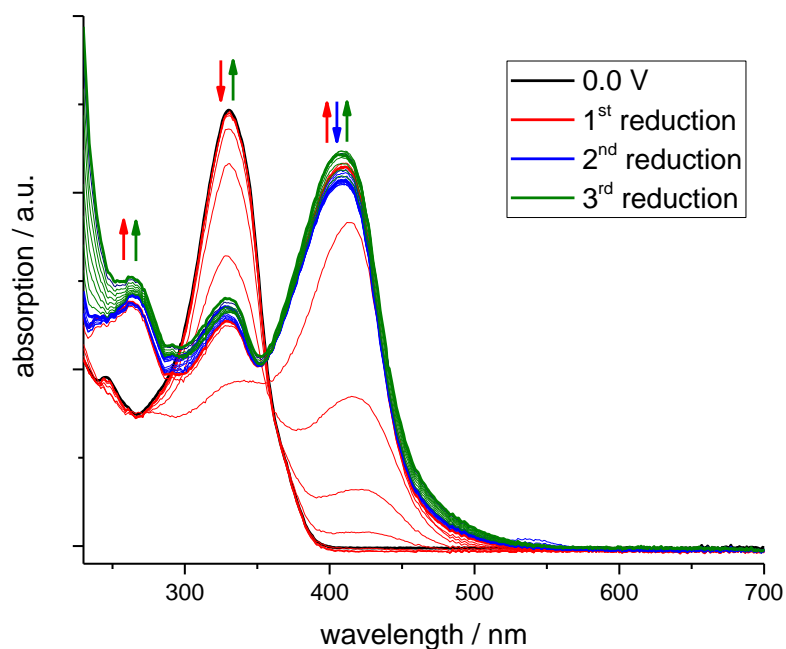


Figure 2.119 SEC-UV/Vis of H₂dap(b)TSCmB in 0.1 M nBu₄PF₆ THF solution during the first reduction with 0.1 V increments.

The difference between the reduction of the thiosemicarbazones is more vivid in H₂Cldap(b)TSCAd. The cyclic voltammogram in Figure 2.120 shows six independent reductions.

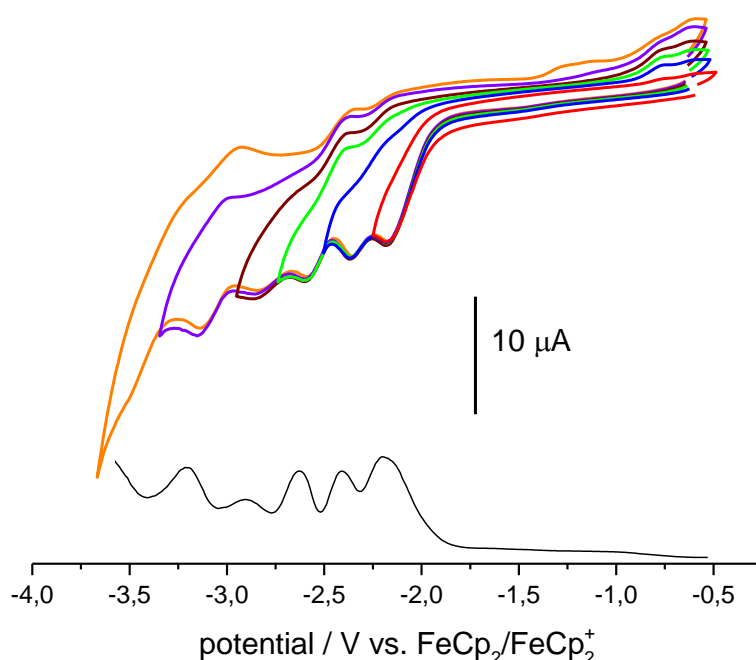


Figure 2.120 Cyclic voltammogram of H₂Cldap(b)TSCAd in 0.1 M nBu₄PF₆ THF solution with a scan rate of 100 mV/s.

The SEC-UV/Vis measurement during the first reduction unveiled a more in depth look at the reduced species (Figure 2.121). Here, the first reduction process is quite like the previously described ones. At lower potentials, another band at 500 nm appears. This band may result from a dianionic ligand with a further extended π -system compared to the mono TSC compounds.

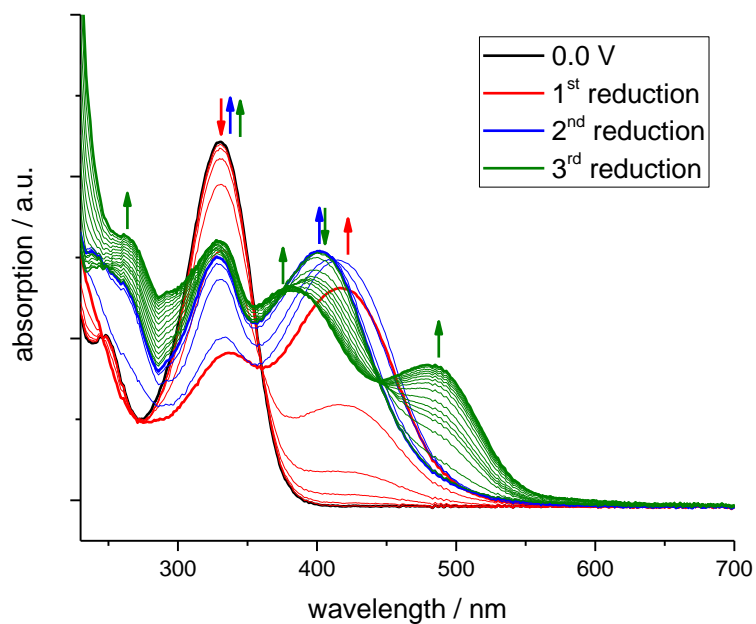


Figure 2.121 SEC-UV/Vis of H₂Cl dap(b)TSCAd in 0.1 M nBu₄PF₆ THF solution during the first reduction with 0.1 V increments.

These results show promising new ligand systems which may become substituted in the *para*-position of the central pyridine ring to allow the functionalization of surfaces or nanoparticles with symmetric pentadentate ligands for a manifold of tasks.

The big obstacle to tackle here, is to find a suitable group for cross coupling in the *para*-position. It may be possible to form the boronic acid of these type of compounds and couple it to the propargyl bromide, but the stability of the pyridine compounds during the reaction process is hard to predict.

3. Conclusion

During this thesis, a total of 48 ligands and 52 complexes were synthesized and analysed. A total of 21 SC-XRD structures could be determined to validate the theoretical structures.

With the synthesis of Ir(III) hydride thiosemicarbazone complexes we were able to analyse the influence of the backbone derivatisations on the electronic properties of the complex. With 8 different hydrides and their ^1H NMR we were able to conclude, that a methylation of the backbone does not affect the hydride shift.

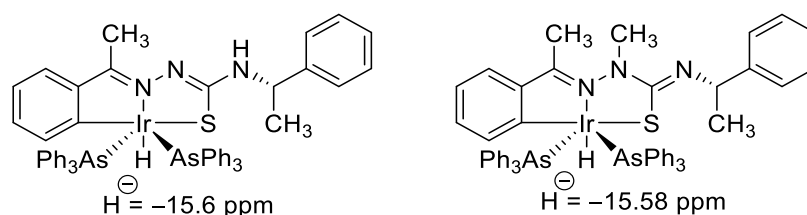


Chart 3.1 The two synthesized hydride complexes $[\text{Ir}(\text{AsPh}_3)_2(\text{aphTSCmB})(\text{H})]$ (left) and $[\text{Ir}(\text{AsPh}_3)_2(\text{aph(m)TSCmB})(\text{H})]$ and their hydride shifts measured in $\text{DMSO-}d_6$ at 300 MHz.

The electronic properties were tested further with the application in catalysis. Here, we were able to synthesize and purify a series of Pd(II) complexes and test for their catalytic properties. We also attempted a biologically active functional group to generate a form of artificial metalloenzyme. Lysine derived structures could be synthesized with various metal ion centres, like Pd(II), to gain access to C-C coupling catalysts. The formation of biotin derived structures was unsuccessful.

Nevertheless, we were able to extend the capabilities of the previously known palladium catalysts by various side chains, leading to catalysts that can be further implemented in peptide structures while keeping their activity. Furthermore, other substitutions lead to increased water solubility and to turn over numbers of 100,000 in aqueous media.

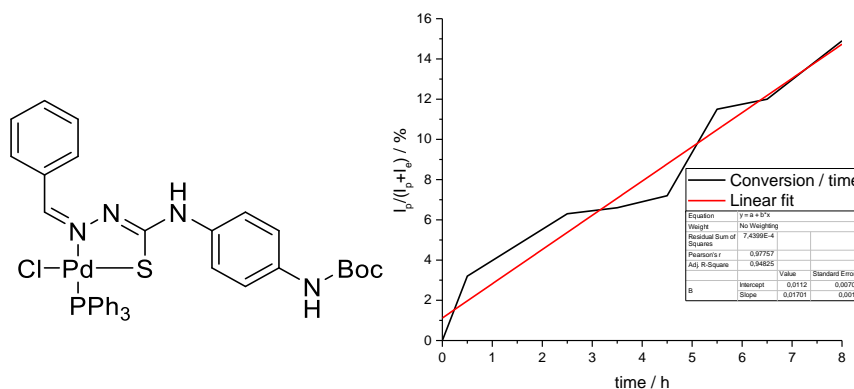


Figure 3.1 Synthesized C-C coupling catalyst $[\text{Pd}(\text{PPh}_3)(\text{bzTSCpba})(\text{Cl})]$ and its activity under *Suzuki-Miyaura* conditions.

In pursuit of new radiopharmaceuticals, we were successful by synthesizing and analysing Pt(II) thiosemicarbazones. We were able to generate promising results for the first *Auger* emitting peptide receptor radionuclide therapy. The synthesis and characterization of the platinum complexes with chlorido and cyanido coligand could be verified by XRD, MS and NMR techniques and their characteristics could be investigated with UV/Vis, cyclic voltammetry, and combined methods alongside extensive calculations.

The synthesis takes 10 steps starting from L-lysine to the final peptide which in case for sC18 derived structures had an overall yield of 10%. Pt(II) could still be coordinated by the N²N¹S binding of the pyridine based thiosemicarbazone. The structure could be investigated by cross referencing it to the model complex [Pt(dpyTSCmB)Cl].

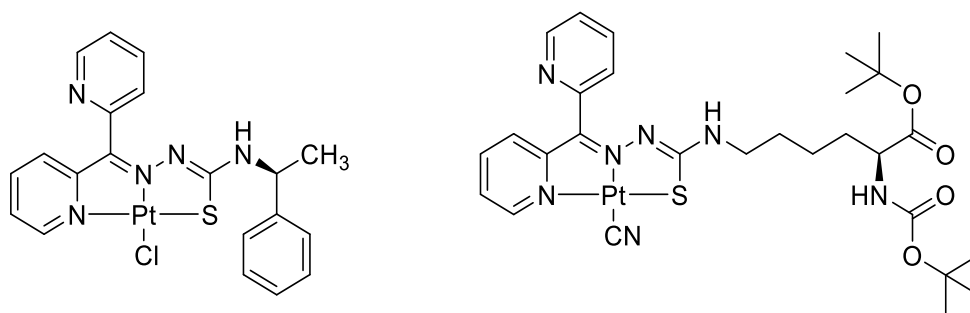


Chart 3.2 Synthesized complexes with [Pt(dpyTSCmB)Cl] and [Pt(dpyTSCLp)CN].

The peptide structures increased the solubility in aqueous medium drastically which allowed for hydrolysis tests. The complexes [Pt(dpyTSCL-sC18)Cl] and [Pt(dpyTSCL-sC18)CN] were quite stable with a degradation of 8% and 15% over 72 h, respectively.

Whilst the ligands HdpyTSCmB and HdpyTSCLp showed remarkable antiproliferative activity towards the human cancer cell lines MCF-7 and as well as the non-cancer cell line HEK-293, peptide structure HdpyTSCL-sC18 showed almost no activity up to 25 μM . In all cases the platinum complexes with chloride as coligand showed lower antiproliferation than their corresponding ligands. The coligand exchange to cyanide even lowers the antiproliferation.

In summary, the complexes are very interesting candidates for late-stage labelling with the radioisotopes ^{189}Pt , ^{191}Pt , $^{193\text{m}}\text{Pt}$, or $^{195\text{m}}\text{Pt}$. The low toxicity, high biostability as well as the ability to be late stage labelled with the radionuclide and being isolated by common HPLC methods could make them promising candidates in nuclear medicine.

Tetradentate thiosemicarbazones of the type 6-(2-hydroxyphenyl)picoline could be synthesized for the first time in this thesis. Their planar dianionic O⁻N⁻N⁻S donor motif showed good chelation of the divalent nickel group elements. The complexes interesting optical properties could be explained by intensive investigation as well as benchmarking DFT calculations.

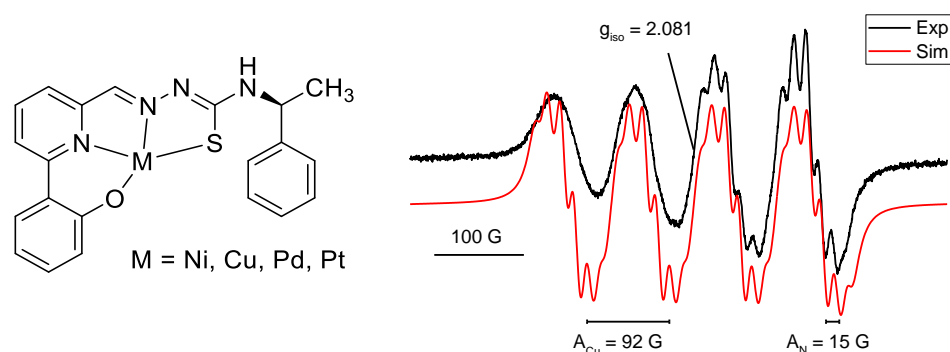


Figure 3.2 Synthesized complexes with hphfpyTSCmB²⁻ as tetradentate ligand and the X-Band EPR of the copper complex in MeCN at room temperature.

The tetradentate binding motif could be synthesized at the protected lysine thiosemicarbazide, yet the deprotection which is necessary to coordinate Pt(II) and enable the coupling to peptides was not possible. On the other hand, during this work further motifs could be attached to the amino acid moiety. One of them was the fluorescent acridine, of which we performed extensive photophysical spectroscopy in correlation with several metal ions.

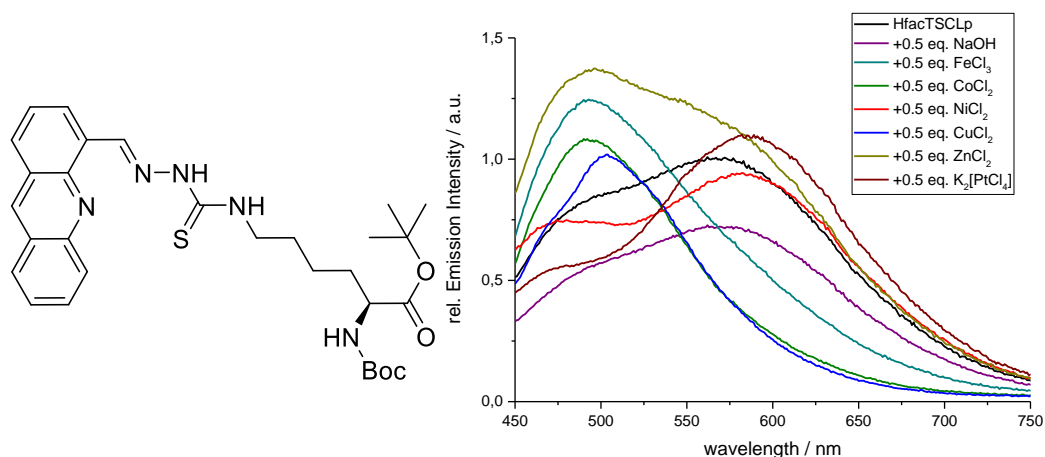


Figure 3.3 Molecular structure of HfacTSCLp and its titration with metal salts in fluorescence spectroscopy.

Cooperation with groups within the institute lead to various new structural motifs. With the group of Prof. *Wickleder*, the first oxygen-free and air stable U(IV) thiosemicarbazones were synthesized. These complexes bear the possibility of being single source precursors for uranium sulphide materials, even though decomposition reactions showed the formation of UO₂.

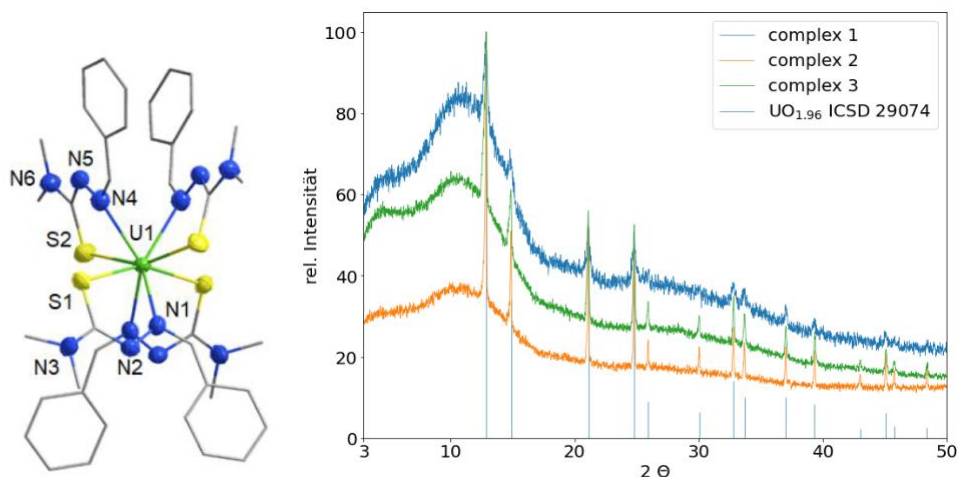


Figure 3.4 XRD crystal structure of $[U(bzTSCdm)_4]$ and the powder diffraction patterns of the thermal decay products.

Working with the group of Prof. *Mathur*, lead to various attempts were made to attach pentadentate TSC to nanoparticles. Whilst the crucial step for the supposed coupling position did not yield the desired product, the electrochemical properties of these bis thiosemicarbazones were investigated in detail.

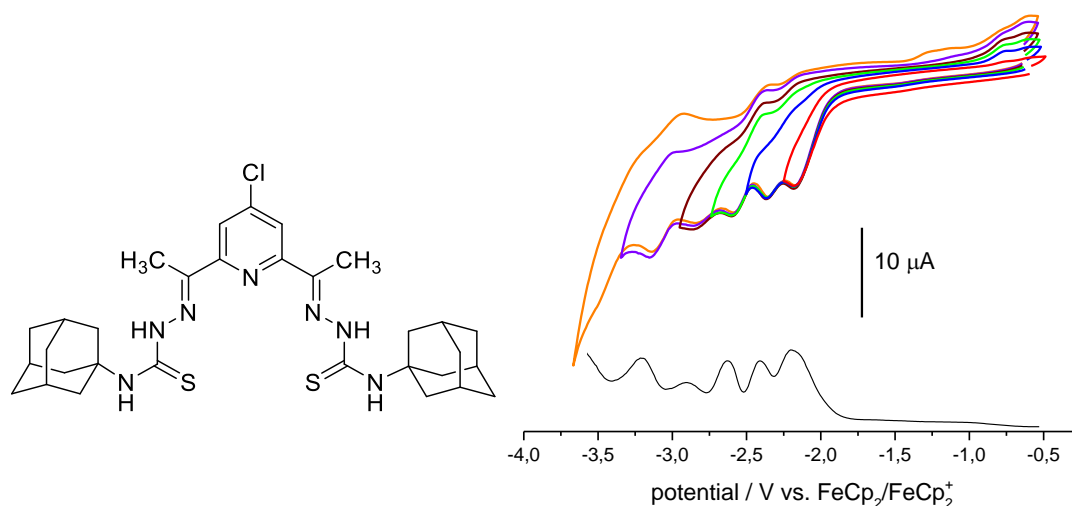


Figure 3.5 Molecular structure of $H_2Cl(dap)(b)TSCAd$ and its cyclic voltammogram in 0.1 M nBu_4NPF_6/THF .

In total the insights gained in this work showed the high potential of *N4* derivatization for thiosemicarbazones in various fields of application. The high substitution capability of the used reaction pathways gave access to tuneable complexes for several applications. The use of new substituted structures and metal ions in the used reactions will advance thiosemicarbazones further into the fields of nuclear medicine and catalysis.

4. Outlook

First and foremost, the synthesis of the peptide derived platinum structures with radioactive nuclides needs to be investigated. The synthesis of radioactive Pt(II) precursors as well as their implementation in the peptide conjugates and purification by HPLC sound easy but may prove to be more challenging than expected. Other radiopharmaceutical isotopes could be introduced as well expanding the use as a multimodal ligand for nuclear medicine.

As stated in the introduction octreotide is a work horse for nuclear medical complexes. By changing the terminal phenylalanine to which the chelator is bound to the lysine derivative, the binding mode of the octreotide should not be changed (Figure 4.1) It should be possible to combine octreotide with the synthesized thiosemicarbazones. These new structures could combine the already well understood effectiveness of octreotide with the possibility for platinum conjugation.

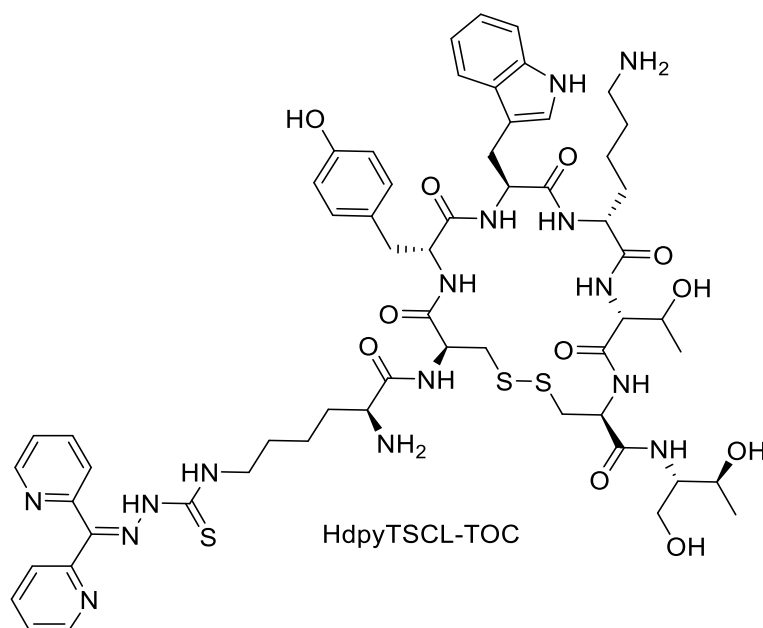


Figure 4.1 Molecular structure of a hypothetical TOC derivative bearing a HdpyTSCL motif as chelator.

Recently a group of bioactive vectors became famous due to their extremely good bioselectivity. Their structure is based of quinolines with a glycine proline structure in position 4. The position 6 of the quinoline is etherified with a propargyl piperazine or piperidine. The most selective structure is FAPI-4, bearing a difluoro cyanopyrrolidine and piperazine bridge (Figure 4.2). Amino acids or the synthesized thiosemicarbazones can be attached to that piperazine using FAPI-4 as a biolinker for further investigations. A thiosemicarbazone with a terminal chloropropargyl piperazine would be favourable for the synthesis of such structures.

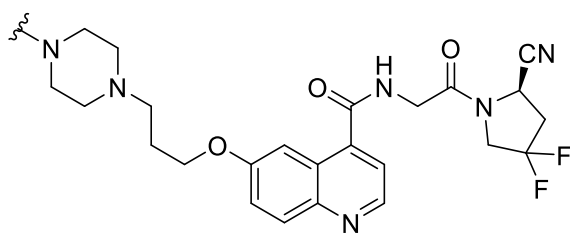


Figure 4.2 Molecular structure of the bioactive vector FAPI-4.

Looking at the tetradentate system as well as the fluorescence system, combination of both may be fused by benzo[h]quinolines, like 10-hydroxybenzo[h]quinoline-2-carbaldehyde (Figure 4.3). This structure contains the previously described 6-(2-hydroxyphenyl) picolinaldehyde motive with an ethene bridge. This bridge extends the π system of the backbone to a possible fluorescent emitter. The carbonyl bridge should condense with thiosemicarbazides as previously mentioned.

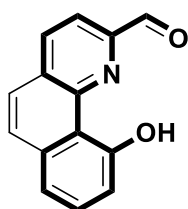
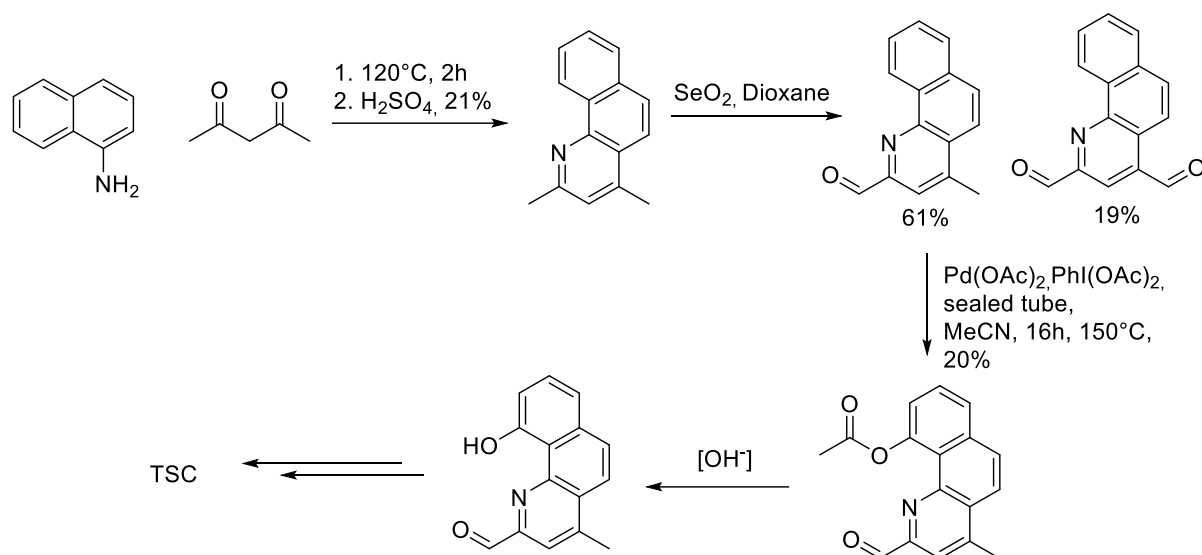


Figure 4.3 Molecular structure of 10-hydroxybenzo[h]quinoline-2-carbaldehyde as carbonyl motif for tetradentate fluorescent thiosemicarbazones.

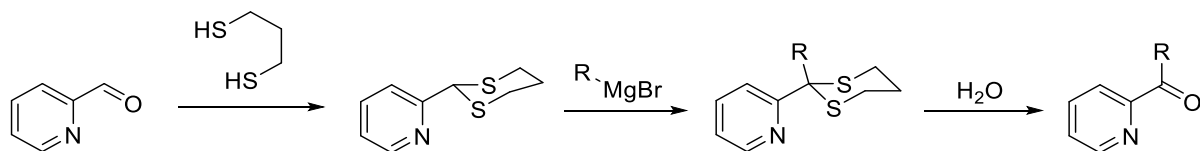
The resulting complexes should be very stable and exhibit a cation specific fluorescence shift. They should also be traceable with fluorescence microscopy methods in small agglomerates. This could help to investigate the binding mode of peptide structures and simultaneously check for the complex stability at different regions of the cell.

A possible synthetic route was published in 2011 by *Gryko* (Scheme 4.1).³⁶⁹ The route is not efficient but produces the acetyl protected derivative of the desired carbaldehyde. This compound could be deprotected and should easily undergo condensation to the corresponding thiosemicarbazone.



Scheme 4.1 Proposed synthesis route for 10-hydroxybenzo[h]quinoline-2-carbaldehyde.

With the synthesized 6-(2-hydroxyphenyl)picoline aldehyde and the prior proposed hydroxybenzoquinoline carbaldehyde two promising structures can be further derivatized using *Corey-Seebach* type chemistry (Scheme 4.2). Herein, the carbaldehyde is converted into a dithiane using dithiols which allows *Grignard* reagents to selectively react with the former carbaldehyde carbon and after aqueous work up a variety of ketones are accessible.



Scheme 4.2 Corey-Seebach reaction scheme with picolinaldehyde as example.

The influence of simple substituents at the coordinating arene is also an achievable task to generate a better understanding of electrochemical properties. As done in this work the influence of the substitution at position 6 of a pyridine showed to have a big influence on the molecular structure.

The tetradentate binding motif employed for the hphfpyTSCmB series can also be changed to different donor atoms Chart 4.1. These donor systems may have the advantage, that they do not need to be protected in the first place. This would be beneficial for the synthesis of the deprotected lysine species. Additionally, they are redox and acid-base active groups that would allow for different metal centres beyond the oxidation state of +2.

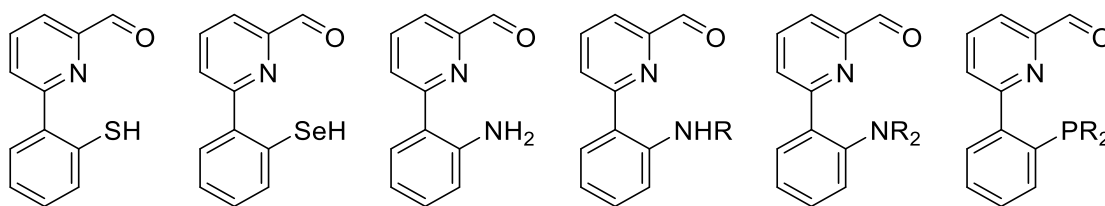
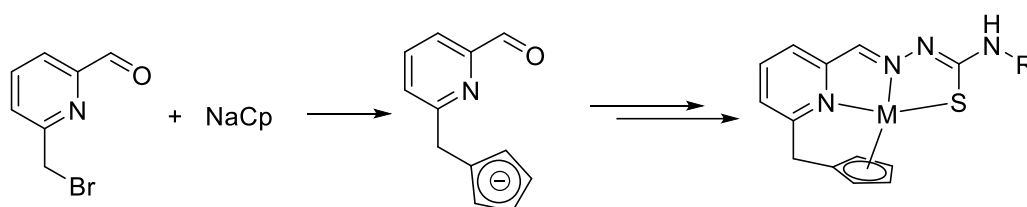


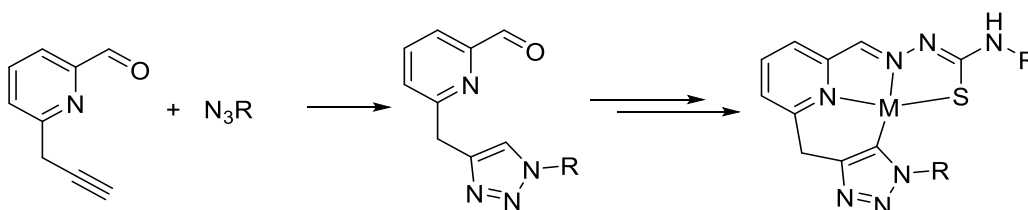
Chart 2.1 Molecular structure of 6-derivatized formyl pyridines with different donor systems.

A methylene bridged cyclopentadienide would be able to function as a half sandwich donor forming a Cp⁻N⁻N⁻S system. This would be able to coordinate bigger cations like f-elements or heavy ions, expressing spherical coordination sphere like Gd(III), Hg(II), Bi(III) or Pb(IV). The introduction of the Cp to the ligand system by salt metathesis and possible complex structure is shown in Scheme 4.3.



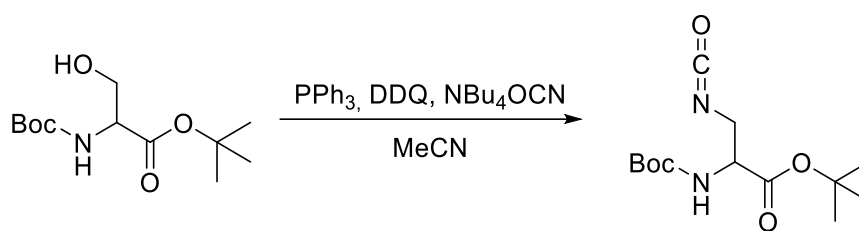
Scheme 4.3 Suggested synthesis of a cyclopentadienide donor containing complex.

Similarly, mesoionic carbenes can be introduced to thiosemicarbazones. An alkyne derivatized pyridine structure can be reacted with azides to generate triazines. These triazines are capable of forming carbenes as shown in Scheme 4.4.



Scheme 4.4 Suggested synthesis of a mesoionic carbene donor containing complex.

Further diversification of the bioconjugation could be achieved by altering the thiosemicarbazone to a semicarbazone or selenosemicarbazone. As mentioned previously, both are accessible through reaction of phosgene or selenophosgene with amines and whilst it is feasible for the selenoderivative, working with phosgene is quite dangerous and triphosgene produces a lot of side products which may react with an isocyanate. In 2005 Akhlaghinia published a method to gain access to isocyanates under very mild conditions starting from alcohols (Scheme 4.5).³⁷⁰ This could be very interesting since it may be transferable to serine and thus form interesting isocyanates of amino acids.



Scheme 4.5 Proposed synthetic route for the synthesis of isocyanates as precursors for amino acid containing semicarbazones.

Very recently the group of *Goicoechea* synthesized phosphinecarboxamides which are a heavier analogue of semicarbazones.³⁷¹ Despite their inherent instability, the group was able to isolate the deprotonated species, which leads to a negatively charged phosphorous atom. In combination with the work of their group in which they synthesized isoelectrical carbondisulfide structures, a new series of semicarbazone analogues may be just around the corner (Chart 4.2).³⁷²

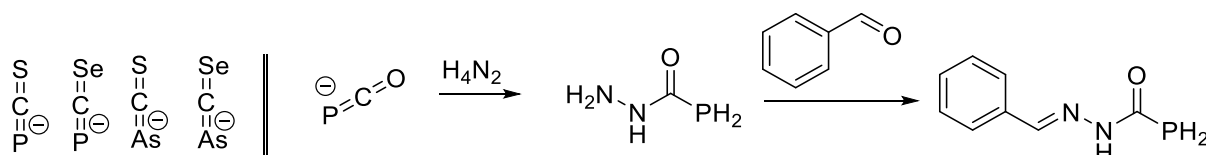


Chart 4.2 Molecular structures of phosphinecarboxamide and heavier analogues of thio and seleno cyanates by the group of *Goicoechea*.

5. Experimental Part

5.1. Materials

Chemicals and glassware

All chemicals were provided by commercial suppliers (*Sigma Aldrich, Merck, ABCR, Acros Organics, Carbolution, Alfa Aesar, TCI* etc.) and used without further purification steps or were synthesized within the research group in advance. Solvents which were not bought with a septum or molecular sieves were absolute from HPLC quality on a MBRAUN MB SPS-800 solvent purification system. THF was afterwards further dried over sodium/potassium alloy (30/70) and freshly distilled at the day of use. All other mentioned solvents were used directly as provided by the supplier in a pure form. Synthesized compounds were stored in a freezer at $-26\text{ }^{\circ}\text{C}$.

Syringes, NMR tubes and equipment for working under argon atmosphere or dry conditions were stored in a drying oven at $60\text{ }^{\circ}\text{C}$. Glassware were baked out in vacuum with a heat gun.

Schlenk-technique

For experiments under inert conditions (air and moisture sensitive reactions) *BIP* argon from *Linde* with a purity of 5.7 (99.998%) was employed.

Distillation via rotary evaporator

Solvents were removed under reduced pressure employing a *Büchi* rotary evaporator. Bath temperature was set between $30\text{ }^{\circ}\text{C}$ and $60\text{ }^{\circ}\text{C}$ depending on the compound's heat stability.

Flash column chromatography

Flash column chromatography was performed using silica gel 60 from *Merck* (0.035- 0.065 mm, CAS: 7631-86-9).

Thin layer chromatography

TLC analyses were done on *Merck* 60/UV₂₅₄ silica aluminium sheets. Visualization was accomplished by UV light, $\lambda = 254\text{ nm}$, and by staining with an aqueous KMnO_4 solution. The solvent fractions are given in volume parts.

5.2. Equipment and analytical methods

Electron paramagnetic resonance spectroscopy (EPR)

All EPR were performed on a X-band Bruker system ELEXSYS 500E with a Bruker Variable Temperature Unit ER 4131VT (500 to 100 K) and an ER4122SHQE wave guide cavity. *g*-factors were referenced against 2,2-diphenyl-1-picrylhydrazyl (dpph) and determined with the MatLab expansion EasySpin. The spectra were simulated with Bruker Simphonia/Bruker SOPHE or Xsophe.

NMR spectroscopy

All NMR spectra were taken at the Bruker Avance II 300. ¹H-NMR spectra were measured at a frequency of 300 MHz, ¹³C-NMR spectra at a frequency of 75 MHz. The assignment was carried out using 1D NMR (¹H, ¹³C) and 2D NMR spectroscopy (¹H,¹H COSY, ¹H,¹³C HSQC, ¹H,¹³C and ¹H,¹⁹⁵Pt HMBC). The chemical shift δ was indicated in ppm and the coupling constant *J* in Hz. All measurements were carried out at 298 K.

The multiplicity was assigned with singlet (s), doublet (d), triplet (t), quartet (q), quintet (quin), multiplet (m) and pseudo (ps). Deuterated chloroform, $\omega(\text{CDCl}_3) = 99.8\%$, $\omega(\text{TMS}) = 0.03\%$, deuterated dimethyl sulfoxide, $\omega(\text{DMSO-}d_6) = 99.8\%$, $\omega(\text{TMS}) = 0.03\%$ and deuterated water $\omega(\text{D}_2\text{O}) = 99.9\%$ were used as solvents. The calibration was done based on the TMS signal or the solvent signal. For ¹H-NMR spectra the chemical shift is 7.26 ppm for CDCl₃, 2.50 ppm for DMSO-*d*₆ and 4.79 ppm for D₂O. For ¹³C-NMR spectra the chemical shift is 77.16 ppm for CDCl₃ and 39.52 ppm for DMSO-*d*₆. The analysis was done using MestReNova 11.0.

Fourier-transform infrared spectroscopy (FTIR)

All FTIR spectra were measured at a Perkin Elmer FTIR-ATR or a Perkin Elmer Spektrum Two spectrometer at ambient temperature. Absorption bands were given in cm⁻¹ and assigned with broad (br), weak (w), medium (m) and strong (s).

Ultraviolet-visible spectroscopy (UV/vis)

UV/vis spectra were recorded on a Varian 50 Scan UV-visible photometer using quartz glass cuvettes with a length of 1 cm. The spectra were baseline corrected.

Spectroelectrochemical measurements

All UV/vis spectroelectrochemical experiments were performed in an OTTLE-cell (optical thin layer electrochemical) at a Varian 50 Scan UV-visible photometer in 0.1 V

intervals.³⁷³ EPR spectroelectrochemical experiments were performed with a two electrode setup.³⁷⁴ *Origin 2017* was used as a data program for the evaluation.

Fluorescence and excitation spectroscopy

All fluorescence spectra were recorded at room temperature on a FluoroMax-3.

Ultraviolet photoelectron spectroscopy (UPS)

For ultraviolet photoelectron spectroscopy (UPS) measurements thin films were prepared on ITO-coated glass substrates (15 Ω /sq sheet resistance), which were sequentially cleaned with chloroform, acetone, a 2% Mucasol soap solution and deionized water before use. Thin films were prepared out of DCM solution via electrospinning at a rate of 4000 rpm for 35 s, to yield layers with thicknesses of about 10 nm. Solid state UV-Vis was recorded using a Cary 50 Bio spectrometer from Varian. Photoelectron spectroscopy measurements were performed in an ultra-high vacuum chamber using a Phoibos 100 hemispherical analyser by Specs. For ultraviolet photoelectron spectroscopy (UPS) a monochromatic helium discharge lamp (He I at 21.22 eV) with a probing depth of around 2 nm at a pass energy of 2 eV and a resolution of 110 meV was used.

Single crystal X-ray diffraction (SC-XRD)

Single crystal XRD were measured at 170(2) K or 293(2) K on an IPDS IIT, at 293(2) K on an IPDS II or IPDS IIT (STOE und Cie.) diffractometers with Mo-K α radiation ($\lambda = 0.71073$ Å) and usage of a ω - ϕ -2 θ scan technique. Cu-K α ($\lambda = 0.40784$ Å) radiation was used on a *Bruker* D8 venture at 100 K or 293 K. Some crystals were measured at the P24 beamline of the PETRA III synchrotron at the DESY facility in Hamburg. Using a *Huber* 4 circle kappa diffractometer and a gas jet cryostat the single crystals were measured at 100 K. The structures were refined by direct methods using SIR92³⁷⁵ or SIR2014³⁷⁶ or charge flip using OLEX2.0.³⁷⁷ The structure refinement were performed with SHELXL 2016³⁷⁸ using the full-matrix least-squares technique against $F_0^2 \geq 2\sigma(F_0^2)$. The numerical absorption correction (X-RED V1.22; Stoe & Cie, 2011) was performed after the optimization of the crystal structure (X-SHAPE V1.06; Stoe & Cie, 1999). Non-hydrogen atoms were, if not otherwise stated, without limitations anisotropically refined. Hydrogen atoms were added by suitable fixation models. The data of the structural solutions and refinements are available at <https://summary.ccdc.cam.ac.uk/structures> of the Cambridge Crystallographic Data Centre (CCDC). The graphical representations of the crystal and molecular structures were created using DIAMOND v4.2.

Hirshfeld surfaces with d_{norm} weighing and fingerprint plots were generated with CrystalExplorer 17.³⁷⁹

Cyclic voltammetry (CV)

Cyclic voltammetry was performed in a baked-out three-necked flask with three electrodes installed: a glazed carbon electrode, a platinum counter electrode and an Ag/AgCl pseudo reference electrode. The measurements were carried out in a 0.1 M $n\text{Bu}_4\text{NPF}_6$ solution in THF and a rate of 100 mV/s if not stated otherwise. Regulation was done via an *Autolab PG STAT* or an *Metrohm Dropsens $\mu\text{Stat}400$* potentiostat. All data collection was referenced employing ferrocene/ferrocenium as redox pair. *Origin 2017* was used as a data program for the evaluation.

Electron ionization mass spectrometry (EI-MS)

EI-MS spectra were recorded on a *Finnigan MAT 95* spectrometer with a positive ionization energy of 20 eV or 70 eV. The Spectra were simulated using ISOPRO 3.0. All measurements were performed by operator *Astrid Baum*.

High resolution mass spectrometry (HR-ESI-MS)

HR-ESI-MS(+) spectra were measured at the *THERMO Scientific LTQ Orbitrap XL* mass spectrometer via electron spray ionization and a FTMS Analyzer. All measurements were performed by operator *Michael Neihls*.

Quantum chemical calculations

Quantum chemical calculations were performed on the basis of the density functional theory (DFT) using „Resolution of Identity“ (RI) Coulomb approximations^{380, 381} with the program package TURBOMOLE³⁸² and the graphical user interface TMoleX.³⁸³ Molecular structures were first optimized using small basis sets and afterwards using bigger basis sets further optimized. Geometry optimization was verified using a vibration calculation with the same functional and basis sets by testing for imaginary vibration modes and verification of a local minimum. Prior to time dependent DFT (TD-DFT) calculations the molecules were geometrically optimized using „Conductor-like Screening Models“(COSMO)^{384, 385} with the dielectricity constant of the corresponding solvent.³⁸⁶ During calculations double- ξ -valence basis set def-SV(P)³⁸⁷ and triple- ξ -valence def2-TZVP³⁸⁸ were used for H, C, N, O, S and Cl. For nickel the extended basis set aug-cc-pVQZ³⁸⁹, for palladium and platinum LanL2DZ with effective core

potentials ecp Hay/Wadt (N-1) and ecp Hay/Wadt 60 respectively were used.³⁹⁰⁻³⁹² For geometry optimization and structural verification Becke's exchange energy corrected functional BP86³⁹³ was mainly used whereas for TD-DFT calculations the hybrid functional B3LYP³⁹⁴⁻³⁹⁶ was used predominantly.

Peptide conjugates

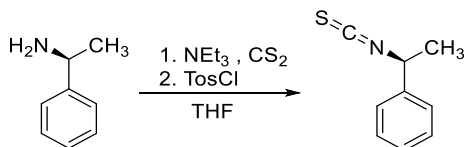
The cell-penetrating peptide was synthesised in the research group of *Prof. Ines Neundorf* by automated solid phase peptide synthesis on a Syro I peptide synthesiser (MultiSynTech). HPLC chromatograms were recorded on an Agilent 1260 HPLC system (column: Nucleodur C18ec; 100-5; Macherey-Nagel; gradient: 10-60% MeCN in water (incl. 0.1 % formic acid) over 15 min; 0.6 mL/min flow rate). ESI-MS(+) spectra were recorded on an LTQ-XL mass spectrometer via electron spray ionisation (Thermo Scientific). Data was evaluated with Xcalibur™ Software (Thermo Scientific).³⁹⁷

Antiproliferative activities

Antiproliferative activity was determined in the group of *Prof. Ines Neundorf* by photo spectrometric measurements. The conversion of resazurin ($\lambda_{\text{ex}} = 550 \text{ nm}$) into the resorufin product ($\lambda_{\text{ex}} = 595 \text{ nm}$) was measured on a Tecan infinite M200 plate reader (Tecan Group AG). Data were normalised to untreated control cells were (100% viability).³⁹⁸

5.3. Synthesis of thiosemicarbazides

5.3.1. Synthesis of ITCmB



Under argon atmosphere, 10.1 mL (78.4 mmol, 1.0 eq.) of (*S*)-(-)- α -methylbenzylamine were dissolved in 60 mL THF and 35.9 mL (259 mmol, 3.3 eq.) of triethylamine were added. The solution was cooled down to 0 °C and 4.7 mL of CS₂ (78 mmol, 1.0 eq.) were slowly added. The reaction mixture was stirred for 1 hour and then 16.5 g (86.2 mmol, 1.1 eq.) of 4-toluenesulfonyl chloride were added. After another 1.5 h of stirring, the liquid as poured into 60 mL of 1N hydrochloric acid. The aqueous phase was extracted with MTBE three times and the combined organic phases were dried over MgSO₄. The crude product was filtered through a silica plug with *n*-hexane, yielding 13.4 g (82.0 mmol, >99%) of product as an orange oil.

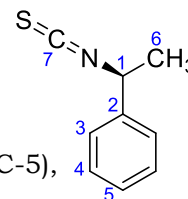
ITCmB: C₉H₉NS (163.24 g/mol).

Yield: 13.4 g (82.0 mmol, >99%).

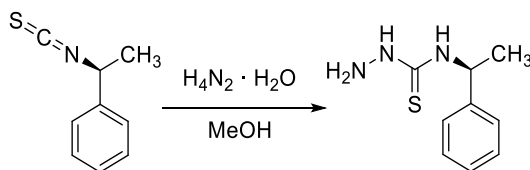
Habitus: Orange oil.

¹H NMR: (DMSO-d₆, 300 MHz) δ [ppm] = 7.32 – 7.45 (m, 5H, H-3 – H-5), 5.22 (q, 1H, *J* = 6.7 Hz, H-6), 1.60 (d, 3H, *J* = 6.8 Hz, H-6).

¹³C NMR: (DMSO-d₆, 75 MHz) δ [ppm] = 140.2 (s, C-2), 128.8 (d), 128.1 (d, C-5), 125.6 (d), 56.4 (d, C-1), 24.2 (q, C-6).



5.3.2. Synthesis of N4-1-phenylethyl thiosemicarbazide



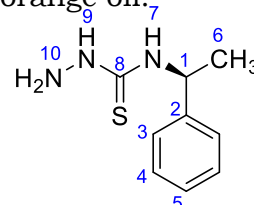
4.0 mL (82 mmol, 1.0 eq.) of hydrazine monohydrate were dissolved in 75 mL of MeOH and the solution was heated to 70 °C. Then, 13.4 g (82.0 mmol, 1.0 eq.) of the isothiocyanate were slowly added and the reaction mixture was stirred for 1.5 hours. The solvent was removed under reduced pressure and the crude product was poured into boiling petrol ether. The formed oil phase separated from the ether phase. 15.8 g (80.9 mmol, 99%) of the thiosemicarbazide were obtained as an orange oil.

TSCmB: C₉H₁₃N₃S (195.29 g/mol).

Yield: 15.8 g (80.9 mmol, 99%).

Habitus: Orange oil.

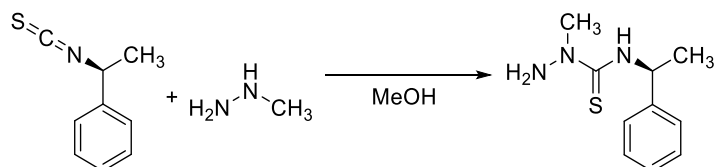
¹H NMR: (DMSO-d₆, 300 MHz) δ [ppm] = 8.72 (br s, 1H, MH-9),



8.02 (d, 1H, $J = 8.9$ Hz, NH-7), 7.14 – 7.41 (m, 5H, H-3 – H-5),
 5.57 (qui, $J = 6.9$ Hz, 1H, H-1), 4.54 (br s, 2H, NH-10), 1.45 (d, 3H, $J = 7.0$
 Hz, H-6).

^{13}C NMR: (DMSO- d_6 , 75 MHz) δ [ppm] = 180.6 (s, C-8), 144.3 (s, C-2), 128.2 (t), 126.7
 (t, C-5), 126.2 (t), 51.8 (d, C-1), 22.1 (q, C-6).

5.3.3. Synthesis of N2-methyl N4-phenylethyl thiosemicarbazide



1.23 mL (30.6 mmol, 1.0 eq.) of methylhydrazine were dissolved in 75 mL of MeOH and the solution was heated to 70 °C. Then, 5 g (30.6 mmol, 1.0 eq.) of the isothiocyanate were slowly added and the reaction mixture was stirred for 2 hours. The solvent was removed under reduced pressure and the crude product was poured into boiling petrol ether. The formed oil phase was separated from the ether phase. 5.16 g of the thiosemicarbazide were obtained as an orange oil.

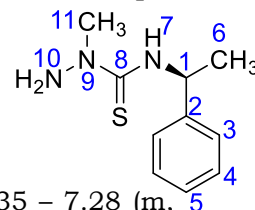
(m)TSCmB: $\text{C}_{10}\text{H}_{15}\text{N}_3\text{S}$ (209.31 g/mol).

Yield: 5.16 g (24.6 mmol, 80%).

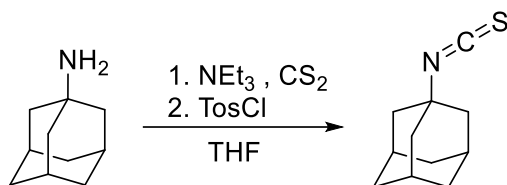
Habitus: Orange oil.

^1H NMR: (DMSO- d_6 , 300 MHz) δ [ppm] = 8.34 (d, $J = 8.9$ Hz, 1H), 7.35 – 7.28 (m, 4H), 7.25 – 7.16 (m, 1H), 5.44 (p, $J = 7.8$ Hz, 1H), 4.93 (s, 2H), 3.44 (s, 3H), 1.44 (d, $J = 7.0$ Hz, 3H).

^{13}C NMR (DMSO- d_6 , 75 MHz) δ [ppm] = 179.99 (C-8), 144.43 (C-2), 128.19 (C-4), 126.61 (C-5), 126.15 (C-3), 53.06 (C-1), 42.42 (C-11), 22.18 (C-6).



5.3.4. Synthesis of 1-isothiocyanatoadamantane



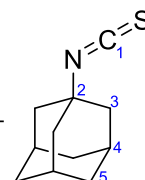
8.5 g of 1-aminoadamantane (56.2 mmol, 1 eq.) were dispersed in 60 mL THF, 23.4 mL NEt_3 and 3.4 mL (56.2 mmol, 1 eq.) CS_2 were added to the mixture. The reaction mixture was stirred for 2 h before 11.9 g (61.8 mmol, 1.1 eq.) tosyl chloride were added and the solution was diluted with 20 mL of 1 N HCl. The aqueous phase was washed with MTBE and the solvent was removed under reduced pressure. The solid was recrystallized from EtOH yielding 850 mg of a colourless crystalline solid.

ITCAAd: $\text{C}_{11}\text{H}_{15}\text{NS}$ (193.09 g/mol).

Yield: 2.70 g (14.0 mmol, 25%).

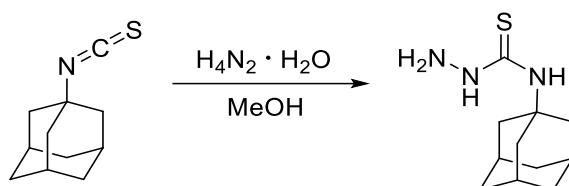
Habitus: Colourless crystals.

^1H NMR: (300 MHz, DMSO- d_6): δ (ppm) = 2.06 (s, 3H, H-4), 1.96 (d, 6H, H-3), 1.61 (s, 6H, H-5).



¹³C NMR (75 MHz, DMSO-d₆): δ (ppm) = 58.7 (C-2), 43.0 (C-3), 34.8 (C-5), 28.7(C-4).

5.3.5.Synthesis of *N*4-adamantyl thiosemicarbazide



2.7 mg (14 mmol, 1 eq.) isothiocyanate were dissolved in 25 mL MeOH and heated to 70 °C before 0.7 mL (14 mmol, 1 eq.) hydrazine hydrate was added. The mixture was heated for 20 minutes. After cooling to ambient temperature, the resulting solid was filtered and washed with cold MeOH yielding 1.3 g of a colourless crystalline solid.

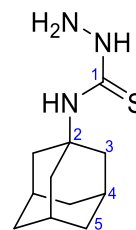
TSCAd: C₁₁H₁₉N₃S (225.13 g/mol).

Yield: 1.3 g (5.8 mmol, 41%).

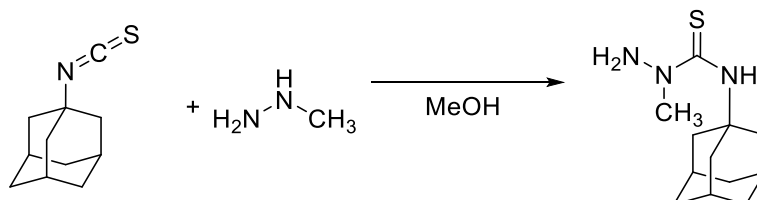
Habitus: Colourless crystalline solid.

¹H NMR: (300 MHz, DMSO-d₆): δ (ppm) = 8.36 (s, 1H, NH), 7.41 (s, 1H, NH), 4.50 (s, 2H, NH₂), 2.18 (d, 6H, H-3), 2.04 (s, 3H, H-4), 1.63 (t, 6H, H-5).

¹³C NMR: (75 MHz, DMSO-d₆): δ (ppm) = 51.9 (C-1), 48.6 (C-2), 41.4 (C-3), 36.0 (C-5), 29.0 (C-4).



5.3.6.Synthesis of *N*2-methyl *N*4-adamantyl thiosemicarbazide



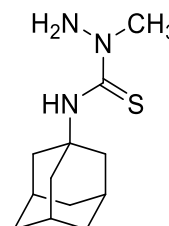
200 mg (1.1 mmol, 1 eq.) isothiocyanate were dissolved in 25 mL MeOH and heated to 70 °C before 0.05 mL (1.1 mmol, 1 eq.) methylhydrazine was added. The mixture was heated for 20 minutes. After cooling to ambient temperature, the resulting solid was filtered and washed with cold MeOH yielding 203 mg of a colourless crystalline solid.

(m)TSCAd: C₁₂H₂₁N₃S (239.15 g/mol).

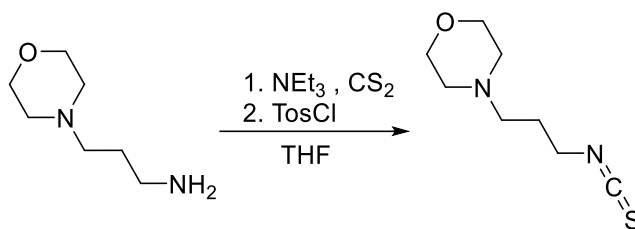
Yield: 203 mg (0.85 mmol, 77%).

Habitus: Colourless crystalline solid.

¹H NMR: (DMSO-d₆, 300 MHz) δ [ppm] = 8.01 (s, 1H), 4.87 (s, 2H), 3.40 (s, 3H), 2.17 (d, *J* = 2.9 Hz, 6H), 2.03 (s, 1H), 1.62 (t, *J* = 3.1 Hz, 6H).



5.3.7. Synthesis of 3-morpholinopropane-1-isothiocyanate



10.1 ml (69.3 mmol, 1.00 eq.) 3-morpholinopropan-1-amine and 28.8 ml (208 mmol, 3.00 eq.) NEt_3 were dissolved in 74 ml anhydrous THF. At 0 °C 4.2 ml (69.3 mmol, 1.00 eq.) carbon disulphide were added dropwise. After stirring the reaction mixture for 1 h, 14.5 g (76.2 mmol, 1.1 eq.) tosyl chloride were added and the reaction mixture was stirred for an additional 30 minutes. The reaction mixture was quenched with 200 ml of 1 N HCl and the phases were separated. The aqueous phase was basified with NaOH to a pH of 10 and extracted three times with MTBE. After drying the organic phases over Na_2SO_4 , filtration and removal of the solvent under reduced pressure 11.3 g of a brown oil was obtained.

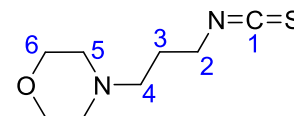
ITCpmo: $\text{C}_8\text{H}_{14}\text{N}_2\text{OS}$ (186.27 g/mol).

Yield: 11.3 g (60.7 mmol, 88%).

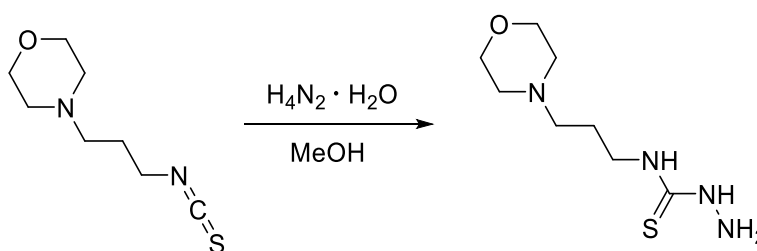
Habitus: Brown oil.

$^1\text{H NMR}$: (DMSO- d_6 , 300 MHz) δ [ppm] = 3.98 (d, 2H, H-2), 3.83 (t, 2H, H-6), 3.69 (t, 2H, H-4), 3.45 (d, 2H, H-5), 2.06 (quin, 2H, H-3).

$^{13}\text{C NMR}$: (DMSO- d_6 , 75 MHz) δ (ppm) = 63.3 (C-6), 53.3 (C-5), 51.2 (C-4), 45.7 (C-2), 42.3 (C-3).



5.3.8. Synthesis of N4-propylmorpholino thiosemicarbazide

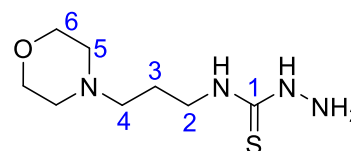


3.13 ml (60.7 mmol, 1.00 eq.) hydrazine were dissolved in 55 ml MeOH and heated to 70 °C. 11.3 g (60.7 mmol, 1.00 eq.) isothiocyanate were added dropwise and the reaction mixture was stirred for 2 hours. The solvent was removed under reduced pressure and the obtained orange oil was poured into boiling petrol ether. The formed precipitate was filtered off and afforded 11.7 g of a yellow solid.

TSCpmo: $\text{C}_8\text{H}_{18}\text{N}_4\text{OS}$ (218.32 g/mol).

Yield: 11.7 g (53.8 mmol, 89%).

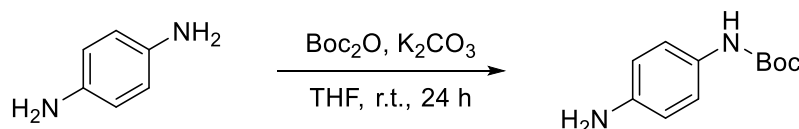
Habitus: yellow oil.



¹H NMR: (DMSO-d₆, 300 MHz) δ [ppm] = 8.54 (s, 1H, NH), 8.10 (s, 1H, NH), 4.43 (s, 2H, NH₂), 3.58 (t, 4H, H-6), 3.48 (q, 2H, H-2), 3.34-2.28 (m, 6H, H-4/5), 1.65 (quin, 2H, H-3).

¹³C NMR: (DMSO-d₆, 75 MHz) δ (ppm) = 66.1 (C-6), 56.5(C-5), 53.4(C-4), 42.1(C-2), 25.5(C-3).

5.3.9. Synthesis of tert-butyl (4-aminophenyl)carbamate



A *Schlenk*-flask was charged with potassium carbonate (3.05 g, 22 mmol, 1.10 eq.), *p*-phenylenediamine (6.50 g, 60.2 mmol, 3.01 eq.) in THF (60.0 ml) under inert conditions. Boc₂O (4.40 g, 20 mmol, 1.00 eq.) were added over a time span of 20 minutes and the mixture was stirred for 24 h. The mixture was diluted with water (140 ml) and extracted with DCM (100 ml) and the organic phase was washed with water (2x 50 ml) and dried over Na₂SO₄. The crude product (brown solid) was concentrated under reduced pressure and purified *via* column chromatography (c-hex/EtOAc, 2:1). The desired product was obtained as a pure slightly yellow solid in yield of 81%.

4-aminophenyl C₁₁H₁₆N₂O₂ (208.1 g/mol).

carbamate:

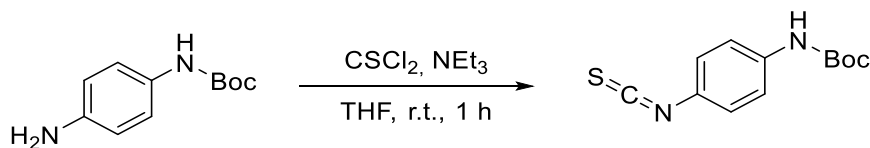
Yield: 3.37 g (16.2 mmol, 81%).

Habitus: Slight yellow powder.

¹H NMR: (DMSO-d₆, 300 MHz) δ [ppm] = 8.76 (s, 1H), 7.06 (d, J = 8.2 Hz, 2H), 6.46 (d, J = 8.8 Hz, 2H), 4.72 (s, 2H), 1.44 (s, 9H).

¹³C NMR: (DMSO-d₆, 75 MHz) δ [ppm] = 114.2, 28.4.

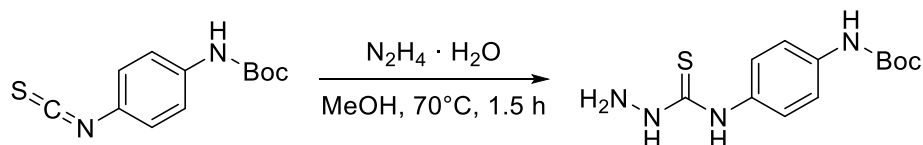
5.3.10. Synthesis of tert-butyl (4-isothiocyanatophenyl)carbamate



In a *Schlenk*-flask the mono protected *p*-phenylenediamine (2.00 g, 9.60 mmol, 1.00 eq.) and triethylamine (2.90 g, 28.8 mmol, 4.00 ml, 3.00 eq.) were dissolved in THF (120 ml) under inert conditions. Thiophosgene (85%, 1.20 g, 10.6 mmol, 0.800 ml, 1.10 eq.) was added at 0 °C. After 1 h stirring at room temperature the mixture was quenched with water (100 ml) and extracted with ether (3x 80.0 ml). The organic phase was dried over Na₂SO₄, and the solvent was removed under reduced pressure. The desired product was obtained as a pure brown solid in a yield of 95%.

4-Boc-aminophenyl ITC: C₁₂H₁₄N₂O₂S (250.1 g/mol).
Yield: 2.28 g (9.12 mmol, 95%).
Habitus: Brown solid.
¹H NMR: (CDCl₃, 300 MHz) δ [ppm] = 7.37 (d, *J* = 8.8 Hz, 2H), 7.14 (d, *J* = 6.8 Hz, 2H), 6.77 (s, 1H), 1.51 (s, 9H).
¹³C NMR: (CDCl₃, 75 MHz) δ (ppm) = 126.2, 119.2, 28.3.
¹⁵N NMR: (CDCl₃, 30 MHz) δ (ppm) = 205.5.

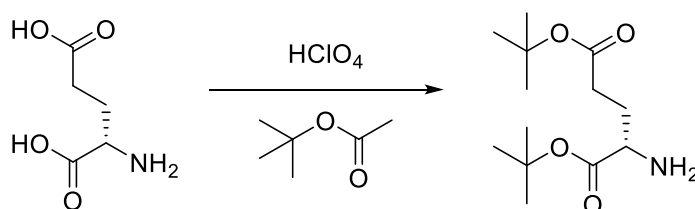
5.3.11. tert-butyl (4-(thiosemicarbazide)phenyl)carbamate



A Schlenk-flask was charged with hydrazine hydrate (420 mg, 12.9 mmol, 0.420 ml, 1.60 eq.) in MeOH (27.0 ml) under inert conditions and was heated up to 70 °C. 2.00 g (8.00 mmol, 1.00 eq.) of the isothiocyanate was added slowly to the MeOH solution and stirred for 1.5 h. The MeOH was removed under reduced pressure and the residue was taken up with chloroform. The mixture was transferred into boiling petrol ether and the solid was filtered and washed with cold petrol ether. The product could be observed as a bright brown solid in a yield of 84%.

TSCpBa: C₁₂H₁₈N₄O₂S (282.1 g/mol).
Yield: 1.89 g (6.69 mmol, 84%).
Habitus: Brown solid.
¹H NMR: (DMSO-*d*₆, 300 MHz) δ [ppm] = 9.52 (s, 1H), 9.27 (s, 1H), 9.00 (s, 1H), 7.40 (dd, *J* = 25.9 Hz, *J* = 8.7 Hz, 4H), 4.74 (s, 2H), 1.48 (s, 9H).
¹³C NMR: (DMSO-*d*₆, 75 MHz) δ (ppm) = 153.1, 124.7, 118.2, 78.9, 28.7.

5.3.12. Synthesis of di-tert-butyl L-glutamate

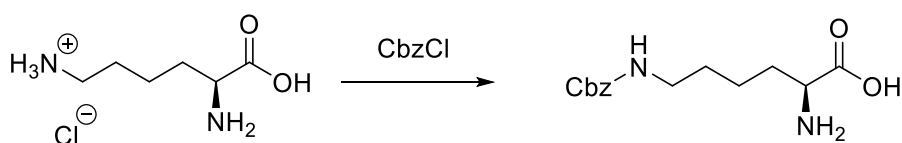


2.16 g (14.7 mmol, 1 eq.) L-glutamic acid were dispersed in 140 mL tert-butyl acetate before 2 mL (18.4 mmol, 1.25 eq.) 60% perchloric acid was added. The reaction mixture was stirred at ambient temperature for 16 h. During the first hour the dispersion cleared up. After 16 h 100 mL 0.5 N HCl was added to the solution and the aqueous phase was separated, neutralized with NaHCO₃, and extracted with

diethyl ether. The combined organic phases were dried over MgSO_4 , and the solvent was removed under reduced pressure yielding a slightly yellow oil.

Glu(tBu)-OtBu: $\text{C}_{13}\text{H}_{25}\text{NO}_4$ (259.35 g/mol).
Yield: 1.5 g (5.8 mmol, 39%).
Habitus: Slight yellow oil.
 $^1\text{H NMR}$: (CDCl_3 , 300 MHz) δ [ppm] = 3.49 (dd, $J = 7.8, 5.4$ Hz, 1H), 3.40 (s, 3H), 2.38 (t, $J = 7.5$ Hz, 2H), 2.05 – 1.97 (m, 1H), 1.92 – 1.79 (m, 1H), 1.48 (s, 9H), 1.45 (s, 8H).
 $^{13}\text{C NMR}$: (CDCl_3 , 75 MHz) δ (ppm) = 173.68, 172.61, 81.95, 80.75, 54.03, 31.80, 29.33, 28.15, 28.09.

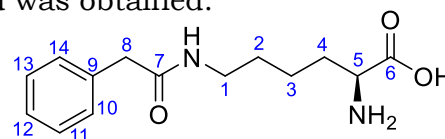
5.3.13. Synthesis of H-Lys(Cbz)-OH



18.25 g (99.92 mmol, 1 eq.) of *L*-lysine hydrochloride were dissolved in 80 mL H_2O to obtain a pale-yellow solution and 8 g (200 mmol, 2 eq.) NaOH were added. Separately 12.48 g (50 mmol, 0.5 eq.) of $\text{CuSO}_4 \cdot 5 \text{H}_2\text{O}$ were dissolved in 40 mL H_2O and added to the Lysine solution. The mixture was cooled in an ice bath and 9.98 g (119 mmol, 1.19 eq.) NaHCO_3 were added. Afterwards 19 mL (22.8 g, 134 mmol, 1.34 eq.) CbzCl was added dropwise over 10 minutes. The reaction was stirred overnight, and the pale-blue voluminous precipitate was collected. The crude product was washed with 200 mL of water and 100 mL of acetone.

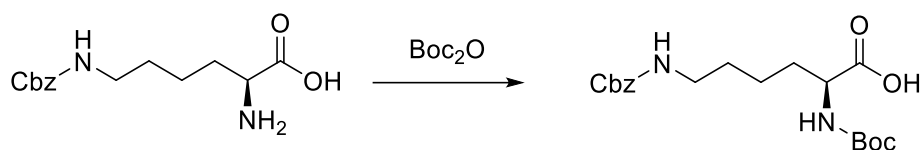
In a 1000 mL three necked flask equipped with a reflux condenser 41.8 g (110 mmol, 1.1 eq.) EDTA sodium salt was dissolved in 400 mL water. The pH was adjusted to 7 using concentrated hydrochloric acid. The mixture was heated to reflux, and the Lysine copper complex was added portion wise. During the addition, the pH was maintained at 7 using hydrochloric acid. After the addition was completed, the mixture was heated to reflux for another 30 minutes before the solution was cooled to room temperature and the precipitate was filtered and washed three times with 100 mL water and two times with 100 mL MeOH. The crude product was recrystallized from EtOH. 29.56 g of a slight blue solid was obtained.

H-Lys(Cbz)-OH: $\text{C}_{20}\text{H}_{19}\text{N}_5\text{S}$ (280.32 g/mol).
Yield: 29.56 g (99.9 mmol, 99%).
 $^1\text{H NMR}$: ($\text{DMSO}-d_6$, 300 MHz) δ [ppm] = 7.43 – 7.27 (m, 4 H, 10-H, 14-H, 11-H, 13-H), 7.23 (t, $J_{\text{H,H}} = 5.5$ Hz, 1 H, 12-H), 5.00 (s, 2 H, 8-H), 3.16 – 3.10 (m, 1 H,



5-H), 2.97 (q, $^3J_{H,H} = 6.5$ Hz, 2 H, 1-H), 1.77 – 1.45 (m, 2 H, 4-H), 1.41 – 1.19 (m, 4 H, 2-H, 3-H).

5.3.14. Synthesis of Boc-Lys(Cbz)-OH



In a 500 mL round-bottomed flask 15 g (53.21 mmol, 1 eq.) *N*⁶-Cbz lysine was treated with a solution of 5.67 g (53.5 mmol, 1 eq.) Na₂CO₃ in 100 mL water 75 mL *tert*-butanol. To the slurry 11.67 g (53.5 mmol, 1 eq.) Boc₂O dissolved in 25 mL *tert*-butanol was added over 10 minutes. The slurry was heated to reflux for 4 hours upon which it cleared up. The mixture was allowed to cool to room temperature and stirred overnight.

The pale-blue suspension was diluted with 450 mL water and extracted with 200 mL *n*-pentane and the organic phase was discarded. The aqueous phase was cooled to 0 °C and carefully acidified with 120 mL of 1.2 M hydrochloric acid. The aqueous phase was extracted with 3 times 250 mL EtOAc, and the combined organic phase was washed with 10% Na₂SO₄ solution and dried over Na₂SO₄. The solvent was removed under reduced pressure yielding 13.85 g of a colourless oil.

Boc-Lys(Cbz)-OH:

C₁₉H₂₈N₂O₆ (380.44 g/mol).

Yield:

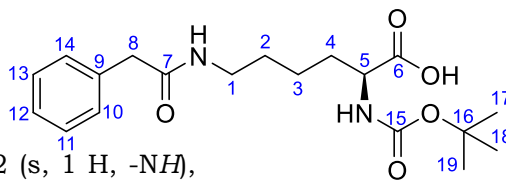
13.85 g (36.4 mmol, 68%).

¹H NMR:

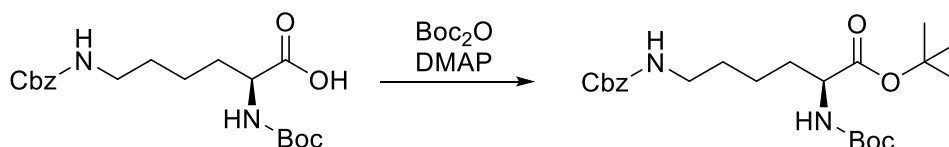
(CDCl₃, 300 MHz) δ [ppm] = 8.62 (s, 1 H, -NH), 7.32 (s, 5 H, 10-H, 11-H, 12-H, 13-H, 14-H), 5.32 (t, $^3J = 8.7$ Hz, 1 H, -NH), 5.07 (s, 2 H, 8-H), 4.27 (d, $^3J_{H,H} = 6.5$ Hz, 1 H, 5H), 3.16 (d, $^3J_{H,H} = 6.5$ Hz, 2 H, 1-H), 1.87 – 1.56 (m, 2 H, 4-H), 1.59 – 1.38 (m, 4 H, 2-H, 3-H), 1.42 (s, 9 H, 17-H, 18-H, 19-H).

¹³C NMR:

(CDCl₃, 75 MHz) δ [ppm] = 176.2 (C-6), 156.8 (C-7), 155.9 (C-15), 136.6 (C-9), 128.6 (C-11, C-12, C-13), 128.2 (C-14, C-10), 80.1 (C-16), 66.8 (C-8), 53.2 (C-5), 40.7 (C-1), 32.1 (C-4), 29.4 (C-2), 28.4 (C-17, C-18, C-19), 22.4 (C-3).



5.3.15. Synthesis of Boc-Lys(Cbz)-OtBu



In a 1000 mL round-bottomed flask 15.2 g (39.95 mmol, 1 eq.) of *N*²-Boc *N*⁶-Cbz lysine was dissolved in 80 mL *tert*-butanol and 488 mg (3.99 mmol, 0.1 eq.) DMAP were added. To the colourless solution 11.34 g (51.94 mmol, 1.3 eq.) Boc₂O were added dropwise over 10 minutes. The mixture was stirred at room temperature for

24 hours before it was stored at 6 °C over night. The solvent was removed under reduced pressure yielding a yellow oil. The residue was dissolved in 300 mL diethyl ether and washed with 160 mL 0.5 M HCl, 160 mL 5% NaHCO₃ and 100 mL 10% Na₂SO₄ solution. The organic phase was dried over Na₂SO₄, and the solvent was removed under reduced pressure yielding a yellow oil. The crude product was purified by flash column chromatography using a *c*-Hex/EtOAc (v/v≈1:1) mixture. The solvent was removed under reduced pressure yielding 14.05 g of a pale-yellow oil.

Boc-Lys(Cbz)-OtBu: C₁₉H₂₈N₂O₆ (380.44 g/mol).

Yield: 14.05 g (32.1 mmol, 80%).

R_f: (*c*-Hex/EtOAc; v/v≈6:4): 0.61.

FTIR-ATR:

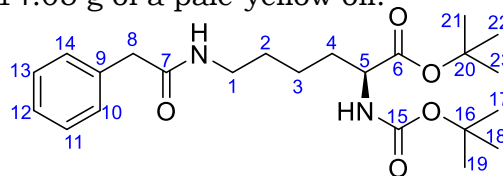
ν [cm⁻¹] = 3855 (w), 3675 (m), 2987 (s), 2901 (s), 2359 (w), 2173 (w), 2116 (w), 1716 (m), 1653 (w), 1507 (w), 1454 (w), 1406 (m), 1394 (m), 1381 (m), 1152 (m), 1075 (s), 1066 (s), 1056 (s), 1028 (m), 892 (w), 880 (w), 776 (w), 737 (w), 697 (w), 618 (w), 611 (w), 599 (w).

¹H NMR:

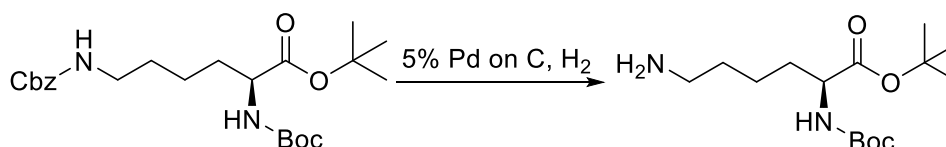
(300 MHz, CDCl₃) δ [ppm] = 7.38 – 7.27 (m, 2 H, 10-H, 11-H, 12-H, 13-H, 14-H), 5.07 (s, 3 H, 5-H, 8-H), 4.93 (s, 1 H, -NH), 3.16 (q, ³J_{H,H} = 6.5 Hz, 2 H, 1-H), 1.85 – 1.67 (m, 1 H, 4 H), 1.66 – 1.47 (m, 5 H, 2-H, 3-H, 4-H), 1.44 (s, 9 H, 21-H, 22-H, 23-H), 1.42 (s, 9 H, 17-H, 18-H, 19-H).

¹³C NMR:

(75 MHz, CDCl₃) δ [ppm] = 156.5 (C-7), 155.5 (C-15), 136.7 (C-6), 128.6 (C-11, C-13), 128.2 (C-12), 128.1 (C-10, C-14), 81.9 (C-16), 79.7 (C-20), 66.6 (C-8), 53.8 (C-5), 40.8 (C-1), 32.7 (C-4), 29.5 (C-2), 28.4 (C-17, C-18, C-19), 28.1 (C-21, C-22, C-23), 22.4 (C-3).



5.3.16. Synthesis of Boc-Lys-OtBu



In a dry 250 mL round-bottom Schlenck flask 13.97 g (32 mmol, 1 eq.) of the protected Lysine were dissolved in 100 mL MeOH and 1.221 g Pd on charcoal (5% Pd-basis) was suspended in the solution. The argon atmosphere was removed under reduced pressure and replaced by a H₂ atmosphere. The mixture was stirred at room temperature for 19 hours. The suspension was filtered over celite and washed three times with 50 mL MeOH. The solvent was removed under reduced pressure yielding 9.26 g of a pale-yellow oil.

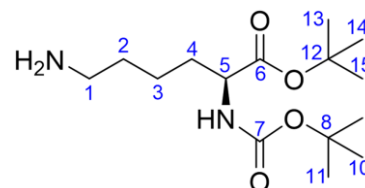
Boc-Lys-OtBu: C₁₅H₃₀N₂O₄ (302.42 g/mol).

Yield: 9.26 g (30.6 mmol, 96%).

R_f: (*c*-Hex/EtOAc; v/v≈6:4): 0.69 (UV-inactive).

FTIR-ATR:

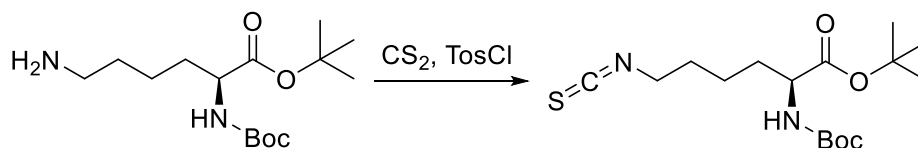
ν [cm⁻¹] = 3675 (m), 2987 (s), 2901 (s), 1713 (m), 1454 (w), 1394 (m), 1369(m), 1249 (m), 1155 (m), 1099 (w), 1065 (s), 1054 (s), 1021 (m), 910 (w), 879 (w), 818 (w), 799 (w), 756 (w), 737 (w), 722 (w), 690 (w), 661 (m), 652 (m), 639 (m), 630 (m), 615 (m), 606 (m), 611 (m), 590 (w), 579 (m), 566 (w), 555 (w), 544 (w), 527 (w).



¹H NMR: (CDCl₃, 300 MHz) δ [ppm] = 5.10 (d, ²J_{H,H} = 8.4 Hz, 2 H, -NH₂), 4.09 (q, ³J_{H,H} = 7.0 Hz, 2 H, 5-H), 2.62 (t, ³J_{H,H} = 6.7 Hz, 2 H, 1 H), 1.79 – 1.63 (m, 1 H, 4-H), 1.61 – 1.45 (m, 5 H, 2-H, 3-H, 4-H'), 1.39 (s, 9 H, 13-H, 14-H, 15), 1.37 (s, 9 H, 9-H, 10-H, 11-H).

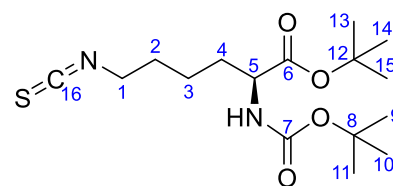
¹³C NMR: (75 MHz, CDCl₃) δ [ppm] = 172.0 (C-6), 155.4 (C-7), 81.7 (C-8), 79.5 (C-12), 53.9 (C-5), 41.9 (C-1), 33.3 (C-4), 32.7 (C-3), 28.4 (C-9, C-10, C-11), 28.0 (C-13, C-14, C-15), 22.5 (C-2).

5.3.17. Synthesis of *tert*-butyl *N*²-(*tert*-butoxycarbonyl)-*N*⁶-thioxomethylidene-*L*-lysinate (ITCLp)



5 g (16.5 mmol, 1 eq.) of the partially unprotected lysine is dissolved under inert conditions in 25 mL dry THF and 7 mL triethylamine. The mixture was cooled to 0 °C and 1 mL (1.26 g, 16.5 mmol, 1 eq.) carbon disulphide was added dropwise over 30 minutes. The reaction mixture was allowed to warm to room temperature and stirred overnight. The mixture was cooled to 0 °C and 3.49 g (18.2 mmol, 1.1 eq.) TosCl was added. To the resulting suspension MTBE was added and the organic phase was separated, and aqueous phase was extracted with two times 50 mL MTBE. The collected organic phases were dried over Na₂SO₄, and the solvent was removed under reduced pressure yielding a yellow oil.

The crude product was purified by flash chromatography (*c*-Hex/EtOAc; v/v≈18:1). The corresponding fractions were collected, and the solvent was removed under reduced pressure yielding a pale-yellow oil.



ITCLp: C₁₅H₃₀N₂O₄ (302.42 g/mol).

Yield: 4.482 g (13 mmol, 79%).

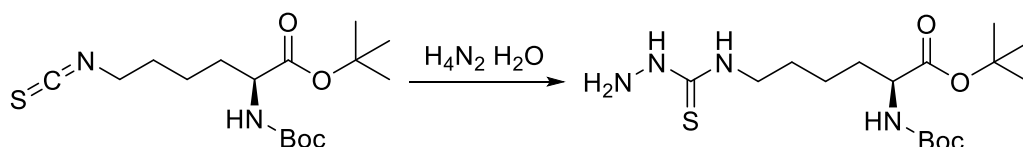
R_f: (*c*-Hex/EtOAc; v/v≈18:1): 0.23.

FTIR-ATR: ν [cm⁻¹] = 3675 (m), 2987 (s), 2901 (s), 2102 (br), 1711 (m), 1506 (m), 1453 (m), 1405 (m), 1394 (s), 1381 (m), 1366 (m), 1250 (m), 1230 (m), 1152 (m), 1069 (s), 1028 (s), 893 (w), 800 (w), 780 (w), 712 (w), 696 (w), 682 (w), 669 (w), 649 (w), 634 (w), 627 (w), 608 (s), 590 (w), 579 (w), 539 (w), 518 (w).

¹H NMR: (CDCl₃, 300 MHz) δ [ppm] = 5.06 (d, ²J_{NH,NH'} = 8.1 Hz, 2 H, -NH₂), 4.16 (q, ³J_{5H,4H} = 7.0 Hz, 2 H, 5-H), 3.50 (t, ³J_{1H,2H} = 6.5 Hz, 2 H, 1 H), 1.86 – 1.53 (m, 6 H, 2-H, 3-H, 4-H), 1.45 (s, 9 H, 13-H, 14-H, 15-H), 1.43 (s, 9 H, 9-H, 10-H, 11-H).

¹³C NMR: (CDCl₃, 75 MHz) δ [ppm] = 171.7 (C-6), 155.4 (C-7), 100.1 (C-16), 82.2 (C-8), 79.8 (C-12), 53.6 (C-5), 44.9 (C-1), 32.4 (C-4), 29.6 (C-3), 28.4 (C-9, C-10, C-11), 28.0 (C-13, C-14, C-15), 22.4 (C-2).

5.3.18. Synthesis of *tert*-butyl *N*²-(*tert*-butoxycarbonyl)-*N*⁶-(hydrazinecarbonothioyl)-*L*-lysinate (TSCLp)



0.63 g (12.6 mmol, 1 eq.) hydrazine hydrate was diluted with 20 mL MeOH and heated to reflux. At that temperature 4.338 g (12.6 mmol, 1 eq.) of the isothiocyanate dissolved in 9 mL MeOH were added dropwise over 20 minutes. The reaction mixture was stirred at 75 °C for 2 hours. The solvent was removed under reduced pressure yielding 4.713 g of a sticky yellow oil.

TSCLp:

(C₁₆H₃₂N₄O₄S) = 376.52 g/mol

Yield:

4.713 g (12.6 mmol, 99%).

R_f:

(*c*-Hex/EtOAc; v/v≈6:4): 0.69 (UV-inactive).

FTIR-ATR:

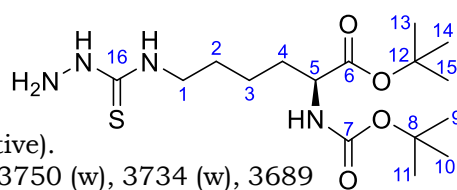
v [cm⁻¹] = 3903 (w), 3853 (w), 3839 (w), 3750 (w), 3734 (w), 3689 (m), 3675 (m), 3566 (w), 3335 (br), 2972 (s), 2900 (s), 2361 (w), 2174 (w), 2116 (w), 1706 (m), 1653 (w), 1635 (w), 1540 (m), 1507 (m), 1456 (m), 1394 (m), 1367 (m), 1250 (m), 1152 (s), 1068 (s), 1028 (m), 950 (w), 892 (w), 864 (w), 848 (w), 774 (w), 737 (w), 629 (w), 621 (w), 614 (w), 602 (w), 582 (w), 570 (w), 558 (w), 539 (w).

¹H NMR:

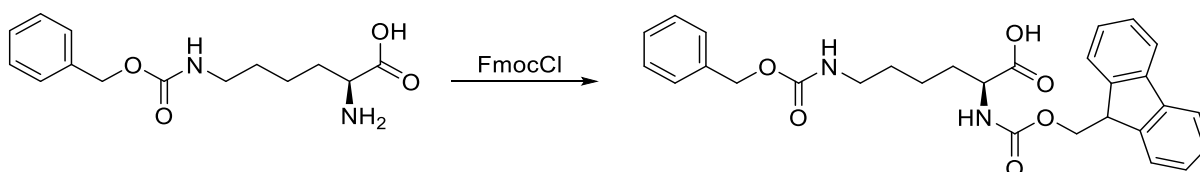
(CDCl₃, 300 MHz) δ [ppm] = 7.76 (s, 1 H, -NH), 7.43 (s, 1 H, -NH), 5.06 (d, ³J_{SCNH,-NH} = 8.3 Hz, 1 H, -SCNH), 4.13 (q, ³J_{5H,4H} = 7.3 Hz, 1 H, 5-H), 3.78 (brs, 1H, -NH), 3.60 (q, ³J_{1H,2H} = 7.1 Hz, 2H), 1.84 – 1.52 (m, 6 H, 2-H, 3-H, 4-H), 1.44 (s, 9 H, 13-H, 14-H, 15-H), 1.42 (s, 9 H, 9-H, 10-H, 11-H).

¹³C NMR:

(CDCl₃, 75 MHz) δ [ppm] = 182.2 (C-16), 172.0 (C-6), 155.5 (C-7), 82.0 (C-8), 79.7 (C-12), 53.9 (C-5), 43.8 (C-1), 32.8 (C-4), 29.1 (C-3), 28.4 (C-9, C-10, C-11), 28.1 (C-13, C-14, C-15), 22.7 (C-2).



5.3.19. Synthesis of Fmoc-Lys(Cbz)-OH

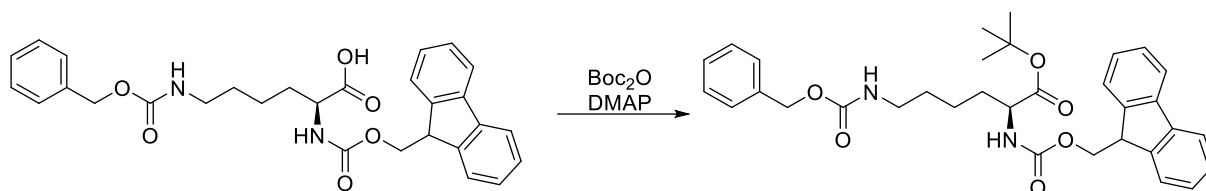


2.25 g (8.01 mmol, 1 eq.) Lys(Z)-OH and 2,5 g (30 mmol, 3.75 eq.) NaHCO₃ were dissolved in 750 mL H₂O/THF mixture (v:v = 1:1) and cooled in an ice bath. 2.3 g (8.81 mmol, 1.1 eq.) FmocCl were dissolved in dry THF and slowly added to the lysine solution. The mixture was stirred for 4h during which the temperature was allowed to reach ambient temperature. THF was removed under reduced pressure and the solution was acidified with HCl to a pH of 3. The mixture was extracted with ethyl acetate and the combined organic phases were dried over Na₂SO₄. The solvent was removed under reduced pressure and the crude product solidified upon cooling. The

mixture was purified by column chromatography on silica (gradient DCM → 10% MeOH in DCM) yielding a white solid.

Fmoc-Lys(Cbz)-OH: C₂₉H₃₀N₂O₆ (502.21 g/mol).
Yield: 0.15 g (0.3 mmol, 4%).
¹H NMR: (CDCl₃, 300 MHz) δ [ppm] = 7.89 (d, *J* = 7.4 Hz, 2H), 7.73 (d, *J* = 7.4 Hz, 2H), 7.61 (d, *J* = 8.0 Hz, 1H), 7.46 – 7.38 (m, 2H), 7.37 – 7.29 (m, 6H), 7.28 – 7.22 (m, 1H), 5.00 (s, 2H), 4.31 – 4.18 (m, 3H), 3.99 – 3.81 (m, 1H), 2.99 (q, *J* = 6.4 Hz, 2H), 1.80 – 1.51 (m, 2H), 1.46 – 1.19 (m, 4H).
¹³C NMR: (CDCl₃, 75 MHz) δ [ppm] = 174.41, 156.61, 144.26, 141.16, 137.73, 128.79, 128.17, 128.09, 127.52, 125.73, 120.56, 66.05, 65.57, 54.25, 47.12, 30.87, 29.43, 23.39.

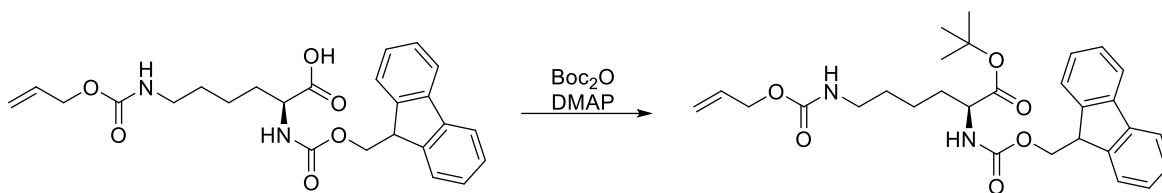
5.3.20. Synthesis of Fmoc-Lys(Cbz)-OtBu



2 g (4 mmol, 1 eq.) Fmoc-Lys(Z)-OH and 0.049 g (0.4 mmol, 0.1 eq.) DMAP were dissolved in 60 mL tert-butanol. 1.135 g (5.2 mmol, 1.3 eq.) Boc₂O were added to the mixture, upon this addition the solution turned slightly yellow. The reaction was stirred at 30 °C for 24 h. The solvent was removed under reduced pressure and the residue was taken up in diethyl ether. The organic phase was washed with 0.5 N HCl, saturated NaHCO₃ solution and 10 wt.% Na₂SO₄ solution and dried over Na₂SO₄ before the diethyl ether was removed under reduced pressure. The residue was purified over silica (c-Hex/EtOAc; v/v = 6:4). Removal of the solvent yielded 2.05 g of a colourless oily substance.

Fmoc-Lys(Cbz)-OtBu: C₃₃H₃₈N₂O₆ (558.68 g/mol).
Yield: 2.05 g (3.7 mmol, 92%).
R_f: (c-Hex/EtOAc; v/v≈6:4): 0.52.
¹H NMR: (CDCl₃, 300 MHz) δ [ppm] = 7.90 (d, *J* = 7.5 Hz, 2H), 7.72 (d, *J* = 7.4 Hz, 2H), 7.63 (d, *J* = 7.8 Hz, 1H), 7.42 (t, *J* = 7.5 Hz, 2H), 7.38 – 7.29 (m, 6H), 7.26 – 7.20 (m, 1H), 5.00 (s, 2H), 4.37 – 4.16 (m, 3H), 3.85 (td, *J* = 8.4, 5.3 Hz, 1H), 2.99 (q, *J* = 6.4 Hz, 2H), 1.63 (q, *J* = 7.6 Hz, 2H), 1.39 (d, *J* = 4.8 Hz, 13H).
¹³C NMR: (CDCl₃, 75 MHz) δ [ppm] = 172.10, 156.54, 141.18, 128.78, 128.09, 127.50, 125.70, 120.57, 65.56, 60.21, 28.10, 26.80, 21.22, 14.55.

5.3.21. Synthesis of Fmoc-Lys(Alloc)-OtBu



2.39 g (5.28 mmol, 1 eq.) Fmoc-Lys(Alloc)-OH and 0.064 g (0.53 mmol, 0.1 eq.) DMAP were dissolved in 70 mL tert-butanol. 1.5 g (6.87 mmol, 1.3 eq.) Boc₂O were added to the mixture, upon this addition the solution turned slightly yellow. The reaction was stirred at 30 °C for 24 h. The solvent was removed under reduced pressure and the residue was taken up in diethyl ether. The organic phase was washed with 0.5 N HCl, saturated NaHCO₃ solution and 10 wt.% Na₂SO₄ solution and dried over Na₂SO₄ before the diethyl ether was removed under reduced pressure. The residue was purified over silica (c-Hex/EtOAc; v/v = 3:2). Removal of the solvent yielded 2.18 g of a colourless oily substance.

Fmoc-Lys(Alloc)-OtBu:

Yield:

R_f:

¹H NMR:

C₂₉H₃₆N₂O₆ (508.26 g/mol).

2.18 g (4.29 mmol, 81%).

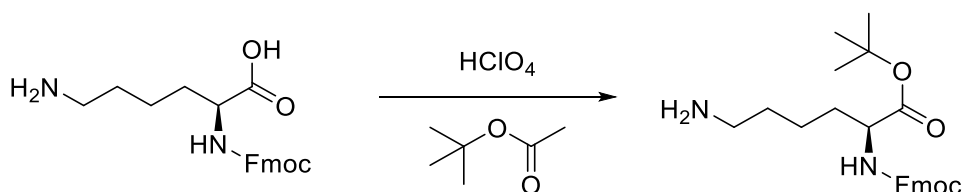
(c-Hex/EtOAc; v/v≈3:2): 0.55.

(DMSO-*d*₆, 300 MHz) δ [ppm] = 7.89 (d, *J* = 7.4 Hz, 2H, H-20), 7.73 (d, *J* = 7.4 Hz, 2H, H-17), 7.63 (d, *J* = 7.8 Hz, 1H, H-12), 7.42 (td, *J* = 7.5, 1.2 Hz, 2H, H-19), 7.33 (td, *J* = 7.4, 1.2 Hz, 2H, H-18), 7.18 (t, *J* = 5.7 Hz, 1H, H-7), 5.90 (ddt, *J* = 17.2, 10.5, 5.3 Hz, 1H, H-10), 5.26 (dq, *J* = 17.3, 1.8 Hz, 1H, H-11_{trans}), 5.16 (dq, *J* = 10.5, 1.5 Hz, 1H, H-11_{cis}), 4.45 (dt, *J* = 5.4, 1.5 Hz, 2H, H-9), 4.34 – 4.26 (m, 2H, H-14), 4.26 – 4.20 (m, 1H, H-15), 3.85 (td, *J* = 8.4, 5.3 Hz, 1H, H-2), 2.98 (q, *J* = 6.4 Hz, 2H, H-6), 1.72 – 1.52 (m, 2H, H-3), 1.46 – 1.26 (m, 13H, H-4/6/23).

¹³C NMR:

(DMSO-*d*₆, 75 MHz) δ [ppm] = 171.64 (C-1), 156.07 (C-8), 155.88 (C-13), 143.77 (C-16), 140.71 (C-21), 133.84 (C-10), 127.62 (C-19), 127.03 (C-18), 125.23 (C-17), 120.09 (C-20), 116.79 (C-11), 80.38 (C-22), 65.56 (C-14), 64.09 (C-9), 54.45 (C-2), 46.66 (C-15), 39.93 (C-6), 30.45 (C-3), 28.94 (C-5), 27.62 (C-23), 22.76 (C-4).

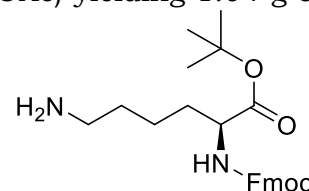
5.3.22. Synthesis of Fmoc-Lys-OtBu



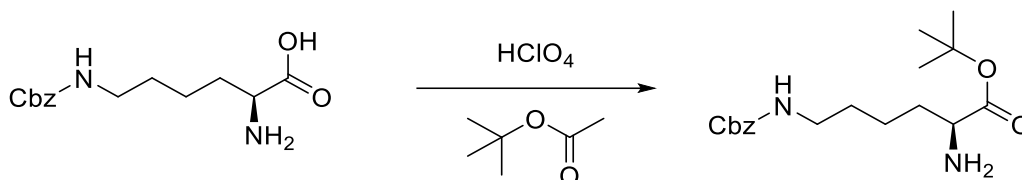
2 g (5.43 mmol, 1 eq.) of Fmoc-Lys-OH were dispersed in 42 mL tBuOAc and cooled with an ice bath. 1.18 mL (10.86 mmol, 2 eq.) 60% perchloric acid (9.2 M) were added

dropwise to the suspension. Over the course of one hour the mixture cleared up. After 4 hours of stirring at ambient temperature, the mixture was diluted with 100 mL water & extracted with three times 100 mL EtOAc. The combined organic phases were dried over Na₂SO₄, and the solvent was removed under reduced pressure. The crude product was purified by column chromatography (100% EtOAc) yielding 1.04 g of a yellow solid.

Fmoc-Lys-OtBu: C₂₅H₃₂N₂O₄ (424.54 g/mol).
Yield: 1.04 g (2.45 mmol, 45%).
R_f: 0.11 (EtOAc)
¹H NMR: (CDCl₃, 300 MHz) δ [ppm] = 7.78 (d, *J* = 7.5 Hz, 2H), 7.55 (s, 2H), 7.49 – 7.27 (m, 4H), 6.07 (s, 1H) 4.72 – 4.49 (m, 2H), 4.43 – 4.21 (m, 3H), 3.43 (s, 1H), 3.15 (s, 2H), 1.51 (s, 6H), 1.41 (s, 9H).



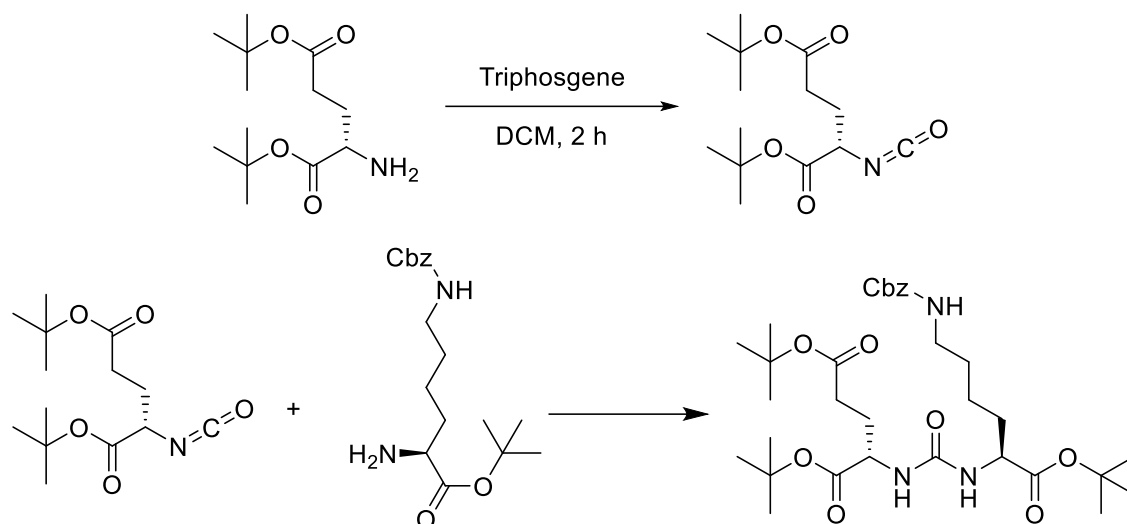
5.3.23. Synthesis of Lys(Cbz)-OtBu



8 g (28.6 mmol) H-Lys(Z)-OH were added to 135 mL tBuOAc and cooled with an ice bath. To the stirred suspension 3.5 mL 60% perchloric acid was slowly added. During the addition, the suspension cleared, and the mixture was stirred for 18 h at ambient temperature. 150 mL water were added, and the phases were separated. The aqueous phase was washed with EtOAc, the combined organic phases were dried over Na₂SO₄, and the solvent was removed under reduced pressure. Subsequent lyophilization yields the product as a colourless oil.

Lys(Cbz)-OtBu: C₁₈H₂₈N₂O₄ (336.43 g/mol).
Yield: 9.55 g (28.4 mmol, 98%).
¹H NMR: (DMSO-*d*₆, 300 MHz) δ [ppm] = 8.18 (s, 3H), 7.44 – 7.26 (m, 4H), 7.26 – 7.11 (m, 1H), 5.01 (s, 2H), 3.89 (d, *J* = 6.1 Hz, 1H), 3.01 (q, *J* = 6.3, 5.8 Hz, 2H), 1.85 – 1.66 (m, 2H), 1.43 (d, *J* = 20.5 Hz, 6H).
¹³C NMR: (DMSO-*d*₆, 75 MHz) δ [ppm] = 172.16, 171.26, 168.85, 156.24, 137.34, 128.48, 127.85, 83.14, 65.30, 52.40, 52.04, 39.95, 31.39, 29.79, 28.95, 28.09, 27.62, 21.74, 21.53, 21.15.

5.3.24. Synthesis of tBuO-Glu(OtBu)-u-Lys(Cbz)-OtBu



1.8 g (7 mmol, 1 eq.) of Glu(OtBu)-OtBu was suspended in a mixture of 30 mL DCM and 60 mL saturated aqueous NaHCO₃ and cooled in an ice bath. 1.1 g (3.8 mmol, 0.6 eq.) triphosgene was added in one portion. The mixture was allowed to warm to ambient temperature and stirred for 2 hours. Afterwards, the mixture was diluted with additional 60 mL DCM and the phases were separated. The organic phases were washed with brine and dried over Na₂SO₄ before the solvent was removed under reduced pressure. This yielded 1.8 g of a colourless low viscous oil which was used without further purification.

1.65 g (5.7 mmol, 1 eq.) of this oil were dissolved in 40 mL dry DCM. Separately, 1.94 g (5.7 mmol, 1 eq.) HLys(Cbz)OtBu were dissolved in 40 mL dry DCM to which 0.6 mL pyridine was added. The isocyanate solution was added slowly to the lysine one and the reaction mixture was stirred for 72 h at ambient temperature. The solvent was removed under reduced pressure and the crude product was purified by column chromatography (gradient 1:4->1:1 EtOAc/c-Hex) yielding 3.3 g of a waxy solid.

tBuO-Glu(OtBu)-u-Lys(Cbz)-OtBu

C₃₂H₅₁N₃O₉ (621.77 g/mol).

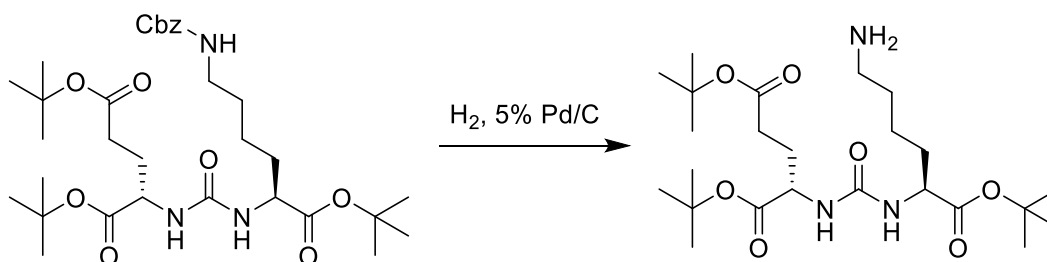
Yield:

3.3 g (5.3 mmol, 93%).

¹H NMR:

(CDCl₃, 300 MHz) δ [ppm] = 7.37 (d, *J* = 4.4 Hz, 5H), 5.28 – 5.05 (m, 5H), 4.43 – 4.27 (m, 2H), 3.19 (q, *J* = 6.8 Hz, 2H), 2.42 – 2.21 (m, 2H), 1.95 – 1.53 (m, 8H), 1.46 (s, 18H), 1.45 (s, 9H).

5.3.25. Synthesis of tBuO-Glu(OtBu)-u-Lys-OtBu



1.2 g of 5% Pd/C were added to a solution of 3 g (4.82 mmol) tBuO-Glu(OtBu)-u-Lys(Cbz)-OtBu in 150 mL dry MeOH. The atmosphere was switched for H₂, and the mixture was stirred for 3 days at ambient temperature. The mixture was filtered through celite, and the solvent was removed under reduced pressure. Further side products were removed by lyophilization.

tBuO-Glu(OtBu)-u-Lys-OtBu

C₂₄H₄₅N₃O₇ (487.64 g/mol).

Yield:

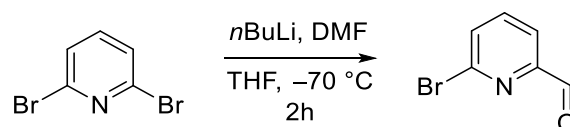
1.05 g (2.15 mmol, 45%).

¹H NMR:

(CDCl₃, 300 MHz) δ [ppm] = 5.51 (dd, *J* = 8.3, 2.9 Hz, 2H), 4.35 (td, *J* = 8.0, 4.1 Hz, 2H), 2.69 (t, *J* = 6.6 Hz, 2H), 2.62 – 2.47 (m, 2H), 2.31 (dt, *J* = 8.8, 6.6 Hz, 2H), 2.16 – 1.98 (m, 1H), 1.96 – 1.70 (m, 2H), 1.70 – 1.55 (m, 1H), 1.45 (d, *J* = 7.5 Hz, 34H).

5.4. Synthesis of ketones

5.4.1. Synthesis of 2-formyl 6-bromo pyridine



13 mL *n*-BuLi (1.6 M in hexane, 20.8 mmol, 0.99 eq.) was dissolved in 20 mL abs. THF and added slowly to a solution of 5.00 g 2,6-dibromopyridine (21 mmol, 1.00 eq.) in 20 mL abs. THF at -78 °C. 30 min later 2.5 mL DMF (32.5 mmol, 1.55 eq.) were added dropwise. The mixture was let warm to 0 °C and stirred for additional 3 h at ambient temperature before 30 mL MeOH was added. 40 mL sat. NaHCO₃ solution was added, and the product was extracted with DCM. The crude product was purified by column chromatography at silica (*c*-Hex:EtOAc v/v=5:1). The product was isolated as a pale-yellow solid.

2-form 6-Br: C₆H₄BrNO (186.01 g/mol).

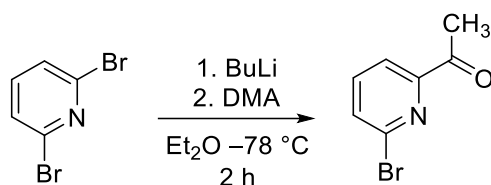
Yield: 0.5 g (2.68 mmol, 64%).

R_f: (*c*-Hex/EtOAc; v/v≈6:4): 0.69 (UV-inactive).

¹H NMR: (CDCl₃, 300 MHz) δ [ppm] = 10.01 (s, 1H), 7.93 (dt, J = 6.3, 1.8, 1H), 7.80 – 7.70 (m, 2H).

¹³C NMR: (CDCl₃, 75 MHz) δ [ppm] = 191.67, 139.33, 132.66, 120.32.

5.4.2. Synthesis of 2-acetyl 6-bromo pyridine



10.0 g (42.2 mmol, 1.0 eq.) 2,6-dibromopyridine were added into 100 ml dry diethyl ether and cooled to -78 °C. 17 ml (2.5 M) butyllithium in hexane were added dropwise and stirred for 0.5 h. 5.6 ml dimethylacetamide were added. The mixture was stirred at -78 °C for 0.5 h, then the mixture was allowed to rise to rt, at rt stirred for 1 h. 50 ml saturated ammonium chloride solution was added, the aqueous layer was washed three times with 50 ml diethyl ether, the united organic layers dried over Na₂SO₄. The solvent was removed and purified via column chromatography at silica (*c*-Hex:EtOAc; 4:1). The product (690 mg, 3.45 mmol, 8 %) was isolated as a colourless solid.

2-acetyl 6-bromo pyridine: C₇H₆BrNO (200.04 g/mol).

Yield:

690 mg (3.45 mmol, 8 %).

R_f:

0.55 (*c*-Hex:EtOAc = 4:1).

Habitus

colourless solid.

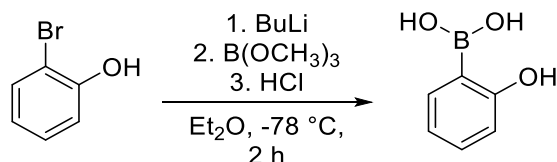
¹H NMR:

(300 MHz, DMSO-*d*₆): δ (ppm) = 7.99 (dd, 1H, J = 6.9, 1.7, H-2), 7.73–7.62 (m, 2H, H-1;3), 2.71 (s, 3H, H-7).

¹³C NMR:

(75 MHz, DMSO-*d*₆): δ (ppm) = 154.28, 141.34, 131.75, 120.45, 25.73.

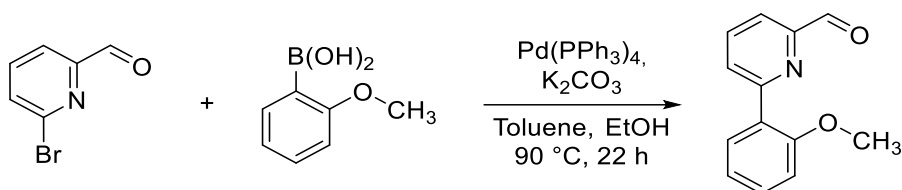
5.4.3. Synthesis of (2-hydroxyphenyl)boronic acid



3.5 ml (30 mmol, 1.0 eq.) **23** dissolved in 60 ml diethyl ether and cooled to -78 °C. 25 ml (2.5 M) *n*-butyllithium in hexane were added slowly. The mixture was allowed to warm up to rt over 2 h. The solution was cooled down to -78 °C and 5.6 ml (50 mmol, 1.7 eq.) trimethyl borate were added slowly, the solution was warmed up to rt and stirred overnight. 20 ml (2 M) hydrochloric acid was added and stirred for 0.5 h. The product (4.20 g, 24.2 mmol, 81%) was isolated as an orange/brown oil.

2-hydroxyphenyl boronic acid: C₆H₇BO₃ (137.93 g/mol).
Yield: 4.20 g (24.2 mmol, 81%)
Habitus: Brown/orange oil.
¹H NMR: (300 MHz, DMSO-d₆): δ (ppm) = 7.44 (dd, 1H, *J* = 8.0, 1.6), 7.19 (ddd, 1H, *J* = 8.2, 7.3, 1.6), 7.00 (dd, 1H, *J* = 8.1, 1.6), 6.78 (ddd, *J* = 8.0, 7.3, 1.6), -OH, BOH2
¹³C NMR: (75 MHz, DMSO-d₆): δ (ppm) = 154.28, 141.34, 131.75, 120.45, 25.73.

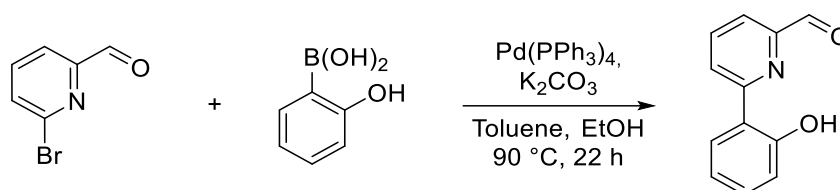
5.4.4.Synthesis of 2-formyl 6-(2-methoxyphenyl) pyridine



930 mg 6-bromo picolinaldehyde (5 mmol, 1.0 eq.), 1400 mg potassium carbonate (10 mmol, 2.0 eq.), 830 mg 2-methoxyphenyl boronic acid (5.5 mmol, 1.1 eq.) and 12 mg tetrakis (triphenylphosphine)palladium(0) (0.1 mmol, 0.02 eq.) were dissolved in 15 mL abs. toluene and 10 mL EtOH and heated to 90 °C for 20 h. The mixture was cooled to ambient temperature and 30 mL of water were added and stirred for 30 min. The aqueous layer was extracted with DCM dried over Na₂SO₄ and the solvent was removed under reduced pressure. The crude product was purified by column chromatography at silica (pure EtOAc). The product was isolated as a yellow oil.

6-(2-mph)formylpyridine C₁₃H₁₁NO₂ (213.24 g/mol).
Yield: 0.94 g (4.41 mmol, 88%)
¹H NMR: (300 MHz, CDCl₃): δ (ppm) = 10.15 (s, 1H, H-13), 8.09 (dd, *J* = 6.3, 2.7, 1H), 7.94 – 7.85 (m, 3H), 7.43 (ddd, *J* = 8.3, 7.4, 1.9, 1H), 7.13 (td, *J* = 7.5, 1.1, 1H), 7.04 (dd, *J* = 8.3, 1.0, 1H), 3.88 (s, 3H).
¹³C NMR: (75 MHz, CDCl₃): δ (ppm) = 194.1, 136.5, 131.1, 130.6, 129.4, 121.2, 119.4, 114.5, 113.9, 111.5, 110.7, 60.4.

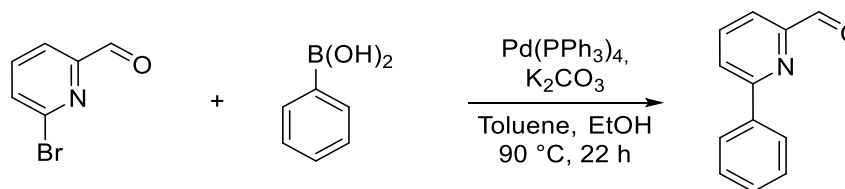
5.4.5.Synthesis of 2-formyl 6-(2-hydroxyphenyl) pyridine by cross coupling



500 mg bromopicolinaldehyde (2.69 mmol, 1.0 eq.), 750 mg potassium carbonate (5.38 mmol, 2.0 eq.), 411 mg hydroxy boronic acid (2.96 mmol, 1.1 eq.) and 6.6 mg tetrakis(triphenylphosphine)palladium(0) (5 mol%) were dissolved in 5.0 ml abs. toluene and 4.5 ml EtOH and heated to 90°C for 20.5 h. The mixture was cooled to rt, and 30 ml of water were added and stirred for 30 min. The aqueous layer was extracted with DCM dried over Na₂SO₄ and the solvent was removed. The crude product was purified by column chromatography over silica (EtOAc). The product (27 mg, 0.14 mmol, 5 %) was isolated as a colourless solid.

6-(2-hph)formylpyridine	C ₁₂ H ₉ NO ₂ (199.21 g/mol).
Yield:	27 mg (0.14 mmol, 5%).
R_f	0.25 (EtOAc).
¹H NMR:	(300 MHz, CDCl ₃): δ (ppm) = 10.11 (d, <i>J</i> = 0.7 Hz, 1H), 8.17 (dd, <i>J</i> = 8.2 Hz, 1.2Hz, 1H), 8.11 – 8.00 (m, 1H), 7.91 (dd, <i>J</i> = 7.5 Hz, 1.1 Hz, 1H), 7.85 (dd, <i>J</i> = 8.0 Hz, 1.7 Hz, 1H), 7.39 (ddd, <i>J</i> = 8.6 Hz, 7.2 Hz, 1.6 Hz, 1H), 7.09 (dd, <i>J</i> = 8.3 Hz, 1.3 Hz, 1H), 6.99 (ddd, <i>J</i> = 8.3 Hz, 7.2 Hz, 1.3 Hz, 1H).
¹³C NMR:	(75 MHz, CDCl ₃): δ (ppm) = 191.1, 159.7, 158.7, 138.8, 138.6, 132.4, 126.6, 123.7, 119.9, 119.4, 118.9.

5.4.6.Synthesis of 6-Phenyl 2-formylpyridine

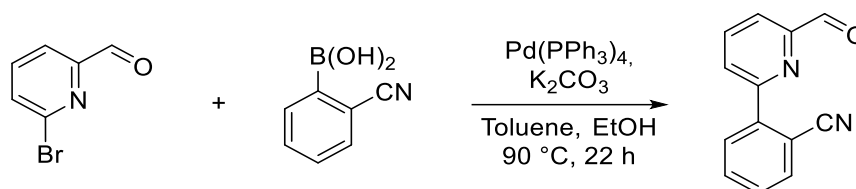


0.5 g (2.7 mmol, 1 eq.) of 6-bromo 2-formylpyridine, 0.366 g (3 mmol, 1,1 eq.) phenylboronic acid, 0.75 g (5.4 mmol, 2 eq.) potassium carbonate and 15 mg (0.135 mmol, 0.05 eq.) [Pd(PPh₃)₄] were added to a dried flask and dissolved in 15 mL toluene and 10 mL EtOH. The mixture was heated to reflux for 22 h. Prior to the addition of 20 mL water, the mixture was cooled to ambient temperature. The mixture was extracted with DCM and the combined organic phases were dried over Na₂SO₄

before the solvent was removed under reduced pressure. The crude product was purified by column chromatography (SiO₂, v/v = 1:2 EtOAc/c-Hex).

6-(2-hph)formylpyridine	C ₁₂ H ₉ NO (183.21 g/mol).
Yield:	420 mg (2.3 mmol, 85%).
R_f	0.8 (EtOAc).
¹H NMR:	(300 MHz, CDCl ₃): δ (ppm) = 10.17 (s, 1H), 8.09 (dd, <i>J</i> = 8.1, 1.6 Hz, 2H), 7.98 – 7.87 (m, 3H), 7.56 – 7.42 (m, 3H).
¹³C NMR:	(75 MHz, CDCl ₃): δ (ppm) = 194.1, 158.1, 152.9, 138.3, 137.9, 129.8, 129.1, 127.1, 124.6, 119.9.

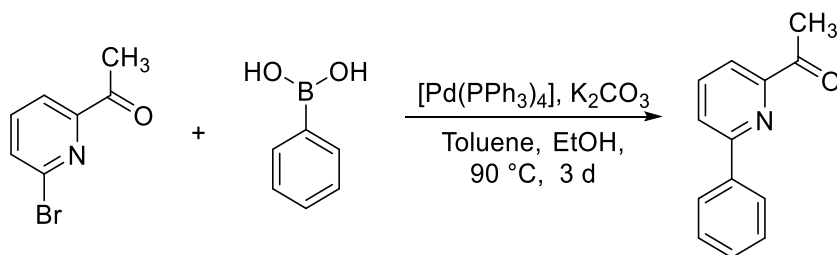
5.4.7.Synthesis of 6-(2-cyanophenyl) picolinaldehyde



500 mg bromopicolinaldehyde (2.69 mmol, 1.0 eq.), 750 mg potassium carbonate (5.38 mmol, 2.0 eq.), 442 mg 2-cyanophenyl boronic acid (2.96 mmol, 1.1 eq.) and 6.6 mg tetrakis(triphenylphosphine)palladium(0) (5 mol%) were dissolved in 5.0 ml abs. toluene and 4.5 ml EtOH and heated to 90°C for 20.5 h. The mixture was cooled to rt, and 30 ml of water were added and stirred for 30 min. The aqueous layer was extracted with DCM dried over Na₂SO₄ and the solvent was removed. The crude product was purified by column chromatography over silica (c-hex:EtOAc). The product (68 mg, 0.37 mmol, 14 %) was isolated as a colourless solid.

6-cyanophenyl picolinaldehyde	C ₁₃ H ₈ N ₂ O (208.22g/mol).
Yield:	68 mg (0.37 mmol, 14%).
Habitus	colourless solid.
¹H NMR:	(300 MHz, CDCl ₃) δ (ppm) = 10.20 (d, <i>J</i> =0.5, 1H), 8.09 – 8.02 (m, 3H), 7.99 – 7.92 (m, 1H), 7.88 (dt, <i>J</i> =7.7, 0.8, 1H), 7.77 (td, <i>J</i> =7.7, 1.4, 1H), 7.60 (td, <i>J</i> =7.6, 1.3, 1H).
¹³C NMR:	(75 MHz, CDCl ₃) δ (ppm) = 193.1, 155.7, 152.9, 142.1, 138.1, 134.4, 133.0, 130.0, 129.4, 127.1, 120.9.

5.4.8.Synthesis of 1-(6-phenyl-pyridin-2-yl)ethan-1-one



0.50 g (2.50 mmol, 1.00 eq.) 2-acetyl 6-bromo pyridine, 0.05 (0.05 mmol, 0.02 eq.) Tetrakis(triphenylphosphine)palladium and 0.69 g (5.00 mmol, 2.00 eq.) potassium carbonate was dissolved in 20 ml dry toluene and stirred for 0.2 h. 0.37 g (3.00 mmol, 1.20 eq.) **26** were added slowly and refluxed for 3 d. After cooling to rt 0.4 ml (30%) hydrogen peroxide were added and the mixture was stirred for 0.5 h, then 10 ml water were added. The aqueous layer was extracted two times with 50 ml diethyl ether, and the combined organic layers were washed two times with saturated sodium chloride solution and dried over sodium sulphate, afterwards the solvent was removed. The crude product (0.69 g, 3.50 mmol, quant.) was isolated as a yellow oil.

2-acetyl 6-phenyl pyridine: C₁₃H₁₁NO (197.24 g/mol).

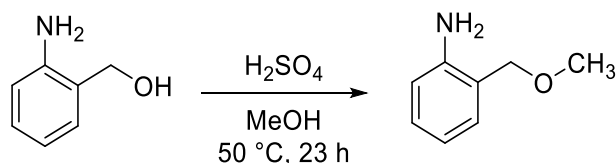
Yield: 0.69 g (3.5 mmol, >99 %).

Habitus yellow solid.

¹H NMR: (300 MHz, CDCl₃) δ (ppm) = 8.10 (dd, 2H, *J* = 8.2, 1.6, H-8), 8.00 – 7.83 (m, 3H, H-3;9), 7.55 – 7.42 (m, 2H, H-9), 7.28 – 7.14 (m, 2H, H-4;10), 2.83 (s, 3H, H-7).

¹³C NMR: (75 MHz, CDCl₃) δ (ppm) = 138.42, 137.63, 129.47, 128.87, 126.89, 123.46, 119.80, 25.79

5.4.9.Synthesis of 2-(methoxymethyl) aniline



5.06 g (41.1 mmol, 1.0 eq.) of aniline were dissolved in 40 ml MeOH and cooled to 0 °C. 4.4 ml (82.2 mmol, 2.0 eq.) conc. H₂SO₄ were added. A white precipitate formed that was resolved after 10 min of continued stirring. The solution was stirred at 50 °C for 23 h. After cooling to room temperature, the reaction was quenched using aqueous sat. Na₂CO₃ solution. 70 ml water were added, and the aqueous phase

extracted with DCM (3x100 ml). The combined organic phases were dried over Na₂SO₄, and the solvent removed under reduced pressure. Column chromatography (c-Hex:EtOAc:Et₃N = 3:1:0.1) of the residue gave aniline as a pale-yellow oil in a yield of 2.92 g (21.6 mmol, 53%).

2-(methoxymethyl) aniline C₈H₁₁NO (137.18 g/mol).

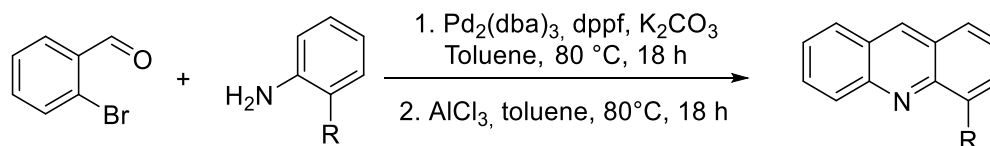
Yield: 2.92 g (21.6 mmol, 53%).

Habitus Pale-yellow oil.

R_f 0.33 (c-Hex:EtOAc:Et₃N = 3:1:0.1).

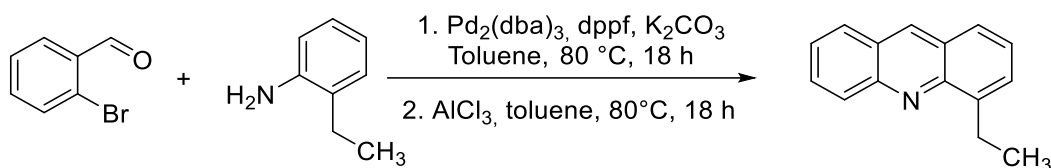
¹H NMR: (300 MHz, CDCl₃) δ (ppm) = 7.12 (td, J = 7.7 Hz, 1.6 Hz, 1H), 7.05 (dd, J = 7.5 Hz, 1.6 Hz, 1H), 6.73 – 6.63 (m, 2H), 4.46 (s, 2H, H-7), 4.13 (bs, 2H, NH₂), 3.32 (s, 3H, H-8).

5.4.10. General Procedure for the synthesis of acridines



Under an argon atmosphere 0.14 g (0.15 mmol, 3 mol%) of Pd₂(dba)₃, 0.15 g (0.27 mmol, 5 mol%) of dppf and 1.50 g (10.8 mmol, 2.0 eq.) of K₂CO₃ were dissolved in 50 ml abs. toluene. 6.5 mmol (1.2 eq.) of the aniline derivatives 12 was added and the solution stirred for 5 min at room temperature. 0.63 ml (1.0 g, 5.4 mmol, 1.0 eq.) of 11 were added and the solution stirred at 80 °C for 18 h. The reaction mixture was cooled to room temperature and filtrated over a celite plug. The solvent was concentrated to approximately 50 ml and 1.48 g (11.1 mmol, 2.0 eq.) AlCl₃ were added. The resulting mixture was stirred at 80 °C for another 18 h. After cooling to room temperature, the reaction was quenched with 50 ml water. The phases were separated, and the aqueous phase extracted with EtOAc (3x100 ml). The combined organic phases were dried over Na₂SO₄, and the solvent removed under reduced pressure. The residue was purified by column chromatography.

5.4.10.1. Synthesis of 4-ethyl acridine



4-ethyl acridine was synthesised according to general procedure A on a 5.4 mmol scale. For column chromatography a solvent mixture of c-Hex:EtOAc = 20:1 was used. The acridine was obtained as a dark yellow oil in a yield of 0.99 g (4.8 mmol, 88%).

4-ethyl acridine: $\text{C}_{15}\text{H}_{13}\text{N}$ (207.28 g/mol).

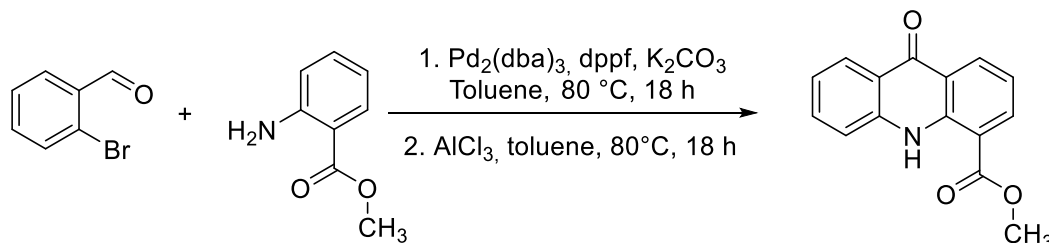
Yield: 0.99 g (4.8 mmol, 88%).

Habitus Dark yellow oil.

R_f 0.57 (c-Hex:EtOAc = 20:1).

¹H NMR: (300 MHz, CDCl_3): δ (ppm) = 8.72 (s, 1H, H-7), 8.32 (d, $J = 8.5$ Hz, 1H), 7.99 (d, $J = 8.5$ Hz, 1H), 7.85 (d, $J = 8.1$ Hz, 1H), 7.81 – 7.75 (m, 1H), 7.66 – 7.62 (m, 1H), 7.58 – 7.46 (m, 2H), 3.52 (q, $J = 7.5$ Hz, 2H, H-14), 1.52 (t, $J = 7.5$ Hz, 3H, H-15).

5.4.10.2. Synthesis of methyl acridone-4-carboxylate



Benzaldehyde and aniline were converted according to general procedure on a 2.7 mmol scale. After column chromatography (c-Hex:EtOAc = 4:1 to 2:1) the acridone was obtained as a dark yellow solid in a yield of 0.21 g (0.84 mmol, 31%). Impurities of acridine were observed in the ¹H-NMR.

methyl acridone-4-carboxylate: $\text{C}_{15}\text{H}_{11}\text{NO}_3$ (253.26 g/mol).

Yield: 0.21 g (0.84 mmol, 31%).

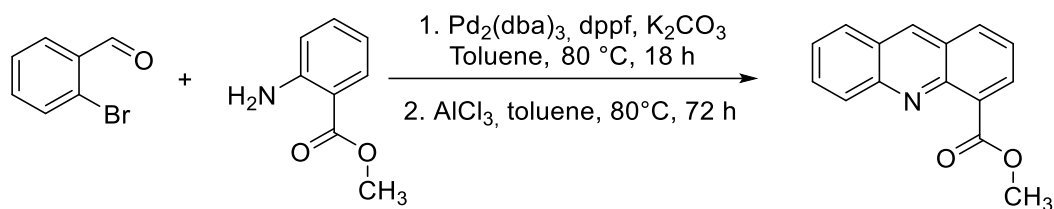
Habitus Dark yellow solid.

R_f 0.26 (c-Hex:EtOAc = 3.5:1).

¹H NMR: (300 MHz, CDCl_3): δ (ppm) = 11.8 (bs, 1H, NH), 8.73 (d, $J = 7.9$ Hz, 1H), 8.43 (t, $J = 7.9$ Hz, 2H), 7.69 (t, $J = 7.7$ Hz, 1H), 7.39 (d, $J = 8.25$ Hz, 1H), 7.31 – 7.21 (m, 2H), 4.02 (s, 3H, H-15).

EI-MS $m/z = 253$ [M^+].

5.4.10.3. Synthesis of methyl acridine-4-carboxylate



Synthesis of acridine was attempted again according to general procedure on a 2.0 mmol scale. This time the reaction mixture was stirred at 80 °C with AlCl₃ for 72 h instead of 18 h, quenched with 50 ml water and extracted four times with 100 ml EtOAc. Purification was done via column chromatography (c-Hex:EtOAc = 4:1 to 2:1). The acridine was obtained in a yield of 0.23 g (0.97 mmol, 48%) as a viscous, yellow oil. Impurities of the acridone were observed in the ¹H-NMR.

methyl acridine 4-carboxylate: C₁₅H₁₂NO₂ (237.26 g/mol).

Yield: 0.23 g (0.97 mmol, 48%).

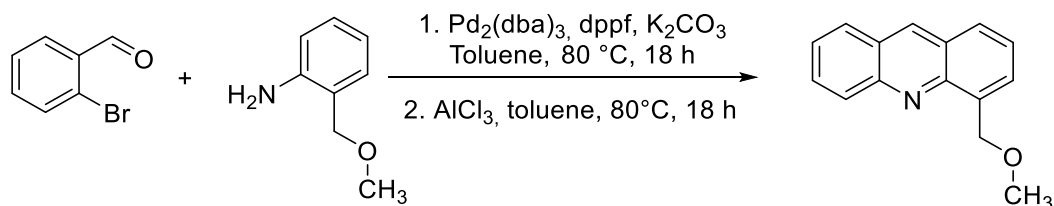
Habitus Yellow oil.

R_f 0.26 (c-Hex:EtOAc = 3.5:1).

¹H NMR: (300 MHz, CDCl₃): δ (ppm) = 8.72 (s, 1H, H-7), 8.32 (d, J = 8.5 Hz, 1H), 7.99 (d, J = 8.5 Hz, 1H), 7.85 (d, J = 8.1 Hz, 1H), 7.81 – 7.75 (m, 1H), 7.66 – 7.62 (m, 1H), 7.58 – 7.46 (m, 2H), 3.52 (q, J = 7.5 Hz, 2H, H-14), 1.52 (t, J = 7.5 Hz, 3H, H-15).

EI-MS m/z = 237 [M⁺].

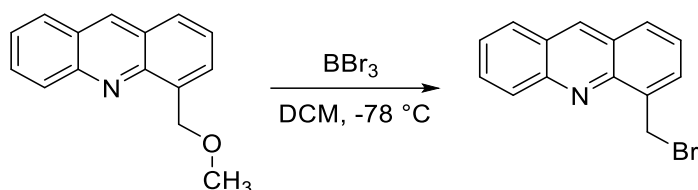
5.4.10.4. Synthesis of 4-(methoxymethyl)-4-acridine



Acridine 2g was synthesised according to general procedure A on a 2.7 mmol scale. The reaction mixture was stirred with AlCl₃ at 80 °C for 72 h. The residue was purified by column chromatography (c-Hex:EtOAc = 4:1) to give the acridine as a yellow oil in a yield of 99 mg (0.44 mmol, 16%).

4-(methoxymethyl)-4-acridine	$C_{15}H_{13}NO$ (223.28 g/mol).
Yield:	99 mg (0.44 mmol, 16%).
Habitus	Yellow oil.
R_f	0.15 (c-Hex:EtOAc = 3.5:1).
¹H NMR:	(300 MHz, CDCl ₃): δ (ppm) = 8.75 (s, 1H, H-7), 8.25 (d, J = 8.9 Hz, 1H) 8.01 (d, J = 8.8 Hz, 1H), 7.93 (d, J = 8.8 Hz, 1H), 7.90 – 7.85 (m, 1H), 7.57 – 7.50 (m, 2H), 7.44 – 7.40 (m, 1H), 5.37 (s, 2H, H-14), 3.65 (s, 3H, H-15).

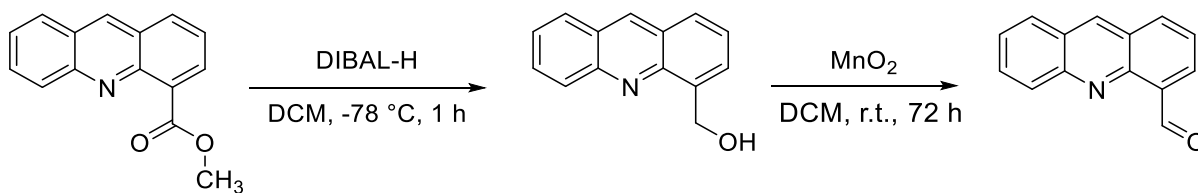
5.4.11. Synthesis of 4-(bromomethyl)acridine



Under an argon atmosphere 99 mg (0.44 mmol, 1.0 eq.) acridine 2g were dissolved in 5 ml abs. DCM. The solution was cooled to $-78\text{ }^{\circ}\text{C}$ and 0.07 ml (0.2 g, 0.7 mmol, 1.7 eq.) boron tribromide were added. The solution turned deep red. The solution was stirred at $-78\text{ }^{\circ}\text{C}$ for one hour, slowly warmed to room temperature and stirred for 3 days. The reaction was quenched by addition of 5 ml water. The phases were separated, and the aqueous phase extracted with DCM (3x20 ml) and chloroform (1x20 ml). The combined organic phases were dried over sodium sulphate and the solvent evaporated under reduced pressure. The residue was purified via column chromatography (c-Hex:EtOAc = 4:1) to give 2h as a brownish solid in a yield of 63 mg (0.24 mmol, 55%).

4-(bromomethyl)-4-acridine	$C_{14}H_{10}BrNO$ (272.15 g/mol).
Yield:	63 mg (0.24 mmol, 55%).
Habitus	Brown solid.
R_f	0.17 (c-Hex:EtOAc = 4:1).
¹H NMR:	(300 MHz, CDCl ₃): δ (ppm) = 8.76 (s, 1H), 8.30 (d, J = 8.8 Hz, 1H), 8.03 – 7.95 (m, 2H), 7.92 (d, J = 7.2 Hz, 1H), 7.83 – 7.76 (m, 1H), 7.59 – 7.52 (m, 1H), 7.49 (dd, J = 8.5 Hz, 7.1 Hz), 5.42 (s, 2H).

5.4.12. Synthesis of acridine-4-carbaldehyde



Under an argon atmosphere 0.198 g (0.835 mmol, 1.0 eq.) of methyl acridine-4-carboxylate were dissolved in 5 ml abs. DCM and cooled to -78 °C. 1.1 ml (1.0 mol/l, 1.1 mmol, 1.25 eq.) of a solution of DIBAL-H in hexane was added dropwise and the solution stirred at -78 °C for 1 h. 2 ml MeOH were added, and the reaction mixture warmed to room temperature. 0.51 g (2.63 mmol, 3.1 eq.) sodium tartrate were dissolved in 5 ml water and added to the reaction mixture. To the orange, viscous dispersion 10 ml of DCM were added. The phases were separated, and the organic phase was washed with water (5 ml) and brine (2x10 ml) and dried over Na₂SO₄. The solvent was removed under reduced pressure and the residue purified by column chromatography (c-Hex:EtOAc = 4:1). 82 mg of impure alcohol was obtained.

The crude alcohol was dissolved in 4.5 ml DCM and 0.34 g (3.9 mmol, 4.7 eq.) MnO₂ were added. The resulting mixture was stirred at room temperature for 72 h and then filtrated over a celite plug. The solvent was removed under reduced pressure and the residue purified by column chromatography (c-Hex:EtOAc = 4:1) to give 30 mg (<0.14 mmol, <17 %) of impure carbaldehyde.

4-(hydroxymethyl)-4-acridine C₁₄H₁₁NO (209.25 g/mol).

Yield: 82 mg (0.39 mmol, 46%).

R_f 0.17 (c-Hex:EtOAc = 4:1).

¹H NMR: (300 MHz, CDCl₃): δ (ppm) = 8.77 (s, 1H, H-7), 8.19 (d, J = , 1H), 7.98 (d, J = , 1H), 7.91 (d, J = , 1H), 7.81 – 7.75 (m, 1H), 7.64 – 7.51 (m, 2H), 7.49 – 7.42 (m, 1H), 5.68 (bs, 1H, OH), 5.29 (s, 2H, H-14).

Acridine-4-carbaldehyde C₁₄H₉NO (207.23 g/mol).

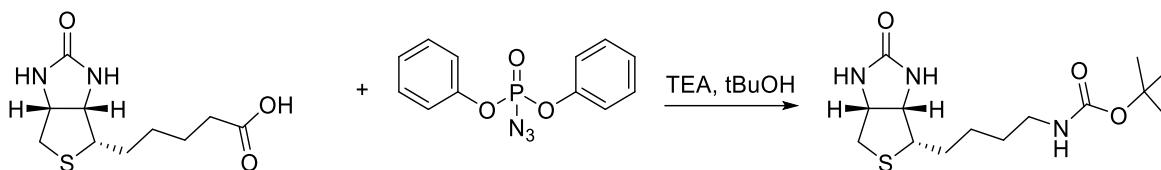
Yield: 30 mg (0.14 mmol, overall 17%).

R_f 0.38 (c-Hex:EtOAc = 4:1).

¹H NMR: (300 MHz, CDCl₃): δ (ppm) = 11.68 (d, J = 0.6 Hz, 1H, H-14), 8.85 (s, 1H, H- 7), 8.44 (dd, J = 6.9 Hz, 1.5 Hz, 1H), 8.31 – 8.25 (m, 2H), 8.03 (d, J = 8.5 Hz, 1H), 7.89 – 7.83 (m, 1H), 7.70 – 7.56 (m, 2H).

5.4.13. Synthesis of biotin derivatives

5.4.13.1. N-Boc norbiotin amine



In a *Schlenk*-flask Biotin (1.50 g, 6.14 mmol, 1.00 eq.) was dissolved in *t*BuOH (22.0 ml) and stirred for 10 minutes. DPPA (1.86 g, 6.75 mmol, 1.46 ml, 1.10 eq.) and triethylamine (0.680 g, 6.75 mmol, 0.940 ml, 1.10 eq.) was added under inert conditions. The mixture was stirred at 95 °C for 24 h. The solvent was removed under reduced pressure and the crude product was purified *via* column chromatography (SiO₂, DCM/MeOH, 19:1 + 5% triethylamine). The desired product could be observed as a brown oil in a yield of 46%.

N-Boc norbiotin amine C₁₄H₂₅N₃O₃S (315.2 g/mol).

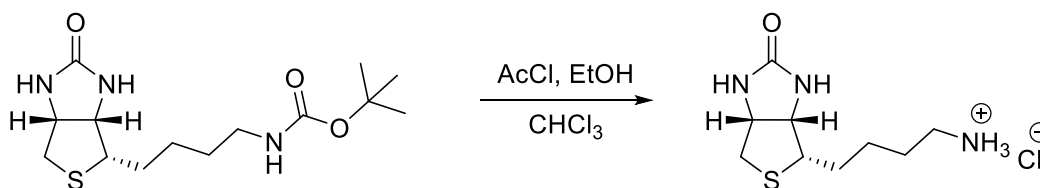
Yield: 0,89 g (2.82 mmol, 46%).

Habitus Brown oil.

R_f 0.44 (MeOH:CH₂Cl₂ = 1:19).

¹H NMR: (300 MHz, DMSO-*d*₆): δ (ppm) = 4.31 (dd, *J* = 7.3, *J* = 5.4 Hz, 1H), 4.13 (dd, *J* = 7.1, *J* = 4.6 Hz, 1H), 2.98 – 2.70 (m, 3H), 2.58 (d, *J* = 12.6 Hz, 1H), 2.28 (dd, *J* = 3.6, *J* = 1.8 Hz, 1H), 1.65 – 1.42 (m, 2H), 1.38 (s, 9H), 1.24 (d, *J* = 7.0 Hz, 4H).

5.4.13.2. Norbiotin amine



A *Schlenk*-flask was charged with chloroform (10.0 ml) and EtOH (1.57 g, 34.1 mmol, 2.00 ml, 23.3 eq.) under inert conditions. Acetyl chloride (2.64 g, 33.6 mmol, 2.40 ml, 23.0 eq.) was added over a dropping funnel over 25 minutes and the mixture was stirred for 10 minutes. The protected Biotin (460 mg, 1.46 mmol, 1.00 eq.) was partially dissolved in chloroform (10.0 ml) and the EtOH/acetyl chloride solution was added over a dropping funnel over 10 minutes at 0 °C. The mixture was stirred for 18 h at room temperature. The mixture was filtrated, and

the crude product was washed with chloroform (45.0 ml) and dried *in vacuo*. The desired product could be obtained as a pure white solid in a yield of 66%.

Norbiotin amine hydrochloride C₉H₁₈ClN₃OS (251.2 g/mol).

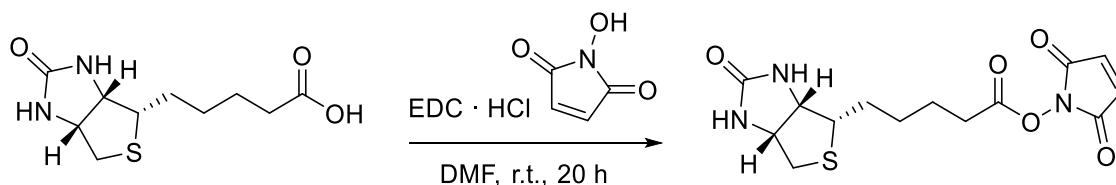
Yield: 243 mg (0.96 mmol, 66%).

Habitus colourless solid.

¹H NMR: (300 MHz, MeOH-*d*₄): δ (ppm) = 1.55 (dd, *J* = 14.7 Hz, 2H), 1.87-1.60 (m, 4H), 2.76 (d, *J* = 12.7 Hz, 1H), 2.96 (dt, *J* = 7.6 Hz, 3.8 Hz, 3H), 3.29 – 3.22 (m, 1H), 4.55 (dd, *J* = 7.8, *J* = 4.1 Hz, 1H), 4.35 (dd, *J* = 7.9, *J* = 4.5 Hz, 1H).

¹³C NMR: (75 MHz, CD₃OD): δ [ppm] = 25.6, 27.4, 28.5, 55.9, 59.5, 61.4, 163.2.

5.4.13.3. Synthesis of biotin NHS



In a *Schlenk*-flask Biotin (500 mg, 2.05 mmol, 1.00 eq.), *N*-hydroxy-succinimide (281 mg, 2.44 mmol, 1.19 eq.) and EDC·HCl (470 mg, 2.44 mmol, 1.19 eq.) were slowly dissolved in DMF (17.0 ml) and stirred for 20 h. The solvent was removed under reduced pressure and the residue was taken up and washed with a solution (100 ml) of EtOH/acetic acid/water (Vol%, 95/4/1). The desired product was obtained as a pure white solid in a yield of 63%.

Biotin-NHS C₁₄H₁₉N₃O₅S (341.1 g/mol).

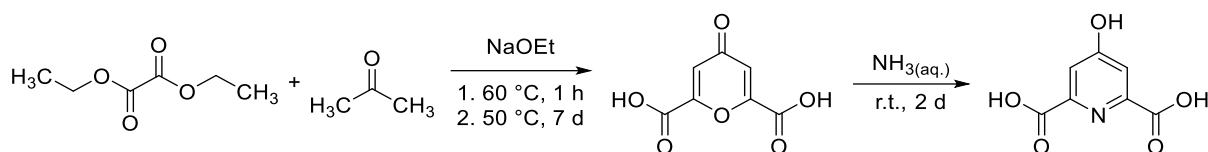
Yield: 439 mg (1.29 mmol, 63%).

Habitus colourless solid.

¹H NMR: (300 MHz, DMSO-*d*₆): δ (ppm) = 6.39 (d, *J* = 17.4 Hz, 2H), 4.38 – 4.25 (m, 1H), 4.20 – 4.09 (m, 1H), 3.15 – 3.06 (m, 1H), 2.93 – 2.77 (m, 5H), 2.76 – 2.54 (m, 3H), 1.74 – 1.32 (m, 6H).

¹³C NMR: (75 MHz, DMSO-*d*₆): δ [ppm] = 24.8, 26.0, 27.9, 28.5, 30.5, 55.9, 59.9, 61.8, 162.2, 163.0, 169.4, 171.0.

5.4.14. Synthesis of 4-hydroxypyridine 2,6-dicarboxylic acid (Chelidamic acid)



Under argon atmosphere 15.0 g (510 mmol, 2.04 eq.) sodium were dissolved in 150 ml EtOH. After dropwise addition of a mixture of 74.0 ml (530 mmol, 2.12 eq.) diethyl oxalate and 19.0 ml (250 mmol, 1.00 eq.) acetone the reaction mixture was heated to 60 °C for 1 hour. The solution was cooled down to 0 °C and 100 ml of 12 M HCl and 50 ml of water were added. The solution was stirred over night at 50 °C. After removal of EtOH under reduced pressure, 25 ml of 12 M HCl and 150 ml of water were added, and the solution was stirred for 7 days at 50 °C. The solution was cooled down to ambient temperature and filtered. After washing the brown precipitate with water and acetone, 500 ml of 13 M ammonia solution were added dropwise at 0 °C. The reaction mixture was allowed to warm to ambient temperature and stirred for two days. After the removal of ammonia under reduced pressure, 300 ml of water and 10 g charcoal were added. The suspension was refluxed for 5 minutes and then filtered off. The filtrate was cooled down to 0 °C and 150 ml of 12 M HCl solution were added to give a pH of 1. The precipitate was filtered off and washed with ice cold water. 10.4 g (56.8 mmol, 30%) of were obtained as a brown solid.

Chelidamic acid: C₇H₅NO₅ (183.12 g/mol).

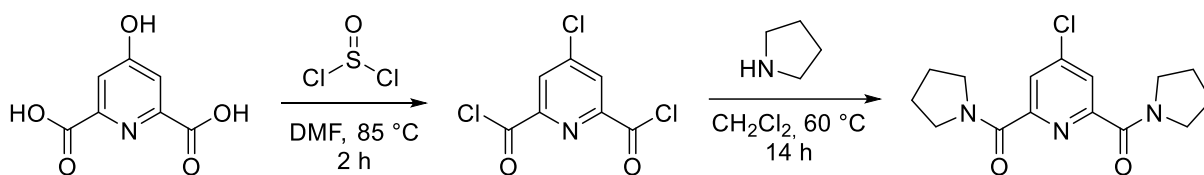
Yield: 10.4 g (56.8 mmol, 30%)

Habitus Brown solid.

¹H NMR: (300 MHz, DMSO-d₆): δ (ppm) = 7.56 (s, 2H, H-3).

¹³C NMR: (75 MHz, DMSO-d₆): δ (ppm) = 165.3 (C-1), 149.2 (C-2), 114.7 (C-3).

5.4.15. Synthesis of (4-chloropyridine-2,6-diyl)bis(pyrrolidine-1-ylmethanone)



At 0 °C 82.4 ml (1.14 mol, 20 eq.) thionyl chloride were added dropwise to a mixture of 10.4 g (56.8 mmol, 1 eq.) chelidamic acid and 5 ml dimethylformamide. The reaction mixture was allowed to warm to ambient temperature and was then refluxed for 2 hours. At ambient temperature, the excess thionyl chloride was removed under reduced pressure and the reaction mixture was washed several times with CH₂Cl₂ to remove all traces of thionyl chloride. Without further purification 4-chloropyridine-2,6-dicarbonyldichloride was dissolved in 35 ml of CH₂Cl₂. 46.6 ml (284 mmol, 10.0 eq.) pyrrolidine dissolved in 65 ml CH₂Cl₂ were added dropwise at 0 °C. The reaction mixture was stirred over night at 60 °C. At 0 °C 200 ml of 5% HCl were added. After filtration, the phases were separated, and the aqueous phase was extracted three times with CH₂Cl₂. The combined organic phases were washed with water and dried over Na₂SO₄. After filtration, removal of the solvent under reduced pressure and washing with *n*-hexane 9.60 g (31.3 mmol, 55%) of (4-chloropyridine-2,6-diyl)bis(pyrrolidine-1-ylmethanone) were obtained as a brown solid.

4-Cl-2,6dpp: C₁₅H₁₈ClN₃O₂ (307.78 g/mol).

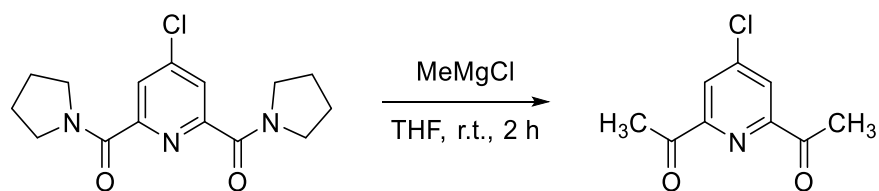
Yield: 9.60 g (31.3 mmol, 55%).

Habitus Brown solid.

¹H NMR: (300 MHz, DMSO-d₆): δ (ppm) = 7.87 (s, 2H, H-2), 3.55-3.48 (m, 8H, H-5), 1.88-1.82 (m, 8H, H-6).

¹³C NMR: (75 MHz, DMSO-d₆): δ (ppm) = 163.9 (C-4), 154.6 (C-1), 144.7 (C-3), 124.1 (C-2), 48.3 (C-5), 46.4 (C-5), 26.0 (C-6), 23.5 (C-6).

5.4.16. Synthesis of 4-chloro-2,6-diacetylpyridine



4.06 g (13.2 mmol, 1.00 eq.) (4-chloropyridine-2,6-diyl)bis(pyrrolidin-1-ylmethanone) were dissolved in 30 ml anhydrous THF and cooled to 0 °C. 11.0 ml methyl magnesium chloride (3 M in Et₂O) was added dropwise. Afterwards, the reaction mixture was allowed to warm to ambient temperature and was stirred for 2 h. After quenching the solution with 100 ml 2 M HCl, the phases were separated, and the aqueous phase was extracted three times with CH₂Cl₂. The combined organic phases were washed with brine and dried over Na₂SO₄. After removal of the solvent under reduced pressure and column chromatographic purification on silica gel with cHex/EtOAc 10:1 410 mg (2.50 mmol, 19%) of were obtained as a beige solid.

4-Cl-2,6dap: C₉H₈ClNO₂ (197,62 g/mol).

Yield: 410 mg (2.50 mmol, 19%).

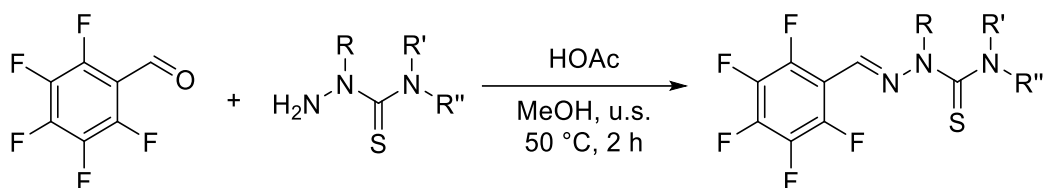
Habitus Beige solid.

¹H NMR: (300 MHz, DMSO-d₆): δ (ppm) = 8.17 (s, H₂, H-2), 2.73 (s, H₆, H-5).

¹³C NMR: (75 MHz, DMSO-d₆): δ (ppm) = 198.1 (C-4), 154.2 (C-3), 146.3 (C-1), 124.8 (C-2), 26.0 (C-5).

5.5. Synthesis of thiosemicarbazones

5.5.1. Synthesis of fluorinated thiosemicarbazones



1 eq. of pentafluorobenzaldehyde were diluted in 20 mL MeOH and 0.1 mL acetic acid were added prior to the corresponding thiosemicarbazide. The mixture was sonicated for 2 h at 60 °C, during that time a solid formed which was filtered off and the filtrate was refrigerated. Overnight a crystalline precipitate formed which was filtered and washed with cold MeOH yielding the product as colourless crystals.

5.5.1.1. Synthesis of HFbzTSC

HFbzTSC:	$\text{C}_8\text{H}_4\text{F}_5\text{N}_3\text{S}$ (269.19 g/mol).	 <chem>Fc1c(F)c(F)c(F)c1C=N-NH-C(=S)-NH2</chem>
Yield:	2.19 g (8.13 mmol, 75%).	
Habitus	colourless solid.	
¹H NMR:	(300 MHz, DMSO- <i>d</i> ₆): δ (ppm) = 11.80 (s, 1H), 8.52 (s, 1H), 8.14 (s, 1H), 7.46 (s, 1H).	
¹³C NMR:	(75 MHz, DMSO- <i>d</i> ₆): δ (ppm) = 178.91, 130.81.	
¹⁹F NMR:	(282 MHz, DMSO- <i>d</i> ₆) δ (ppm) = -141.72 – -142.50 (m, 2F), -153.45 (t, <i>J</i> = 22.2 Hz, 1F), -162.75 (td, <i>J</i> = 21.8, 6.6 Hz, 2F).	
EI-MS (+)	[<i>m/z</i>] = 269 (calc. 269).	

5.5.1.2. Synthesis of HFbzTSCm

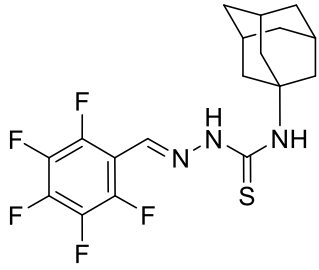
HFbzTSCm:	$\text{C}_9\text{H}_6\text{F}_5\text{N}_3\text{S}$ (283.22 g/mol).	 <chem>Fc1c(F)c(F)c(F)c1C=N-NH-C(=S)-N(CH3)</chem>
Yield:	1.73 g (6.1 mmol, 64%).	
Habitus	colourless solid.	
¹H NMR:	(300 MHz, DMSO- <i>d</i> ₆): δ (ppm) = 11.83 (s, 1H), 8.35 – 7.91 (m, 1H), 3.01 (d, <i>J</i> = 4.6 Hz, 3H).	
¹³C NMR:	(75 MHz, DMSO- <i>d</i> ₆): δ (ppm) = 1177.93, 129.63, 31.10.	
¹⁹F NMR:	(282 MHz, DMSO- <i>d</i> ₆) δ (ppm) = -141.96 (dd), -153.64 (t, <i>J</i> = 22.2 Hz), -162.85 (td, <i>J</i> = 22.1, 6.9 Hz).	
EI-MS (+)	[<i>m/z</i>] = 283 (calc. 283).	

5.5.1.3. Synthesis of HFbzTSCdm

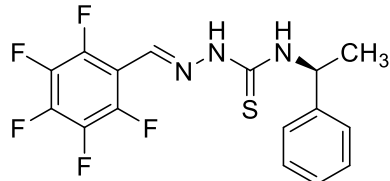
HFbzTSCdm:	$\text{C}_{10}\text{H}_8\text{F}_5\text{N}_3\text{S}$ (297.25 g/mol).	 <chem>Fc1c(F)c(F)c(F)c1C=N-NH-C(=S)-N(CH3)2</chem>
Yield:	1.77 g (5.96 mmol, 72%).	

Habitus	yellow solid.
¹H NMR:	(300 MHz, DMSO- <i>d</i> ₆): δ (ppm) = 11.26 (s, 1H), 8.24 (s, 1H), 3.29 (s, 6H).
¹³C NMR:	(75 MHz, DMSO- <i>d</i> ₆): δ (ppm) = 180.46, 130.78, 42.53.
¹⁹F NMR:	(282 MHz, DMSO- <i>d</i> ₆) δ (ppm) = -142.51 – -143.49 (m, 2F), -154.36 (t, <i>J</i> = 22.2 Hz, 1F), -162.89 (td, <i>J</i> = 22.4, 7.3 Hz, 2F)
EI-MS (+)	[<i>m/z</i>] = 297 (calc. 297).

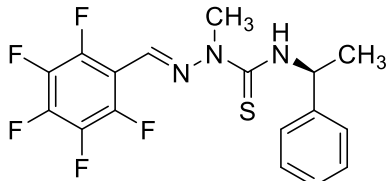
5.5.1.4. Synthesis of HFbzTSCAd

HFbzTSCAd:	C ₁₈ H ₁₈ F ₅ N ₃ S (403.42 g/mol).	
Yield:	0.35 g (0.86 mmol, 98%).	
Habitus	colourless solid.	
¹H NMR:	(300 MHz, DMSO- <i>d</i> ₆): δ (ppm) = 11.72 (s, 1H), 8.12 (s, 1H), 7.45 (s, 1H), 2.25 (d, <i>J</i> = 17.9 Hz, 6H), 2.08 (s, 4H), 1.66 (s, 6H).	
¹⁹F NMR:	(282 MHz, DMSO- <i>d</i> ₆) δ (ppm) = -143.13 (d, <i>J</i> = 21.3 Hz), -153.59 (t, <i>J</i> = 22.1 Hz), -161.88 – -163.33 (m).	
HR-ESI-MS (+)	[<i>m/z</i>] = [M+H] ⁺ 404.12131 (calc. 404.12143), [M+Na] ⁺ 426.10334 (calc. 426.10338).	

5.5.1.5. Synthesis of HFbzTSCmB

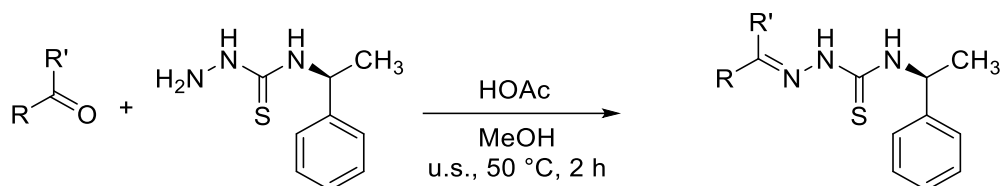
HFbzTSCmB:	C ₁₆ H ₁₂ F ₅ N ₃ S (373.35 g/mol).	
Yield:	0.58 g (1.55 mmol, 76%).	
Habitus	colourless solid.	
¹H NMR:	(300 MHz, DMSO- <i>d</i> ₆): δ (ppm) = 11.99 (s, 1H), 9.33 (s, 1H), 8.39 – 7.99 (m, 1H), 7.46 – 7.14 (m, 5H), 5.71 – 5.39 (m, 1H), 1.53 (d, <i>J</i> = 6.9 Hz, 2H).	
¹⁹F NMR:	(282 MHz, DMSO- <i>d</i> ₆) δ (ppm) = -142.42 (dd, <i>J</i> = 22.9, 7.5 Hz), -153.37 (t, <i>J</i> = 22.2 Hz), -162.57 (td, <i>J</i> = 22.6, 7.3 Hz).	
HR-ESI-MS (+)	[<i>m/z</i>] = [M+H] ⁺ 374.07439 (calc. 374.07448), [M+Na] ⁺ 396.05629 (calc. 396.05643).	

5.5.1.6. Synthesis of HFbz(m)TSCmB

HFbzTSCmB:	C ₁₇ H ₁₄ F ₅ N ₃ S (385.08 g/mol).	
Yield:	0.65 g (1.68 mmol, 88%).	
Habitus	colourless solid.	
¹H NMR:	(300 MHz, DMSO- <i>d</i> ₆): δ (ppm) = 8.70 (d, <i>J</i> = 8.3 Hz, 1H), 7.80 (s, 1H), 7.35 (d, <i>J</i> = 4.3 Hz, 4H), 7.31 – 7.22 (m, 1H), 5.59 – 5.39 (m, 1H), 3.81 (s, 3H), 1.52 (d, <i>J</i> = 6.9 Hz, 3H).	

¹³C NMR:	(DMSO- <i>d</i> ₆ , 75 MHz) δ [ppm] = 178.60, 143.11, 128.48, 127.38, 127.12, 125.94, 54.17, 32.62, 22.06.
¹⁹F NMR:	(282 MHz, DMSO- <i>d</i> ₆) δ (ppm) = -142.48 – -143.66 (m), -153.34 (t, <i>J</i> = 22.3 Hz), -162.36 (td, <i>J</i> = 21.4, 6.1 Hz).
HR-ESI-MS (+)	[<i>m/z</i>] = [M+H] ⁺ 388.09011 (calc. 388.09014), [M+Na] ⁺ 410.07196 (calc. 410.072080).

5.5.2. Synthesis of the Thiosemicarbazones from TSCmB



1 equivalent of aldehyde or ketone and 1 equivalent of thiosemicarbazide were dissolved in MeOH and 0.1 mL of acetic acid were added. The solution was sonicated at 60 °C for 2 hours. The precipitate was filtrated and washed with cold MeOH to yield the desired thiosemicarbazone.

5.5.2.1. Synthesis of HfpyTSCmB

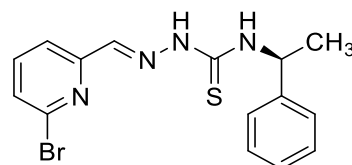
HfpyTSCmB was synthesized using the procedure described in chapter 5.5.2. using 2-formylpyridine as aldehyde.

HfpyTSCmB:	C ₁₅ H ₁₆ N ₄ S (284.38 g/mol).	
Yield:	1.37 g (4.82 mmol, > 99%).	
¹H NMR:	(DMSO- <i>d</i> ₆ , 300 MHz) δ [ppm] = 11.77 (s, 1H, MH-9), 8.76 (d, 1H, <i>J</i> = 8.6 Hz), 8.57 (d, 1H, <i>J</i> = 4.2 Hz), 8.31 (d, 1H, <i>J</i> = 7.9 Hz), 8.76 (s, 1H, H-10), 7.85 (t, 1H, <i>J</i> = 7.3 Hz), 7.32 – 7.44 (m, 5H), 7.24 (t, 1H, <i>J</i> = 7.1 Hz), 5.75 (qui, 1H, <i>J</i> = 6.8 Hz, H-1), 1.58 (s, 1H, H-6).	
¹³C NMR:	(DMSO- <i>d</i> ₆ , 75 MHz) δ [ppm] = 176.7 (s, C-8), 153.2 (s, C-11), 149.4 (d, C-10), 143.7 (s, C-2), 142.9 (d), 136.5 (d), 128.2 (d, 2C), 126.7 (d), 126.3 (d, 2C), 124.2 (d), 120.4 (d), 52.5 (d, C-1), 21.2 (s, C-6).	

5.5.2.2. Synthesis of H6-BrfpyTSCmB

HBrfpyTSCmB was synthesized using the procedure described in chapter 5.5.2. using 6-bromo 2-formylpyridine as aldehyde. The crude product was purified by column chromatography (SiO₂, v:v=1:2 EtOAc/*c*-Hex).

H6-BrfpyTSCmB:	C ₁₅ H ₁₅ BrN ₄ S (363.28 g/mol).
Yield:	0.12 g (0.33 mmol, 62%).
Habitus	Yellow solid.
R_f	0.35 (1:2 EtOAc/ <i>c</i> -Hex).



¹H NMR: (300 MHz, CDCl₃): δ (ppm) = 13.59 (s, 1H), 9.25 (s, 1H), 7.78 (d, *J* = 1.0 Hz, 1H), 7.68 (dt, *J* = 7.8, 3.4 Hz, 1H), 7.58 (t, *J* = 7.8 Hz, 1H), 7.48 (dd, *J* = 7.9, 1.0 Hz, 1H), 7.45 – 7.27 (m, 4H), 5.81 – 5.68 (m, 1H), 1.68 (d, *J* = 6.9 Hz, 3H).

¹³C NMR: (75 MHz, CDCl₃) δ [ppm] = 177.04, 153.53, 140.67, 138.87, 128.94, 127.80, 126.49, 119.34, 53.80, 21.48.

5.5.2.3. Synthesis of H6-phfpyTSCmB

HphfpyTSCmB was synthesized using the procedure described in chapter 5.5.2. using 6-phenyl 2-formylpyridine as aldehyde. The crude product was purified by column chromatography (SiO₂, v:v=1:2 EtOAc/c-Hex).

H6-PhfpyTSCmB: C₂₁H₂₀N₄S (360.48 g/mol).

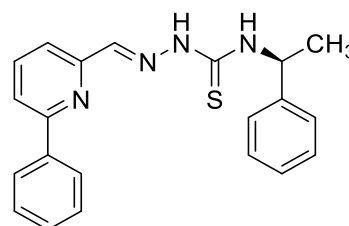
Yield: 0.23 g (0.64 mmol, 84%).

Habitus Yellow solid.

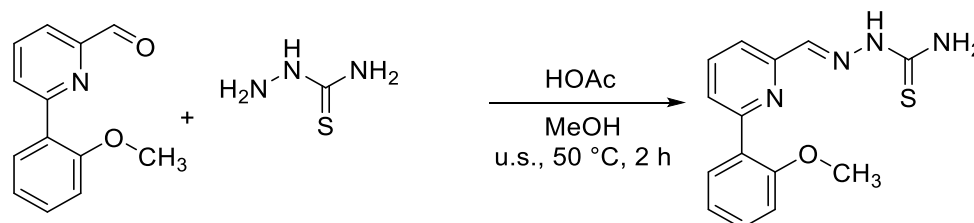
R_f 0.35 (1:2 EtOAc/c-Hex).

¹H NMR: (300 MHz, CDCl₃): δ (ppm) = 10.86 (s, 0H), 9.05 (s, 1H), 8.05 – 7.97 (m, 2H), 7.93 (d, *J* = 1.0 Hz, 1H), 7.81 – 7.75 (m, 2H), 7.73 (dd, *J* = 6.0, 3.0 Hz, 1H), 7.55 – 7.30 (m, 7H), 5.84 – 5.67 (m, 1H), 1.70 (d, *J* = 7.0 Hz, 3H).

¹³C NMR: (75 MHz, CDCl₃) δ [ppm] = 143.08, 137.37, 129.53, 128.95, 127.76, 127.06, 126.49, 121.29, 118.85, 53.77, 27.07.



5.5.2.4. Synthesis of HmphfpyTSC



0.5 g (2.34 mmol, 1 eq.) of 6-(methoxyphenyl) 2-formyl pyridine, 0.1 mL acetic acid and 0.23 g (2.5 mmol, 1.1 eq.) thiosemicarbazide were dissolved in 20 mL MeOH and sonicated at 60 °C for 2 h. The solvent was removed, and the crude product was purified by column chromatography (c-Hex:EtOAc = 1:1) yielding a yellow solid.

HmphfpyTSC: C₁₄H₁₄N₄OS (286.35 g/mol).

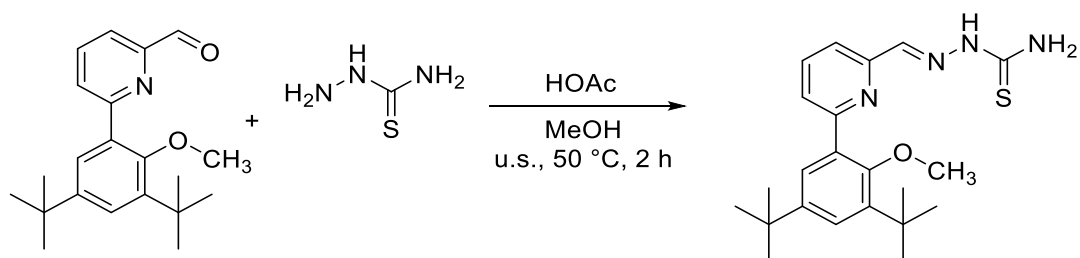
Yield: 660 mg (2.23 mmol, 95%).

R_f: 0.45 (c-Hex:EtOAc = 1:1).

¹H NMR: (CDCl₃, 300 MHz) δ [ppm] = 14.91 (s, 1H), 9.14 (s, 1H), 8.03 – 7.94 (m, 3H), 7.91 – 7.82 (m, 2H), 7.82 – 7.69 (m, 3H), 7.48 – 7.30 (m, 4H), 7.23 – 7.16 (m, 2H), 7.10 (td, *J* = 7.5, 1.1 Hz, 1H), 7.06 – 6.99 (m, 2H), 6.30 (d, *J* = 43.1 Hz, 2H), 3.89 (d, *J* = 12.1 Hz, 3H).

¹³C NMR: (CDCl₃, 75 MHz) δ [ppm] = 144.60, 137.39, 136.31, 134.55, 131.67, 131.18, 130.56, 126.37, 125.96, 123.58, 121.76, 121.32, 118.59, 111.62, 55.98.

5.5.2.5. Synthesis of Hm(tBu)phfpyTSC



0.2 g (0.6 mmol, 1 eq.) of 6-(2-methoxy 3,5-ditertbutyl phenyl) 2-formyl pyridine, 0.1 mL acetic acid and 0.07 g (0.77 mmol, 1.2 eq.) thiosemicarbazide were dissolved in 20 mL MeOH and sonicated at 60 °C for 2 h. The solvent was removed, and the crude product was purified by column chromatography (c-Hex:EtOAc = 1:1) yielding a pale-yellow solid.

Hm(tBu)phfpyTSCmB: C₂₂H₃₀N₄OS (398.21 g/mol).
Yield: 72 mg (0.18 mmol, 30%).
R_f: 0.5 (c-Hex:EtOAc = 1:1).
¹H NMR: (CDCl₃, 300 MHz) δ [ppm] = 9.25 (s, 1H), 8.03 (s, 1H), 7.89 – 7.73 (m, 3H), 7.52 – 7.43 (m, 2H), 7.33 (s, 1H), 6.44 (s, 1H), 3.34 (s, 3H), 1.46 (s, 9H), 1.36 (s, 9H).
¹³C NMR: (CDCl₃, 75 MHz) δ [ppm] = 146.05, 144.47, 136.76, 126.40, 126.07, 125.34, 118.56, 61.58, 31.66, 31.06.

5.5.2.6. Synthesis of H₂hphfpyTSC

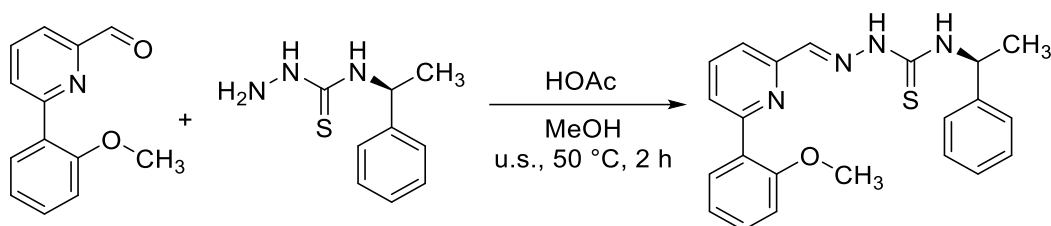


100 mg (0.25 mmol, 1 eq.) of the methoxyphenyl derivative were dissolved in 30 mL dry CH₂Cl₂. 0.35 mL (0.35 mmol, 1.4 eq.) 1 M solution of BBr₃ in CH₂Cl₂ was slowly added to the solution. The mixture was stirred at ambient temperature overnight. 50 mL water were slowly added to the reaction and the bilayer mixture was extracted with DCM. The combined organic phases were dried over Na₂SO₄, and the solvent was evaporated yielding a pale-yellow solid.

H2(tBu)hphfyTSCmB: C₂₁H₂₈N₄OS (384.54 g/mol).
Yield: 72 mg (0.19 mmol, 76%).
¹H NMR: (CDCl₃, 300 MHz) δ [ppm] = 14.53 (s, 1H), 9.28 (s, 1H), 7.96 (d, *J* = 8.2 Hz, 1H), 7.91 (s, 1H), 7.87 (d, *J* = 8.1 Hz, 1H), 7.66 (d, *J* = 2.4 Hz, 1H), 7.61 (dd, *J* = 7.5, 1.0 Hz, 1H), 7.44 (d, *J* = 2.4 Hz, 1H), 6.42 (s, 1H), 5.30 (s, 1H), 1.48 (s, 9H), 1.36 (s, 9H).

HR-ESI MS [M+H]⁺ 385.20533 (calc. 385.20565)
[M+Na]⁺ 407.18732 (calc. 407.18760).

5.5.2.7. Synthesis of HmphfyTSCmB



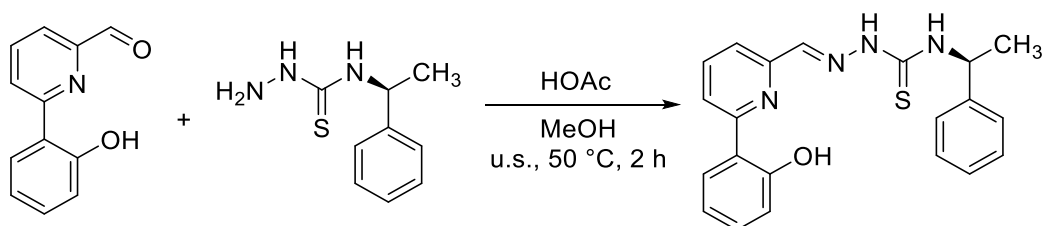
300 mg aldehyde (1.40 mmol, 1.0 eq.) were dissolved in 1.0 ml MeOH and 272 mg thiosemicarbazide (1.40 mmol, 1.0 eq.) in 2.0 ml MeOH and 0.1 ml HOAc were added. Then added in an ultra-sonic bath at 50°C for 1 h and cooled to rt. The solvent was removed, and the crude product was purified by column chromatography over silica (c-hex:EtOAc). The product (320 mg, 0.82 mmol, 59%) was isolated as a yellow oil.

HmphfyTSCmB: C₂₂H₂₂N₄OS (390.51 g/mol).
Yield: 320 mg (0.82 mmol, 59%).
R_f: 0.4 (c-Hex:EtOAc = 2:1).
¹H NMR: (CDCl₃, 300 MHz) δ [ppm] = 8.09 – 7.90 (m, 1H, arom.), 7.88 – 7.72 (m, 3H, arom.), 7.48 – 7.23 (m, 6H, arom.), 7.13 – 6.96 (m, 2H, arom.), 5.77 (dt, *J*=8.5, 6.5, 1H, NCH), 4.12 (q, *J*=7.1, 1H, CH), 3.86 (d, *J*=9.9, 3H, -OMe), 1.66 (dd, *J*=10.7, 7.0, 3H, CH₃).

¹³C NMR: (CDCl₃, 75 MHz) δ [ppm] = 143.3, 137.1, 136.1, 133.0, 131.6, 131.1, 131.0, 130.3, 128.8, 128.6, 128.6, 127.5, 127.3, 126.4, 125.9, 125.5, 123.2, 121.6, 118.4, 60.4, 26.9.

EI MS (70 eV) [m/z] = 390 [M⁺].

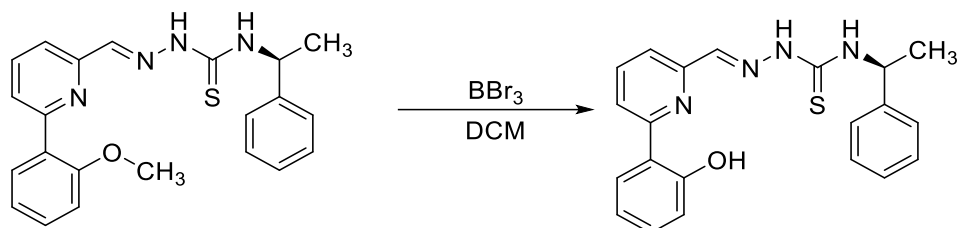
5.5.2.8. Synthesis of H₂hphfyTSCmB



27 mg aldehyde (0.1 mmol, 1.0 eq.) were dissolved in 1.0 ml MeOH and 27 mg thiosemicarbazide (0.1 mmol, 1.0 eq.) in 2.0 ml MeOH and 0.1 ml HOAc were added. Then added in an ultra-sonic bath at 50°C for 1 h and cooled to rt. The solvent was

removed, and the crude product was purified by column chromatography over silica (c-hex:EtOAc, v:v = 1:1). The product (27.7 mg, 0.07 mmol, 51%) was isolated as a yellow solid.

5.5.2.9. Synthesis of H₂hphfpyTSCmB by deprotection



330 mg of the 2-methoxy-phenyl thiosemicarbazone (0.85 mmol) was dissolved in 5 mL CH₂Cl₂. 160 μL (426 mg, 1.7 mmol) BBr₃ were added slowly at ambient temperature. The mixture was stirred for 22 h and slowly quenched with 20 mL H₂O. The aqueous layer was extracted with CH₂Cl₂, and the combined organic phases were dried over Na₂SO₄. The crude product was purified by column chromatography (silica; c-hex:EtOAc v:v = 1:1) yielding a yellow solid.

HhphfpyTSCmB: C₂₁H₂₀N₄OS (376.48 g/mol).

Yield: 201 mg (0.53 mmol, 62%).

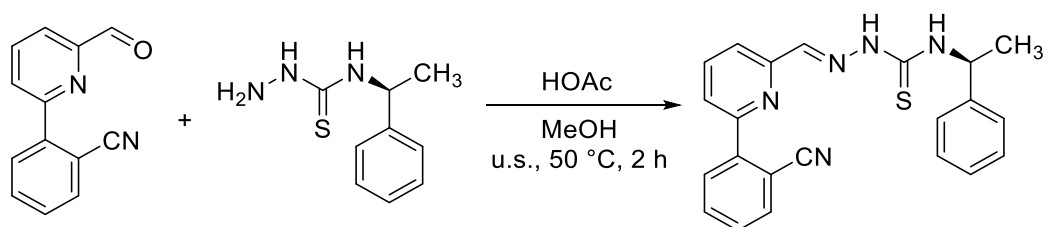
R_f: 0.29 (c-Hex:EtOAc = 2:1).

¹H NMR: (CDCl₃, 300 MHz) δ [ppm] = 10.42 (s, 1H), 8.03 (d, J=8.5, 1H), 7.90 – 7.76 (m, 4H), 7.56 – 7.48 (m, 2H), 7.42 – 7.21 (m, 5H), 7.03 (dd, J=8.3, 1.3, 1H), 6.91 (ddd, J=8.3, 7.2, 1.3, 1H), 5.83 – 5.61 (m, 1H), 1.73 (d, J=6.9, 3H, CH₃).

¹³C NMR: (CDCl₃, 75 MHz) δ [ppm] = 176.64, 160.63, 157.96, 148.11, 142.67, 138.41, 137.99, 131.97, 128.73, 127.47, 126.54, 126.26, 120.63, 119.34, 118.88, 118.70, 118.17, 53.98, 22.28.

EI-MS (70 eV) [m/z] = 376 [M⁺].

5.5.2.10. Synthesis of HcphfpyTSCmB



68 mg aldehyde (1.40 mmol, 1.0 eq.) were dissolved in 1.0 ml MeOH and 71 mg of the thiosemicarbazide (1.40 mmol, 1.0 eq.) in 2.0 ml MeOH and 0.1 ml HOAc were added. Then added in an ultra-sonic bath at 50°C for 1 h and cooled to rt. The solvent was removed, and the crude product was purified by column chromatography over

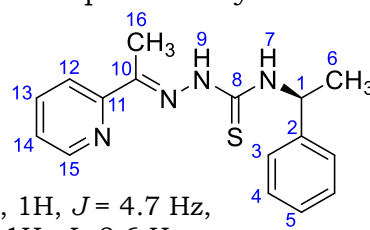
silica (*c*-hex:EtOAc, 1:1 + Et₃N). The product (121 mg, 0.31 mmol, 83%) was isolated as a yellow solid.

HcphfpyTSCmB: C₂₂H₂₂N₄OS (385.49 g/mol).
Yield: 121 mg (0.07 mmol, 51%).
R_f: 0.63 (*c*-Hex:EtOAc = 1:1).
¹H NMR: (CDCl₃, 300 MHz) δ [ppm] = 9.91 (s, 1H), 8.03 (s, 1H), 8.02 – 7.96 (m, 1H), 7.92 – 7.68 (m, 6H), 7.58 – 7.44 (m, 3H), 7.44 – 7.25 (m, 3H), 1.71 (d, *J*=7.0, 3H).
¹³C NMR: (CDCl₃, 75 MHz) δ [ppm] = 138.40, 138.11, 134.38, 134.01, 133.80, 133.02, 131.91, 130.87, 129.99, 129.71, 129.39, 128.64, 127.39, 127.11, 126.38, 124.68, 123.76, 120.89, 60.38.
EI-MS (70 eV) [*m/z*] = 385 [M⁺].

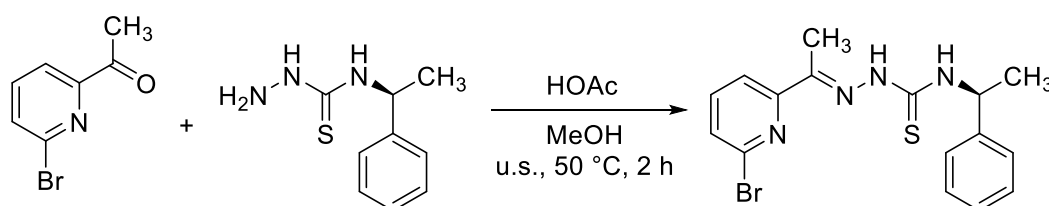
5.5.2.11. Synthesis of HapyTSCmB

HapyTSCmB was synthesized using the procedure described in chapter 5.5.2. using 2-acetylpyridine as ketone. The crude product was purified by column chromatography (SiO₂, *v:v*=1:2 EtOAc/*c*-Hex).

HapyTSCmB: C₁₆H₁₈N₄S (298.41 g/mol).
Yield: 0.91 g (3.1 mmol, 74%).
¹H NMR: (DMSO-*d*₆, 300 MHz) δ [ppm] = 10.41 (s, 1H, NH-9), 8.70 (d, 1H, *J* = 8.8 Hz, NH-7), 8.59 (d, 1H, *J* = 4.7 Hz, H-15), 8.34 (d, 1H, *J* = 8.1 Hz, H-12), 7.84 (t, 1H, *J* = 8.6 Hz, H-13), 7.32 – 7.44 (m, 5H, H-3 – H-5), 7.24 (t, 1H, *J* = 7.2 Hz, H-14), 5.76 (qui, 1H, *J* = 7.0 Hz, H-1), 2.41 (s, 3H, H-16), 1.58 (d, 3H, *J* = 7.0 Hz, H-6).
¹³C NMR: (DMSO-*d*₆, 75 MHz) δ [ppm] = 177.6 (s, C-8), 154.6 (s, C-10), 148.8 (s, C-11), 148.5 (d, C-15), 143.6 (s, C-2), 136.5 (d, C-13), 128.2 (d, 2C), 126.7 (d, C-14), 126.3 (d, 2C), 124.0 (d, C-5), 120.9 (d, C-12), 52.7 (d, C-1), 21.3 (q, C-6), 12.4 (q, C-16).



5.5.2.12. Synthesis of H6-BrapyTSCmB



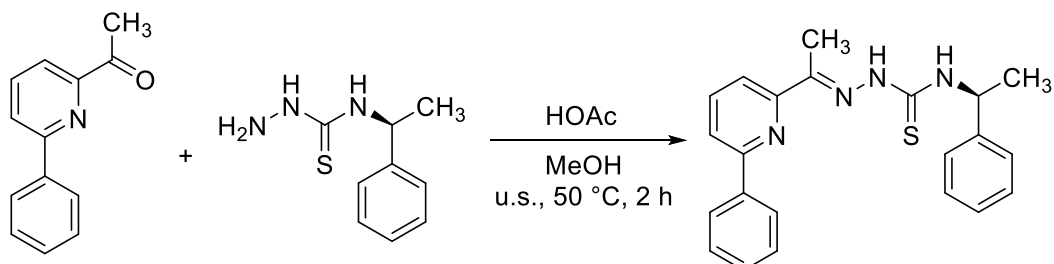
500 mg (2.50 mmol, 1.0 eq.) aldehyde dissolved in 3 ml MeOH. 488 mg (2.50 mmol, 1.0 eq.) thiosemicarbazide in 3 ml MeOH and 0.3 ml HOAc added. The reaction mixture immediately turned yellow and was put in an ultrasonic bath at 50 °C for 1 h. The mixture was cooled in the freezer, the solid was filtered of and washed with MeOH. The product (103 mg, 0.284 mmol, 11 %) was isolated as a yellow solid.

H6-BrapyTSCmB: C₁₅H₁₅BrN₄S (363.28 g/mol).
Yield: 103 mg (0.284 mmol, 11%).

¹H NMR: (300 MHz, CDCl₃) δ (ppm) = 8.18 (dd, 2H, *J* = 7.7, 1.0, H-3;5), 7.61 (t, 2H, *J* = 7.8, H-4), 7.55-7.35 (m, 5H, H-12-15), 2.31 (s, 3H, H-7), 1.68 (d, 1H, *J* = 6.9, H-9), 1.56 (s, 3H, H-10).

¹³C NMR: (75 MHz, CDCl₃) δ (ppm) = 141.09, 138.52, 128.79, 128.46, 126.25, 119.91, 53.55, 13.91

5.5.2.13. Synthesis of H6-phapyTSCmB



350 mg (1.77 mmol, 1.0 eq.) ketone dissolved in 1 ml MeOH. 347 mg (1.77 mmol, 1.0 eq.) TSCmB in 3 ml MeOH and 0.2 ml HOAc added. The reaction mixture turned yellow and was sonicated at 50 °C for 1 h. The mixture was cooled in the freezer, the solid was filtered off and washed with diethyl ether. The product (370 mg, 1.03 mmol, 58 %) was isolated as a pale-yellow solid.

H6-PhapyTSCmB: C₂₁H₂₀N₄S (360.48 g/mol).

Yield: 370 mg (1.03 mmol, 58%).

¹H NMR: (300 MHz, CDCl₃) δ (ppm) = 8.10 – 8.02 (m, 1H, H-4), 7.84 – 7.73 (m, 1H, H-3;5), 7.52 – 7.31 (m, 10H, H-11-14; H-15-18), 3.48 (s, 3H, H-7), 2.53 (s, 1H, H-9), 1.70 (s, 3H, H-10).

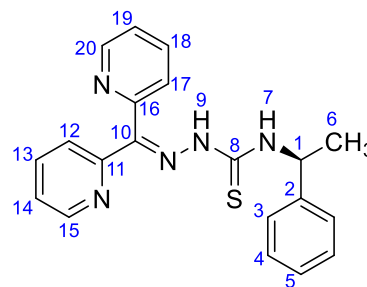
¹³C NMR: (75 MHz, CDCl₃) δ (ppm) = 137.12, 130.00, 129.26, 128.79, 128.61, 127.53, 127.50, 126.79, 126.44, 126.33, 126.25, 120.38, 118.49, 53.48, 50.83, 21.63, 11.52.

5.5.2.14. Synthesis of HdpyTSCmB

HdpyTSCmB was synthesized using the procedure described in chapter 5.5.2. using 6-bromo 2-formylpyridines as ketone. The crude product was purified by column chromatography (SiO₂, v:v=1:2 EtOAc/c-Hex).

HdpyTSCmB: C₂₀H₁₉N₅S (361.47 g/mol).

Yield: 1.30 g (3.60 mmol, 66%).



¹H NMR: (DMSO-*d*₆, 300 MHz) δ [ppm] = 13.31 (s, 1H, NH-9), 8.97 (d, 1H, *J* = 8.7 Hz, NH-7), 8.82 (d, 1H, *J* = 4.2 Hz), 8.58 (d, 1H, *J* = 4.6 Hz), 8.21 (d, 1H, *J* = 7.9 Hz), 7.94 – 8.01 (m, 2H), 7.55 – 7.59 (m, 1H), 7.41 – 7.49 (m, 4H), 7.34 (t, 2H, *J* = 7.4 Hz), 7.24 (t, 1H, *J* = 7.2 Hz), 5.71 (qui, *J* = 7.1 Hz, 1H, H-1), 1.59 (d, 3H, *J* = 7.0 Hz, H-6).

¹³C NMR: (DMSO-*d*₆, 75 MHz) δ [ppm] = 177.45 (C-8), 155.46 (C-16), 151.56 (C-11), 148.84 (C-12), 148.59 (C-17), 143.76 (C-2), 138.01 (C-20), 137.59 (C-15), 128.70 (C-4), 127.56 (C-5), 127.29 (C-19), 127.08 (C-14), 126.76 (C-3), 125.19 (C-10), 124.37 (C-13), 124.31 (C-18), 53.57 (C-1), 21.54 (C-6).

5.5.2.15. Synthesis of H₂bzTSCmB

H₂bzTSCmB was synthesized using the procedure described in chapter 5.5.2. using benzaldehyde as aldehyde.

H₂bzTSCmB C₁₆H₁₇N₃S (283.39 g/mol).

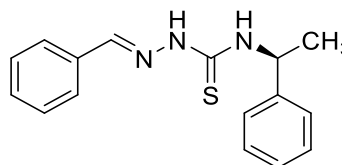
Yield: 1.09 g (3.85 mmol, 82%).

Habitus: Yellow solid.

EI-MS (70 eV): [m/z]: 283 ([M]⁺), 177, 120, 106, 105.

¹H NMR: (DMSO-*d*₆, 300 MHz) δ [ppm] = 11.56 (s, 1H, NH-9), 8.60 (d, 1H, *J* = 8.9 Hz, MH-7), 8.10 (s, 1H, H-10), 7.81 – 7.84 (m, 2H, H-12), 7.41 – 7.44 (m, 5H, H-3 – H-5), 7.34 (t, 2H, *J* = 7.5 Hz, H-13), 7.24 (t, 2H, *J* = 7.5 Hz, H-14), 5.74 (qui, *J* = 7.0 Hz, 1H, H- 1), 1.57 (d, 3H, *J* = 7.0 Hz, H-6).

¹³C NMR: (DMSO-*d*₆, 75 MHz) δ [ppm] = 176.4 (s, C-8), 143.8 (s), 142.6 (d, C-10), 134.1 (s), 129.9 (d), 128.7 (d), 128.2 (d), 127.4 (d), 126.7 (d), 126.3 (d), 52.4 (d, C-1), 21.3 (s, C-6).



5.5.2.16. Synthesis of H₂aphTSCmB

H₂aphTSCmB was synthesized using the procedure described in chapter 5.5.2. using acetophenone as ketone.

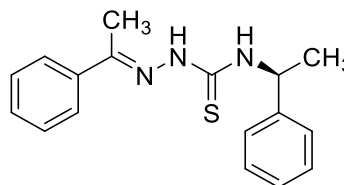
H₂aphTSCmB C₁₇H₁₉N₃S (297.42 g/mol).

Yield: 0.22 g (0.73 mmol, 29%).

Habitus: Yellow solid.

¹H NMR: (DMSO-*d*₆, 300 MHz) δ [ppm] = 10.32 (1H, s, NH), 8.81 (1H, *J* = 9 Hz, d, NH), 7.90-7.87 (2H, m, Ar-H), 7.43-7.40 (5H, m, Ar-H), 7.34 (2H, *J* = 8 Hz, t, Ar-H), 7.24 (2H, *J* = 8 Hz, d, Ar-H), 5.72 (1H, *J* = 8 Hz, quint, CH), 2.33 (3H, s, CH₃), 1.57 (3H, *J* = 7 Hz, d, CH₃)

¹³C NMR: (DMSO-*d*₆, 75 MHz) δ [ppm] = 177.92 (NCS), 149.00 (NCC), 144.18 (Ar-C), 138.13 (Ar-C), 129.74 (Ar-C), 128.80 (Ar-C), 128.71 (Ar-C), 127.22 (Ar-C), 127.07 (Ar-C), 126.70 (Ar-C), 53.04 (NCC), 21.87 (CH₃), 14.85 (CH₃).



5.5.2.17. Synthesis of H₂bphTSCmB

H₂bphTSCmB was synthesized using the procedure described in chapter 5.5.2. using benzophenone as ketone.

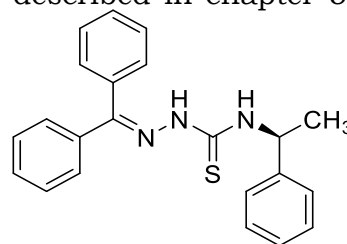
H₂bphTSCmB C₂₂H₂₁N₃S (359.49 g/mol).

Yield: 0.22 g (0.73 mmol) 24%.

Habitus: Yellow solid.

¹H NMR: (DMSO-*d*₆, 300 MHz) δ [ppm] = 8.97 (1H, *J* = 9 Hz, d, NH), 8.62 (1H, s, NH), 7.66-7.61 (5H, m, Ar-H), 7.46-7.23 (10H, m, Ar-H), 5.69 (1H, *J* = 7 Hz, quint, CH), 1.60 (3H, *J* = 7 Hz, d, CH₃).

¹³C NMR: (DMSO-*d*₆, 75 MHz) δ [ppm] = 176.90 (NCS), 149.98 (NCC), 143.85 (Ar-C), 136.81 (Ar-C), 133.15 (Ar-C), 131.92 (Ar-C), 130.47 (Ar-C), 130.27 (Ar-C), 128.84 (Ar-C), 128.71 (Ar-C), 128.14 (Ar-C), 127.30 (Ar-C), 126.81 (Ar-C), 53.71 (NCC), 21.59 (CH₃).



5.5.2.18. Synthesis of H₂tetTSCmB

H₂tetTSCmB was synthesized using the procedure described in chapter 5.5.2. using tetralone as ketone.

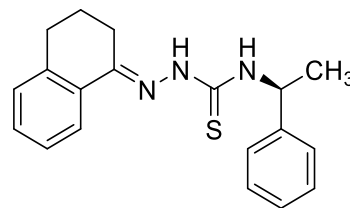
H₂tetTSCmB C₂₂H₂₁N₃S (359.49 g/mol).

Yield: 0.28 g (0.87 mmol) 34%.

Habitus: Yellow solid.

¹H NMR: (DMSO-*d*₆, 300 MHz) δ [ppm] = 10.21 (1H, s, NH), 8.56 (1H, *J* = 9 Hz, d, NH), 8.22 (1H, *J* = 8 Hz, d, Ar-H), 7.42 (2H, *J* = 8 Hz, d, Ar-H), 7.35 (2H, *J* = 8 Hz, t, Ar-H), 7.29-7.17 (4H, m, Ar-H), 5.74 (1H, *J* = 8 Hz, quint, CH), 2.73-2.70 (4H, m, CH₂), 1.83- 1.79 (2H, m, CH₂), 1.57 (3H, *J* = 7 Hz, d, CH₃).

¹³C NMR: (DMSO-*d*₆, 75 MHz) δ [ppm] = 177.31 (NCS), 148.38 (CN), 143.73 (Ar-C), 140.19 (Ar-C), 131.83 (Ar-C), 192.20 (Ar-C), 128.47 (Ar-C), 128.23 (Ar-C), 126.73 (Ar-C), 126.24 (Ar-C), 125.12 (Ar-C), 52.55 (NCC), 28.88 (CH₂), 25.97 (CH₂), 21.37 (CH₃), 21.32 (CH₂).



5.5.2.19. Synthesis of H₂vanTSCmB

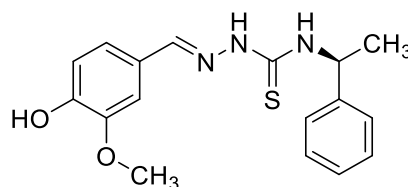
H₂vanTSCmB was synthesized using the procedure described in chapter 5.5.2. using vanillin as aldehyde.

H₂vanTSCmB C₁₇H₁₉N₃O₂S (329.42 g/mol).

Yield: 0.27 g (0.82 mmol) 31%.

Habitus: Yellow solid.

¹H NMR: (DMSO-*d*₆, 300 MHz) δ [ppm] = 11.42 (1H, s, NH), 9.94 (1H, s, OH), 8.42 (1H, *J* = 9 Hz, d, NH), 7.98 (1H, s, CH), 7.43 (2H, *J* = 7 Hz, d, Ar-H), 7.36-7.27 (3H, m, Ar-H), 7.24 (2H, *J* = 8 Hz, t, Ar-H), 6.80 (2H, *J* =



8 Hz, d, Ar-H), 5.70 (1H, $J = 8$ Hz, quint, CH), 3.83 (3H, s, CH₃), 1.56 (3H, $J = 7$ Hz, d, CH₃).

¹³C NMR: (DMSO-*d*₆, 75 MHz) δ [ppm] = 176.01 (NCS), 148.86 (COH), 147.82 (Ar-C), 143.87 (Ar-C), 143.06 (NCH), 128.22 (Ar-C), 126.73 (Ar-C), 126.27 (Ar-C), 126.36 (Ar-C), 121.54 (Ar-C), 115.55 (Ar-C), 110.81 (Ar-C), 55.75 (NCC), 52.34 (CH₃), 21.50 (CH₃).

5.5.2.20. Synthesis of H₂4-NO₂aphTSCmB

H₂4-NO₂aphTSCmB was synthesized using the procedure described in chapter 5.5.2. using *p*-nitro acetophenone as ketone.

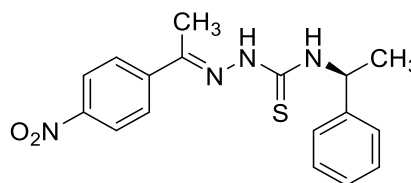
H₂4-NO₂aphTSCmB C₁₇H₁₈N₄O₂S (342.42 g/mol).

Yield: 0.53 g (1.55 mmol) 60%.

Habitus: Intense yellow solid.

¹H NMR: (DMSO-*d*₆, 300 MHz) δ [ppm] = 10.54 (1H, s, NH), 8.70 (1H, $J = 9$ Hz, d, NH), 8.20 (4H, $J = 9$ Hz, q, Ar-H), 7.42 (2H, $J = 7$ Hz, d, Ar-H), 7.35 (2H, $J = 7$ Hz, t, Ar-H), 7.24 (1H, $J = 7$ Hz, t, Ar-H), 5.75 (1H, $J = 7$ Hz, quint, CH), 2.38 (3H, s, CH₃), 1.58 (3H, $J = 7$ Hz, d, CH₃).

¹³C NMR: (DMSO-*d*₆, 75 MHz) δ [ppm] = 177.68 (NCS), 147.42 (Ar-C), 164.00 (NCC), 143.90 (Ar-C), 143.55 (Ar-C), 128.22 (Ar-C), 127.76 (Ar-C), 126.74 (Ar-C), 126.23 (Ar-C), 123.35 (Ar-C), 52.75 (NCC), 21.27 (CH₃), 14.30 (CH₃).



5.5.2.21. Synthesis of H₂SalTSCmB

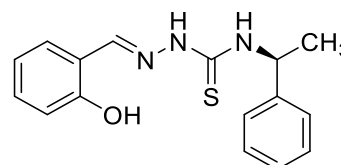
H₂SalTSCmB was synthesized using the procedure described in chapter 5.5.2. using salicylic aldehyde as aldehyde.

H₂SalTSCmB C₁₆H₁₇N₃OS (299.39 g/mol).

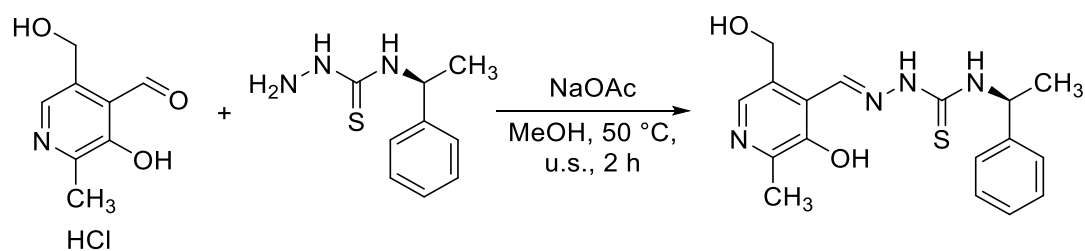
Yield: 0.50 g (1.67 mmol) 41%.

Habitus: Pale yellow solid.

¹H NMR: (DMSO-*d*₆, 300 MHz) δ [ppm] = 11.48 (s, 1H), 9.93 (s, 1H), 8.53 (d, $J = 8.9$ Hz, 1H), 8.41 (s, 1H), 7.94 (d, $J = 7.6$ Hz, 1H), 7.42 (d, $J = 7.2$ Hz, 2H), 7.34 (t, $J = 7.6$ Hz, 2H), 7.28 – 7.16 (m, 2H), 6.93 – 6.77 (m, 2H), 5.72 (p, $J = 7.2$ Hz, 1H), 1.55 (d, $J = 7.0$ Hz, 3H).



5.5.2.22. Synthesis of HpyxTSCmB



0.55 g (2.74 mmol, 1 eq.) pyridoxaldehyde hydrochloride, 0.48 g (2.74 mmol, 1 eq.) and 0.2 g sodium acetate were dissolved in 15 mL MeOH. The mixture was sonicated at 50 °C for 2 hours. The formed precipitate was filtered off and washed with diethyl ether.

HpyxTSCmB: (C₁₇H₂₀N₄O₂S) = 344.43 g/mol

Yield: 0.45 g (1.31 mmol, 48%).

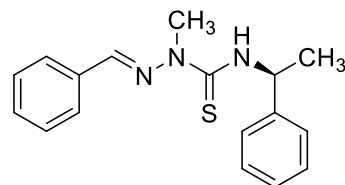
¹H NMR: (DMSO-*d*₆, 300 MHz) δ [ppm] = 11.88 (s, 1H), 9.05 (d, *J* = 8.5 Hz, 1H), 8.57 (s, 1H), 7.97 (s, 1H), 7.43 – 7.30 (m, 4H), 7.29 – 7.18 (m, 1H), 5.63 (p, *J* = 7.1 Hz, 1H), 4.58 (d, *J* = 5.3 Hz, 2H), 2.41 (s, 3H), 1.51 (d, *J* = 7.0 Hz, 3H).

5.5.3. Synthesis of Thiosemicarbazones from (m)TSCmB

1 eq. Thiosemicarbazide were dissolved in MeOH and 0.1 mL HOAc were added. 1 eq. of the corresponding aldehyde were added to the mixture prior to 2 hours of sonification at 60 °C. The mixture was cooled to -26 °C overnight. The precipitate was filtered off and washed with Et₂O yielding a colourless crystalline solid.

5.5.3.1. H₂bz(m)TSCmB

H₂bz(m)TSCmB was synthesized using the procedure described in chapter 5.5.3. using benzaldehyde as aldehyde.



Hbz(m)TSCmB: C₁₇H₁₉N₃S (297.13 g/mol).

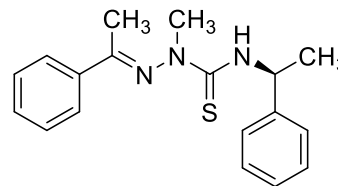
Yield: 1.11 g (3.7 mmol, 78%).

¹H NMR: (DMSO-*d*₆, 300 MHz) δ [ppm] = 8.93 (d, *J* = 8.6 Hz, 1H), 8.02 (s, 1H), 7.93 – 7.86 (m, 2H), 7.50 – 7.38 (m, 5H), 7.34 (ddd, *J* = 7.8, 6.7, 1.2 Hz, 2H), 7.27 – 7.18 (m, 1H), 5.78 – 5.57 (m, 1H), 3.82 (s, 3H), 1.59 (d, *J* = 7.0 Hz, 3H).

¹³C NMR (DMSO-*d*₆, 75 MHz) δ [ppm] = 141.51, 130.35, 129.18, 128.72, 128.19, 127.20, 126.65, 54.58, 34.21, 22.10.

5.5.3.2. H₂aph(m)TSCmB

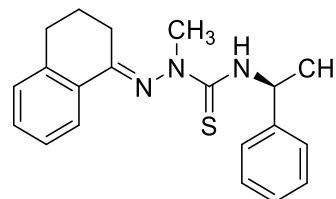
H₂aph(m)TSCmB was synthesized using the procedure described in chapter 5.5.3. using acetophenone as ketone.



H₂aph(m)TSCmB: C₁₇H₂₀N₄O₂S (311.45 g/mol)
Yield: 0.96 g (3.1 mmol, 69%).
¹H NMR: (DMSO-*d*₆, 300 MHz) δ [ppm] = 8.35 (d, *J* = 8.8 Hz, 1H), 7.78 – 7.66 (m, 0H), 7.63 – 7.52 (m, 1H), 7.39 – 7.25 (m, 4H), 7.28 – 7.16 (m, 1H), 5.44 (p, *J* = 7.2 Hz, 1H), 4.93 (s, 2H), 3.44 (s, 3H), 1.44 (d, *J* = 7.0 Hz, 3H).
¹³C NMR (DMSO-*d*₆, 75 MHz) δ [ppm] = 180.46, 144.90, 133.16, 130.06, 128.66, 127.09, 126.62, 53.53, 42.90, 22.65.

5.5.3.3. H₂tet(m)TSCmB

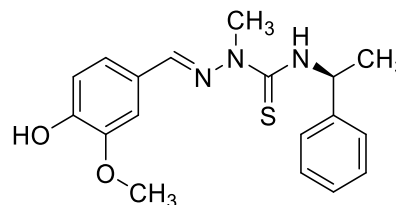
H₂tet(m)TSCmB was synthesized using the procedure described in chapter 5.5.3. using tetralone as ketone.



H₂tet(m)TSCmB C₂₀H₂₃N₃S (337.49 g/mol).
Yield: 0.4 g (1.21 mmol) 51%.
Habitus: colourless solid.
¹H NMR: (DMSO-*d*₆, 300 MHz) δ [ppm] = 8.17 (1H, *J* = 8 Hz, q, Ar-H), 7.63 (1H, *J* = 8 Hz, d, NH), 7.43 (1H, *J* = 7 Hz, t, Ar-H), 7.34-7.26 (6H, m, Ar-H), 7.23-7.17 (1H, m, Ar-H), 5.65 (1H, *J* = 8 Hz, quint, CH), 3.41 (3H, s, CH₃), 2.86 (2H, *J* = 6 Hz, t, CH₂), 2.65 (2H, *J* = 6 Hz, t, CH₂), 1.92- 1.82 (2H, m, CH₂), 1.45 (3H, *J* = 7 Hz, d, CH₃).

5.5.3.4. H₂van(m)TSCmB

H₂van(m)TSCmB was synthesized using the procedure described in chapter 5.5.3. using vanillin as aldehyde.



H₂van(m)TSCmB C₂₀H₂₃N₃S (337.49 g/mol).
Yield: 0.4 g (1.15 mmol) 49 %.
Habitus: Pale yellow solid.
¹H NMR: (DMSO-*d*₆, 300 MHz) δ [ppm] = 9.52 (1H, s, OH), 8.85 (1H, *J* = 9 Hz, d, NH), 7.90 (1H, s, CH), 7.44 (2H, *J* = 8 Hz, d, Ar-H), 7.33 (2H, *J* = 7 Hz, t, Ar-H), 7.27- 7.25 (2H, m, Ar-H), 6.84 (2H, *J* = 8 Hz, d, Ar-H), 5.61 (1H, *J* = 7 Hz, quint, CH), 3.83 (3H, s, CH₃), 3.78 (3H, s, CH₃), 1.56 (3H, *J* = 7 Hz, d, CH₃).
¹³C NMR (DMSO-*d*₆, 75 MHz) δ [ppm] = 178.18 (NCS), 148.79 (COH), 147.84 (Ar- C), 143.82 (Ar-C), 141.17 (NCH), 128.36 (Ar-C), 126.90 (Ar-C), 126.22 (Ar-C), 125.75 (Ar-C), 121.10 (Ar-C), 115.50 (Ar-C), 110.29 (Ar-C), 55.42 (NCC), 54.18 (OMe), 33.52 (CH₃), 21.86 (CH₃).

5.5.3.5. H₂4-NO₂aph(m)TSCmB

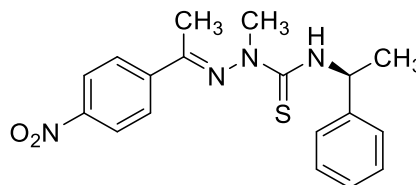
H₂4-NO₂aph(m)TSCmB was synthesized using the procedure described in chapter 5.5.3. using *p*-nitro acetophenone as ketone.

H₂4-NO₂aph(m)TSCmB C₁₈H₂₀N₄O₂S (356.13 g/mol).

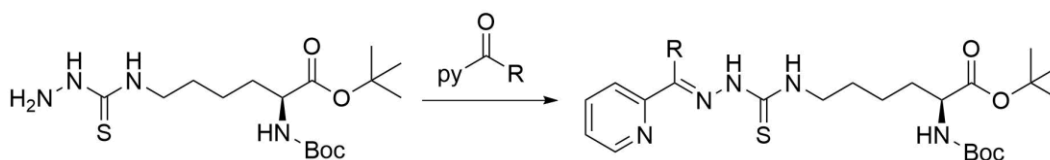
Yield: 0.19 g (0.53 mmol) 23%.

Habitus: Intense yellow solid.

¹H NMR: (DMSO-*d*₆, 300 MHz) δ [ppm] = 8.26 (4H, *J* = 9 Hz, q, Ar-H), 7.81 (1H, *J* = 9 Hz, d, NH), 7.37-7.19 (5H, m, Ar-H), 5.67 (1H, *J* = 7 Hz, quint, CH), 3.47 (3H, s, CH₃), 2.41 (3H, s, CH₃), 1.47 (3H, *J* = 7 Hz, d, CH₃).



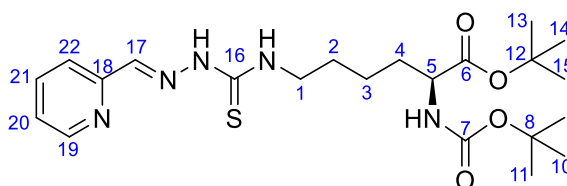
5.5.4. Synthesis of Thiosemicarbazones from TSCLp



Synthesis of HapyTSCLp as example: In a 5 mL pear shaped flask 989 mg (2.63 mmol, 1 eq.) of the thiosemicarbazone was dissolved in 3.5 mL MeOH and 0.1 mL acetic acid. To the colourless solution 0.3 mL (2.63 mmol, 1 eq.) 2-acetylpyridine was added and the reaction mixture was sonicated at 50 °C for 30 minutes. The solvent was removed under reduced pressure and the crude product was purified by flash chromatography (first *c*-hex/EtOAc; *v/v*≈4:6; then pure EtOAc). The solvent was removed under reduced pressure.

5.5.4.1. Synthesis of HfpyTSCLp

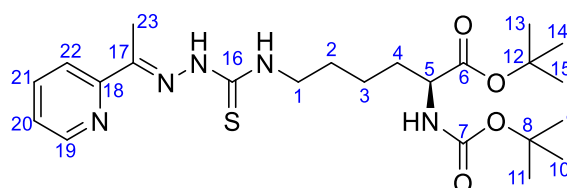
HfpyTSCLp: (C₂₂H₃₅N₅O₄S) = 465.61 g/mol
Yield: 0.25 g (0.58 mmol, 58%).



¹H NMR: (DMSO-*d*₆, 300 MHz) δ [ppm] = 10.00 (1H, -NH-N), 9.81 (s, 1H, 17-H), 8.15 (t, ³*J*_{19H,20H} = 6.0 Hz, 1H, 19-H), 8.06 (td, ³*J*_{22H,21} = 7.6, ⁴*J*_{22H,20H} = 1.6 Hz, 1H, 22-H), 7.94 (dt, ³*J*_{21H,20H/22H} = 7.8, ⁴*J*_{21H,19H} = 1.2 Hz, 1H, 21-H), 7.72 (ddd, *J* = 7.5, 4.7, 1.4 Hz, 1H, 20-H), 7.09 (d, ³*J*_{NH,5H} = 7.7 Hz, 1H, -NH), 3.75 (q, ³*J*_{1H,2H/NH} = 7.5 Hz, 1H, 5-H), 3.49 (m, 2H, 1-H), 1.54 (m, 6H, 2-H, 3-H, 4-H), 1.38 (s, 18H, 9-H, 10-H, 11-H, 13-H, 14-H, 15-H).

5.5.4.2. Synthesis of HapyTSCLp

HapyTSCLp: (C₂₃H₃₇N₅O₄S) = 479.64 g/mol
Yield: 1.13 g (2.36 mmol, 91%).
R_f: (*c*-hex/EtOAc 9:1) = 0.26.
HR-ESI-MS(+): [m/z] [M+Na]⁺: 502.24584 (calc. 502.24585)



FTIR-ATR: ν [cm⁻¹] = 3675 (m), 2987 (s), 2901 (s), 1701 (m), 1533 (m), 1455 (m), 1405 (m), 1384 (s), 1250 (m), 1152 (m), 1075 (s), 1028 (s), 880 (w), 785 (w), 747 (w), 737 (w), 704 (w), 689 (w), 670 (w), 662 (w), 626 (m), 615 (s), 600 (w), 579 (w), 545 (w).

¹H NMR: (CDCl₃, 300 MHz) δ [ppm] = 10.28 (s, 1 H, -NH-N), 8.66 (t, J = 5.7 Hz, 1 H, -NH), 8.59 (dt, $^3J_{22H,21H}$ = 7.8 Hz, $^4J_{22H,20H}$ = 1.3 Hz, 1 H, 22-H), 8.39 (d, $^3J_{19H,20H}$ = 8.1 Hz, 1 H, 19-H), 7.84 (td, $^3J_{21H,20H/22H}$ = 7.8 Hz, $^4J_{21H,19H}$ = 1.8 Hz, 1 H, 21-H), 7.40 (ddd, $^3J_{20H,19H/21H}$ = 8.1 Hz, $^4J_{20H,22H}$ = 1.2 Hz, 1 H, 20-H), 7.08 (d, $^3J_{NH,5H}$ = 7.0 Hz, 1 H, -NH), 3.77 (td, $^3J_{5H,4H}$ = 8.2 Hz, J = 5.5 Hz, 1 H, 5-H), 3.59 (q, $^3J_{1H,2H/NH}$ = 7.0 Hz, 2 H, 1-H), 2.38 (s, 3 H, 23-H), 1.60 (m, 3.7 Hz, 6 H, 2-H, 3-H, 4-H), 1.37 (s, 18 H, 9-H, 10-H, 11-H, 13-H, 14-H, 15-H).

¹³C NMR: (CDCl₃, 75 MHz) δ [ppm] = 177.9 (C-16), 171.9 (C-6), 155.5 (C-7), 154.4 (C-17), 148.2 (C-22), 147.5 (C-18), 136.7 (C-21), 123.9 (C-20), 120.9 (C-19), 80.1 (C-8), 77.9 (C-12), 54.4 (C-5), 43.5 (C-1), 30.6 (C-4), 28.4 (C-3), 28.2 (C-9, C-10, C-11), 27.6 (C-13, C-14, C-15), 23.0 (C-2), 12.1 (C-23).

5.5.4.3. Synthesis of HdpyTSClp

HdpyTSClp: (C₂₇H₃₈N₆O₄S) = 542.70 g/mol

Yield: 5.2 g (9.7 mmol, 92%).

R_f: (100% EtOAc) = 0.16-0.47.

HR-ESI-

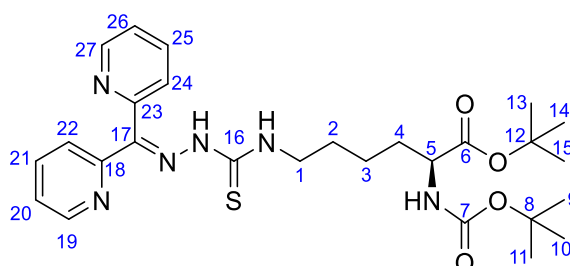
MS(+): [m/z] [M+Na]⁺: 565.25674

(calc. 565.2567455)

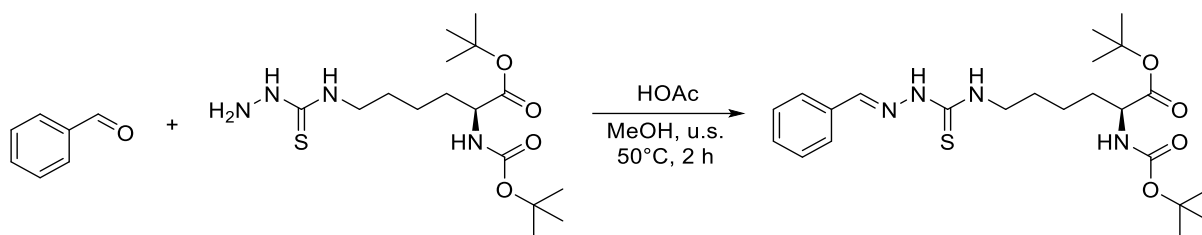
FTIR-ATR: ν [cm⁻¹] = 3853 (w), 3839 (w), 3801 (w), 3734 (w), 3684 (m), 3675 (m), 3566 (w), 3335 (w), 2987 (s), 2972 (s), 2091 (s), 2360 (w), 2173 (w), 2112 (w), 1923 (w), 1706 (m), 1653 (w), 1636 (w), 1588 (w), 1558 (w), 1522 (w), 1507 (w), 1455 (m), 1433 (w), 1406 (m), 1394 (s), 1230 (m), 1152 (m), 1075 (s), 1066 (s), 1057 (s), 949 (w), 892 (w), 880 (w), 868 (w), 803 (w), 774 (w), 747 (w), 679 (w), 663 (w), 650 (w), 616 (w), 608 (w), 598 (w), 591 (w), 567 (w), 546 (w), 537 (w), 518 (w).

¹H NMR: (CDCl₃, 300 MHz) δ [ppm] = 8.93 – 8.77 (m, 1 H, 22-H), 8.68 (d, 1H, -NH-N), 8.59 – 8.47 (m, 1 H, 27-H), 8.22 (d, 1 H, 26-H), 8.08 – 7.93 (m, 3 H, 19-H, 24-H, 21-H), 7.66 – 7.59 (m, 1 H, 20-H), 7.59 – 7.53 (m, 1 H, 25-H), 7.08 (d, J = 7.6 Hz, 1 H, -NH), 3.82 – 3.70 (m, 1 H, 5-H), 3.66 – 3.36 (m, 2 H, 1-H), 1.69 – 1.43(m, 6 H, 2-H, 3-H, 4-H), 1.38 (s, 9 H, 13-H, 14-H, 15-H), 1.36 (s, 9 H, 9-H, 10-H, 11-H).

¹³C NMR: (CDCl₃, 75 MHz) δ [ppm] = 177.2 (C-16), 171.9 (C-6), 155.5 (C-7), 155.1 (C-23), 154.3 (18), 151.1 (C-17), 148.9 (C-22, C-27), 137.1 (C-21, C-26), 126.6 (C-20, C-25), 124.0 (C-19, C-24), 80.1 (C-8), 77.9 (C-12), 54.4 (psd, C-5), 43.7 (C-1), 30.5 (C-4), 28.8 (C-3), 28.2 (psd, C-9, C-10, C-11), 27.63 (psd, C-13, C-14, C-15), 22.9 (C-2).



5.5.4.5. Synthesis of HbzTSCLp



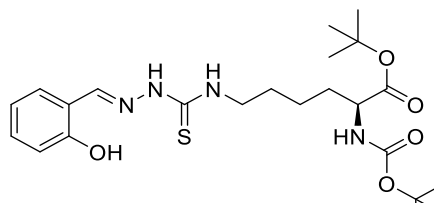
0.50 g (1.3 mmol, 1.0 eq.) amino acid derived thiosemicarbazide was dissolved in 1.8 ml MeOH and 0.53 ml (9.3 mmol, 7.2 eq.) HOAc was added. To the colourless solution 0.17 ml (1.3 mmol, 1.0 eq.) benzaldehyde was added and the mixture was reacted in the sonicator bath for 40 min at 50 °C. Overnight the product was cooled in the freezer and the next day the solvent was removed under reduced pressure, to get a yellow oil as a crude product. The oil was lyophilized with 10 ml CH₂Cl₂, and the product was yielded after column chromatography with cyclohexane/EtOAc (3:1) as 0.14 g (0.29 mmol, 22%) of a colourless to yellow oil.

HbzTSCLp: (C₂₃H₃₆N₄O₄S) = 464.63 g/mol.

Yield: 0.14 g (0.29 mmol, 22%).

¹H NMR: (300 MHz, DMSO-*d*₆) δ [ppm] = 10.12 (s, 1H, -NH-N), 8.46 (t, 3J = 5.73 Hz, 1H, -CSNH), 7.94–7.86 (m, 2H, H-14), 7.44–7.35 (m, 3H, H-15, H-16), 7.07 (d, 3J = 7.57 Hz, 1H, -NH), 3.80–3.67 (m, 1H, H-5), 3.62–3.51 (m, 2H, H-1), 2.28 (s, 3H, H-17), 1.68–1.48 (m, 6H, H-2, H-3, H-4), 1.36 (s, 18H, H-8, H-11).

5.5.4.6. Synthesis of HSaltTSCLp



HfactTSCLp: (C₂₃H₃₆N₄O₅S) = 480.62 g/mol.

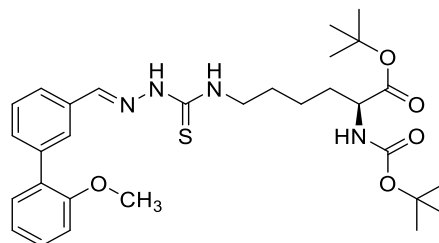
Yield: 0.29 g (0.60 mmol, 72%).

¹H NMR: (300 MHz, DMSO-*d*₆) δ [ppm] = 11.34 (s, 1H), 9.86 (s, 1H), 8.41 (t, J = 5.9 Hz, 1H), 8.36 (s, 1H), 7.92 (dd, J = 7.8, 1.7 Hz, 1H), 7.21 (ddd, J = 8.6, 7.3, 1.7 Hz, 1H), 7.08 (d, J = 7.6 Hz, 1H), 6.89 – 6.81 (m, 2H), 3.83 – 3.70 (m, 1H), 3.53 (d, J = 6.9 Hz, 2H), 1.57 (d, J = 11.2 Hz, 4H), 1.38 (d, J = 1.9 Hz, 19H).

5.5.4.7. Synthesis of HmphfpyTSCLp

0.22 g (1.03 mmol, 1.0 eq.) 6-(2-Methoxyphenyl)-2-pyridinecarboxaldehyde and 0.39 g (1.03 mmol, 1.0 eq.) TSCLp were dissolved in 3 and 5 mL MeOH, respectively. To the thiosemicarbazide solution, 0.2 mL acetic acid were added, and the solutions were mixed. The mixture was sonicated at 50 °C for 3 h. The solvent was removed under reduced pressure, and the crude product was purified via silica gel column chromatography (eluent: cyclohexane/ethyl acetate = 3:1 v/v) to afford the product in 0.47 g (0.82 mmol, 80%) yield as a yellow solid.

HmphfpyTSCLp: (C₂₃H₃₆N₄O₅S) = 480.62 g/mol.
Yield: 0.47 g (0.82 mmol, 80%).
R_f: 0.39 (v:v = 3:1 c-Hex/EtOAc).

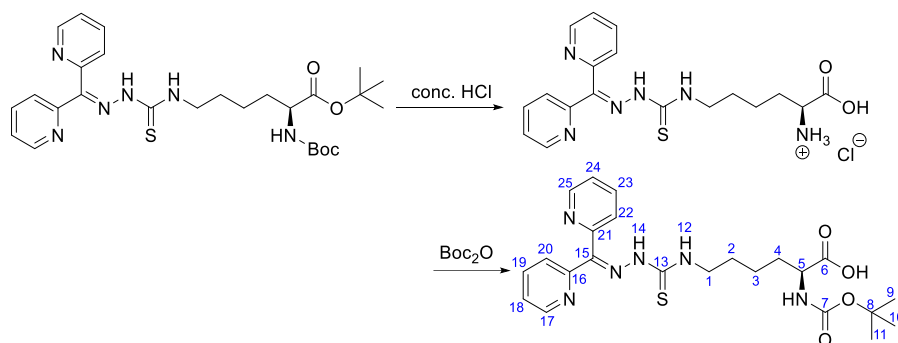


¹H NMR: (600 MHz, CDCl₃) δ [ppm] = 14.59 (s, 1H), 9.69 (s, 1H), 7.93 (dd, *J* = 7.7, 1.6 Hz, 2H), 7.89 – 7.84 (m, 1H), 7.77 – 7.72 (m, 1H), 7.70 (ddd, *J* = 5.8, 3.9, 1.9 Hz, 1H), 7.66 – 7.62 (m, 2H), 7.58 (t, *J* = 5.9 Hz, 1H), 7.31 (dddd, *J* = 15.5, 8.7, 7.4, 1.8 Hz, 2H), 7.24 – 7.18 (m, 1H), 7.11 (td, *J* = 7.5, 1.0 Hz, 1H), 7.00 (dd, *J* = 7.5, 1.0 Hz, 1H), 6.92 (ddd, *J* = 8.4, 3.5, 0.9 Hz, 2H), 5.04 (t, *J* = 8.7 Hz, 1H), 4.11 (h, *J* = 5.5 Hz, 1H), 3.80 (s, 3H), 3.64 (q, *J* = 6.6 Hz, 3H), 1.81 – 1.69 (m, 2H), 1.68 – 1.53 (m, 3H), 1.36 (dd, *J* = 12.3, 3.2 Hz, 33H).

¹³C NMR: (151 MHz, CDCl₃) δ [ppm] = 178.49, 177.70, 171.97, 157.16, 157.03, 156.14, 155.44, 155.27, 152.15, 151.51, 143.13, 137.10, 136.12, 132.96, 131.61, 131.10, 130.96, 130.33, 128.32, 127.00, 125.85, 123.22, 121.60, 121.08, 118.65, 111.47, 111.42, 81.85, 79.59, 55.77, 53.85, 44.37, 43.92, 32.73, 29.71, 28.88, 28.37, 28.04, 26.92, 22.67.

HR-ESI-MS [M+H]⁺ 572.28980 (calc. 572.29011) [M+Na]⁺ 594.27191 (calc. 594.27206).

5.5.4.8. Synthesis of HdpyTSCLBoc



0.64 g (1.18 mmol) of HdpyTSCLp were dissolved in 150 mL concentrated HCl and stirred at ambient temperature for 48 h. The protected amino acid dissolves rapidly under gas formation. The solvent was removed under reduced pressure yielding 0.26 g of a dark yellow solid. The product was used without further purification. Yield: 0.26 g (0.61 mmol, 52%).

123 mg (0.3 mmol, 1 eq.) of the unprotected amino acid and 50 mg (0.45 mmol, 1.5 eq.) Na₂CO₃ were dissolved in 10 mL H₂O and 7.5 mL *t*-BuOH. 65 mg (0.3 mmol, 1 eq.) Boc₂O were added to the mixture. The reaction mixture was heated to reflux overnight. Then stirring was continued for 24 h at ambient temperature. 100 mL of H₂O were added to the reaction followed by 100 mL of *n*-pentane. The organic phase was discarded, and the aqueous phase was acidified with concentrated HCl to a *pH* of 1. Then, the aqueous phase was extracted with 3 × 100 mL EtOAc. The combined organic phases were washed with 10 wt.% Na₂SO₄ solution, dried over Na₂SO₄ and

the solvent was evaporated under reduced pressure yielding 130 mg (0.27 mmol, 90%) of yellow oil.

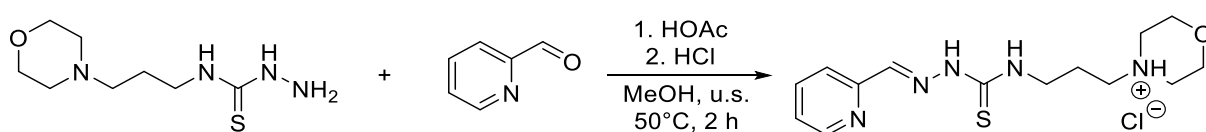
HmphfpyTSCLp: C₂₃H₃₀N₆O₄S (486.59 g/mol)
Yield: 130 mg (0.27 mmol, 47%).
¹H NMR: (300 MHz, DMSO-*d*₆) δ [ppm] = δ 13.15 (s, 1H, NH14), 8.89 (t, 1H, *J* = 5.9 Hz, H17), 8.83 (m, 1H, H25), 8.58 (d, 1H, H22), 8.28-8.18 (m, 1H, H20), 7.98 (m, 2H, H19,23), 7.55-7.42 (m, 2H, H18,24), 7.06 (d, 1H, *J* = 8.0 Hz, NH12), 3.84 (dd, 1H, *J* = 8.5, 4.5 Hz, H5), 3.58 (q, 2H, *J* = 6.9 Hz, H1), 1.65 (m, 6H, H2,3,4), 1.36 (s, 9H, H9,10,11).

5.5.4.9. Synthesis of HdpyTSCL-sC18

sC18 (Gly-Leu-Arg-Lys-Arg-Leu-Arg-Lys-Phe-Arg-Asn-Lys-Ile-Lys-Glu-Lys-NH₂) was synthesised as previously described.³¹⁰ HdpyTSCL (15 μmol, 2 eq.) was coupled manually to the resin using 2 eq. HATU (O-(7-azabenzotriazol-1-yl)-*N,N,N',N'*-tetramethyluronium hexafluorophosphate) and 2 eq. DIPEA (*N,N*-diisopropyl-ethyl-amine) in DMF for 2 h at r.t. The resulting HdpyTSCL-sC18 conjugate was cleaved from the resin with trifluoroacetic acid/triisopropylsilane/H₂O (95/2.5/2.5, v/v/v) and precipitated in ice cold diethyl ether. Then it was purified by preparative HPLC (column: Nucleodur C18ec; 100-5; Macherey-Nagel; solvent: 10-60% MeCN in H₂O (incl. 0.1% TFA) over 45 min, 6.0 mL/min flow rate). The product was identified via HPLC-ESI MS (column: Nucleodur C18ec; 100-5; Macherey-Nagel; gradient: 10-60% MeCN in H₂O (incl. 0.1 % formic acid) over 15 min; 0.6 mL/min flow rate). After purification, a yield of 19.7 mg (8.08 μmol, 53.8%) was determined.

5.5.5. Synthesis from other thiosemicarbazides

5.5.5.1. Synthesis of HfpyTSCpm



In a 50 mL pear-shaped flask 501 mg morpholine thiosemicarbazide (2.29 mmol, 1.00 eq.) in 30 mL MeOH and 0.1 mL HOAc (105 mg, 1.75 mmol, 0.67 eq.) were added. To the pale-yellow solution 0.22 mL 2-formylpyridine (245 mg, 2.29 mmol, 1.00 eq.) were added. The reaction mixture was put in a sonicator bath at 50 °C for 90 min. The brown solution was concentrated under reduced pressure to obtain a yellow oil. The crude product was dissolved in 15 mL MeOH and acidified via conc. HCl (pH = ~1). The solvent was evaporated. The brown solid was washed with 3 x 5 mL MeOH to obtain a yellow solid which was washed with 3 x 5 mL Et₂O and dried

under reduced pressure to obtain 527 mg morpholine fpy-thiosemicarbazone as hydrochloride (M = 341.90 g/mol, 1.54 mmol, 67% yield).

HfpyTSCpm: (C₁₄H₂₂N₅O₂Cl) = 343.87 g/mol.

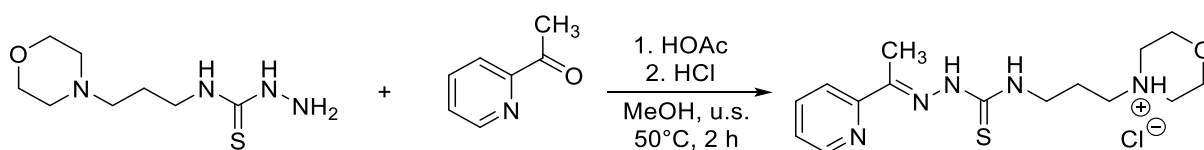
Yield: 0.527 g (1.54 mmol, 67%).

FTIR-ATR: ν [cm⁻¹] = 3675 (br), 3125 (w), 2987 (s), 2901 (s), 2439 (br), 1610 (w), 1586 (w), 1555 (w), 1539 (w), 1518 (w), 1455 (w), 1406 (w), 1394 (w), 1382 (w), 1325 (w), 1287 (w), 1254 (m), 1233 (w), 1203 (m), 1169 (w), 1137 (m), 1077 (s), 1066 (s), 1051 (s), 1028 (m), 954 (w), 908 (w), 880 (w), 871 (w), 825 (w), 766 (m), 747 (w), 728 (w), 689 (w), 662 (w), 627 (w), 619 (w), 607 (w), 590 (w), 582 (w), 528 (w).

¹H NMR: (DMSO-*d*₆, 300 MHz) δ [ppm] = 8.78 (dd, ³J_{14H,13H} = 5.9 Hz, ⁴J_{14H,12H} = 1.5 Hz, 1 H, 14-H), 8.62 (td, ³J_{12H,11H/13H} = 8.0 Hz, ⁴J_{12H,14H} = 1.6 Hz, 1 H, 12-H), 8.22 (d, ³J_{11H,12H} = 8.1 Hz, 1 H, 11-H), 8.15 (s, 1 H, 9-H), 8.03 (ddd, ³J_{13H,12H} = 7.5 Hz, ³J_{13H,14H} = 5.8 Hz, ⁴J_{13H,11H} = 1.3 Hz, 1 H, 13-H), 4.14 (dd, ²J_{6H,6H'} = 13.3 Hz, ³J_{6H,5H} = 3.6 Hz, 2 H, 6-H)*, 3.96 – 3.73 (m, 4 H, 7-H*, 2-H), 3.64 – 3.51 (m, 2 H, 5-H)**, 3.37 – 3.29 (m, 2 H, 4-H), 3.23 (td, ²J_{8H,8H'} = 12.6 Hz, ³J_{8H,7H} = 3.7 Hz, 2 H, 8-H)**, 2.37 – 1.96 (m, 2 H, 3-H, 3-H).
*,**Assignment interconvertible.

¹³C NMR: (DMSO-*d*₆, 75 MHz) δ [ppm] = 178.23 (C-1), 148.07 (C-12), 145.84 (C-10), 142.65 (C-14), 133.43 (C-13), 127.57 (psd, C-11), 64.43 (C-6, C-7), 55.23 (C-4), 52.40 (C-5, C-8), 41.59 (C-2), 23.73 (C-3).

5.5.5.2. Synthesis of HapyTSCpm



In a 50 mL pear-shaped flask 506 mg morpholine thiosemicarbazide (2.29 mmol, 1.00 eq.) in 30 mL MeOH and 0.1 mL HOAc (105 mg, 1.75 mmol, 0.67 eq.) were added. To the pale-yellow solution 0.26 mL 2-acetylpyridine (280 mg, 2.29 mmol, 1.00 eq.) were added. The reaction mixture was put in a sonicator bath at 50 °C for 90 min. The yellow solution was concentrated under reduced pressure to obtain a yellow oil. The crude product was dissolved in 15 mL MeOH and acidified via conc. HCl (pH = ~1). The solvent was evaporated to obtain yellow solid which was washed with 3 x 5 mL Et₂O and dried under reduced pressure to obtain 728 mg morpholine apy-thiosemicarbazone as hydrochloride (M = 355.93 g/mol, 2.05 mmol, 89% yield).

HapyTSCpm: C₁₅H₂₄N₅O₂Cl (341.90 g/mol)

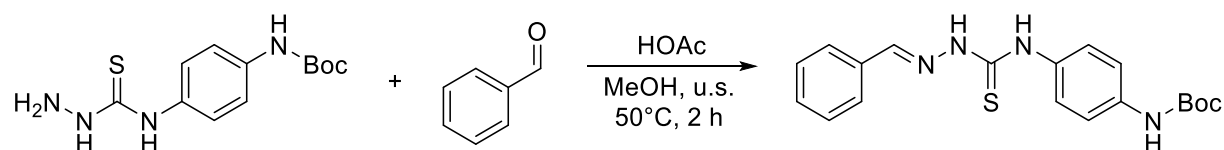
Yield: 0.527 g (1.54 mmol, 67%).

FIR-ATR: ν [cm⁻¹] = 3684 (m), 3675 (m), 3177 (br), 3087 (w), 2987 (s), 2872 (s), 2901 (s), 2434 (s), 1616 (w), 1583 (w), 1549 (w), 1498 (w), 1454 (w), 1406 (m), 1394 (m), 1381 (w), 1354 (w), 1315 (w), 1301 (w), 1289 (w), 1250 (w), 1234 (m), 1198 (m), 1149 (w), 1130 (w), 1077 (s), 1066 (s), 1051 (s), 1028 (m), 969 (w), 954 (w), 906 (w), 891 (w), 878 (m), 816 (w), 772 (m), 745 (w), 729 (w), 634 (w), 621 (w), 606 (w), 597 (w), 590 (w), 570 (w), 550 (w), 539 (w), 510 (w).

¹H NMR: (DMSO-*d*₆, 300 MHz) δ [ppm] = 8.79 (dd, ³*J*_{14H,13H} = 5.8 Hz, ⁴*J*_{14H,12H} = 1.5 Hz, 1 H, 14-H), 8.68 (td, ³*J*_{12H,11H/13H} = 8.3 Hz, ⁴*J*_{12H,14H} = 1.6 Hz, 1 H, 12-H), 8.34 (dd, ³*J*_{11H,12H} = 8.3 Hz, ⁴*J*_{11H,13H} = 1.2 Hz, 1 H, 11-H), 8.06 (ddd, ³*J*_{13H,12H} = 8.0 Hz, ³*J*_{13H,14H} = 5.8 Hz, ⁴*J*_{13H,11H} = 1.2 Hz, 1 H, 13-H), 4.14 (dd, ²*J*_{6H,6H'} = 13.0 Hz, ³*J*_{6H,5H} = 3.2 Hz, 2 H, 6-H)*, 3.92 – 3.71 (m, 4 H, 7-H*, 2-H), 3.66 – 3.47 (m, 2 H, 5-H)**, 3.41 – 3.28 (m, 2 H, 4-H), 3.23 (td, ²*J*_{8H,8H'} = 12.6 Hz, ³*J*_{8H,7H} = 3.7 Hz, 2 H, 8-H)**, 2.45 (s, 3 H, 15-H), 2.32 – 1.98 (m, 2 H, 3-H). *,**Assignment interconvertible.

¹³C NMR: (DMSO-*d*₆, 75 MHz) δ [ppm] = 178.52 (C-1), 148.40 (C-12), 147.26 (C-10), 142.51 (C-14), 140.28 (C-9), 127.39 (C-13), 126.18 (C-11), 64.45 (C-6, C-7), 55.23 (C-4), 52.39 (C-5, C-8), 41.64 (C-2), 23.73 (C-3), 12.75 (C-15).

5.5.5.3. Synthesis of H2bzTSCbap



868 mg (83.10 mmol, 1.00 eq.) thiosemicarbazide was added to a *Schlenk*-flask, suspended in MeOH (20.0 ml), and stirred for 5 minutes at room temperature under inert conditions. Benzaldehyde (361 mg, 3.41 mmol, 0.350 ml, 1.10 eq.) and acetic acid (0.210 g, 0.200 ml, 100 mol%) were added to the mixture and sonicated at 50 °C for 30 minutes. The crude product was purified *via* column chromatography (c-hex/EtOAc, 2:1). The desired product could be obtained as an orange-yellow solid in a yield of 50%.

H2bzTSCbap C₁₉H₂₂N₄O₂S (370.1 g/mol).

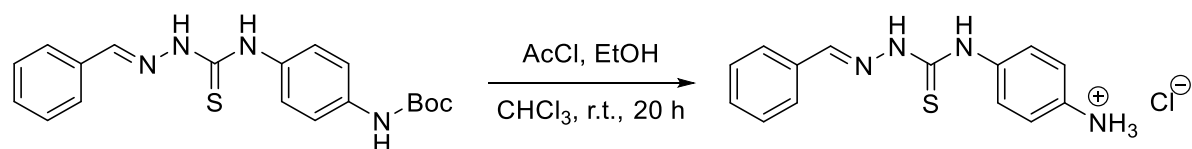
Yield: 570 mg (3.09 mmol, 50%).

Habitus Brown solid.

¹H NMR: (300 MHz, DMSO-*d*₆): δ (ppm) = 11.76 (s, 1H), 10.02 (s, 1H), 9.36 (s, 1H), 8.15 (s, 1H), 7.99 – 7.84 (m, 2H), 7.57 – 7.31 (m, 7H), 1.49 (s, 9H).

¹³C NMR: (75 MHz, DMSO-*d*₆): δ [ppm] = 176.7, 153.3, 143.1, 137.6, 134.6, 133.8, 133.4, 130.4, 129.7, 129.0, 128.0, 127.0, 118.1, 79.3, 28.5.

5.5.5.4. Synthesis of H2bzTSCap



H2bzTSCbap (510 mg, 1.38 mmol, 1.00 eq.) was partially dissolved in chloroform (9.00 ml). Another flask was charged with EtOH (1.47 g, 32.0 mmol, 1.90 ml, 23.0 eq.) and chloroform (10.0 ml) under inert conditions and acetyl

chloride (2.46 g, 31.7 mmol, 2.30 ml, 23.0 eq.) was added *via* a dropping funnel over a time span of 20 minutes. The EtOH/acetyl chloride solution was added to the chloroform solution at 0 °C over a time span of 15 minutes and was stirred for 20 h. The resulted residue was filtered and washed with chloroform. The product could be obtained as a pure yellow solid in a yield of 94%.

H2bzTSCap C₁₄H₁₅N₄ClS (406.1 g/mol).

Yield: 526 mg (1.3 mmol, 94%).

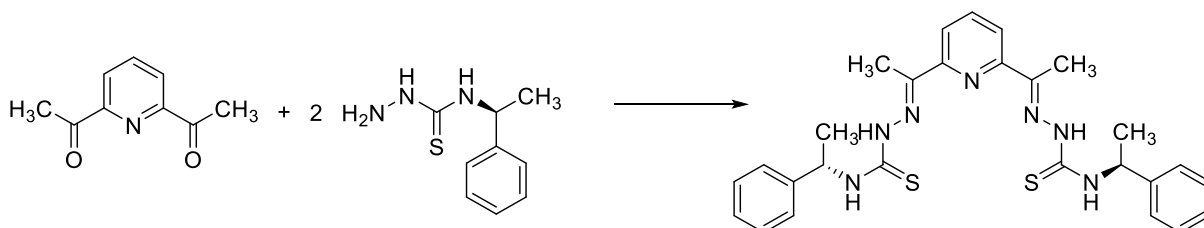
Habitus Brown solid.

¹H NMR: (300 MHz, DMSO-*d*₆): δ (ppm) = 11.94 (s, 1H), 10.20 (s, 1H), 8.19 (s, 1H), 7.91 (d, *J* = 2.9 Hz, 2H), 7.68 (d, *J* = 8.2 Hz, 2H), 7.39 (dd, *J* = 20.1 Hz, *J* = 11.4 Hz, 5H), 5.01 (s, 2H).

¹³C NMR: (75 MHz, DMSO-*d*₆): δ [ppm] = 143.9, 130.5, 129.3, 128.2, 127.4, 123.5.

5.6. Synthesis of Bisthiosemicarbazones

5.6.1. Synthesis of (2*E*, 2'*E*)-2,2'-((4-chloropyridine-2,6-diyl)bis(ethan-1-yl-1-ylidene))bis(*N*-(1-phenylethyl)hydrazine-1-carbothioamid



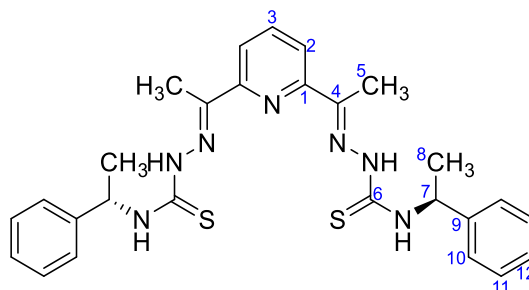
100 mg (0.610 mmol, 1.00 eq.) 2,6-Diacetylpyridine were dissolved in 2 ml EtOH and 299 mg (1.53 mmol, 2.50 eq.) *N*-(1-phenylethyl)hydrazine carbothioamide and one drop of acetic acid were added, and the reaction mixture was sonicated at 50 °C for 20 min. After removal of the solvent under reduced pressure 220 mg (0.425 mmol, 70%) of a yellow solid were obtained.

H2dapTSCmB: C₂₇H₃₁N₇S₂ (517.71 g/mol).

Yield: 220 mg (0.425 mmol, 65%).

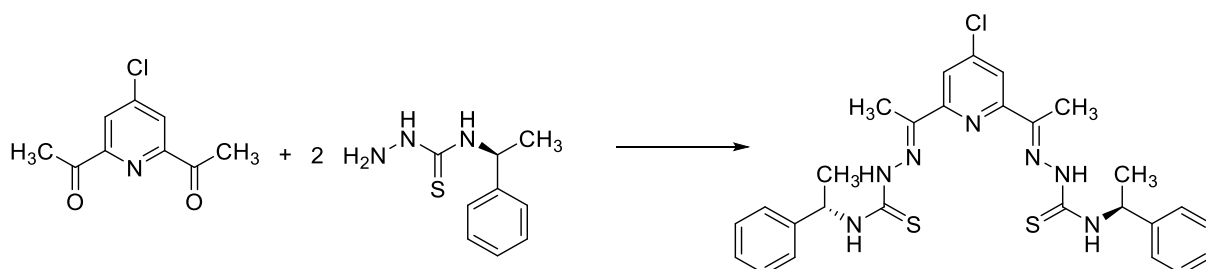
Habitus Yellow solid.

¹H NMR: (300 MHz, DMSO-*d*₆): δ (ppm) = 10.42 (s, 2H, NH), 8.74 (d, 2H, NH), 8.38 (d, 2H, H-2), 7.89 (t, 1H, H-3), 7.43 (d, 4H, H-10), 7.35 (t, 4H, H-11), 7.25 (t, 2H, H-12), 5.81-5.72 (m, 2H, H-7), 2.47 (s, 6H, H-5), 1.59 (d, 6H, H-8).



¹³C NMR: (75 MHz, DMSO-d₆): δ (ppm) = 177.5 (C-6), 153.4(C-1), 148.5(C-4), 143.6 (C-9), 136.8 (C-3), 128.2 (C-11), 127.7 (C-10), 126.2 (C-12), 120.9 (C-2), 52.7 (C-7), 21.2 (C-8), 12.3 (C-5).

5.6.2.Synthesis of (2*E*, 2'*E*)-2,2'-((4-chloropyridine-2,6-diyl)bis(ethan-1-yl-1-ylidene))bis(*N*-(1-phenylethyl)hydrazine-1-carbothioamid

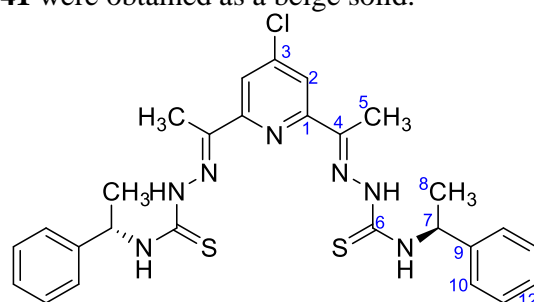


500 mg (2.53 mmol, 1.00 eq.) 4-chloro-2,6-diacetylpyridine were dissolved in 30 ml EtOH. 1.10 g (5.63 mmol, 2.23 eq.) *N*-(1-phenylethyl)hydrazine carbothioamide (**39**) and three drops of HOAc were added and the reaction mixture was sonicated at 50 °C for 1 h. The precipitate was filtered off and washed with EtOH. 280 mg (0.51 mmol, 20%) of **41** were obtained as a beige solid.

H₂Cl₂dapTSCmB: C₂₇H₃₀ClN₇S₂ (552,16 g/mol).

Yield: 280 mg (0.51 mmol, 20%).

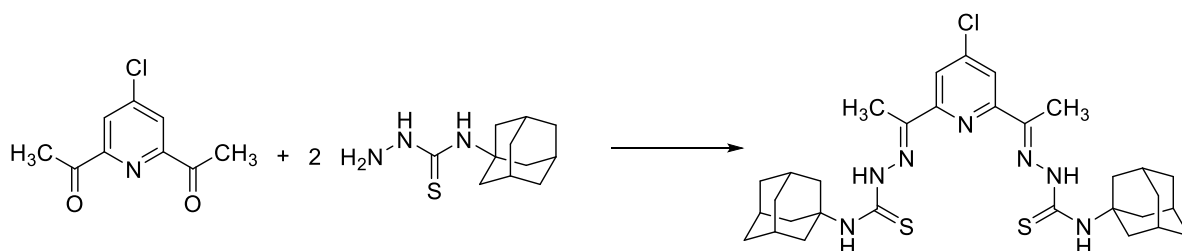
Habitus beige solid.



¹H NMR: (300 MHz, DMSO-d₆): δ (ppm) = 10.44 (s, 2H, NH), 8.91 (d, 2H, NH), 8.43 (s, 2H, H-2), 7.44 (d, 4H, H-10), 7.36 (t, 4H, H-11), 7.25 (t, 2H, H-12), 5.82-5.73 (m, 2H, H-7), 2.46 (s, 6H, H-5), 1.61 (d, 6H, H-8).

¹³C NMR: (75 MHz, DMSO-d₆): δ (ppm) = 143.5 (C-9), 128.2 (C-11), 126.7 (C-10), 126.2 (C-12), 120.3 (C-2), 99.5, 52.8 (C-7), 21.1 (C-8), 12.4 (C-5).

5.6.3.Synthesis of (2*E*,2'*E*)-2,2'-((4-chloropyridine-2,6-diyl)bis(ethan-1-yl-1-ylidene))bis(*N*-((3*s*,5*s*,7*s*)-adamantan-1-yl)-hydrazine-1-carbothioamid



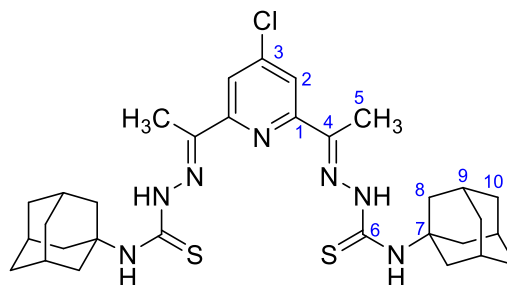
570 mg (2.53 mmol, 2.50 eq.) adamantylthiosemicarbazone and 200 mg (1.01 mmol, 1.00 eq.) 4-chloro-2,6-diacetylpyridine were dissolved in 40 ml MeOH and two drops of acetic acid were added. The reaction mixture was sonicated for 2 hours at 50 °C, filtered over a silica plug and washed with cHex/EtOAc 10:1. After removal of the solvent under reduced pressure 230 mg (0.380 mmol, 38%) of were obtained as a yellow solid.

H₂dapTSCmB: C₃₁H₄₂ClN₇S₂ (612,30 g/mol).

Yield: 230 mg (0.380 mmol, 38%).

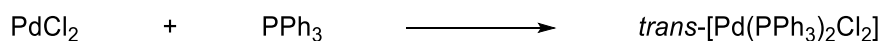
Habitus yellow solid.

¹H NMR: (300 MHz, DMSO-*d*₆): δ (ppm) = 10.28 (s, 2H, NH), 8.35 (d, 2H, H-2), 7.92 (d, 2H, NH), 2.88 (s, 6H, H-5), 2.32 (s, 12H, H-8), 2.10 (s, 6H, H-9), 1.87 (s, 12H, H-10).



5.7. Metal precursor synthesis

5.7.1. Synthesis of [Pd(PPh₃)₂Cl₂]



0.526 g (2 mmol, 2 eq.) triphenyl phosphine were dissolved in 10 mL DCM. Separately, 0.177 g (1 mmol, 1 eq.) PdCl₂ was dispersed in 14 mL MeCN and added to the first solution. Stirred at room temperature over the weekend and the solvent was removed under reduced pressure. The residue was dissolved in chloroform and filtered. The solvent was removed, and the residue was washed with hot water, hot EtOH, and diethyl ether (each 3 times with 10 mL) yielding a yellow solid.

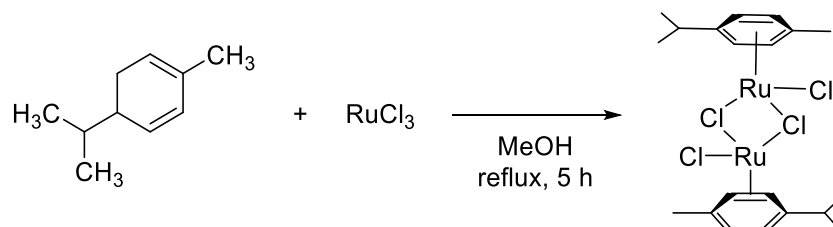
[Pd(PPh₃)₂Cl₂]: C₃₆H₃₀Cl₂P₂Pd (701.9 g/mol).

Yield: 0.35 g (0.57 mmol, 57%).

¹H NMR: (300 MHz, Chloroform-*d*) δ [ppm] = 7.71 (m, 4H), 7.51 – 7.31 (m, 6H).

³¹P NMR: (121 MHz, Chloroform-*d*) δ [ppm] = 23.27.

5.7.2. Synthesis of [Ru(*p*-Cymene)Cl₂]₂



2.00 g (7.61 mmol, 1 eq.) RuCl₃ trihydrate were dissolved in 100 mL EtOH. Afterwards, 10 mL *p*-phellandrene (62.4 mmol, 8.2 eq.) were added to the solution and the mixture was heated

to reflux for 5 hours before it was stirred over night at ambient temperature. The precipitate was filtered off and dried in vacuo, yielding a red solid.

[Ru(*p*-Cymene)Cl₂]₂ (C₂₀H₂₈Cl₄Ru₂) = 612.39 g/mol
Yield: 0.55 g (1.36 mmol, 88%).
¹H NMR: (300 MHz, Chloroform-*d*) δ [ppm] = 5.48 (d, *J* = 5.9 Hz, 2H), 5.34 (d, *J* = 5.9 Hz, 2H), 2.92 (hept, *J* = 7.0 Hz, 1H), 2.17 (d, *J* = 3.9 Hz, 3H), 1.28 (d, *J* = 6.9 Hz, 6H).

5.7.3.Synthesis of PPh₃-*d*₁₅

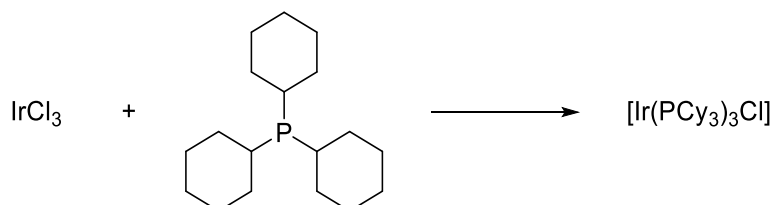
A three neck Schlenk flask was baked out with 1.05 g (43.2 mmol, 3.1 eq.) magnesium in it. 20 mL dry diethyl ether were added the flask. Separately 5 mL (7.7 g, 47.5 mmol, 3.4 eq.) bromobenzene-*d*₅ were diluted with 15 mL dry diethyl ether in a dropping funnel. The bromobenzene-*d*₅ was slowly added to the magnesium to ensure a mild reflux. After 30 minutes, 1.4 mL (3.8 g, 14 mmol, 1 eq.) PBr₃ was diluted in 20 mL dry diethyl ether and added slowly to the mixture in an ice bath. The mixture was stirred at 0 °C for 1.5 hours before 60 mL 1 M HCl were added. The phases were separated, the aqueous phase was washed 4 times with 100 mL diethyl ether each, and the combined organic phases were dried over MgSO₄. The solvent was removed under reduced pressure yielding a yellow oil which solidified overnight in the freezer. ³¹P{¹H}-NMR revealed a mixture of triphenylphosphine and triphenylphosphine oxide at a ratio of about 1 to 7.

PPh₃-*d*₁₅ C₁₈D₁₅P (277.38 g/mol).
O=PPh₃-*d*₁₅ C₁₈D₁₅PO (293.38 g/mol).
Yield: 4.1 g (14 mmol, >99%). Calculated as mixture (291.3 g/mol).
³¹P NMR (300 MHz, DMSO-*d*₆) δ [ppm] = 25.3, -7.36.

5.7.4.Synthesis of [Ir(PPh₃-*d*₁₅)₃Cl]

[Ir(PPh₃-*d*₁₅)₃Cl] C₅₄D₄₅ClIrP₃ (1059.49 g/mol).
Yield: 0.22 g (0.21 mmol, 45%).
³¹P NMR: (121 MHz, DMSO-*d*₆) δ [ppm] = 25.36, 20.20.

5.7.5.Synthesis of [Ir(PCy₃)₃Cl]

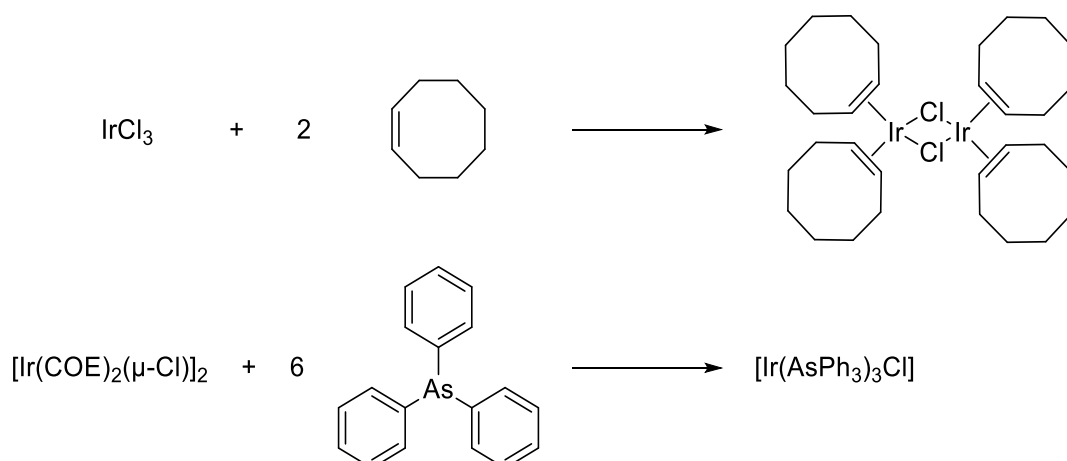


281.7 mg (1 mmol, 3 eq.) tricyclohexyl phosphine were dissolved in 20 mL tert-butanol. The solution was purged with a stream of argon for 5 minutes, before 100 mg (0.335 mmol, 1 eq.) iridium (III) chloride hydrate was added to the solution. The mixture was heated for 72 h at

85 °C. The formed precipitate was filtered off and washed with diethyl ether yielding a yellow solid.

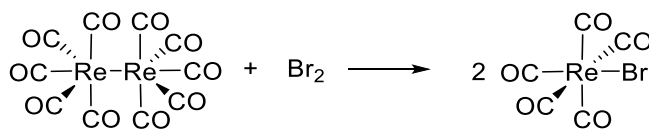
[Ir(PCy₃)₃Cl] (C₅₄H₉₀ClIrP₃) = 1059.90 g/mol.
Yield: 81.3 mg (0.08 mmol, 8%).
¹H NMR: (300 MHz, CDCl₃) δ [ppm] = 1.74 (m, 54H), 1.31 (m, 36H).
³¹P NMR (300 MHz, CDCl₃) δ [ppm] = -29.18.

5.7.6.Synthesis of [Ir(AsPh₃)₃Cl]



30 mL isopropanol were degassed for 20 minutes with a stream of argon. 200 mg (0.57 mmol, 1 eq.) iridium (III) chloride hydrate and 1 mL (5.7 mmol, 10 eq.) cyclooctene were added to the solution and heated to reflux for 3 hours. Afterwards, 523.3 mg (1.71 mmol, 6 eq.) triphenyl arsine was added to the solution and heated for another hour to reflux. During that time, a yellow precipitate formed which was filtered under inert conditions and washed with dry diethyl ether. The product was used without further purification.

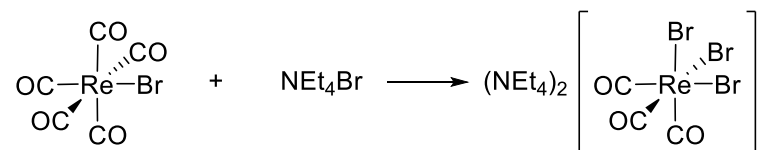
5.7.7.Synthesis of [Re(CO)₅Br]



0.5 g (0.77 mmol, 1 eq.) Re₂(CO)₁₀ were dissolved in 20 mL CS₂. Separately, 0.1 mL bromine were dissolved in 10 mL CS₂. Of the latter solution, 5 mL were added to the rhenium solution. The mixture was stirred at ambient temperature for 72 hours upon which a white precipitate formed. Additional product could be generated upon evaporating of the solvent.

Re(CO)₅Br: (C₅BrO₅Re) = 542.70 g/mol
Yield: 0.55 g (1.36 mmol, 88%).
FTIR-ATR: ν [cm⁻¹] = 2152, 2078, 2058, 2023, 1960, 1928.

5.7.8.Synthesis of $(\text{NEt}_4)_2\text{fac}[\text{Re}(\text{CO})_3\text{Br}_3]$



0.2 g (0.5 mmol, 1 eq.) $\text{Re}(\text{CO})_5\text{Br}$ and 0.11 g (1.1 mmol, 2.2 eq.) NEt_4Br were dispersed in 20 mL diglyme. The mixture was heated to 115 °C upon which the dispersion cleared up. After 5 hours a solid slowly appeared. The mixture was stirred at elevated temperature overnight. After cooling a white solid could be isolated.

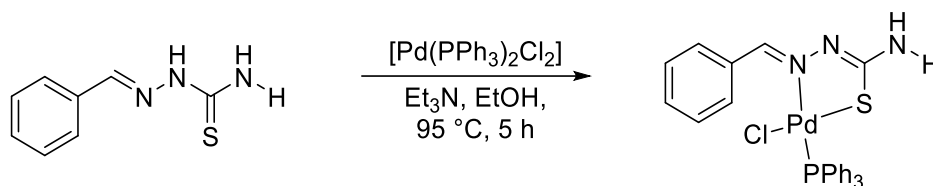
$(\text{NEt}_4)_2[\text{Re}(\text{CO})_3\text{Br}_3]$: $(\text{C}_{19}\text{H}_{40}\text{Br}_3\text{N}_2\text{O}_3\text{Re}) = 770.46 \text{ g/mol}$

Yield: 0.145 g (0.19 mmol, 38%).

FTIR-ATR: $\nu [\text{cm}^{-1}] = 1998, 1865, 1849, 1455, 1405, 1184, 1032, 1005, 795.$

5.8. Synthesis of complexes

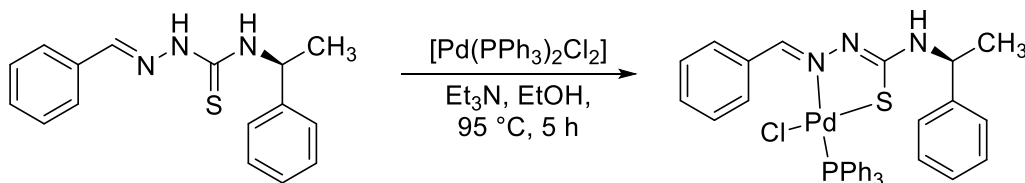
5.8.1. Synthesis of $[\text{Pd}(\text{PPh}_3)(\text{HbzTSC})\text{Cl}]$



0.0254 g (0.142 mmol, 1.0 eq.) ligand HbzTSC was dissolved in 30 ml EtOH at 40 °C. 0.02 ml (0.14 mmol, 1.0 eq.) triethyl amine was added. After the addition of 0.0984 g (0.142 mmol, 1 eq.) dichloro bistrisphenylphosphine palladium the mixture was refluxed at 95 °C for 5 h. The mixture was allowed to cool down, the solvent was removed, and the crude product was purified by column chromatography with Toluene/EtOAc (10:1) as the eluent. 86.8 mg (> 100%) of an orange solid were isolated.

$[\text{Pd}(\text{PPh}_3)(\text{bzTSC})\text{Cl}]$ $\text{C}_{26}\text{H}_{23}\text{ClN}_3\text{PPdS}$ (582.4 g/mol).
Yield: 86.8 mg (0.142 mmol, >99%).
Habitus Orange solid.
 $^1\text{H NMR}$: (300 MHz, DMSO- d_6) δ [ppm] = 8.59 (d, $3J = 4.40$ Hz, 1H, H-2), 7.92–7.86 (m, 2H), 4.81 (s, 2H, H2N-).
 $^{31}\text{P NMR}$ (161.9 MHz, CDCl_3) δ [ppm] = 27.4.

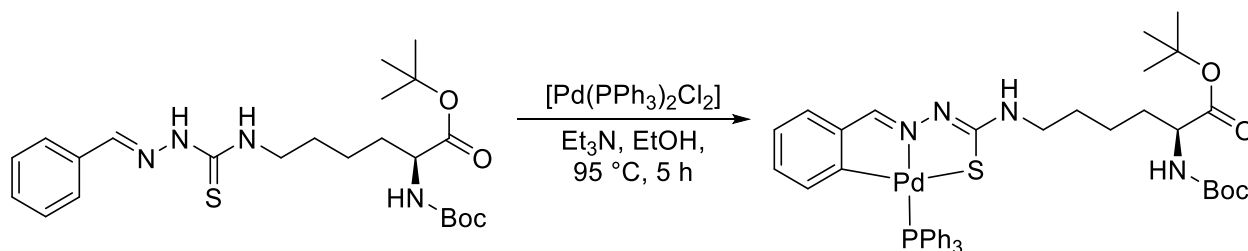
5.8.2. Synthesis of $[\text{Pd}(\text{PPh}_3)(\text{bzTSCmB})\text{Cl}]$



0.0395 g (0.142 mmol, 1.0 eq.) ligand HbzTSCmB was dissolved in 30 ml EtOH at 40 °C. 0.02 ml (0.14 mmol, 1.0 eq.) triethyl amine was added. After the addition of 0.0985 g (0.142 mmol, 1.0 eq.) dichloro bistrisphenylphosphine palladium the mixture was refluxed at 95 °C for 5 h. The mixture could cool down, the solvent was removed, and the crude product was purified by column chromatography with Toluene/EtOAc (15:1) as the eluent. 93.8 mg (0.137 mmol, 96%) of an orange solid were isolated.

$[\text{Pd}(\text{PPh}_3)(\text{bzTSCmB})\text{Cl}]$ $\text{C}_{34}\text{H}_{30}\text{ClN}_3\text{PPdS}$ (686.6 g/mol).
Yield: 93.8 mg (0.137 mmol, 96%).
Habitus Orange solid.
 $^1\text{H NMR}$: (300 MHz, DMSO- d_6) δ [ppm] = 8.14–8.01 (m, 1H), 7.94 (d, $3J = 7.85$ Hz, 1H), 7.81 (d, $3J = 7.68$ Hz, 1H), 7.19–7.14 (m, 1H, H-11), 4.91 (t, $3J = 6.71$ Hz, 1H, H-2), 2.42 (s, 3H, H-14), 1.76–1.67 (m, 3H, H-7).
 $^{31}\text{P NMR}$ (161.9 MHz, CDCl_3) δ [ppm] = 28.1.

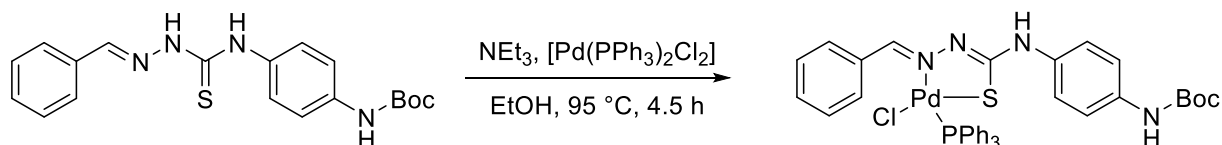
5.8.3. Synthesis of [Pd(PPh₃)(bzTSCLP)]



0.015 g (0.031 mmol, 1.0 eq.) ligand HbzTSCLP was dissolved in 30 ml EtOH at 40 °C. 0.004 ml (0.03 mmol, 1.0 eq.) triethyl amine was added. After the addition of 0.026 g (0.037 mmol, 1.2 eq.) dichloro bistrisphenylphosphine palladium the mixture was refluxed at 95 °C for 5 h. The mixture was allowed to cool down, the solvent was removed, and the crude product was purified by column chromatography with toluene/EtOAc (10:1 → 3:1) as the eluent. 76.4 mg of a yellow solid were isolated.

[Pd(PPh₃)(aphTSCLP)Cl] C₄₁H₄₉N₄O₄PPdS (831.32 g/mol).
Yield: 76.4 mg (0.03 mmol, 97%).
Habitus: yellow solid.
¹H NMR: (300 MHz, CDCl₃) δ [ppm] = 7.96–7.90 (m, 1H), 5.00 (d, 1H, -NH), 4.23–4.10 (m, 1H, H-5), 3.38–3.22 (m, 2H, H-1), 2.38 (s, 3H, H-18), 1.47 (s, 9H, H-8), 1.45 (s, 9H, H-11).

5.8.4. Synthesis of [Pd(PPh₃)(HbzTSCbap)Cl]



A Schlenk-flask was charged with 50 mg (0.13 mmol, 1.00 eq.) ligand in EtOH (28.0 ml) at 40 °C under inert conditions. Triethylamine (13.0 mg, 0.130 mmol, 0.019 ml, 1.00 eq.) and Pd(PPh₃)₂Cl₂ (91.0 mg, 0.130 mmol, 1.00 eq.) were added slowly and the mixture was stirred under reflux for 4.5 h at 95 °C. The EtOH was removed under reduced pressure and the crude product was purified *via* column chromatography (SiO₂, Toluene/EE, 15:1). The desired complex could be obtained as a pure yellow-orange solid in a yield of 80%.

[Pd(PPh₃)(HbzTSCbap)Cl] C₃₇H₃₆ClN₄O₂PPdS (772.1 g/mol).
Yield: 80 mg (0.103 mmol, 80%).
Habitus: yellow solid.
R_f: 0.54 (Tol/EtOAc = 15:1).
¹H NMR: (300 MHz, CDCl₃) δ [ppm] = 9.47 (s, 1H), 9.23 (s, 1H), 8.51 (d, J = 4.1 Hz, 1H), 8.14 (d, J = 7.4 Hz, 2H), 7.75–7.25 (m, 24H), 1.47 (s, 9H).
¹³C NMR: (75 MHz, CDCl₃): δ [ppm] = 28.9, 128.6, 129.2, 134.6.
³¹P NMR: (121 MHz, CDCl₃): δ [ppm] = 28.0.

5.8.5. Synthesis of Ir(III) complexes

All iridium complexes were synthesized following the same procedure:

1 eq. (1 mmol scale) of the corresponding benzyl thiosemicarbazone were dissolved in 50 mL toluene and 2 eq. of triethylamine were added before the reaction was degassed. Afterwards, 1 eq. of the Ir(I) precursor was added, and the mixture was heated to reflux overnight. The solvent was removed under reduced pressure and the crude mixture was purified by column chromatography using a toluene/ethyl acetate mixture (19:1) yielding dark yellow solids. Typically, the chloro complex is eluted before the hydrido complex.

5.8.5.1. Iridium complexes of H₂bzTSCmB

[Ir(PPh₃)₂(bzTSCmB)H]

C₅₂H₄₆IrN₃P₂S (999.19 g/mol).

Yield:

24 mg (0.024 mmol, 24%).

Habitus

yellow solid.

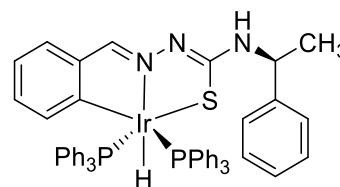
¹H NMR:

(300 MHz, DMSO-*d*₆) δ [ppm] = 7.51 – 7.42 (m, 5H), 7.42 – 7.21 (m, 27H), 7.22 – 7.10 (m, 20H), 6.88 (s, 1H), 6.74 – 6.63 (m, 1H), 6.54 (d, *J* = 7.5 Hz, 1H), 6.42 (t, *J* = 7.4 Hz, 1H), 5.99 (td, *J* = 7.4, 1.5 Hz, 1H), 4.50 (t, *J* = 7.4 Hz, 1H), 1.15 (d, *J* = 7.0 Hz, 3H), -14.65 (t, *J* = 17.3 Hz, 1H).

HR-ESI-MS

[M+H]⁺ calc.: 1000.25897 found: 1000.25569.

[M-PPh₃]⁺ calc.: 738.16783 found: 738.16519.



[Ir(PPh₃-*d*₁₅)₂(bzTSCmB)H]

C₅₂H₁₆D₃₀IrN₃P₂S (1029.44 g/mol).

Yield:

27 mg (0.026 mmol, 26%).

Habitus

yellow solid.

¹H NMR:

(300 MHz, DMSO-*d*₆) δ [ppm] = 7.70 (dd, *J* = 4.5, 2.9 Hz, 1H), 7.52 – 7.00 (m, 16H), 6.75 (d, *J* = 7.5 Hz, 1H), 6.41 (t, *J* = 7.3 Hz, 1H), 6.29 (s, 0H), 6.14 (d, *J* = 7.1 Hz, 1H), 6.01 (t, *J* = 7.2 Hz, 1H), 5.89 (td, *J* = 7.4, 1.3 Hz, 1H), 4.39 (t, *J* = 7.0 Hz, 1H), 1.14 (d, *J* = 7.2 Hz, 3H), -14.25 (t, *J* = 16.4 Hz, 1H), -14.52 (t, *J* = 16.7 Hz, 1H).

³¹P NMR:

(121 MHz, DMSO-*d*₆) δ [ppm] = 15.94 (dd, *J* = 67.5, 17.2 Hz), 14.60 (dd, *J* = 39.1, 16.6 Hz).

[Ir(PPh₃)₂(bzTSCmB)Cl]

C₅₂H₄₅ClIrN₃P₂S (1033.21 g/mol).

Yield:

78 mg (0.075 mmol, 75%).

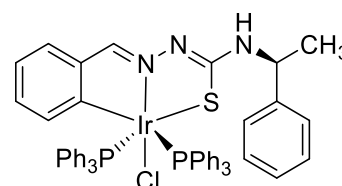
Habitus

yellow solid.

HR-ESI-MS

[M+H]⁺ calc.: 1034.22000 found: 1034.21780.

[M-PPh₃]⁺ calc.: 772.12886 found: 772.12379.



[Ir(PPh₃-d₁₅)₂(bzTSCmB)Cl] C₅₂H₁₅D₃₀ClIrN₃P₂S (1062.40 g/mol).

Yield: 67 mg (0.066 mmol, 66%).

Habitus yellow solid.

5.8.5.2. Iridium complexes of H₂bz(m)TSCmB

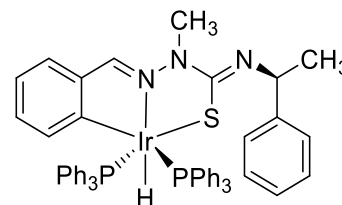
[Ir(PPh₃)₂(bz(m)TSCmB)H] C₅₃H₄₈IrN₃P₂S (1013.27 g/mol).

Yield: 17 mg (0.017 mmol, 17%).

Habitus yellow solid.

¹H NMR: (300 MHz, DMSO-d₆) δ [ppm] =

8.94 (d, *J* = 8.6 Hz, 1H), 8.02 (s, 1H), 7.95 – 7.82 (m, 2H), 7.74 – 7.51 (m, 6H), 7.50 – 7.12 (m, 14H), 7.03 – 6.84 (m, 2H), 5.77 – 5.61 (m, 1H), 3.83 (s, 3H), 1.59 (d, *J* = 7.0 Hz, 3H), -11.06 (td, *J* = 20.5, 4.9 Hz, 1H), -11.49 (td, *J* = 20.6, 5.1 Hz, 1H).



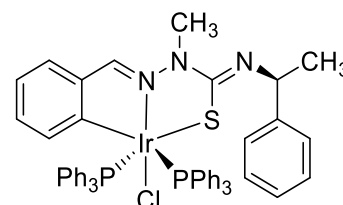
[Ir(PPh₃)₂(bz(m)TSCmB)Cl] C₅₃H₄₇ClIrN₃P₂S (1047.65 g/mol).

Yield: 24 mg (0.024 mmol, 24%).

Habitus yellow solid.

¹H NMR (as PPh₃-d₁₅):

(300 MHz, DMSO-d₆) δ [ppm] = 7.52 – 7.44 (m, 1H), 7.37 – 7.27 (m, 6H), 7.27 – 7.22 (m, 6H), 7.21 – 7.11 (m, 12H), 7.09 – 6.98 (m, 4H), 6.12 (q, *J* = 7.2 Hz, 1H), 3.80 (s, 3H), 1.61 (d, *J* = 7.3 Hz, 3H).



5.8.5.3. Iridium complexes of H₂aphTSCmB

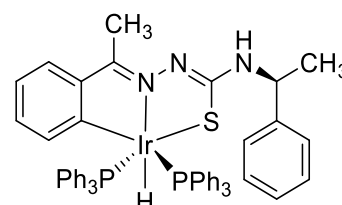
[Ir(PPh₃)₂(aphTSCmB)H] C₅₃H₄₈IrN₃P₂S (1013.27 g/mol).

Yield: 30.4 mg (0.03 mmol, 30%).

Habitus yellow solid.

¹H NMR: (300 MHz, DMSO-d₆) δ [ppm] =

7.98 – 7.84 (m, 0H), 7.70 – 7.52 (m, 15H), 7.53 – 7.32 (m, 19H), 7.30 – 7.07 (m, 23H), 7.07 – 6.84 (m, 10H), 6.81 – 6.58 (m, 2H), 6.44 (td, *J* = 7.3, 1.6 Hz, 1H), 4.00 (s, 1H), 1.10 (d, *J* = 7.0 Hz, 3H), -14.34 (t, *J* = 16.6 Hz, 1H).



[Ir(PPh₃-d₁₅)₂(aphTSCmB)H] C₅₃H₁₈D₃₀IrN₃P₂S (1043.36 g/mol).

Yield: 23.1 mg (0.023 mmol, 23%).

Habitus yellow solid.

¹H NMR: (300 MHz, DMSO-d₆) δ [ppm] = 7.43 – 7.08 (m, 24H), 6.90 (s, 1H), 6.64 (d, *J* = 7.5 Hz, 2H), 6.54 (d, *J* = 8.1 Hz, 1H), 6.43 (t, *J* = 7.3 Hz, 1H), 5.99 (t, *J* = 7.5 Hz, 1H), 4.52 (d,

$J = 10.6$ Hz, 1H), 1.16 (d, $J = 6.9$ Hz, 3H), -14.65 (td, $J = 17.4, 1.6$ Hz, 1H).

[Ir(PPh₃)₂(aphTSCmB)Cl]

Yield:

Habitus

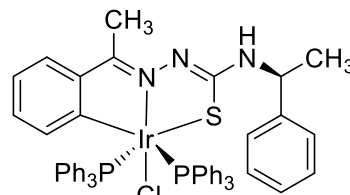
HR-ESI-MS

C₅₃H₄₇ClIrN₃P₂S (1047.23 g/mol).

7.1 mg (0.007 mmol, 7%).

yellow solid.

[M+H]⁺ calc.: 1046.23331 found: 1046.23396.



[Ir(PPh₃-d₁₅)₂(aphTSCmB)Cl]

Yield:

Habitus

C₅₃H₁₇D₃₀IrN₃P₂SCl (1076.42 g/mol).

29 mg (0.137 mmol, 29%).

yellow solid.

[Ir(AsPh₃)₂(aphTSCmB)H]

Yield:

Habitus

¹H NMR:

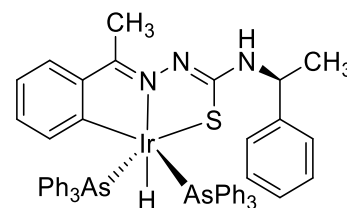
C₅₃H₄₈IrN₃As₂S (1101.16 g/mol).

25.6 mg (0.025 mmol, 25%).

yellow solid.

(300 MHz, DMSO-d₆) δ [ppm] =

7.78 – 7.64 (m, 1H), 7.51 – 6.92 (m, 27H), 6.89 – 6.68 (m, 2H), 6.66 – 6.53 (m, 1H), 6.45 (td, $J = 7.4, 1.3$ Hz, 0H), 6.06 (td, $J = 7.3, 2.4$ Hz, 0H), 4.70 (q, $J = 7.1$ Hz, 0H), 1.24 (d, $J = 6.9$ Hz, 1H), -15.59 (s, 1H).



[Ir(AsPh₃)₂(aphTSCmB)Cl]

Yield:

Habitus

¹H NMR:

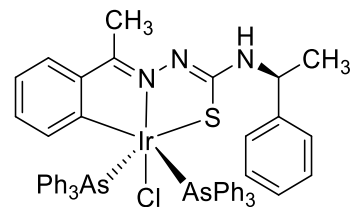
C₅₃H₄₇IrN₃As₂S (1135.12 g/mol).

17.3 mg (0.017 mmol, 17%).

yellow solid.

(300 MHz, DMSO-d₆) δ [ppm] =

8.52 (d, $J = 8.8$ Hz, 1H), 7.77 – 7.66 (m, 1H), 7.49 – 7.09 (m, 24H), 5.86 – 5.57 (m, 1H), 2.33 (s, 3H), 1.57 (d, $J = 7.0$ Hz, 3H).



[Ir(PCy₃) (aphTSCmB)H]

Yield:

Habitus

¹H NMR:

³¹P NMR:

HR-ESI-MS

C₃₅H₅₁IrN₃PS (769.06 g/mol).

26 mg (0.034 mmol, 34%).

yellow solid.

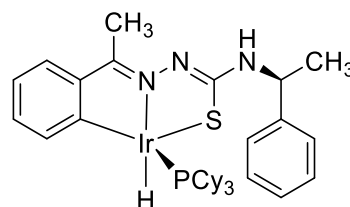
(300 MHz, DMSO-d₆) δ [ppm] =

-30.64 (d, $J = 18.0$ Hz, 1H).

(121 MHz, DMSO-d₆) δ [ppm] = 2.62.

[M+Na]⁺ calc.: 792.30628 found: 790.29063.

[M-H]⁺ calc.: 768.30195 found: 767.29645.

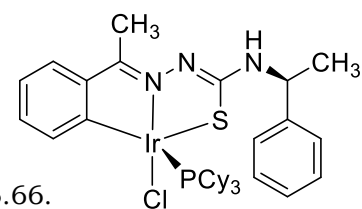


[Ir(PCy₃)(aphTSCmB)Cl]C₃₅H₅₀IrN₃PClS (803.28 g/mol).**Yield:**

8 mg (0.01 mmol, 10%).

Habitus

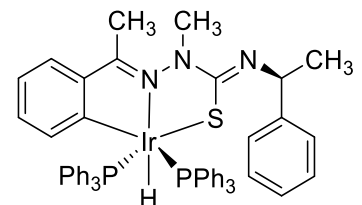
yellow solid.

³¹P NMR:(121 MHz, DMSO-d₆) δ [ppm] = -15.66.**HR-ESI-MS**[M+H]⁺ calc.: 804.28536 found: 804.13877.**5.8.5.4. Iridium complexes of H₂aph(m)TSCmB****[Ir(PPh₃)₂(aph(m)TSCmB)H]**C₅₄H₄₉IrN₃P₂S (1027.28 g/mol).**Yield:**

15.9 mg (0.015 mmol, 15%).

Habitus

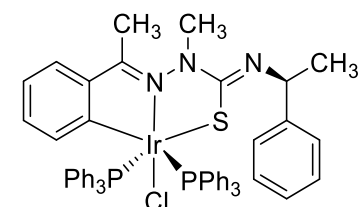
yellow solid.

¹H NMR:(300 MHz, DMSO-d₆) δ [ppm] = -14.50 (t, *J* = 18.0 Hz, 1H).**¹H NMR as PPh₃-d₁₅:**(300 MHz, DMSO-d₆) δ [ppm] = 7.70 (d, *J* = 4.2 Hz, 0H), 7.55 – 6.89 (m, 10H), 6.74 (d, *J* = 7.6 Hz, 0H), 6.56 (t, *J* = 7.2 Hz, 2H), 6.30 (d, *J* = 7.7 Hz, 1H), 6.14 (d, *J* = 7.1 Hz, 1H), 5.89 (t, *J* = 7.5 Hz, 1H), 4.13 (t, *J* = 6.8 Hz, 2H), 1.97 (s, 4H), 1.25 (d, *J* = 7.9 Hz, 13H), -14.25 (t, *J* = 16.4 Hz, 1H), -14.52 (t, *J* = 16.7 Hz, 1H).**[Ir(PPh₃)₂(aph(m)TSCmB)Cl]**C₅₄H₄₉ClIrN₃P₂S (1061.68 g/mol).**Yield:**

4.4 mg (0.004 mmol, 4%).

Habitus

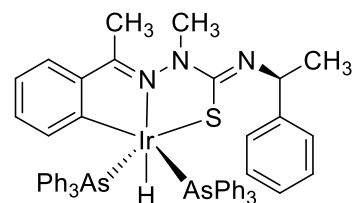
yellow solid.

¹H NMR as PPh₃-d₁₅:(300 MHz, DMSO-d₆) δ [ppm] = 7.60 – 7.42 (m, 1H), 7.38 – 7.24 (m, 5H), 7.06 (dd, *J* = 7.4, 2.5 Hz, 4H), 6.13 (q, *J* = 7.3 Hz, 1H), 3.80 (s, 3H), 1.61 (d, *J* = 7.3 Hz, 3H).**HR-ESI-MS**[M+H]⁺ calc.: 1084.24655 found: 1084.22049.**[Ir(AsPh₃)₂(aph(m)TSCmB)H]**C₅₄H₅₀IrN₃As₂S (1115.14 g/mol).**Yield:**

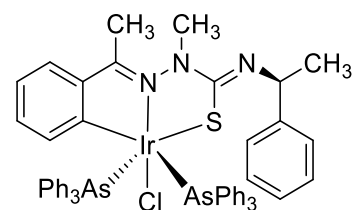
7.3 mg (0.007 mmol, 7%).

Habitus

yellow solid.

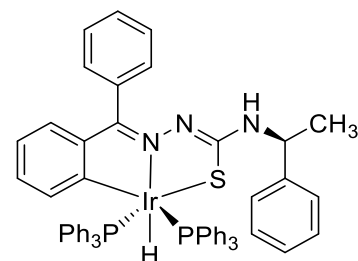
¹H NMR:(300 MHz, DMSO-d₆) δ [ppm] =7.82 – 7.65 (m, 3H), 7.64 – 7.55 (m, 3H), 7.39 (m, 37H), 7.34 – 7.15 (m, 32H), 7.15 – 6.87 (m, 15H), 6.82 – 6.61 (m, 2H), 6.53 (td, *J* = 7.3, 1.6 Hz, 1H), 4.27 (d, *J* = 11.3 Hz, 2H), 1.55 (s, 3H), 1.15 (d, *J* = 7.0 Hz, 3H), -15.59 (s, 1).

[Ir(AsPh₃)₂(aphTSCmB)Cl] C₅₄H₄₉ClIrN₃As₂S (1149.14 g/mol).
Yield: 10.3 mg (0.010 mmol, 10%).
Habitus yellow solid.



5.8.5.5. Iridium complexes of H₂bphTSCmB

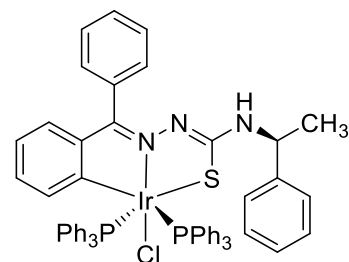
[Ir(PPh₃)₂(bphTSCmB)H] C₅₈H₅₀IrN₃P₂S (1075.28 g/mol).
Yield: 62 mg (0.06 mmol, 58%).
Habitus yellow solid.
¹H NMR: (300 MHz, DMSO-d₆) δ [ppm] =



7.69 – 7.58 (m, 1H), 7.53 – 7.41 (m, 6H), 7.35 – 7.10 (m, 23H), 7.05 (t, *J* = 7.6 Hz, 6H), 6.89 – 6.74 (m, 3H), 6.52 – 6.36 (m, 2H), 6.29 (dd, *J* = 7.8, 1.4 Hz, 1H), 6.03 (td, *J* = 7.3, 1.5 Hz, 1H), 4.06 (d, *J* = 14.0 Hz, 1H), 1.04 (dd, *J* = 6.6, 2.3 Hz, 3H), -14.57 (t, *J* = 18.0 Hz, 1H).

³¹P NMR: (121 MHz, DMSO-d₆) δ [ppm] = 11.68 (t, *J* = 6.3 Hz).

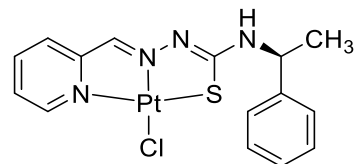
[Ir(PPh₃)₂(bphTSCmB)Cl] C₅₈H₄₉ClIrN₃P₂S (1109.73 g/mol).
Yield: 45 mg (0.04 mmol, 40%). PPh₃ impurities.
Habitus yellow solid.
³¹P NMR: (121 MHz, DMSO-d₆) δ [ppm] = 11.59 (s).



5.8.6. Synthesis of [Pt(fpyTSCmB)Cl]

1 eq. of the protoligands HfpyTSCmB and 1 eq. of K₂[PtCl₄] were dissolved in MeCN and stirred for 2 h at ambient temperature. The colour changes from yellow to dark red. Upon evaporation of the solvent a red solid form that could be isolated by filtration.

[Pt(fpyTSCmB)Cl] C₁₅H₁₇ClN₄SPt (513.91 g/mol).
Yield: 119.9 mg (0.23 mmol, 97%).
Habitus red solid.



¹H NMR: (300 MHz, DMSO-d₆) δ [ppm] = 8.87 (d, 1H, *J* = 8.0 Hz, NH7), 8.70 (d, 1H, *J* = 5.6 Hz, H15), 8.35 (s, 1H, H10), 8.13 (t, 1H, *J* = 7.7 Hz, H13), 7.70 (t, 1H, *J* = 7.9 Hz, H14), 7.33 (d, 5H, *J* = 5.9 Hz, H3,4,5), 7.25 (dd, 1H, *J* = 6.1, 2.1 Hz, H12), 5.06 (qui, 1H, *J* = 7.4 Hz, H1), 1.42 (d, 3H, *J* = 7.1 Hz, H6).

5.8.7.Synthesis of [Pt(fpyTSClp)Cl]

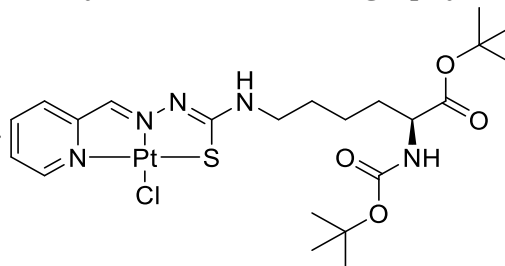
1 eq. of the ligand was dissolved in MeCN and added to a solution of 1 eq. $K_2[PtCl_4]$. The colour changes from yellow to dark red. After 2 h the solvent was evaporated under reduced pressure and the residue was purified by column chromatography.

[Pt(fpyTSClp)Cl] $C_{22}H_{34}ClN_5O_4SPt$ (695.14 g/mol).

Yield: 127 mg (0.18 mmol, 75%).

Habitus red solid.

1H NMR: (300 MHz, DMSO- d_6) δ [ppm] = 8.81-8.68 (m, 1H), 8.40 (s, 1H), 8.30 (d, 1H J = 4.5 Hz), 8.15 (t, 1H, J = 8.2 Hz), 7.71 (t, 1H, J = 9.0 Hz), 7.10 (s, 1H), 5.07 (d, 1H, J = 8.3 Hz, NH), 3.75 (q, 2H, J = 6.7 Hz), 3.65-3.55 (m, 2H) 1.69-1.47 (m, 4H), 1.39 (s, 20H).



5.8.8.Synthesis of [Pt(6-phfpyTSCmB)Cl]

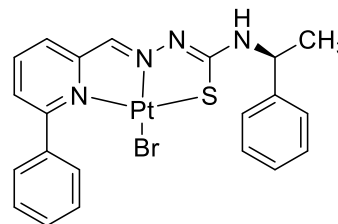
[Pt(6-phfpyTSCmB)Cl] was synthesized according to the method described in chapter 5.8.6.

[Pt(6-phfpyTSCmB)Cl] $C_{22}H_{34}ClN_5O_4SPt$ (695.14 g/mol).

Yield: 127 mg (0.18 mmol, 75%).

Habitus red solid.

1H NMR: (300 MHz, DMSO- d_6) δ [ppm] = 8.81-8.68 (m, 1H), 8.40 (s, 1H), 8.30 (d, 1H J = 4.5 Hz), 8.15 (t, 1H, J = 8.2 Hz), 7.71 (t, 1H, J = 9.0 Hz), 7.10 (s, 1H), 5.07 (d, 1H, J = 8.3 Hz, NH), 3.75 (q, 2H, J = 6.7 Hz), 3.65-3.55 (m, 2H) 1.69-1.47 (m, 4H), 1.39 (s, 20H).



5.8.9.Synthesis of [Ni(hphfpyTSCmB)]

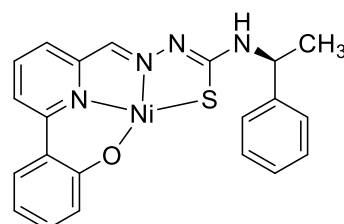
13 mg (0.035 mmol, 1 eq.) H₂hphfpyTSCmB were dissolved in 5 mL MeCN, and 2 mL triethylamine were added upon which the solution darkens. 8 mg NiCl₂ were dissolved in 5 mL water and added to the ligand solution. The solution changed quickly to a red colour. The reaction mixture was stirred at ambient temperature overnight. Solvent was removed under reduced pressure and the residue was purified by column chromatography (100% EtOAc) yielding a dark red solid.

[Ni(hphfpyTSCmB)] $C_{21}H_{18}N_4OSNi$ (433.16 g/mol).

Yield: 18.6 mg (0.43 mmol, 86%).

R_f: 0.8 (pure EtOAc)

Habitus red solid.



¹H NMR: (300 MHz, CDCl₃) δ [ppm] = 8.17 (d, *J* = 8.6 Hz, 1H), 8.05 – 7.85 (m, 3H), 7.35 (d, *J* = 5.8 Hz, 6H), 7.07 (d, *J* = 7.7 Hz, 1H), 6.71 (d, *J* = 7.1 Hz, 1H), 5.03 (d, *J* = 19.5 Hz, 1H), 1.58 (s, 3H).

EI-MS [m/z]: 432 (calc. 432).

5.8.10. Synthesis of [Pd(hphfpyTSCmB)]

Synthesized according to the procedure described in chapter 5.8.9. using K₂[PdCl₄] as metal ion source.

[Pd(hphfpyTSCmB)] C₂₁H₁₈N₄OSPd (480.88 g/mol).

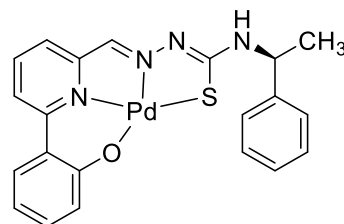
Yield: 21.6 mg (0.45 mmol, 90%).

R_f: 0.8 (pure EtOAc)

Habitus orange solid.

¹H NMR: (300 MHz, CDCl₃) δ [ppm] = 8.17 (d, *J* = 8.6 Hz, 1H), 8.02 – 7.83 (m, 2H), 7.46 (s, 1H), 7.41 – 7.16 (m, 5H), 6.74 (ddd, *J* = 8.2, 6.3, 1.7 Hz, 1H), 5.10 (s, 1H), 1.57 (d, *J* = 9.7 Hz, 14H).

EI-MS [m/z]: 480 (calc. 480).



5.8.11. Synthesis of [Pt(hphfpyTSCmB)]

Synthesized according to the procedure described in chapter 5.8.9. using K₂[PtCl₄] as metal ion source.

[Pt(hphfpyTSCmB)] C₂₁H₁₈N₄OSPt (569.55 g/mol).

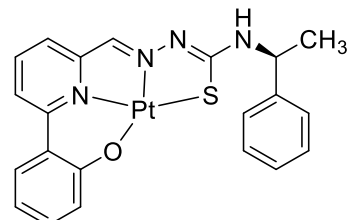
Yield: 26.3 mg (0.46 mmol, 92%).

R_f: 0.8 (pure EtOAc)

Habitus Red solid.

¹H NMR: (300 MHz, CDCl₃) δ [ppm] = 8.37 (d, *J* = 8.5 Hz, 1H), 8.19 – 8.03 (m, 2H), 7.86 (s, 1H), 7.37 (d, *J* = 4.5 Hz, 9H), 6.86 – 6.73 (m, 1H), 5.23 (t, *J* = 7.2 Hz, 1H), 1.60 (d, *J* = 6.8 Hz, 4H).

EI-MS [m/z]: 569 (calc. 569).



5.8.12. Synthesis of [Cu(hphfpyTSCmB)]

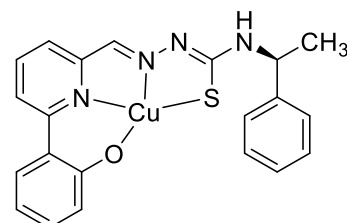
Synthesized according to the procedure described in chapter 5.8.9. using CuSO₄ hydrate as metal ion source.

[Cu(hphfpyTSCmB)] C₂₁H₁₈N₄OSCu (438.01 g/mol).

Yield: 30 mg (0.069 mmol, 62%).

R_f: 0.8 (pure EtOAc)

Habitus brown solid.



HR-ESI-MS[M+H]⁺ calc.: 438.05701 found: 438.05718.[M+Na]⁺ calc.: 460.03895 found: 460.03913.**5.8.13. Synthesis of [Cu((tBu)hphfpyTSC)]**

Synthesized according to the procedure described in chapter 5.8.9. using CuSO₄ hydrate as metal ion source and H₂(tBu)hphfpyTSC as ligand.

[Cu(hphfpyTSCmB)]C₂₁H₂₆N₄OSCu (446.07 g/mol).**Yield:**

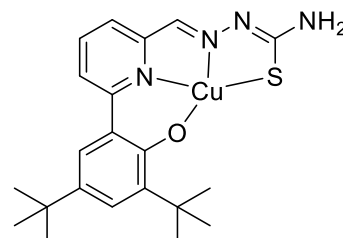
20.1 mg (0.045 mmol, 90%).

R_f:

0.8 (pure EtOAc)

Habitus

brown solid.

EI-MS[M+H]⁺ calc.: 446.11961 found: 446.11921.[M+Na]⁺ calc.: 468.10155 found: 468.10162.**5.8.14. Synthesis of [Cu((tBu)hphfpyTSCmB)]**

Synthesized according to the procedure described in chapter 5.8.9. using CuSO₄ hydrate as metal ion source and H₂(tBu)hphfpyTSCmB as ligand.

[Cu(hphfpyTSCmB)]C₂₉H₃₄N₄OSCu (550.22 g/mol).**Yield:**

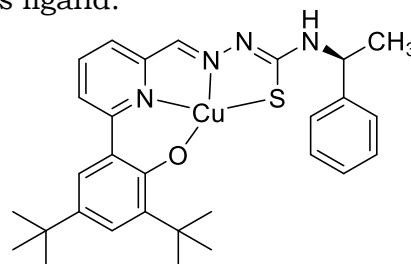
27 mg (0.049 mmol, 82%).

R_f:

0.8 (pure EtOAc)

Habitus

brown solid.

EI-MS[M+H]⁺ calc.: 550.18221 found: 550.18157.[M+Na]⁺ calc.: 572.16415 found: 572.16376.**5.8.15. Synthesis of [Ni(apyTSCmB)Cl]**

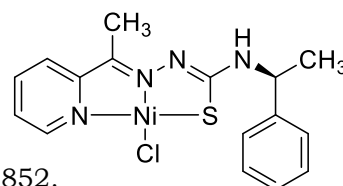
[Ni(apyTSCmB)Cl] was synthesized according to the method described in chapter 5.8.6 using NiCl₂ hydrate as metal ion source and HapyTSCmB as ligand.

[Ni(apyTSCmB)Cl]C₁₆H₁₇N₄ClNi (390.54 g/mol).**Yield:**

320 mg (0.82 mmol, 93%).

Habitus

brown solid.

HR-ESI-MS[M+H]⁺ calc.: 391.02886 found: 391.02852.[M+Na]⁺ calc.: 413.01081 found: 413.01055.

5.8.16. Synthesis of [Ni(apyTSCmB)(NCS)]

[Ni(apyTSCmB)(NCS)] was synthesized according to the method described in chapter 5.8.6 using Ni(NCS)₂ as metal ion source and HapyTSCmB as ligand.

[Ni(apyTSCmB)NCS] C₁₇H₁₇N₅S₂Ni (414.17 g/mol).

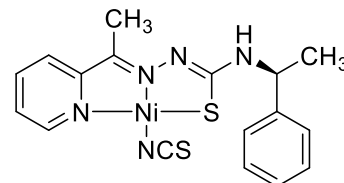
Yield: 110 mg (0.282 mmol, 96%).

Habitus brown solid.

¹H NMR: (300 MHz, DMSO-*d*₆) δ [ppm] = 8.63 (d, *J* = 7.5 Hz, 1H), 8.53 (dd, *J* = 5.4, 1.5 Hz, 1H), 8.14 (td, *J* = 7.9, 1.7 Hz, 1H), 7.79 (d, *J* = 8.0 Hz, 1H), 7.61 (t, *J* = 6.6 Hz, 1H), 7.33 (d, *J* = 4.3 Hz, 3H), 7.24 (q, *J* = 4.3 Hz, 1H), 5.02 – 4.77 (m, 1H), 1.41 (d, *J* = 7.1 Hz, 3H).

HR-ESI-MS [M+H]⁺ calc.: 414.03516 found: 414.03502.

[M+Na]⁺ calc.: 436.01711 found: 436.01703.



5.8.17. Synthesis of [Pd(apyTSCmB)Cl]

[Pd(apyTSCmB)Cl] was synthesized according to the method described in chapter 5.8.6 using K₂[PdCl₄] as metal ion source and HapyTSCmB as ligand.

[Pd(apyTSCmB)Cl] C₁₆H₁₇ClN₄PdS (439.27 g/mol).

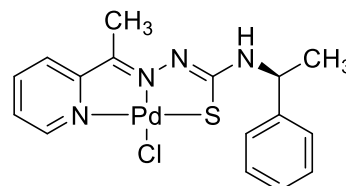
Yield: 0.15 g (0.343 mmol, >99%).

Habitus yellow solid.

¹H NMR: (300 MHz, DMSO-*d*₆) δ [ppm] = 8.63 (d, 3*J* = 6.80 Hz, 1H, -CSNH), 8.53 (d, 3*J* = 4.82 Hz, 1H, H-13), 8.14 (td, 3*J* = 7.82 Hz, 4*J* = 1.40 Hz, 1H, H-12), 7.79 (d, 3*J* = 7.91 Hz, 1H, H-10), 7.61 (t, 3*J* = 6.43 Hz, 1H, H-6), 7.37–7.29 (m, 4H, H-4, H-5), 7.24 (st, 3*J* = 4.20 Hz, 1H, H-11), 4.91 (t, 3*J* = 7.01 Hz, 1H, H-2), 2.28 (s, 3H, H-14), 1.41 (d, 3*J* = 7.13 Hz, 3H, H-7).

HR-ESI-MS [M+H]⁺ calc.: 437.99861 found: 437.99859.

[M+Na]⁺ calc.: 459.98055 found: 459.98059.



5.8.18. Synthesis of [Pt(apyTSCmB)Cl]

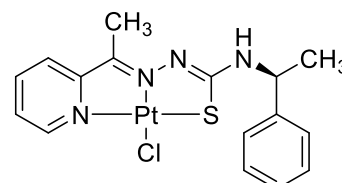
[Pt(apyTSCmB)Cl] was synthesized according to the method described in chapter 5.8.6 using K₂[PtCl₄] as metal ion source and HapyTSCmB as ligand.

[Pt(apyTSCmB)Cl] C₁₆H₁₇ClN₄SPt (527.93 g/mol).

Yield: 0.121 g (0.23 mmol, 96%).

Habitus red solid.

¹H NMR: (300 MHz, DMSO-*d*₆) δ [ppm] = 8.76 (m, 2H, NH7, H15), 8.16 (t, 1H, *J* = 7.9 Hz, H13), 7.74 (d, 1H, *J* = 8.1 Hz, H15), 7.68 (d, 1H, *J* = 6.8 Hz, H12), 7.41–7.29 (m, 4H, H3,4), 7.24 (m, 1H, H5), 5.13–



4.93 (m, 1H, H1), 2.26 (d, 3H, $J = 6.9$ Hz, H16), 1.43 (d, 3H, $J = 7.0$ Hz, H6).

HR-ESI-MS

[M+H]⁺ calc.: 527.05619 found: 527.05655.

[M+Na]⁺ calc.: 549.03813 found: 549.03826.

5.8.19. Synthesis of [Pt(apyTSClP)Cl]

In a 20 mL vial 113 mg HapyTSClP (0.235 mmol, 0.98 eq.) were dissolved in 3 mL MeOH und the bright-yellow solution was combined with an orange solution of 100 mg K₂[PtCl₄] (0.241 mmol, 1.00 eq.), dissolved in 6 mL H₂O. The mixture was stirred until after 5 min a solid precipitated. The mixture was stirred for additional 1 h and filtrated. The precipitate was washed with ice-cold 1 mL MeOH in portions and dried to obtain 110 mg of a red powder. TLC-control indicated several impurities. The crude product was purified via flash column chromatography (*c*-hex/EtOAc 60:40, then product elution with 100% EtOAc) to give 141 mg [Pt(apyTSClP)Cl] as red solid (0.2 mmol, 83% yield).

[Pt(apyTSClP)Cl]

C₂₃H₃₆ClN₅O₄SPt (709.17 g/mol).

Yield:

141 mg (0.2 mmol, 83%).

Habitus

red solid.

FTIR-ATR

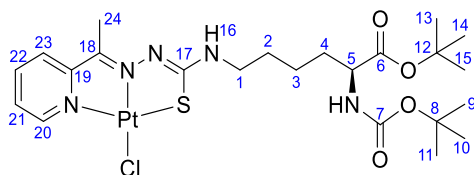
3853 (w), 3675 (m), 3424 (w), 2987 (s), 2901 (s), 2359 (w), 1715 (m), 1558 (w), 1507 (m), 1455 (m), 1406 (m), 1394 (m), 1380 (m), 1250 (m), 1230 (m), 1154 (m), 1075 (s), 1066 (s), 1056 (s), 1028 (m), 891 (w), 789 (w), 706 (w), 642 (w), 626 (w), 618 (m), 606 (m), 591 (w), 581 (w), 570 (w), 560 (w), 546 (w), 540 (w), 526 (w).

¹H NMR:

(300 MHz, DMSO-*d*₆) δ [ppm] = 8.88 (d, 1H, $J = 5.5$ Hz, H20), 7.90 (t, 1H, $J = 7.6$ Hz, H22), 7.38 (d, 2H, H21,23), 5.07 (d, 1H, $J = 8.3$ Hz, NH), 4.24-4.01 (m, 1H, H5), 3.47 (q, 2H, $J = 6.7$ Hz, H1), 2.29 (s, 3H, H24), 1.86-1.52 (m, 6H, H2,3,4), 1.45 (s, 9H, H13,14,15), 1.43 (s, 9H, H9,10,11). ¹H/¹⁹⁵Pt-HMBC NMR: (300 MHz, CDCl₃) δ [ppm] = -3108 (³J_{Pt,20H}, ⁴J_{Pt,21H/23H}, ⁴J_{Pt,24H}).

HR-ESI-MS

m/z [M+Na]⁺ 730.16964 (calc. 730.1695382).



5.8.20. Synthesis of [Pt(6-BrapyTSCmB)Cl]

[Pt(6-BrapyTSCmB)Cl] was synthesized according to the method described in chapter 5.8.19 using H6-BrapyTSCmB as ligand.

[Pt(6-BrapyTSCmB)Cl]

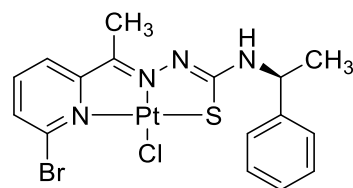
C₁₇H₂₂BrClN₄SPt (623.89 g/mol).

Yield:

80 mg (0.12 mmol, 99%).

Habitus

orange solid.



¹H NMR: (300 MHz, DMSO-*d*₆) δ [ppm] = 8.19 (d, 1H, *J* = 7.7, H-3), 8.00 – 7.69 (m, 2H, H-2;4), 7.44 – 7.21 (m, 5H, H-11-13), 3.45 (d, 1H, *J* = 3.2, H- 6), 3.17 (s, 1H, H-8), 2.65 – 2.36 (s, 3H, H-9).

5.8.21. Synthesis of [Pt(6-PhapyTSCmB)Cl]

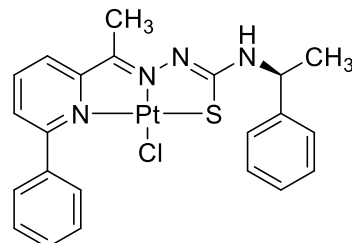
[Pt(6-PhapyTSCmB)Cl] was synthesized according to the method described in chapter 5.8.19 using H6-PhapyTSCmB as ligand.

[Pt(6-PhapyTSCmB)Cl] C₂₃H₂₇ClN₄SPt (622.09 g/mol).

Yield: 78 mg (0.13 mmol, 92%).

Habitus orange solid.

¹H NMR (300 MHz, DMSO-*d*₆) δ [ppm] = 8.16 (dt, 2H, *J* = 6.0, 1.5, H-3), 8.01 – 7.90 (m, 2H, H-2;4), 7.58 – 7.18 (m, 10H, H-10-13; H-14-17), 3.44 (s, 1H, H-6), 3.17 (s, 1H, H-8), 2.59 – 2.39 (m, 3H, H-9).



5.8.22. Synthesis of [Pd(dpyTSCmB)Cl]

120 mg (0.36 mmol, 1.0 eq.) of K₂PdCl₄ and 130 mg (0.36 mmol, 1.0 eq.) of HdpyTSCmB were dissolved in 40 mL of MeCN and stirred for one hour at room temperature. The orange precipitate was filtrated and dried under reduced pressure. 78 mg (0.16 mmol, 44%) of [Pd(dpyTSCmB)Cl] were obtained.

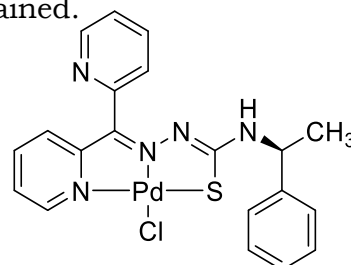
[Pd(dpyTSCmB)Cl] C₂₀H₁₈ClN₅SPd (502.33 g/mol).

Yield: 78 mg (0.16 mmol, 44%).

Habitus yellow solid.

¹H NMR: (300 MHz, DMSO-*d*₆) δ [ppm] = 8.77 (d, *J* = 4.7 Hz, 1H), 8.61 (d, *J* = 5.5 Hz, 1H), 7.96 – 8.05 (m, 2H), 7.57 – 7.65 (d, 2H), 7.44 (d, *J* = 7.6 Hz, 1H), 7.38 – 7.18 (m, 4H), 6.99 (d, *J* = 6.9 Hz, 2H), 4.45 – 4.54 (m, 1H, H-1), 1.30 (d, *J* = 7.1 Hz, 3H, H-6).

EI-MS m/z = [M]⁺ 502, [M-Cl]⁺ 465.



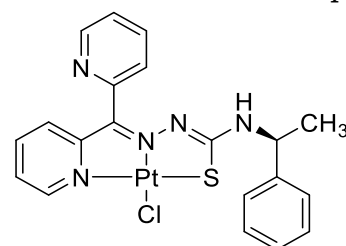
5.8.23. Synthesis of [Pt(dpyTSCmB)Cl]

[Pt(dpyTSCmB)Cl] was synthesized according to the method described in chapter 5.8.19 using HdpyTSCmB as ligand.

[Pt(dpyTSCmB)Cl] C₂₀H₁₈ClN₅SPt (590.99 g/mol).

Yield: 0.131 g (0.22 mmol, 93%).

Habitus red solid.



¹H NMR: (300 MHz, DMSO-*d*₆) δ [ppm] = 8.93 (d, *J* = 7.2 Hz, 1H), 8.77 (d, *J* = 4.7 Hz, 1H), 8.61 (d, *J* = 5.5 Hz, 1H), 7.96 – 8.05 (m, 2H), 7.57 – 7.65 (d, 2H), 7.44 (d, *J* = 7.6 Hz, 1H), 7.38 – 7.18 (m, 4H), 6.99 (d, *J* = 6.9 Hz, 2H), 4.45 – 4.54 (m, 1H, H-1), 1.30 (d, *J* = 7.1 Hz, 3H, H-6).

HR-ESI-MS [M+H]⁺ calc.: 590.06708 found: 590.06731.

[M+Na]⁺ calc.: 612.04903 found: 612.04947.

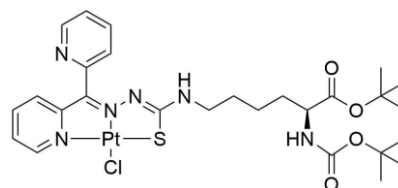
5.8.24. Synthesis of [Pt(dpyTSCLp)Cl]

[Pt(dpyTSCLp)Cl] was synthesized according to the method described in chapter 5.8.6 using K₂[PtCl₄] as metal ion source and HdpyTSCLp as ligand.

[Pt(dpyTSCLp)Cl] C₂₇H₃₇ClN₆O₄SPt (772.23 g/mol).

Yield: 162 mg (0.21 mmol, 87%).

Habitus red solid.



¹H NMR: (300 MHz, CDCl₃) δ [ppm] = 8.94-8.87 (m, 1H), 8.76 (d, 1H, *J* = 4.7), 8.51 (t, 1H, *J* = 5.5 Hz), 8.08 (td, 1H, *J* = 7.9, 1.6 Hz), 7.98 (td, 1H, *J* = 7.8, 1.7 Hz), 7.85 (d, 1H, *J* = 7.9 Hz), 7.73 (td, 1H, *J* = 7.9, 4.1 Hz), 7.53 (m, 1H), 7.43 (d, 1H, *J* = 8.1 Hz), 7.06 (d, 1H, *J* = 7.7 Hz), 4.03 (q, 1H, *J* = 7.1 Hz), 3.16 (d, 2H, *J* = 6.4 Hz), 1.49 (m, 6H, *J* = 7.4 Hz), 1.38 (d, 18H, *J* = 3.0 Hz).

HR-ESI-MS [M+Na]⁺ calc.: 793.18082 found: 793.18082.

[M-Cl]⁺ calc.: 735.22181 found: 735.22206.

5.8.25. Synthesis of [Pt(dpyTSCL-sC18)Cl]

For complex formation HdpyTSCL-sC18 and K₂PtCl₄ were dissolved in H₂O (concentration of stocks: 5 mM; ratio: 1:1) and incubated for 3 h under shaking at r.t. Complex formation was determined by an undergoing colour change and was verified by ESI mass spectrometry. The crude complex was desalted using a C18ec cartridge (Chromafix C18ec, Macherey-Nagel), solvent was evaporated, and the red residue lyophilised.

5.8.26. Synthesis of U(IV) Complexes

5.8.26.1. Synthesis of [U(bzTSC)₄]

Method A: 53.4 mg UCl₄ (0.141 mmol, 1.0 eq.) was dissolved in 3 mL THF and a solution of 100.7 mg HbzTSC (0.562 mmol, 4.0 eq.) in 1 mL THF was added dropwise. 79 μL triethylamine (0.562 mmol, 4.0 eq.) was added to the mixture and after stirring for 1 h at room temperature the suspension was filtered through a PTFE membrane with 0.2 μm pore size. After 30 min yellow crystals formed from the supersaturated THF solution. 48.3 mg [U(bzTSC)₄] (0.051 mmol) was obtained in a yield of 36%.

Method B: 35.9 mg UCl_4 (0.095 mmol, 1.0 eq.) was dissolved in 1 mL THF and a solution of 75.9 mg NabzTSC (0.139 mmol, 4.0 eq.) in 1 mL THF was added dropwise. The mixture was stirred for 6 h at room temperature and after all volatiles were removed under reduced pressure the complex was extracted with THF (5 x 2 mL). The solvent was removed under reduced pressure to afford 30.0 mg $[\text{U}(\text{bzTSC})_4]$ (0.029 mmol) in a yield of 31%.

$[\text{U}(\text{bzTSC})_4] \cdot \text{THF}$	$\text{C}_{48}\text{H}_{64}\text{N}_{12}\text{O}_4\text{S}_4\text{U}$ (1239.38 g/mol).
Habitus	yellow crystalline solid.
FTIR-ATR	3339, 3244, 3163 $\nu(\text{NH})$, 3034 $\nu(\text{CH})_{\text{Ph}}$, 2987 $\nu(=\text{CH})$, 1604 $\nu(\text{C}=\text{N})$, 1578 $\nu(\text{NH})$, 1538 $\delta(\text{HNCS})$, 1100, 1057, 946 $\nu(\text{C}=\text{S})$.
CHNS-Analysis	Anal. Calcd. for $\text{C}_{32}\text{H}_{32}\text{N}_{12}\text{S}_4\text{U} \times \text{C}_4\text{H}_8\text{O}$ (mol. wt. 1023.07): C, 42.26; H, 3.94; N, 16.43; S, 12.53. Found: C, 42.32; H, 4.46; N, 16.46; S, 11.69.

5.8.26.2. Synthesis of $[\text{U}(\text{bzTSCm})_4]$

Method A: 31.5 mg UCl_4 (0.083 mmol, 1.0 eq.) was dissolved in 2 mL THF and a solution of 63.9 mg HbzTSCm (0.332 mmol, 4.0 eq.) in 1 mL THF was added dropwise. 47 μL triethylamine (0.332 mmol, 4.0 eq.) was added to the mixture and after stirring for 1 h at rt the suspension was filtered through a PTFE membrane with 0.2 μm pore size. After 10 min yellow octahedral crystals formed from the supersaturated solution. 21.7 mg $[\text{U}(\text{bzTSCm})_4]$ (0.022 mmol) was obtained in a yield of 26%.

Method B: 13.2 mg UCl_4 (0.035 mmol, 1.0 eq.) was dissolved in 1 mL THF and a solution of 30.0 mg NaBzTSCm (0.139 mmol, 4.0 eq.) in 1 mL THF was added dropwise. The mixture was stirred for 10 min at room temperature and the suspension was filtered through a PTFE membrane with 0.2 μm pore size. After 10 min yellow octahedral crystals formed from the supersaturated solution. 10.9 mg $[\text{U}(\text{bzTSCm})_4]$ (0.011 mmol) was obtained in a yield of 31%.

$[\text{U}(\text{bzTSCm})_4]$	$\text{UC}_{36}\text{H}_{40}\text{N}_{12}\text{S}_4$ (1007.07 g/mol).
Habitus	yellow crystalline solid.
FTIR-ATR	3364 $\nu(\text{NH})$, 2931 $\nu(\text{CH})_{\text{Ph}}$, 2987 $\nu(=\text{CH})$, 2860 $\nu(-\text{CH})_{\text{Me}}$, 1540 $\nu(\text{C}=\text{N})$, 1489 $\nu(\text{NH})$, 1437 $\delta(\text{HNCS})$, 1063, 1039, 944 $\nu(\text{C}=\text{S})$
CHNS-Analysis	Anal. Calcd. for $\text{C}_{36}\text{H}_{40}\text{N}_{12}\text{S}_4\text{U}$ (mol. wt. 1007.07): C, 42.94; H, 4.00; N, 16.69; S, 12.73. Found: C, 42.27; H, 4.16; N, 15.39; S, 9.99.

5.8.26.3. Synthesis of [U(bzTSCdm)₄]

Method A: 7.1 mg UCl₄ (0.019 mmol, 1.0 eq.) was dissolved in 1 mL THF and a solution of 15.5 mg HbzTSCdm (0.075 mmol, 4.0 eq.) in 1 mL THF was added dropwise. 11 μ L triethylamine (0.075 mmol, 4.0 eq.) was added to the mixture and after stirring for 1 h at rt the suspension was filtered through a PTFE membrane with 0.2 μ m pore size. After 30 min orange irregular crystals were grown from the supersaturated solution. 12.7 mg [U(bzTSCdm)₄] (0.012 mmol) was obtained in a yield of 63%.

Method B: 12.4 mg UCl₄ (0.033 mmol, 1.0 eq.) was dissolved in 1 mL THF and a solution of 30.0 mg NabzTSCdm (0.131 mmol, 4.0 eq.) in 1 mL THF was added dropwise. The mixture was stirred for 15 min at room temperature and the suspension was filtered through a PTFE membrane with 0.2 μ m pore size. After 30 min orange irregular crystals were grown from the supersaturated solution. 20.7 mg [U(bzTSCdm)₄] (0.019 mmol) was obtained in a yield of 59%.

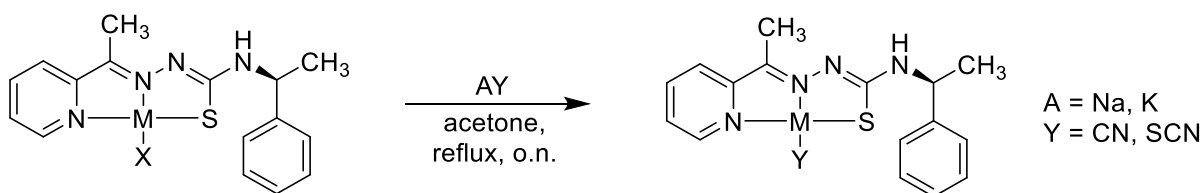
[U(bzTSCdm)₄] UC₄₀H₅₂N₁₂S₄ (1063.17 g/mol).

Habitus orange crystalline solid.

FTIR-ATR 2929 ν (CH)_{Ph}, 2929 ν (=CH), 2810 ν (-CH)_{Me}, 1506 ν (C=N), 1447 ν (NH), 1370 δ (HNCS), 932, 907, 864, 756 ν (C=S).

CHNS-Analysis Anal. Calcd for C₄₀H₄₈N₁₂S₄U (mol. wt. 1063.18): C, 45.19; H, 4.55; N, 15.81; S, 12.06. Found: C, 44.87; H, 4.57; N, 15.13; S, 10.07

5.8.27. Co-Ligand exchange reactions



1 equivalent of the chlorido complex was dissolved in acetone. An alkali salt bearing the desired coligand was added to the solution which was refluxed overnight. After cooling to room temperature, the solvent was removed under reduced pressure and the complex was isolated by column chromatography (SiO₂, MeOH).

[Ni(apyTSCmB)CN] C₁₇H₁₇N₅NiS (382.11 g/mol).

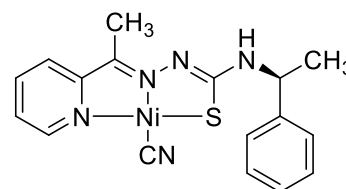
Yield: 0.085 g (0.22 mmol, 89%).

Habitus Bright red solid.

¹H NMR: (300 MHz, DMSO-d₆) δ [ppm] = 8.63 (d, *J* = 7.6 Hz, 1H), 8.44 (d, *J* = 5.4 Hz, 1H), 8.12 (td, *J* = 7.8, 1.5 Hz, 1H), 7.68 (d, *J* = 7.9 Hz, 1H), 7.56 (t, *J* = 6.6 Hz, 1H), 7.33 (d, *J* = 4.3 Hz, 4H), 7.29 – 7.19 (m, 1H), 5.05 – 4.84 (m, 1H), 2.23 (s, 3H), 1.41 (d, *J* = 7.1 Hz, 3H).

HR-ESI-MS [M+H]⁺ calc.: 382.06309 found: 382.06284.

[M+Na]⁺ calc.: 404.04535 found: 404.04478.



[Pd(apyTSCmB)NCS] C₁₇H₁₇N₅PdS₂ (461.00 g/mol).

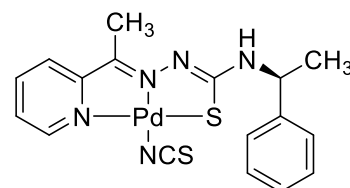
Yield: 0.16 g (0.343 mmol, >99%).

Habitus yellow solid.

¹H NMR: (300 MHz, DMSO-d₆) δ [ppm] = 8.83–8.68 (m, 1H), 8.32–8.12 (d, *J* = 4.82 Hz, 1H), 7.84 (d, *J* = 7.80 Hz, 1H), 7.62 (t, *J* = 6.50 Hz, 1H), 7.37–7.30 (m, 4H), 7.24 (t, *J* = 4.02 Hz, 1H), 5.00–4.82 (m, 1H), 2.31 (s, 3H), 1.42 (d, *J* = 6.68 Hz, 3H, H-7).

HR-ESI-MS [M+H]⁺ calc.: 461.00489 found: 461.00503.

[M+Na]⁺ calc.: 482.98684 found: 482.98708.



[Pd(apyTSCmB)CN] C₁₇H₁₇N₅PdS (429.84 g/mol).

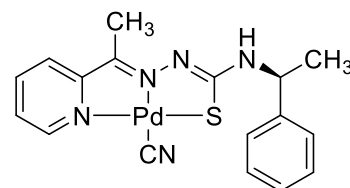
Yield: 0.041 g (0.095 mmol, 95%).

Habitus yellow solid.

¹H NMR: (300 MHz, DMSO-d₆) δ [ppm] = 8.72 (d, *J* = 7.5 Hz, 1H), 8.53 (dd, *J* = 5.3, 1.5 Hz, 1H), 8.18 (td, *J* = 7.9, 1.6 Hz, 1H), 7.83 (d, *J* = 8.0 Hz, 1H), 7.63 (t, *J* = 6.7 Hz, 1H), 7.48 – 7.23 (m, 4H), 7.25 – 7.12 (m, 1H), 4.95 (t, *J* = 7.2 Hz, 1H), 2.31 (s, 3H), 1.42 (d, *J* = 7.0 Hz, 3H).

HR-ESI-MS [M+H]⁺ calc.: 429.03282 found: 429.03311.

[M+Na]⁺ calc.: 482.98684 found: 482.98708.



[Pt(apyTSCmB)NCS] C₁₇H₁₇N₅PtS₂ (550.56 g/mol).

Yield: 0.034 g (0.062 mmol, 82%).

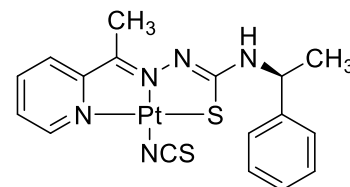
Habitus red solid.

R_f 0.63 (SiO₂, EtOAc)

¹H NMR: (300 MHz, DMSO-d₆) δ [ppm] = 8.90 (d, *J* = 7.5 Hz, 1H), 8.44 (dd, *J* = 23.7, 5.5 Hz, 1H), 8.28 – 8.13 (m, 1H), 7.80 (d, *J* = 8.0 Hz, 1H), 7.73 (t, *J* = 6.7 Hz, 1H), 7.63 (t, *J* = 6.7 Hz, 1H), 7.43 – 7.28 (m, 4H), 7.25 (m, 1H), 5.04 (qui, *J* = 7.3 Hz, 1H), 2.31 (s, 3H), 1.47 – 1.40 (m, 3H).

HR-ESI-MS [M+H]⁺ calc.: 550.06247 found: 550.06269.

[M+Na]⁺ calc.: 572.04442 found: 572.04452.

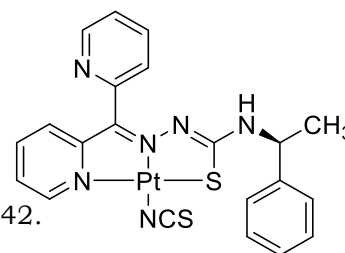


[Pt(dpyTSCmB)NCS]C₁₇H₁₇N₅PtS₂ (613.62 g/mol).**Yield:**

0.046 g (0.07 mmol, >99%).

Habitus

red solid.

HR-ESI-MS[M+H]⁺ calc.: 613.07337 found: 613.07342.[M+Na]⁺ calc.: 635.05532 found: 635.05564.**[Pt(dpyTSCmB)CN]**C₁₇H₁₇N₅PtS (581.56 g/mol).**Yield:**

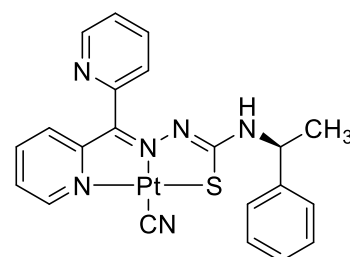
0.053 g (0.09 mmol, >99%).

Habitus

Bright red solid.

¹H NMR:

(300 MHz, DMSO-d₆) δ [ppm] = 9.19 (d, 1H, *J* = 7.1 Hz, NH7), 8.85 (d, 1H, *J* = 5.4 Hz, ³*J*_{PtH} = 35 Hz, HPy6), 8.77 (d, 1H, *J* = 4.9 Hz, HPy'6), 8.10 (t, 1H, *J* = 8.0 Hz, HPy4), 7.99 (t, 1H, *J* = 7.2 Hz, HPy'4), 7.66 (t, 1H, *J* = 7.7, 1.8 Hz, HPy5'), 7.59 (t, 1H, *J*_{HH} = 7.8 Hz, HPy5), 7.49 (m, 1H, HPy'3), 7.44 (m, 1H, HPy3), 7.35-7.19 (m, 3H, H4,5), 7.04 (d, 2H, *J* = 8.1 Hz, H3), 4.77-4.62 (m, 1H, H1), 1.34 (d, 3H, *J* = 7.0 Hz, H6).

HR-ESI-MS[M+H]⁺ calc.: 581.10131 found: 581.10133.[M+Na]⁺ calc.: 603.08325 found: 603.08393.

6. Literature

1. B. R. Srinivasan, P. Raghavaiah and V. S. Nadkarni, Reinvestigation of growth of urea thiosemicarbazone monohydrate crystal, *Spectrochim. Acta A Mol. Biomol. Spectrosc.*, 2013, **112**, 84-89.
2. E. G. Jayasree and S. Sreedevi, Density functional evaluation and a feasibility study of intramolecular thione–thiol tautomerization, *J. Quantum Chem.*, 2017, **117**, e25427.
3. N. M. El-Metwaly and M. S. Refat, Elaborated ¹H NMR study for the ligitional behavior of two thiosemicarbazide derivatives towards some heavy metals (Sn(II), Sb(III), Pb(II) and Bi(III)), thermal, antibacterial and antifungal studies, *Spectrochim. Acta A Mol. Biomol. Spectrosc.*, 2011, **81**, 519-528.
4. M. S. El-Shahawi, W. Ahmad, G. I. Mohammed, Y. M. Moustafa, G. A. Al-Hazmi and A. A. El-Asmy, Impact and correlation of pK_a and dn electrons of some selected thiosemicarbazone Schiff base metal Co, Ni, Cu complexes: a study of electrochemical behavior, excitation and optical energies, *New J. Chem.*, 2017, **41**, 4853-4861.
5. M. J. Campbell and R. Grzeskowiak, Some copper(II) complexes of thiosemicarbazide, *J. Chem. Soc. A*, 1967, 396-401.
6. S. M. Siddiqui, A. Salahuddin and A. Azam, Thiosemicarbazone fragment embedded within 1, 2, 4-triazole ring as inhibitors of *Entamoeba histolytica*, *Bioorg. Med. Chem. Lett.*, 2012, **22**, 2768-2771.
7. P. P. T. Sah and T. C. Daniels, Thiosemicarbazide as a reagent for the identification of aldehydes, ketones, and quinones, *Recl. Trav. Chim. Pays-Bas*, 1950, **69**, 1545-1556.
8. B. Yoshio, The Gas Chromatographic Determination of Carbonyl Compounds as Their Thiosemicarbazone, *Bull. Chem. Soc. Jpn.*, 1975, **48**, 270-272.
9. D. M. McLean, Methisazone therapy in pediatric vaccinia complications, *Ann. NY. Acad. Sci.*, 1977, **284**, 118-121.
10. K. E. Omari and D. K. Stammers, The design and development of drugs acting against the smallpox virus, *Expert Opin. Drug Discov.*, 2007, **2**, 1263-1272.
11. D. J. Bauer, Clinical experience with the antiviral drug marboran®(1-methylisatin 3-thiosemicarbazone), *Ann. NY. Acad. Sci.*, 1965, **130**, 110-117.
12. F. A. Beckford, G. Leblanc, J. Thessing, M. Shaloski, B. J. Frost, L. Li and N. P. Seeram, Organometallic ruthenium complexes with thiosemicarbazone ligands: Synthesis, structure and cytotoxicity of [(η⁶-p-cymene)Ru(NS)Cl]⁺ (NS=9-anthraldehyde thiosemicarbazones), *Inorg. Chem. Commun.*, 2009, **12**, 1094-1098.
13. R. Carballo, J. S. Casas, E. García-Martínez, G. Pereiras-Gabián, A. n. Sánchez, J. Sordo, E. M. Vázquez-López, J. C. Garcia-Monteaudo and U. Abram, Reaction of bromopentacarbonylrhenium(I) with ferrocenylcarbaldehyde thiosemicarbazones: the first X-ray diffraction studies of metal carbonyl complexes containing bidentate thiosemicarbazone ligands, *J. Organomet. Chem.*, 2002, **656**, 1-10.
14. S. Sharma, F. Athar, M. R. Maurya, F. Naqvi and A. Azam, Novel bidentate complexes of Cu(II) derived from 5-nitrofur-2-carboxaldehyde thiosemicarbazones with antiamoebic activity against *E. histolytica*, *Eur. J. Med. Chem.*, 2005, **40**, 557-562.
15. S. Chandra, S. Bargujar, R. Nirwal and N. Yadav, Synthesis, spectral characterization and biological evaluation of copper(II) and nickel(II) complexes with

- thiosemicarbazones derived from a bidentate Schiff base, *Spectrochim. Acta A Mol. Biomol. Spectrosc.*, 2013, **106**, 91-98.
16. T. Stringer, B. Therrien, D. T. Hendricks, H. Guzgay and G. S. Smith, Mono- and dinuclear (η^6 -arene) ruthenium(II) benzaldehyde thiosemicarbazone complexes: Synthesis, characterization and cytotoxicity, *Inorg. Chem. Commun.*, 2011, **14**, 956-960.
 17. P. Chellan, S. Nasser, L. Vivas, K. Chibale and G. S. Smith, Cyclopalladated complexes containing tridentate thiosemicarbazone ligands of biological significance: Synthesis, structure and antimalarial activity, *J. Organomet. Chem.*, 2010, **695**, 2225-2232.
 18. S. Halder, P. Paul, S.-M. Peng, G.-H. Lee, A. Mukherjee, S. Dutta, U. Sanyal and S. Bhattacharya, Benzaldehyde thiosemicarbazone complexes of platinum: Syntheses, structures and cytotoxic properties, *Polyhedron*, 2012, **45**, 177-184.
 19. R. Acharyya, S. Dutta, F. Basuli, S.-M. Peng, G.-H. Lee, L. R. Falvello and S. Bhattacharya, Rhodium Assisted C-H Activation of Benzaldehyde Thiosemicarbazones and Their Oxidation via Activation of Molecular Oxygen, *Inorg. Chem.*, 2006, **45**, 1252-1259.
 20. D. Pandiarajan and R. Ramesh, Catalytic transfer hydrogenation of ketones by ruthenium(II) cyclometallated complex containing para-chloroacetophenone thiosemicarbazone, *Inorg. Chem. Commun.*, 2011, **14**, 686-689.
 21. I. G. Santos, U. Abram, R. Alberto, E. V. Lopez and A. Sanchez, Tricarbonylrhenium(I) Complexes with Thiosemicarbazone Derivatives of 2-Acetylpyridine and 2-Pyridine Formamide Showing Two Unusual Coordination Modes of Tridentate Thiosemicarbazone Ligands, *Inorg. Chem.*, 2004, **43**, 1834-1836.
 22. R. Pedrido, M. J. Romero, M. R. Bermejo, M. Martínez-Calvo, A. M. González-Noya and G. Zaragoza, Coordinative trends of a tridentate thiosemicarbazone ligand: synthesis, characterization, luminescence studies and desulfurization processes, *Dalton Trans.*, 2009, 8329-8340.
 23. A. Hazra, A. K. Barik, S. Pal, S. Gupta, S. Roy, R. J. Butcher, S.-M. Peng, G. H. Lee and S. K. Kar, Synthesis and structural studies on di-oxovanadium(V) complexes of N(4)-substituted pyrazole based thiosemicarbazones, *Polyhedron*, 2007, **26**, 773-781.
 24. D. K. Sau, R. J. Butcher, S. Chaudhuri and N. Saha, Synthesis and spectroscopic characterization of new cobalt(III) complexes with 5-methyl-3-formyl pyrazole 3-hexamethyleneiminyl thiosemicarbazone (HMPz₃Hex): X-ray crystallographic identification of HMPz₃Hex and [Co(MPz₃Hex)₂]Br·H₂O with evidence for unusual rotation about the azomethine double bond of the ligand on complexation with cobalt(III), *Polyhedron*, 2004, **23**, 5-14.
 25. S. Sen, S. Shit, S. Mitra and S. R. Batten, Structural and spectral studies of a new copper(II) complex with a tridentate thiosemicarbazone ligand, *J. Struct. Chem.*, 2008, **19**, 137-142.
 26. A. R. Rettondin, Z. A. Carneiro, A. C. R. Gonçalves, V. F. Ferreira, C. G. Oliveira, A. N. Lima, R. J. Oliveira, S. de Albuquerque, V. M. Deflon and P. I. S. Maia, Gold(III) complexes with ONS-Tridentate thiosemicarbazones: Toward selective trypanocidal drugs, *Eur. J. Med. Chem.*, 2016, **120**, 217-226.
 27. M. Şahin, T. Bal-Demirci, G. Pozan-Soylu and B. Ülküseven, Synthesis, characterization and thermal decomposition of dioxouranium(VI) complexes with

- N1,N4-diarylidene-S-propyl-thiosemicarbazone: Crystal structure of [UO₂(LI)(C₄H₉OH)], *Inorg. Chim. Acta*, 2009, **362**, 2407-2412.
28. R. Ramachandran, G. Prakash, P. Vijayan, P. Viswanathamurthi and J. Grzegorz Malecki, Synthesis of heteroleptic copper(I) complexes with phosphine-functionalized thiosemicarbazones: An efficient catalyst for regioselective N-alkylation reactions, *Inorg. Chim. Acta*, 2017, **464**, 88-93.
 29. R. Ramachandran, G. Prakash, M. Nirmala, P. Viswanathamurthi and J. G. Malecki, Ruthenium(II) carbonyl complexes designed with arsine and PNO/PNS ligands as catalysts for N-alkylation of amines via hydrogen autotransfer process, *J. Organomet. Chem.*, 2015, **791**, 130-140.
 30. A. Castiñeiras and R. Pedrido, Auophilicity in gold(I) thiosemicarbazone clusters, *Dalton Trans.*, 2012, **41**, 1363-1372.
 31. G. Argay, A. Kálmán, L. Párkányi, V. M. Leovac, I. D. Brceski and P. N. Radivojsa, Transition Metal Complexes with Thiosemicarbazide-Based Ligands. Part 37.* Synthesis and Study of the first Thiosemi-Carbazide-Derived Copper(I) Complexes: Crystal Structure of [2-(Diphenylphosphino)Benzaldehyde Thiosemicarbazonato(-1)] Copper(I)-Nitrate-Methanol Solvate, *J. Coord. Chem.*, 2000, **51**, 9-20.
 32. T. S. Lobana, Rekha, R. J. Butcher, A. Castineiras, E. Bermejo and P. V. Bharatam, Bonding Trends of Thiosemicarbazones in Mononuclear and Dinuclear Copper(I) Complexes: Syntheses, Structures, and Theoretical Aspects, *Inorg. Chem.*, 2006, **45**, 1535-1542.
 33. D. X. West, Y. Yang, T. L. Klein, K. I. Goldberg, A. E. Liberta, J. Valdes-Martinez and R. A. Toscano, Binuclear copper(II) complexes of 2-hydroxyacetophenone 4N-substituted thiosemicarbazones, *Polyhedron*, 1995, **14**, 1681-1693.
 34. J. S. Casas, M. S. García-Tasende and J. Sordo, Main group metal complexes of semicarbazones and thiosemicarbazones. A structural review, *Coord. Chem. Rev.*, 2000, **209**, 197-261.
 35. S. Padhyé and G. B. Kauffman, Transition metal complexes of semicarbazones and thiosemicarbazones, *Coord. Chem. Rev.*, 1985, **63**, 127-160.
 36. M. Bakir, M. W. Lawrence and M. Bohari Yamin, Novel κ^2 -N_{im},S- and κ^4 -C,N_{im},(μ -S),(μ -S)-coordination of di-2-thienyl ketone thiosemicarbazone (dtkts). Hydrogen evolution and catalytic properties of palladacyclic [Pd(κ^4 -C,N_{im},(μ -S),(μ -S)-dtkts-2H)]₄, *Inorg. Chim. Acta*, 2020, **507**, 119592.
 37. W. R. P. Costa, R. A. C. Souza, V. M. Deflon and C. G. Oliveira, Preparation, structural characterization, voltammetry and Hirshfeld surface analysis of homoleptic iron(III) thiosemicarbazone complexes, *Trans. Met. Chem.*, 2020, **45**, 511-521.
 38. M. Papadakis, A. Barrozo, T. Straistari, N. Queyriaux, A. Putri, J. Fize, M. Giorgi, M. Réglie, J. Massin, R. Hardré and M. Orió, Ligand-based electronic effects on the electrocatalytic hydrogen production by thiosemicarbazone nickel complexes, *Dalton Trans.*, 2020, **49**, 5064-5073.
 39. N. Raja and R. Ramesh, Mononuclear ruthenium(III) complexes containing chelating thiosemicarbazones: Synthesis, characterization and catalytic property, *Spectrochim. Acta A Mol. Biomol. Spectrosc.*, 2010, **75**, 713-718.
 40. S. Datta, D. K. Seth, R. J. Butcher and S. Bhattacharya, Mixed-ligand thiosemicarbazone complexes of nickel: Synthesis, structure and catalytic activity, *Inorg. Chim. Acta*, 2011, **377**, 120-128.

41. B. L. Souza, L. A. Faustino, F. S. Prado, R. N. Sampaio, P. I. S. Maia, A. E. H. Machado and A. O. T. Patrocínio, Spectroscopic characterization of a new Re(I) tricarbonyl complex with a thiosemicarbazone derivative: towards sensing and electrocatalytic applications, *Dalton Trans.*, 2020, **49**, 16368-16379.
42. P. Adak, B. Ghosh, A. Bauzá, A. Frontera, S. R. Herron and S. K. Chattopadhyay, Binuclear and tetranuclear Zn(II) complexes with thiosemicarbazones: synthesis, X-ray crystal structures, ATP-sensing, DNA-binding, phosphatase activity and theoretical calculations, *RSC Advances*, 2020, **10**, 12735-12746.
43. B. S. Garg and V. K. Jain, Analytical applications of thiosemicarbazones and semicarbazones, *Microchem. J.*, 1988, **38**, 144-169.
44. K. J. Reddy, J. R. Kumar, C. Ramachandraiah, T. Thriveni and A. V. Reddy, Spectrophotometric determination of zinc in foods using N-ethyl-3-carbazolecarboxaldehyde-3-thiosemicarbazone: Evaluation of a new analytical reagent, *Food Chem.*, 2007, **101**, 585-591.
45. G. P. Volynets, M. A. Tukalo, V. G. Bdzhola, N. M. Derkach, M. I. Gumeniuk, S. S. Tarnavskiy, S. A. Starosyla and S. M. Yarmoluk, Benzaldehyde thiosemicarbazone derivatives against replicating and nonreplicating Mycobacterium tuberculosis, *J. Antibiot.*, 2019, **72**, 218-224.
46. D. Rogolino, A. Gatti, M. Carcelli, G. Pelosi, F. Bisceglie, F. M. Restivo, F. Degola, A. Buschini, S. Montalbano, D. Feretti and C. Zani, Thiosemicarbazone scaffold for the design of antifungal and antiaflatoxigenic agents: evaluation of ligands and related copper complexes, *Sci. Rep.*, 2017, **7**, 11214.
47. E. Baruffini, R. Ruotolo, F. Bisceglie, S. Montalbano, S. Ottonello, G. Pelosi, A. Buschini and T. Lodi, Mechanistic insights on the mode of action of an antiproliferative thiosemicarbazone-nickel complex revealed by an integrated chemogenomic profiling study, *Sci. Rep.*, 2020, **10**, 10524.
48. P. Chellan, K. M. Land, A. Shokar, A. Au, S. H. An, C. M. Clavel, P. J. Dyson, C. d. Kock, P. J. Smith, K. Chibale and G. S. Smith, Exploring the Versatility of Cycloplatinated Thiosemicarbazones as Antitumor and Antiparasitic Agents, *Organometal.*, 2012, **31**, 5791-5799.
49. L. Wei, J. Easmon, R. K. Nagi, B. D. Muegge, L. A. Meyer and J. S. Lewis, ⁶⁴Cu-azabicyclo [3.2.2] nonane thiosemicarbazone complexes: radiopharmaceuticals for PET of topoisomerase II expression in tumors, *J. Nucl. Med.*, 2006, **47**, 2034-2041.
50. A. E. Stacy, D. Palanimuthu, P. V. Bernhardt, D. S. Kalinowski, P. J. Jansson and D. R. Richardson, Zinc(II)-Thiosemicarbazone Complexes Are Localized to the Lysosomal Compartment Where They Transmetallate with Copper Ions to Induce Cytotoxicity, *J. Med. Chem.*, 2016, **59**, 4965-4984.
51. R. Anjum, D. Palanimuthu, D. S. Kalinowski, W. Lewis, K. C. Park, Z. Kovacevic, I. U. Khan and D. R. Richardson, Synthesis, Characterization, and in Vitro Anticancer Activity of Copper and Zinc Bis(Thiosemicarbazone) Complexes, *Inorg. Chem.*, 2019, **58**, 13709-13723.
52. L. W. Yue Zhao, C. Guo, B. Jiang, X. Li, K. Liu, D. Shi, Metal Complexes of Thiosemicarbazones as Potent Anticancer Agents: a Minireview, *Med. Res.*, 2018, **2**, 180009.

53. S. Mylonas and A. Mamalis, Synthesis and antitumor activity of new thiosemicarbazones of 2-acetylimidazo[4,5-b]pyridine, *J. Heterocyclic Chem.*, 2005, **42**, 1273-1281.
54. H.-H. Lin, W.-Y. Wu, S.-L. Cao, J. Liao, L. Ma, M. Gao, Z.-F. Li and X. Xu, Synthesis and antiproliferative evaluation of piperazine-1-carbothiohydrazide derivatives of indolin-2-one, *Bioorg. Med. Chem. Lett.*, 2013, **23**, 3304-3307.
55. A. Dobrova, S. Platzer, F. Bacher, M. N. M. Milunovic, A. Dobrov, G. Spengler, É. A. Enyedy, G. Novitchi and V. B. Arion, Structure–antiproliferative activity studies on l-proline- and homoproline-4-N-pyrrolidine-3-thiosemicarbazone hybrids and their nickel(II), palladium(II) and copper(II) complexes, *Dalton Trans.*, 2016, **45**, 13427-13439.
56. I.-J. Kang, L.-W. Wang, T.-A. Hsu, A. Yueh, C.-C. Lee, Y.-C. Lee, C.-Y. Lee, Y.-S. Chao, S.-R. Shih and J.-H. Chern, Isatin- β -thiosemicarbazones as potent herpes simplex virus inhibitors, *Bioorg. Med. Chem. Lett.*, 2011, **21**, 1948-1952.
57. R. Wong and S. J. Dolman, Isothiocyanates from Tosyl Chloride Mediated Decomposition of in Situ Generated Dithiocarbamic Acid Salts, *J. Org. Chem.*, 2007, **72**, 3969-3971.
58. A. P. d. Silva, G. de Freitas Gauze, N. P. Coelho, C. C. da Silva and E. A. Basso, Addition of hydrazine to natural terpene-based isothiocyanates derivatives: density functional theory investigation, *Tetrahedron Lett.*, 2011, **52**, 62-64.
59. E. C. Rodriguez, L. A. Marcaurrelle and C. R. Bertozzi, Aminoxy-, Hydrazide-, and Thiosemicarbazide-Functionalized Saccharides: Versatile Reagents for Glycoconjugate Synthesis, *J. Org. Chem.*, 1998, **63**, 7134-7135.
60. B. N. Goswami, J. C. S. Katakya and J. N. Baruah, Synthesis and antibacterial activity of 1-(2,4-dichlorobenzoyl)-4-substituted thiosemicarbazides, 1,2,4-triazoles and their methyl derivatives, 1984, **21**, 1225-1229.
61. F. Buccheri, G. Cusmano, M. Gruttadauria, R. Noto and G. Werber, A study of the behaviour of 2,4-substituted thiosemicarbazides toward orthoesters: Formation of mesoionic compounds, *J. Heterocyclic Chem.*, 1997, **34**, 1447-1451.
62. E. Fischer, Ueber die Hydrazinverbindungen; Erste Abhandlung, *Liebigs Ann. Chem.*, 1878, **190**, 67-183.
63. W. Marckwald, Ueber stereoisomere Thiosemicarbazide. II, *Ber. Dtsch. Chem. Ges.*, 1899, **32**, 1081-1087.
64. S. Carradori, D. Secci, M. D'Ascenzio, P. Chimenti and A. Bolasco, Microwave and Ultrasound-Assisted Synthesis of Thiosemicarbazones and Their Corresponding (4,5-Substituted-thiazol-2-yl)hydrazines, *J. Heterocyclic Chem.*, 2014, **51**, 1856-1861.
65. P. Paul, P. Sengupta and S. Bhattacharya, Palladium mediated C–H bond activation of thiosemicarbazones: Catalytic application of organopalladium complexes in C–C and C–N coupling reactions, *J. Organometal. Chem.*, 2013, **724**, 281-288.
66. R. Carballo, A. Castiñeiras and T. Pérez, Group 12 Metal Complexes of 2-Formylpyrrole-(4PL1) and 2-Acetylpyrrole-N(4)-phenylthiosemicarbazone (4PL2), as Examples form Different Donor Modes. Crystal and Molecular Structures of [Hg(4PL1-H)Br]₂ and [Zn(4PL2)₂Br₂] · 2 EtOH, *Z. Naturforsch. B*, 2001, **56**, 881-888.
67. J. Valdés-Martínez, A. Sierra-Romero, C. Alvarez-Toledano, R. A. Toscano and H. García-Tapia, Semicarbazones and thiosemicarbazones: IX. Tungsten carbonyl

- thiosemicarbazone organometallic compounds, *Jo. Organometal. Chem.*, 1988, **352**, 321-326.
68. D. Kovala-Demertzi, M. A. Demertzis, J. R. Miller, C. Papadopoulou, C. Dodorou and G. Filousis, Platinum(II) complexes with 2-acetyl pyridine thiosemicarbazone: Synthesis, crystal structure, spectral properties, antimicrobial and antitumour activity, *J. Inorg. Biochem.*, 2001, **86**, 555-563.
 69. M. Maji, S. Ghosh, S. K. Chattopadhyay and T. C. W. Mak, Binary, Ternary, and Quarternary Complexes of Ruthenium(II) Involving the Flexidentate ONNS Donor Mono(4-(4-tolyl)thiosemicarbazone) of 2,6-Diacetylpyridine (L2H). First Report on Ruthenium Complexes of a Mono(thiosemicarbazone) of a Diketone: Crystal Structure of [Ru(L2)(PPh₃)₂]ClO₄, *Inorg. Chem.*, 1997, **36**, 2938-2943.
 70. R. Pedrido, M. R. Bermejo, M. J. Romero, M. Vázquez, A. M. González-Noya, M. Maneiro, M. J. Rodríguez and M. I. Fernández, Syntheses and X-ray characterization of metal complexes with the pentadentate thiosemicarbazone ligand bis(4-N-methylthiosemicarbazone)-2,6-diacetylpyridine. The first pentacoordinate lead(II) complex with a pentagonal geometry, *Dalton Trans.*, 2005, 572-579.
 71. I. Pal, F. Basuli, T. C. W. Mak and S. Bhattacharya, Synthesis, Structure, and Properties of a Novel Heterooctametallate Complex Containing a Cyclic Ru₄Ni₄ Core, *ACIE*, 2001, **40**, 2923-2925.
 72. T. S. Lobana, G. Bawa and R. J. Butcher, Synthesis of CuII–RuII–CuII Trinuclear Complexes via Redox Reaction of Copper(I) Across Thiosemicarbazones Coordinated to Ruthenium(II), *Inorg. Chem.*, 2008, **47**, 1488-1495.
 73. S. Argibay-Otero, L. Gano, C. Fernandes, A. Paulo, R. Carballo and E. M. Vázquez-López, Chemical and biological studies of Re(I)/Tc(I) thiosemicarbazone complexes relevant for the design of radiopharmaceuticals, *J. Inorg. Biochem.*, 2020, **203**, 110917.
 74. Y. Kang, N. Yang, S. O. Kang, J. Ko, C.-H. Lee and Y.-H. Lee, Synthesis and Characterization of Aluminum and Gallium Complexes of Heterocyclic Carboxaldehyde Thiosemicarbazones. Single-Crystal Structure of [(MeAl){NC₄H₃CHNNC(S)NiC₃H₇}(AlMe₂)₂]₂ and (GaMe₂)₂[SC₄H₃CHNNC(S)NPh], *Organometallics*, 1997, **16**, 5522-5527.
 75. C. K. Oza, M. Jain, N. Jain and D. Verma, Synthesis, Characterization, Antimicrobial Activities, and Structural Studies of Lanthanide (III) Complexes with 1-(4-Chlorophenyl)-3-(4-fluoro/hydroxyphenyl)prop-2-en-1-thiosemicarbazone, *Phosphorus, Sulfur, Silicon Rel. Elem.*, 2010, **185**, 377-386.
 76. B. M. Paterson and P. S. Donnelly, Copper complexes of bis (thiosemicarbazones): from chemotherapeutics to diagnostic and therapeutic radiopharmaceuticals, *Chem. Soc. Rev.*, 2011, **40**, 3005-3018.
 77. N. P. Prajapati and H. D. Patel, Novel thiosemicarbazone derivatives and their metal complexes: Recent development, *Syn. Commun.*, 2019, **49**, 2767-2804.
 78. M. S. More, P. G. Joshi, Y. K. Mishra and P. K. Khanna, Metal complexes driven from Schiff bases and semicarbazones for biomedical and allied applications: a review, *Mater. Today Chem.*, 2019, **14**, 100195.
 79. E. Noulisri, D. R. Richardson, S. Lerdwana, S. Fucharoen, T. Yamagishi, D. S. Kalinowski and K. J. Pattananyasat, Antitumor activity and mechanism of action of the iron chelator, Dp44mT, against leukemic cells, *Am. J. Hematol.*, 2009, **84**, 170-176.

80. D. B. Lovejoy, P. J. Jansson, U. T. Brunk, J. Wong, P. Ponka and D. R. Richardson, Antitumor activity of metal-chelating compound Dp44mT is mediated by formation of a redox-active copper complex that accumulates in lysosomes, *Cancer Res.*, 2011, **71**, 5871-5880.
81. V. A. Rao, S. R. Klein, K. K. Agama, E. Toyoda, N. Adachi, Y. Pommier and E. B. Shacter, The Iron Chelator Dp44mT Causes DNA Damage and Selective Inhibition of Topoisomerase II α in Breast Cancer Cells, *Cancer Res.*, 2009, **69**, 948-957.
82. P. J. Jansson, C. L. Hawkins, D. B. Lovejoy and D. R. Richardson, The iron complex of Dp44mT is redox-active and induces hydroxyl radical formation: An EPR study, *J. Inorg. Biochem.*, 2010, **104**, 1224-1228.
83. Z. Chen, D. Zhang, F. Yue, M. Zheng, Z. Kovacevic and D. R. Richardson, The iron chelators Dp44mT and DFO inhibit TGF- β -induced epithelial-mesenchymal transition via up-regulation of N-Myc downstream-regulated gene 1 (NDRG1), *J. Biol. Chem.*, 2012, **287**, 17016-17028.
84. M. A. González, A. G. Algarra, M. G. Basallote, P. V. Bernhardt, M. J. Fernández-Trujillo and M. Martínez, Proton-assisted air oxidation mechanisms of iron(II) bis-thiosemicarbazone complexes at physiological pH: a kinetic-mechanistic study, *Dalton Trans.*, 2019, **48**, 16578-16587.
85. D. S. Kalinowski, P. Quach and D. R. Richardson, Thiosemicarbazones: the new wave in cancer treatment, *Future Med. Chem.*, 2009, **1**, 1143-1151.
86. E. Gutierrez, D. R. Richardson and P. J. Jansson, The anticancer agent Di-2-pyridylketone 4, 4-dimethyl-3-thiosemicarbazone (Dp44mT) overcomes prosurvival autophagy by two mechanisms persistent induction of autophagosome synthesis and impairment of lysosomal integrity, *J. Biol. Chem.*, 2014, **289**, 33568-33589.
87. J. Yuan, D. B. Lovejoy and D. R. Richardson, Novel di-2-pyridyl-derived iron chelators with marked and selective antitumor activity: in vitro and in vivo assessment, *Blood*, 2004, **104**, 1450-1458.
88. Y. Fujibayashi, H. Taniuchi, Y. Yonekura, H. Ohtani, J. Konishi and A. Yokoyama, Copper-62-ATSM: a new hypoxia imaging agent with high membrane permeability and low redox potential, *J. Nucl. Med.*, 1997, **38**, 1155.
89. J. S. Lewis, D. W. McCarthy, T. J. McCarthy, Y. Fujibayashi and M. J. Welch, Evaluation of ⁶⁴Cu-ATSM in vitro and in vivo in a hypoxic tumor model, *J. Nucl. Med.*, 1999, **40**, 177-183.
90. A. L. Vāvere and J. S. Lewis, Cu-ATSM: A radiopharmaceutical for the PET imaging of hypoxia, *Dalton Trans.*, 2007, 4893-4902.
91. J. S. Lewis, R. Laforest, F. Dehdashti, P. W. Grigsby, M. J. Welch and B. A. Siegel, An imaging comparison of ⁶⁴Cu-ATSM and ⁶⁰Cu-ATSM in cancer of the uterine cervix, *J. Nucl. Med.*, 2008, **49**, 1177-1182.
92. C. P. Soon, P. S. Donnelly, B. J. Turner, L. W. Hung, P. J. Crouch, N. A. Sherratt, J.-L. Tan, N. K.-H. Lim, L. Lam, L. Bica, S. Lim, J. L. Hickey, J. Morizzi, A. Powell, D. I. Finkelstein, J. G. Culvenor, C. L. Masters, J. Duce, A. R. White, K. J. Barnham and Q.-X. Li, Diacetylbis (N (4)-methylthiosemicarbazono) copper (II)(CuII (atsm)) protects against peroxynitrite-induced nitrosative damage and prolongs survival in amyotrophic lateral sclerosis mouse model, *J. Biol. Chem.*, 2011, **286**, 44035-44044.
93. E. Lopci, I. Grassi, D. Rubello, P. M. Colletti, S. Cambioli, A. Gamboni, F. Salvi, G. Cicoria, F. Lodi, C. Dazzi, S. Mattioli and S. Fanti, Prognostic evaluation of disease

- outcome in solid tumors investigated with ^{64}Cu -ATSM PET/CT, *Clin. Nucl. Med.*, 2016, **41**, e87-e92.
94. X. Nie, G. J. Randolph, A. Elvington, N. Bandara, A. Zheleznyak, R. J. Gropler, P. K. Woodard, S. Lapi and biology, Imaging of hypoxia in mouse atherosclerotic plaques with ^{64}Cu -ATSM, *Eur. J. Nucl. Med.*, 2016, **43**, 534-542.
 95. P. N. Fonteh, F. K. Keter and D. Meyer, New bis(thiosemicarbazone) gold(III) complexes inhibit HIV replication at cytostatic concentrations: Potential for incorporation into virostatic cocktails, *J. Inorg. Biochem.*, 2011, **105**, 1173-1180.
 96. J. G. Rajendran, D. L. Schwartz, J. O'Sullivan, L. M. Peterson, P. Ng, J. Scharnhorst, J. R. Grierson and K. A. Krohn, Tumor Hypoxia Imaging with [F-18] Fluoromisonidazole Positron Emission Tomography in Head and Neck Cancer, *Clin. Cancer Res.*, 2006, **12**, 5435-5441.
 97. D. M. Brizel, G. S. Sibley, L. R. Prosnitz, R. L. Scher and M. W. Dewhirst, Tumor hypoxia adversely affects the prognosis of carcinoma of the head and neck, *Int. J. Radiat. Oncol. Biol. Phys.*, 1997, **38**, 285-289.
 98. X. Sun, G. Niu, N. Chan, B. Shen and X. Chen, Tumor Hypoxia Imaging, *Mol. Imaging Biol.*, 2011, **13**, 399-410.
 99. P. Zanzonico, J. O'Donoghue, J. D. Chapman, R. Schneider, S. Cai, S. Larson, B. Wen, Y. Chen, R. Finn, S. Ruan, L. Gerweck, J. Humm and C. Ling, Iodine-124-labeled iodoazomycin-galactoside imaging of tumor hypoxia in mice with serial microPET scanning, *Eur. J. Nucl. Med. Mol. Imaging*, 2004, **31**, 117-128.
 100. C. Stefani, Z. Al-Eisawi, P. J. Jansson, D. S. Kalinowski and D. R. Richardson, Identification of differential anti-neoplastic activity of copper bis(thiosemicarbazones) that is mediated by intracellular reactive oxygen species generation and lysosomal membrane permeabilization, *J. Inorg. Biochem.*, 2015, **152**, 20-37.
 101. F. A. Berends and R. Kleiss, Distributions for electron-positron annihilation into two and three photons, *Nucl. Phys B*, 1981, **186**, 22-34.
 102. B. Singh, Nuclear Data Sheets for A = 64, *Nuclear Data Sheets*, 2007, **108**, 197-364.
 103. J. S. Lewis, M. R. Lewis, P. D. Cutler, A. Srinivasan, M. A. Schmidt, S. W. Schwarz, M. M. Morris, J. P. Miller and C. J. Anderson, Radiotherapy and Dosimetry of ^{64}Cu -TETA-Tyr³-Octreotate in a Somatostatin Receptor-positive, Tumor-bearing Rat Model, *Clin. Cancer Res.*, 1999, **5**, 3608-3616.
 104. J. Czernin, I. Sonni, A. Razmaria and J. Calais, The future of nuclear medicine as an independent specialty, *J. Nucl. Med.*, 2019, **60**, 3S-12S.
 105. M. Sollini, F. Bandera, M. Kirienko and m. imaging, Quantitative imaging biomarkers in nuclear medicine: from SUV to image mining studies. Highlights from annals of nuclear medicine, *Eur. J. Nucl. Med.*, 2018, 2019, 1-9.
 106. C. Van de Wiele, C. Lahorte, W. Oyen, O. Boerman, I. Goethals, G. Slegers and R. A. Dierckx, Nuclear medicine imaging to predict response to radiotherapy: a review, *Int. J. Radiat. Oncol. Biol. Phys.*, 2003, **55**, 5-15.
 107. U. Eberlein, J. H. Bröer, C. Vandevoorde, P. Santos, M. Bardiès, K. Bacher, D. Nosske, M. Lassmann and m. imaging, Biokinetics and dosimetry of commonly used radiopharmaceuticals in diagnostic nuclear medicine—a review, *Eur. J. Nucl. Med.*, 2011, **38**, 2269-2281.

108. P. Chilra, S. Gnesin, G. Allenbach, M. Monteiro, J. O. Prior, L. Vieira and J. A. Pires Jorge, Cardiac PET/CT with Rb-82: optimization of image acquisition and reconstruction parameters, *EJNMMI Physics*, 2017, **4**, 10.
109. T. Jones, D. Chesler and M. M. Ter-Pogossian, The continuous inhalation of oxygen-15 for assessing regional oxygen extraction in the brain of man, *Br. J. Radiol.*, 1976, **49**, 339-343.
110. R. Frackowiak, G.-L. Lenzi, T. Jones and J. D. J. J. o. c. a. t. Heather, Quantitative measurement of regional cerebral blood flow and oxygen metabolism in man using ^{15}O and positron emission tomography: theory, procedure, and normal values, *J. Comput. Assist. Tomogr.*, 1980, **4**, 727-736.
111. K. Wagatsuma, K. Oda, M. Sakata, M. Inaji, K. Miwa, M. Sasaki, J. Toyohara and K. Ishii, Validation of scatter limitation correction to eliminate scatter correction error in oxygen-15 gas-inhalation positron emission tomography images, *Nucl. Med. Commun.*, 2018, **39**, 936-944.
112. S. V. Nesterov, E. Deshayes, R. Sciagrà, L. Settimo, J. M. Declerck, X.-B. Pan, K. Yoshinaga, C. Katoh, P. J. Slomka, G. Germano, C. Han, V. Aalto, A. M. Alessio, E. P. Ficaro, B. C. Lee, S. G. Nekolla, K. L. Gwet, R. A. deKemp, R. Klein, J. Dickson, J. A. Case, T. Bateman, J. O. Prior and J. M. Knuuti, Quantification of Myocardial Blood Flow in Absolute Terms Using ^{82}Rb PET Imaging, *The RUBY-10 Study, JACC Cardiovasc. Imaging*, 2014, **7**, 1119-1127.
113. K. Fukushima, M. S. Javadi, T. Higuchi, R. Lautamäki, J. Merrill, S. G. Nekolla and F. M. J. Bengel, Prediction of short-term cardiovascular events using quantification of global myocardial flow reserve in patients referred for clinical ^{82}Rb PET perfusion imaging, *J. Nucl. Med.*, 2011, **52**, 726-732.
114. K. Yoshinaga, O. Manabe, C. Katoh, L. Chen, R. Klein, M. Naya, R. A. Dekemp, K. Williams, R. S. Beanlands and N. Tamaki, Quantitative analysis of coronary endothelial function with generator-produced ^{82}Rb PET: comparison with ^{15}O -labelled water PET, *Eur. J. Nucl. Med. Mol. Imaging*, 2010, **37**, 2233-2241.
115. S. Sheikhabaei, C. V. Marcus, R. S. Fragomeni, S. P. Rowe, M. S. Javadi and L. B. Solnes, Whole-body ^{18}F -FDG pet and ^{18}F -FDG PET/CT in patients with suspected paraneoplastic syndrome: a systematic review and meta-analysis of diagnostic accuracy, *J. Nucl. Med.*, 2017, **58**, 1031-1036.
116. C. Rohleder, D. Wiedermann, B. Neumaier, A. Drzezga, L. Timmermann, R. Graf, F. M. Leweke and H. Endepols, The Functional Networks of Prepulse Inhibition: Neuronal Connectivity Analysis Based on FDG-PET in Awake and Unrestrained Rats, *Front Behav. Neurosci.*, 2016, **10**.
117. L. Evangelista, L. Cuppari, L. Bellu, D. Bertin, M. Caccese, P. Reccia, V. Zagonel and G. Lombardi, Comparison between ^{18}F -Dopa and ^{18}F -Fet pet/Ct in patients with suspicious recurrent high grade glioma: a literature review and our experience, *Curr. Radiopharm.*, 2019, **12**, 220-228.
118. P. Lohmann, G. Stoffels, G. Ceccon, M. Rapp, M. Sabel, C. P. Filss, M. A. Kamp, C. Stegmayr, B. Neumaier, N. J. Shah, K.-J. Langen and N. Galldiks, Radiation injury vs. recurrent brain metastasis: combining textural feature radiomics analysis and standard parameters may increase ^{18}F -FET PET accuracy without dynamic scans, *Eur. Radiol.*, 2017, **27**, 2916-2927.

119. K. Hamacher, H. H. Coenen and G. Stöcklin, Efficient stereospecific synthesis of no-carrier-added 2-[¹⁸F]-fluoro-2-deoxy-D-glucose using aminopolyether supported nucleophilic substitution, *J. Nucl. Med.*, 1986, 235-238.
120. S. M. Qaim and H. H. Coenen, Produktion pharmazeutisch relevanter Radionuklide: An Reaktoren und Zyklotronen, *Pharm. Unserer Zeit*, 2005, **34**, 460-466.
121. D. Pauleit, G. Stoffels, A. Bachofner, F. W. Floeth, M. Sabel, H. Herzog, L. Tellmann, P. Jansen, G. Reifenberger and K. Hamacher, Comparison of ¹⁸F-FET and ¹⁸F-FDG PET in brain tumors, *Nucl. Med. Biol.*, 2009, **36**, 779-787.
122. T. S. Lee, S. H. Ahn, B. S. Moon, K. S. Chun, J. H. Kang, G. J. Cheon, C. W. Choi and S. M. Lim, Comparison of ¹⁸F-FDG, ¹⁸F-FET and ¹⁸F-FLT for differentiation between tumor and inflammation in rats, *Nucl. Med. Biol.*, 2009, **36**, 681-686.
123. A. H. Kaim, B. Weber, M. O. Kurrer, G. Westera, A. Schweitzer, J. Gottschalk, G. K. von Schulthess and A. Buck, ¹⁸F-FDG and ¹⁸F-FET uptake in experimental soft tissue infection, *Eur. J. Nucl. Med. Mol. Imaging*, 2002, **29**, 648-654.
124. T. Ertay, M. S. Eren, M. Karaman, G. Oktay, H. Durak, ¹⁸F-FDG-PET/CT in Initiation and Progression of Inflammation and Infection, *Mol. Imaging Radionucl. Ther.*, 2017, **26**, 47.
125. D. Pauleit, A. Zimmermann, G. Stoffels, D. Bauer, J. Risse, M. O. Flüss, K. Hamacher, H. H. Coenen and K.-J. Langen, ¹⁸F-FET PET compared with ¹⁸F-FDG PET and CT in patients with head and neck cancer, *J. Nucl. Med.*, 2006, **47**, 256-261.
126. A. Bhatnagar, R. Hustinx and A. Alavi, Nuclear imaging methods for non-invasive drug monitoring, *Adv. Drug Deliv. Rev.*, 2000, **41**, 41-54.
127. J. M. Farma, A. A. Santillan, M. Melis, J. Walters, D. Belinc, D.-T. Chen, E. A. Eikman and M. Malafa, PET/CT fusion scan enhances CT staging in patients with pancreatic neoplasms, *Ann. Surg. Oncol.*, 2008, **15**, 2465-2471.
128. S. Carlson, A Glance At The History Of Nuclear Medicine, *Acta Oncol.*, 1995, **34**, 1095-1102.
129. G. de Hevesy, Some applications of isotopic indicators, *Nobel Lecture*, 1944, **12**.
130. E. Tapscott, Nuclear Medicine Pioneer, Hal O. Anger, 1920-2005, *J. Nucl. Med. Technol.*, 2005, **33**, 250.
131. R. R. Buechel, B. A. Herzog, L. Husmann, I. A. Burger, A. P. Pazhenkottil, V. Treyer, I. Valenta, P. von Schulthess, R. Nkoulou and C. A. Wyss, Ultrafast nuclear myocardial perfusion imaging on a new gamma camera with semiconductor detector technique: first clinical validation, *Eur. J. Nucl. Med. Mol. Imaging*, 2010, **37**, 773-778.
132. D. Macey and R. Marshall, Absolute quantitation of radiotracer uptake in the lungs using a gamma camera, *J. Nucl. Med.*, 1982, **23**, 731-734.
133. T. E. Peterson and L. R. Furenlid, SPECT detectors: the Anger Camera and beyond, *Phys. Med. Biol.*, 2011, **56**, R145.
134. M. Rosenthal, J. Cullom, W. Hawkins, S. Moore, B. Tsui and M. Yester, Quantitative SPECT imaging: a review and recommendations by the Focus Committee of the Society of Nuclear Medicine Computer and Instrumentation Council, *J. Nucl. Med.*, 1995, **36**, 1489-1513.

135. G. Mariani, L. Bruselli, T. Kuwert, E. E. Kim, A. Flotats, O. Israel, M. Dondi and N. Watanabe, A review on the clinical uses of SPECT/CT, *Eur. J. Nucl. Med. Mol. Imaging*, 2010, **37**, 1959-1985.
136. D. L. Bailey and K. P. Willowson, An evidence-based review of quantitative SPECT imaging and potential clinical applications, *J. Nucl. Med.*, 2013, **54**, 83-89.
137. X. Li, G. Zubal, M. A. King and L. R. Furenlid, Design of a modular SPECT camera with improved spatial resolution near edges, *IEEE*, 2017.
138. D. Stentz, P. Sankar, R. Arseneau, W. Chang, J. Karp and S. Metzler, Spatial and Energy Resolutions Measurements for C-SPECT, *J. Nucl. Med.*, 2018, **59**, 218-218.
139. A. Heinzl, S. M. Shali, M. Dafotakis, F. A. Verburg, F. M. Mottaghy and O. H. Winz, Comparison of automatic versus manual procedures for the quantification of dopamine D2 receptor availability using I-123-IBZM-SPECT, *Nucl. Med. Comm.*, 2015, **36**, 1120-1126.
140. N. Abbasi Gharibkandi and S. J. Hosseinimehr, Radiotracers for imaging of Parkinson's disease, *Eur. J. Med. Chem.*, 2019, **166**, 75-89.
141. G. Vandegrift, D. Chaiko, R. Heinrich, E. Kucera, K. Jensen, D. Poa, R. Varma and D. Vissers, Preliminary Investigations for Technology Assessment of ⁹⁹Mo Production from LEU Targets, 1986.
142. A. Tataurov and O. S. Feinberg, Molten salt reactor for ⁹⁹Mo production, *Atomic Energy*, 2017, **122**, 299-303.
143. R. Lewis and T. J. Butler, Production of ³³P from ³⁶Cl and ³³S by Fast-Neutron Irradiation, *Nucl. Appl.*, 1966, **2**, 102-105.
144. Y. A. Karelin, V. Efimov, V. Filimonov, R. Kuznetsov, Y. L. Revyakin, O. Andreev, I. Y. Zhemkov, V. Bukh, V. Lebedev and Y. N. Spiridonov, Radionuclide production using a fast flux reactor, 2000, *Appl. Radiat. Isot.* **53**, 825-827.
145. E. O. Lawrence and M. S. Livingston, The production of high speed protons without the use of high voltages, *Phys. Rev.*, 1931, **38**, 834.
146. S. M. Qaim, Cyclotron production of medical radionuclides, *Handbook of Nuclear Chemistry*, 2011.
147. J. J. Livingood, *Principles of cyclic particle accelerators*, 1961.
148. N. Bohr, Conservation laws in quantum theory, *Nature*, 1936, **138**, 25-26.
149. E. Fermi, Versuch einer Theorie der β -Strahlen. I, *Zeitschrift für Physik*, 1934, **88**, 161-177.
150. W. Pauli, *Pauli letter collection: letter to Lise Meitner*, 1956.
151. C. L. Cowan, F. Reines, F. B. Harrison, H. W. Kruse and A. D. McGuire, Detection of the Free Neutrino: a Confirmation, *Science*, 1956, **124**, 103-104.
152. F. Reines and C. L. Cowanjun, The Neutrino, *Nature*, 1956, **178**, 446-449.
153. S. Berkoand H. N. Pendleton, Positronium, *Ann. Rev. Nucl. Particl. Sci.*, 1980, **30**, 543-581.
154. A. Al-Ramadhan and D. W. Gidley, New precision measurement of the decay rate of singlet positronium, *Phys. Rev. Lett.*, 1994, **72**, 1632.
155. R. S. Vallery, P. Zitzewitz and D. W. Gidley, Resolution of the orthopositronium-lifetime puzzle, *Phys. Rev. Lett.*, 2003, **90**, 203402.

156. H. Quigley, S. J. Colloby and J. T. O'Brien, PET imaging of brain amyloid in dementia: a review, *Int. J. Geriatr. Psychiatry*, 2011, **26**, 991-999.
157. A. Sánchez-Crespo, P. Andreo and S. A. Larsson, Positron flight in human tissues and its influence on PET image spatial resolution, *Eur. J. Nucl. Med. Mole. Imaging*, 2004, **31**, 44-51.
158. B. Bai, A. Ruangma, R. Laforest, Y.-C. Tai and R. M. Leahy, Positron Range Modeling for Statistical PET Image Reconstruction, *IEEE*, 2003.
159. J. Cal-González, J. Herraiz, S. España, M. Desco, J. Vaquero and J. M. Udías, Positron range effects in high resolution 3D PET imaging, *IEEE*, 2009.
160. V. C. Spanoudaki and C. S. Levin, Photo-detectors for time of flight positron emission tomography (ToF-PET), *Sensors*, 2010, **10**, 10484-10505.
161. L. Barnes, S. Gilbert and C. Surko, Energy-resolved positron annihilation for molecules, *Phys. Rev. A*, 2003, **67**, 032706.
162. G. Gribakin, J. A. Young and C. M. Surko, Positron-molecule interactions: Resonant attachment, annihilation, and bound states, *Rev. Modern Phys.*, 2010, **82**, 2557.
163. T. L. Rosenblat, M. R. McDevitt, D. A. Mulford, N. Pandit-Taskar, C. R. Divgi, K. S. Panageas, M. L. Heaney, S. Chanel, A. Morgenstern, G. Sgouros, S. M. Larson, D. A. Scheinberg and J. G. Jurcic, Sequential cytarabine and α -particle immunotherapy with bismuth-213–lintuzumab (HuM195) for acute myeloid leukemia, *Clin. Cancer Res.*, 2010, **16**, 5303-5311.
164. C. Parker, S. Nilsson, D. Heinrich, S. I. Helle, J. O'sullivan, S. D. Fosså, A. Chodacki, P. Wiechno, J. Logue and M. Seke, Alpha emitter radium-223 and survival in metastatic prostate cancer, *N. Eng. J. Med.*, 2013, **369**, 213-223.
165. N. A. Thiele, V. Brown, J. M. Kelly, A. Amor-Coarasa, U. Jermilova, S. N. MacMillan, A. Nikolopoulou, S. Ponnala, C. F. Ramogida and A. K. Robertson, An eighteen-membered macrocyclic ligand for actinium-225 targeted alpha therapy, *ACIE*, 2017, **56**, 14712-14717.
166. Y.-S. Kim and M. W. Brechbiel, An overview of targeted alpha therapy, *Tumour Biol.*, 2012, **33**, 573-590.
167. A. I. Kassis and S. J. Adelstein, Radiobiologic principles in radionuclide therapy, *J. Nucl. Med.*, 2005, **46**, 4S-12S.
168. H. Yukawa, On the interaction of elementary particles. I, *Prog. Theor. Phys.*, 1935, **17**, 48-57.
169. L. W. Alvarez, Nuclear K electron capture, *Phys. Rev.*, 1937, **52**, 134.
170. F. Bosch and Y. A. Litvinov, Observation of non-exponential orbital electron-capture decay of stored hydrogen-like ions, *Prog. Part. Nucl. Phys.*, 2010, **64**, 435-438.
171. D. Hoekzema, G. Schooten, E. van den Berg and P. Lijnse, Conservation Laws, Symmetries, and Elementary Particles, *Phys. Teach.* 2005, **43**, 266-271.
172. XENON Collaboration, Observation of two-neutrino double electron capture in ^{124}Xe with XENON1T, *Nature*, 2019, **568**, 532-535.
173. P. Auger, Sur les rayons β secondaires produits dans un gaz par des rayons X, *Cr Acad. Sci.* 1923, **177**, 169.

174. D. Coster and R. D. L. Kronig, New type of auger effect and its influence on the x-ray spectrum, *Physica*, 1935, **2**, 13-24.
175. L. Davis and L. Feldkamp, Resonant photoemission involving super-Coster-Kronig transitions, *Phys. Rev. B*, 1981, **23**, 6239.
176. S. Forberg, E. Odeblad, R. Söremark and S. Ullberg, Autoradiography with isotopes emitting internal conversion electrons and Auger electrons, *Acta Radiol. Ther. Phys. Biol.*, 1964, **2**, 241-262.
177. K. F. Eckerman and A. Endo, *MIRD: radionuclide data and decay schemes*, Snmml, 2007.
178. M. Fjälling, P. Andersson, E. Forssell-Aronsson, J. Gretarsdottir, V. Johansson, L. Tisell, B. Wangberg, O. Nilsson, G. Berg and A. Michanek, Systemic radionuclide therapy using indium-111-DTPA-D-Phe¹-octreotide in midgut carcinoid syndrome, *J. Nucl. Med.*, 1996, **37**, 1519-1521.
179. M. de Jong, W. A. Breeman, B. F. Bernard, E. J. Rolleman, L. J. Hoflande, T. J. Visser, B. Setyono-Han, W. H. Bakker, M. E. van der Pluijm and E. P. Krenning, Evaluation in vitro and in rats of ¹⁶¹Tb-DTPA-octreotide, a somatostatin analogue with potential for intraoperative scanning and radiotherapy, *Eur. J. Nucl. Med.*, 1995, **22**, 608-616.
180. J. E. Gains, V. Moroz, M. D. Aldridge, S. Wan, K. Wheatley, J. Laidler, C. Peet, J. B. Bomanji and M. Gaze, A phase IIa trial of molecular radiotherapy with ¹⁷⁷lutetium DOTATATE in children with primary refractory or relapsed high-risk neuroblastoma, *Eur. J. Nucl. Med. Mol. Imaging*, 2020, **47**, 2348-2357.
181. J. M. van Dodewaard-de Jong, J. M. de Klerk, H. J. Bloemendal, D. E. Oprea-Lager, O. S. Hoekstra, H. P. van den Berg, M. Los, A. Beeker, M. A. Jonker, J. M. O'Sullivan, H. M. W. Verheul, A. J. M. van den Eertwegh, A randomised, phase II study of repeated rhenium-188-HEDP combined with docetaxel and prednisone versus docetaxel and prednisone alone in castration-resistant prostate cancer (CRPC) metastatic to bone; the Taxium II trial, *Eur. J. Nucl. Med. Mol. Imaging*, 2017, **44**, 1319-1327.
182. F. F. Knapp Jr., Rhenium-188-A generator-derived radioisotope for cancer therapy, *Cancer Biother. Radiopharm.*, 1998, **13**, 337-349.
183. S. Aghevlian, A. J. Boyle and R. M. Reilly, Radioimmunotherapy of cancer with high linear energy transfer (LET) radiation delivered by radionuclides emitting α -particles or Auger electrons, *Adv. Drug Deliv. Rev.*, 2017, **109**, 102-118.
184. A. Ku, V. J. Facca, Z. Cai and R. M. Reilly, Auger electrons for cancer therapy—a review, *EJNMMI Radiopharm. Chem.*, 2019, **4**, 1-36.
185. V. W. Hu, D. S. Heikka, P. B. Dieffenbach and U. Ha, Metabolic radiolabeling: experimental tool or Trojan horse? ³⁵S-Methionine induces DNA fragmentation and p53-dependent ROS production, *FASEB*, 2001, **15**, 1562-1568.
186. A. Haimovitz-Friedman, C.-C. Kan, D. Ehleiter, R. S. Persaud, M. Mcloughlin, Z. Fuks and R. N. Kolesnick, Ionizing radiation acts on cellular membranes to generate ceramide and initiate apoptosis, *J. Exp. Med.*, 1994, **180**, 525-535.
187. P. Iyengar, Z. Wardak, D. E. Gerber, V. Tumati, C. Ahn, R. S. Hughes, J. E. Dowell, N. Cheedella, L. Nedzi, K. D. Westover, S. Pulippracharuvil, H. Choy, R. D. Timmerman, Consolidative radiotherapy for limited metastatic non-small-cell lung cancer: A phase 2 randomized clinical trial, *JAMA Oncol.*, 2018, **4**, e173501-e173501.

188. P. D. Brown, K. Jaeckle, K. V. Ballman, E. Farace, J. H. Cerhan, S. K. Anderson, X. W. Carrero, F. G. Barker, R. Deming and S. H. Burri, Effect of radiosurgery alone vs radiosurgery with whole brain radiation therapy on cognitive function in patients with 1 to 3 brain metastases: a randomized clinical trial, *JAMA*, 2016, **316**, 401-409.
189. S. M. Hiniker, S. A. Reddy, H. T. Maecker, P. B. Subrahmanyam, Y. Rosenberg-Hasson, S. M. Swetter, S. Saha, L. Shura and S. J. Knox, A prospective clinical trial combining radiation therapy with systemic immunotherapy in metastatic melanoma, *Int. J. Radiat. Oncol. Biol. Phys.*, 2016, **96**, 578-588.
190. R. J. Hicks, D. J. Kwekkeboom, E. Krenning, L. Bodei, S. Grozinsky-Glasberg, R. Arnold, I. Borbath, J. Cwikla, C. Toumpanakis, G. Kaltsas, P. Davies, D. Hörsch, E. Tiensuu Janson and J. Ramage, ENETS Consensus Guidelines for the Standards of Care in Neuroendocrine Neoplasms: Peptide Receptor Radionuclide Therapy with Radiolabelled Somatostatin Analogues, *Neuroendocrinology*, 2017, **105**, 295-309.
191. W. Yang, C. Wang and G. Huang, Receptor-Targeted Radionuclide Imaging (PTRI) and Peptide Receptor Radionuclide Therapy (PRRT), *Nucl. Med. Oncol.*, Springer, 2019, pp. 177-199.
192. D. L. Chan, N. Pavlakis, G. P. Schembri, E. J. Bernard, E. Hsiao, A. Hayes, T. Barnes, C. Diakos, M. Khasraw and J. Samra, Dual somatostatin receptor/FDG PET/CT imaging in metastatic neuroendocrine tumours: proposal for a novel grading scheme with prognostic significance, *Tharnostics*, 2017, **7**, 1149.
193. R. Mikołajczak and H. R. Maecke, Radiopharmaceuticals for somatostatin receptor imaging, *Nucl. Med. Rev.*, 2016, **19**, 126-132.
194. S. W. J. Lamberts and L. J. Hofland, Anniversary Review: Octreotide, 40 years later, *Eur. J. Endocrinol.*, 2019, **181**, R173-R183.
195. S. A. Deppen, J. Blume, A. J. Bobbey, C. Shah, M. M. Graham, P. Lee, D. Delbeke and R. C. Walker, ⁶⁸Ga-DOTATATE compared with ¹¹¹In-DTPA-octreotide and conventional imaging for pulmonary and gastroenteropancreatic neuroendocrine tumors: a systematic review and meta-analysis, *J. Nucl. Med.*, 2016, **57**, 872-878.
196. R. P. Baum, A. W. Kluge, H. Kulkarni, U. Schorr-Neufing, K. Niepsch, N. Bitterlich and C. J. van Echteld, [¹⁷⁷Lu-DOTA] 0-D-Phe¹-Tyr³-octreotide (¹⁷⁷Lu-DOTATOC) for peptide receptor radiotherapy in patients with advanced neuroendocrine tumours: a phase-II study, *Tharnostics*, 2016, **6**, 501.
197. L. Y. I. Yamaga, M. L. Cunha, G. C. C. Neto, M. R. Garcia, J. H. Yang, C. P. Camacho, J. Wagner and M. B. G. Funari, ⁶⁸Ga-DOTATATE PET/CT in recurrent medullary thyroid carcinoma: a lesion-by-lesion comparison with ¹¹¹In-octreotide SPECT/CT and conventional imaging, *Eur. J. Nucl. Med. Mol. Imaging*, 2017, **44**, 1695-1701.
198. D. Storch, M. Béhé, M. A. Walter, J. Chen, P. Powell, R. Mikolajczak and H. R. Mäcke, Evaluation of [^{99m}Tc/EDDA/HYNIC0] octreotide derivatives compared with [¹¹¹In-DOTA0, Tyr3, Thr8] octreotide and [¹¹¹In-DTPA0] octreotide: does tumor or pancreas uptake correlate with the rate of internalization?, *J. Nucl. Med.* 2005, **46**, 1561-1569.
199. D. J. Kwekkeboom, W. H. Bakker, P. P. Kooij, M. W. Konijnenberg, A. Srinivasan, J. L. Erion, M. A. Schmidt, J. L. Bugaj, M. de Jong and E. P. Krenning, [¹⁷⁷Lu-DOTA 0, Tyr 3] octreotate: comparison with [¹¹¹In-DTPA 0] octreotide in patients, *Eur. J. Nucl. Med.*, 2001, **28**, 1319-1325.

200. C. Waldherr, M. Pless, H. Maecke, A. Haldemann and J. Mueller-Brand, The clinical value of [⁹⁰Y-DOTA]-D-Phe1-Tyr3-octreotide (⁹⁰Y-DOTATOC) in the treatment of neuroendocrine tumours: a clinical phase II study, *Ann. Oncol.*, 2001, **12**, 941-945.
201. C. Bruns, I. Lewis, U. Briner, G. Meno-Tetang and G. Weckbecker, SOM230: a novel somatostatin peptidomimetic with broad somatotropin release inhibiting factor (SRIF) receptor binding and a unique antiseecretory profile, *Eur. J. Endocrinol.*, 2002, **146**, 707-716.
202. H. A. Schmid, Pasireotide (SOM230): Development, mechanism of action and potential applications, *Mol. Cell. Endocrinol.*, 2008, **286**, 69-74.
203. L. J. Hofland, J. v. d. Hoek, R. Feelders, M. O. v. Aken, P. M. v. Koetsveld, M. Waaijers, D. Sprij-Mooij, C. Bruns, G. Weckbecker, W. W. d. Herder, A. Beckers and S. W. J. Lamberts, The multi-ligand somatostatin analogue SOM230 inhibits ACTH secretion by cultured human corticotroph adenomas via somatostatin receptor type 5, *Eur. J. Endocrinol.*, 2005, **152**, 645.
204. S. Petersenn, J. Schopohl, A. Barkan, P. Mohideen, A. Colao, R. Abs, A. Buchelt, Y.-Y. Ho, K. Hu and A. J. Farrall, Pasireotide (SOM230) demonstrates efficacy and safety in patients with acromegaly: a randomized, multicenter, phase II trial, *J. Clin. Endocrinol. Metab.*, 2010, **95**, 2781-2789.
205. T. Murakami, Y. Hiroshima, R. Matsuyama, Y. Homma, R. M. Hoffman and I. Endo, Role of the tumor microenvironment in pancreatic cancer, *Ann. Gastroenterol. Surg.*, 2019, **3**, 130-137.
206. T. Murakami, Y. Hiroshima, R. Matsuyama, Y. Homma, R. M. Hoffman and I. J. A. o. G. S. Endo, Role of the tumor microenvironment in pancreatic cancer, 2019, **3**, 130-137.
207. L. Bodei, M. Cremonesi, C. Grana, P. Rocca, M. Bartolomei, M. Chinol and G. Paganelli, Receptor radionuclide therapy with ⁹⁰Y-[DOTA] 0-Tyr 3-octreotide (⁹⁰Y-DOTATOC) in neuroendocrine tumours, *Eur. J. Nucl. Med. Mol. Imaging*, 2004, **31**, 1038-1046.
208. L. Bodei, M. Cremonesi, S. Zoboli, C. Grana, M. Bartolomei, P. Rocca, M. Caracciolo, H. R. Mäcke, M. Chinol and G. Paganelli, Receptor-mediated radionuclide therapy with ⁹⁰Y-DOTATOC in association with amino acid infusion: a phase I study, *Eur. J. Nucl. Med. Mol. Imaging*, 2003, **30**, 207-216.
209. M. Hofmann, H. Maecke, A. Börner, E. Weckesser, P. Schöffski, M. Oei, J. Schumacher, M. Henze, A. Heppeler, J. Meyer, H. Knapp, Biokinetics and imaging with the somatostatin receptor PET radioligand ⁶⁸Ga-DOTATOC: preliminary data, *Eur. J. Nucl. Med.*, 2001, **28**, 1751-1757.
210. F. Forrer, H. Uusijärvi, C. Waldherr, M. Cremonesi, P. Bernhardt, J. Mueller-Brand and H. R. Maecke, A comparison of ¹¹¹In-DOTATOC and ¹¹¹In-DOTATATE: biodistribution and dosimetry in the same patients with metastatic neuroendocrine tumours, *Eur. J. Nucl. Med. Mol. Imaging*, 2004, **31**, 1257-1262.
211. I. Buchmann, M. Henze, S. Engelbrecht, M. Eisenhut, A. Runz, M. Schäfer, T. Schilling, S. Haufe, T. Herrmann and U. Haberkorn, Comparison of ⁶⁸Ga-DOTATOC PET and ¹¹¹In-DTPAOC (Octreoscan) SPECT in patients with neuroendocrine tumours, *Eur. J. Nucl. Med. Mol. Imaging* 2007, **34**, 1617-1626.

212. F. Forrer, H. Uusijärvi, D. Storch, H. R. Maecke and J. Mueller-Brand, Treatment with ^{177}Lu -DOTATOC of patients with relapse of neuroendocrine tumors after treatment with ^{90}Y -DOTATOC, *J. Nucl. Med.*, 2005, **46**, 1310-1316.
213. U. Hennrich and K. J. P. Kopka, Lutathera®: The First FDA-and EMA-approved radiopharmaceutical for peptide receptor radionuclide therapy, 2019, **12**, 114.
214. P. Anitha, P. Viswanathamurthi, D. Kesavan and R. J. Butcher, Ruthenium (II) 9, 10-phenanthrenequinone thiosemicarbazone complexes: synthesis, characterization, and catalytic activity towards the reduction as well as condensation of nitriles, *J. Coord. Chem.*, 2015, **68**, 321-334.
215. P. Anitha, R. Manikandan and P. Viswanathamurthi, Palladium(II) 9,10-phenanthrenequinone N-substituted thiosemicarbazone/semicarbazone complexes as efficient catalysts for N-arylation of imidazole, *J. Coord. Chem.*, 2015, **68**, 3537-3550.
216. M. Muthukumar and P. Viswanathamurthi, Synthesis, spectral characterization and catalytic studies of new ruthenium(II) chalcone thiosemicarbazone complexes, *Open Chem. J.*, 2010, **8**, 229.
217. M. Mohamed Subarkhan and R. Ramesh, Binuclear ruthenium(III) bis(thiosemicarbazone) complexes: Synthesis, spectral, electrochemical studies and catalytic oxidation of alcohol, *Spectrochim. Acta A Mol. Biomol. Spectrosc.*, 2015, **138**, 264-270.
218. M. Hakimi, H. Vahedi, R. Takjoo and A. J. Rezaeifard, Nanoporous Silica Supported Novel Copper (II) Thiosemicarbazone Complexes as Selective and Reusable Catalysts for Oxidation of Alcohols Using H_2O_2 , *Int. J. Chemtech Res.* 2012, **4**, 1658-1665.
219. M. Salavati-Niasari, Host (nanocage of zeolite–Y)/guest (manganese(II), cobalt(II), nickel(II) and copper(II) complexes of 12-membered macrocyclic Schiff-base ligand derived from thiosemicarbazide and glyoxal) nanocomposite materials: Synthesis, characterization and catalytic oxidation of cyclohexene, *J. Mol. Catal. A Chem.*, 2008, **283**, 120-128.
220. A. Manimaran and C. Jayabalakrishnan, DNA-binding, catalytic oxidation, CC coupling reactions and antibacterial activities of binuclear Ru(II) thiosemicarbazone complexes: Synthesis and spectral characterization, *J. Adv. Res.*, 2012, **3**, 233-243.
221. S S. Datta, D. K. Seth, R. J. Butcher and S. Bhattacharya, Mixed-ligand thiosemicarbazone complexes of nickel: Synthesis, structure and catalytic activity, *Inorg. Chim. Acta*, 2011, **377**, 120-128.
222. L. Lu, P. Chellan, G. S. Smith, X. Zhang, H. Yan and J. Mao, Thiosemicarbazone salicylaldiminato palladium(II)-catalyzed alkynylation couplings between arylboronic acids and alkynes or alkynyl carboxylic acids, *Tetrahedron*, 2014, **70**, 5980-5985.
223. I. D. Kostas, F. J. Andreadaki, D. Kovala-Demertzi, P. Christos and M. A. Demertzis, Suzuki–Miyaura cross-coupling reaction of aryl bromides and chlorides with phenylboronic acid under aerobic conditions catalyzed by palladium complexes with thiosemicarbazone ligands, *Tetrahedron Lett.*, 2005, **46**, 1967-1970.
224. S. Datta, D. K. Seth, S. Gangopadhyay, P. Karmakar and S. Bhattacharya, Nickel complexes of some thiosemicarbazones: Synthesis, structure, catalytic properties and cytotoxicity studies, *Inorg. Chim. Acta*, 2012, **392**, 118-130.
225. Z. Moradi-Shoeili, D. M. Boghaei, M. Amini, M. Bagherzadeh and B. Notash, New molybdenum(VI) complex with ONS-donor thiosemicarbazone ligand: Preparation,

- structural characterization, and catalytic applications in olefin epoxidation, *Inorg. Chem. Commun.*, 2013, **27**, 26-30.
226. J. Pisk, B. Prugovečki, D. Matković-Čalogović, R. Poli, D. Agustin and V. Vrdoljak, Charged dioxomolybdenum(VI) complexes with pyridoxal thiosemicarbazone ligands as molybdenum(V) precursors in oxygen atom transfer process and epoxidation (pre)catalysts, *Polyhedron*, 2012, **33**, 441-449.
227. N. S. Youssef, A. M. A. El-Seidy, M. Schiavoni, B. Castano, F. Ragaini, E. Gallo and A. Caselli, Thiosemicarbazone copper complexes as competent catalysts for olefin cyclopropanations, *J. Organomet. Chem.*, 2012, **714**, 94-103.
228. K. Sivadasan Chettiar and K. Sreekumar, Polystyrene-supported thiosemicarbazone–transition metal complexes: synthesis and application as heterogeneous catalysts, *Polym. Int.*, 1999, **48**, 455-460.
229. R. Manikandan, P. Anitha, P. Viswanathamurthi and J. G. Malecki, Palladium(II) pyridoxal thiosemicarbazone complexes as efficient and recyclable catalyst for the synthesis of propargylamines by a three-component coupling reactions in ionic liquids, *Polyhedron*, 2016, **119**, 300-306.
230. X. Jing, P. Wu, X. Liu, L. Yang, C. He and C. Duan, Light-driven hydrogen evolution with a nickel thiosemicarbazone redox catalyst featuring Ni···H interactions under basic conditions, *New J. Chem.*, 2015, **39**, 1051-1059.
231. P. Paul, S. Datta, S. Halder, R. Acharyya, F. Basuli, R. J. Butcher, S.-M. Peng, G.-H. Lee, A. Castineiras, M. G. B. Drew and S. Bhattacharya, Syntheses, structures and efficient catalysis for C–C coupling of some benzaldehyde thiosemicarbazone complexes of palladium, *J. Mol. Catal. A Chem.*, 2011, **344**, 62-73.
232. K. Thapa, P. Paul and S. Bhattacharya, A group of diphosphine-thiosemicarbazone complexes of palladium: Efficient precursors for catalytic CC and CN coupling reactions, *Inorg. Chim. Acta*, 2019, **486**, 232-239.
233. T. Straistari, J. Fize, S. Shova, M. Réglie, V. Artero and M. Orio, A Thiosemicarbazone–Nickel(II) Complex as Efficient Electrocatalyst for Hydrogen Evolution, *ChemCatChem*, 2017, **9**, 2262-2268.
234. T. Straistari, R. Hardré, J. Fize, S. Shova, M. Giorgi, M. Réglie, V. Artero and M. Orio, Hydrogen Evolution Reactions Catalyzed by a Bis(thiosemicarbazone) Cobalt Complex: An Experimental and Theoretical Study, *Chem. Eur. J.*, 2018, **24**, 8779-8786.
235. S. Panagiotakis, G. Landrou, V. Nikolaou, A. Putri, R. Hardré, J. Massin, G. Charalambidis, A. G. Coutsolelos and M. Orio, Efficient Light-Driven Hydrogen Evolution Using a Thiosemicarbazone-Nickel (II) Complex, *Front. Chem.*, 2019, **7**, 405.
236. A. Barrozo and M. Orio, Unraveling the catalytic mechanisms of H₂ production with thiosemicarbazone nickel complexes, *RSC Advances*, 2021, **11**, 5232-5238.
237. F. H. Arnold, Innovation by evolution: Bringing new chemistry to life (Nobel Lecture), *ACIE*, 2019, **58**, 14420-14426.
238. E. Gibney, R. Van Noorden, H. Ledford, D. Castelvecchi and M. Warren, 'Test-tube' evolution wins Chemistry Nobel Prize, *Nature*, 2018, **562**, 176.
239. S. C. Hammer, A. M. Knight and F. H. Arnold, Design and evolution of enzymes for non-natural chemistry, *Curr. Opin. Green Sustain. Chem.*, 2017, **7**, 23-30.

240. R. Chowdhury and C. D. Maranas, From directed evolution to computational enzyme engineering—A review, *AiChE J.*, 2020, **66**, e16847.
241. I. Coluzza, Computational protein design: a review, *J. Condens. Matter Phys.*, 2017, **29**, 143001.
242. P.-S. Huang, S. E. Boyken and D. Baker, The coming of age of de novo protein design, *Nature*, 2016, **537**, 320-327.
243. S. Bähr, S. Brinkmann-Chen, M. Garcia-Borràs, J. M. Roberts, D. E. Katsoulis, K. N. Houk and F. H. Arnold, Selective Enzymatic Oxidation of Silanes to Silanols, *ACIE*, 2020, **59**, 15507-15511
244. S. J. Kan, R. D. Lewis, K. Chen and F. H. Arnold, Directed evolution of cytochrome c for carbon–silicon bond formation: Bringing silicon to life, *Science*, 2016, **354**, 1048-1051.
245. K. Engström, E. V. Johnston, O. Verho, K. P. J. Gustafson, M. Shakeri, C.-W. Tai and J.-E. Bäckvall, Co-immobilization of an Enzyme and a Metal into the Compartments of Mesoporous Silica for Cooperative Tandem Catalysis: An Artificial Metalloenzyme, *ACIE*, 2013, **52**, 14006-14010.
246. F. Schwizer, Y. Okamoto, T. Heinisch, Y. Gu, M. M. Pellizzoni, V. Lebrun, R. Reuter, V. Köhler, J. C. Lewis and T. R. Ward, Artificial metalloenzymes: reaction scope and optimization strategies, *Chem. Rev.*, 2018, **118**, 142-231.
247. V V. Sabatino and T. R. Ward, Aqueous olefin metathesis: recent developments and applications, *J. Org. Chem.*, 2019, **15**, 445-468.
248. T. Heinisch and T. R. Ward, Artificial metalloenzymes based on the biotin–streptavidin technology: challenges and opportunities, *Acc. Chem Rev.*, 2016, **49**, 1711-1721.
249. W. A. Hendrickson, A. Pähler, J. L. Smith, Y. Satow, E. A. Merritt and R. P. Phizackerley, Crystal structure of core streptavidin determined from multiwavelength anomalous diffraction of synchrotron radiation, *PNAS*, 1989, **86**, 2190-2194.
250. P. S. Stayton, S. Freitag, L. A. Klumb, A. Chilkoti, V. Chu, J. E. Penzotti, R. To, D. Hyre, I. Le Trong, T. P. Lybrand and R. E. Stenkamp, Streptavidin–biotin binding energetics, *Biomol. Eng.*, 1999, **16**, 39-44.
251. S. Freitag, I. Le Trong, A. Chilkoti, L. A. Klumb, P. S. Stayton and R. E. Stenkamp, Structural studies of binding site tryptophan mutants in the high-affinity streptavidin–biotin complex, *J. Mol. Biol.*, 1998, **279**, 211-221.
252. A. D. Liang, J. Serrano-Plana, R. L. Peterson and T. R. Ward, Artificial metalloenzymes based on the biotin–streptavidin technology: enzymatic cascades and directed evolution, *Acc. Chem. Res.*, 2019, **52**, 585-595.
253. H. J. Davis and T. R. Ward, Artificial Metalloenzymes: Challenges and Opportunities, *ACS Cent. Sci.*, 2019, **5**, 1120-1136.
254. U. Markel, D. F. Sauer, J. Schiffels, J. Okuda and U. Schwaneberg, Towards the Evolution of Artificial Metalloenzymes—A Protein Engineer's Perspective, *ACIE*, 2019, **58**, 4454-4464.
255. C. Zeymer and D. Hilvert, Directed evolution of protein catalysts, *Ann. Rev. Biochem.*, 2018, **87**, 131-157.
256. K. K. Yang, Z. Wu and F. H. Arnold, Machine-learning-guided directed evolution for protein engineering, *Nat. Methods*, 2019, **16**, 687-694.

257. M. Kasha, Characterization of electronic transitions in complex molecules, *Discuss. Faraday Soc.*, 1950, **9**, 14-19.
258. J. C. Del Valle and J. Catalán, Kasha's rule: a reappraisal, *Phys. Chem. Chem. Phys.*, 2019, **21**, 10061-10069.
259. K. D. Piatkevich, J. Hulit, O. M. Subach, B. Wu, A. Abdulla, J. E. Segall and V. V. Verkhusha, Monomeric red fluorescent proteins with a large Stokes shift, *PNAS*, 2010, **107**, 5369-5374.
260. T. Kogure, H. Kawano, Y. Abe and A. Miyawaki, Fluorescence imaging using a fluorescent protein with a large Stokes shift, *Methods*, 2008, **45**, 223-226.
261. P. Dierks, A. Pöpcke, O. S. Bokareva, B. Altenburger, T. Reuter, K. Heinze, O. Kühn, S. Lochbrunner and M. Bauer, Ground- and Excited-State Properties of Iron(II) Complexes Linked to Organic Chromophores, *Inorg. Chem.*, 2020, **59**, 14746-14761.
262. M. Kleinschmidt, C. van Wüllen and C. M. Marian, Intersystem-crossing and phosphorescence rates in fac-Ir III (ppy) 3: A theoretical study involving multi-reference configuration interaction wavefunctions, *J. Chem. Phys.*, 2015, **142**, 094301.
263. B. Valeur, Molecular Fluorescence, in *digital Encyclopedia of Applied Physics*, pp. 477-531.
264. L. Möckl, D. C. Lamb and C. Bräuchle, Super-resolved Fluorescence Microscopy: Nobel Prize in Chemistry 2014 for Eric Betzig, Stefan Hell, and William E. Moerner, 2014, *ACIE*, **53**, 13972-13977.
265. J. W. Lichtman and J.-A. Conchello, Fluorescence microscopy, *Nat. Methods*, 2005, **2**, 910-919.
266. B. Huang, M. Bates and X. Zhuang, Super-resolution fluorescence microscopy, *Ann. Rev. Biochem.*, 2009, **78**, 993-1016.
267. S. W. Hell and J. Wichmann, Breaking the diffraction resolution limit by stimulated emission: stimulated-emission-depletion fluorescence microscopy, *Opt. Lett.*, 1994, **19**, 780-782.
268. Y. Zhu, S. Mohapatra and J. C. Weisshaar, Rigidification of the Escherichia coli cytoplasm by the human antimicrobial peptide LL-37 revealed by superresolution fluorescence microscopy, *PNAS*, 2019, **116**, 1017-1026.
269. G. H. Patterson, S. M. Knobel, W. D. Sharif, S. R. Kain and D. W. Piston, Use of the green fluorescent protein and its mutants in quantitative fluorescence microscopy, *Biophys. J.*, 1997, **73**, 2782.
270. V. A. Byvaltsev, L. A. Bardonova, R. A. Polkin, S. V. Ochkal, V. V. Shepelev, M. A. Aliyev, D. A. Ptashnikov and A. A. Potapov, Acridine orange: a Review of Novel Applications for Surgical Cancer Imaging and Therapy, *Front Oncol.*, 2019, **9**, 925.
271. G. Shute and T. Sodeman, Identification of malaria parasites by fluorescence microscopy and acridine orange staining, *Bull. World Health Organ.* 1973, **48**, 591.
272. A. Zelenin, Fluorescence microscopy of lysosomes and related structures in living cells, *Nature*, 1966, **212**, 425-426.
273. O. Shimomura, F. H. Johnson and Y. Saiga, Extraction, Purification and Properties of Aequorin, a Bioluminescent Protein from the Luminous Hydromedusan, Aequorea, *J. Cell. Physiol.*, 1962, **59**, 223-239.

274. C. J. Peddie, K. Blight, E. Wilson, C. Melia, J. Marrison, R. Carzaniga, M.-C. Domart, P. O'Toole, B. Larijani and L. M. Collinson, Correlative and integrated light and electron microscopy of in-resin GFP fluorescence, used to localise diacylglycerol in mammalian cells, *Ultramicroscopy*, 2014, **143**, 3-14.
275. S. Cabantous and G. S. Waldo, In vivo and in vitro protein solubility assays using split GFP, *Nat. Methods*, 2006, **3**, 845-854.
276. Q. Li, S. S. H. Wu and K. C. Chou, Subdiffraction-Limit Two-Photon Fluorescence Microscopy for GFP-Tagged Cell Imaging, *Biophys. J.*, 2009, **97**, 3224-3228.
277. D. M. Damas-Souza, R. Nunes and H. F. Carvalho, An improved acridine orange staining of DNA/RNA, *Acta Histochem.*, 2019, **121**, 450-454.
278. L. Lerman, The structure of the DNA-acridine complex, *PNAS*, 1963, **49**, 94.
279. A. Karmakar, S. Banerjee, B. Singh and N. C. Mandal, Study of hydrogen bonding interaction of acridine orange with different acceptor molecules by spectroscopic, theoretical, and antimicrobial studies, *J.Mol. Struct.*, 2019, **1177**, 418-429.
280. Y. Dai, K. Xu, Q. Li, C. Wang, X. Liu and P. Wang, Acridine-based complex as amino acid anion fluorescent sensor in aqueous solution, *Spectrochim. Acta A Mol. Biomol. Spectrosc.*, 2016, **157**, 1-5.
281. M. C. Nunes, F. dos Santos Carlos, O. Fuganti, D. D. M. Galindo, L. De Boni, G. Abate and F. S. Nunes, Turn-on fluorescence study of a highly selective acridine-based chemosensor for Zn²⁺ in aqueous solutions, *Inorg. Chim. Acta*, 2020, **499**, 119191.
282. A. K. Ghosh, A. Samanta and P. Bandyopadhyay, Cu²⁺-Induced Micellar Charge Selective Fluorescence Response of Acridine Orange: Effect of Micellar Charge, pH, and Mechanism, *J. Phys. Chem. B*, 2011, **115**, 11823-11830.
283. E. E. Frieben, S. Amin and A. K. Sharma, Development of Isoselenocyanate Compounds' Syntheses and Biological Applications, *J. Med. Chem.*, 2019, **62**, 5261-5275.
284. Ó. López, S. Maza, V. Ulgar, I. Maya and J. G. Fernández-Bolaños, Synthesis of sugar-derived isoselenocyanates, selenoureas, and selenazoles, *Tetrahedron*, 2009, **65**, 2556-2566.
285. P. Liska, N. Vlachopoulos, M. K. Nazeeruddin, P. Comte and M. Graetzel, cis-Diaquabis(2,2'-bipyridyl-4,4'-dicarboxylate)ruthenium(II) sensitizes wide band gap oxide semiconductors very efficiently over a broad spectral range in the visible, *JACS*, 1988, **110**, 3686-3687.
286. S. Basu, R. Acharyya, F. Basuli, S.-M. Peng, G.-H. Lee, G. Mostafa and S. Bhattacharya, Iridium assisted S-H and C-H activation of benzaldehyde thiosemicarbazones. Synthesis, structure and electrochemical properties of the resulting complexes, *Inorg. Chim. Acta*, 2010, **363**, 2848-2856.
287. K. A. Bunten, L. Chen, A. L. Fernandez and A. J. Poë, Cone angles: Tolman's and Plato's, 2002, *Coord. Chem. Rev.*, **233**, 41-51.
288. C. A. Tolman, Phosphorus ligand exchange equilibriums on zerovalent nickel. Dominant role for steric effects, *JACS*, 1970, **92**, 2956-2965.
289. S. Otto and A. Roodt, Quantifying the electronic cis effect of phosphine, arsine and stibine ligands by use of rhodium (I) Vaska-type complexes, *Inorg. Chim. Acta*, 2004, **357**, 1-10.

290. J. C. Röder, F. Meyer, I. Hyla-Kryspin, R. F. Winter and E. Kaifer, Electronic Coupling in a Highly Preorganized Bimetallic Complex Comprising Pyrazolate-Bridged CpMn(CO)₂ Moieties, *Chem. Eur. J.*, 2003, **9**, 2636-2648.
291. J. Maurer, B. Sarkar, B. Schwederski, W. Kaim, R. F. Winter and S. Záliš, Divinylphenylene-Bridged Diruthenium Complexes Bearing Ru(CO)Cl(PiPr₃)₂ Entities, *Organometallics*, 2006, **25**, 3701-3712.
292. A. A. H. Van Der Zeijden, C. Sontag, H. William Bosch, V. Shklover, H. Berke, D. Nanz and W. V. Philipsborn, IR, Multinuclear-NMR, and Structural Studies on [WH(CO)₂(NO)(PR₃)₂]: cis-Influence of Phosphorus Ligands on Hydride Character, 1991, *Helv. Chim. Acta*, **74**, 1194-1204.
293. A. L. Allred and E. G. Rochow, A scale of electronegativity based on electrostatic force, *J. Inorg. Nucl. Chem.*, 1958, **5**, 264-268.
294. H. Pritchard and H. Skinner, The concept of electronegativity, *Chem. Rev.*, 1955, **55**, 745-786.
295. M. C. DeRosa, G. D. Enright, C. E. Evans and R. J. Crutchley, The photodecomposition product μ -oxalato-1 κ 2O, O': 2 κ 2O'', O'''-bis {bis [2-(2-pyridyl) phenyl- κ 2C, N] iridium (III)}-acetone (1/1.974), *Acta Cryst. E*, 2005, **61**, m967-m969.
296. M. Graf, R. Czerwieniec and K. Sünkel, Synthesis and Molecular Structure of the New Green Emitting Complex [Ir₂(μ ₂-oxamidato-N,N',O,O')(2-(p-tolyl)pyridinato)₄], *ZAAC*, 2013, **639**, 1090-1094.
297. W.-S. Sie, J.-Y. Jian, T.-C. Su, G.-H. Lee, H. M. Lee and K.-B. Shiu, Synthesis, structures, and properties of iridium(III) bis-cyclometallated complexes containing three-atom chelates, *J. Organomet. Chem.*, 2008, **693**, 1510-1517.
298. T. J. Schmeier, G. E. Dobereiner, R. H. Crabtree and N. Hazari, Secondary Coordination Sphere Interactions Facilitate the Insertion Step in an Iridium(III) CO₂ Reduction Catalyst, *JACS*, 2011, **133**, 9274-9277.
299. F. J. Fernández-Alvarez, M. Iglesias, L. A. Oro and V. Polo, CO₂ Activation and Catalysis Driven by Iridium Complexes, *ChemCatChem*, 2013, **5**, 3481-3494.
300. F. R. Louka, F. A. Mautner, R. Vicente and S. S. Massoud, μ ₂-Oxalato-bridged tricopper (II) complex derived from 1, 4, 8, 12-tetraazacyclopentadecane: Synthesis, structure and magnetic characterization, *Inorg. Chem. Comm.*, 2008, **11**, 438-441.
301. K. Gutkowski, E. Freire and R. Baggio, Poly [[tetra- μ ₃-acetato-hexa- μ ₂-acetato-diaqua- μ ₂-oxalato-tetrapraseodymium (III)] dihydrate], *Acta Crystall. C*, 2011, **67**, m77-m80.
302. M. Bakir, M. A. Lawrence, M. Ferhat and R. R. Conry, Spectroscopic, electrochemical and X-ray crystallographic properties of a novel palladium (II) complex of thioamide deprotonated di-2-pyridyl ketone thiosemicarbazone (dpkts-c-H)⁻, *J. Coord. Chem.*, 2017, **70**, 3048-3064.
303. A. Haseloer, Master of Science, Universität zu Köln, 2017.
304. K. R. Koch, A Multinuclear NMR Study of Platinum(II) Complexes of N-Phenyl and N-(3-Allyl) Substituted 2-(2-Pyridinemethylene) Hydrazine Carbothioamides, *J. Coord. Chem.*, 1990, **22**, 289-298.
305. M. J. Arendse, I. R. Green and K. R. Koch, Synthesis and spectral studies of platinum complexes of para-substituted 4-phenylthiosemicarbazides, *Spectrochim. Acta A Mol. Biomol. Spectrosc.*, 1997, **53**, 1537-1545.

306. K. R. Koch, Cationic and neutral bis(4-p-tolylthiosemicarbazido)platinum(II) complexes: a preparative as well as ^1H and ^{195}Pt NMR study of the question of cis/trans isomerism, *Inorg. Chim. Acta*, 1988, **147**, 227-232.
307. J. Li and Y. Sha, A convenient synthesis of amino acid methyl esters, *Molecules*, 2008, **13**, 1111-1119.
308. N. Sun, B. Li, J. Shao, W. Mo, B. Hu, Z. Shen and X. Hu, A general and facile one-pot process of isothiocyanates from amines under aqueous conditions, *J. Org. Chem.*, 2012, **8**, 61-70.
309. J. Nath, L. Jamir and B. K. Patel Improved procedure for the preparation of isothiocyanates via iodine-mediated desulfurization of dithiocarbamic acid salts, *Green Chem. Res. Lett. Rev.*, 2011, **4**, 1-34.
310. M. Horn and I. Neundorf, Design of a novel cell-permeable chimeric peptide to promote wound healing, *Sci. Rep.*, 2018, **8**, 16279-16279.
311. A. Gronewold, M. Horn and I. Neundorf, Design and biological characterization of novel cell-penetrating peptides preferentially targeting cell nuclei and subnuclear regions, *J. org. chem.*, 2018, **14**, 1378-1388.
312. J. Hoyer, U. Schatzschneider, M. Schulz-Siegmund and I. Neundorf, Dimerization of a cell-penetrating peptide leads to enhanced cellular uptake and drug delivery, *J. org. chem.*, 2012, **8**, 1788-1797.
313. S. Richter, V. Bouvet, M. Wuest, R. Bergmann, J. Steinbach, J. Pietzsch, I. Neundorf and F. Wuest, ^{18}F -Labeled phosphopeptide-cell-penetrating peptide dimers with enhanced cell uptake properties in human cancer cells, *Nucl. med. biol.*, 2012, **39**, 1202-1212.
314. S. Yoichi, A Quantitative Scale of the Spectrochemical Series for the Mixed Ligand Complexes of d6 Metals, *Bull. Chem. Soc. Jpn.*, 1988, **61**, 693-698.
315. E. Lee, J. Seo, S. S. Lee and K.-M. Park, A Triple-Stranded Ladder-Type Coordination Polymer, *Cryst. Growth & Des.*, 2012, **12**, 3834-3837.
316. J.-C. Berthet, P. Thuéry and M. Ephritikhine, Advances in f-element cyanide chemistry, *Dalton Trans.*, 2015, **44**, 7727-7742.
317. T.-y. Li, T. Meyer, R. Meerheim, M. Höppner, C. Körner, K. Vandewal, O. Zeika and K. Leo, Aza-BODIPY dyes with heterocyclic substituents and their derivatives bearing a cyanide co-ligand: NIR donor materials for vacuum-processed solar cells, *J. Mater. Chem. A*, 2017, **5**, 10696-10703.
318. A. Lüning, J. Schur, L. Hamel, I. Ott and A. Klein, Strong cytotoxicity of organometallic platinum complexes with alkynyl ligands, *Organometallics*, 2013, **32**, 3662-3672.
319. S. N. Maqbool, S. C. Lim, K. C. Park, R. Hanif, D. R. Richardson, P. J. Jansson and Z. Kovacevic, Overcoming tamoxifen resistance in oestrogen receptor-positive breast cancer using the novel thiosemicarbazone anti-cancer agent, DpC, *Br. J. Pharmacol.*, 2020, **177**, 2365-2380.
320. P. J. Jansson, D. S. Kalinowski, D. J. Lane, Z. Kovacevic, N. A. Seebacher, L. Fouani, S. Sahni, A. M. Merlot and D. R. Richardson, The renaissance of polypharmacology in the development of anti-cancer therapeutics: Inhibition of the "Triad of Death" in cancer by Di-2-pyridylketone thiosemicarbazones, *Pharmacol. Res.*, 2015, **100**, 255-260.

321. S. Krishan, S. Sahni, L. Leck, P. Jansson and D. Richardson, Regulation of autophagy and apoptosis by Dp44mT-mediated activation of AMPK in pancreatic cancer cells, *Biochim. Biophys. Acta Mol. Basis Dis.*, 2020, **1866**, 165657.
322. D. S. Kalinowski, C. Stefani, S. Toyokuni, T. Ganz, G. J. Anderson, N. V. Subramaniam, D. Trinder, J. K. Olynyk, A. Chua and P. J. Jansson, Redox cycling metals: Pedaling their roles in metabolism and their use in the development of novel therapeutics, *Biochim. Biophys. Acta Mol. Cell Res.*, 2016, **1863**, 727-748.
323. D. J. Lane, T. M. Mills, N. H. Shafie, A. M. Merlot, R. S. Moussa, D. S. Kalinowski, Z. Kovacevic and D. R. Richardson, Expanding horizons in iron chelation and the treatment of cancer: Role of iron in the regulation of ER stress and the epithelial–mesenchymal transition, *Biochim. Biophys. Acta Rev. Cancer*, 2014, **1845**, 166-181.
324. P. J. Jansson, T. Yamagishi, A. Arvind, N. Seebacher, E. Gutierrez, A. Stacy, S. Maleki, D. Sharp, S. Sahni and D. R. Richardson, Di-2-pyridylketone 4, 4-dimethyl-3-thiosemicarbazone (Dp44mT) overcomes multidrug resistance by a novel mechanism involving the hijacking of lysosomal P-glycoprotein (Pgp), *J. Biol. Chem.*, 2015, **290**, 9588-9603.
325. Y. Geldmacher, K. Splith, I. Kitanovic, H. Alborzinia, S. Can, R. Rubbiani, M. A. Nazif, P. Wefelmeier, A. Prokop and I. Ott, Cellular impact and selectivity of half-sandwich organorhodium (III) anticancer complexes and their organoiridium (III) and trichloridorhodium (III) counterparts, *J. Biol. Inorg. Chem.*, 2012, **17**, 631-646.
326. W. Hu, K. Splith, I. Neundorf, K. Merz and U. Schatzschneider, Influence of the metal center and linker on the intracellular distribution and biological activity of organometal–peptide conjugates, *J. Biol. Inorg. Chem.*, 2012, **17**, 175-185.
327. K. Splith, I. Neundorf, W. Hu, H. W. P. N'Dongo, V. Vasylyeva, K. Merz and U. Schatzschneider, Influence of the metal complex-to-peptide linker on the synthesis and properties of bioactive CpMn(CO)₃ peptide conjugates, *Dalton Trans.*, 2010, **39**, 2536-2545.
328. C. Cullinane, G. B. Deacon, P. R. Drago, A. P. Erven, P. C. Junk, J. Luu, G. Meyer, S. Schmitz, I. Ott and J. Schur, Synthesis and antiproliferative activity of a series of new platinum and palladium diphosphane complexes, *Dalton Transactions*, 2018, **47**, 1918-1932.
329. V. Lingen, A. Lüning, A. Krest, G. B. Deacon, J. Schur, I. Ott, I. Pantenburg, G. Meyer and A. Klein, Labile Pd-sulphur and Pt-sulphur bonds in organometallic palladium and platinum complexes [(COD) M (alkyl)(S-ligand)]ⁿ⁺—A speciation study, *J. Inorg. Biochem.*, 2016, **165**, 119-127.
330. A. Lüning, M. Neugebauer, V. Lingen, A. Krest, K. Stirnat, G. B. Deacon, P. R. Drago, I. Ott, J. Schur and I. Pantenburg, Platinum diolefin complexes—synthesis, structures, and cytotoxicity, *Eur. J. Inorg. Chem.*, 2015, **2015**, 226-239.
331. F. N. Akladios, S. D. Andrew and C. J. Parkinson, Cytotoxic activity of expanded coordination bis-thiosemicarbazones and copper complexes thereof, *J. Biol. Inorg. Chem.*, 2016, **21**, 931-944.
332. A. Gaál, V. G. Mihucz, S. Bősze, I. Szabó, M. Baranyi, P. Horváth, C. Strelci and N. Szoboszlai, Comparative in vitro investigation of anticancer copper chelating agents, *Microchem. J.*, 2018, **136**, 227-235.
333. E. Potuckova, H. Jansova, M. Machacek, A. Vavrova, P. Haskova, L. Tichotova, V. Richardson, D. S. Kalinowski, D. R. Richardson and T. Simunek, Quantitative analysis

- of the anti-proliferative activity of combinations of selected iron-chelating agents and clinically used anti-neoplastic drugs, *PLoS One*, 2014, **9**, e88754.
334. R. Ettari, F. Bova, M. Zappalà, S. Grasso and N. Micale, Falcipain-2 inhibitors, *Med. Res. Rev.*, 2010, **30**, 136-167.
335. G. Pelosi, F. Bisceglie, F. Bignami, P. Ronzi, P. Schiavone, M. C. Re, C. Casoli and E. Pilotti, Antiretroviral activity of thiosemicarbazone metal complexes, *J. med. chem.*, 2010, **53**, 8765-8769.
336. A. Gaál, G. Orgován, V. G. Mihucz, I. Pape, D. Ingerle, C. Strelí and N. Szoboszlai, Metal transport capabilities of anticancer copper chelators, *J. Trace Elem. Med. Biol.*, 2018, **47**, 79-88.
337. D. B. Lovejoy, P. J. Jansson, U. T. Brunk, J. Wong, P. Ponka and D. R. Richardson, Antitumor activity of metal-chelating compound Dp44mT is mediated by formation of a redox-active copper complex that accumulates in lysosomes, *Cancer res.*, 2011, **71**, 5871-5880.
338. I. Neundorf, R. Rennert, J. Hoyer, F. Schramm, K. Löbner, I. Kitanovic and S. Wöfl, Fusion of a short HA2-derived peptide sequence to cell-penetrating peptides improves cytosolic uptake, but enhances cytotoxic activity, *Pharmaceuticals*, 2009, **2**, 49-65.
339. A. Gronewold, M. Horn, I. Randelović, J. Tóvári, S. M. Vázquez, K. Schomäcker and I. Neundorf, Characterization of a cell-penetrating peptide with potential anticancer activity, *ChemMedChem*, 2017, **12**, 42.
340. M. Horn and I. Neundorf, Design of a novel cell-permeable chimeric peptide to promote wound healing, *Sci. Rep.*, 2018, **8**, 1-12.
341. L. Feni, S. Parente, C. m. Robert, S. Gazzola, D. Arosio, U. Piarulli and I. Neundorf, Kiss and run: Promoting effective and targeted cellular uptake of a drug delivery vehicle composed of an integrin-targeting diketopiperazine peptidomimetic and a cell-penetrating peptide, *Bioconjug. chem.*, 2019, **30**, 2011-2022
342. A. I. Matesanz, J. M. Herrero, E. J. Faraco, L. Cubo and A. G. Quiroga, New platinum (II) triazole thiosemicarbazone complexes: analysis of their reactivity and potential antitumoral action, *ChemBioChem*, 2020, **21**, 1226-1232.
343. E. Boros and A. B. Packard, Radioactive transition metals for imaging and therapy, *Chem. Rev.*, 2018, **119**, 870-901.
344. J. O'donoghue and T. Wheldon, Targeted radiotherapy using Auger electron emitters, *Phys. Med. Biol.*, 1996, **41**, 1973.
345. H. Obata, M. U. Khandaker, E. Furuta, K. Nagatsu and M.-R. Zhang, Excitation functions of proton- and deuteron-induced nuclear reactions on natural iridium for the production of ¹⁹¹Pt, *Appl. Radiat. Isot.*, 2018, **137**, 250-260.
346. S. M. Qaim, Nuclear data for production and medical application of radionuclides: Present status and future needs, *Nucl. Med. Biol.*, 2017, **44**, 31-49.
347. S. M. Qaim and I. Spahn, Development of novel radionuclides for medical applications, *J. Label. Compd. Rad.*, 2018, **61**, 126-140.
348. F. Buchegger, F. Perillo-Adamer, Y. M. Dupertuis and A. B. Delaloye, Auger radiation targeted into DNA: a therapy perspective, *Eur. J. Nucl. Med. Mol. Imaging*, 2006, **33**, 1352-1363.

349. K. Peng, V. Mawamba, E. Schulz, M. Löhr, C. Hagemann and U. Schatzschneider, iClick Reactions of Square-Planar Palladium(II) and Platinum(II) Azido Complexes with Electron-Poor Alkynes: Metal-Dependent Preference for N1 vs N2 Triazolate Coordination and Kinetic Studies with ^1H and ^{19}F NMR Spectroscopy, *Inorg. Chem.*, 2019, **58**, 11508-11521.
350. H. Masai, K. Sonogashira and N. Hagihara, Electronic spectra of square-planar bis (tertiary phosphine) dialkynyl complexes of nickel (II), palladium (II), and platinum (II), *Bull. Chem. Soc. Jpn.*, 1971, **44**, 2226-2230.
351. A. Kochem, G. Gellon, O. Jarjayes, C. Philouze, A. du Moulinet d'Hardemare, M. van Gastel and F. Thomas, Nickel(II) radical complexes of thiosemicarbazone ligands appended by salicylidene, aminophenol and aminothiophenol moieties, *Dalton Trans.*, 2015, **44**, 12743-12756.
352. K. Butsch, T. Günther, A. Klein, K. Stirnat, A. Berkessel and J. Neudörfl, Redox chemistry of copper complexes with various salen type ligands, *Inorg. Chim. Acta*, 2013, **394**, 237-246.
353. K. Butsch, A. Klein, S. Nitsche, K. Stirnat, J. R. Hawkett, E. J. McInnes and M. Bauer, Generation and characterisation of the phenoxyl-radical containing Cu (II) complex $[\text{Cu}(\text{triaz})_2]^+(\text{triaz}=\text{O}, \text{N}$ chelating triazole-phenolate), *Dalton Trans.*, 2012, **41**, 11464-11475.
354. K. Kamaraj, E. Kim, B. Galliker, L. N. Zakharov, A. L. Rheingold, A. D. Zuberbühler and K. D. Karlin, Copper (I) and Copper (II) complexes possessing cross-linked imidazole-phenol ligands: structures and dioxygen reactivity, *JACS*, 2003, **125**, 6028-6029.
355. B. D. Zlatopolskiy, H. Endepols, P. Krapf, M. Guliyev, E. A. Urusova, R. Richarz, M. Hohberg, M. Dietlein, A. Drzezga and B. Neumaier, Discovery of ^{18}F -JK-PSMA-7, a PET Probe for the Detection of Small PSMA-Positive Lesions, *J. Nucl. Med.*, 2019, **60**, 817-823.
356. A. Frei, E. Fischer, B. C. Childs, J. P. Holland and R. Alberto, Two is better than one: difunctional high-affinity PSMA probes based on a $[\text{CpM}(\text{CO})_3]$ ($\text{M} = \text{Re}/^{99\text{m}}\text{Tc}$) scaffold, *Dalton Trans.*, 2019, **48**, 14600-14605.
357. C. Kratochwil, F. Bruchertseifer, F. L. Giesel, M. Weis, F. A. Verburg, F. Mottaghy, K. Kopka, C. Apostolidis, U. Haberkorn and A. Morgenstern, ^{225}Ac -PSMA-617 for PSMA-Targeted α -Radiation Therapy of Metastatic Castration-Resistant Prostate Cancer, *J. Nucl. Med.*, 2016, **57**, 1941-1944.
358. S. Fukuzumi and K. Ohkubo, Fluorescence maxima of 10-methylacridone– metal ion salt complexes: A convenient and quantitative measure of lewis acidity of metal ion salts, *JACS*, 2002, **124**, 10270-10271.
359. T.-J. Wang, W.-W. Chen, Y. Li and M.-H. Xu, Facile synthesis of acridines via Pd (0)-diphosphine complex-catalyzed tandem coupling/cyclization protocol, *J. Org. Chem.*, 2015, **13**, 6580-6586.
360. S. Lai and D. G. Lee, Lewis acid assisted permanganate oxidations, *Tetrahedron*, 2002, **58**, 9879-9887.
361. Abbott Laboratories, 1992; Platelet Activating Antagonist, US5149704.
362. B. P. Bade, S. S. Garje, Y. S. Niwate, M. Afzaal and P. O'Brien, Tribenzyltin(IV)chloride Thiosemicarbazones: Novel Single Source Precursors for Growth of SnS Thin Films, *Chem. Vap. Depos.*, 2008, **14**, 292-295.

363. A. M. Palve, Deposition of Zinc Sulfide Thin Films From Zinc(II) Thiosemicarbazones as Single Molecular Precursors Using Aerosol Assisted Chemical Vapor Deposition Technique, *Front. Mater.*, 2019, **6**.
364. M. B. Schütz, A. M. Renner, S. Ilyas, K. Lê, M. Guliyev, P. Krapf, B. Neumaier and S. Mathur, ¹⁸F-Labeled magnetic nanovectors for bimodal cellular imaging, *Biomater. Sci.*, 2021, **9**, 4717-4727.
365. G. Howáth, C. Rusa, Z. Köntös, J. Gerencsér and P. Huszthy, A new Efficient Method for the Preparation of 2, 6-Pyridinediethyl Ditosylates from Dimethyl 2, 6-Pyridinedicarboxylates, *Syn. Commun.*, 1999, **29**, 3719-3731.
366. A. Dumont, V. Jacques and J. F. Desreux, New synthons for the synthesis of lanthanide containing macrocyclic schiff bases featuring substituents available for tethering, *Tetrahedron*, 2000, **56**, 2043-2052.
367. N. De Rycke, F. Couty and O. R. David, Toward reactant encapsulation for substrate-selectivity, *Tetrahedron Lett.*, 2012, **53**, 462-466.
368. P. V. Ivchenko, I. E. Nifant'ev and I. V. Buslov, A convenient approach for the synthesis of 2, 6-diformyl- and 2, 6-diacetylpyridines, *Tetrahedron Lett.*, 2013, **54**, 217-219.
369. J. Piechowska and D. T. Gryko, Preparation of a Family of 10-Hydroxybenzo[h]quinoline Analogues via a Modified Sanford Reaction and Their Excited State Intramolecular Proton Transfer Properties, *J. Org. Chem.*, 2011, **76**, 10220-10228.
370. B. Akhlaghinia, A new and convenient method of generating alkyl isocyanates from alcohols, thiols and trimethylsilyl ethers using triphenylphosphine/2, 3-dichloro-5, 6-dicyanobenzoquinone/Bu₄NOCN, *Synthesis*, **2005**, 1955-1958.
371. E. N. Faria, A. R. Jupp and J. M. Goicoechea, Novel primary phosphinecarboxamides derived from diamines, *Dalton Trans.*, 2021, DOI: 10.1039/D1DT01198G.
372. F. Tambornino, A. Hinz, R. Köppe and J. M. Goicoechea, A General Synthesis of Phosphorus- and Arsenic-Containing Analogues of the Thio- and Seleno-cyanate Anions, *ACIE*, 2018, **57**, 8230-8234.
373. M. Krejčík, M. Daněk and F. Hartl, Simple construction of an infrared optically transparent thin-layer electrochemical cell: Applications to the redox reactions of ferrocene, Mn₂(CO)₁₀ and Mn(CO)₃(3,5-di-t-butyl-catecholate)⁻, *J. Electroanal. Chem. Interf. Electrochem.*, 1991, **317**, 179-187.
374. W. Kaim, S. Ernst and V. Kasack, ESR of homo- and heteroleptic mono- and dinuclear tris (α-diimine) ruthenium radical complexes, *JACS*, 1990, **112**, 173-178.
375. A. Altomare, G. Casciarano, C. Giacovazzo, A. Guagliardi, M. Burla, G. t. Polidori and M. Camalli, SIRPOW. 92—a program for automatic solution of crystal structures by direct methods optimized for powder data, *J. Appl. Cryst.*, 1994, **27**, 435-436.
376. M. C. Burla, R. Caliandro, B. Carrozzini, G. L. Casciarano, C. Cuocci, C. Giacovazzo, M. Mallamo, A. Mazzone and G. Polidori, Crystal structure determination and refinement via SIR2014, *J. Appl. Cryst.*, 2015, **48**, 306-309.
377. O. V. Dolomanov, L. J. Bourhis, R. J. Gildea, J. A. Howard and H. J. J. o. a. c. Puschmann, OLEX2: a complete structure solution, refinement and analysis program, *J. Appl. Cryst.*, 2009, **42**, 339-341.
378. G. M. Sheldrick, A short history of SHELX, *Acta Cryst. A*, 2008, **64**, 112-122.

379. M. Turner, J. McKinnon, S. Wolff, D. Grimwood, P. Spackman, D. Jayatilaka and M. Spackman, *CrystalExplorer17. IUCrJ*, 2017, **4**, 575-587.
380. J. Mintmire and B. I. Dunlap, Fitting the Coulomb potential variationally in linear-combination-of-atomic-orbitals density-functional calculations, *Phys. Rev. A*, 1982, **25**, 88.
381. C. K. Skylaris, L. Gagliardi, N. C. Handy, A. G. Ioannou, S. Spencer and A. Willetts, On the resolution of identity Coulomb energy approximation in density functional theory, *J. Mol. Struct. Theochem.*, 2000, **501-502**, 229-239.
382. R. Ahlrichs, M. Armbruster, R. Bachorz, M. Bär, H. Baron, R. Bauernschmitt, F. Bischoff, S. Böcker, A. Burow and N. Crawford, TURBOMOLE V7.0; TURBOMOLE GmbH: Karlsruhe, Germany, 2015.
383. C. Steffen, K. Thomas, U. Huniar, A. Hellweg, O. Rubner and A. Schroer, TmoleX—a graphical user interface for TURBOMOLE, *J. Comput. Chem.*, 2010, **31**, 2967-2970.
384. A. Klamt, Conductor-like screening model for real solvents: a new approach to the quantitative calculation of solvation phenomena, *J. Phys. Chem.*, 1995, **99**, 2224-2235.
385. A. Klamt, V. Jonas, T. Bürger and J. C. W. Lohrenz, Refinement and parametrization of COSMO-RS, *J. Phys. Chem. A*, 1998, **102**, 5074-5085.
386. J. R. Rumble and T. J. Bruno, *CRC Handbook of Chemistry and Physics 2019-2020: A Ready-reference Book of Chemical and Physical Data*, Taylor & Francis Group, 2019.
387. A. Schäfer, H. Horn and R. Ahlrichs, Fully optimized contracted Gaussian basis sets for atoms Li to Kr, *J. Chem. Phys.*, 1992, **97**, 2571-2577.
388. A. Schäfer, C. Huber and R. Ahlrichs, Fully optimized contracted Gaussian basis sets of triple zeta valence quality for atoms Li to Kr, *J. Chem. Phys.*, 1994, **100**, 5829-5835.
389. N. B. Balabanov and K. A. Peterson, Systematically convergent basis sets for transition metals. I. All-electron correlation consistent basis sets for the 3 d elements Sc–Zn, 2005, *J. Chem. Phys.*, **123**, 064107.
390. P. J. Hay and W. R. Wadt, Ab initio effective core potentials for molecular calculations. Potentials for the transition metal atoms Sc to Hg, *J. Chem. Phys.*, 1985, **82**, 270-283.
391. W. R. Wadt and P. J. Hay, Ab initio effective core potentials for molecular calculations. Potentials for main group elements Na to Bi, *J. Chem. Phys.*, 1985, **82**, 284-298.
392. P. J. Hay and W. R. Wadt, Ab initio effective core potentials for molecular calculations. Potentials for K to Au including the outermost core orbitals, *J. Chem. Phys.*, 1985, **82**, 299-310.
393. A. D. Becke, Density-functional exchange-energy approximation with correct asymptotic behavior, *Phys. Rev. A*, 1988, **38**, 3098.
394. C. Lee, W. Yang and R. G. Parr, Development of the Colle-Salvetti correlation-energy formula into a functional of the electron density, *Phys. Rev. B*, 1988, **37**, 785-789.
395. A. D. Becke, Density-functional thermochemistry. III. The role of exact exchange, *J. Phys. Chem.*, 1993, **98**, 5648-5652.
396. A. D. Becke, Density-functional thermochemistry. III. The role of exact exchange, 1993, **98**, 5648-5652.
397. Xcalibur™ Software, Data acquisition, Version 2.2/Windows, Thermo Scientific, Darmstadt, Germany **2011**.

398. T. L. Riss, R. Moravec, A. Niles, S. Duellman, H. Benink, T. Worzella and L. Minor, Cell viability assays assay guidance manual, 2004, 1-23.

7. Appendix

7.1. NMR spectra of thiosemicarbazides and their precursors

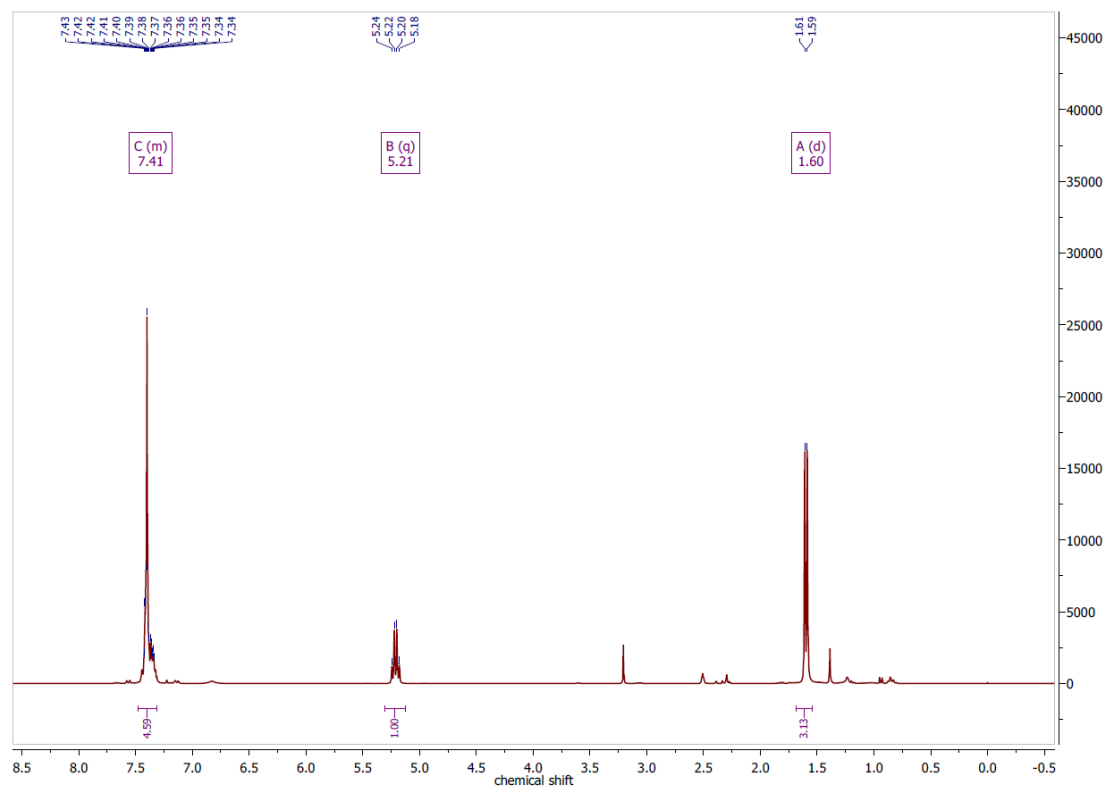


Figure 7.1 ^1H NMR spectrum of ITCmB in $\text{DMSO-}d_6$ at 300 MHz.

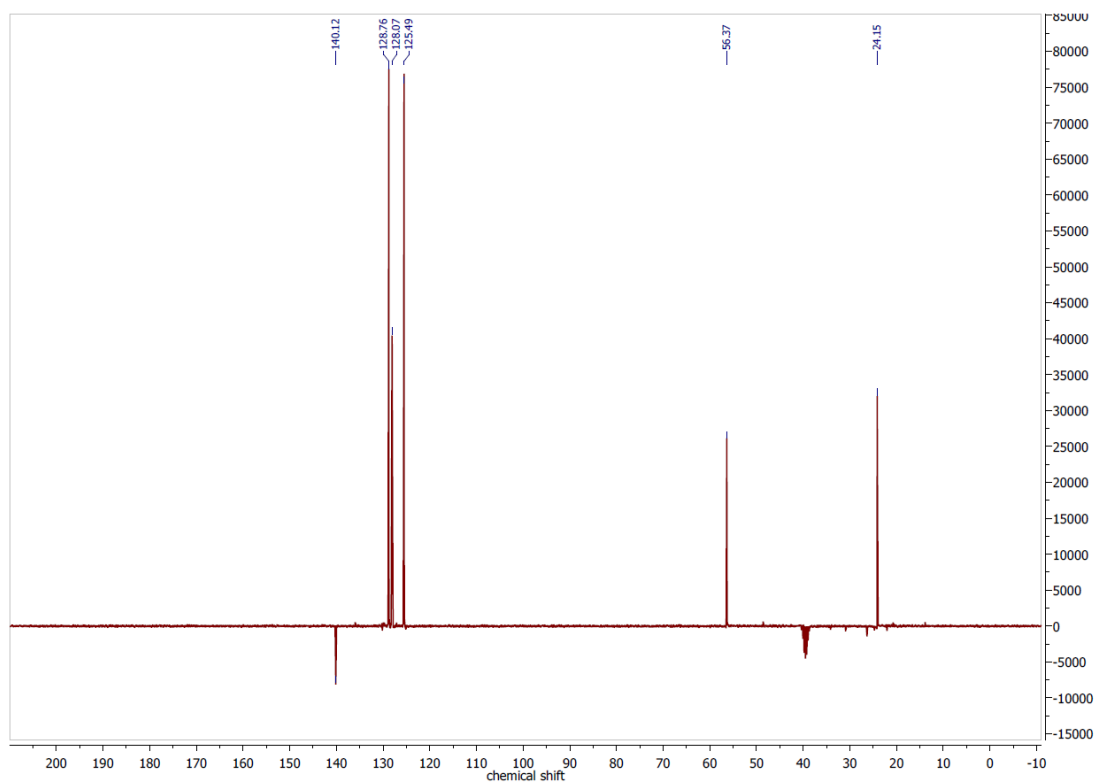


Figure 7.2 ^{13}C APT NMR spectrum of ITCmB in $\text{DMSO-}d_6$ at 75 MHz.

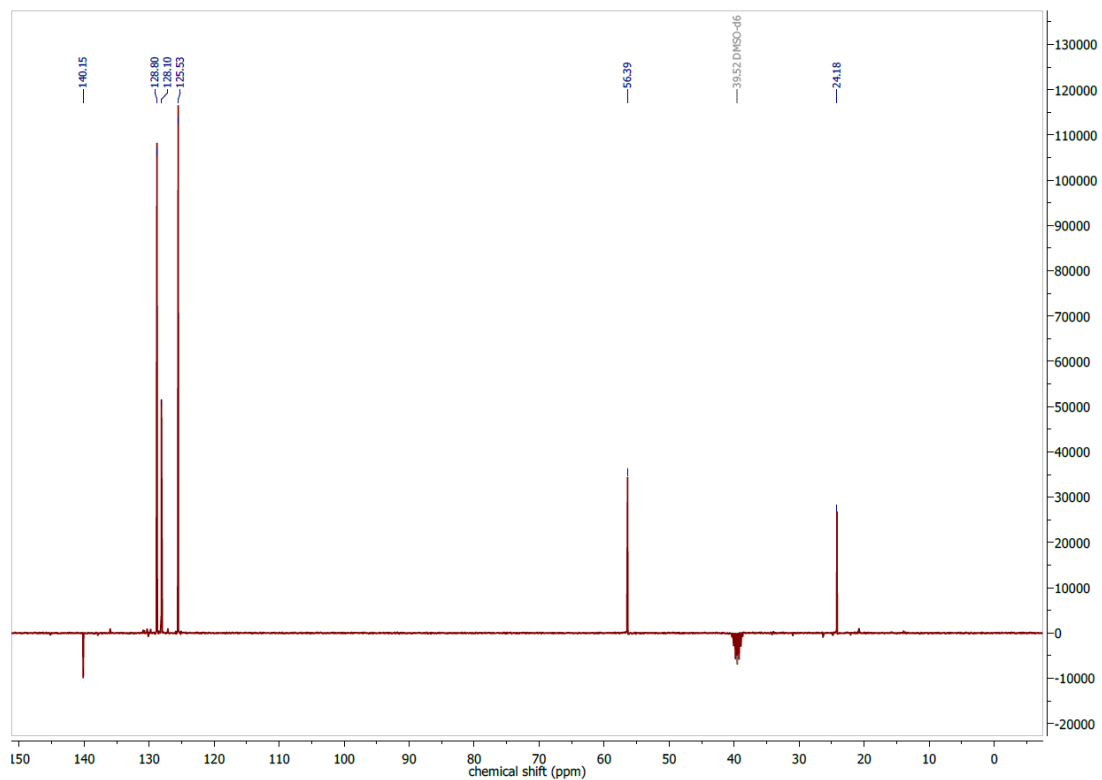


Figure 7.3 $^{13}\text{C}\{^1\text{H}\}$ DEPTQ NMR spectrum of ITCmB in $\text{DMSO-}d_6$ at 75 MHz.

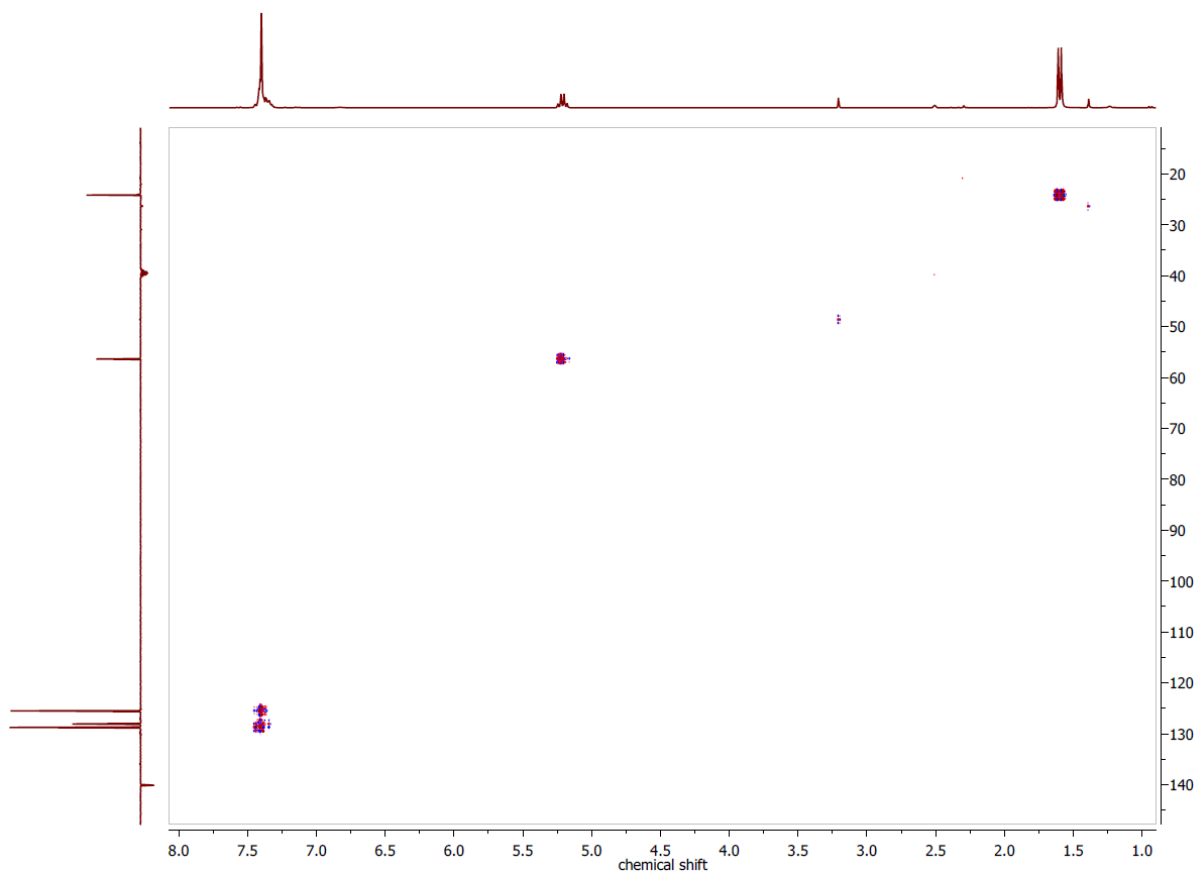


Figure 7.4 $^1\text{H}, ^{13}\text{C}$ HSQC NMR spectrum of ITCmB in $\text{DMSO-}d_6$.

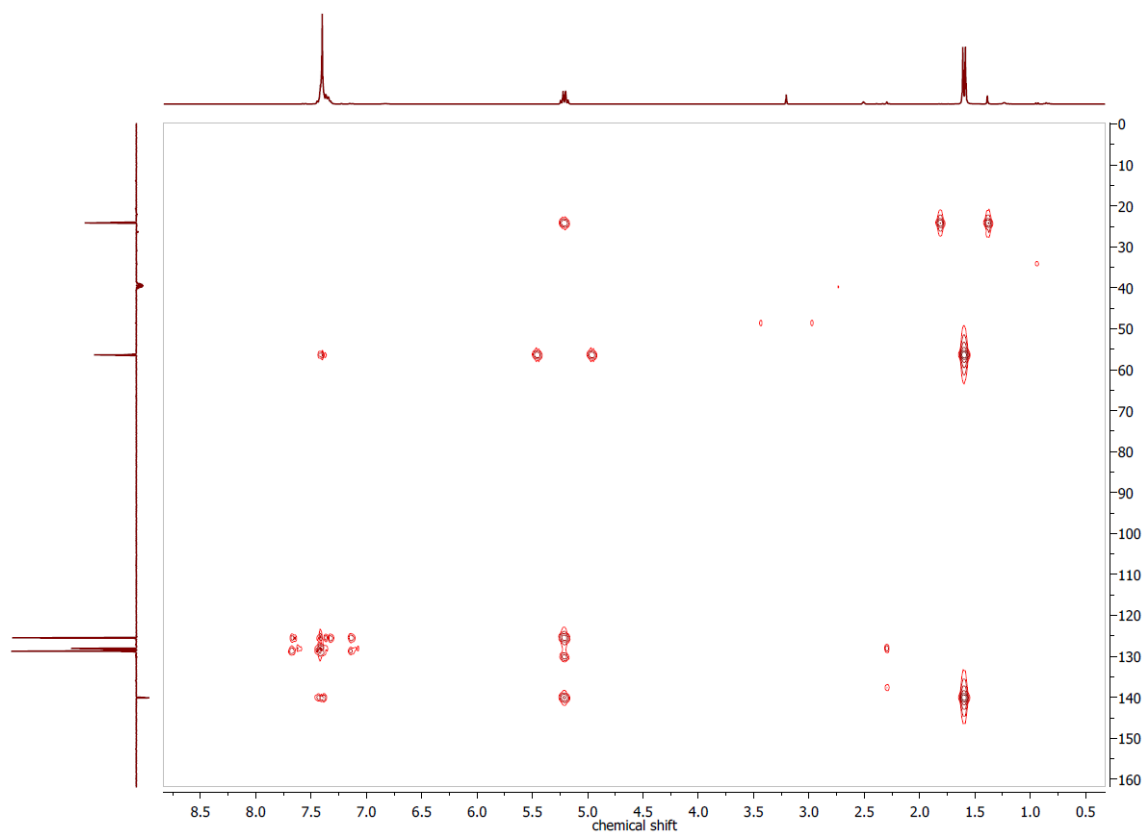


Figure 7.5 ^1H , ^{13}C HMBC NMR spectrum of ITCmB in $\text{DMSO-}d_6$.

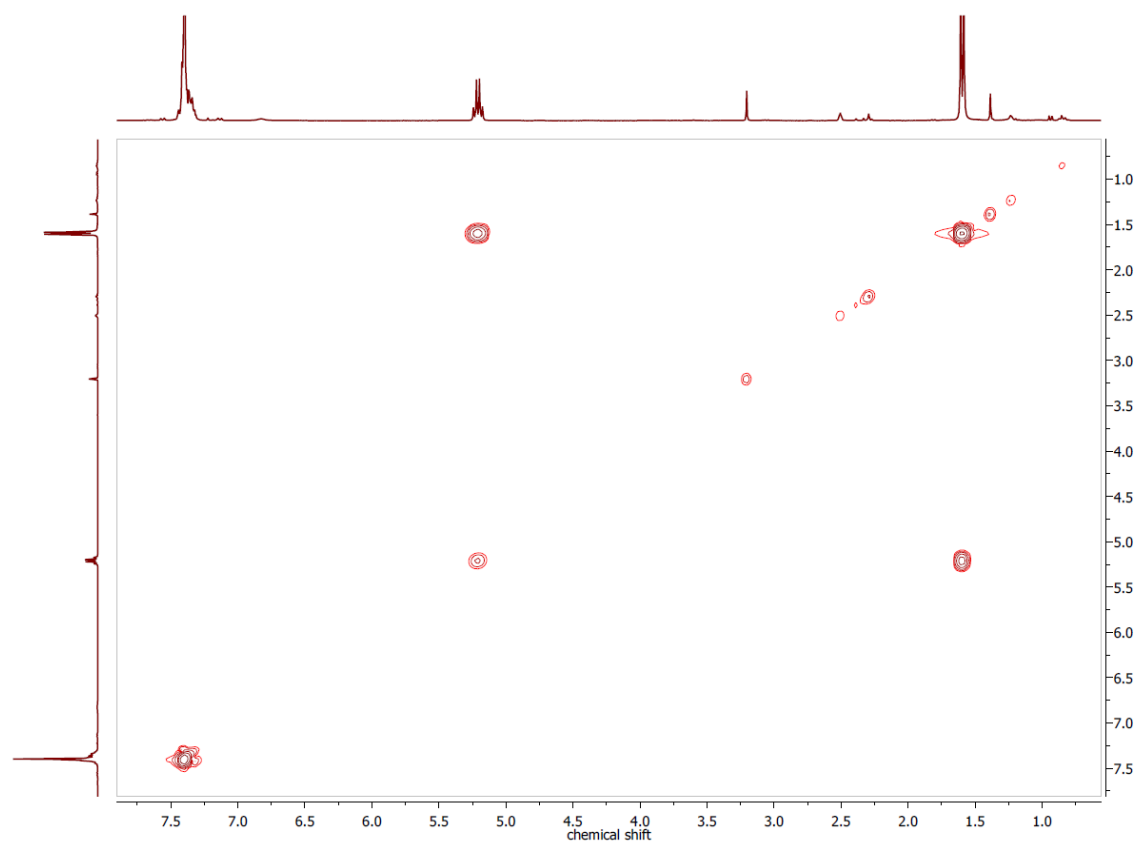


Figure 7.6 ^1H , ^1H COSY NMR spectrum of ITCmB in $\text{DMSO-}d_6$.

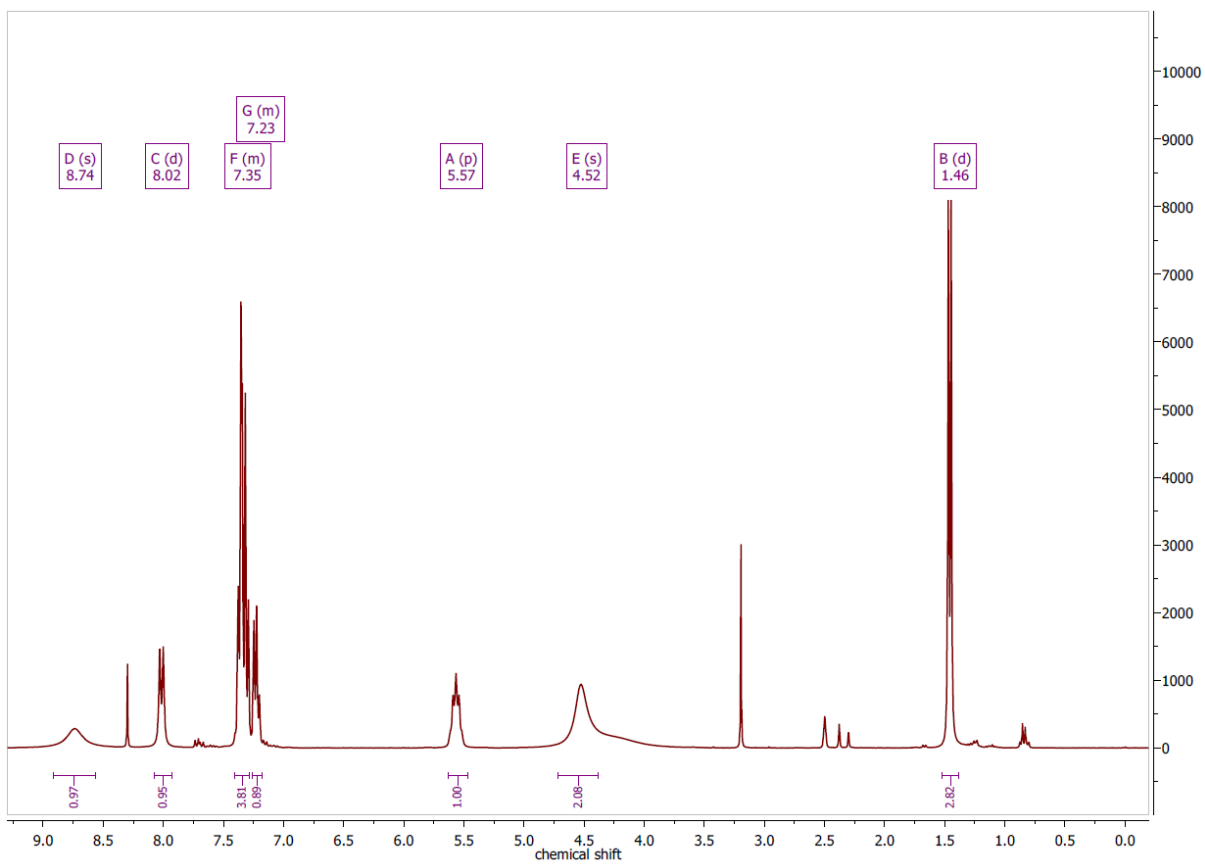


Figure 7.7 ^1H NMR spectrum of TSCmB in $\text{DMSO-}d_6$ at 300 MHz.

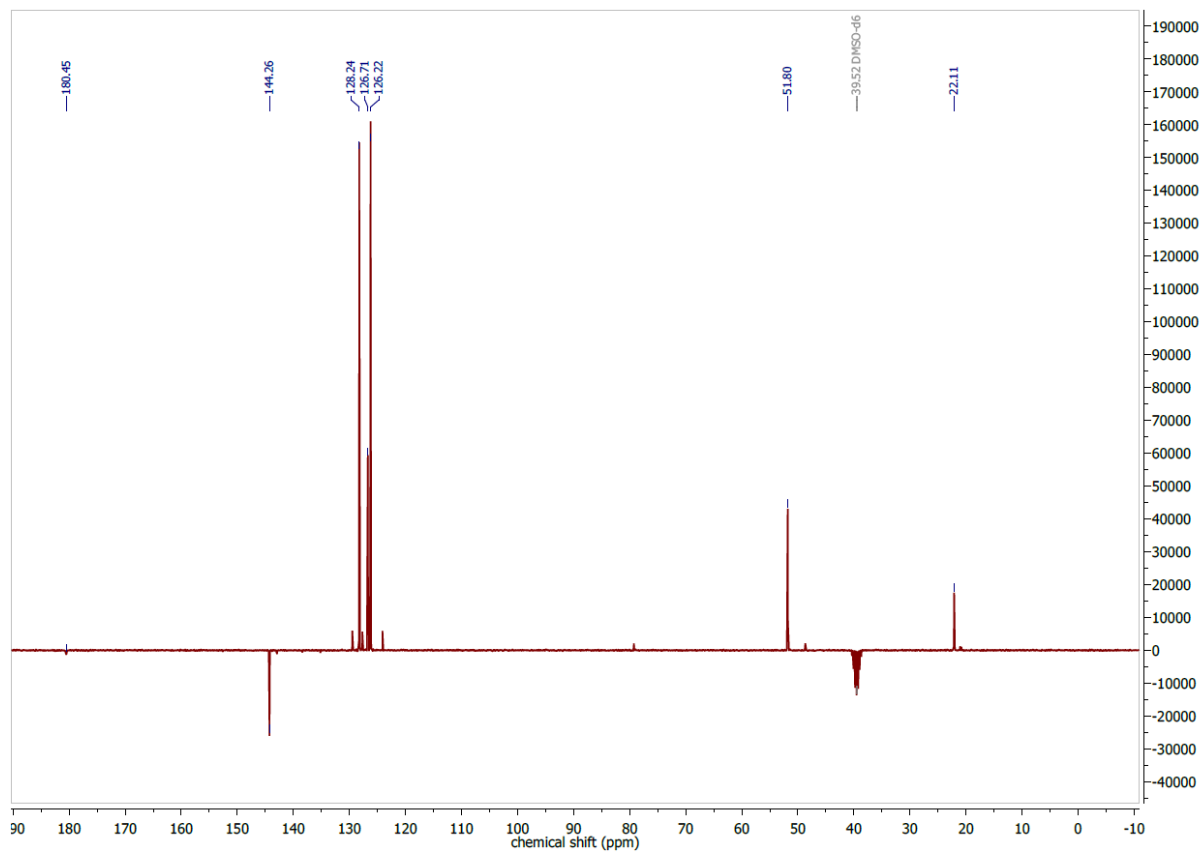


Figure 7.8 $^{13}\text{C}\{^1\text{H}\}$ DEPTQ NMR spectrum of TSCmB in $\text{DMSO-}d_6$ at 75 MHz.

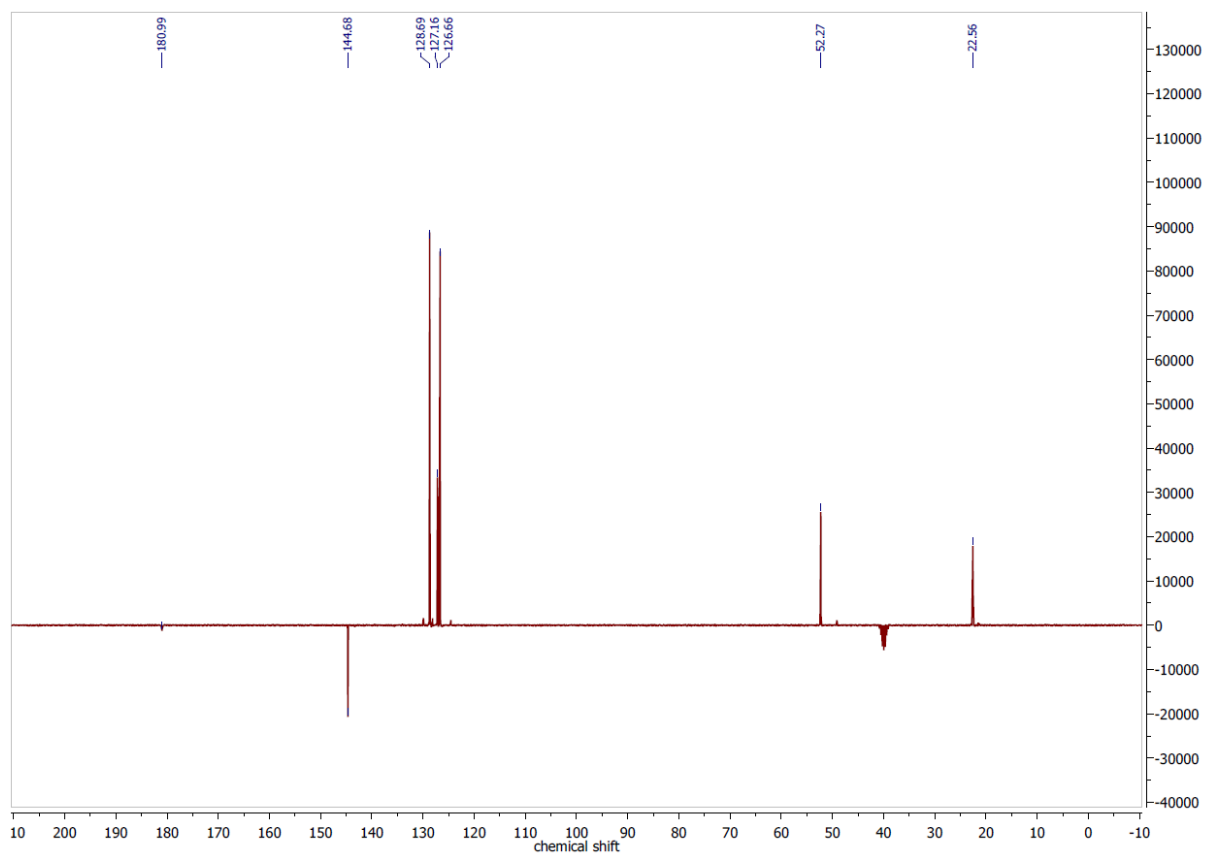


Figure 7.9 ^{13}C APT NMR spectrum of TSCmB in $\text{DMSO-}d_6$ at 75 MHz.

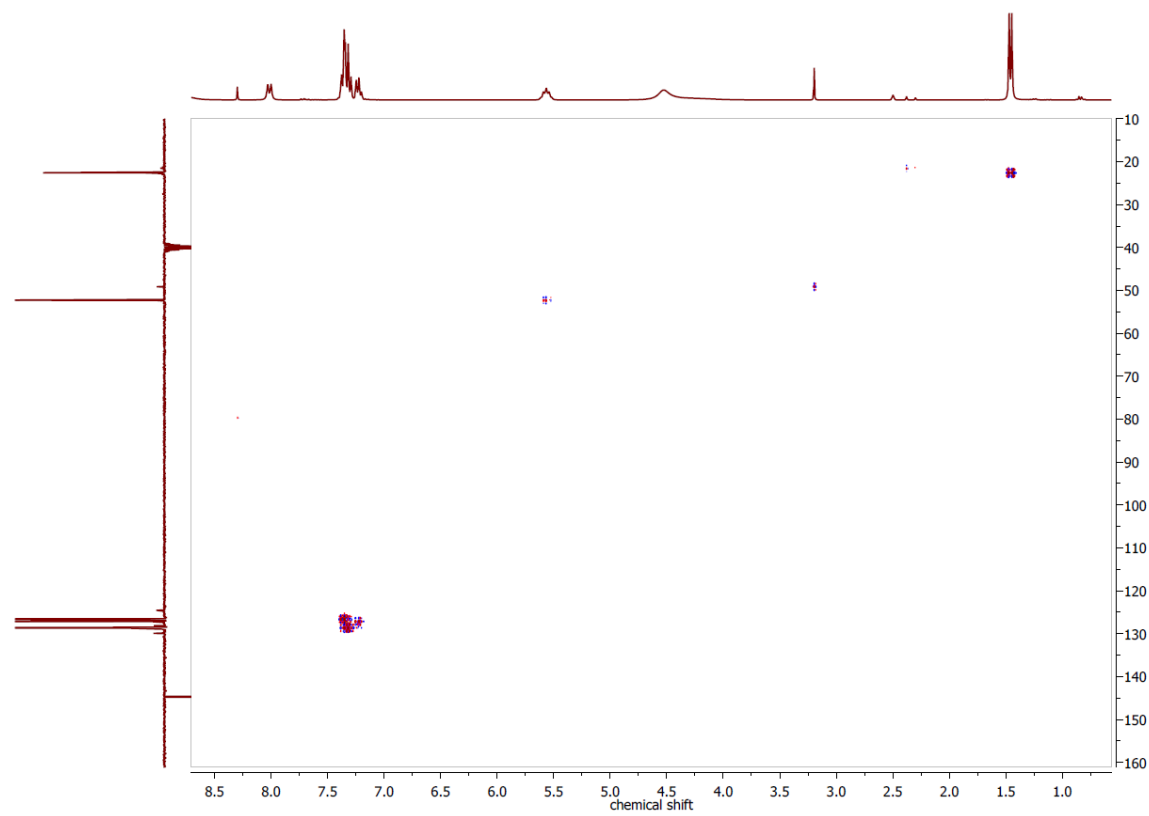


Figure 7.10 ^1H , ^{13}C HSQC NMR spectrum of TSCmB in $\text{DMSO-}d_6$.

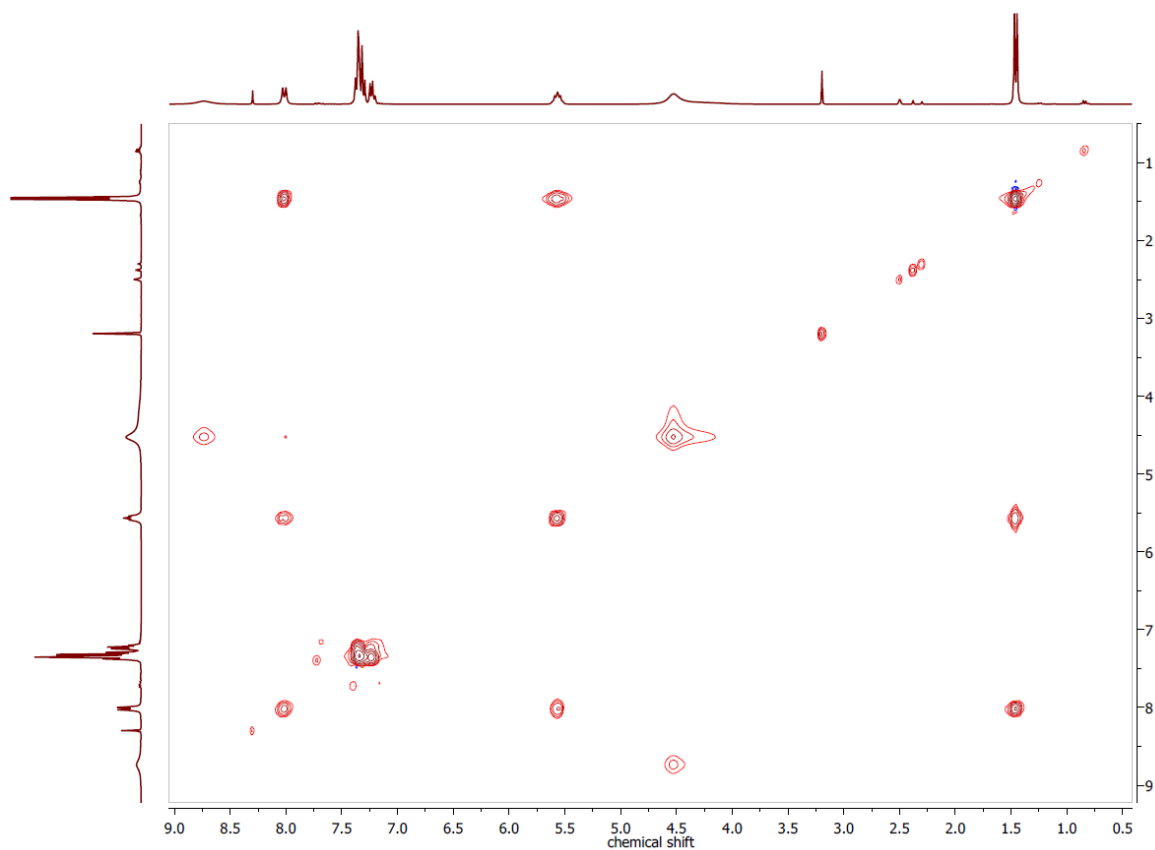


Figure 7.13 ^1H , ^1H TOCSY NMR spectrum of TSCmB in $\text{DMSO-}d_6$.

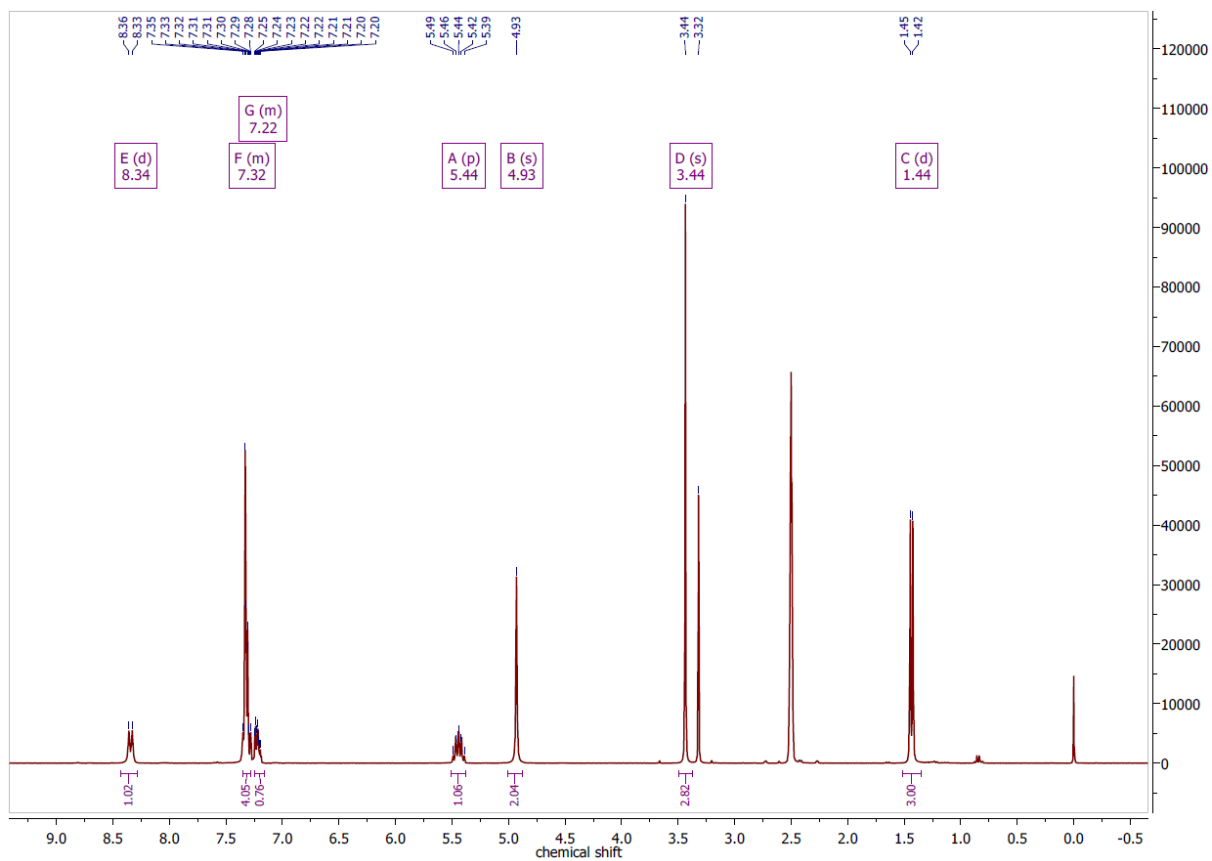


Figure 7.14 ^1H NMR spectrum of (m)TSCmB in $\text{DMSO-}d_6$ at 300 MHz.

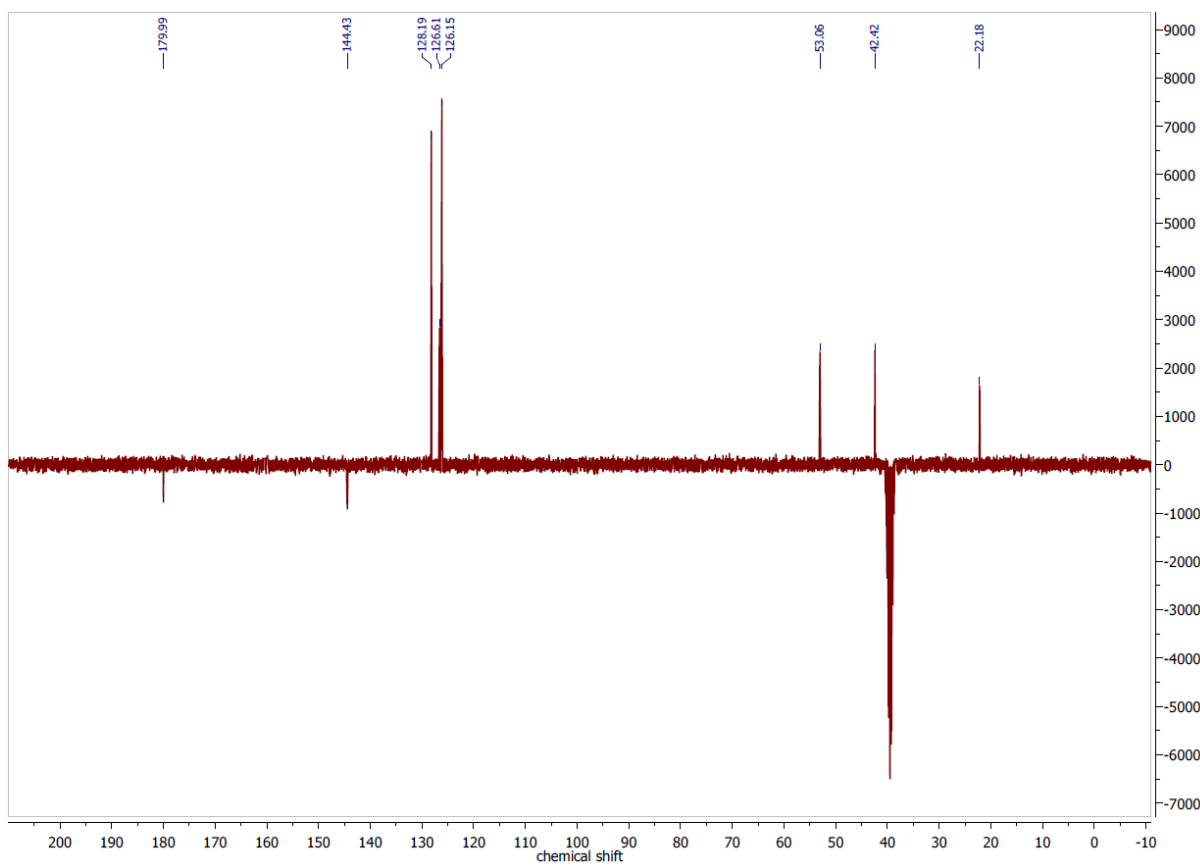


Figure 7.15 $^{13}\text{C}\{^1\text{H}\}$ DEPTQ NMR spectrum of (m)TSCmB in $\text{DMSO-}d_6$ at 75 MHz.

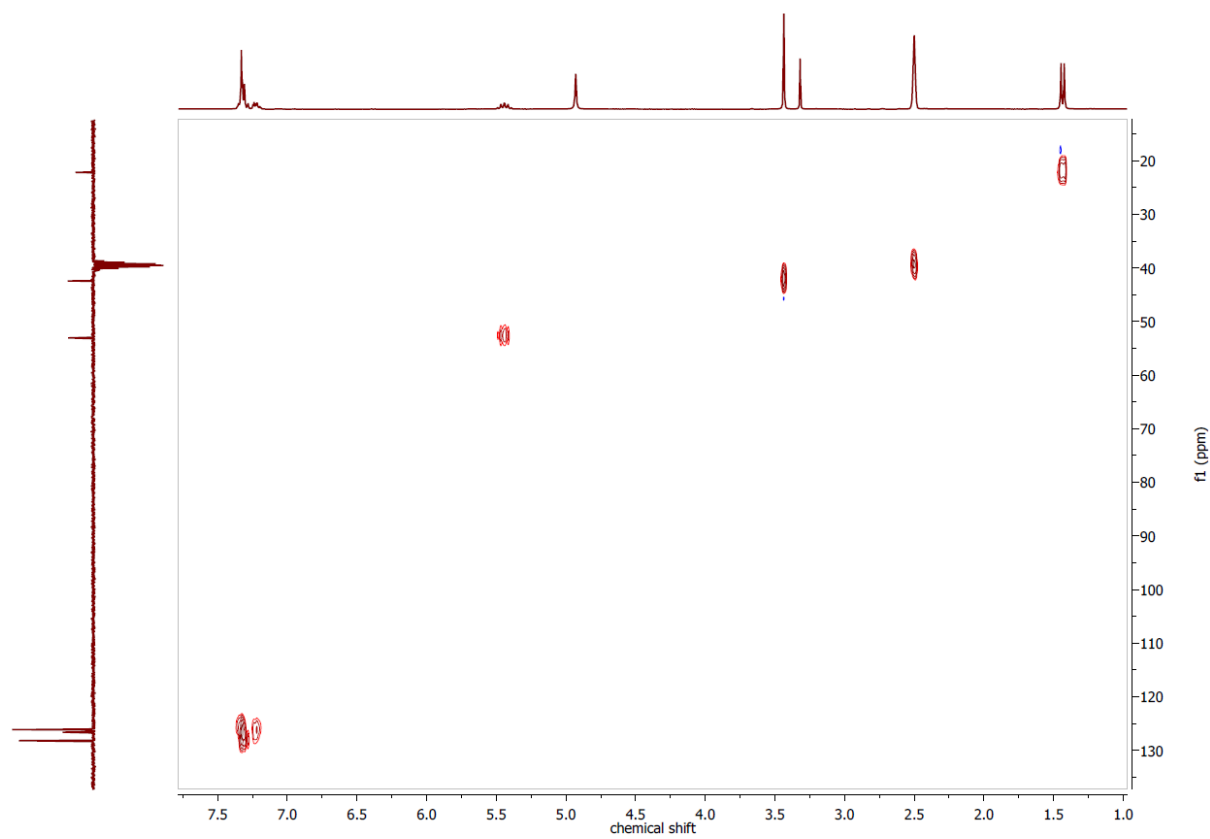


Figure 7.16 $^1\text{H}, ^{13}\text{C}$ HSQCed NMR spectrum of (m)TSCmB in $\text{DMSO-}d_6$.

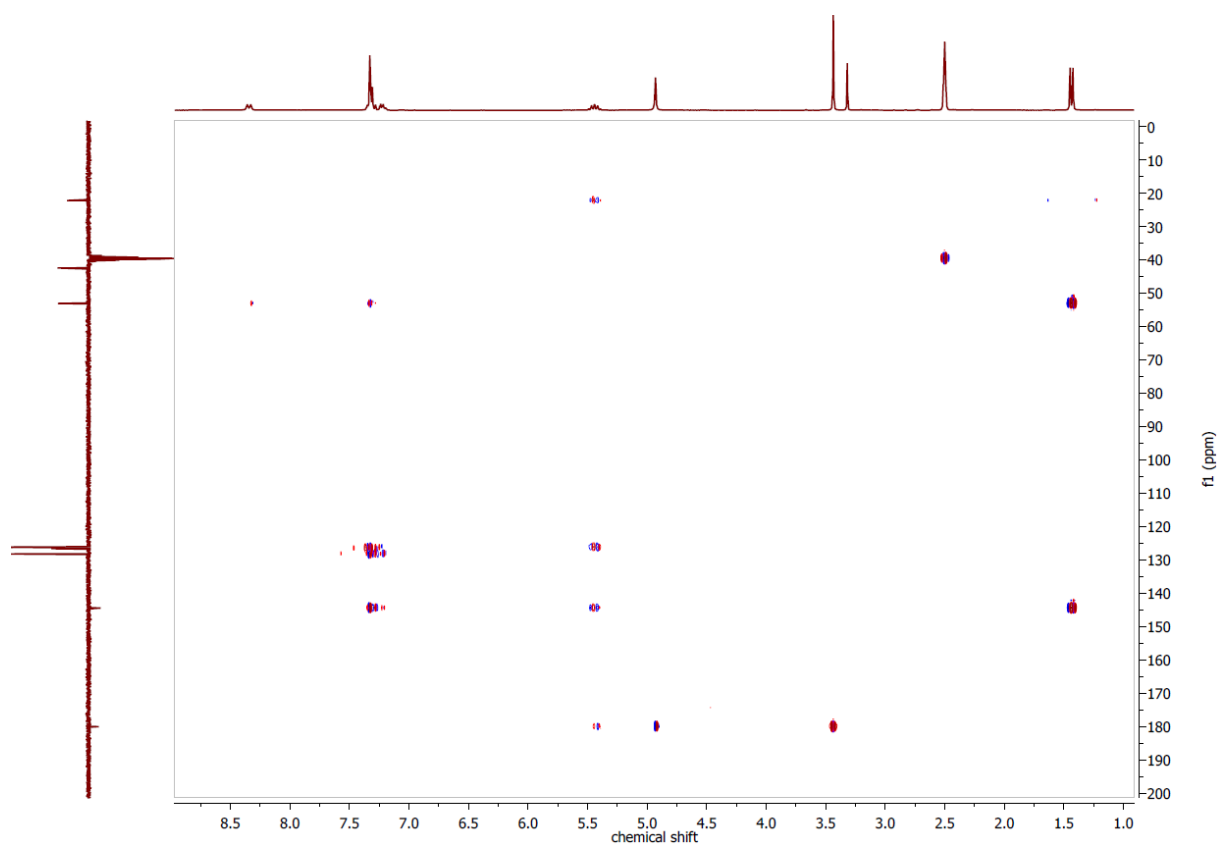


Figure 7.17 ^1H , ^{13}C HMBC NMR spectrum of (m)TSCmB in DMSO- d_6 .

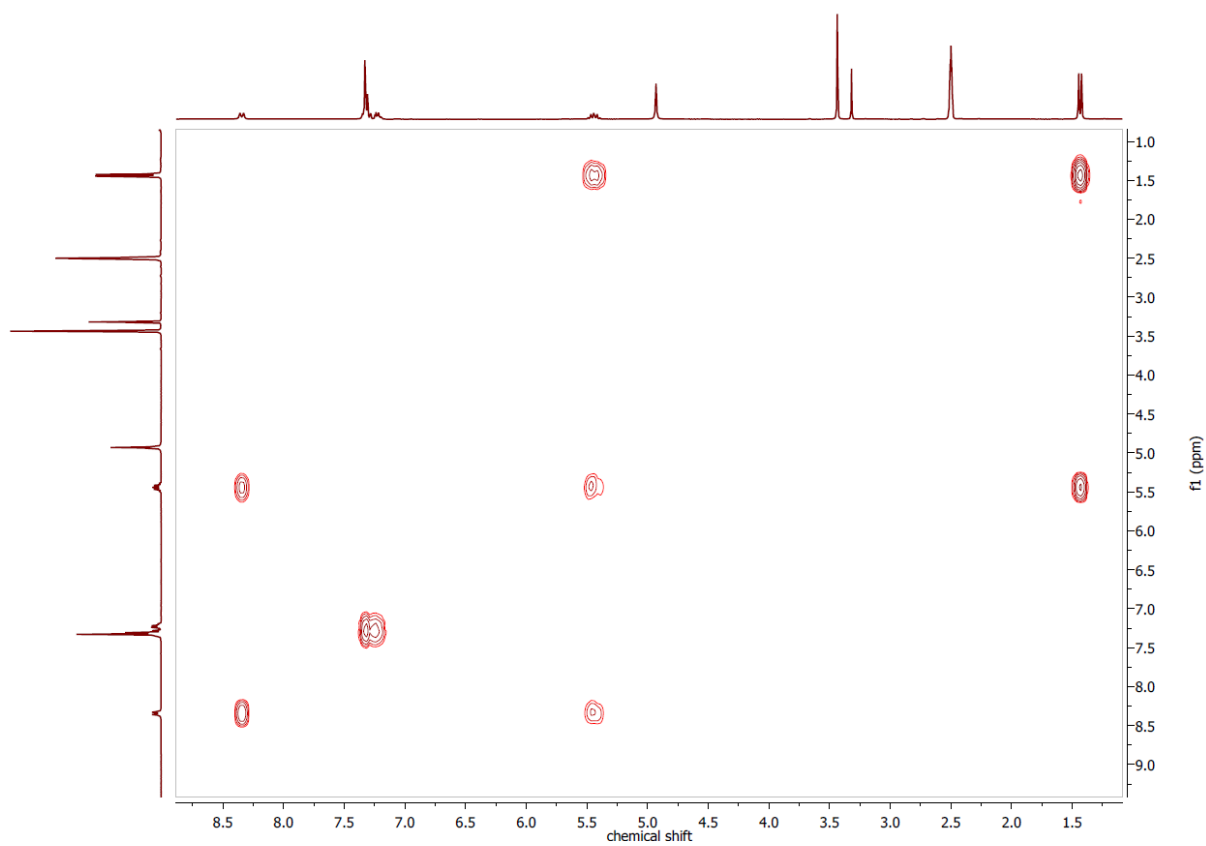


Figure 7.18 ^1H , ^1H COSY NMR spectrum of (m)TSCmB in DMSO- d_6 .

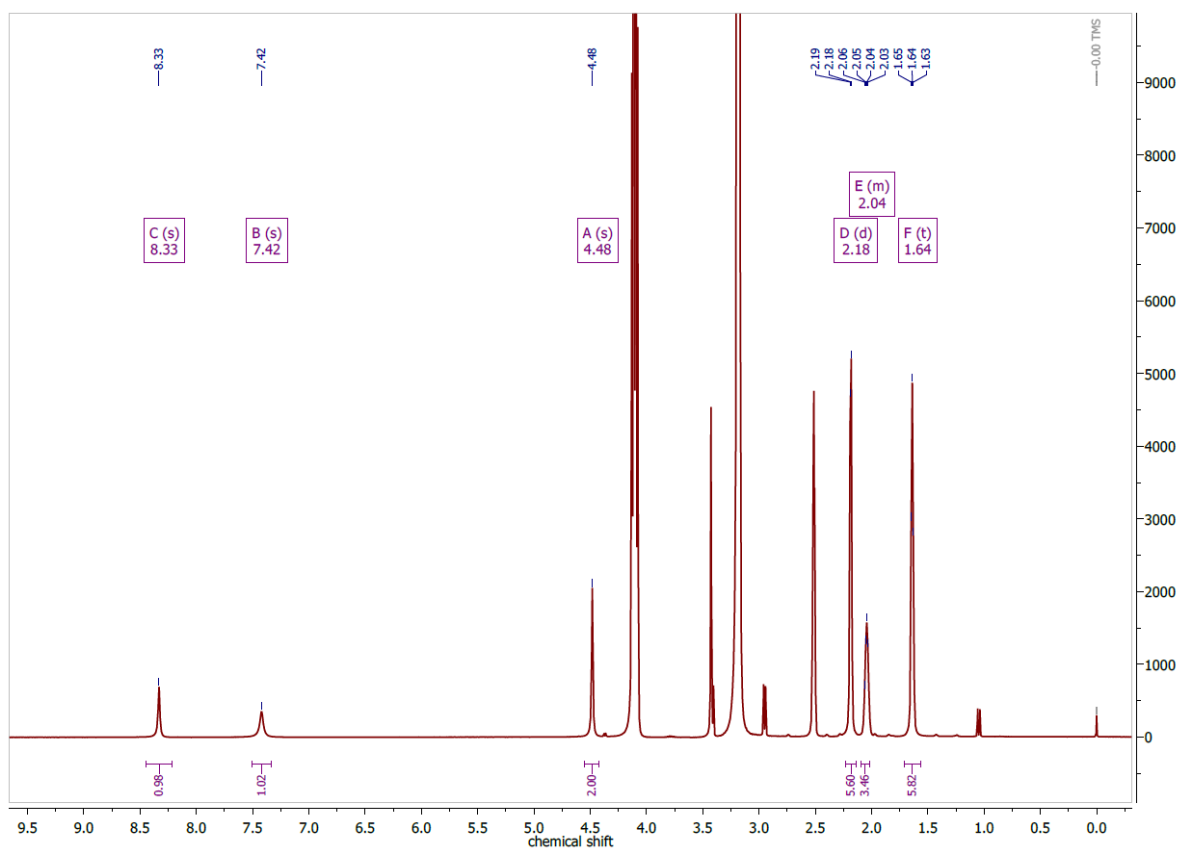


Figure 7.19 ^1H NMR spectrum of TSCAd in $\text{DMSO-}d_6$ at 300 MHz.

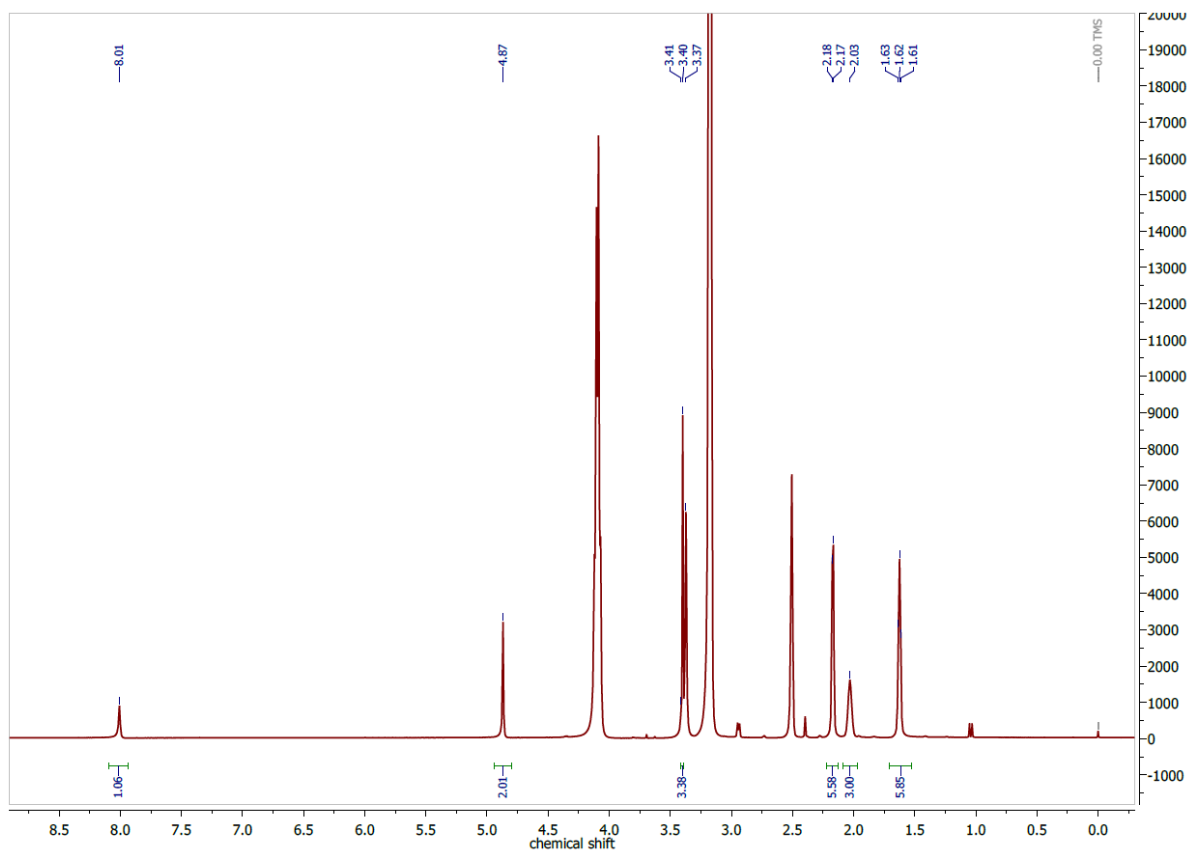


Figure 7.20 ^1H NMR spectrum of (m)TSCAd in $\text{DMSO-}d_6$ at 300 MHz.

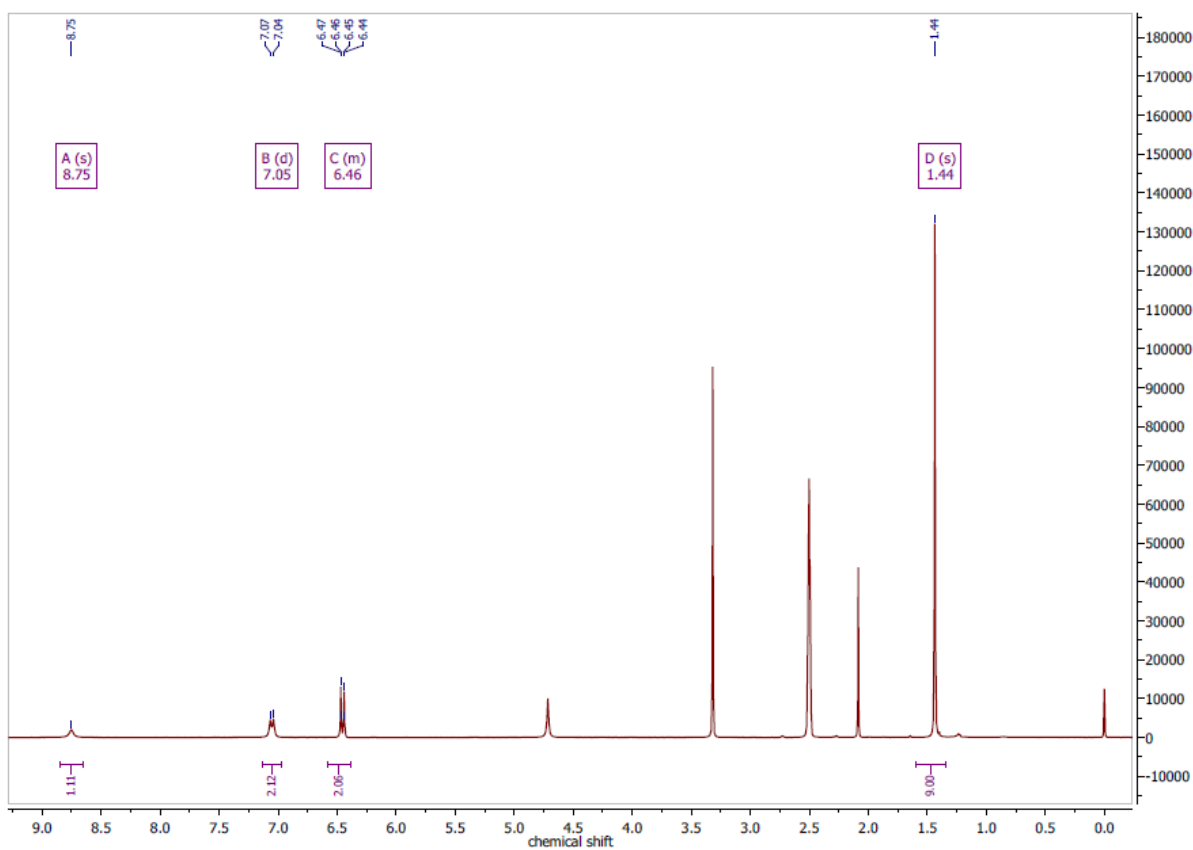


Figure 7.21 ^1H NMR spectrum of *p*-(bocamino) aniline in $\text{DMSO-}d_6$ at 300 MHz.

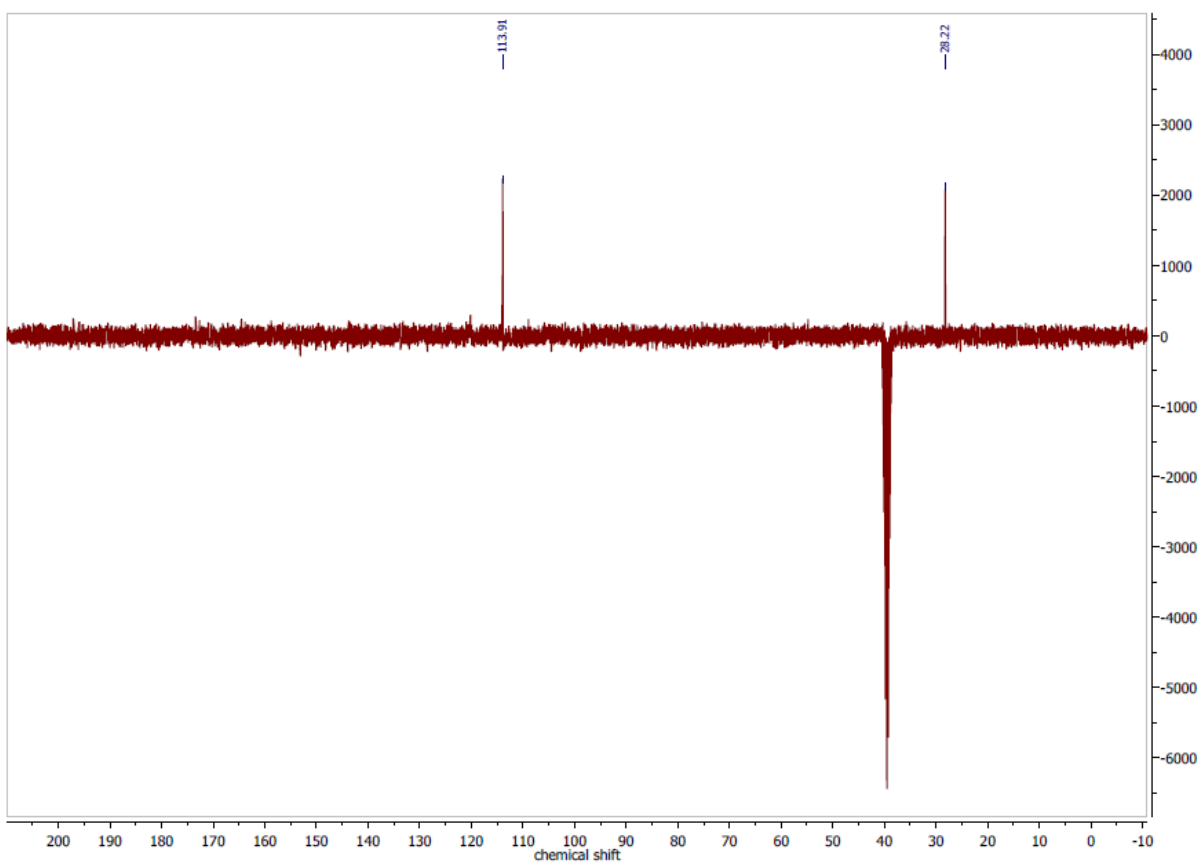


Figure 7.22 $^{13}\text{C}\{^1\text{H}\}$ DEPTQ NMR spectrum of *p*-(bocamino) aniline in $\text{DMSO-}d_6$ at 75 MHz.

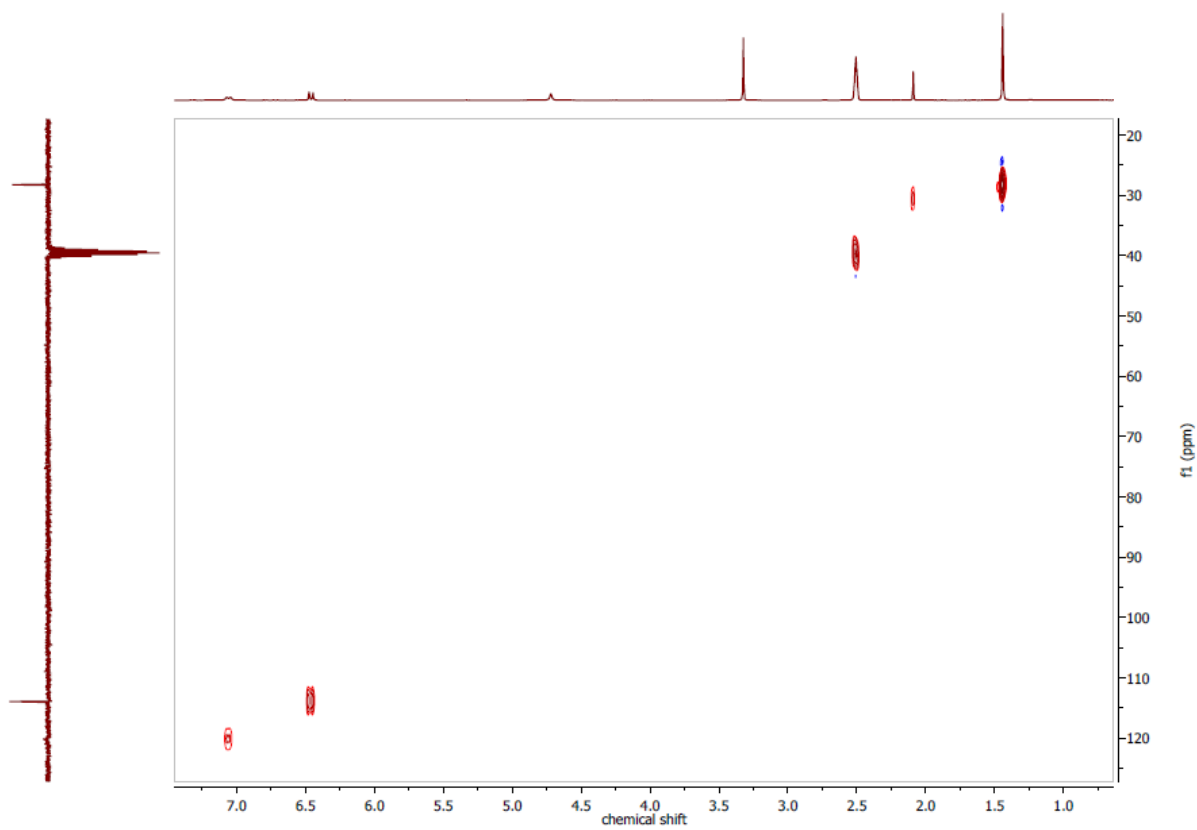


Figure 7.23 ^1H , ^{13}C HSQC NMR spectrum of *p*-(bocamino) aniline in $\text{DMSO-}d_6$.

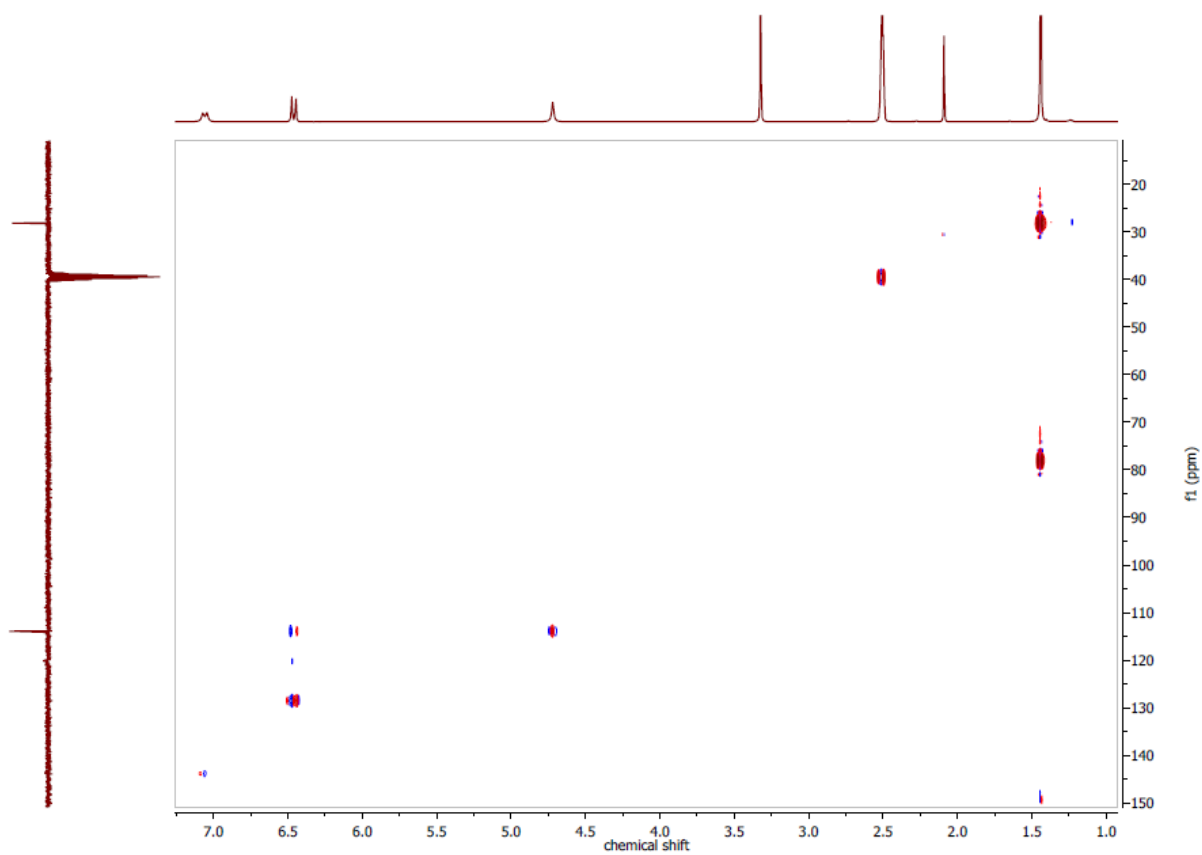


Figure 7.24 ^1H , ^{13}C HMBC NMR spectrum of *p*-(bocamino) aniline in $\text{DMSO-}d_6$.

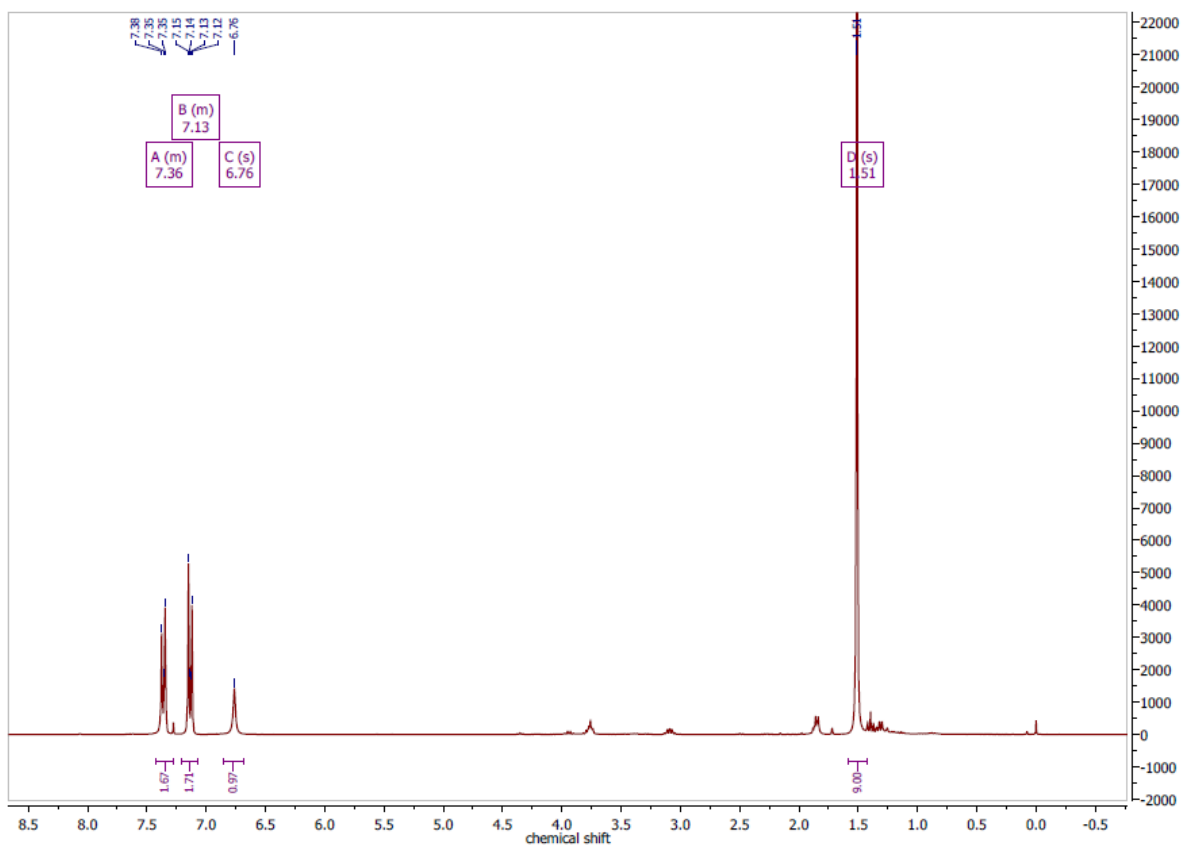


Figure 7.25 ^1H NMR spectrum of tert-butyl (4-isothiocyanatophenyl)carbamate in $\text{DMSO-}d_6$ at 300 MHz.

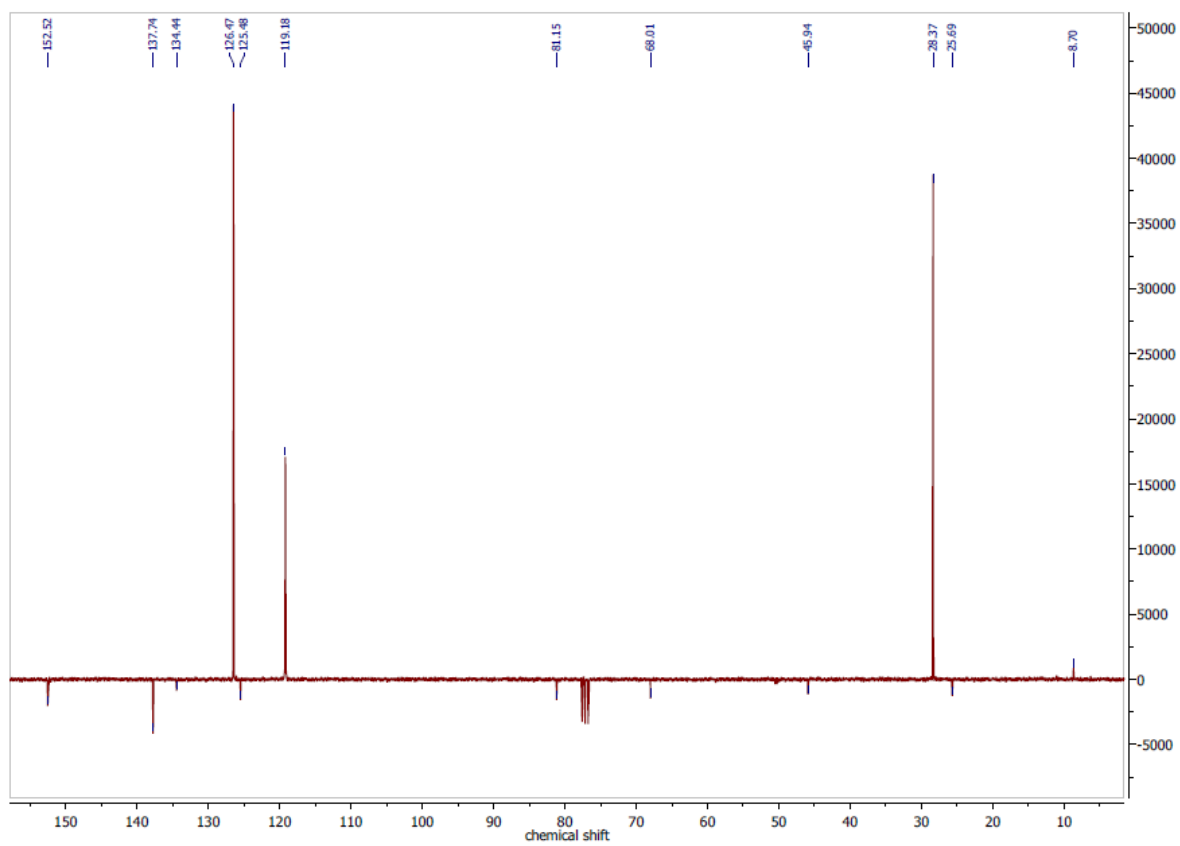


Figure 7.26 $^{13}\text{C}\{^1\text{H}\}$ DEPTQ NMR spectrum of tert-butyl (4-isothiocyanatophenyl)carbamate in $\text{DMSO-}d_6$ at 300 MHz.

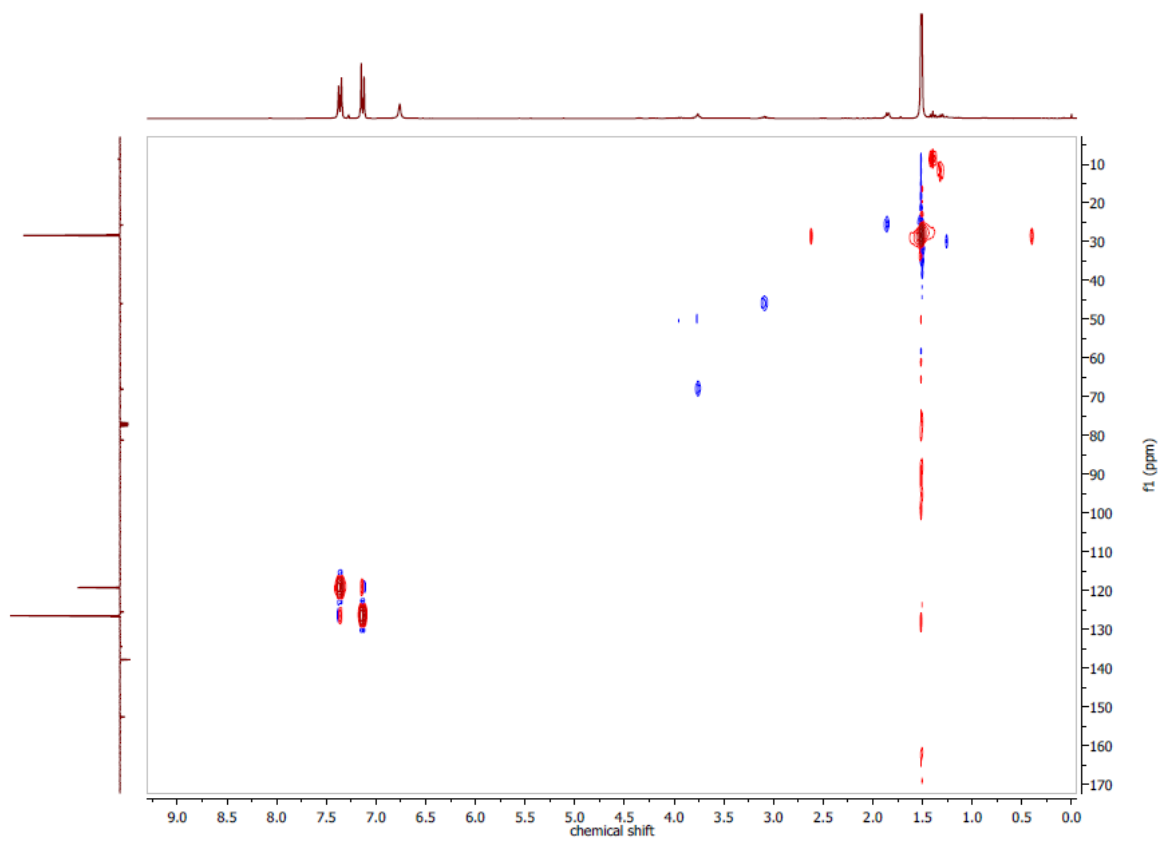


Figure 7.27 ^1H , ^{13}C HSQC NMR spectrum of tert-butyl (4-isothiocyanatophenyl)carbamate in $\text{DMSO-}d_6$.

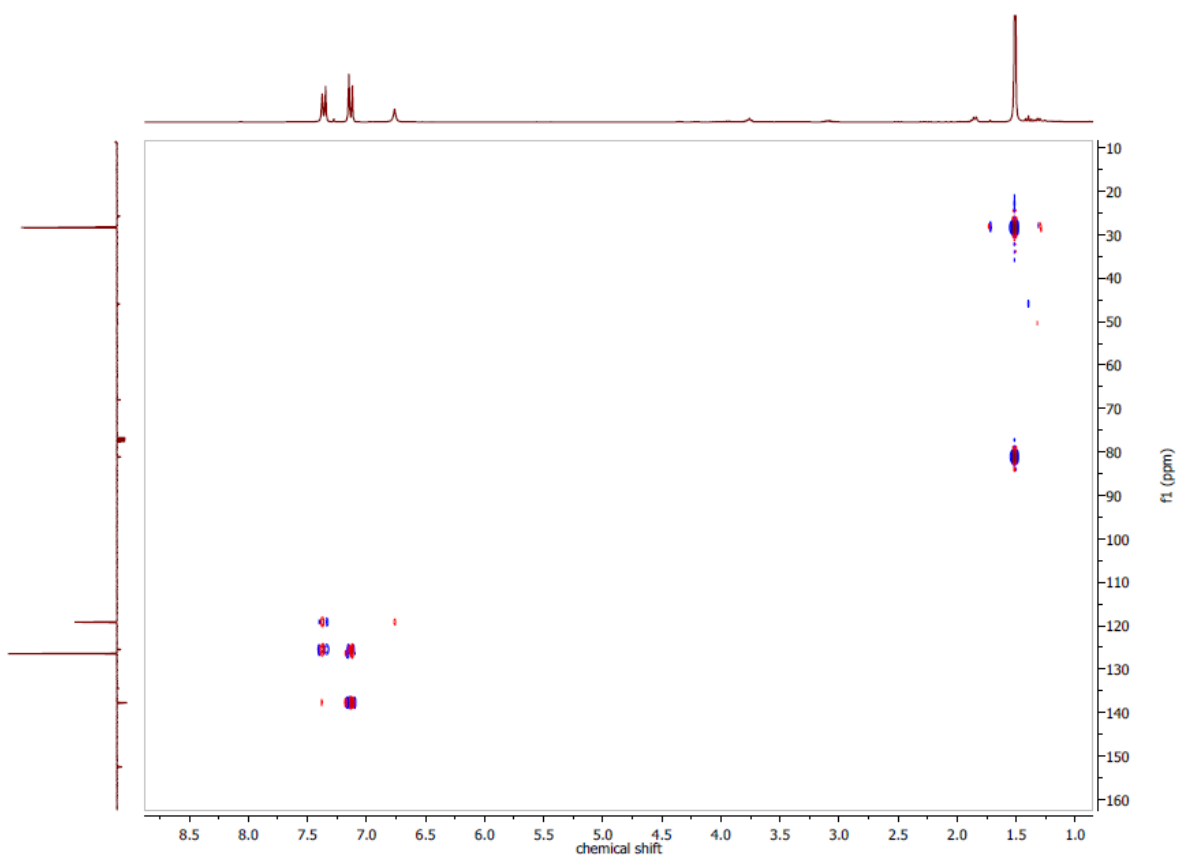


Figure 7.28 ^1H , ^{13}C HMBC NMR spectrum of tert-butyl (4-isothiocyanatophenyl)carbamate in $\text{DMSO-}d_6$.

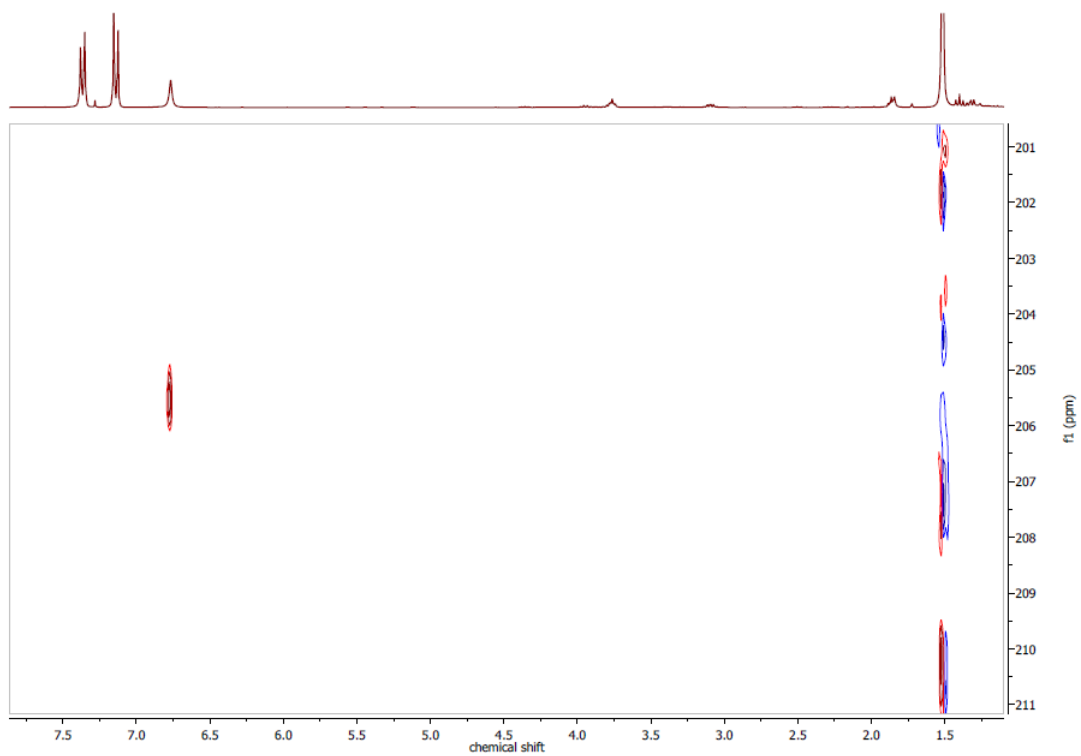


Figure 7.29 ^1H , ^{15}N HMBC NMR spectrum of tert-butyl (4-isothiocyanatophenyl)carbamate in $\text{DMSO-}d_6$.

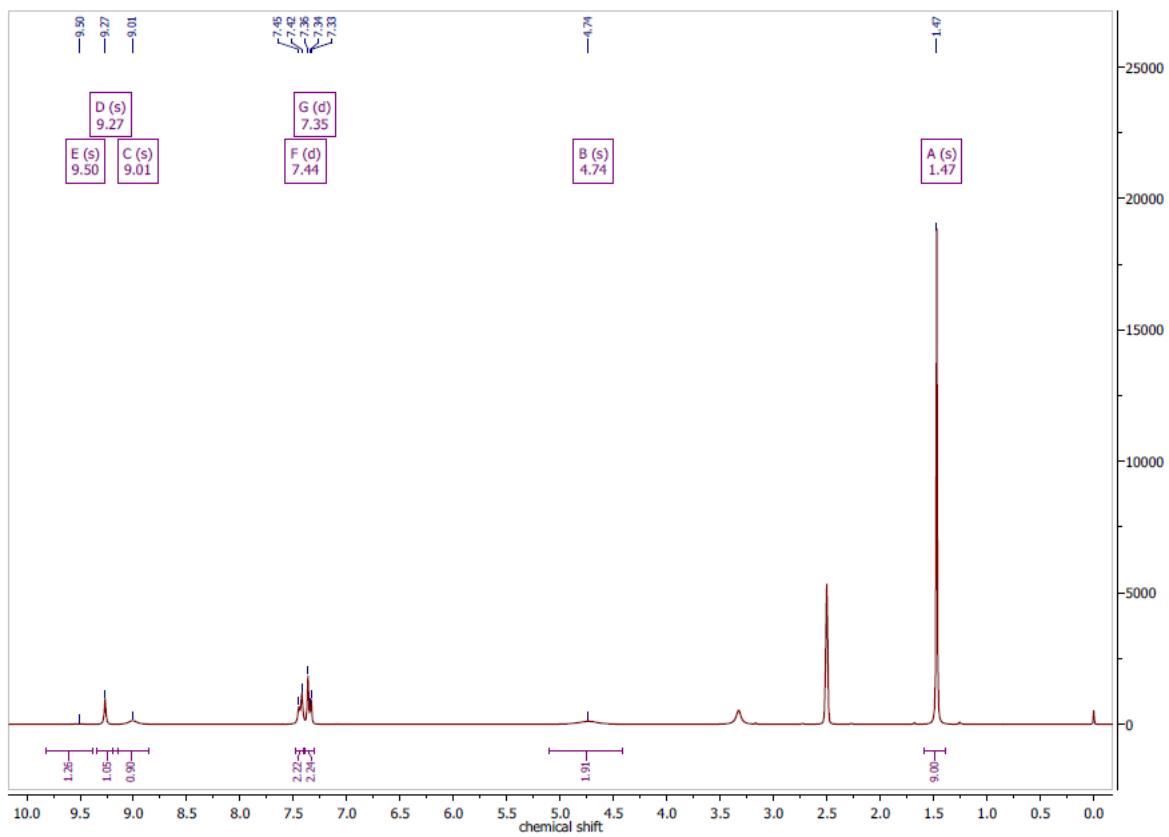


Figure 7.30 ^1H NMR spectrum of TSCpBa in $\text{DMSO-}d_6$ at 300 MHz.

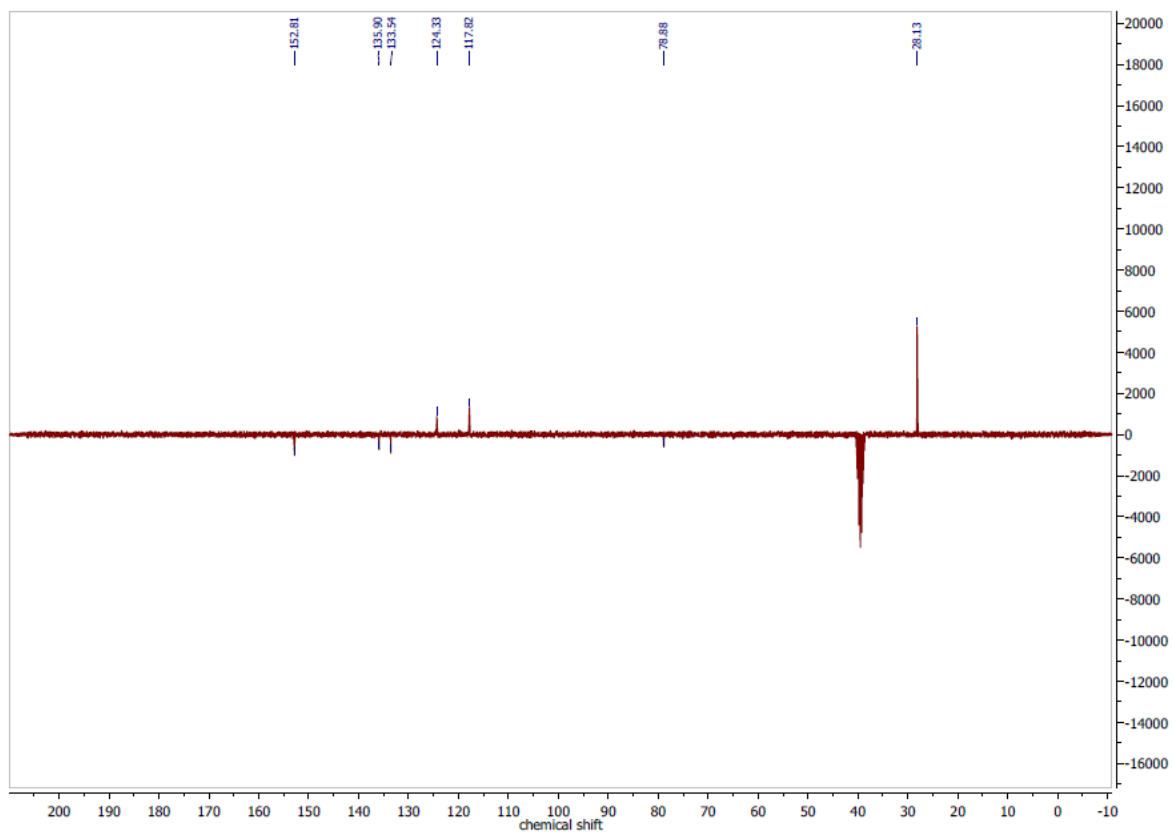


Figure 7.31 $^{13}\text{C}\{^1\text{H}\}$ DEPTQ NMR spectrum of TSCpBa in $\text{DMSO-}d_6$ at 75 MHz.

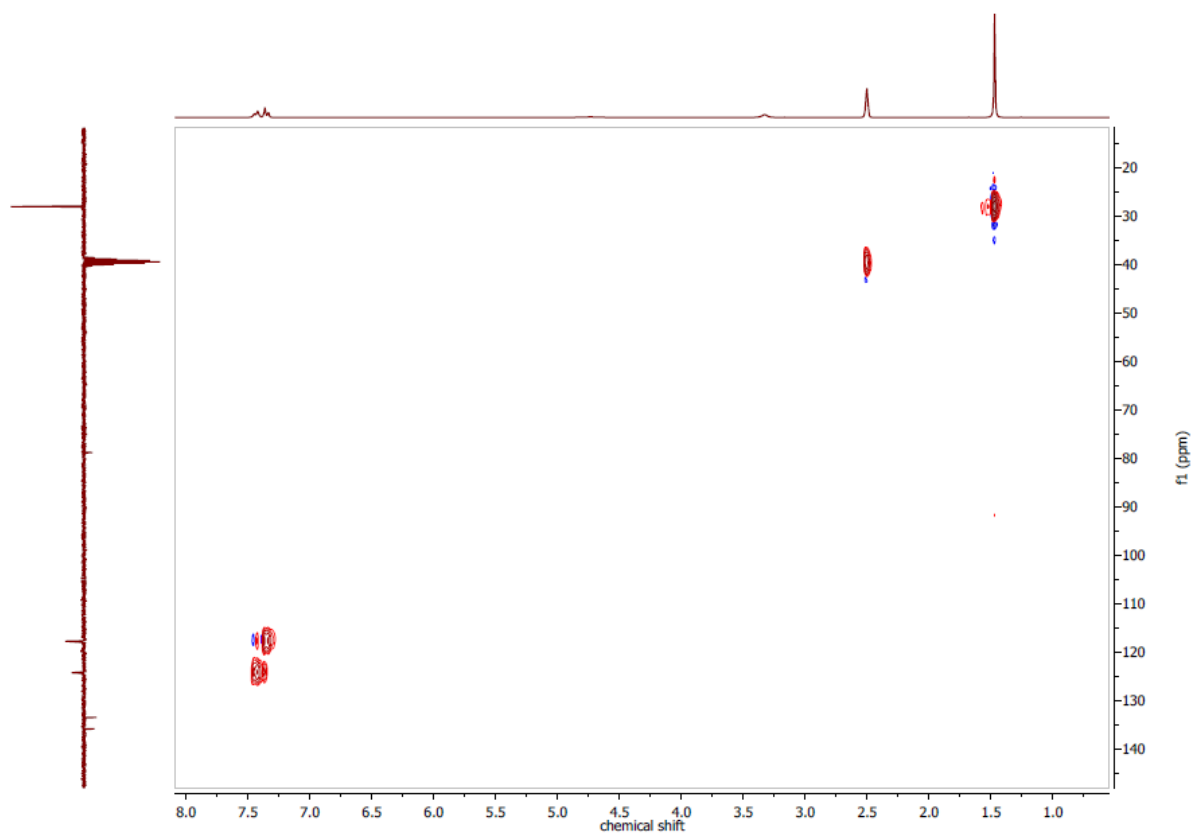


Figure 7.32 $^1\text{H}, ^{13}\text{C}$ HSQCed NMR spectrum of TSCpBa in $\text{DMSO-}d_6$.

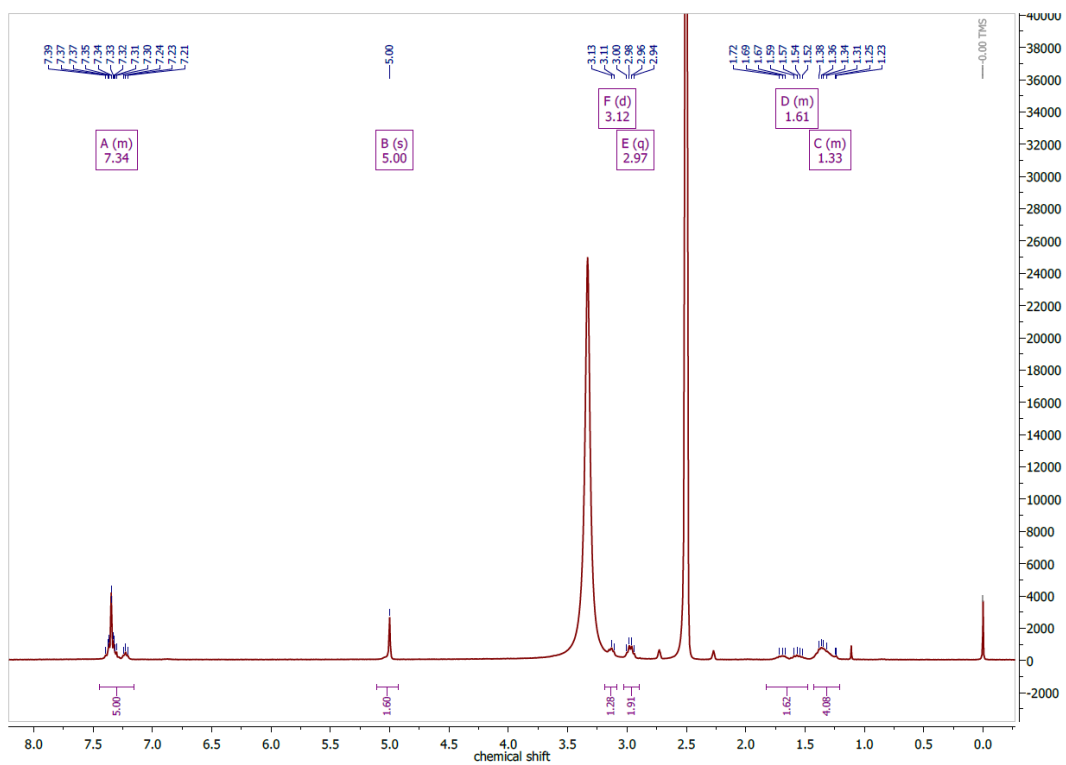


Figure 7.33 ^1H NMR spectrum of H-Lys(Cbz)-OH in DMSO- d_6 at 300 MHz.

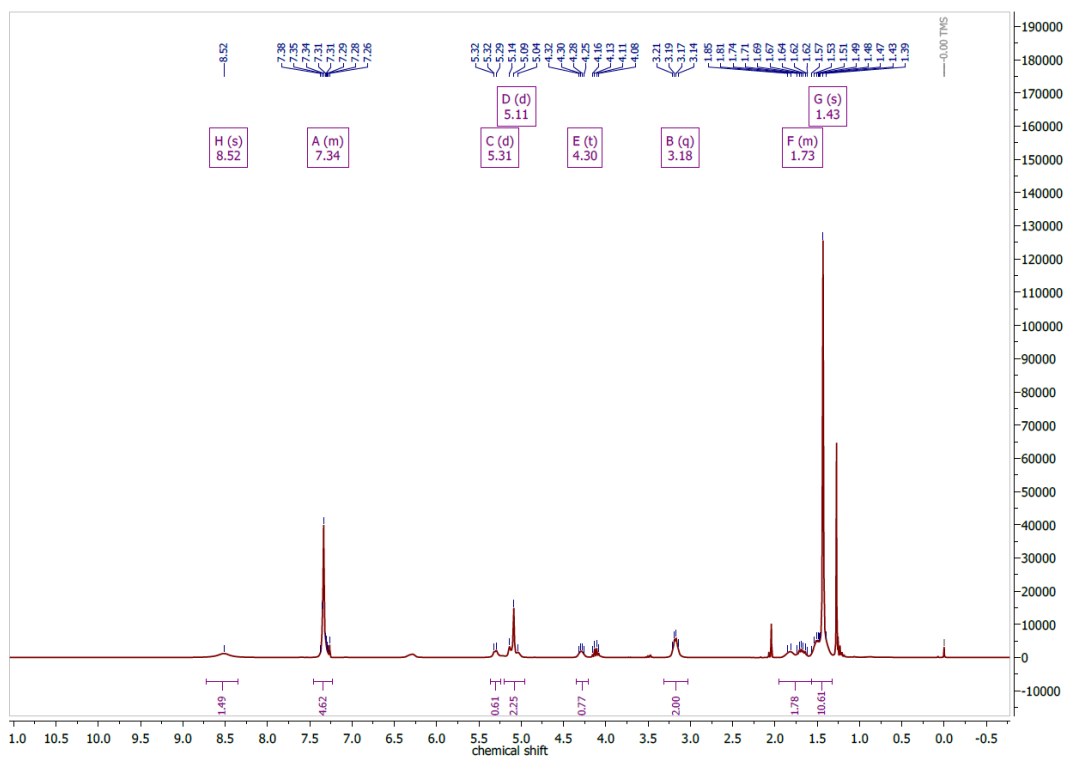


Fig. 7.34 ^1H NMR spectrum of Boc-Lys(Cbz)-OH in CDCl_3 at 300 MHz.

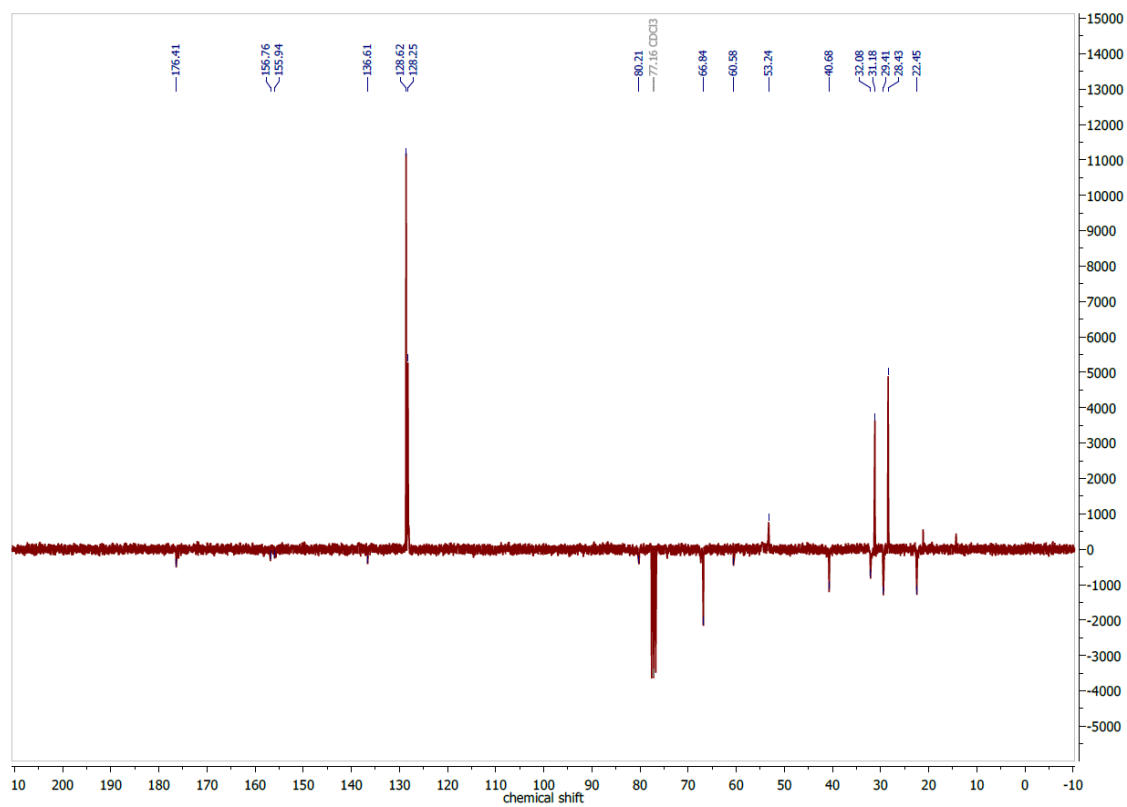


Figure 7.35 $^{13}\text{C}\{^1\text{H}\}$ DEPTQ NMR spectrum of Boc-Lys(Cbz)-OH in CDCl_3 at 75 MHz.

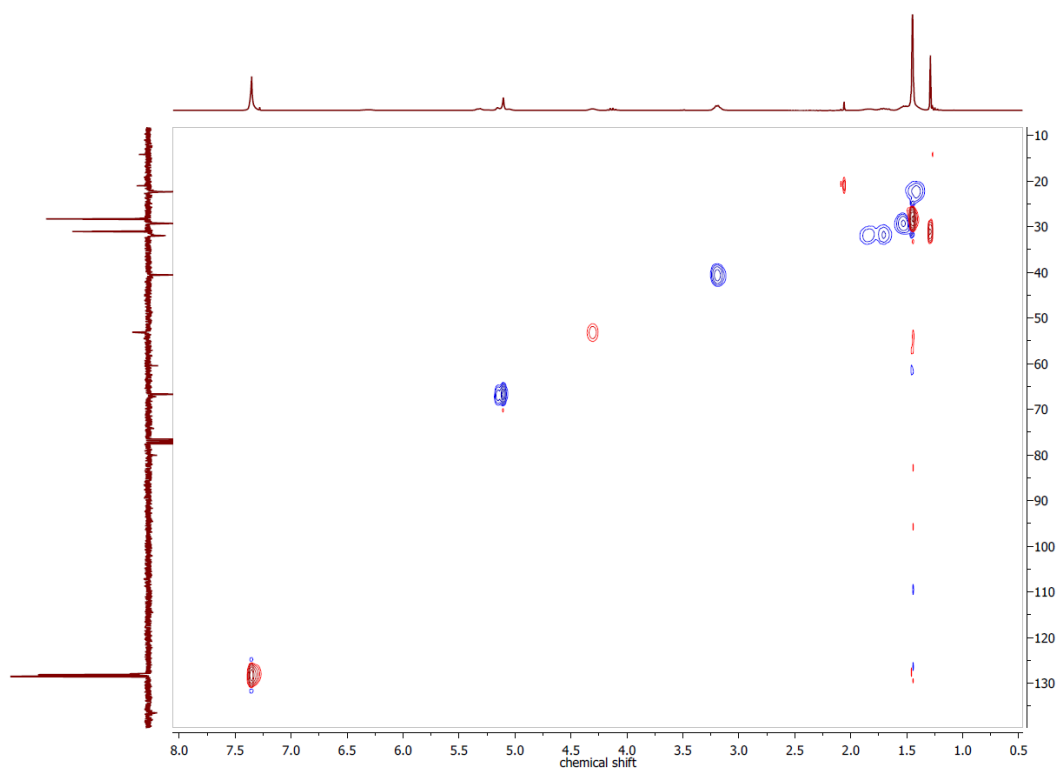


Figure 7.36 $^1\text{H},^{13}\text{C}$ HSQC NMR spectrum of Boc-Lys(Cbz)-OH in CDCl_3 .

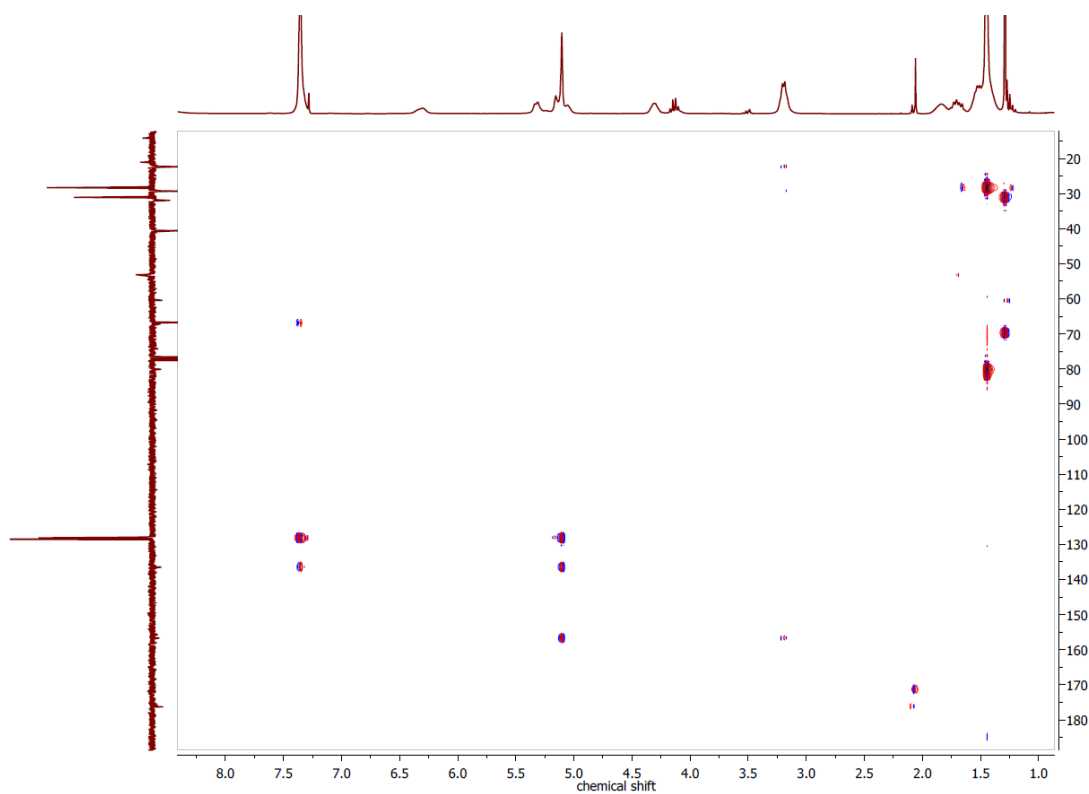


Figure 7.37 ^1H , ^{13}C HMBC NMR spectrum of Boc-Lys(Cbz)-OH in CDCl_3 .

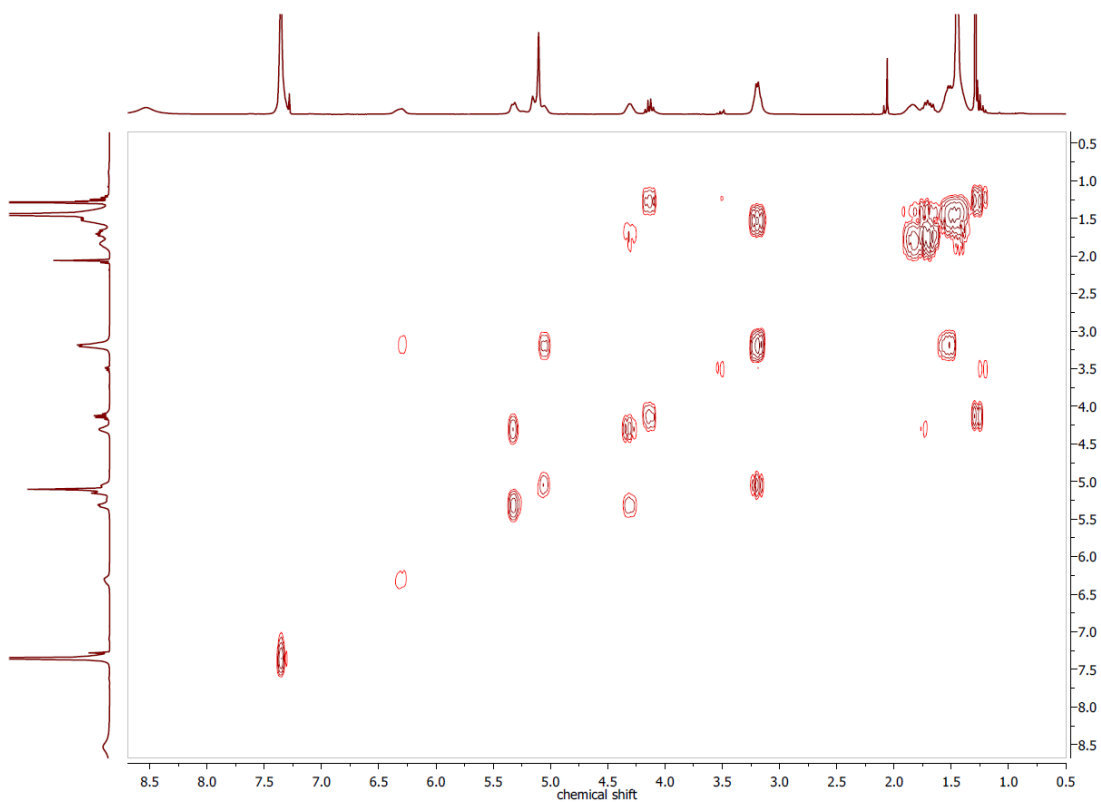


Figure 7.38 ^1H , ^1H COSY NMR spectrum of Boc-Lys(Cbz)-OH in CDCl_3 .

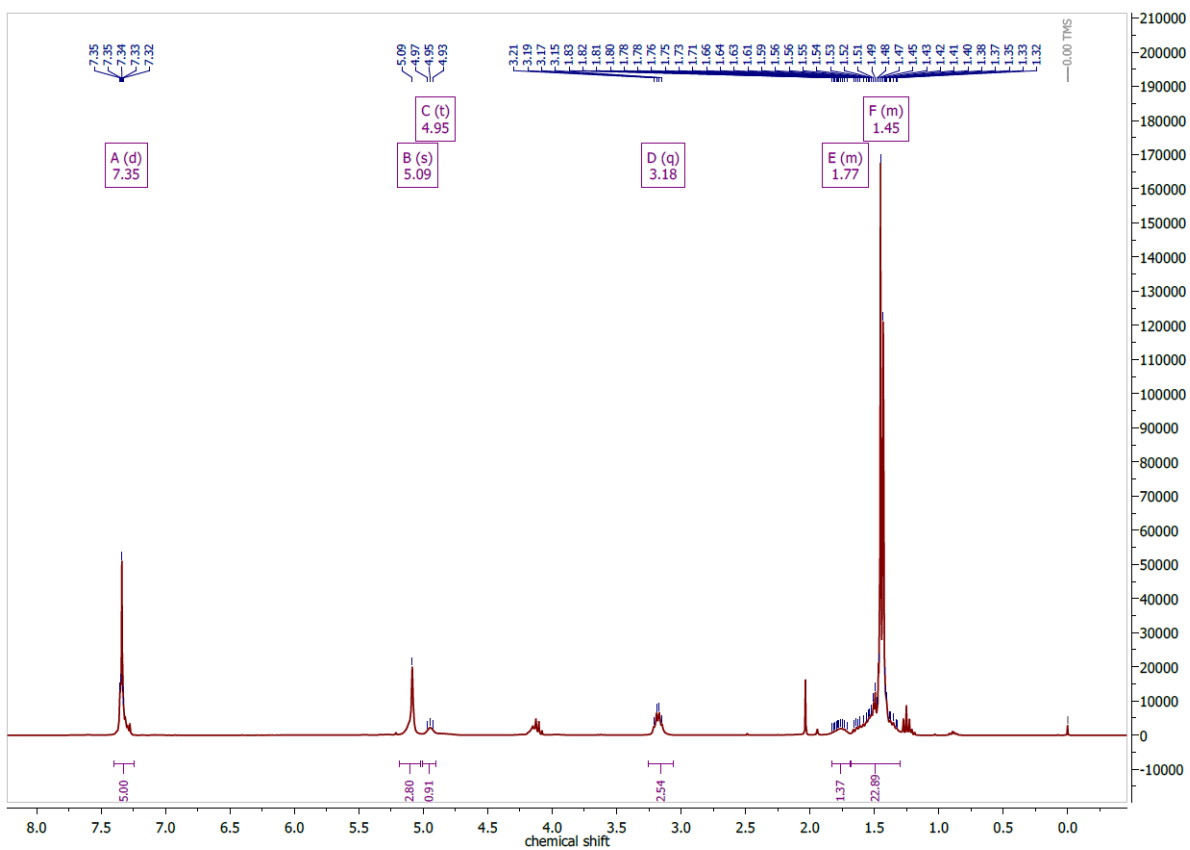


Figure 7.39 ^1H NMR spectrum of Boc-Lys(Cbz)-OtBu in CDCl_3 at 300 MHz.

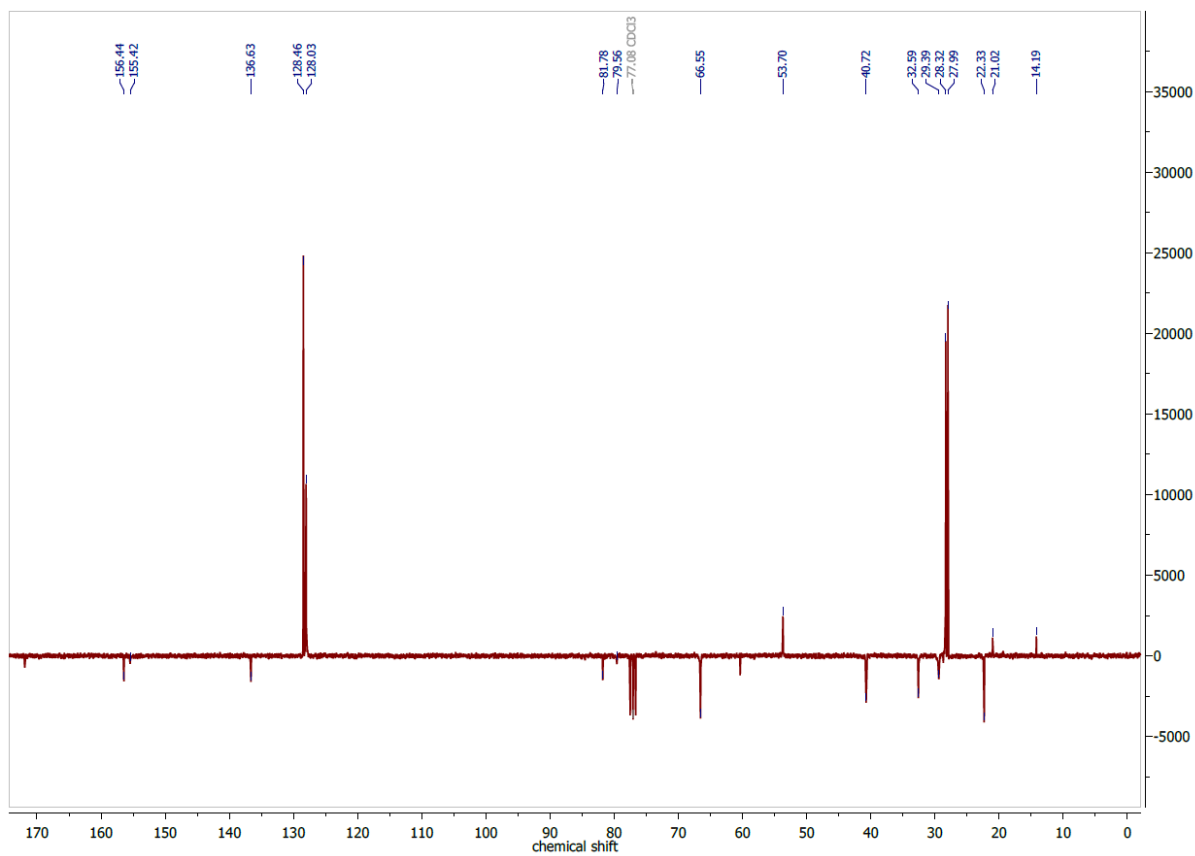


Figure 7.40 $^{13}\text{C}\{^1\text{H}\}$ DEPTQ NMR spectrum of Boc-Lys(Cbz)-OtBu in CDCl_3 at 75 MHz.

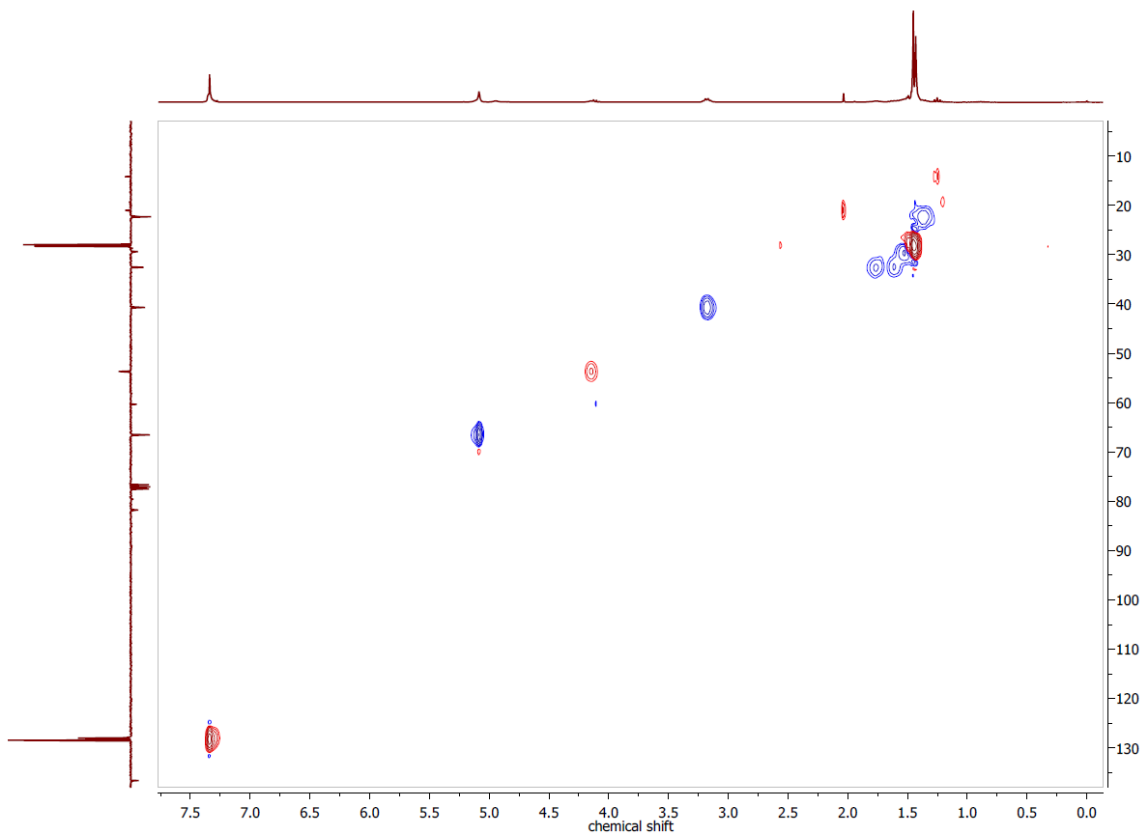


Figure 7.41 ^1H , ^{13}C HSQC NMR spectrum of Boc-Lys(Cbz)-OtBu lysine in CDCl_3 .

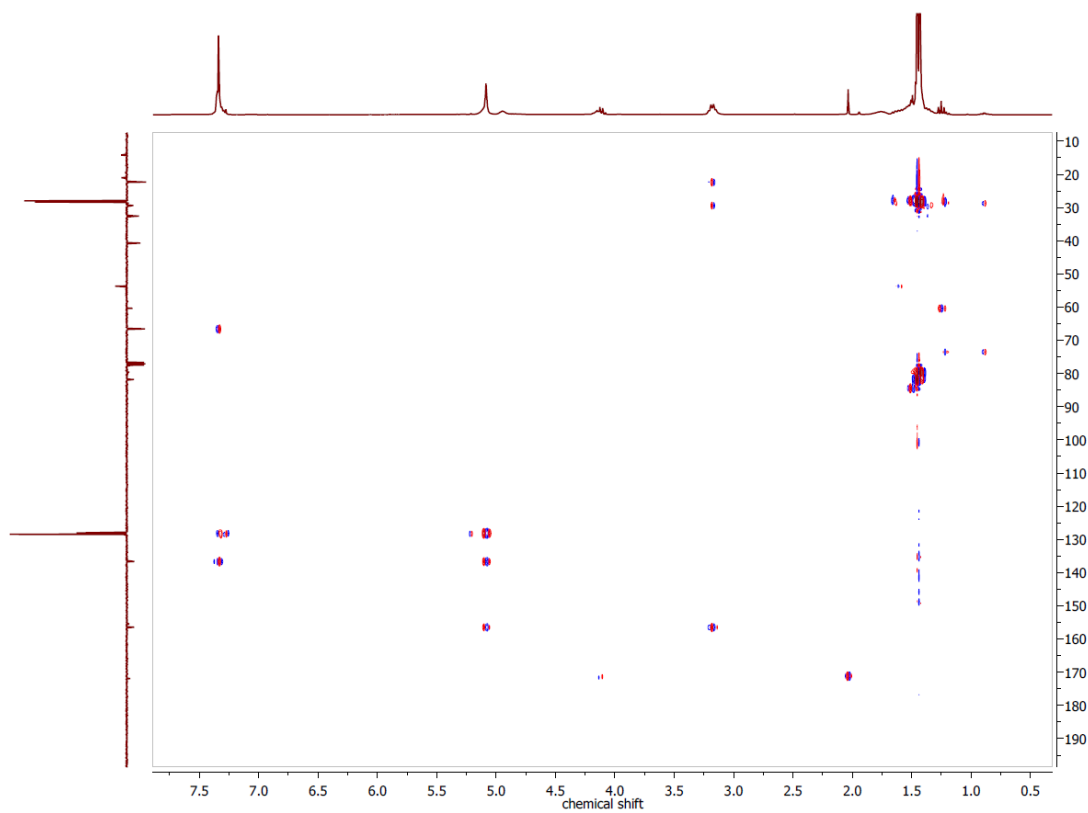


Figure 7.42 ^1H , ^{13}C HMBC NMR spectrum of Boc-Lys(Cbz)-OtBu in CDCl_3 .

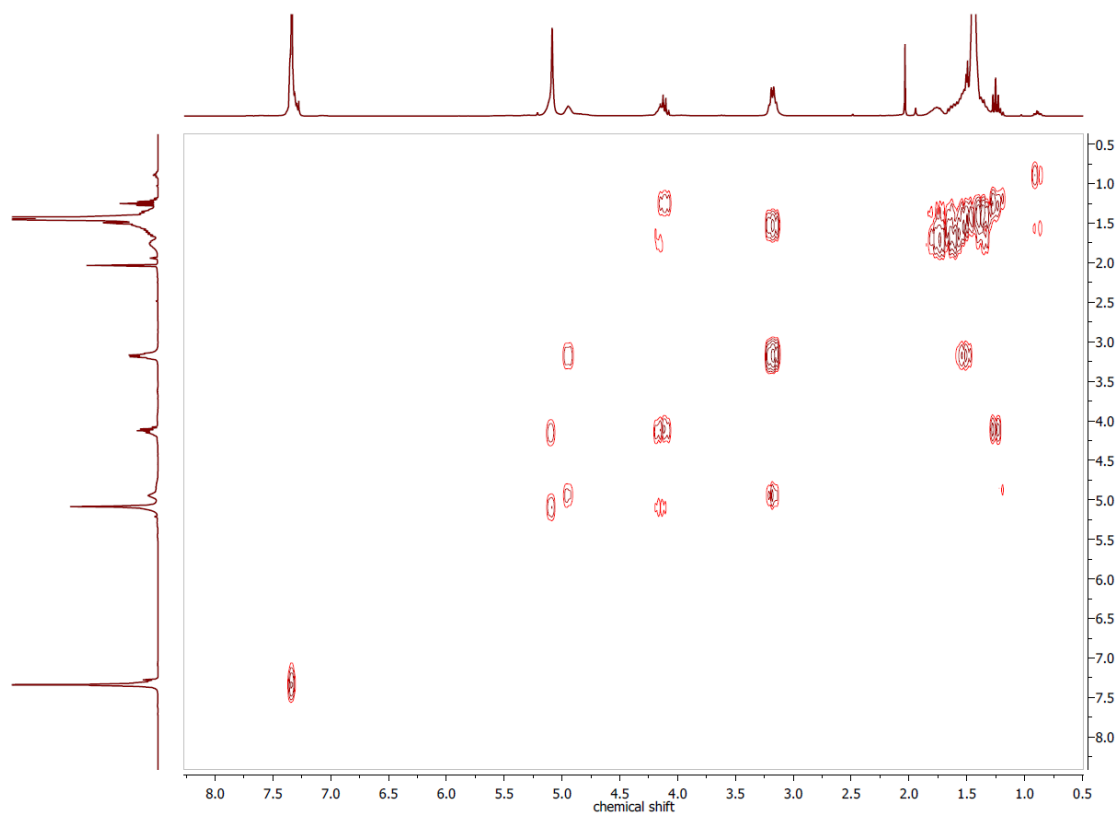


Figure 7.43 $^1\text{H},^1\text{H}$ COSY NMR spectrum of Boc-Lys(Cbz)-OtBu in CDCl_3 .

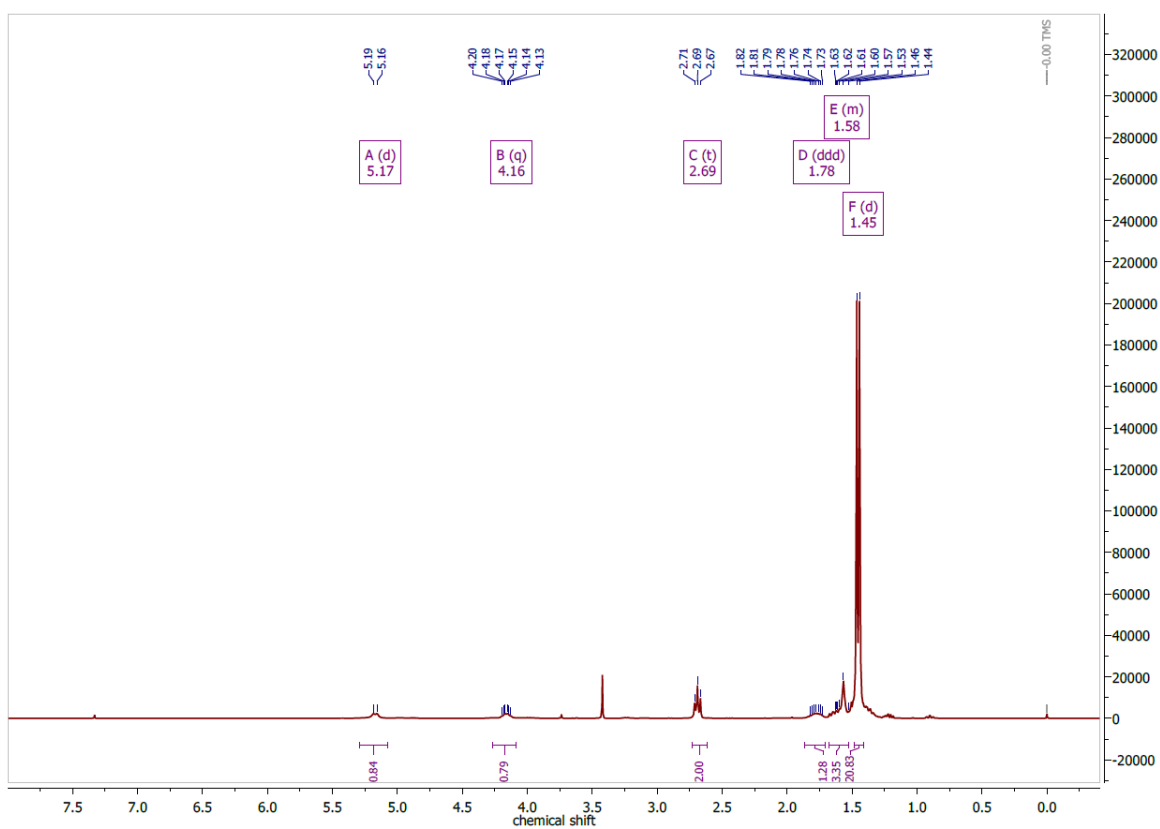


Figure 7.44 ^1H NMR spectrum of Boc-Lys-OtBu in CDCl_3 at 300 MHz.

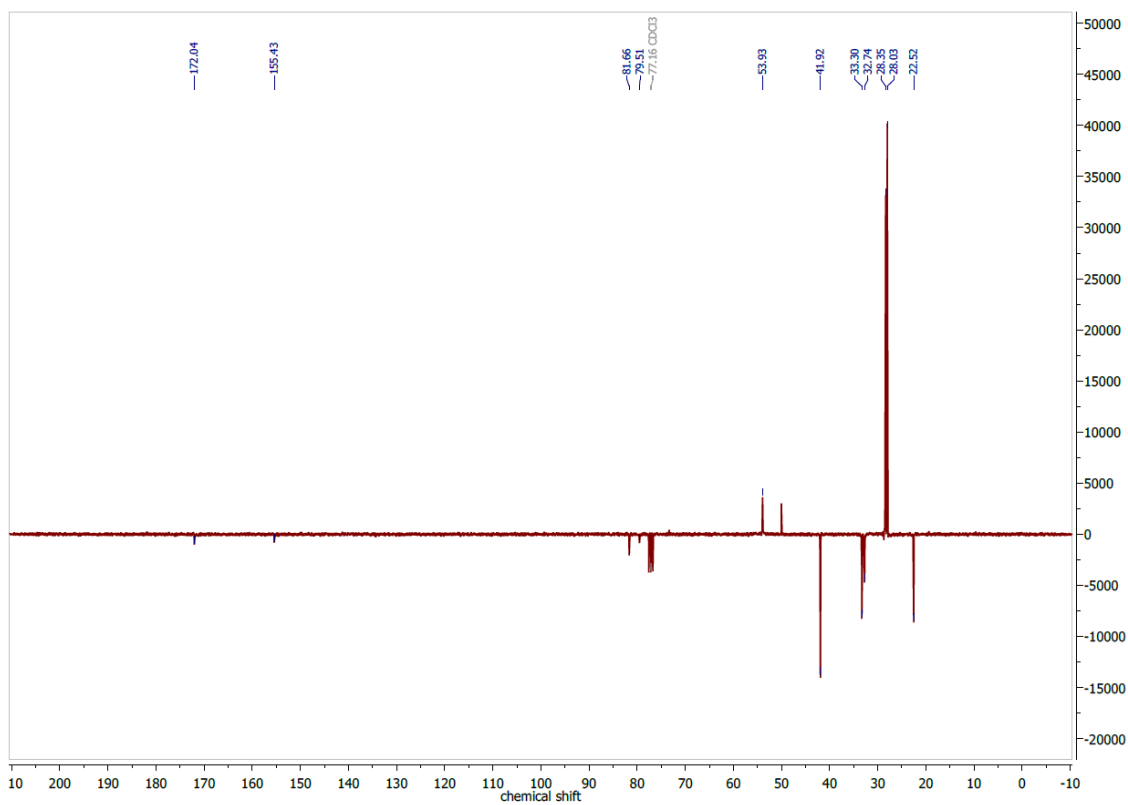


Figure 7.45 $^{13}\text{C}\{^1\text{H}\}$ DEPTQ NMR spectrum of Boc-Lys-OtBu in CDCl_3 at 75 MHz.

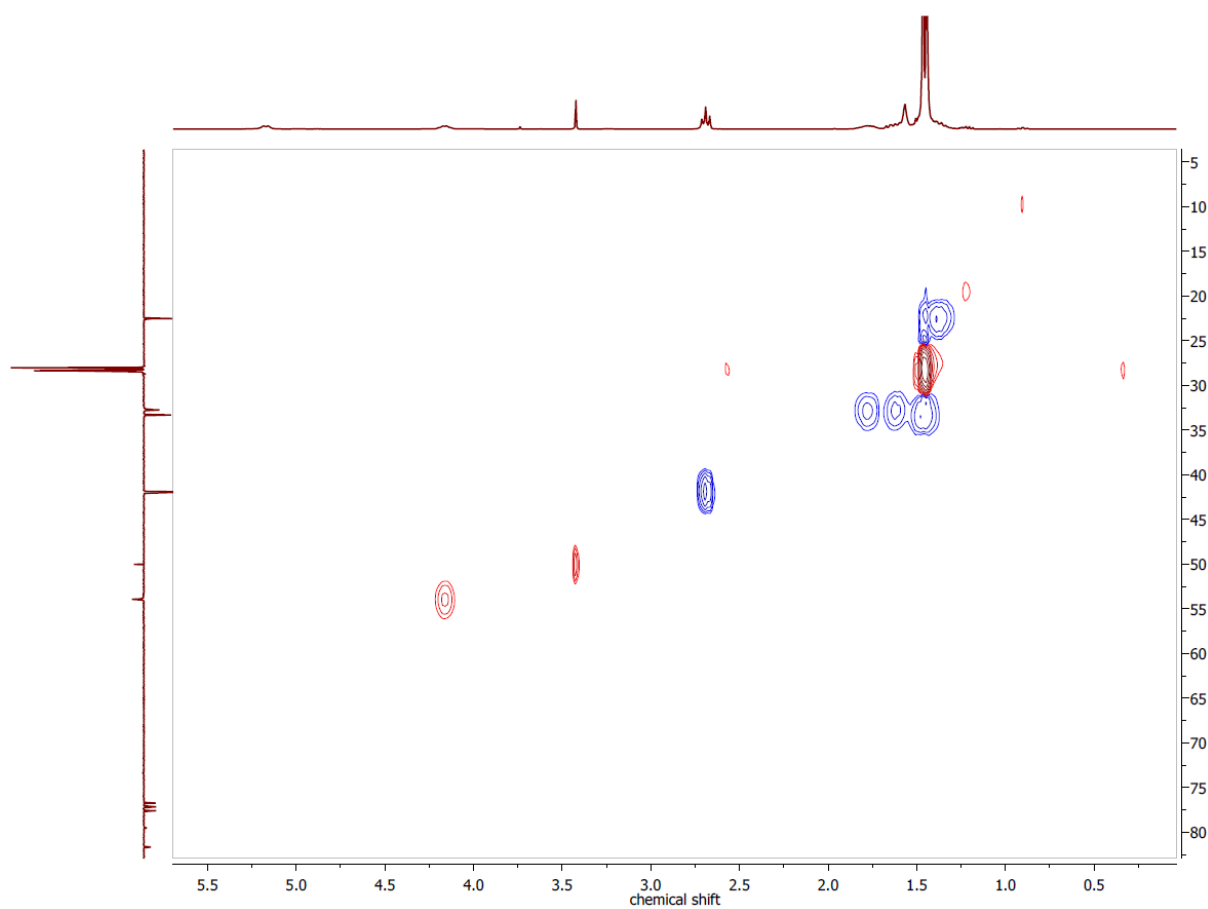


Figure 7.46 $^1\text{H},^{13}\text{C}$ HSQC NMR spectrum of Boc-Lys-OtBu in CDCl_3 .

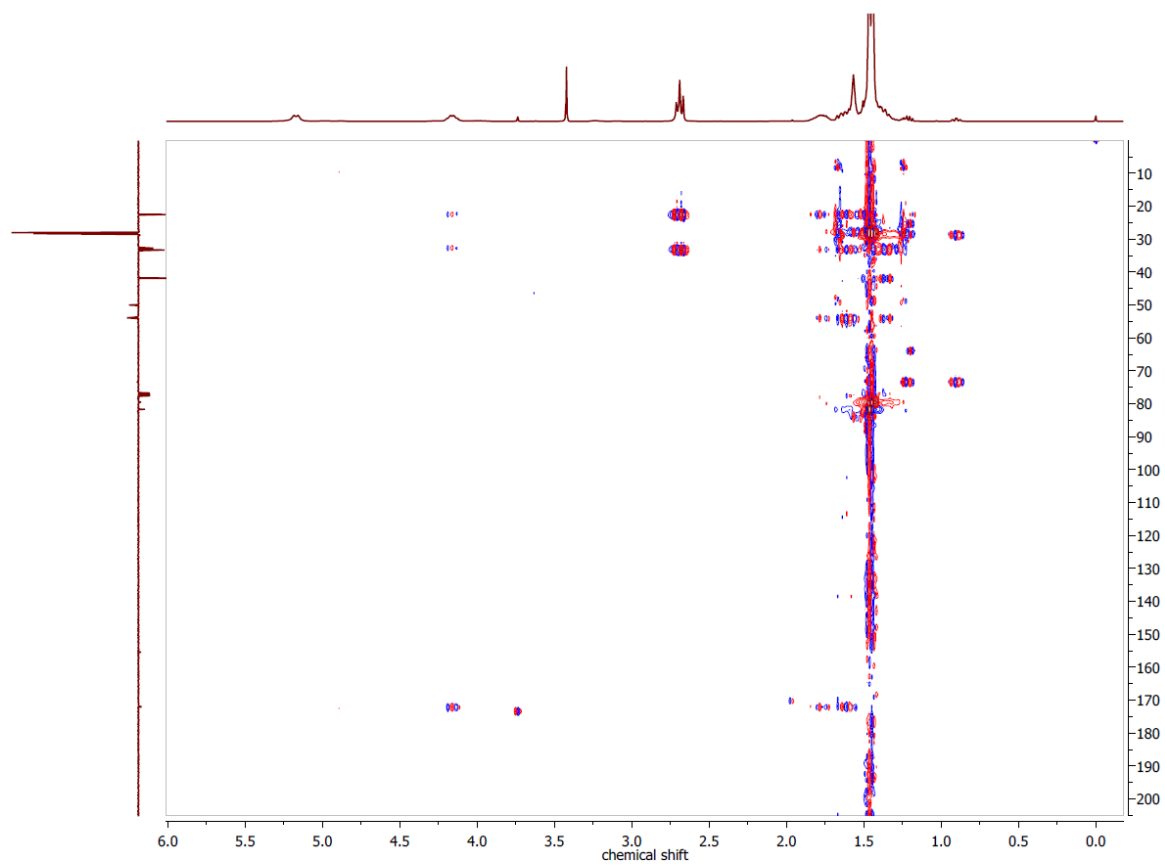


Figure 7.47 ^1H , ^{13}C HMBC NMR spectrum of Boc-Lys-OtBu in CDCl_3 .

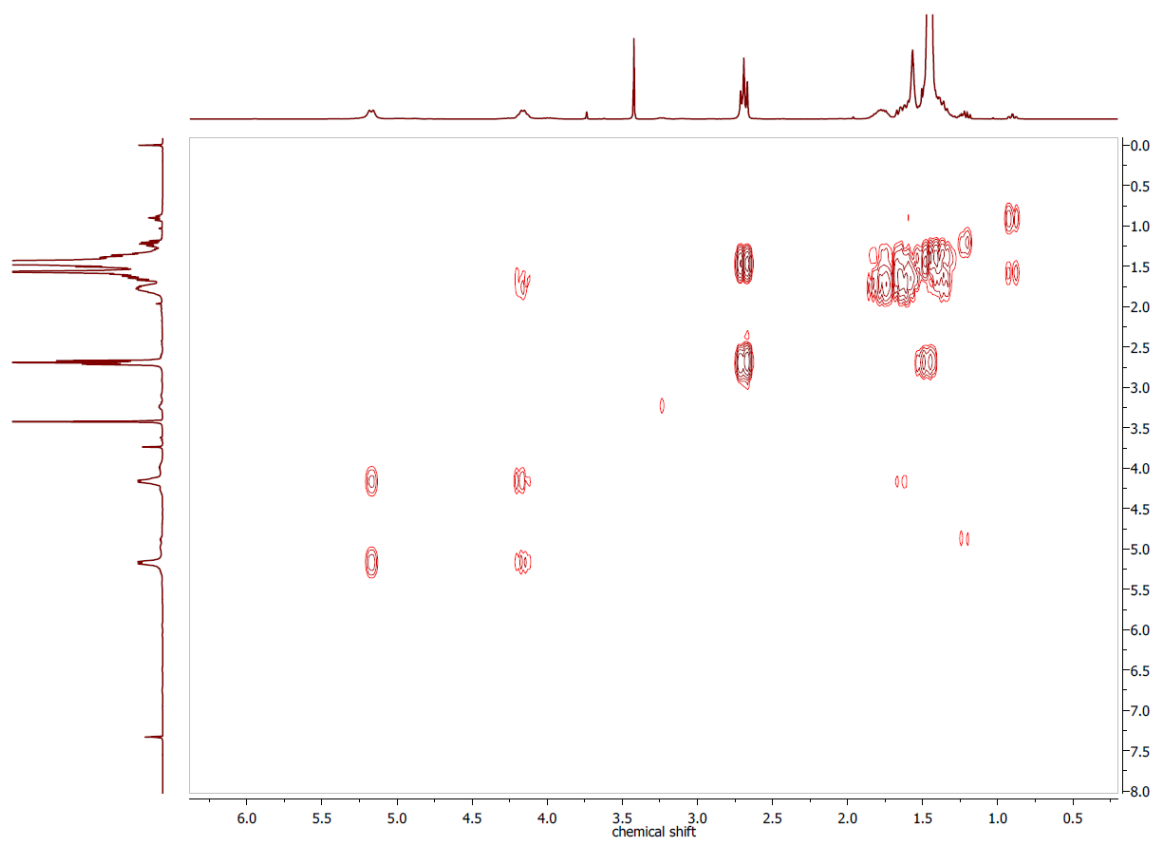


Figure 7.48 ^1H , ^1H COSY NMR spectrum of Boc-Lys-OtBu in CDCl_3 .

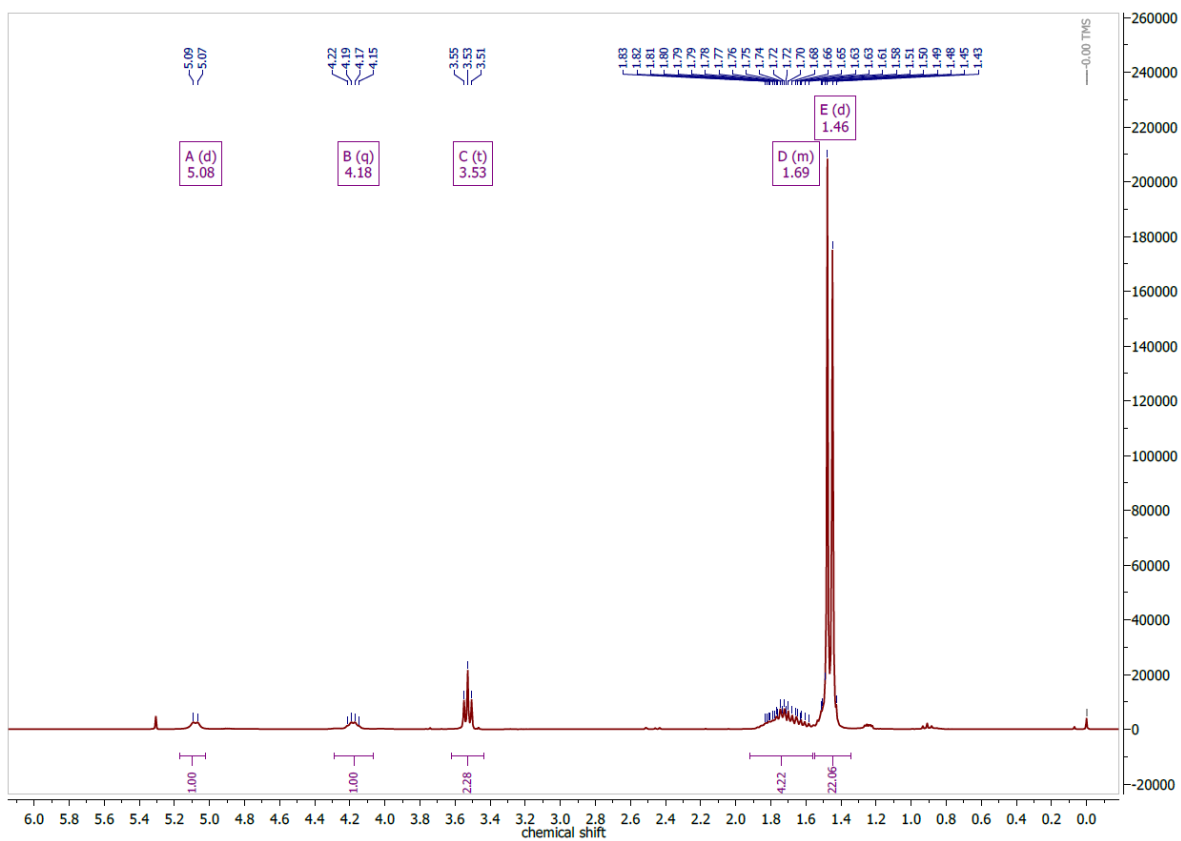


Figure 7.49 ^1H NMR spectrum of ITCLp in CDCl_3 at 300 MHz.

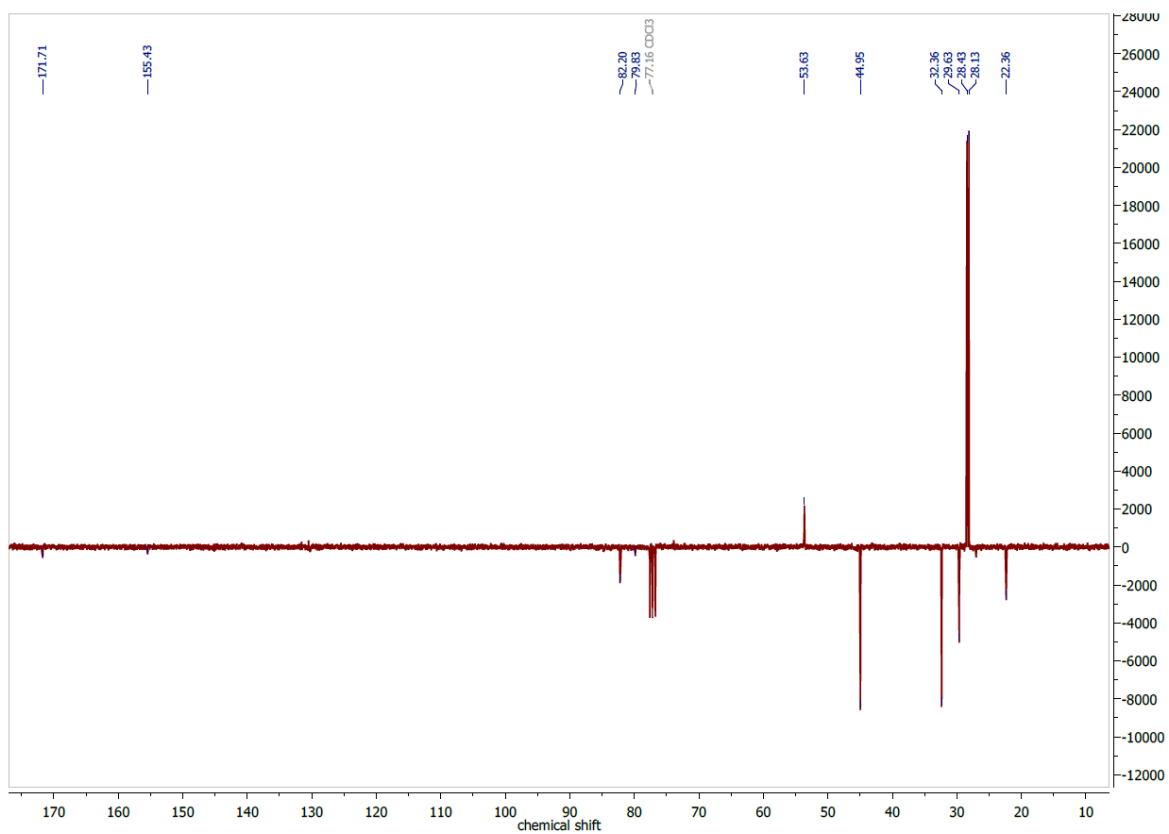


Figure 7.50 $^{13}\text{C}\{^1\text{H}\}$ DEPTQ NMR spectrum of ITCLp in CDCl_3 at 75 MHz.

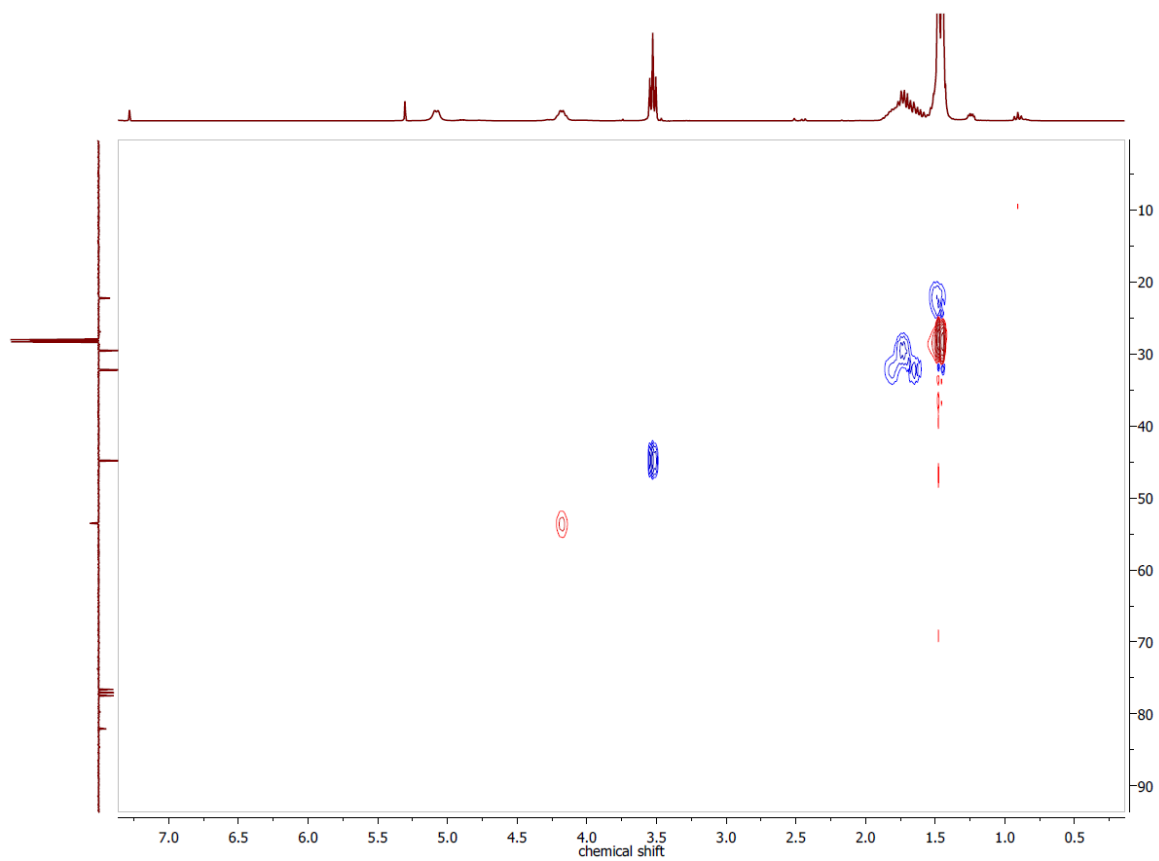


Figure 7.51 ^1H , ^{13}C HSQC NMR spectrum of ITCLp in CDCl_3 .

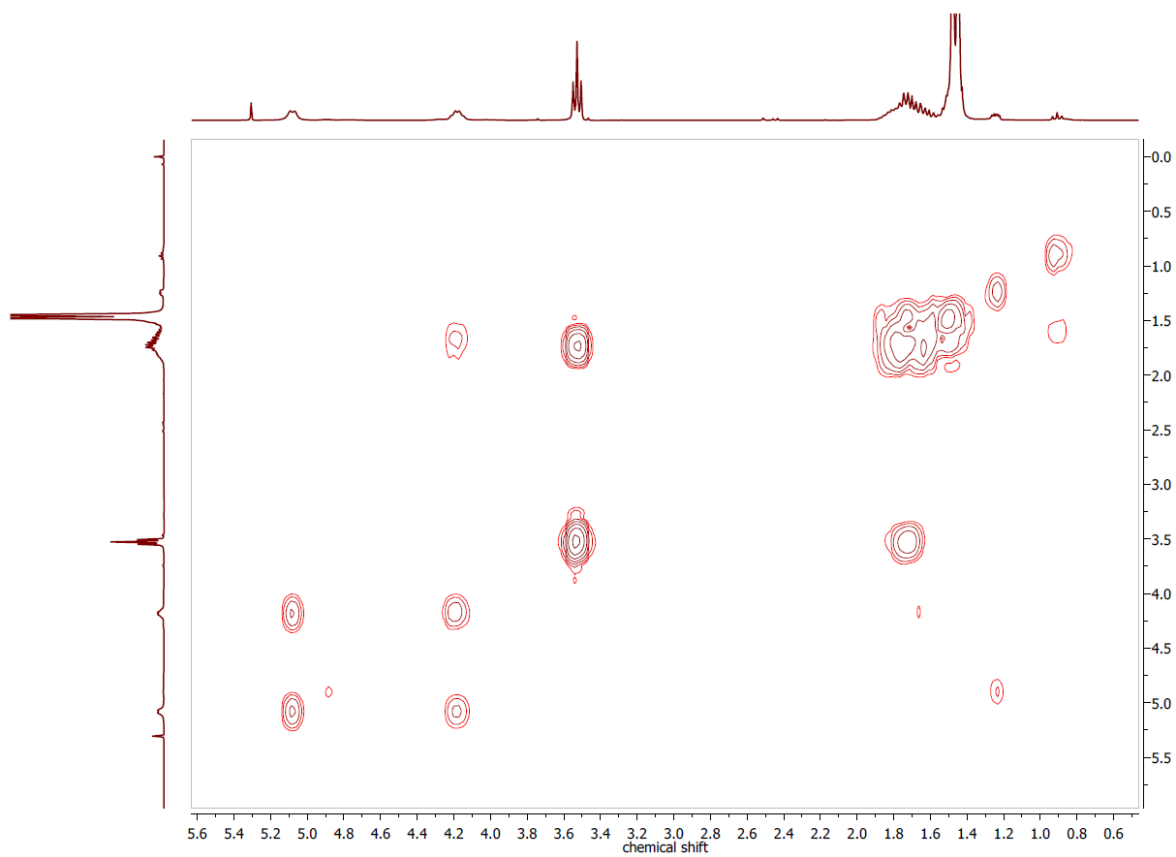


Figure 7.52 ^1H , ^1H COSY NMR spectrum of ITCLp in CDCl_3 .

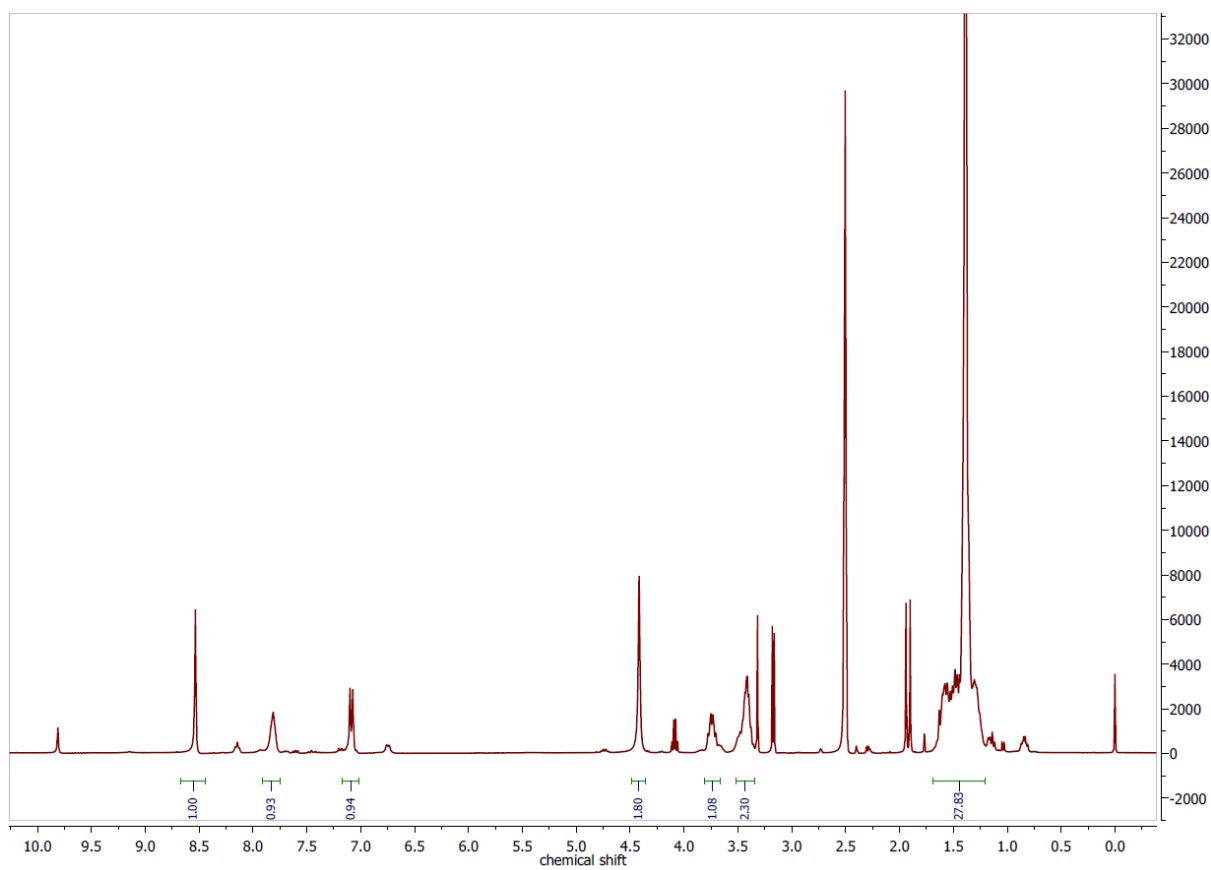


Figure 7.53 ^1H NMR spectrum of TSCLp in $\text{DMSO-}d_6$ at 300 MHz.

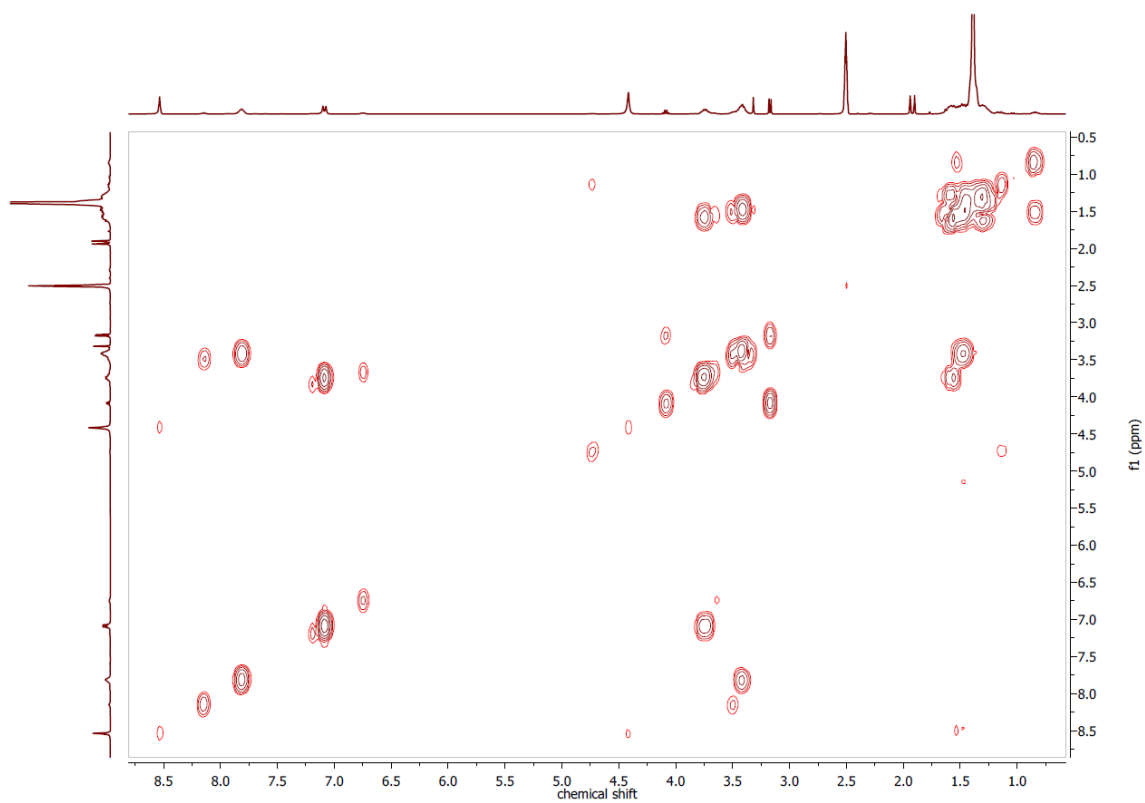


Figure 7.54 ^1H , ^1H COSY-NMR spectrum of TSCLp in $\text{DMSO-}d_6$.

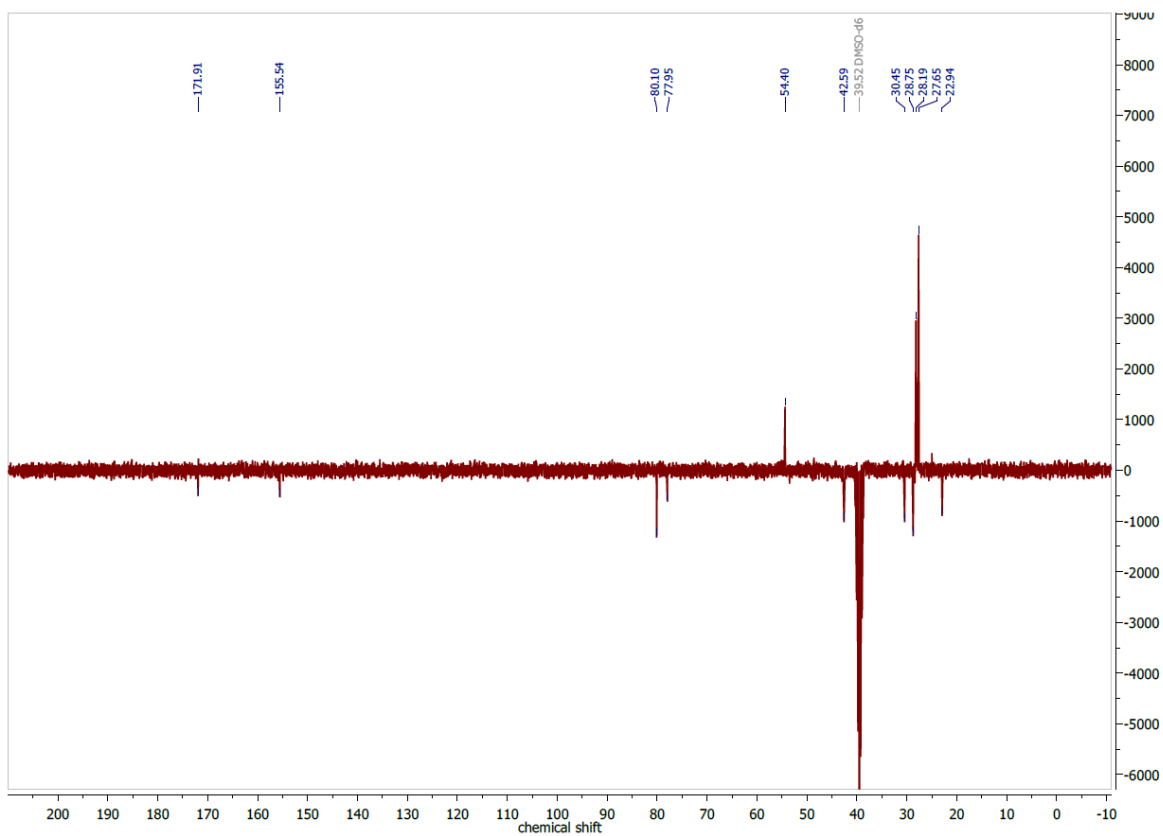


Figure 7.55 $^{13}\text{C}\{^1\text{H}\}$ DEPTQ NMR spectrum of TSCLp in $\text{DMSO-}d_6$ at 75 MHz.

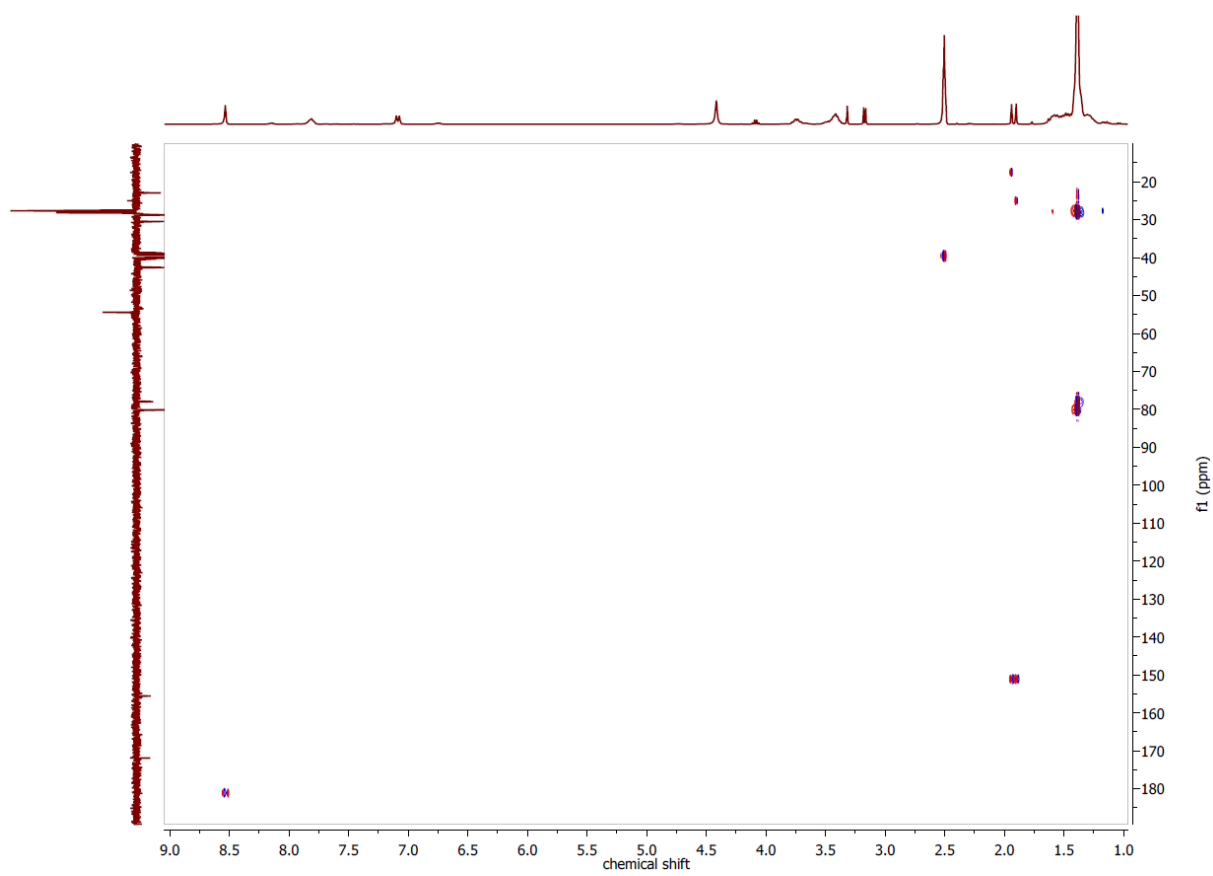


Figure 7.56 $^1\text{H},^{13}\text{C}$ HMBC-NMR spectrum of TSCLp in $\text{DMSO-}d_6$.

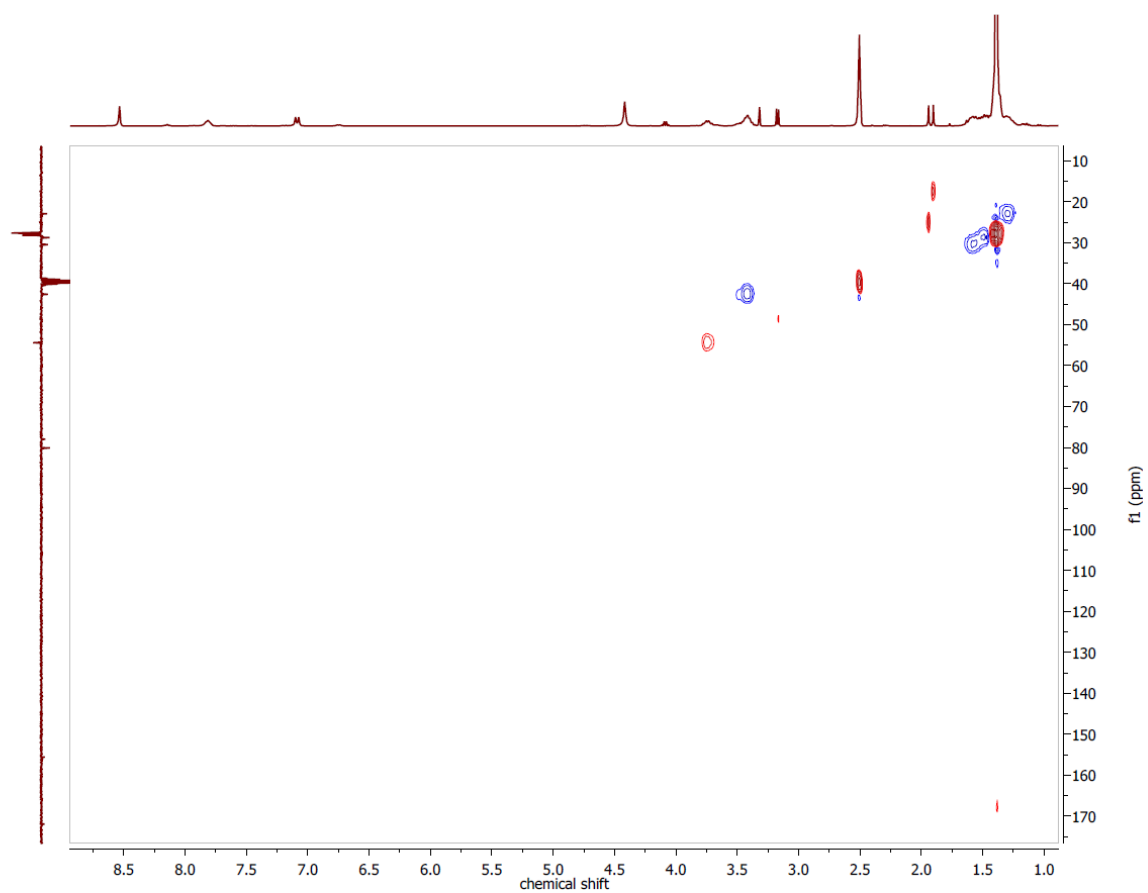


Figure 7.57 ^1H , ^{13}C HSQCed-NMR spectrum of TSCLp in $\text{DMSO}-d_6$.

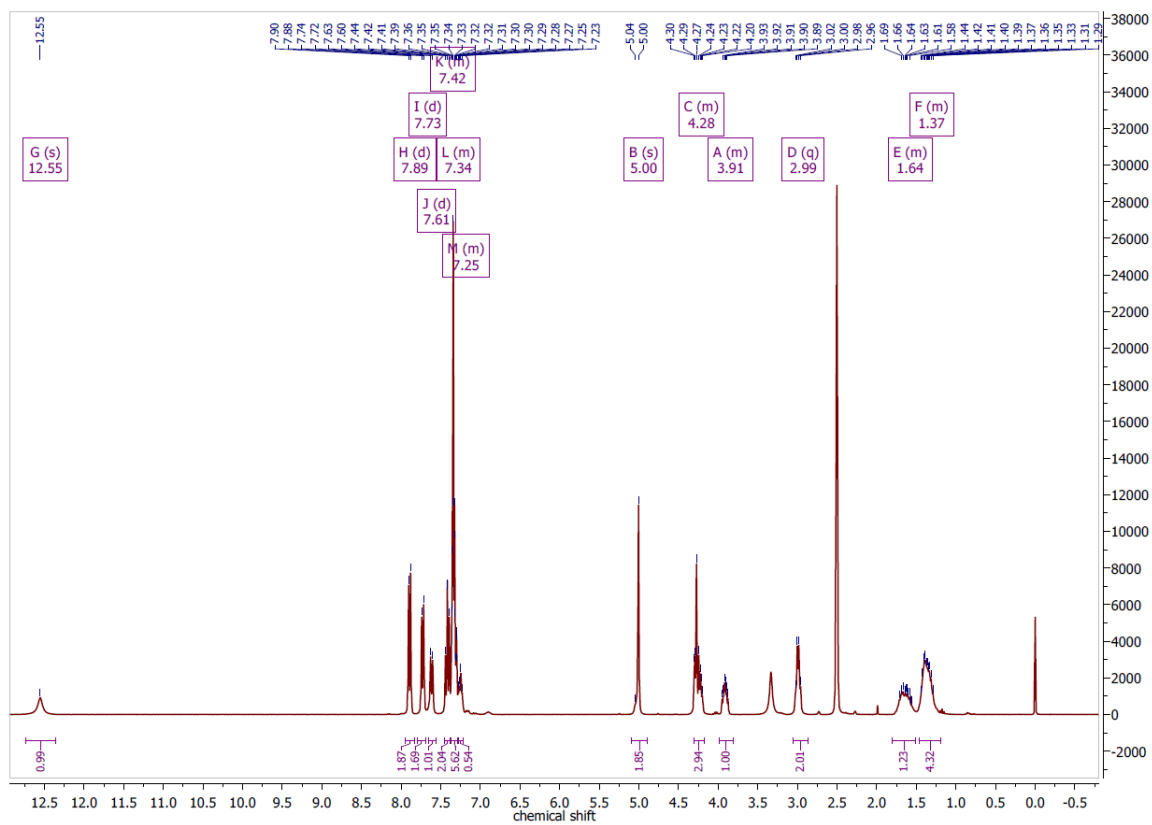


Figure 7.58 ^1H NMR of Fmoc-Lys(Cbz)-OH in $\text{DMSO}-d_6$ at 300 MHz.

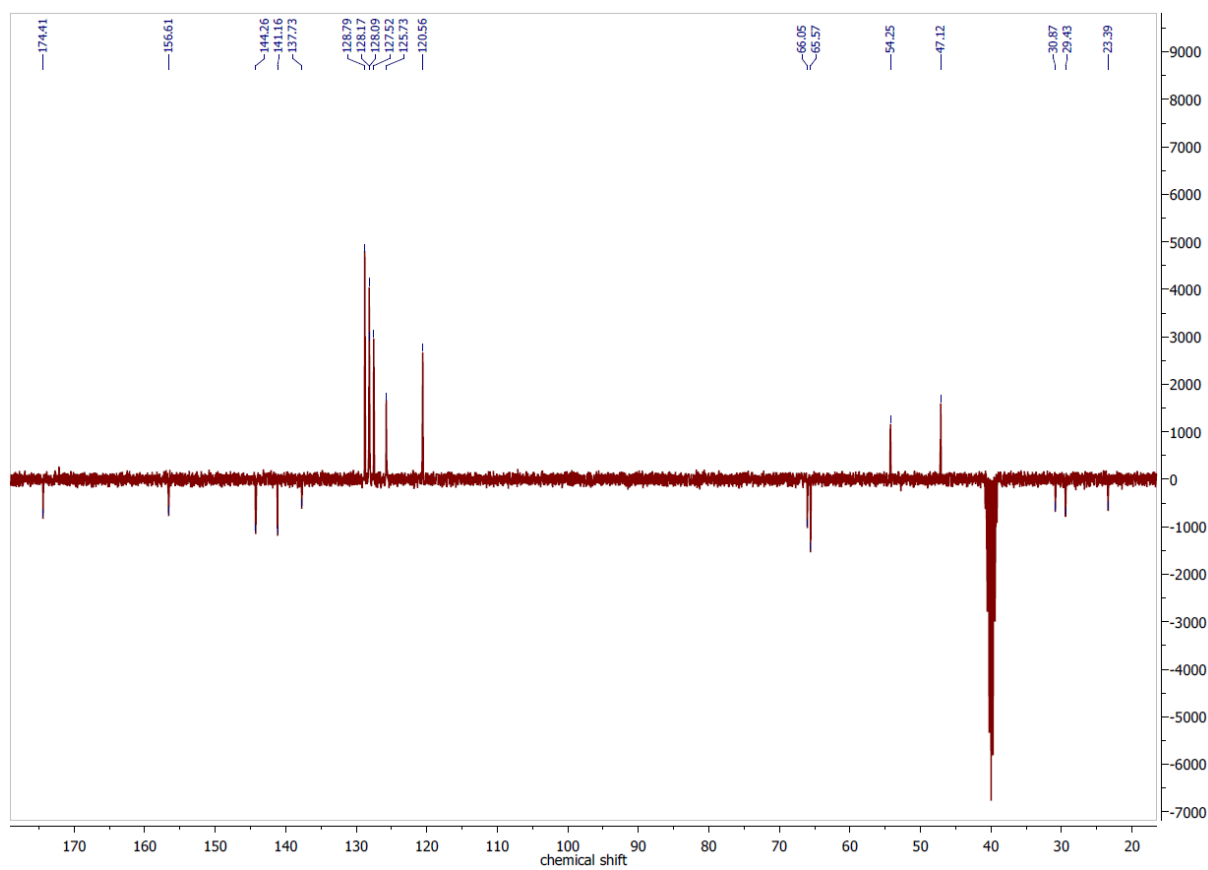


Figure 7.59 $^{13}\text{C}\{^1\text{H}\}$ DEPTQ NMR of Fmoc-Lys(Cbz)-OH in $\text{DMSO-}d_6$ at 75MHz.

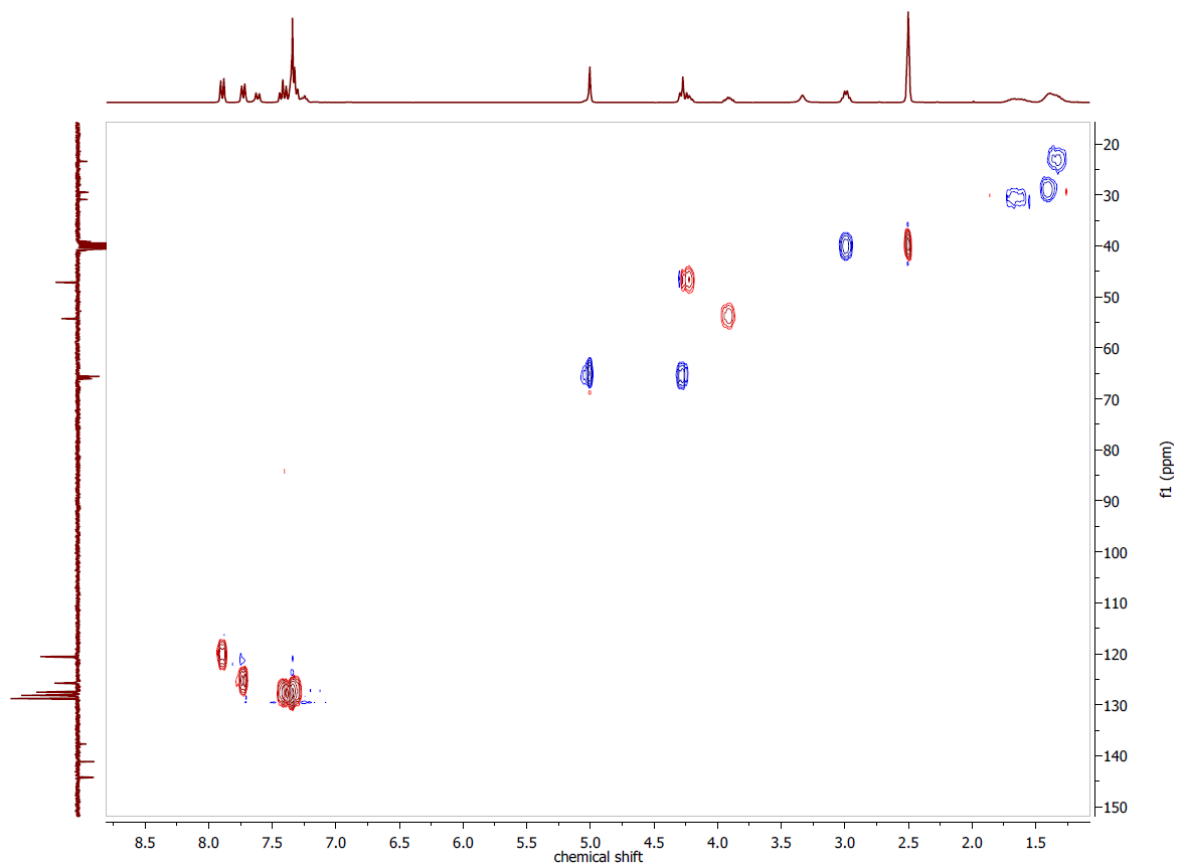


Figure 7.60 $^1\text{H},^{13}\text{C}$ HSQCed NMR of Fmoc-Lys(Cbz)-OH in $\text{DMSO-}d_6$.

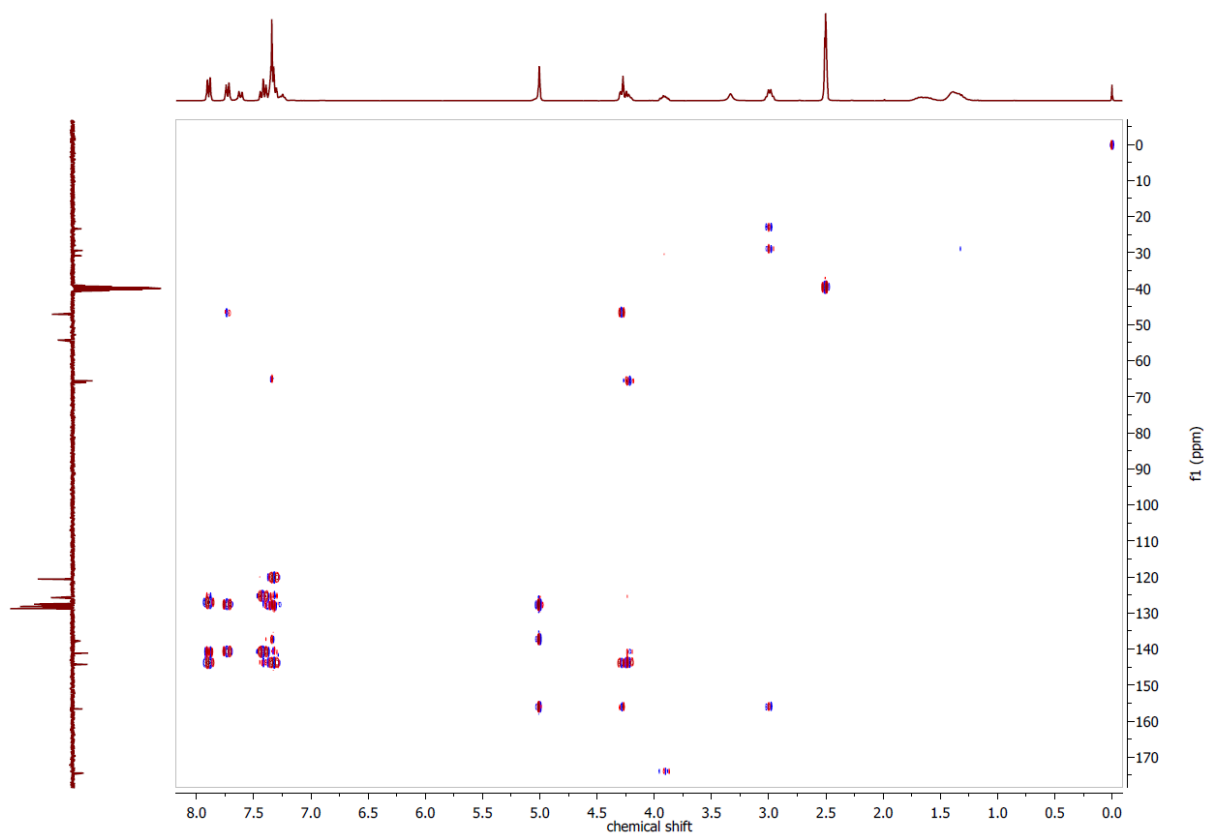


Figure 7.61 ^1H , ^{13}C HMBC NMR of Fmoc-Lys(Cbz)-OH in DMSO- d_6 .

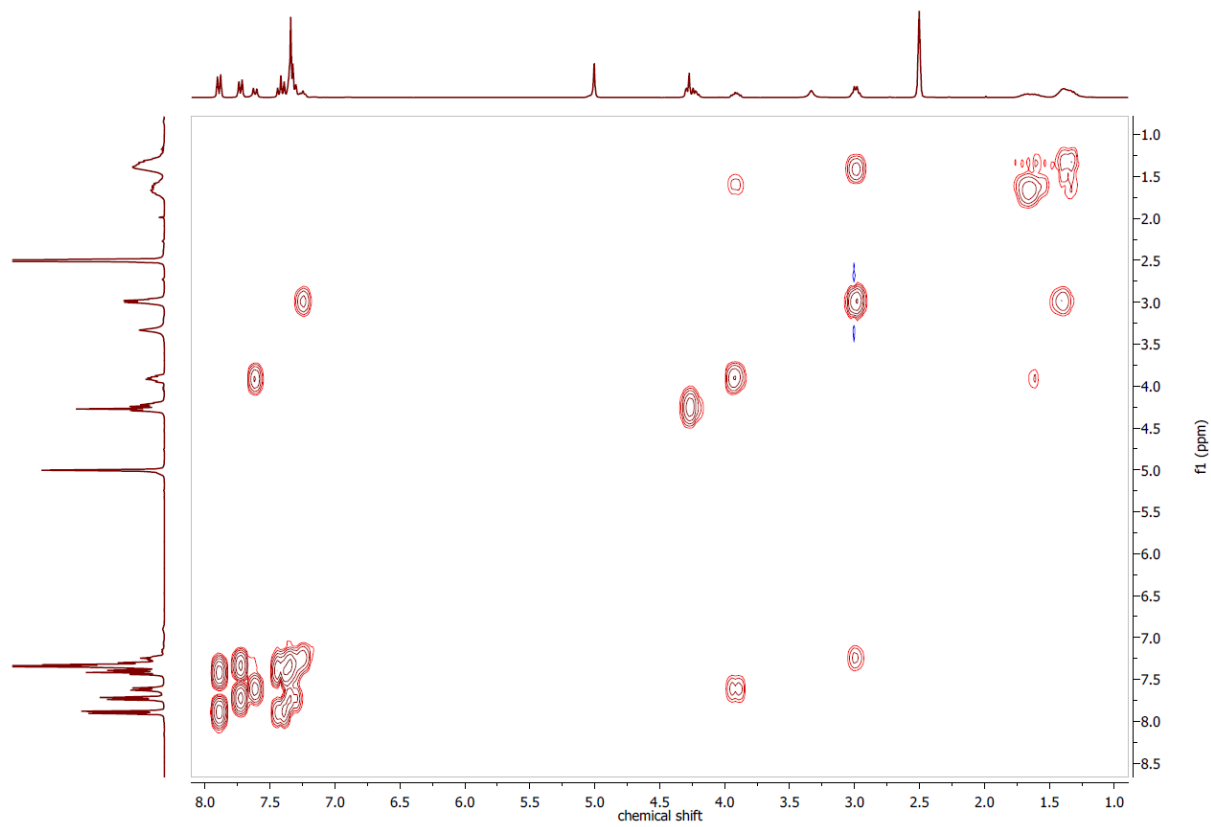


Figure 7.62 ^1H , ^1H COSY NMR of Fmoc-Lys(Cbz)-OH in DMSO- d_6 .

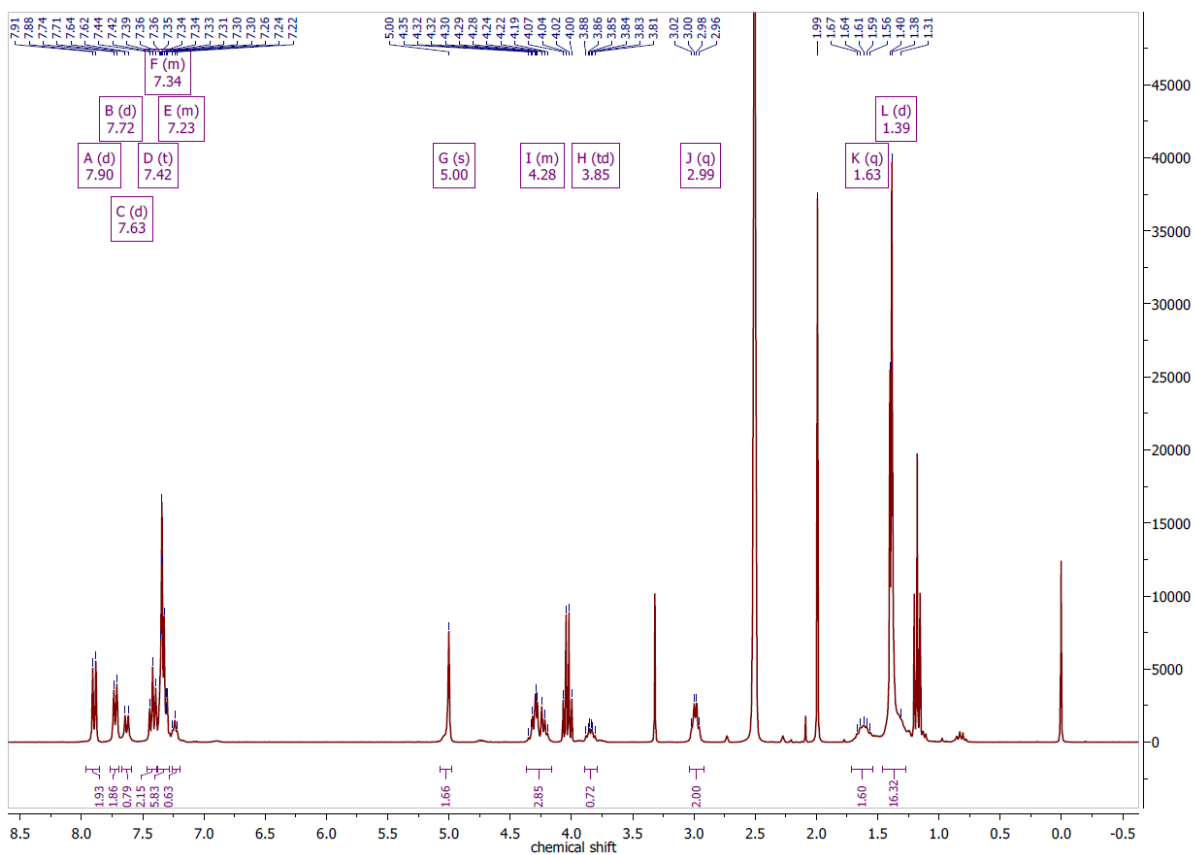


Figure 7.63 ^1H NMR of Fmoc-Lys(Cbz)-OtBu in $\text{DMSO-}d_6$ at 300 MHz.

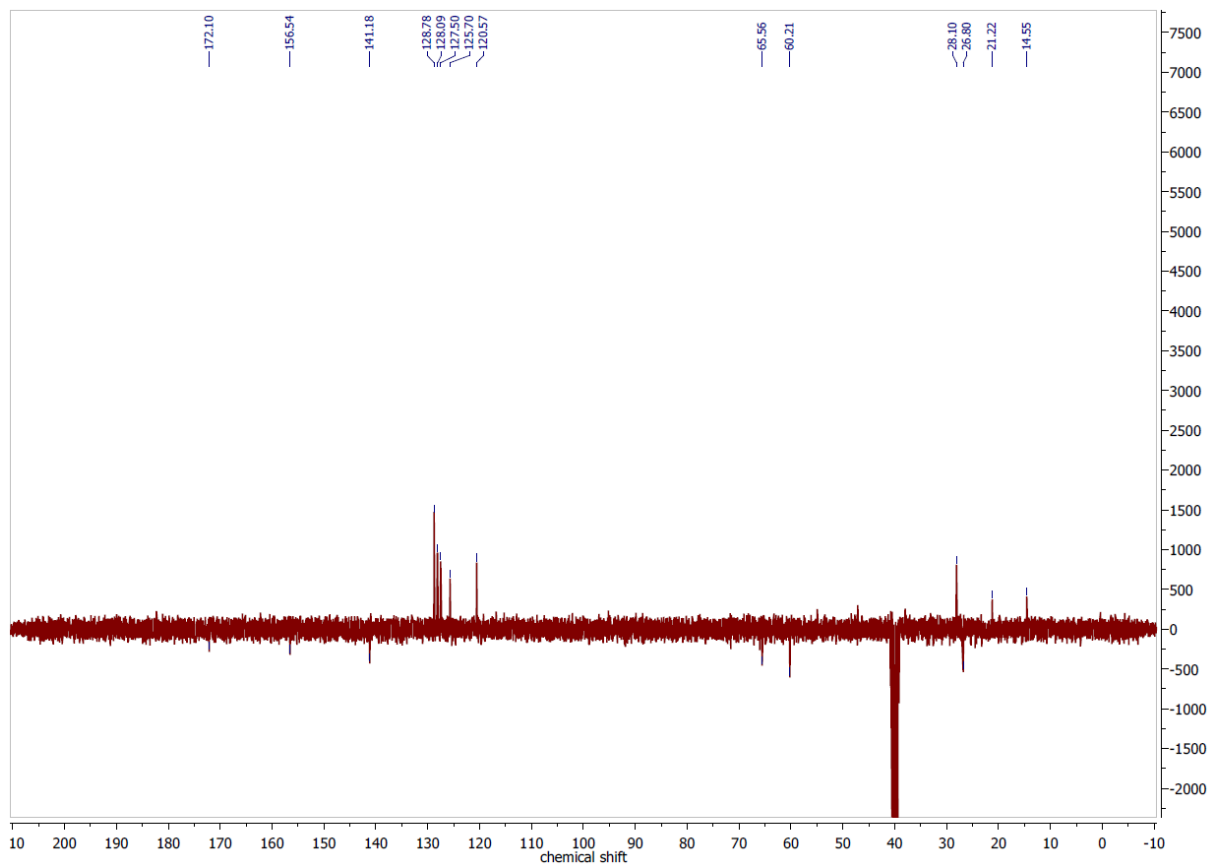


Figure 7.64 $^{13}\text{C}\{^1\text{H}\}$ DEPTQ NMR of Fmoc-Lys(Cbz)-OtBu in $\text{DMSO-}d_6$ at 75 MHz.

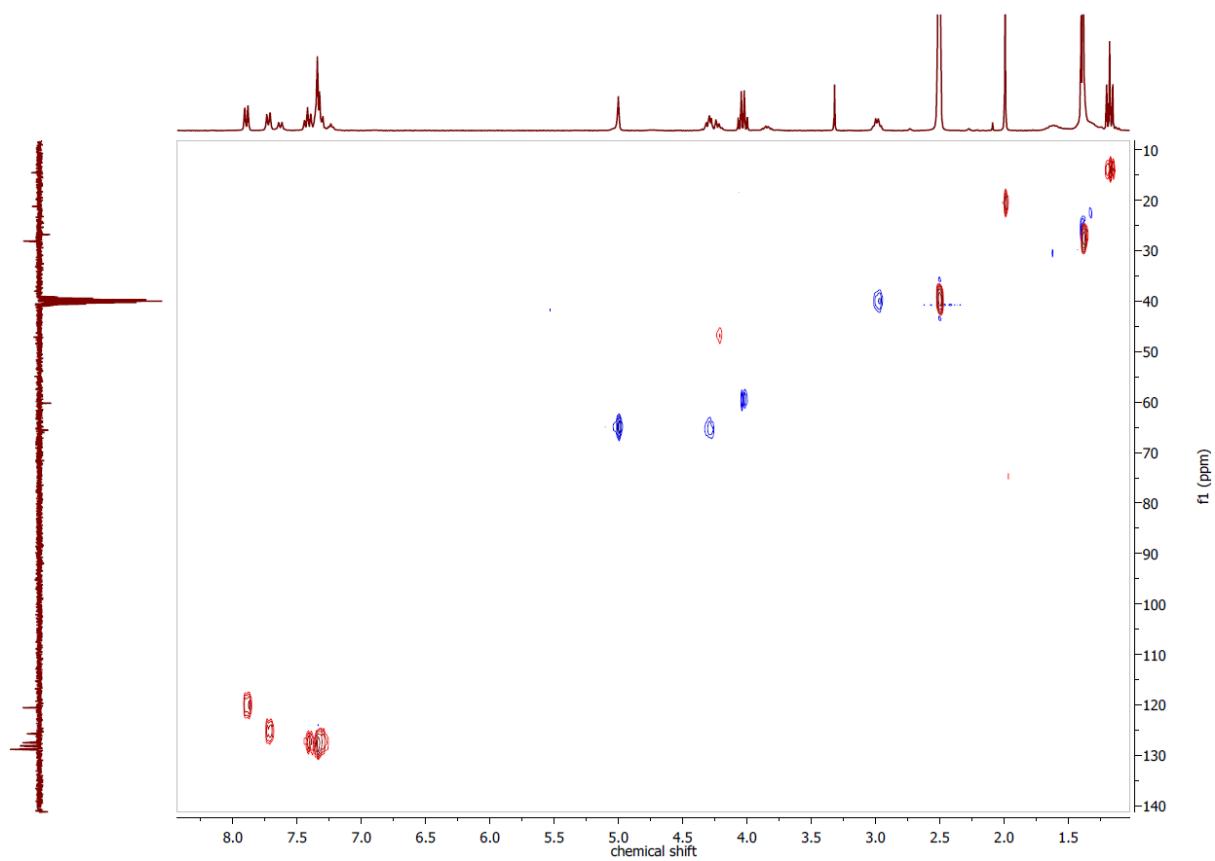


Figure 7.65 ^1H , ^{13}C HSQCed NMR of Fmoc-Lys(Cbz)-OtBu in $\text{DMSO-}d_6$.

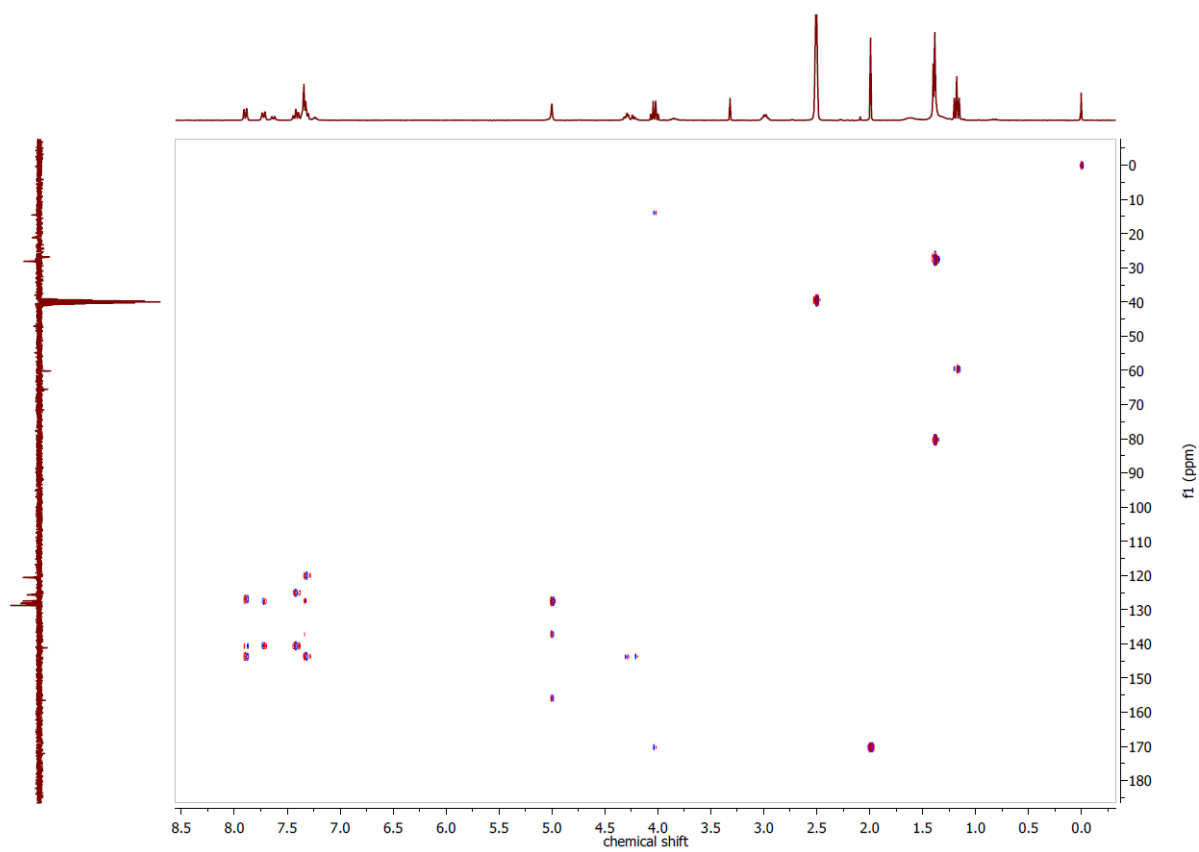


Figure 7.66 ^1H , ^{13}C HMBC NMR of Fmoc-Lys(Cbz)-OtBu in $\text{DMSO-}d_6$.

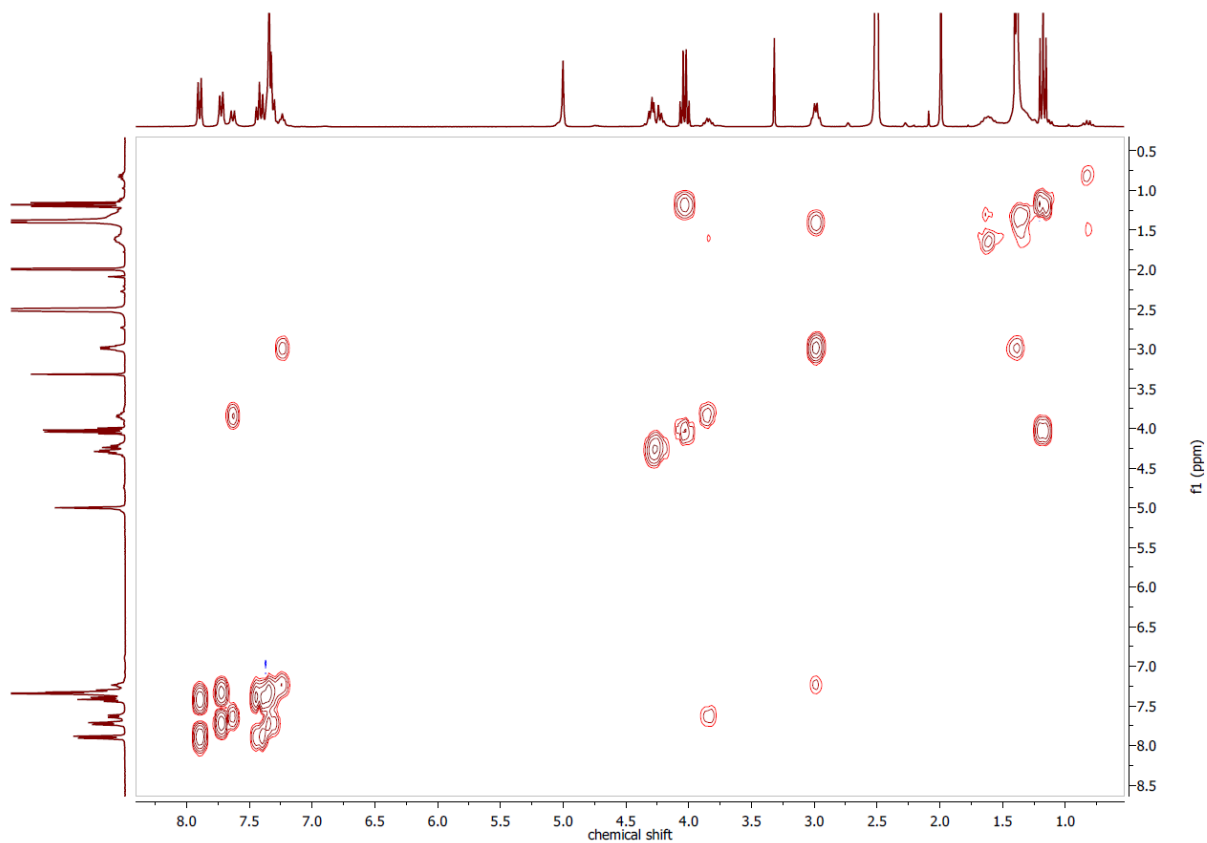


Figure 7.67 $^1\text{H},^1\text{H}$ COSY NMR of Fmoc-Lys(Cbz)-OtBu in DMSO- d_6 .

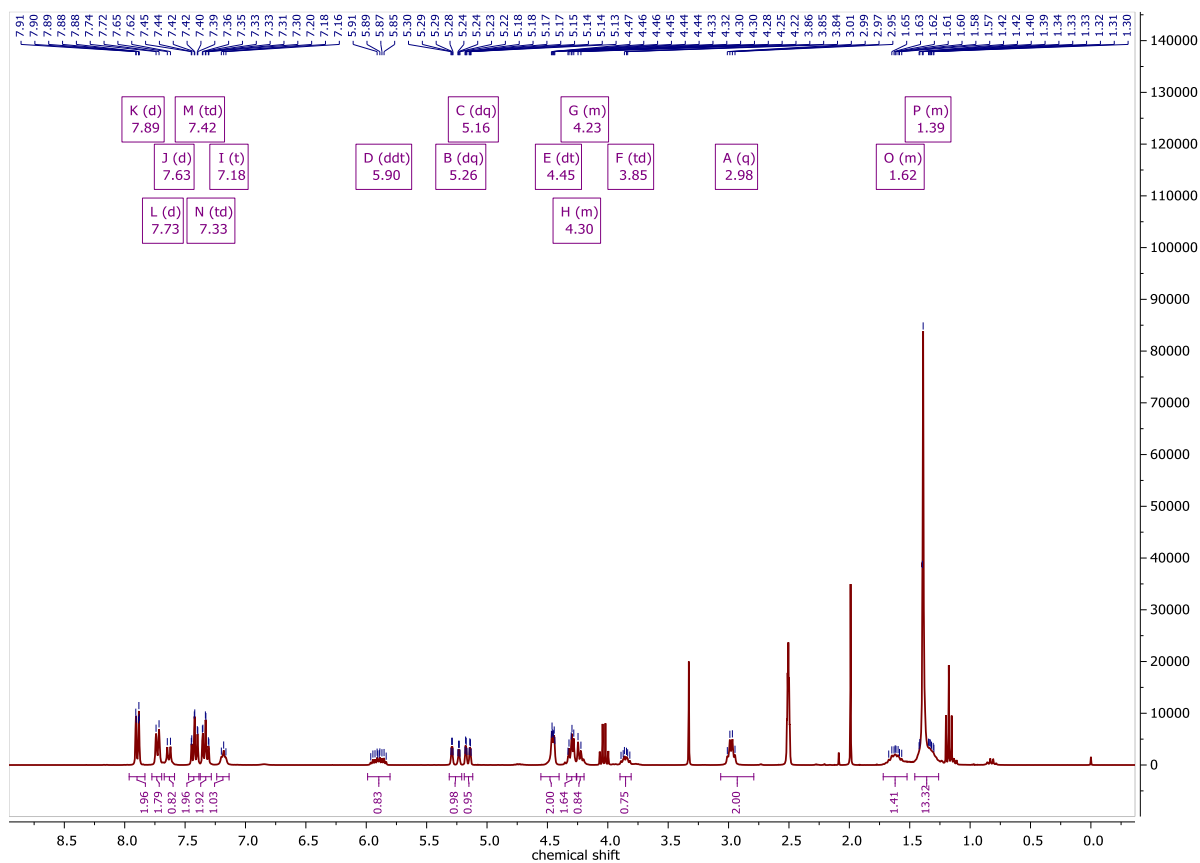


Figure 7.68 ^1H NMR of Fmoc-Lys(Alloc)-OtBu in DMSO- d_6 at 300 MHz.

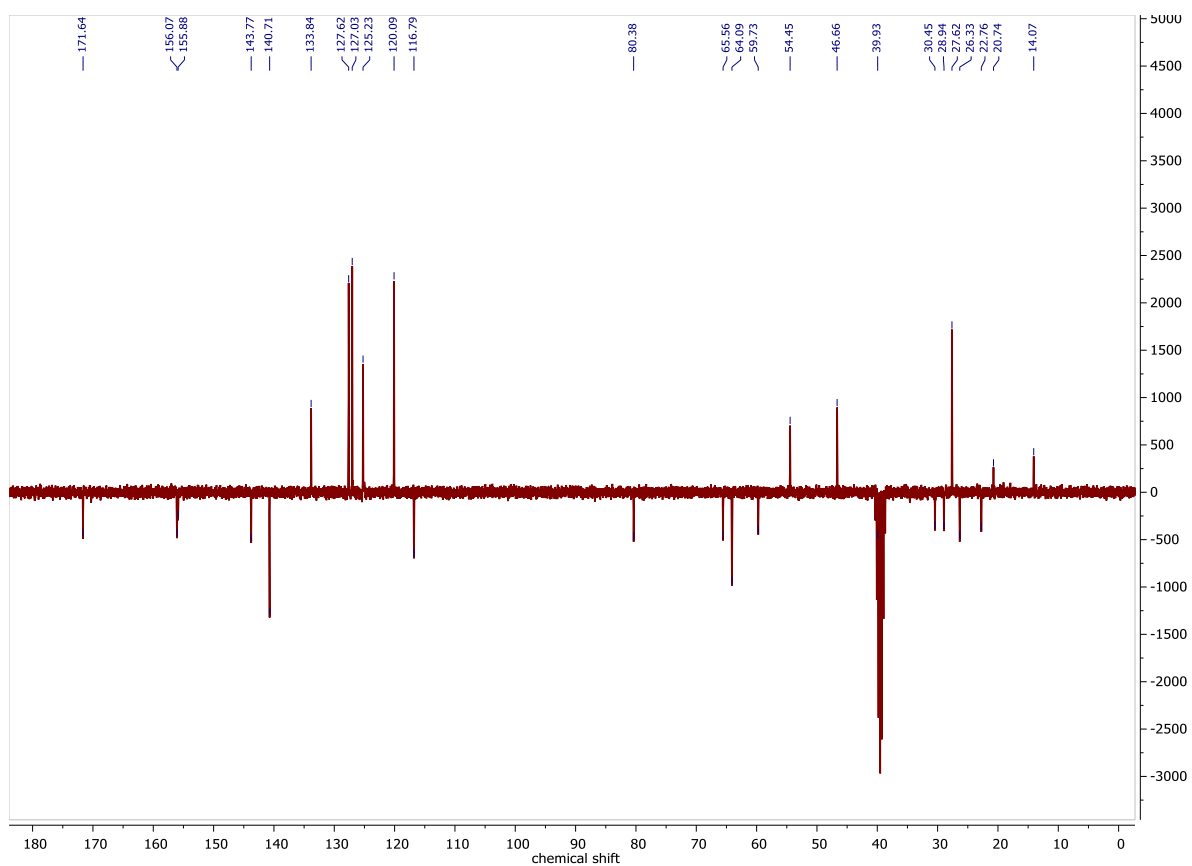


Figure 7.69 $^{13}\text{C}\{^1\text{H}\}$ DEPTQ NMR of Fmoc-Lys(Alloc)-OtBu in DMSO- d_6 at 300 MHz.

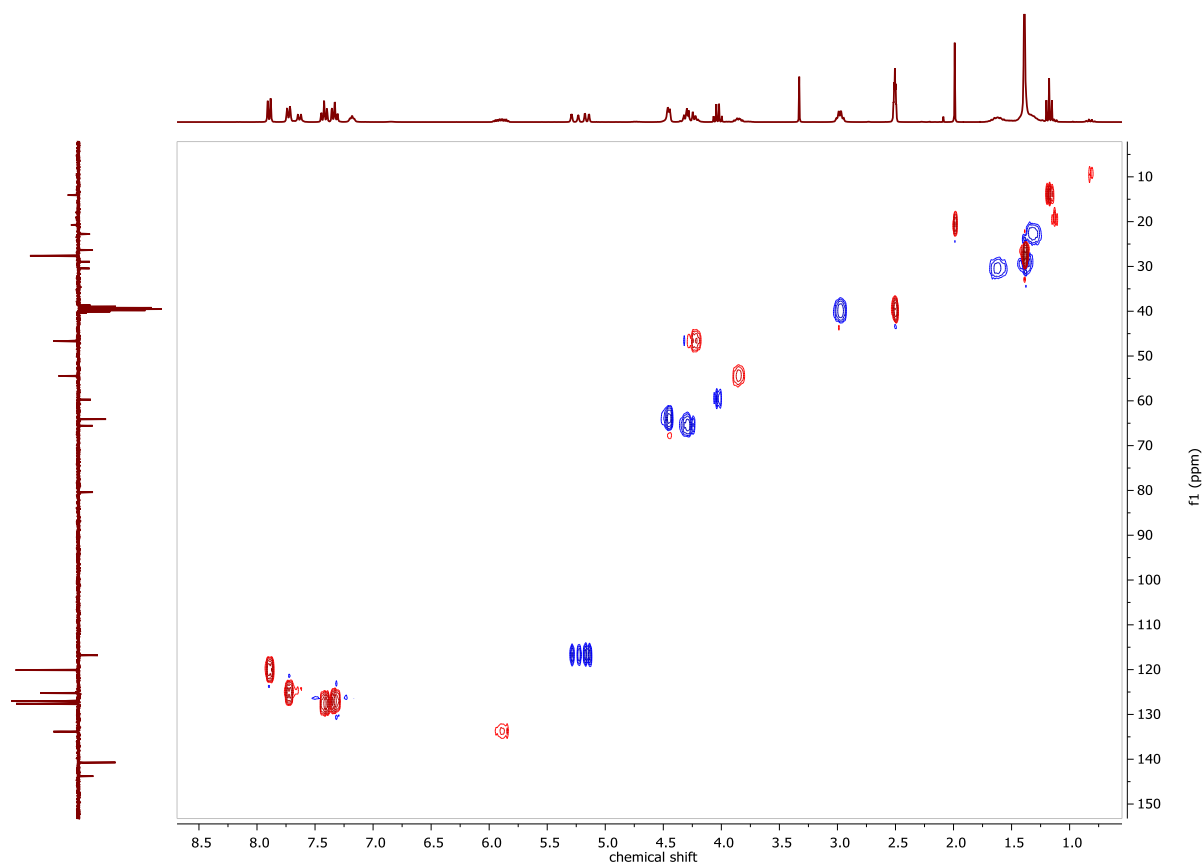


Figure 7.70 $^1\text{H},^{13}\text{C}$ HSQC NMR of Fmoc-Lys(Alloc)-OtBu in DMSO- d_6 .

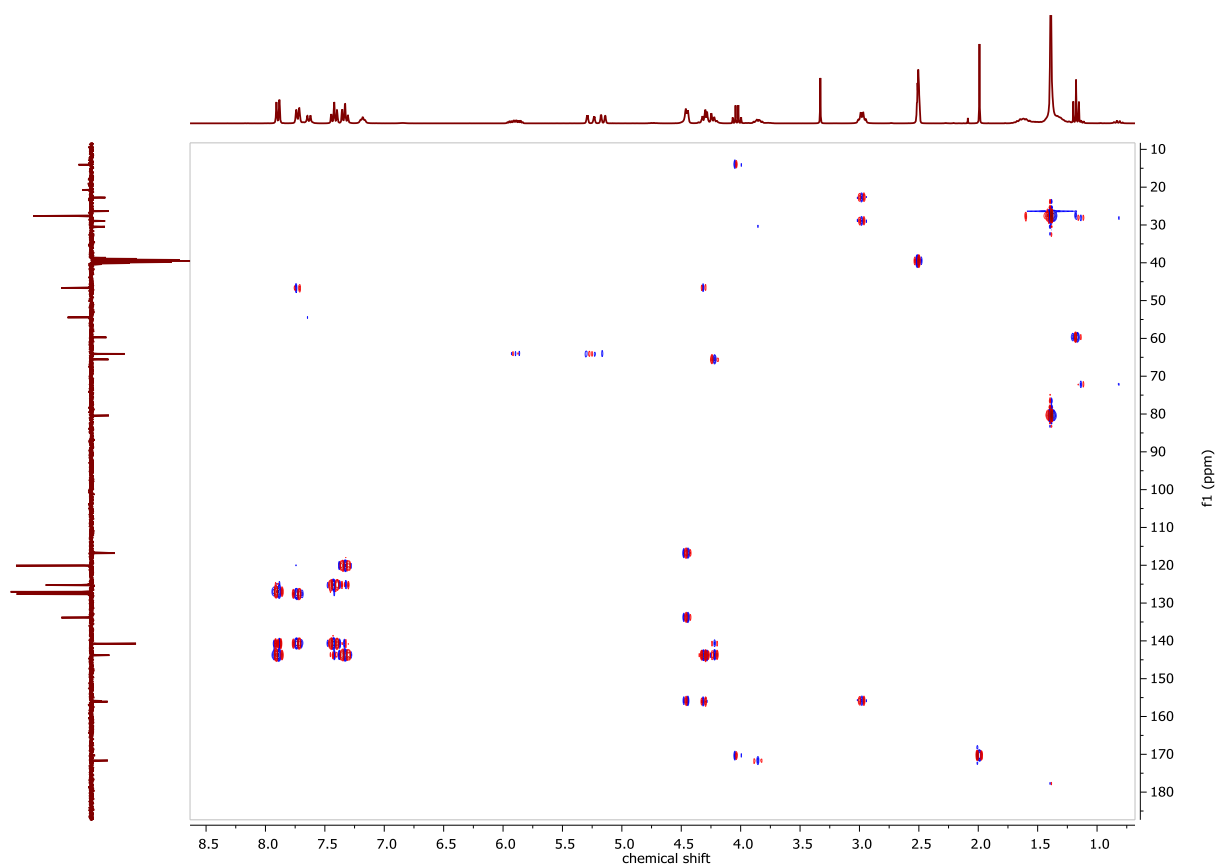


Figure 7.71 ^1H , ^{13}C HMBC NMR of Fmoc-Lys(Alloc)-OtBu in $\text{DMSO}-d_6$.

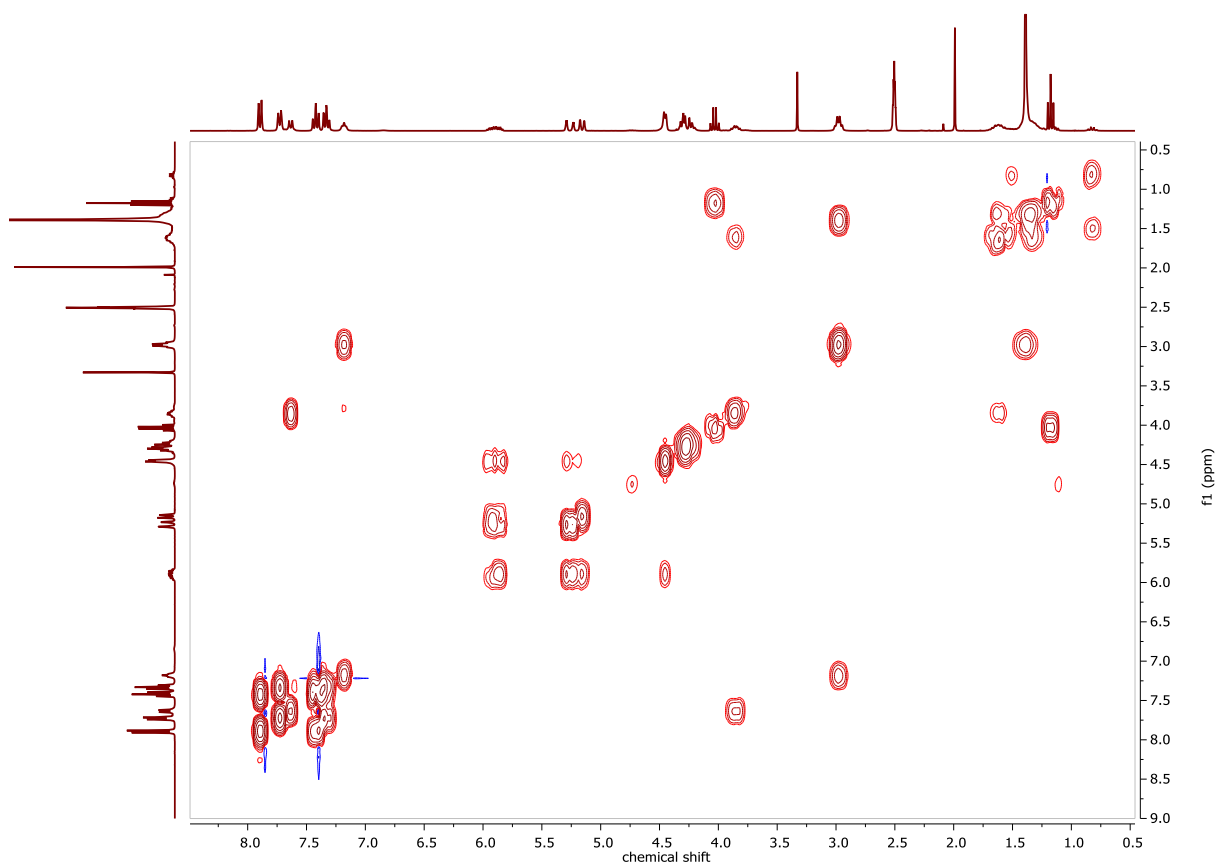


Figure 7.72 ^1H , ^1H COSY NMR of Fmoc-Lys(Alloc)-OtBu in $\text{DMSO}-d_6$.

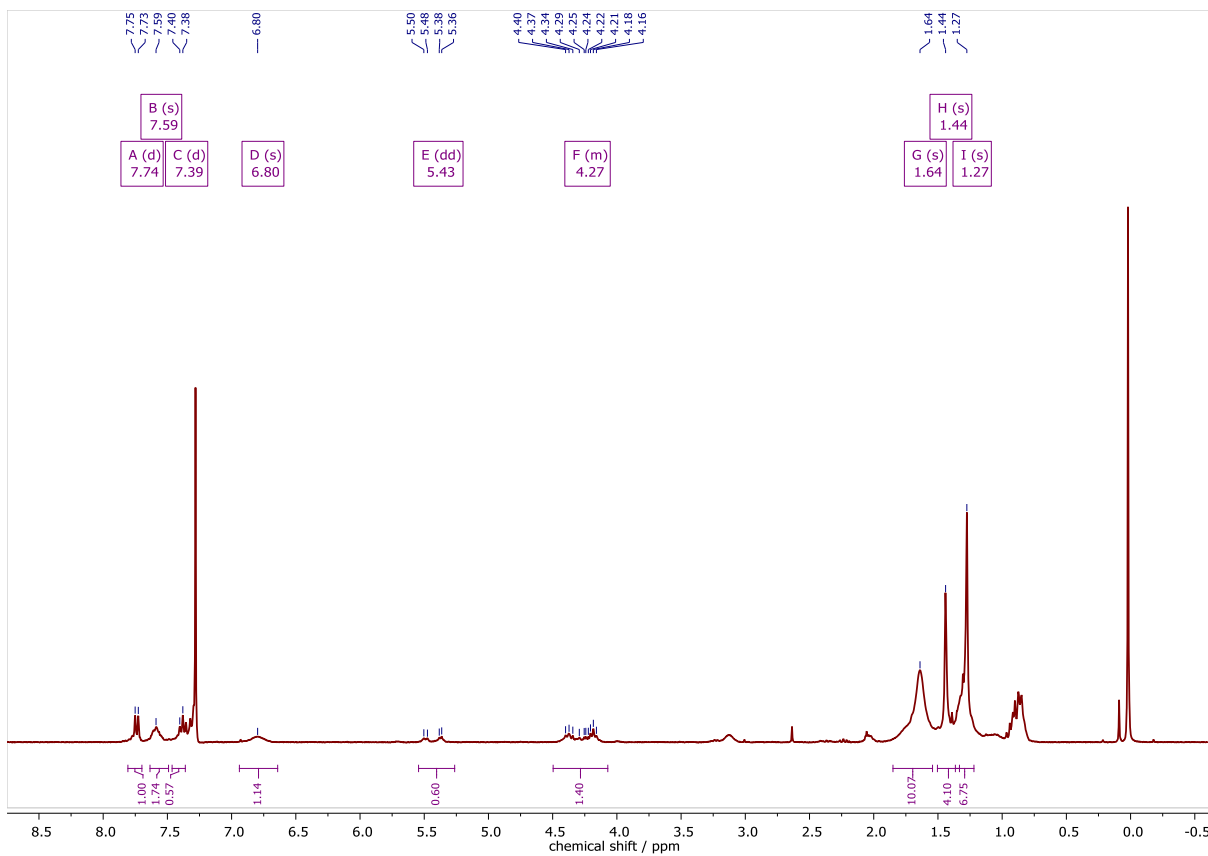


Figure 7.73 ^1H NMR of Fmoc-Lys-OtBu in CDCl_3 at 300 MHz.

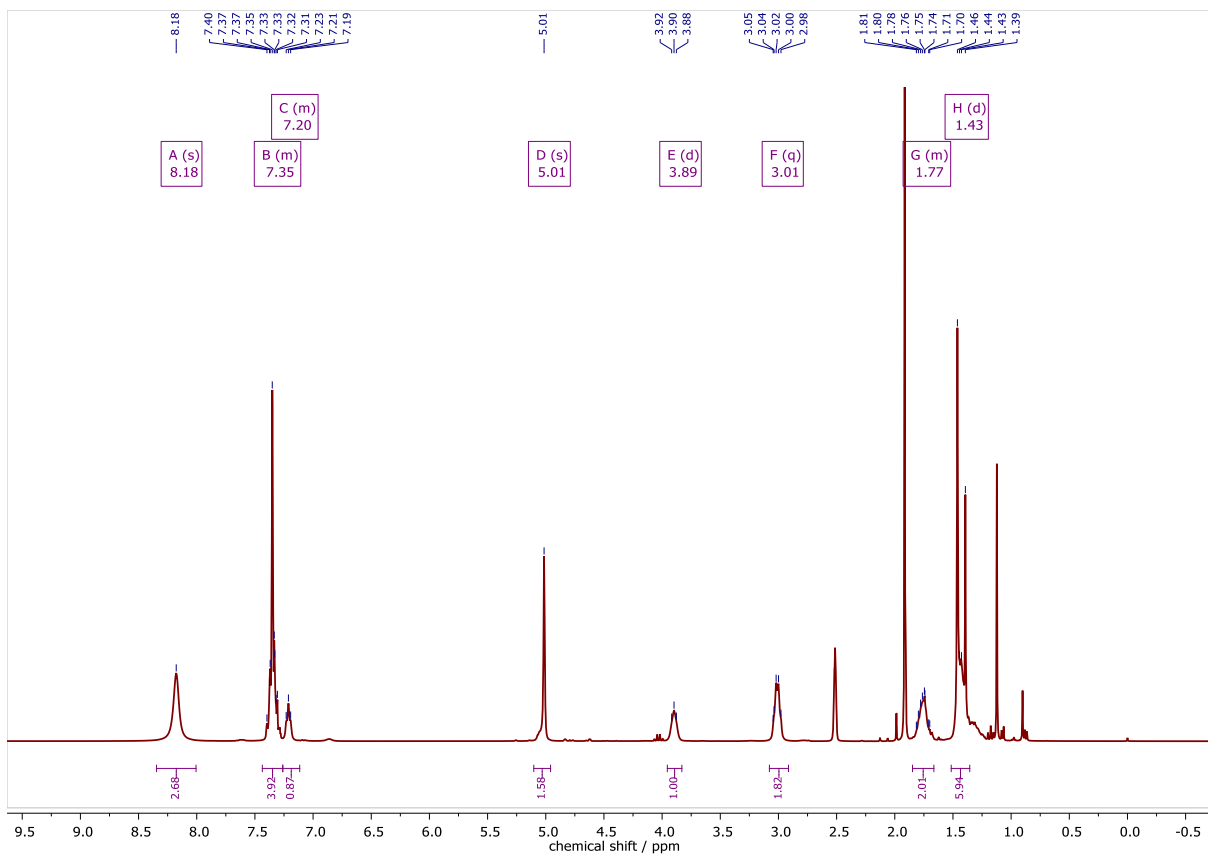


Figure 7.74 ^1H NMR of HLys(Cbz)-OtBu in $\text{DMSO}-d_6$ at 300 MHz.

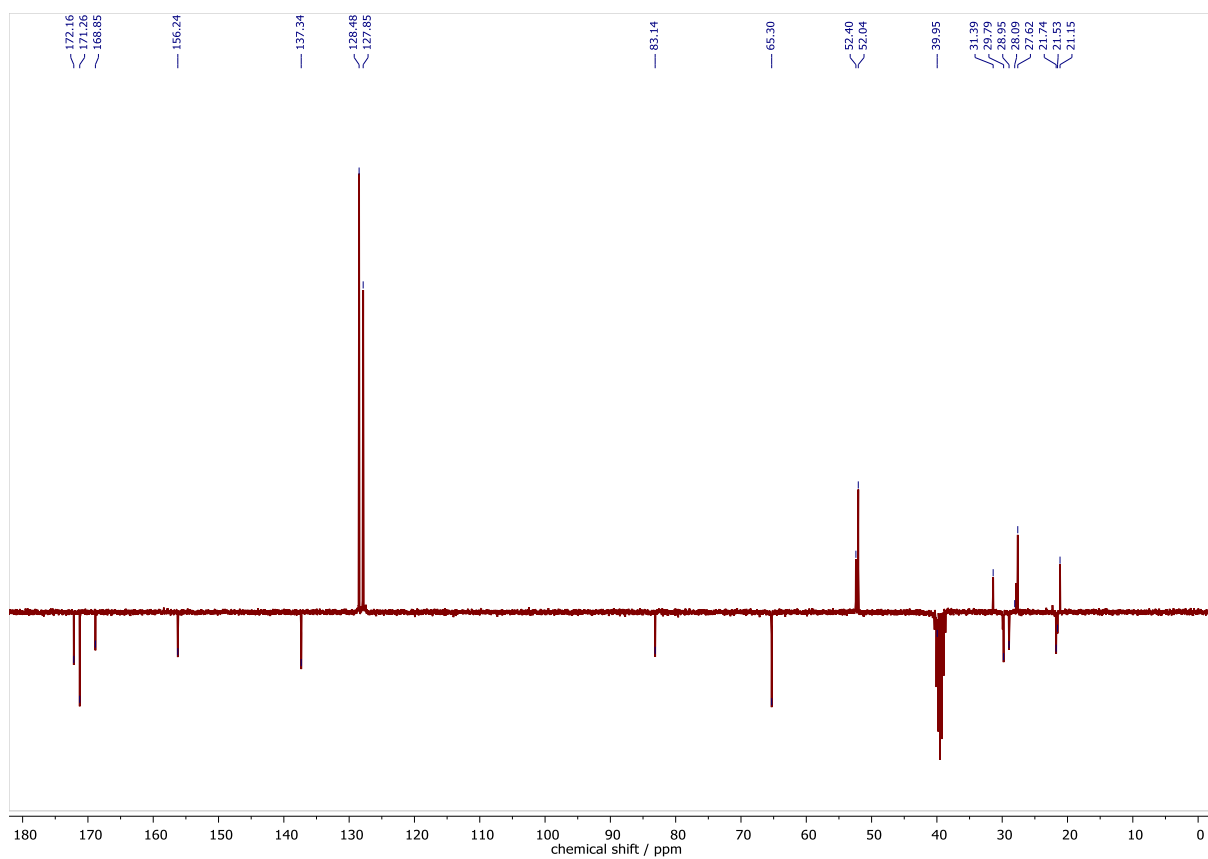


Figure 7.75 $^{13}\text{C}\{^1\text{H}\}$ DEPTQ NMR of HLys(Cbz)-OtBu in DMSO- d_6 at 75 MHz.

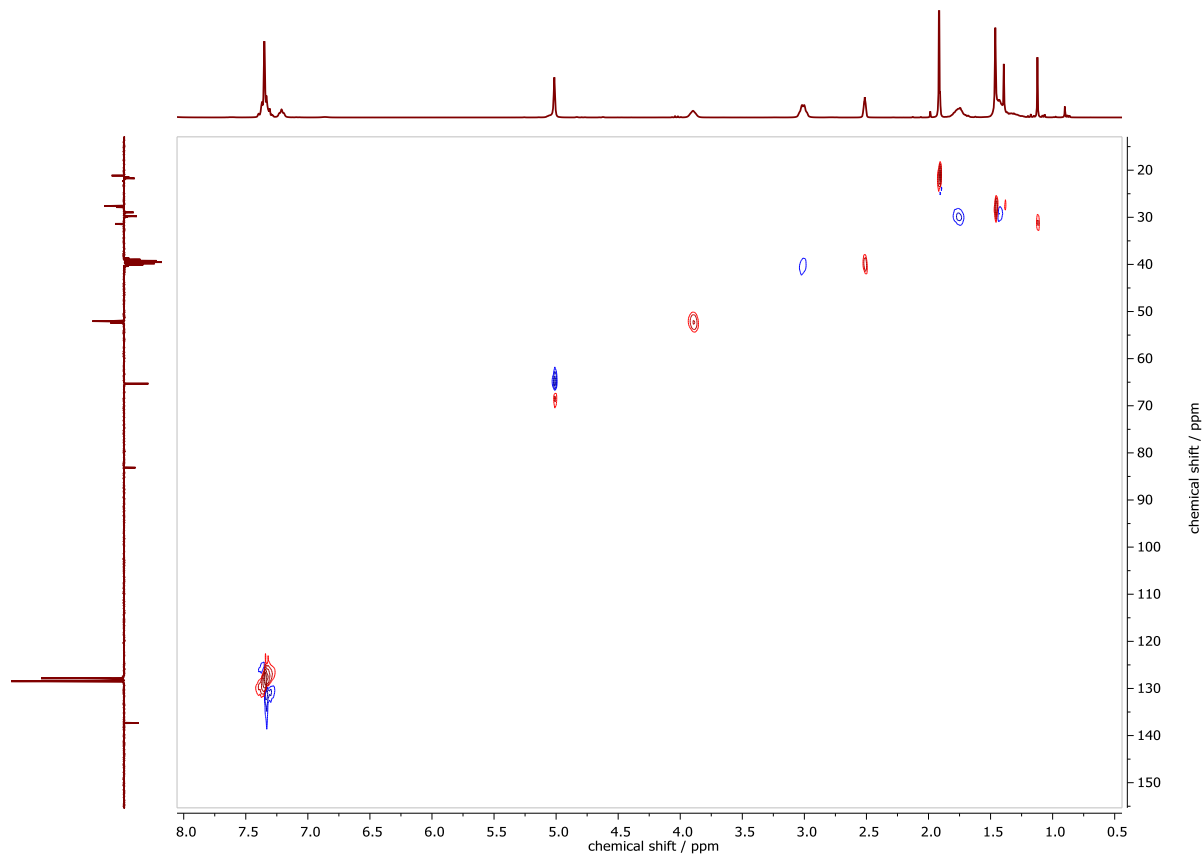


Figure 7.76 ^1H , ^{13}C HSQCed NMR of HLys(Cbz)-OtBu in DMSO- d_6 .

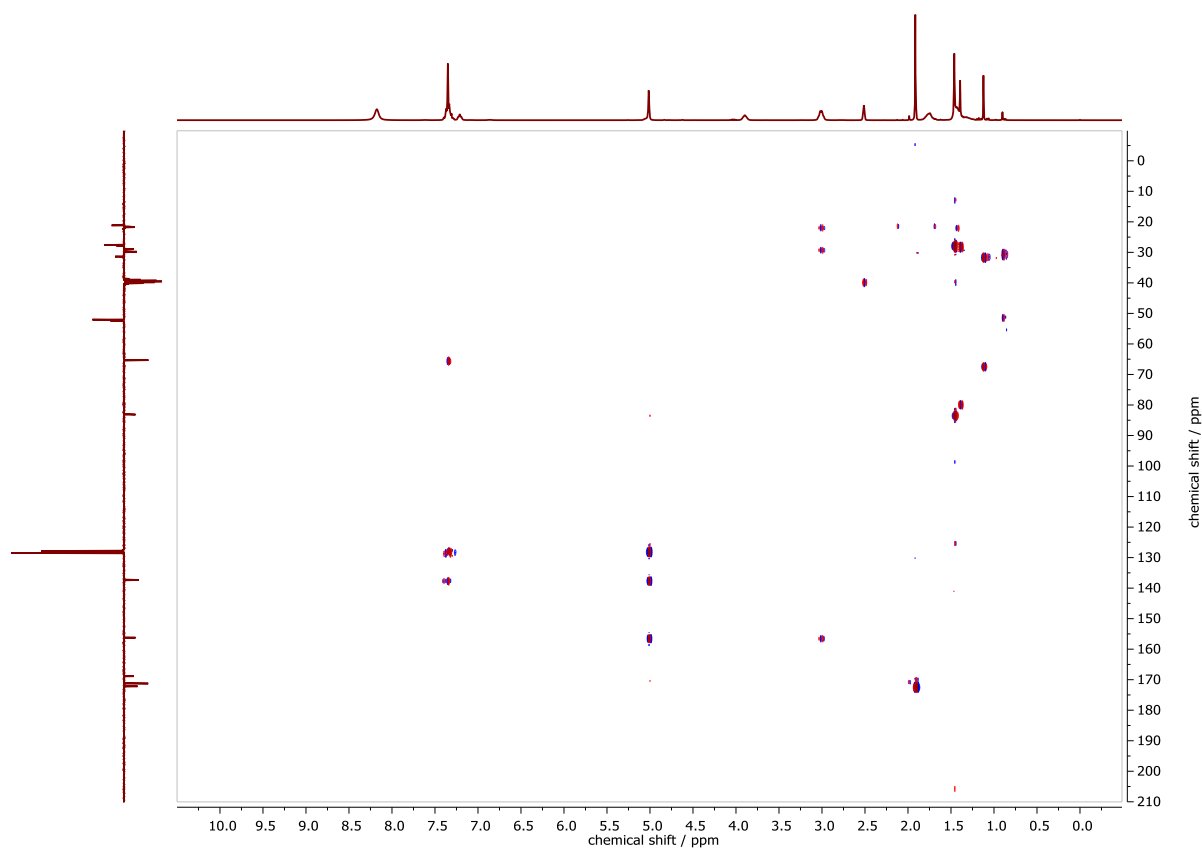


Figure 7.77 ^1H , ^{13}C HMBC NMR of HLys(Cbz)-OtBu in DMSO- d_6 .

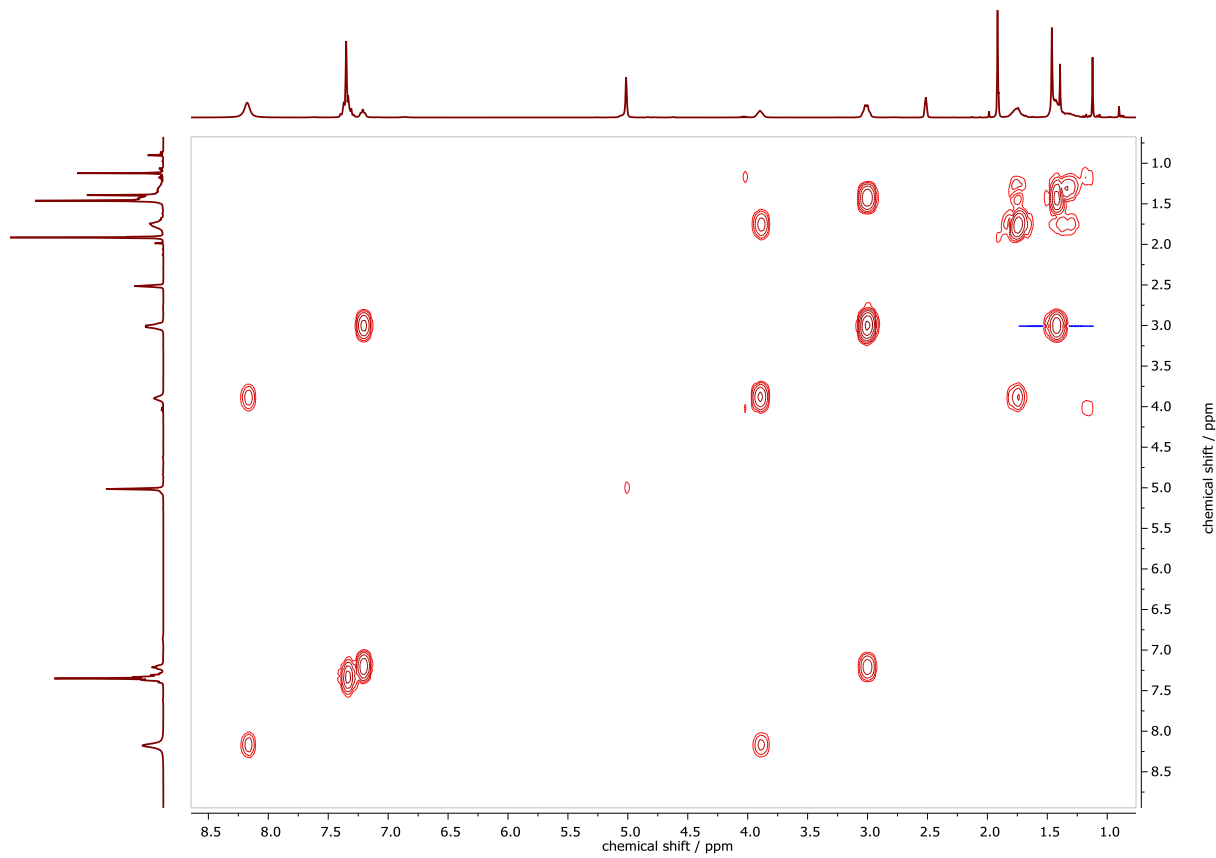


Figure 7.78 ^1H , ^1H COSY NMR of HLys(Cbz)-OtBu in DMSO- d_6 .

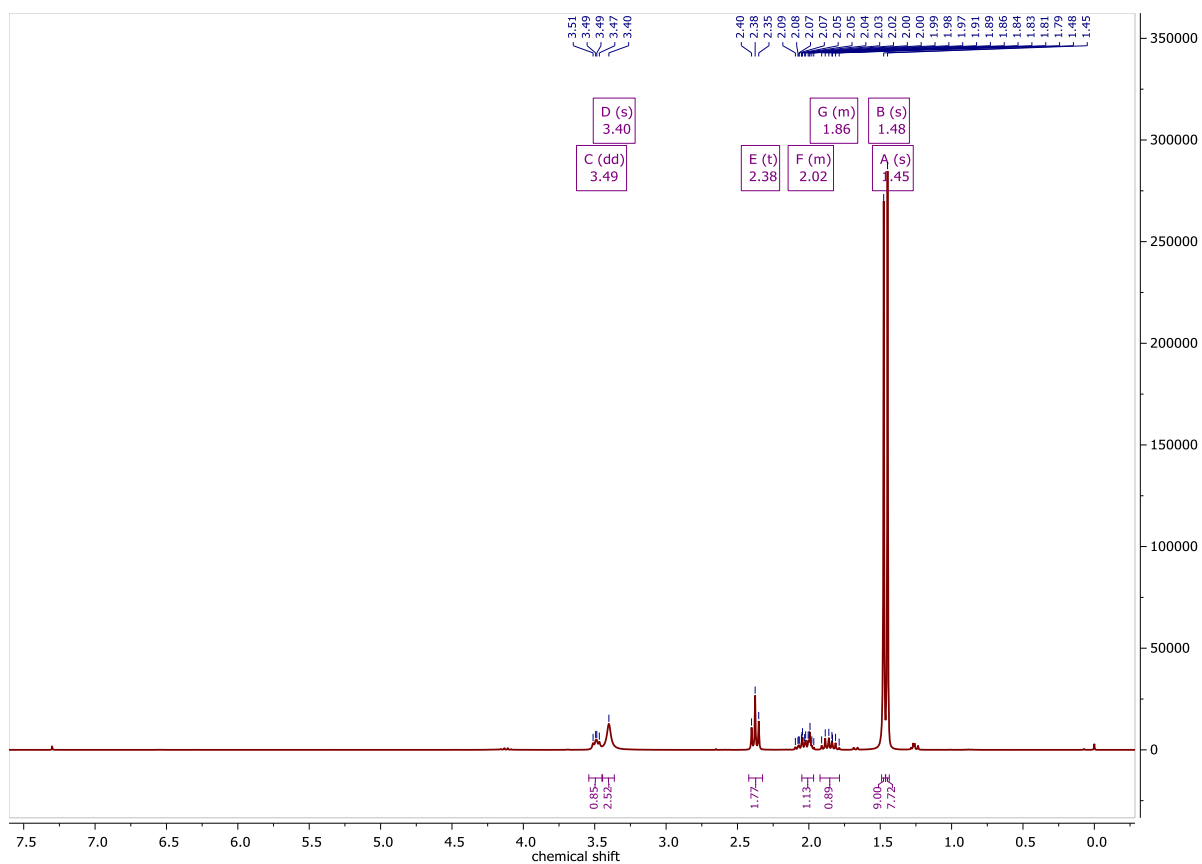


Figure 7.79 ^1H NMR of Glu(OtBu)-OtBu in CDCl_3 at 300 MHz.

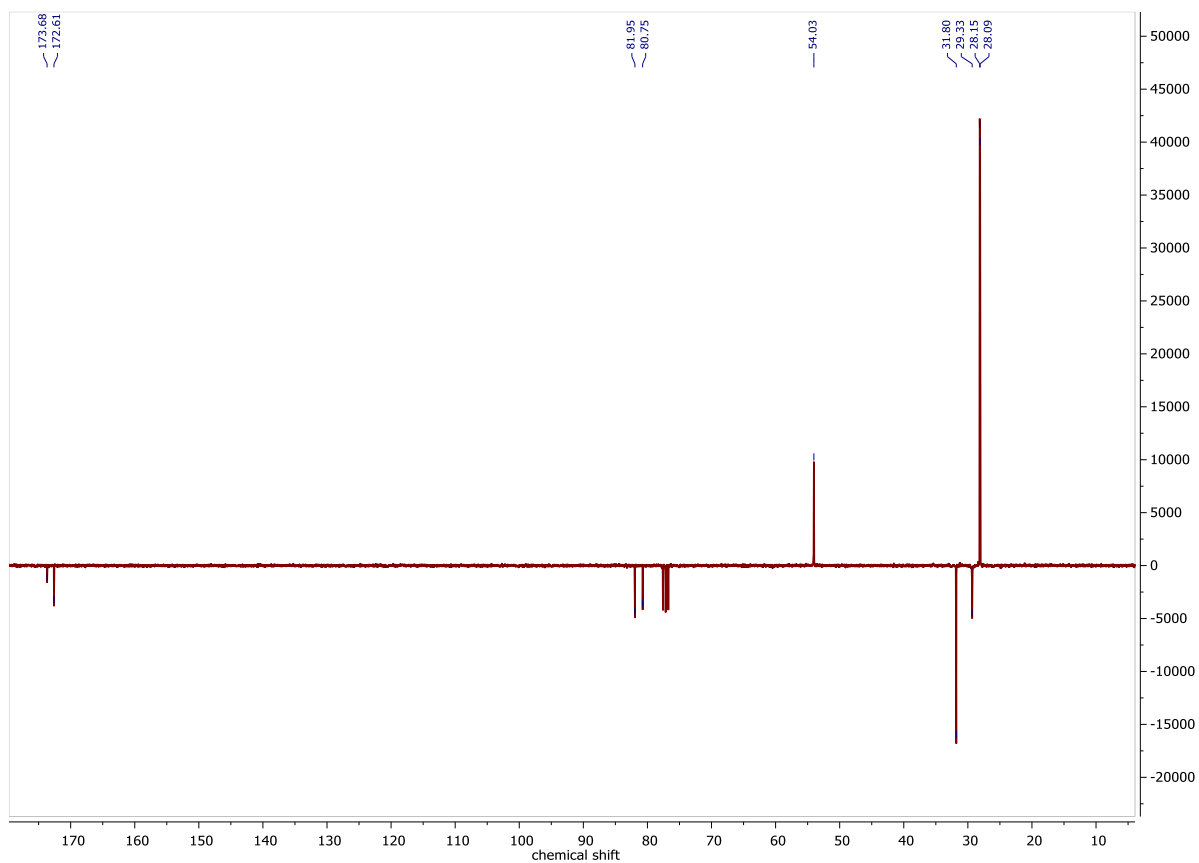


Figure 7.80 $^{13}\text{C}\{^1\text{H}\}$ DEPTQ NMR of Glu(OtBu)-OtBu in CDCl_3 at 75 MHz.

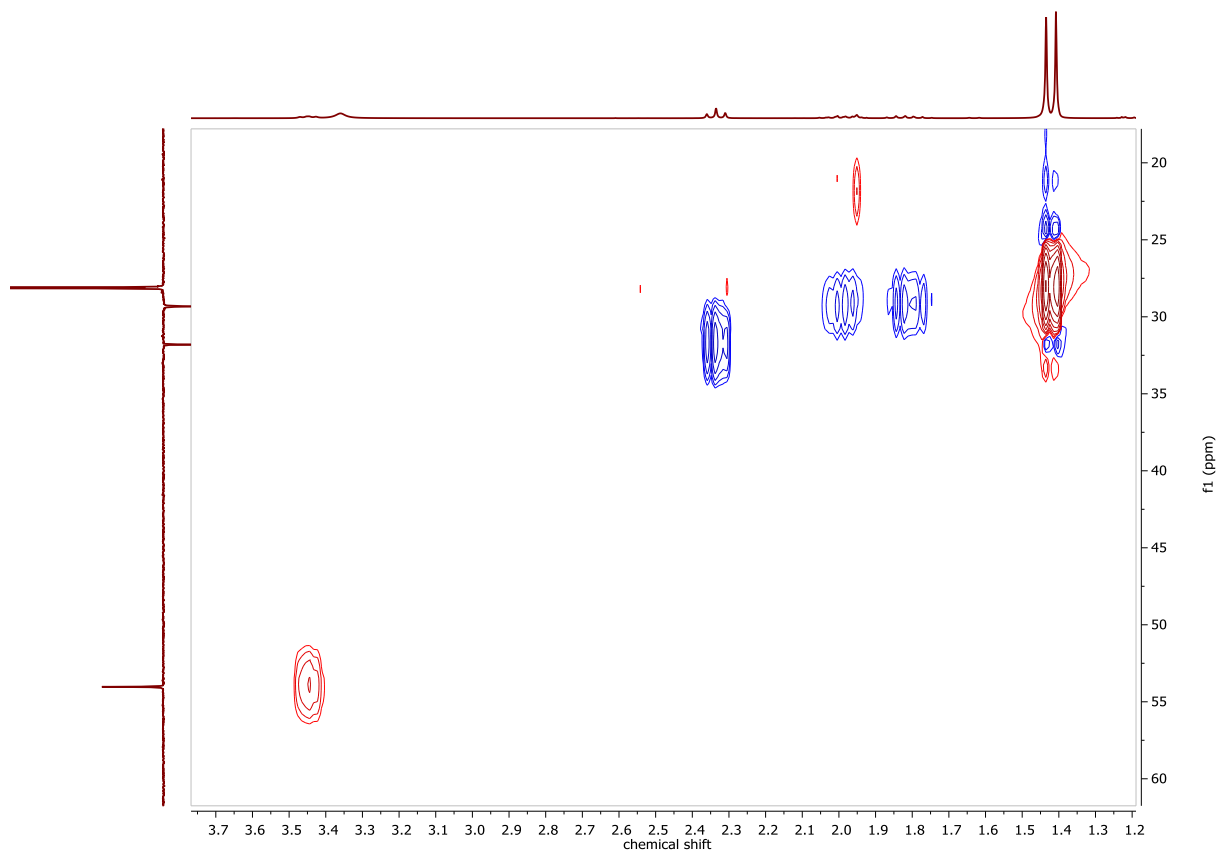


Figure 7.81 $^1\text{H},^{13}\text{C}$ HSQCed NMR of Glu(OtBu)-OtBu in CDCl_3 .

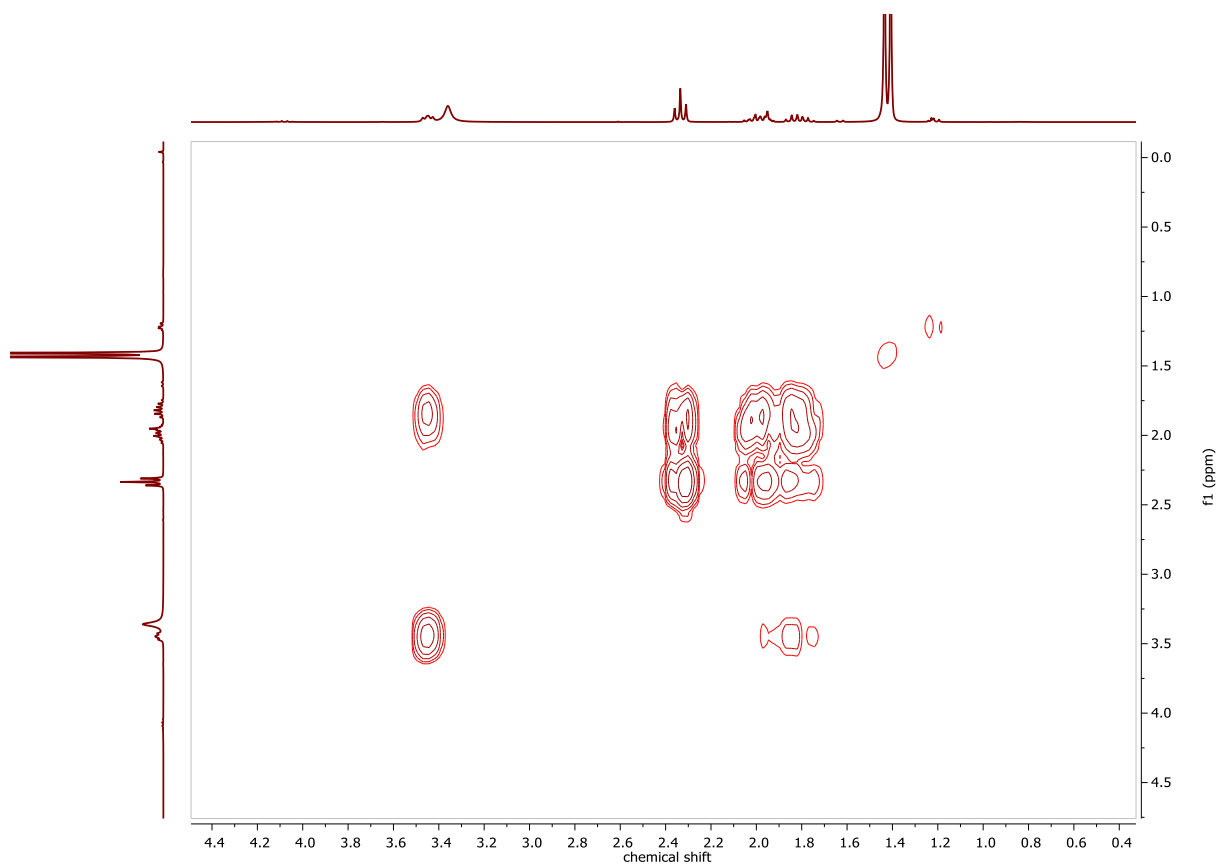


Figure 7.82 $^1\text{H},^1\text{H}$ COSY NMR of Glu(OtBu)-OtBu in CDCl_3 .

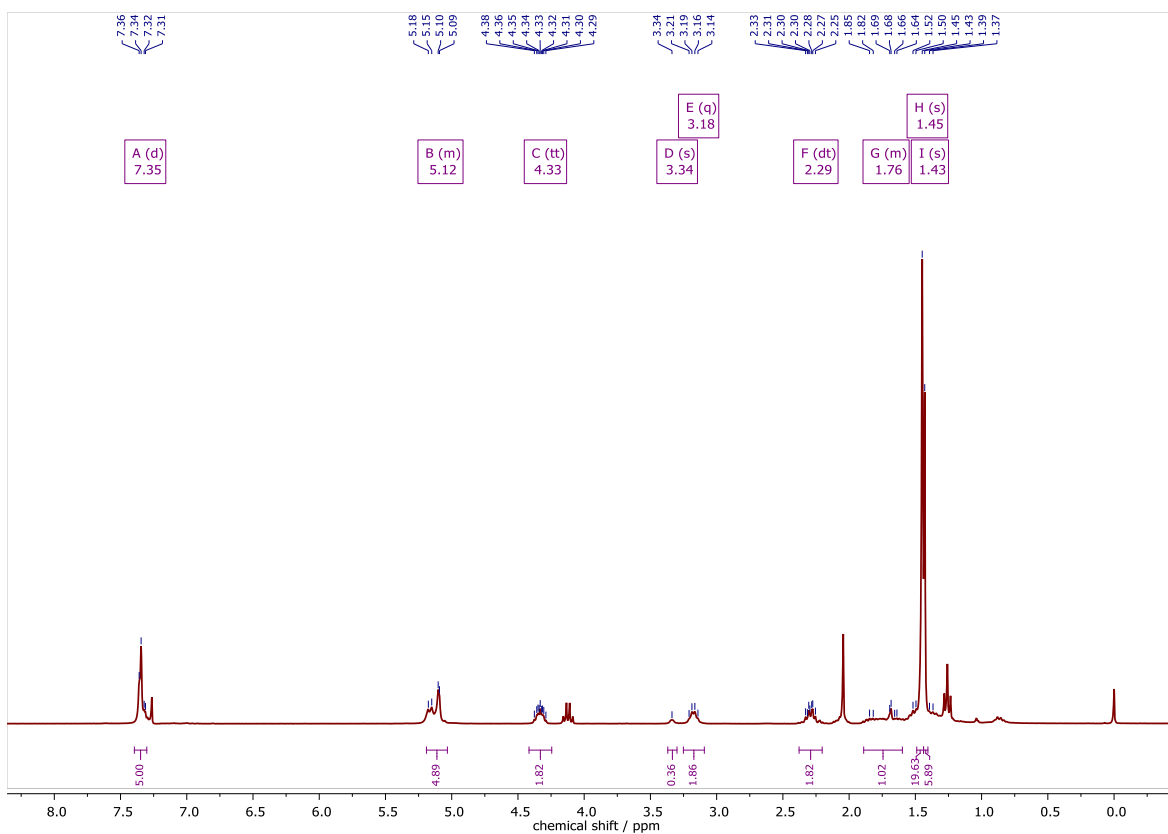


Figure 7.83 ^1H NMR of tBuO-Glu(OtBu)-u-Lys(Cbz)-OtBu in CDCl_3 at 300 MHz.

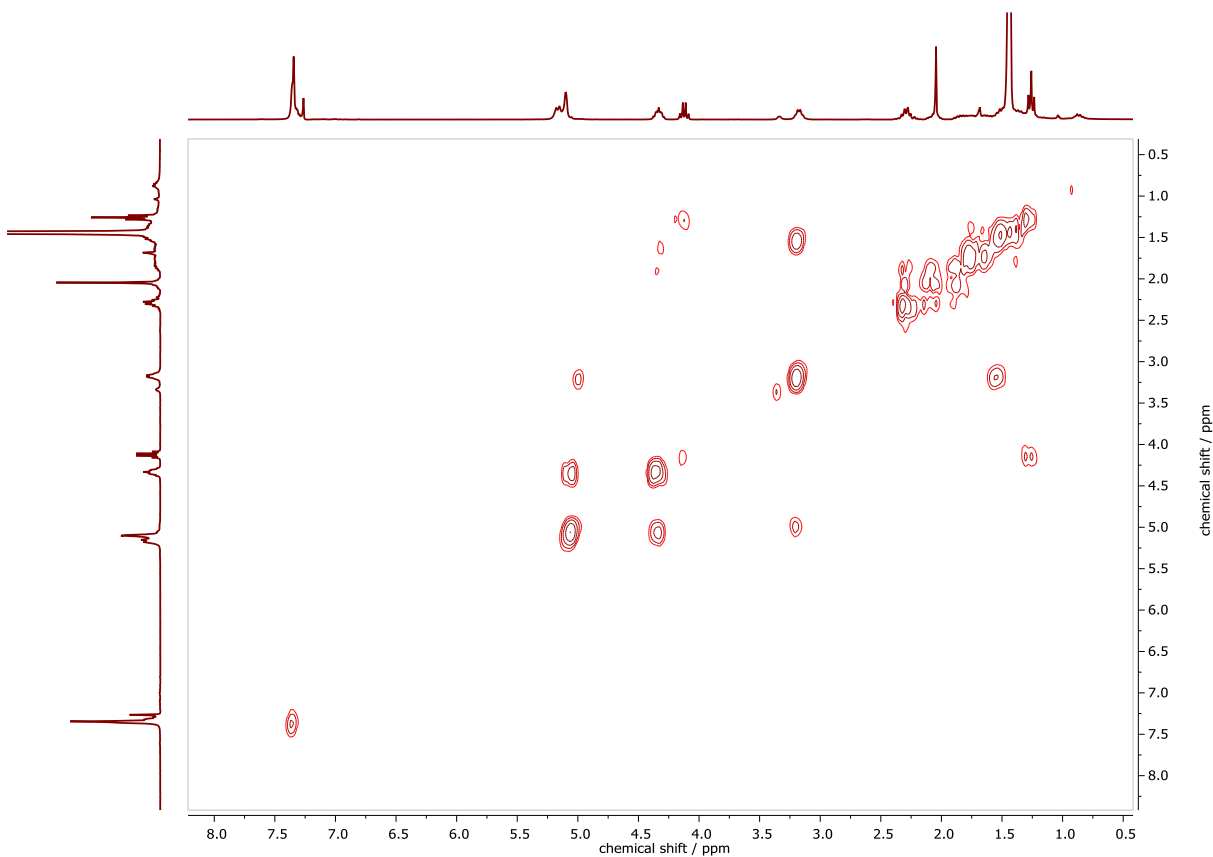


Figure 7.84 $^1\text{H}, ^1\text{H}$ COSY NMR of tBuO-Glu(OtBu)-u-Lys(Cbz)-OtBu in CDCl_3 .

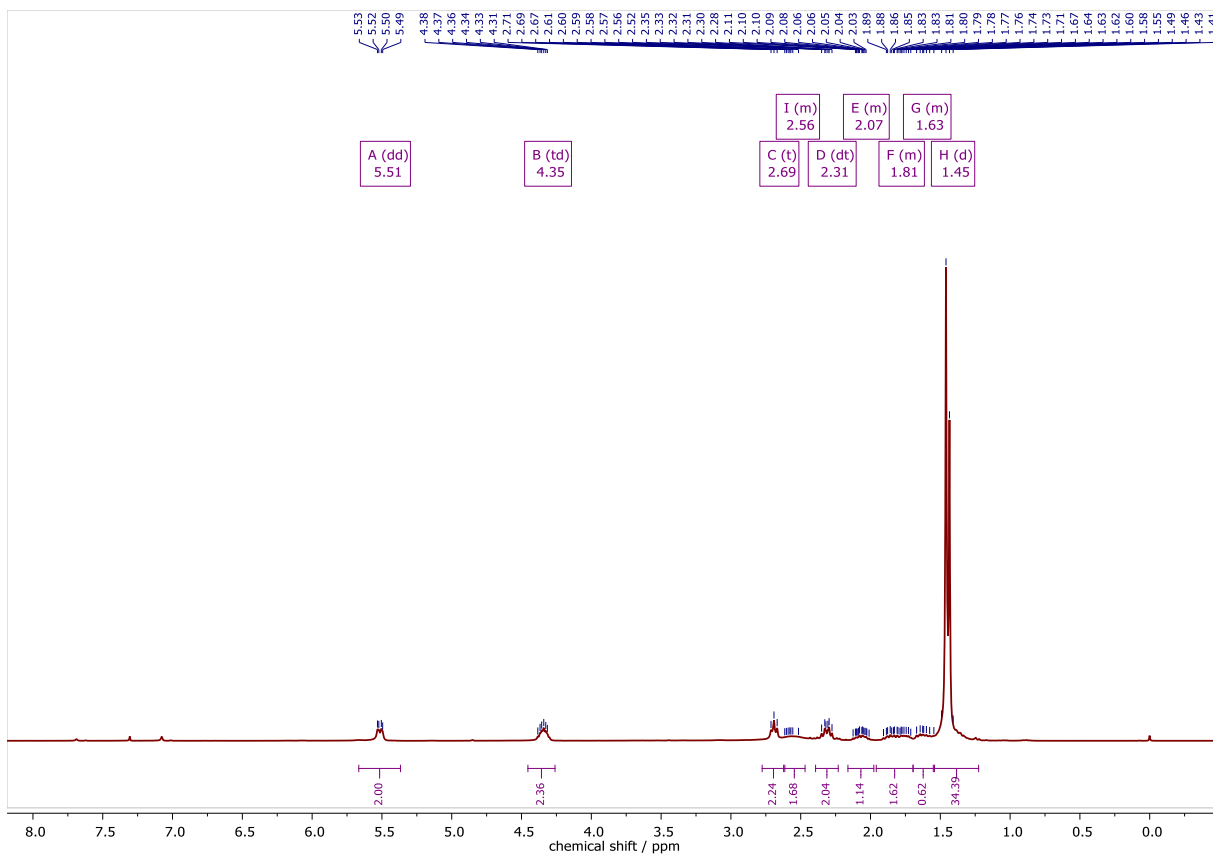


Figure 7.85 ^1H NMR of tBuO-Glu(OtBu)-u-Lys-OtBu in CDCl_3 at 300 MHz.

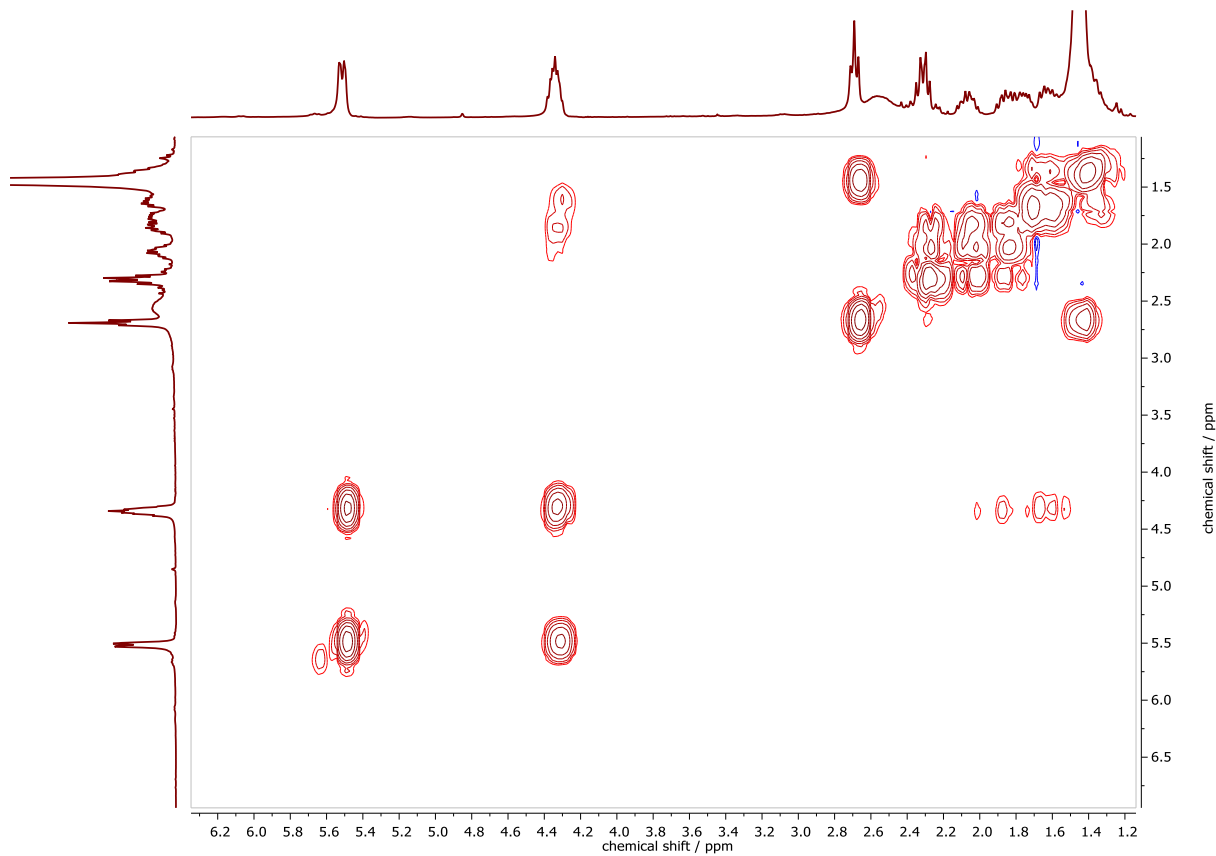


Figure 7.86 $^1\text{H}, ^1\text{H}$ COSY NMR of tBuO-Glu(OtBu)-u-Lys-OtBu in CDCl_3 .

7.2. NMR spectra of the synthesized ketones and their precursors

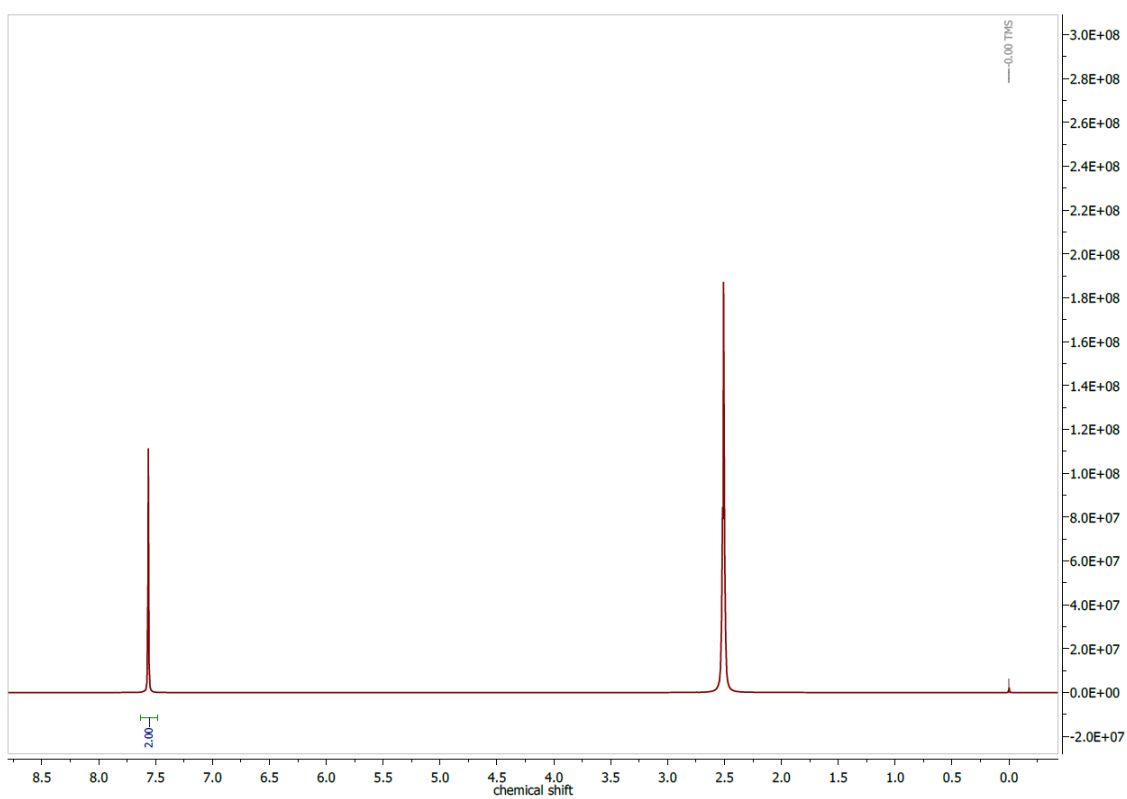


Figure 7.87 ^1H NMR spectrum of chelidamic acid in $\text{DMSO-}d_6$ at 300 MHz.

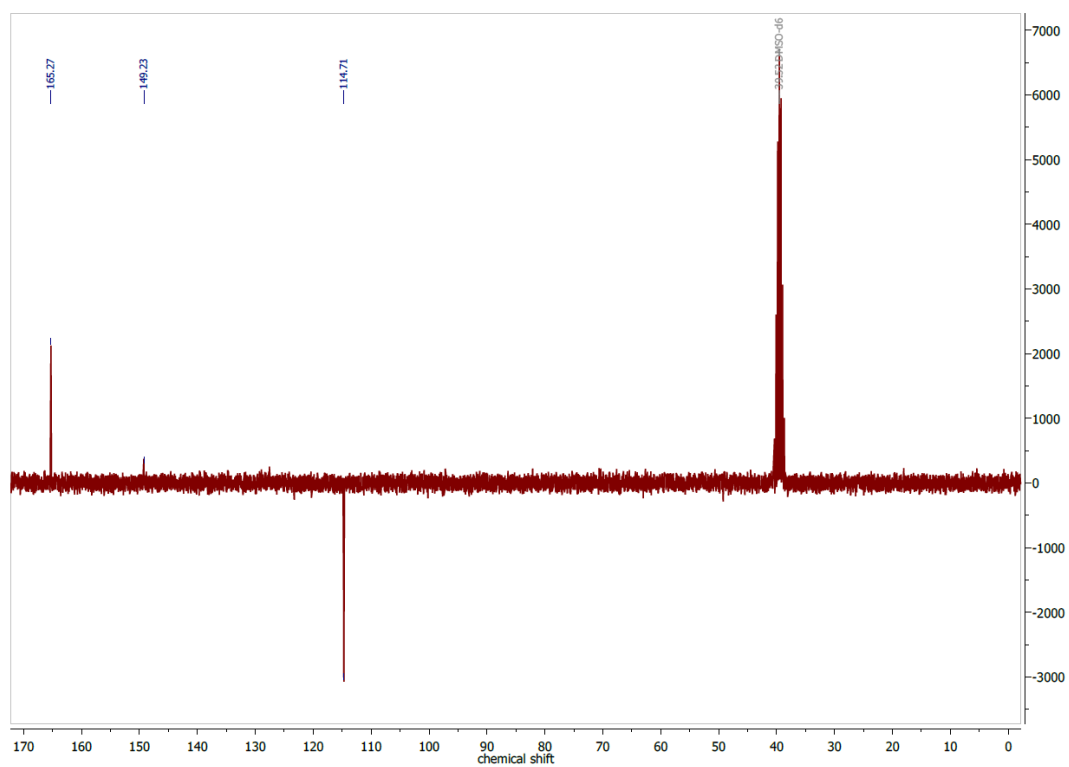


Figure 7.88 ^{13}C APT NMR spectrum of chelidamic acid in $\text{DMSO-}d_6$ at 75 MHz.

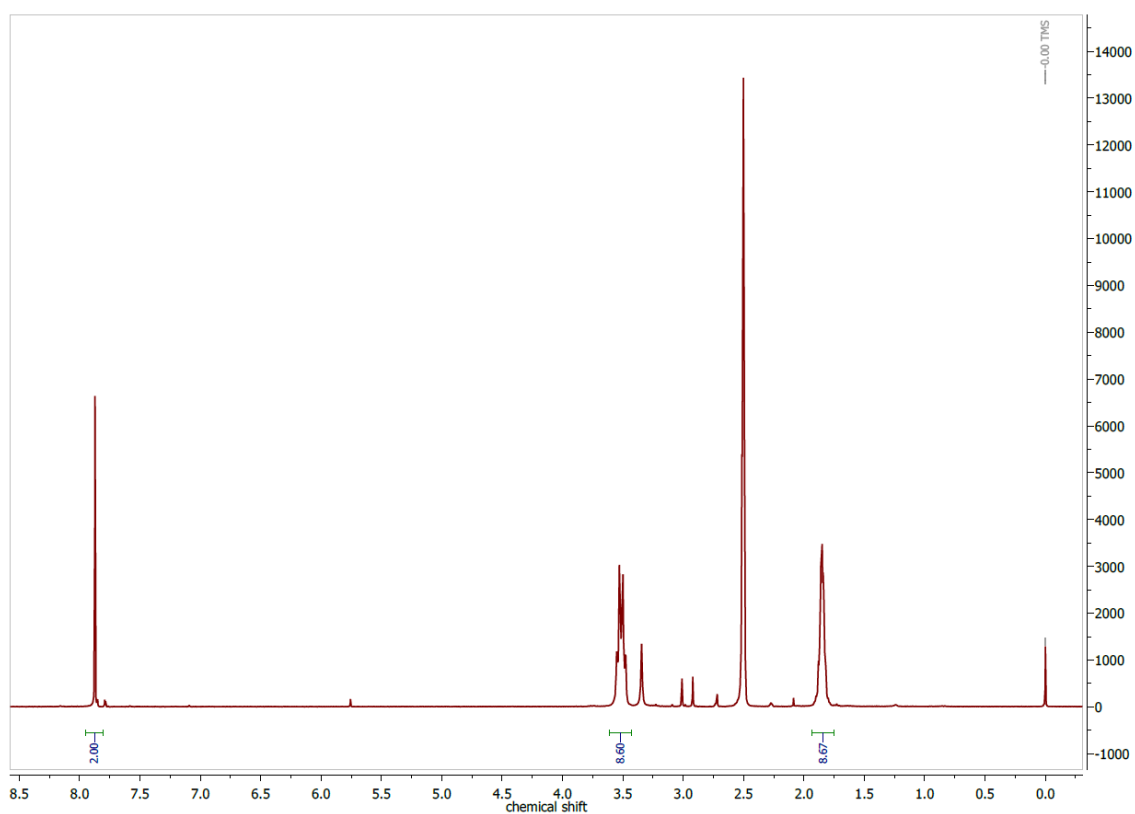


Figure 7.89 ^1H NMR spectrum of (4-chloropyridine-2,6-diyl)bis(pyrrolidine-1-ylmethanone) in $\text{DMSO-}d_6$ at 300 MHz.

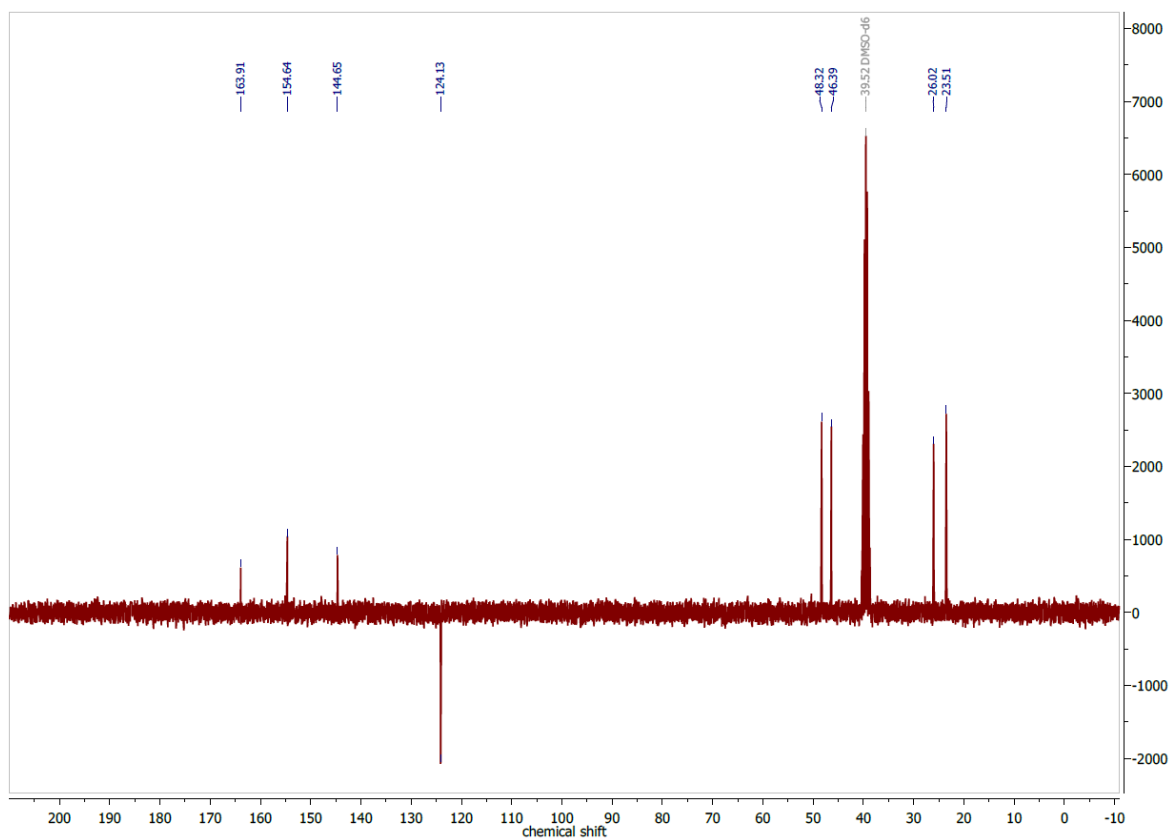


Figure 7.90 ^{13}C APT NMR spectrum of (4-chloropyridine-2,6-diyl)bis(pyrrolidine-1-ylmethanone) in $\text{DMSO-}d_6$ at 75 MHz.

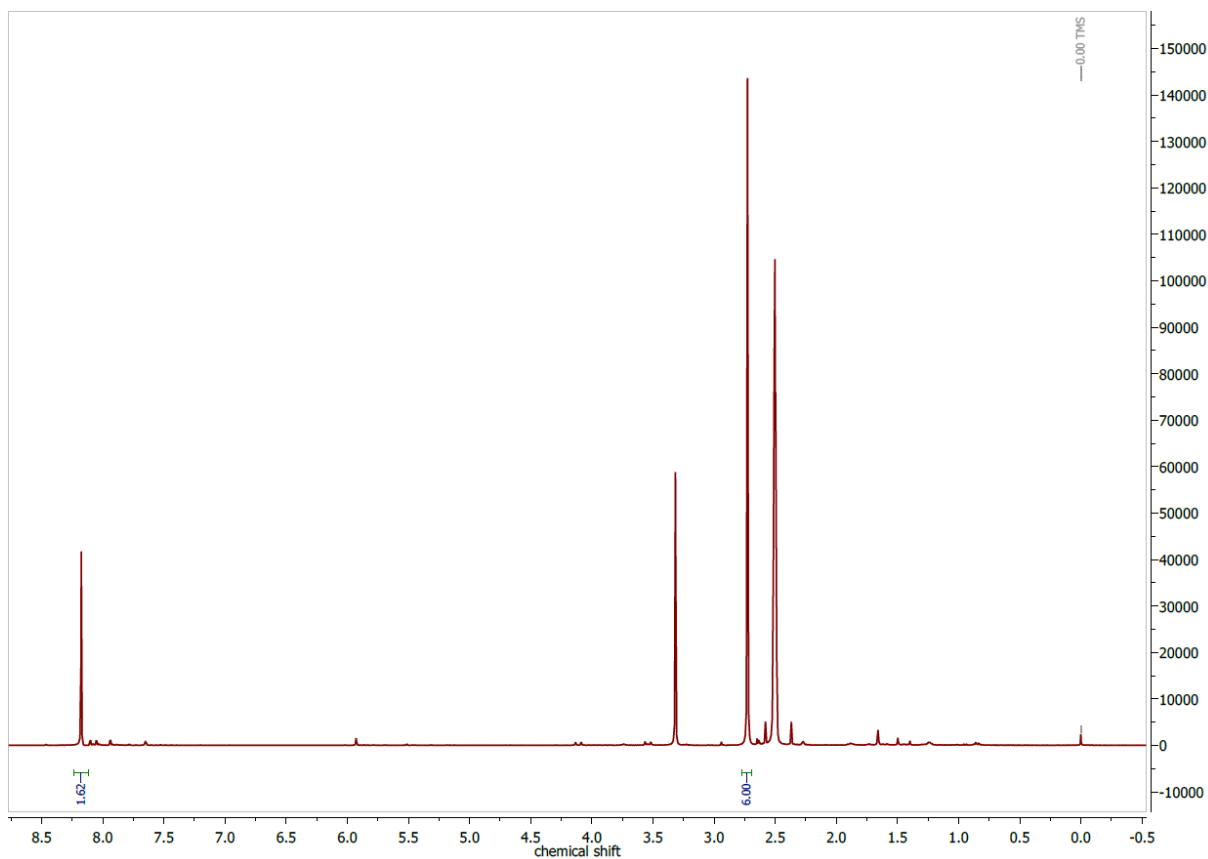


Figure 7.91 ^1H NMR spectrum of 2,6-diacetyl 4-chloropyridine in $\text{DMSO}-d_6$ at 300 MHz.

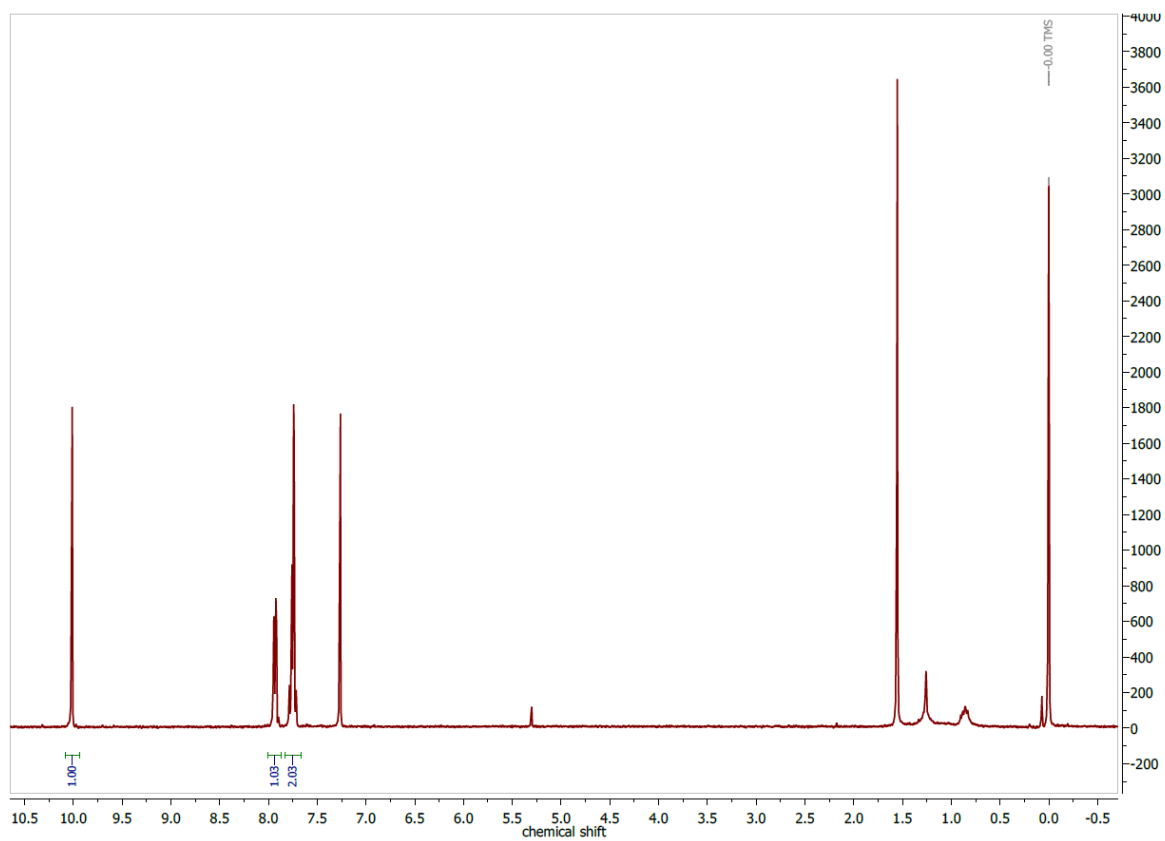


Figure 7.92 ^1H NMR spectrum of 6-bromo picolinaldehyde in $\text{DMSO}-d_6$ at 300 MHz.

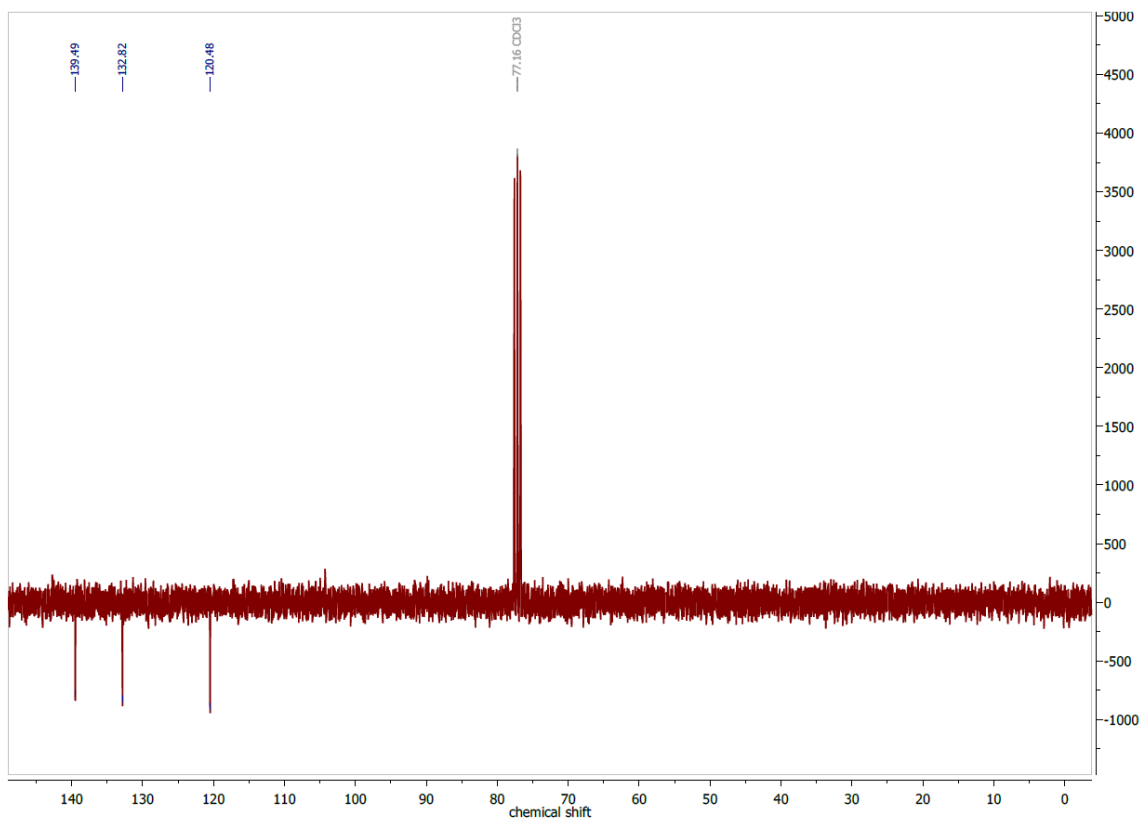


Figure 7.93 $^{13}\text{C}\{^1\text{H}\}$ DEPTQ NMR spectrum of 6-bromo picolinaldehyde in DMSO- d_6 at 75 MHz.

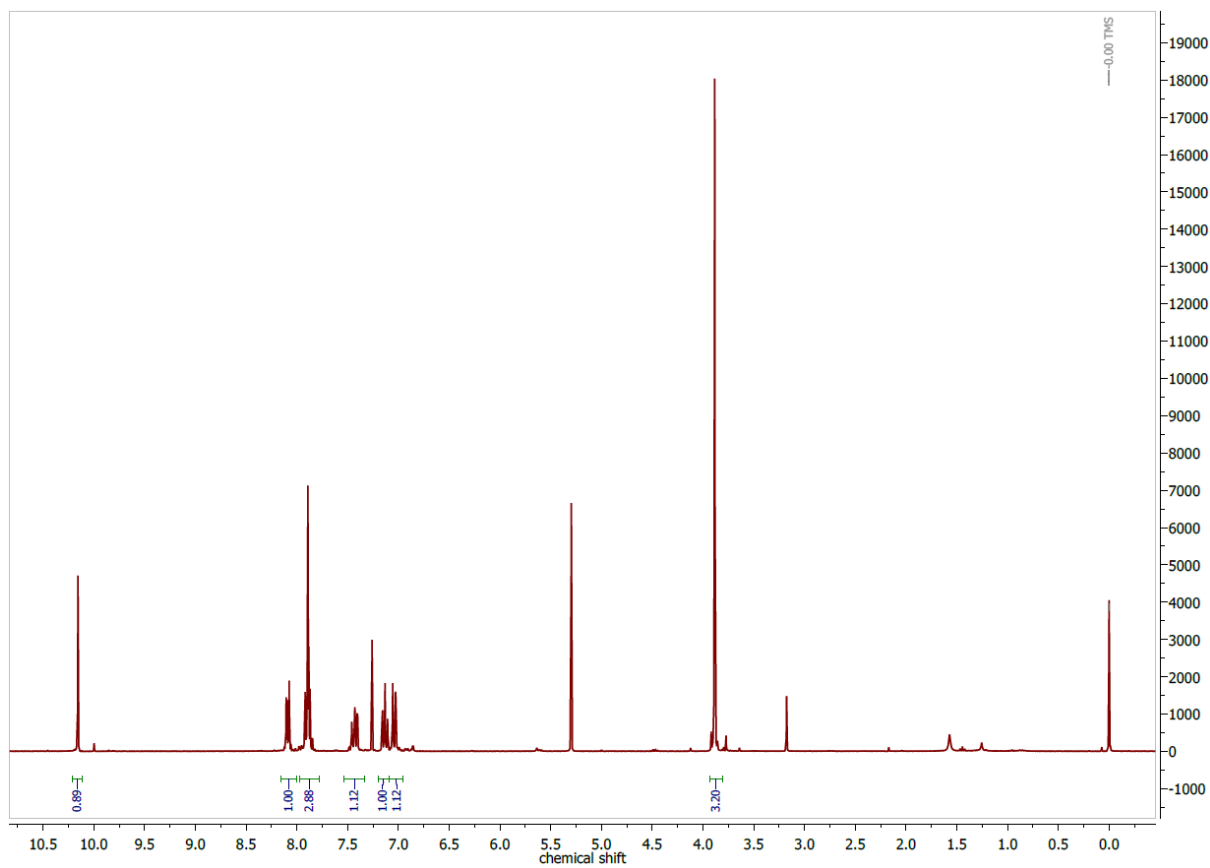


Figure 7.94 ^1H NMR spectrum of 6-(2-methoxyphenyl) picolinaldehyde in DMSO- d_6 at 300 MHz.

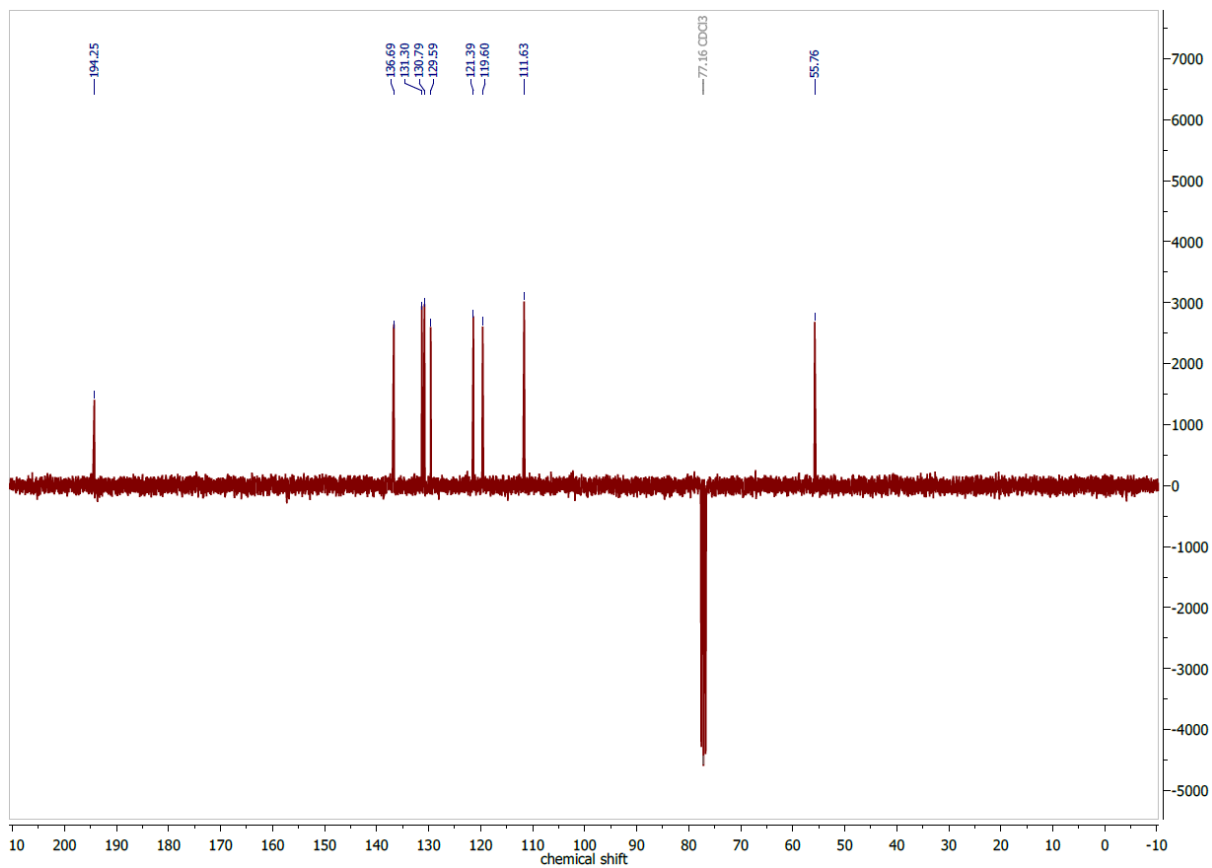


Figure 7.95 $^{13}\text{C}\{^1\text{H}\}$ DEPTQ NMR spectrum of 6-(2-methoxyphenyl) picolinaldehyde in $\text{DMSO}-d_6$ at 75 MHz.

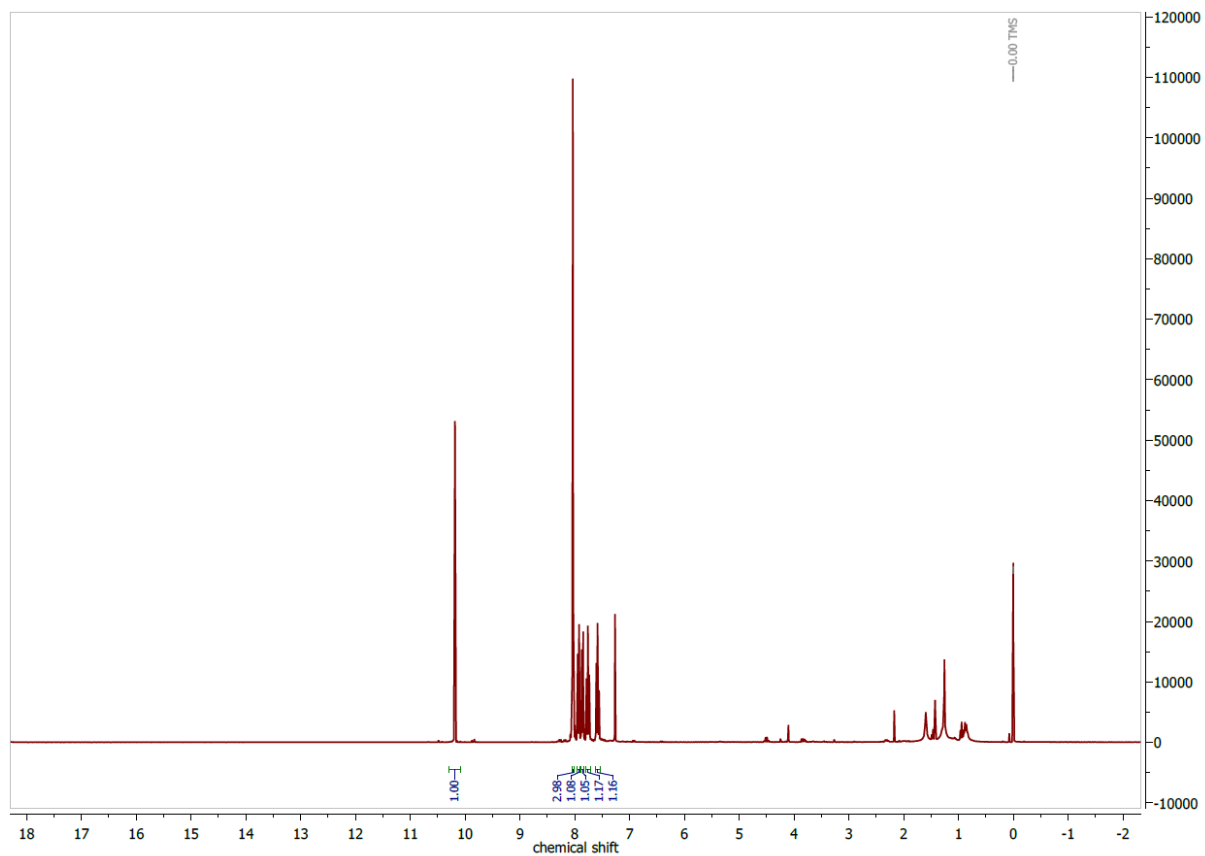


Figure 7.96 ^1H NMR spectrum of 6-(2-cyanophenyl) picolinaldehyde in $\text{DMSO}-d_6$ at 300 MHz.

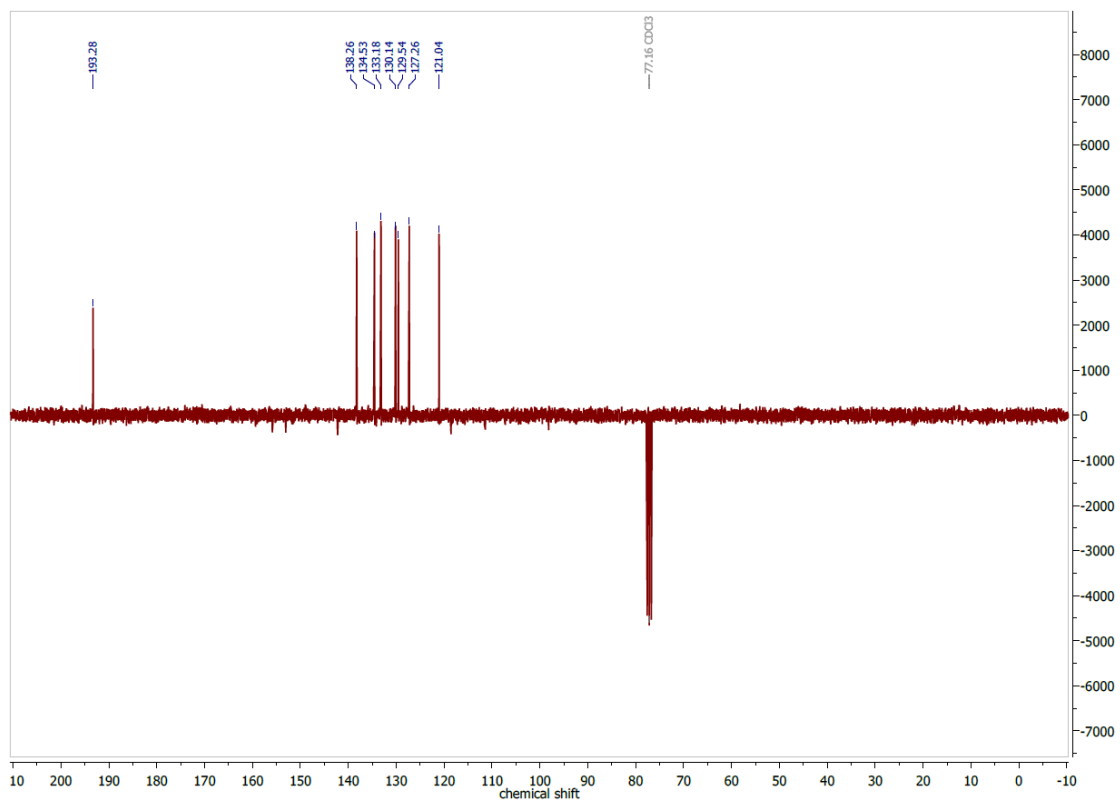


Figure 7.97 $^{13}\text{C}\{^1\text{H}\}$ DEPTQ NMR spectrum of 6-(2-cyanophenyl) picolinaldehyde in $\text{DMSO-}d_6$ at 75 MHz.

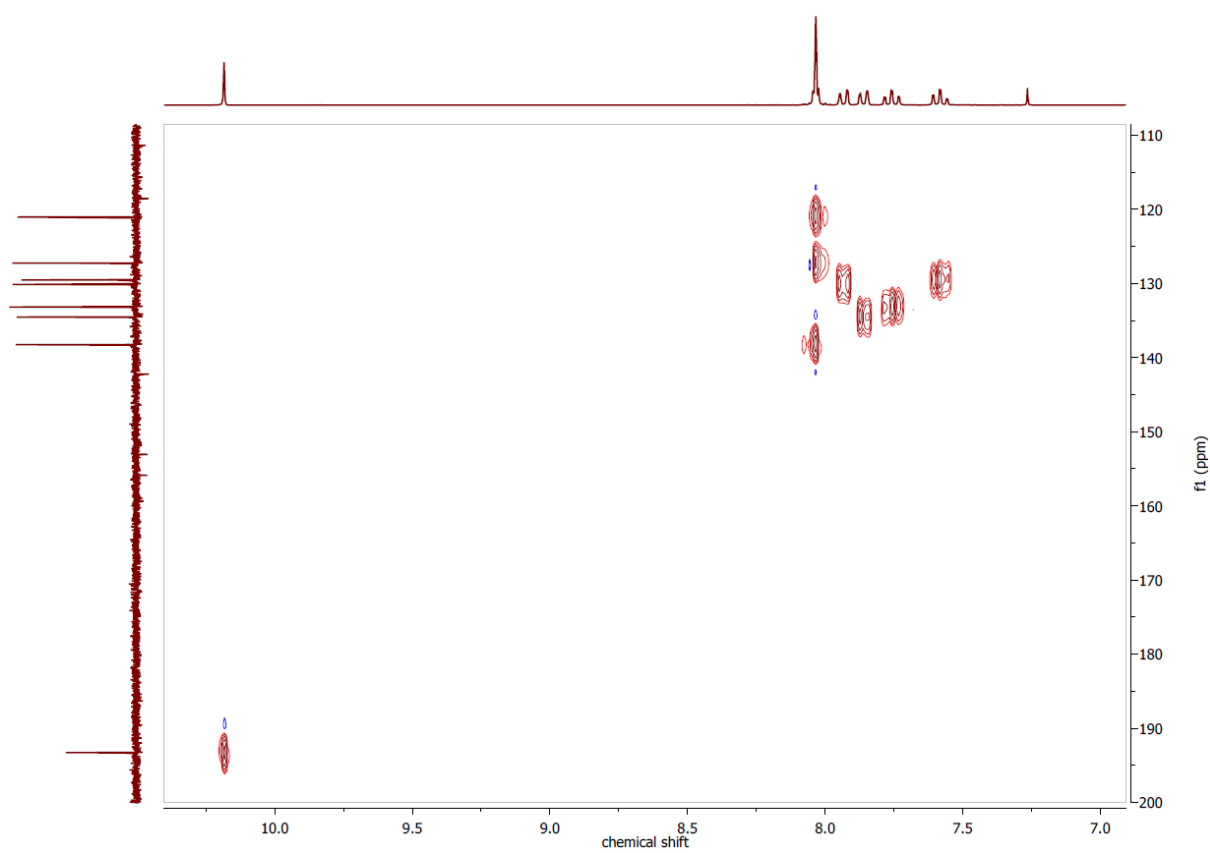


Figure 7.98 $^1\text{H},^{13}\text{C}$ HSQCed NMR spectrum of 6-(2-cyanophenyl) picolinaldehyde in $\text{DMSO-}d_6$.

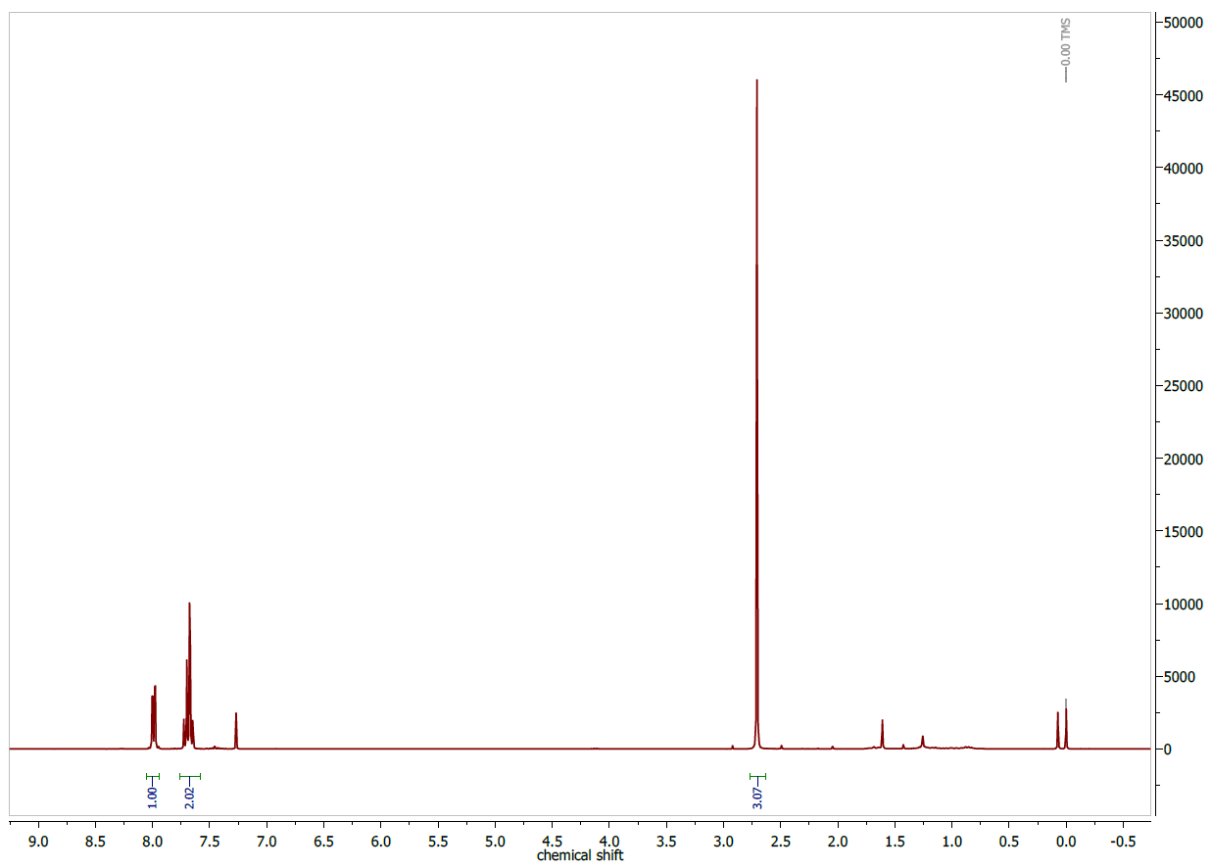


Figure 7.99 ^1H NMR spectrum of 2-acetyl 6-bromo pyridine in CDCl_3 at 300 MHz.

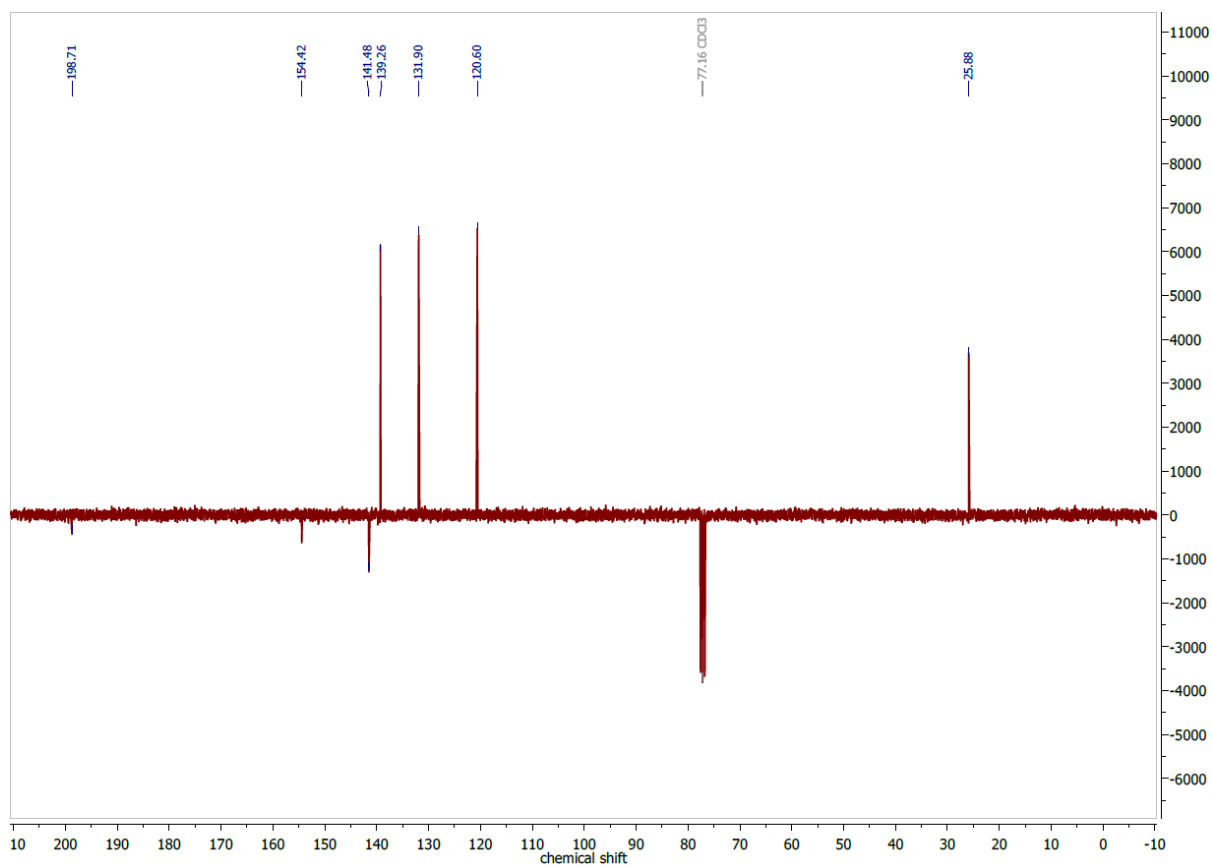


Figure 7.100 $^{13}\text{C}\{^1\text{H}\}$ DEPTQ NMR spectrum of 2-acetyl 6-bromo pyridine in CDCl_3 at 75 MHz.

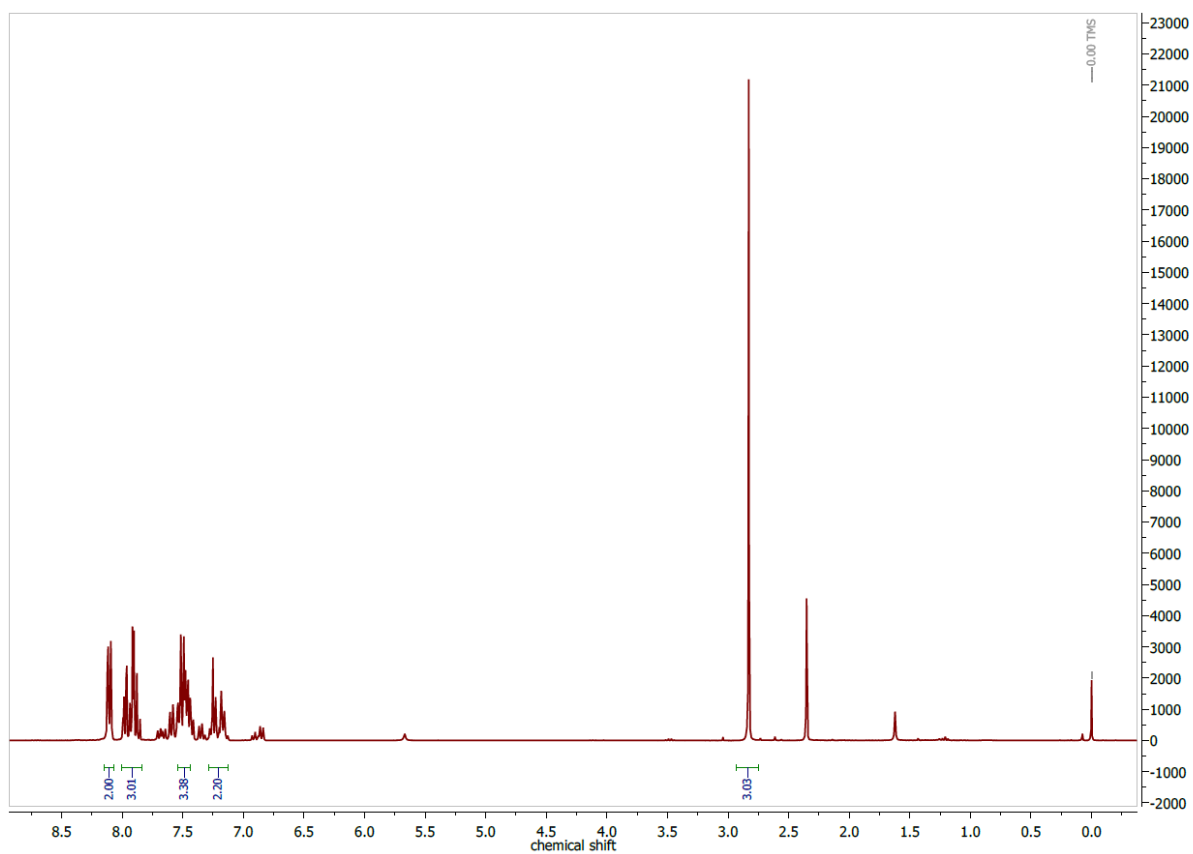


Figure 7.101 ^1H NMR spectrum of 2-acetyl 6-phenyl pyridine in CDCl_3 at 300 MHz.

7.2.1. Acridine synthesis

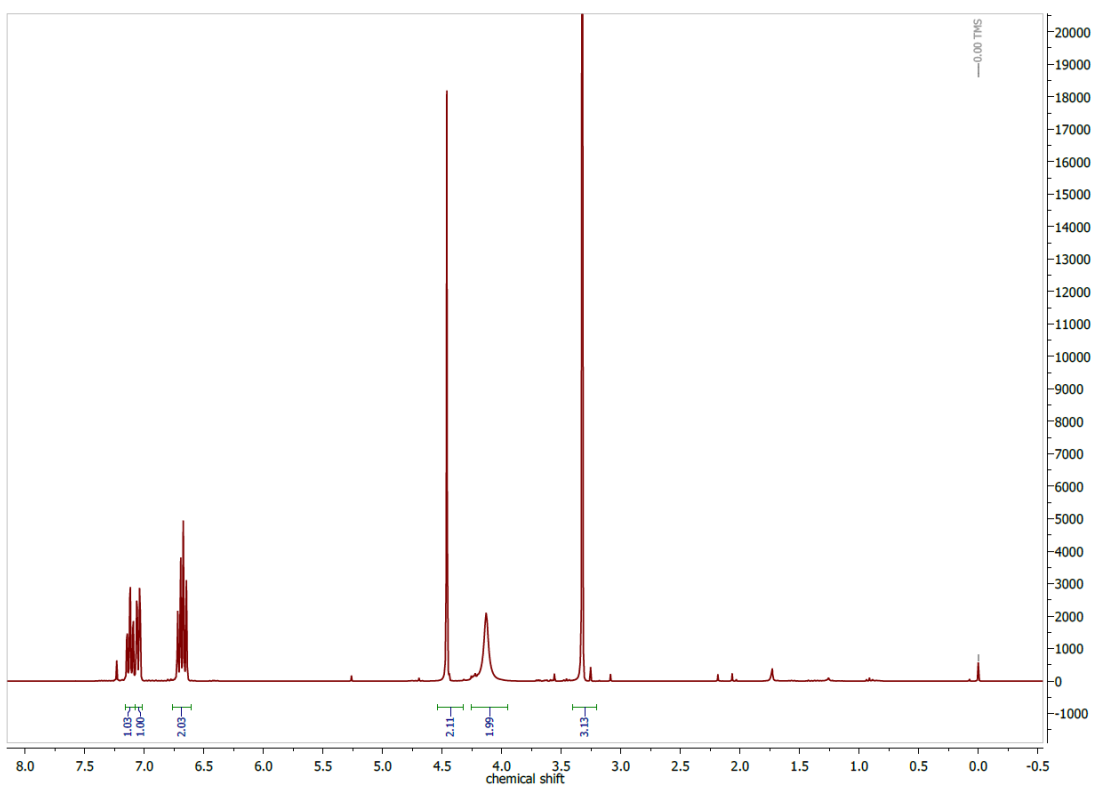


Figure 7.102 ^1H NMR spectrum of 2-methoxymethyl aniline in CDCl_3 at 300 MHz.

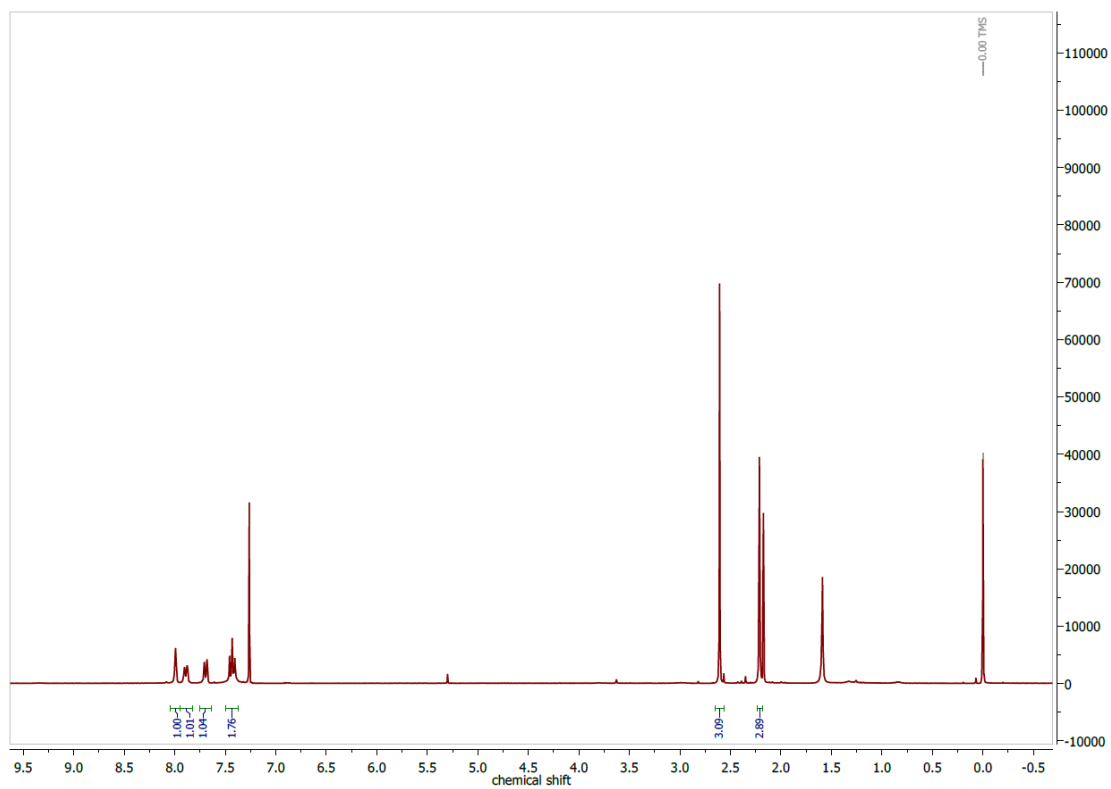


Figure 7.103 ^1H NMR spectrum of N-(3-acetylphenyl)acetamide in CDCl_3 at 300 MHz.

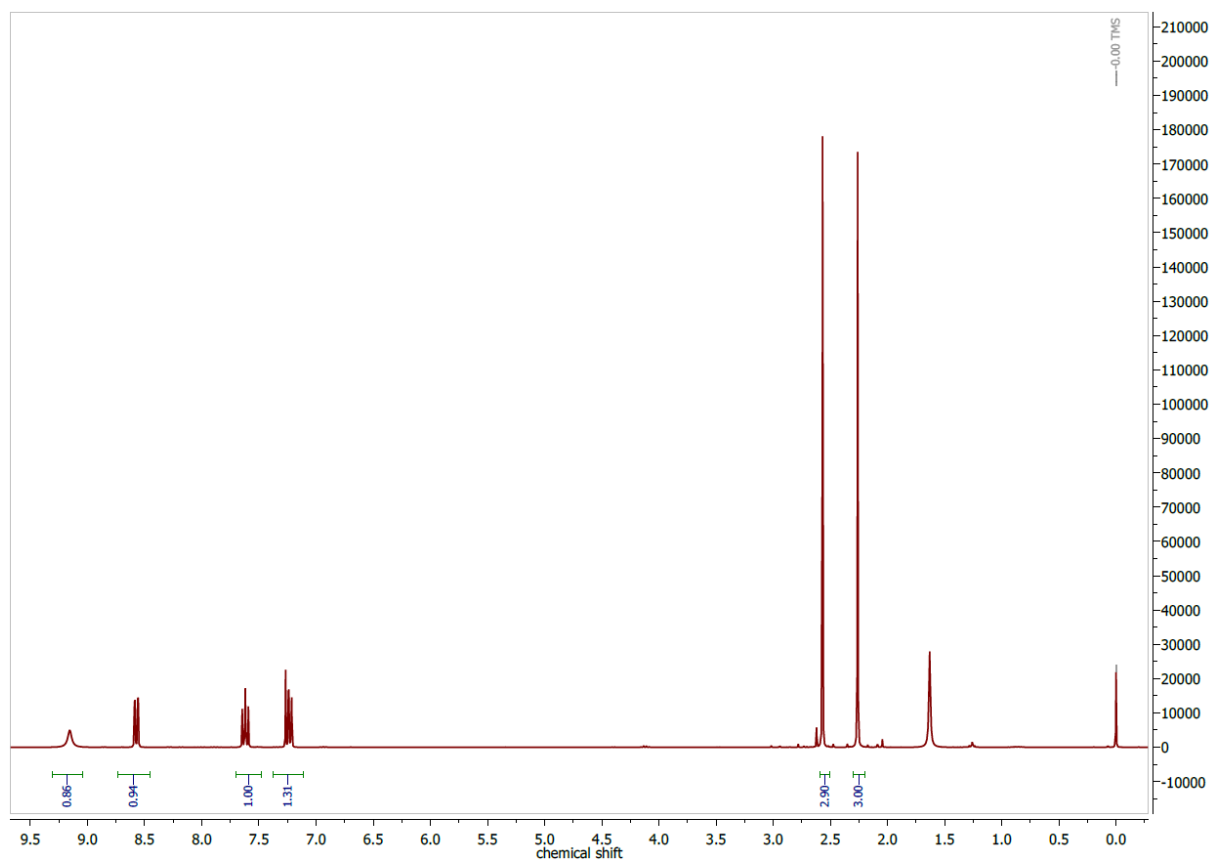


Figure 7.104 ^1H NMR spectrum of N-(3-acetyl-2-nitrophenyl)acetamide in CDCl_3 at 300 MHz.

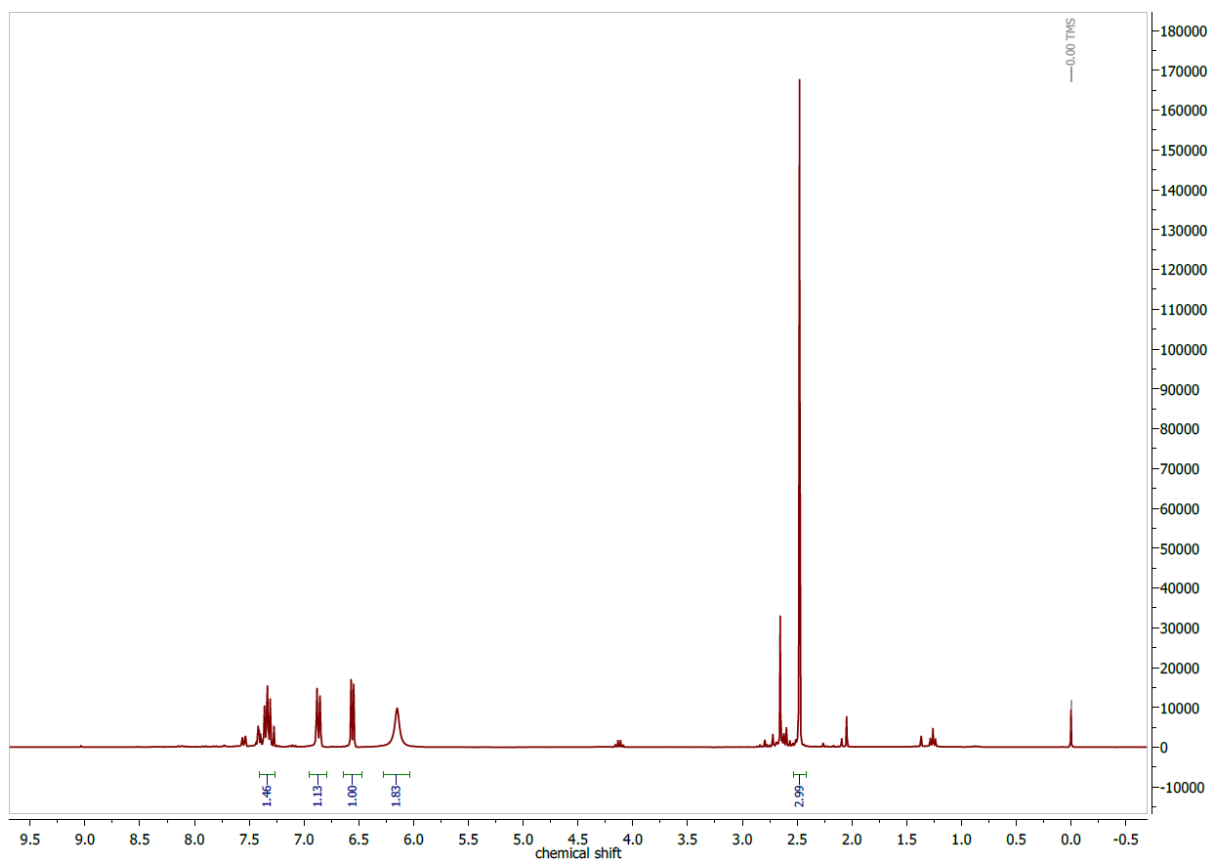


Figure 7.105 ^1H NMR spectrum of 1-(3-amino-2-nitrophenyl)ethan-1-one in CDCl_3 at 300 MHz.

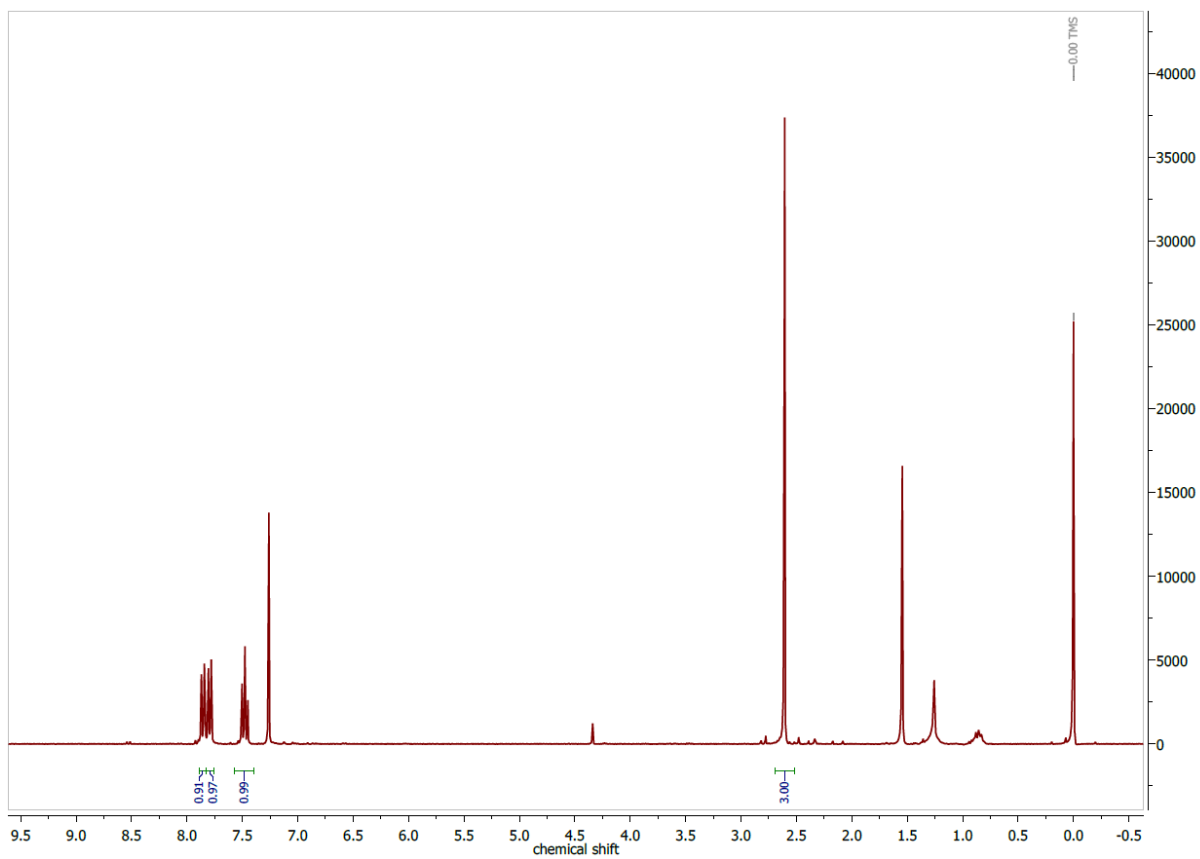


Figure 7.106 ^1H NMR spectrum of 1-(3-bromo-2-nitrophenyl)ethan-1-one in CDCl_3 at 300 MHz.

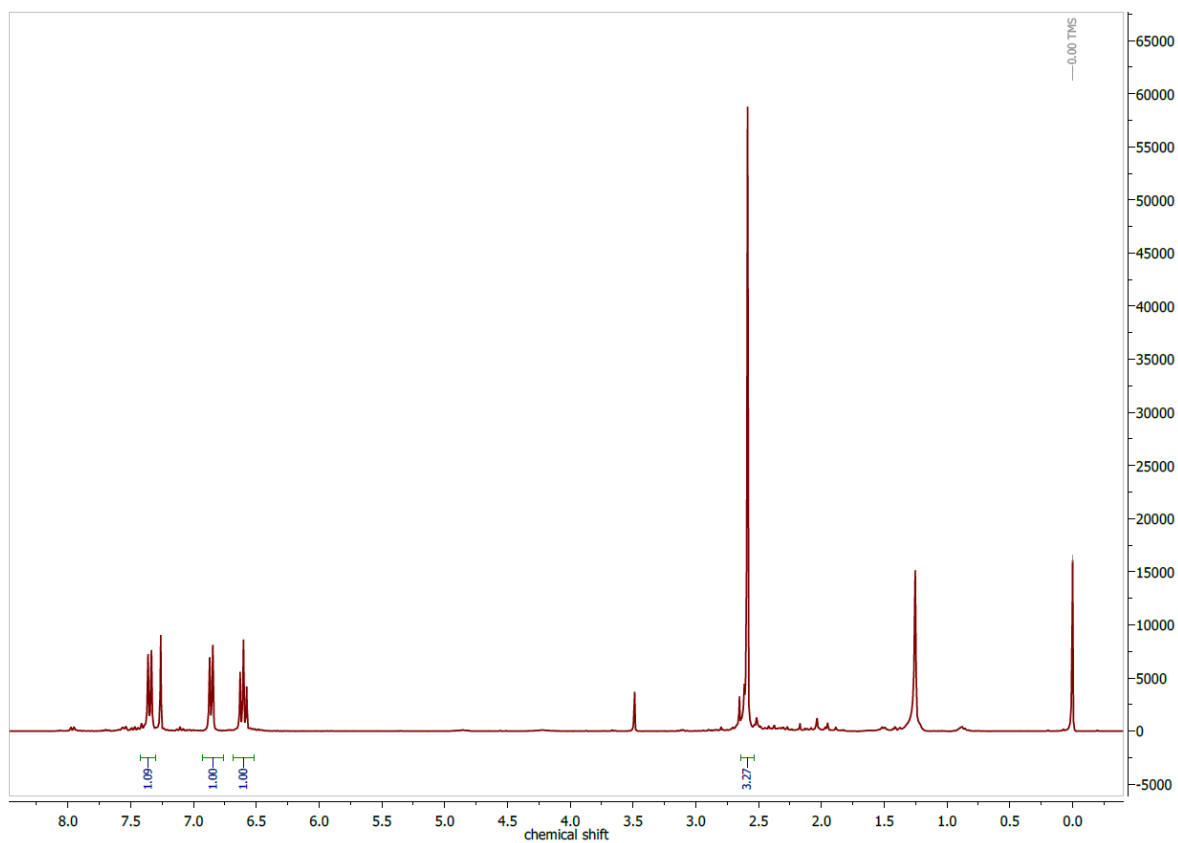


Figure 7.107 ¹H NMR spectrum of 1-(2,3-diaminophenyl)ethan-1-one in CDCl₃ at 300 MHz.

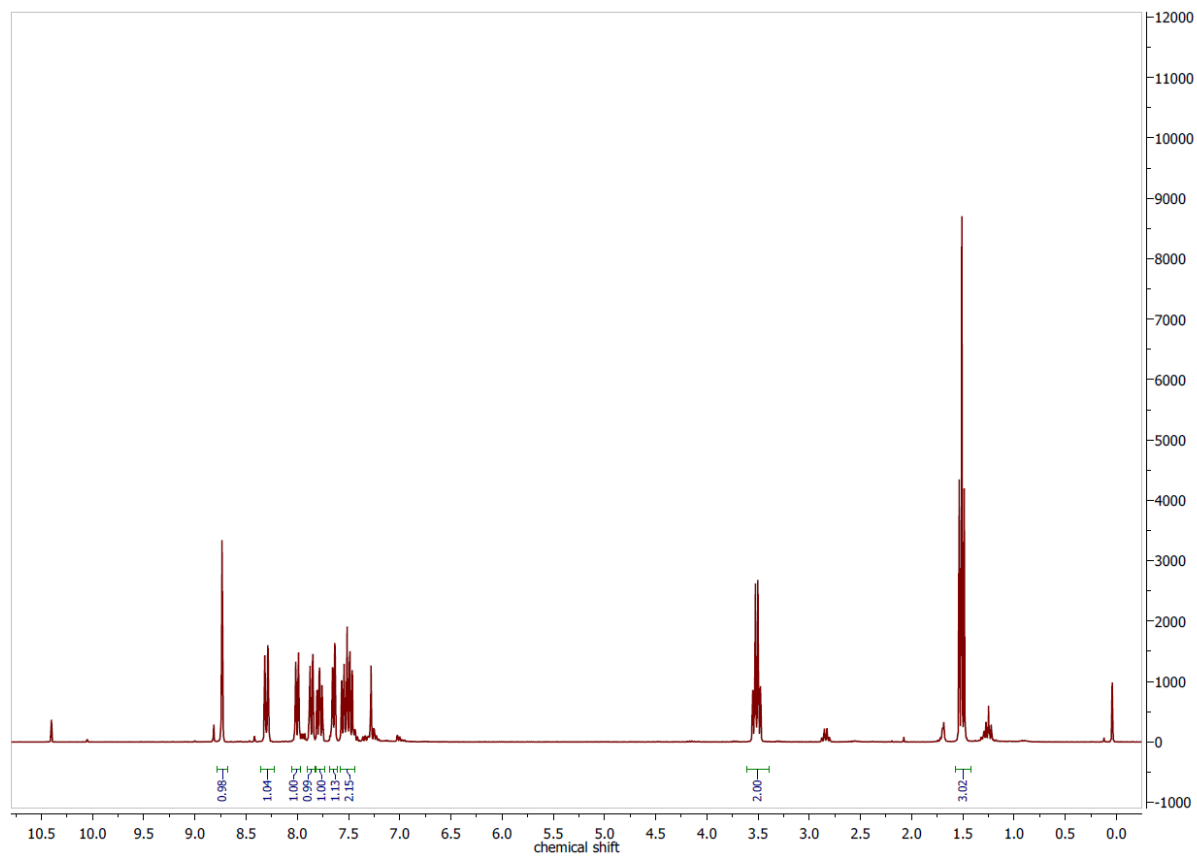


Figure 7.108 ¹H NMR spectrum of 4-ethylacridine in CDCl₃ at 300 MHz.

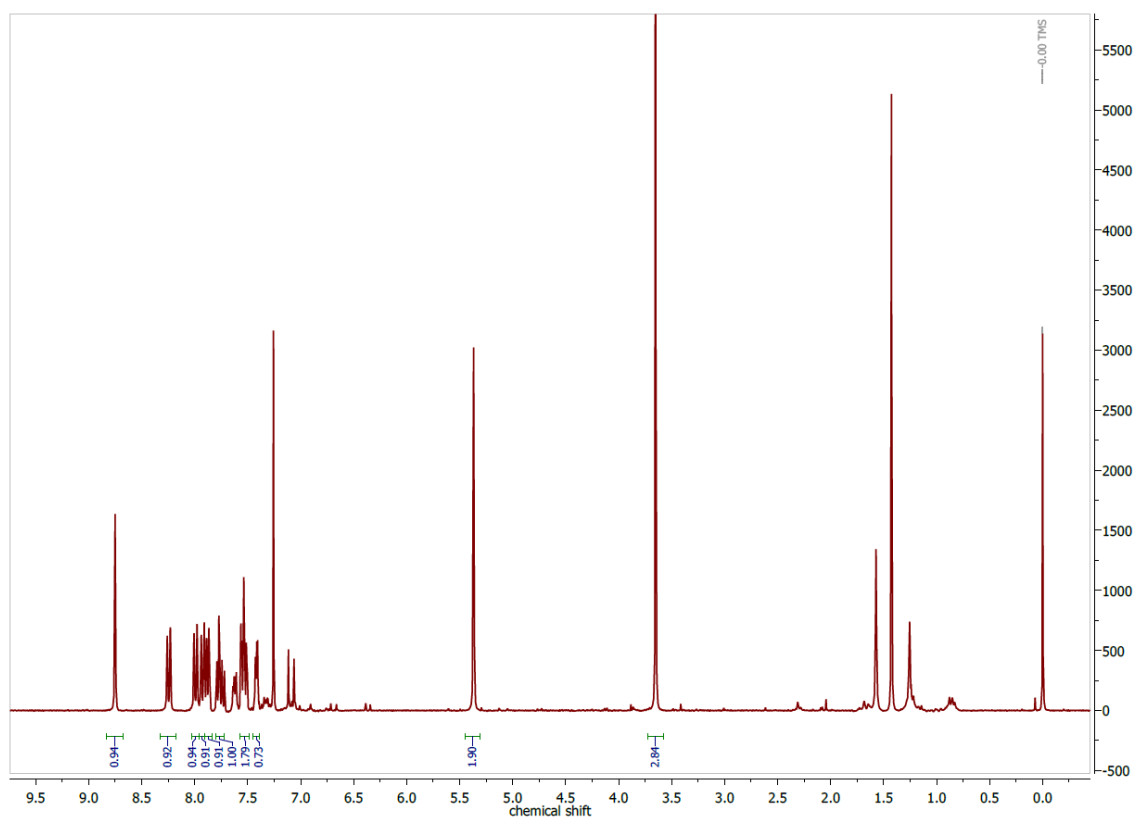


Figure 7.109 ¹H NMR spectrum of 4-methoxymethylacridine in CDCl₃ at 300 MHz.

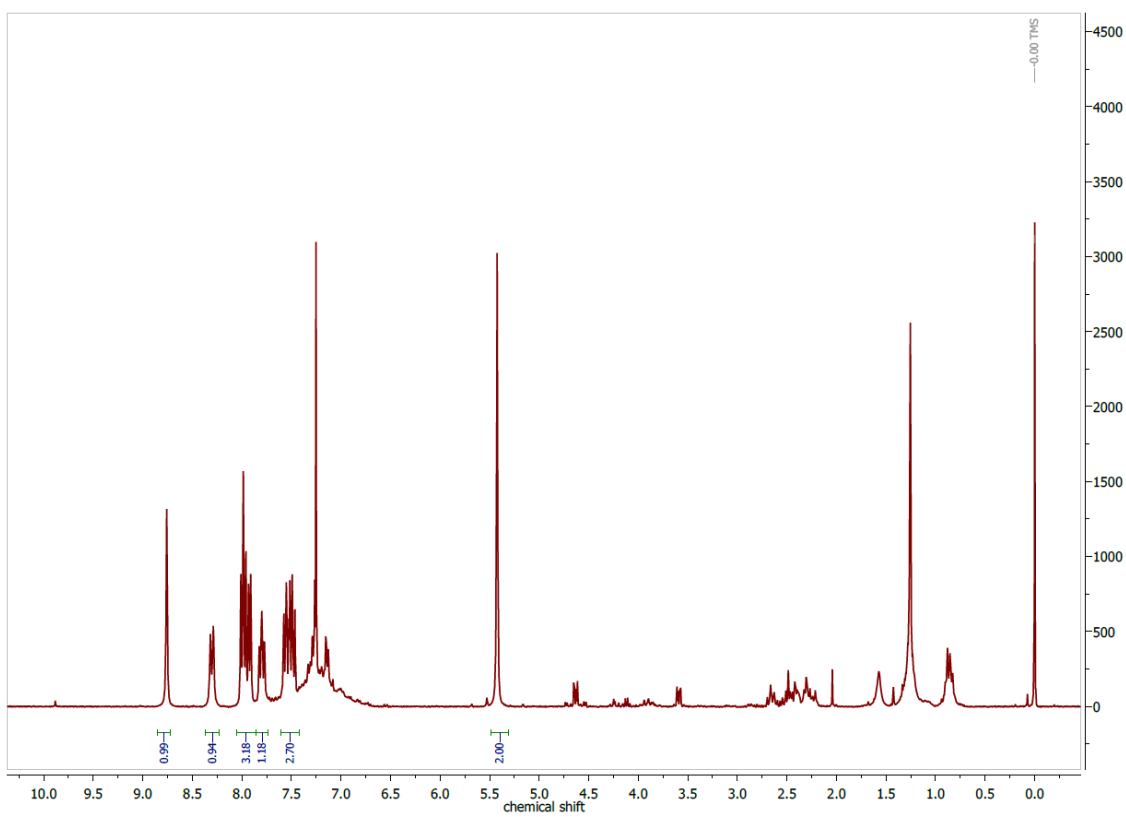


Figure 7.110 ¹H NMR spectrum of 4-bromomethylacridine in CDCl₃ at 300 MHz.

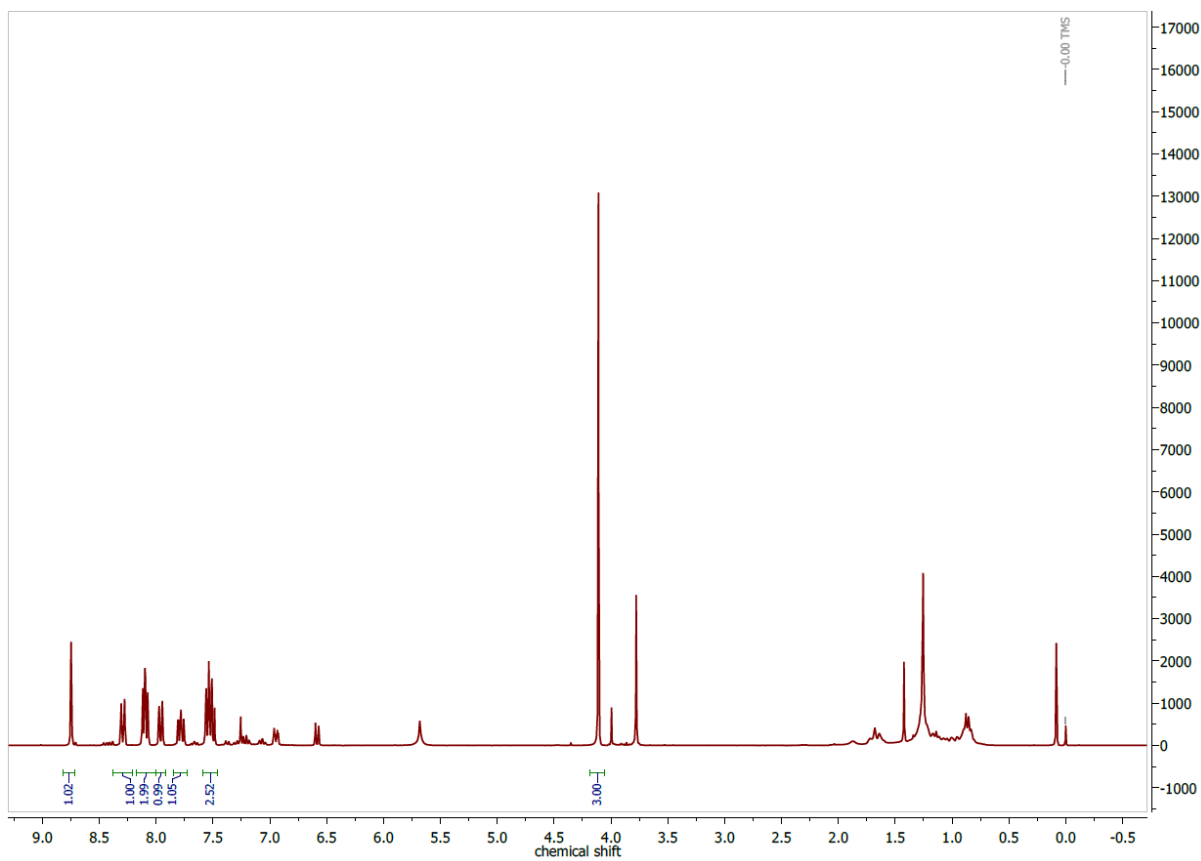


Figure 7.111 ¹H NMR spectrum of methyl acridine-4-carboxylate in CDCl₃ at 300 MHz.

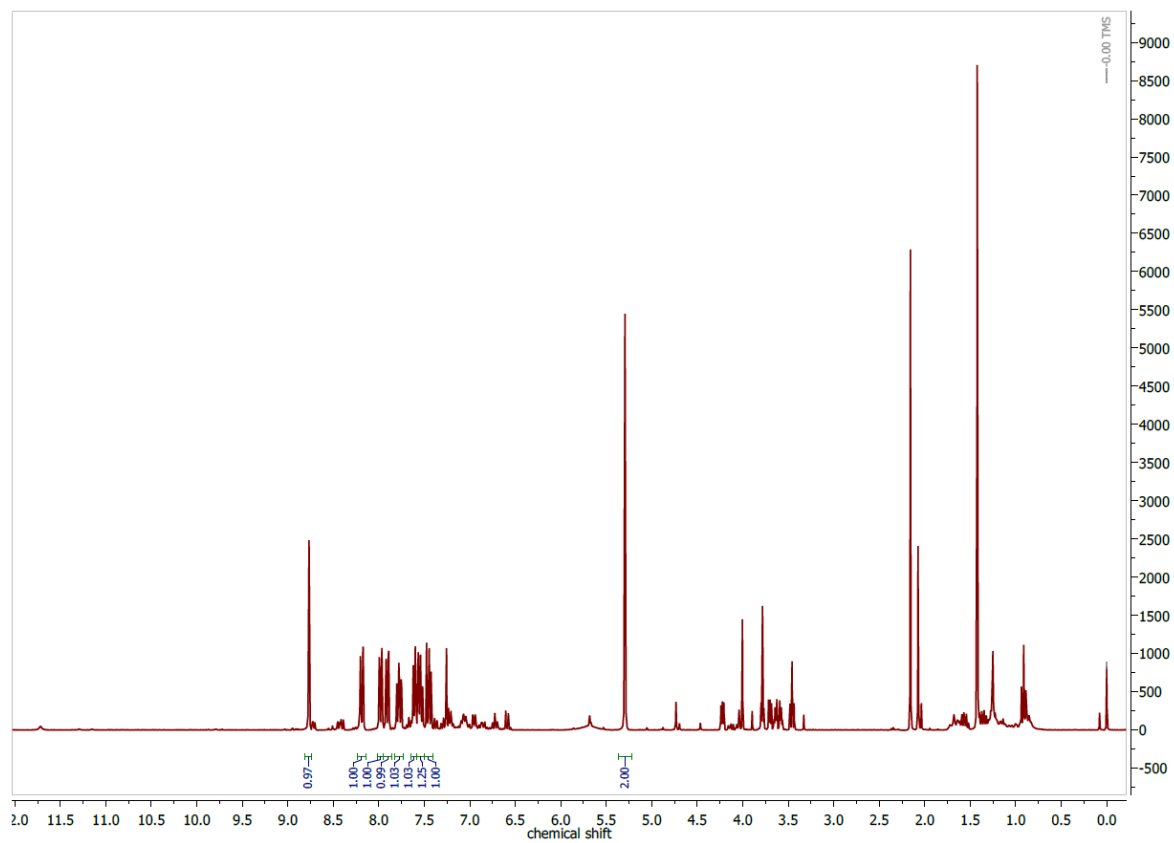


Figure 7.112 ¹H NMR spectrum of acridine-4-ylMeOH in CDCl₃ at 300 MHz.

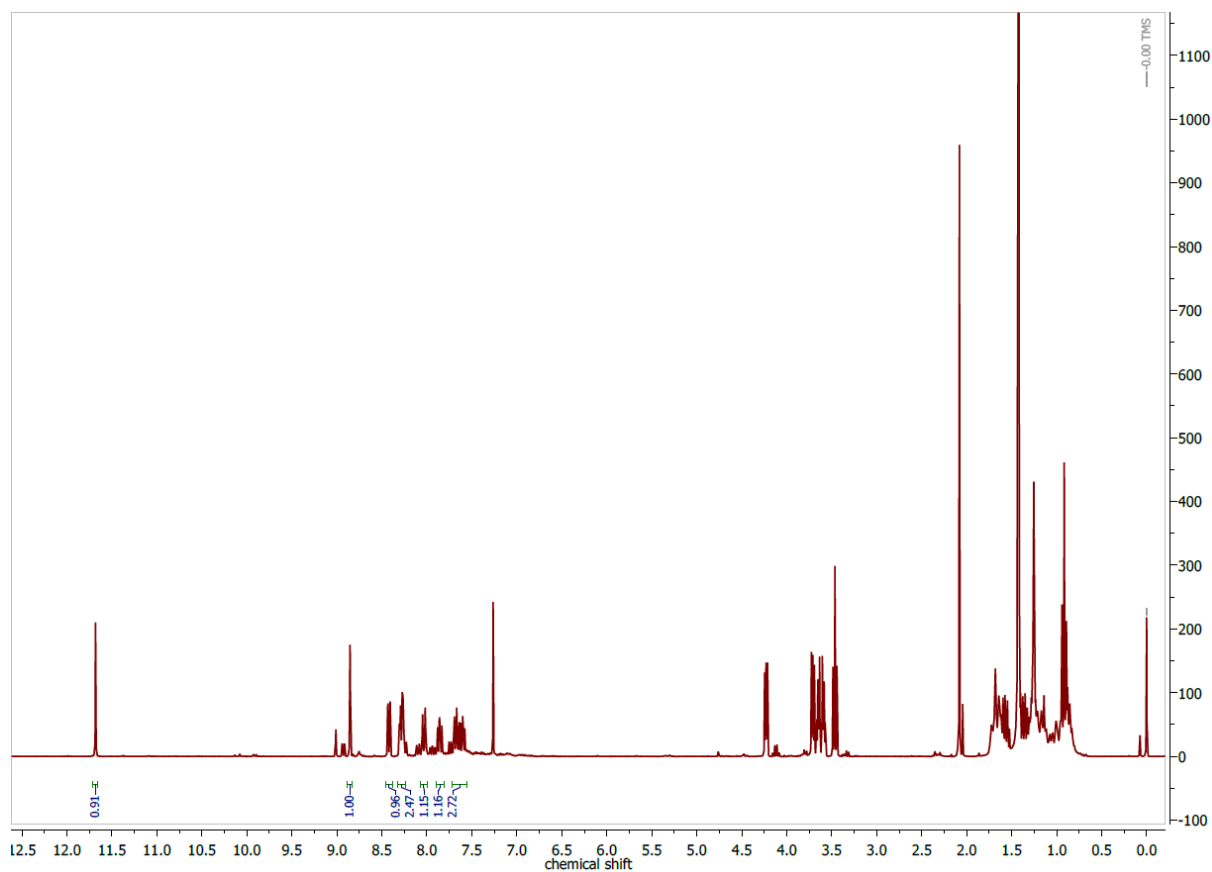


Figure 7.113 ^1H NMR spectrum of methyl acridine-4ylcarbaldehyde in CDCl_3 at 300 MHz.

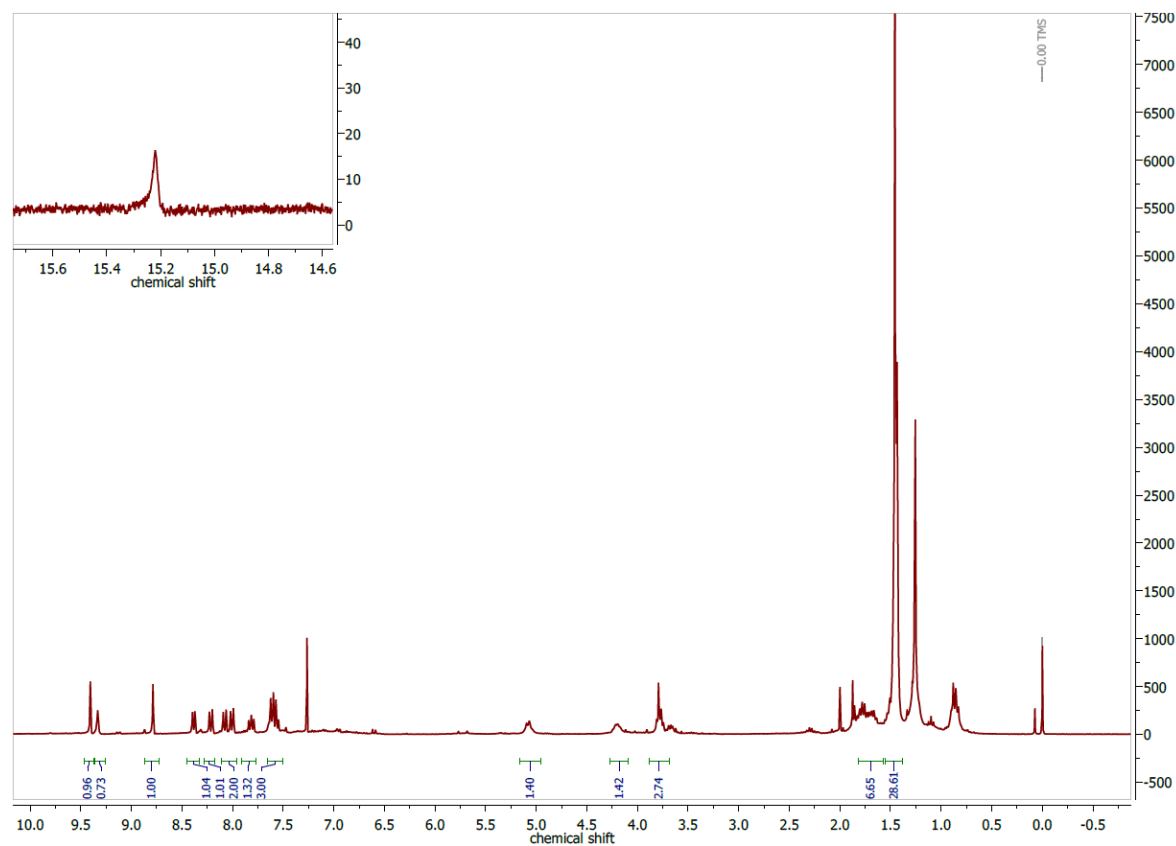


Figure 7.114 ^1H NMR spectrum of HfacTSClP in CDCl_3 at 300 MHz.

7.3. NMR spectra of biotin derivatives

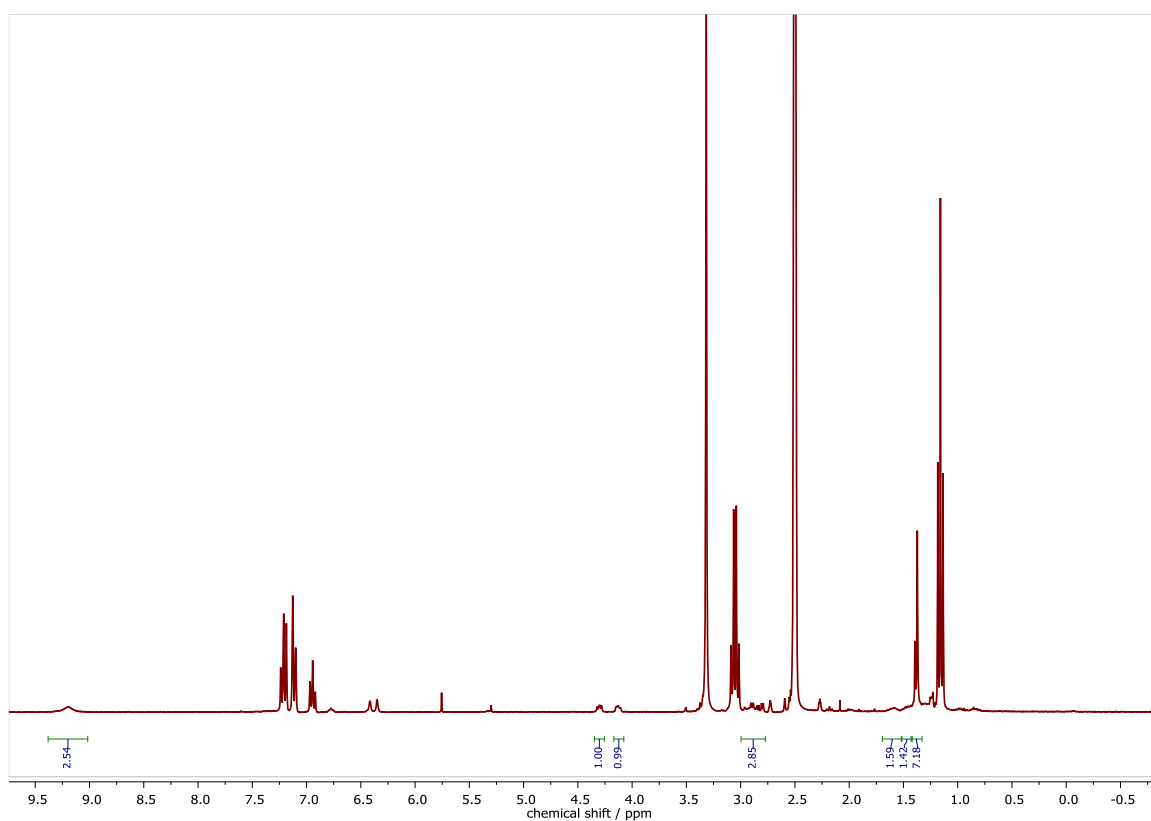


Figure 7.115 ^1H NMR spectrum of Boc-norbiotinamine in $\text{DMSO-}d_6$ at 300 MHz.

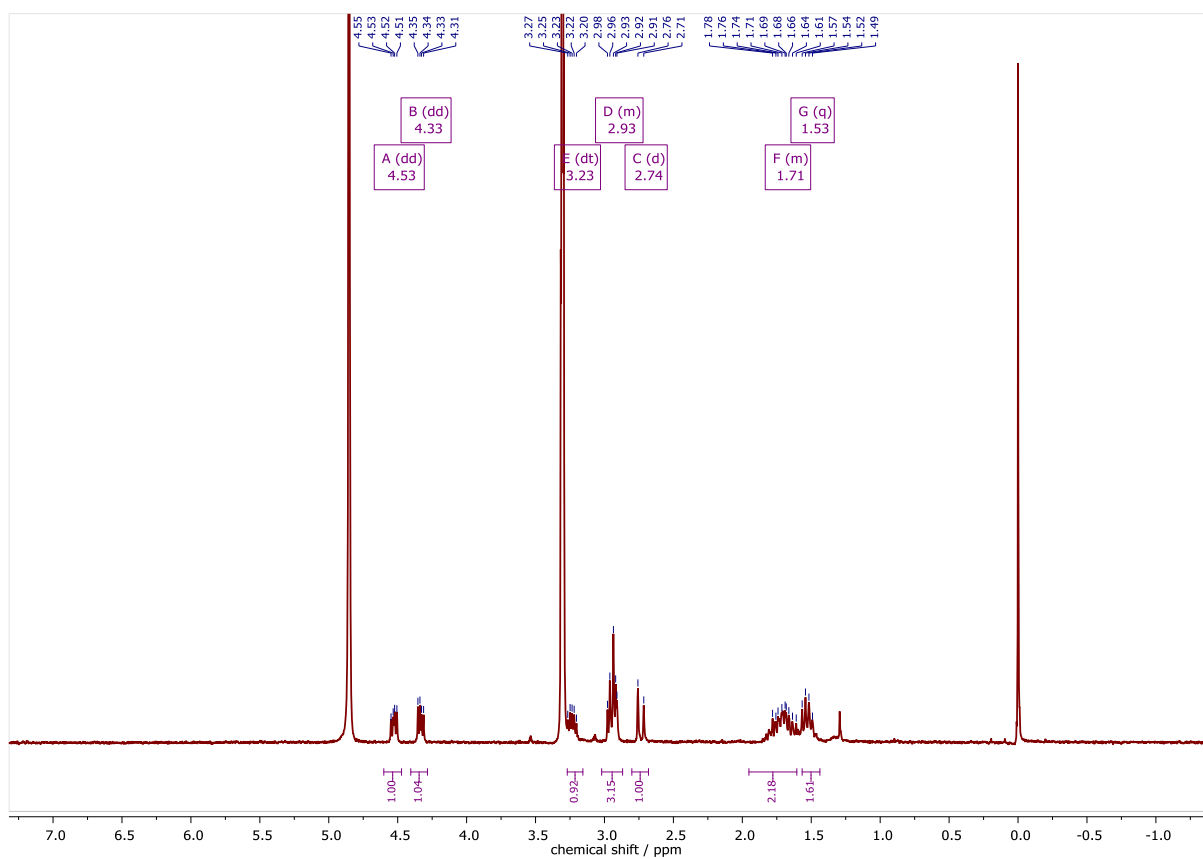


Figure 7.116 ^1H NMR spectrum of norbiotinamine in $\text{MeOH-}d_4$ at 300 MHz.

7.4. NMR spectra of thiosemicarbazones

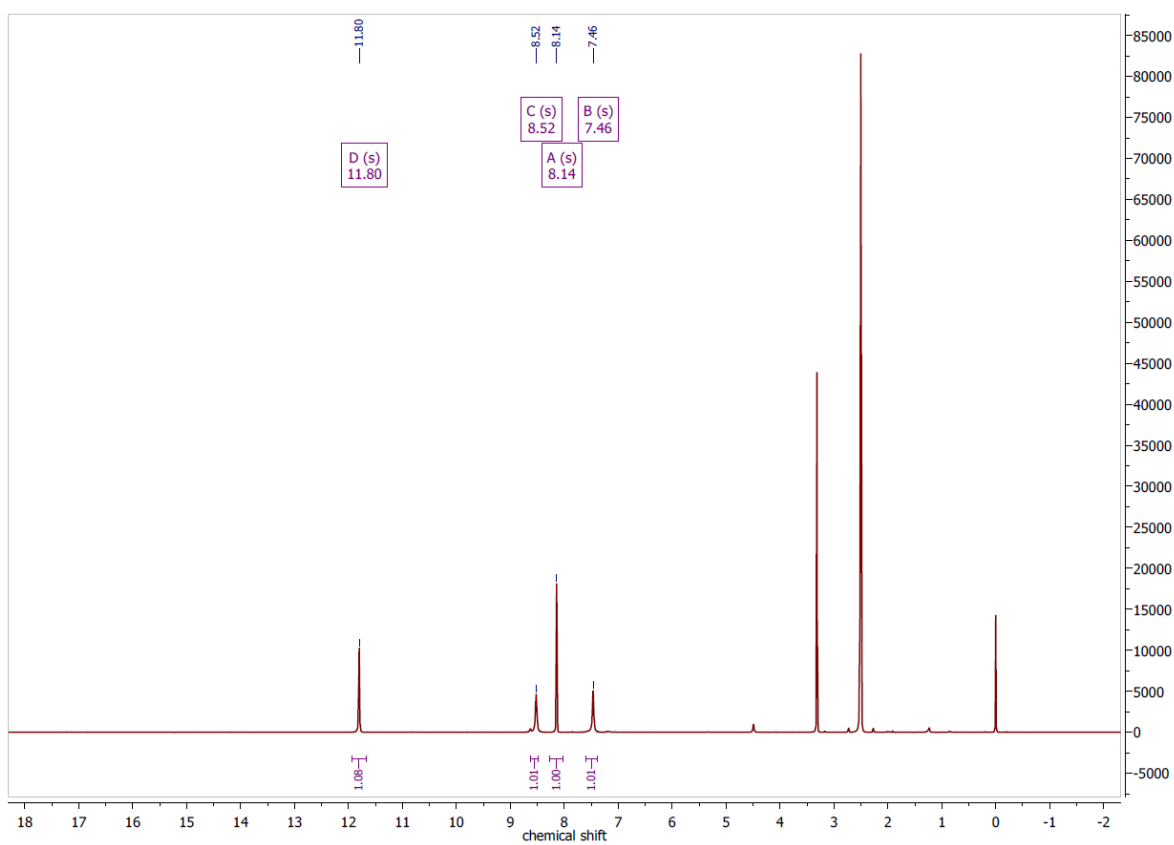


Figure 7.117 ^1H NMR spectrum of HFbzTSC in $\text{DMSO-}d_6$ at 300 MHz.

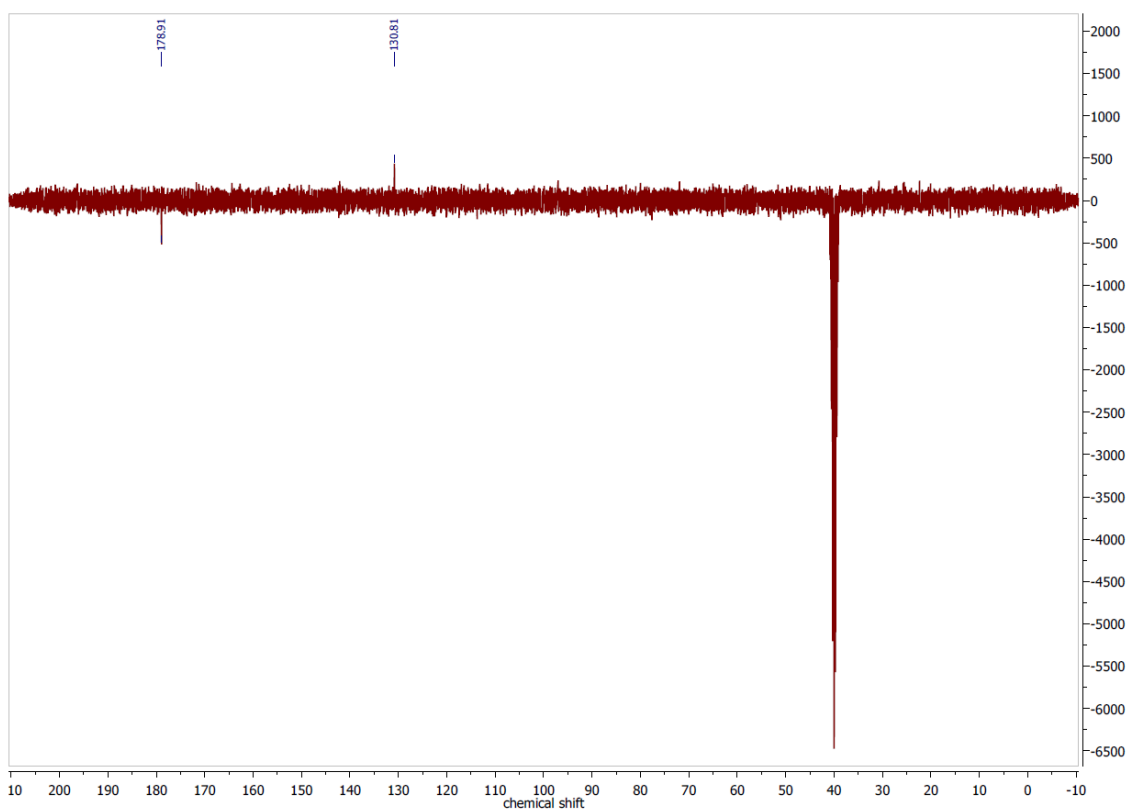


Figure 7.118 $^{13}\text{C}\{^1\text{H}\}$ DEPTQ NMR spectrum of HFbzTSC in $\text{DMSO-}d_6$ at 75 MHz.

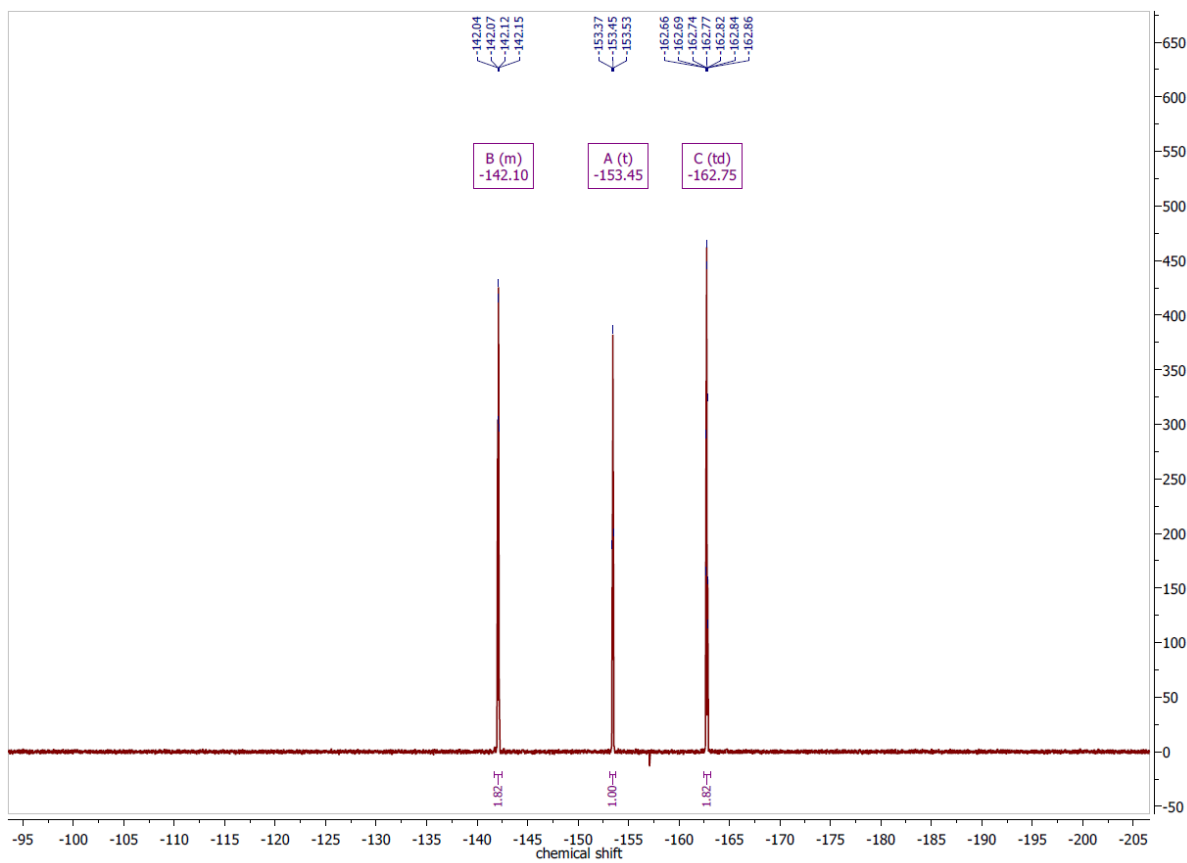


Figure 7.119 ^{19}F NMR spectrum of HFbzTSC in $\text{DMSO-}d_6$ at 282 MHz.

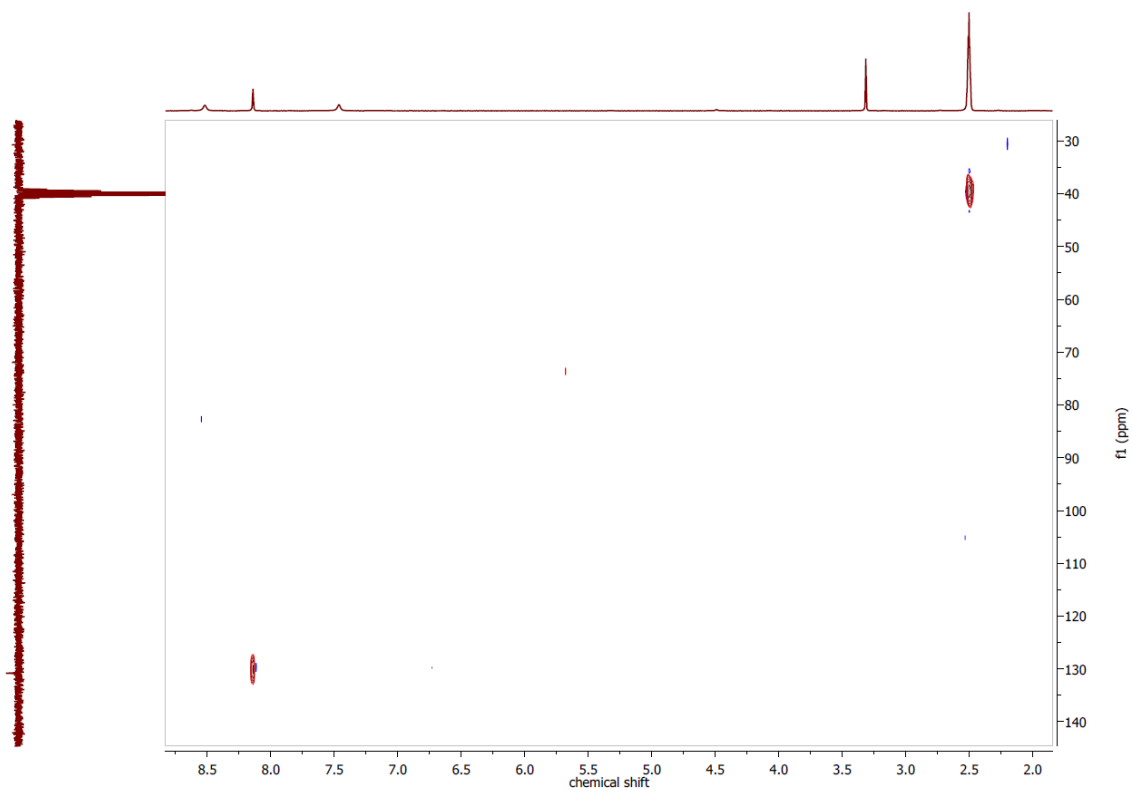


Figure 7.120 ^1H , ^{13}C HSQCed NMR spectrum of HFbzTSC in $\text{DMSO-}d_6$.

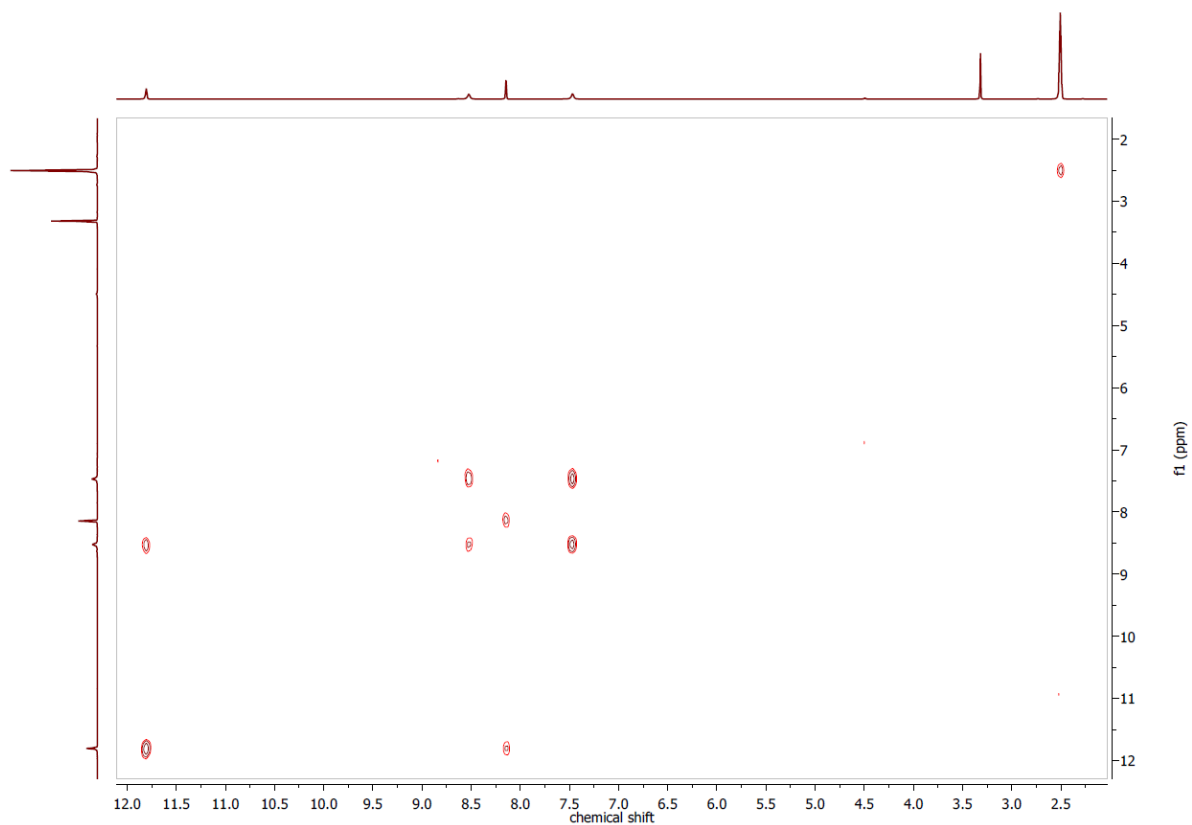


Figure 7.121 $^1\text{H},^1\text{H}$ COSY NMR spectrum of HFbzTSC in $\text{DMSO-}d_6$.

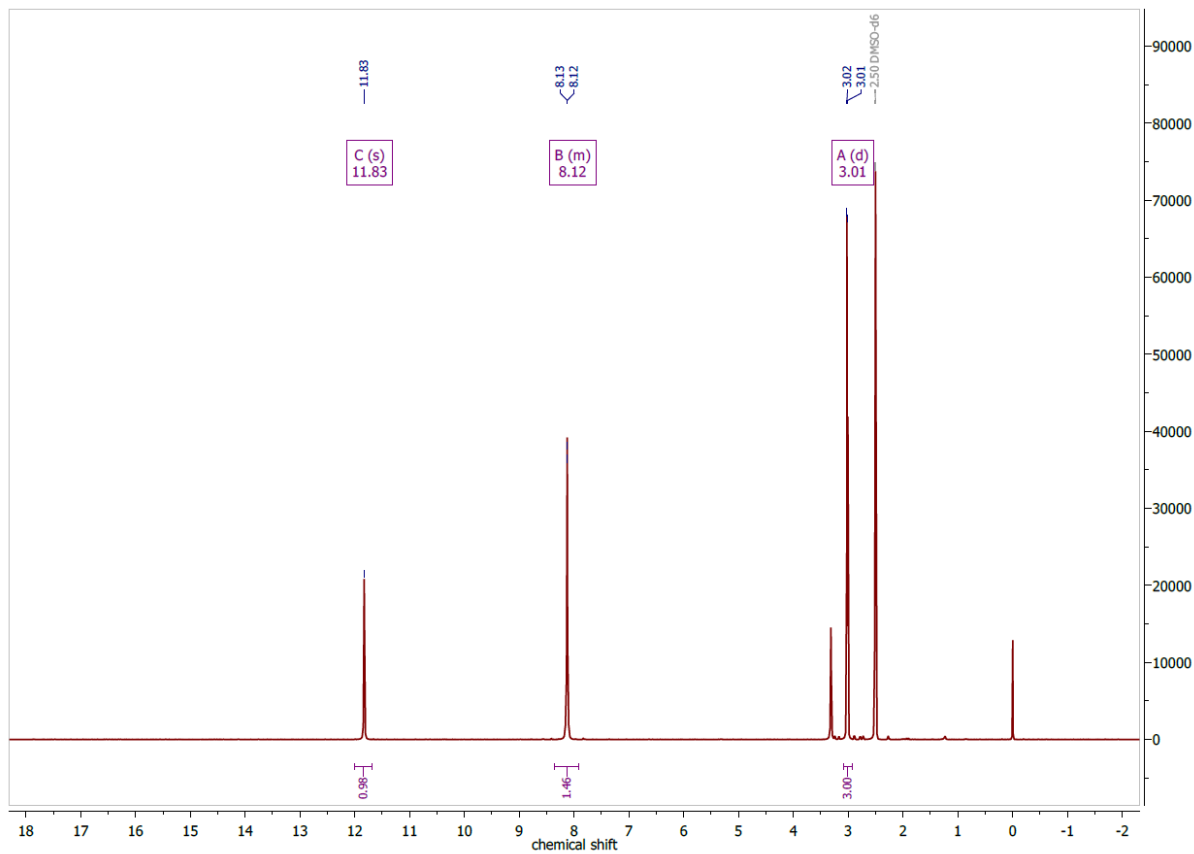


Figure 7.122 ^1H NMR spectrum of HFbzTSCm in $\text{DMSO-}d_6$ at 300 MHz.

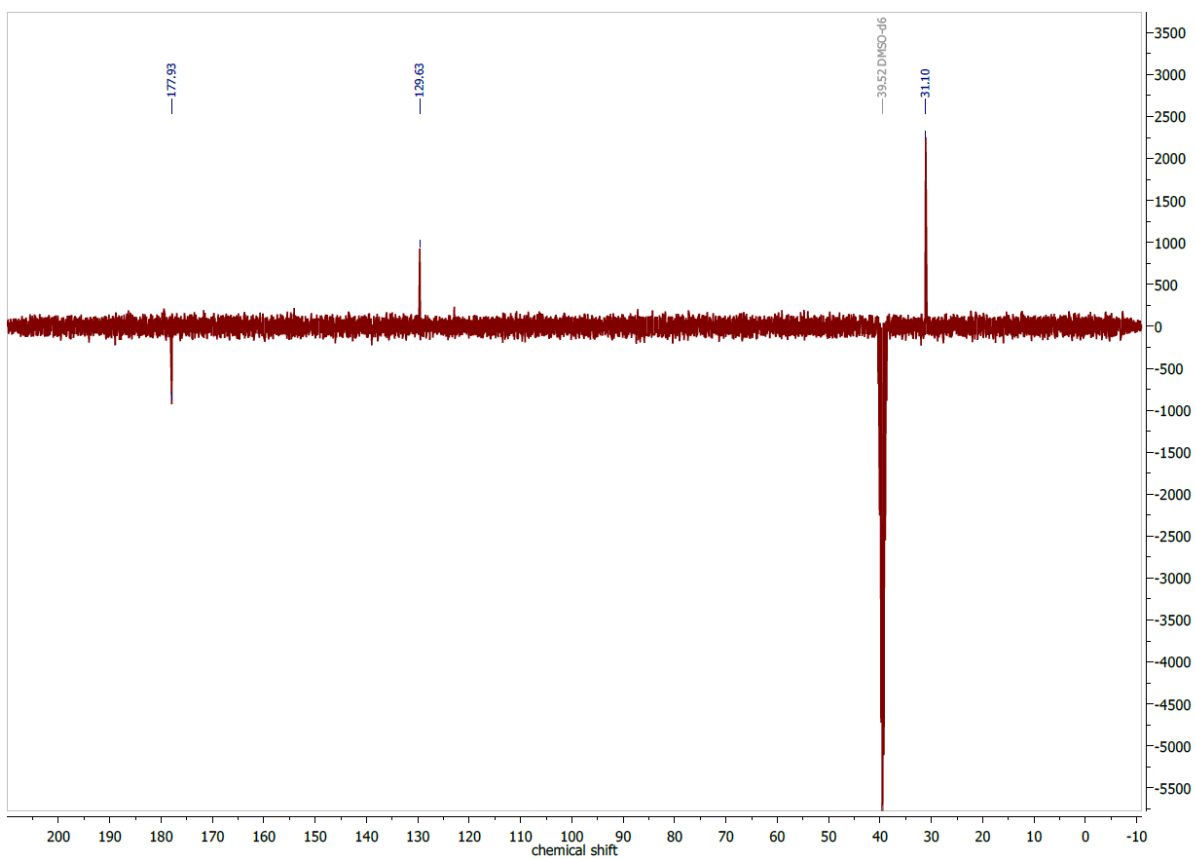


Figure 7.123 $^{13}\text{C}\{^1\text{H}\}$ DEPTQ NMR spectrum of HFbzTSCm in $\text{DMSO-}d_6$ at 75 MHz.

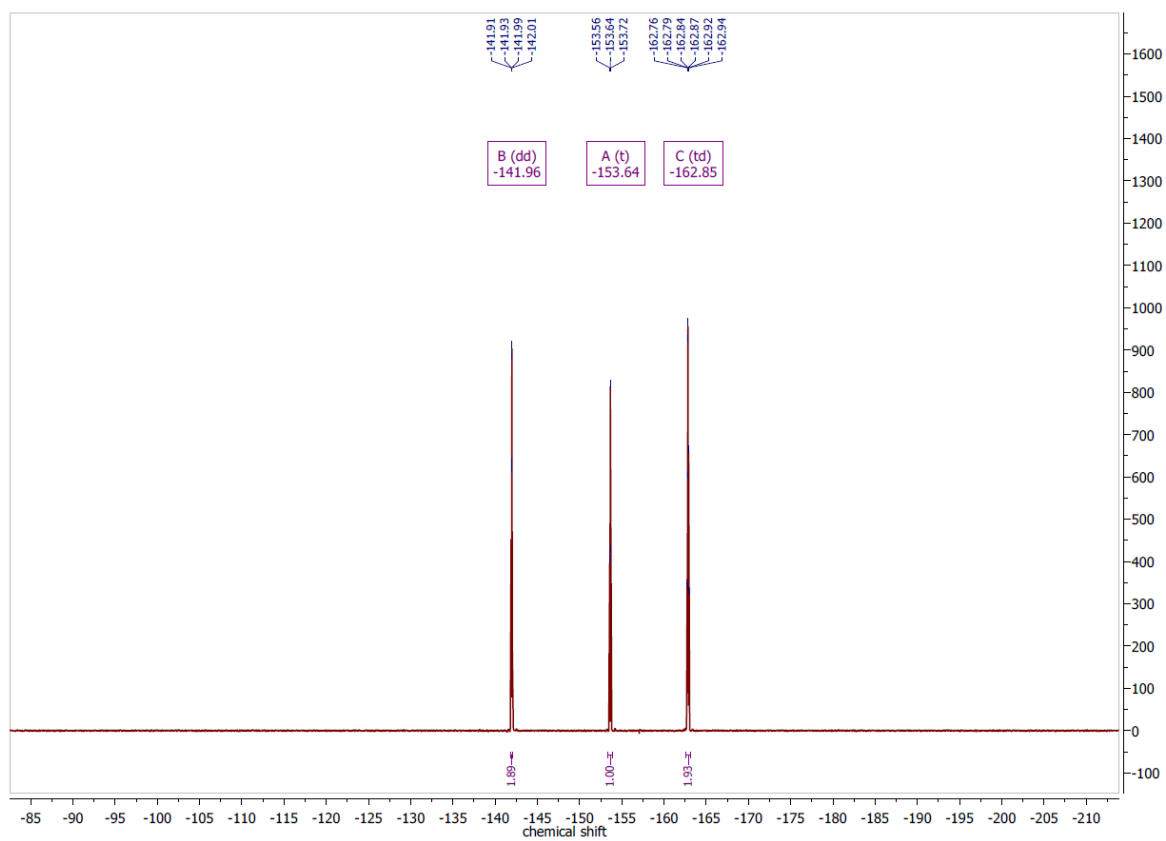


Figure 7.124 ^{19}F NMR spectrum of HFbzTSCm in $\text{DMSO-}d_6$ at 282 MHz.

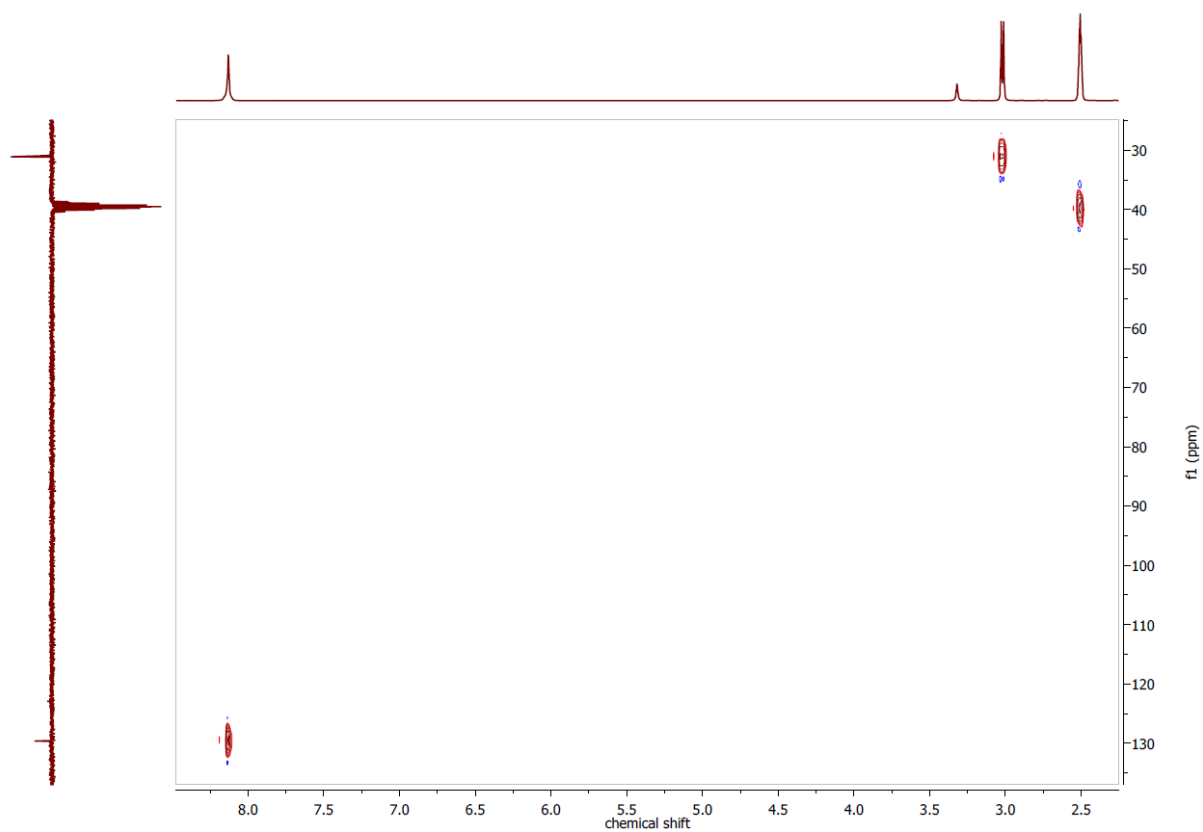


Figure 7.125 ^1H , ^{13}C HSQCed NMR spectrum of HFbzTSCm in $\text{DMSO-}d_6$.

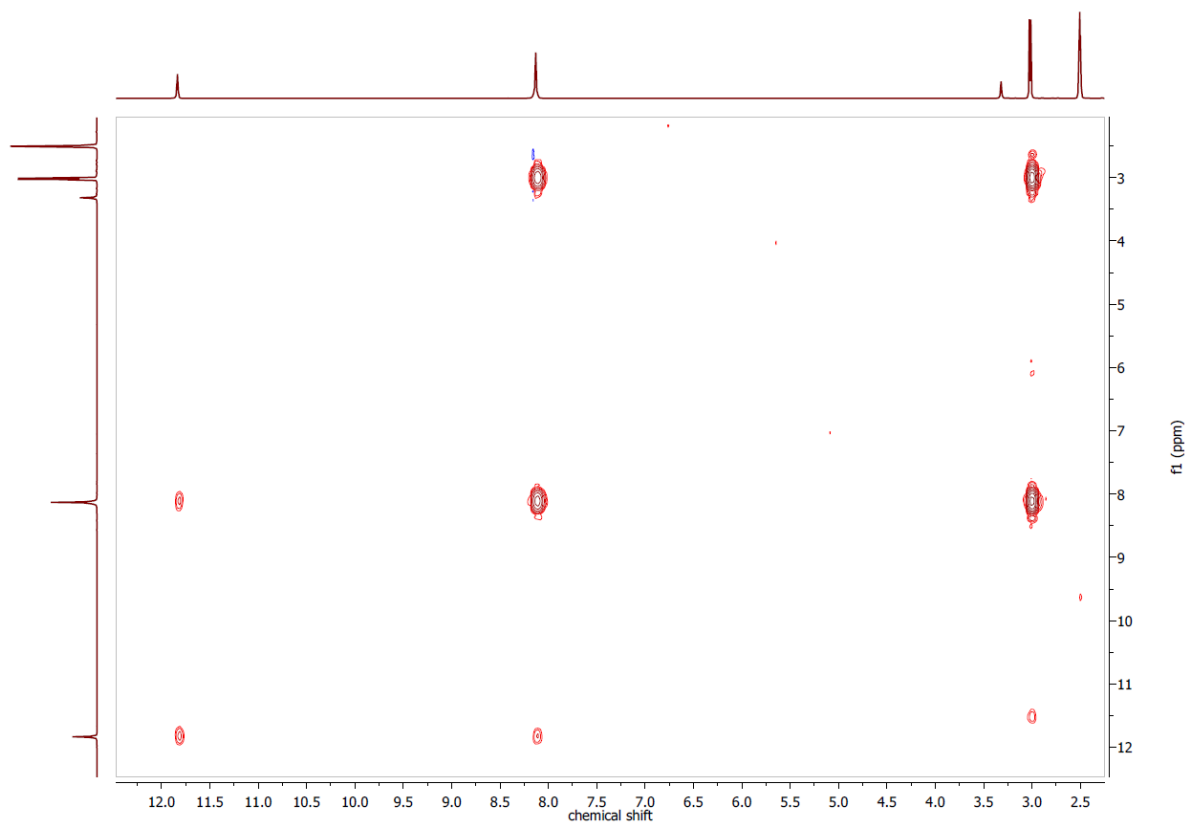


Figure 7.126 ^1H , ^1H COSY NMR spectrum of HFbzTSCm in $\text{DMSO-}d_6$.

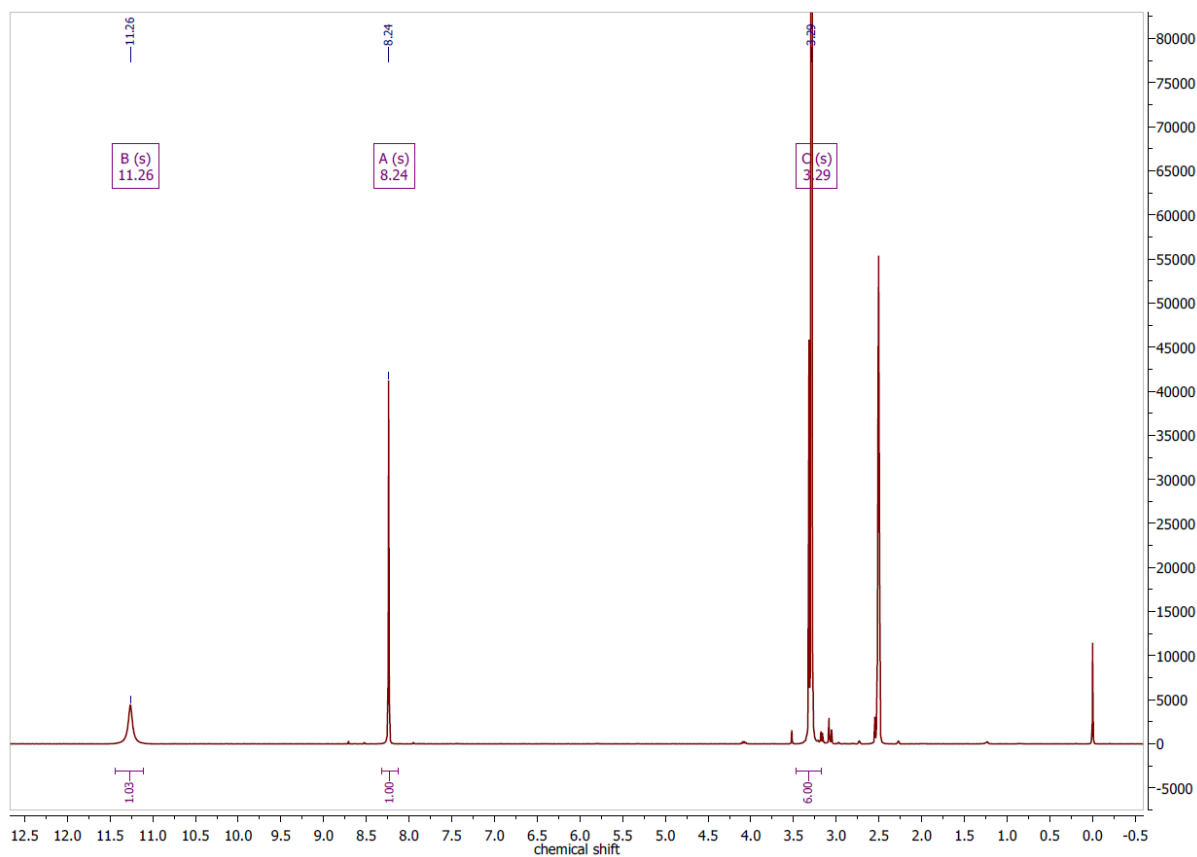


Figure 7.127 ^1H NMR spectrum of HFbzTSCdm in $\text{DMSO-}d_6$ at 300 MHz.

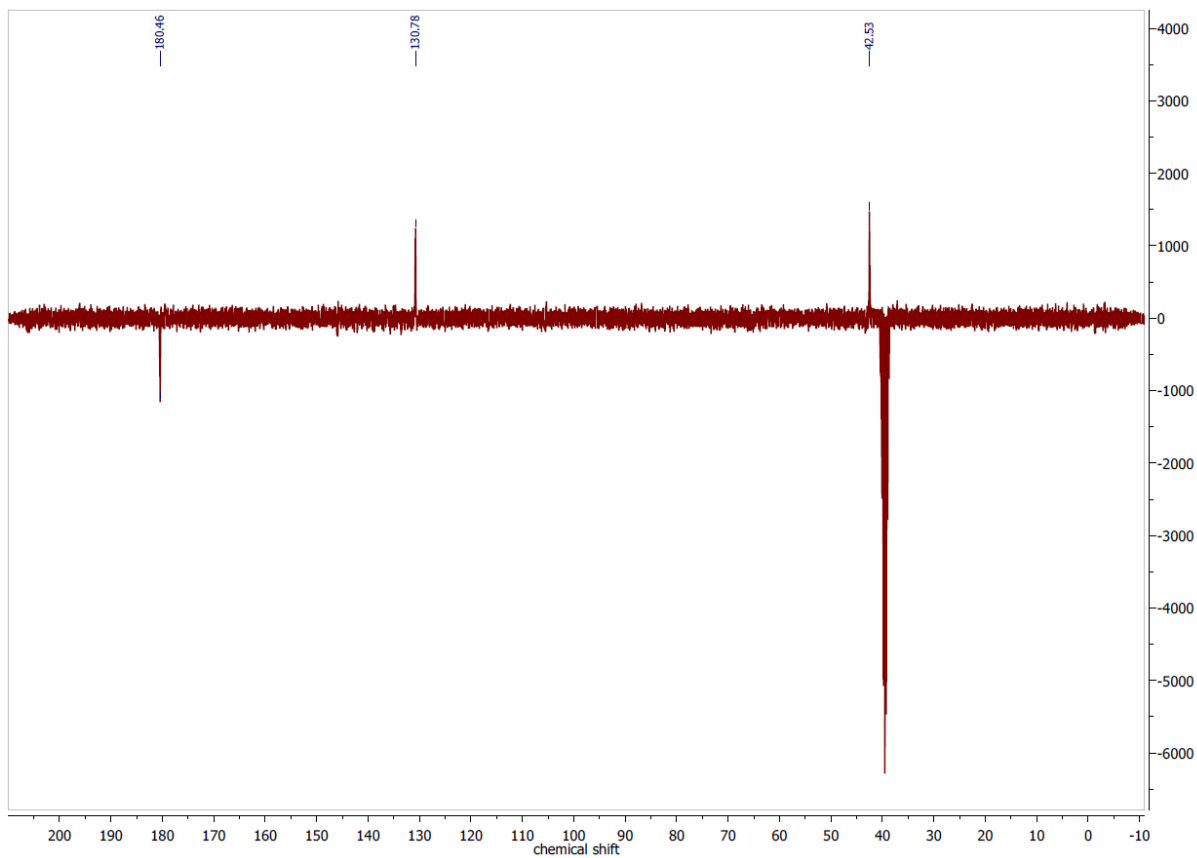


Figure 7.128 $^{13}\text{C}\{^1\text{H}\}$ DEPTQ NMR spectrum of HFbzTSCdm in $\text{DMSO-}d_6$ at 75 MHz.

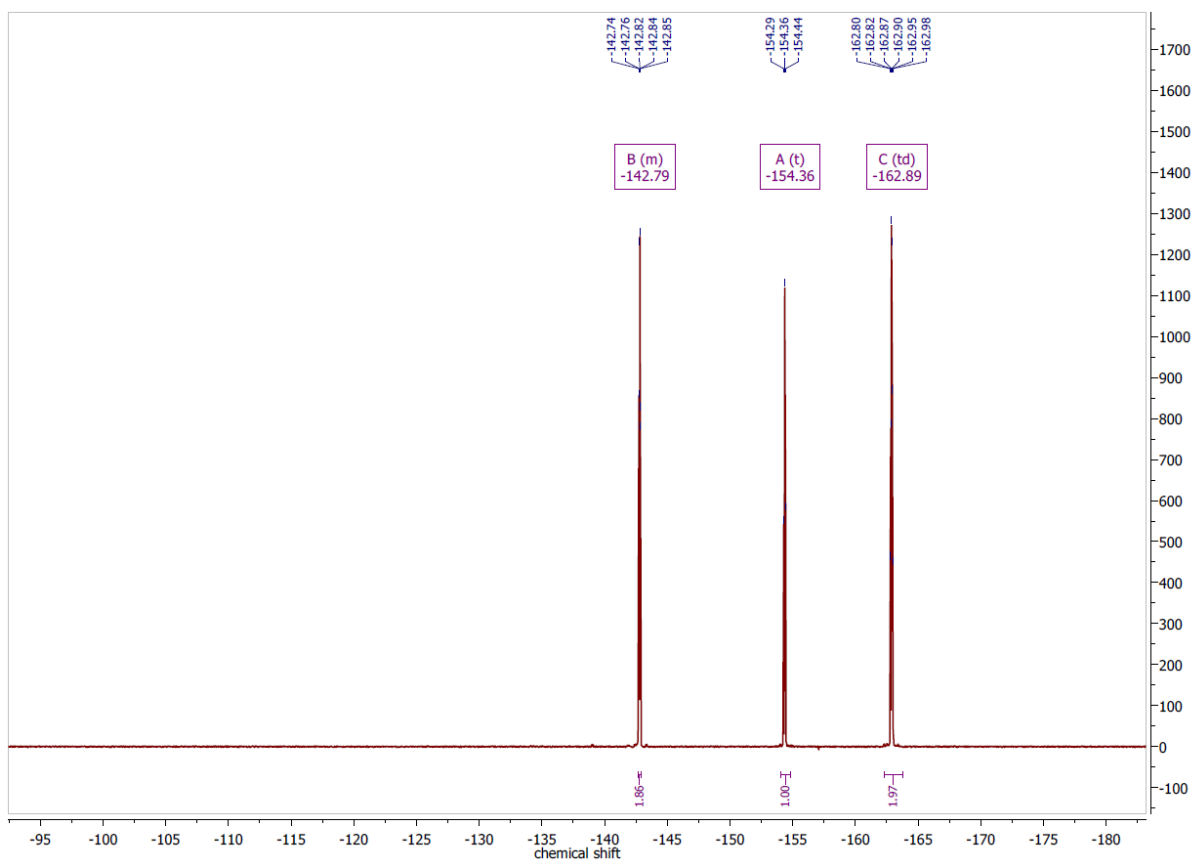


Figure 7.129 ^{19}F NMR spectrum of HFbzTSCdm in $\text{DMSO-}d_6$ at 282 MHz.

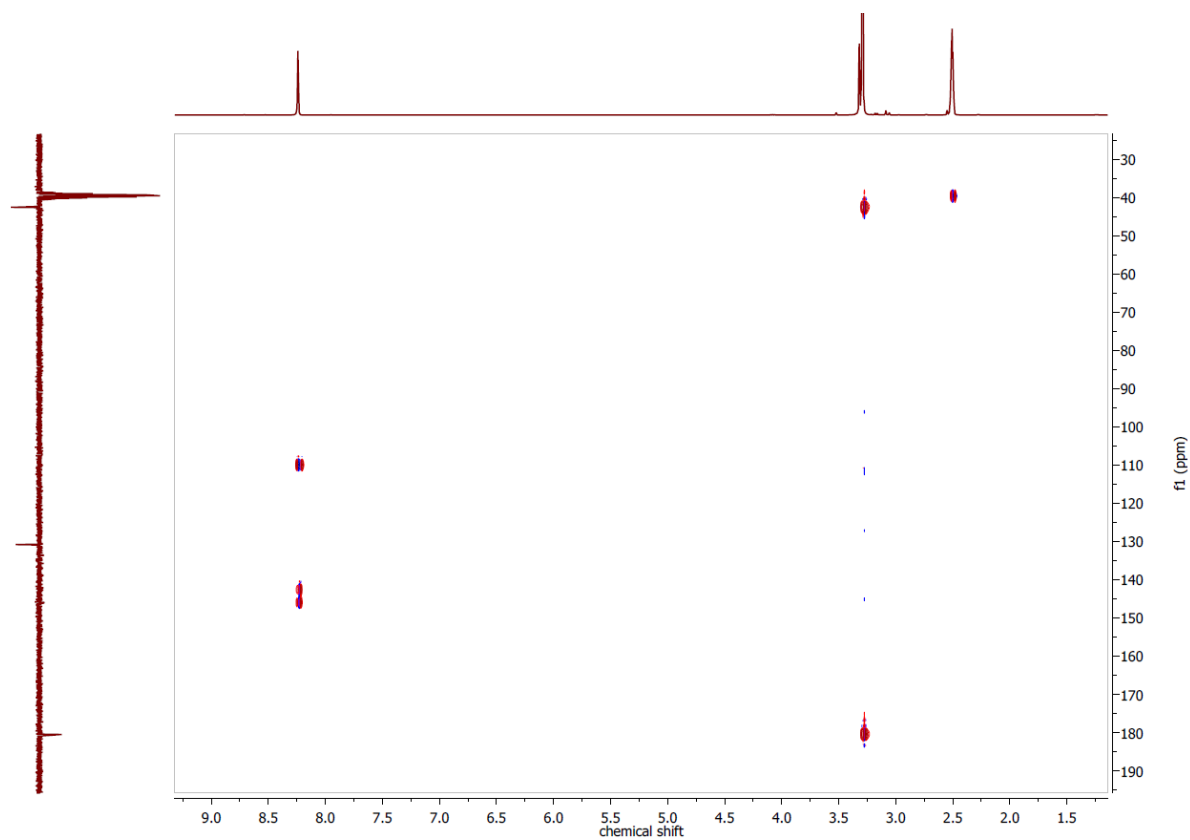


Figure 7.130 $^1\text{H},^{13}\text{C}$ HMBC NMR spectrum of HFbzTSCdm in $\text{DMSO-}d_6$.

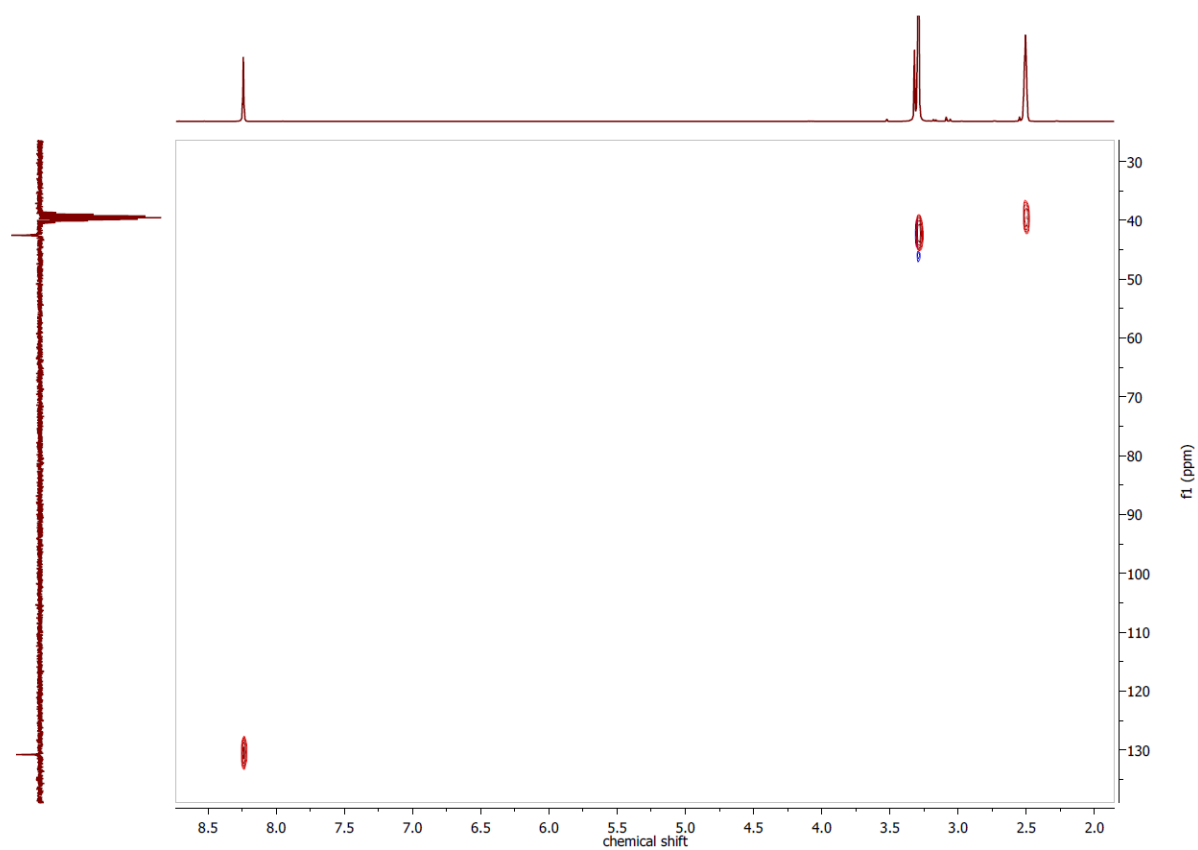


Figure 7.131 ^1H , ^{13}C HSQCed NMR spectrum of HFbzTSCdm in $\text{DMSO-}d_6$.

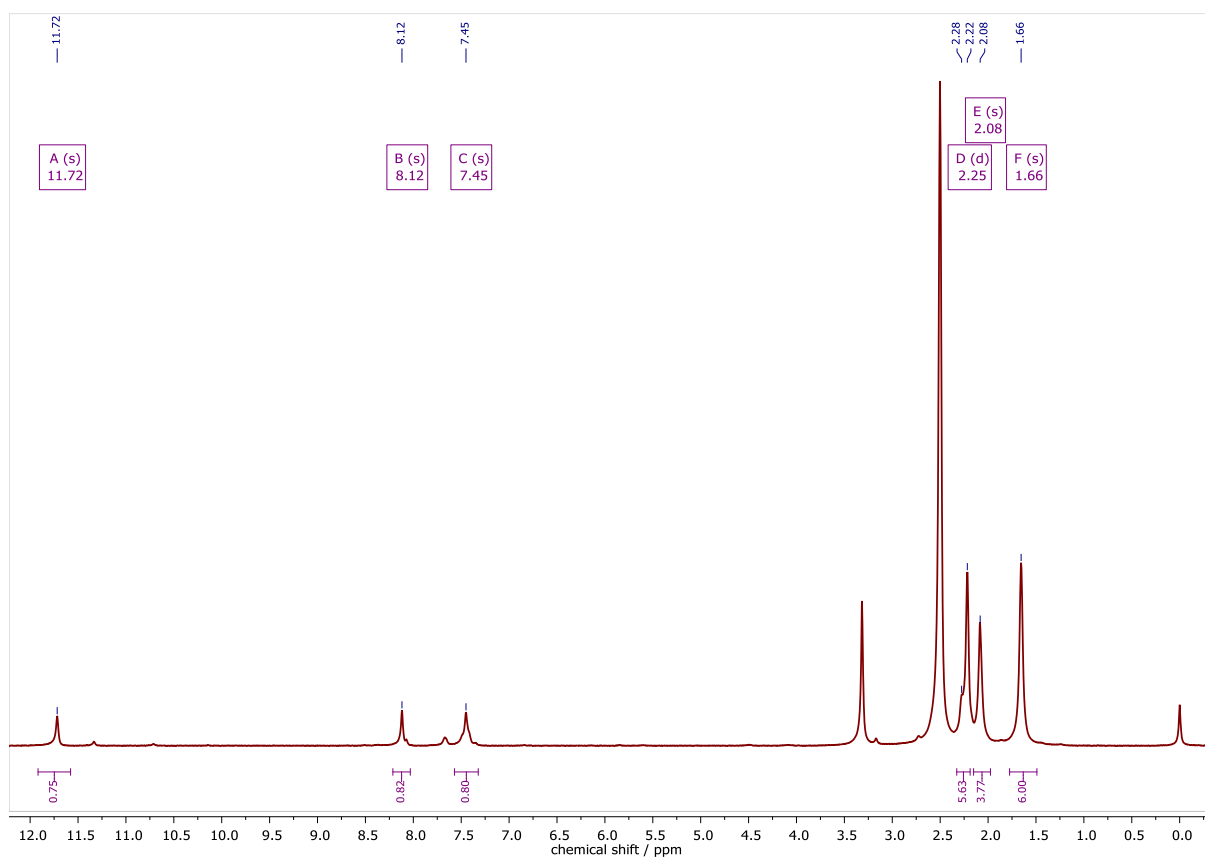


Figure 7.132 ^1H NMR spectrum of HFbzTSCAd in $\text{DMSO-}d_6$ at 300 MHz.

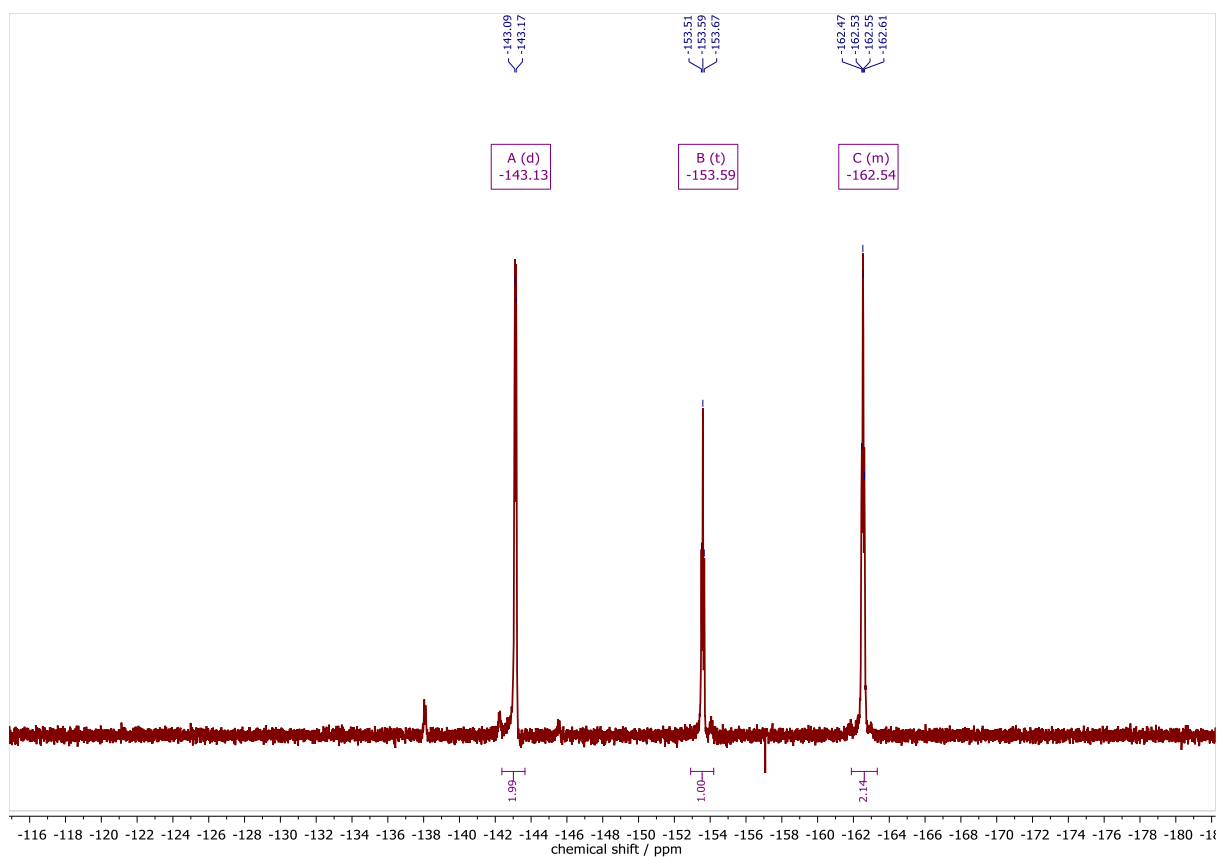


Figure 7.133 ^{19}F NMR spectrum of HFbzTSCAd in $\text{DMSO-}d_6$ at 282 MHz.

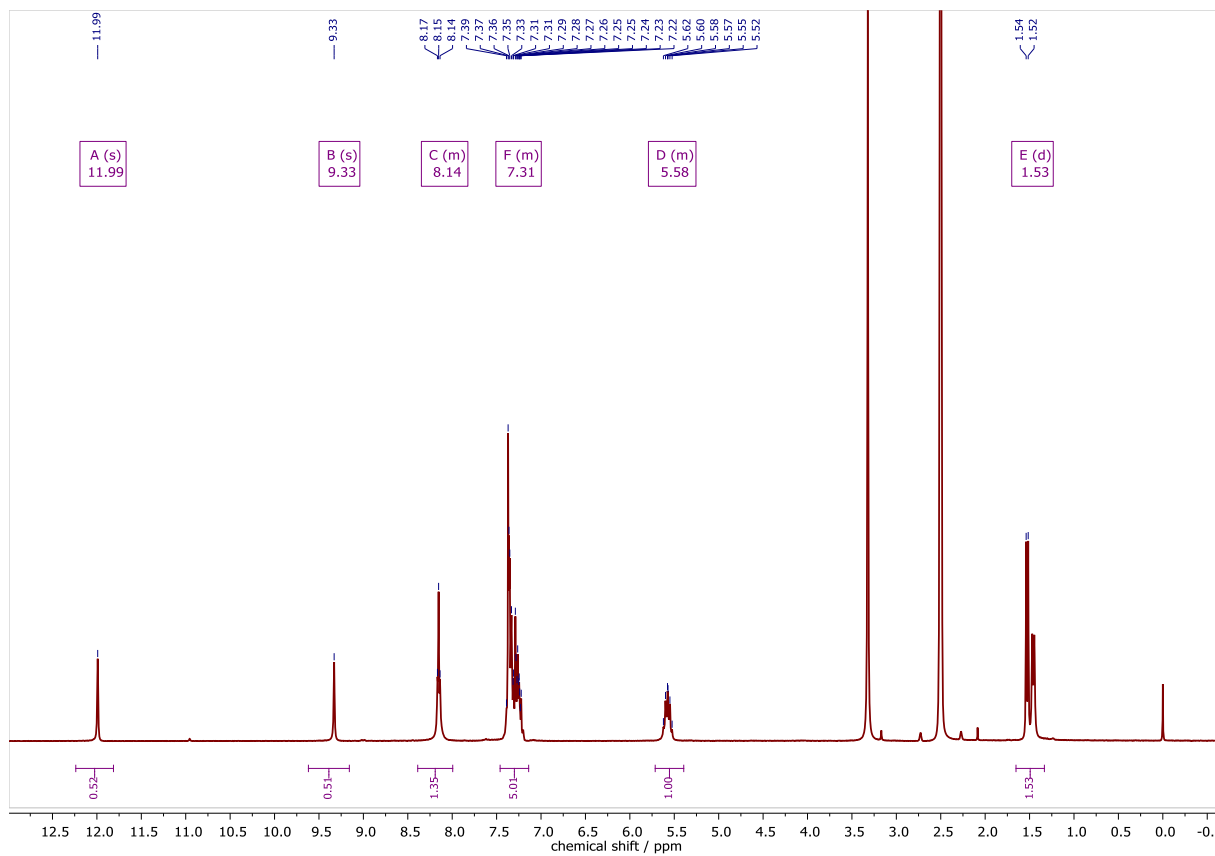


Figure 7.134 ^1H NMR spectrum of HFbzTSCmB in $\text{DMSO-}d_6$ at 300 MHz.

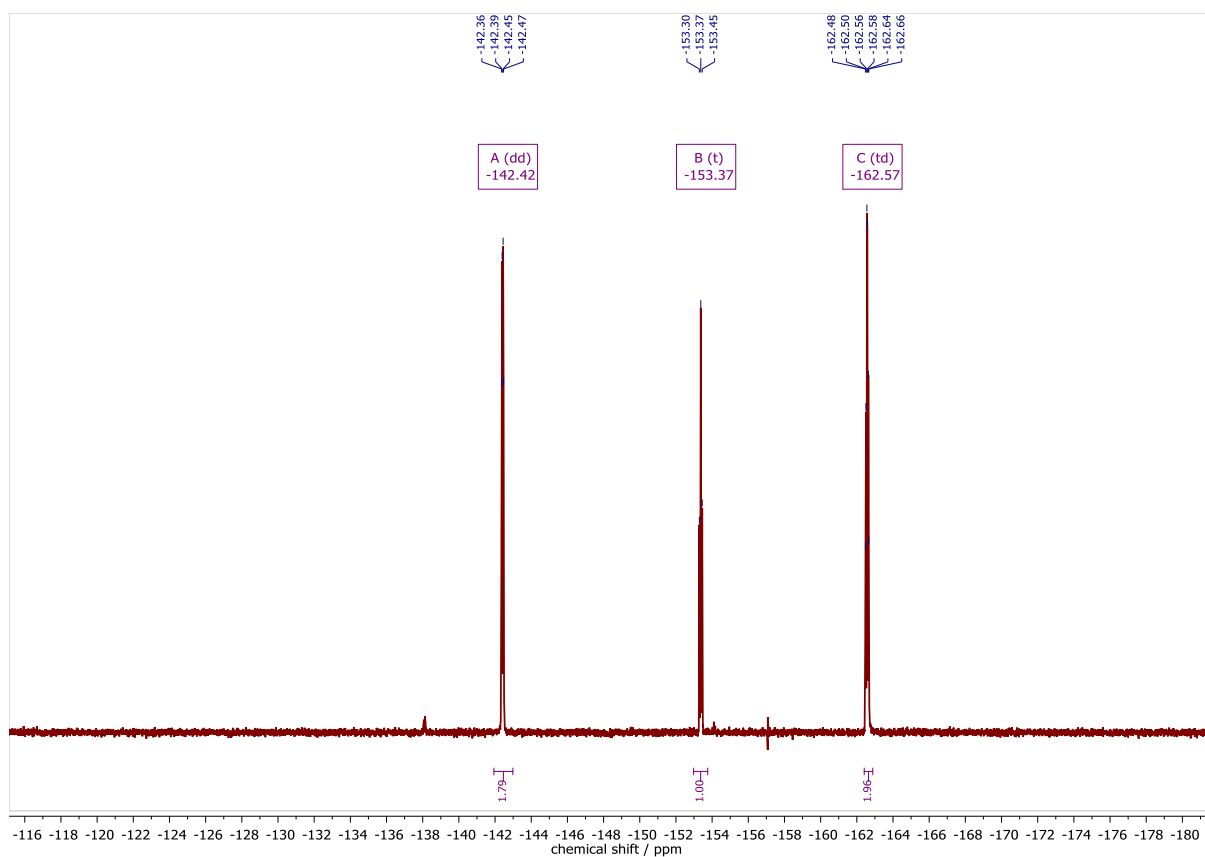


Figure 7.135 ^{19}F NMR spectrum of HFbzTSCmB in $\text{DMSO-}d_6$ at 282 MHz.

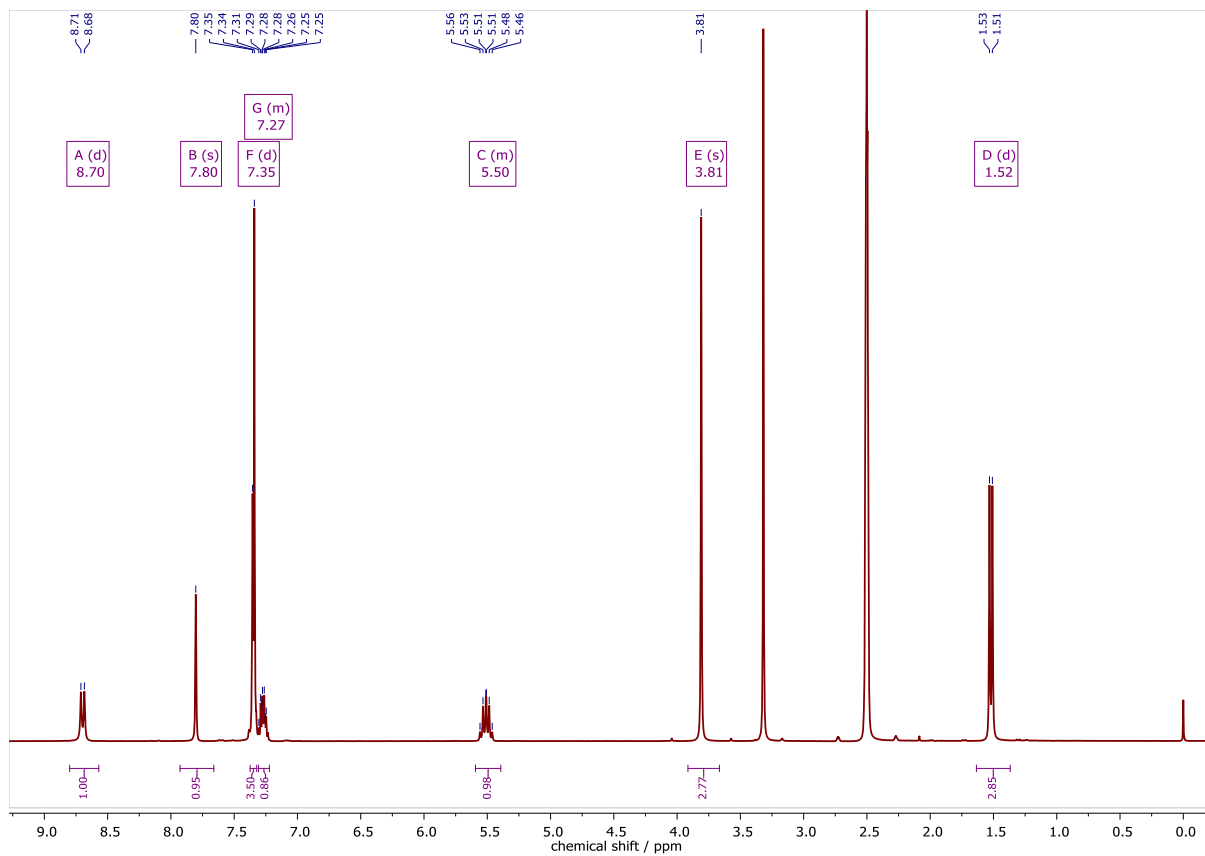


Figure 7.136 ^1H NMR spectrum of HFbz(m)TSCmB in $\text{DMSO-}d_6$ at 300 MHz.

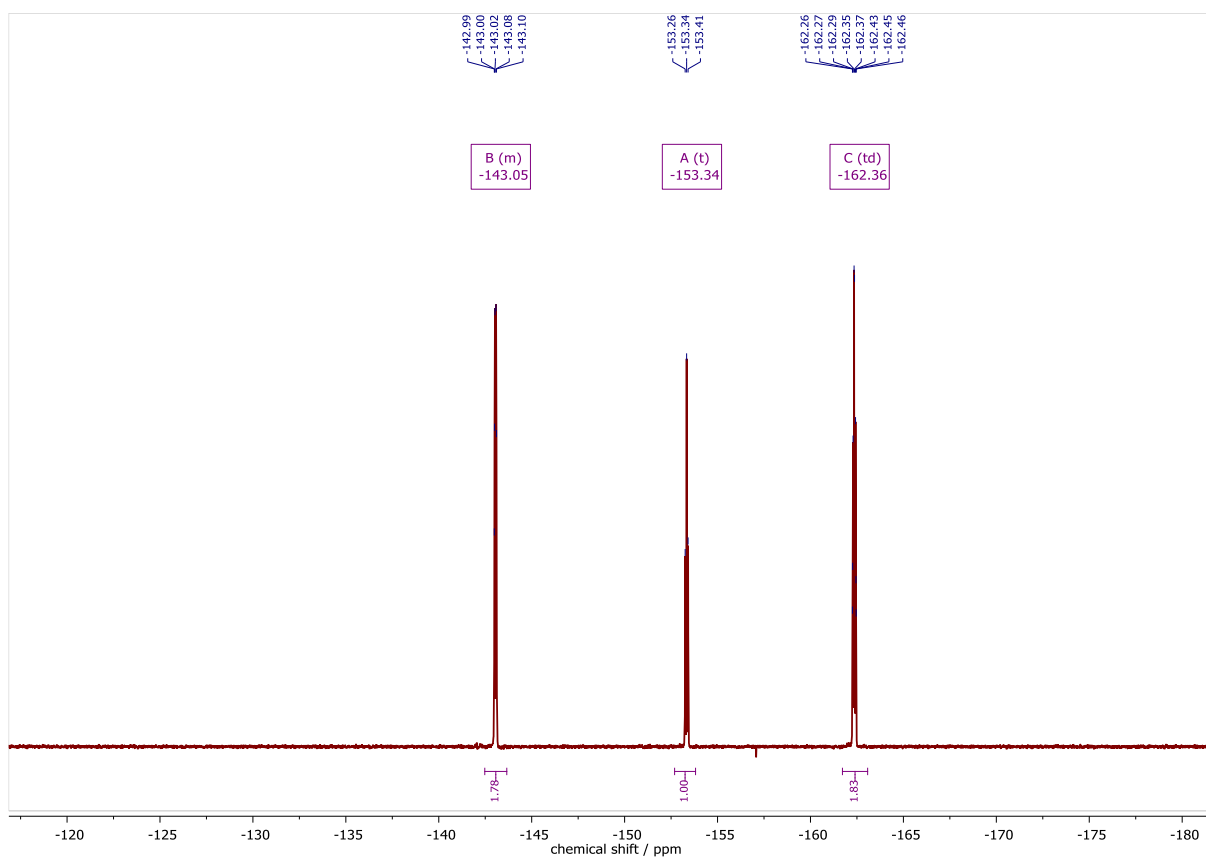


Figure 7.137 ^{19}F NMR spectrum of HFbz(m)TSCmB in DMSO- d_6 at 282 MHz.

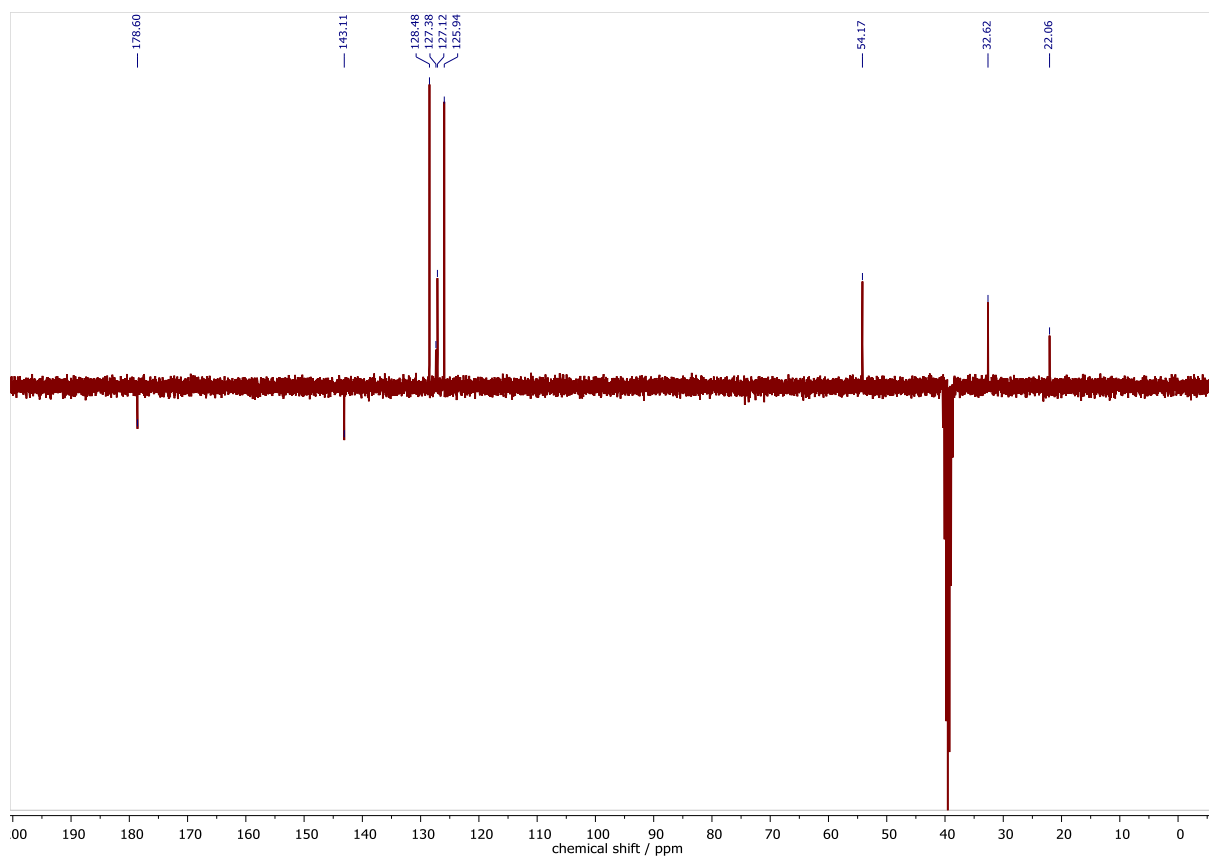


Figure 7.138 $^{13}\text{C}\{^1\text{H}\}$ DEPTQ NMR spectrum of HFbz(m)TSCmB in DMSO- d_6 at 75 MHz.

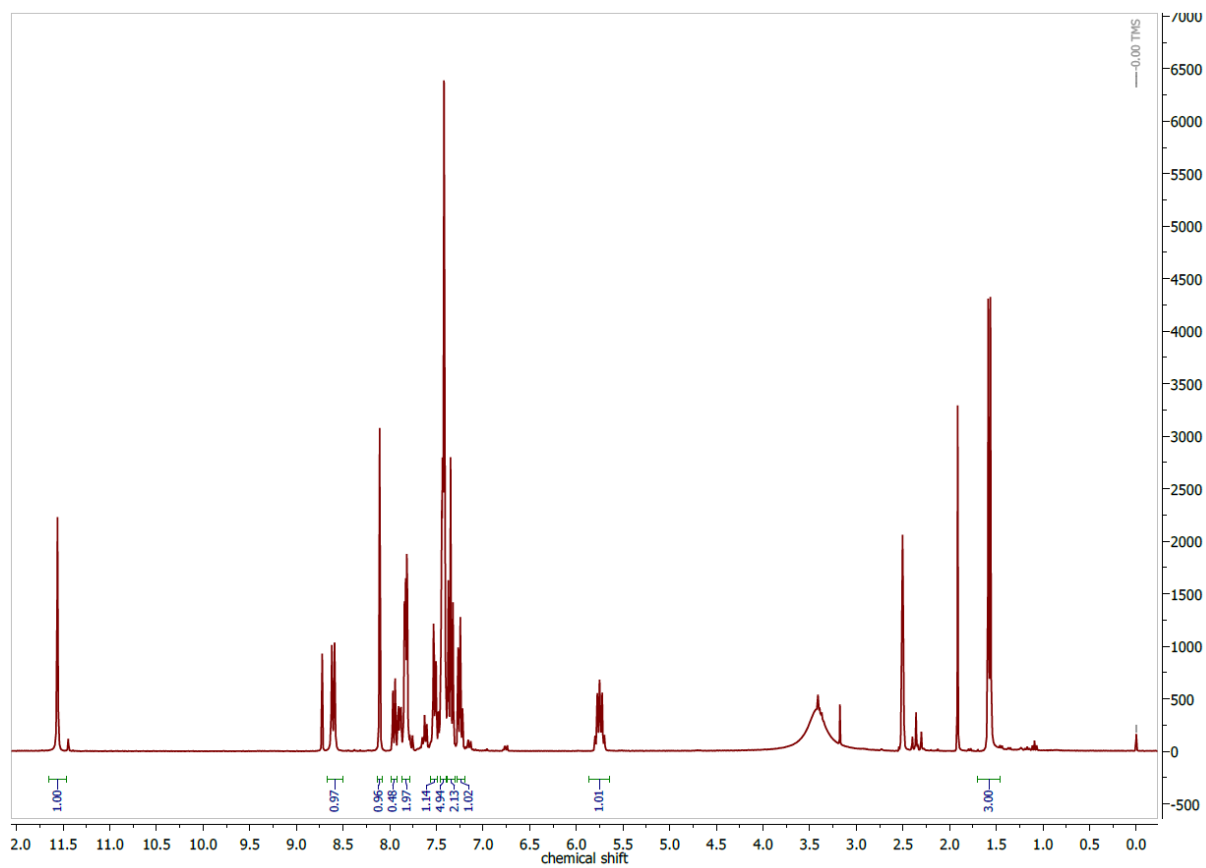


Figure 7.139 ^1H NMR spectrum of HbzTSCmB in $\text{DMSO-}d_6$ at 300 MHz.

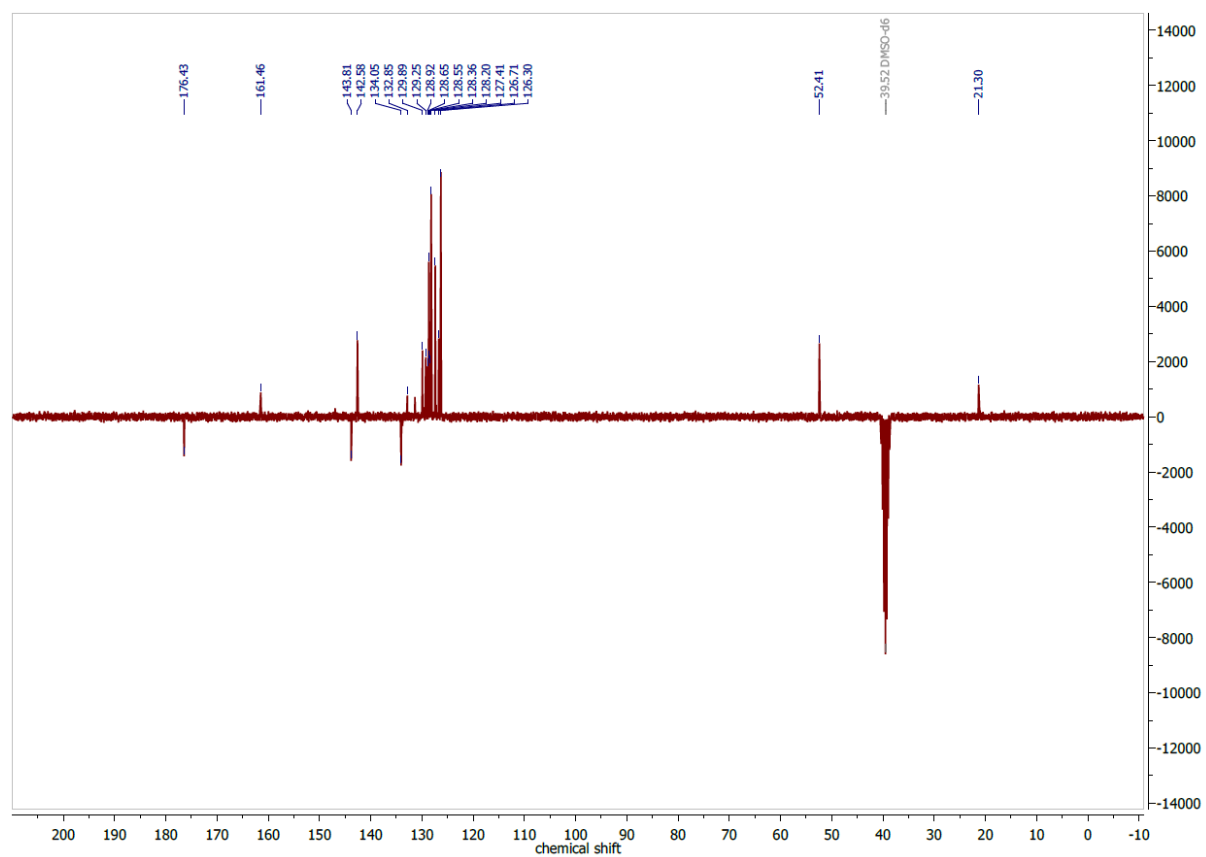


Figure 7.140 $^{13}\text{C}\{^1\text{H}\}$ DEPTQ NMR spectrum of HFbzTSCdm in $\text{DMSO-}d_6$ at 75 MHz.

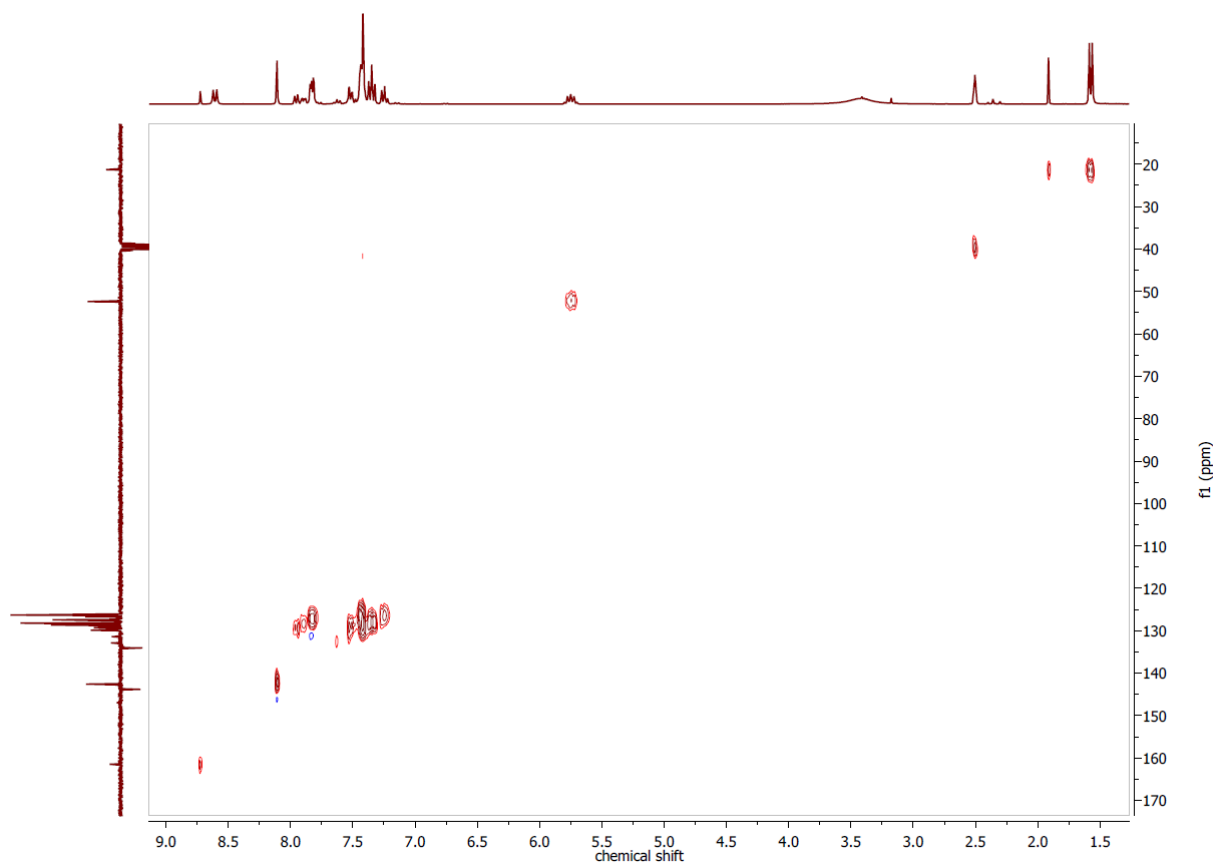


Figure 7.141 ^1H , ^{13}C HSQCed NMR spectrum of HFbzTSCdm in $\text{DMSO-}d_6$.

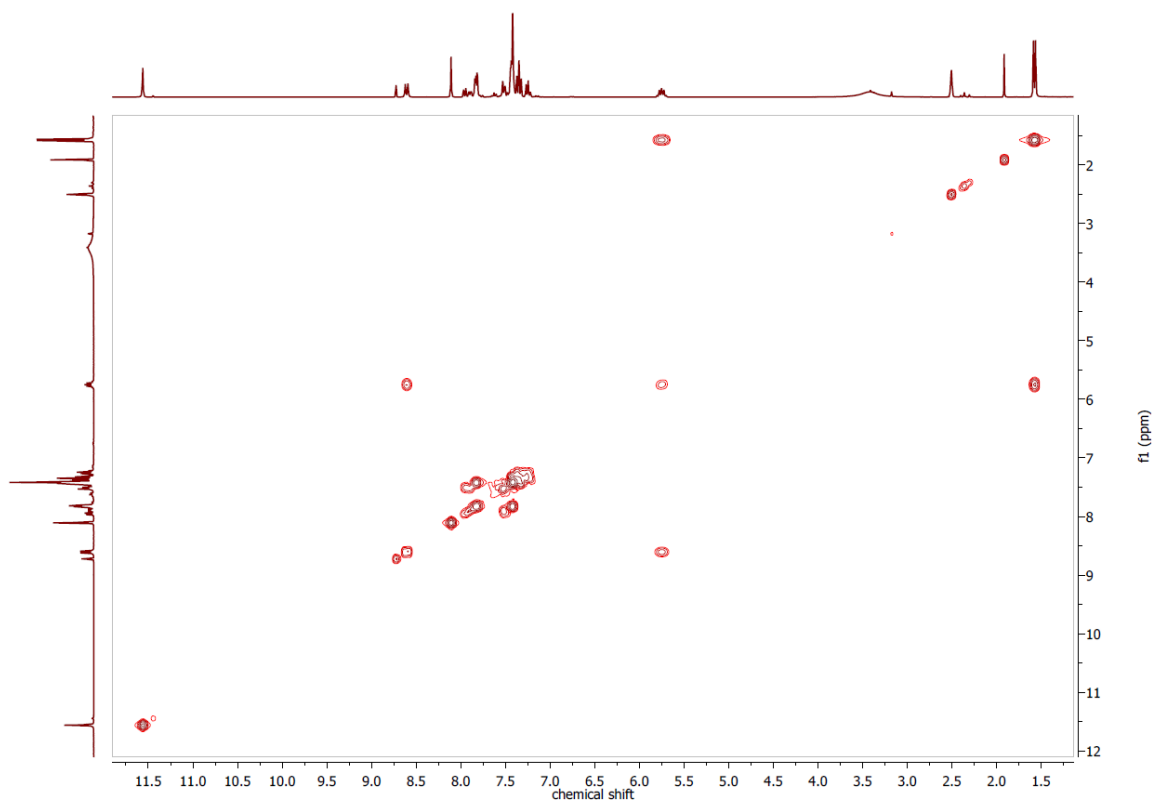


Figure 7.142 ^1H , ^1H COSY NMR spectrum of HFbzTSCdm in $\text{DMSO-}d_6$.

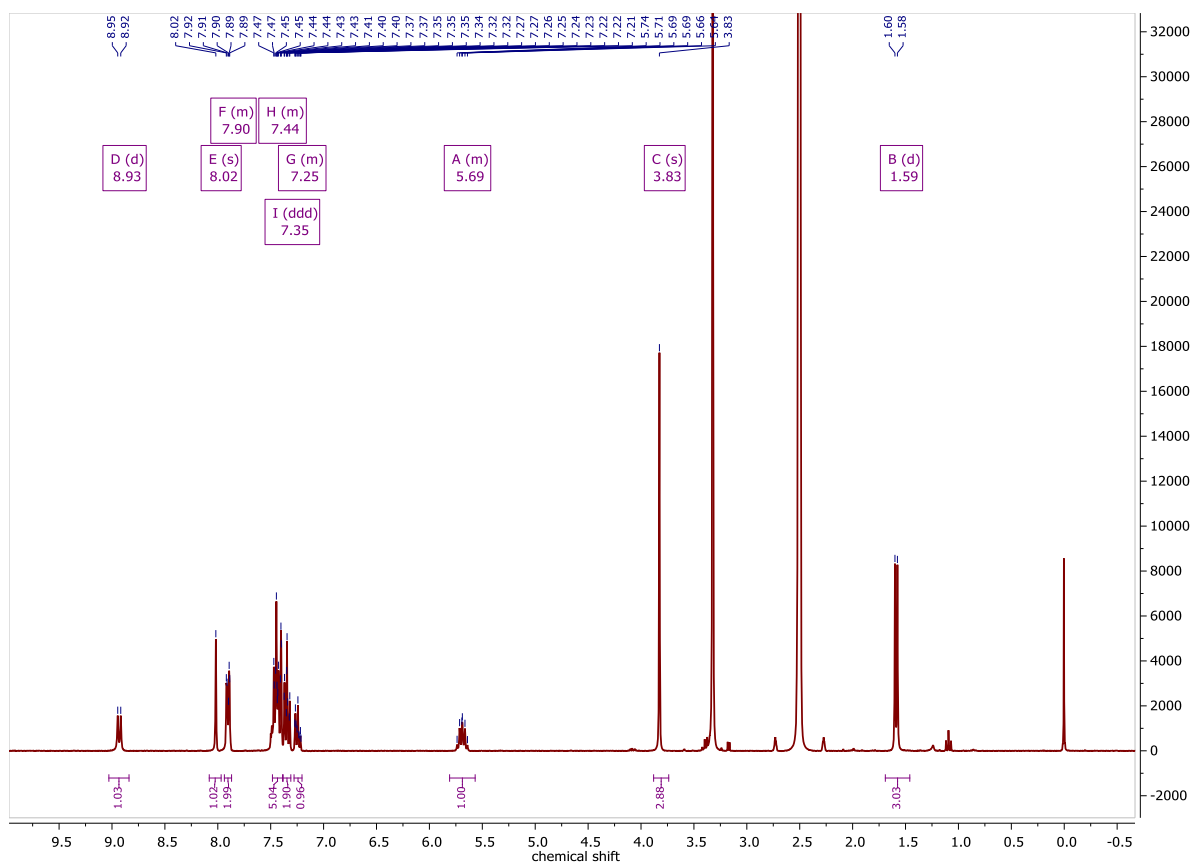


Figure 7.143 ^1H NMR spectrum of Hbz(m)TSCmB in $\text{DMSO-}d_6$ at 300 MHz.

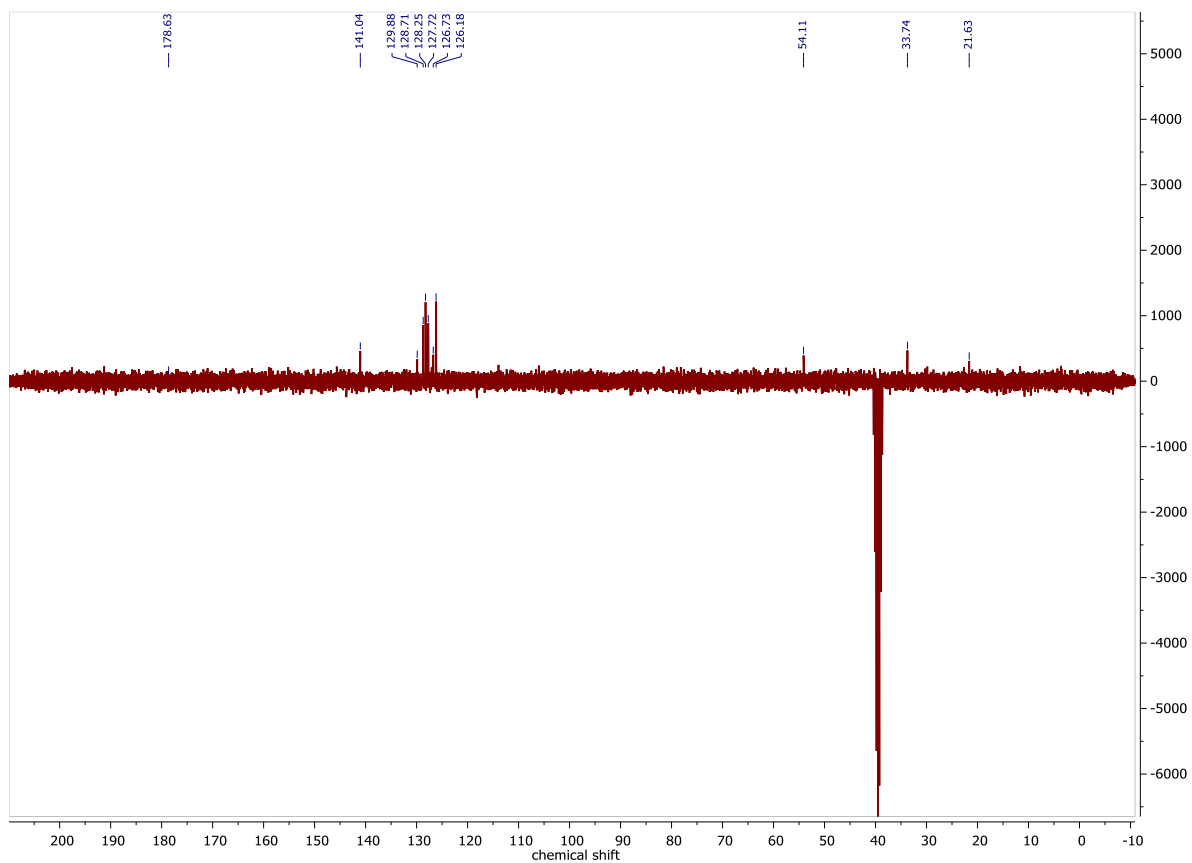


Figure 7.144 $^{13}\text{C}\{^1\text{H}\}$ DEPTQ NMR spectrum of Hbz(m)TSCmB in $\text{DMSO-}d_6$ at 75 MHz.

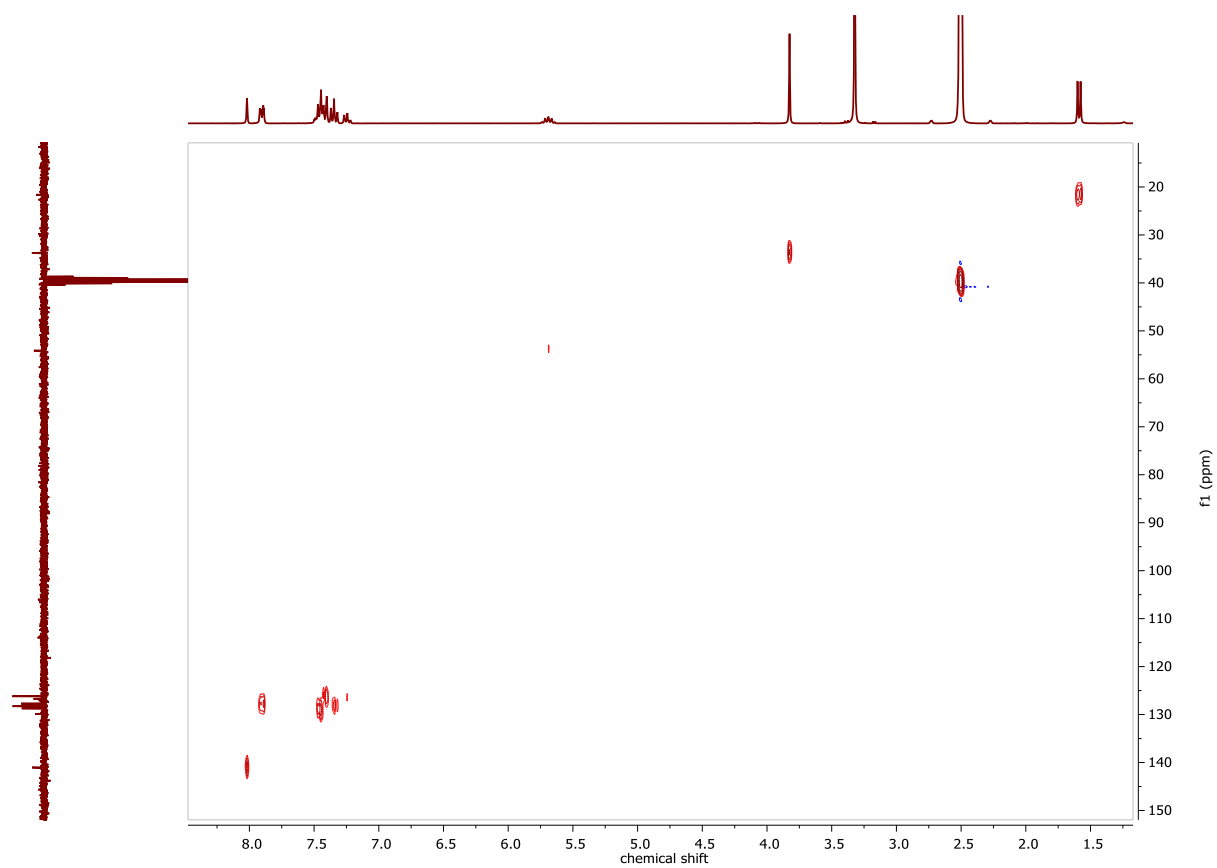


Figure 7.145 $^1\text{H},^{13}\text{C}$ HSQCed NMR spectrum of Hbz(m)TSCmB in $\text{DMSO-}d_6$.

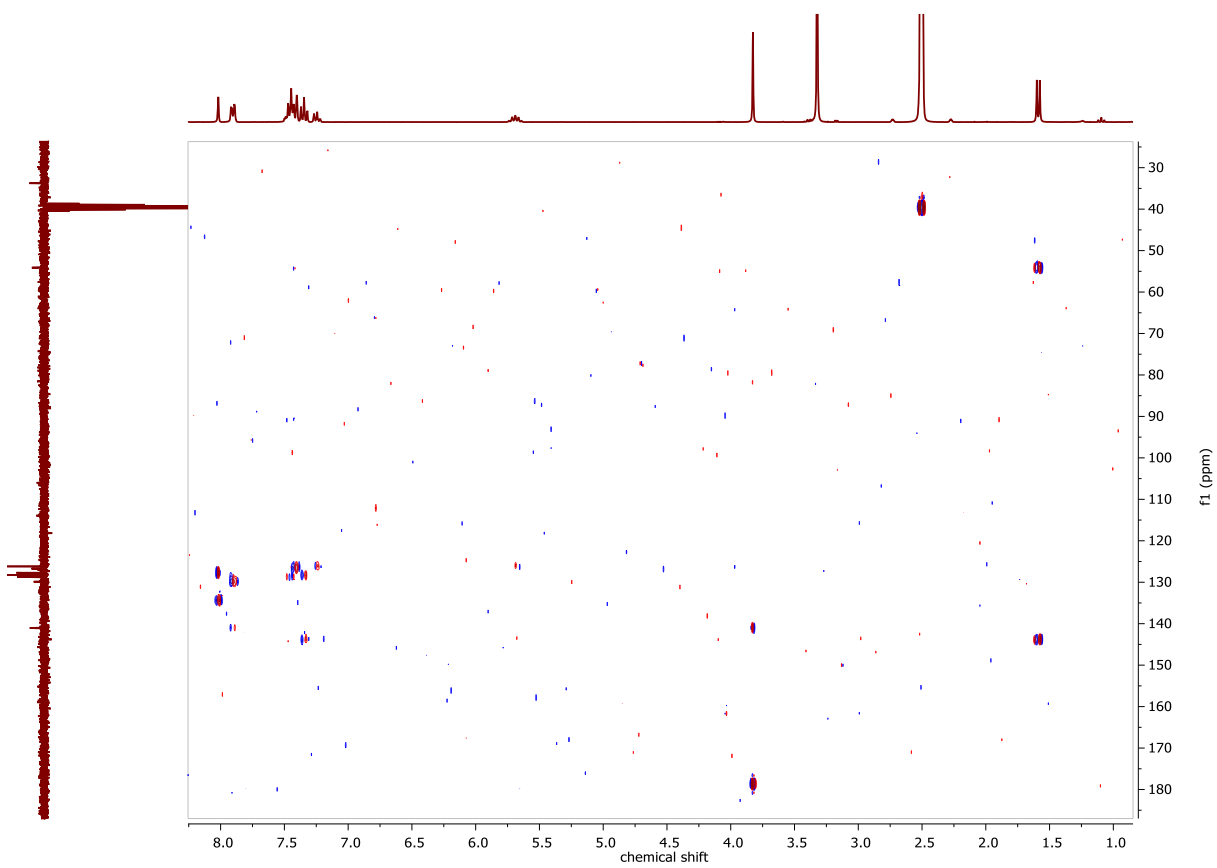


Figure 7.146 $^1\text{H},^{13}\text{C}$ HMBC NMR spectrum of Hbz(m)TSCmB in $\text{DMSO-}d_6$.

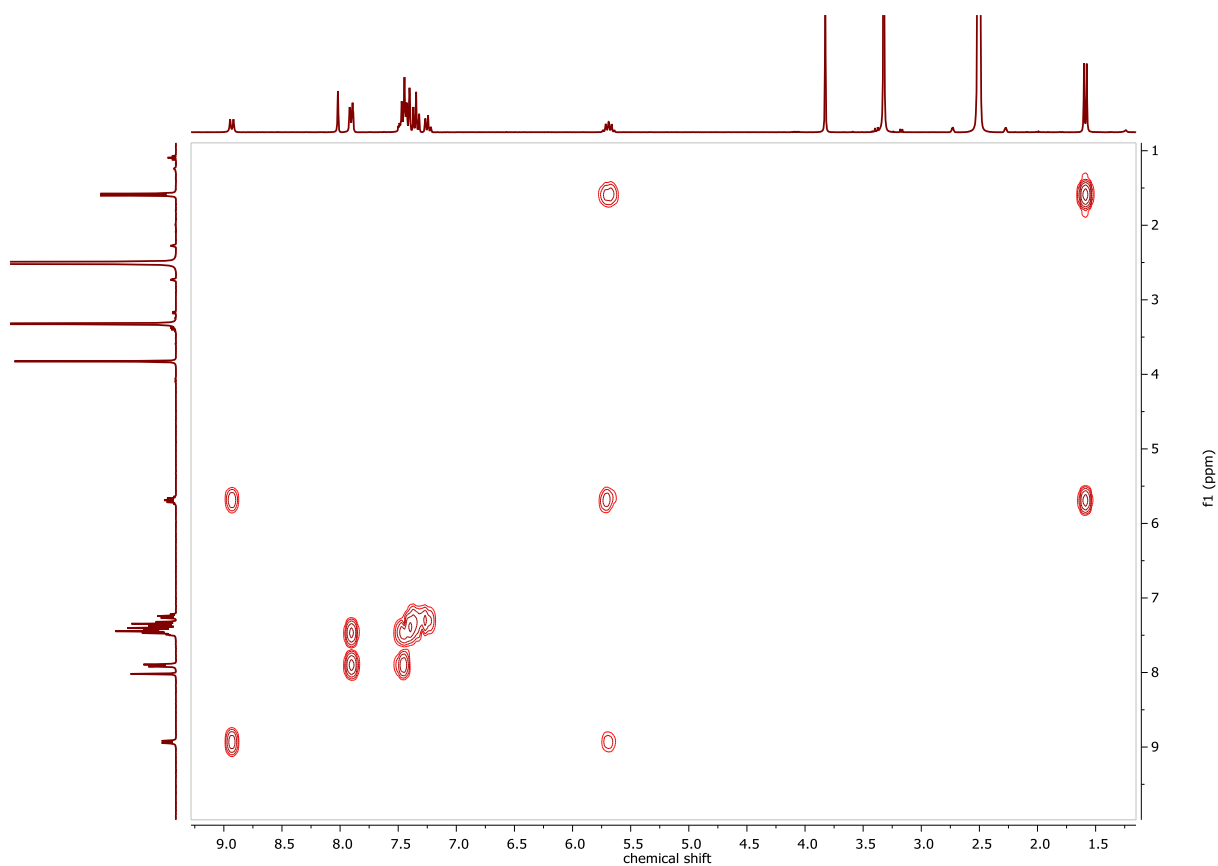


Figure 7.147 ¹H, ¹H COSY NMR spectrum of Hbz(m)TSCmB in DMSO-*d*₆.

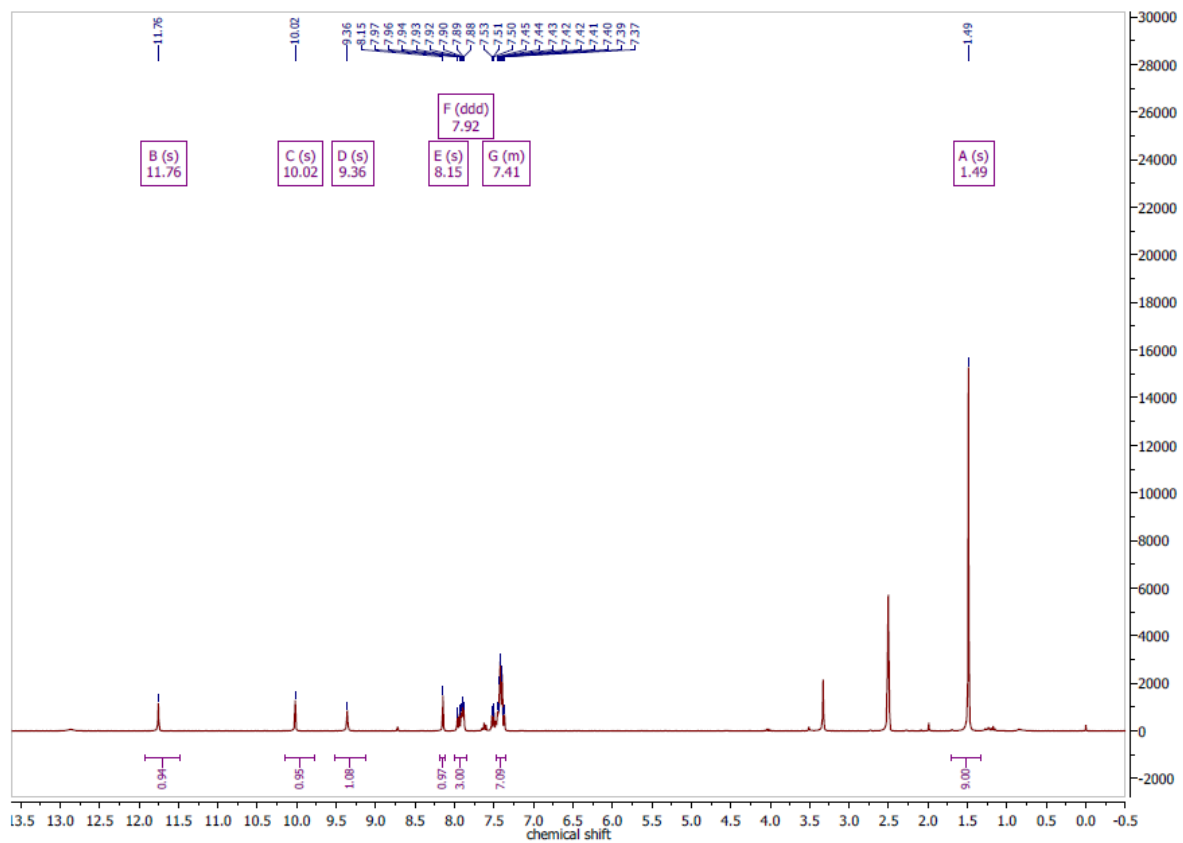


Figure 7.148 ¹H NMR spectrum of HbzTSCbap in DMSO-*d*₆ at 300 MHz.

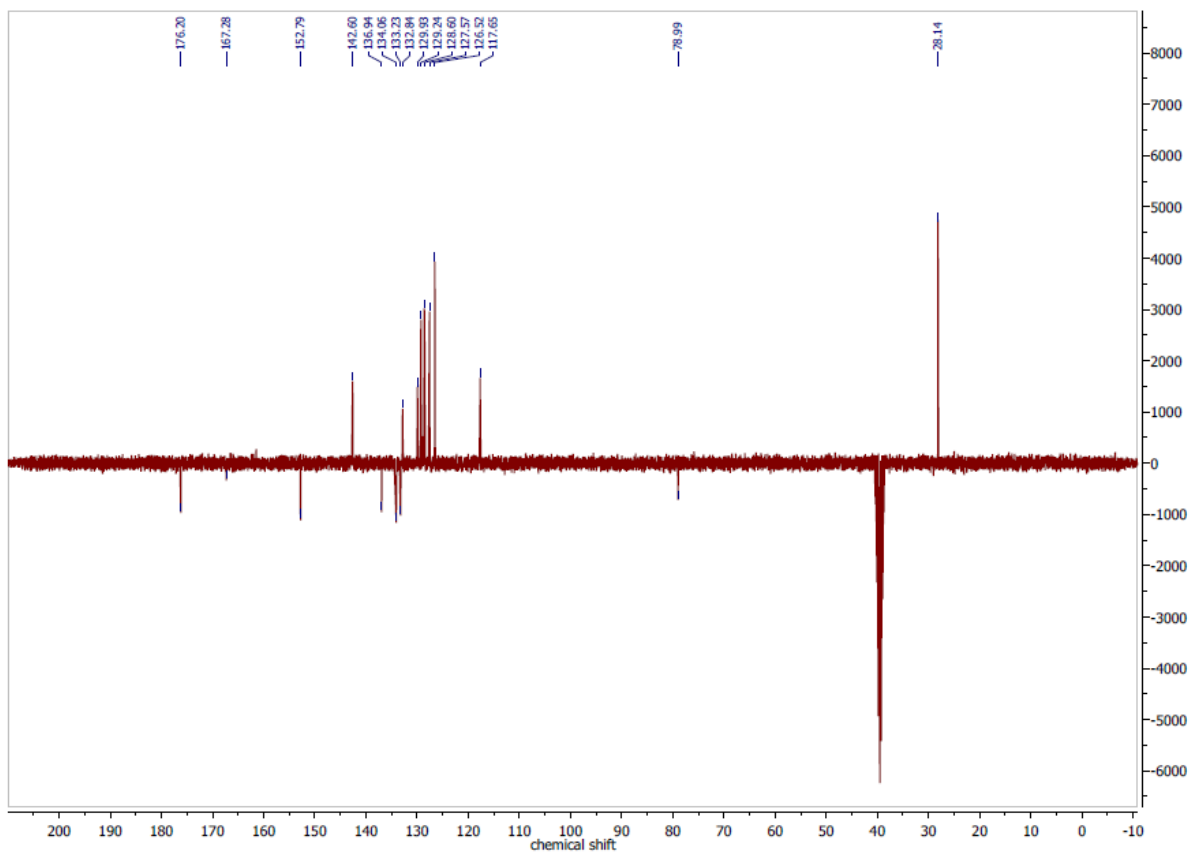


Figure 7.149 $^{13}\text{C}\{^1\text{H}\}$ DEPTQ NMR spectrum of HbzTSCap in $\text{DMSO-}d_6$ at 75 MHz.

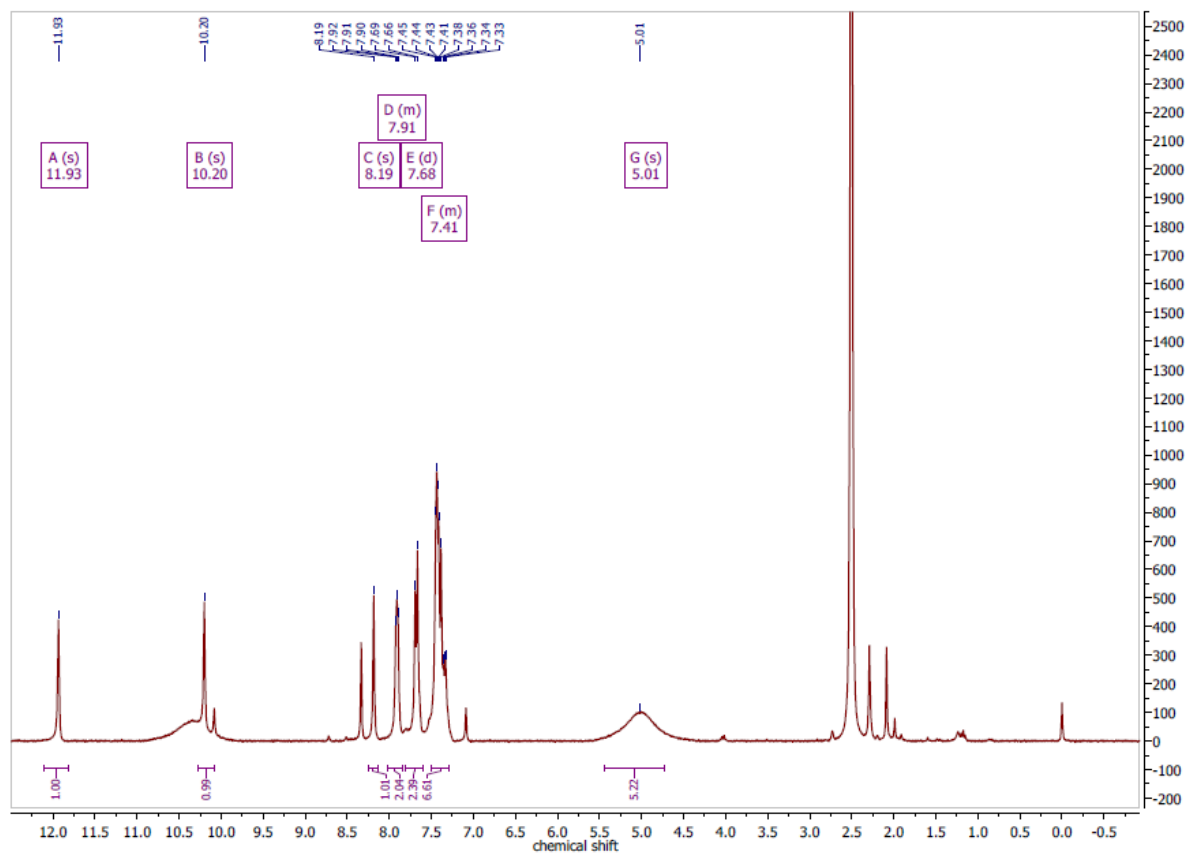


Figure 7.150 ^1H NMR spectrum of HbzTSCap in $\text{DMSO-}d_6$ at 300 MHz.

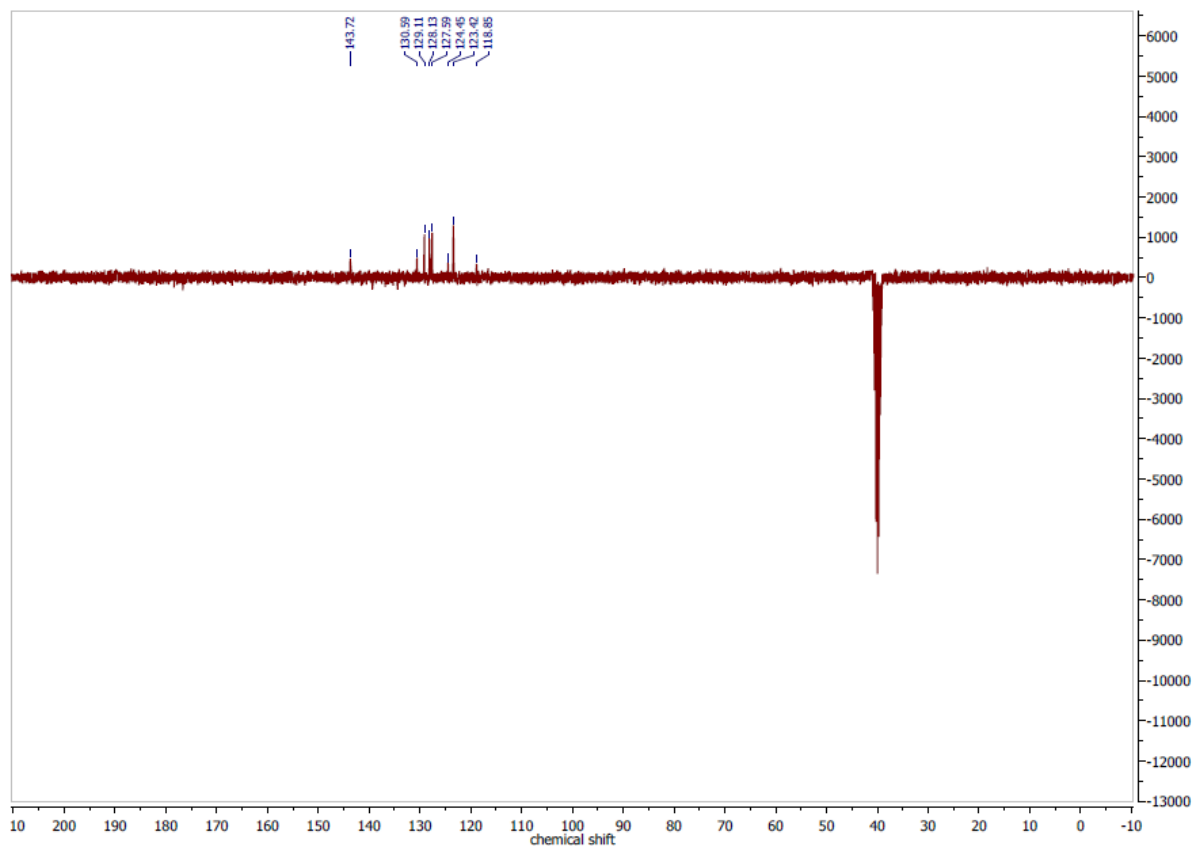


Figure 7.151 $^{13}\text{C}\{^1\text{H}\}$ DEPTQ NMR spectrum of HbzTSCap in $\text{DMSO-}d_6$ at 75 MHz.

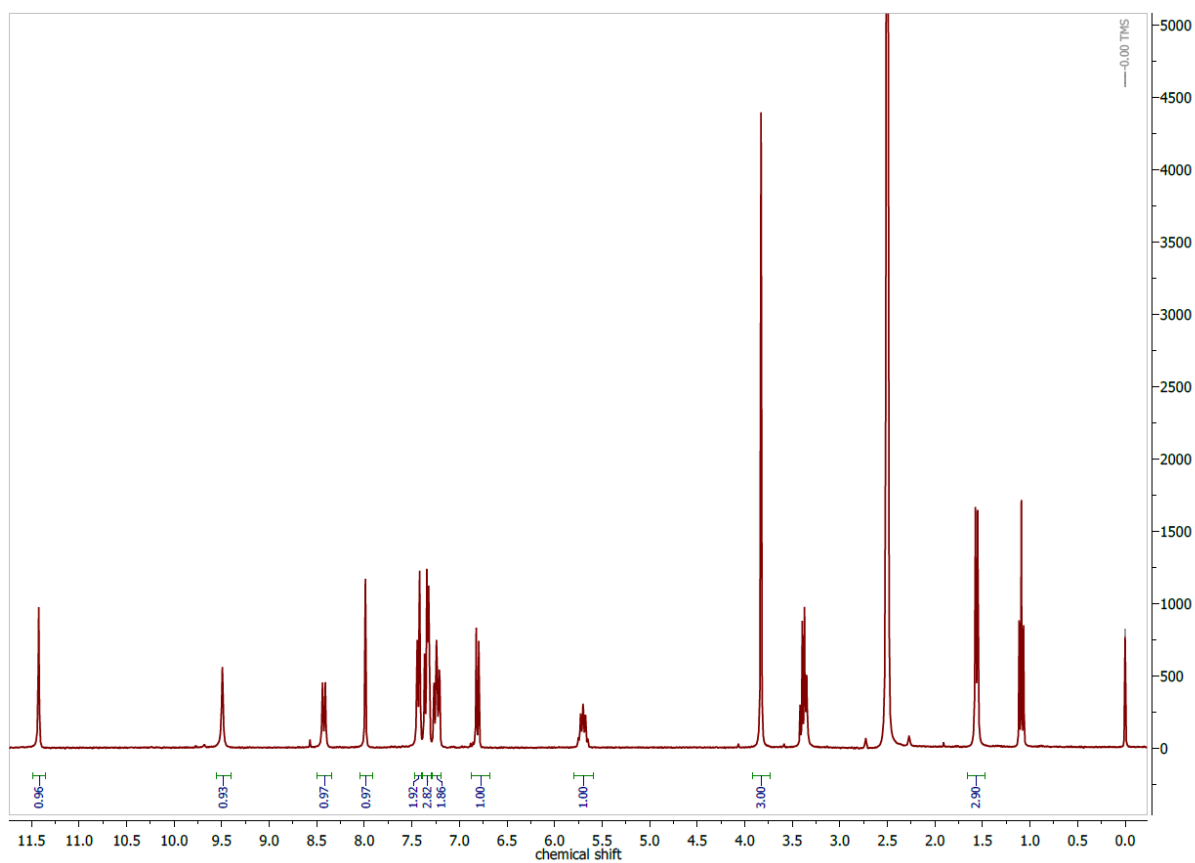


Figure 7.152 ^1H NMR spectrum of $\text{H}_2\text{vanTSCmB}$ in $\text{DMSO-}d_6$ at 300 MHz.

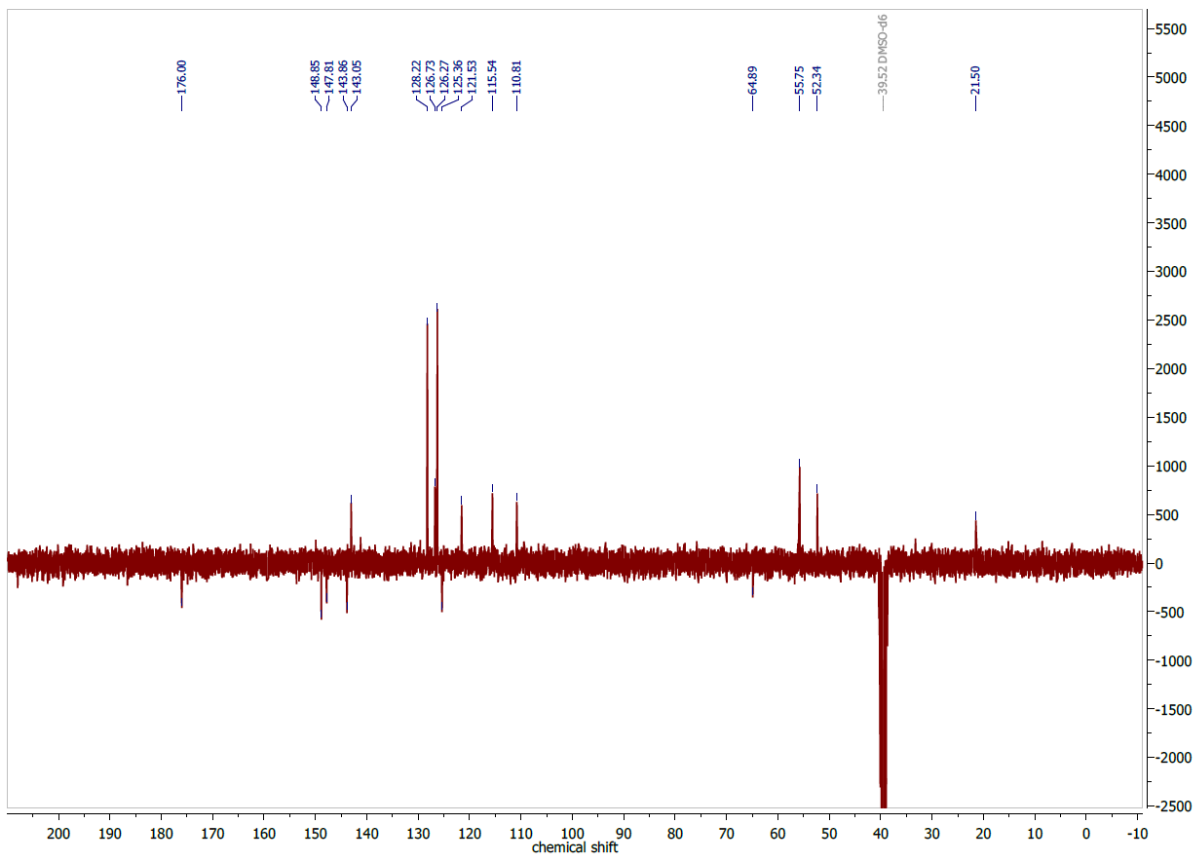


Figure 7.153 ^{13}C APT NMR spectrum of $\text{H}_2\text{vanTSCmB}$ in $\text{DMSO-}d_6$ at 75 MHz.

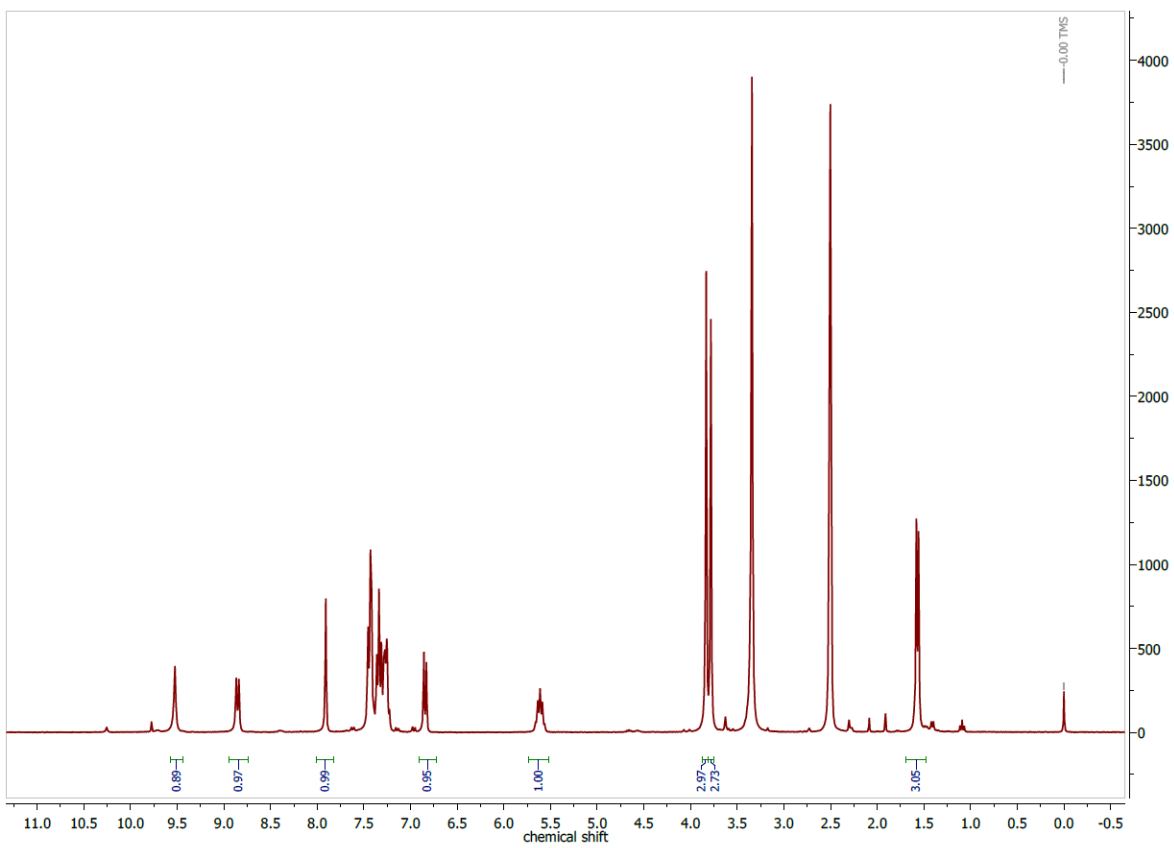


Figure 7.154 ^1H NMR spectrum of $\text{H}_2\text{van(m)TSCmB}$ in $\text{DMSO-}d_6$ at 300 MHz.

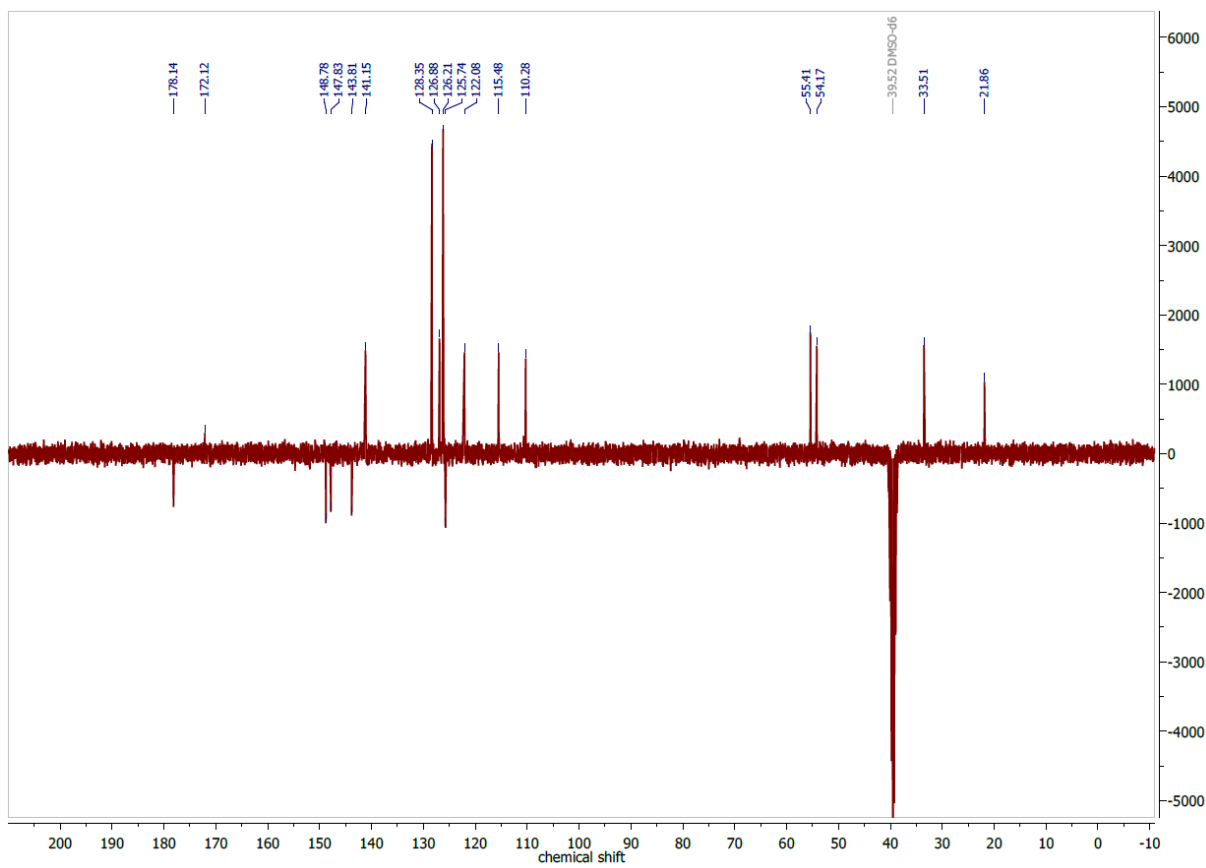


Figure 7.155 ^{13}C APT NMR spectrum of $\text{H}_2\text{van(m)TSCmB}$ in $\text{DMSO-}d_6$ at 75 MHz.

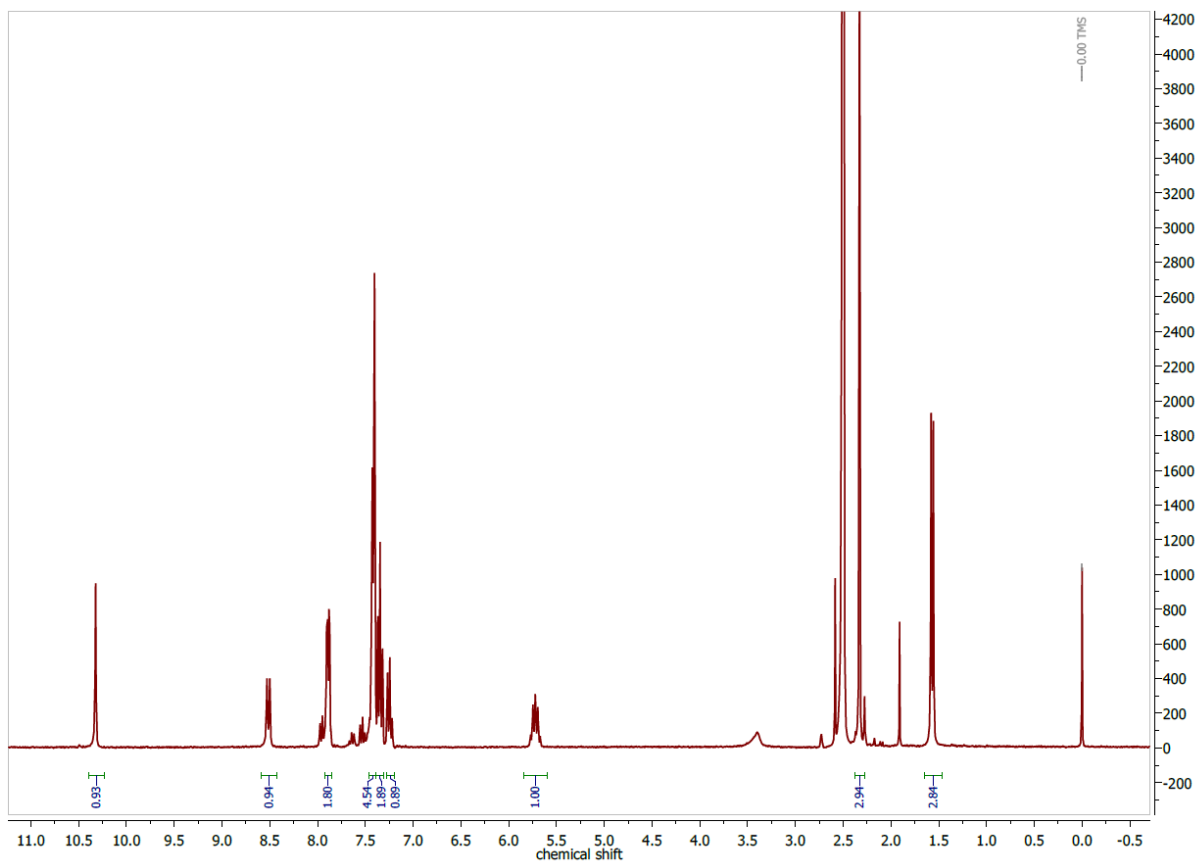


Figure 7.156 ^1H NMR spectrum of $\text{H}_2\text{aphTSCmB}$ in $\text{DMSO-}d_6$ at 300 MHz.

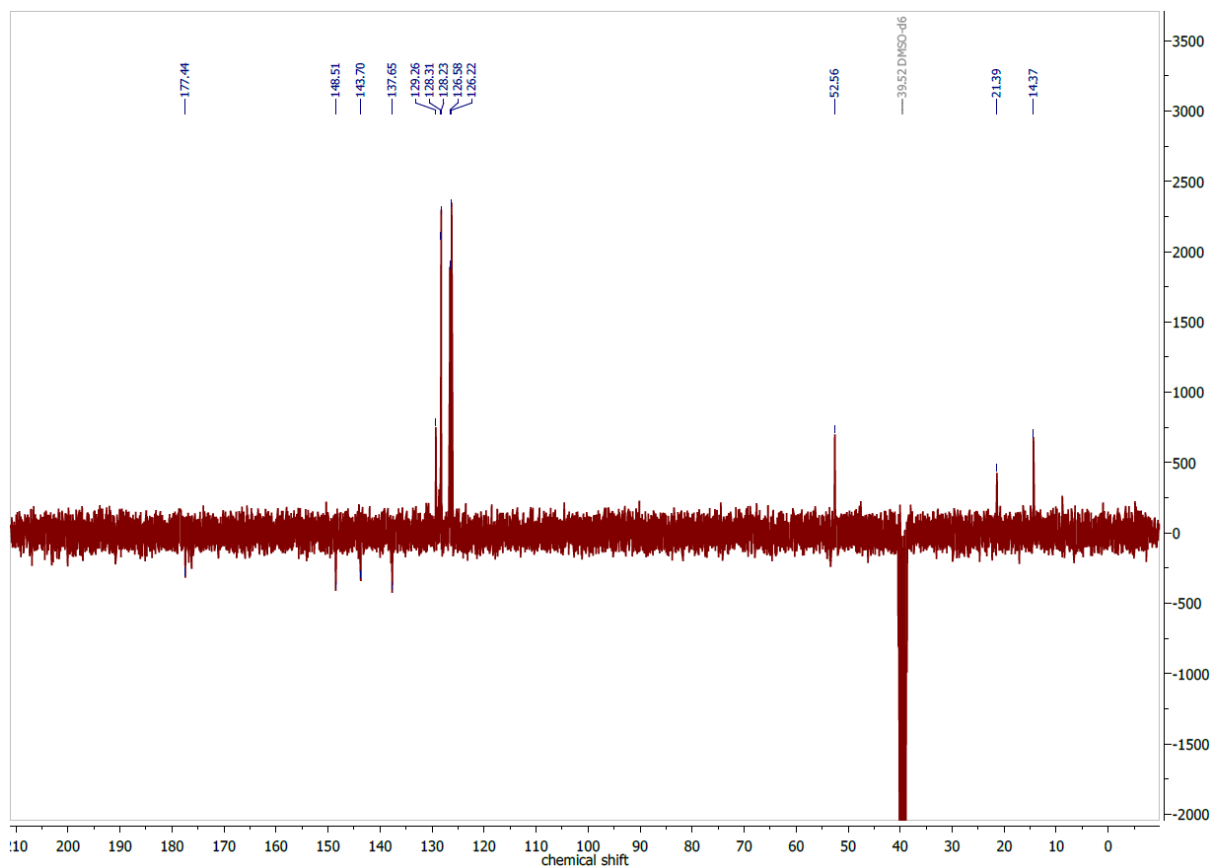


Figure 7.157 $^{13}\text{C}\{^1\text{H}\}$ DEPTQ NMR spectrum of $\text{H}_2\text{aphTSCmB}$ in $\text{DMSO-}d_6$ at 75 MHz.

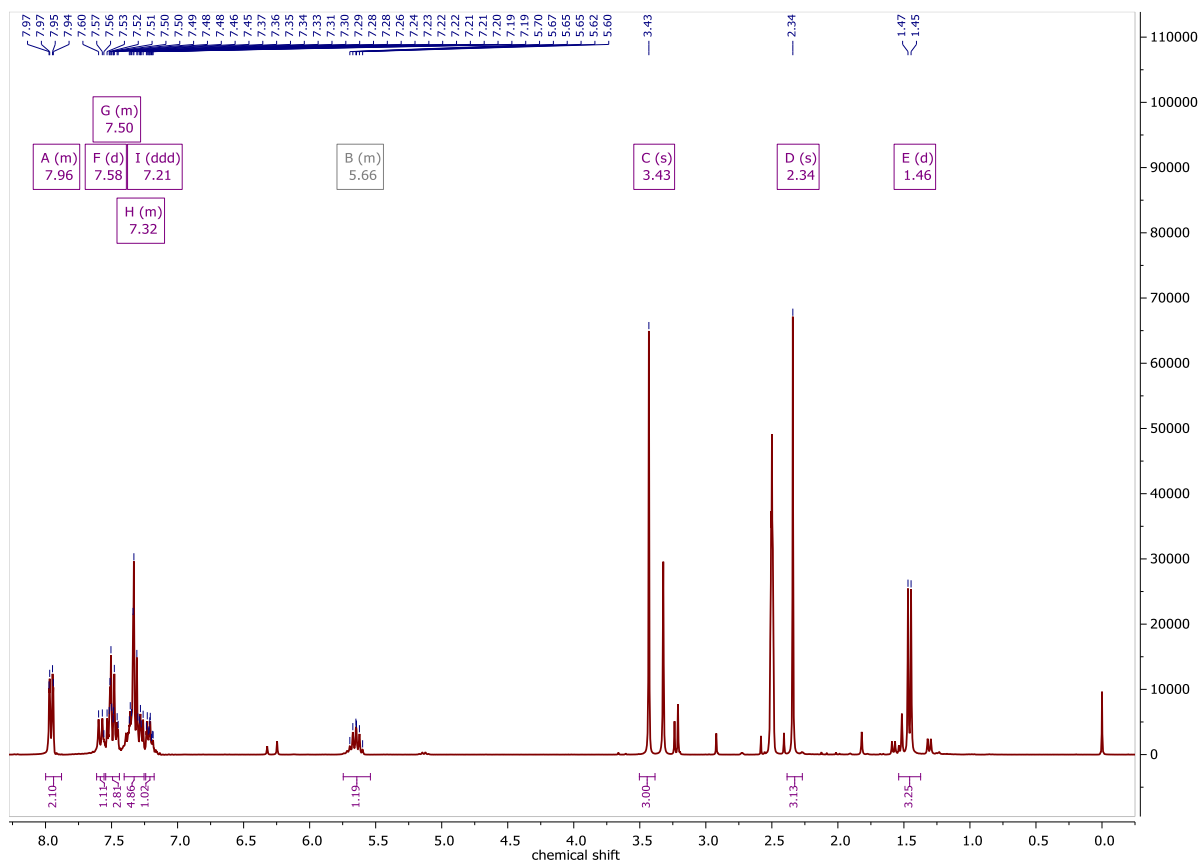


Figure 7.158 ^1H NMR spectrum of $\text{H}_2\text{aph(m)TSCmB}$ in $\text{DMSO-}d_6$ at 300 MHz.

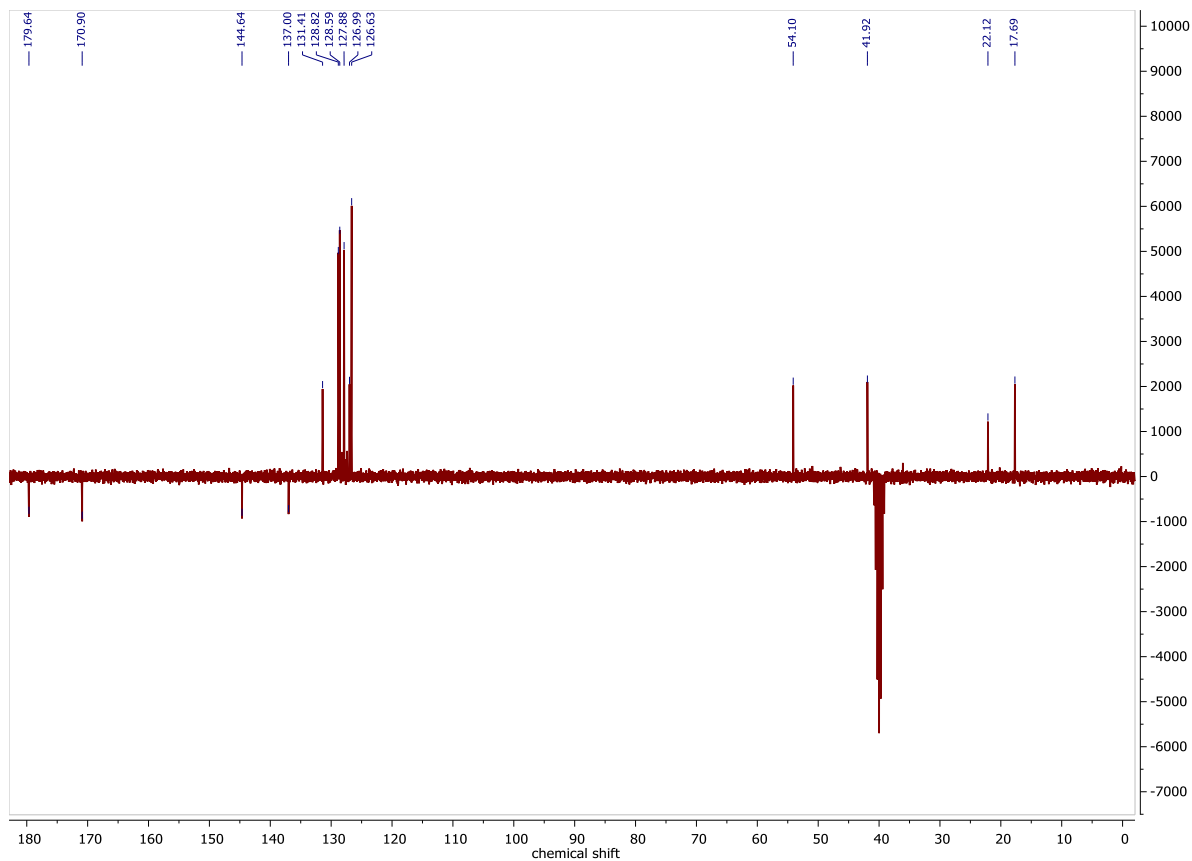


Figure 7.159 $^{13}\text{C}\{^1\text{H}\}$ DEPTQ NMR spectrum of $\text{H}_2\text{aph(m)TSCmB}$ in $\text{DMSO-}d_6$ at 75 MHz.

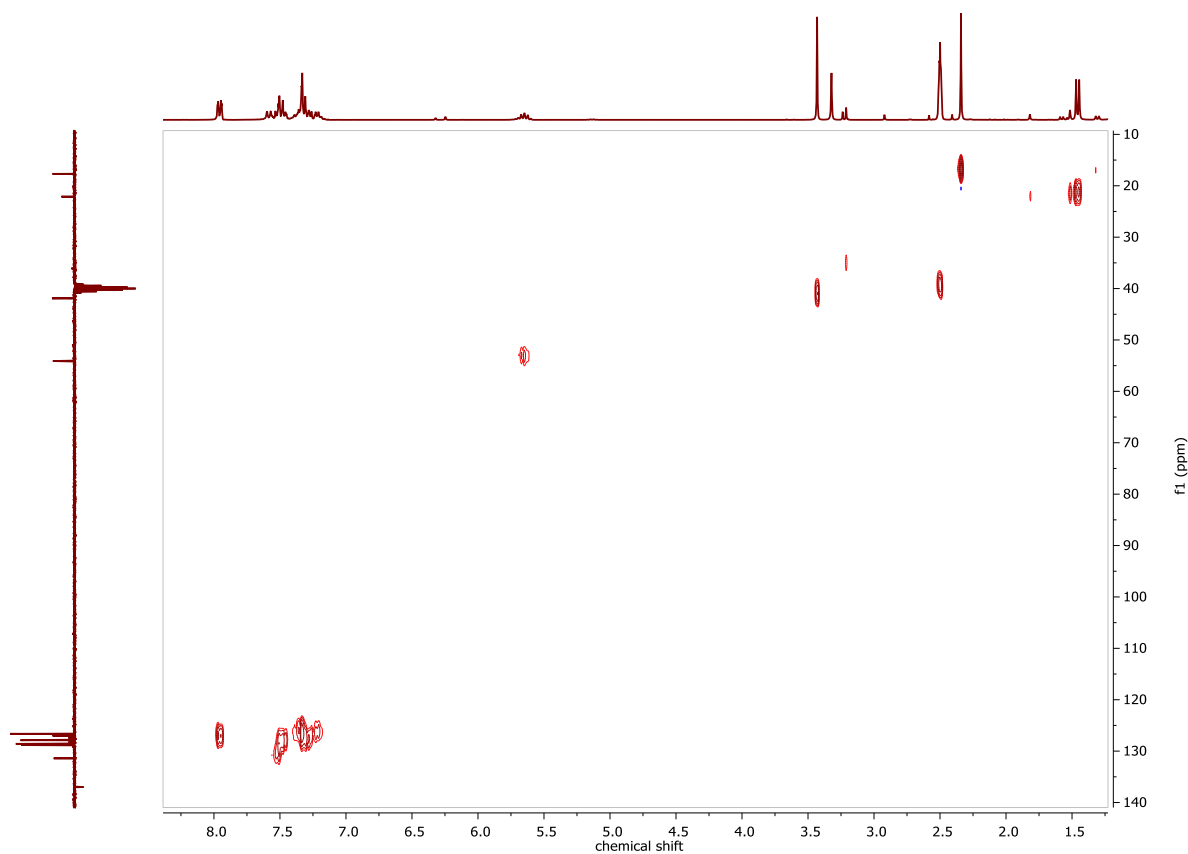


Figure 7.160 $^1\text{H}, ^{13}\text{C}$ HSQCed NMR spectrum of $\text{H}_2\text{aph(m)TSCmB}$ in $\text{DMSO-}d_6$.

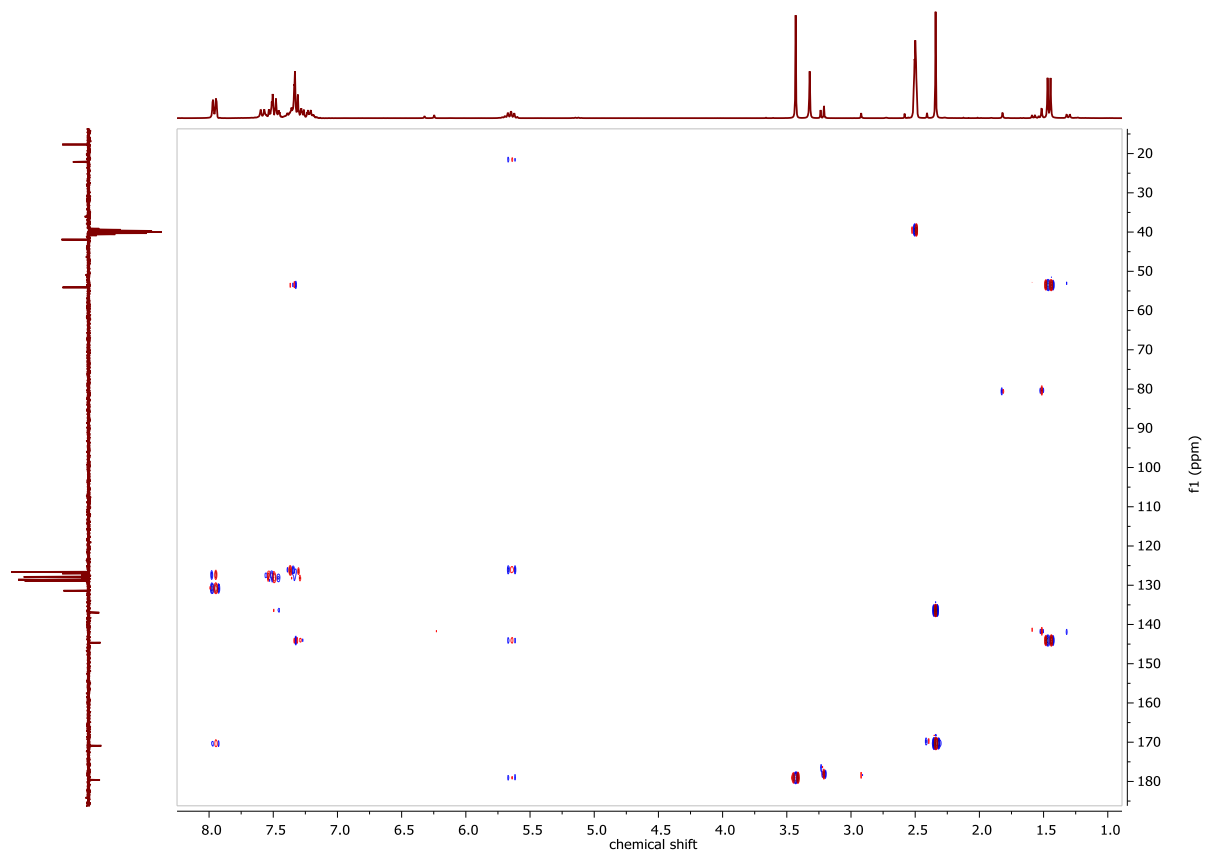


Figure 7.161 ^1H , ^{13}C HMBC NMR spectrum of $\text{H}_2\text{aph(m)TSCmB}$ in $\text{DMSO-}d_6$.

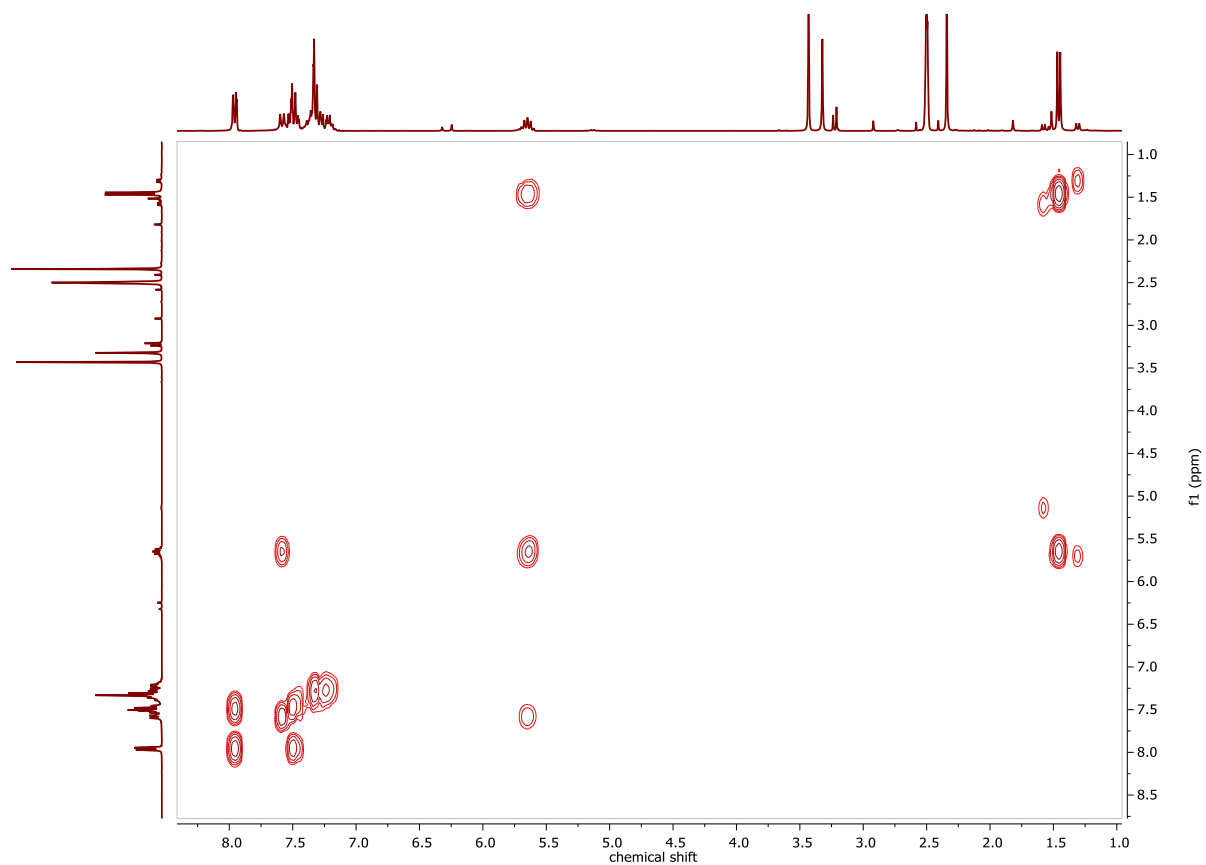


Figure 7.162 ^1H , ^1H COSY NMR spectrum of $\text{H}_2\text{aph(m)TSCmB}$ in $\text{DMSO-}d_6$.

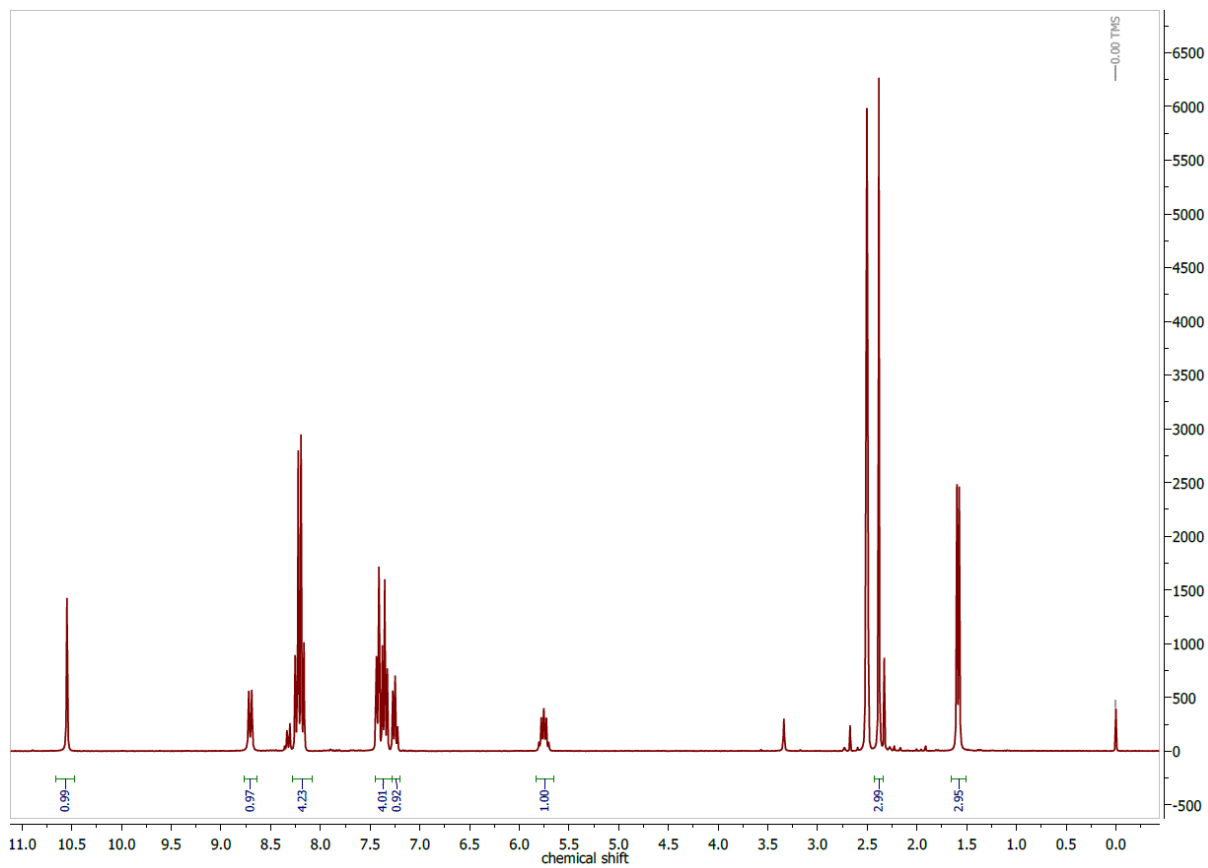


Figure 7.163 ^1H NMR spectrum of $\text{H}_{24}\text{-NO}_2\text{aphTSCmB}$ in $\text{DMSO-}d_6$ at 300 MHz.

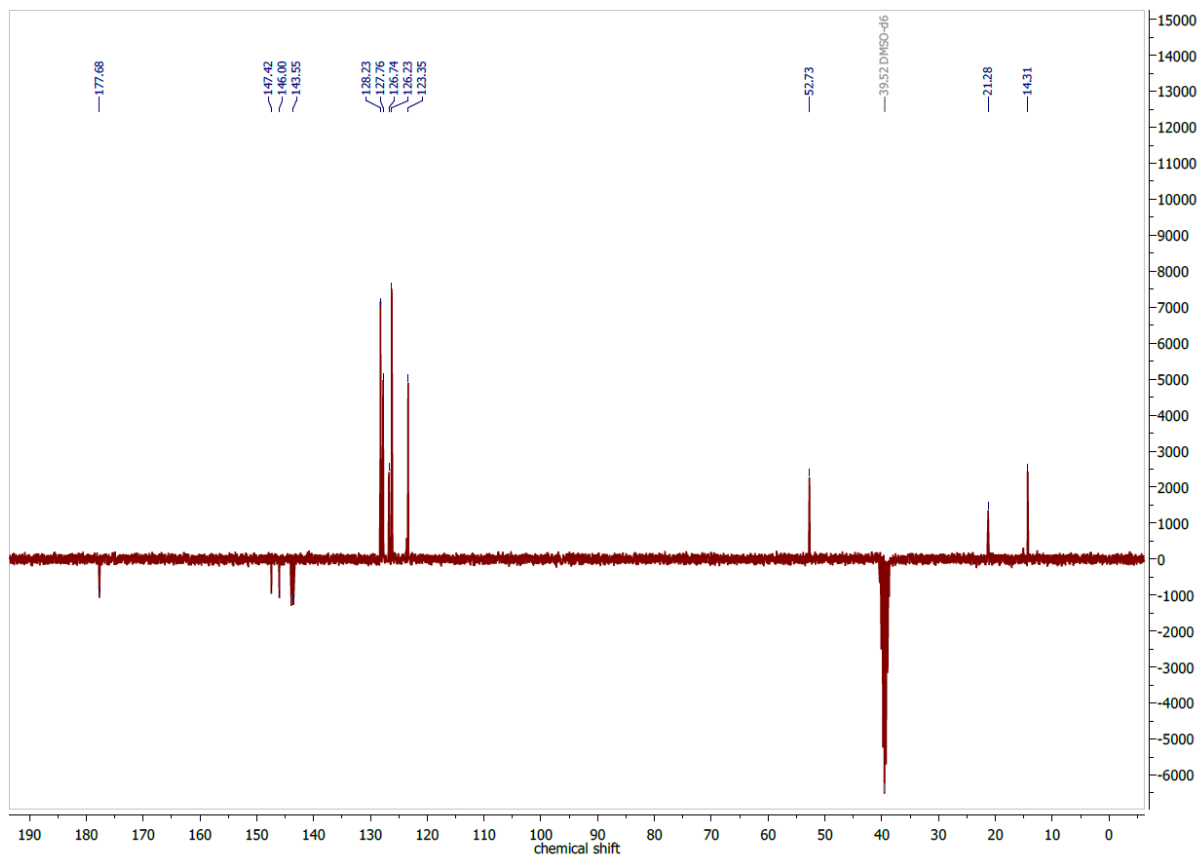


Figure 7.164 ^{13}C APT NMR spectrum of $\text{H}_{24}\text{-NO}_2\text{aphTSCmB}$ in $\text{DMSO-}d_6$ at 75 MHz.

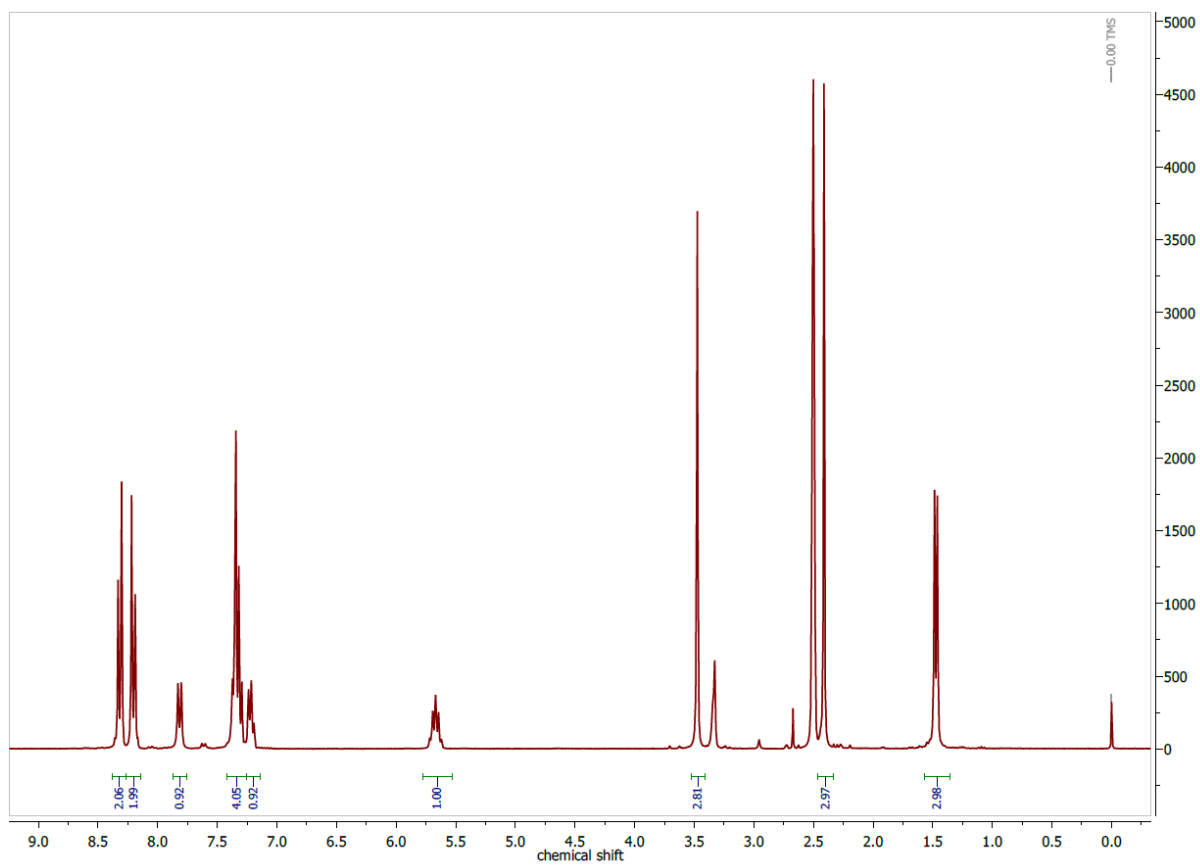


Figure 7.165 ^1H NMR spectrum of $\text{H}_{24}\text{-NO}_2\text{aph(m)TSCmB}$ in $\text{DMSO-}d_6$ at 300 MHz.

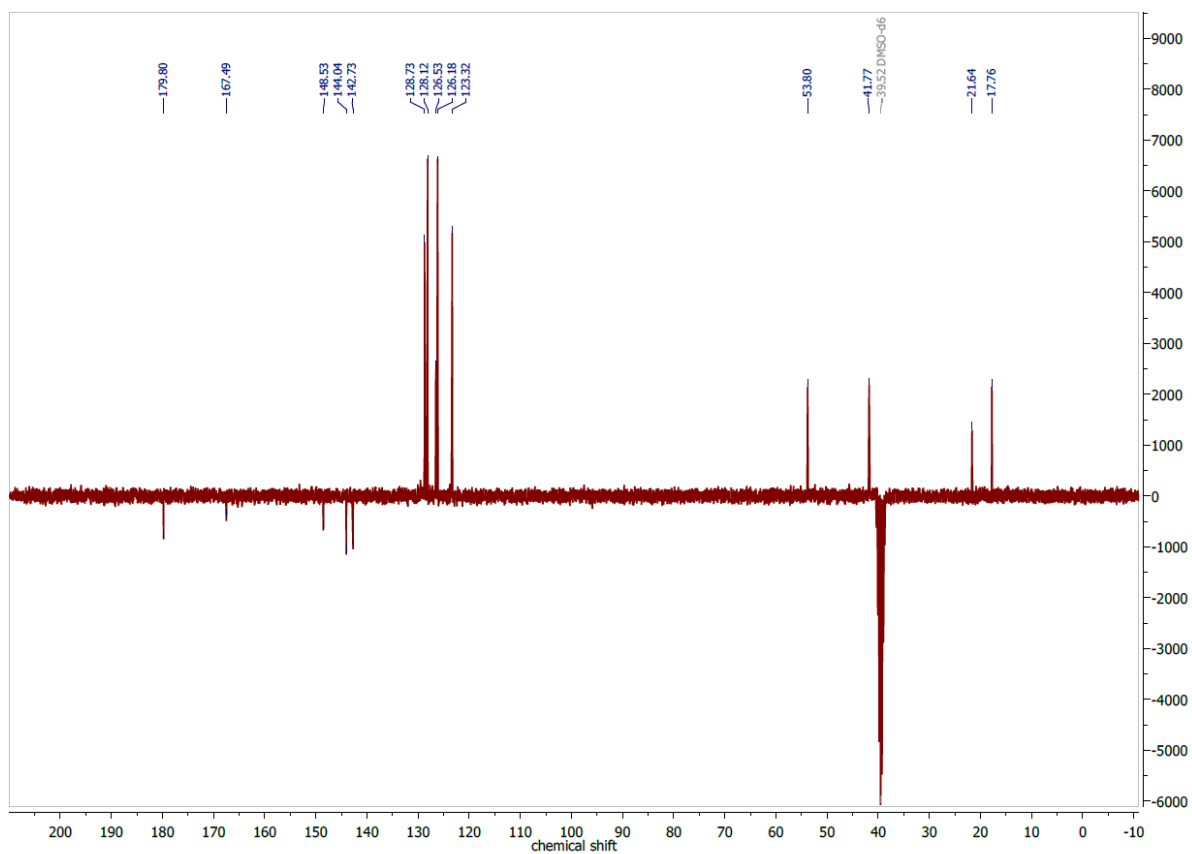


Figure 7.166 ^{13}C APT NMR spectrum of $\text{H}_{24}\text{-NO}_2\text{aph(m)TSCmB}$ in $\text{DMSO-}d_6$ at 75 MHz.

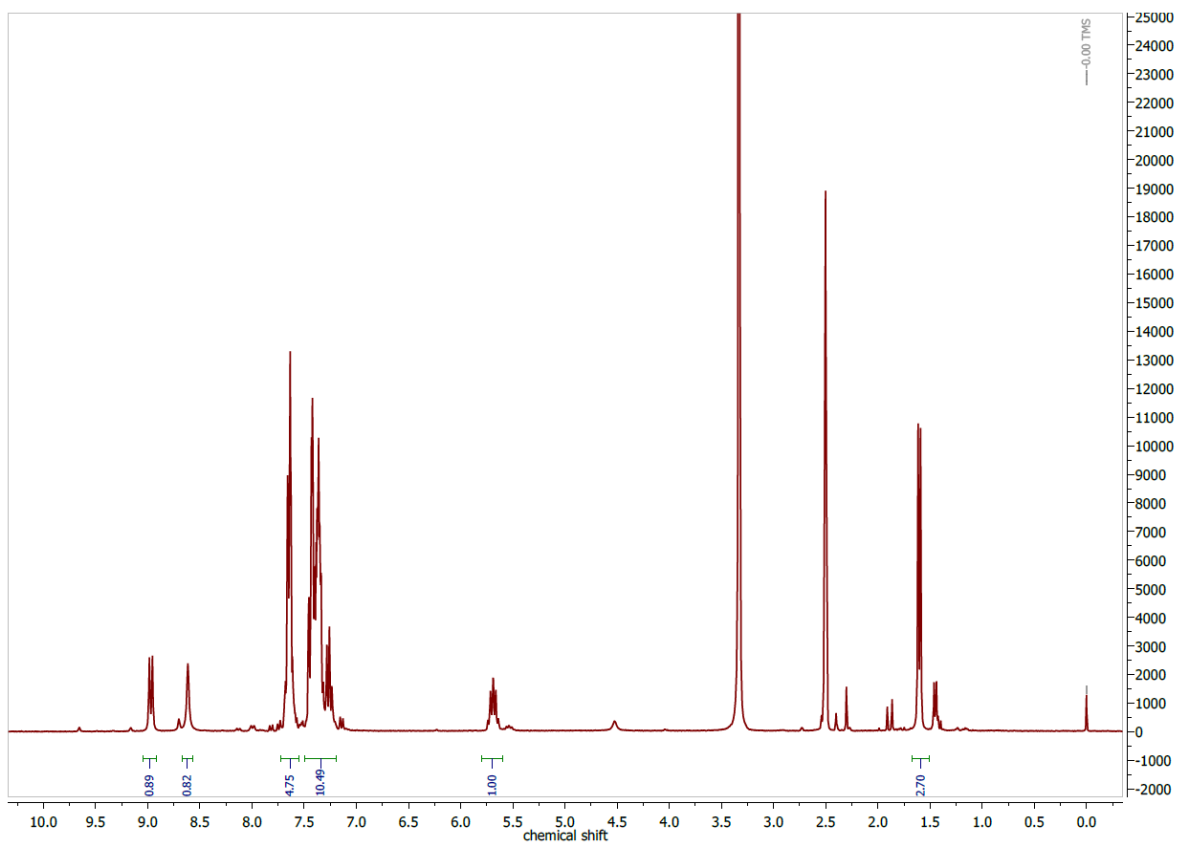


Figure 7.167 ^1H NMR spectrum of $\text{H}_2\text{bphTSCmB}$ in $\text{DMSO-}d_6$ at 300 MHz.

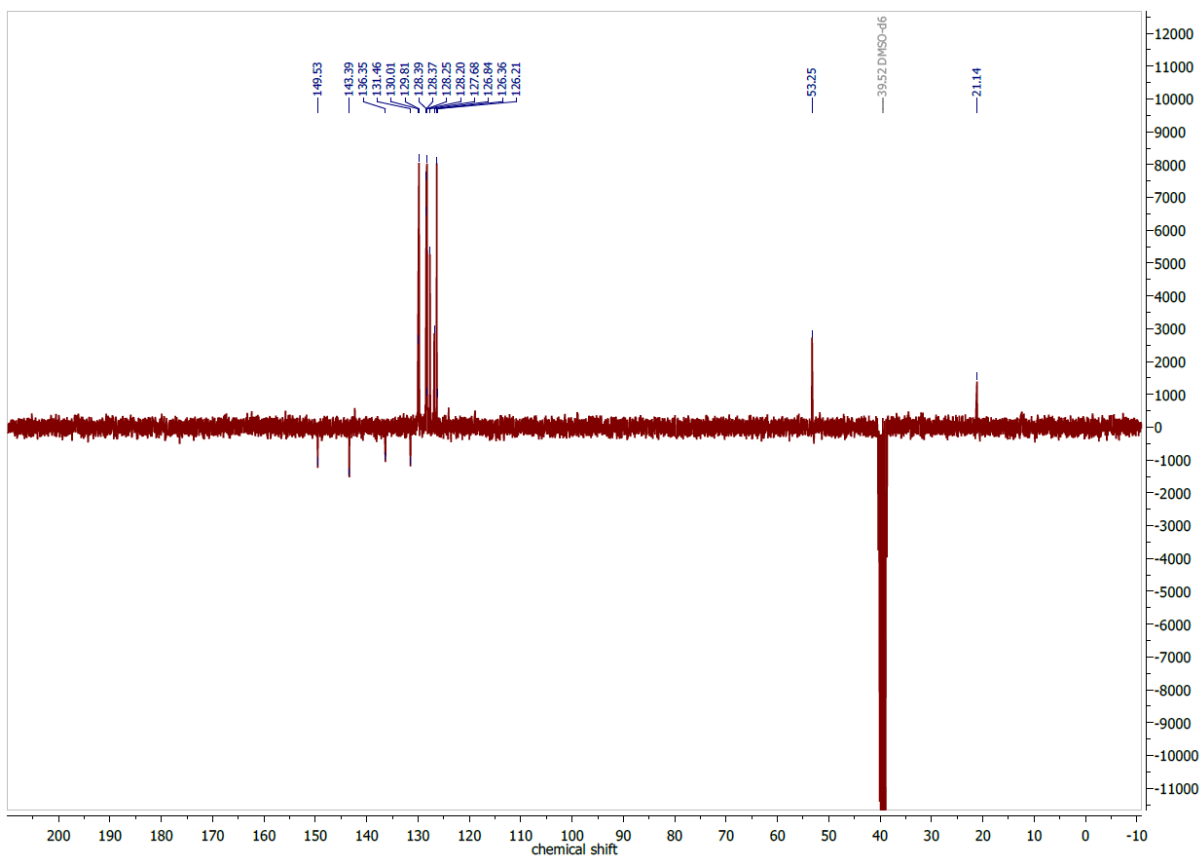


Figure 7.168 $^{13}\text{C}\{^1\text{H}\}$ DEPTQ NMR spectrum of $\text{H}_2\text{bphTSCmB}$ in $\text{DMSO-}d_6$ at 300 MHz.

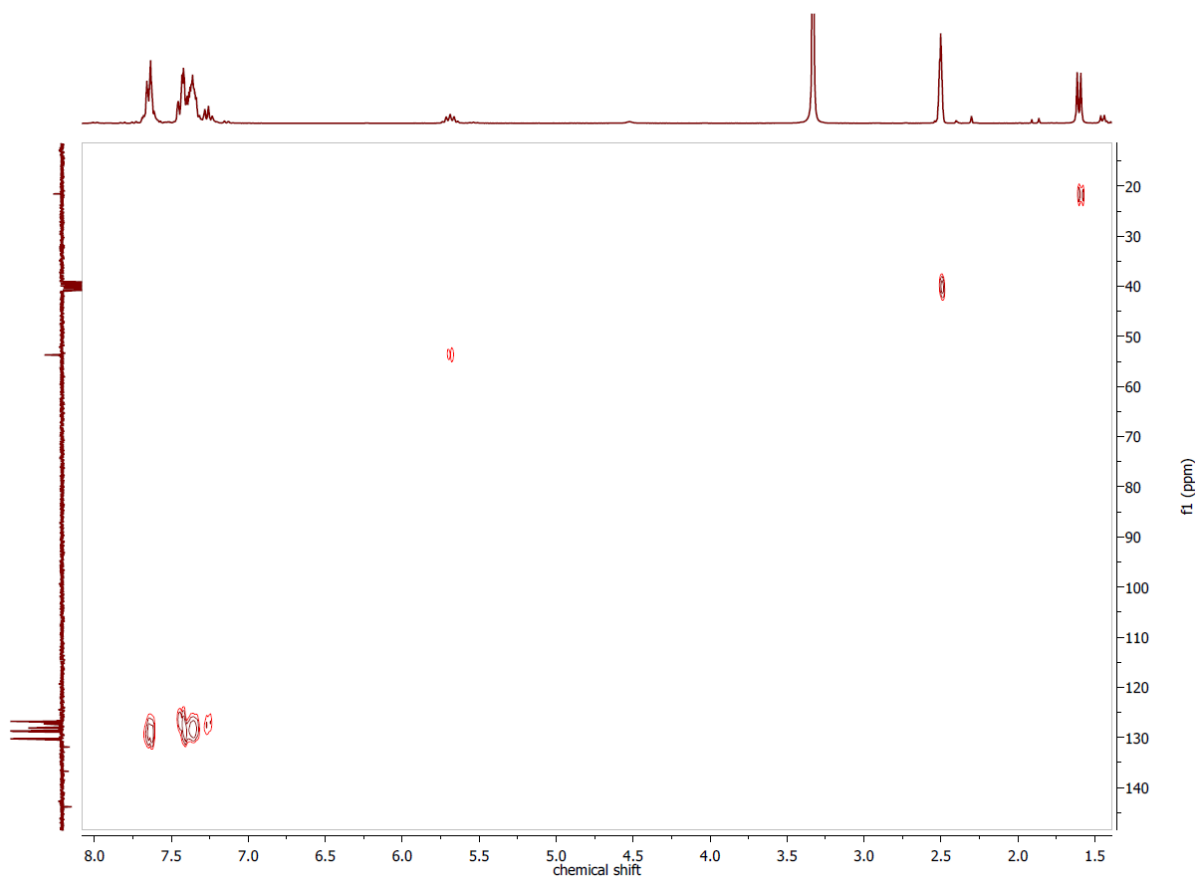


Figure 7.169 ^1H , ^{13}C HSQC NMR spectrum of $\text{H}_2\text{bphTSCmB}$ in $\text{DMSO}-d_6$ at 300 MHz.

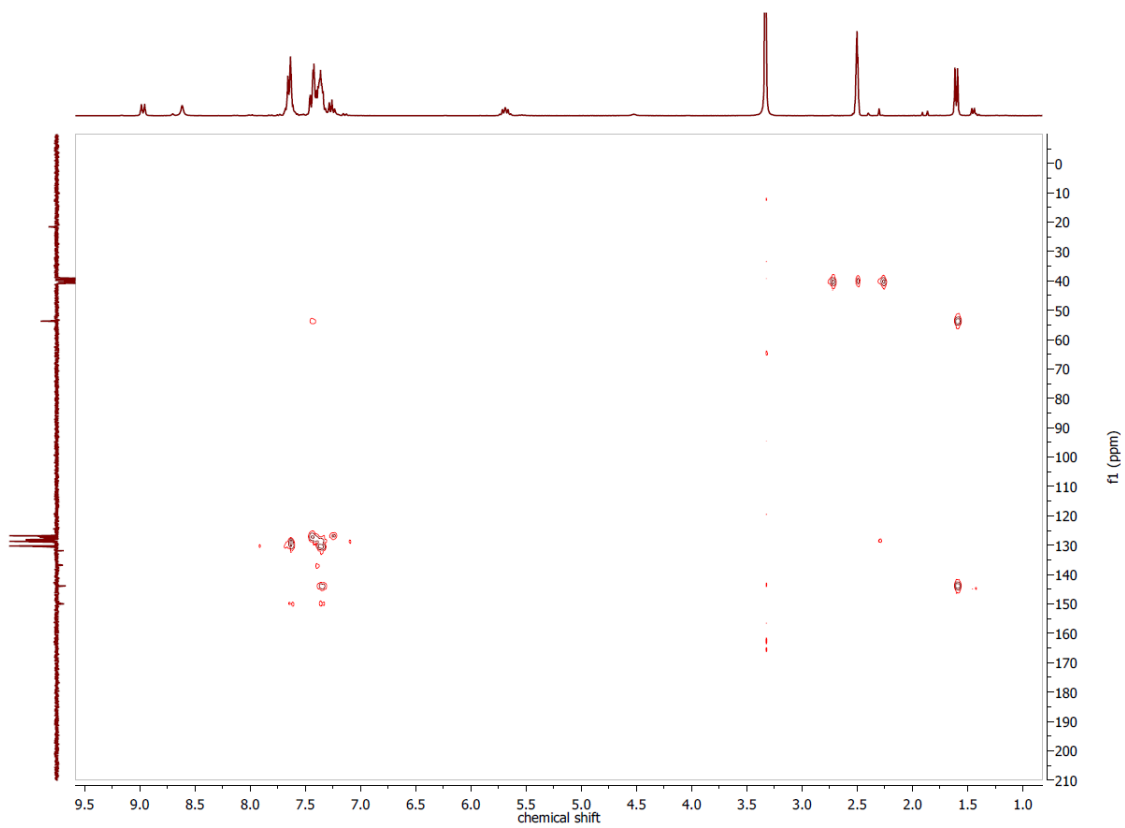


Figure 7.170 ^1H , ^{13}C HMBC NMR spectrum of $\text{H}_2\text{bphTSCmB}$ in $\text{DMSO}-d_6$ at 300 MHz.

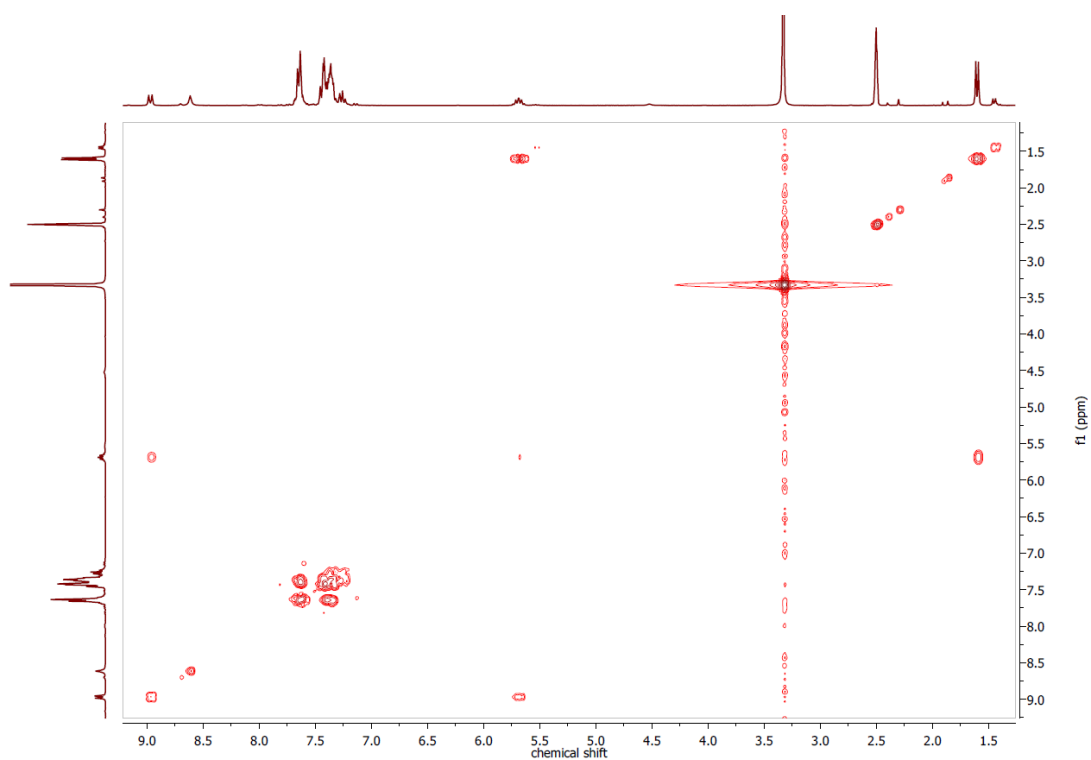


Figure 7.171 $^1\text{H}, ^1\text{H}$ COSY NMR spectrum of $\text{H}_2\text{bphTSCmB}$ in $\text{DMSO}-d_6$ at 300 MHz.

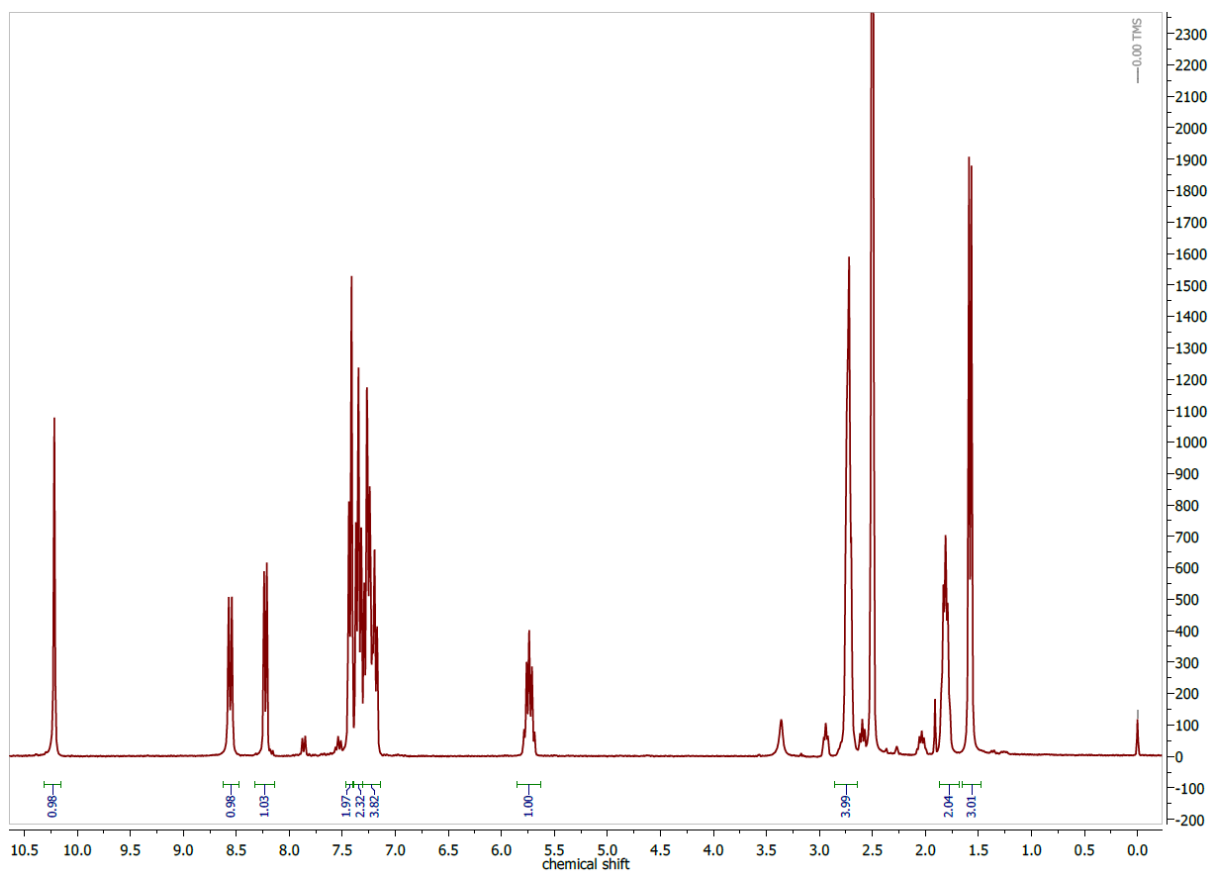


Figure 7.172 ^1H NMR spectrum of $\text{H}_2\text{tetTSCmB}$ in $\text{DMSO}-d_6$ at 300 MHz.

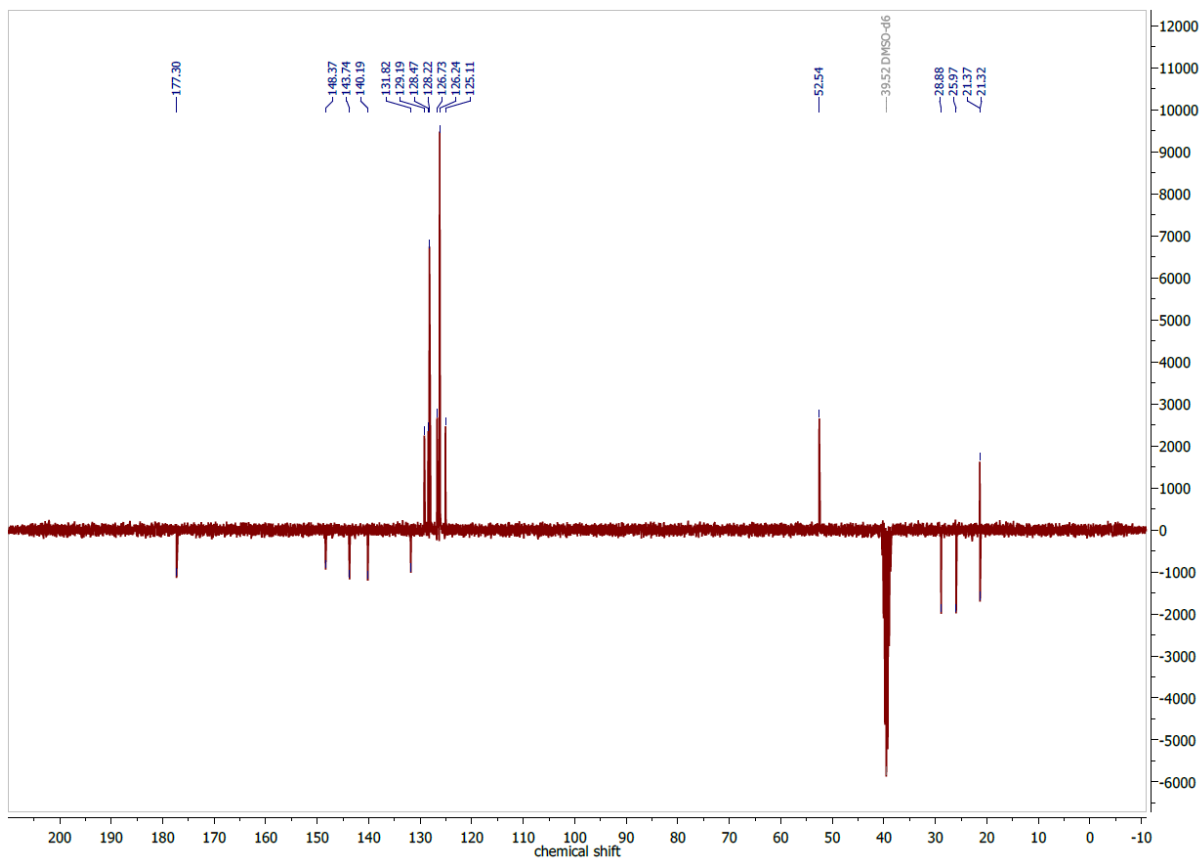


Figure 7.173 ^{13}C APT NMR spectrum of $\text{H}_2\text{tetTSCmB}$ in $\text{DMSO-}d_6$ at 75 MHz.

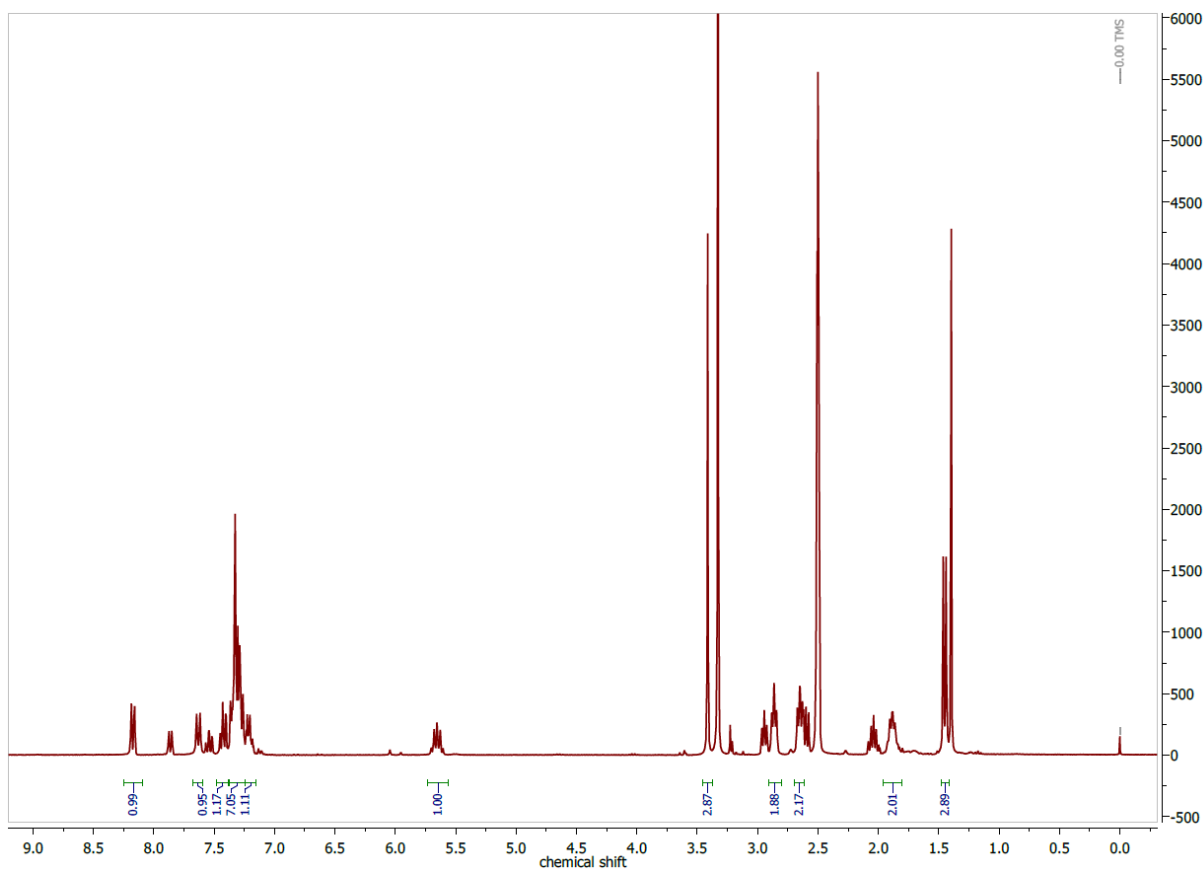


Figure 7.174 ^1H NMR spectrum of $\text{H}_2\text{tet(m)TSCmB}$ in $\text{DMSO-}d_6$ at 300 MHz.

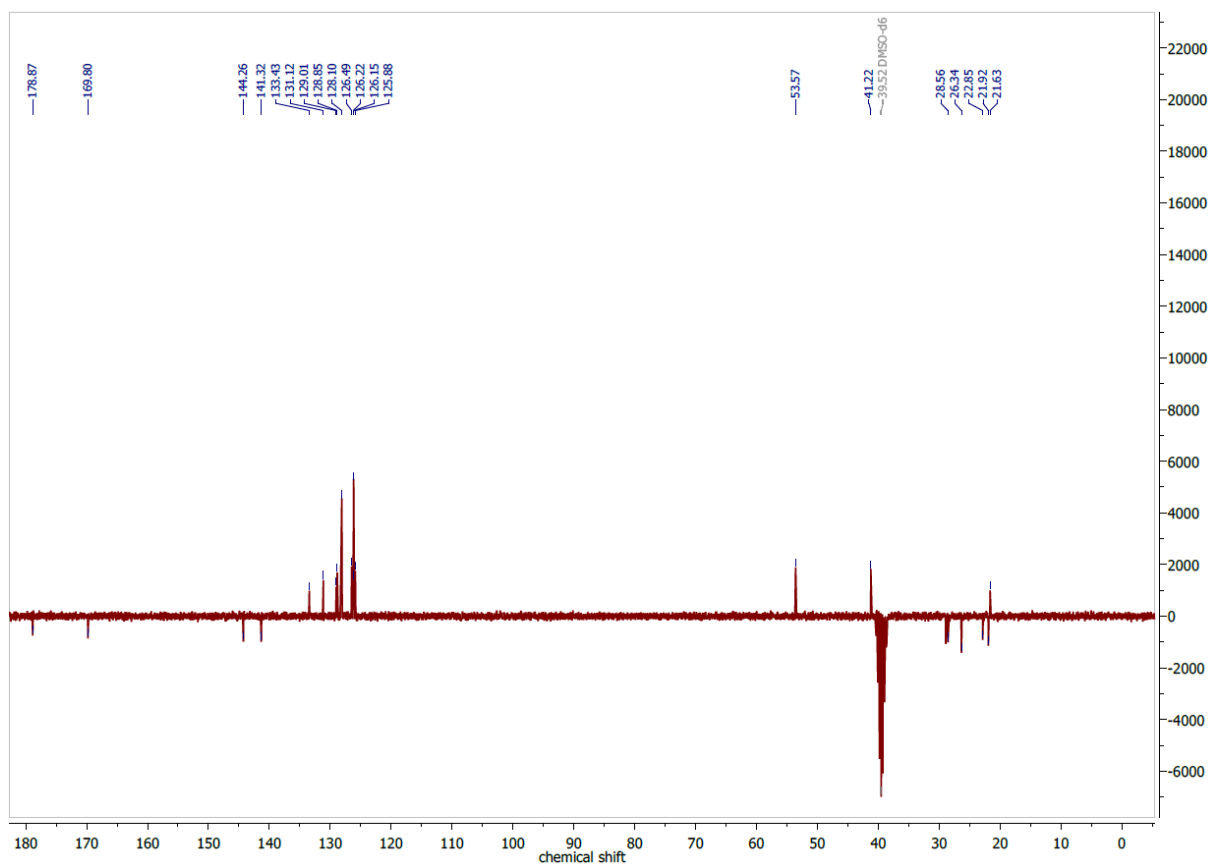


Figure 7.175 ^{13}C APT NMR spectrum of $\text{H}_2\text{tet(m)TSCmB}$ in $\text{DMSO-}d_6$ at 75 MHz.

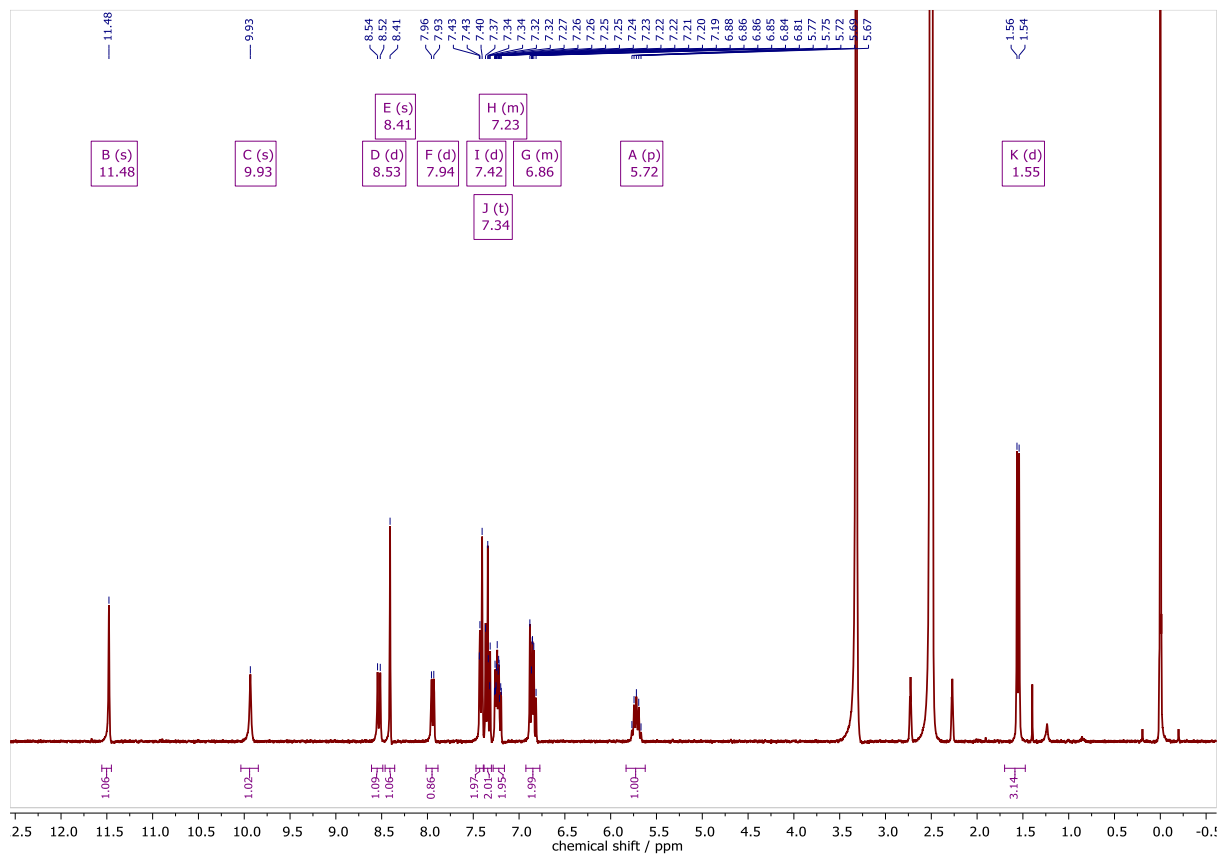


Figure 7.176 ^1H NMR spectrum of $\text{H}_2\text{SalTSCmB}$ in $\text{DMSO-}d_6$ at 300 MHz.

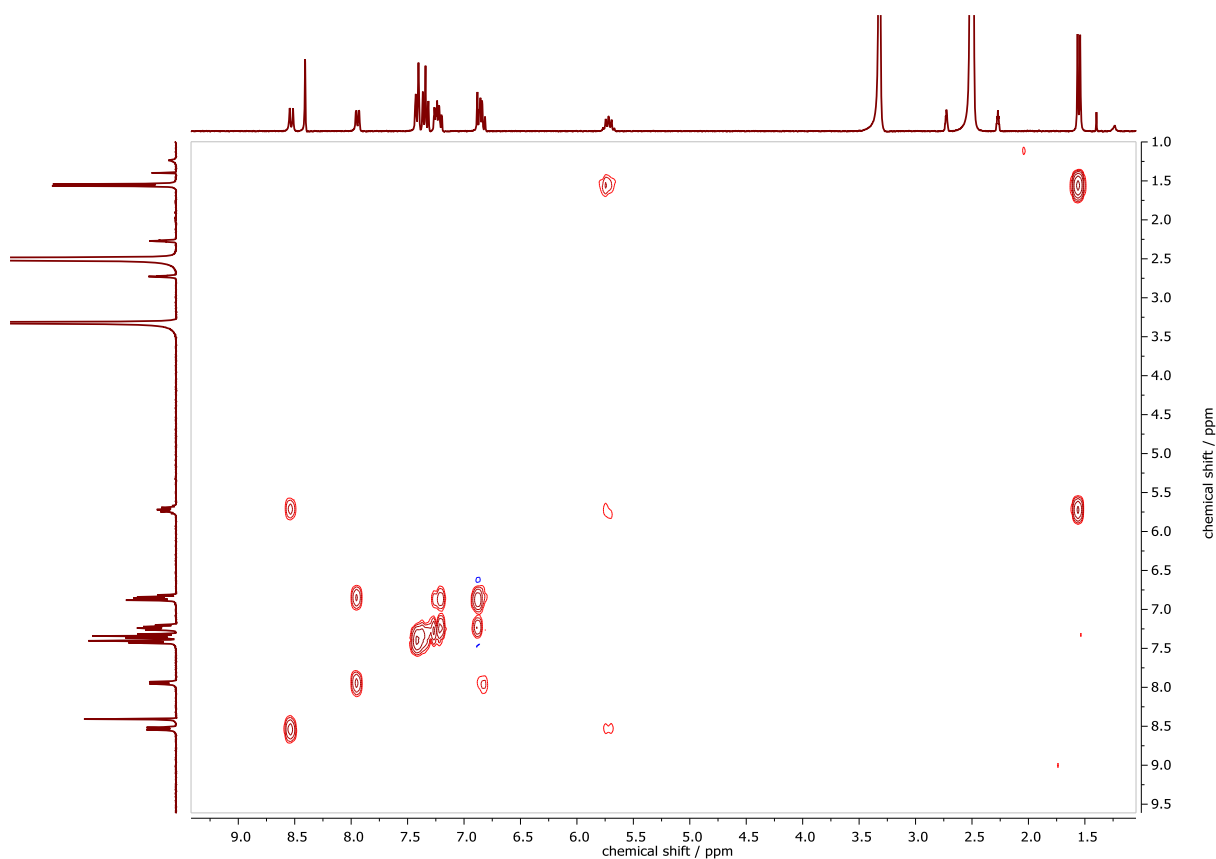


Figure 7.177 $^1\text{H}, ^1\text{H}$ COSY NMR spectrum of $\text{H}_2\text{SalTSCmB}$ in $\text{DMSO}-d_6$.

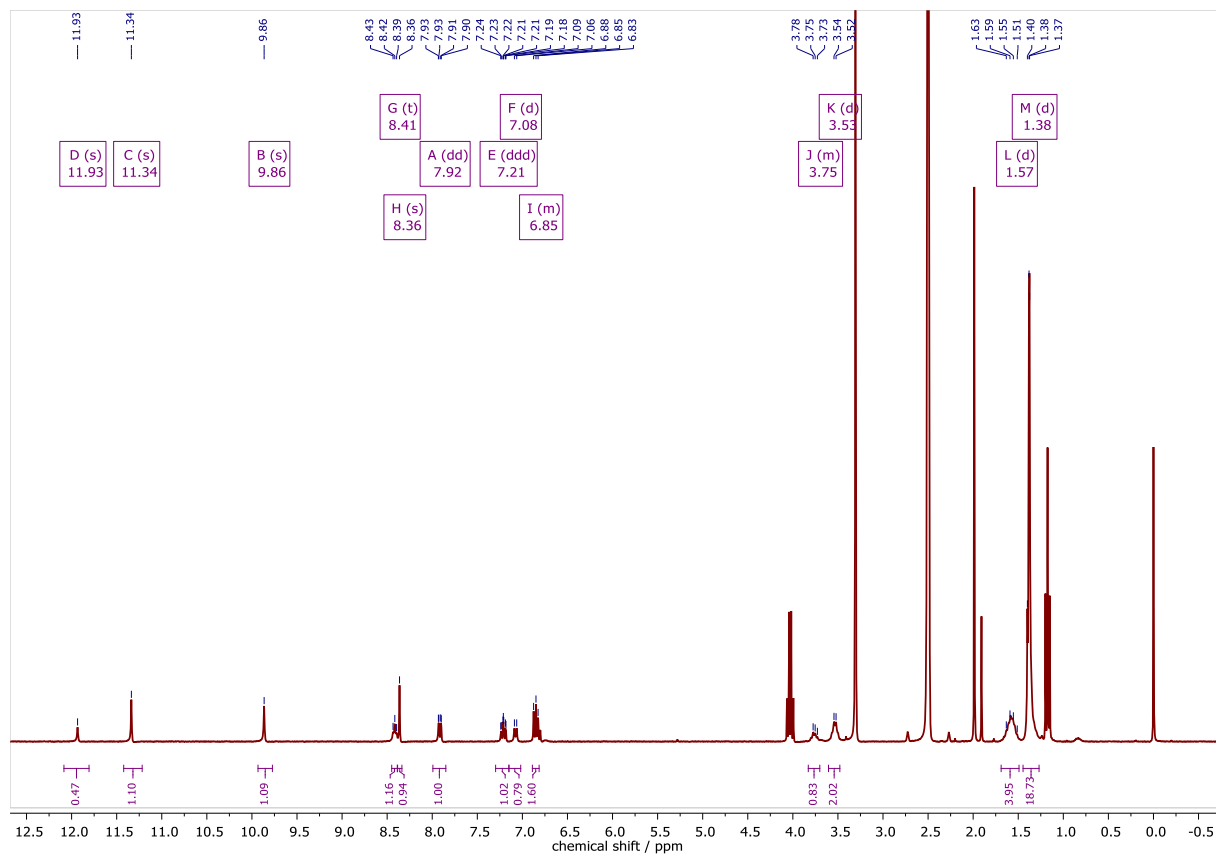


Figure 7.178 ^1H NMR spectrum of $\text{H}_2\text{SalTSLp}$ in $\text{DMSO}-d_6$ at 300 MHz.

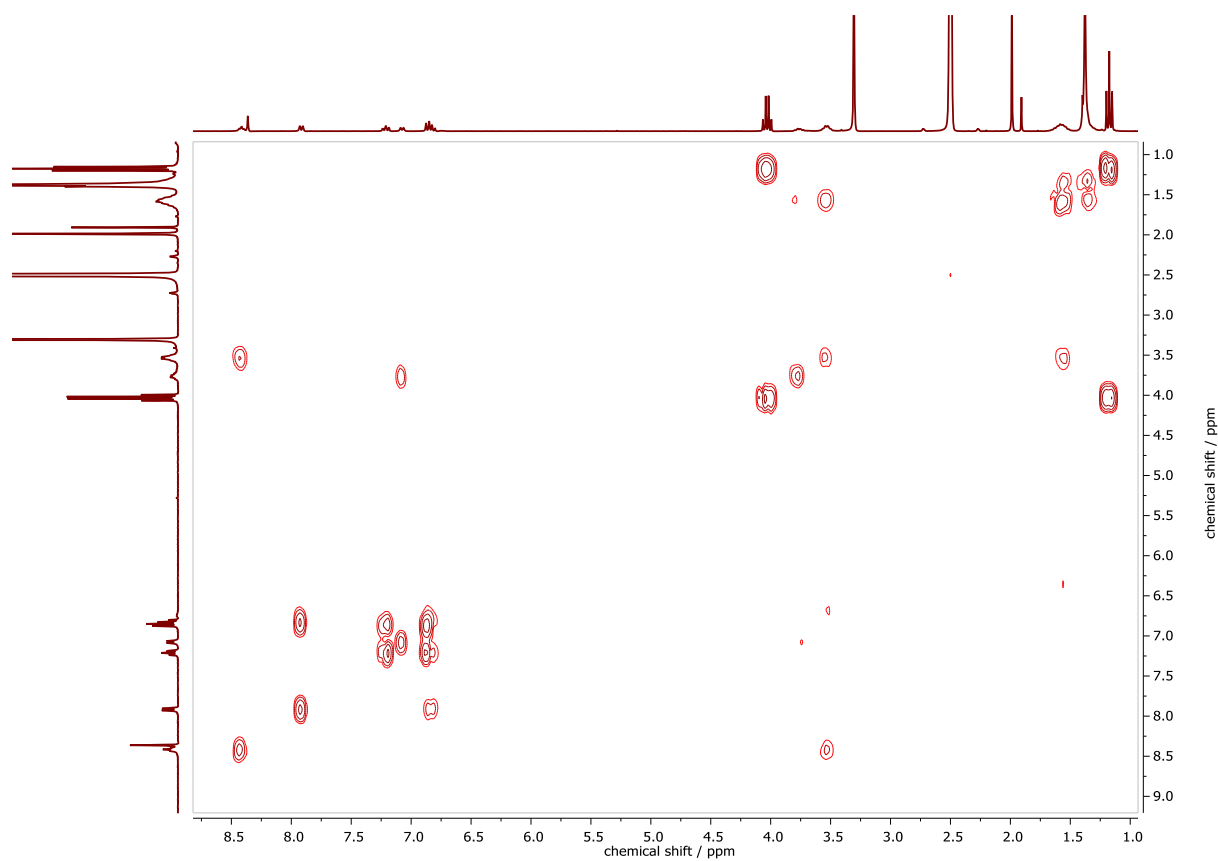


Figure 7.179 $^1\text{H}, ^1\text{H}$ COSY NMR spectrum of $\text{H}_2\text{SalTSClP}$ in $\text{DMSO-}d_6$.

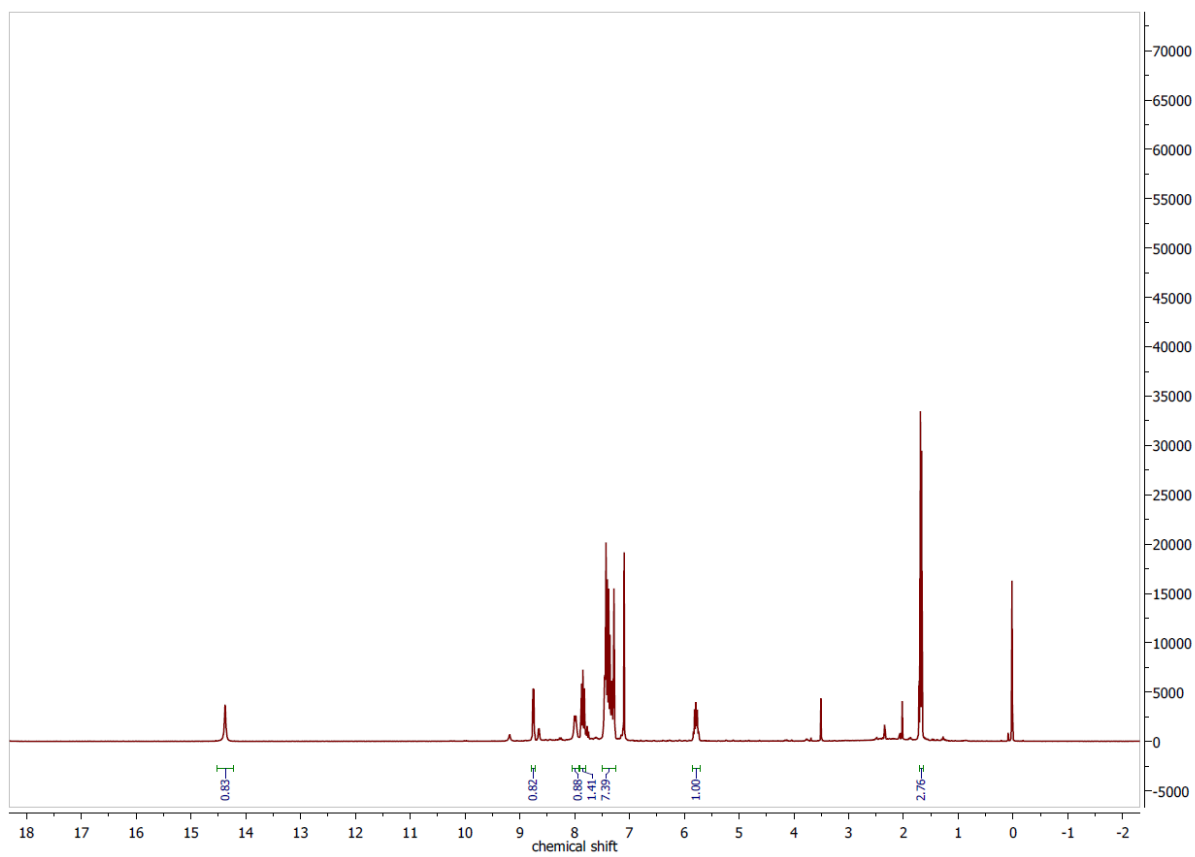


Figure 7.180 ^1H NMR spectrum of HfpyTSCmB in CDCl_3 at 300 MHz.

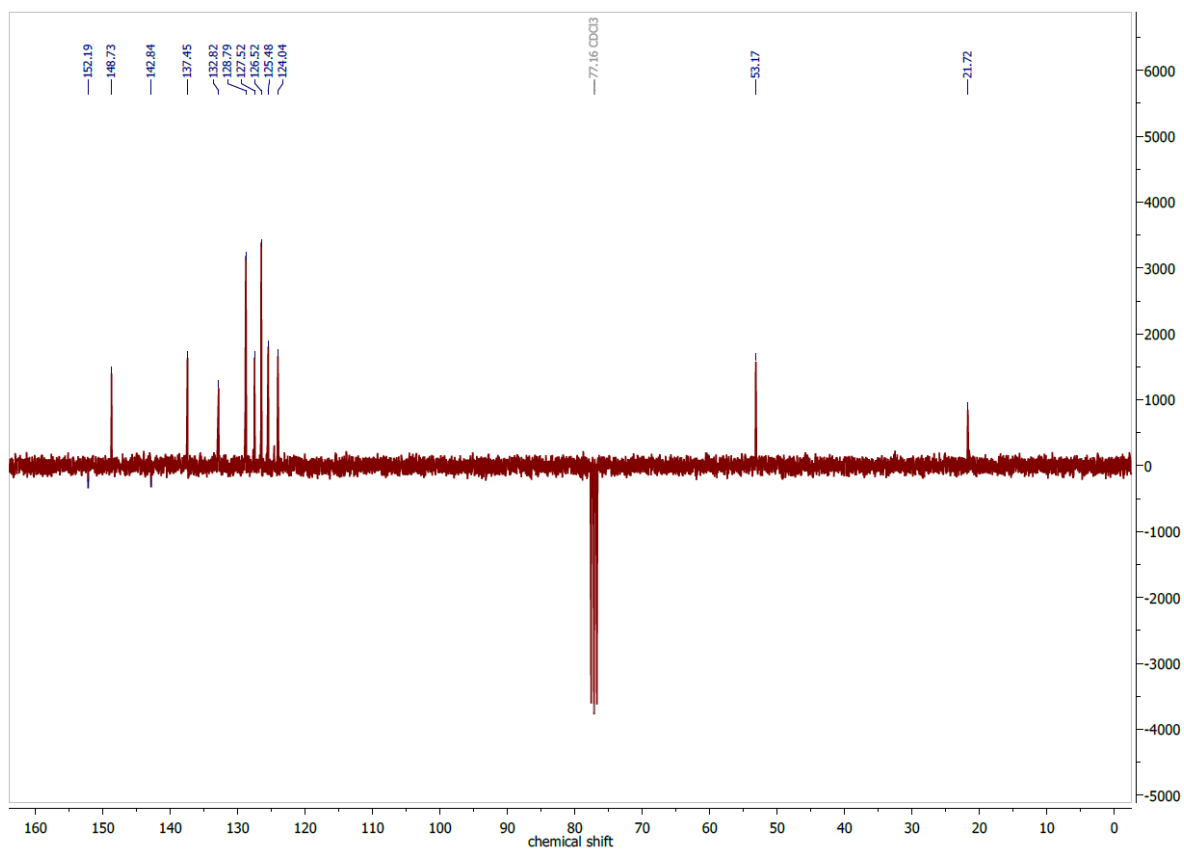


Figure 7.181 ^{13}C APT NMR spectrum of HfpyTSCmB in CDCl_3 at 75 MHz.

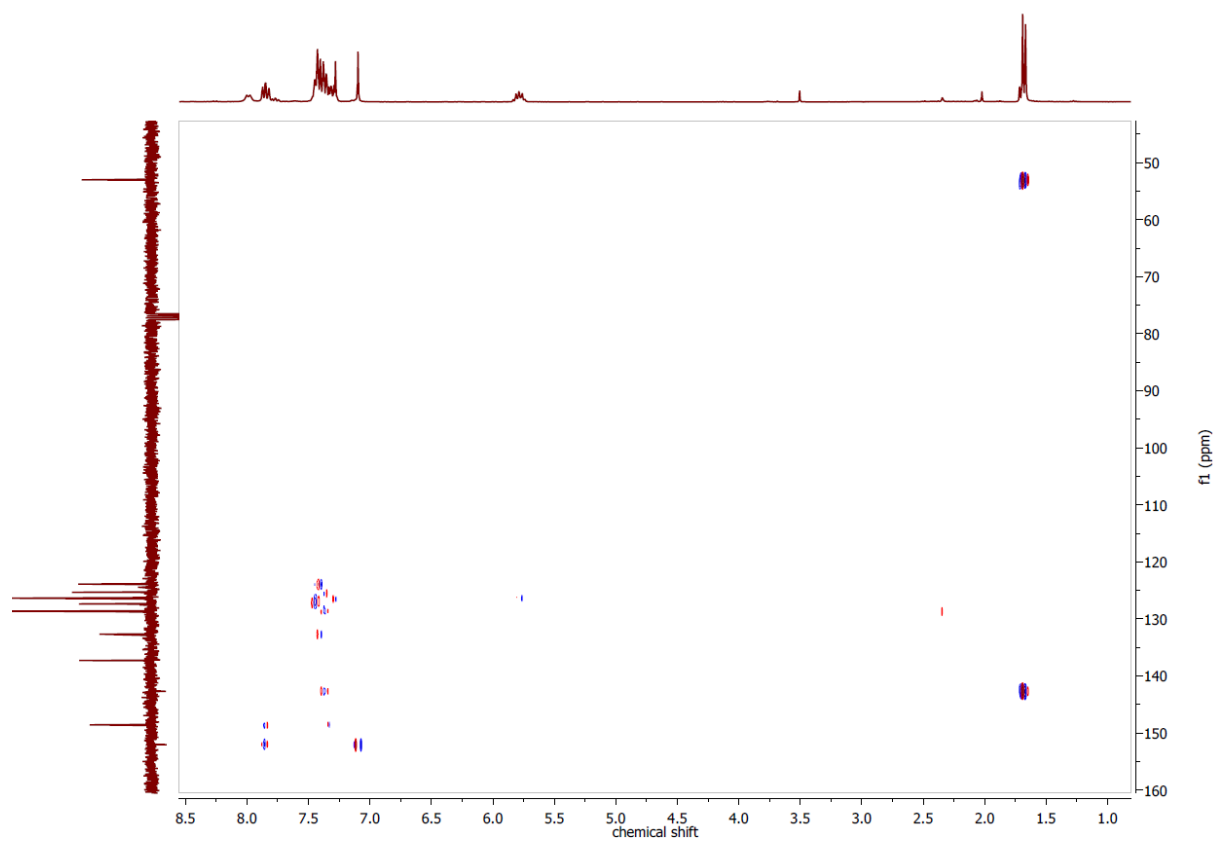


Figure 7.182 ^1H , ^{13}C HSQC NMR spectrum of HfpyTSCmB in CDCl_3 .

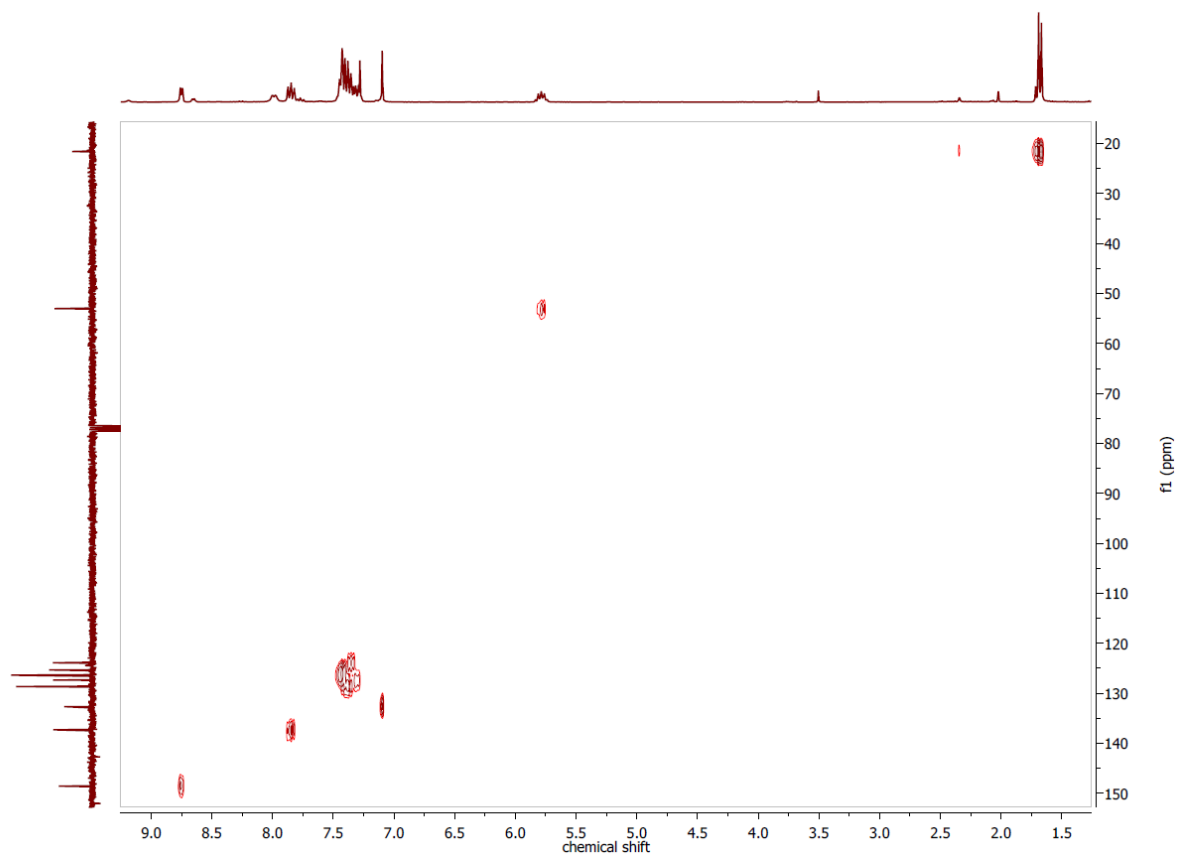


Figure 7.183 ^1H , ^{13}C HMBC NMR spectrum of HfpyTSCmB in CDCl_3 .

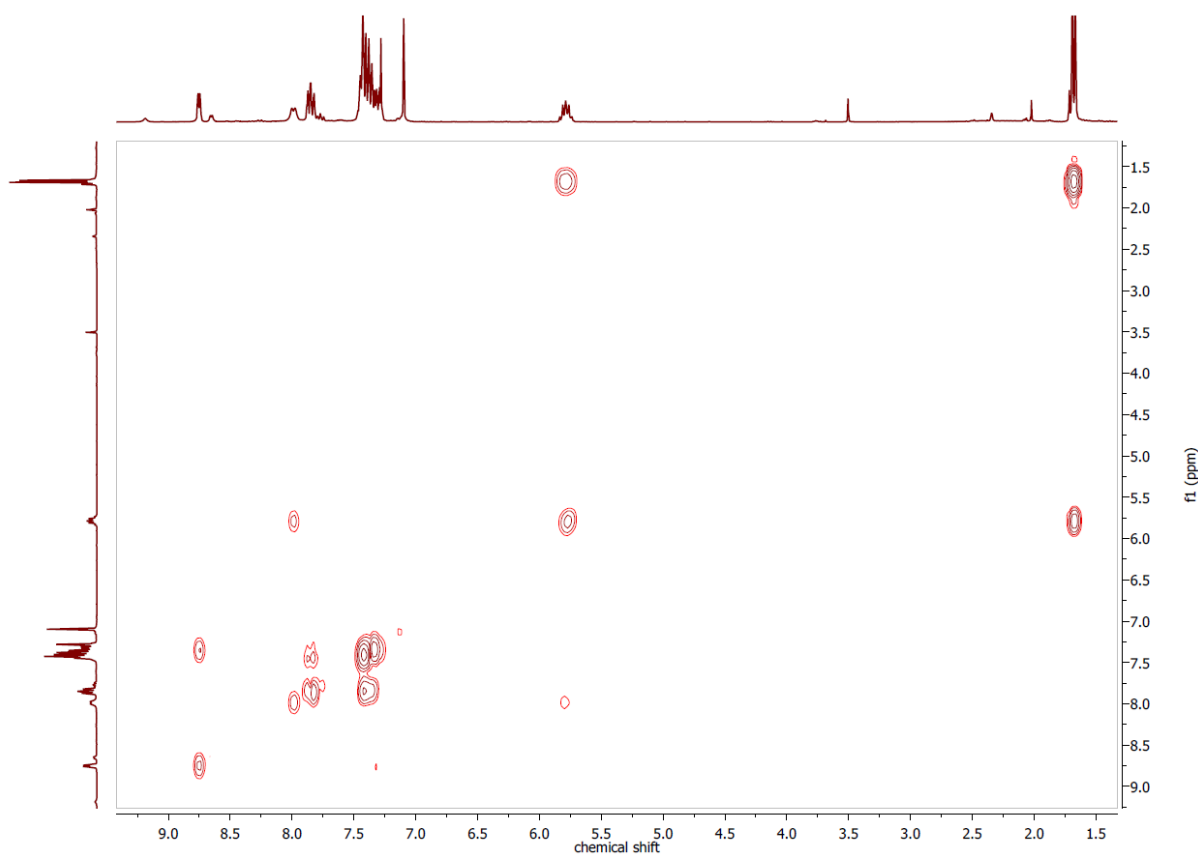


Figure 7.184 ^1H , ^1H COSY NMR spectrum of HfpyTSCmB in CDCl_3 .

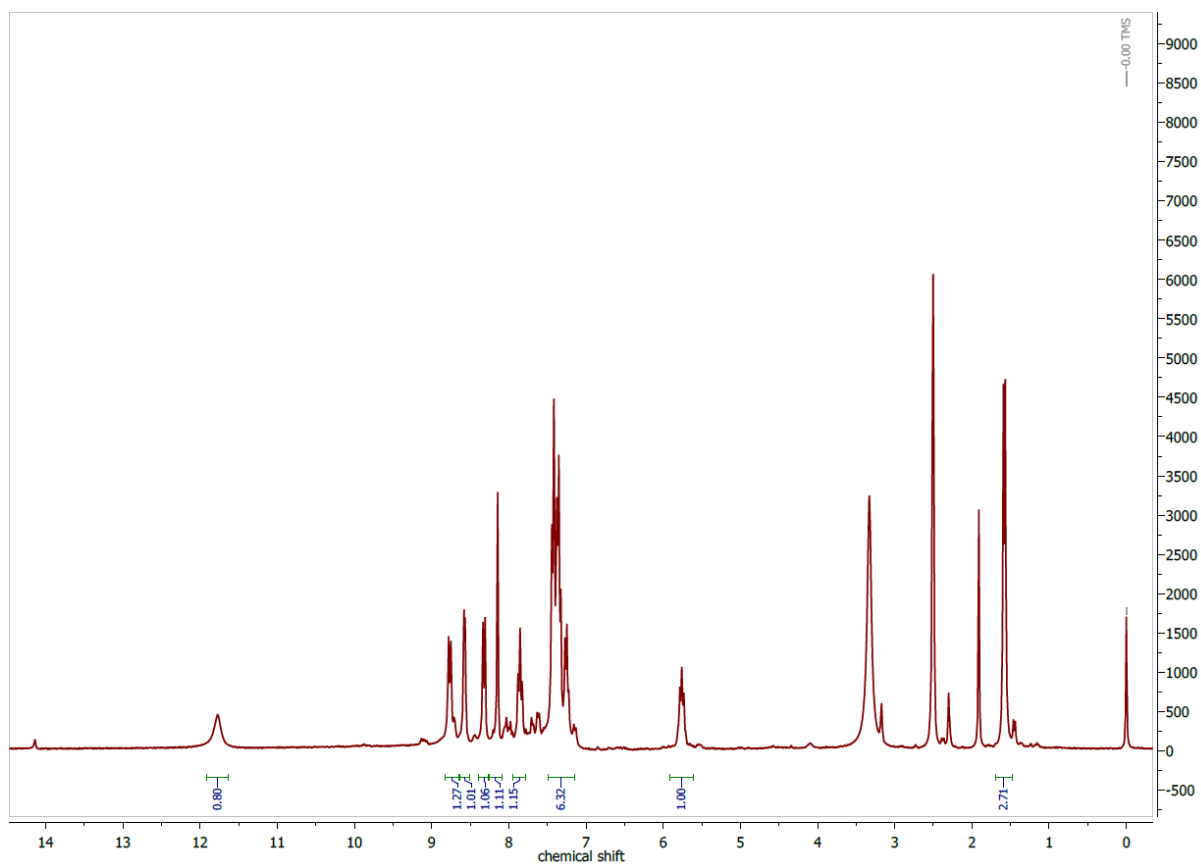


Figure 7.185 ^1H NMR spectrum of HfpyTSCmB in $\text{DMSO-}d_6$ at 300 MHz.

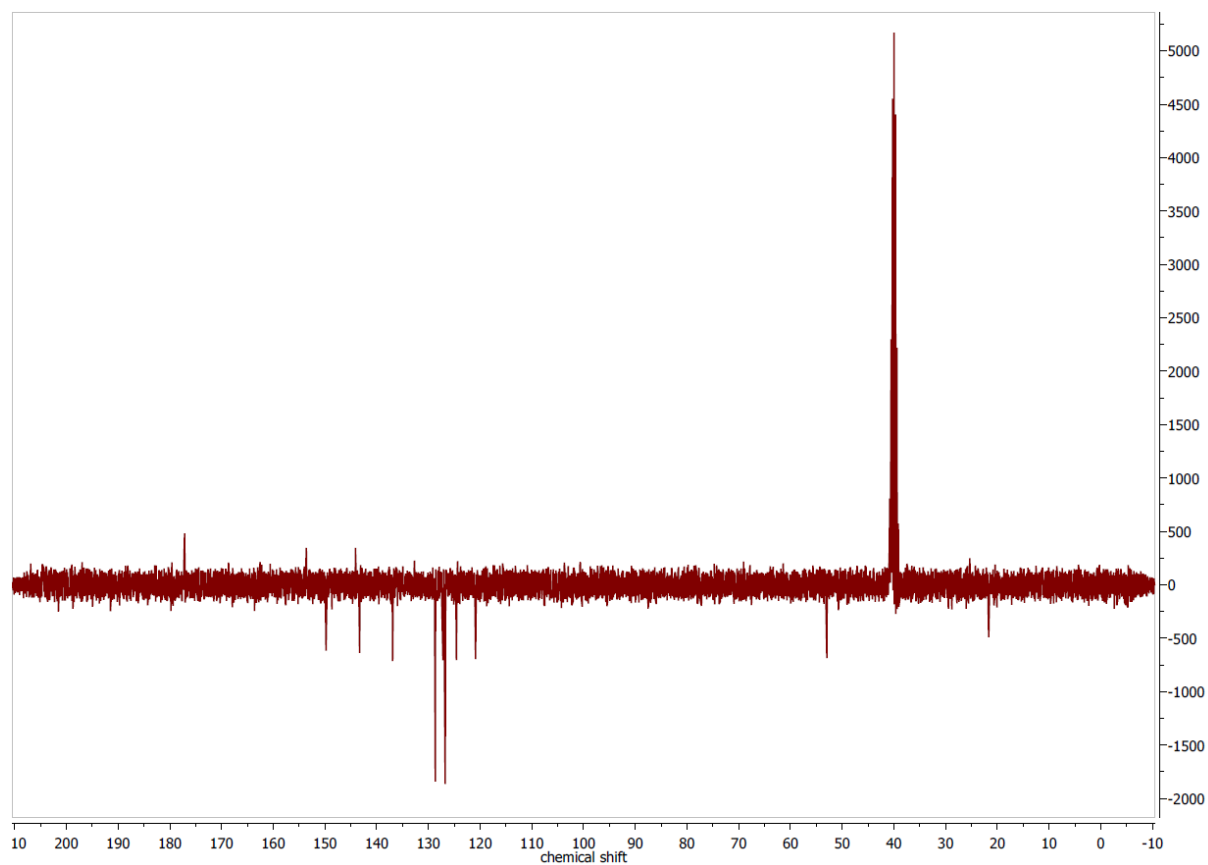


Figure 7.186 $^{13}\text{C}\{^1\text{H}\}$ DEPTQ NMR spectrum of HfpyTSCmB in $\text{DMSO-}d_6$ at 75 MHz.

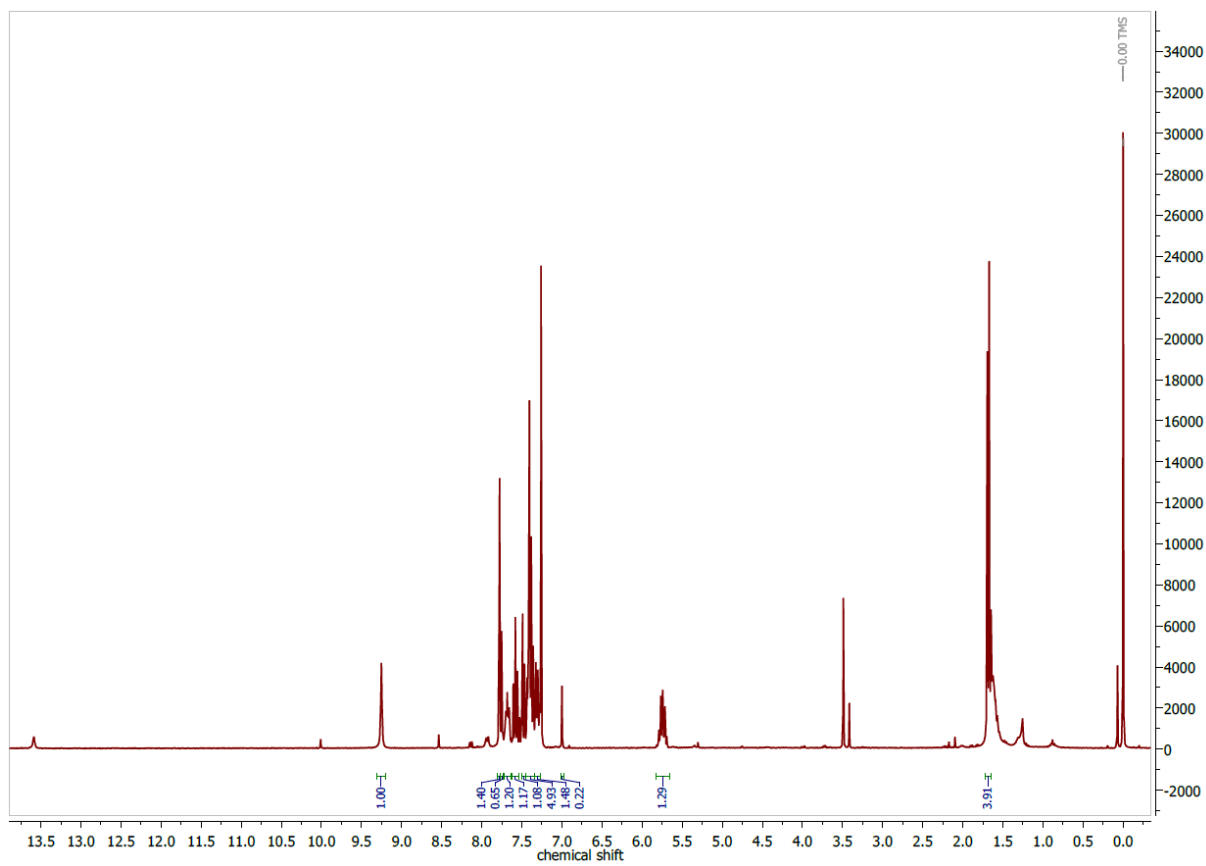


Figure 7.187 ^1H NMR spectrum of H6-BrfpyTSCmB in CDCl_3 at 300 MHz.

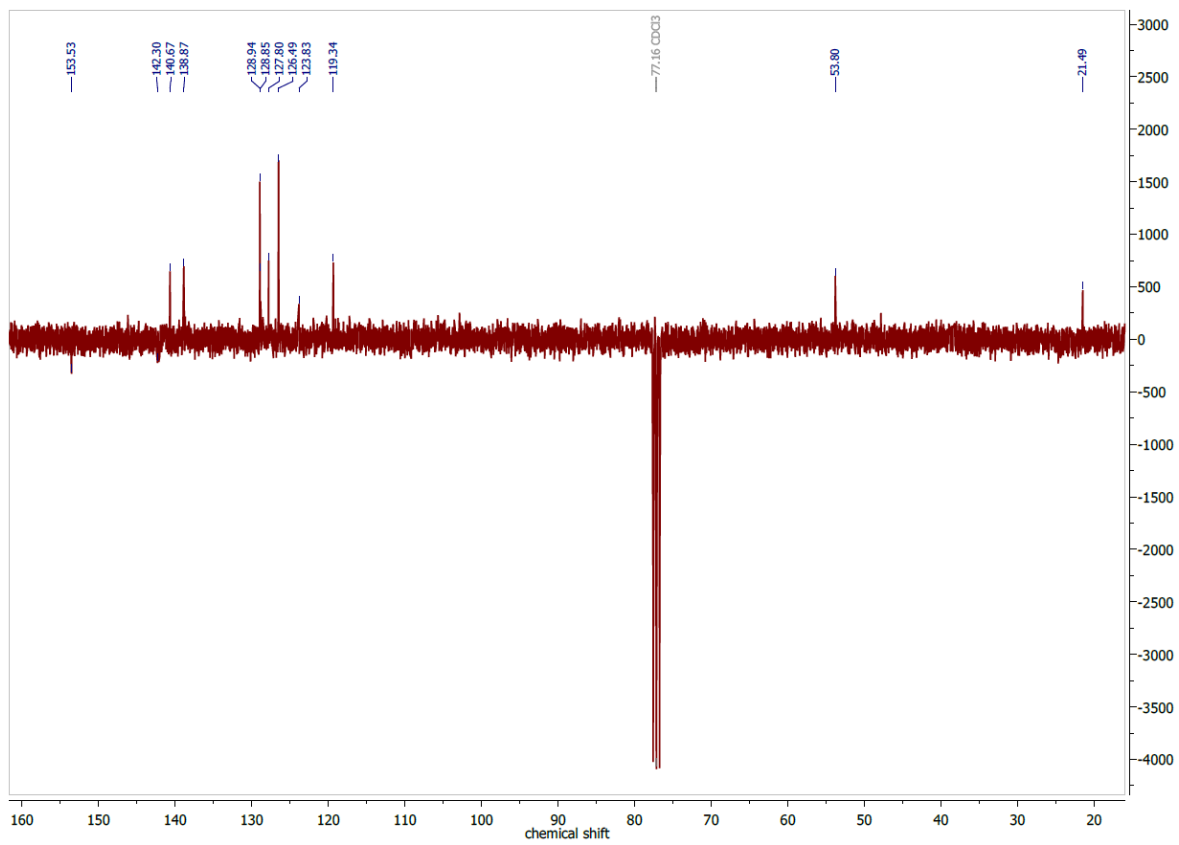


Figure 7.188 $^{13}\text{C}\{^1\text{H}\}$ DEPTQ NMR spectrum of H6-BrfpyTSCmB in CDCl_3 at 300 MHz.

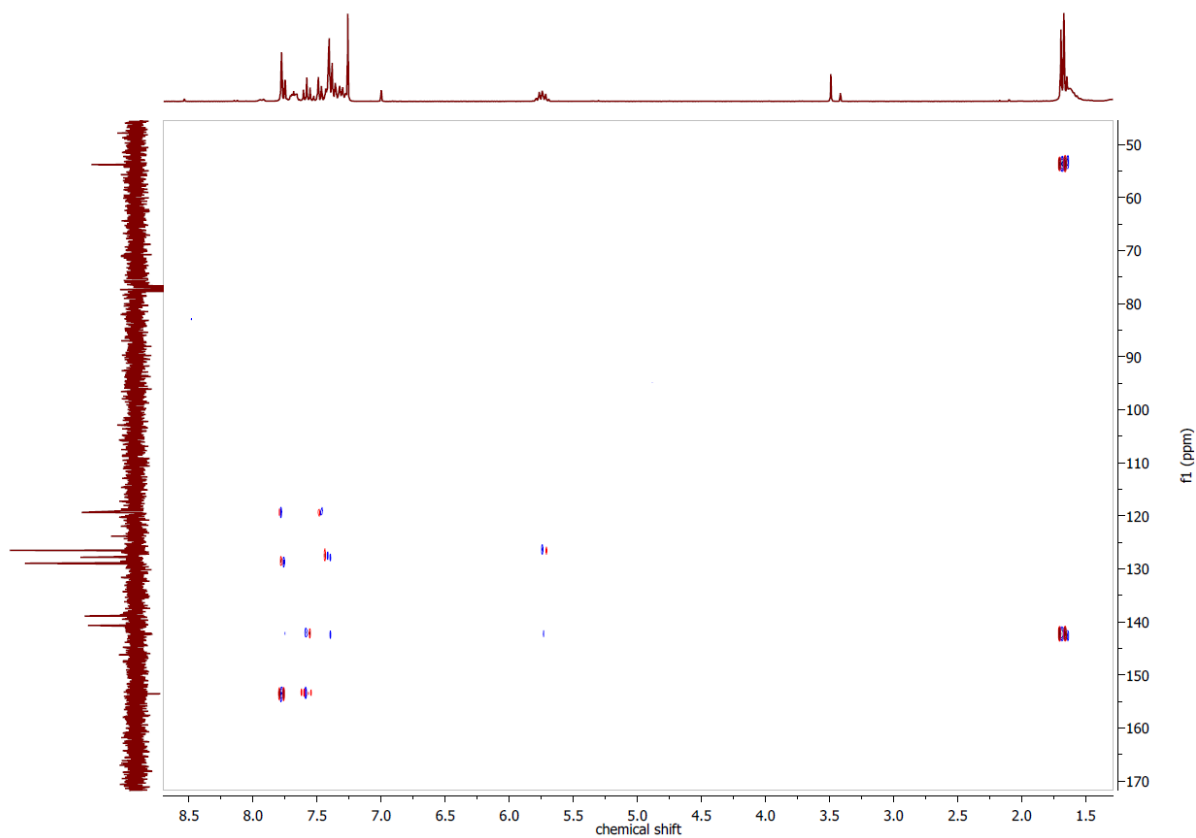


Figure 7.189 ^1H , ^{13}C HMBC NMR spectrum of H6-BrfpyTSCmB in CDCl_3 .

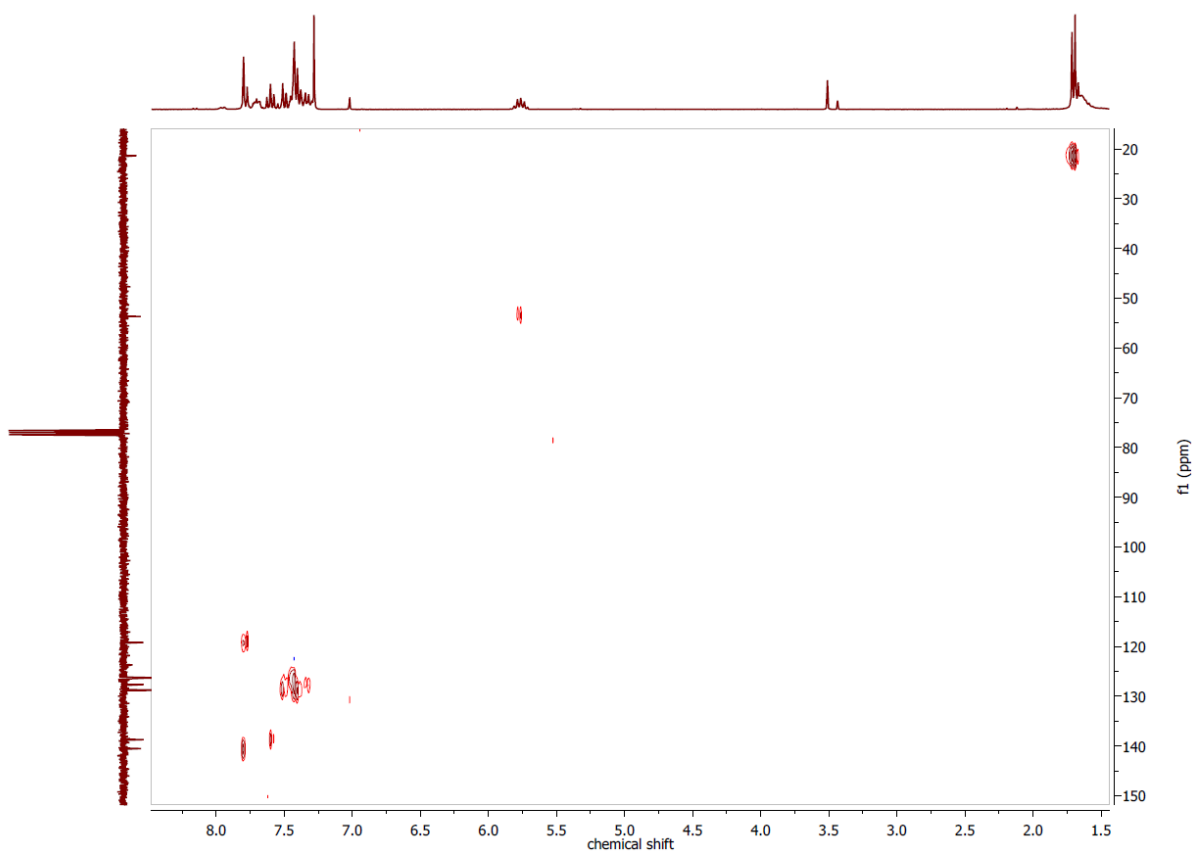


Figure 7.190 ^1H , ^{13}C HSQC NMR spectrum of H6-BrfpyTSCmB in CDCl_3 .

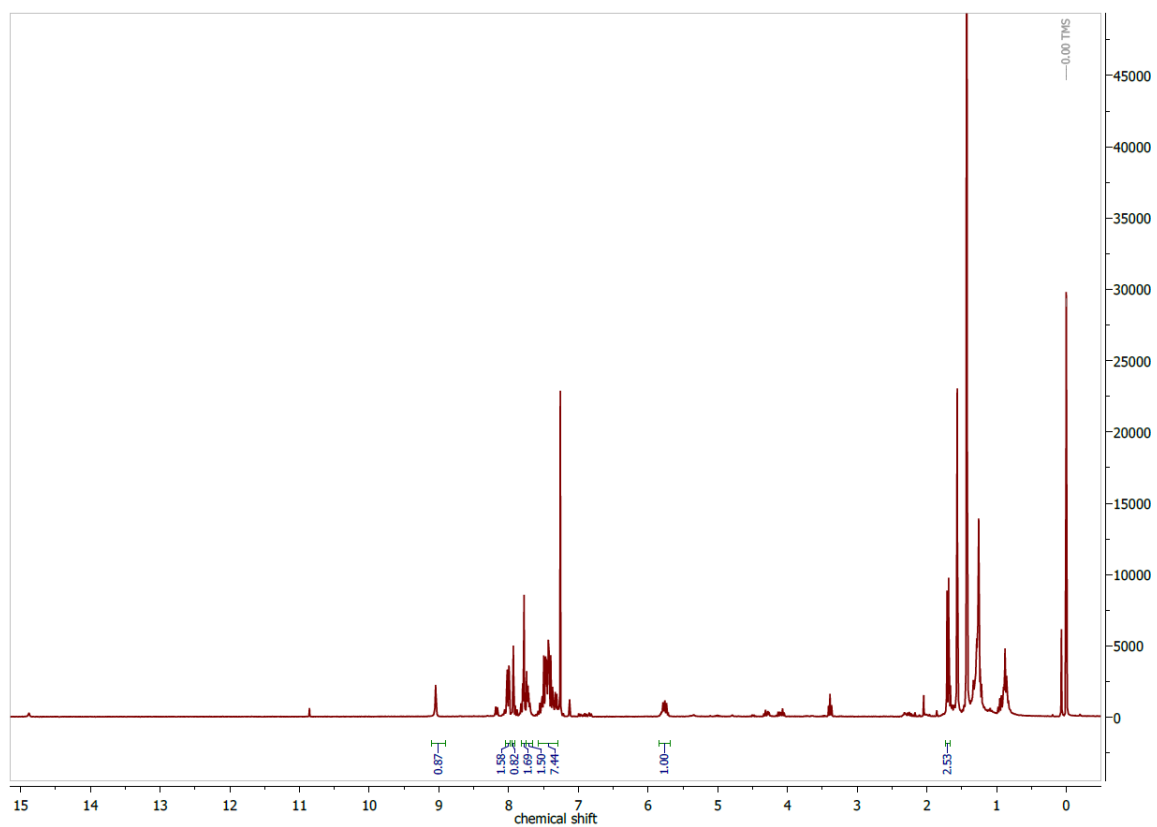


Figure 7.191 ^1H NMR spectrum of H6-phfpyTSCmB in CDCl_3 at 300 MHz.

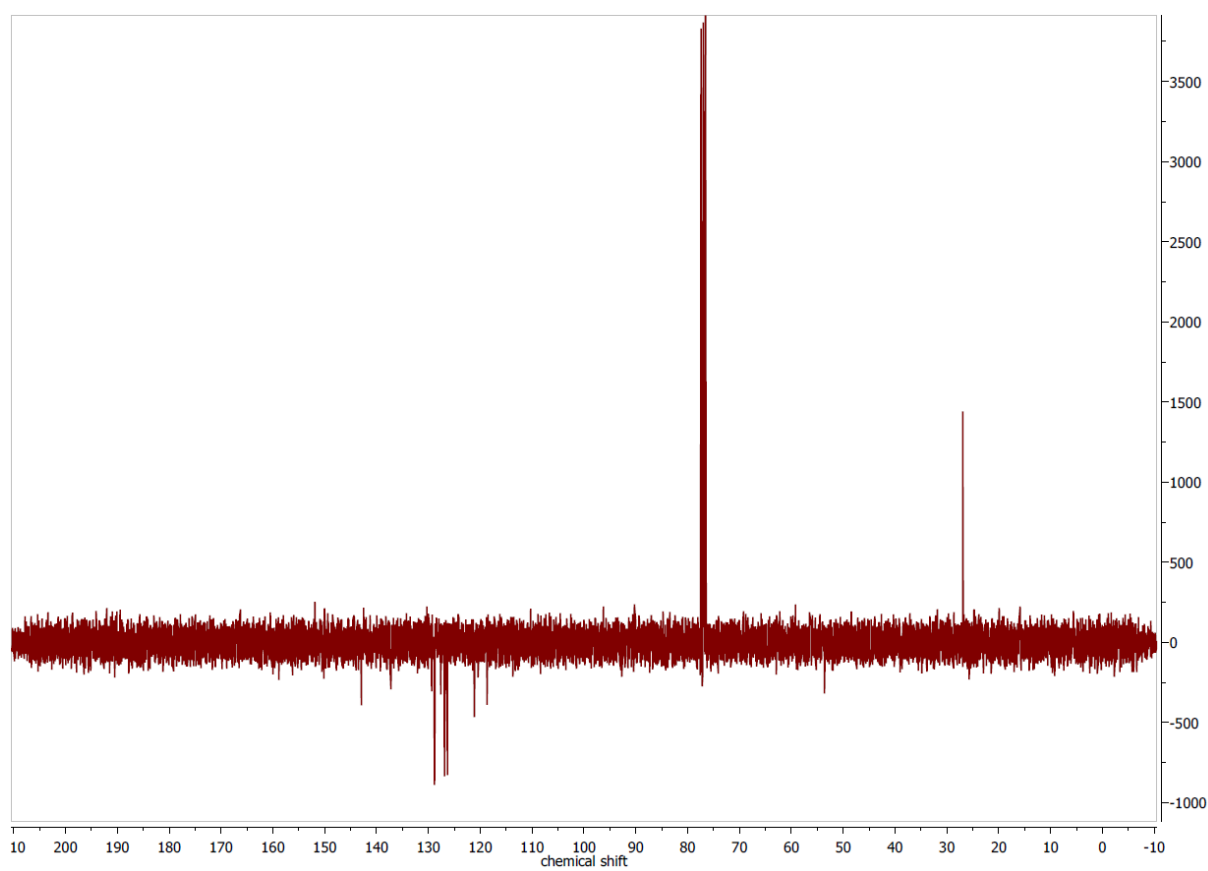


Figure 7.192 $^{13}\text{C}\{^1\text{H}\}$ DEPTQ NMR spectrum of H6-phfpyTSCmB in CDCl_3 at 75 MHz.

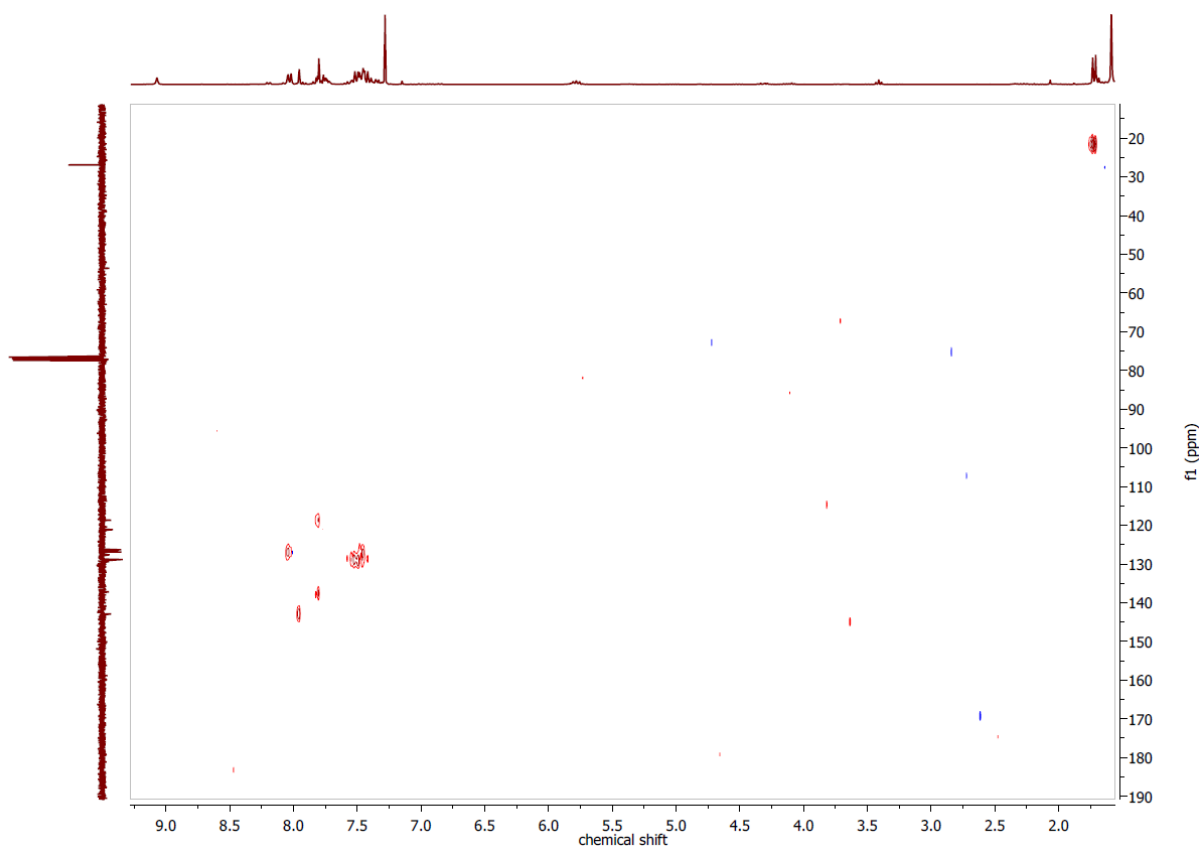


Figure 7.193 ^1H , ^{13}C HSQC NMR spectrum of H6-phfpyTSCmB in CDCl_3 .

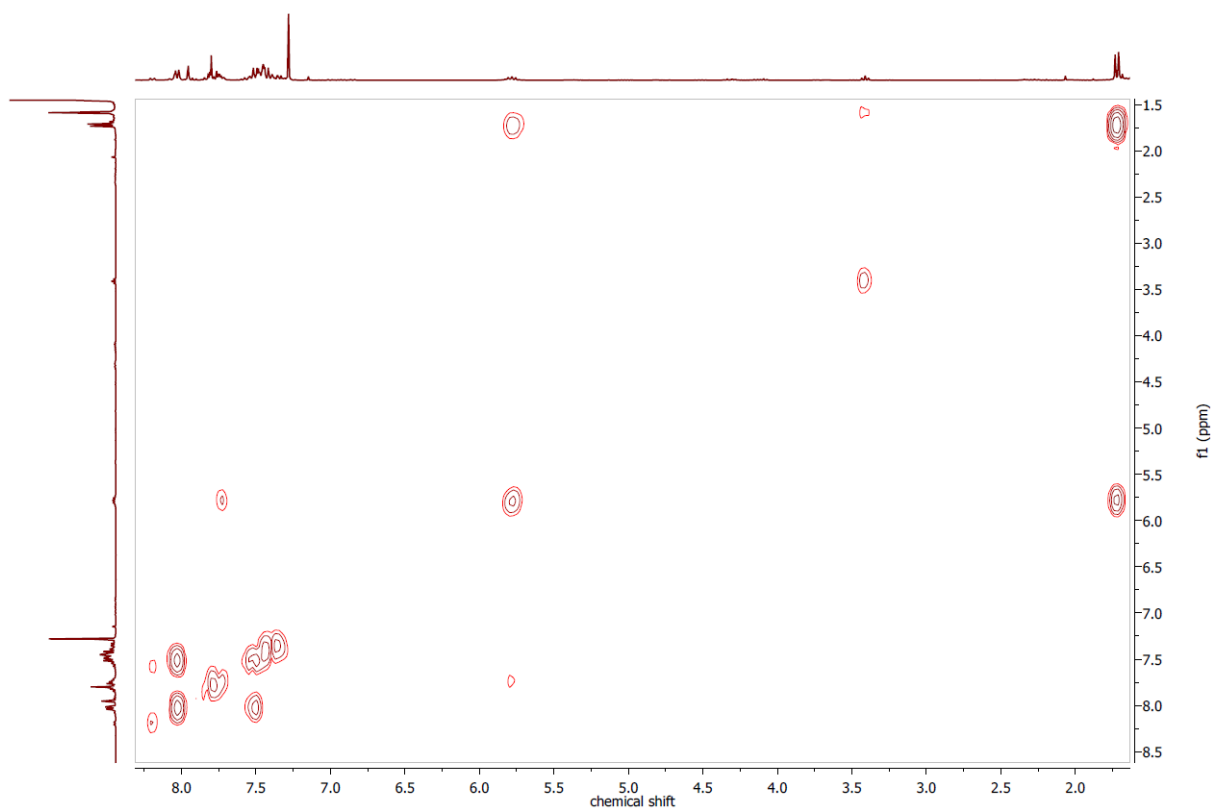


Figure 7.194 ^1H , ^1H COSY NMR spectrum of H6-phfpyTSCmB in CDCl_3 .

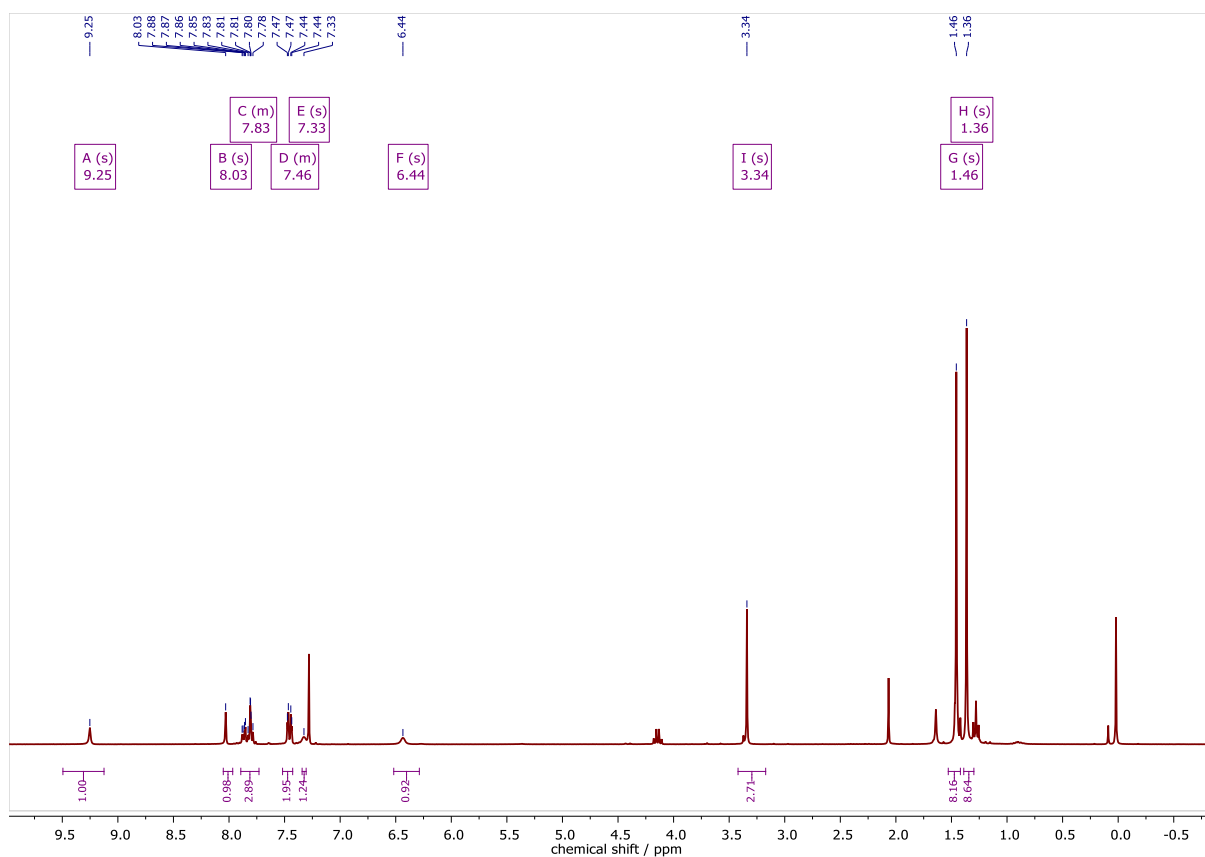


Figure 7.195 ^1H NMR spectrum of H(tBu)mphfyTSCmB in CDCl_3 at 300 MHz.

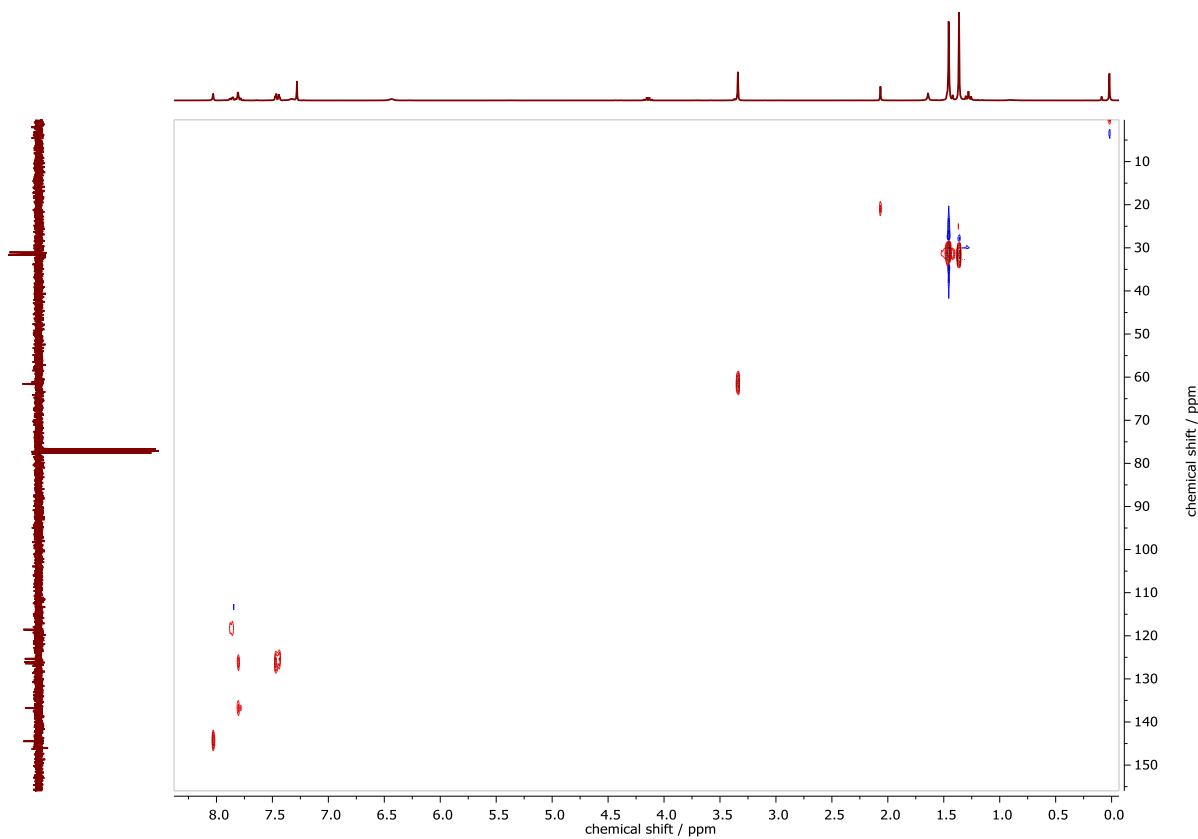


Figure 7.196 ^1H , ^{13}C HSQCed NMR spectrum of H(tBu)mphfyTSCmB in CDCl_3 .

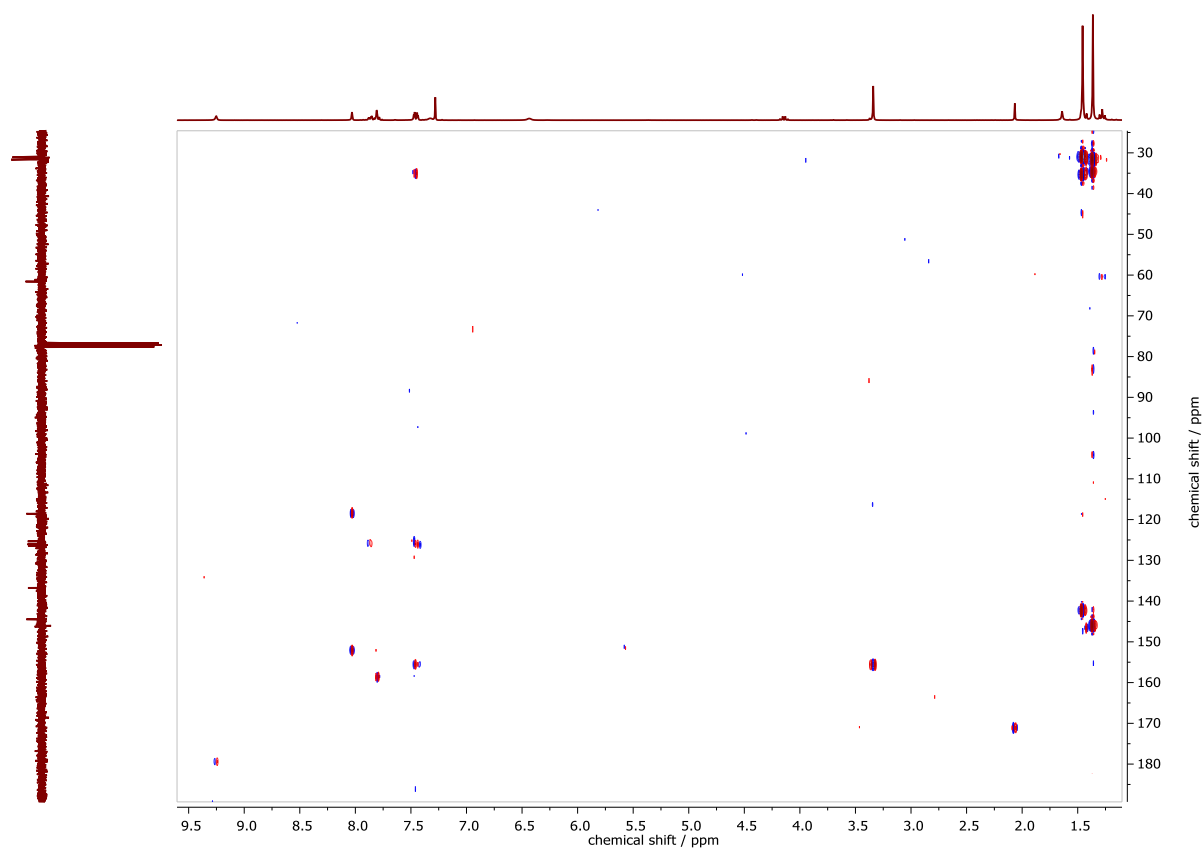


Figure 7.197 ^1H , ^{13}C HMBC NMR spectrum of H(tBu)mphfpyTSCmB in CDCl_3 .

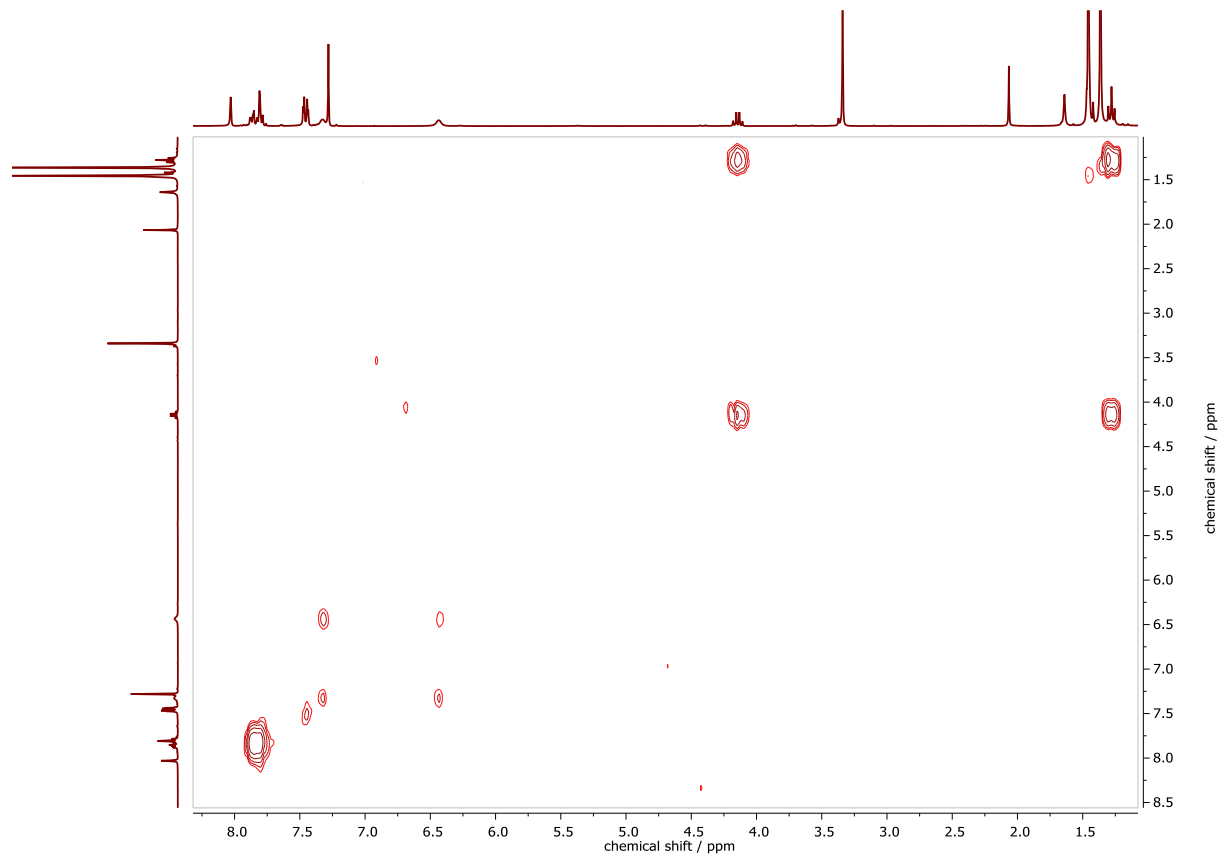


Figure 7.198 ^1H , ^1H COSY NMR spectrum of H(tBu)mphfpyTSCmB in CDCl_3 .

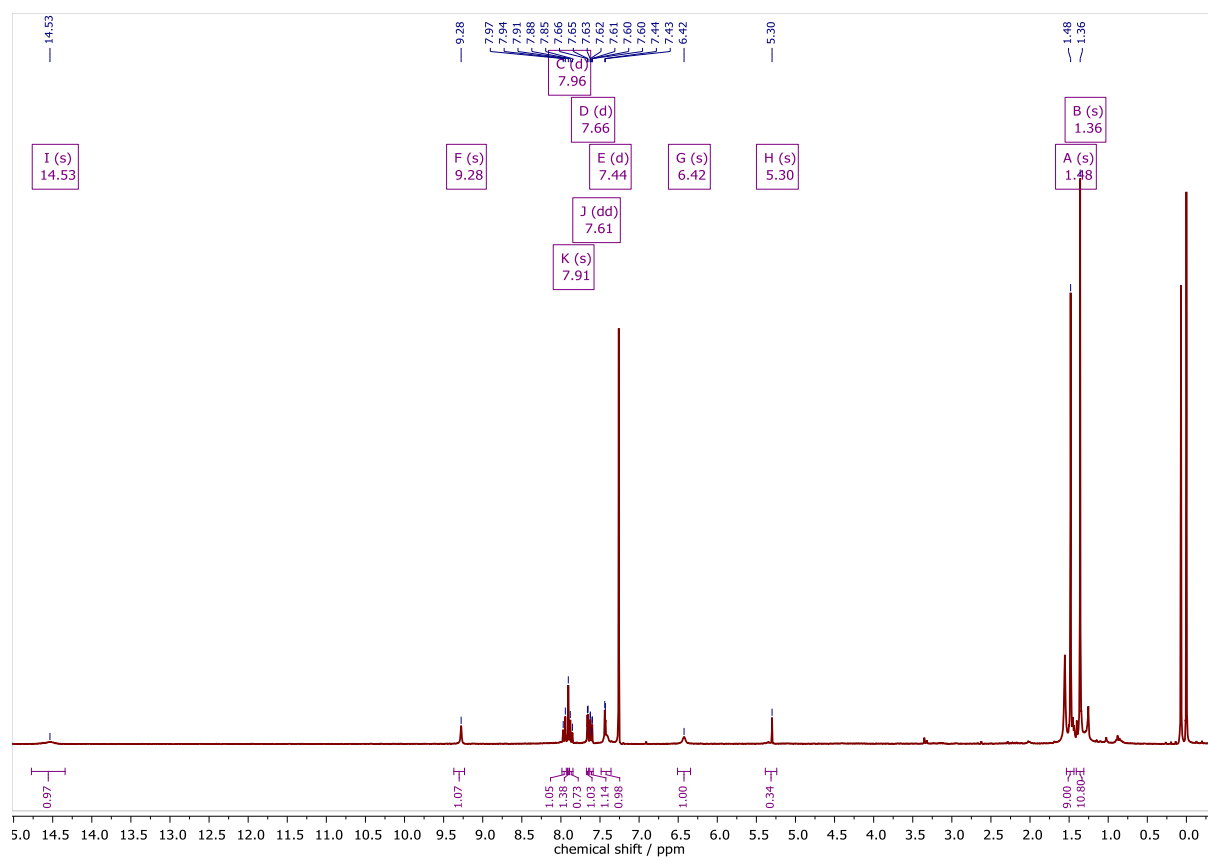


Figure 7.199 ^1H NMR spectrum of $\text{H}_2(\text{tBu})\text{hphfpyTSCmB}$ in CDCl_3 at 300 MHz.

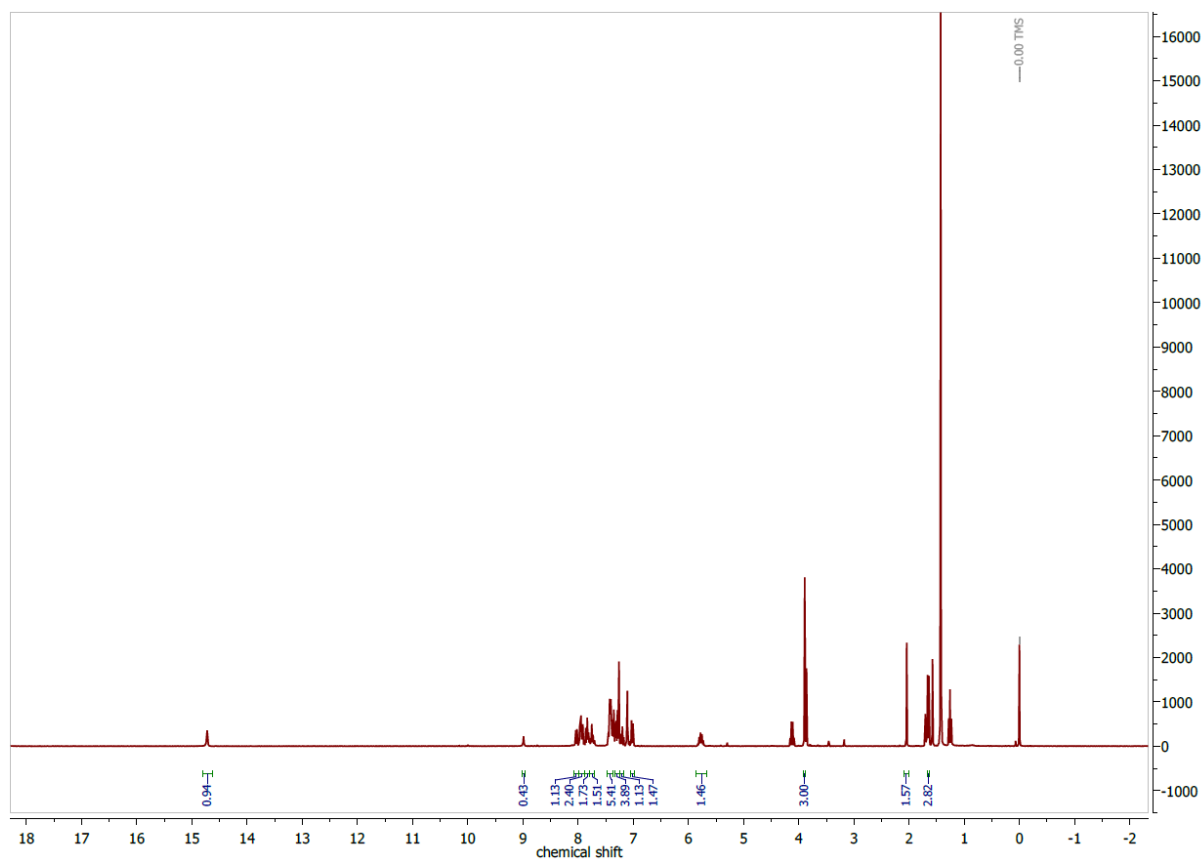


Figure 7.200 ^1H NMR spectrum of HmhpfpTSCmB in CDCl_3 at 300 MHz.

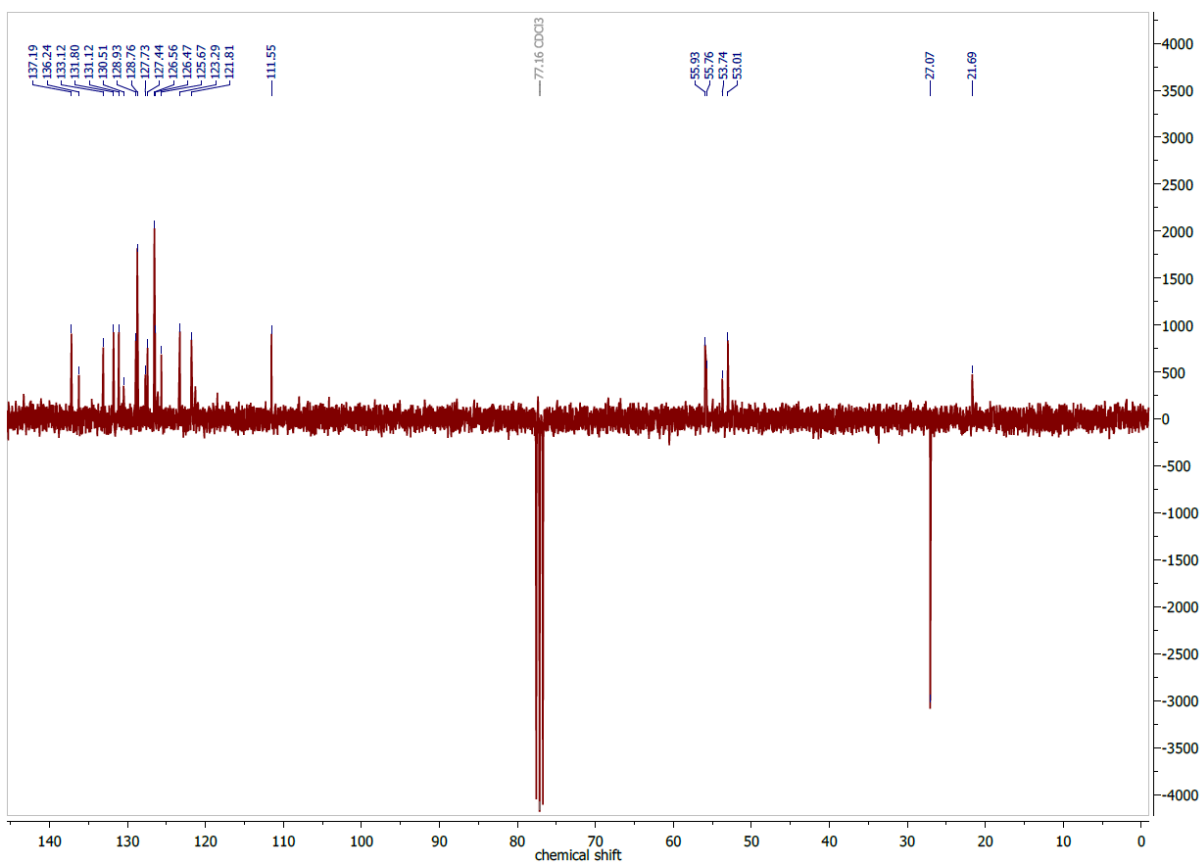


Figure 7.201 $^{13}\text{C}\{^1\text{H}\}$ DEPTQ NMR spectrum of HmphfyTSCmB in CDCl_3 at 75 MHz.

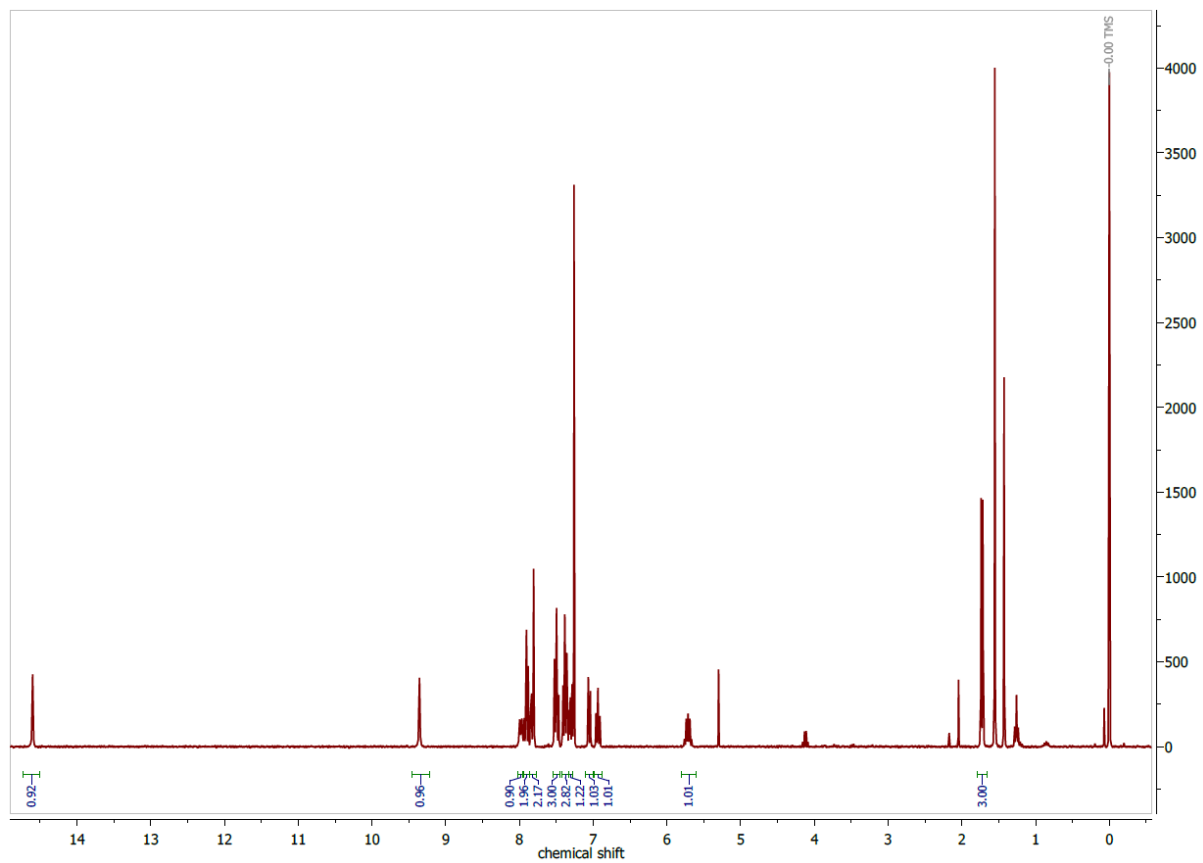


Figure 7.202 ^1H NMR spectrum of $\text{H}_2\text{hphfyTSCmB}$ in CDCl_3 at 300 MHz.

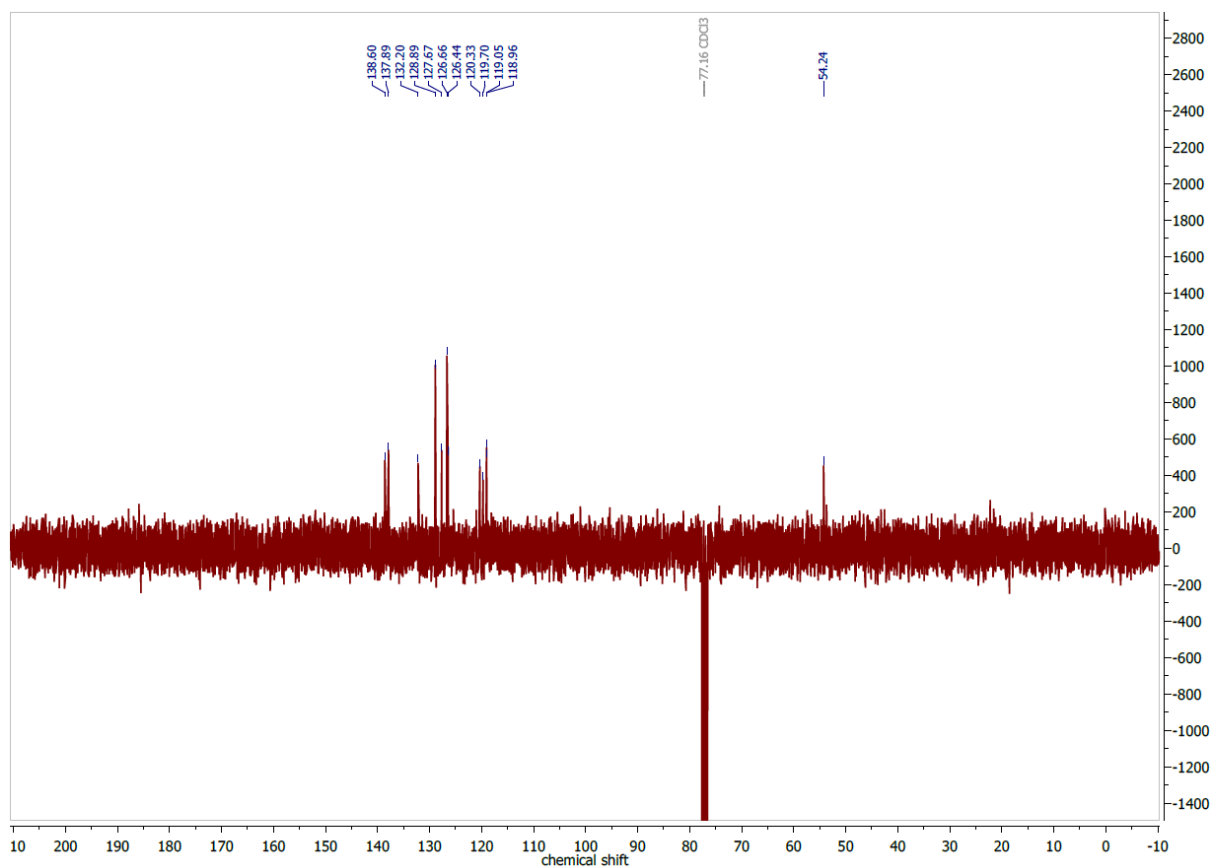


Figure 7.203 $^{13}\text{C}\{^1\text{H}\}$ DEPTQ NMR spectrum of $\text{H}_2\text{hphfyTSCmB}$ in CDCl_3 at 75 MHz.

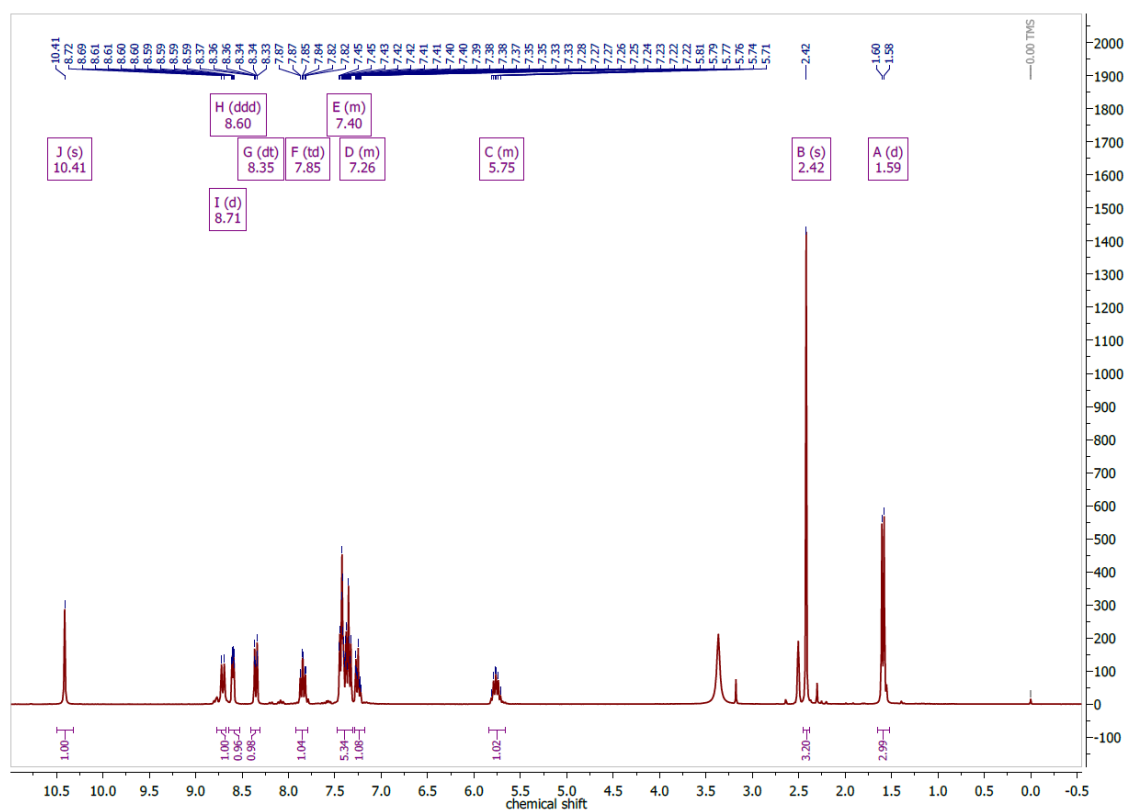


Figure 7.204 ^1H NMR spectrum of HapyTSCmB in $\text{DMSO}-d_6$ at 300 MHz.

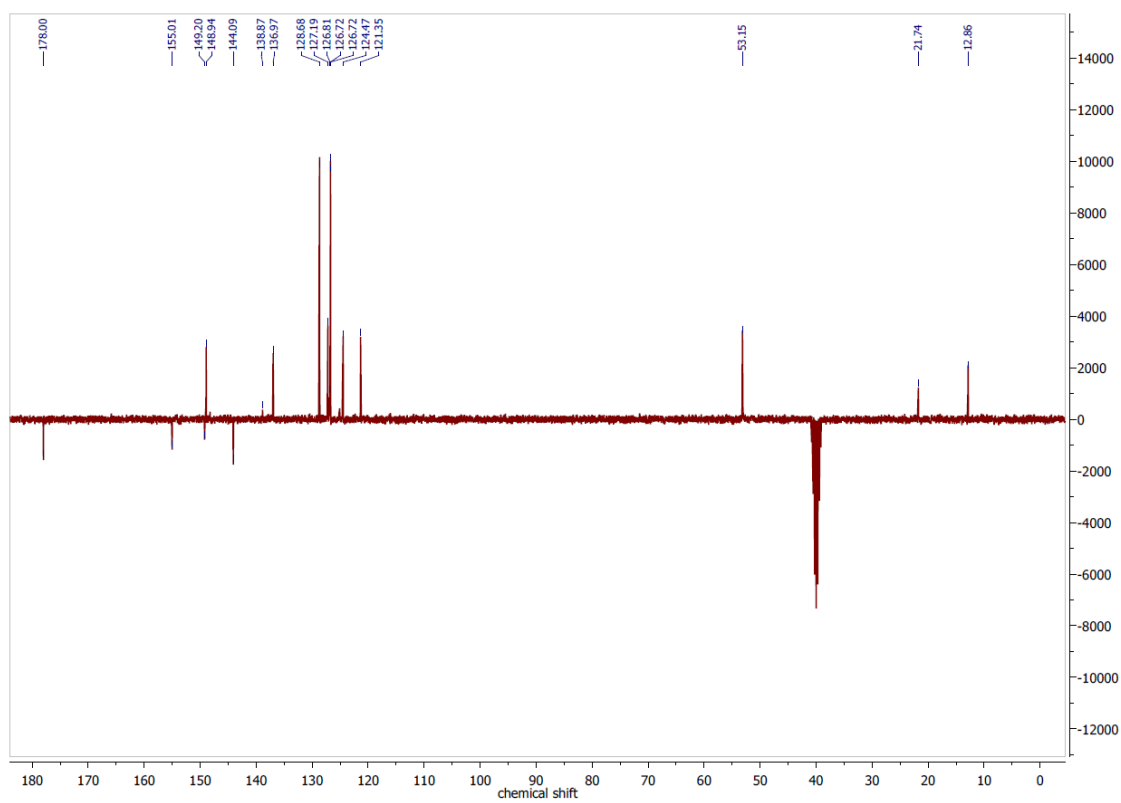


Figure 7.205 $^{13}\text{C}\{^1\text{H}\}$ DEPTQ NMR spectrum of HapyTSCmB in $\text{DMSO-}d_6$ at 75 MHz.

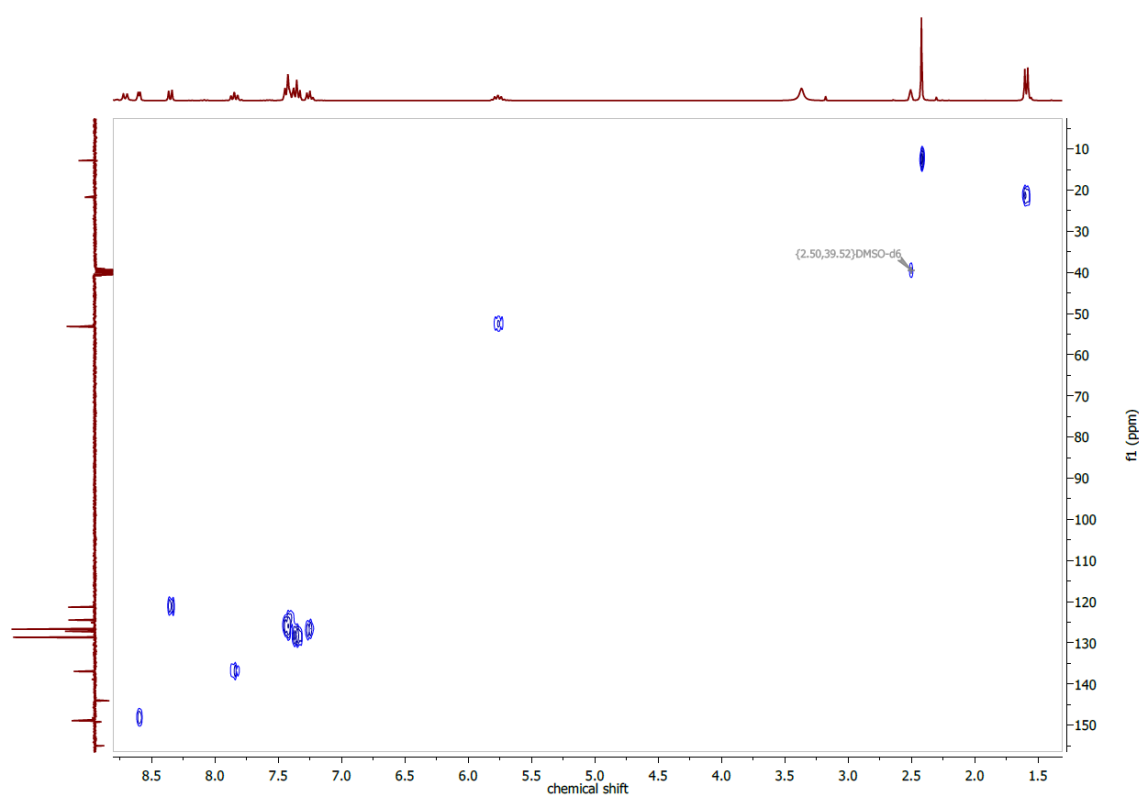


Figure 7.206 $^1\text{H}, ^{13}\text{C}$ HSQCed NMR spectrum of HapyTSCmB in $\text{DMSO-}d_6$.

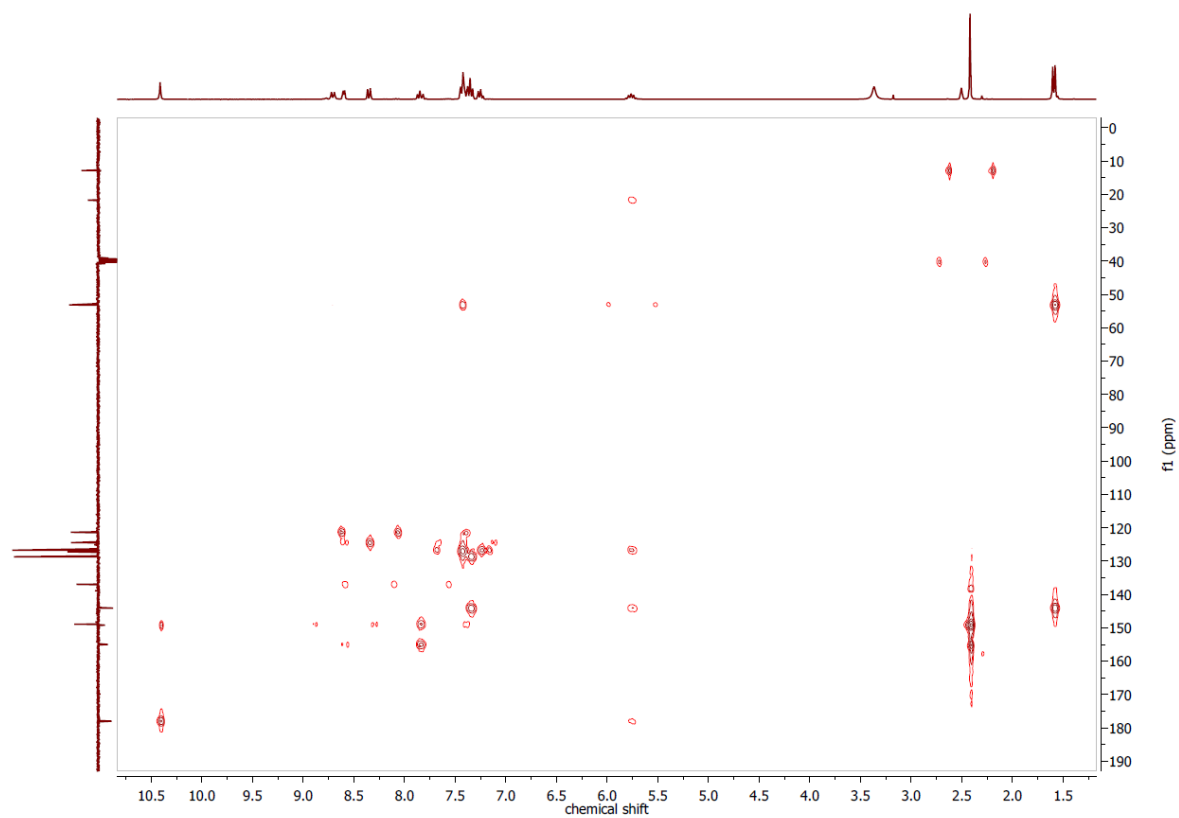


Figure 7.207 ^1H , ^{13}C HMBC NMR spectrum of HapyTSCmB in $\text{DMSO}-d_6$.

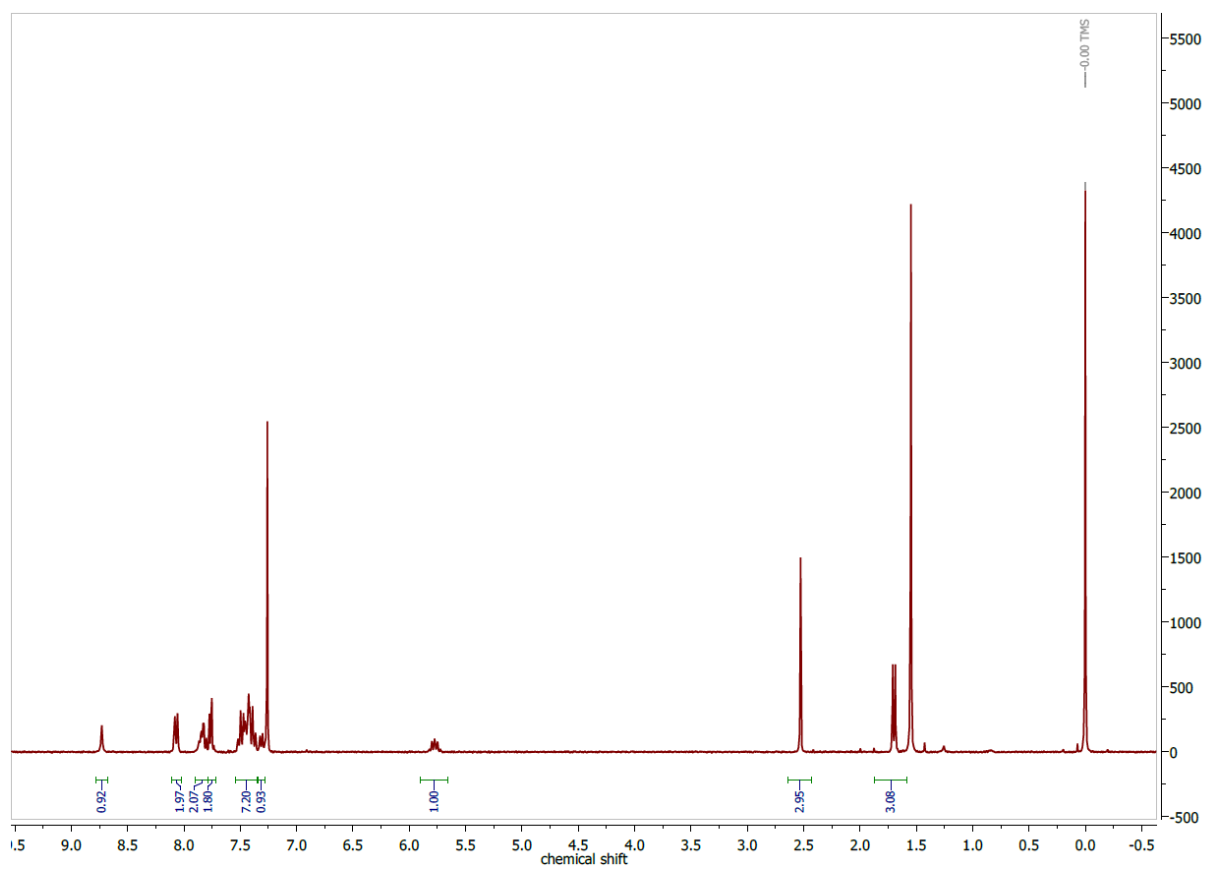


Figure 7.208 ^1H NMR spectrum of H6-phapyTSCmB in CDCl_3 at 300 MHz.

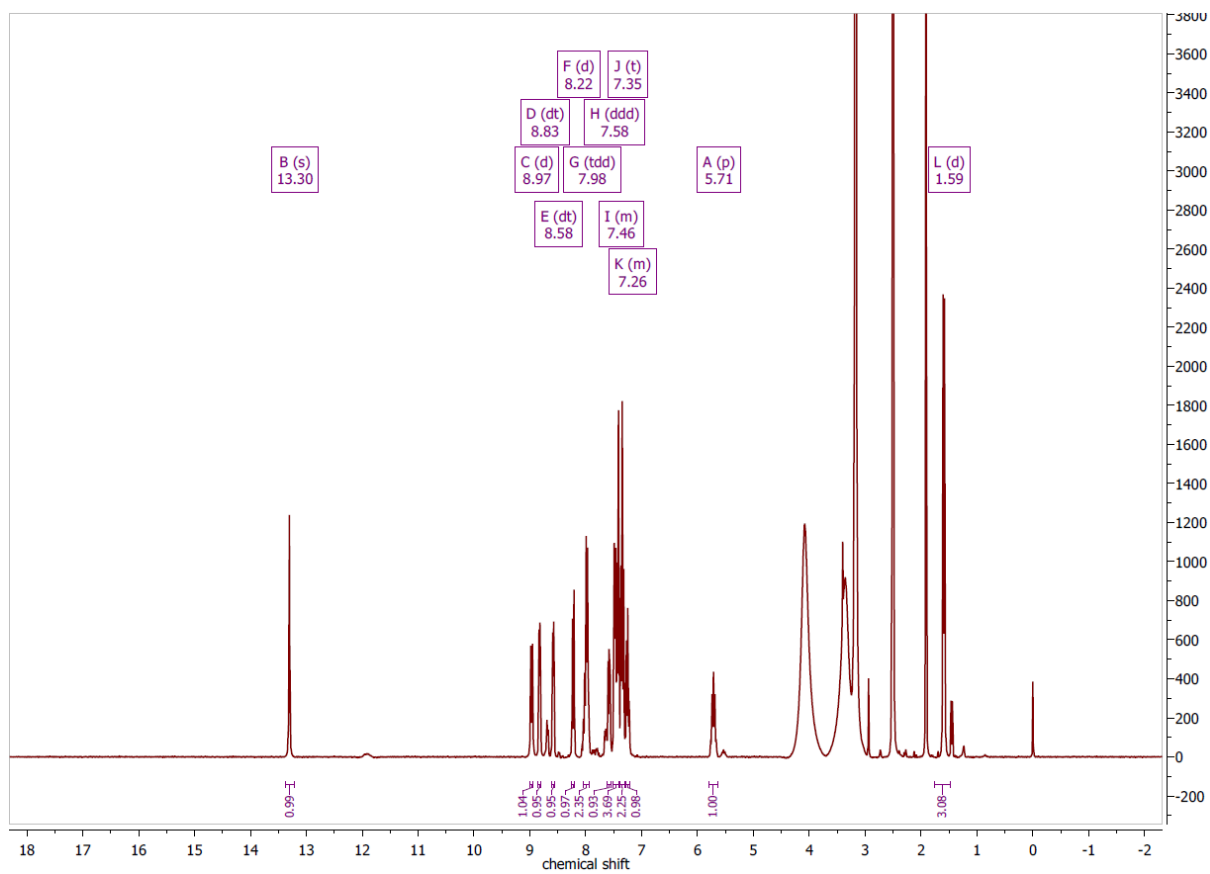


Figure 7.209 ^1H NMR spectrum of HdpyTSCmB in $\text{DMSO-}d_6$ at 300 MHz.

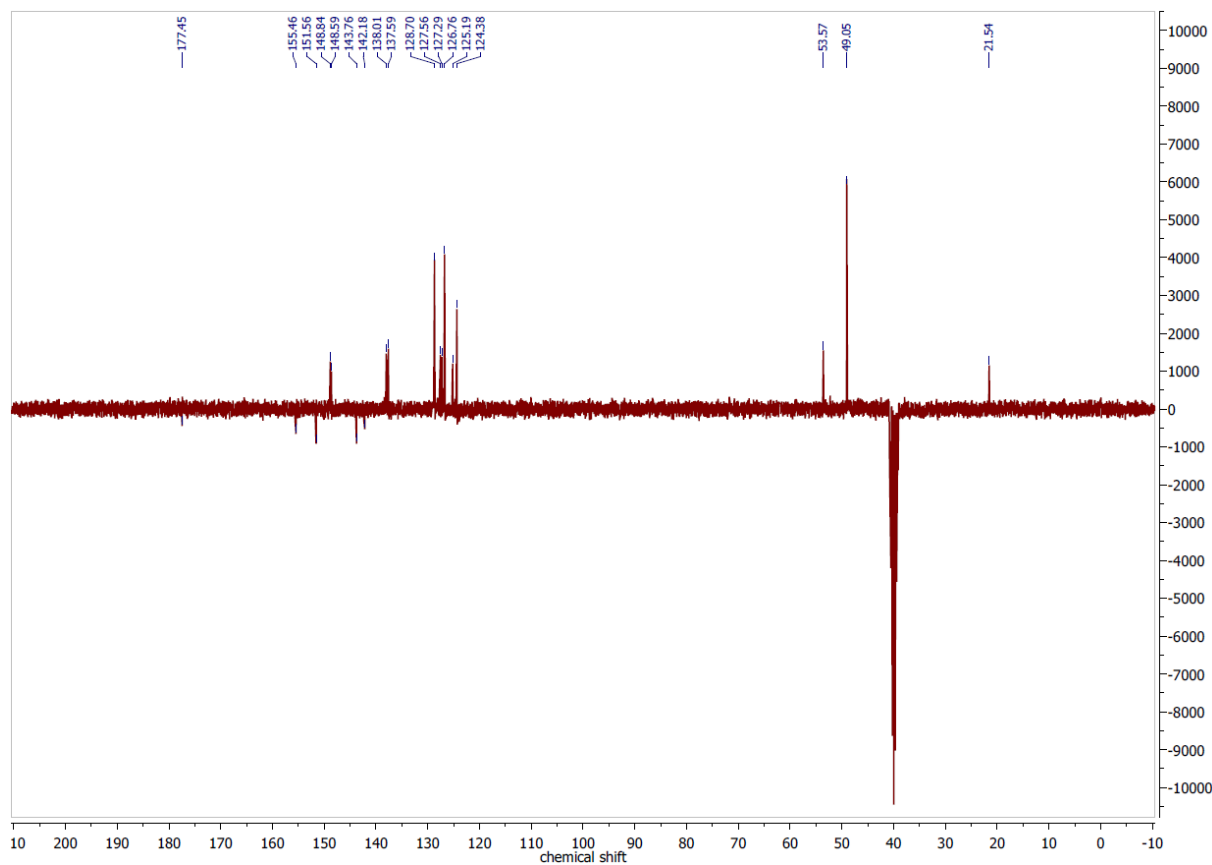


Figure 7.210 ^{13}C APT NMR spectrum of HdpyTSCmB in $\text{DMSO-}d_6$ at 75 MHz.

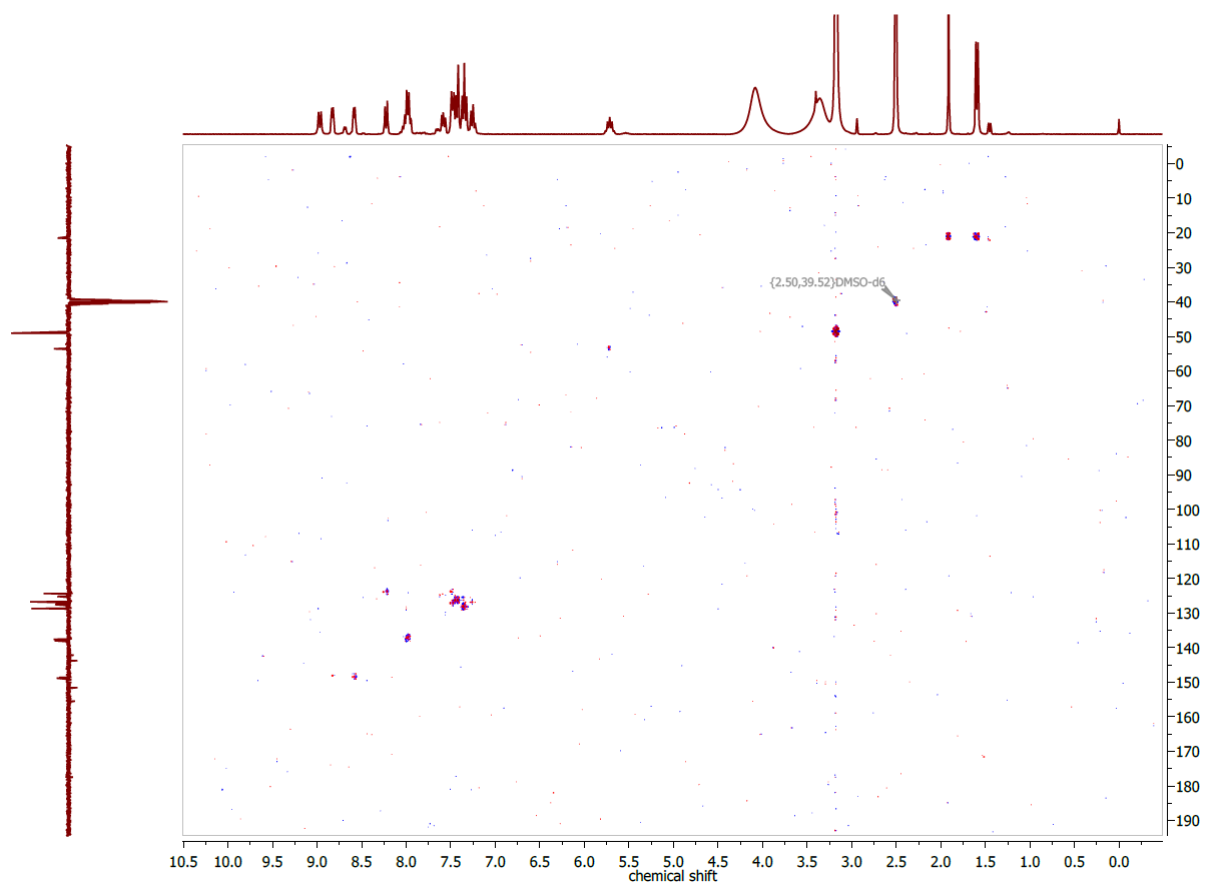


Figure 7.211 ^1H , ^{13}C HSQC NMR spectrum of HdpyTSCmB in $\text{DMSO-}d_6$.

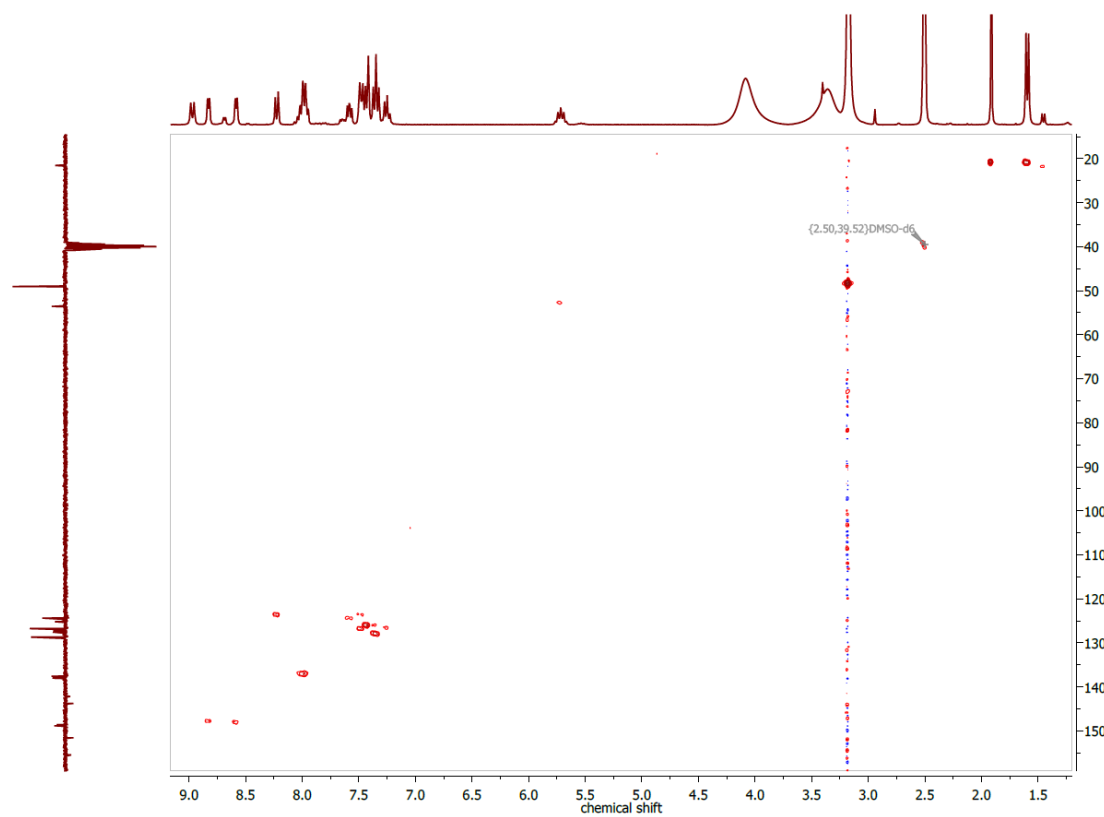


Figure 7.212 ^1H , ^{13}C HMBC NMR spectrum of HdpyTSCmB in $\text{DMSO-}d_6$.

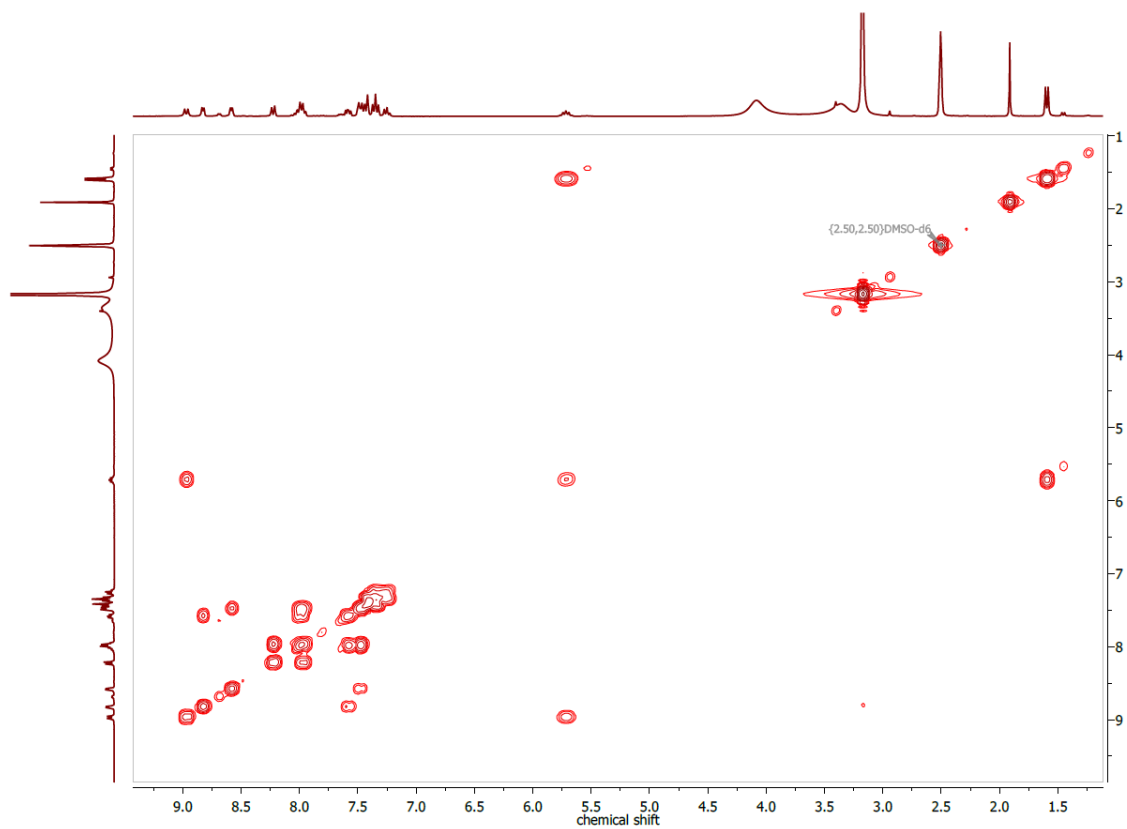


Figure 7.213 ^1H , ^1H COSY NMR spectrum of HdpyTSCmB in $\text{DMSO-}d_6$.

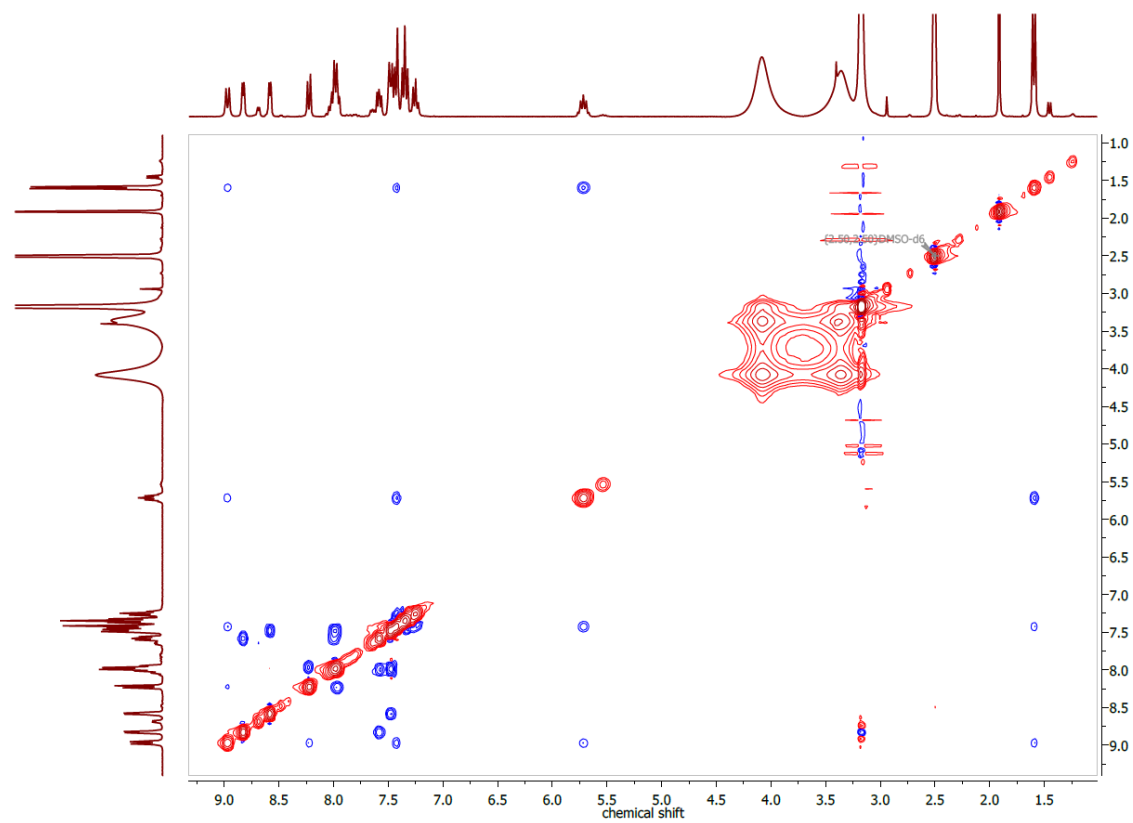


Figure 7.214 ^1H , ^1H NOESY NMR spectrum of HdpyTSCmB in $\text{DMSO-}d_6$.

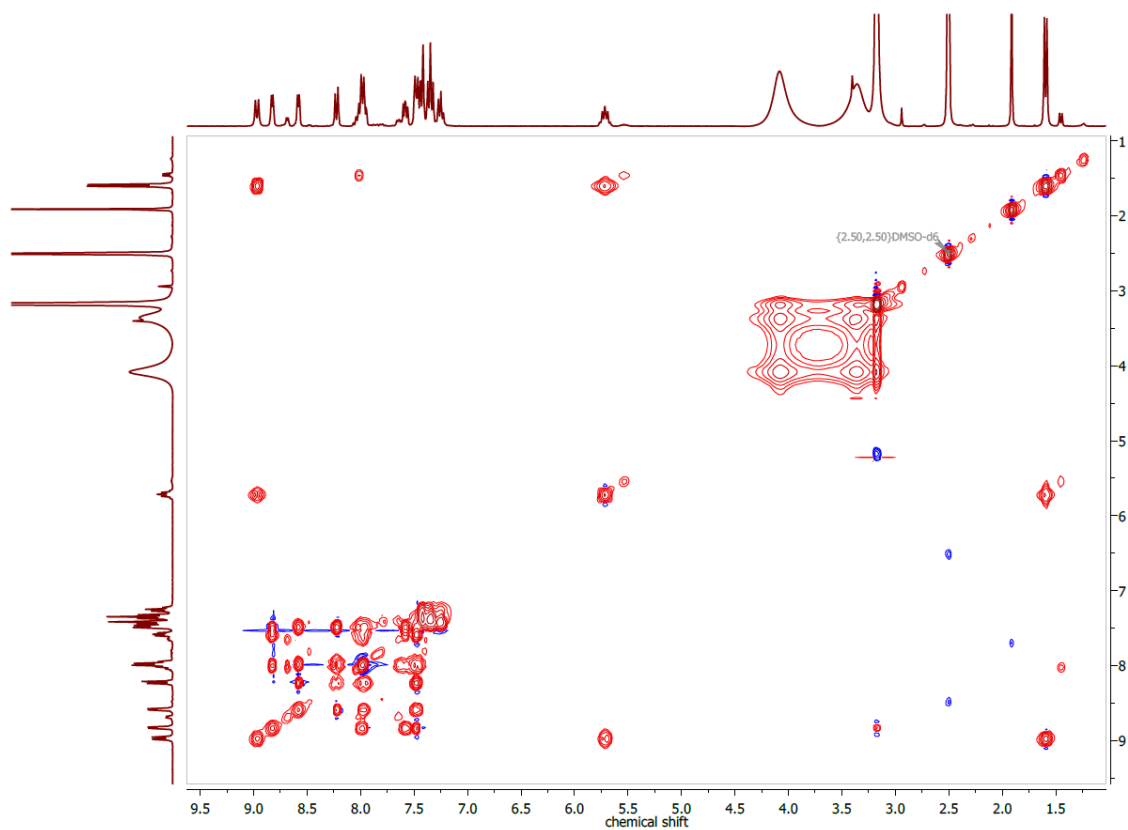


Figure 7.215 $^1\text{H}, ^1\text{H}$ TOCSY NMR spectrum of HdpyTSCmB in $\text{DMSO-}d_6$.

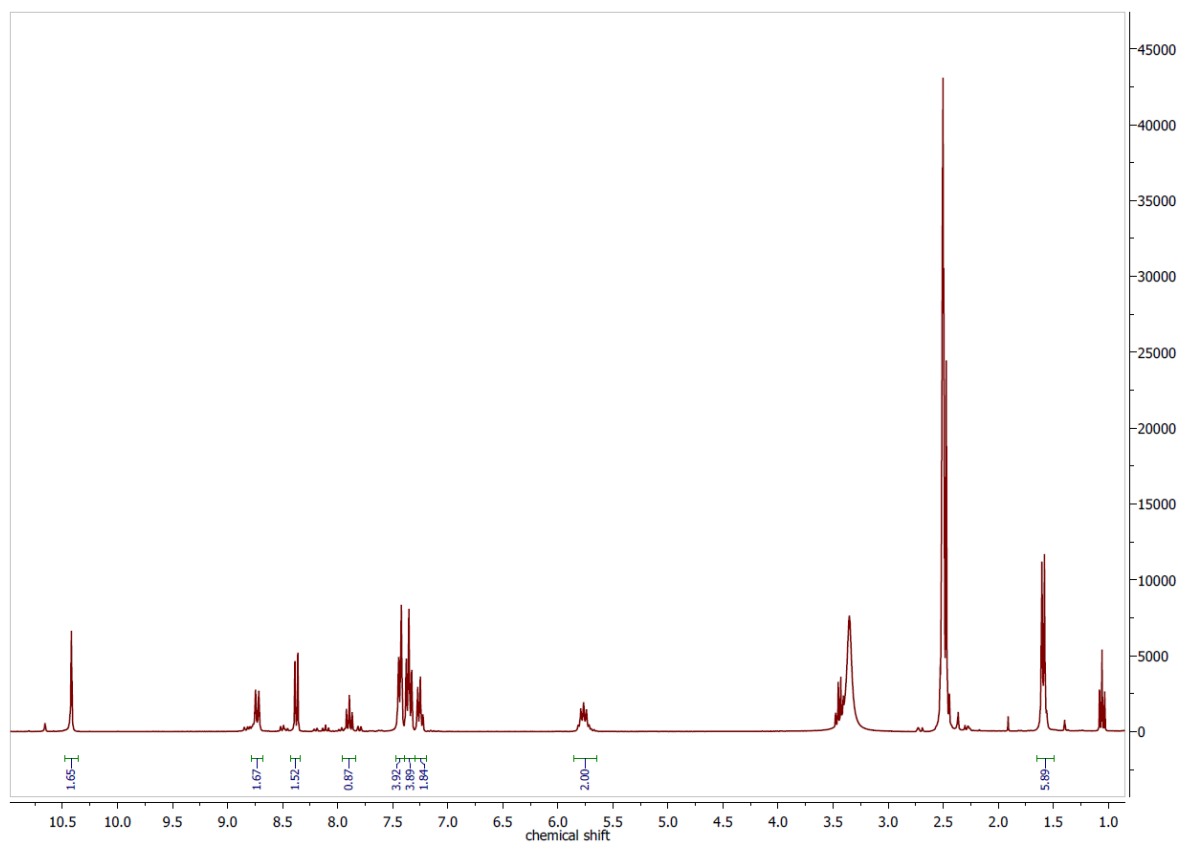


Figure 7.216 ^1H NMR spectrum of $\text{H}_2\text{dap(b)TSCmB}$ in $\text{DMSO-}d_6$ at 300 MHz.

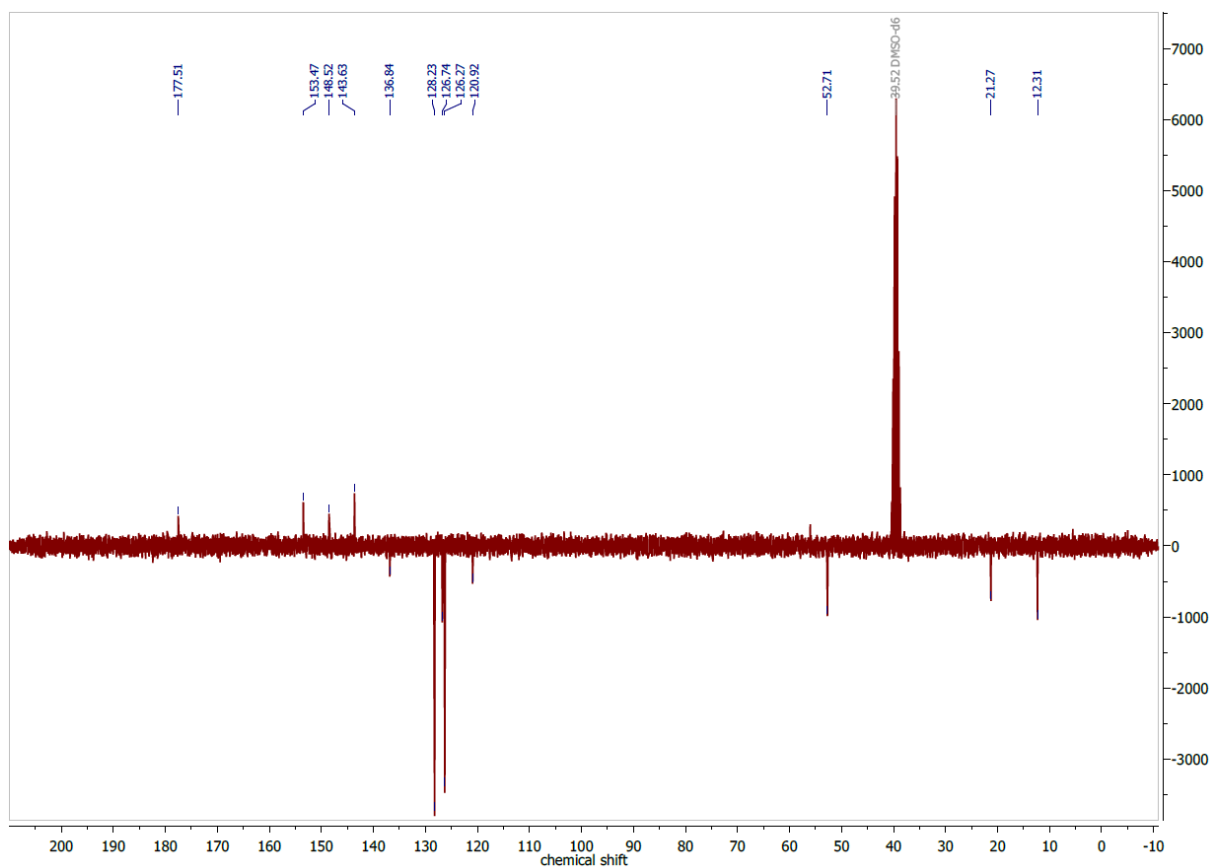


Figure 7.217 ^{13}C APT NMR spectrum of $\text{H}_2\text{dap}(\text{b})\text{TSCmB}$ in $\text{DMSO-}d_6$ at 75 MHz.

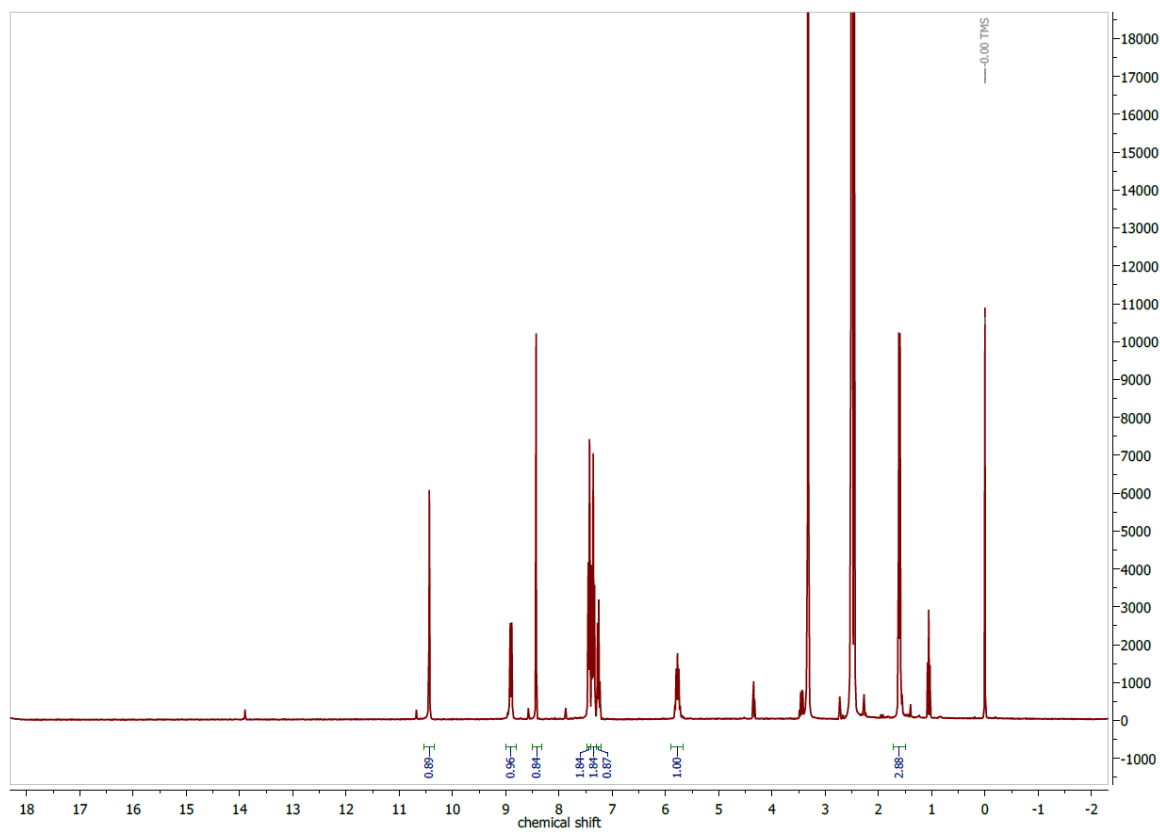


Figure 7.218 ^1H NMR spectrum of $\text{H}_24\text{-Cl dap}(\text{b})\text{TSCAd}$ in $\text{DMSO-}d_6$ at 300 MHz.

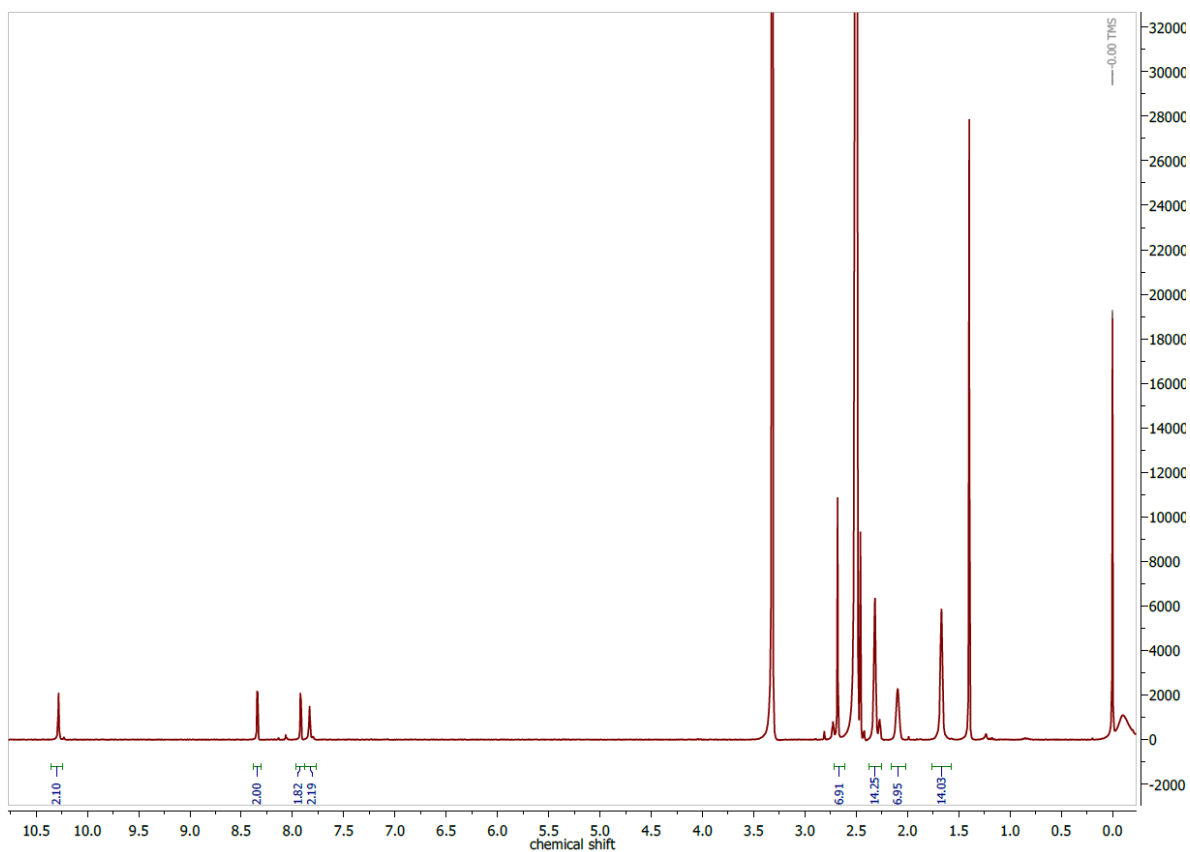


Figure 7.219 ^{13}C APT NMR spectrum of $\text{H}_24\text{-Cl dap(b)TSCAd}$ in $\text{DMSO-}d_6$ at 75 MHz.

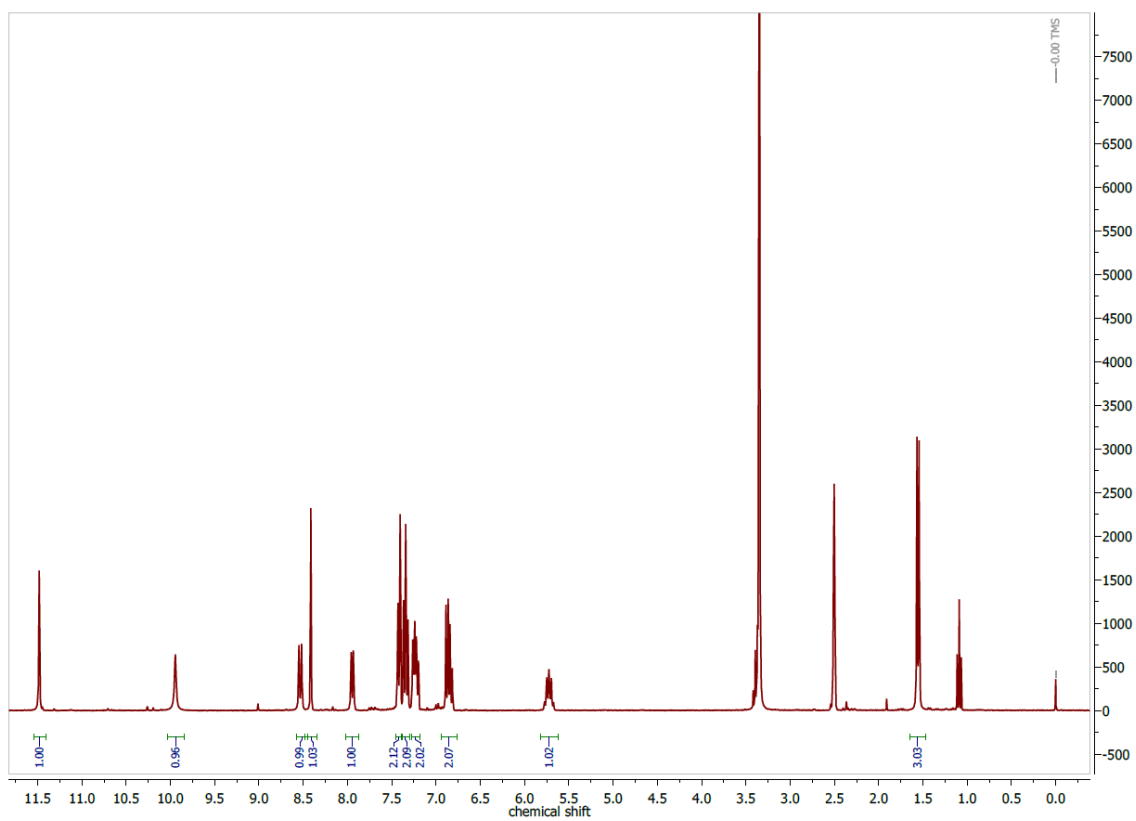


Figure 7.220 ^1H NMR spectrum of $\text{H}_2\text{SalTSCmB}$ in $\text{DMSO-}d_6$ at 300 MHz.

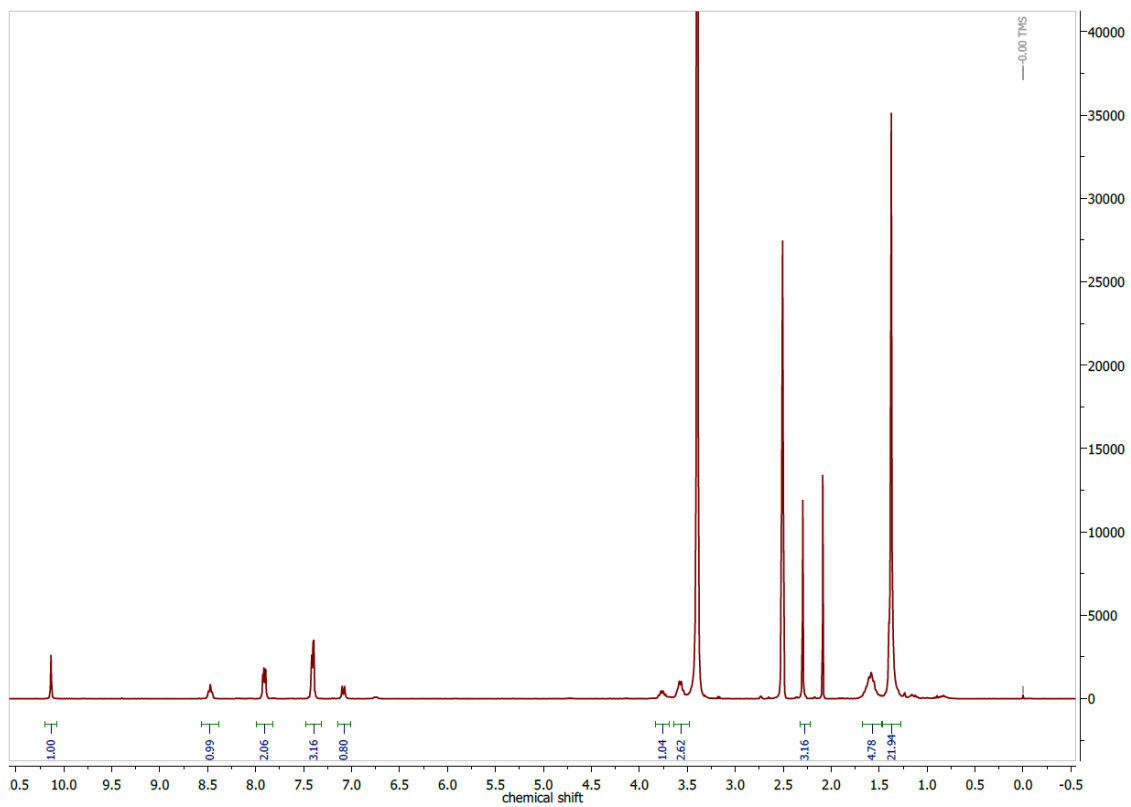


Figure 7.221 ^1H NMR spectrum of $\text{H}_2\text{aphTSCLp}$ in $\text{DMSO}-d_6$ at 300 MHz.

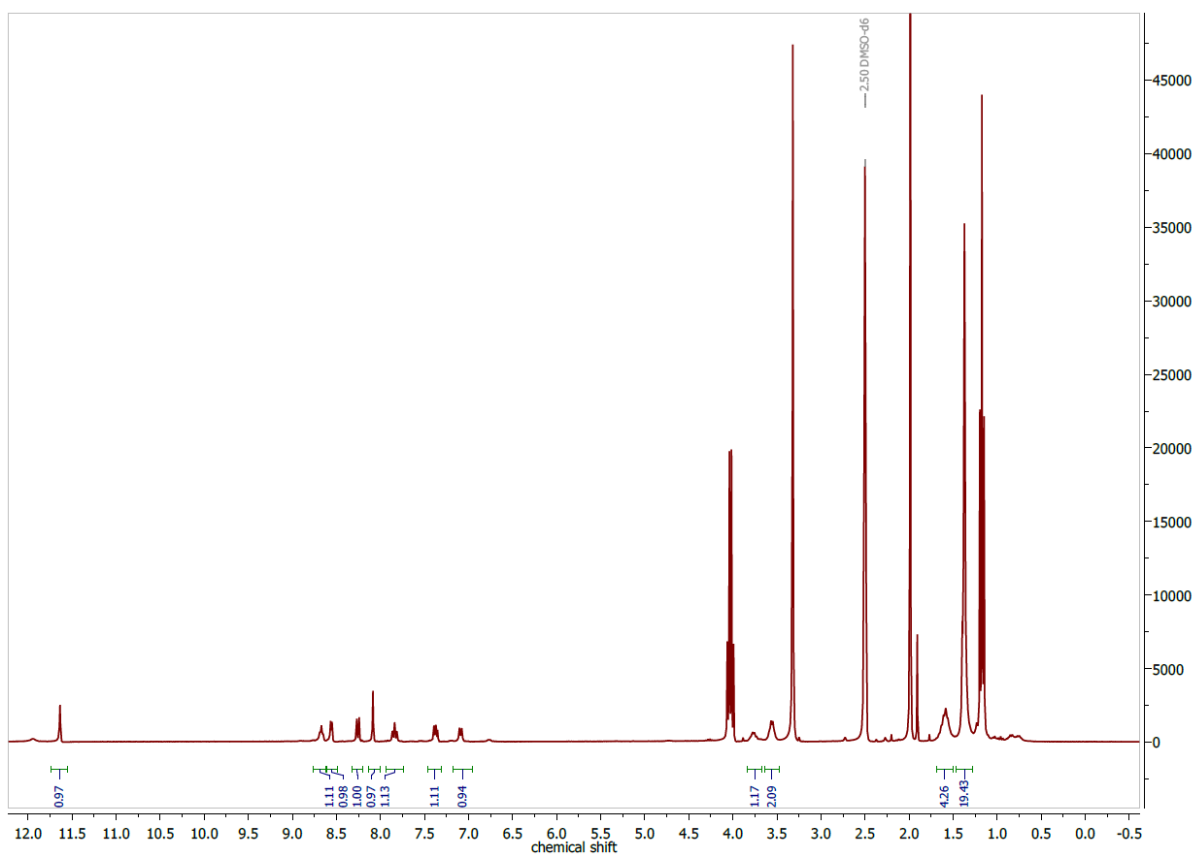


Figure 7.222 ^1H NMR spectrum of HfpyTSCLp in $\text{DMSO}-d_6$ at 300 MHz.

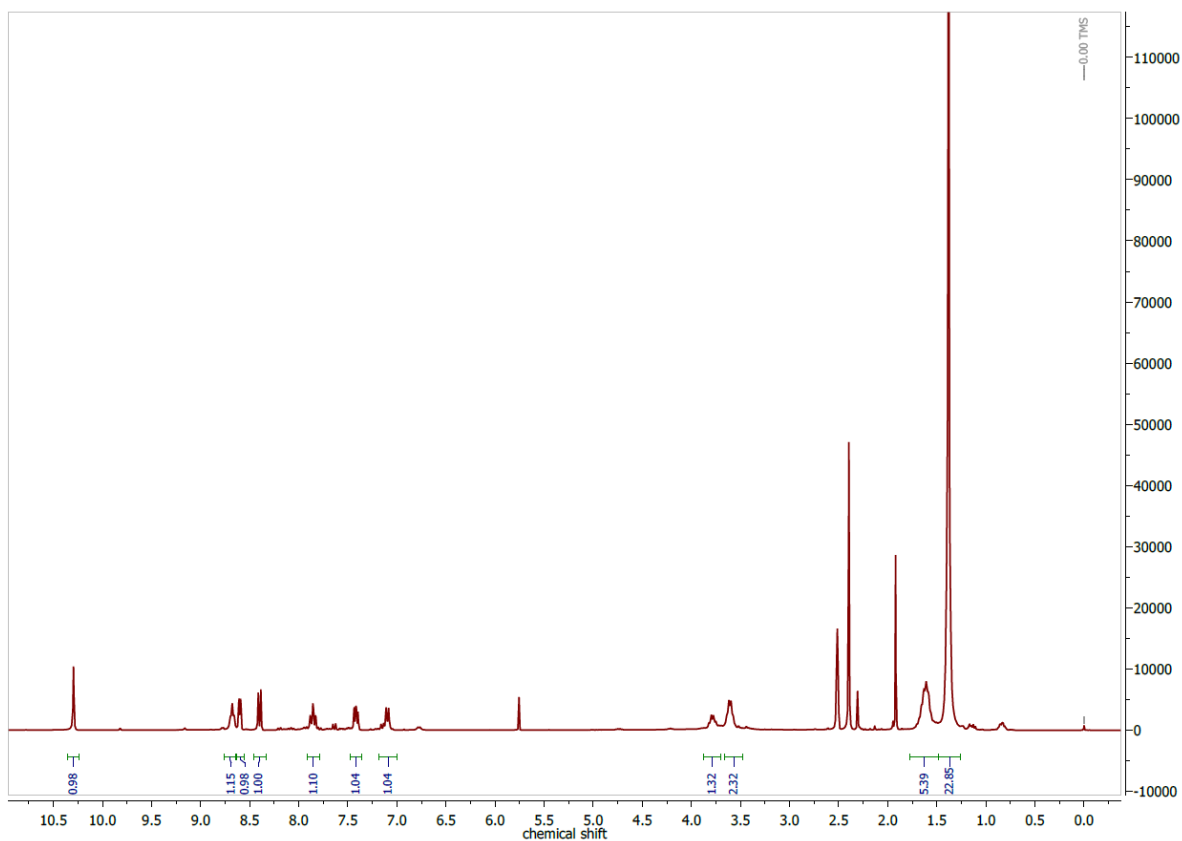


Figure 7.223 ^1H NMR spectrum of HapyTSCLp in $\text{DMSO-}d_6$ at 300 MHz.

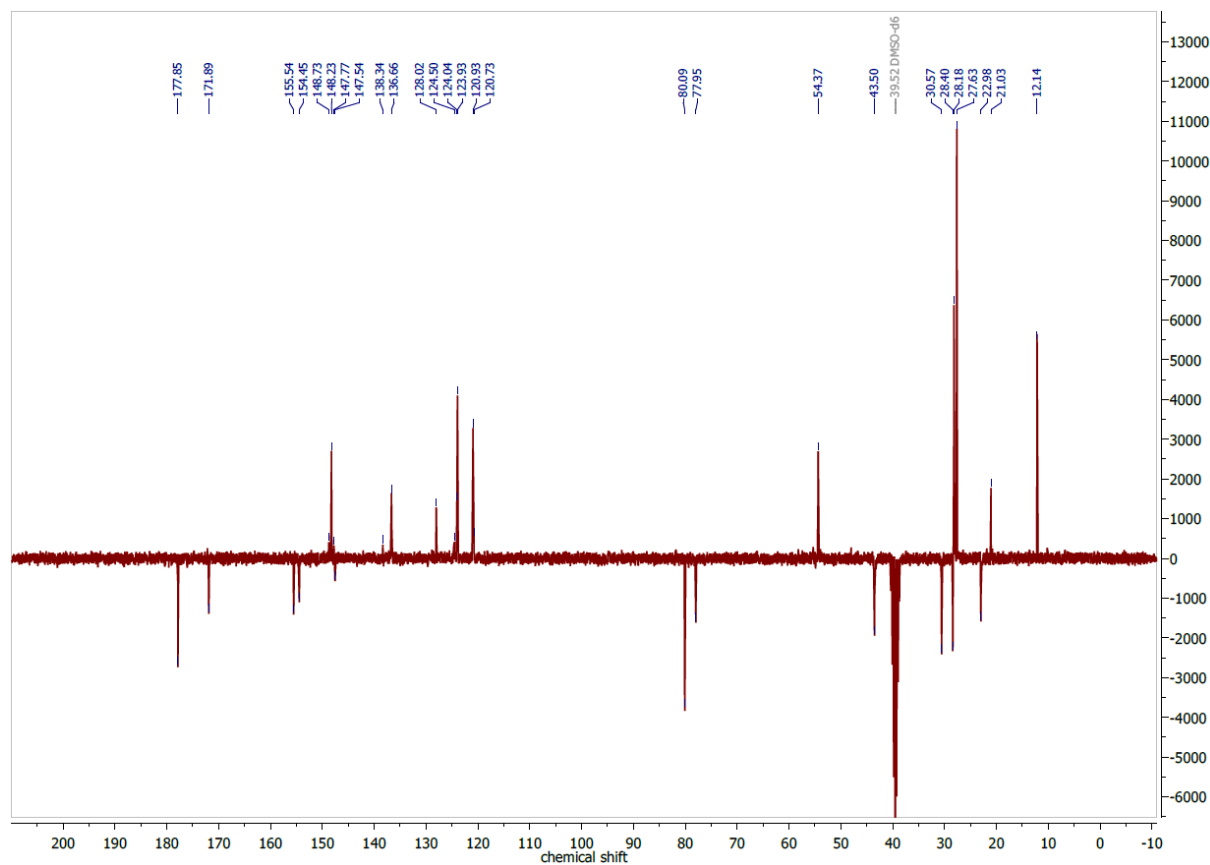


Figure 7.224 $^{13}\text{C}\{^1\text{H}\}$ DEPTQ NMR spectrum of HapyTSCLp in $\text{DMSO-}d_6$ at 75 MHz.

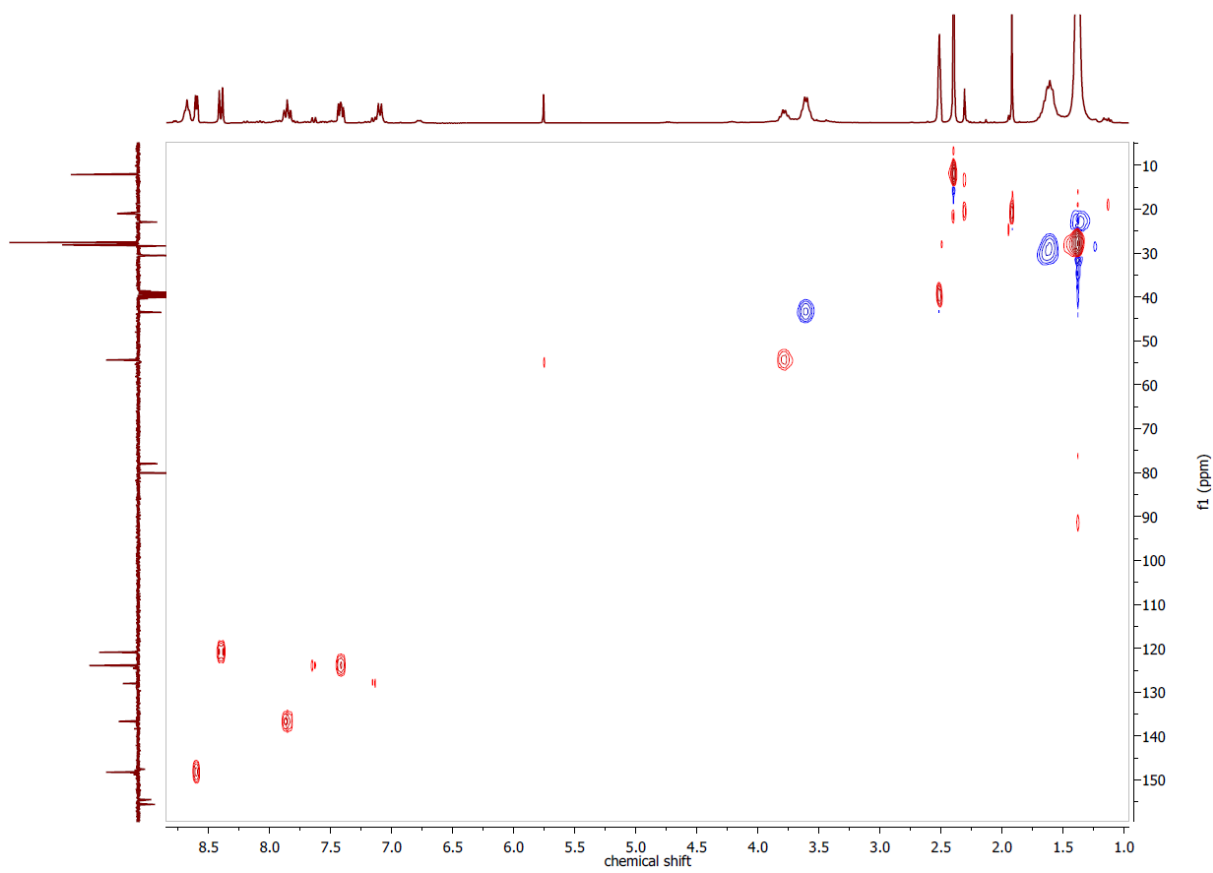


Figure 7.225 ^1H , ^{13}C HSQCed NMR spectrum of HapyTSCLp in $\text{DMSO-}d_6$.

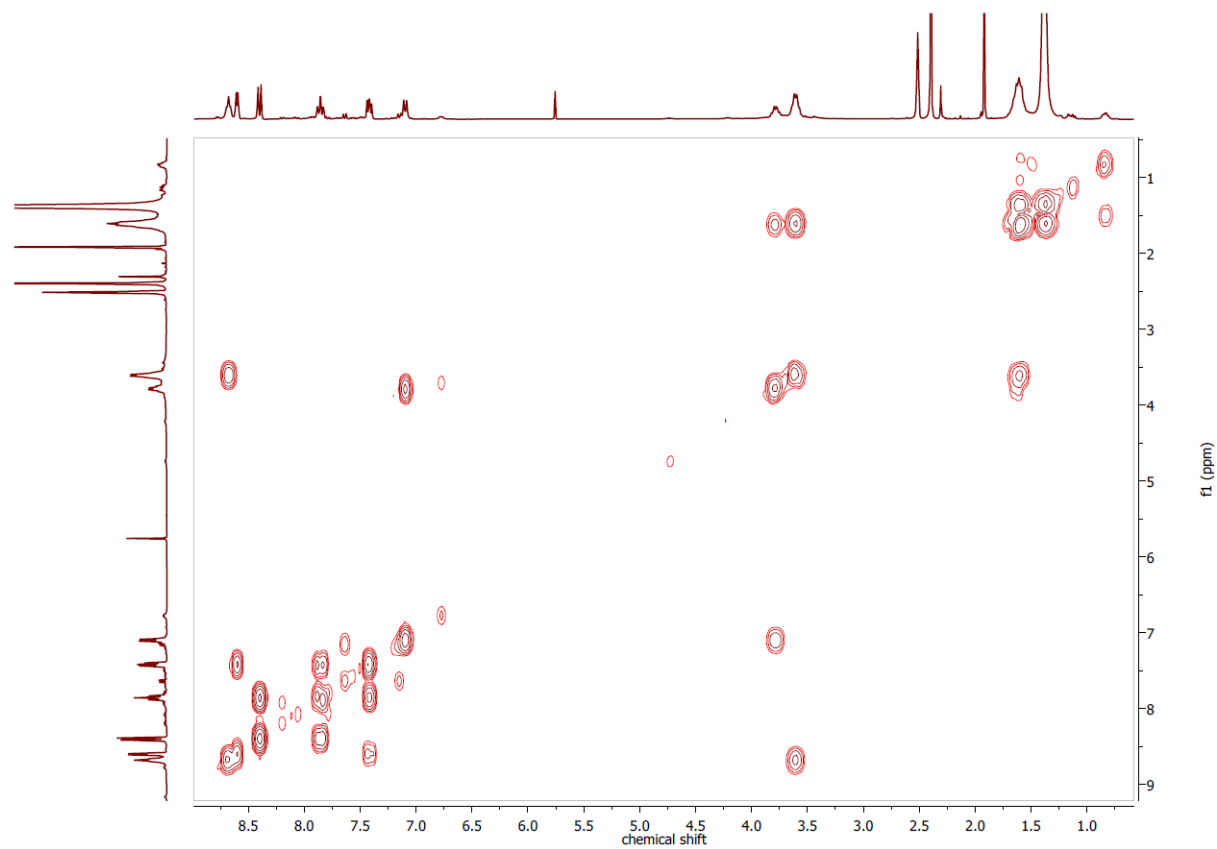


Figure 7.226 ^1H , ^1H COSY NMR spectrum of HapyTSCLp in $\text{DMSO-}d_6$.

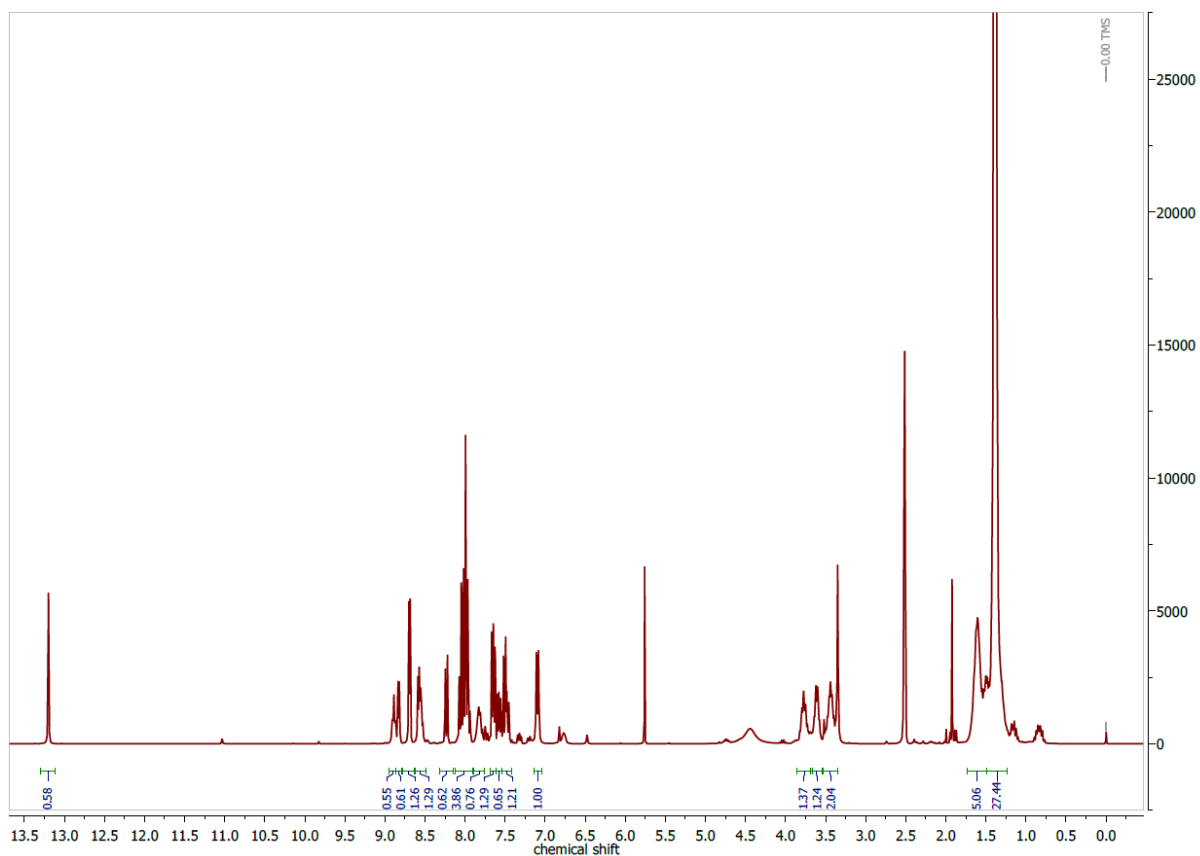


Figure 7.227 ^1H NMR spectrum of HdpyTSCLp in $\text{DMSO-}d_6$ at 300 MHz.

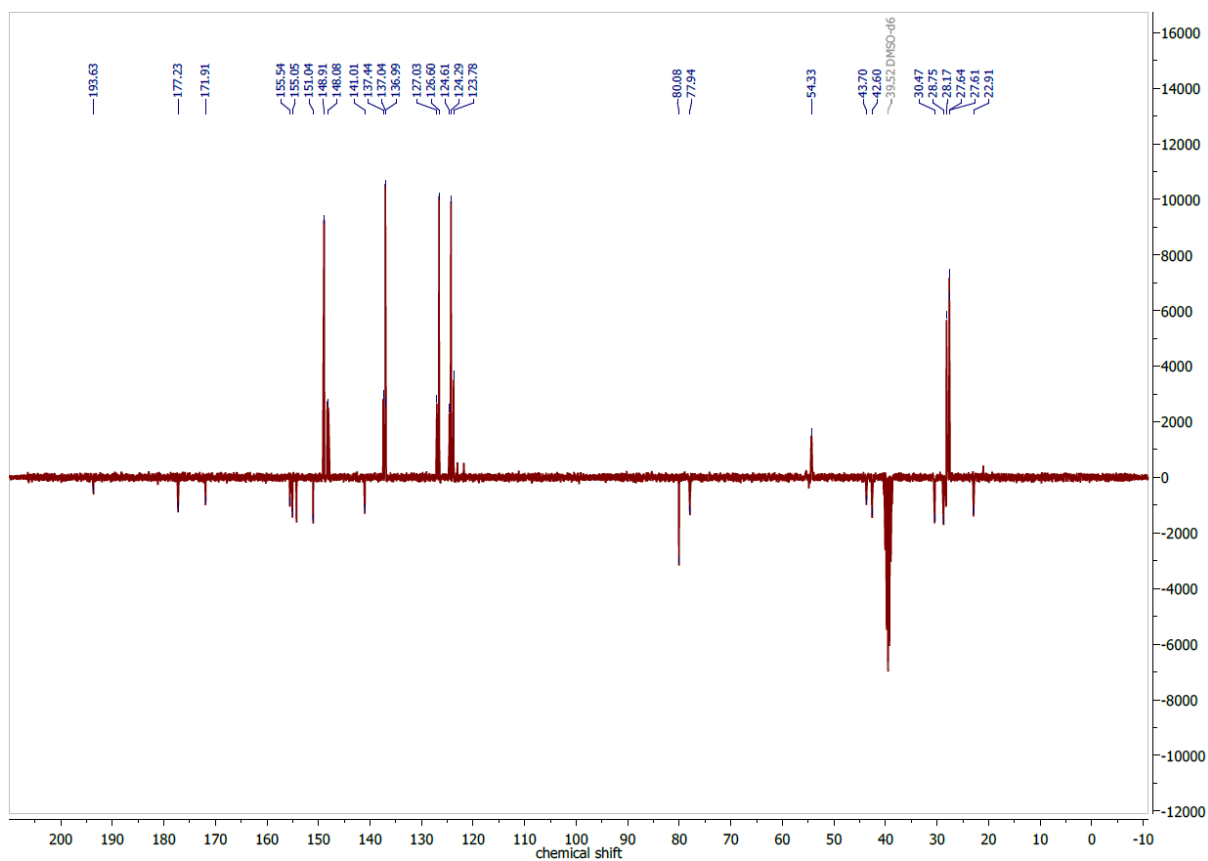


Figure 7.228 ^{13}C NMR spectrum of HdpyTSCLp in $\text{DMSO-}d_6$ at 75 MHz.

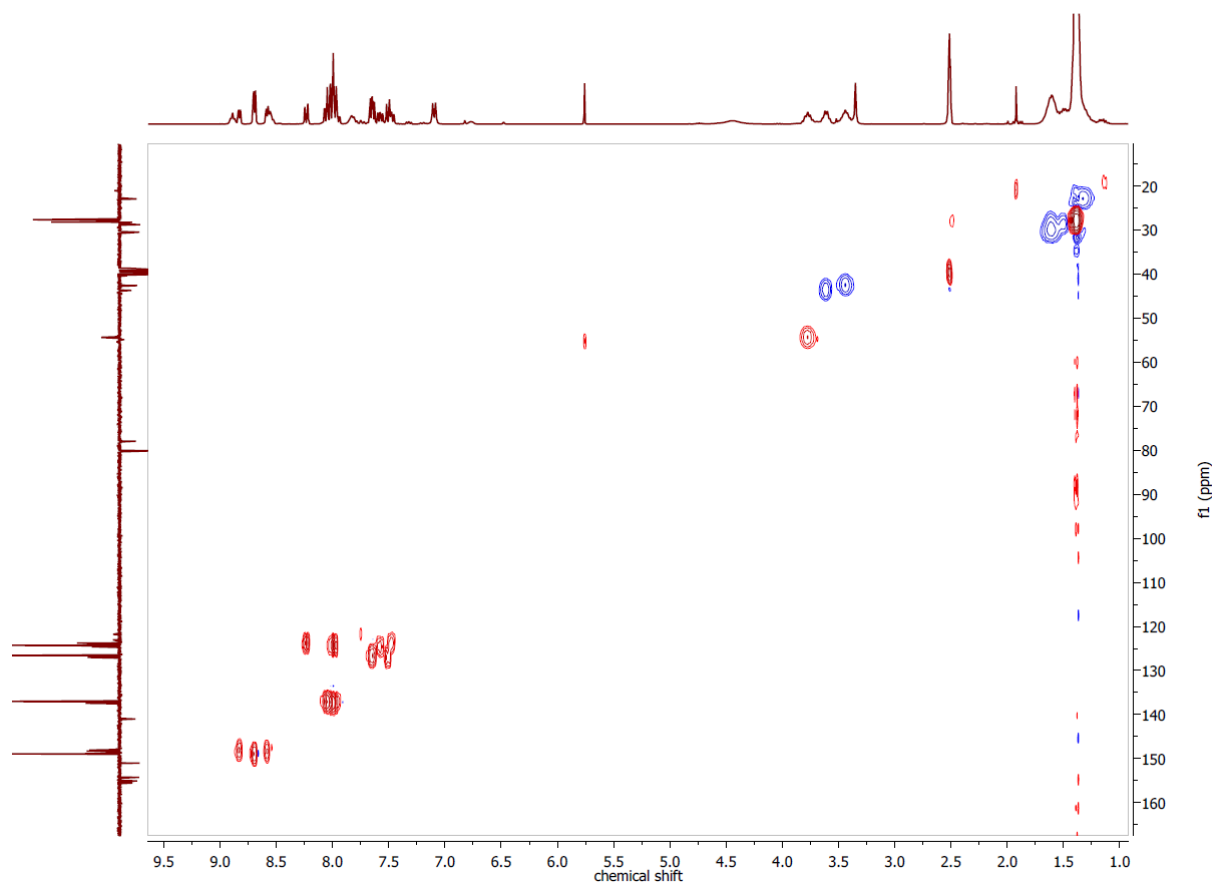


Figure 7.229 ^1H , ^{13}C HSQCed NMR spectrum of HdpyTSCLp in $\text{DMSO-}d_6$.

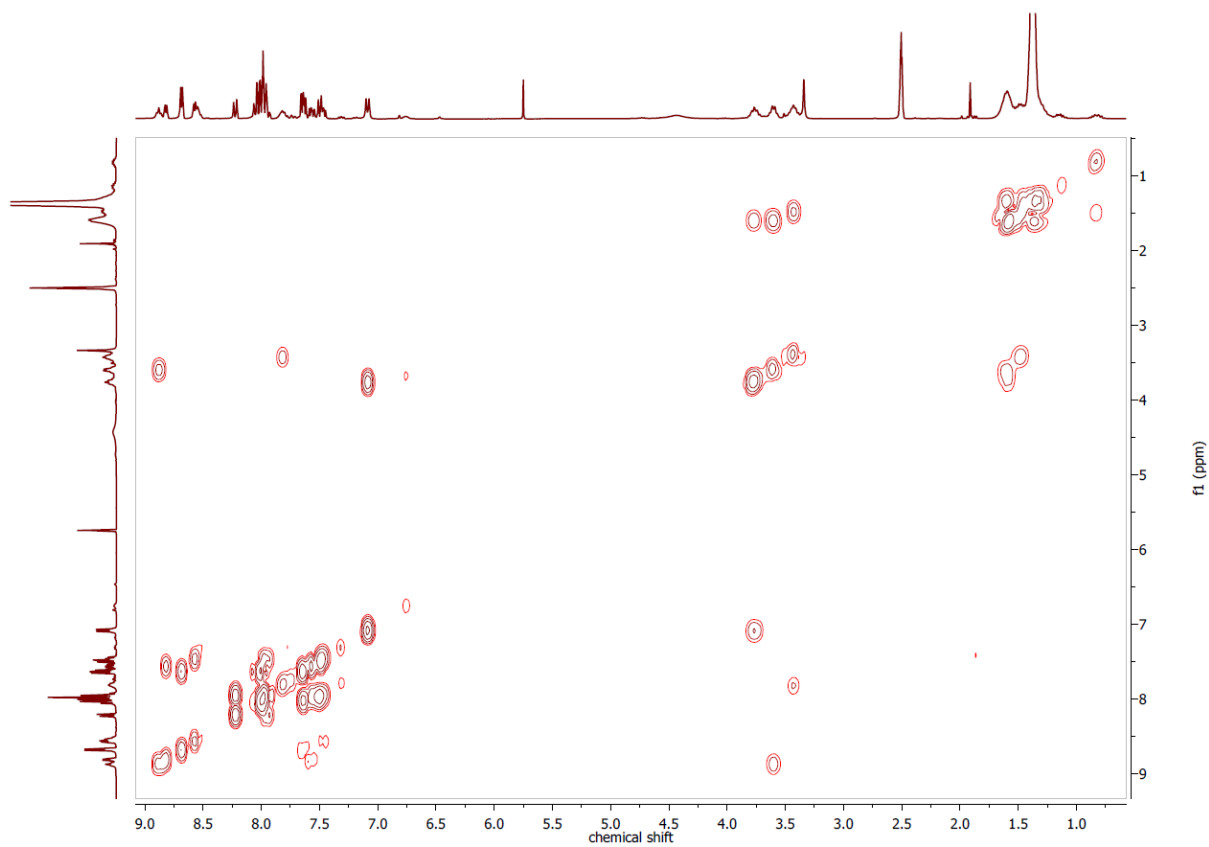


Figure 7.230 ^1H , ^1H COSY NMR spectrum of HdpyTSCLp in $\text{DMSO-}d_6$.

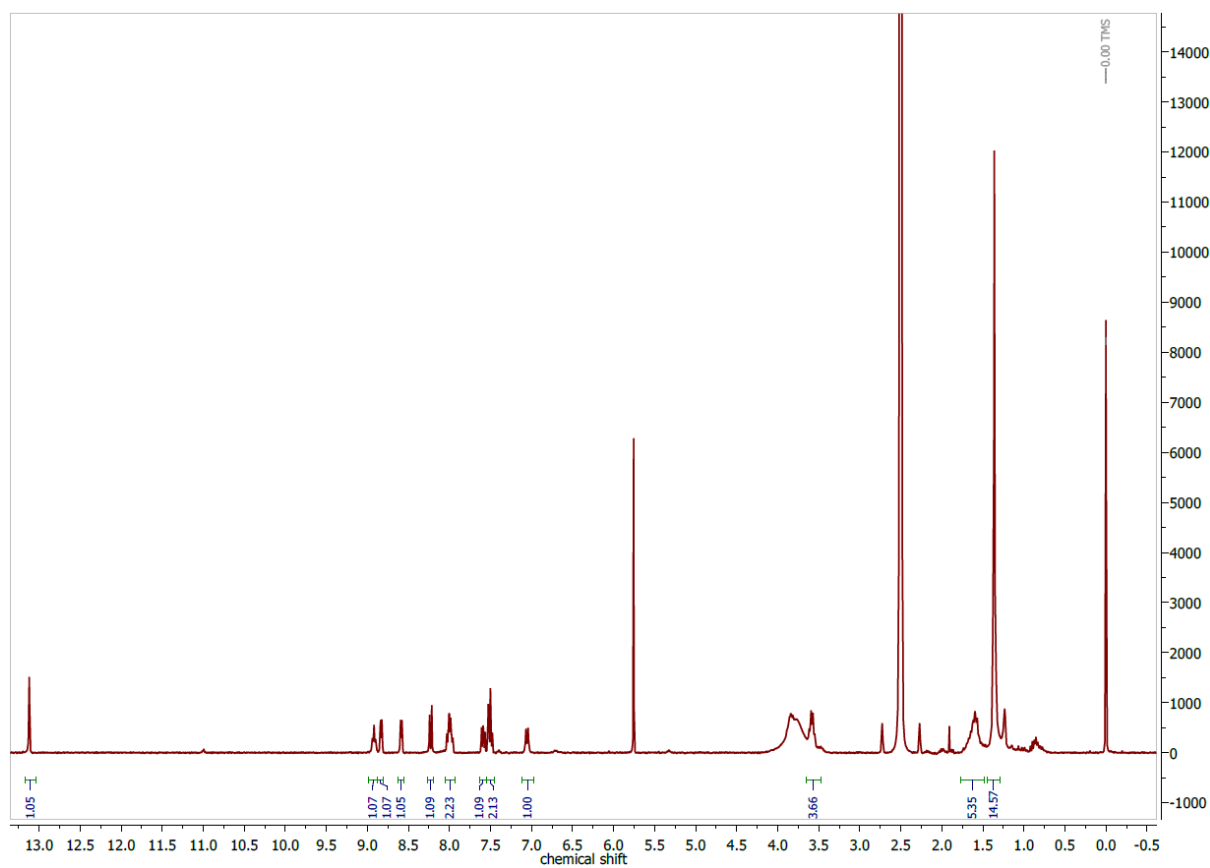


Figure 7.231 ^1H NMR spectrum of HdpyTSLBoc in $\text{DMSO}-d_6$ at 300 MHz.

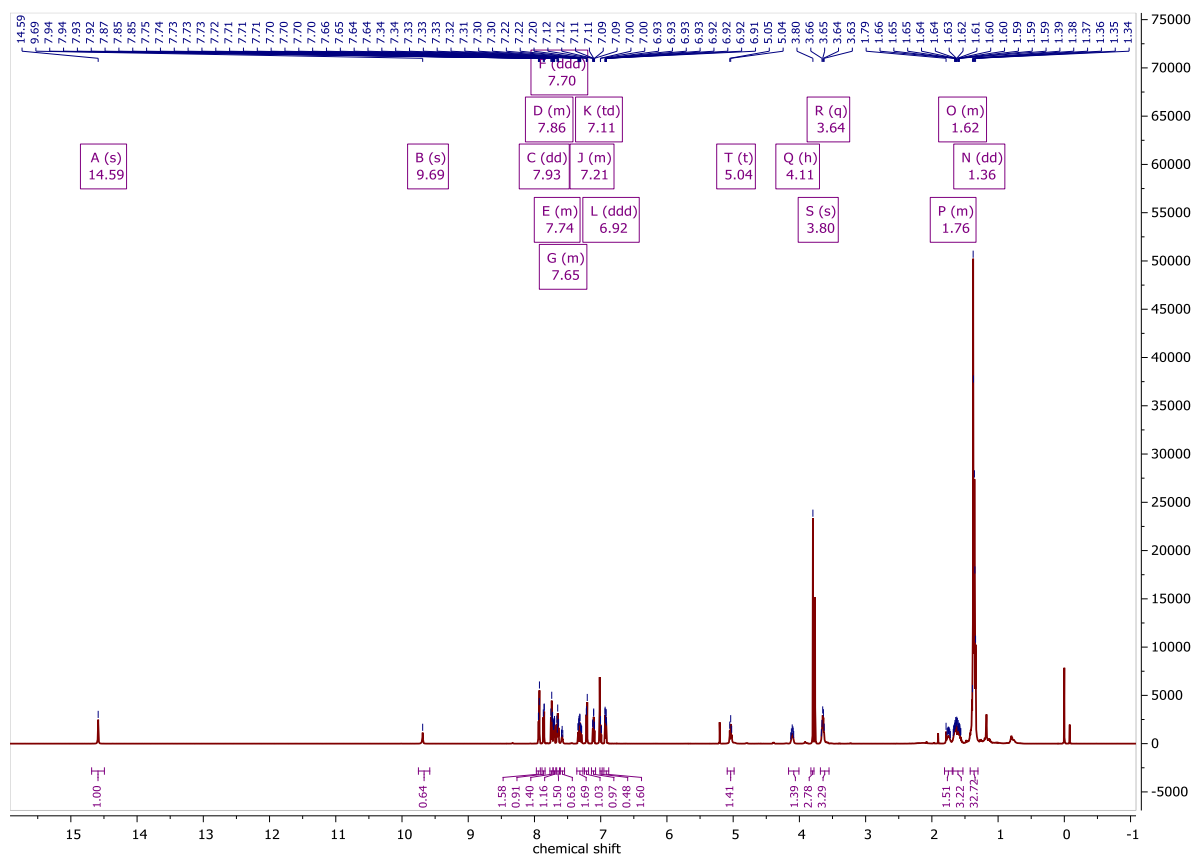


Figure 7.232 ^1H NMR spectrum of HmphfpyTSLp in CDCl_3 at 600 MHz.

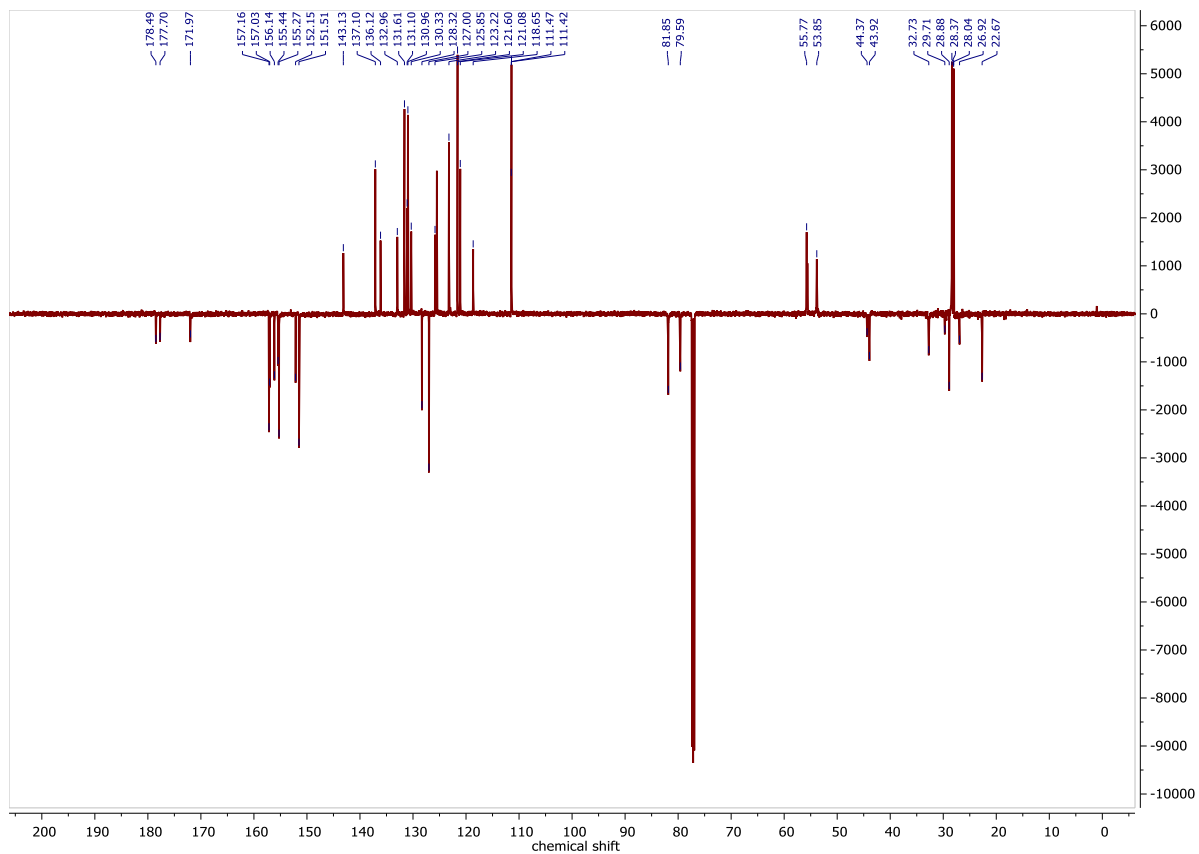


Figure 7.233 ^{13}C APT NMR spectrum of HmphfpyTSCLp in CDCl_3 at 152 MHz.

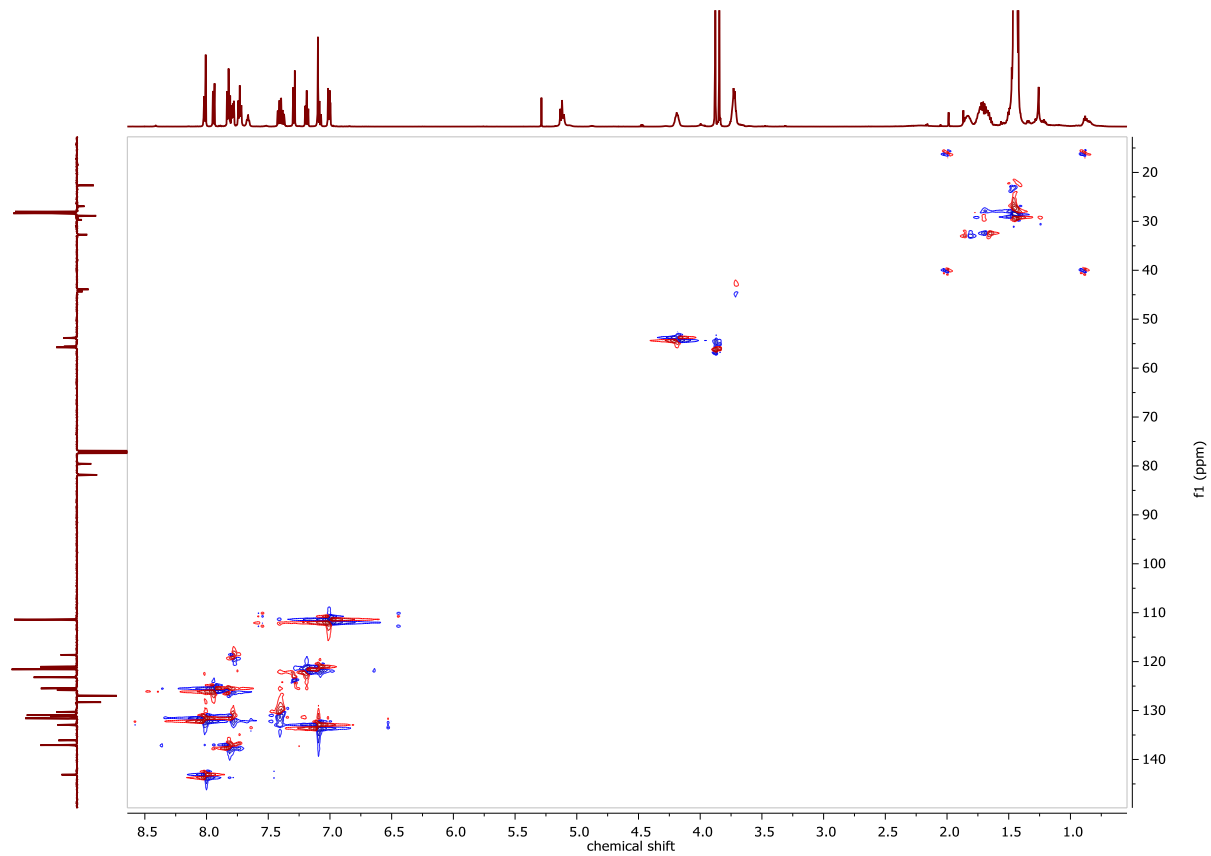


Figure 7.234 ^1H , ^{13}C HSQCed NMR spectrum of HmphfpyTSCLp in CDCl_3 .

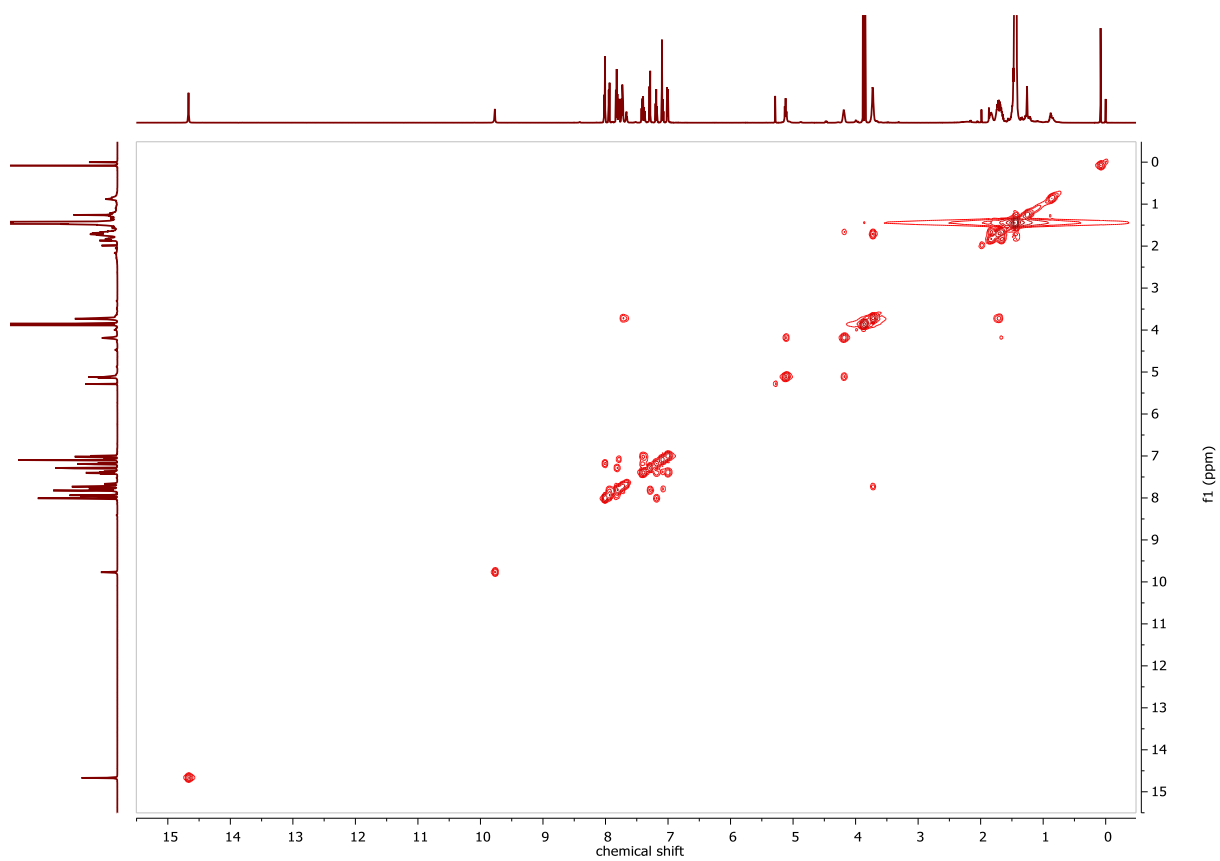


Figure 7.235 $^1\text{H}, ^1\text{H}$ COSY NMR spectrum of HmphfpyTSCLp in CDCl_3 .

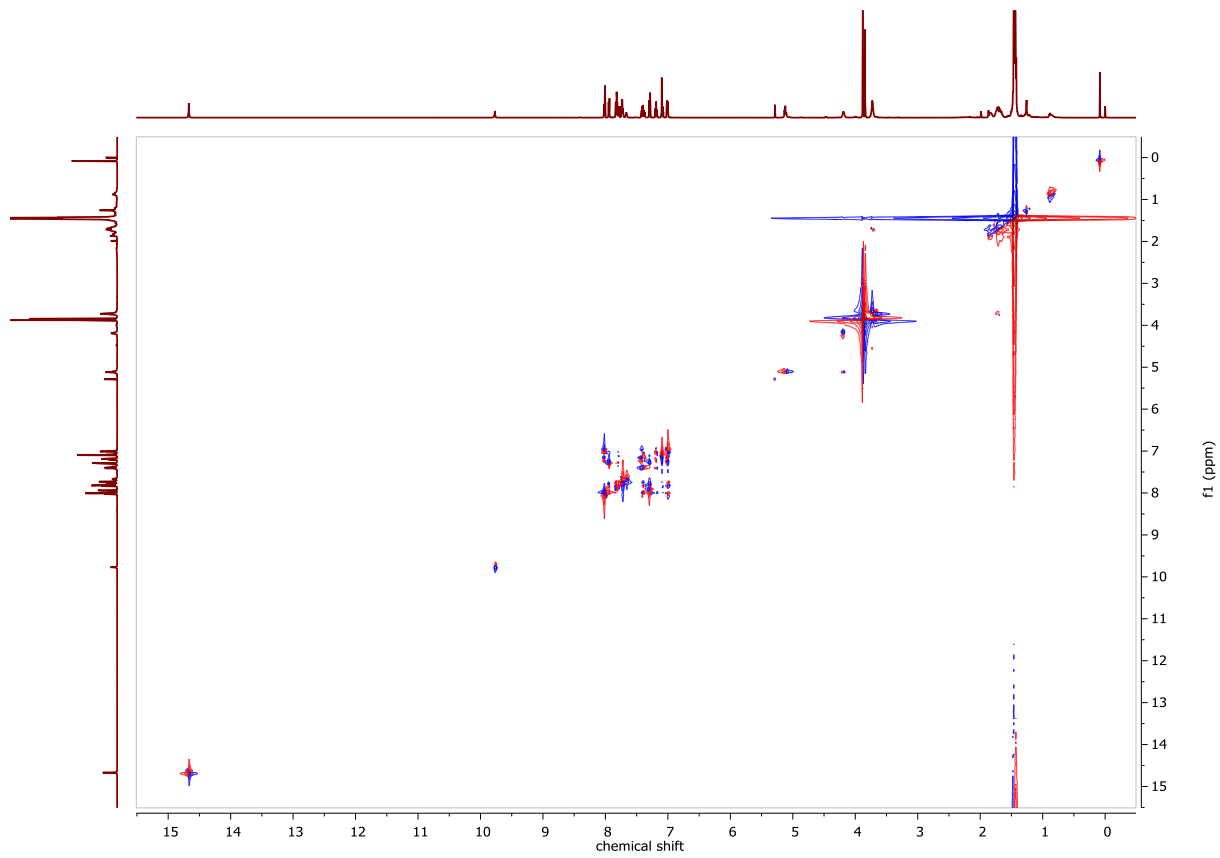


Figure 7.236 $^1\text{H}, ^1\text{H}$ TOCSY NMR spectrum of HmphfpyTSCLp in CDCl_3 .

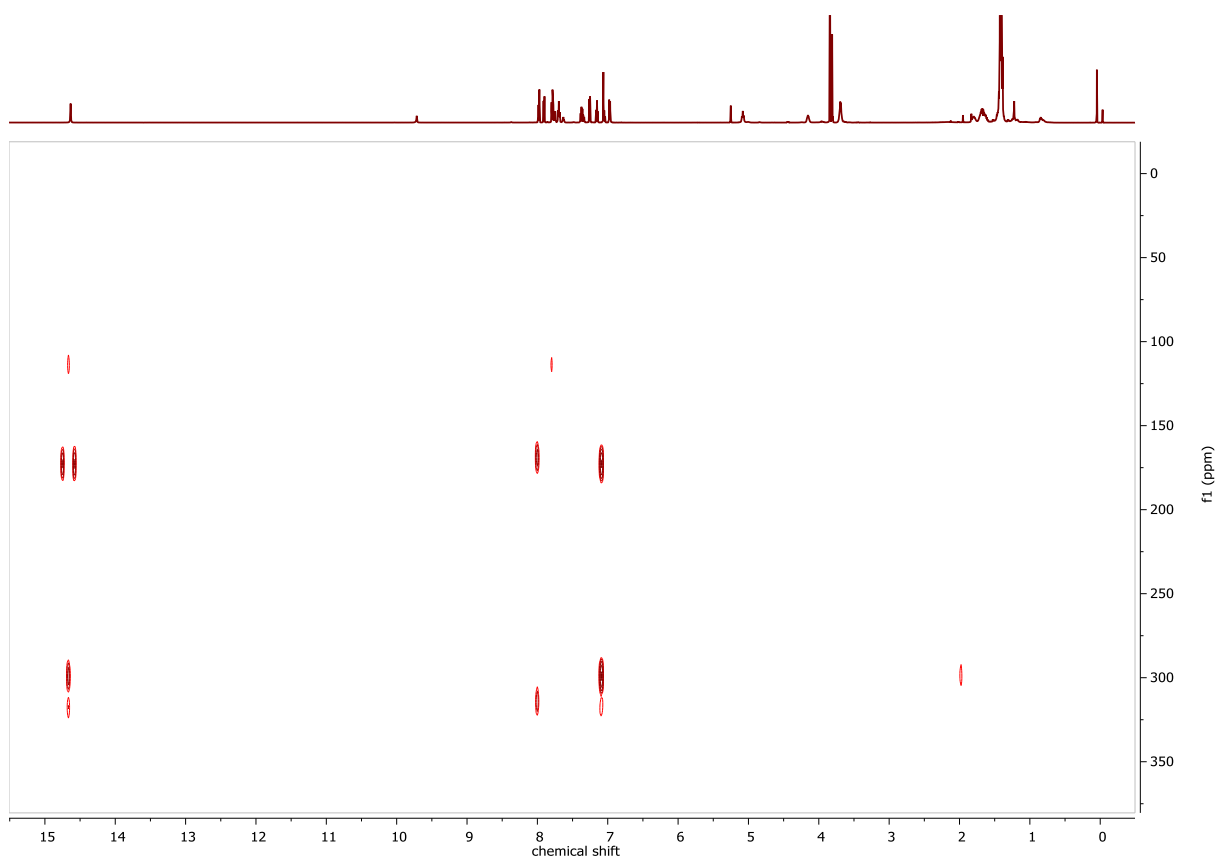


Figure 7.237 ^1H , ^{15}N HMBC NMR spectrum of HmphfpyTSLp in CDCl_3 ($J = 7$ Hz).

7.5. NMR spectra of metal precursor

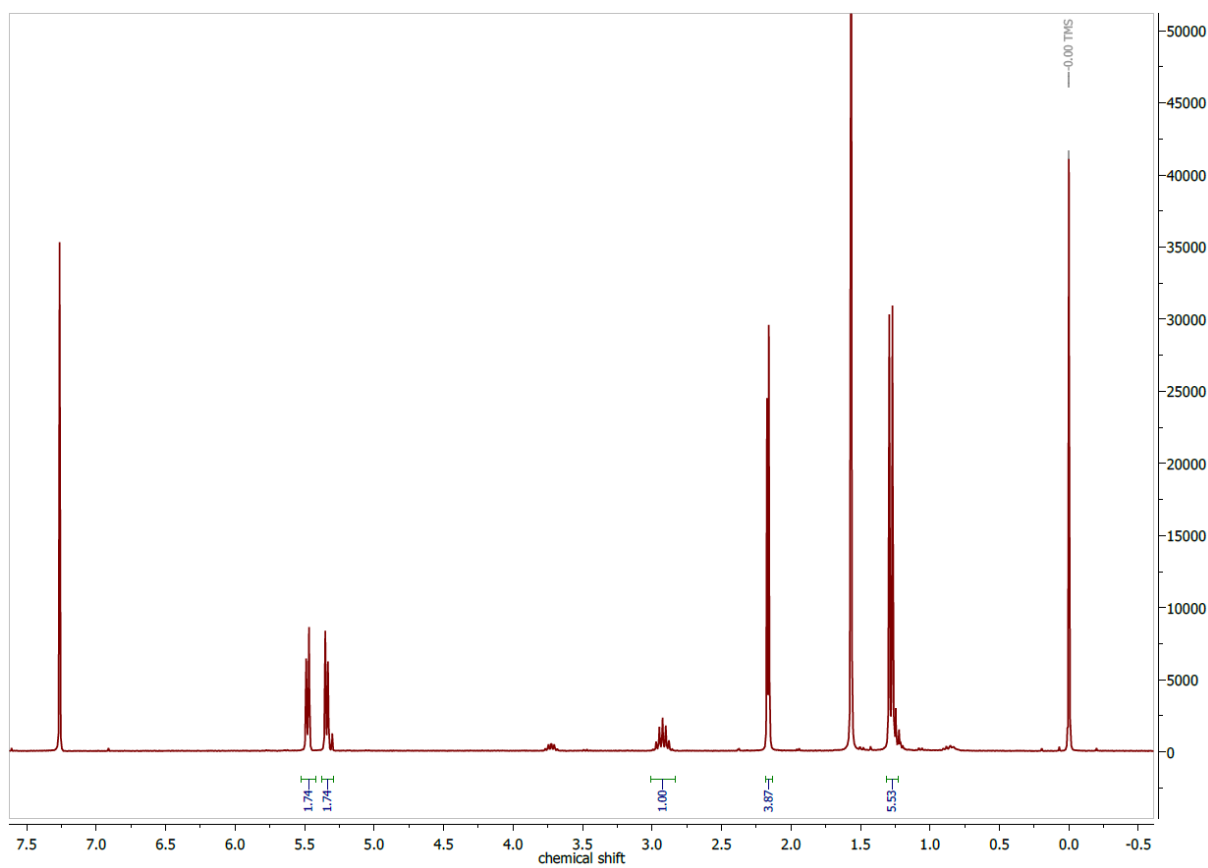


Figure 7.238 ¹H NMR spectrum of [Ru(p-cymene)Cl₂]₂ in CDCl₃ at 300 MHz.

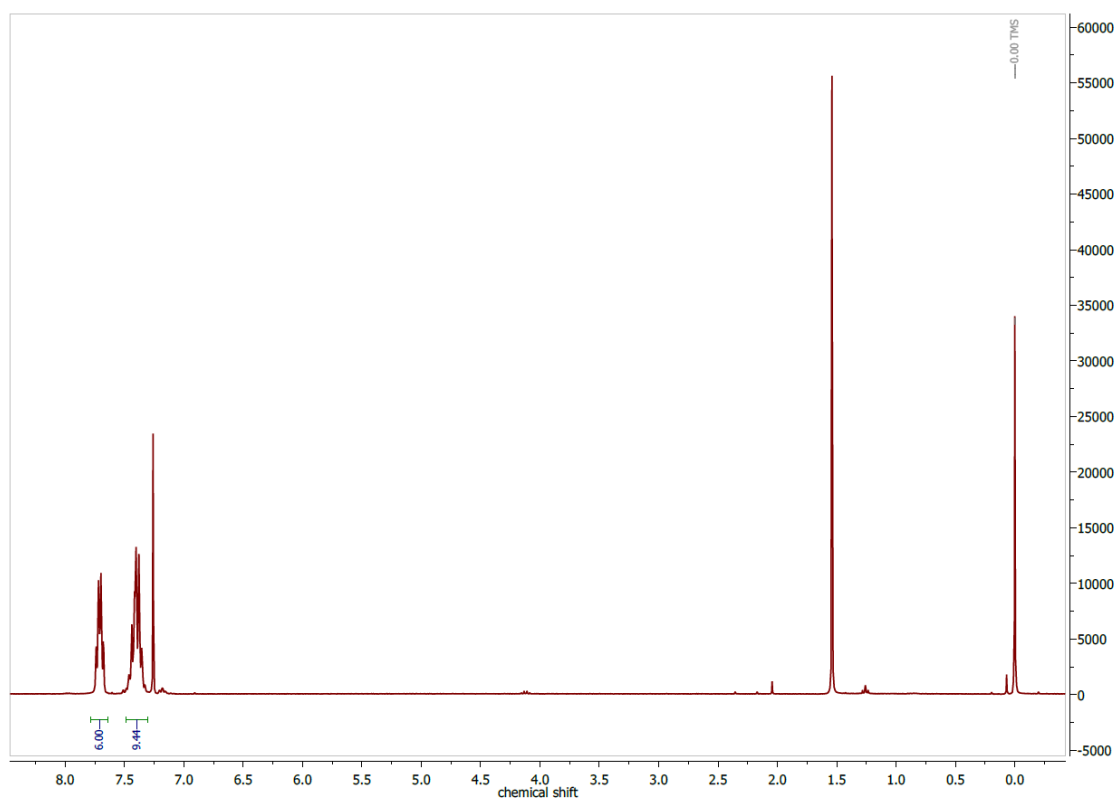


Figure 7.239 ¹H NMR spectrum of [Pd(PPh₃)₂Cl₂] in CDCl₃ at 300 MHz.

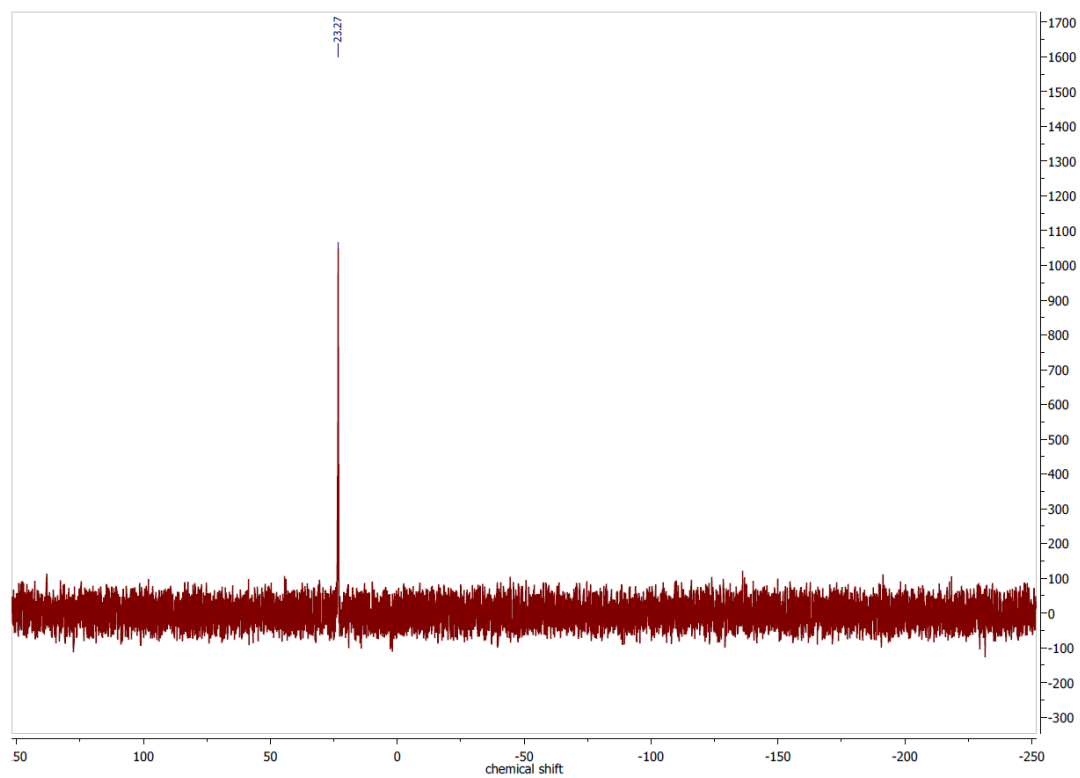


Figure 7.240 $^{31}\text{P}\{^1\text{H}\}$ NMR spectrum of $[\text{Pd}(\text{PPh}_3)_2\text{Cl}_2]$ in CDCl_3 at 121 MHz.

7.6. NMR spectra of complexes

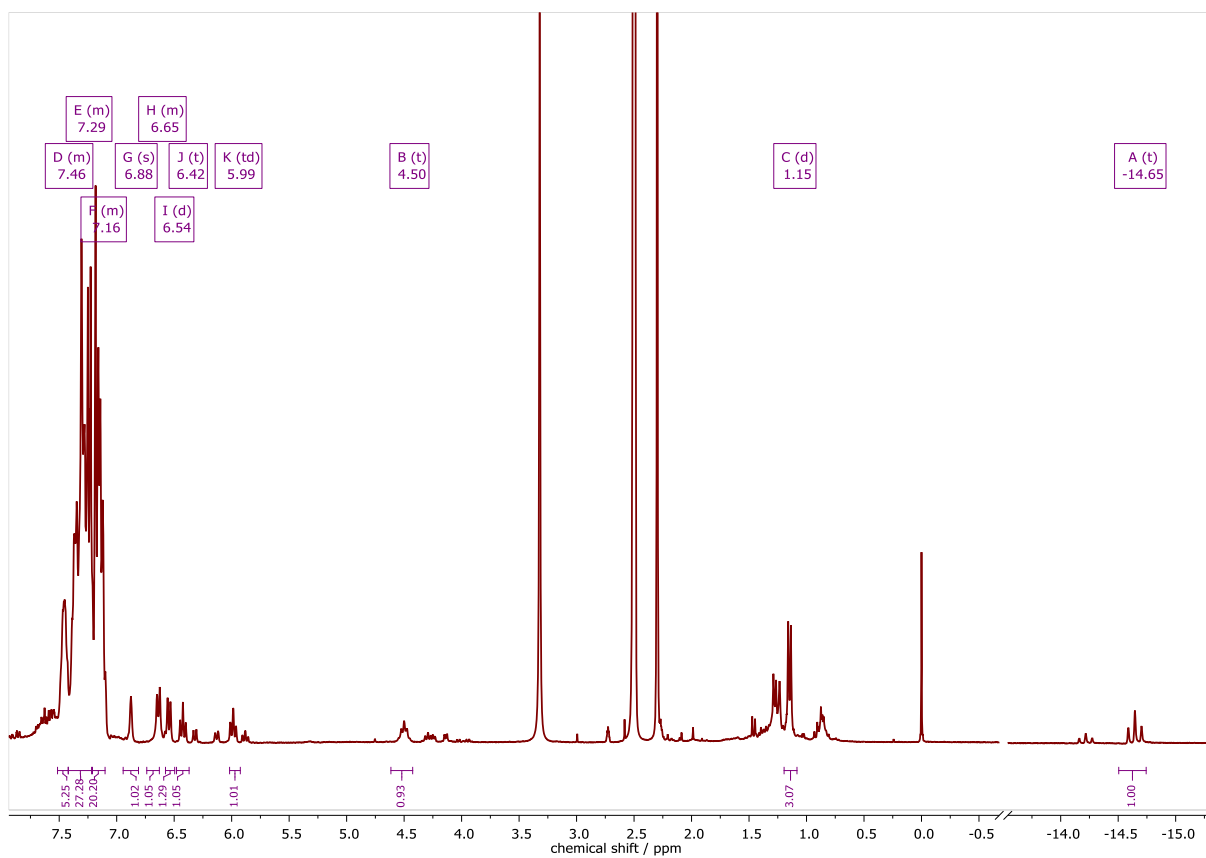


Figure 7.241 ^1H NMR spectrum of $[\text{Ir}(\text{PPh}_3)_2(\text{bzTSCmB})\text{H}]$ in $\text{DMSO}-d_6$ at 300 MHz.

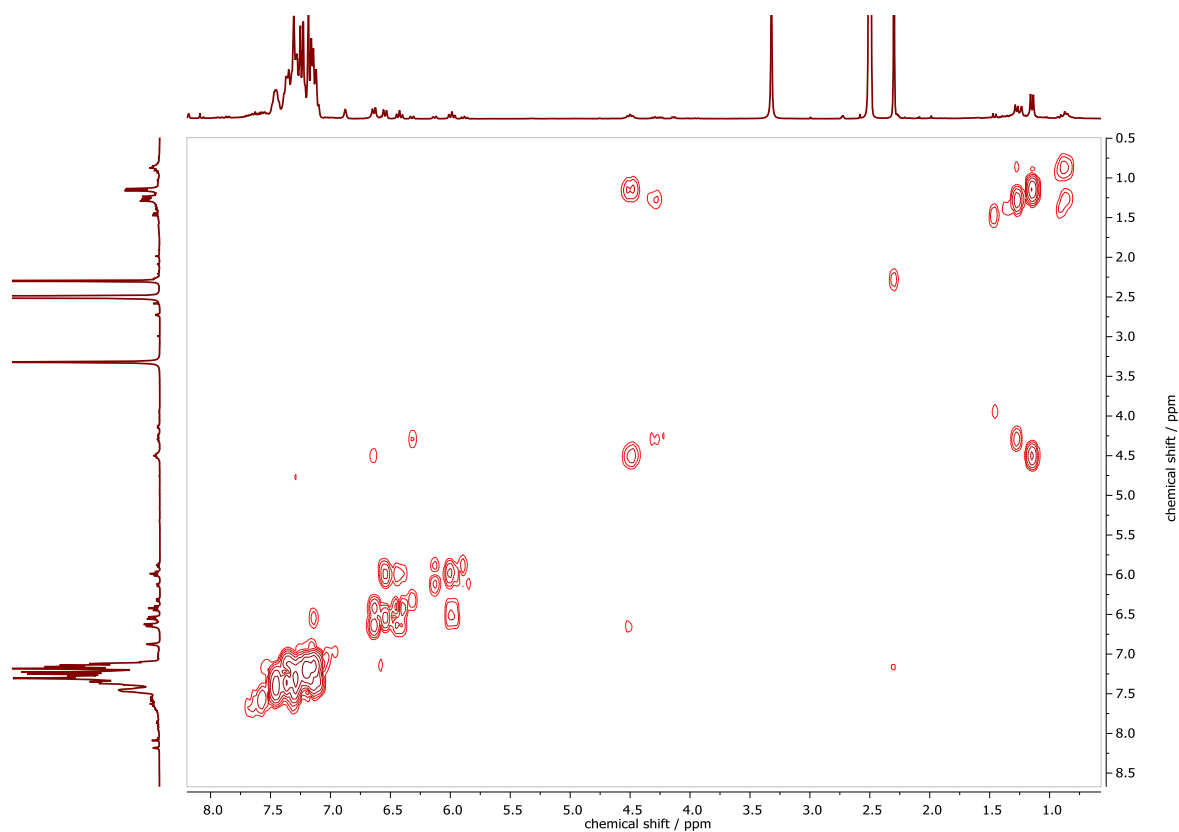


Figure 7.242 $^1\text{H}, ^1\text{H}$ COSY NMR spectrum of $[\text{Ir}(\text{PPh}_3)_2(\text{bzTSCmB})\text{H}]$ in $\text{DMSO}-d_6$ at 300 MHz.

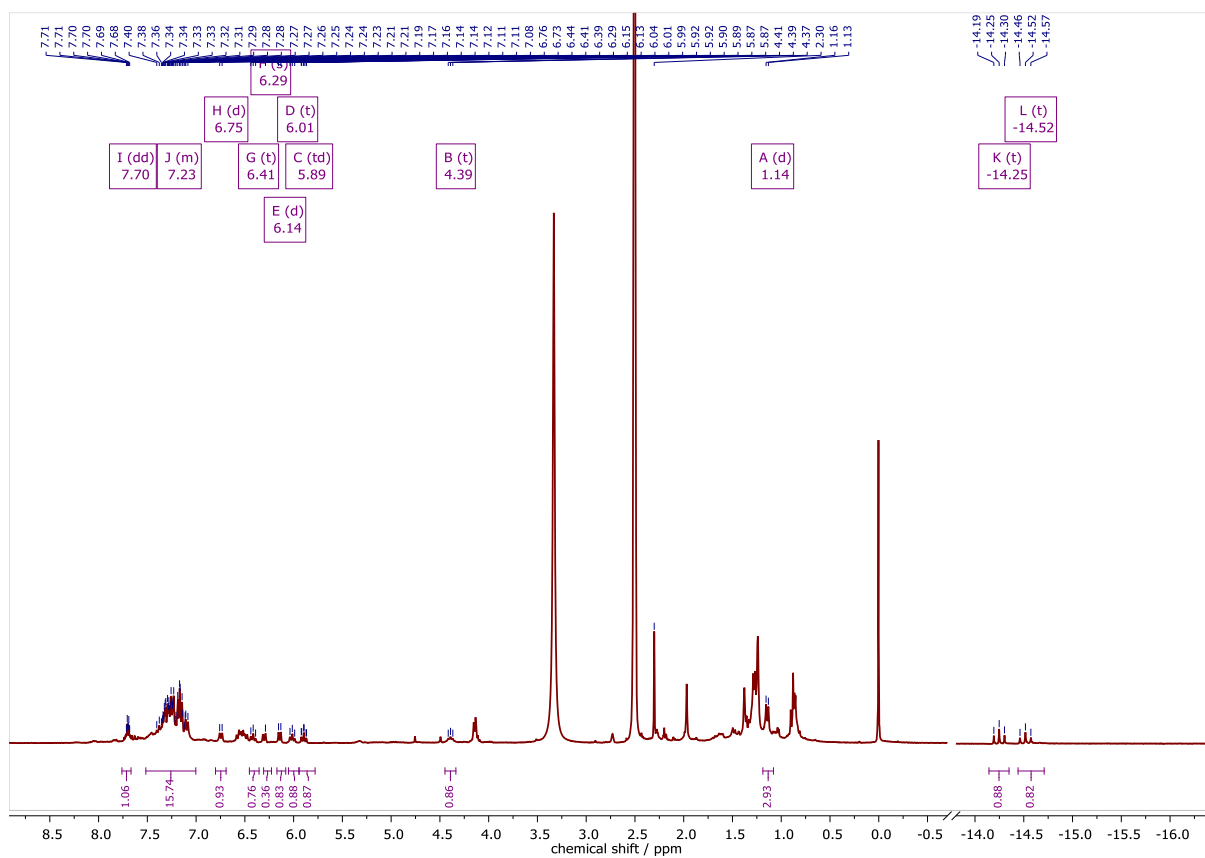


Figure 7.243 ^1H NMR spectrum of $[\text{Ir}(\text{PPh}_3-d_{15})_2(\text{bzTSCmB})\text{H}]$ in $\text{DMSO}-d_6$ at 300 MHz.

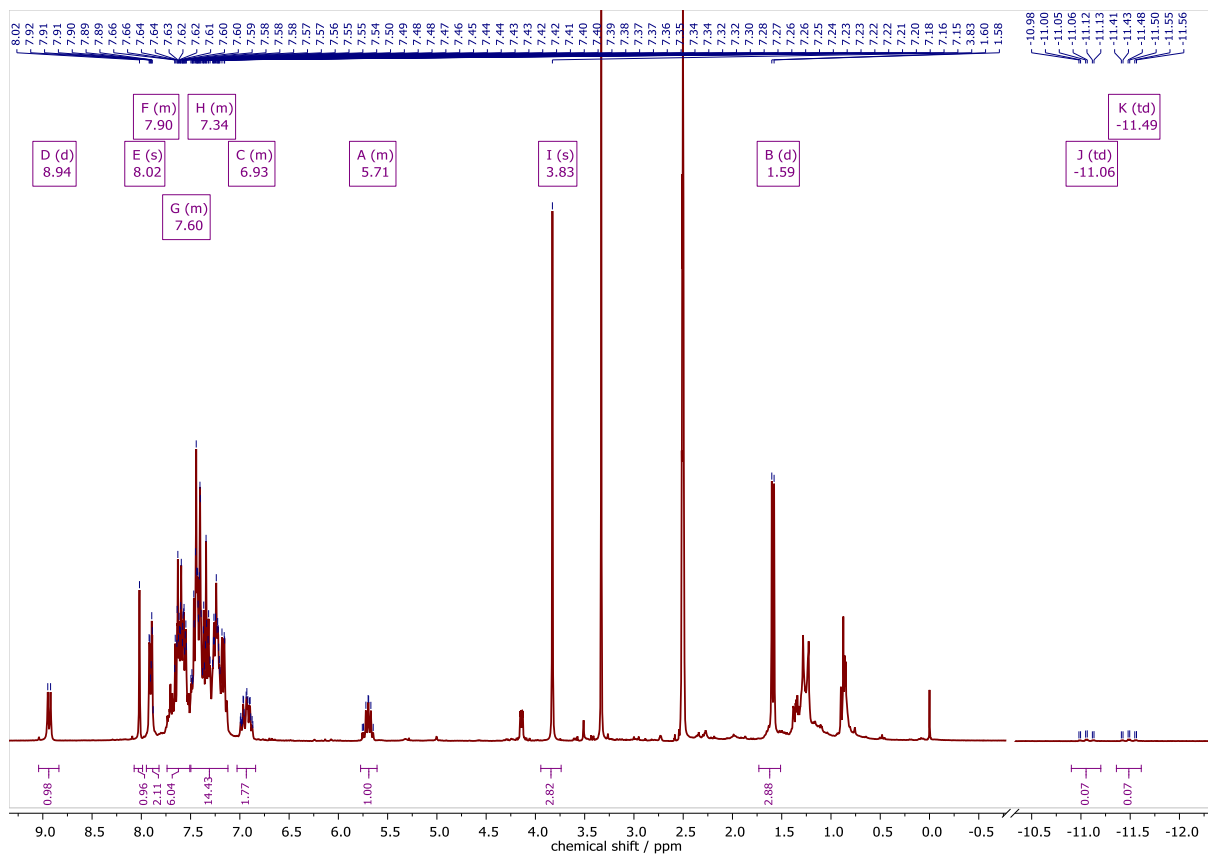


Figure 7.244 ^1H NMR spectrum of $[\text{Ir}(\text{PPh}_3)_2(\text{bz}(\text{m})\text{TSCmB})\text{H}]$ in $\text{DMSO}-d_6$ at 300 MHz.

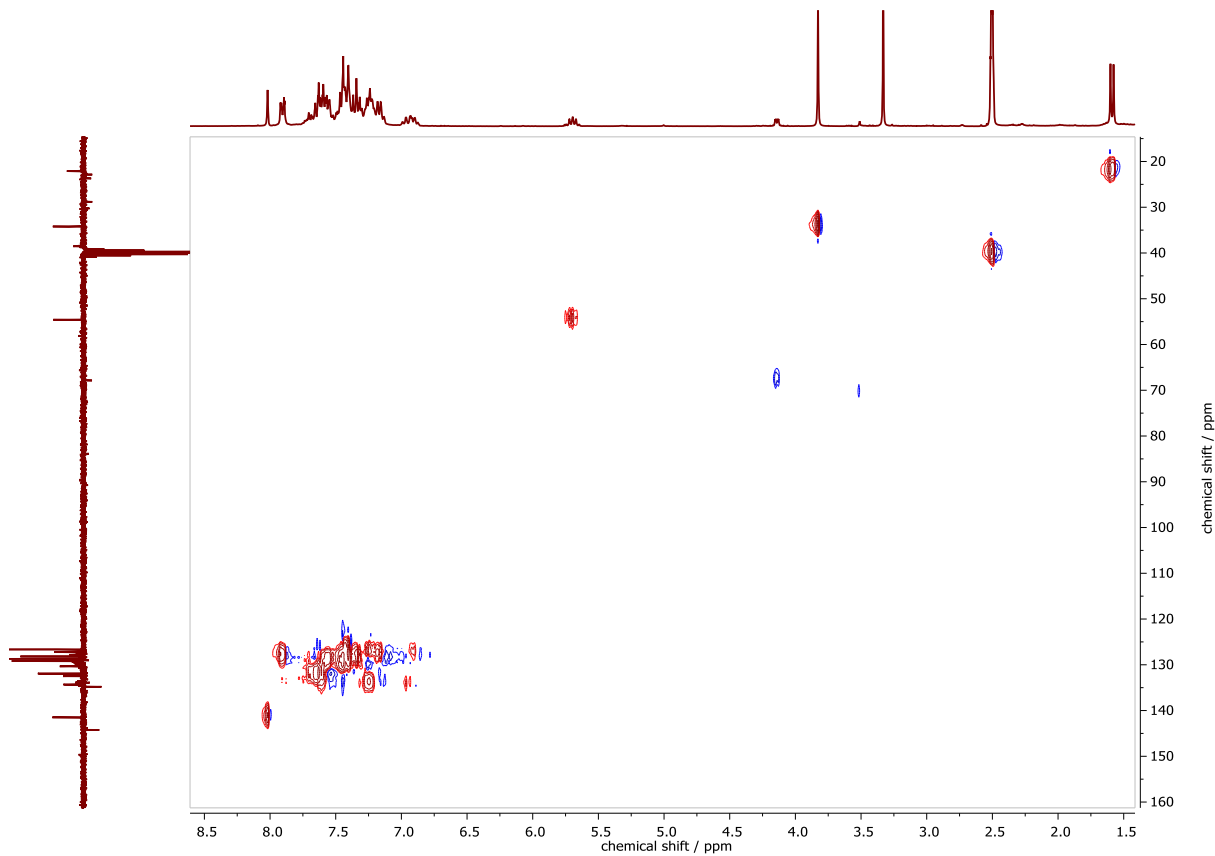


Figure 7.245 ^1H , ^{13}C HSQCed NMR spectrum of $[\text{Ir}(\text{PPh}_3)_2(\text{bz}(\text{m})\text{TSCmB})\text{H}]$ in $\text{DMSO}-d_6$.

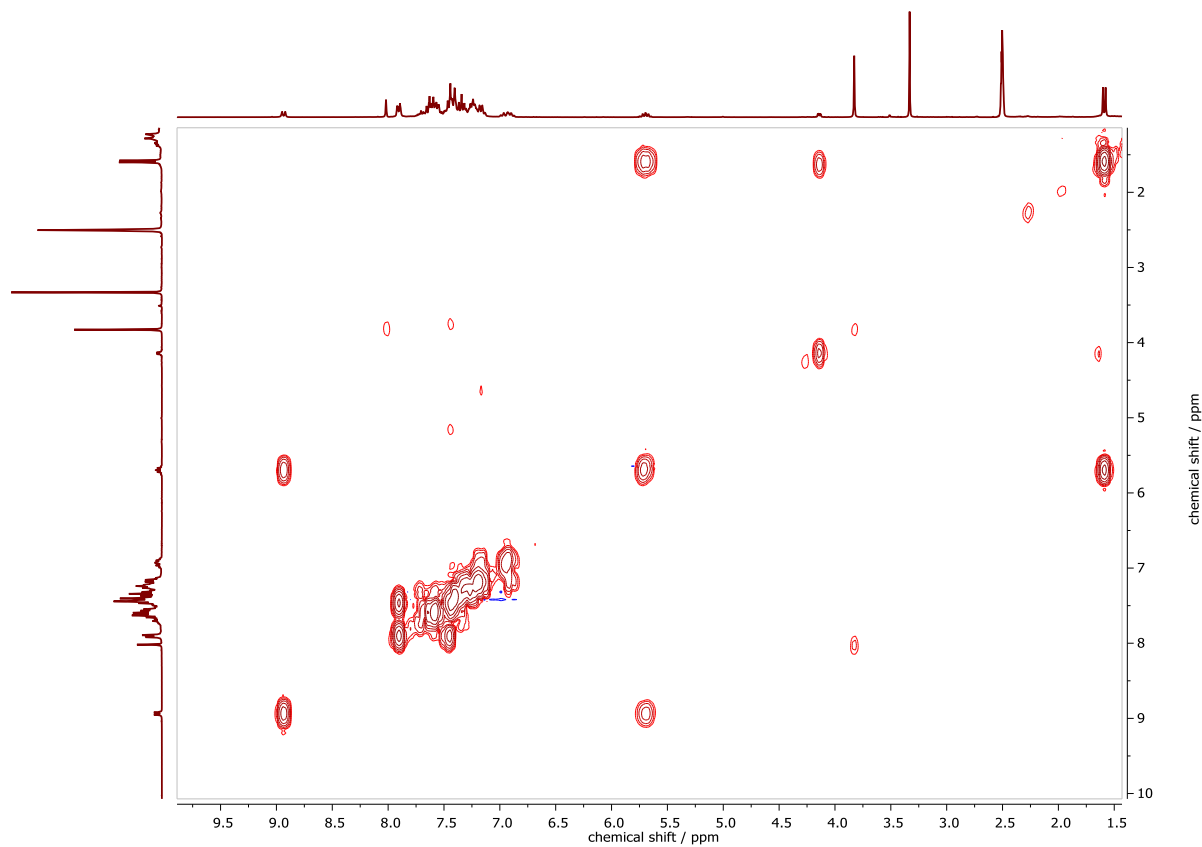


Figure 7.246 ¹H, ¹H COSY NMR spectrum of [Ir(PPh₃)₂(bz(m)TSCmB)H] in DMSO-*d*₆.

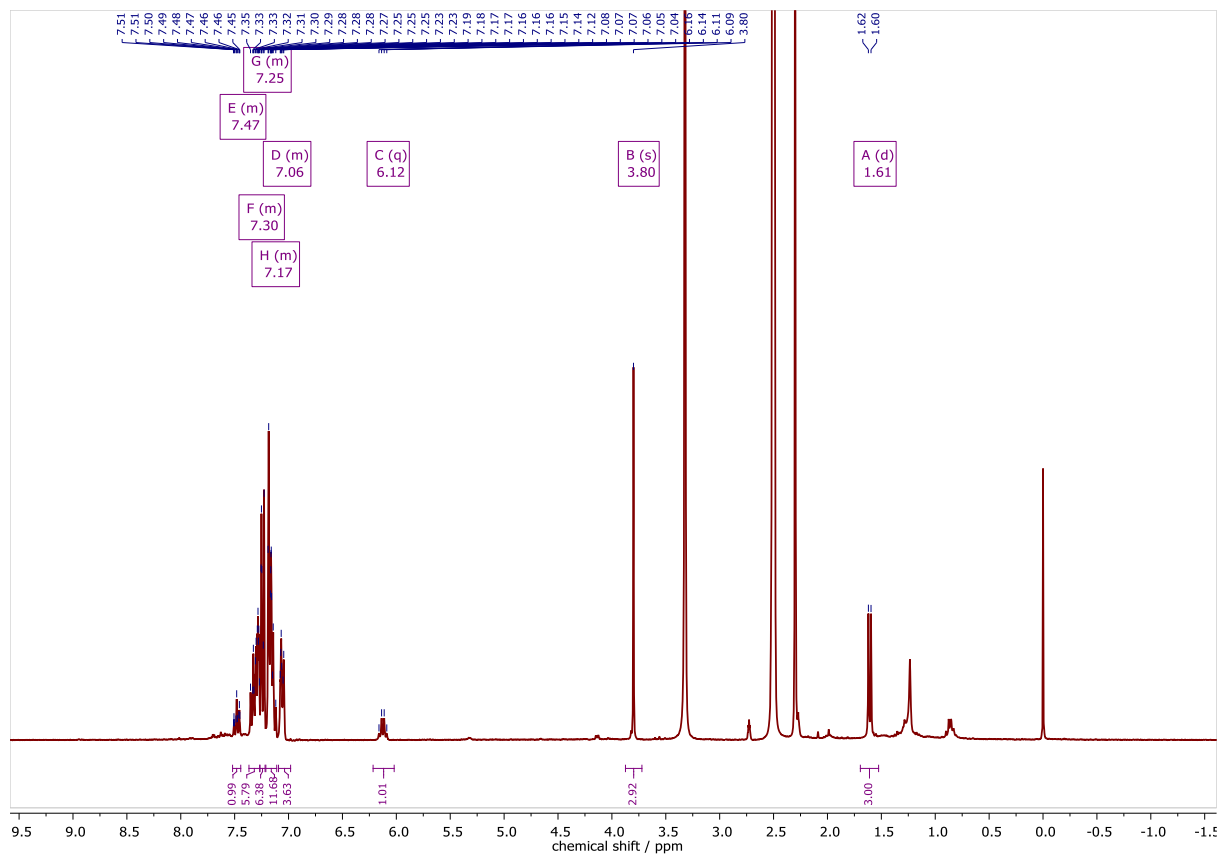


Figure 7.247 ¹H NMR spectrum of [Ir(PPh₃-*d*₁₅)₂(bz(m)TSCmB)Cl] in DMSO-*d*₆ at 300 MHz.

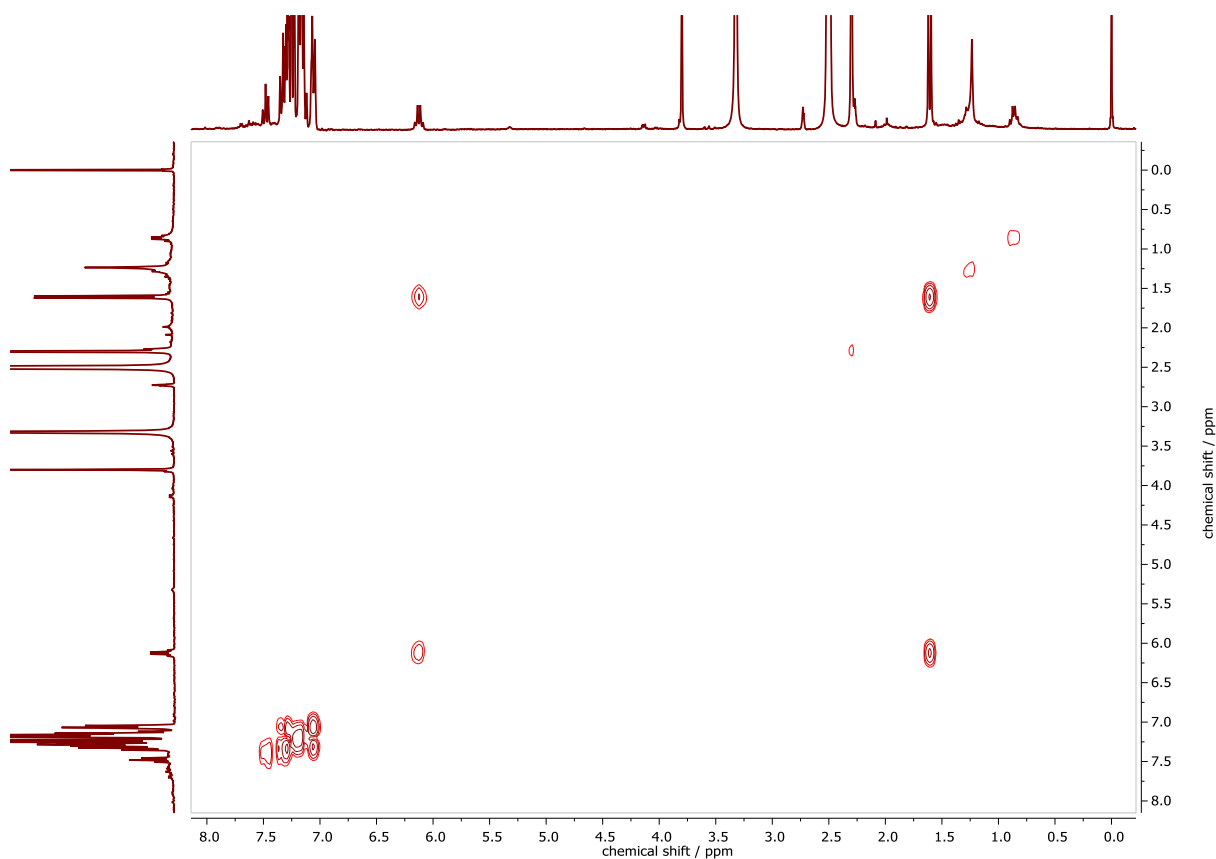


Figure 7.248 ¹H, ¹H COSY NMR spectrum of [Ir(PPh₃-d₁₅)₂(bz(m)TSCmB)Cl] in DMSO-*d*₆.

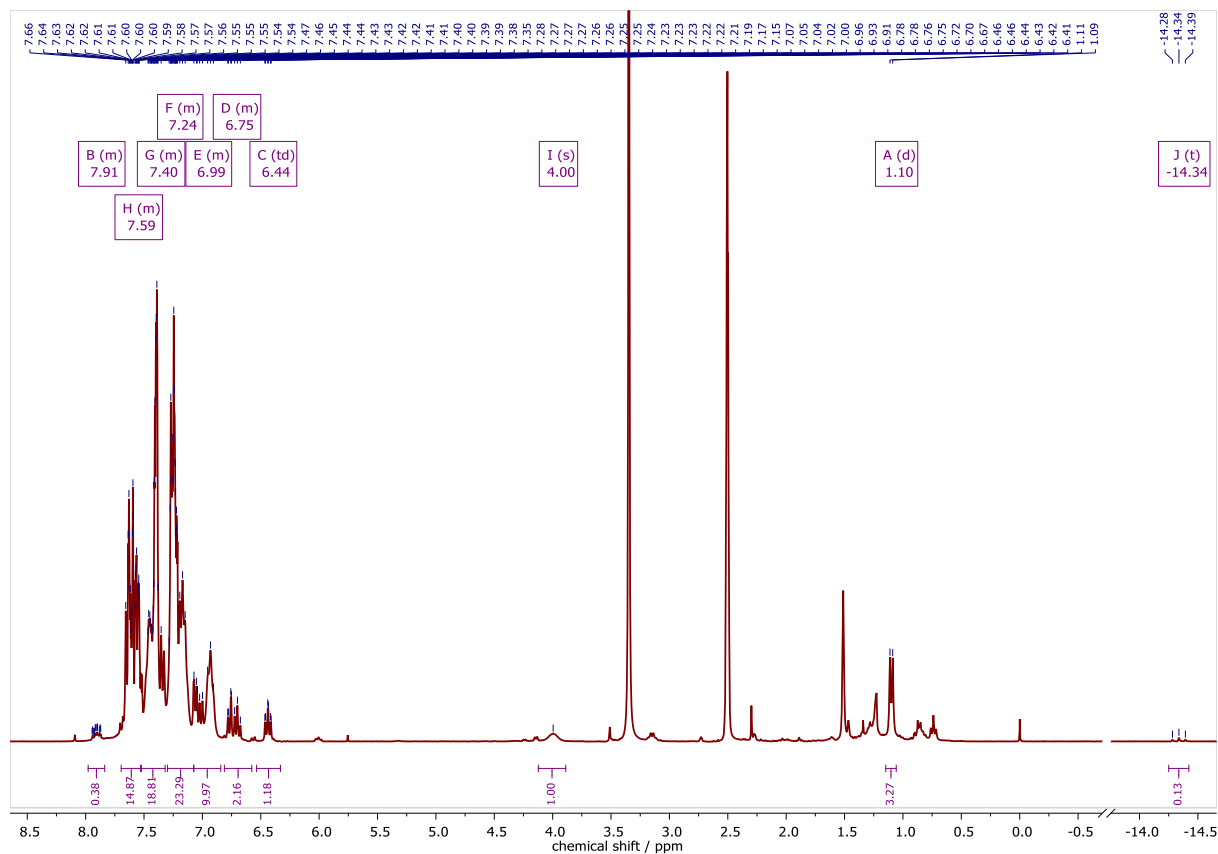


Figure 7.249 ¹H NMR spectrum of [Ir(PPh₃)₂(aphTSCmB)H] in DMSO-*d*₆ at 300 MHz.

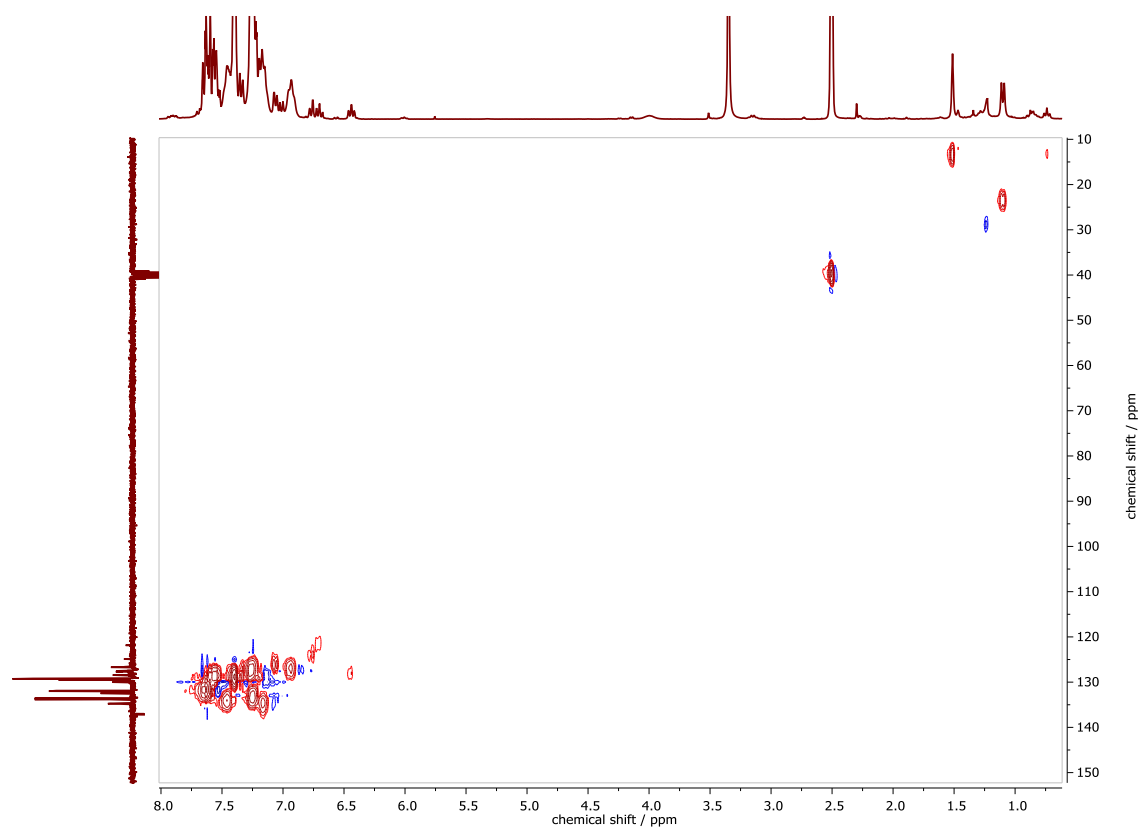


Figure 7.250 ^1H , ^{13}C HSQCed NMR spectrum of $[\text{Ir}(\text{PPh}_3)_2(\text{aphTSCmB})\text{H}]$ in $\text{DMSO-}d_6$.

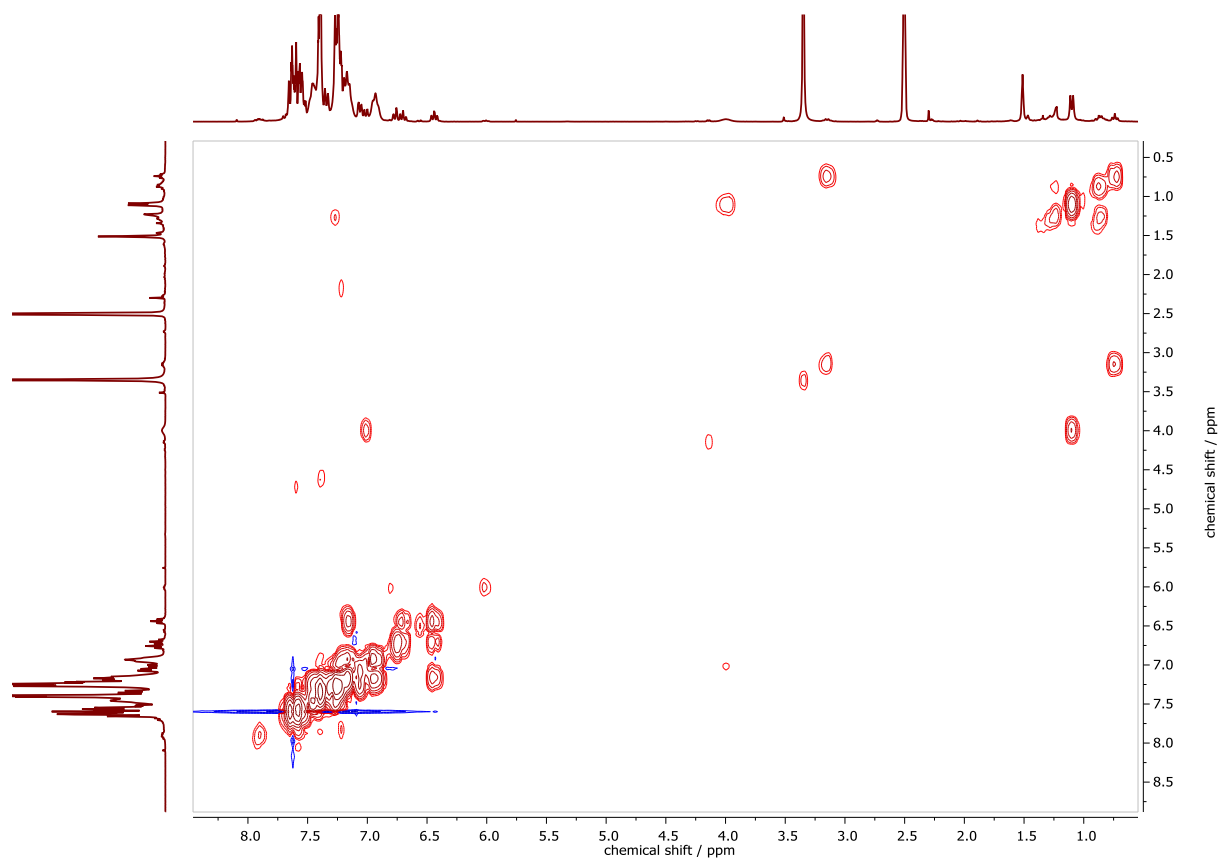


Figure 7.251 ^1H , ^1H COSY NMR spectrum of $[\text{Ir}(\text{PPh}_3)_2(\text{aphTSCmB})\text{H}]$ in $\text{DMSO-}d_6$.

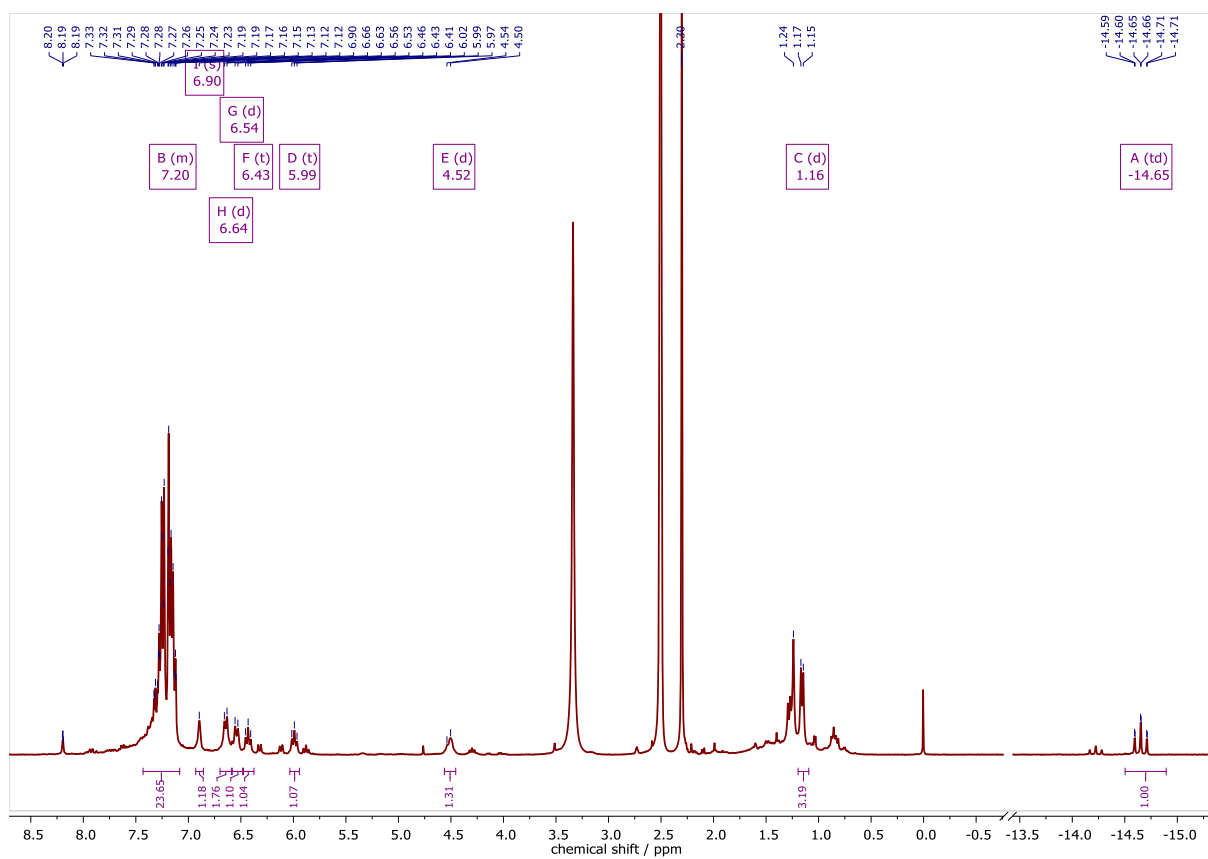


Figure 7.252 ^1H NMR spectrum of $[\text{Ir}(\text{PPh}_3\text{-}d_{15})_2(\text{aphTSCmB})\text{H}]$ in $\text{DMSO-}d_6$ at 300 MHz.

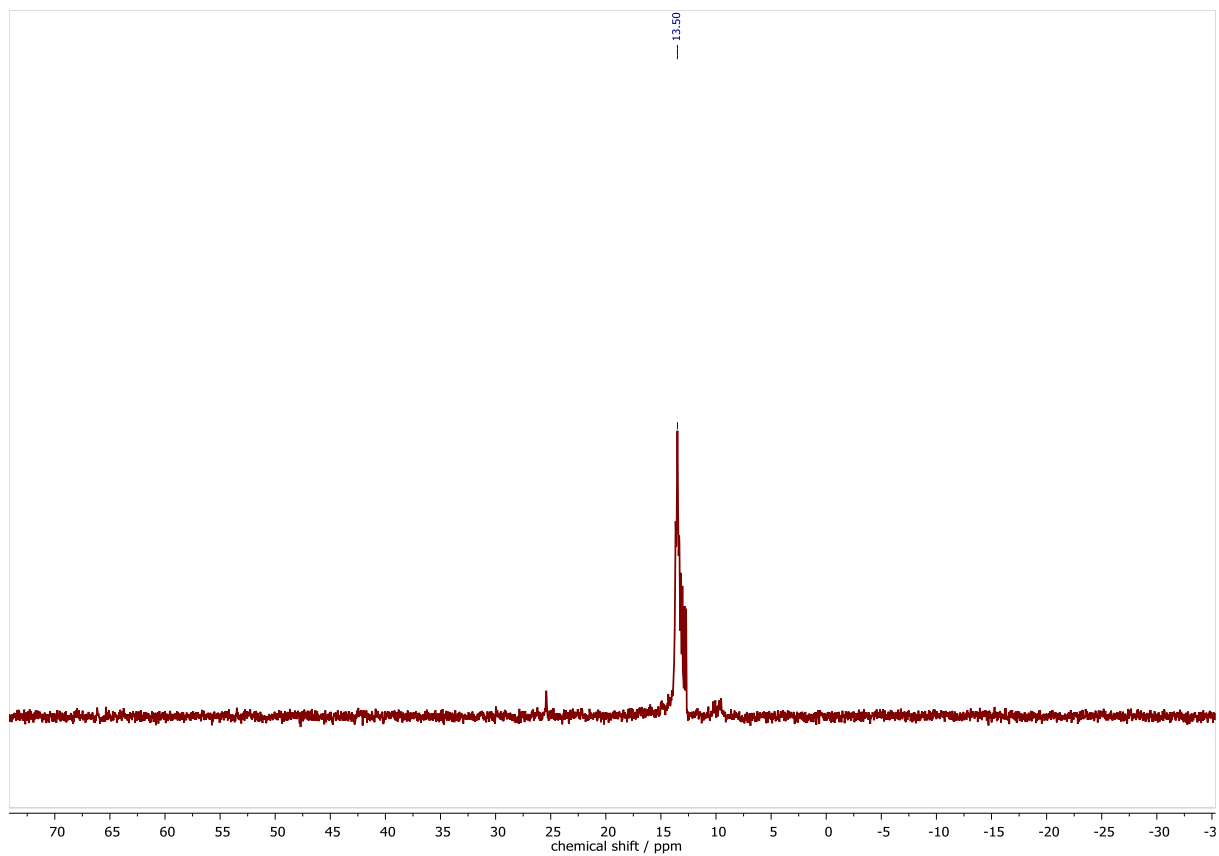


Figure 7.253 $^{31}\text{P}\{^1\text{H}\}$ NMR spectrum of $[\text{Ir}(\text{PPh}_3\text{-}d_{15})_2(\text{aphTSCmB})\text{H}]$ in $\text{DMSO-}d_6$ at 121 MHz.

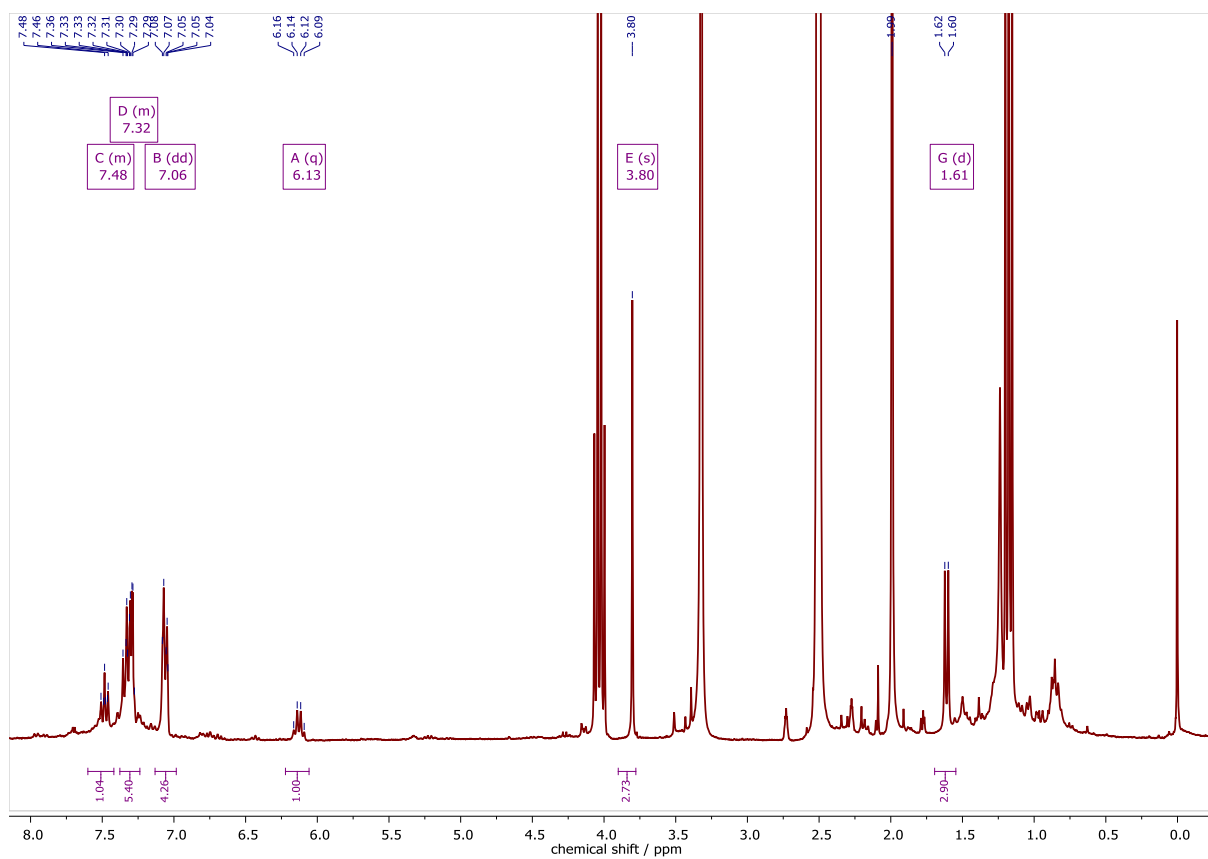


Figure 7.254 ^1H NMR spectrum of $[\text{Ir}(\text{PPh}_3\text{-}d_{15})_2(\text{aph}(\text{m})\text{TSCmB})\text{H}]$ in $\text{DMSO-}d_6$ at 300 MHz.

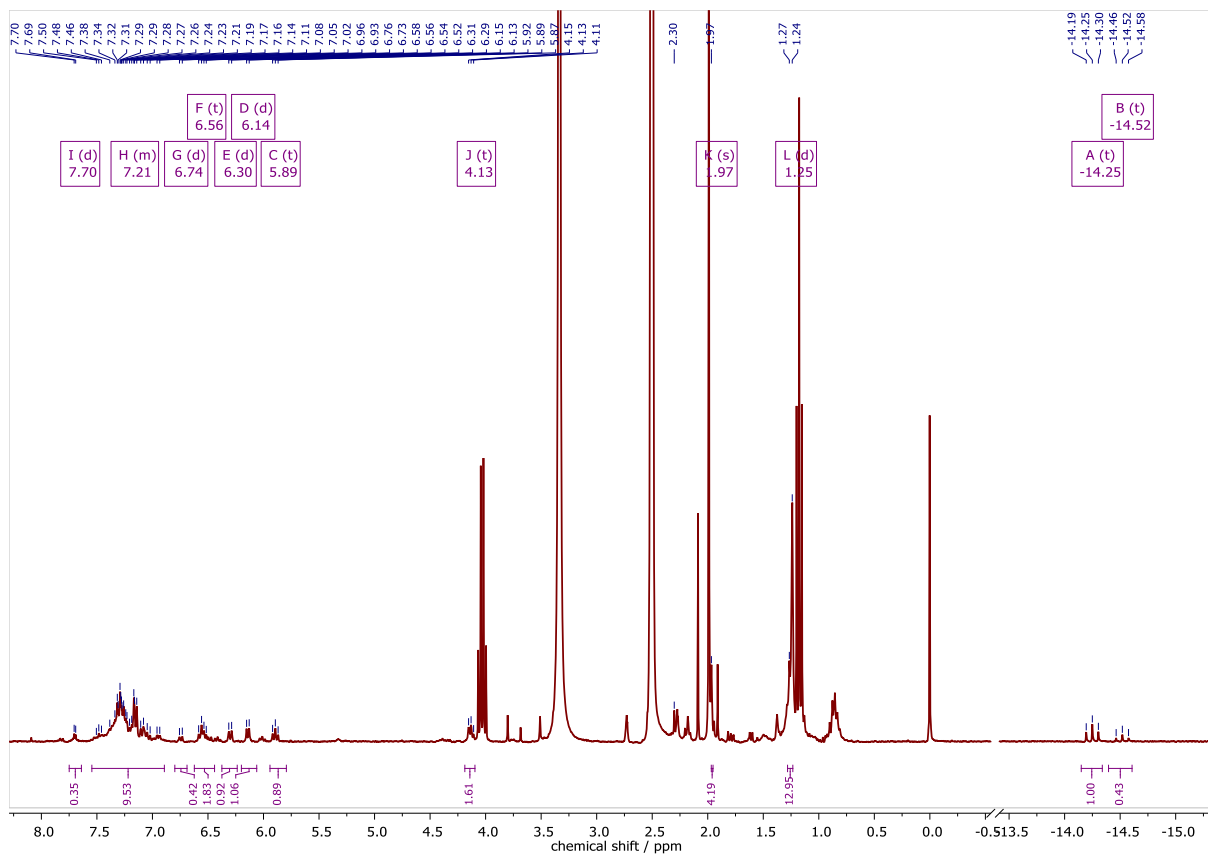


Figure 7.255 ^1H NMR spectrum of $[\text{Ir}(\text{PPh}_3\text{-}d_{15})_2(\text{aph}(\text{m})\text{TSCmB})\text{H}]$ in $\text{DMSO-}d_6$ at 300 MHz.

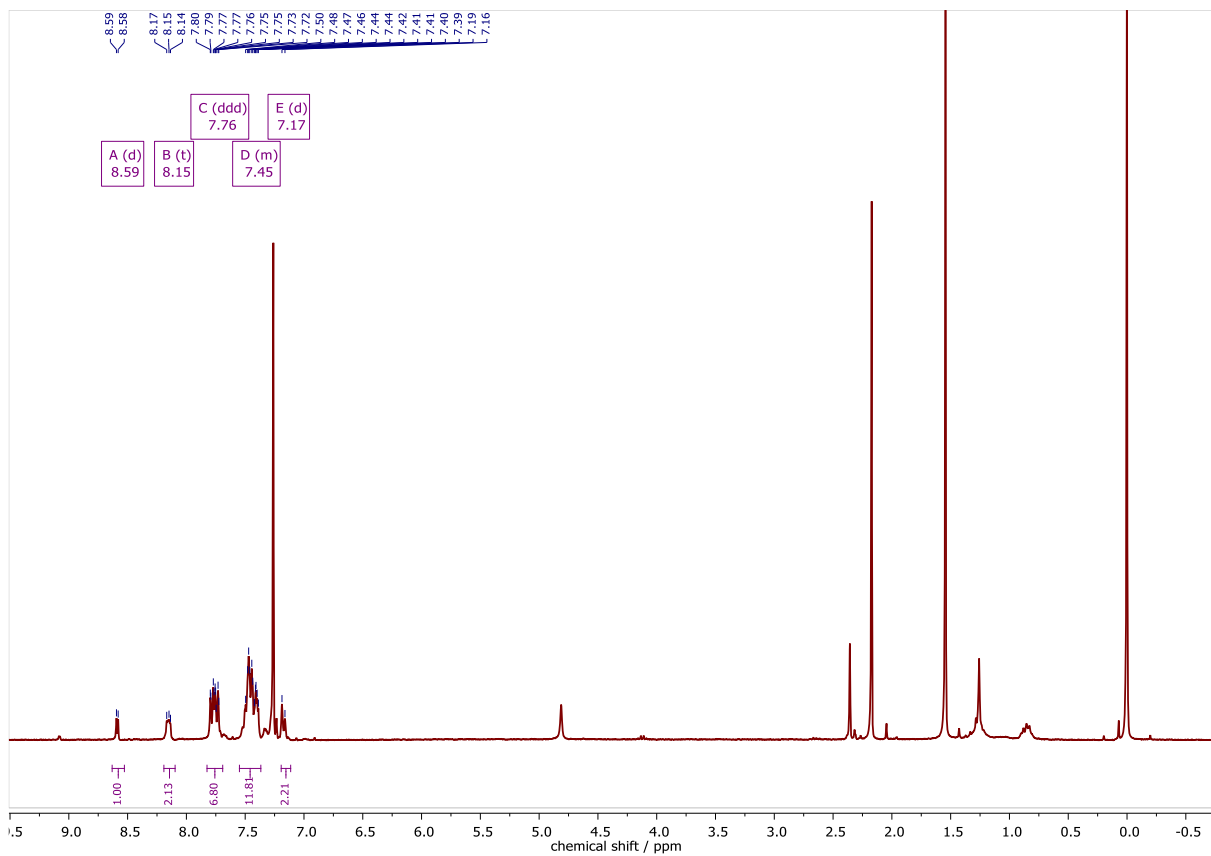


Figure 7.256 ^1H NMR spectrum of $[\text{Pd}(\text{PPh}_3)(\text{HbzTSC})\text{Cl}]$ in CDCl_3 at 300 MHz.

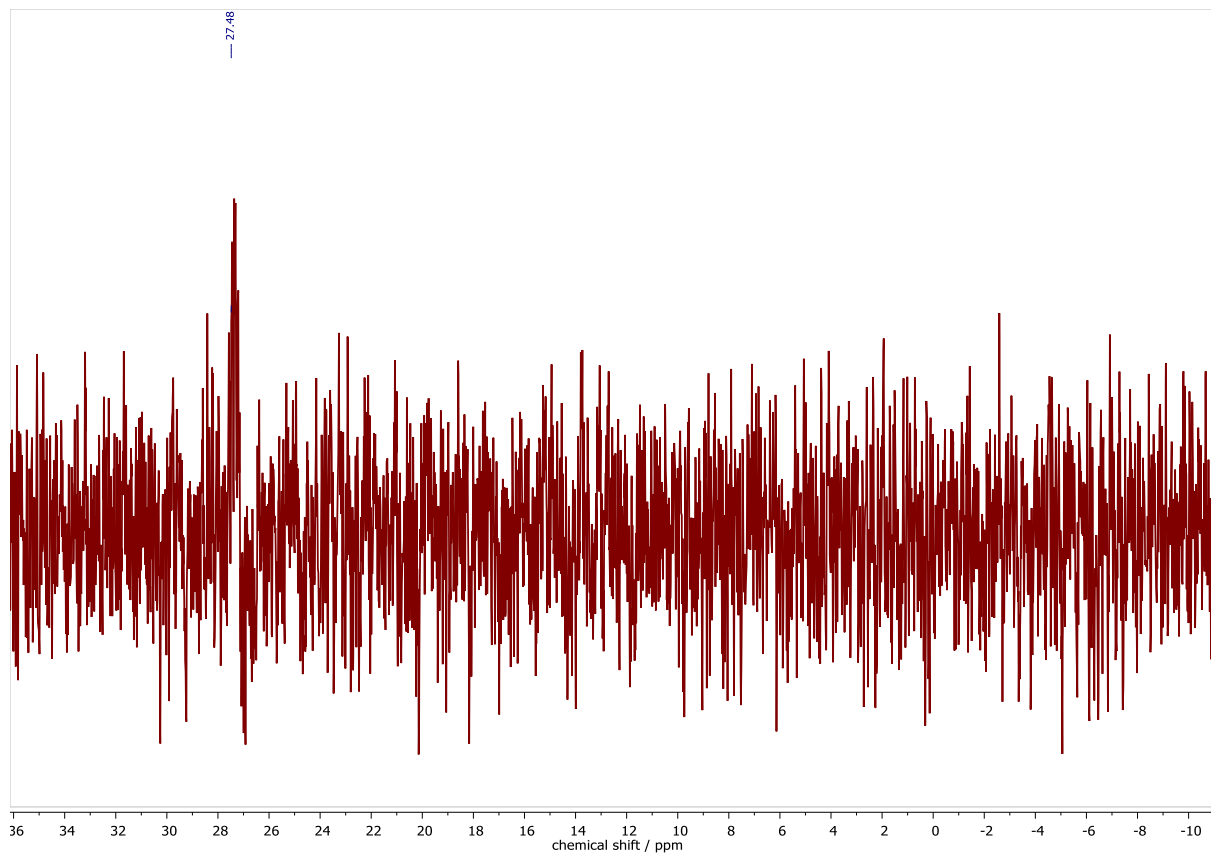


Figure 7.257 $^{31}\text{P}\{^1\text{H}\}$ NMR spectrum of $[\text{Pd}(\text{PPh}_3)(\text{HbzTSC})\text{Cl}]$ in CDCl_3 at 121 MHz.

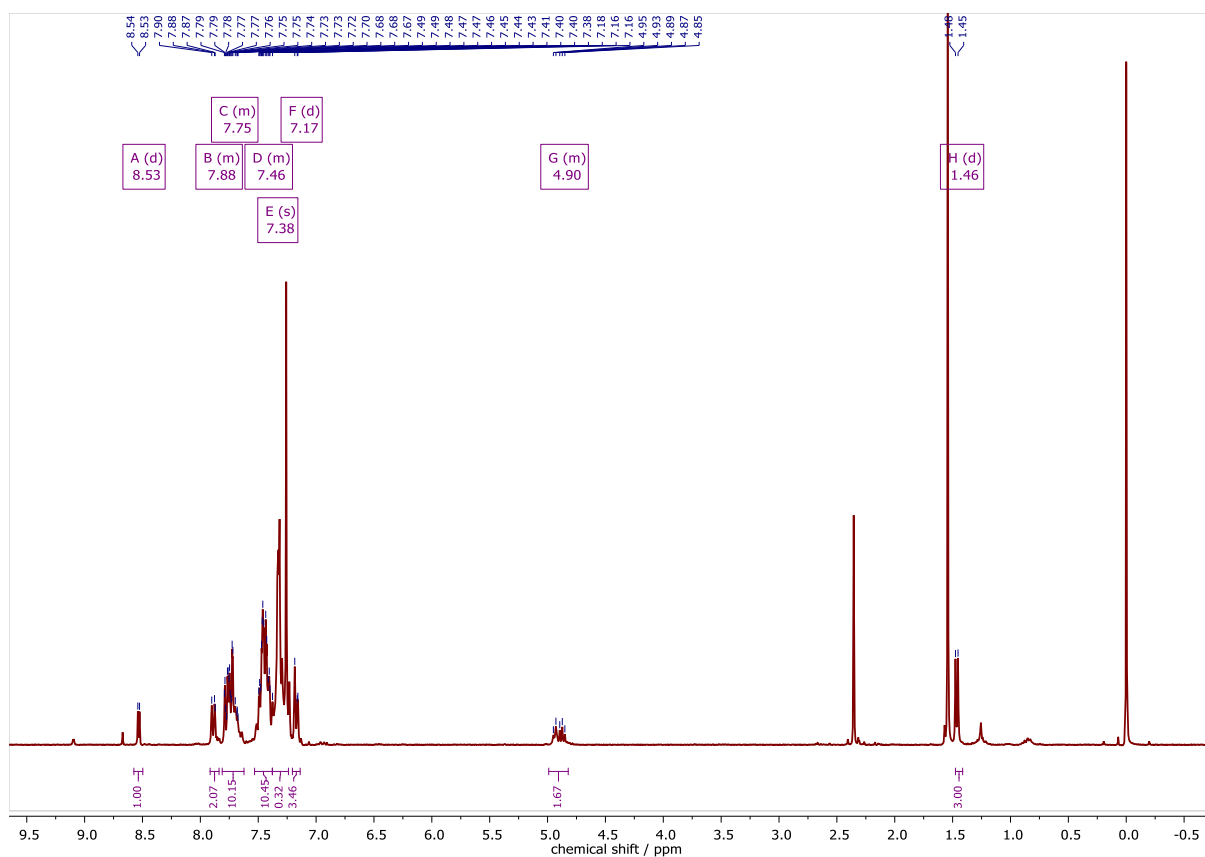


Figure 7.258 ^1H NMR spectrum of $[\text{Pd}(\text{PPh}_3)(\text{HbzTSCmB})\text{Cl}]$ in CDCl_3 at 300 MHz.

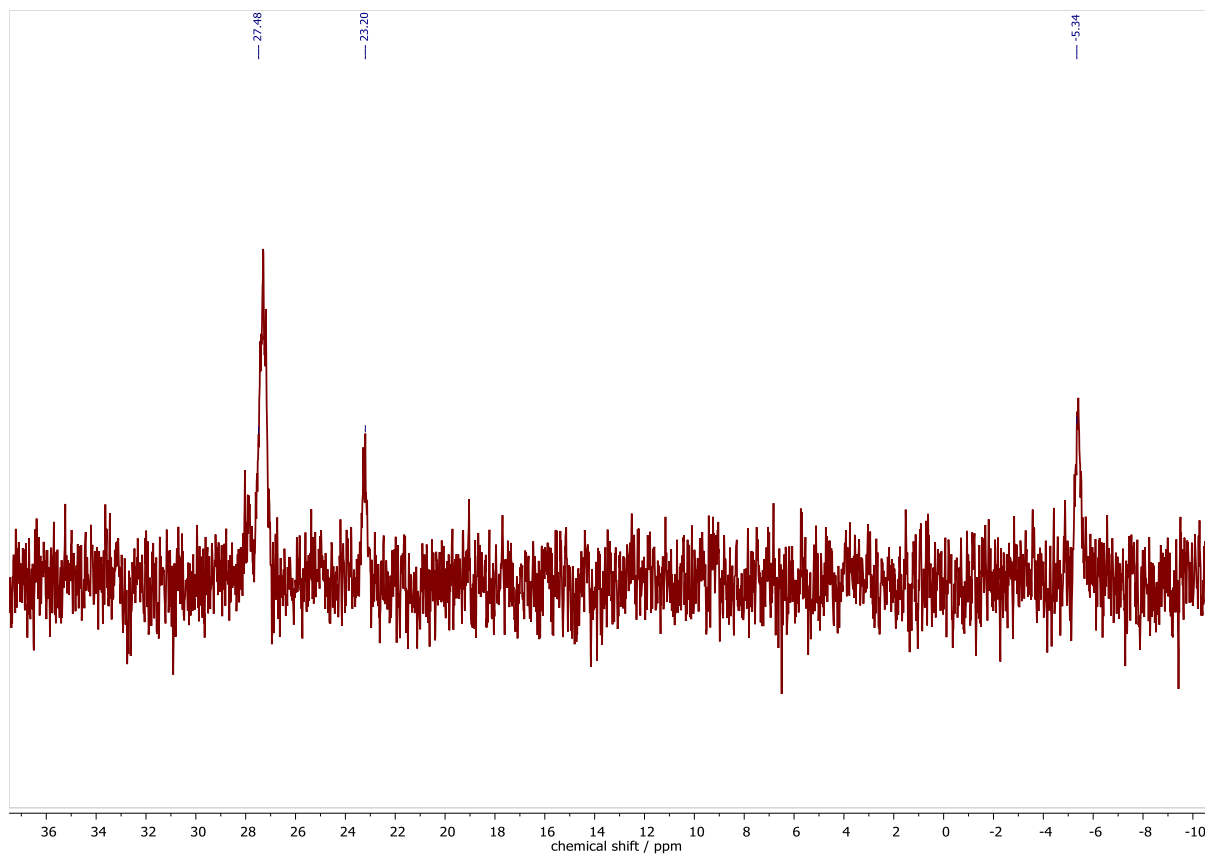


Figure 7.259 $^{31}\text{P}\{^1\text{H}\}$ NMR spectrum of $[\text{Pd}(\text{PPh}_3)(\text{HbzTSCmB})\text{Cl}]$ in CDCl_3 at 121 MHz.

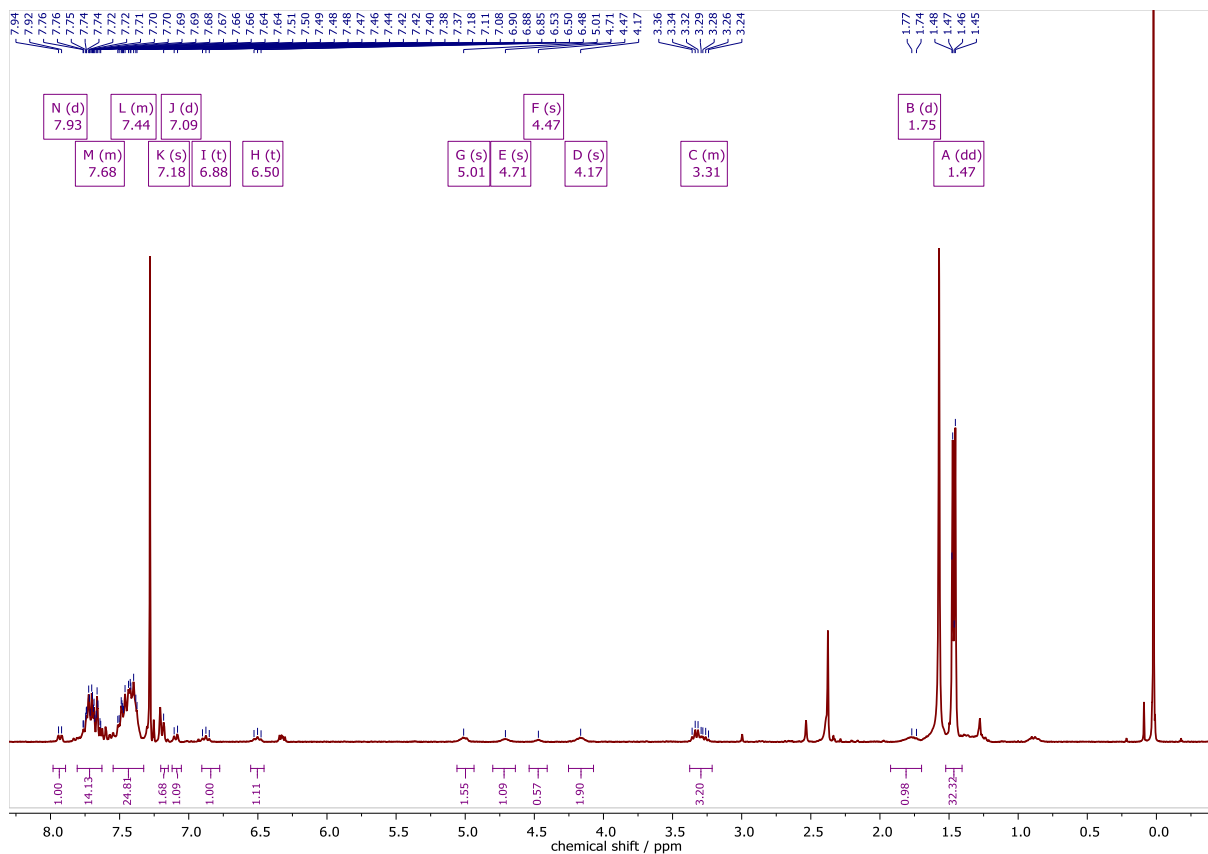


Figure 7.260 ^1H NMR spectrum of $[\text{Pd}(\text{PPh}_3)(\text{bzTSClP})]$ in CDCl_3 at 300 MHz.

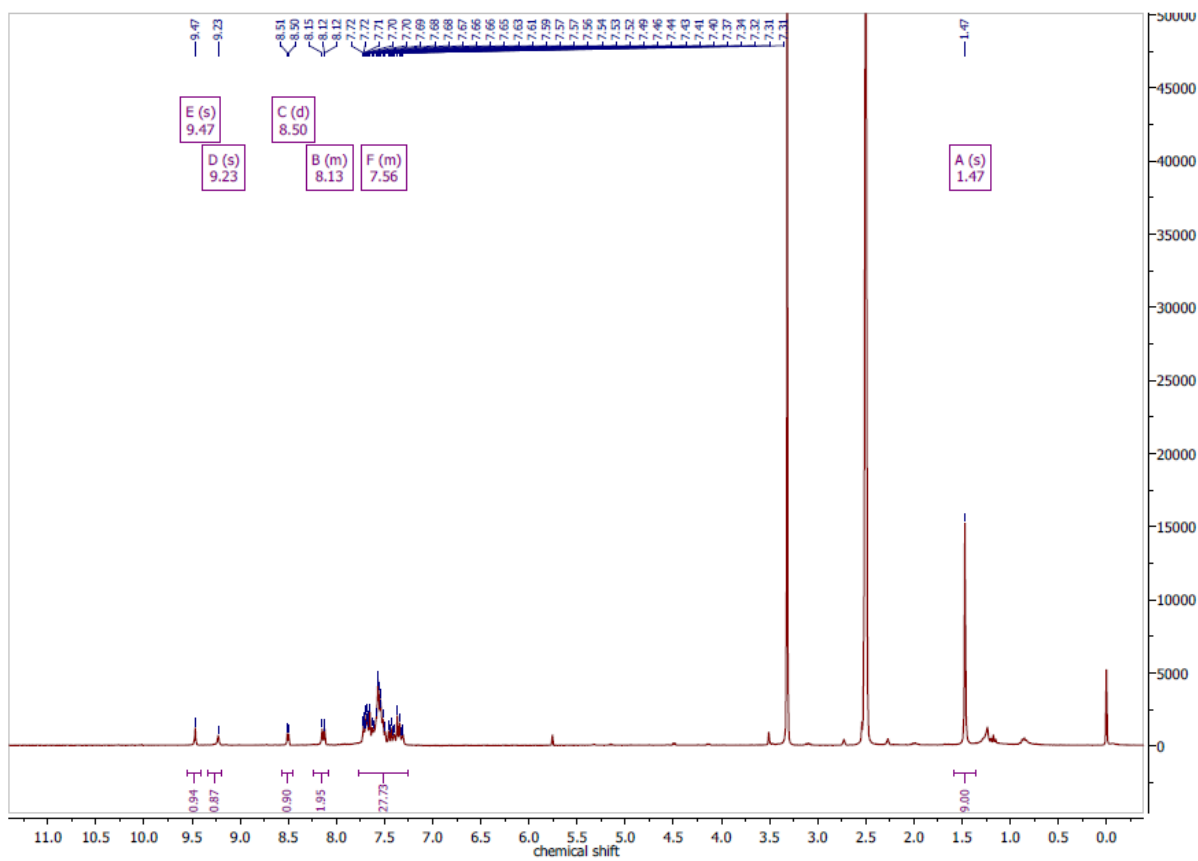


Figure 7.261 ^1H NMR spectrum of $[\text{Pd}(\text{PPh}_3)(\text{HbzTSCbap})\text{Cl}]$ in $\text{DMSO}-d_6$ at 300 MHz.

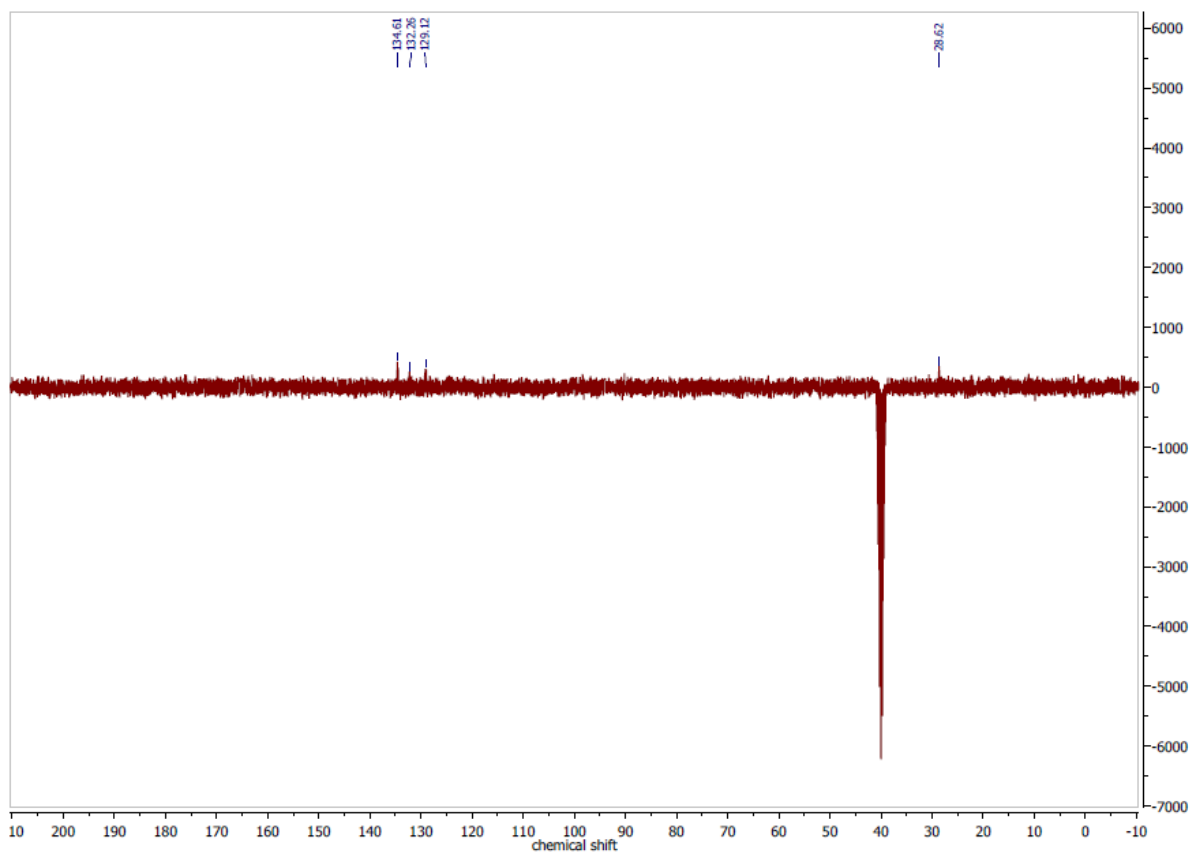


Figure 7.262 $^{13}\text{C}\{^1\text{H}\}$ DEPTQ NMR spectrum of $[\text{Pd}(\text{PPh}_3)(\text{HbzTSCbap})\text{Cl}]$ in $\text{DMSO-}d_6$ at 75 MHz.

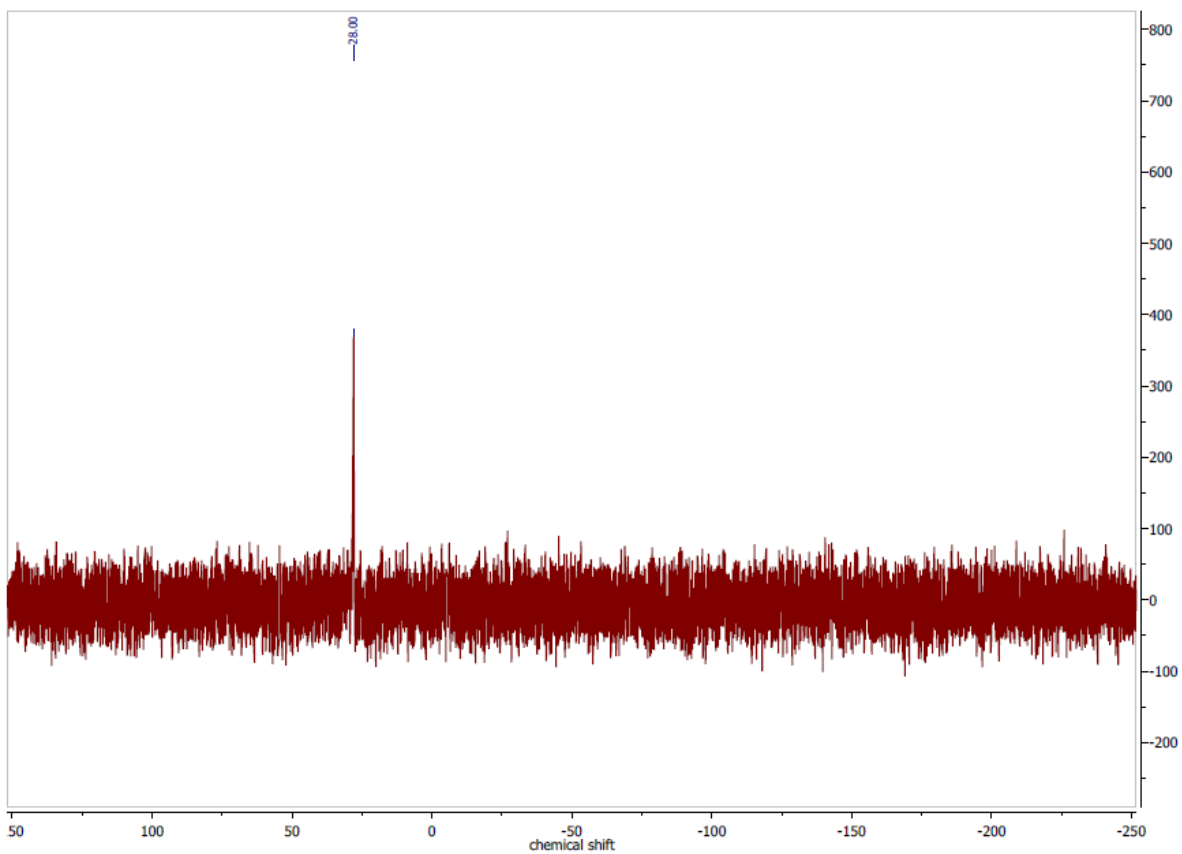


Figure 7.263 $^{31}\text{P}\{^1\text{H}\}$ NMR spectrum of $[\text{Pd}(\text{PPh}_3)(\text{HbzTSCbap})\text{Cl}]$ in $\text{DMSO-}d_6$ at 121 MHz.

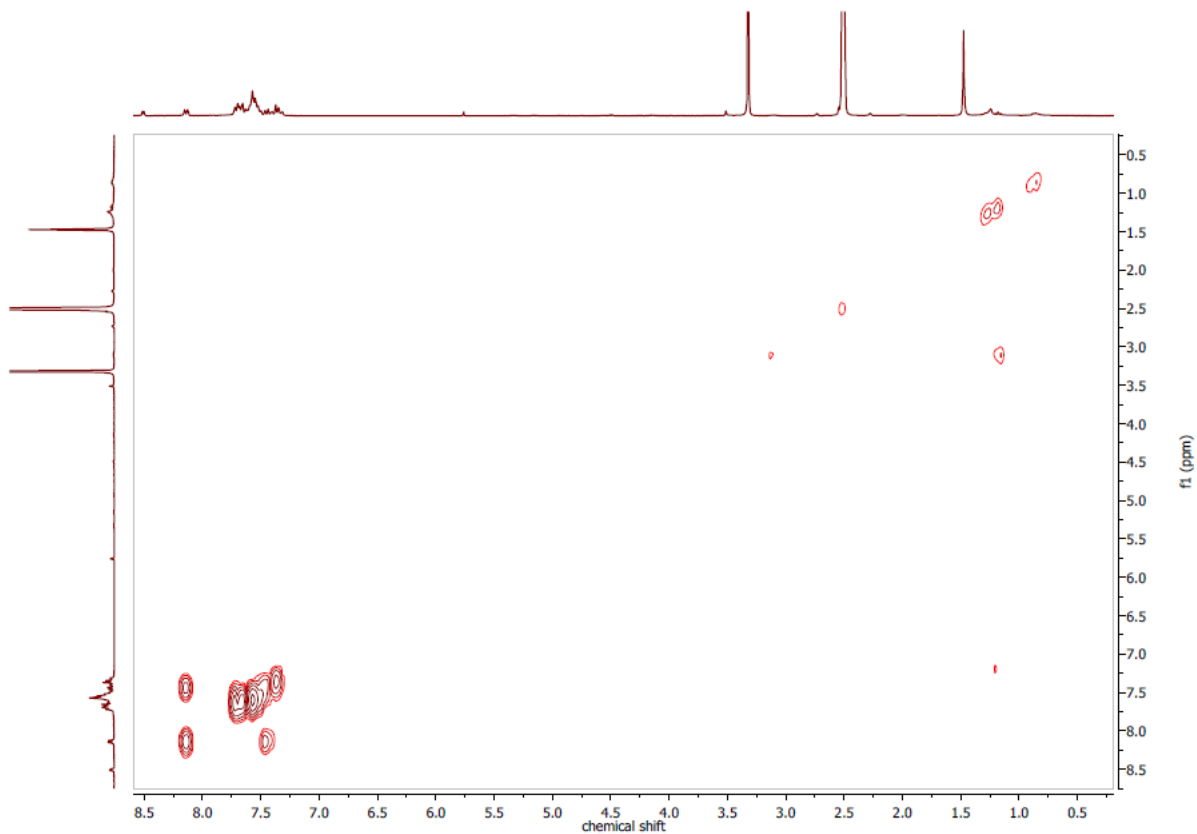


Figure 7.264 ¹H, ¹H COSY NMR spectrum of [Pd(PPh₃)(HbzTSCbap)Cl] in DMSO-*d*₆.

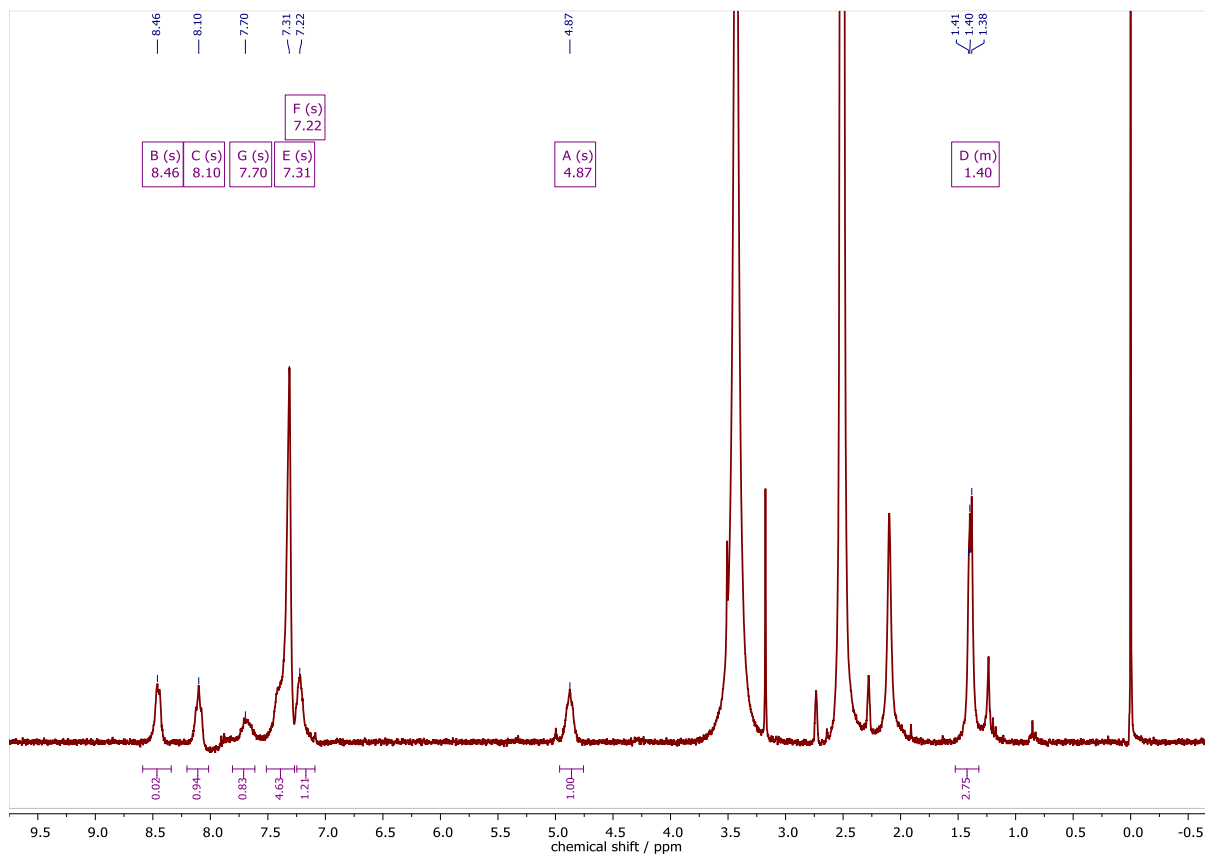


Figure 7.265 ¹H NMR spectrum of [Ni(apyTSCmB)Cl] in DMSO-*d*₆ at 300 MHz.

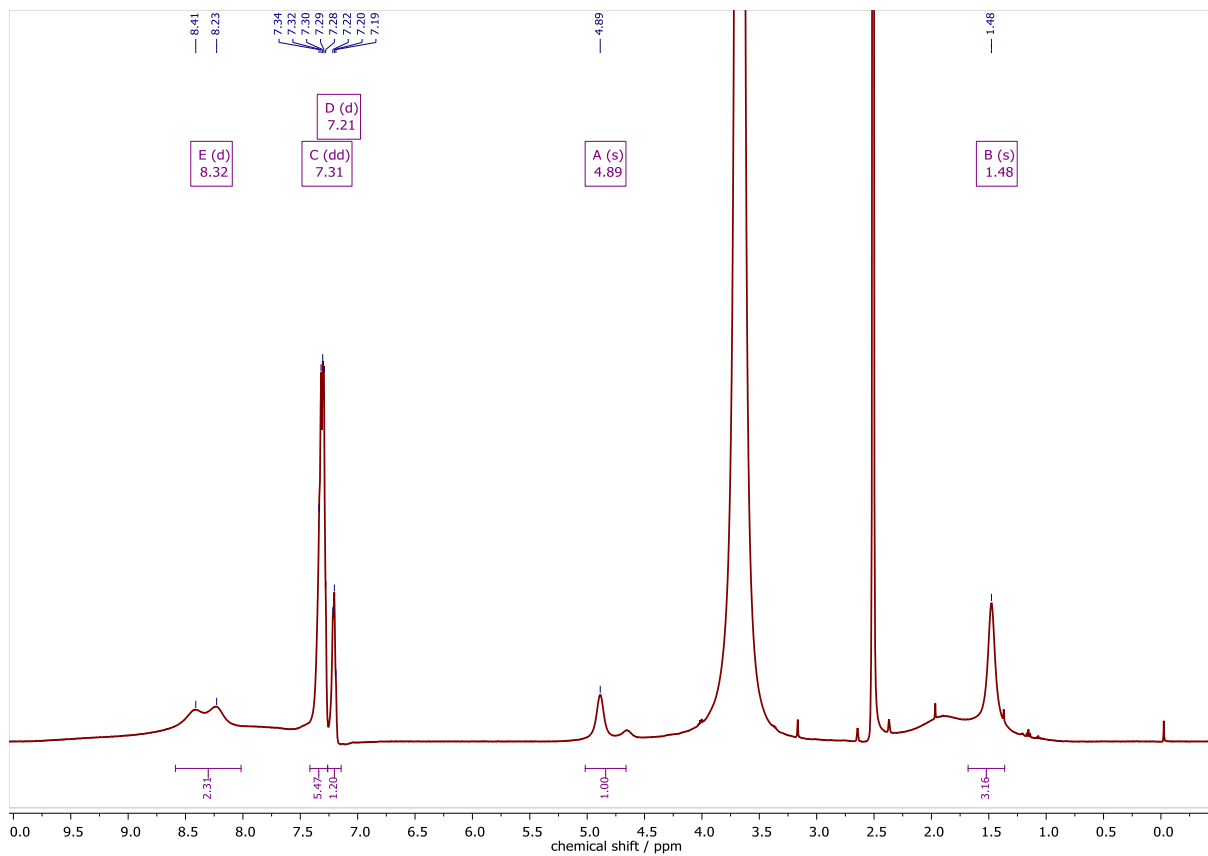


Figure 7.266 ^1H NMR spectrum of $[\text{Ni}(\text{apyTSCmB})\text{NCS}]$ in $\text{DMSO}-d_6$ at 499 MHz.

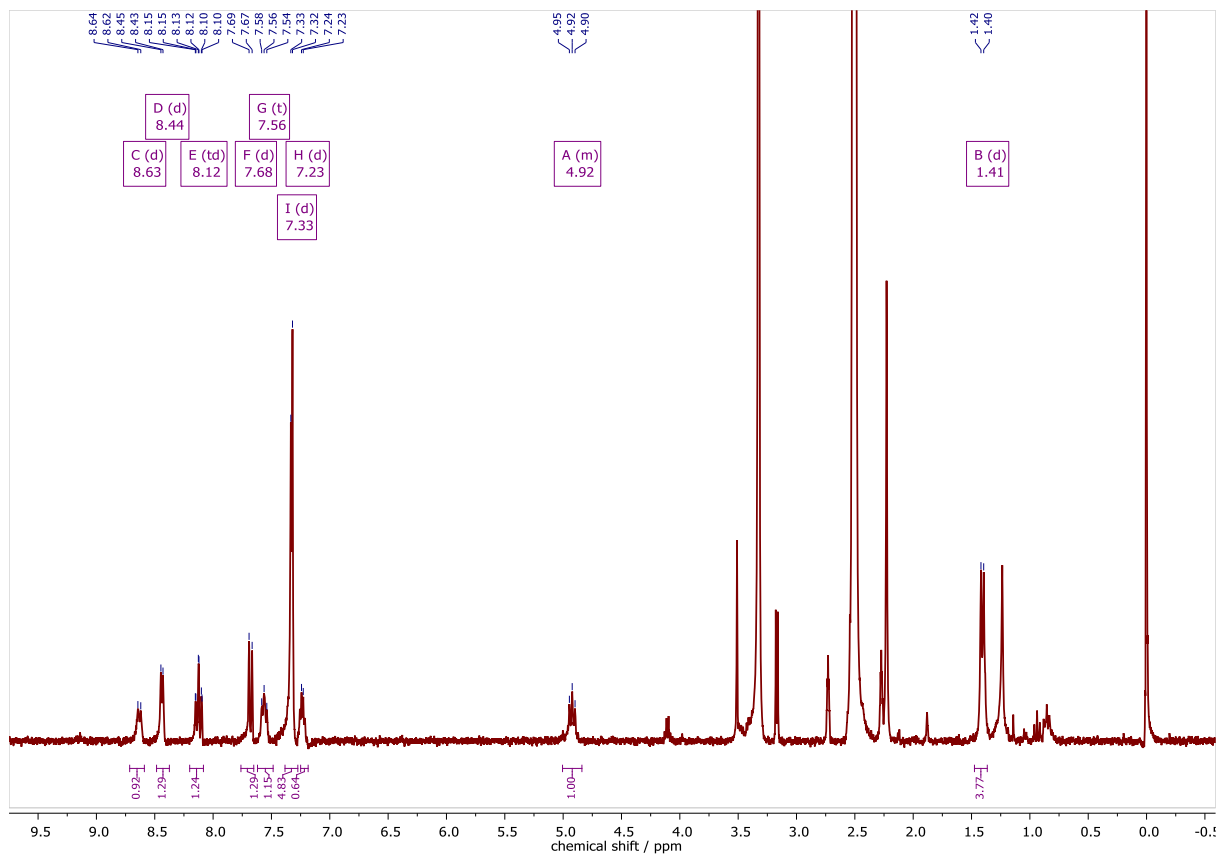


Figure 7.267 ^1H NMR spectrum of $[\text{Ni}(\text{apyTSCmB})\text{CN}]$ in $\text{DMSO}-d_6$ at 300 MHz.

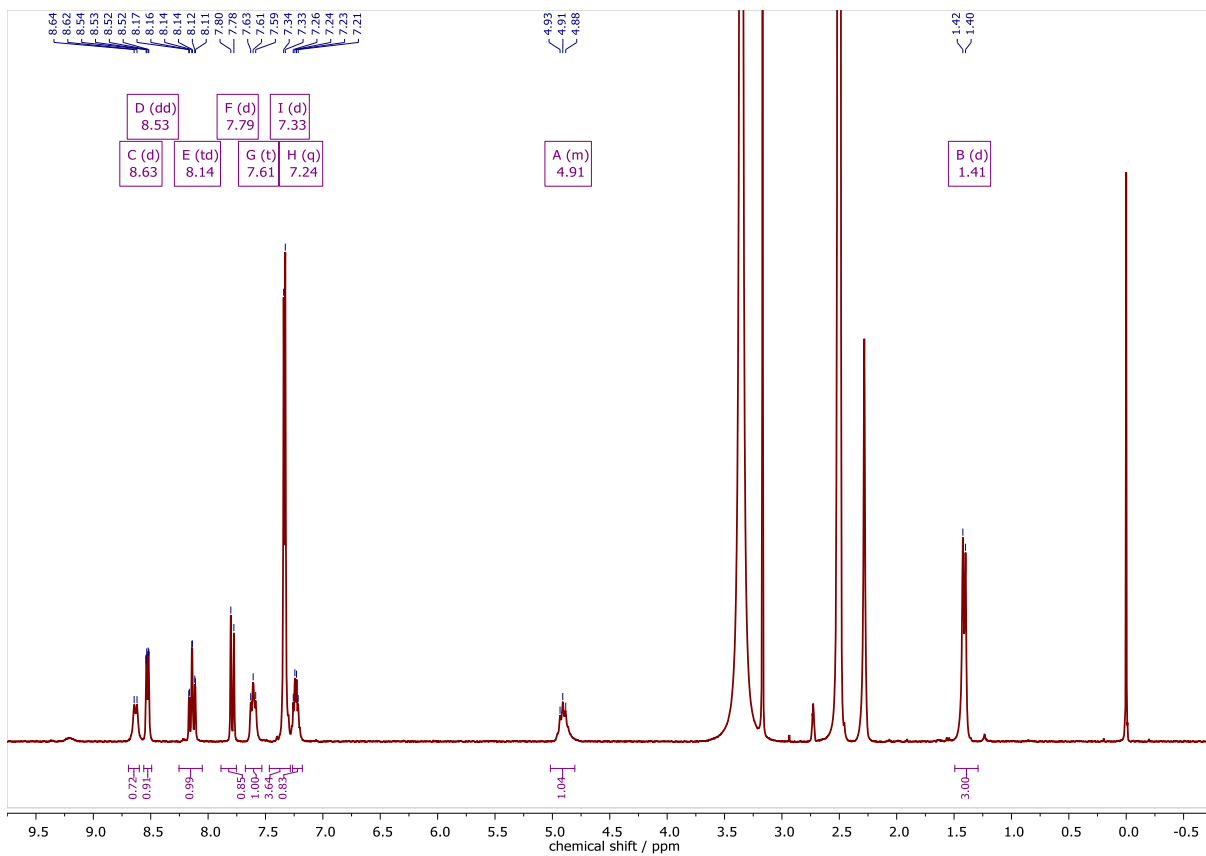


Figure 7.268 ^1H NMR spectrum of $[\text{Pd}(\text{apyTSCmB})\text{Cl}]$ in $\text{DMSO-}d_6$ at 300 MHz.

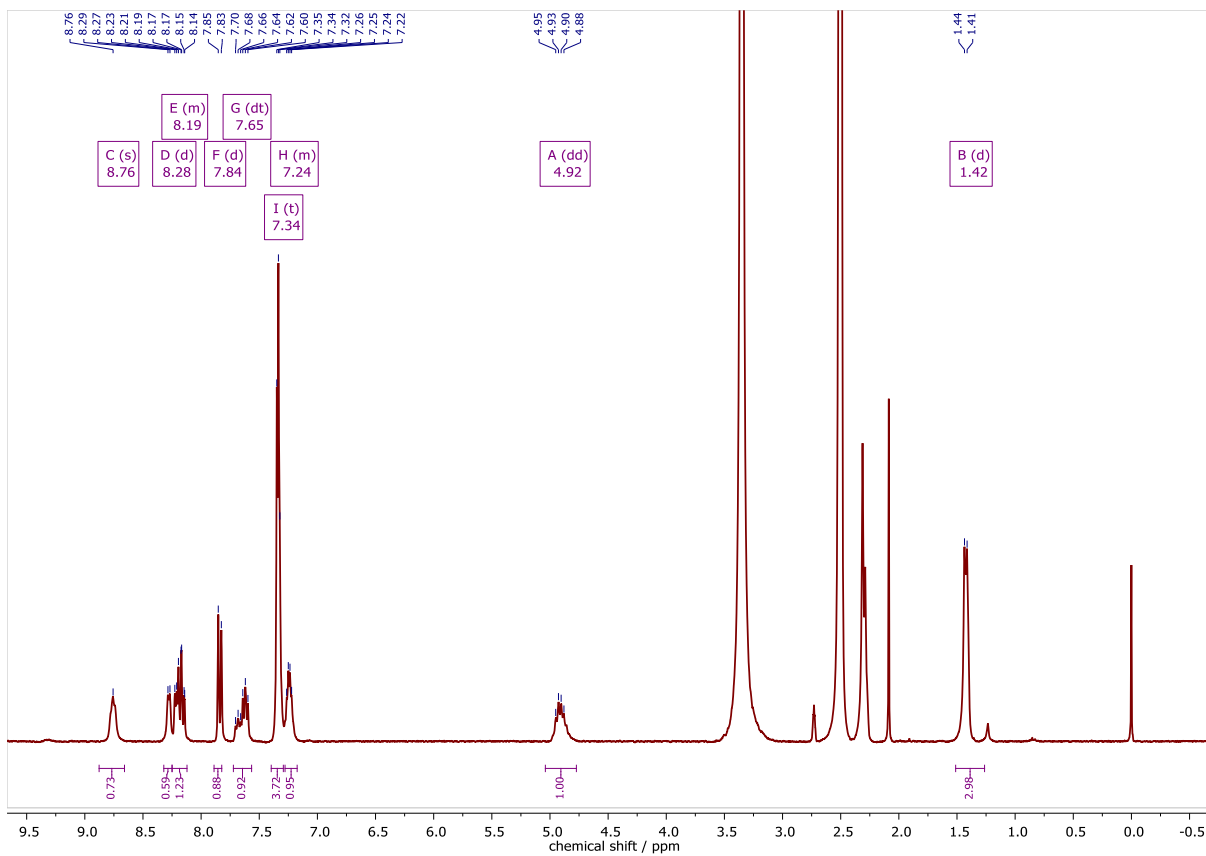


Figure 7.269 ^1H NMR spectrum of $[\text{Pd}(\text{apyTSCmB})\text{NCS}]$ in $\text{DMSO-}d_6$ at 300 MHz.

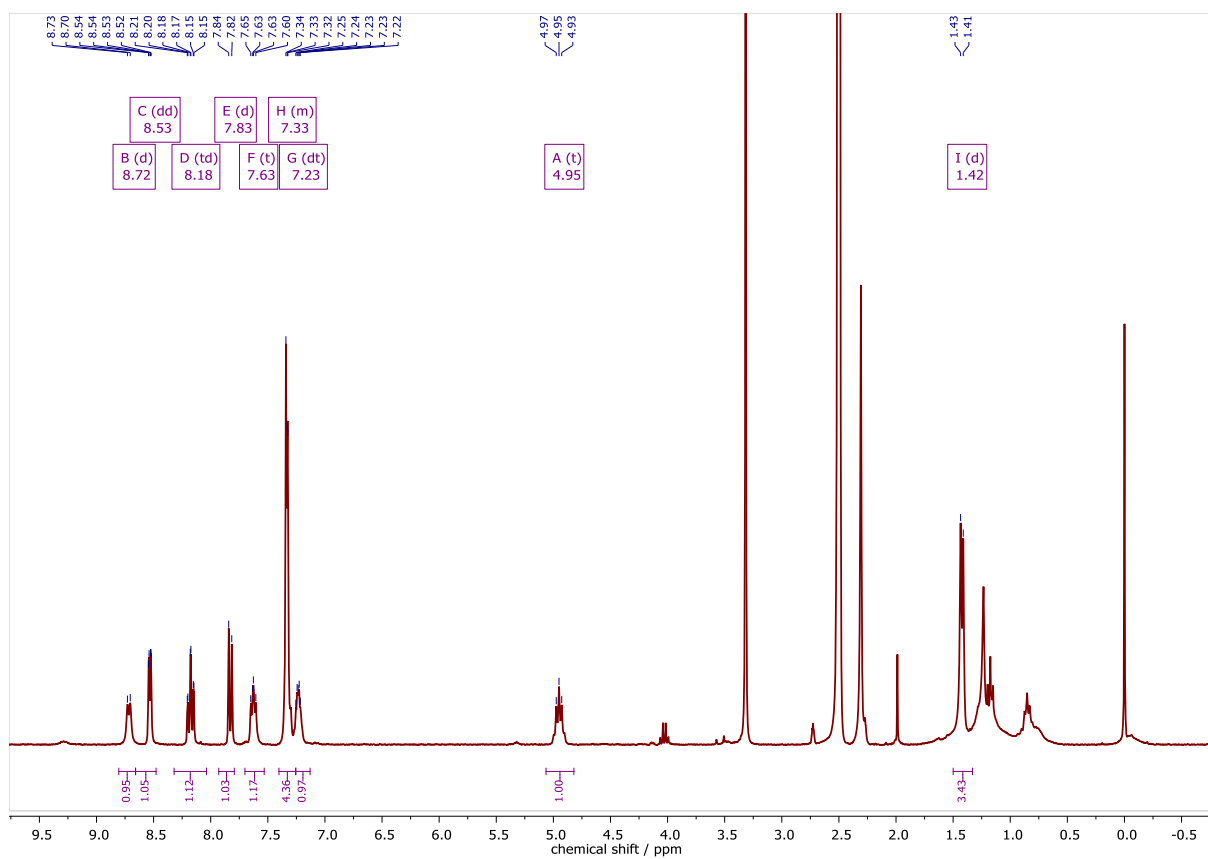


Figure 7.270 ^1H NMR spectrum of $[\text{Pd}(\text{apyTSCmB})\text{CN}]$ in $\text{DMSO-}d_6$ at 300 MHz.

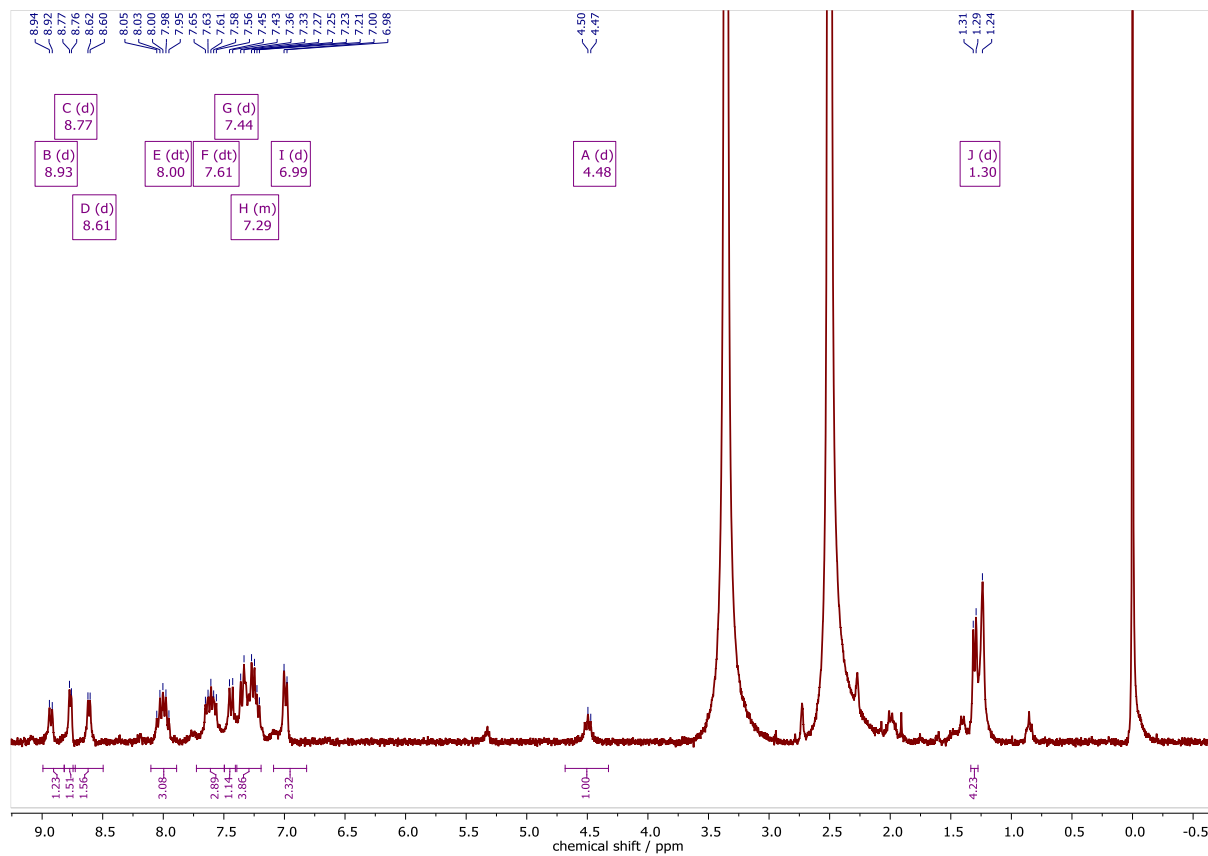


Figure 7.271 ^1H NMR spectrum of $[\text{Pd}(\text{dpyTSCmB})\text{Cl}]$ in $\text{DMSO-}d_6$ at 300 MHz.

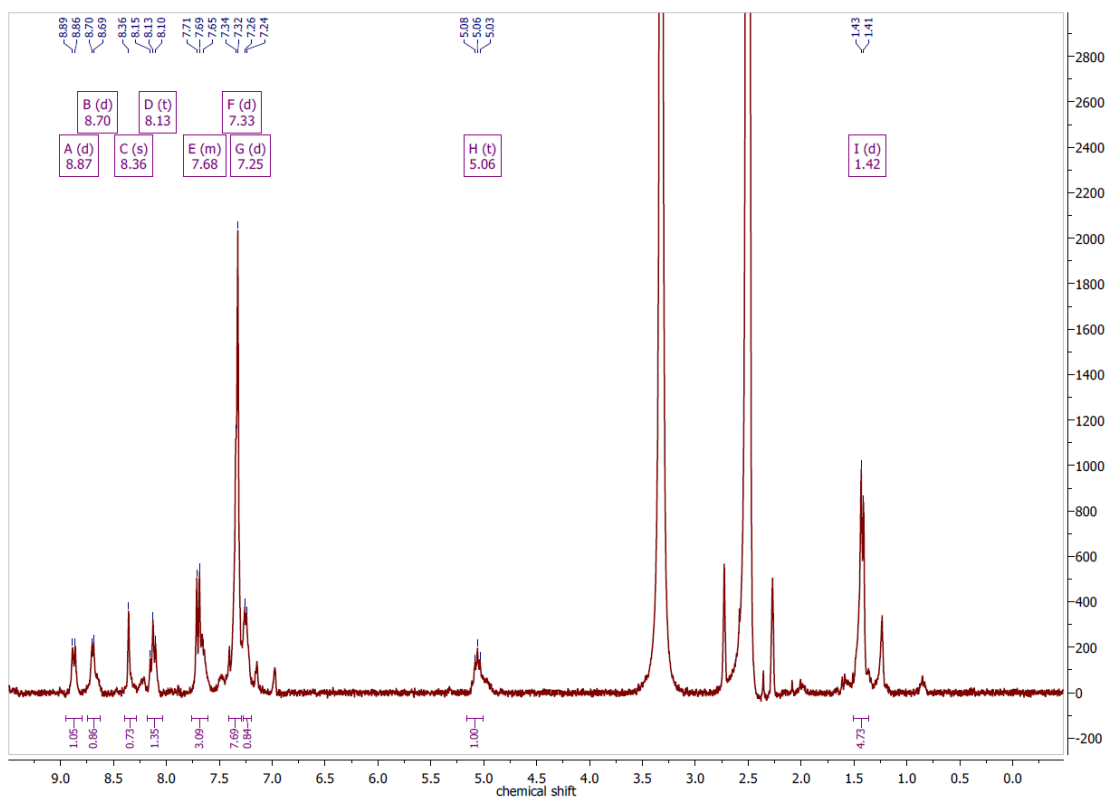


Figure 7.272 ^1H NMR spectrum of $[\text{Pt}(\text{fpyTSCmB})\text{Cl}]$ in $\text{DMSO}-d_6$ at 300 MHz.

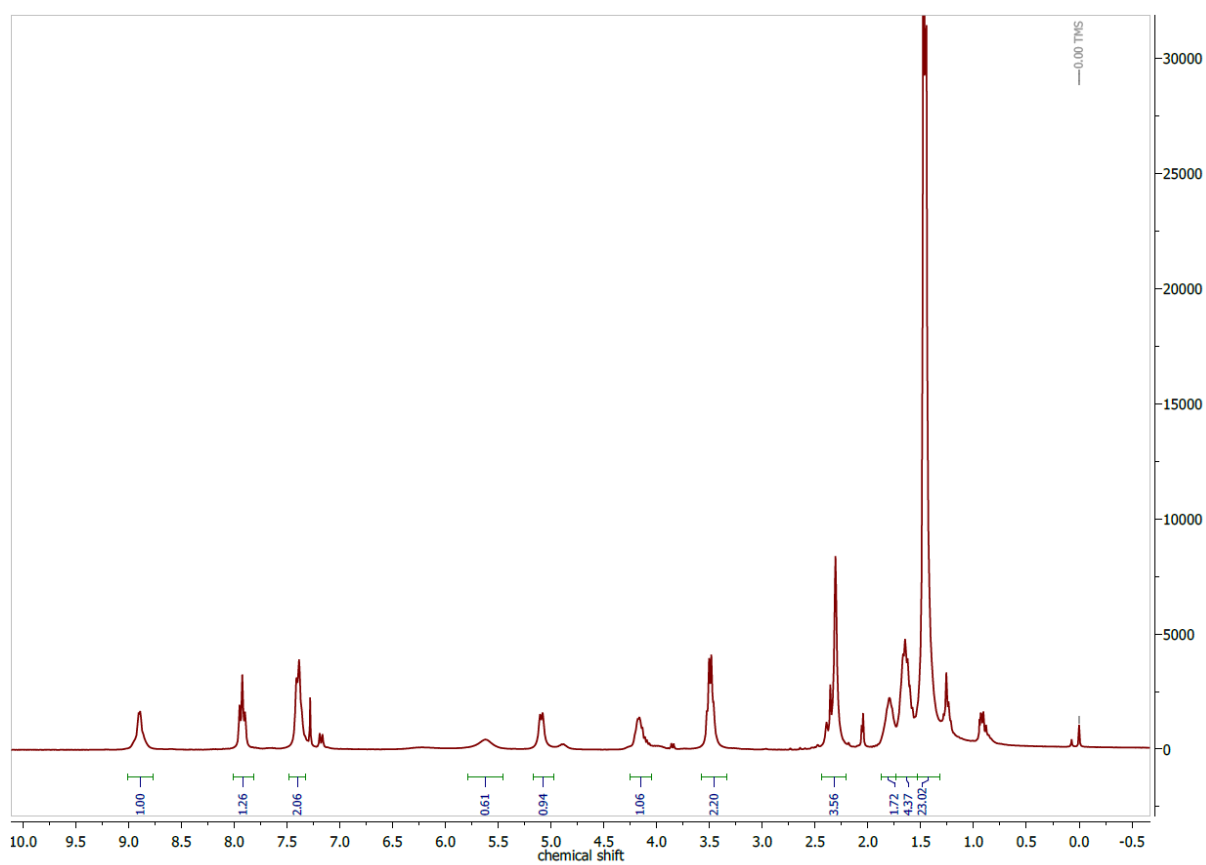


Figure 7.273 ^1H NMR spectrum of $[\text{Pt}(\text{apyTSCmB})\text{Cl}]$ in CDCl_3 at 300 MHz.

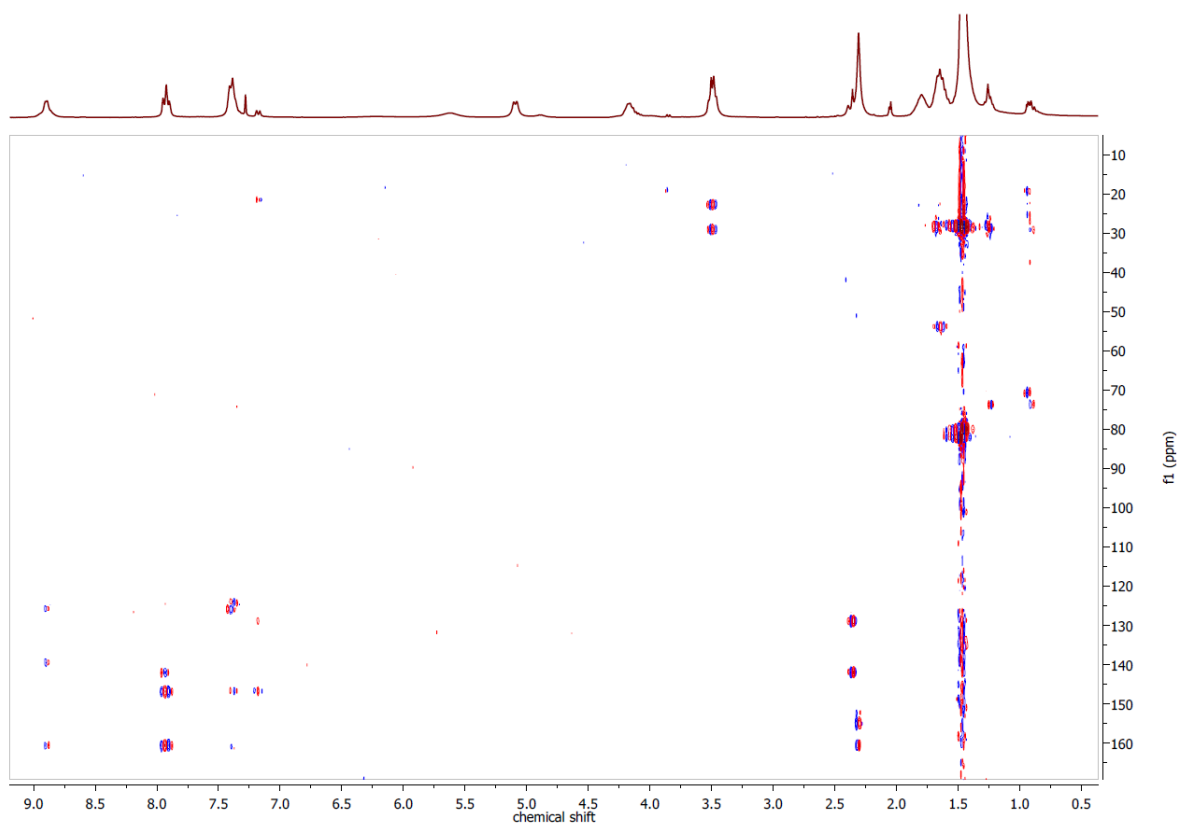


Figure 7.274 ^1H , ^{13}C HMBC NMR spectrum of $[\text{Pt}(\text{apyTSCmB})\text{Cl}]$ in CDCl_3 .

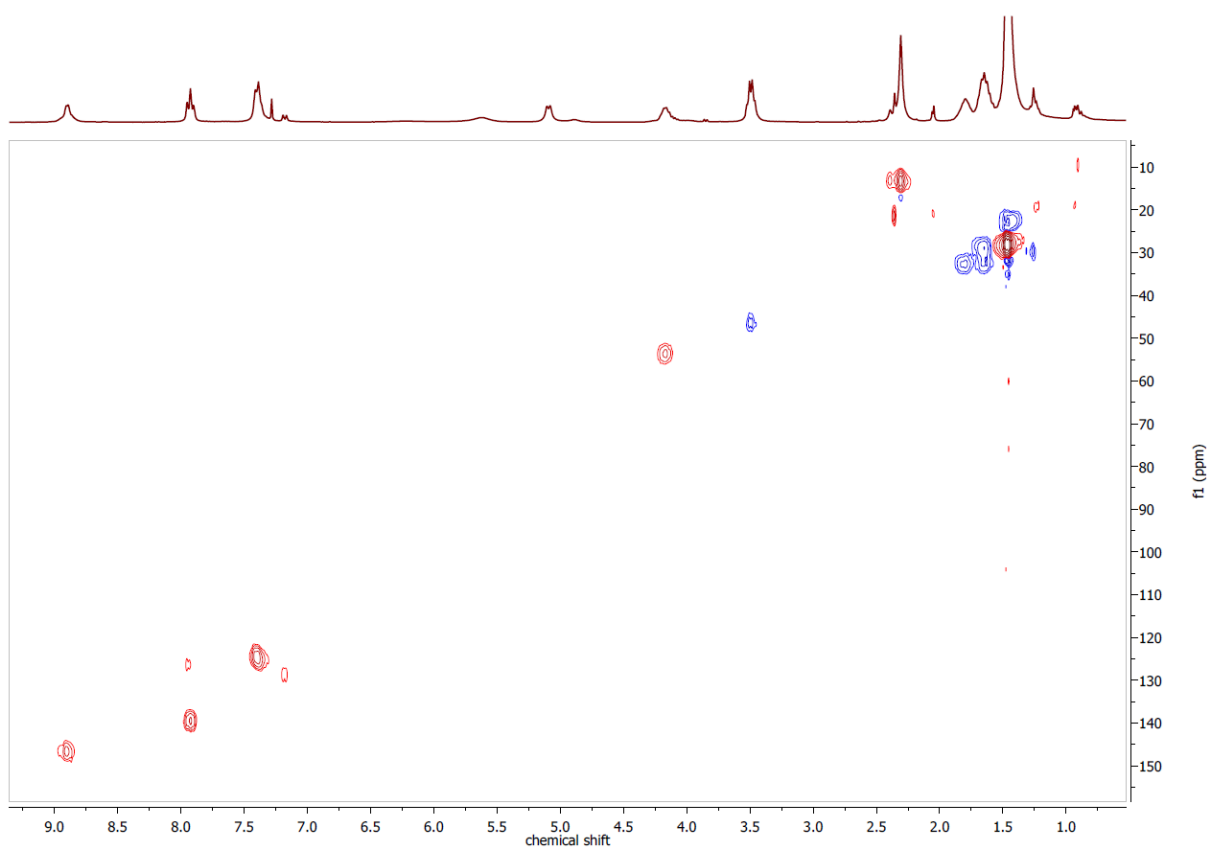


Figure 7.275 ^1H , ^{13}C HSQC NMR spectrum of $[\text{Pt}(\text{apyTSCmB})\text{Cl}]$ in CDCl_3 .

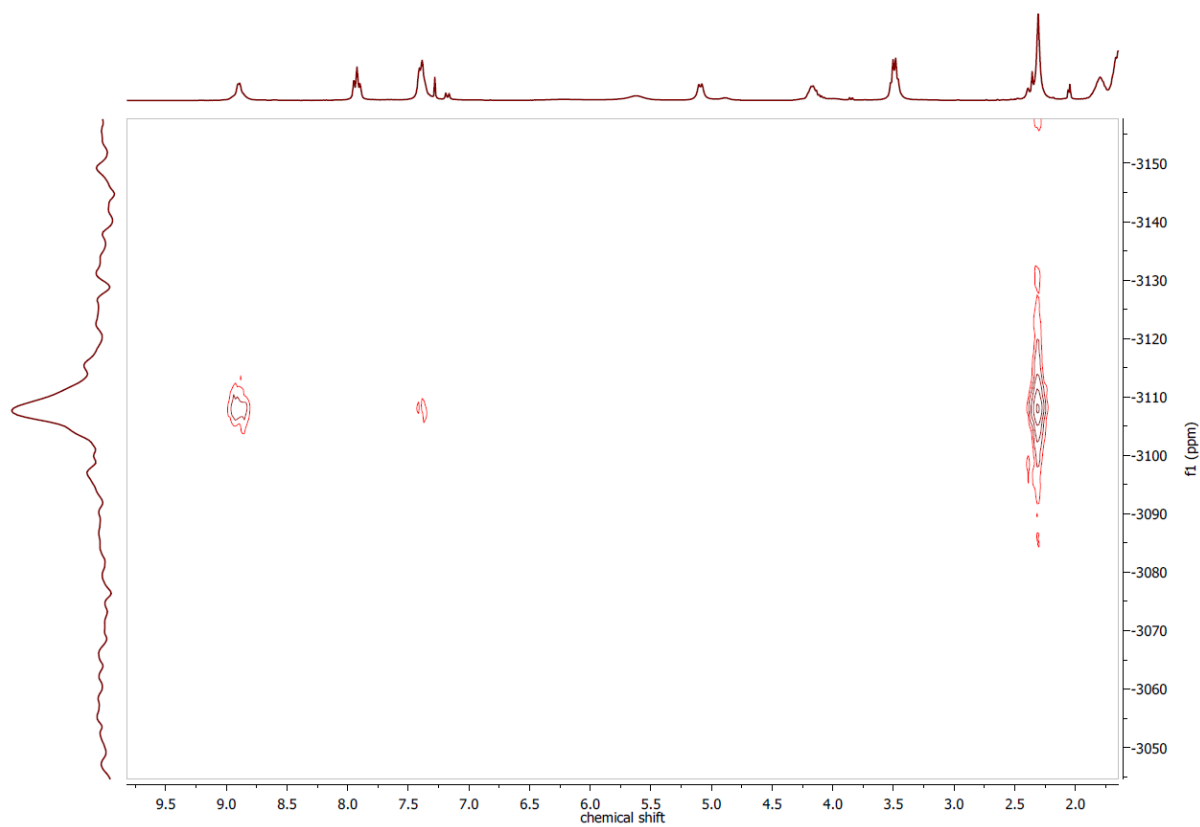


Figure 7.276 ^1H , ^{195}Pt HMBC NMR spectrum of $[\text{Pt}(\text{apyTSCmB})\text{Cl}]$ in CDCl_3 .

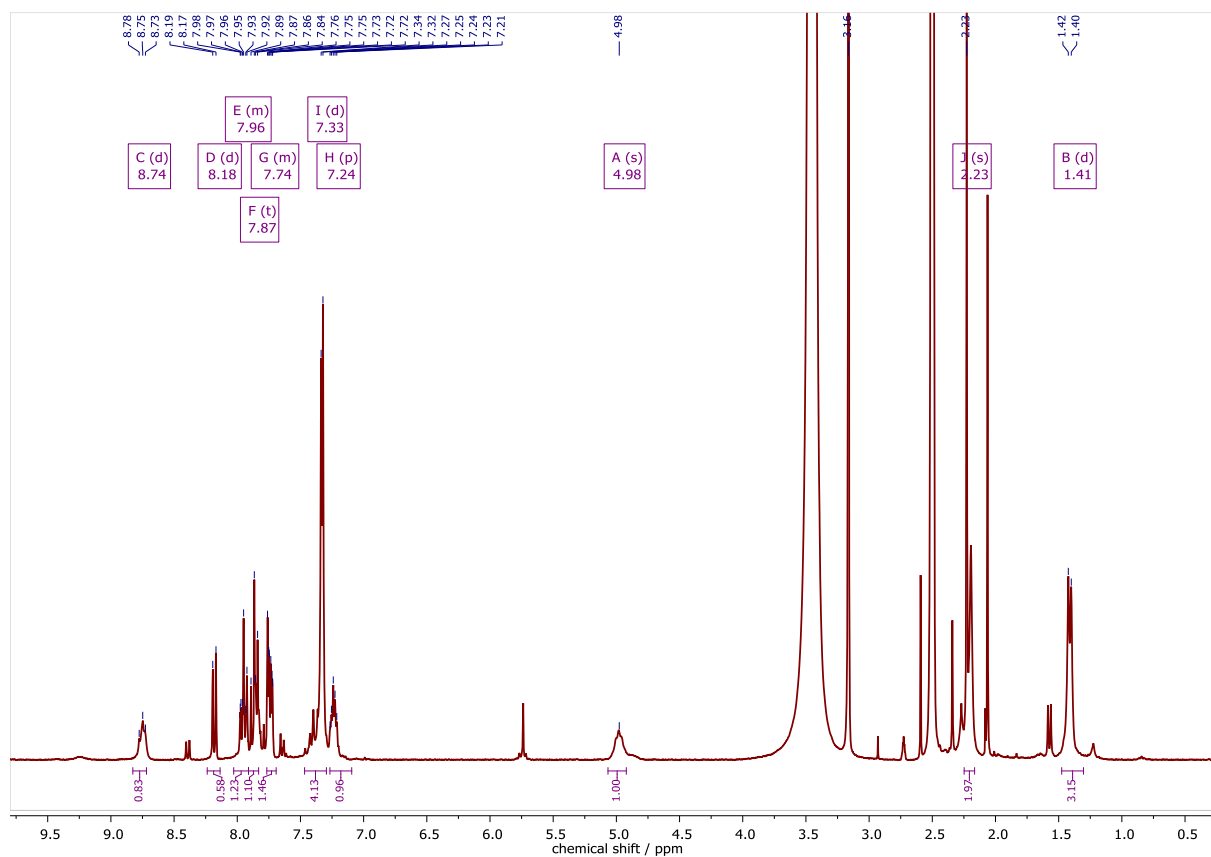


Figure 7.277 ^1H NMR spectrum of $[\text{Pt}(6\text{-BrpyTSCmB})\text{Cl}]$ in CDCl_3 at 300 MHz.

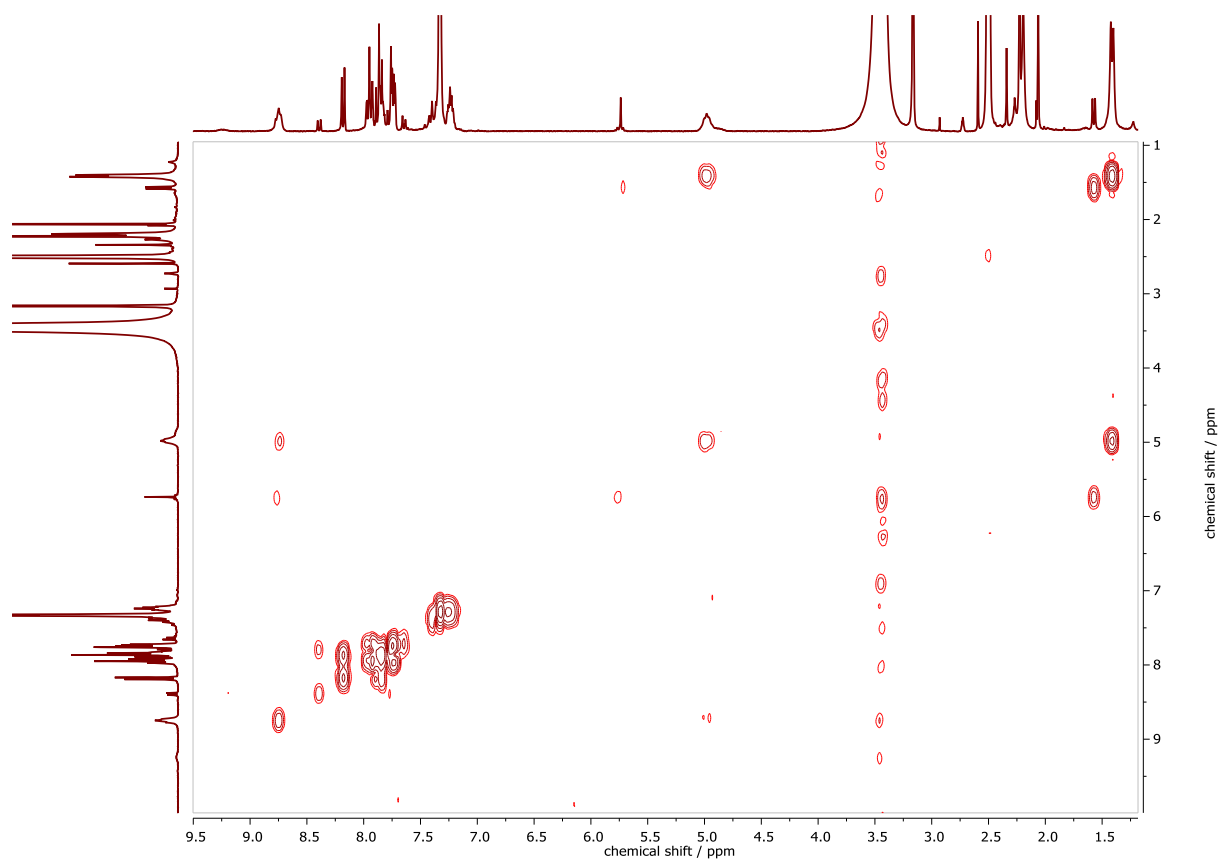


Figure 7.278 ^1H , ^1H COSY NMR spectrum of $[\text{Pt}(6\text{-BrapyTSCmB})\text{Cl}]$ in $\text{DMSO-}d_6$.

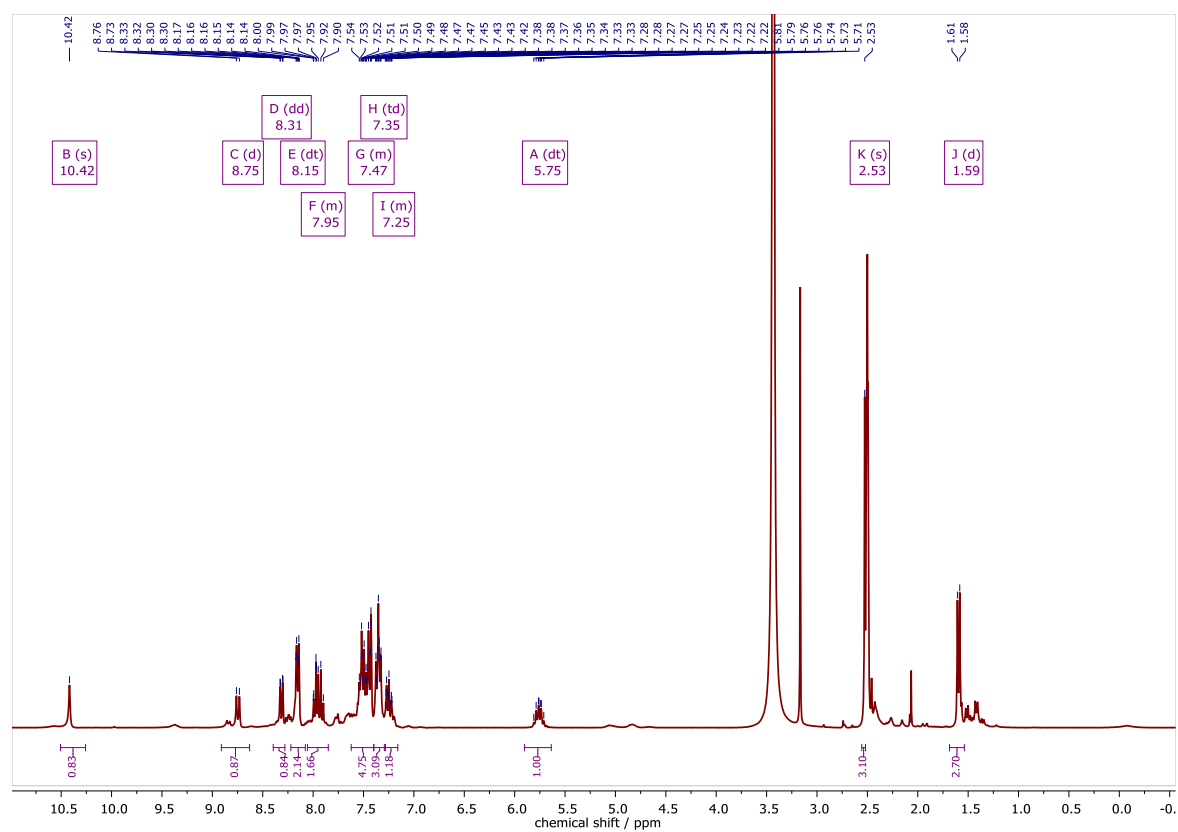


Figure 7.279 ^1H NMR spectrum of $[\text{Pt}(6\text{-PhapyTSCmB})\text{Cl}]$ in CDCl_3 at 300 MHz.

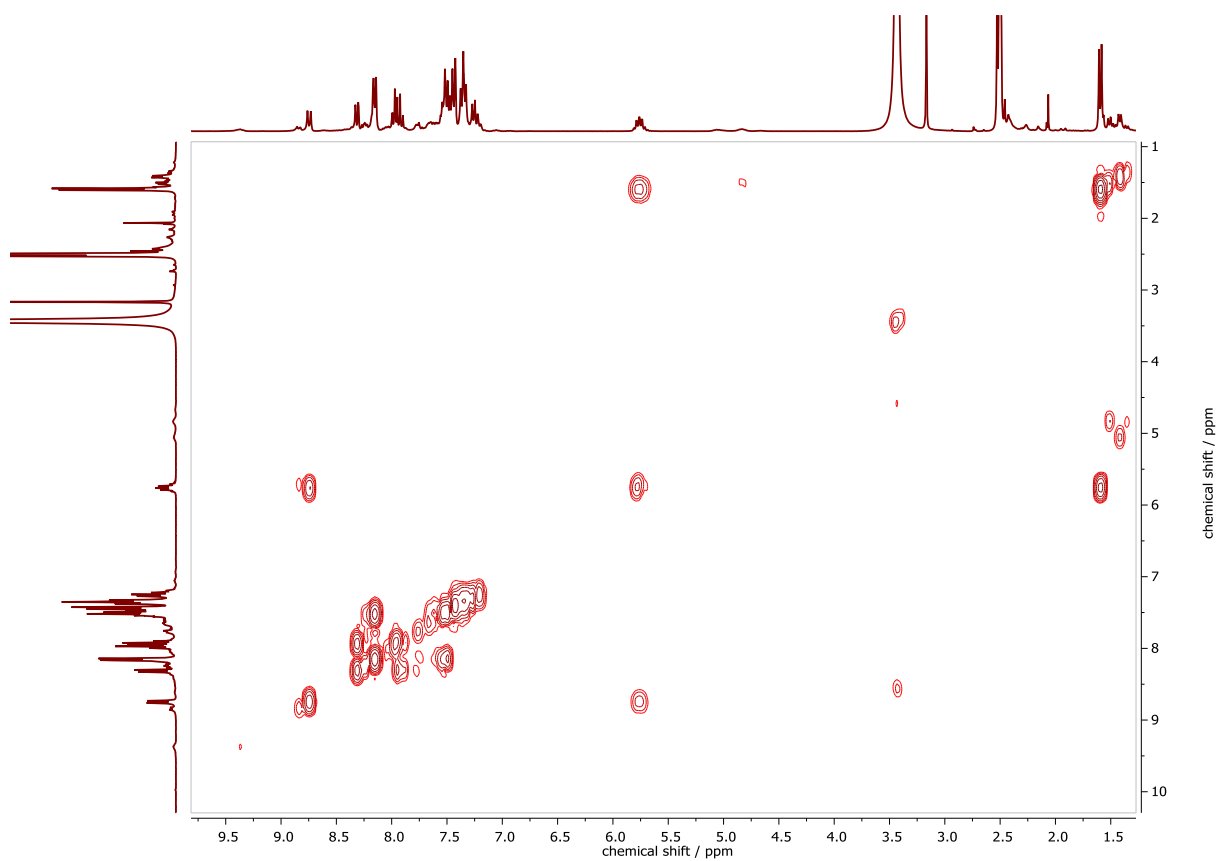


Figure 7.280 ^1H , ^1H COSY NMR spectrum of $[\text{Pt}(6\text{-BrapyTSCmB})\text{Cl}]$ in $\text{DMSO-}d_6$.

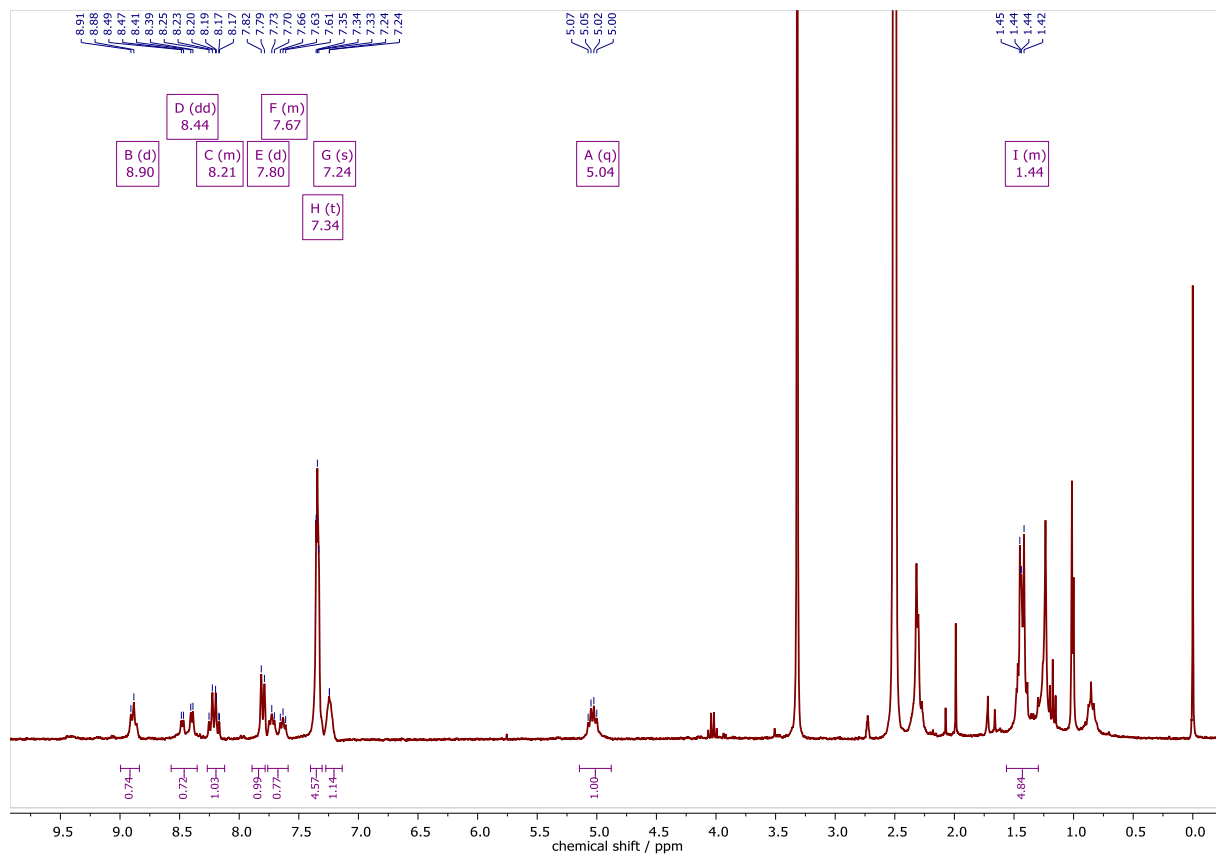


Figure 7.281 ^1H NMR spectrum of $[\text{Pt}(\text{apyTSCmB})\text{NCS}]$ in $\text{DMSO-}d_6$ at 300 MHz.

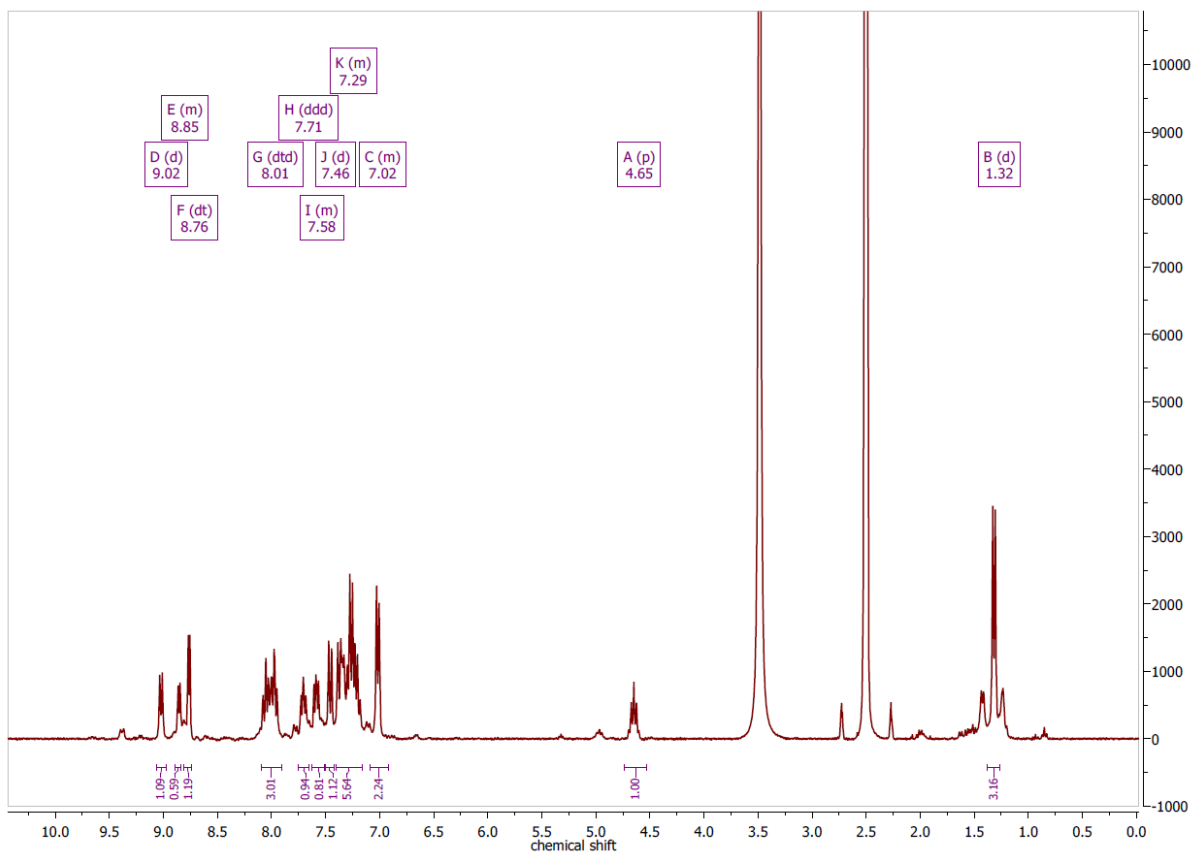


Figure 7.282 ^1H NMR spectrum of $[\text{Pt}(\text{dpyTSCmB})\text{Cl}]$ in $\text{DMSO-}d_6$ at 300 MHz.

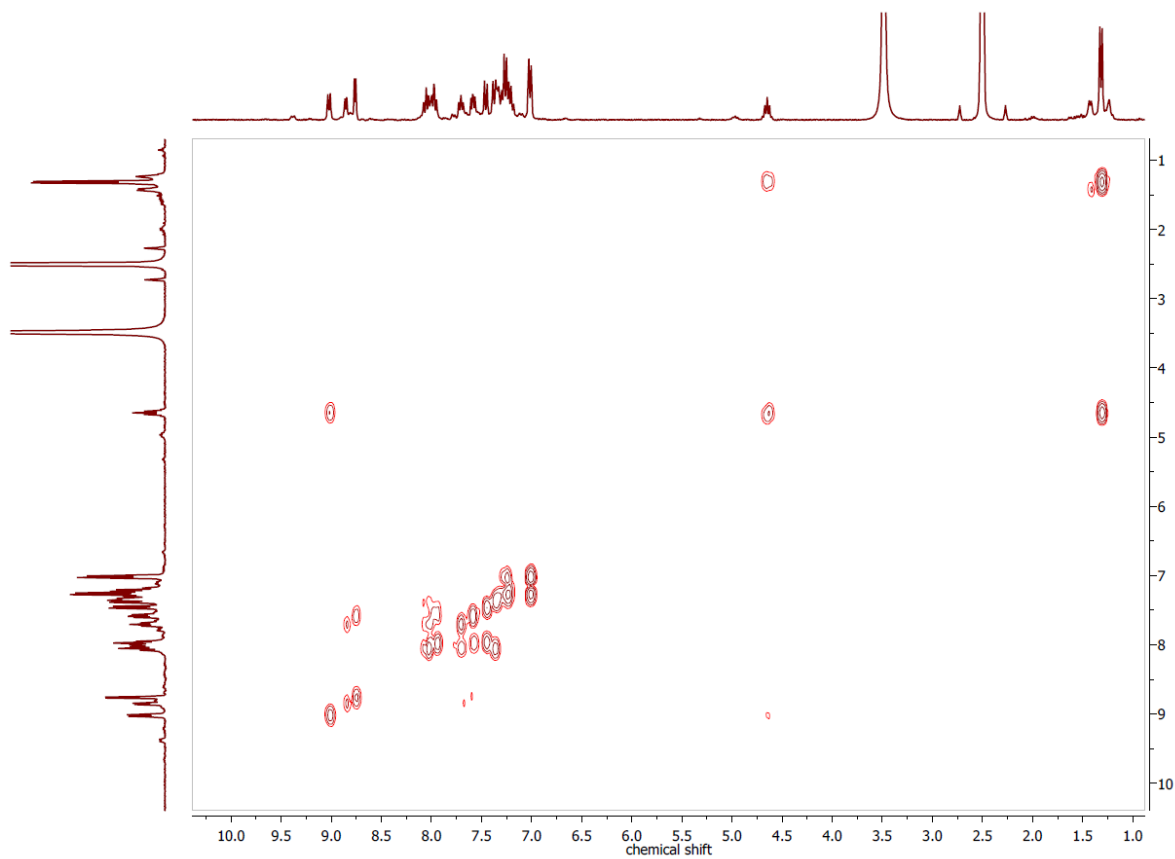


Figure 7.283 $^1\text{H}, ^1\text{H}$ COSY NMR spectrum of $[\text{Pt}(\text{dpyTSCmB})\text{Cl}]$ in $\text{DMSO-}d_6$.

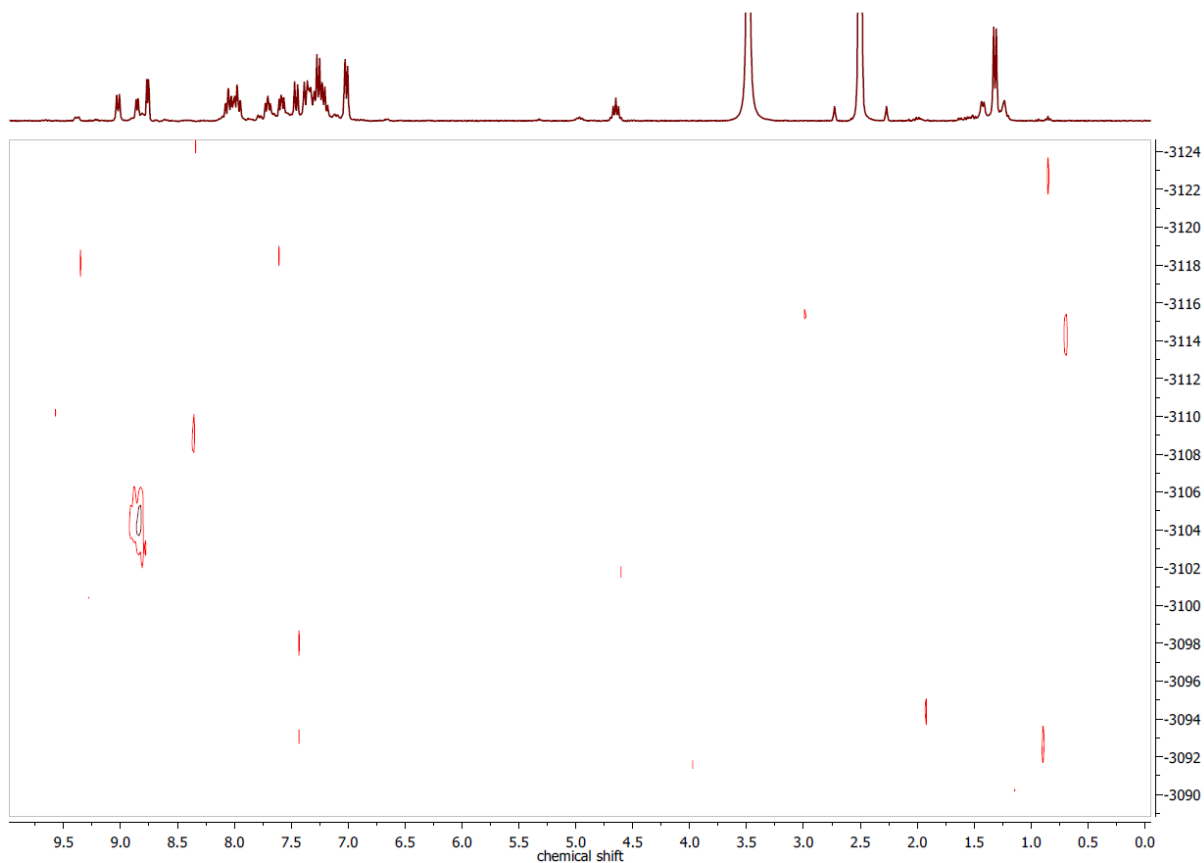


Figure 7.284 ^1H , ^{195}Pt HMBC NMR spectrum of $[\text{Pt}(\text{dpyTSCmB})\text{Cl}]$ in $\text{DMSO-}d_6$.

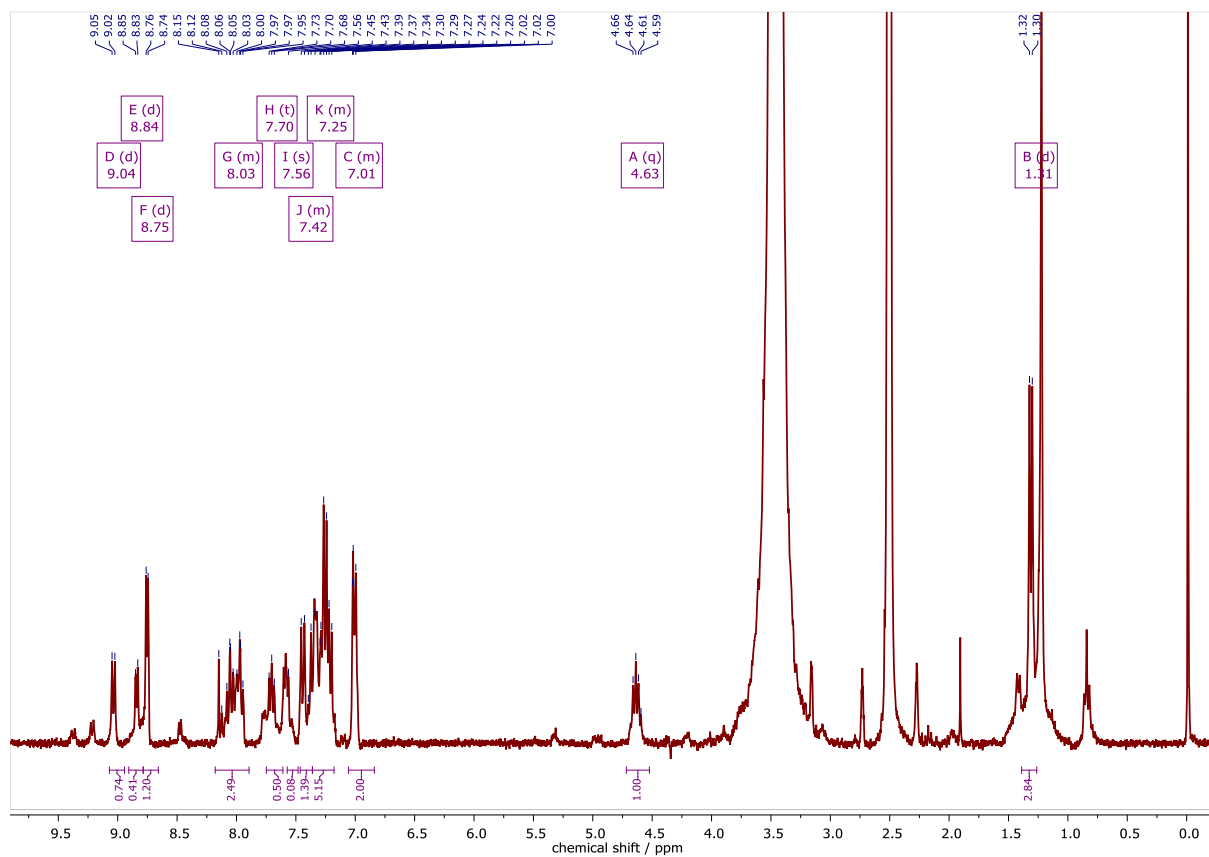


Figure 7.285 ^1H NMR spectrum of $[\text{Pt}(\text{dpyTSCmB})\text{NCS}]$ in $\text{DMSO-}d_6$ at 300 MHz.

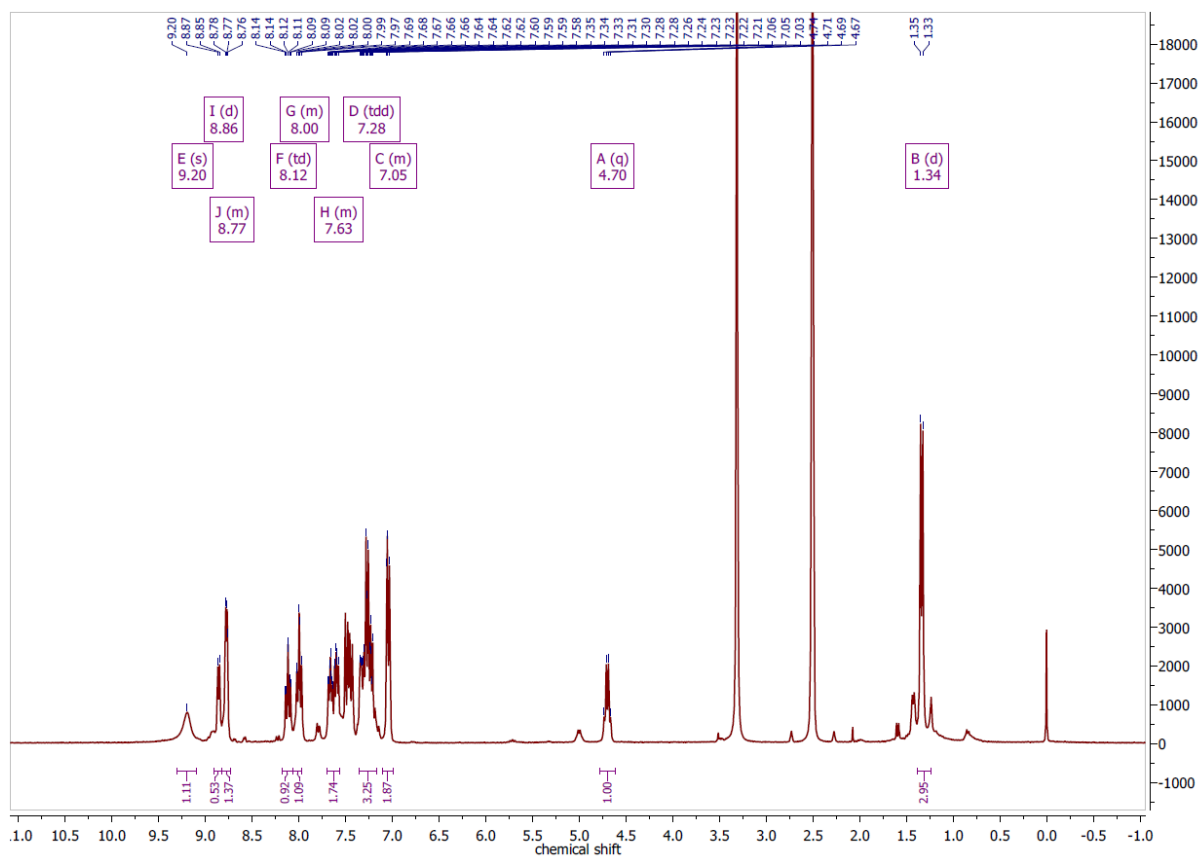


Figure 7.286 ^1H NMR spectrum of $[\text{Pt}(\text{dpyTSCmB})\text{CN}]$ in $\text{DMSO}-d_6$ at 300 MHz.

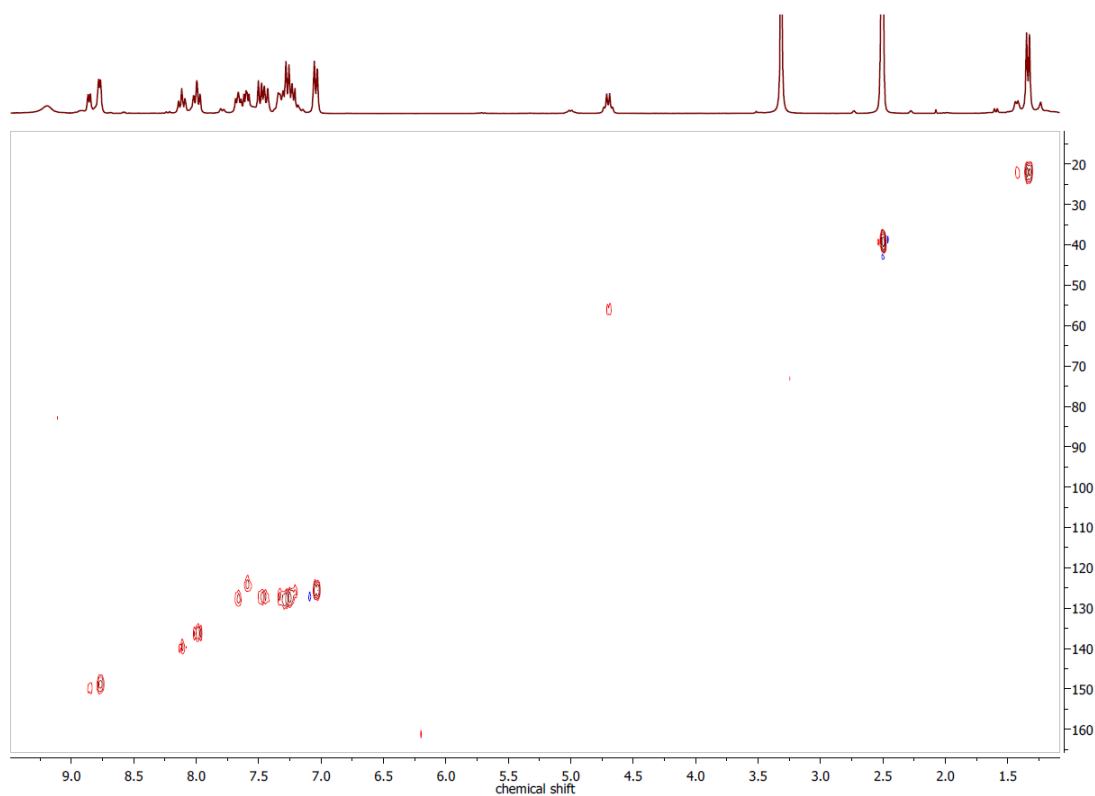


Figure 7.287 $^1\text{H}, ^{13}\text{C}$ HSQCed NMR spectrum of $[\text{Pt}(\text{dpyTSCmB})\text{CN}]$ in $\text{DMSO}-d_6$.

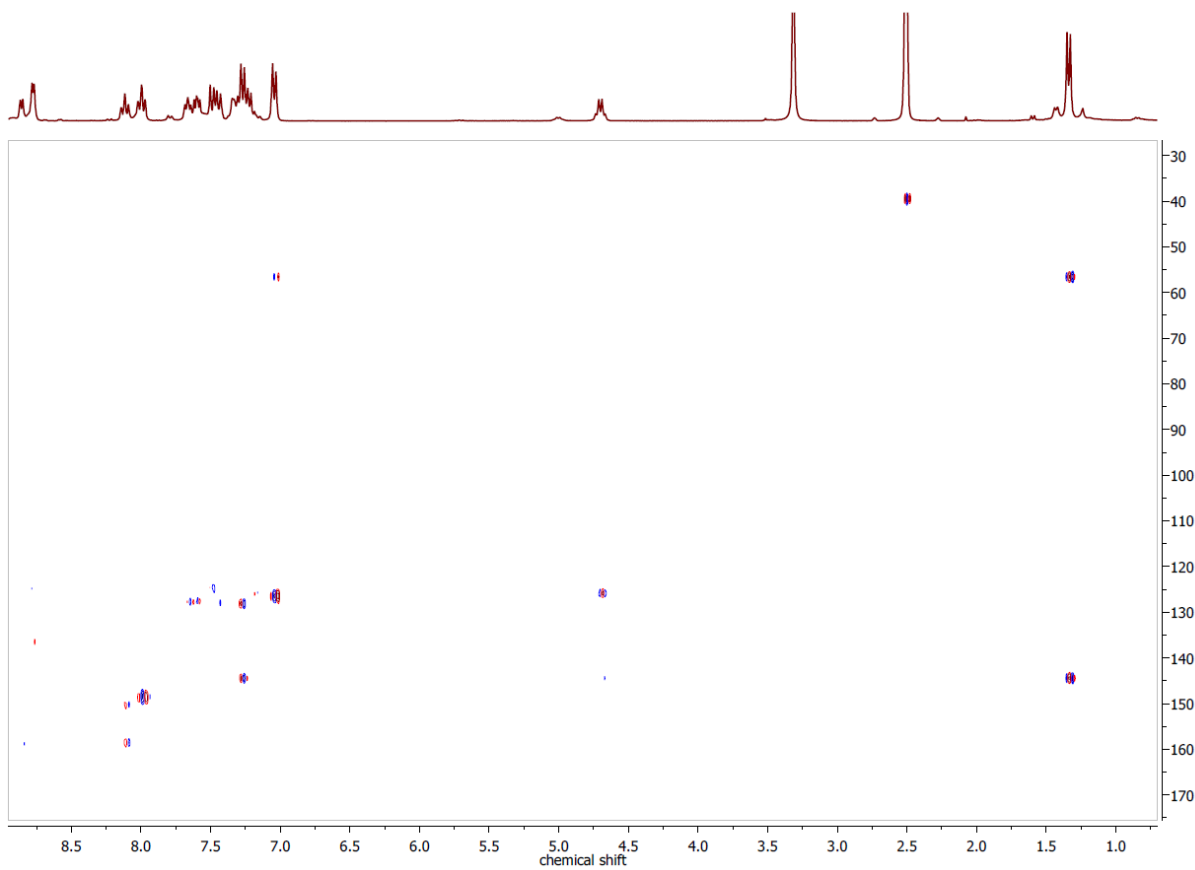


Figure 7.288 ^1H , ^{13}C HMBC NMR spectrum of $[\text{Pt}(\text{dpyTSCmB})\text{CN}]$ in $\text{DMSO-}d_6$.

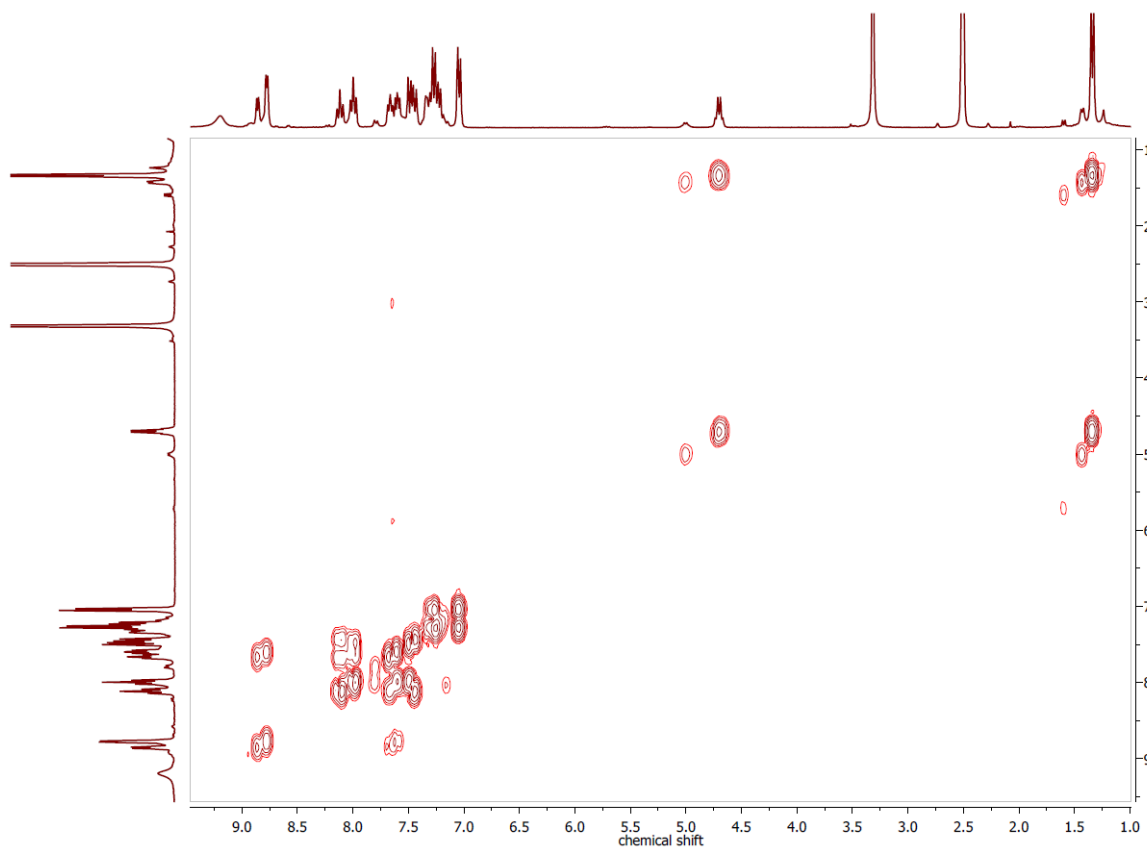


Figure 7.289 ^1H , ^1H COSY NMR spectrum of $[\text{Pt}(\text{dpyTSCmB})\text{CN}]$ in $\text{DMSO-}d_6$.

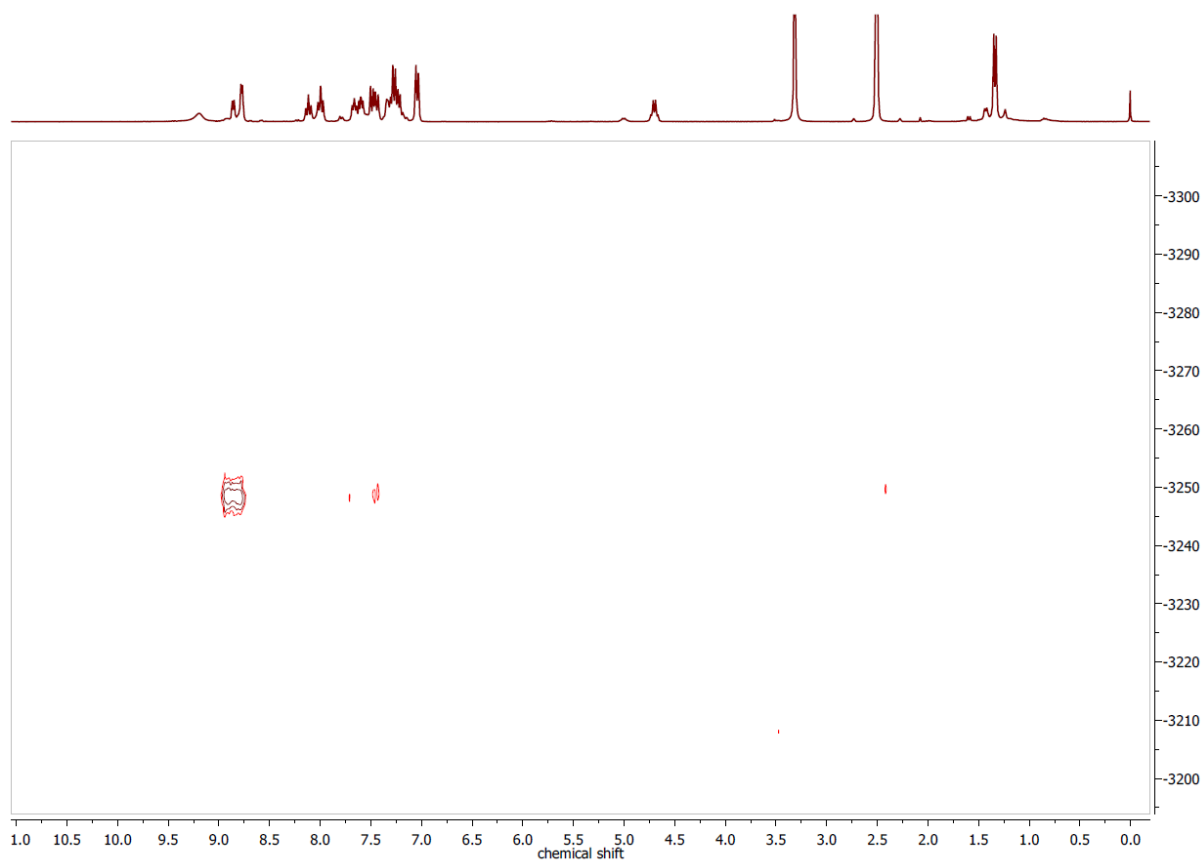


Figure 7.290 ^1H , ^{195}Pt HMBC NMR spectrum of $[\text{Pt}(\text{dpyTSCmB})\text{CN}]$ in $\text{DMSO-}d_6$.

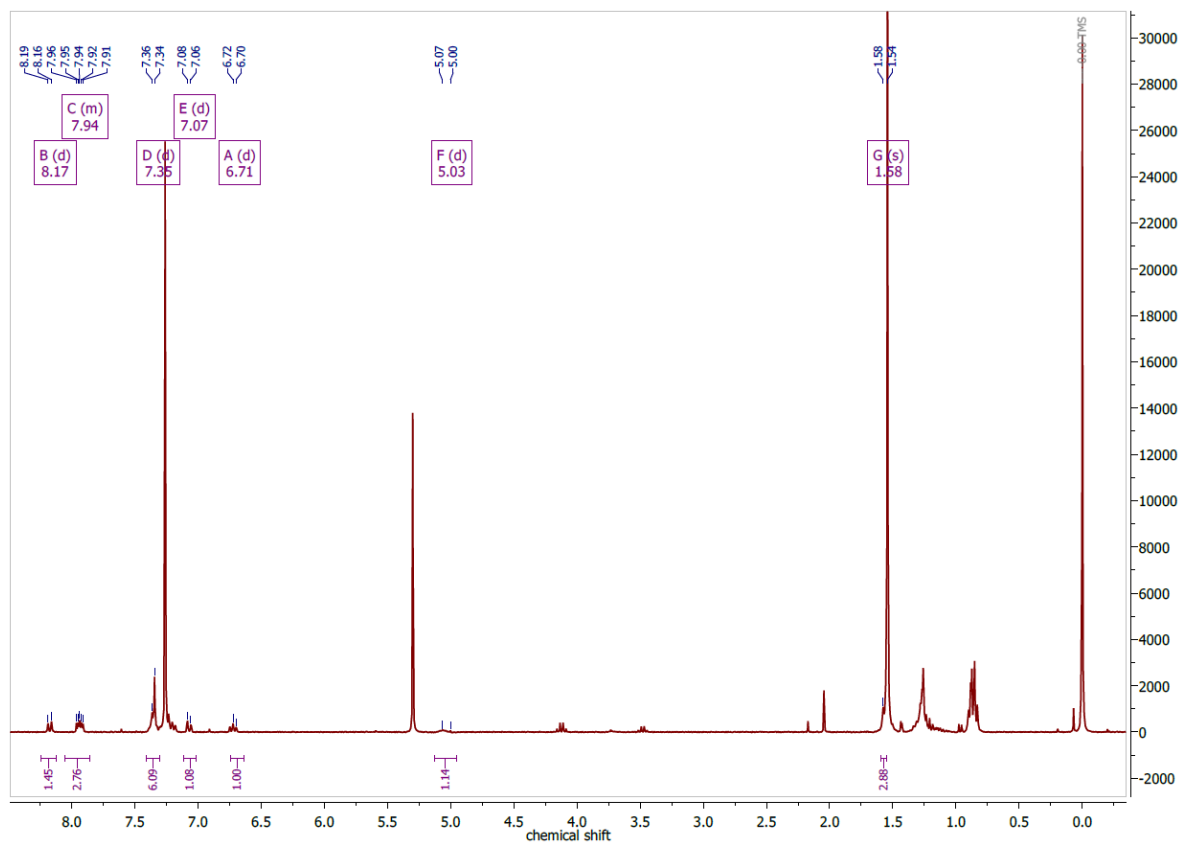


Figure 7.291 ^1H NMR spectrum of $[\text{Ni}(\text{hphfpyTSCmB})]$ in CDCl_3 at 300 MHz.

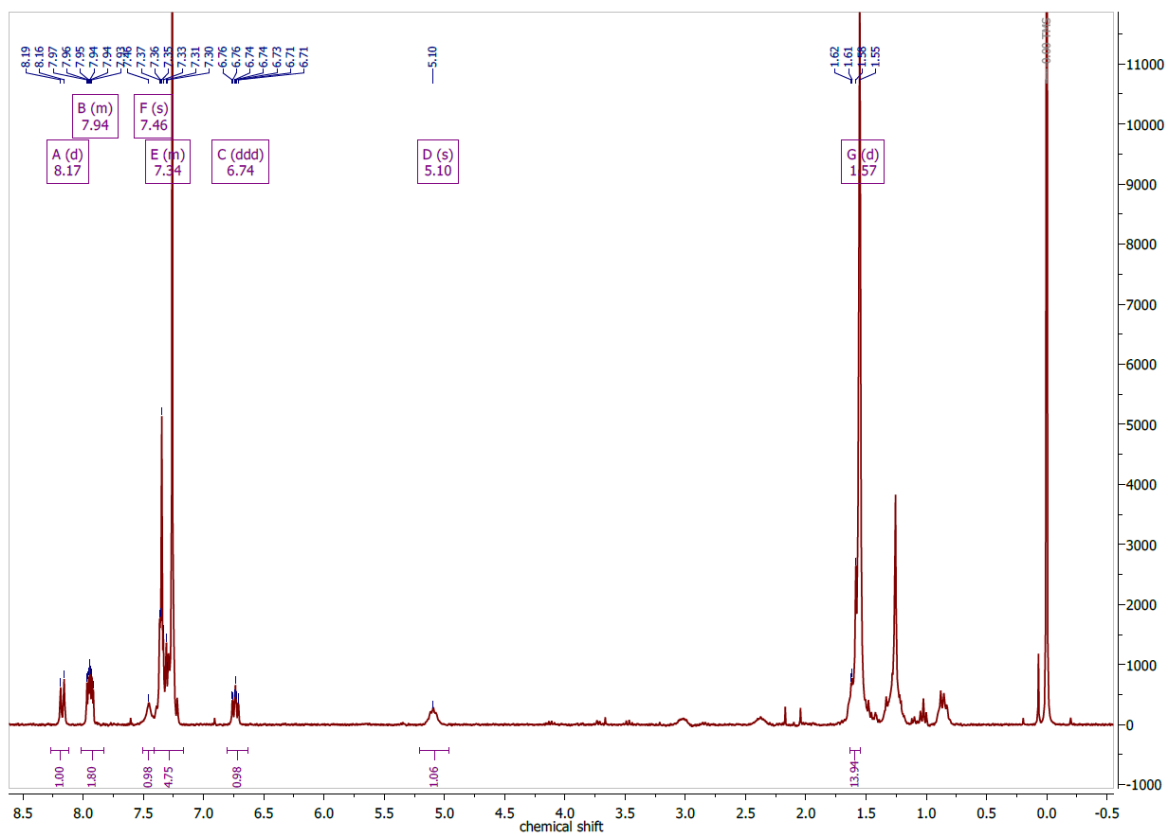


Figure 7.292 ^1H NMR spectrum of $[\text{Pd}(\text{hphfpyTSCmB})]$ in CDCl_3 at 300 MHz.

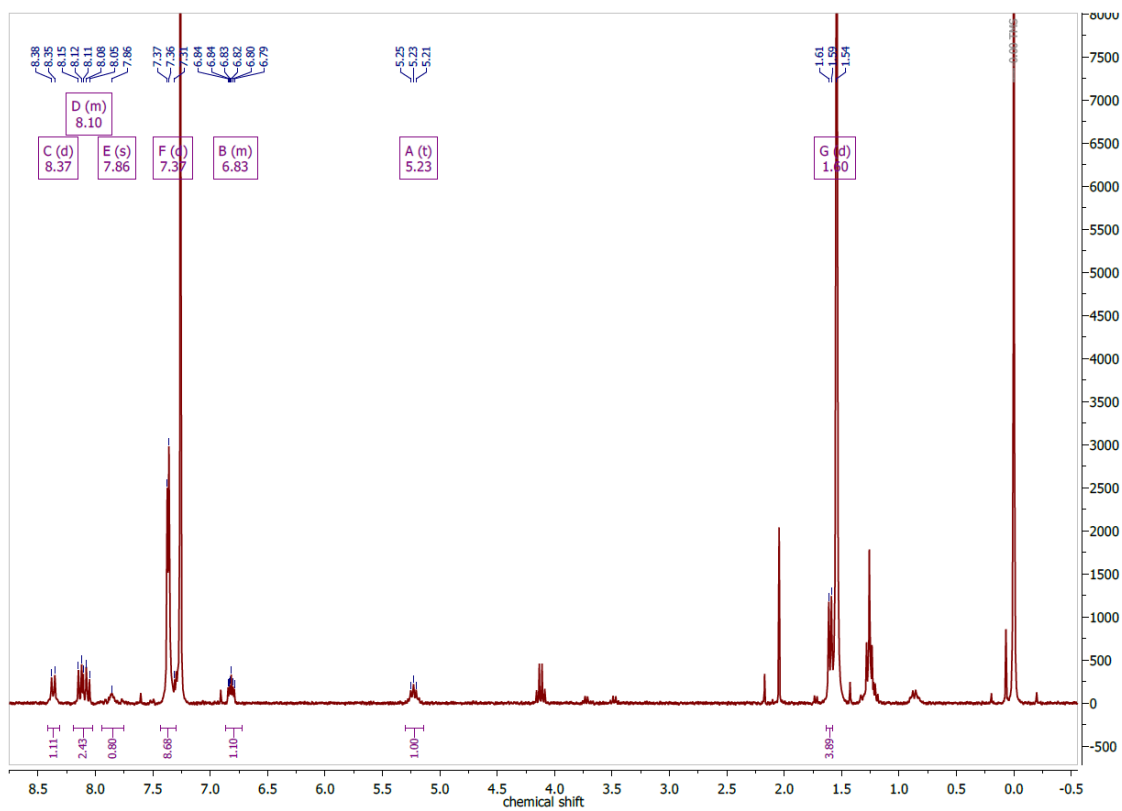


Figure 7.293 ^1H NMR spectrum of $[\text{Pt}(\text{hphfpyTSCmB})]$ in CDCl_3 at 300 MHz.

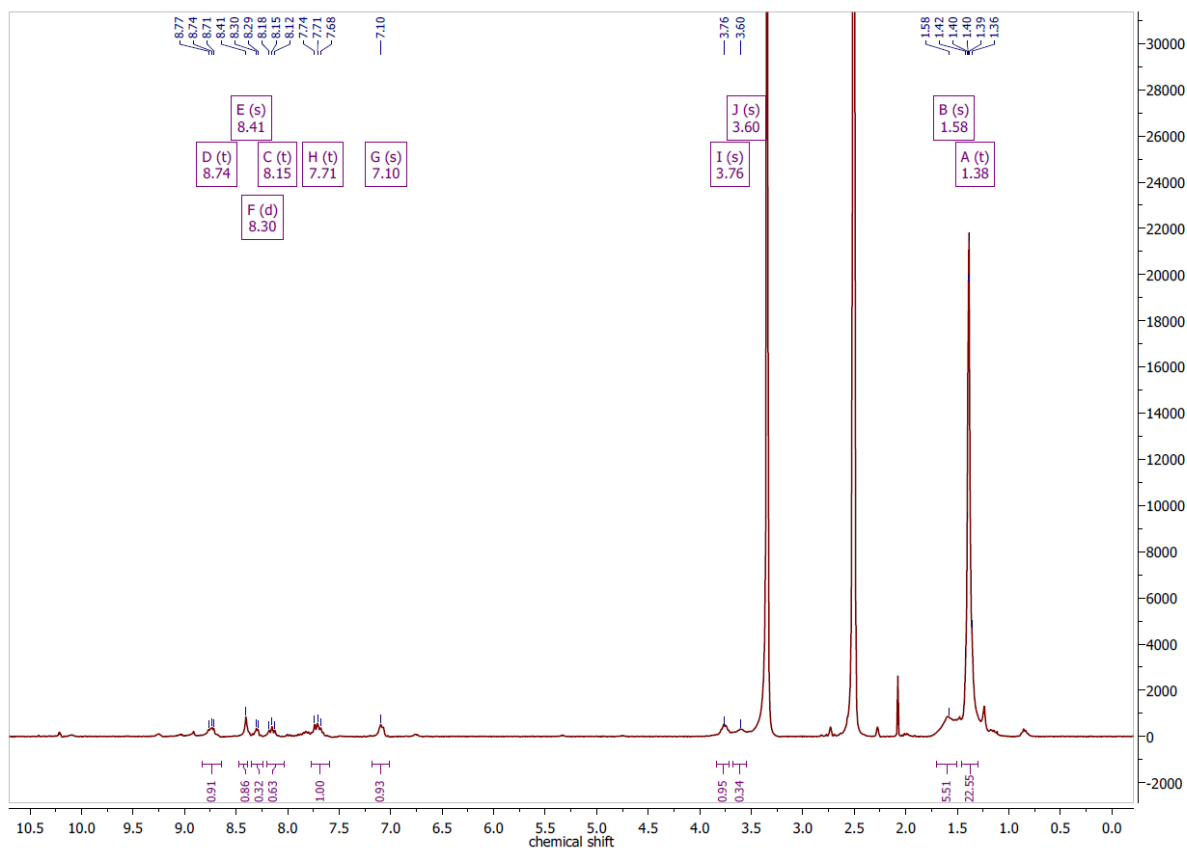


Figure 7.294 ^1H NMR spectrum of $[\text{Pt}(\text{fpyTSCLp})\text{Cl}]$ in $\text{DMSO}-d_6$ at 300 MHz.

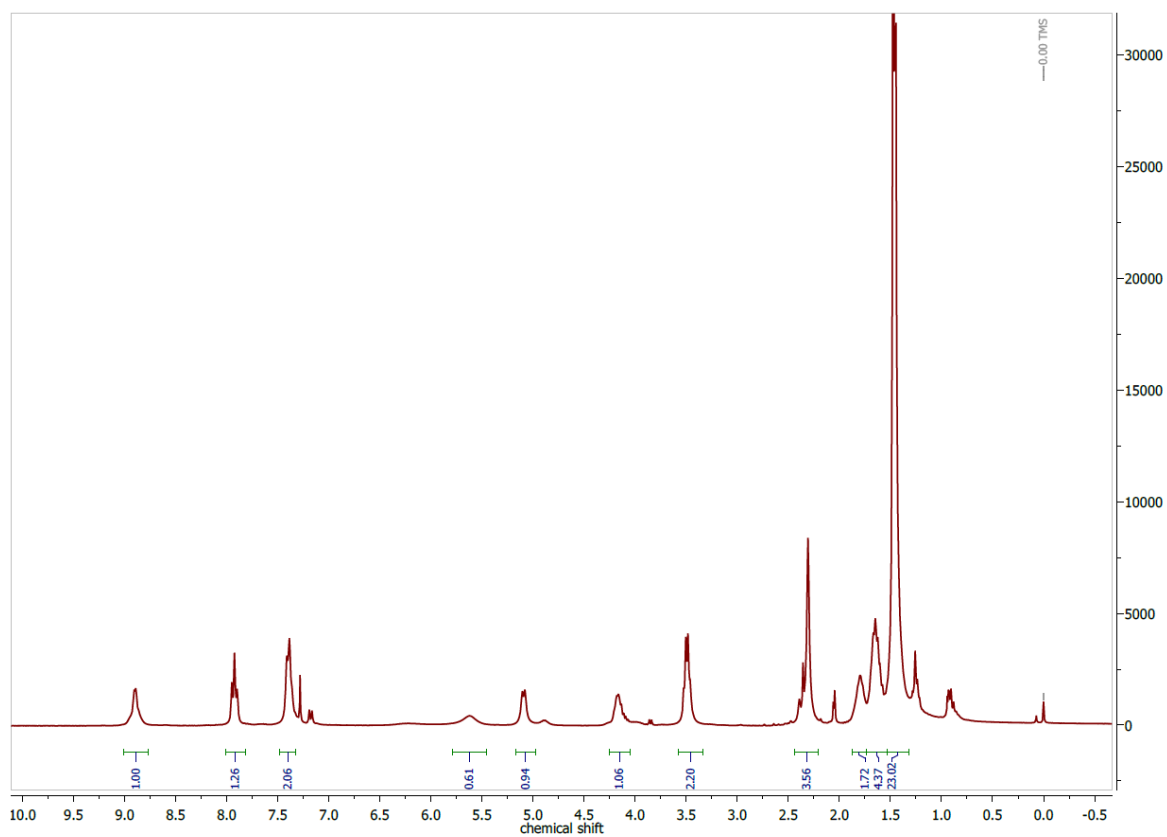


Figure 7.295 ^1H NMR spectrum of $[\text{Pt}(\text{apyTSCLp})\text{Cl}]$ in $\text{DMSO}-d_6$ at 300 MHz.

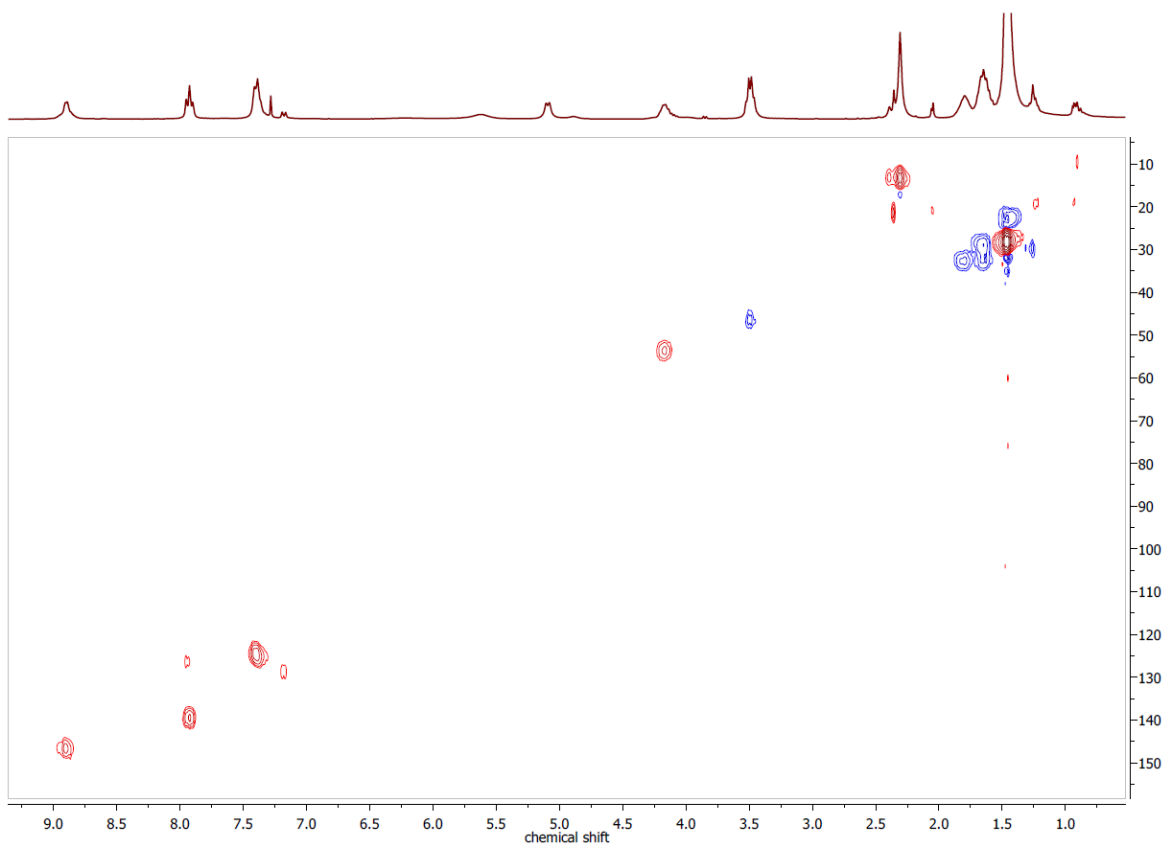


Figure 7.296 ^1H , ^{13}C HSQCed NMR spectrum of $[\text{Pt}(\text{apyTSCLp})\text{Cl}]$ in $\text{DMSO-}d_6$.

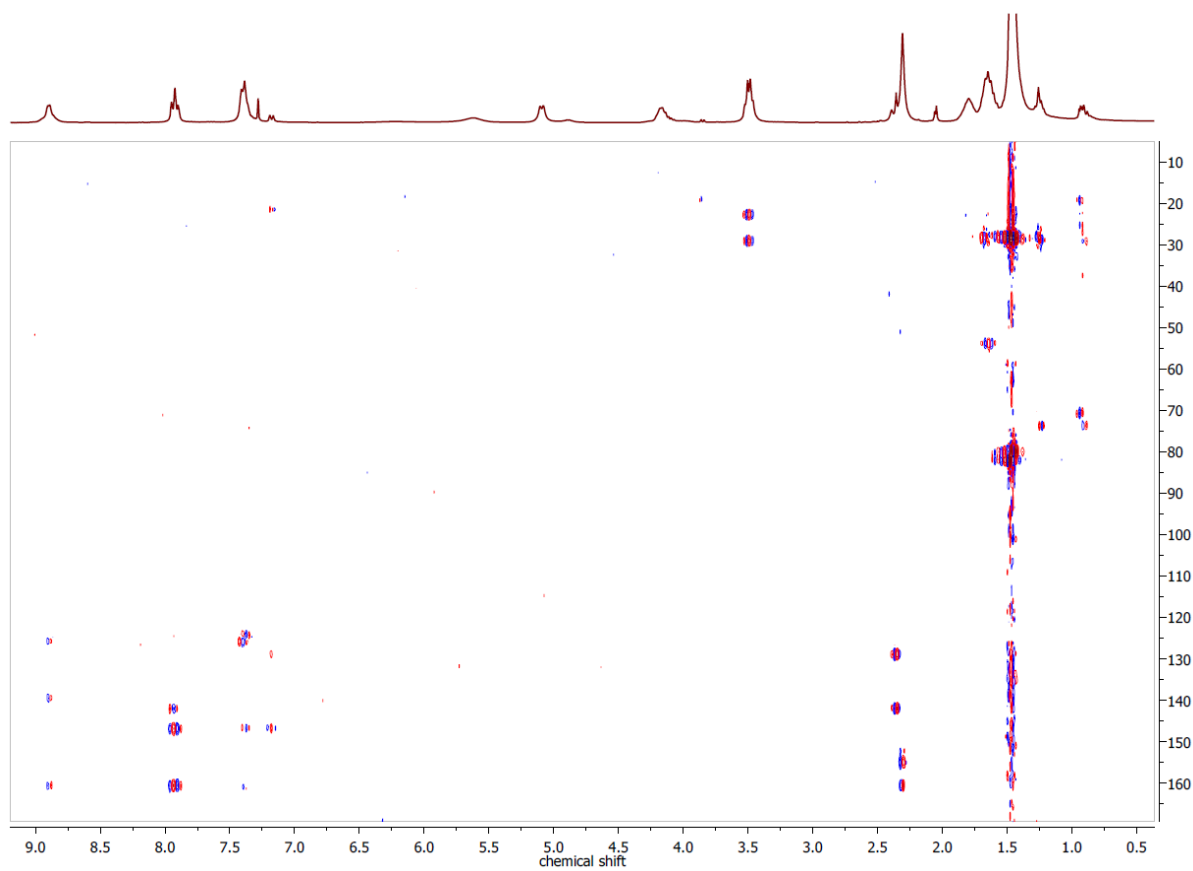


Figure 7.297 ^1H , ^{13}C HMBC NMR spectrum of $[\text{Pt}(\text{apyTSCLp})\text{Cl}]$ in $\text{DMSO-}d_6$.

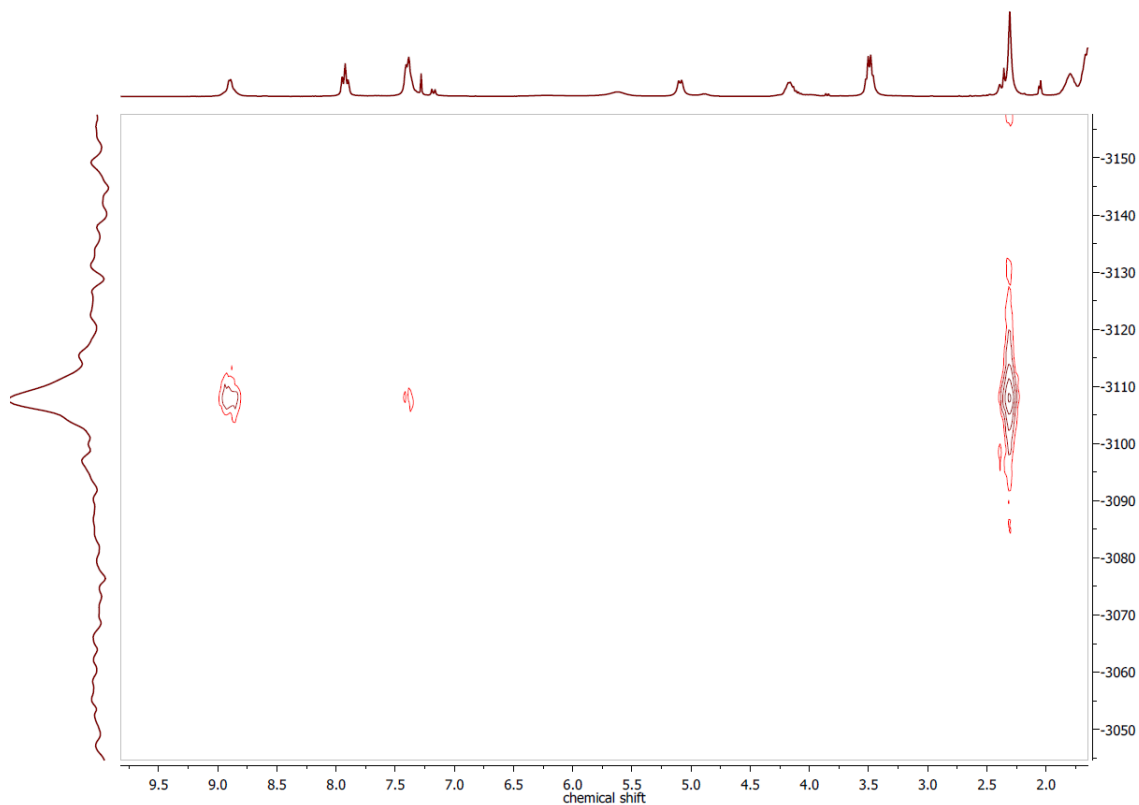


Figure 7.298 $^1\text{H}, ^{195}\text{Pt}$ HMBC NMR spectrum of $[\text{Pt}(\text{apyTSCLp})\text{Cl}]$ in $\text{DMSO-}d_6$.

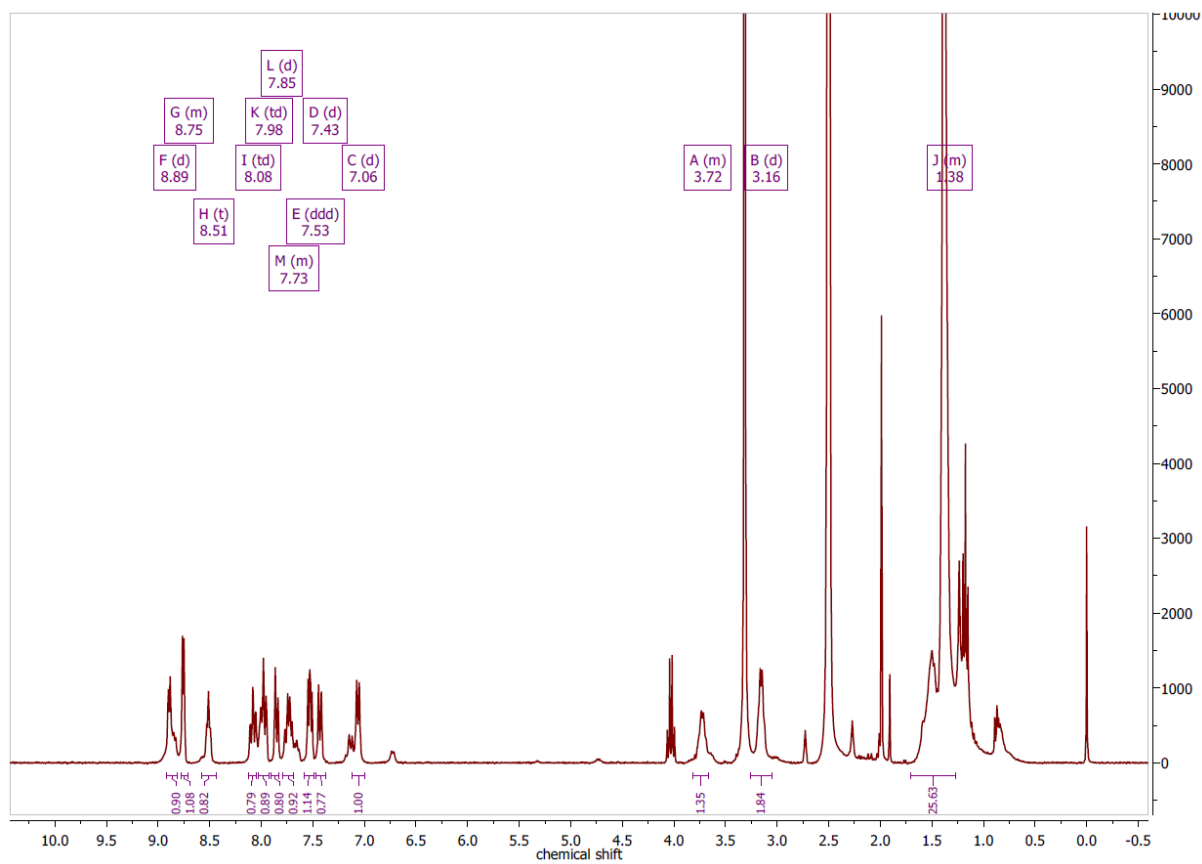


Figure 7.299 ^1H NMR spectrum of $[\text{Pt}(\text{dpyTSCLp})\text{Cl}]$ in $\text{DMSO-}d_6$ at 300 MHz.

7.7. NMR of catalysis crude mixtures

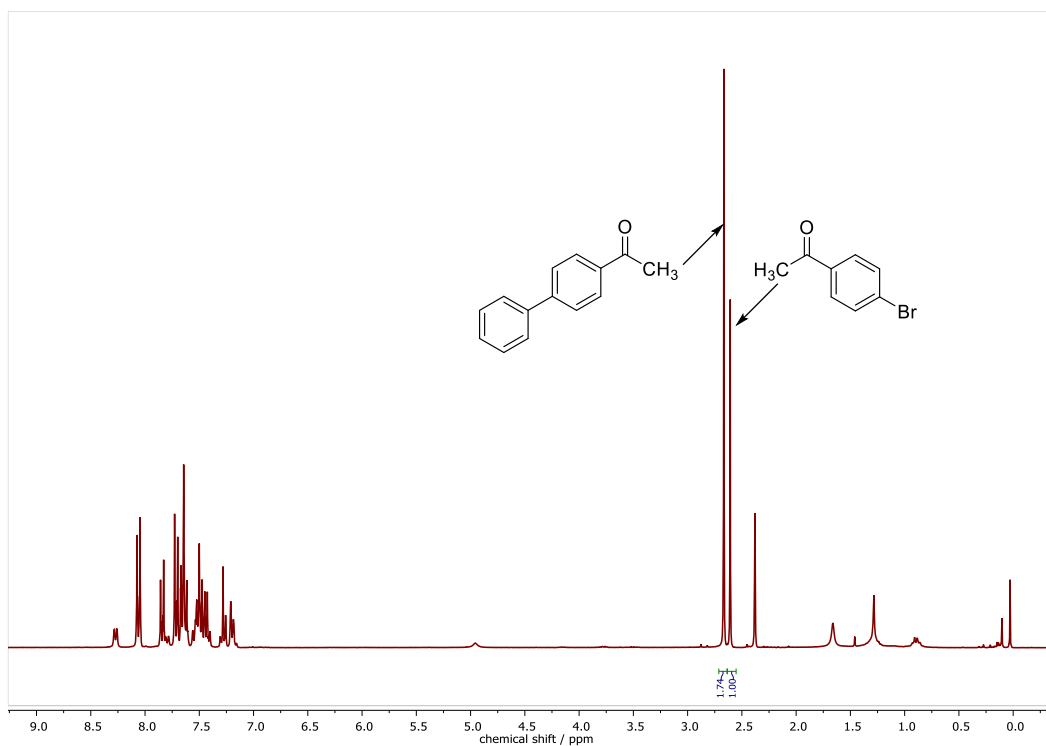


Figure 7.300 ^1H NMR spectrum of the crude mixture of the *Suzuki* reaction between 4-iodo acetophenone and phenyl boronic acid with $[\text{Pd}(\text{PPh}_3)(\text{bzTSCpBa})\text{Cl}]$ as catalyst in CDCl_3 at 300 MHz. The integrals of the acetyl moiety are used for quantification.

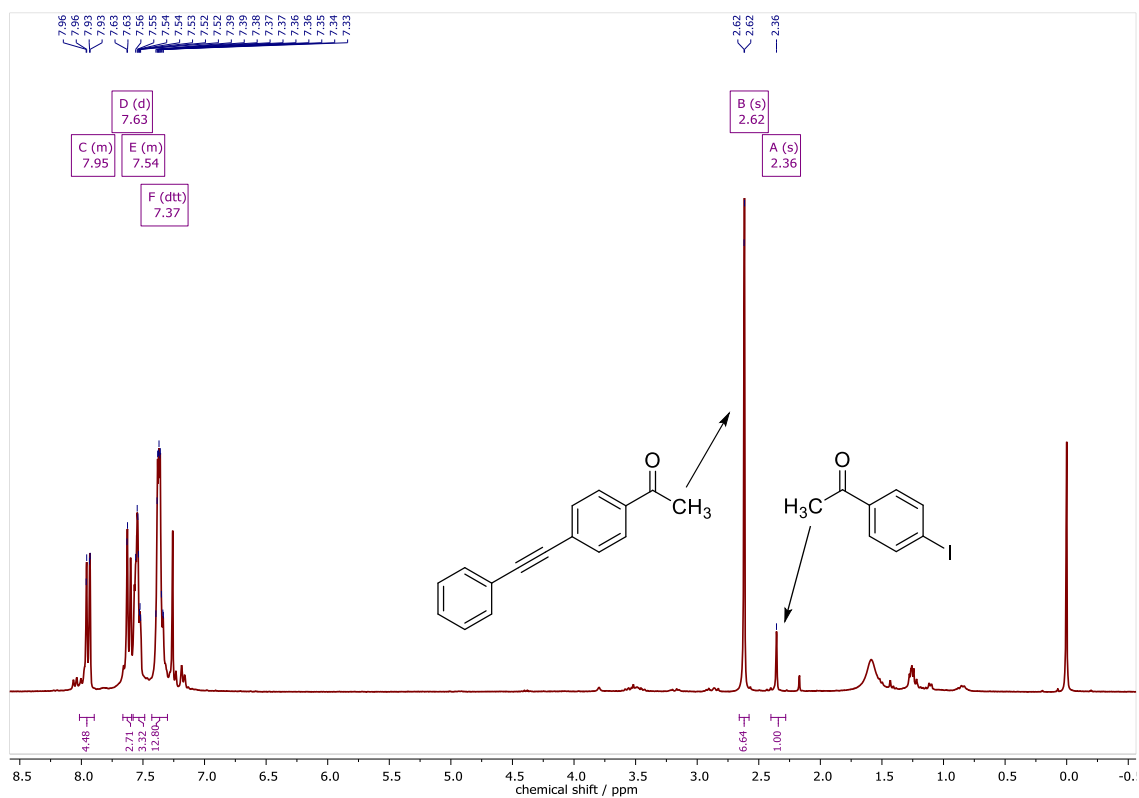


Figure 7.301 ^1H NMR spectrum of the crude mixture of the *Sonogashira* reaction between 4-iodo acetophenone and phenyl boronic acid with $[\text{Pd}(\text{PPh}_3)(\text{aphTSClP})\text{Cl}]$ as catalyst in CDCl_3 at 300 MHz. The integrals of the acetyl moiety are used for quantification.

7.8. Mass spectra

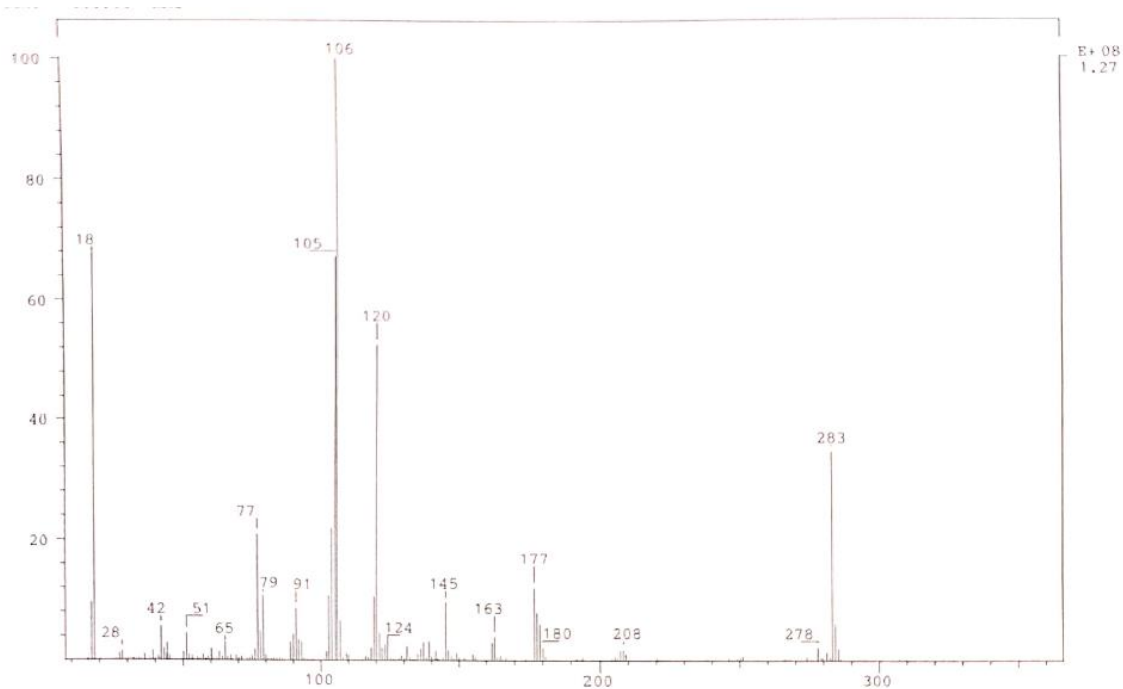


Figure 7.302 EI-MS spectrum of H₂bzTSCmB at 70 eV.

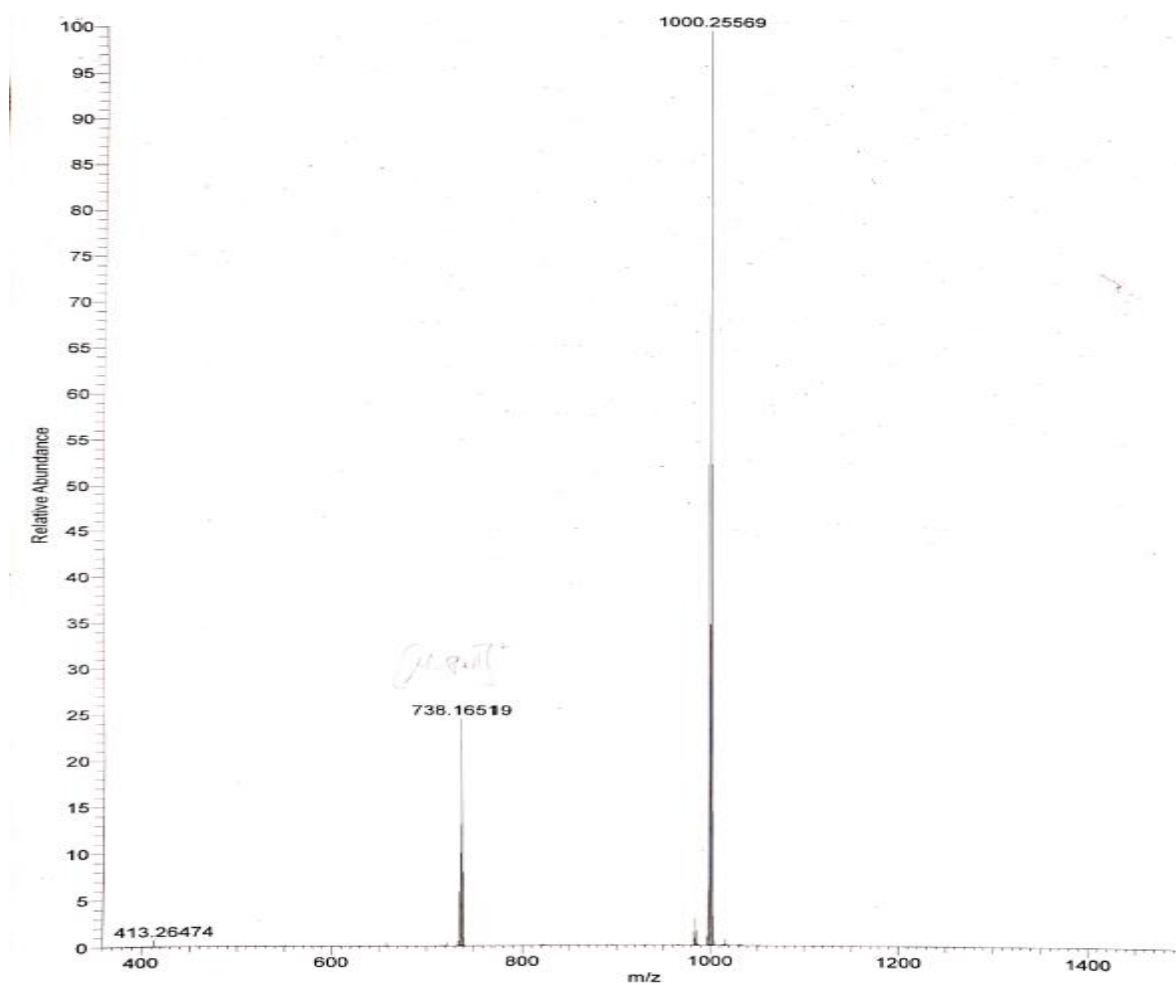


Figure 7.303 HR-ESI-MS spectrum of [Ir(PPh₃)₂(bzTSCmB)H].

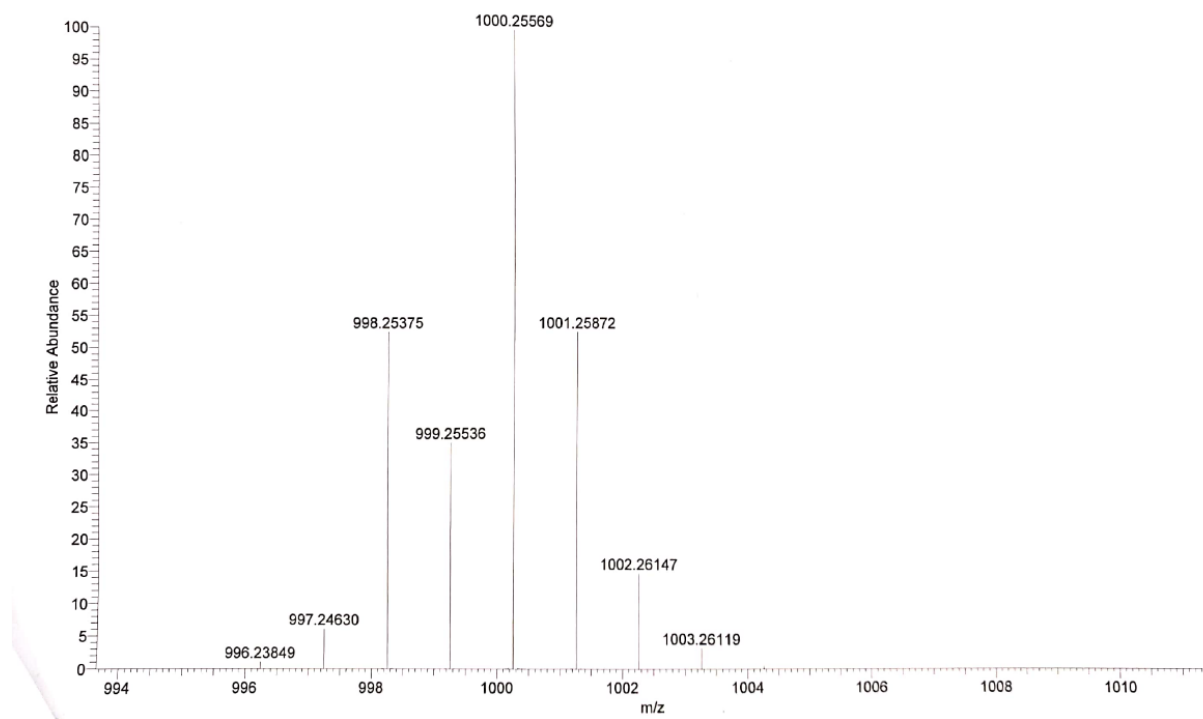


Figure 7.304 Excerpt of HR-ESI-MS spectrum of $[\text{Ir}(\text{PPh}_3)_2(\text{bzTSCmB})\text{H}]$.

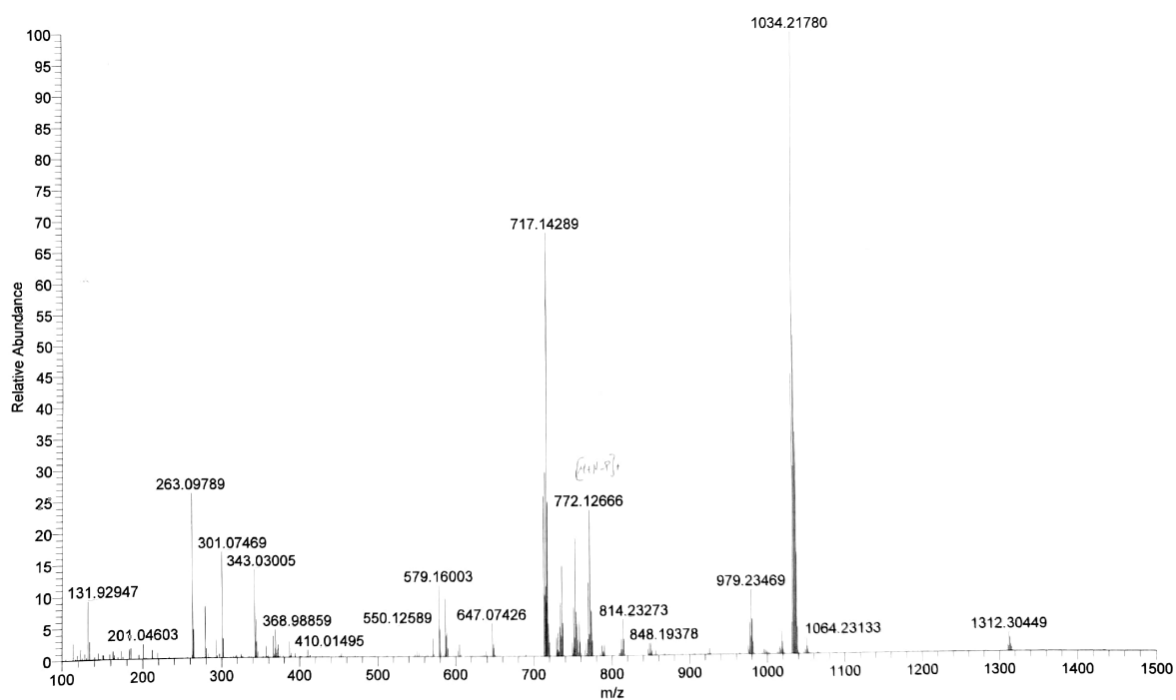


Figure 7.305 HR-ESI-MS spectrum of $[\text{Ir}(\text{PPh}_3)_2(\text{bzTSCmB})\text{Cl}]$.

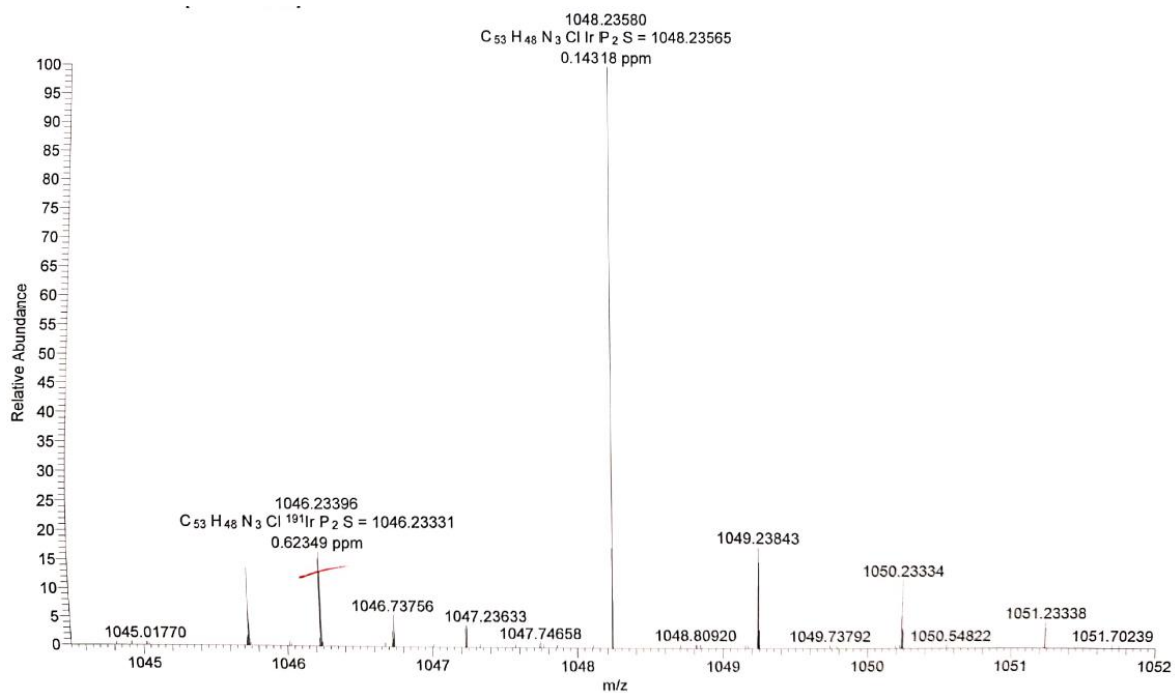


Figure 7.306 HR-ESI-MS spectrum of $[\text{Ir}(\text{PPh}_3)_2(\text{aphTSCmB})\text{Cl}]$.

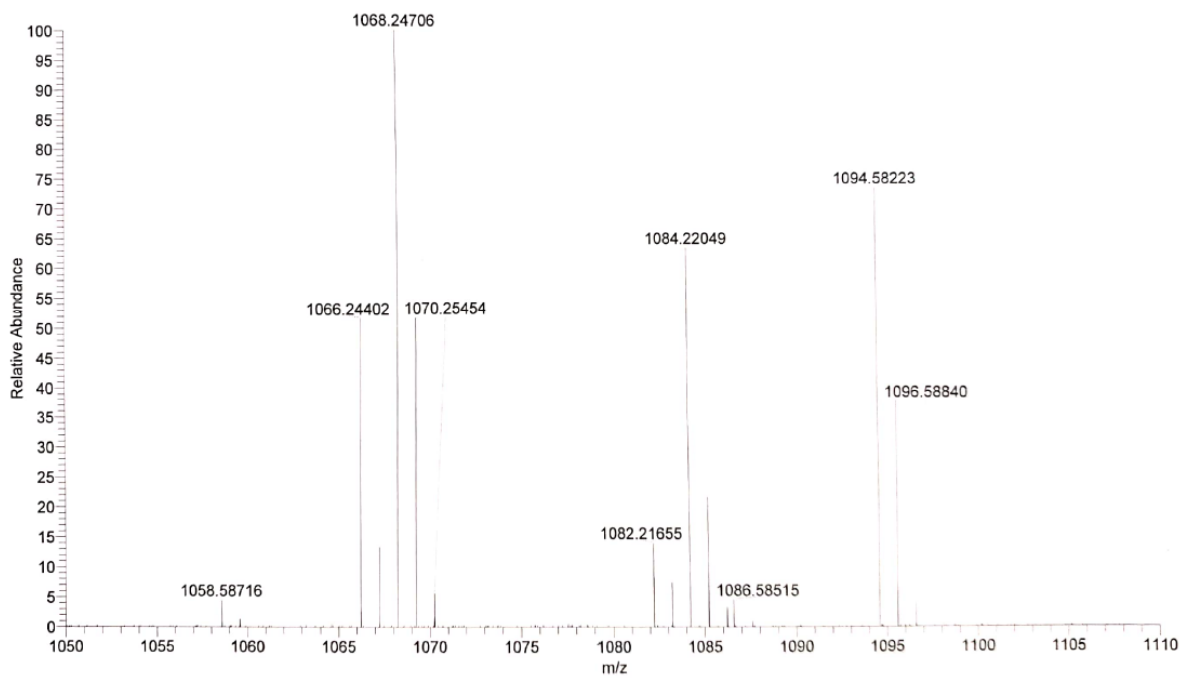


Figure 7.307 HR-ESI-MS spectrum of $[\text{Ir}(\text{PPh}_3)_2(\text{aph(m)TSCmB})\text{Cl}]$.

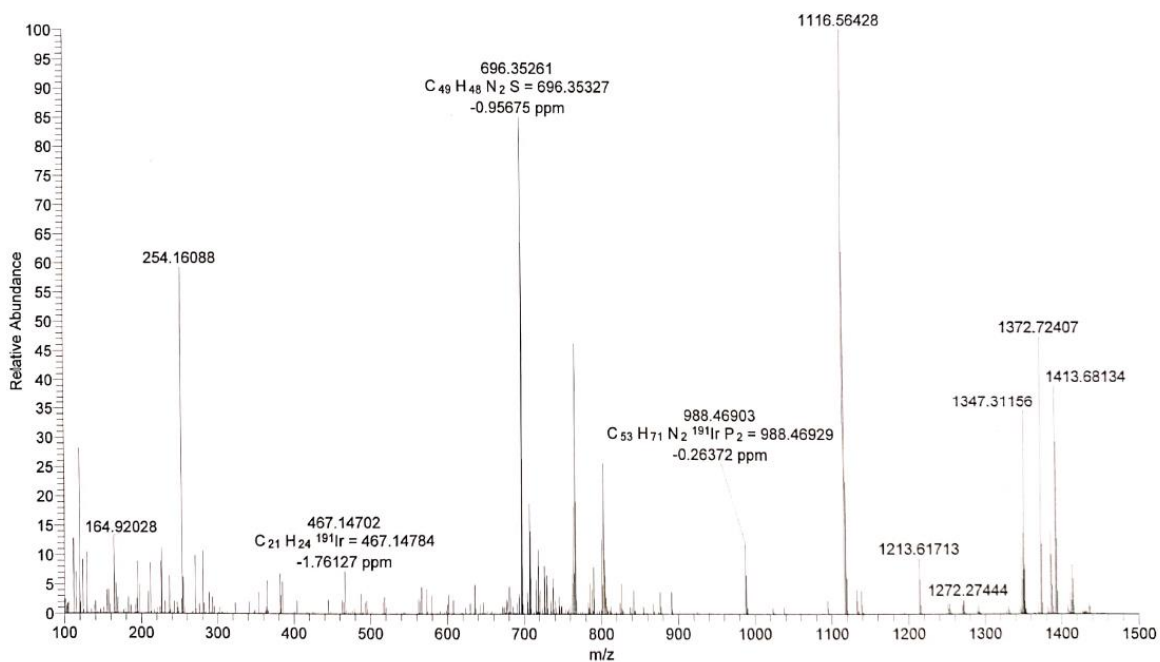


Figure 7.308 HR-ESI-MS spectrum of $[\text{Ir}(\text{PCy}_3)(\text{aphTSCmB})\text{H}]$.

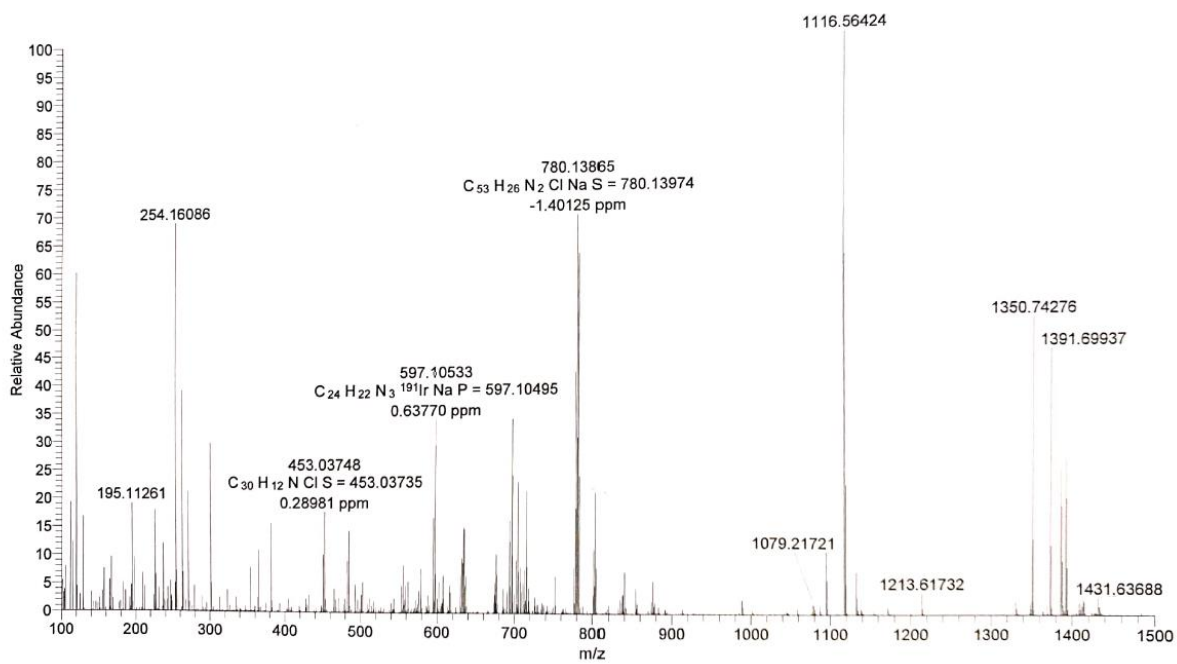


Figure 7.309 HR-ESI-MS spectrum of $[\text{Ir}(\text{PCy}_3)(\text{aphTSCmB})\text{Cl}]$.

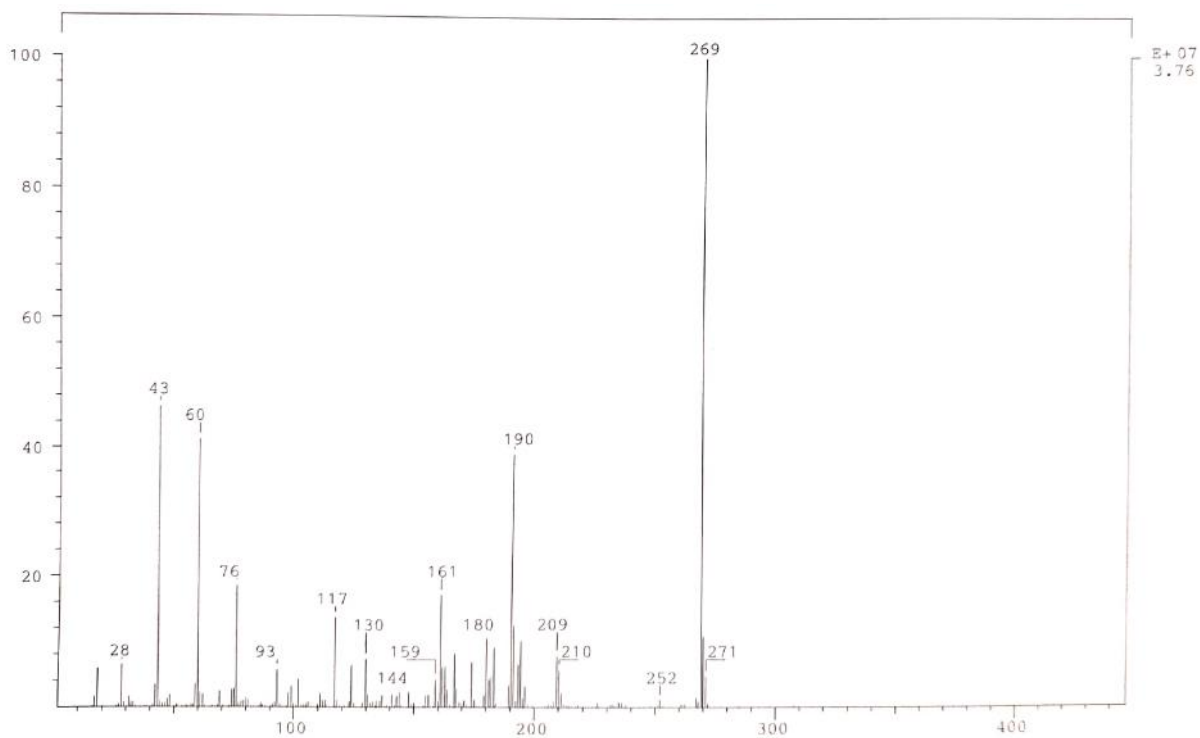


Figure 7.310 EI-MS spectrum of HFbzTSC at 70 eV.

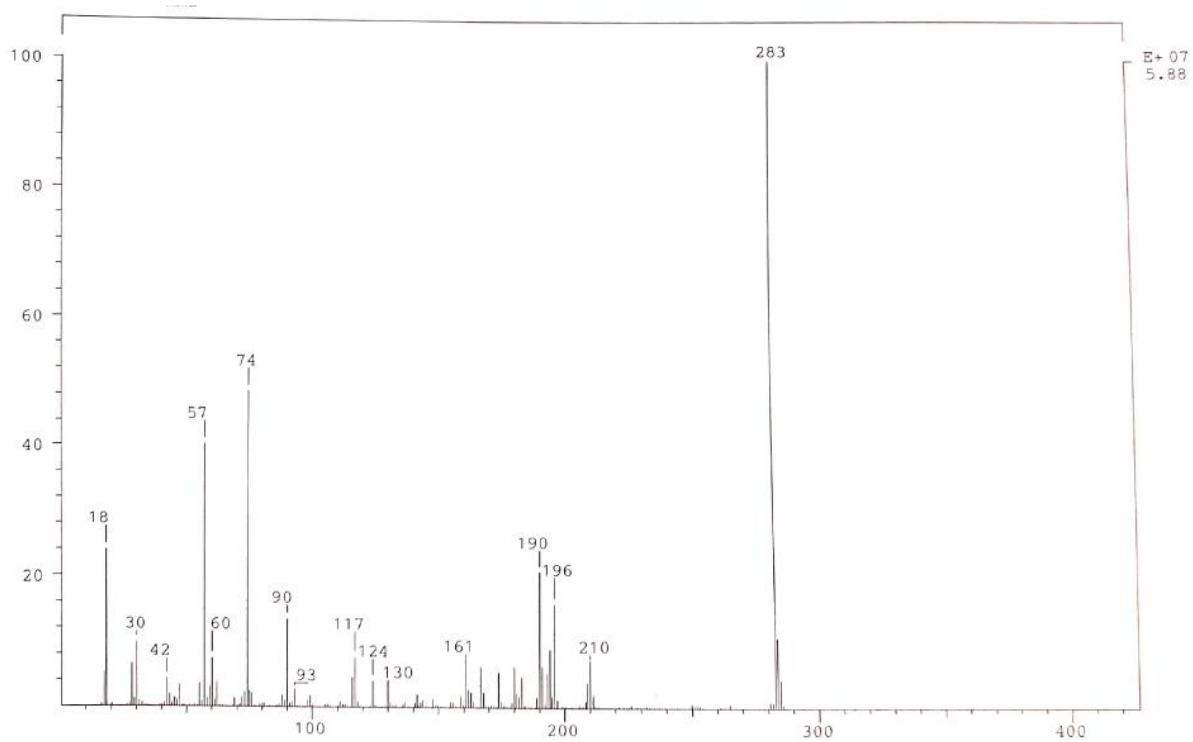


Figure 7.311 EI-MS spectrum of HFbzTSCm at 70 eV.

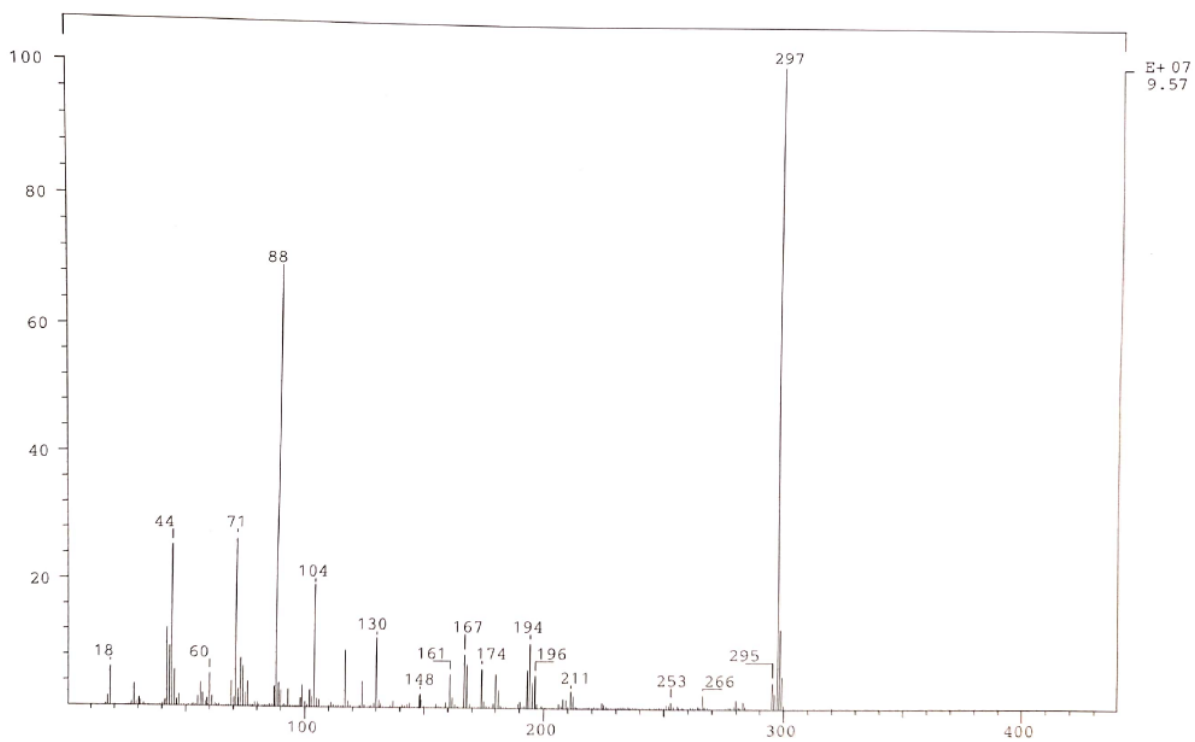


Figure 7.312 EI-MS spectrum of HFbzTSCdm at 70 eV.

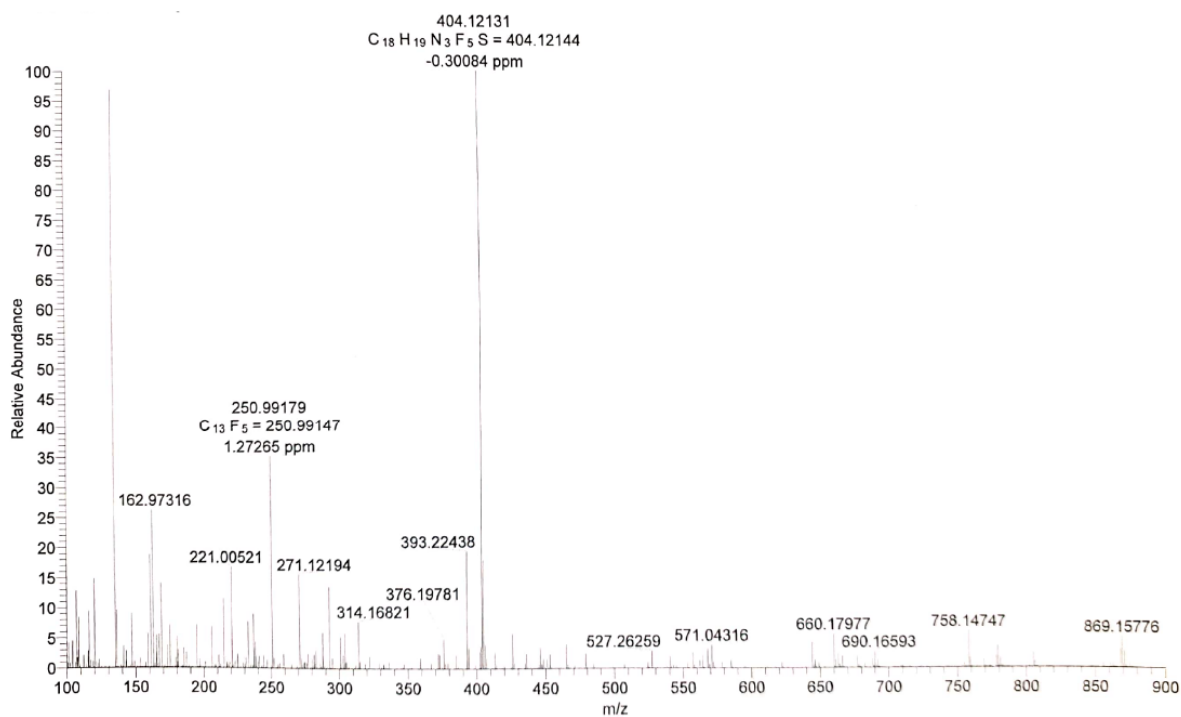


Figure 7.313 HR-ESI-MS spectrum of HFbzTSCAd.

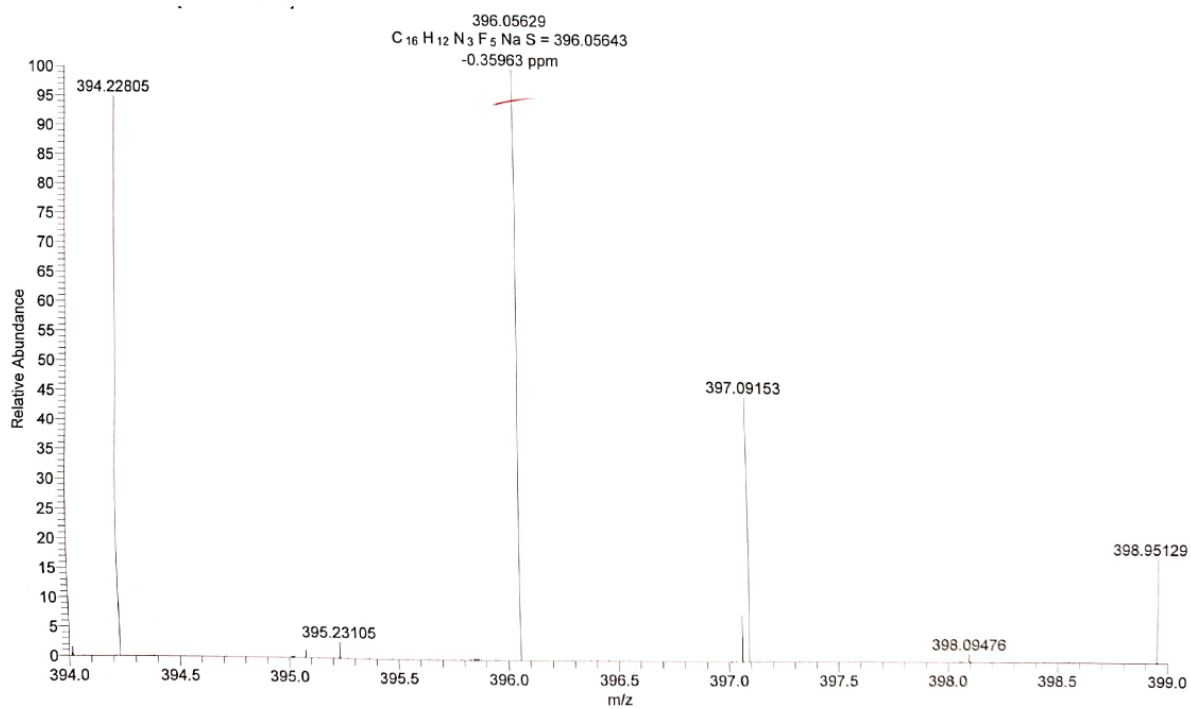


Figure 7.314 HR-ESI-MS spectrum of HFbzTSCmB.

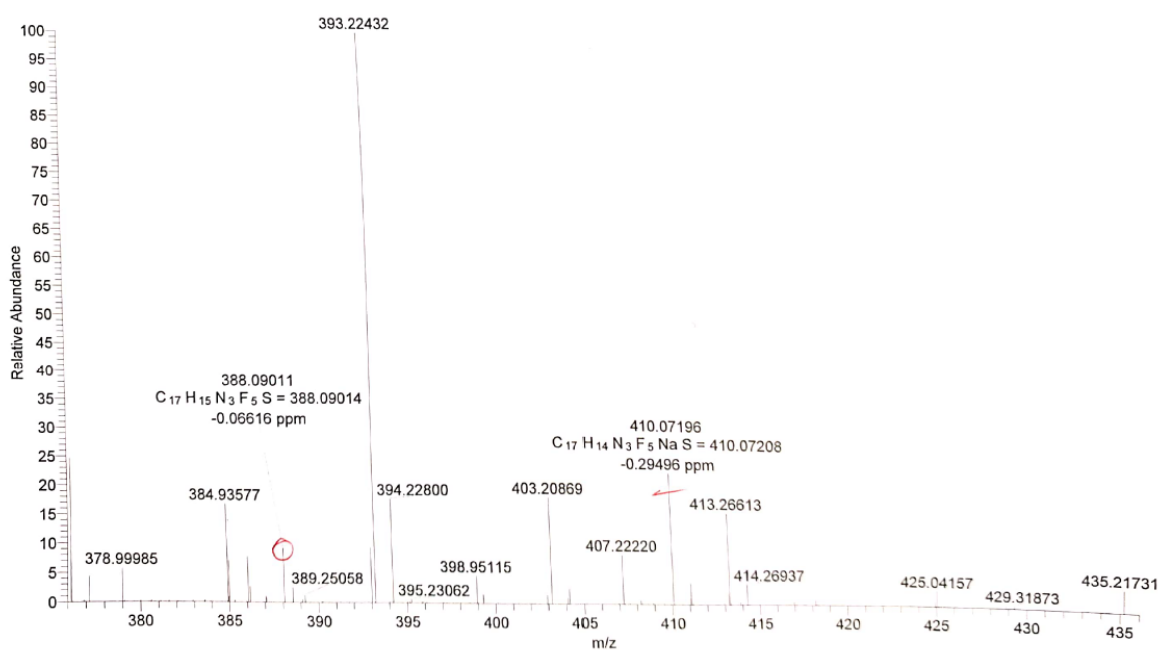


Figure 7.315 HR-ESI-MS spectrum of HFbz(m)TSCmB.

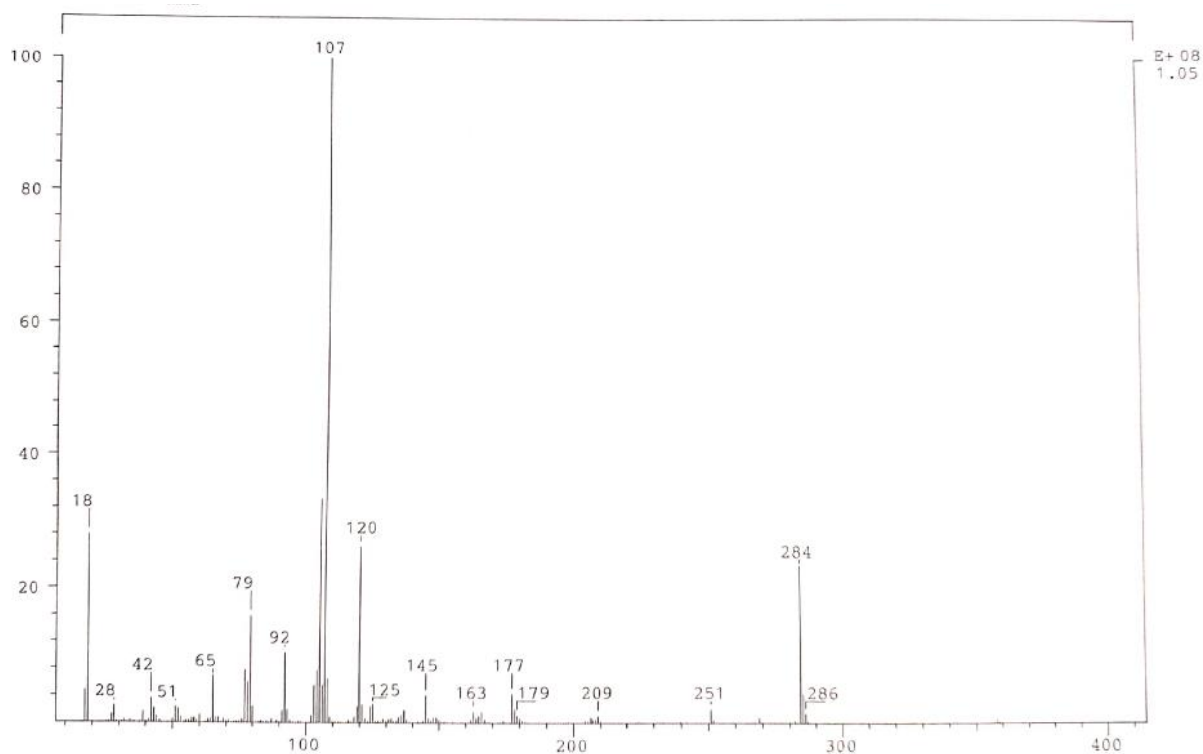


Figure 7.316 EI-MS spectrum of HfpyTSCmB at 70 eV.

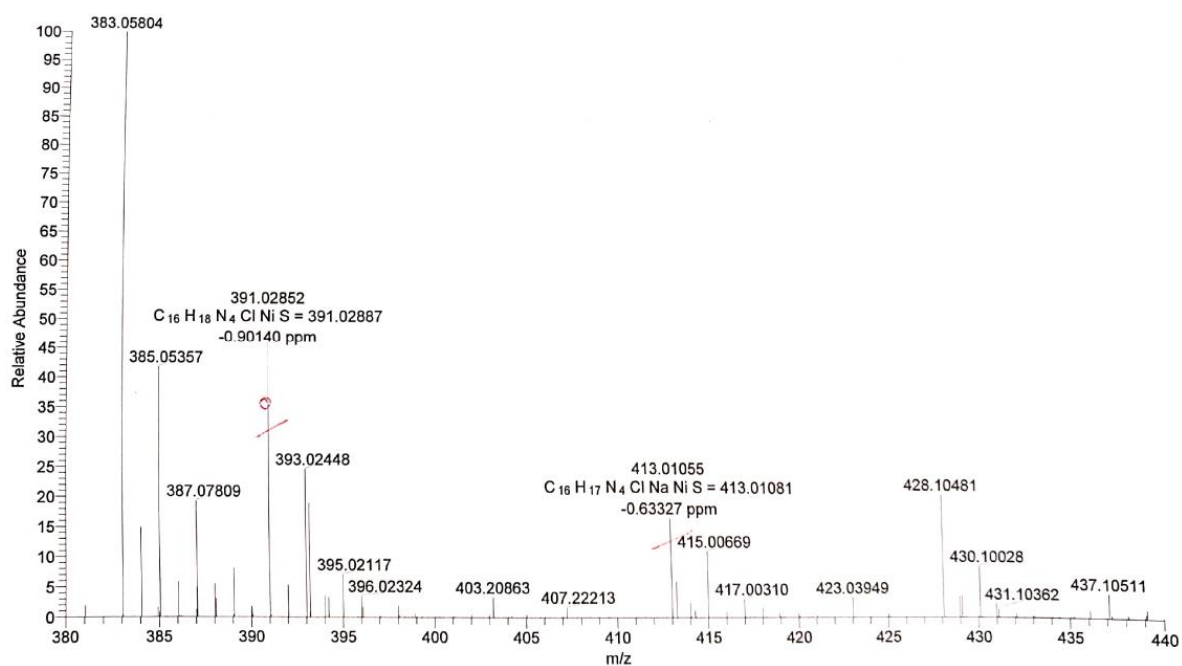


Figure 7.317 HR-ESI-MS spectrum of [Ni(apyTSCmB)Cl].

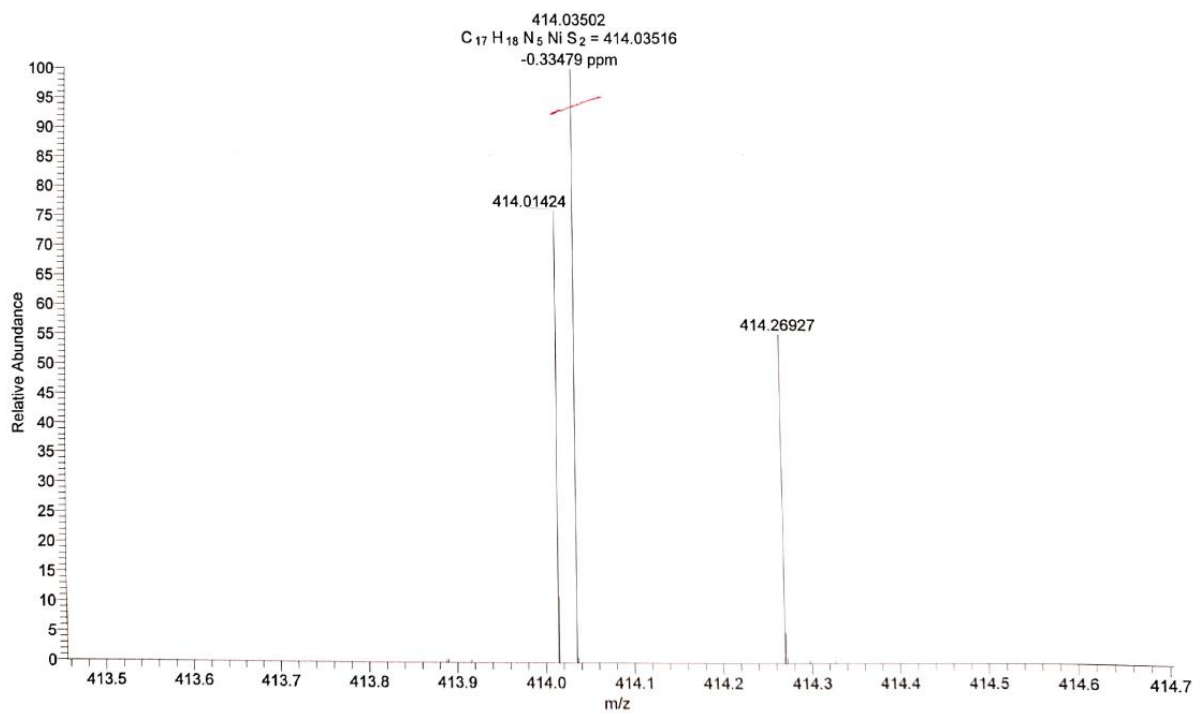


Figure 7.318 HR-ESI-MS spectrum of [Ni(apyTSCmB)NCS].

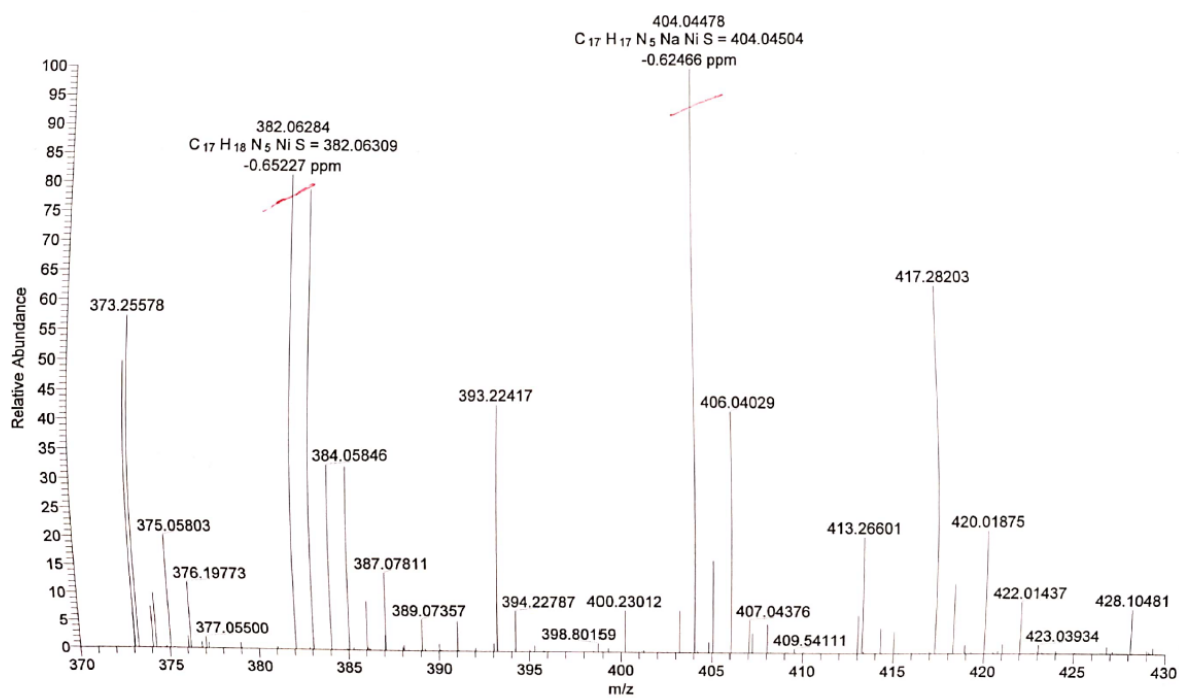


Figure 7.319 HR-ESI-MS spectrum of [Ni(apyTSCmB)CN].

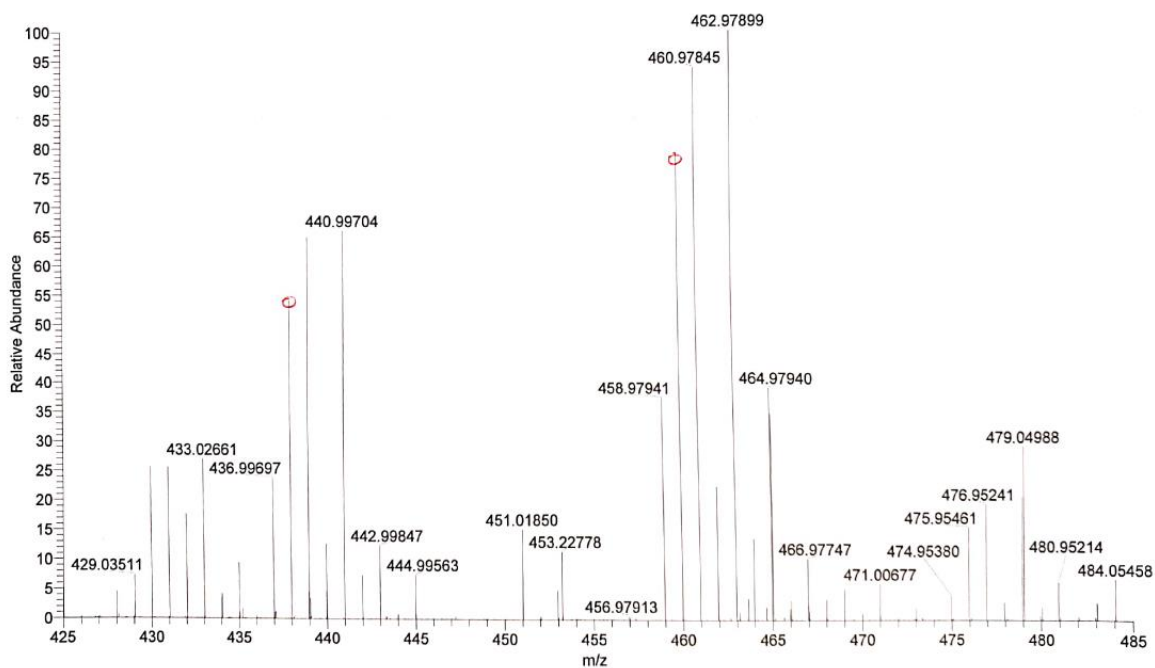


Figure 7.320 HR-ESI-MS spectrum of [Pd(apyTSCmB)Cl].

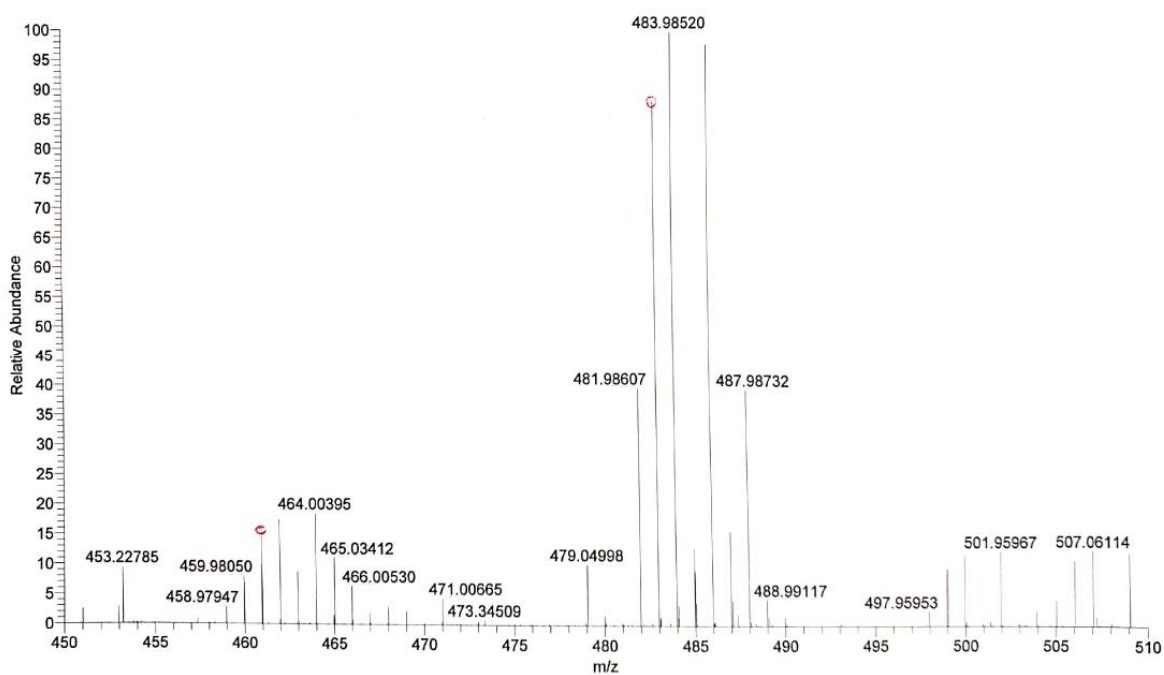


Figure 7.321 HR-ESI-MS spectrum of [Pd(apyTSCmB)NCS].

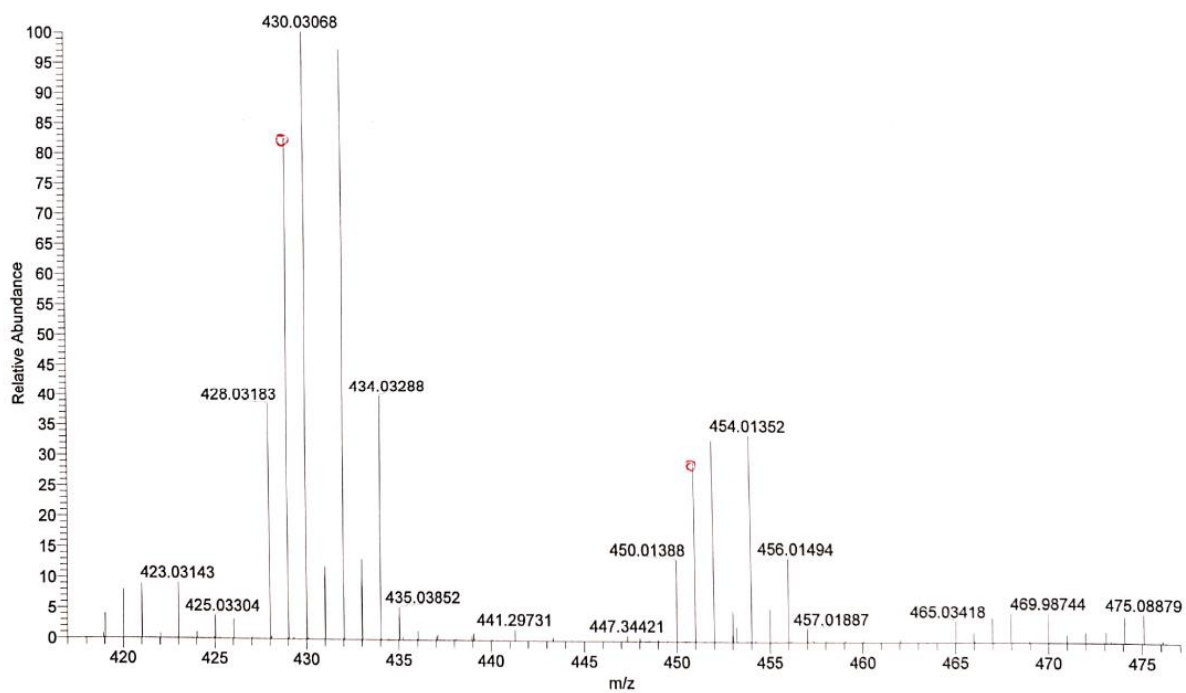


Figure 7.322 HR-ESI-MS spectrum of [Pd(apyTSCmB)CN].

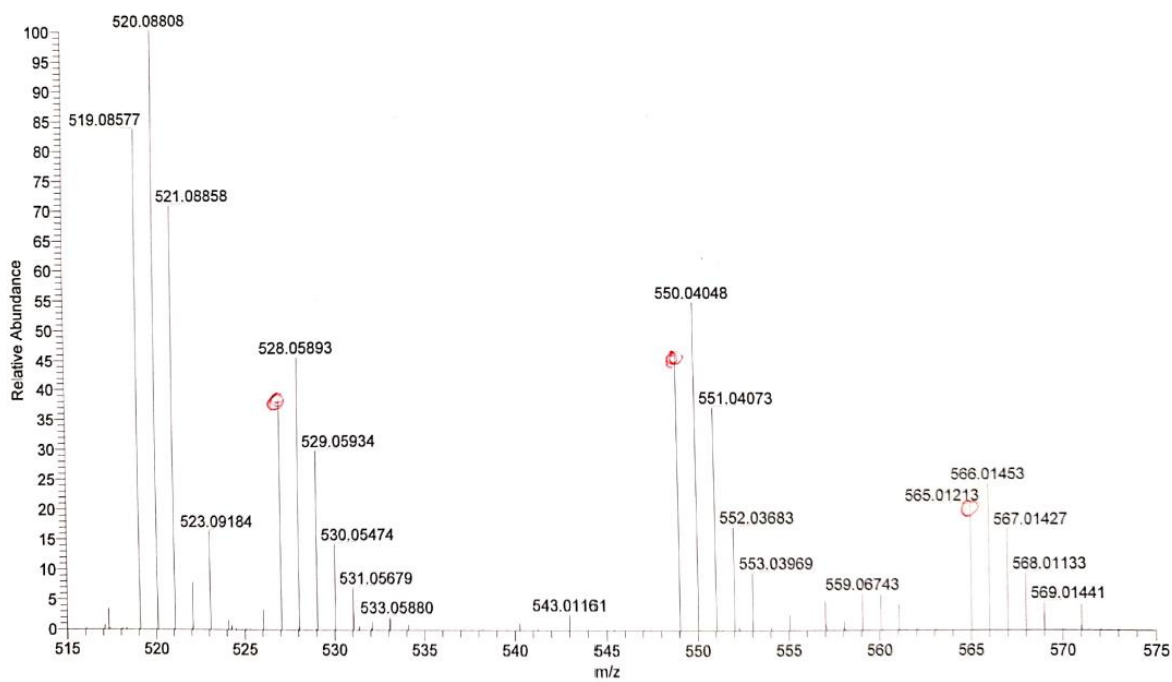


Figure 7.323 HR-ESI-MS spectrum of [Pt(apyTSCmB)Cl].

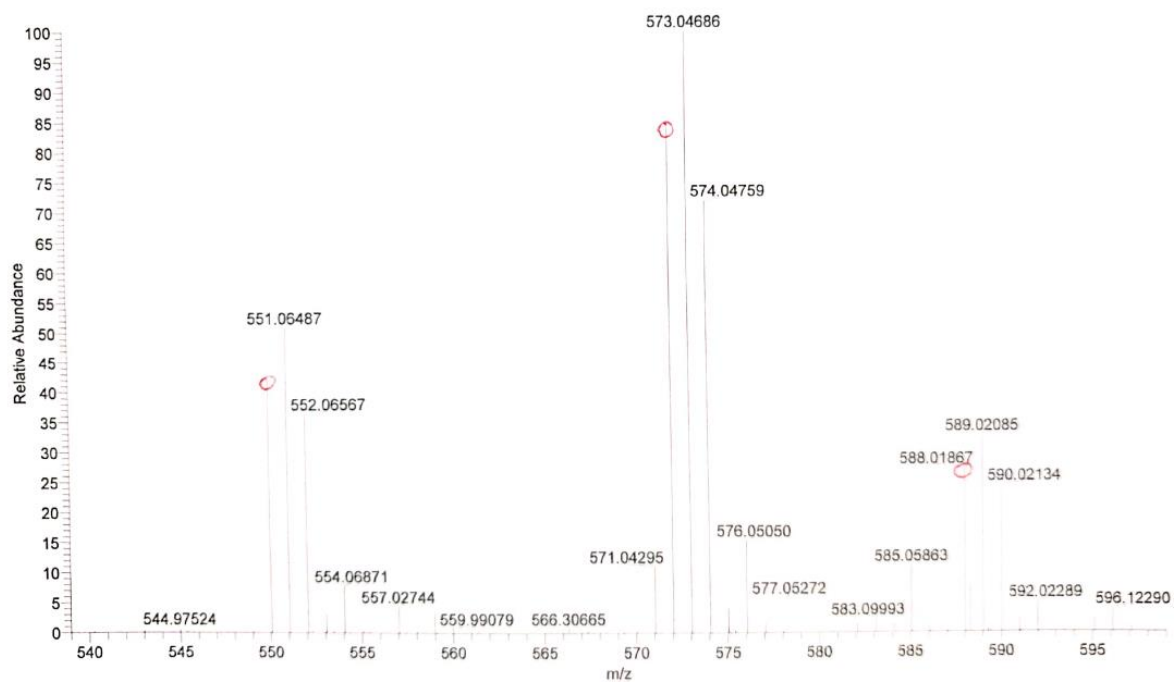


Figure 7.324 HR-ESI-MS spectrum of [Pt(apyTSCmB)NCS].

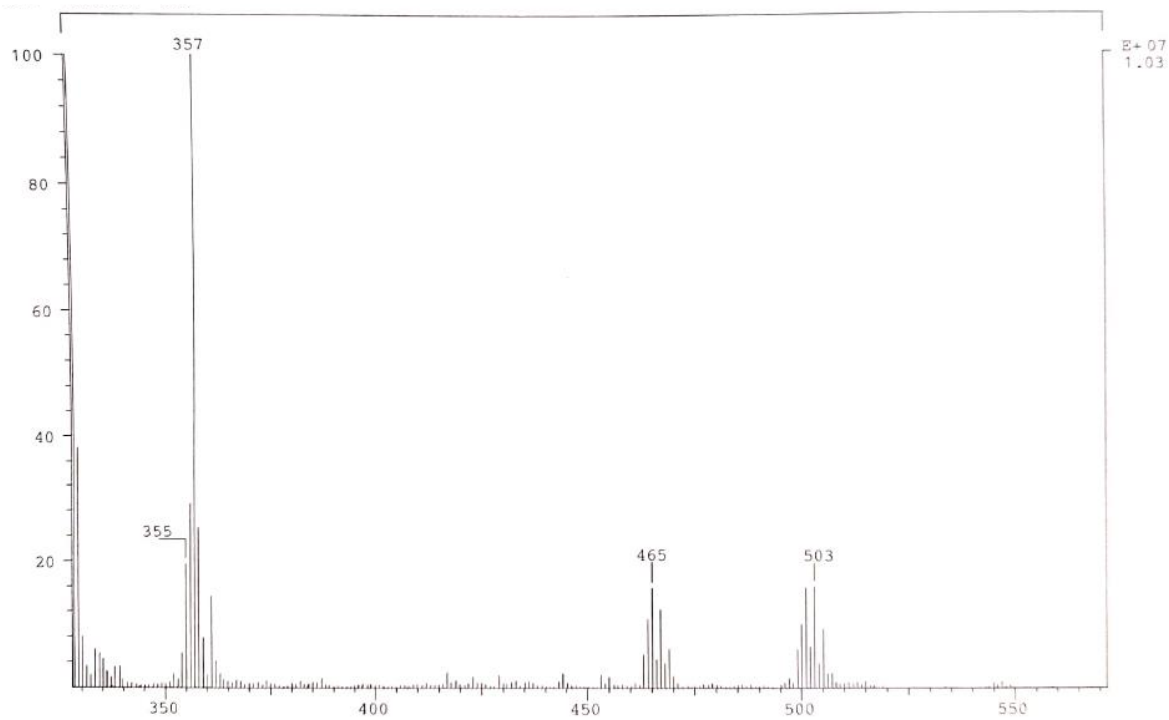


Figure 7.325 EI-MS spectrum of [Pd(dpyTSCmB)Cl].

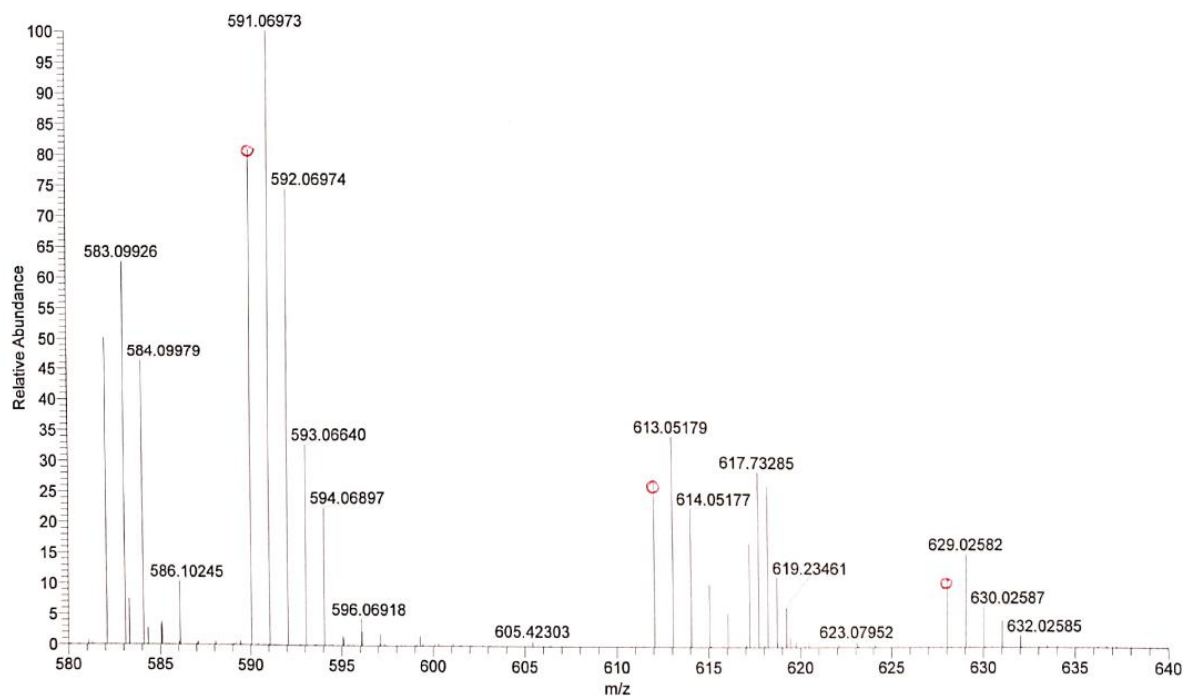


Figure 7.326 HR-ESI-MS spectrum of [Pt(dpyTSCmB)Cl].

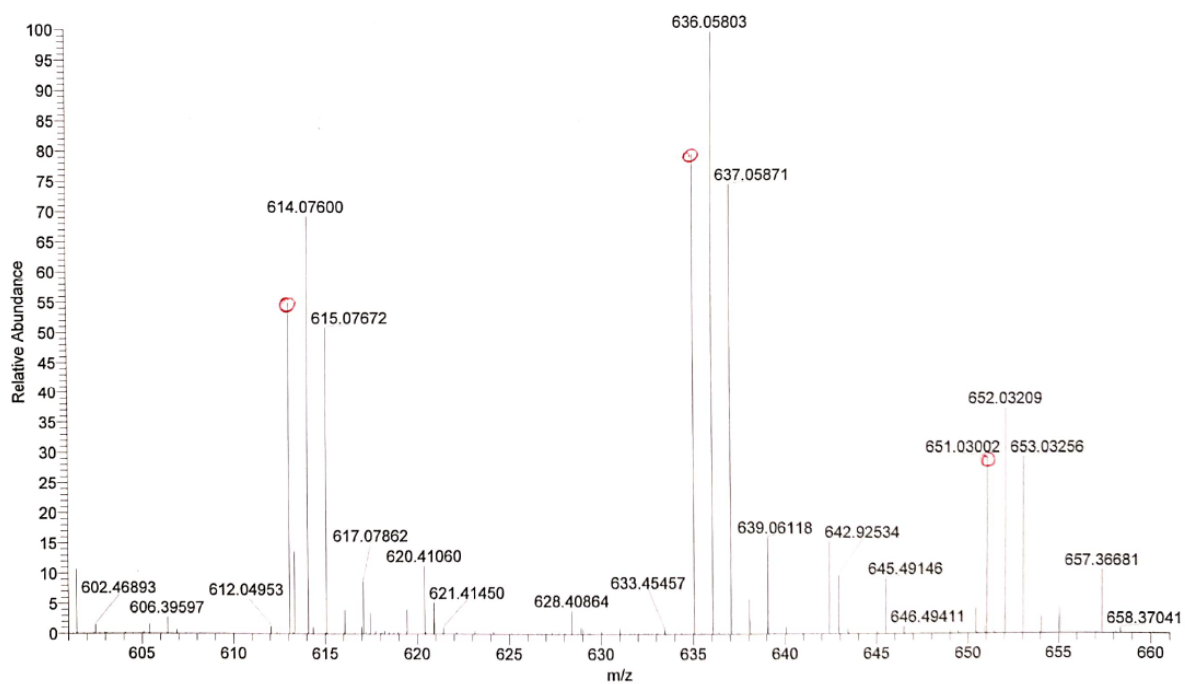


Figure 7.327 HR-ESI-MS spectrum of [Pt(dpyTSCmB)NCS].

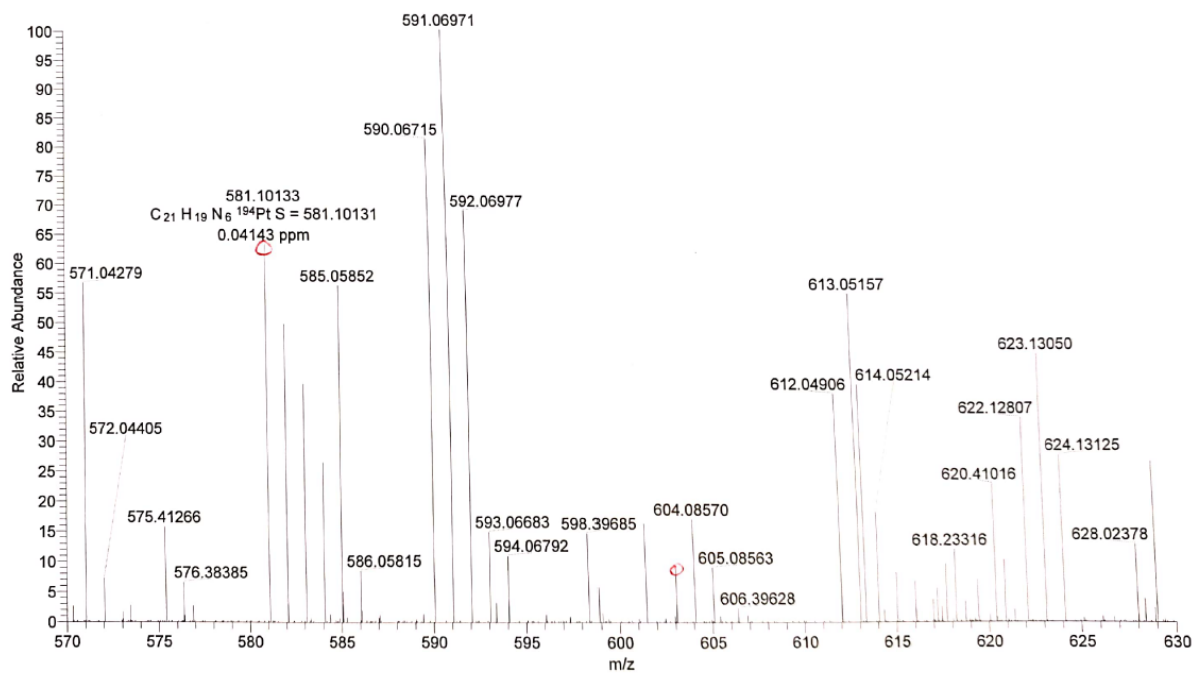


Figure 7.328 HR-ESI-MS spectrum of [Pt(dpyTSCmB)CN].

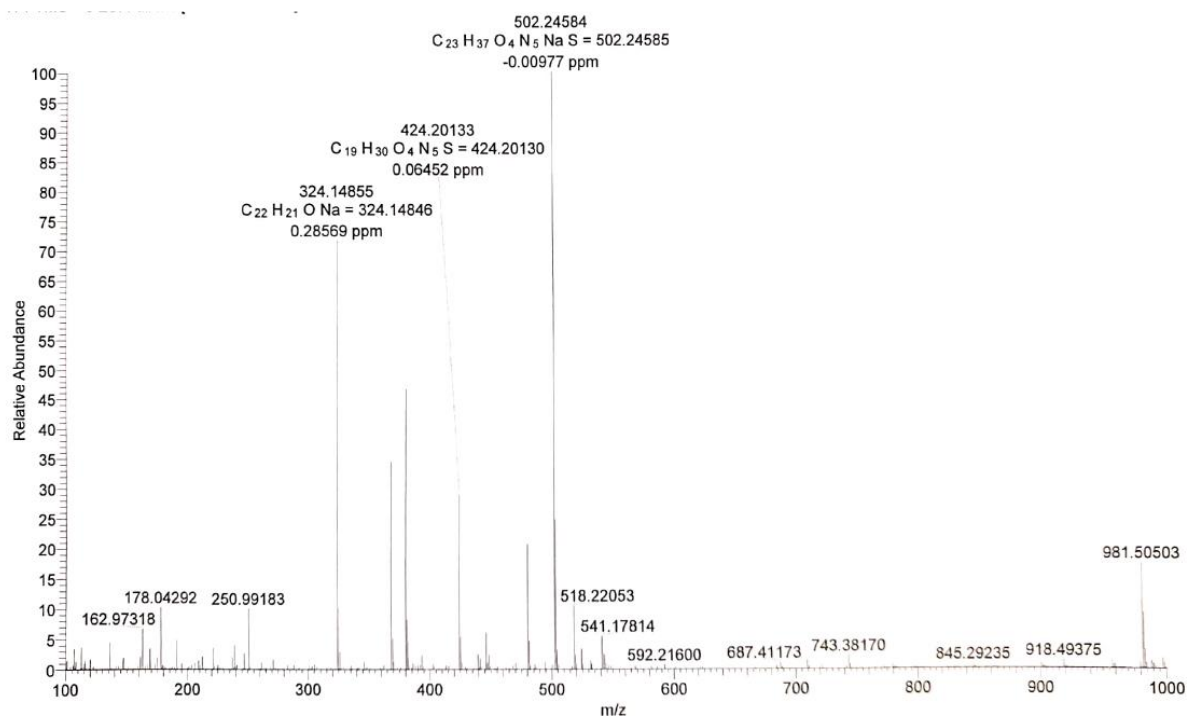


Figure 7.329 HR-ESI-MS spectrum of HapyTSCLp.

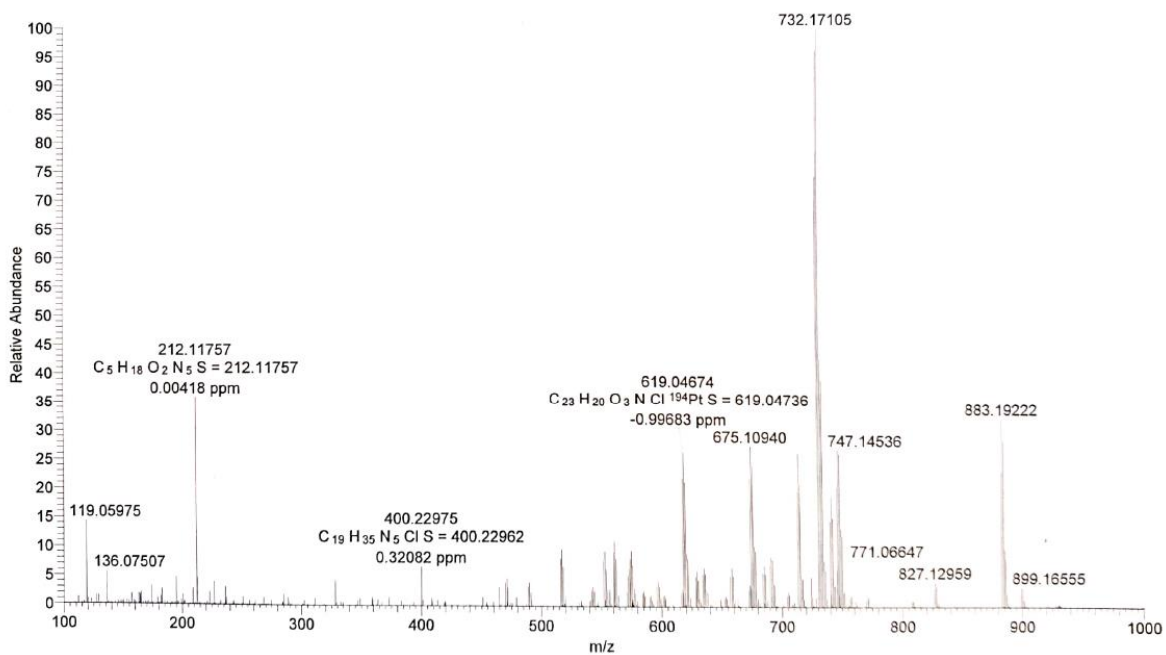


Figure 7.330 HR-ESI-MS spectrum of [Pt(apyTSCLp)Cl].

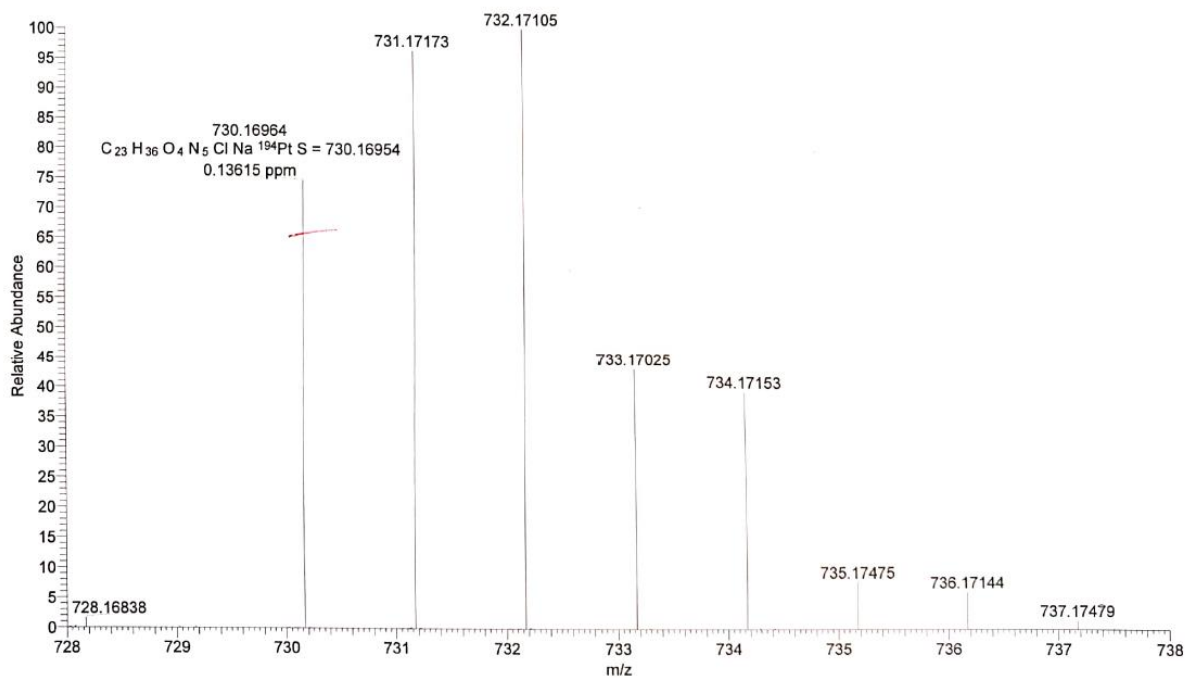


Figure 7.331 Excerpt of HR-ESI-MS spectrum of [Pt(apyTSCLp)Cl].

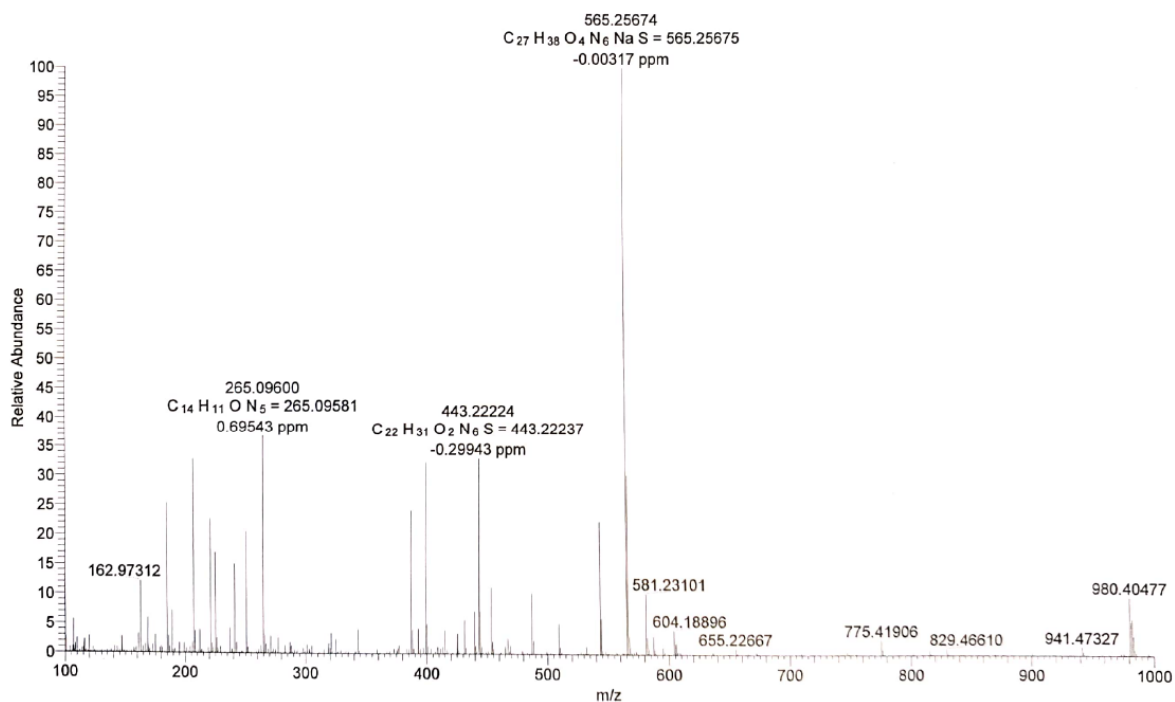


Figure 7.332 HR-ESI-MS spectrum of HdpyTSCLp.

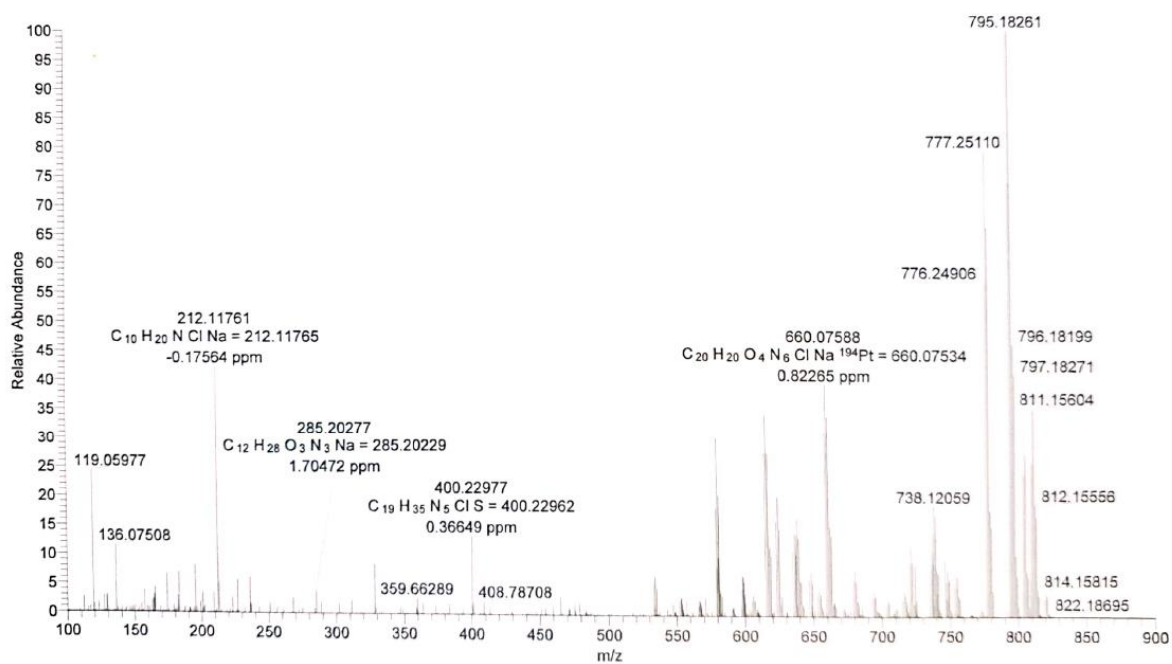


Figure 7.333 HR-ESI-MS spectrum of [Pt(dpyTSCLp)Cl].

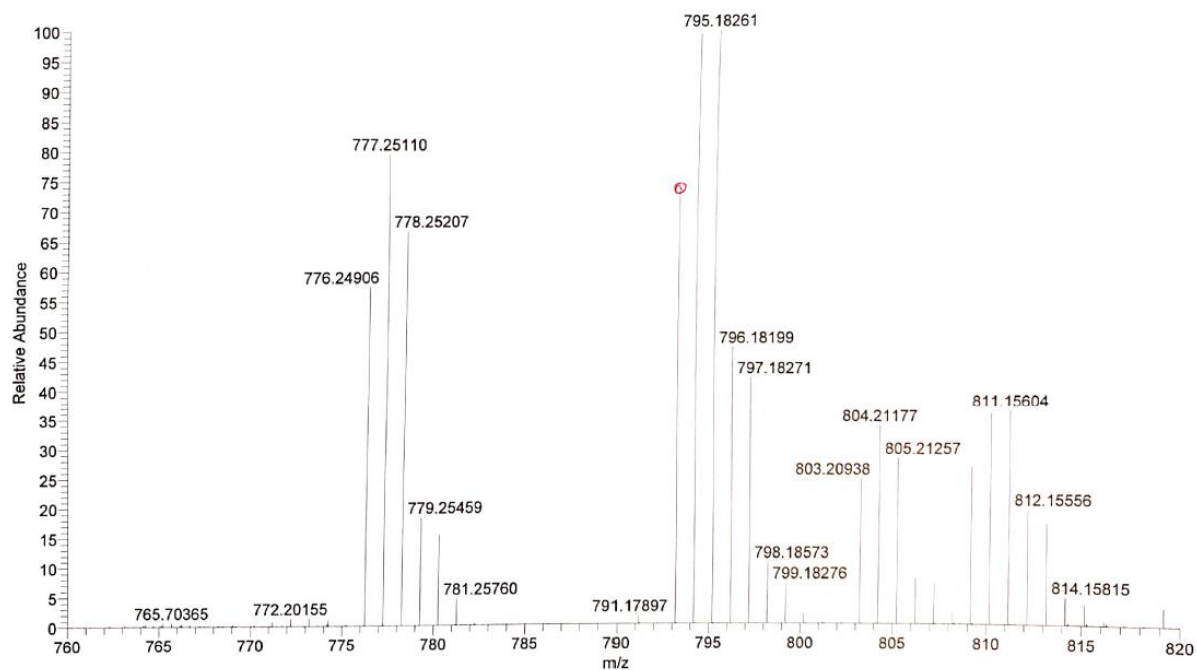


Figure 7.334 Excerpt of HR-ESI-MS spectrum of [Pt(dpyTSCl)Cl].

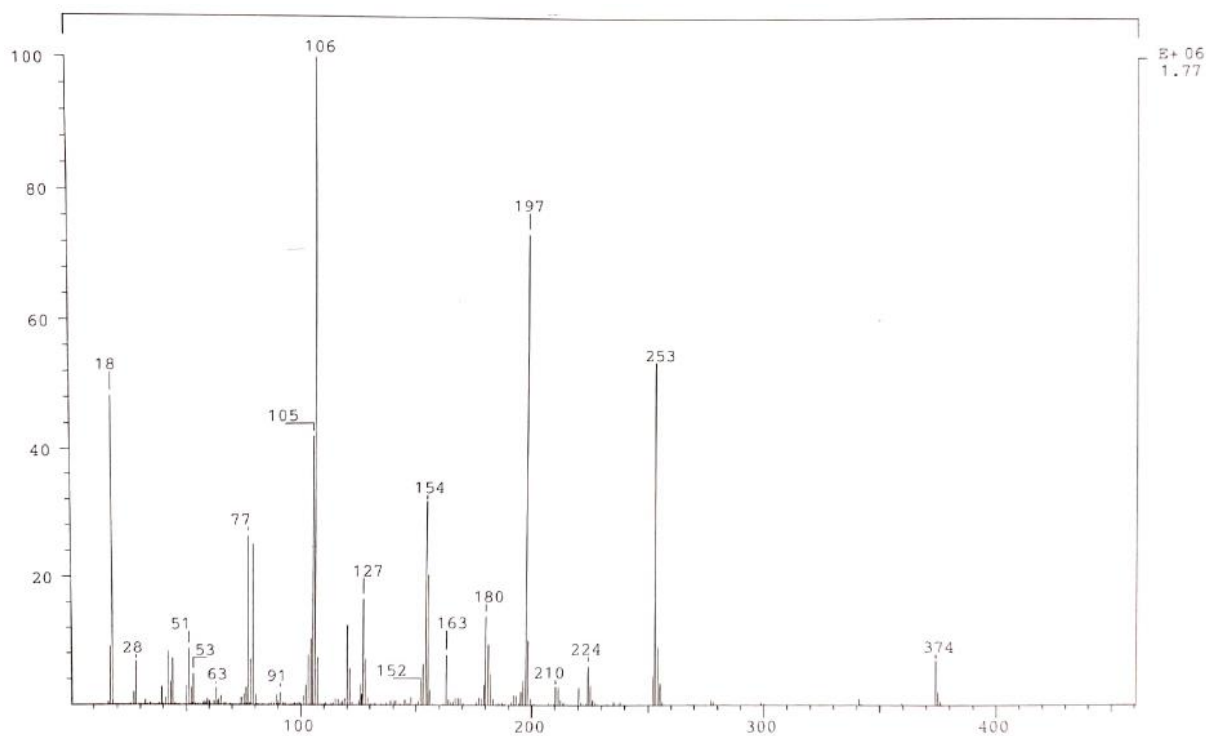


Figure 7.335 EI-MS spectrum of HphapyTSCmB at 70 eV.

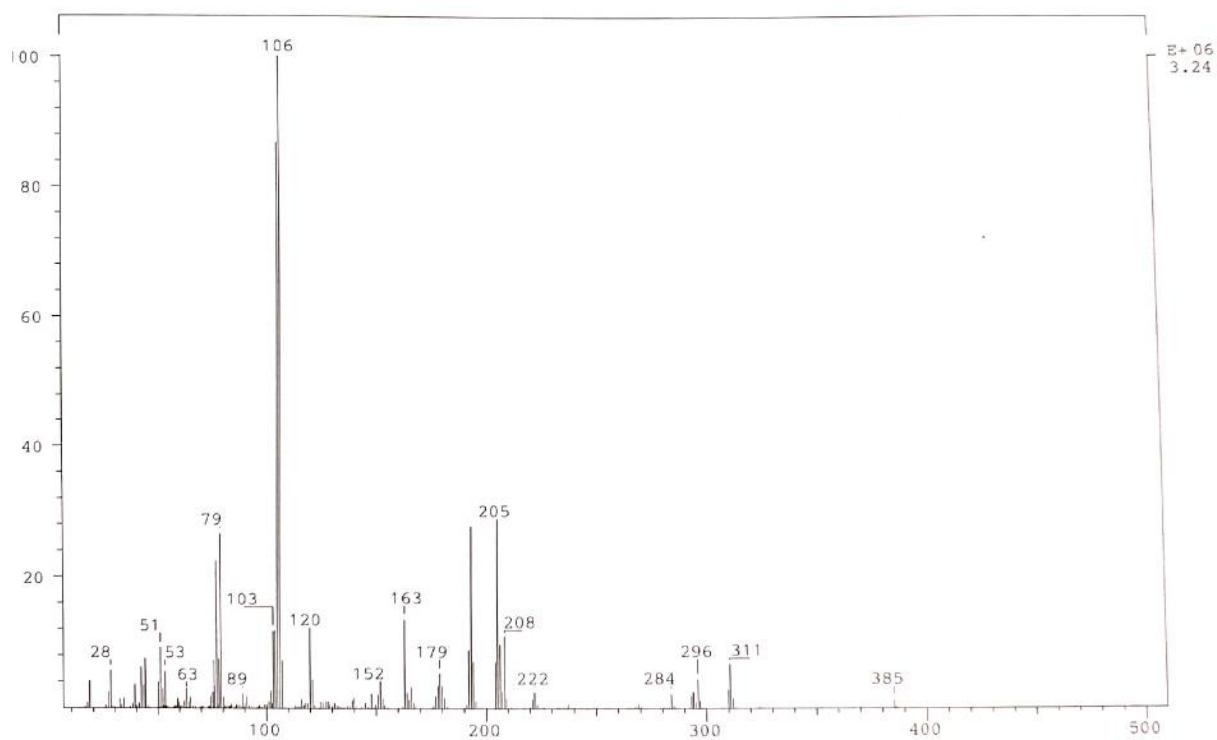


Figure 7.336 EI-MS spectrum of HcphfpyTSCmB at 70 eV.

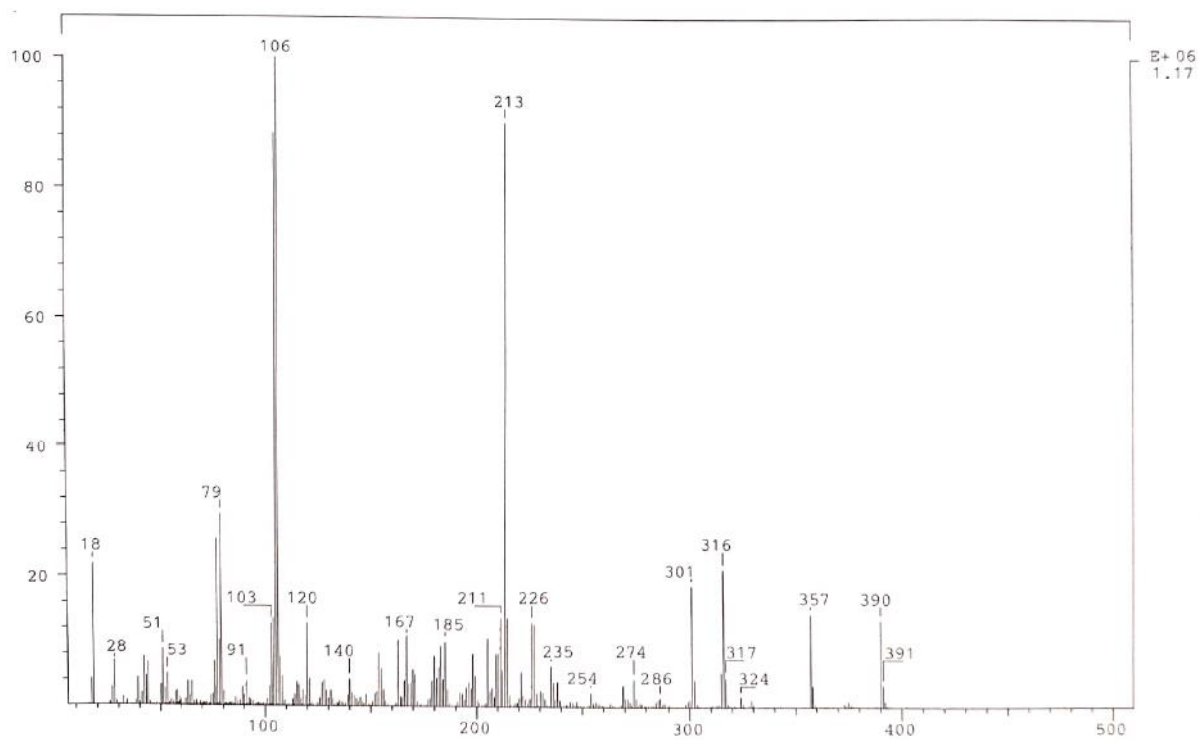


Figure 7.337 EI-MS spectrum of HmphfpyTSCmB at 70 eV.

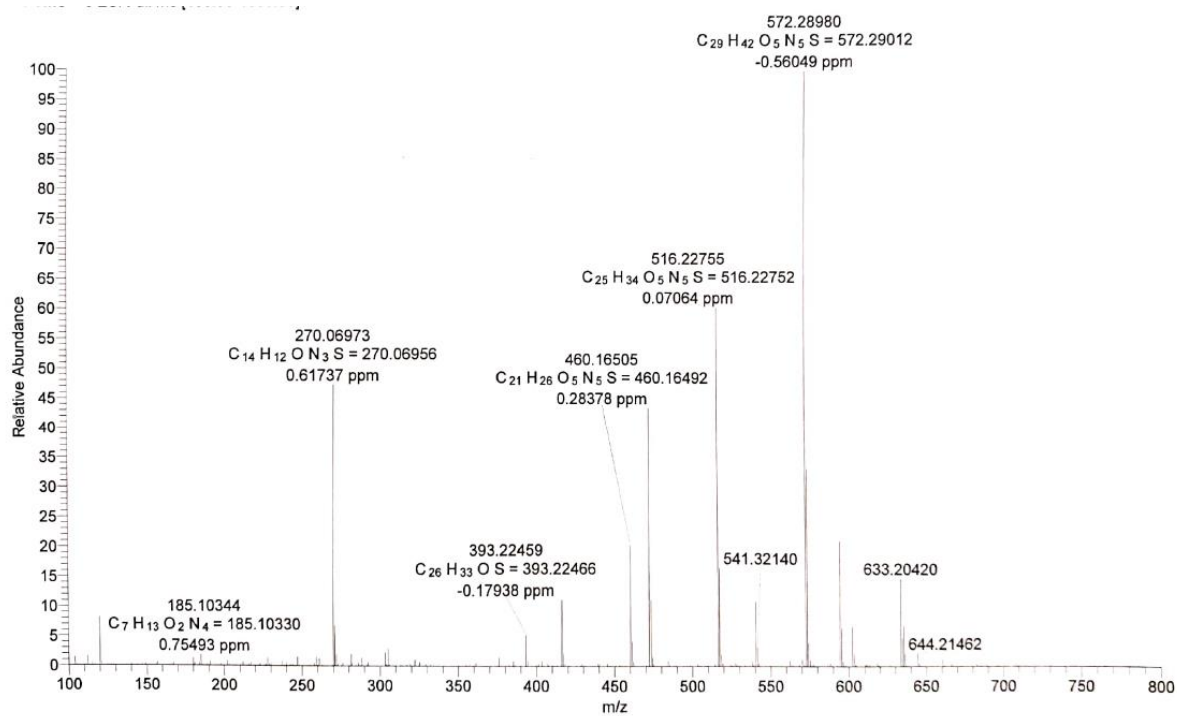


Figure 7.338 HR-ESI-MS spectrum of HmphpyTSLp.

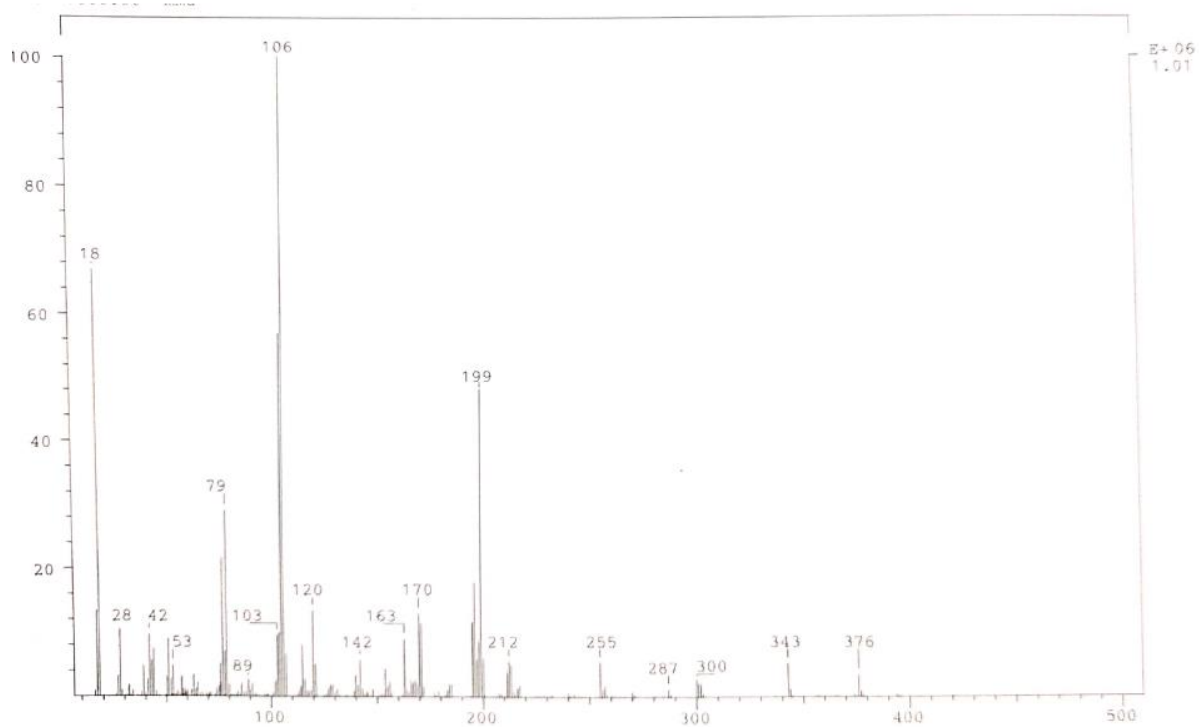


Figure 7.339 EI-MS spectrum of H₂hphpyTSCmB at 70 eV.

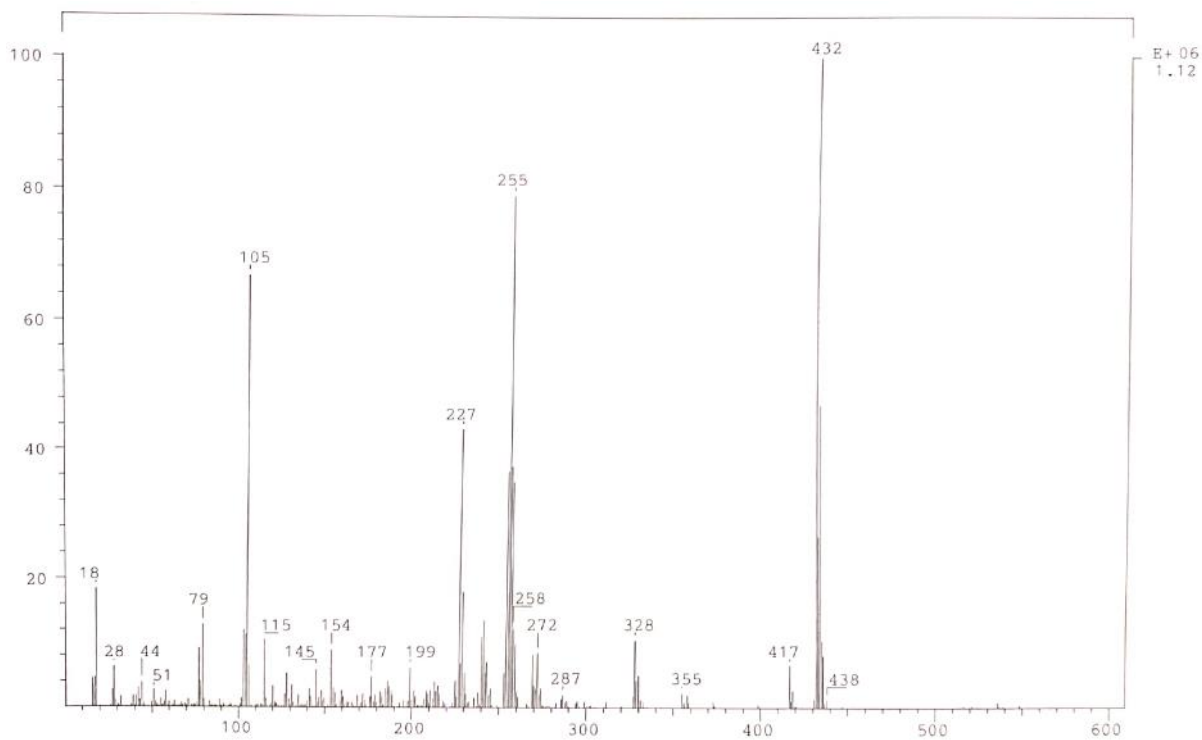


Figure 7.340 EI-MS spectrum of [Ni(hphfyTSCmB)] at 70 eV.

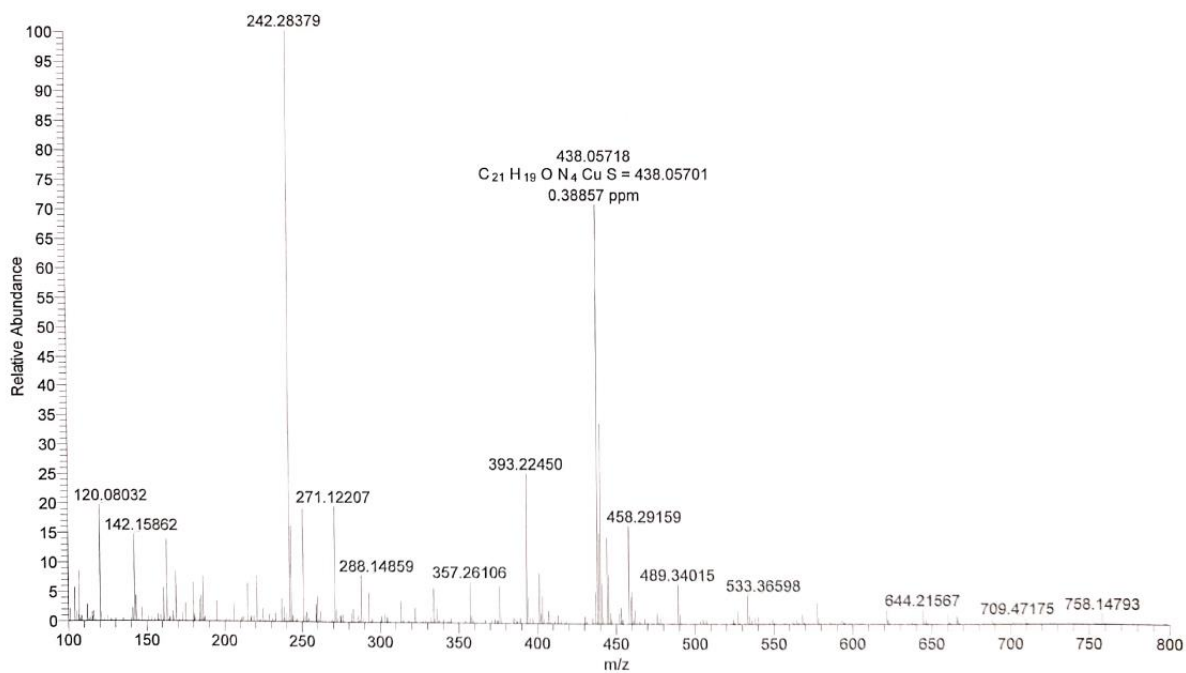


Figure 7.341 HR-ESI-MS spectrum of [Cu(hphfyTSCmB)].

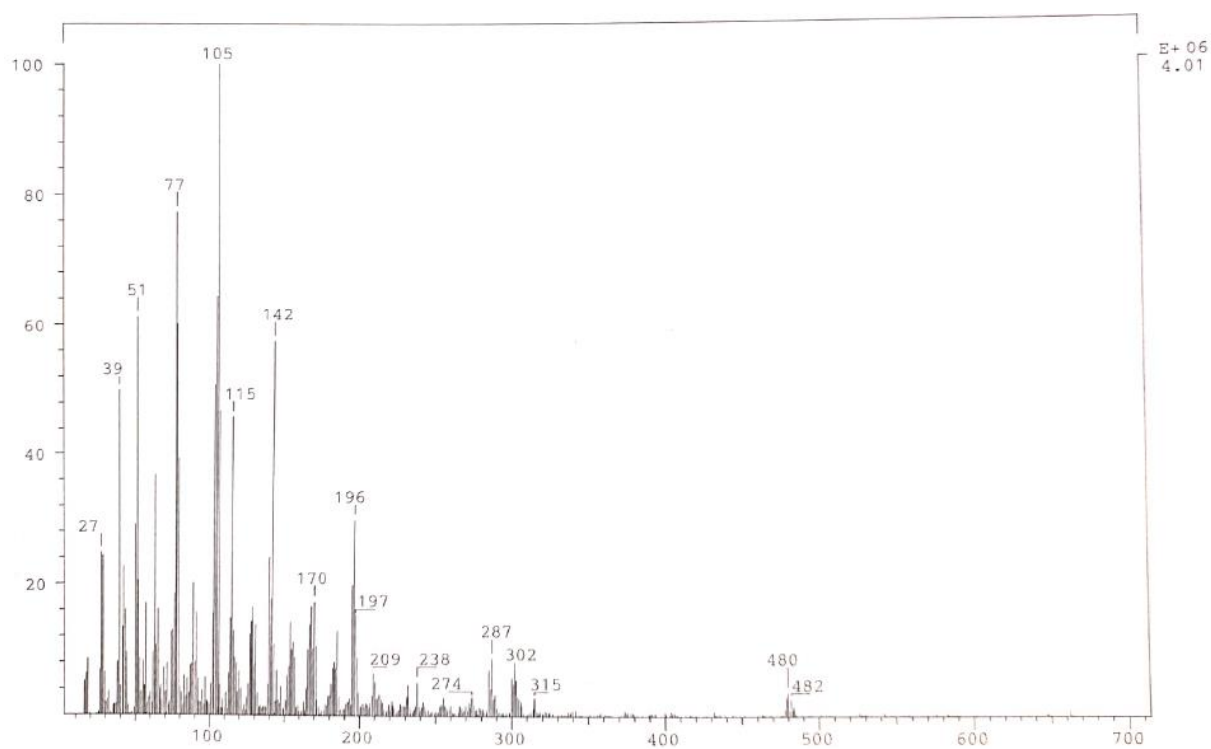


Figure 7.342 EI-MS spectrum of [Pd(hphfpyTSCmB)] at 70 eV.

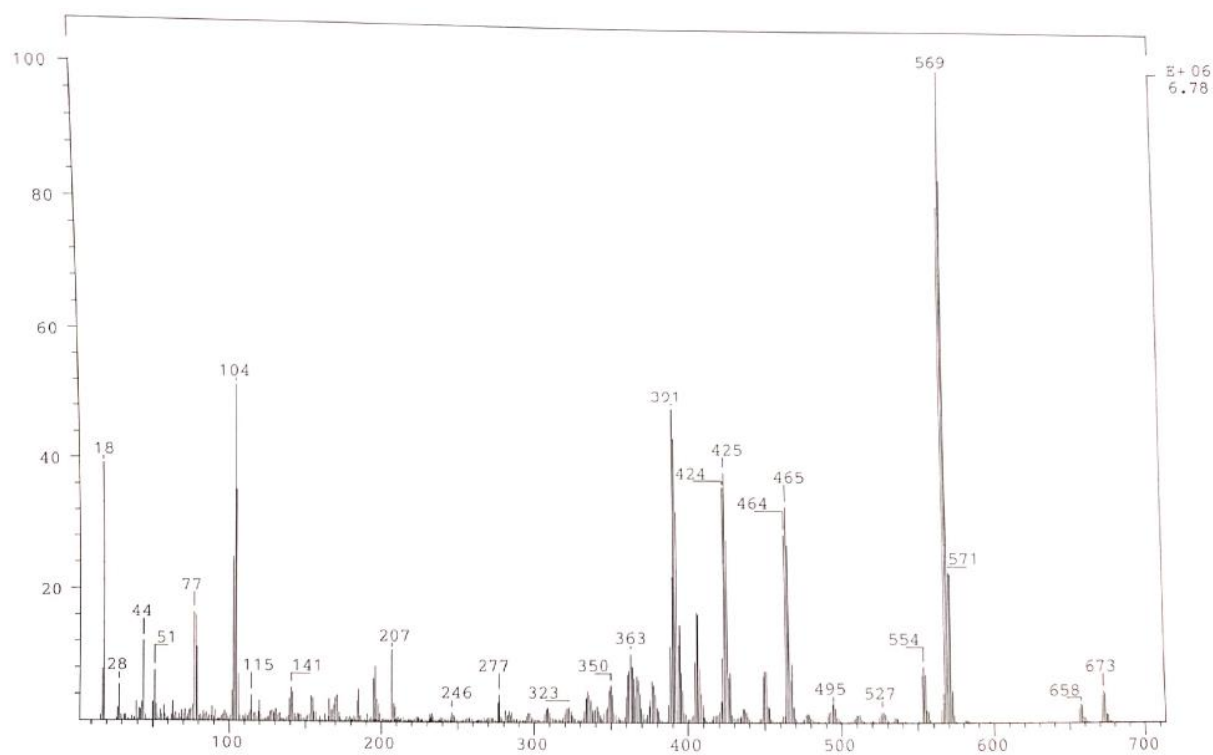


Figure 7.343 EI-MS spectrum of [Pt(hphfpyTSCmB)] at 70 eV.

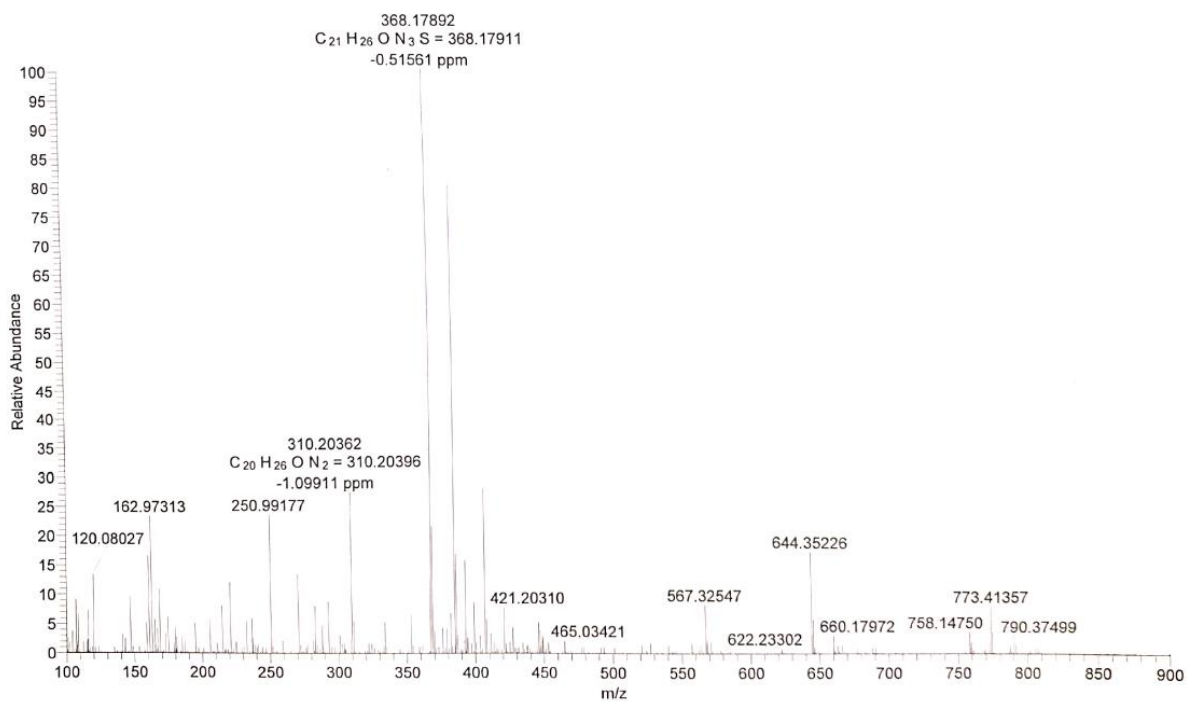


Figure 7.344 HR-ESI-MS spectrum of $H_2(tBu)hphfyTSC$.

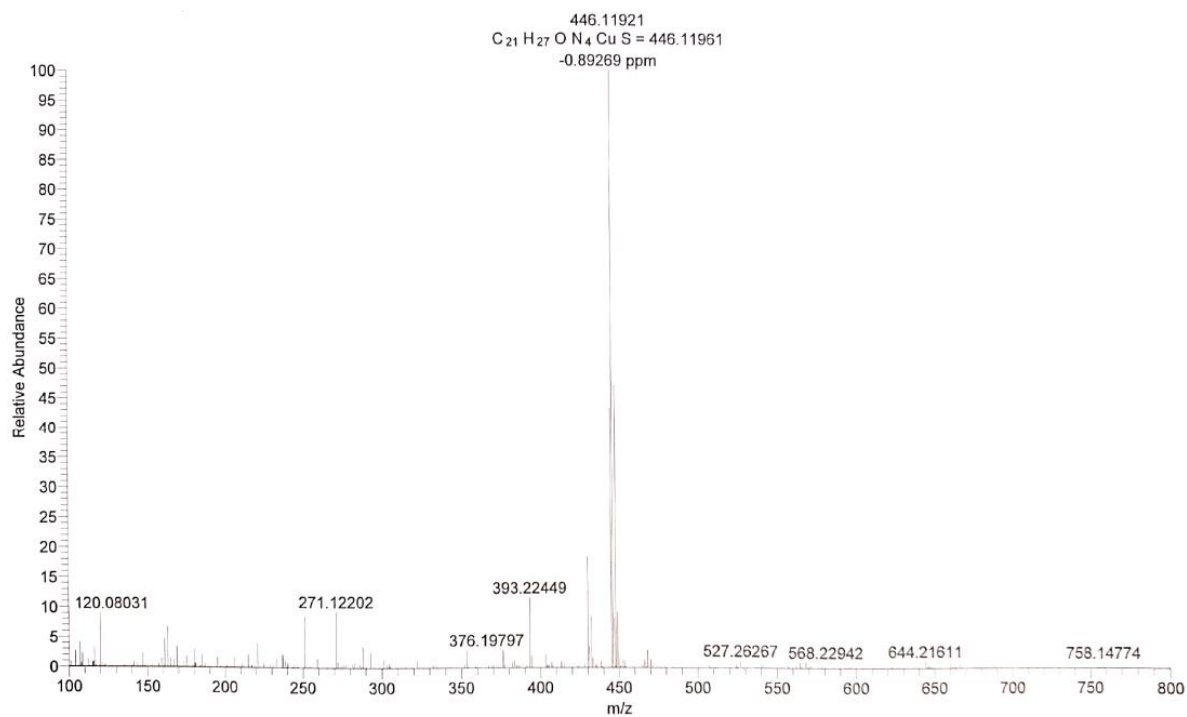


Figure 7.345 HR-ESI-MS spectrum of $[Cu((tBu)hphfyTSC)]$.

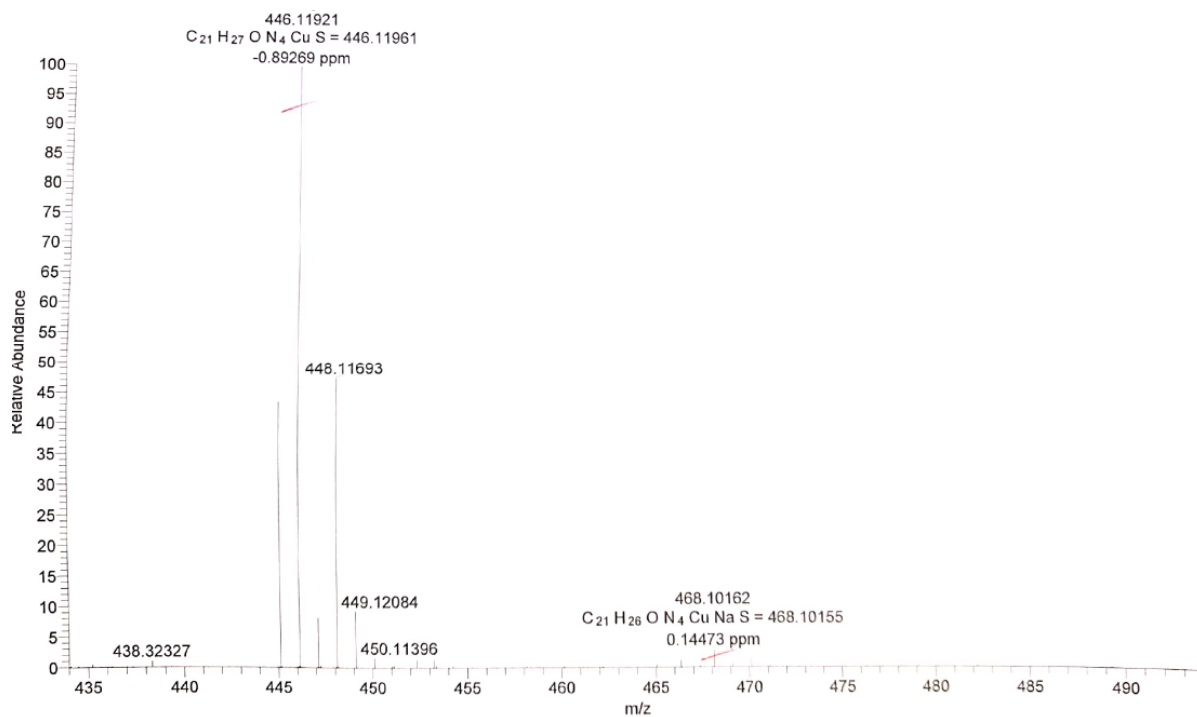


Figure 7.346 Excerpt of HR-ESI-MS spectrum of [Cu((tBu)hphfpyTSC)].

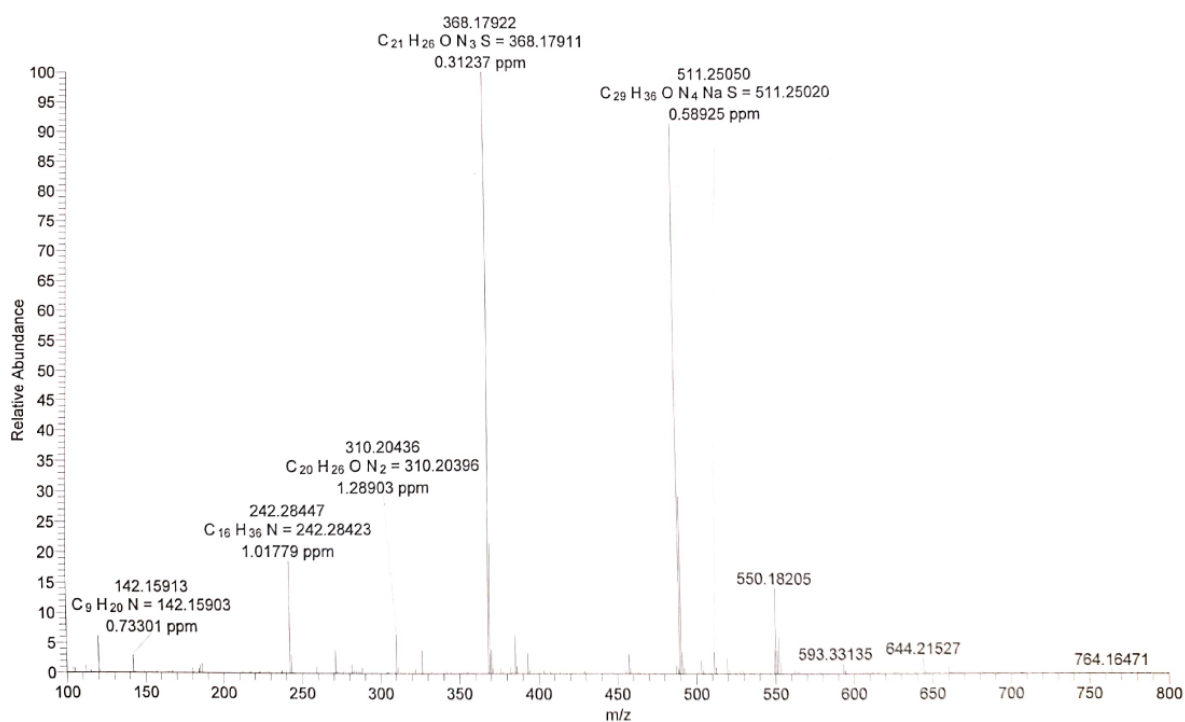


Figure 7.347 HR-ESI-MS spectrum of H₂(tBu)hphfpyTSCmB.

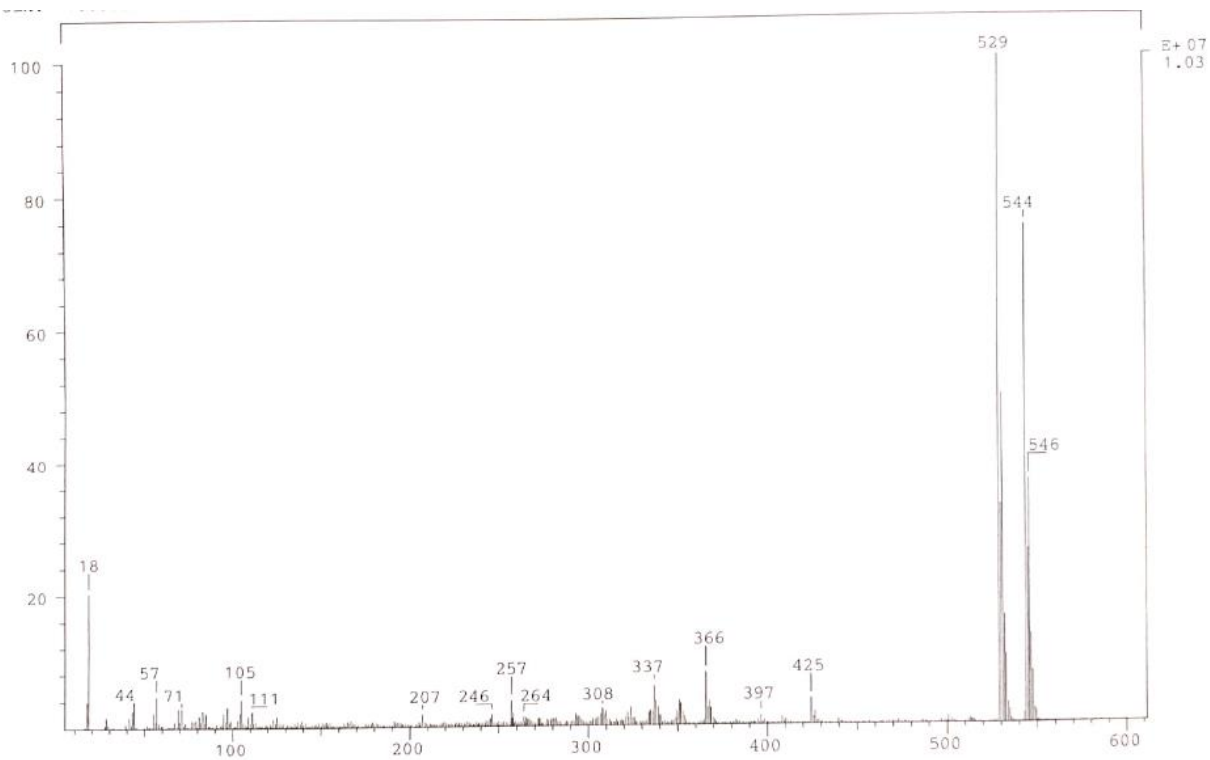


Figure 7.348 EI-MS spectrum of [Ni((tBu)hphfyTSCmB)] at 70 eV.

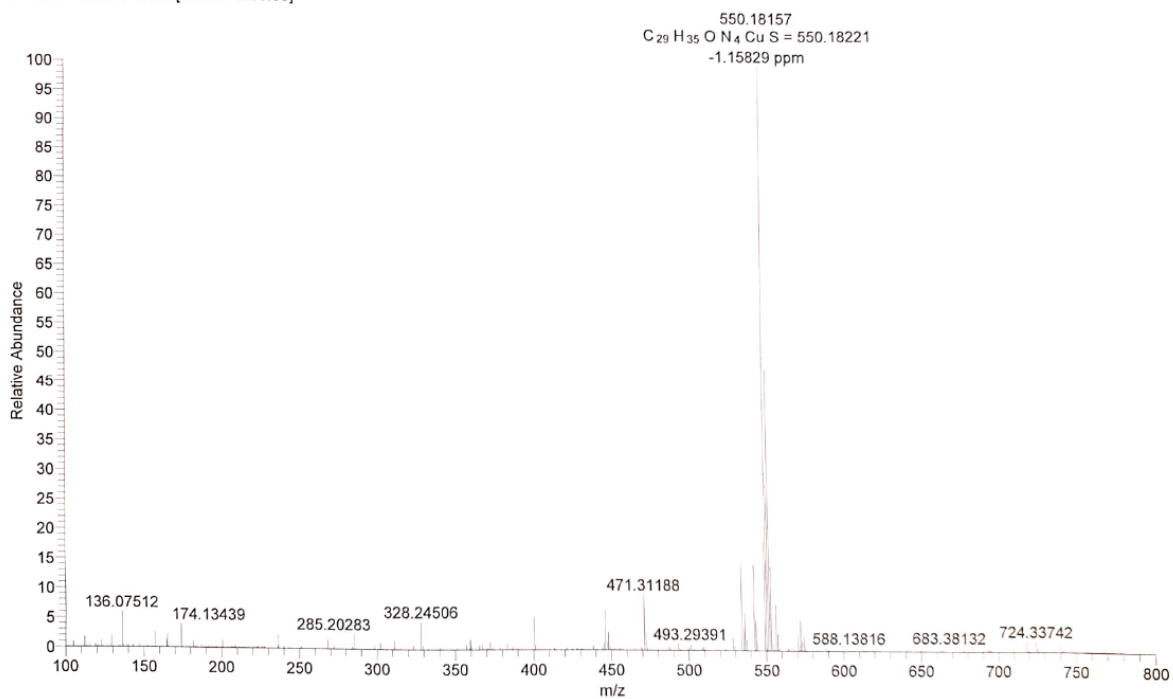


Figure 7.349 HR-ESI-MS spectrum of [Cu((tBu)hphfyTSCmB)].

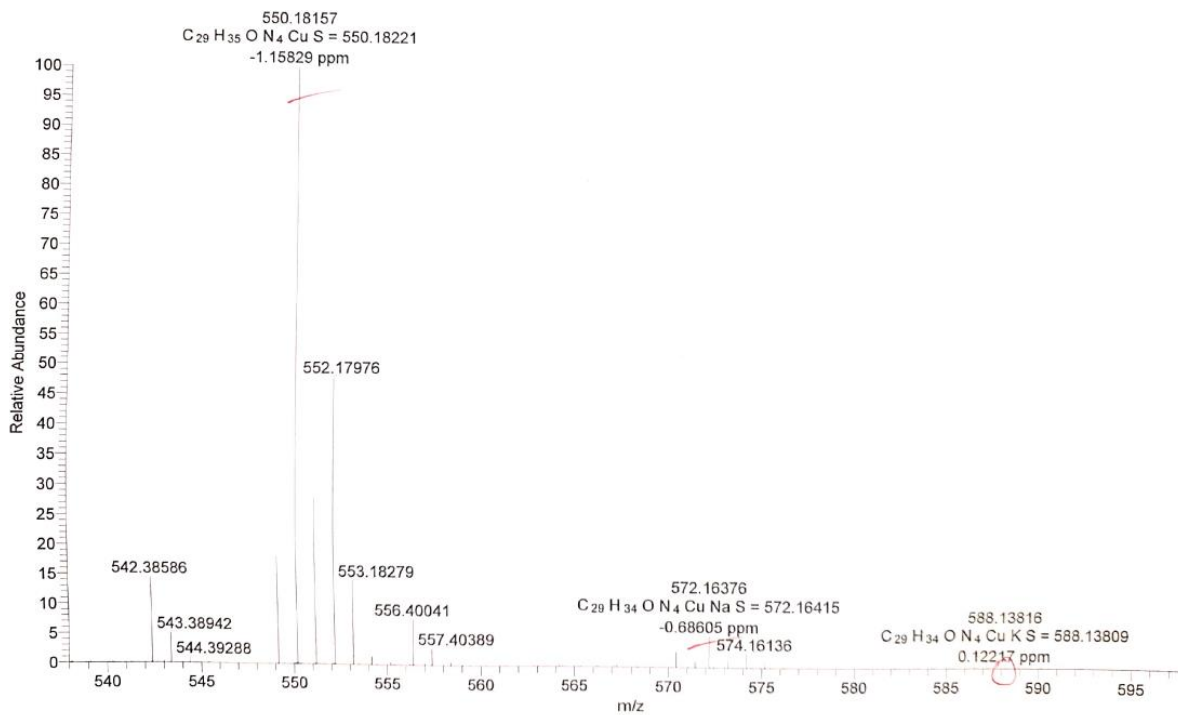


Figure 7.350 Excerpt of HR-ESI-MS spectrum of $[\text{Cu}((\text{tBu})\text{hphfyTSCmB})]$.

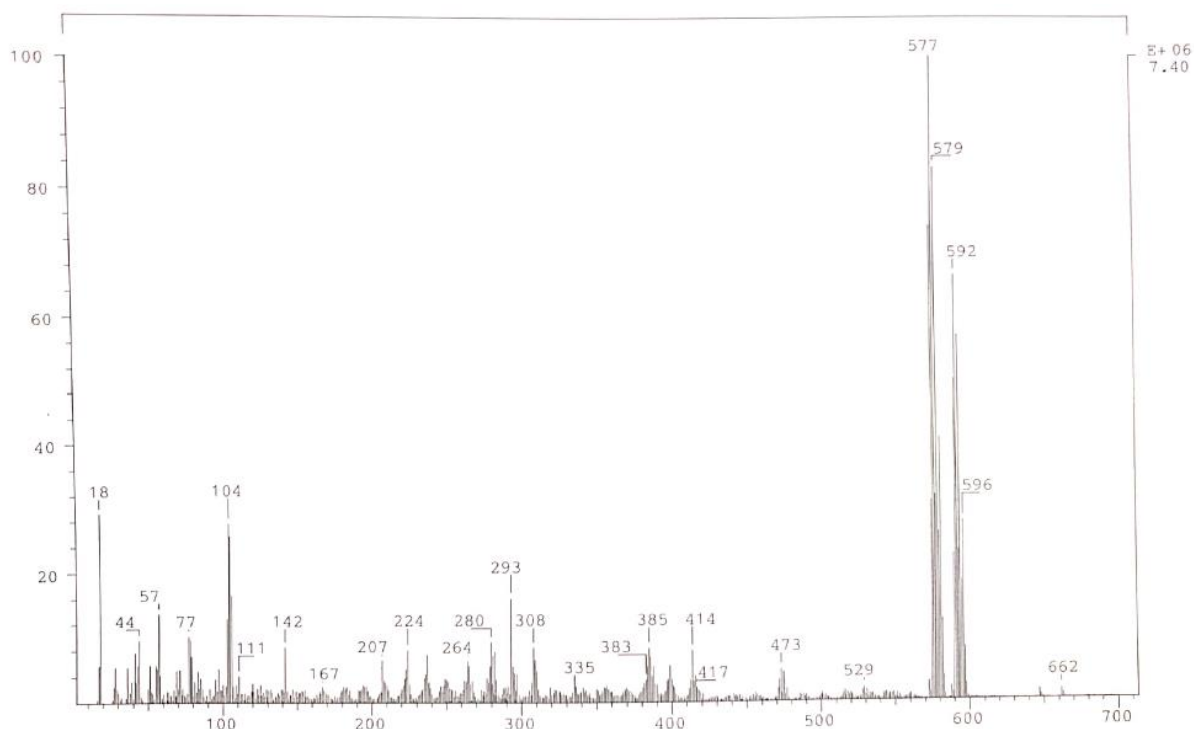


Figure 7.351 EI-MS spectrum of $[\text{Pd}((\text{tBu})\text{hphfyTSCmB})]$ at 70 eV.

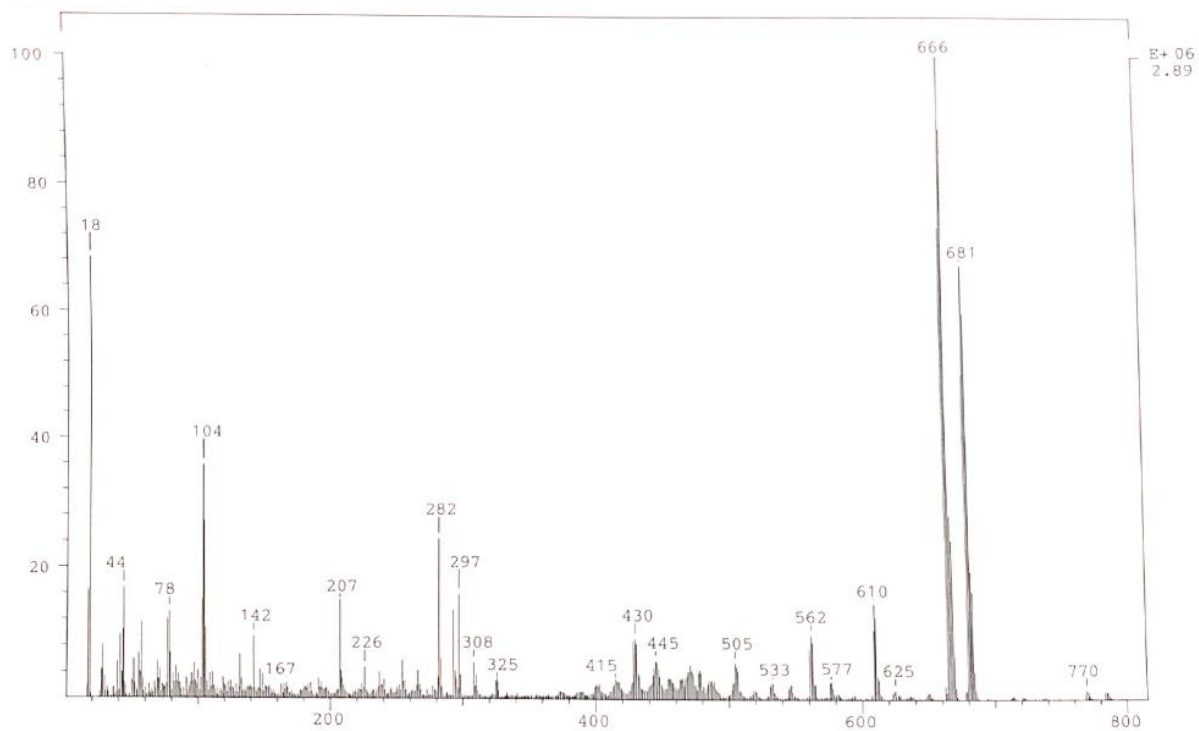


Figure 7.352 EI-MS spectrum of [Pt((tBu)hphfyTSCmB)] at 70 eV.

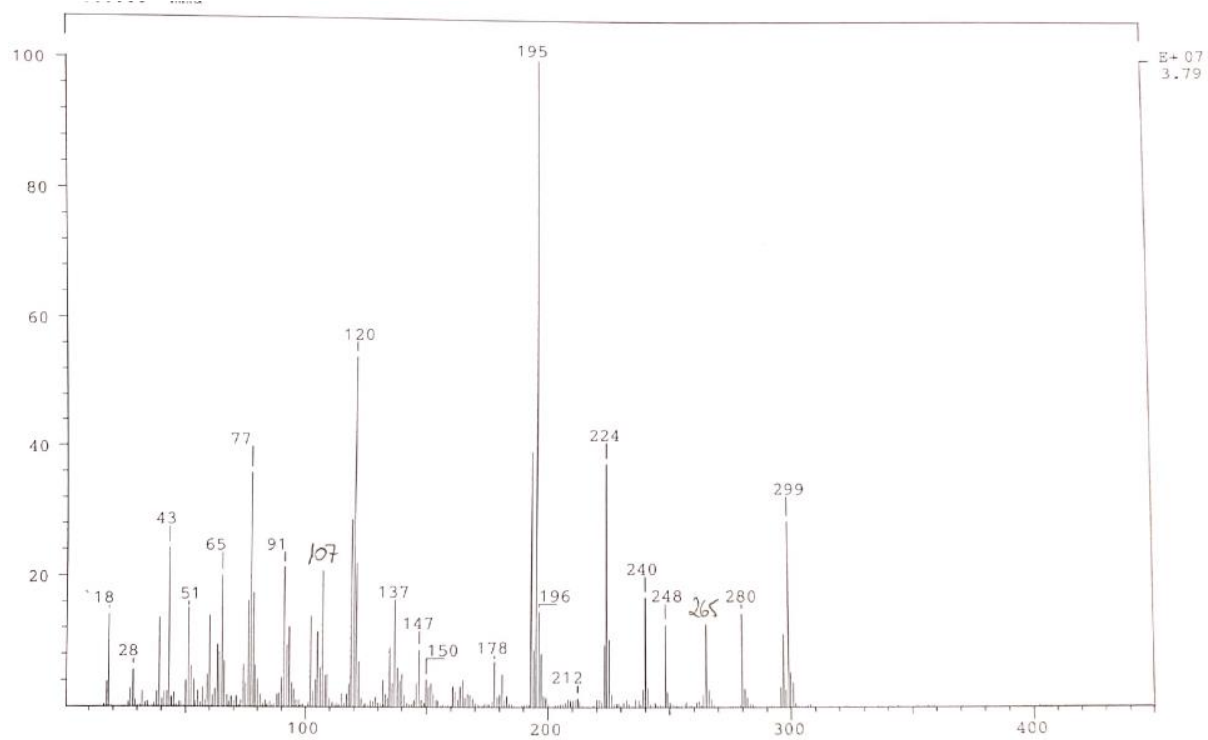


Figure 7.353 EI-MS spectrum of H₂SalTSCmB at 70 eV.

7.9. Cyclic voltammograms

7.9.1. Ligands

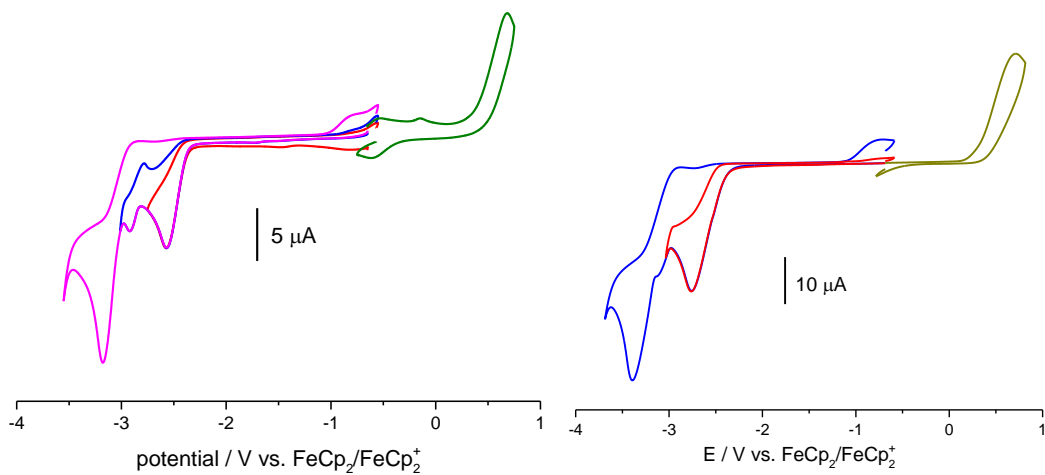


Figure 7.354 Cyclic voltammograms of HbzTSC (left) and HbzTSCm (right) in 0.1 M Bu₄NPF₆/THF at 100 mV/s scan rate.

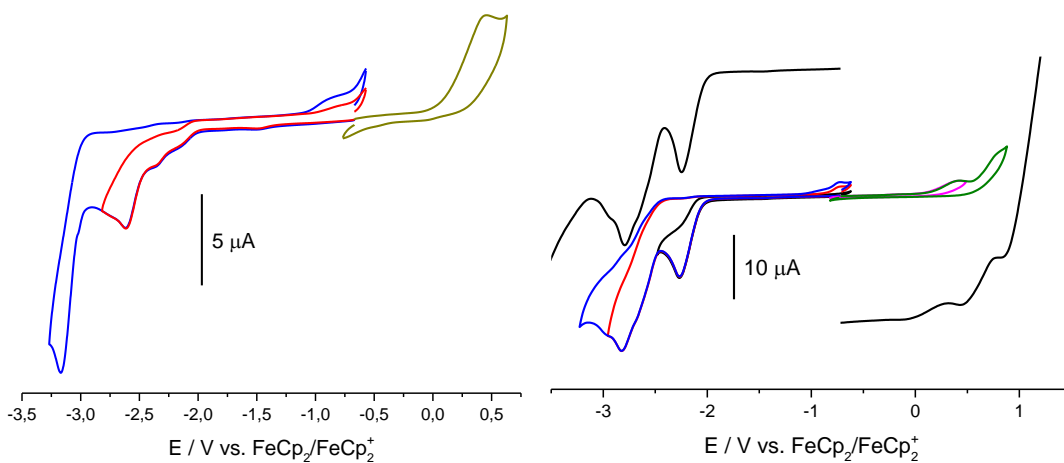


Figure 7.355 Cyclic voltammograms of HbzTSCdm (left) and HFbzTSC in 0.1 M Bu₄NPF₆/THF at 100 mV/s scan rate.

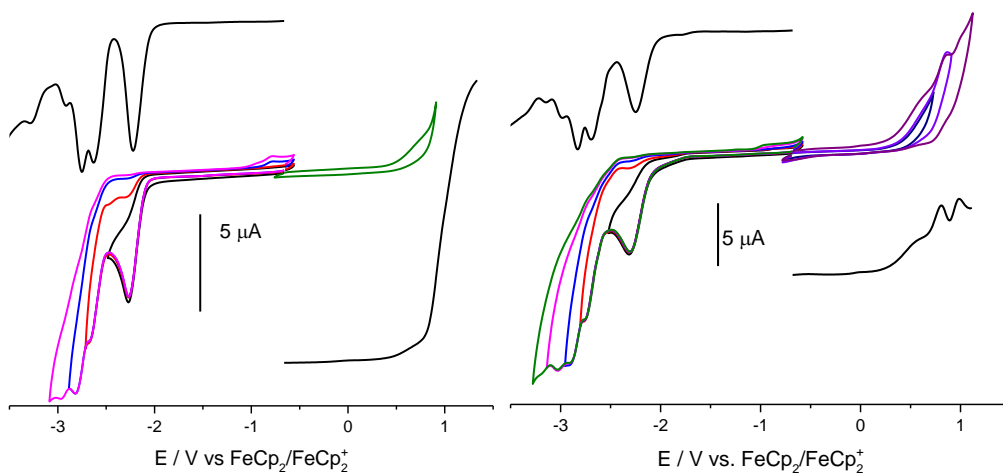


Figure 7.356 Cyclic voltammograms of HFbzTSCm (left) and HFbzTSCdm (right) in 0.1 M Bu₄NPF₆/THF at 100 mV/s scan rate.

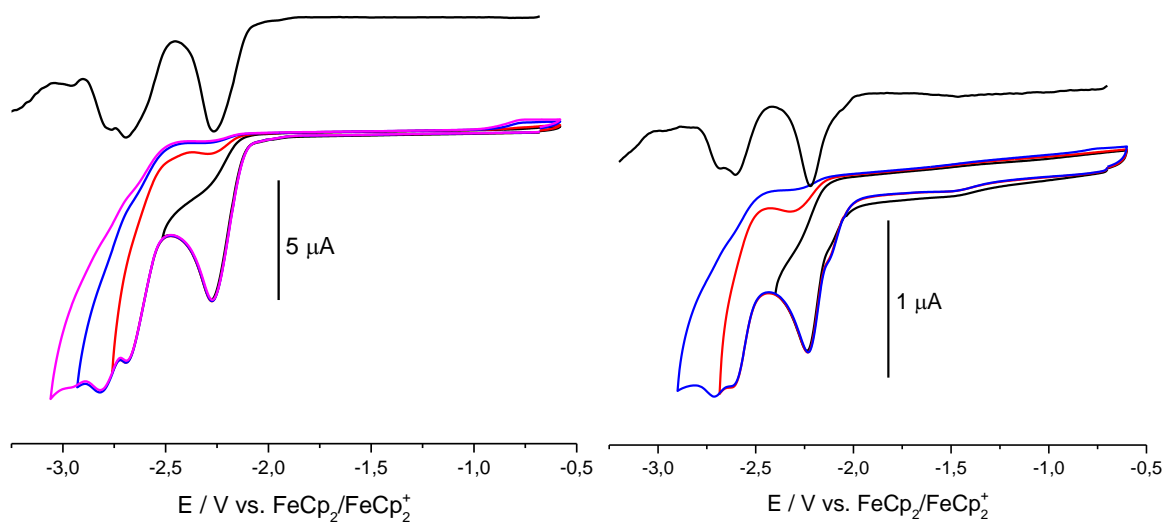


Figure 7.357 Cyclic voltammograms of HFbzTSCAd (left) and HFbzTSCmB(right) in 0.1 M Bu₄NPF₆/THF at 100 mV/s scan rate.

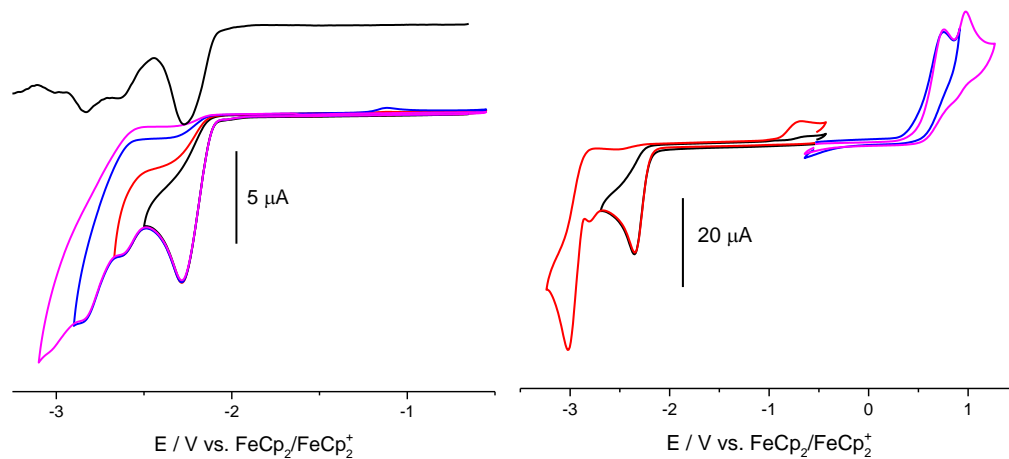


Figure 7.358 Cyclic voltammograms of HFbz(m)TSCmB (left) in 0.1 M Bu₄NPF₆/THF and HbzTSCmB(right) in 0.1 M Bu₄NPF₆/MeCN at 100 mV/s scan rate.

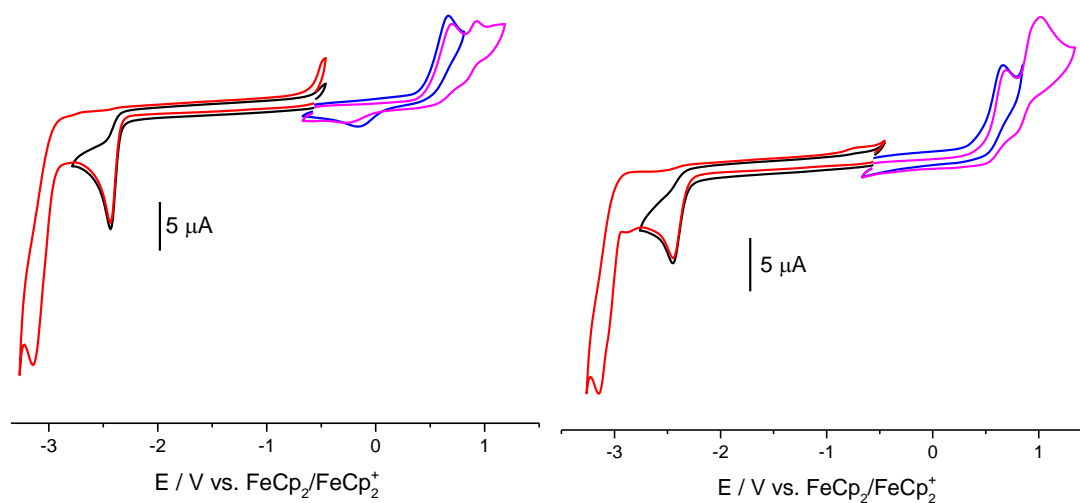


Figure 7.359 Cyclic voltammograms of Hbz(m)TSCmB (left) and HaphTSCmB (right) in 0.1 M Bu₄NPF₆/MeCN solution at 100 mV/s scan rate.

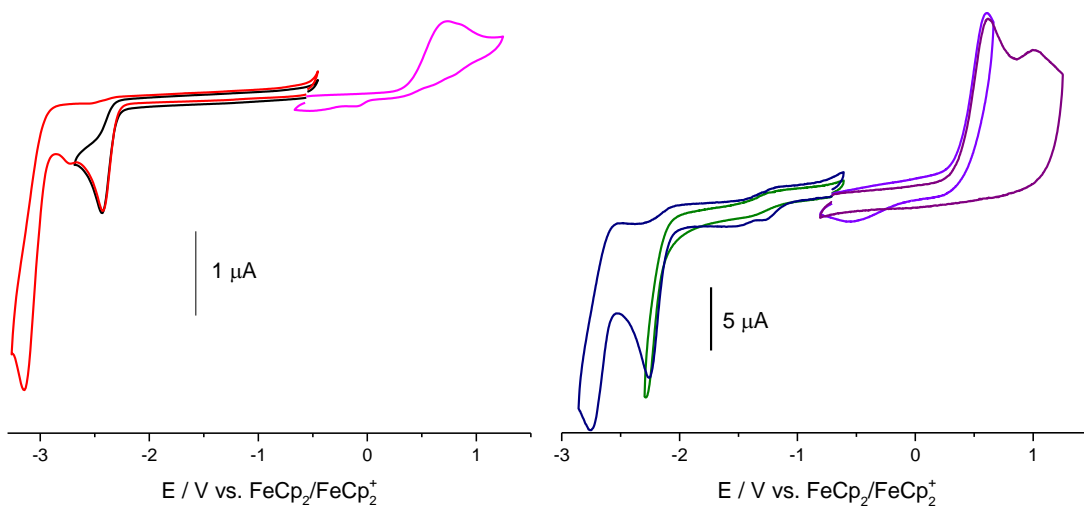


Figure 7.360 Cyclic voltammograms of Haph(m)TSCmB (left) and H₂SalTSC (right) in 0.1 M Bu₄NPF₆/MeCN solution at 100 mV/s scan rate.

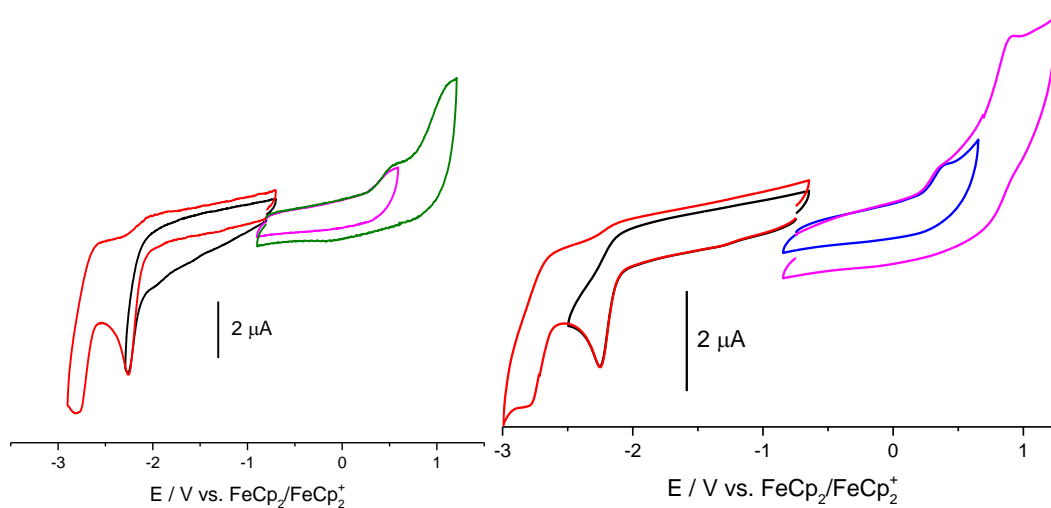


Figure 7.361 Cyclic voltammograms of H₂SalTSCmB (left) and H₂SalTSClp (right) in 0.1 M Bu₄NPF₆/MeCN solution at 100 mV/s scan rate.

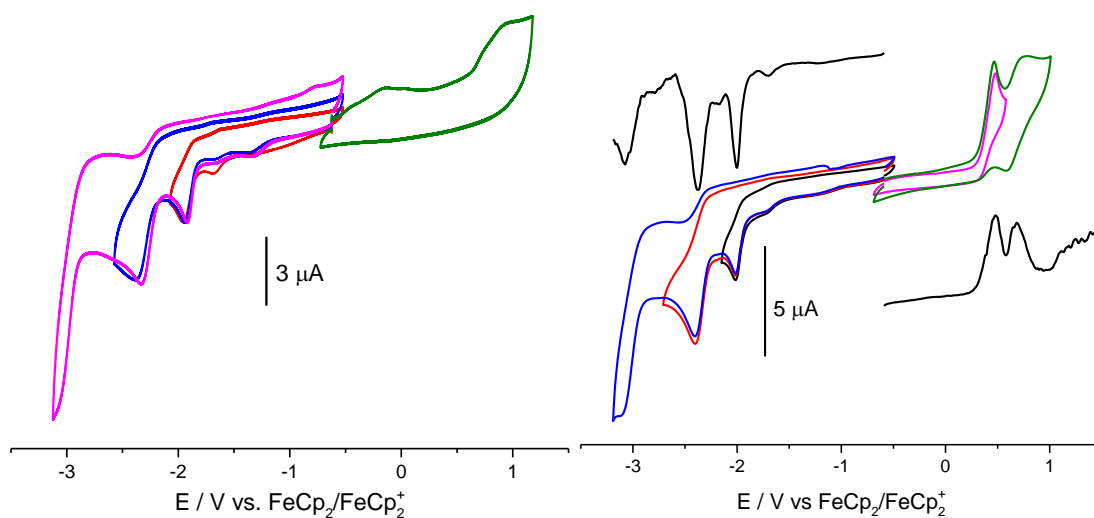


Figure 7.362 Cyclic voltammograms of H₂hphfpyTSCmB (left) and H₂tBuhphfpyTSC (right) in 0.1 M Bu₄NPF₆/MeCN solution at 100 mV/s scan rate.

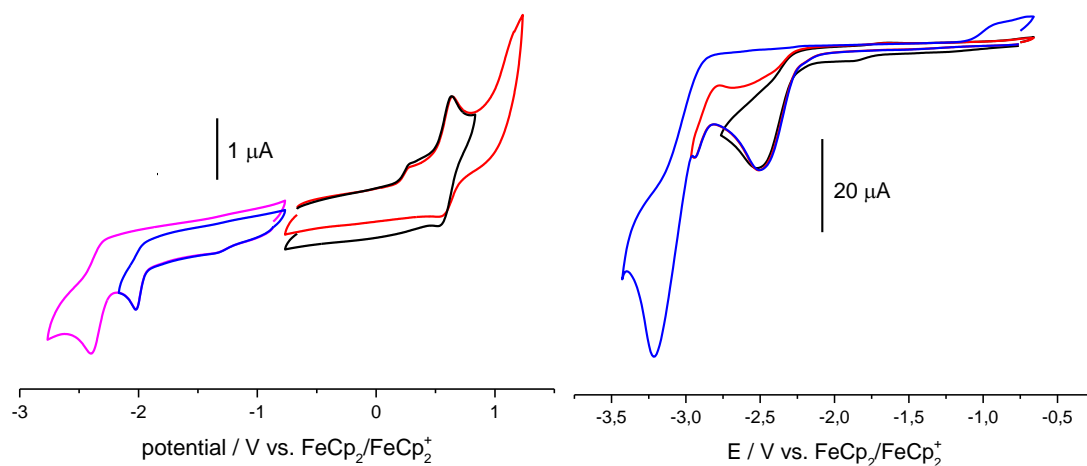


Figure 7.363 Cyclic voltammograms of H₂tBuhphfpyTSCmB (left) and HapyTSCmB (right) in 0.1 M Bu₄NPF₆/MeCN solution at 100 mV/s scan rate.

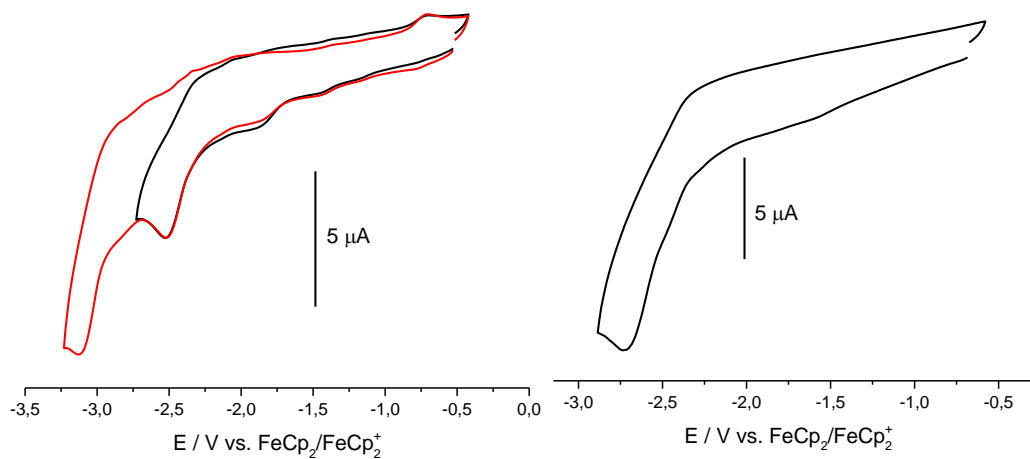


Figure 7.364 Cyclic voltammograms of HapyTSCAd (left) and HapyTSClp (right) in 0.1 M Bu₄NPF₆/MeCN solution at 100 mV/s scan rate.

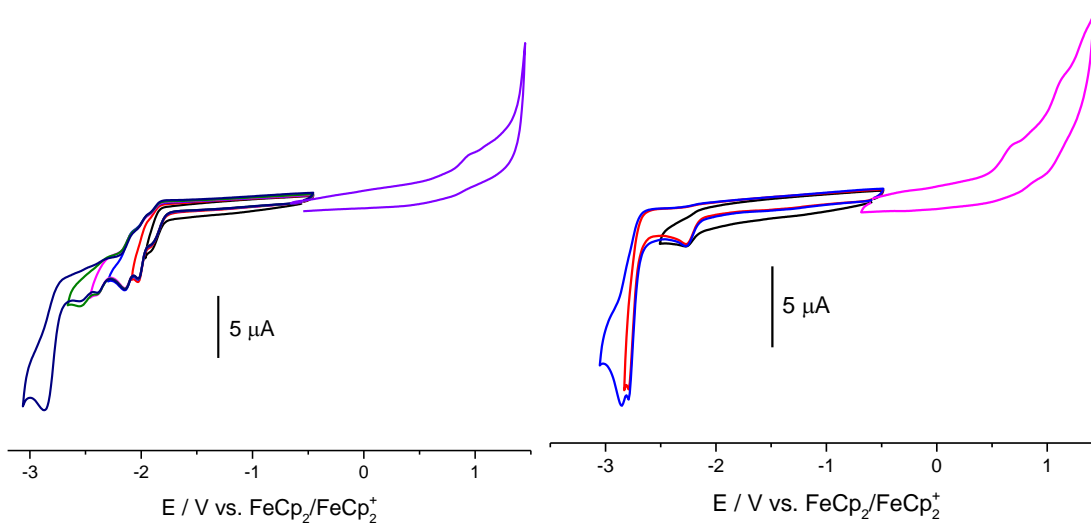


Figure 7.365 Cyclic voltammograms of H6-BrapyTSCmB (left) and of H6-phapyTSCmB (right) in 0.1 M Bu₄NPF₆/MeCN solution at 100 mV/s scan rate.

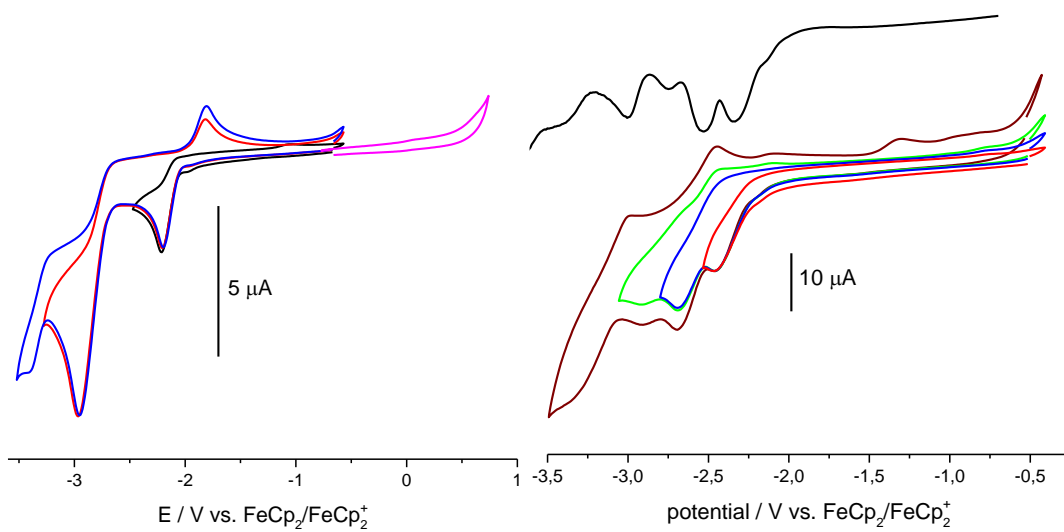


Figure 7.366 Cyclic voltammograms of HdpYTSCmB (left) and H₂dap(b)TSC (right) in 0.1 M Bu₄NPF₆/THF solution at 100 mV/s scan rate.

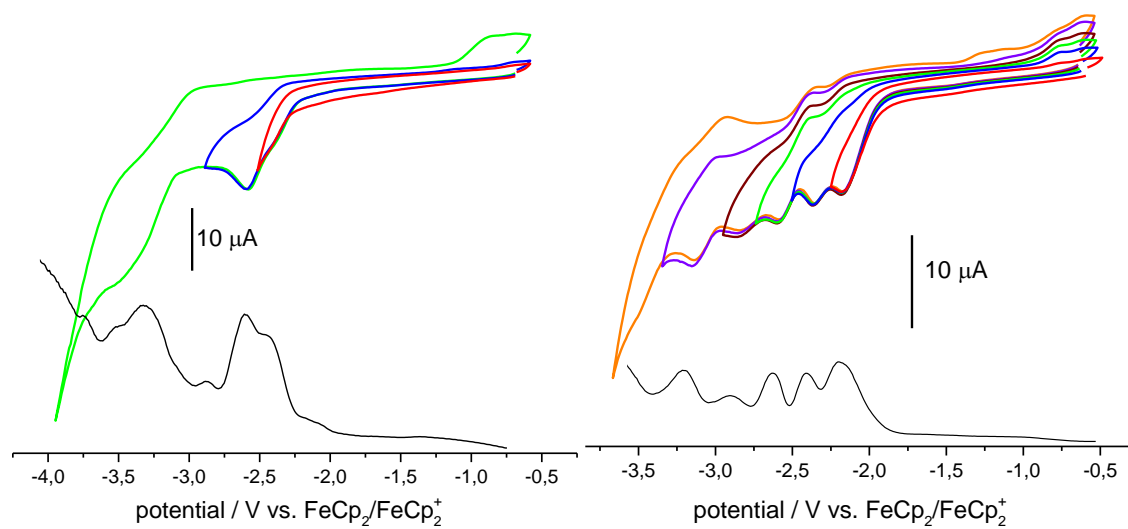


Figure 7.367 Cyclic voltammograms of H₂dap(b)TSCmB (right) and H₂Cldap(b)TSCAd (left) in 0.1 M Bu₄NPF₆/THF at 100 mV/s scan rate.

7.9.2. Complexes

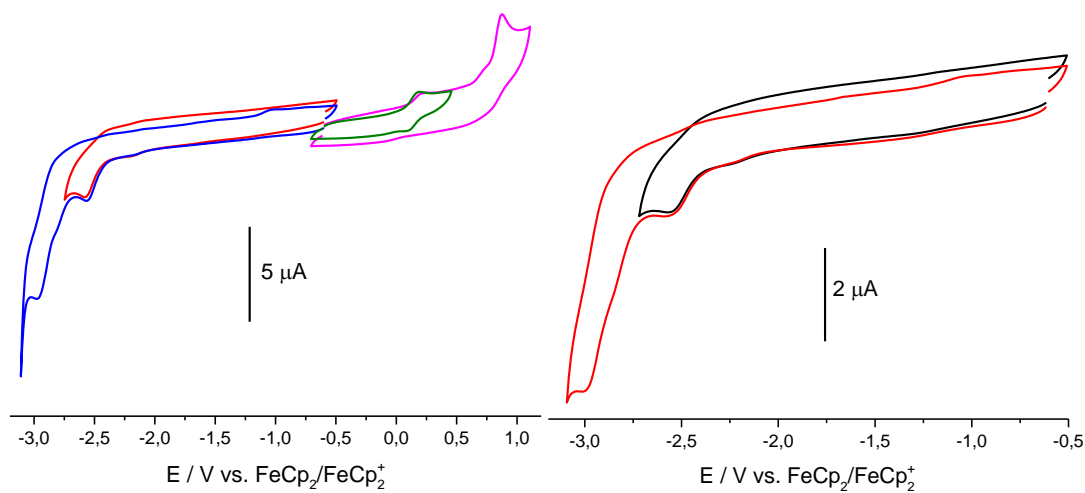


Figure 7.368 Cyclic voltammograms of [Ir(PPh₃)₂(bzTSCmB)(H)] (left) and [Ir(PPh₃)₂(bzTSCmB)(Cl)] (right) in 0.1 M Bu₄NPF₆ / MeCN at a scan rate of 100 mV/s.

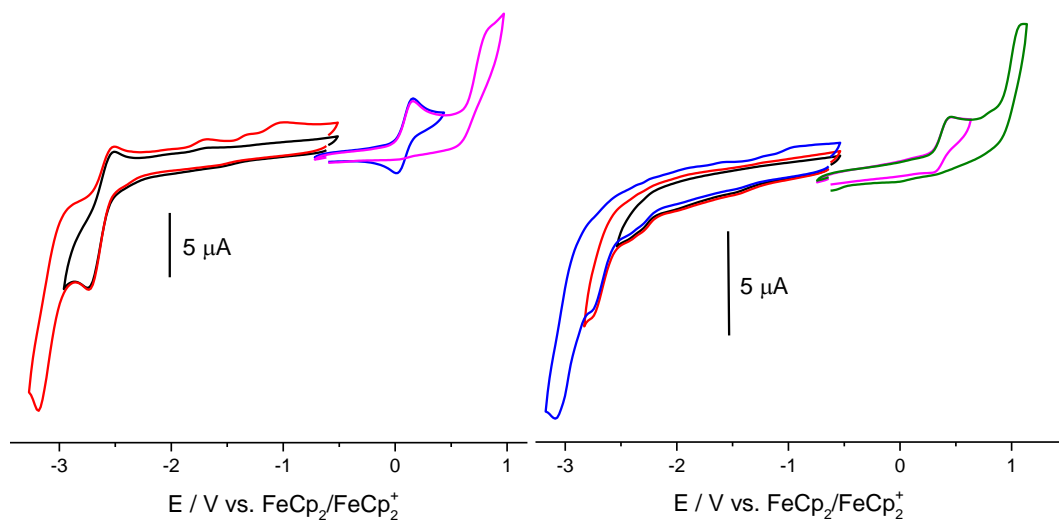


Figure 7.369 Cyclic voltammograms of [Ir(PPh₃)₂(bzTSCmB)(H)] (left) and [Ir(PPh₃)₂(bzTSCmB)(Cl)] (right) in 0.1 M Bu₄NPF₆ / THF at a scan rate of 100 mV/s.

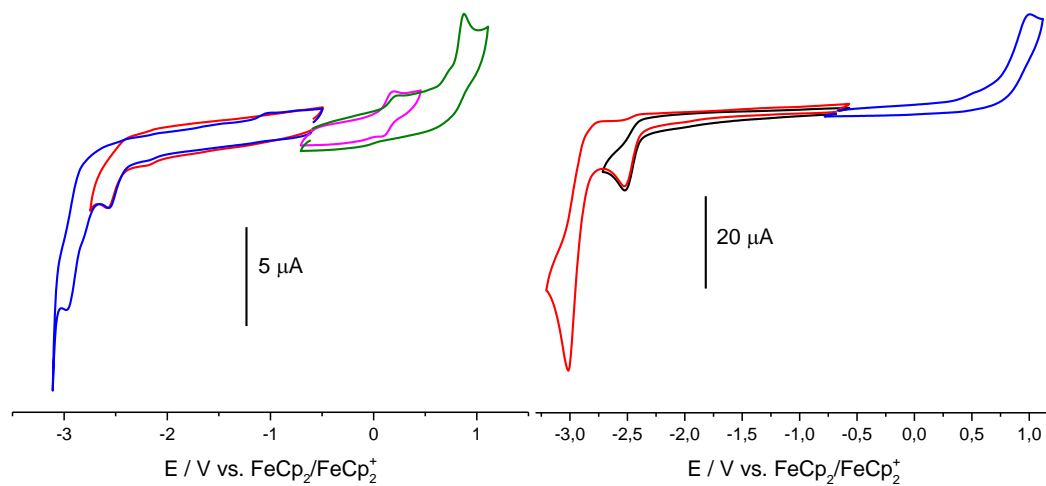


Figure 7.370 Cyclic voltammograms of [Ir(PPh₃)₂(bz(m)TSCmB)(H)] (left) and [Ir(PPh₃)₂(bz(m)TSCmB)(Cl)] (right) in 0.1 M Bu₄NPF₆ / MeCN at a scan rate of 100 mV/s.

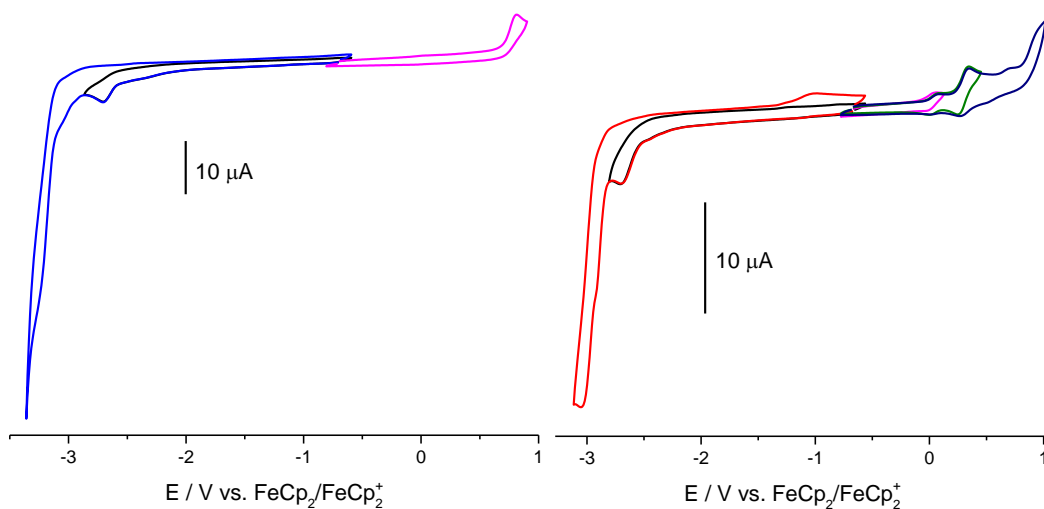


Figure 7.371 Cyclic voltammograms of [Ir(PPh₃)₂(aphTSCmB)(H)] (left) and [Ir(PPh₃)₂(aphTSCmB)(Cl)] (right) in 0.1 M Bu₄NPF₆ / MeCN at a scan rate of 100 mV/s.

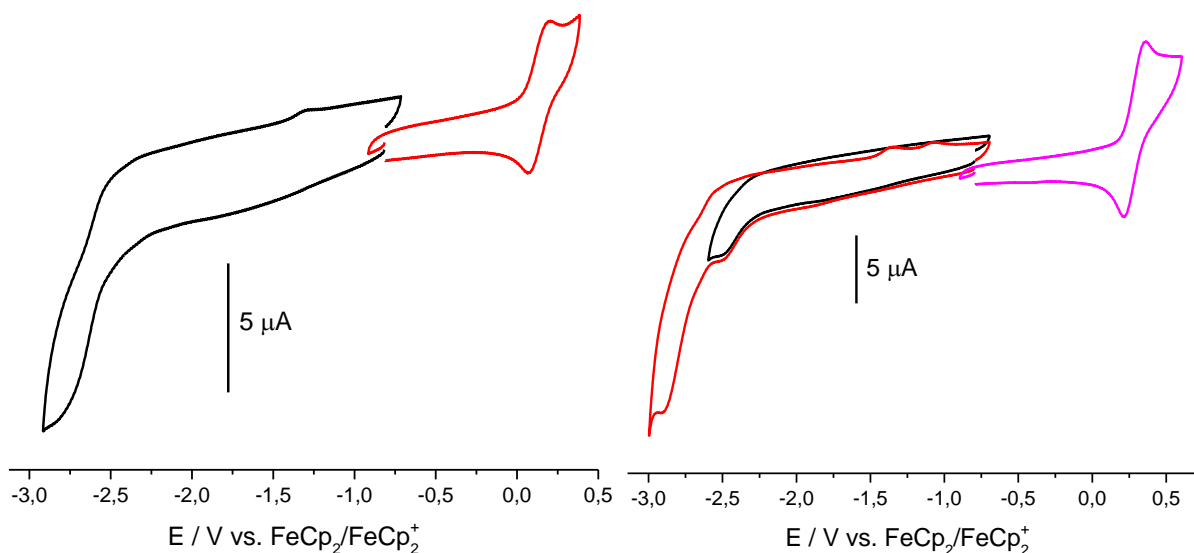


Figure 7.372 Cyclic voltammograms of [Ir(PPh₃)₂(aphTSCmB)(H)] (left) and [Ir(PPh₃)₂(aphTSCmB)(Cl)] (right) in 0.1 M Bu₄NPF₆ / THF at a scan rate of 100 mV/s.

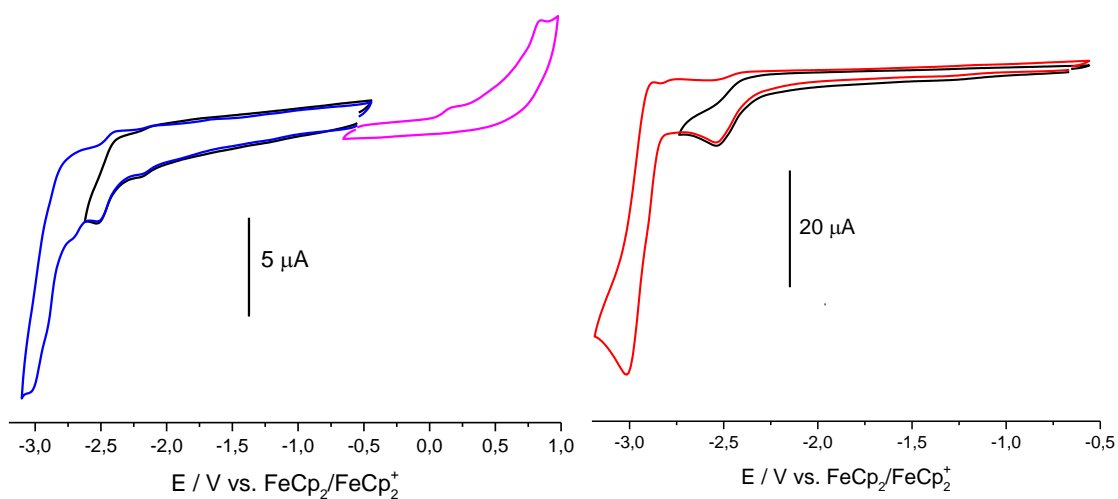


Figure 7.373 Cyclic voltammograms of $[\text{Ir}(\text{PPh}_3)_2(\text{aph}(m)\text{TSCmB})(\text{H})]$ (left) and $[\text{Ir}(\text{PPh}_3)_2(\text{aph}(m)\text{TSCmB})(\text{Cl})]$ (right) in 0.1 M $\text{Bu}_4\text{NPF}_6 / \text{MeCN}$ at a scan rate of 100 mV/s.

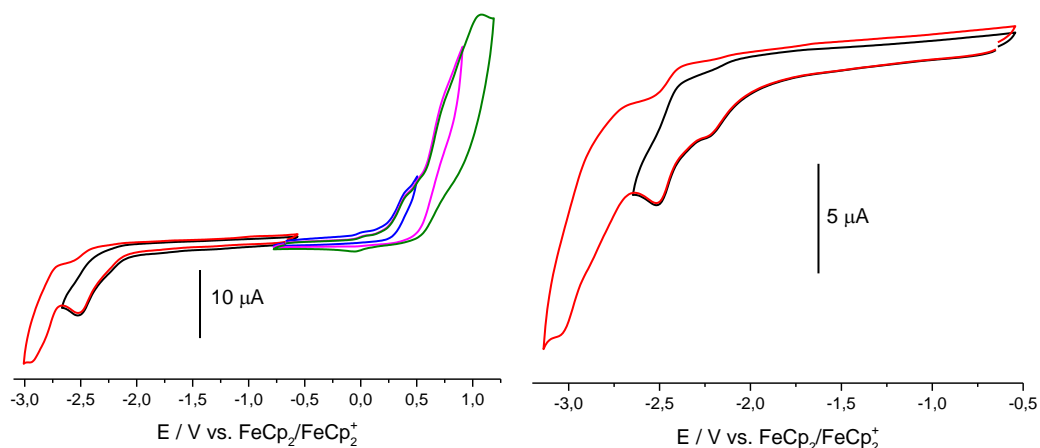


Figure 7.374 Cyclic voltammograms of $[\text{Ir}(\text{AsPh}_3)_2(\text{bzTSCmB})(\text{H})]$ (left) and $[\text{Ir}(\text{AsPh}_3)_2(\text{bzTSCmB})(\text{Cl})]$ (right) in 0.1 M $\text{Bu}_4\text{NPF}_6 / \text{MeCN}$ at a scan rate of 100 mV/s.

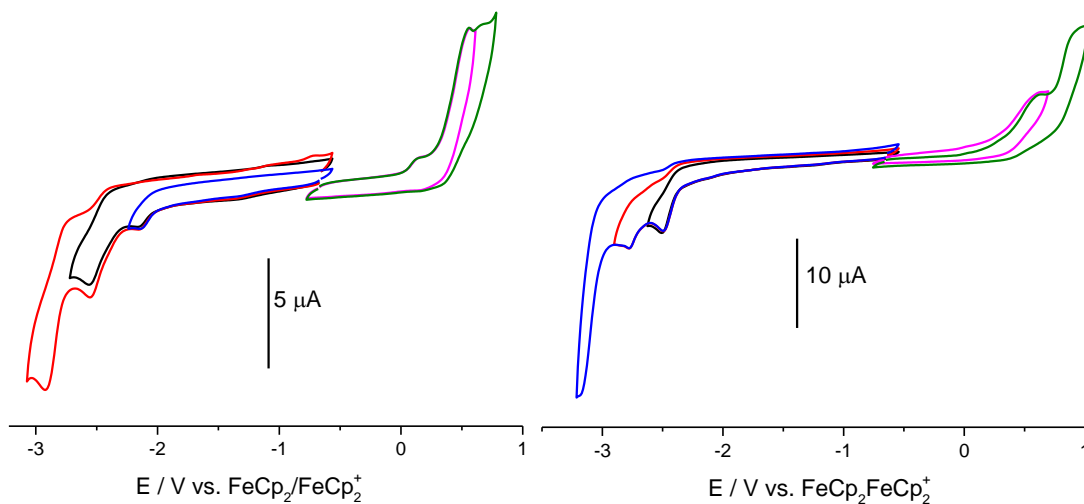


Figure 7.375 Cyclic voltammograms of $[\text{Ir}(\text{AsPh}_3)_2(\text{aphTSCmB})(\text{H})]$ (left) and $[\text{Ir}(\text{AsPh}_3)_2(\text{aphTSCmB})(\text{Cl})]$ (right) in 0.1 M $\text{Bu}_4\text{NPF}_6 / \text{MeCN}$ at a scan rate of 100 mV/s.

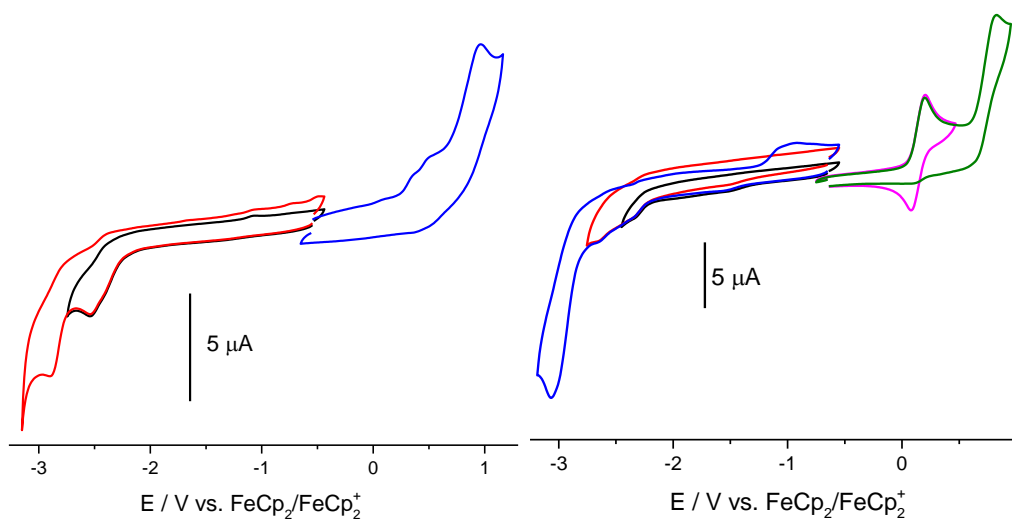


Figure 7.376 Cyclic voltammograms of $[\text{Ir}(\text{AsPh}_3)_2(\text{bz}(m)\text{TSCmB})(\text{H})]$ in 0.1 M $\text{Bu}_4\text{NPF}_6 / \text{MeCN}$ and $[\text{Ir}(\text{PPh}_3)_2(\text{bphTSCmB})(\text{H})]$ (right) in 0.1 M $\text{Bu}_4\text{NPF}_6 / \text{THF}$ at a scan rate of 100 mV/s.

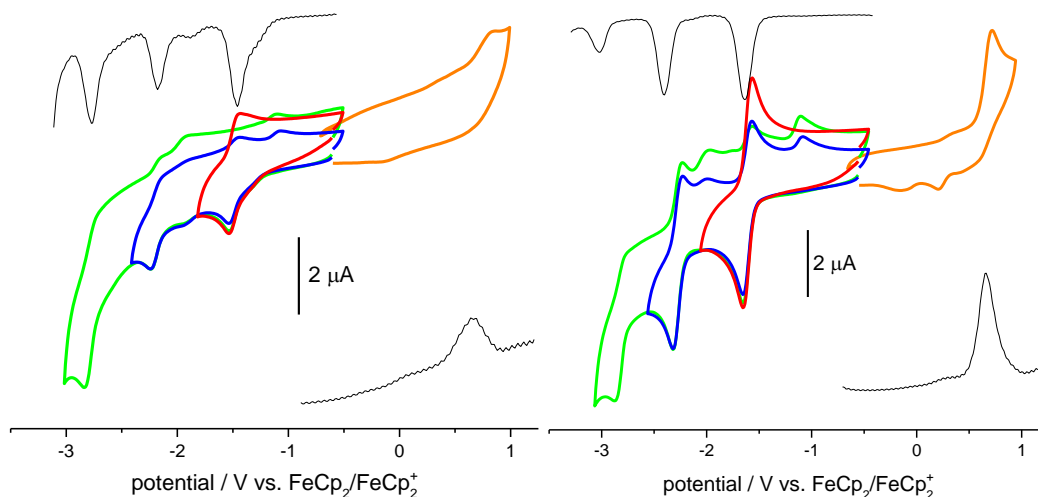


Figure 7.377 Cyclic voltammograms of [Pt(fpyTSCmB)Cl] (left) [Pt(apyTSCmB)Cl] (right) in 0.1 M Bu₄NPF₆/MeCN solution at 100 mV/s scan rate. Square wave measurements in black.

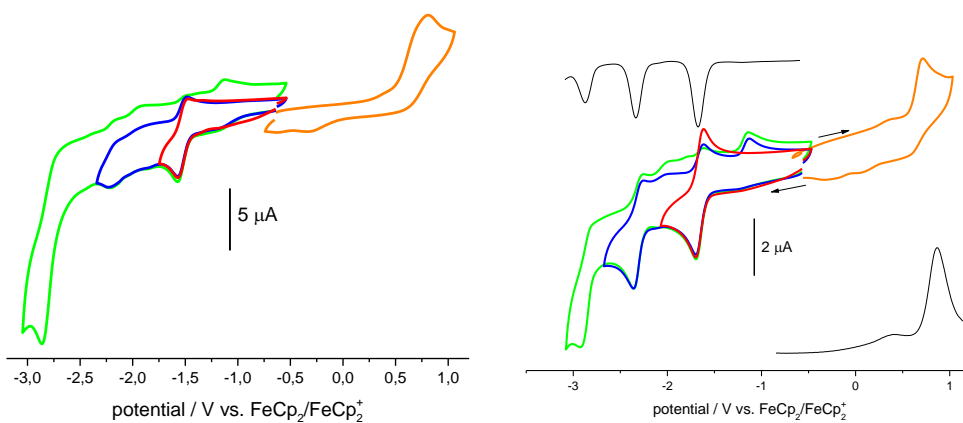


Figure 7.378 Cyclic voltammograms of [Pt(fpyTSCLp)Cl] (left) and [Pt(apyTSCLp)Cl] (right) in 0.1 M Bu₄NPF₆/MeCN solution at 100 mV/s scan rate. Square wave measurements in black.

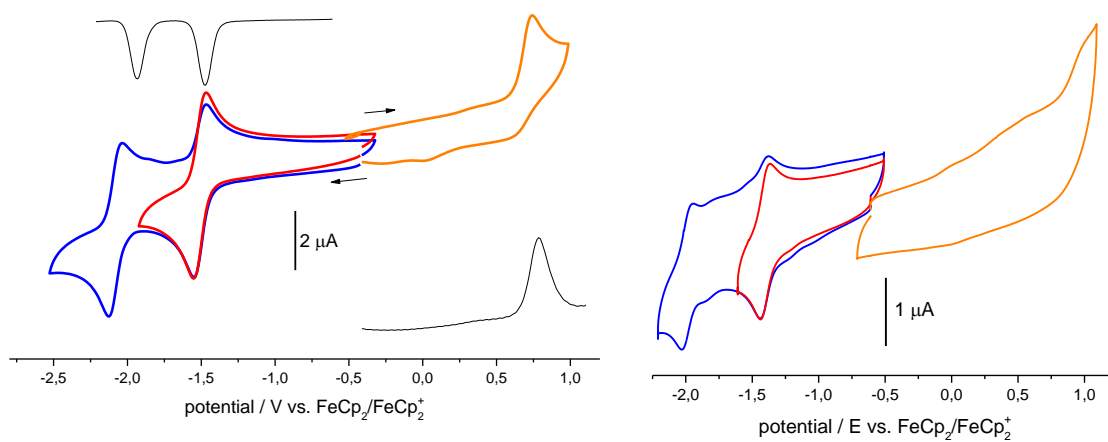


Figure 7.379 Cyclic voltammograms of [Pt(dpyTSCLp)Cl] (left) and [Pt(dpyTSCmB)CN] (right) in 0.1 M Bu₄NPF₆/MeCN solution at 100 mV/s scan rate. Square wave measurements in black.

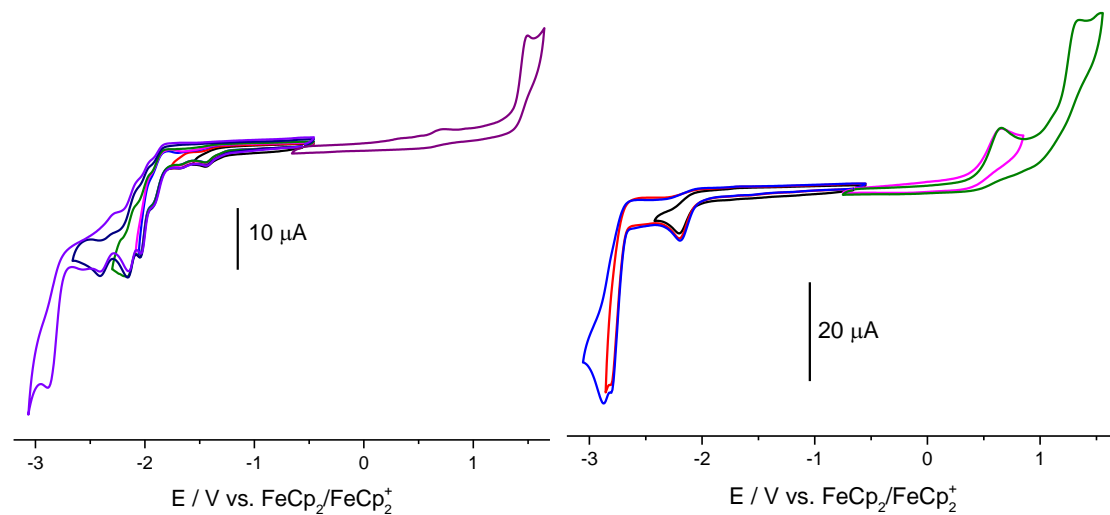


Figure 7.380 Cyclic voltammograms of [Pt(6-BrapyTSCmB)Cl] (left) and [Pt(6-PhapyTSCmB)Cl] (right) in 0.1 M Bu₄NPF₆/MeCN solution at 100 mV/s scan rate. Square wave measurements in black.

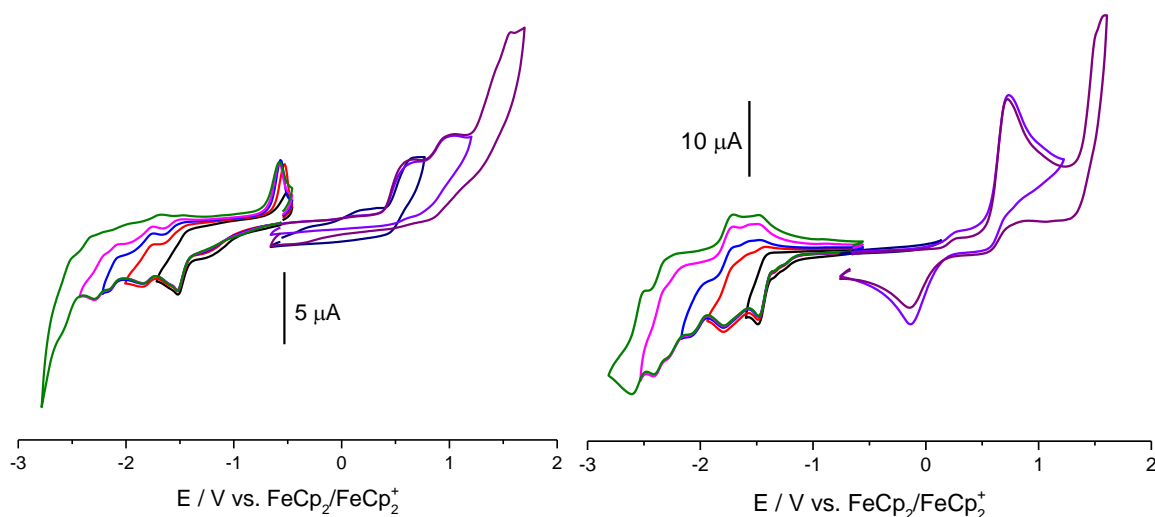


Figure 7.381 Cyclic voltammograms of [Ni(apyTSCmB)Cl] (left) and [Ni(apyTSCmB)NCS] (right) in 0.1 M Bu₄NPF₆/MeCN solution at 100 mV/s scan rate.

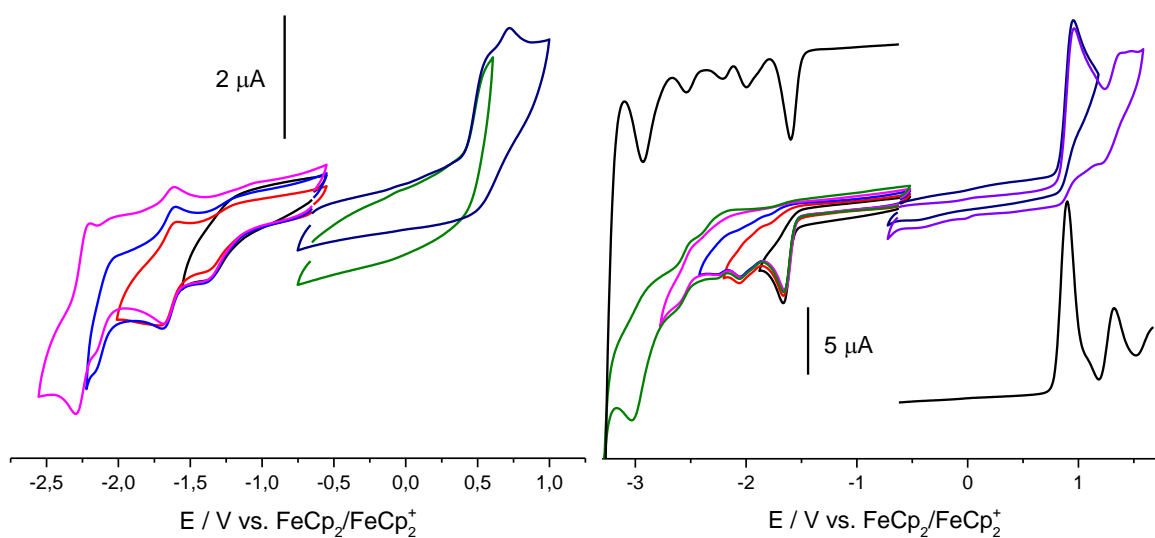


Figure 7.382 Cyclic voltammograms of [Ni(apyTSCmB)CN] (left) and [Pd(apyTSCmB)Cl] (right) in 0.1 M Bu₄NPF₆/MeCN solution at 100 mV/s scan rate.

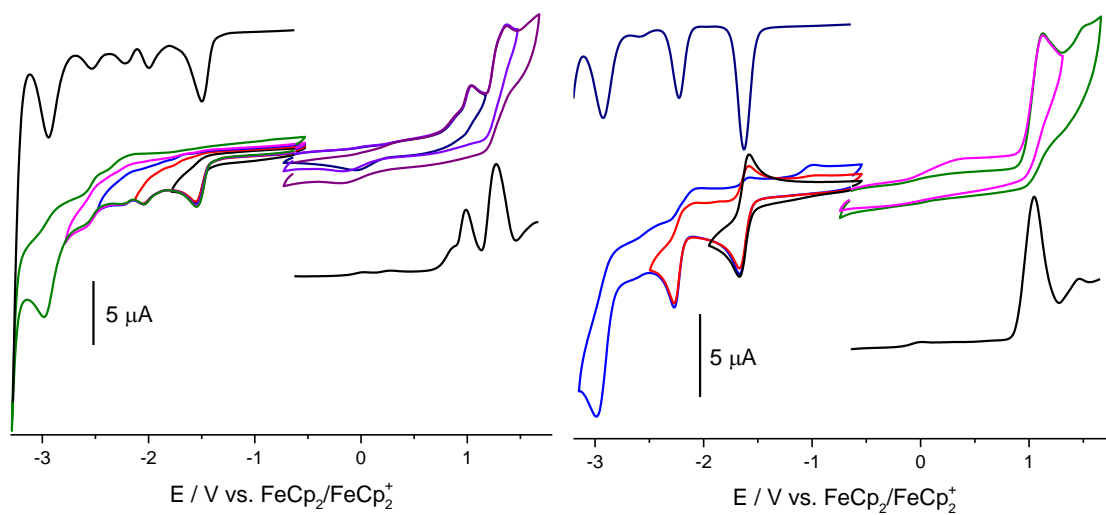


Figure 7.383 Cyclic voltammograms of [Pd(apyTSCmB)NCS] (left) and [Pd(apyTSCmB)CN] (right) in 0.1 M Bu₄NPF₆/MeCN solution at 100 mV/s scan rate.

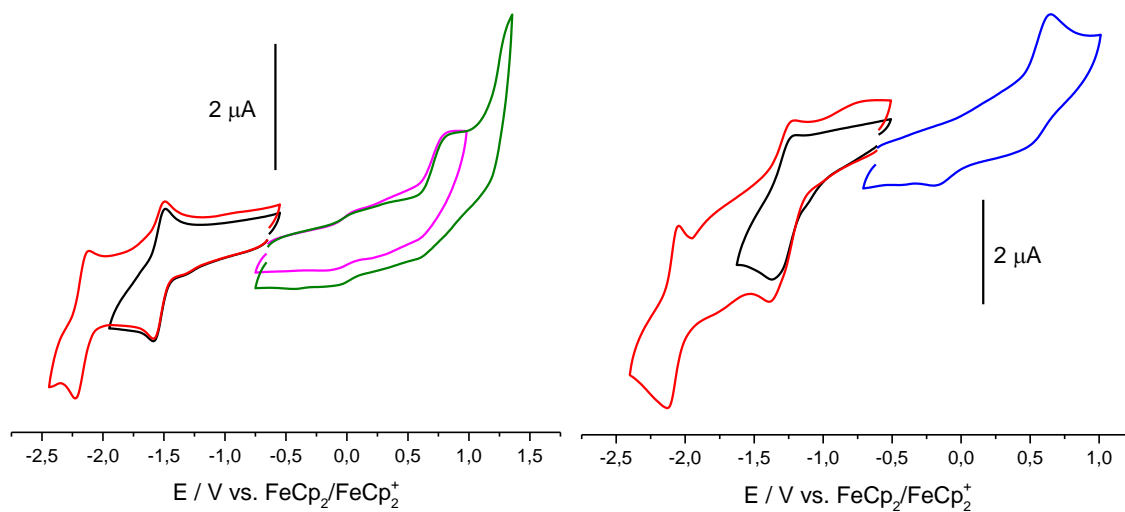


Figure 7.384 Cyclic voltammograms of [Pt(apyTSCmB)NCS] (left) and [Pt(dpyTSCmB)Cl] (right) in 0.1 M Bu₄NPF₆/MeCN solution at 100 mV/s scan rate.

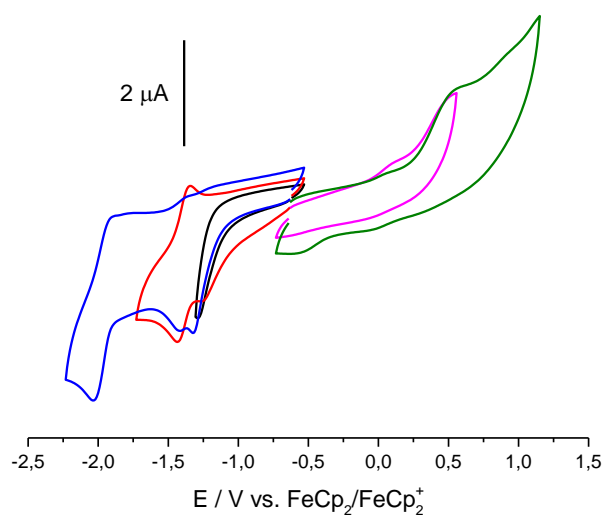


Figure 7.385 Cyclic voltammogram of [Pt(dpyTSCmB)NCS] (left) in 0.1 M Bu₄NPF₆/MeCN solution at 100 mV/s scan rate.

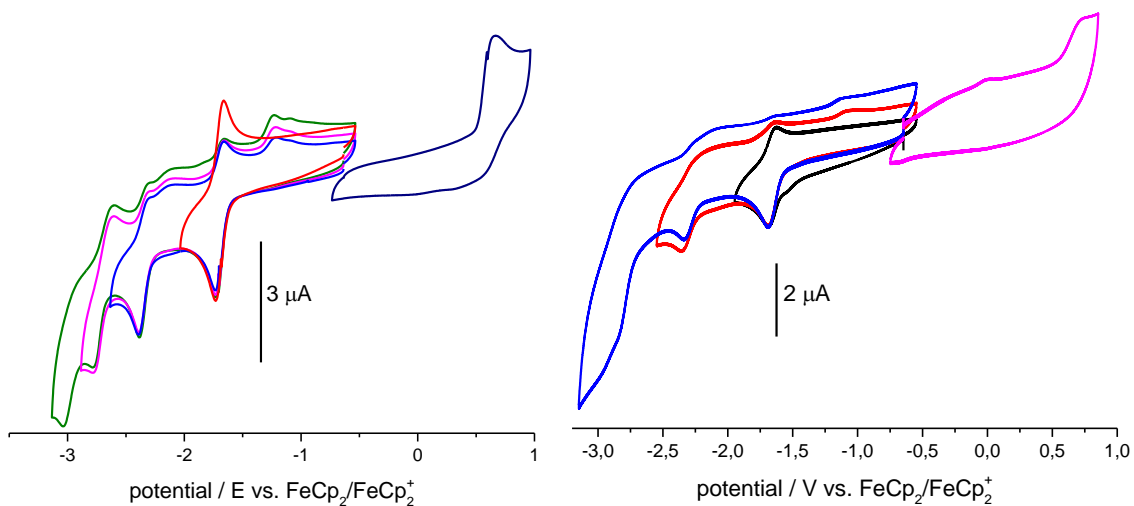


Figure 7.386 Cyclic voltammograms of [Ni(hphfyTSCmB)] (left) and [Pd(hphfyTSCmB)] (right) in 0.1 M Bu₄NPF₆ / MeCN at a feed rate of 100 mV/s.

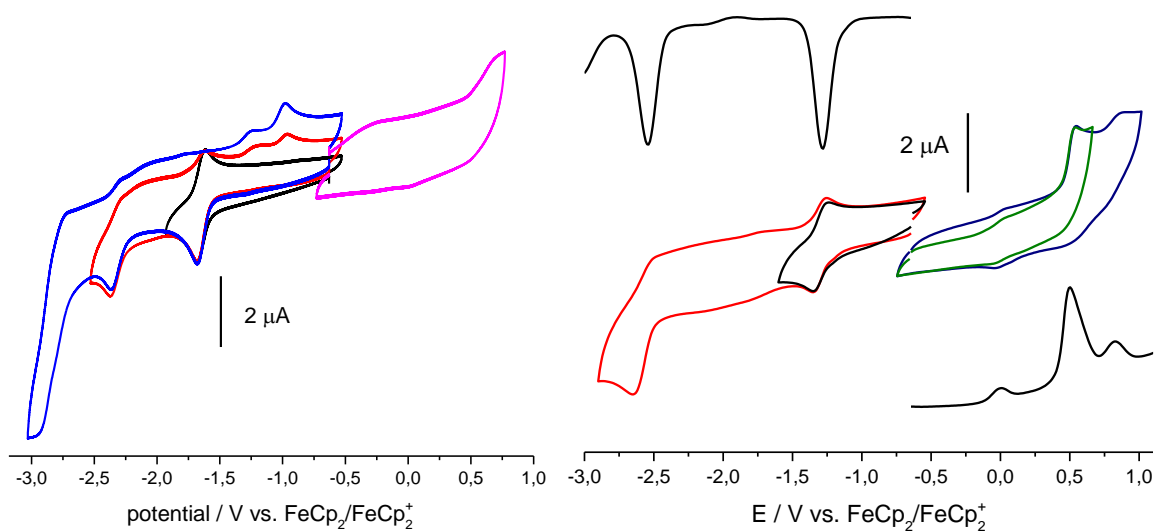


Figure 7.387 Cyclic voltammograms of [Pt(hphfyTSCmB)] and [Cu(hphfyTSCmB)] in 0.1 M Bu₄NPF₆ / MeCN at a feed rate of 100 mV/s.

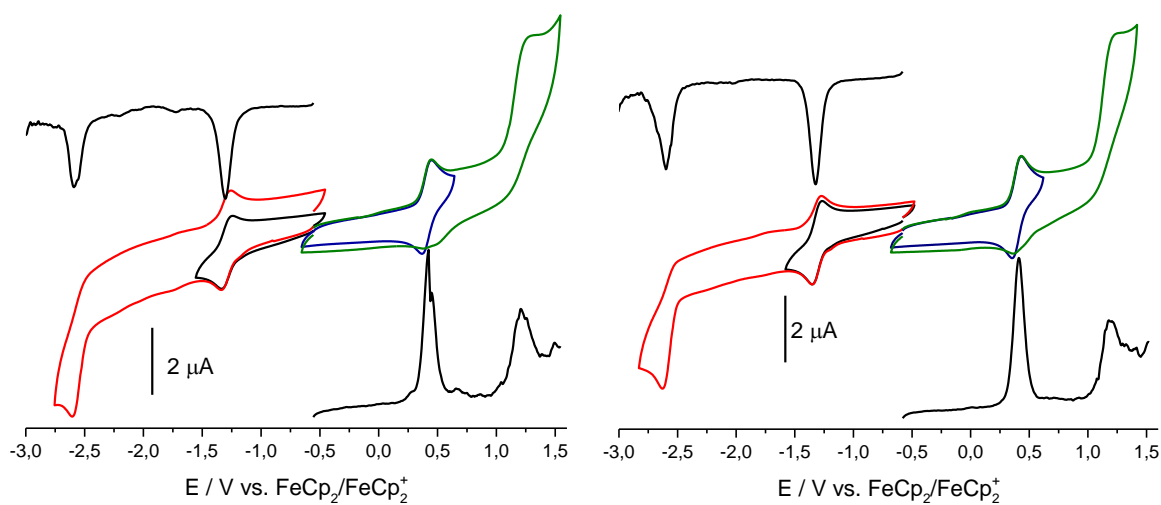


Figure 7.388 Cyclic voltammograms of [Cu(tBuhphfyTSC)] and [Cu(tBuhphfyTSCmB)] in 0.1 M Bu₄NPF₆ / MeCN at a feed rate of 100 mV/s.

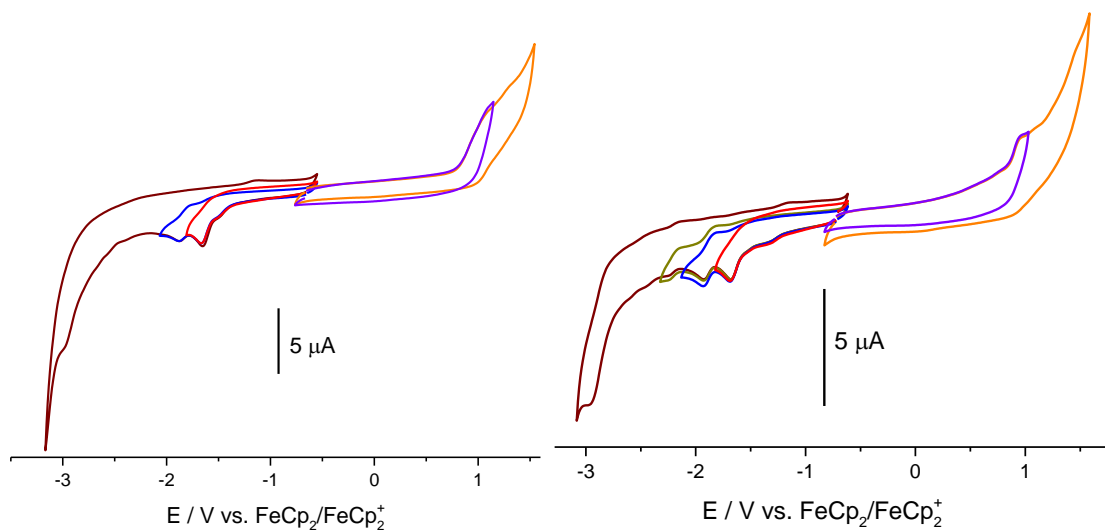


Figure 7.389 Cyclic voltammograms of [Pd(PPh₃)(bzTSC)Cl] (left) and [Pd(PPh₃)(bzTSCmB)Cl] (right) in 0.1 M Bu₄NPF₆ / MeCN at a feed rate of 100 mV/s.

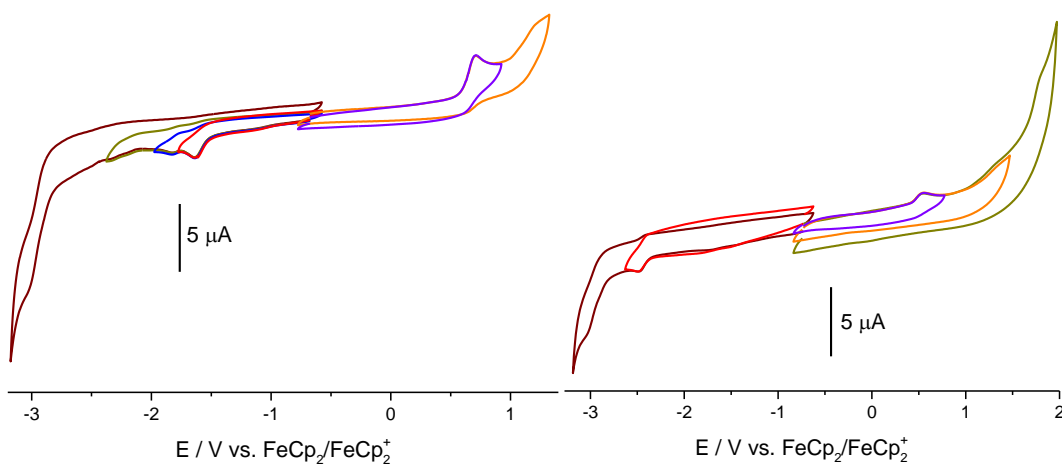


Figure 7.390 Cyclic voltammograms of [Pd(PPh₃)(bzTSCpBa)Cl] (left) and [Pd(PPh₃)(bzTSClp)] (right) in 0.1 M Bu₄NPF₆ / MeCN at a feed rate of 100 mV/s.

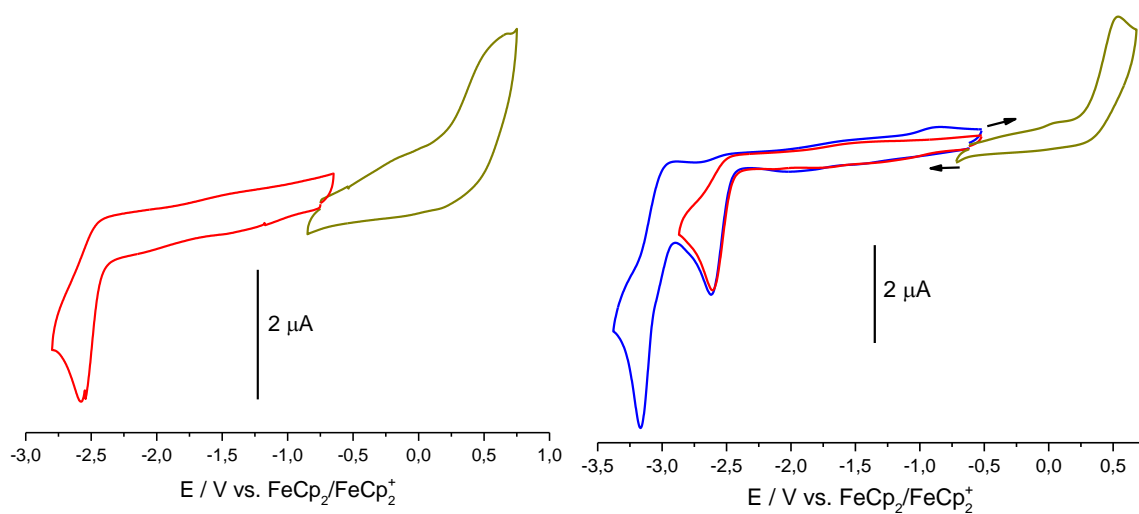


Figure 7.391 Cyclic voltammograms of [U(bzTSC)₄] (left) and [U(bzTSCm)₄] (right) in 0.1 M Bu₄NPF₆ / THF at a feed rate of 100 mV/s.

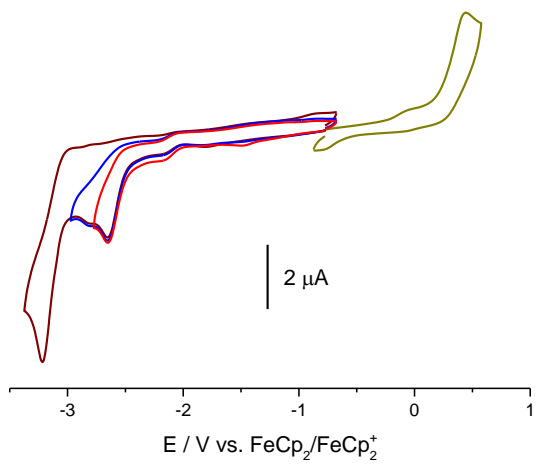


Figure 7.392 Cyclic voltammograms of $[\text{U}(\text{bzTSCdm})_4]$ in 0.1 M $\text{Bu}_4\text{NPF}_6 / \text{THF}$ at a scan rate of 100 mV/s.

7.10. Spectroelectrochemical UV/Vis spectra

7.10.1. Ligands

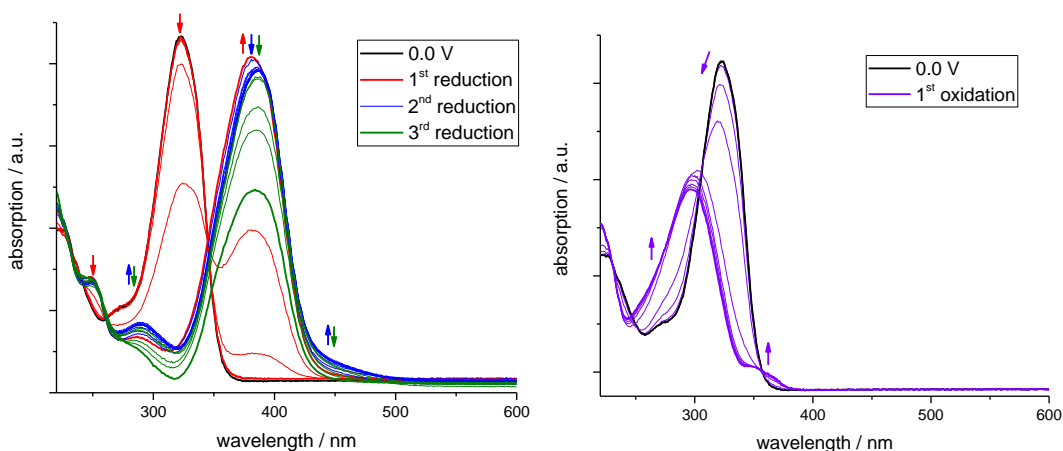


Figure 7.393 Spectroelectrochemical UV/Vis measurements during the reduction (left) and oxidation (right) of HbZTSC in 0.1 M Bu₄NPF₆ / THF with 0.1 V increments.

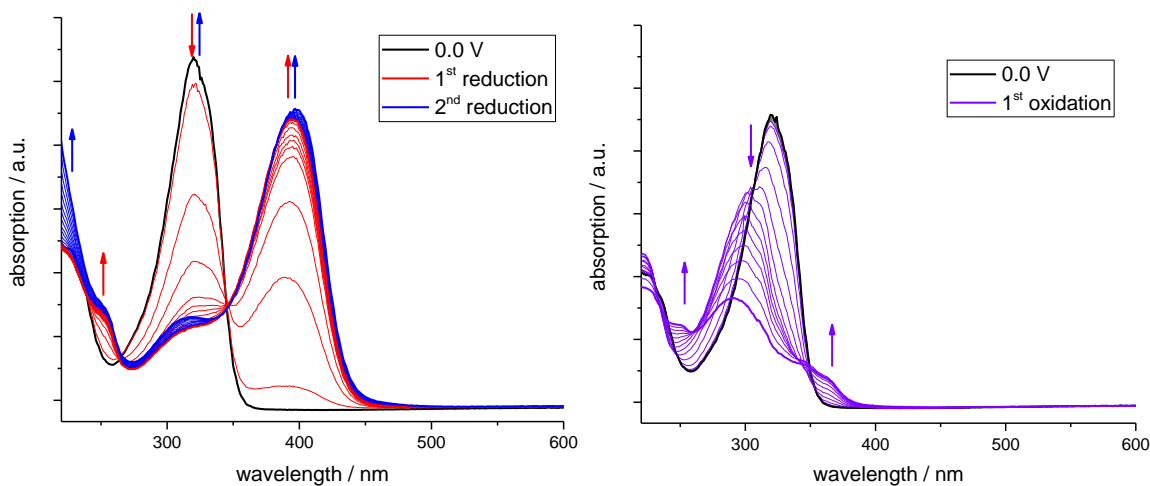


Figure 7.394 Spectroelectrochemical UV/Vis measurements during the reduction (left) and oxidation (right) of HbZTSCm in 0.1 M Bu₄NPF₆ / THF with 0.1 V increments.

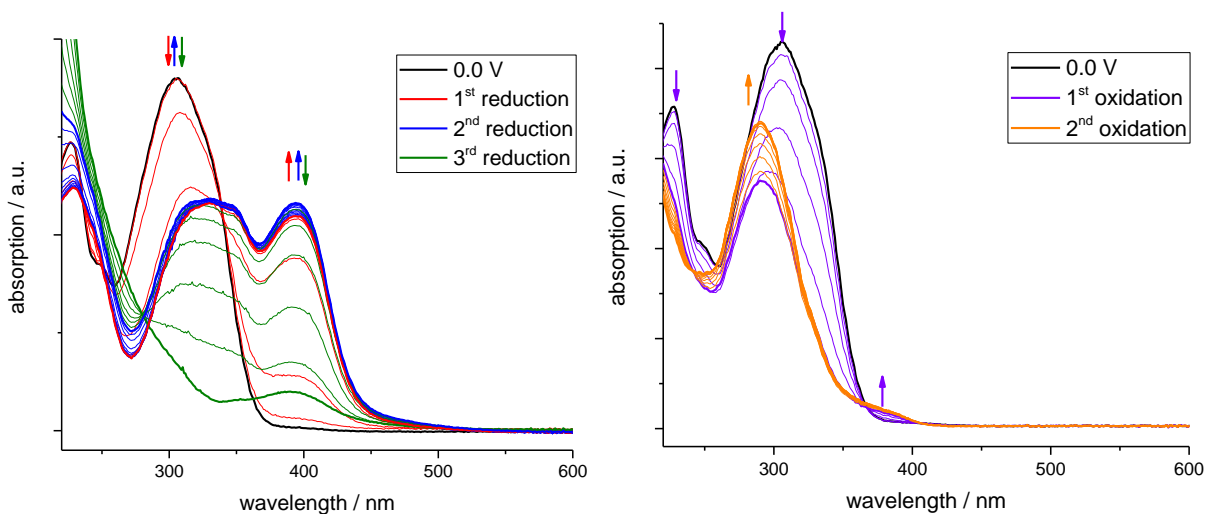


Figure 7.395 Spectroelectrochemical UV/Vis measurements during the reduction (left) and oxidation (right) of HbZTSCdm in 0.1 M Bu₄NPF₆ / THF with 0.1 V increments.

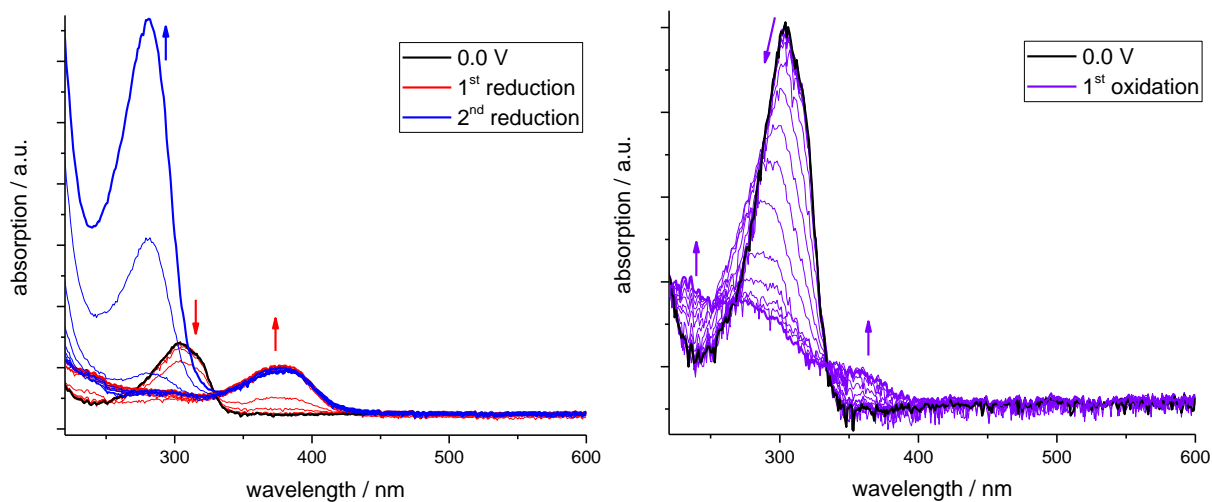


Figure 7.396 Spectroelectrochemical UV/Vis measurements during the reduction (left) and oxidation (right) of HbzTSCmB in 0.1 M Bu₄NPF₆ / MeCN with 0.1 V increments.

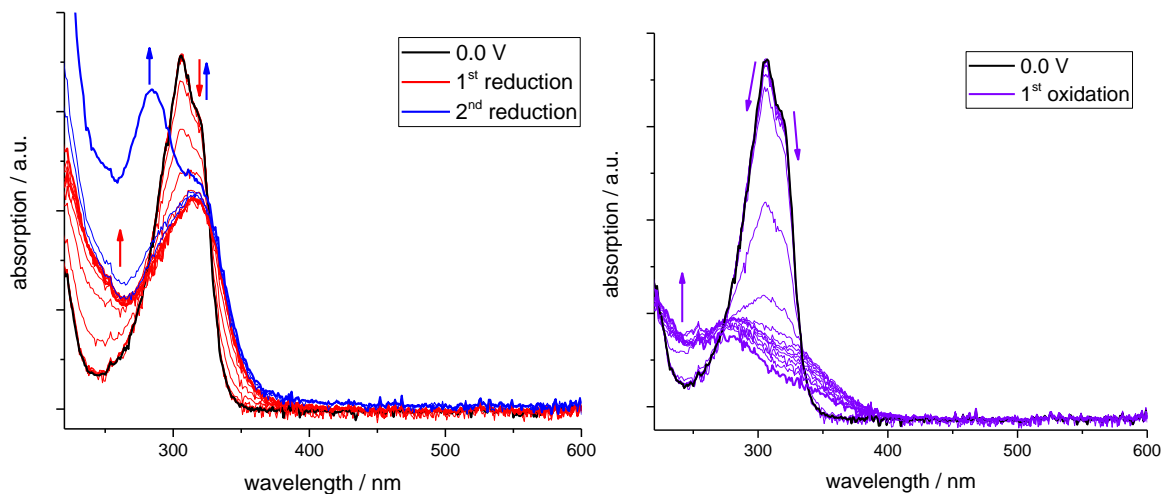


Figure 7.397 Spectroelectrochemical UV/Vis measurements during the reduction (left) and oxidation (right) of Hbz(m)TSCmB in 0.1 M Bu₄NPF₆ / MeCN with 0.1 V increments.

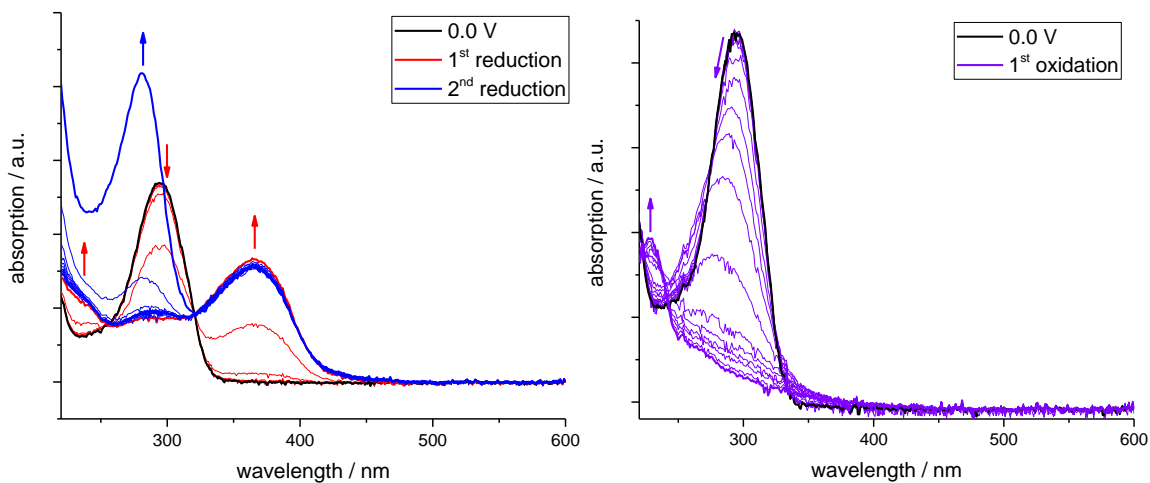


Figure 7.398X Spectroelectrochemical UV/Vis measurements during the reduction (left) and oxidation (right) of HaphTSCmB in 0.1 M Bu₄NPF₆ / MeCN with 0.1 V increments.

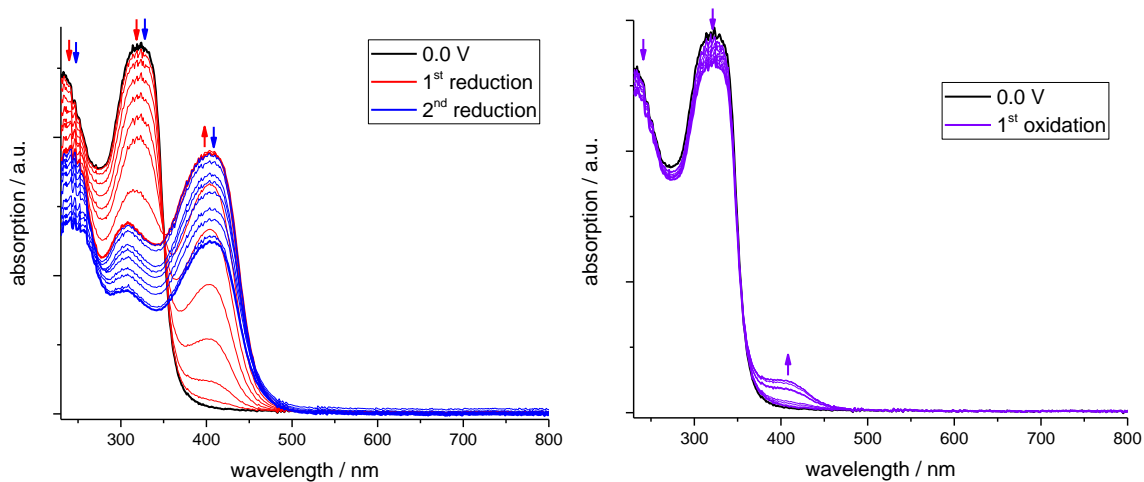


Figure 7.399 Spectroelectrochemical UV/Vis measurements during the reduction (left) and oxidation (right) of HbphTSCmB in 0.1 M Bu₄NPF₆ / MeCN with 0.1 V increments.

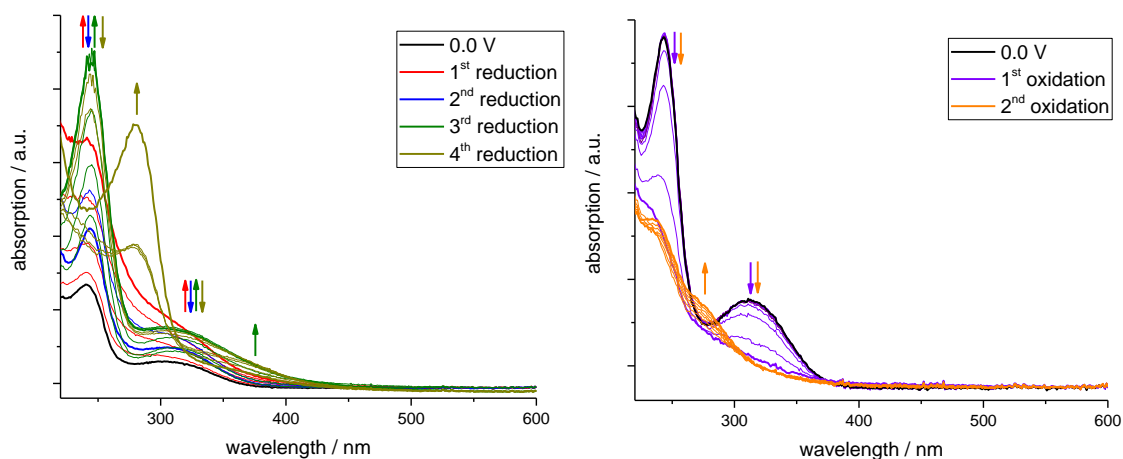


Figure 7.400 Spectroelectrochemical UV/Vis measurements during the reduction (left) and oxidation (right) of Haph(m)TSCmB in 0.1 M Bu₄NPF₆ / MeCN with 0.1 V increments.

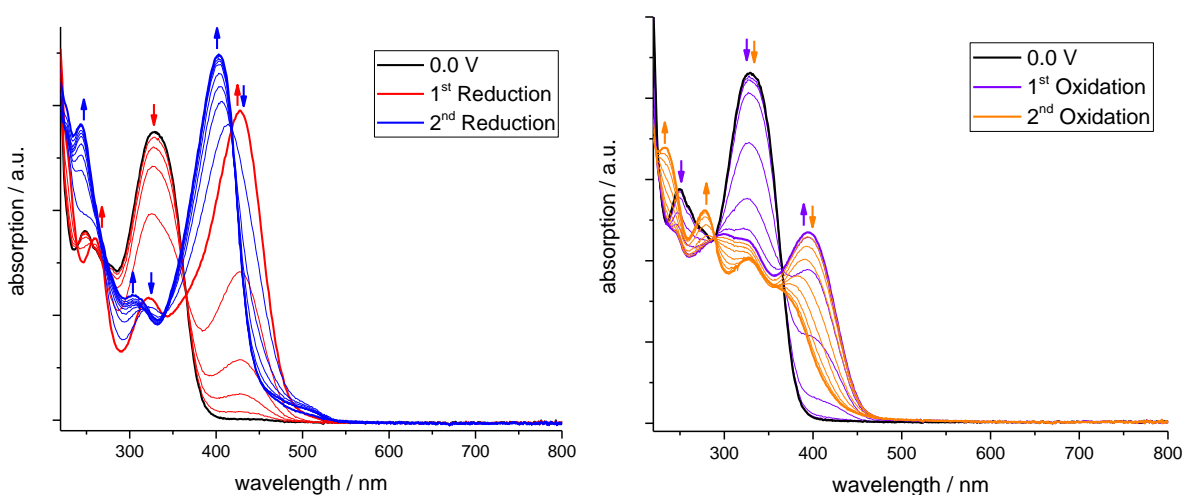


Figure 7.401 Spectroelectrochemical UV/Vis measurements during the reduction (left) and oxidation (right) of H₂hphpyTSCmB in 0.1 M Bu₄NPF₆ / MeCN with 0.1 V increments.

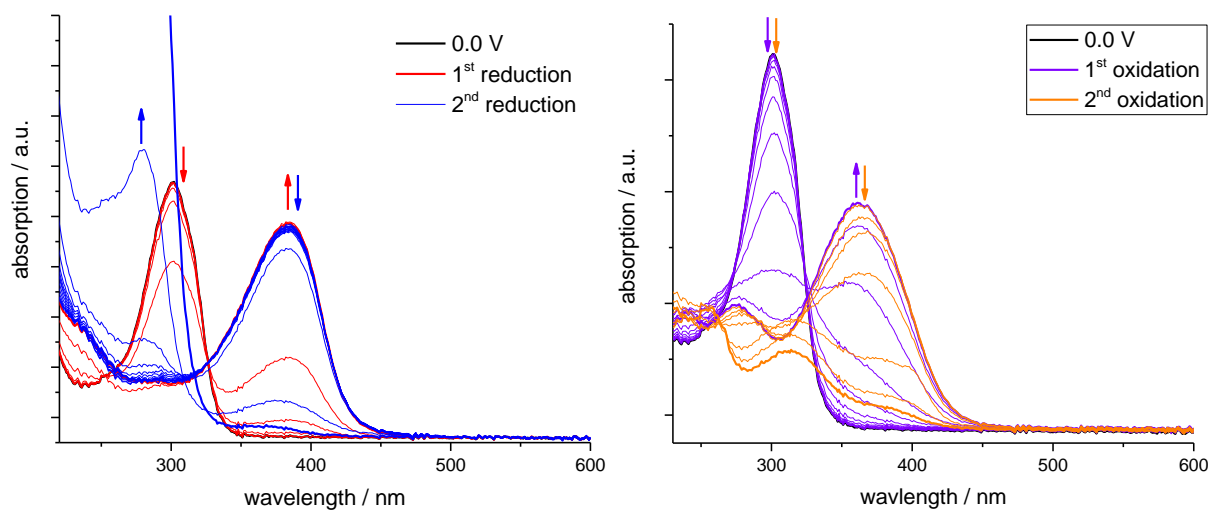


Figure 7.402 Spectroelectrochemical UV/Vis measurements during the reduction (left) and oxidation (right) of HapyTSCmB in 0.1 M Bu₄NPF₆ / MeCN with 0.1 V increments.

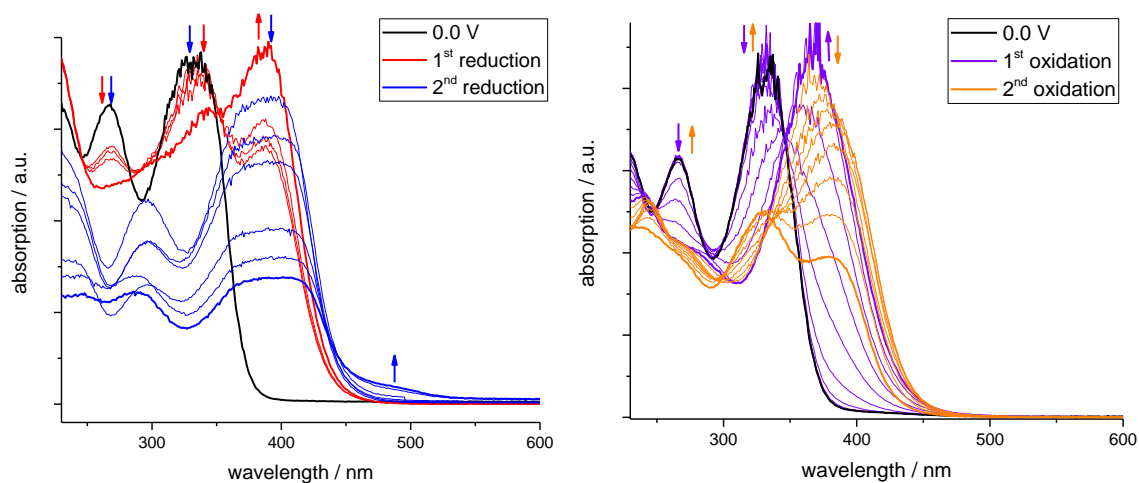


Figure 7.403 Spectroelectrochemical UV/Vis measurements during the reduction (left) and oxidation (right) of HdpyTSCmB in 0.1 M Bu₄NPF₆ / MeCN with 0.1 V increments.

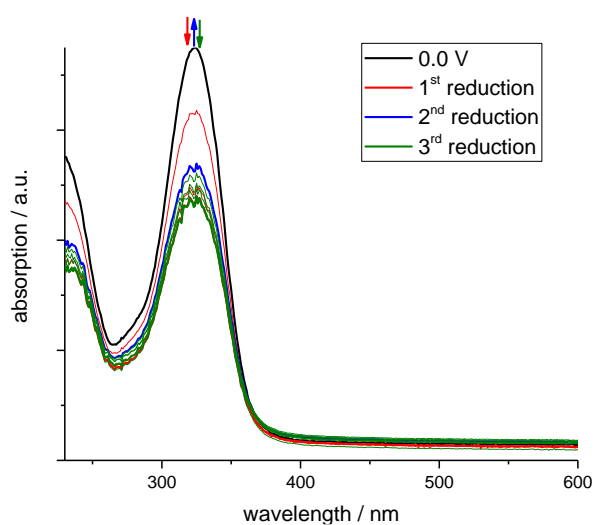


Figure 7.404 Spectroelectrochemical UV/Vis measurements during the reduction (left) and oxidation (right) of Hdap(b)TSC in 0.1 M Bu₄NPF₆ / THF with 0.1 V increments.

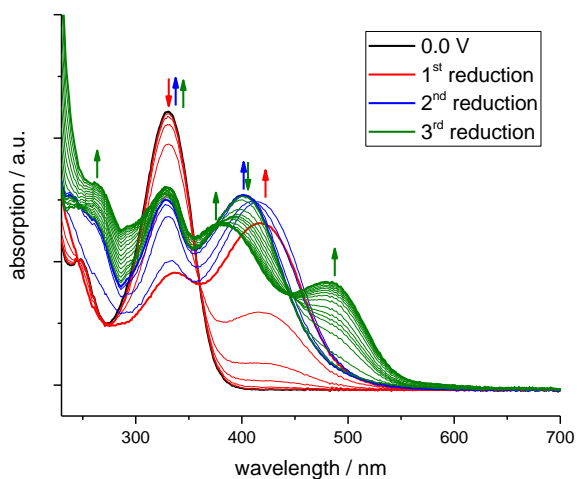


Figure 7.405 Spectroelectrochemical UV/Vis measurements during the reduction of Hdap(b)TSCAd in 0.1 M Bu₄NPF₆ / THF with 0.1 V increments.

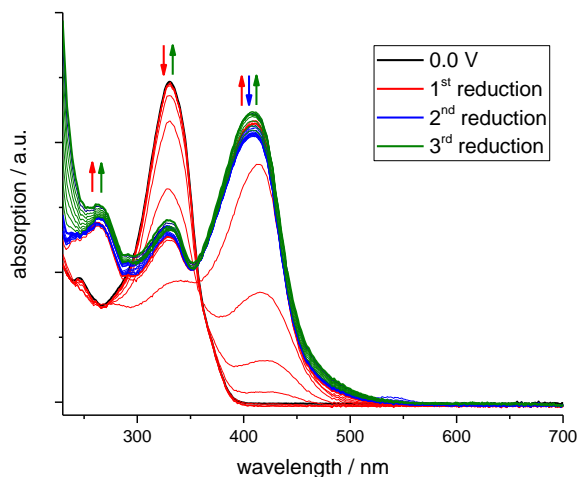


Figure 7.406 Spectroelectrochemical UV/Vis measurements during the reduction of Hdap(b)TSCmB in 0.1 M Bu₄NPF₆ / THF with 0.1 V increments.

7.10.2. Complexes

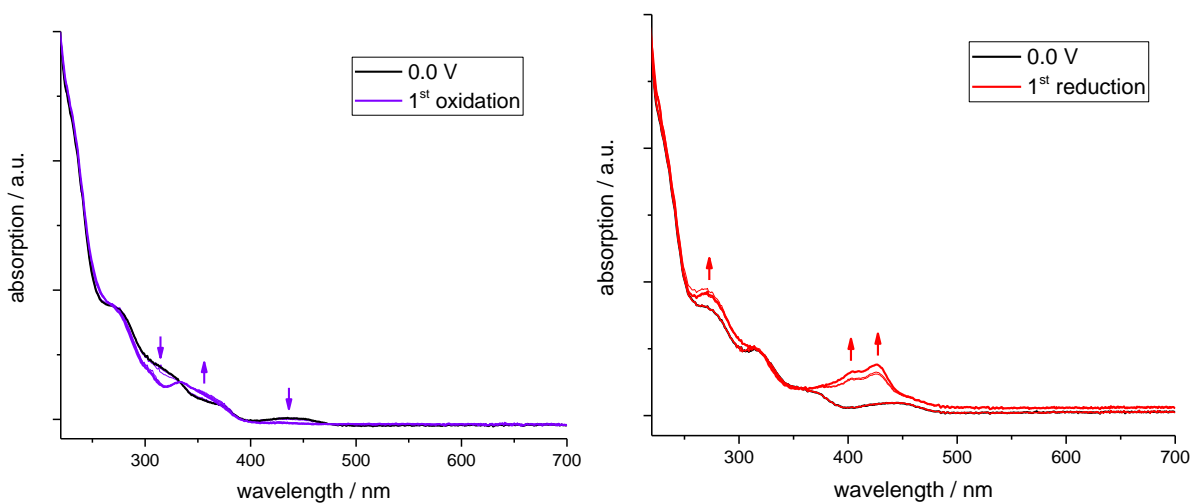


Figure 7.407 Spectroelectrochemical UV/Vis measurements during the reduction (left) and oxidation (right) of [Ir(PPh₃)₂(bz)TSCmB(H)] in 0.1 M Bu₄NPF₆ / MeCN with 0.1 V increments.

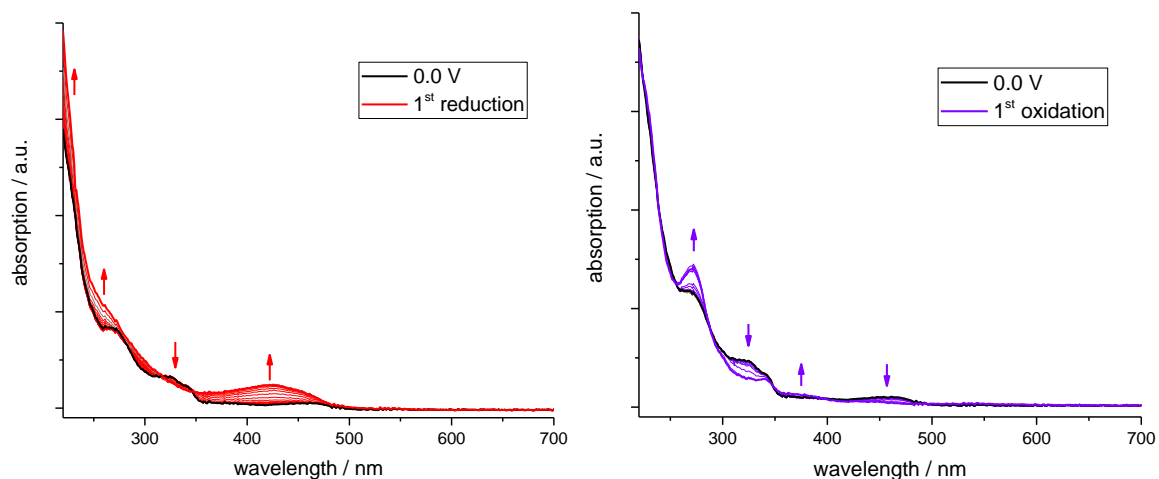


Figure 7.408 Spectroelectrochemical UV/Vis measurements during the reduction (left) and oxidation (right) of $[\text{Ir}(\text{PPh}_3)_2(\text{bzTSCmB})(\text{Cl})]$ in 0.1 M $\text{Bu}_4\text{NPF}_6 / \text{MeCN}$ with 0.1 V increments.

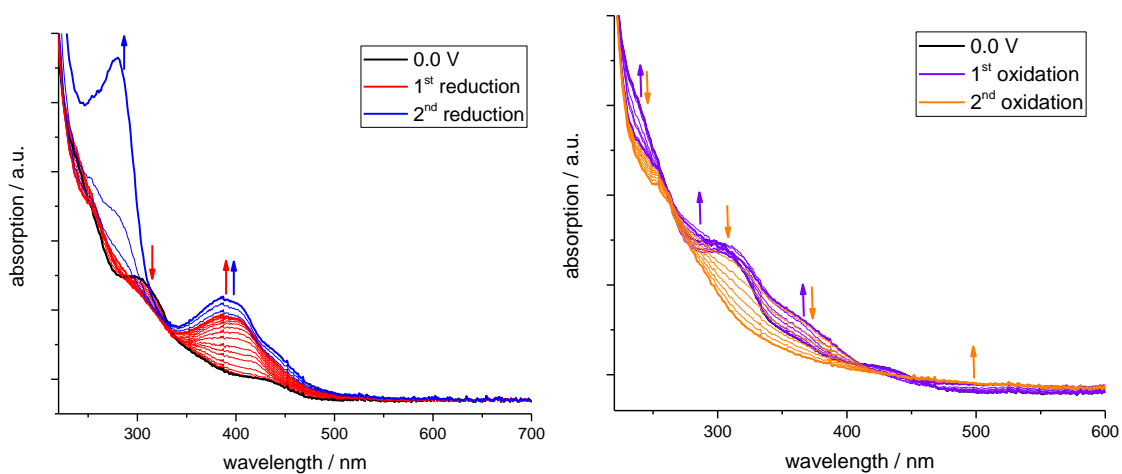


Figure 7.409 Spectroelectrochemical UV/Vis measurements during the reduction (left) and oxidation (right) of $[\text{Ir}(\text{AsPh}_3)_2(\text{aph}(\text{m})\text{TSCmB})(\text{H})]$ in 0.1 M $\text{Bu}_4\text{NPF}_6 / \text{MeCN}$ with 0.1 V increments.

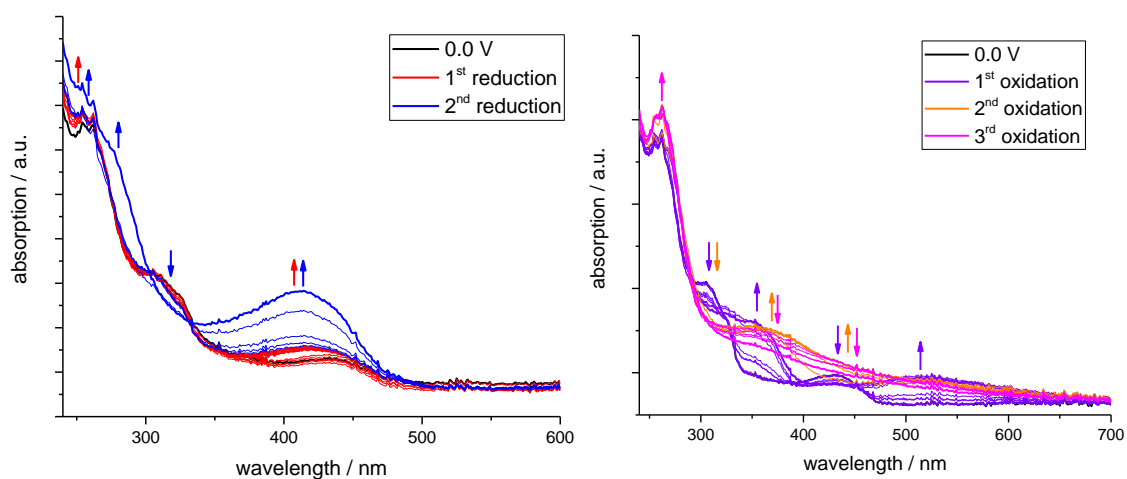


Figure 7.410 Spectroelectrochemical UV/Vis measurements during the reduction (left) and oxidation (right) of $[\text{Ir}(\text{PPh}_3)_2(\text{aphTSCmB})(\text{H})]$ in 0.1 M $\text{Bu}_4\text{NPF}_6 / \text{MeCN}$ with 0.1 V increments.

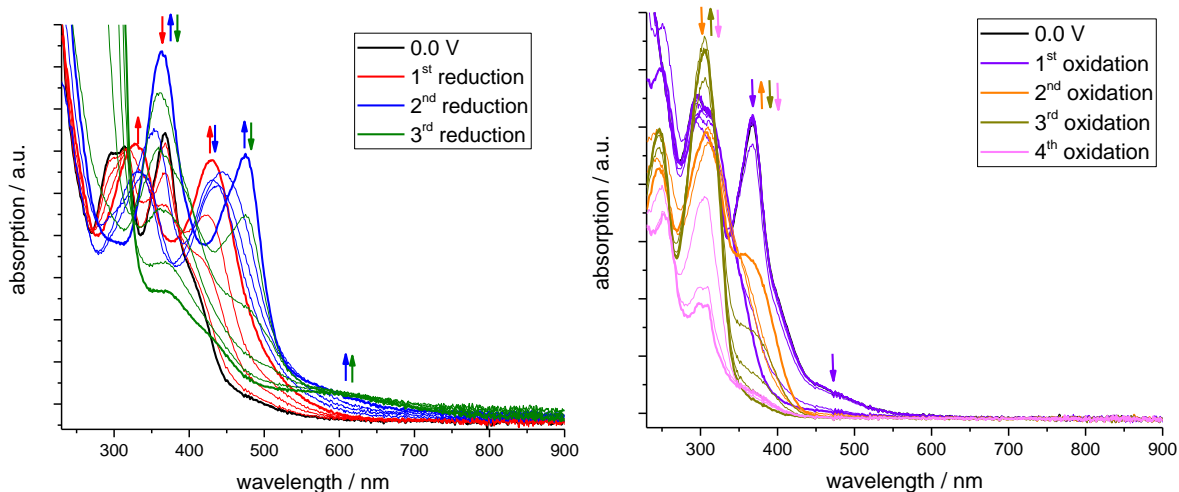


Figure 7.411 Spectroelectrochemical UV/Vis measurements during the reduction (left) and oxidation (right) of [Ni(apyTSCmB)Cl] in 0.1 M Bu₄NPF₆ / MeCN with 0.1 V increments.

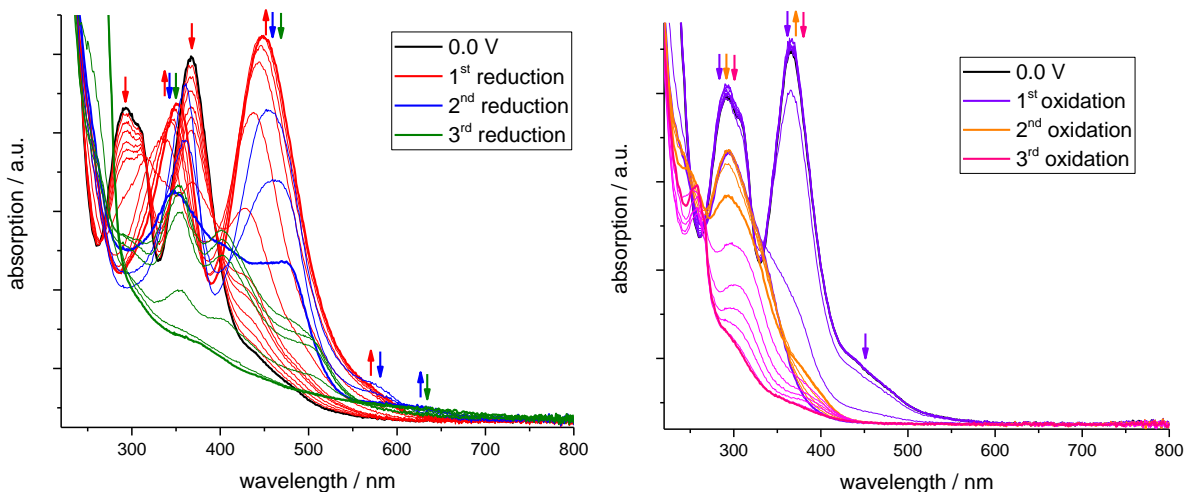


Figure 7.412 Spectroelectrochemical UV/Vis measurements during the reduction (left) and oxidation (right) of [Ni(apyTSCmB)NCS] in 0.1 M Bu₄NPF₆ / MeCN with 0.1 V increments.

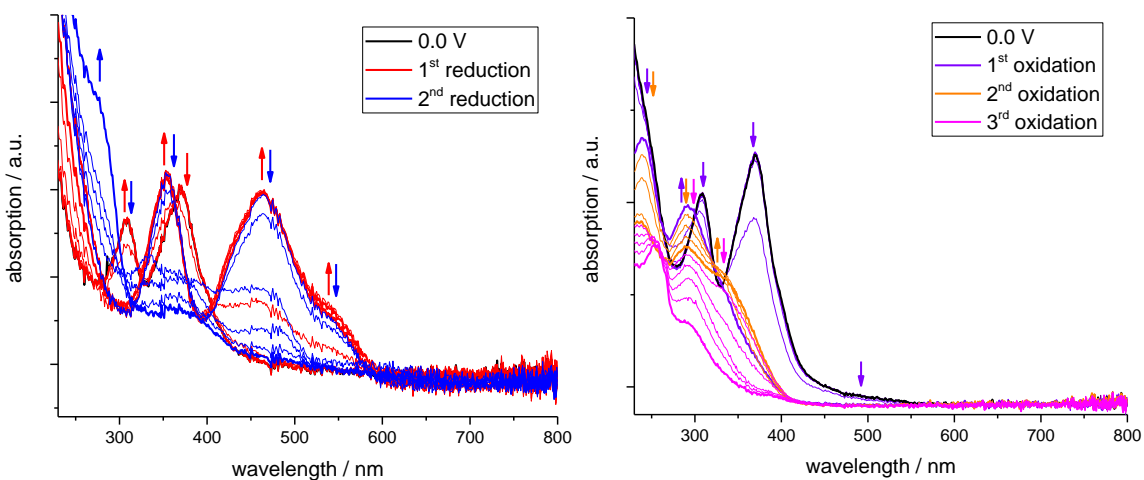


Figure 7.413 Spectroelectrochemical UV/Vis measurements during the reduction (left) and oxidation (right) of [Ni(apyTSCmB)CN] in 0.1 M Bu₄NPF₆ / MeCN with 0.1 V increments.

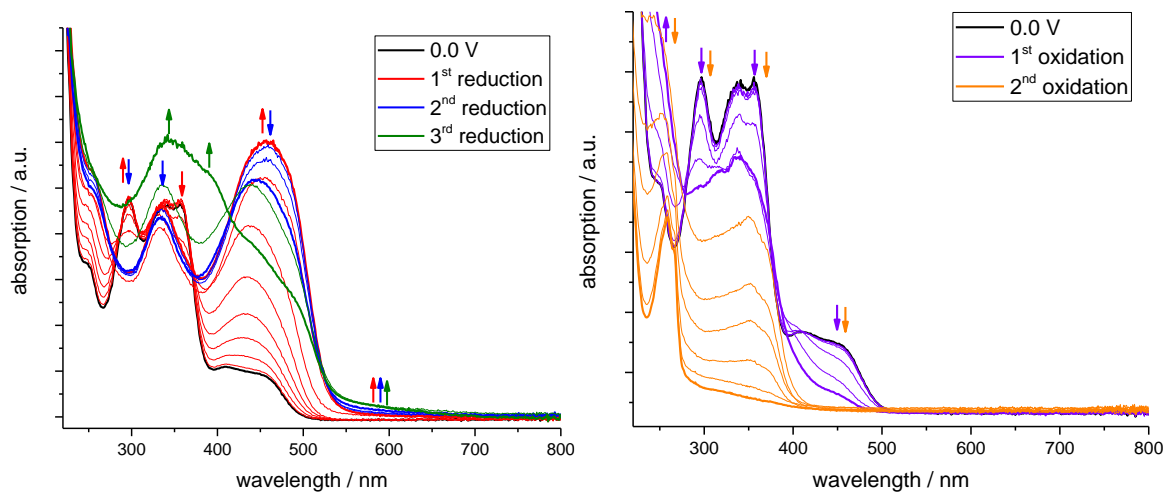


Figure 7.414 Spectroelectrochemical UV/Vis measurements during the reduction (left) and oxidation (right) of [Pd(apvTSCmB)Cl] in 0.1 M Bu₄NPF₆ / MeCN with 0.1 V increments.

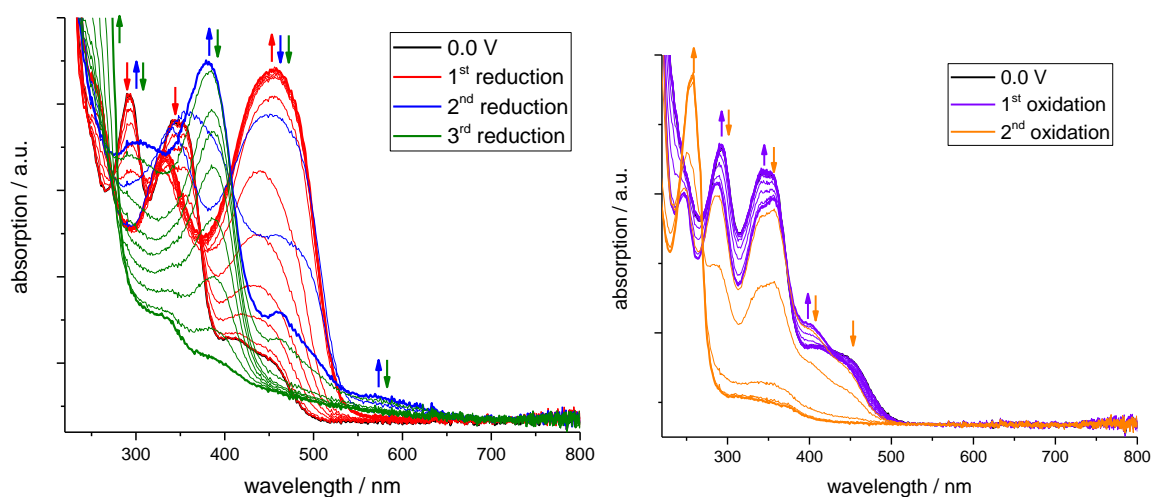


Figure 7.415 Spectroelectrochemical UV/Vis measurements during the reduction (left) and oxidation (right) of [Pd(apvTSCmB)NCS] in 0.1 M Bu₄NPF₆ / MeCN with 0.1 V increments.

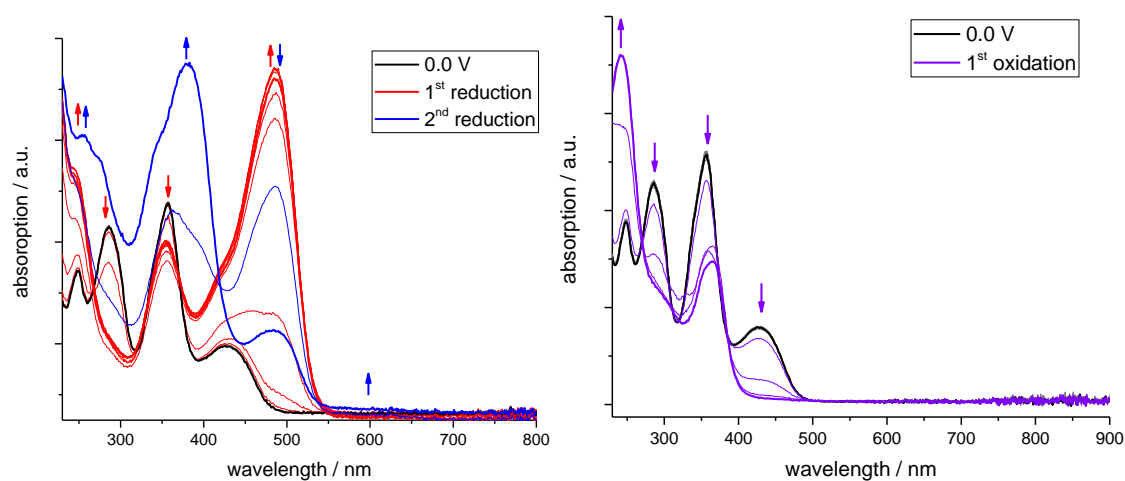


Figure 7.416 Spectroelectrochemical UV/Vis measurements during the reduction (left) and oxidation (right) of [Pd(apvTSCmB)CN] in 0.1 M Bu₄NPF₆ / MeCN with 0.1 V increments.

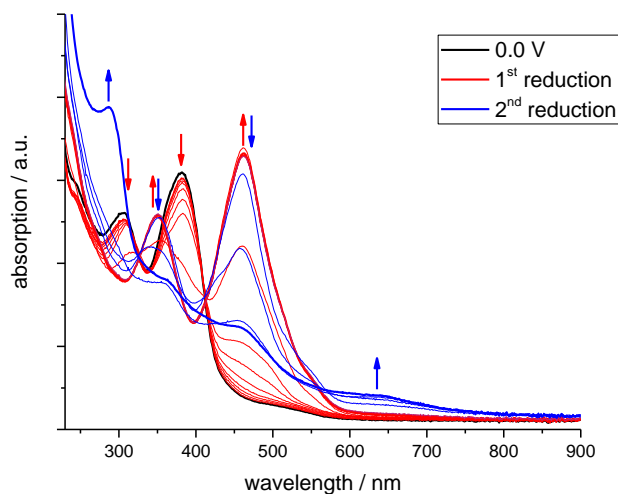


Figure 7.417 Spectroelectrochemical UV/Vis measurements during the reduction of [Pt(fpyTSCmB)Cl] in 0.1 M Bu₄NPF₆ / MeCN with 0.1 V increments.

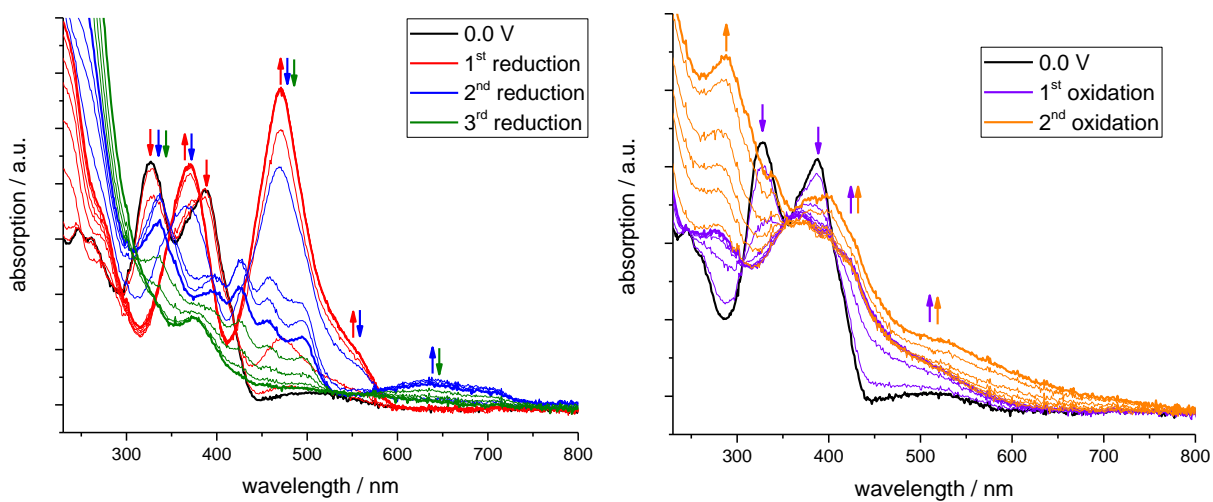


Figure 7.418 Spectroelectrochemical UV/Vis measurements during the reduction (left) and oxidation (right) of [Pt(apyTSCmB)Cl] in 0.1 M Bu₄NPF₆ / MeCN with 0.1 V increments.

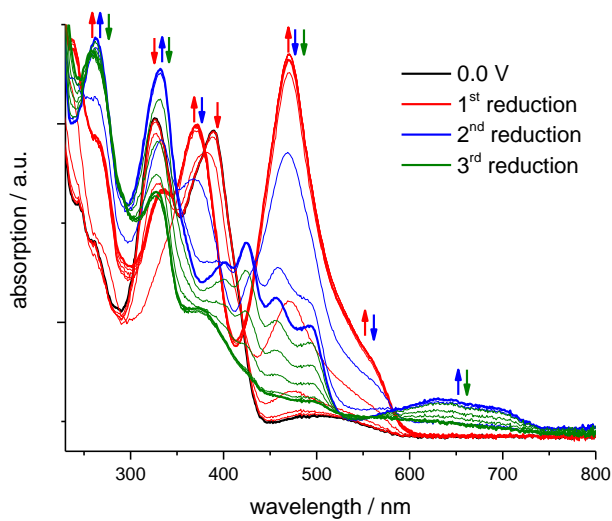


Figure 7.419 Spectroelectrochemical UV/Vis measurements during the reduction of [Pt(apyTSCLp)Cl] in 0.1 M Bu₄NPF₆ / MeCN with 0.1 V increments.

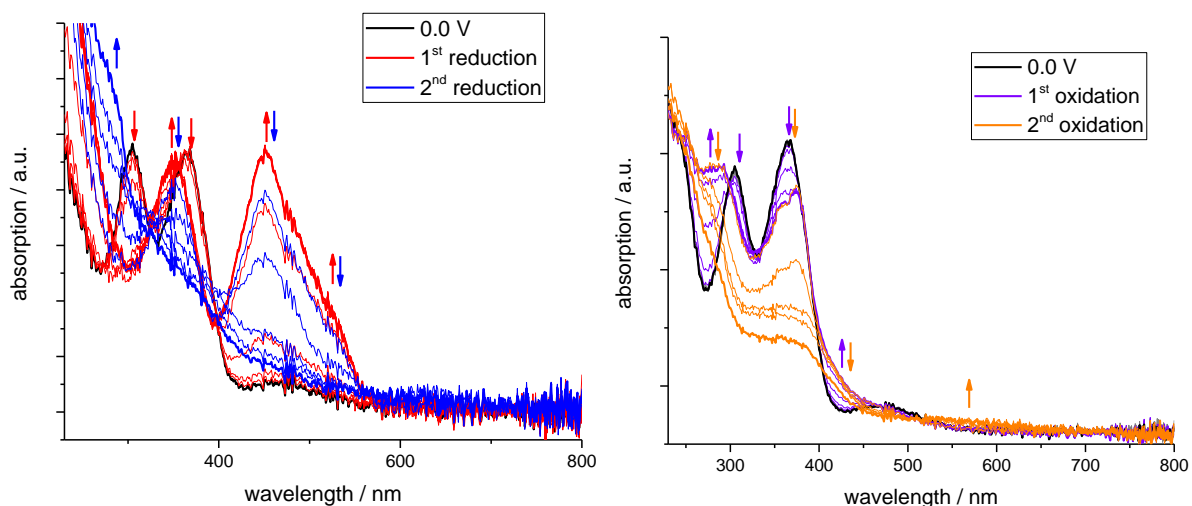


Figure 7.420 Spectroelectrochemical UV/Vis measurements during the reduction (left) and oxidation (right) of [Pt(apvTSCmB)NCS] in 0.1 M Bu₄NPF₆ / MeCN with 0.1 V increments.

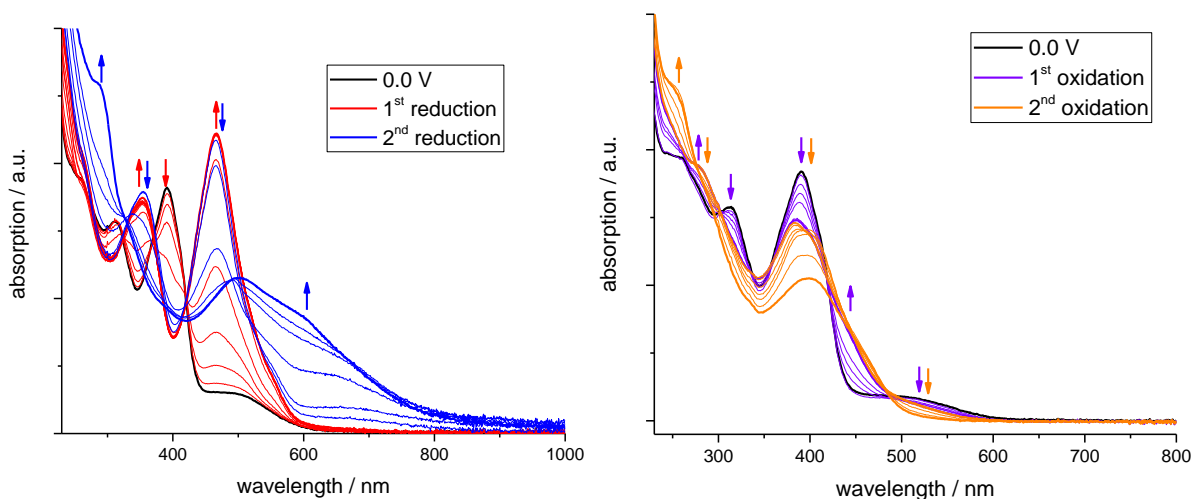


Figure 7.421 Spectroelectrochemical UV/Vis measurements during the reduction (left) and oxidation (right) of [Pt(dpyTSCmB)Cl] in 0.1 M Bu₄NPF₆ / MeCN with 0.1 V increments.

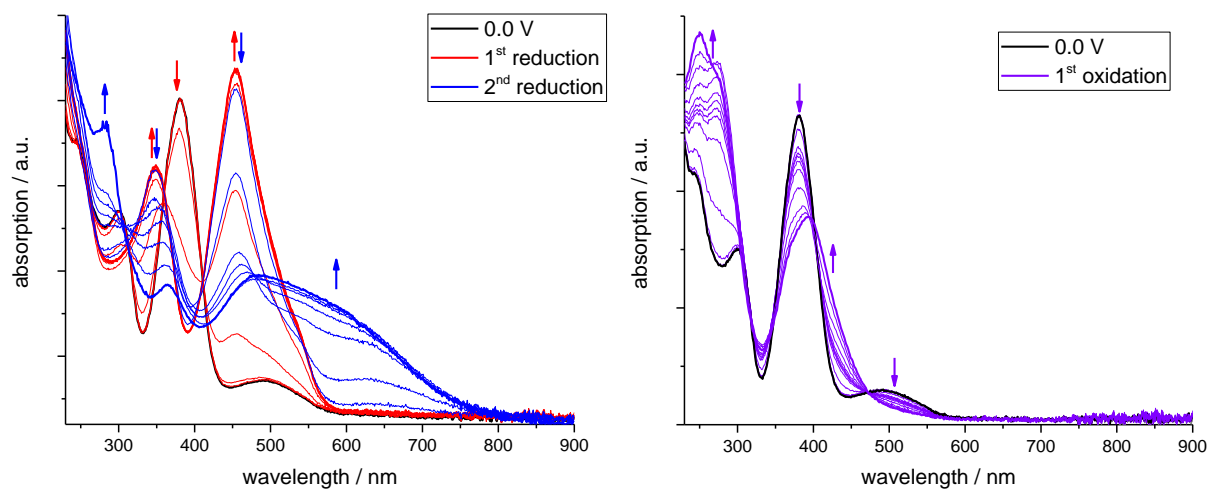


Figure 7.422 Spectroelectrochemical UV/Vis measurements during the reduction (left) and oxidation (right) of [Pt(dpyTSCmB)NCS] in 0.1 M Bu₄NPF₆ / MeCN with 0.1 V increments.

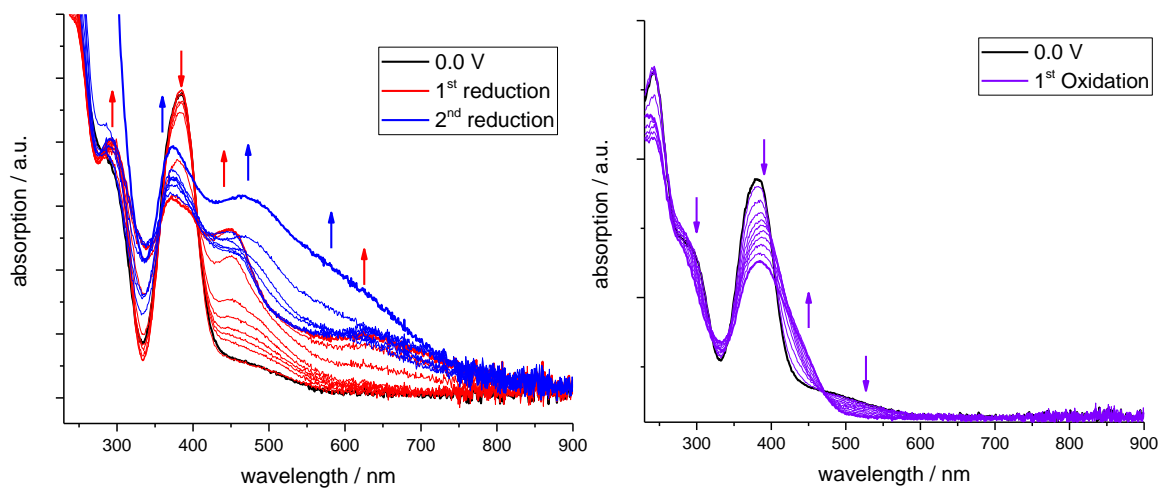


Figure 7.423 Spectroelectrochemical UV/Vis measurements during the reduction (left) and oxidation (right) of [Pt(dpyTSCmB)CN] in 0.1 M Bu₄NPF₆ / MeCN with 0.1 V increments.

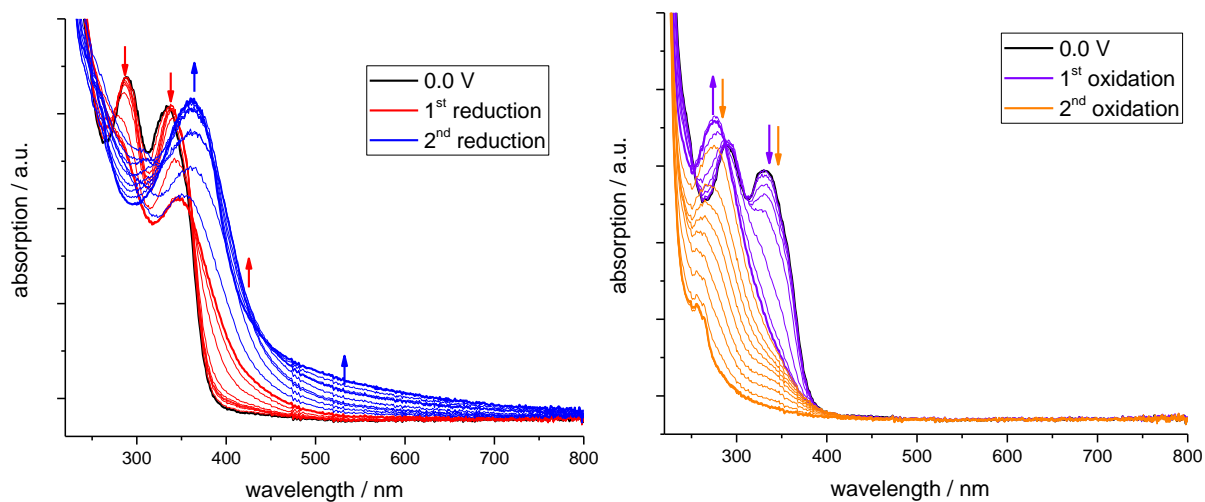


Figure 7.424 Spectroelectrochemical UV/Vis measurements during the reduction (left) and oxidation (right) of [Pd(PPh₃)(bzTSC)Cl] in 0.1 M Bu₄NPF₆ / MeCN with 0.1 V increments.

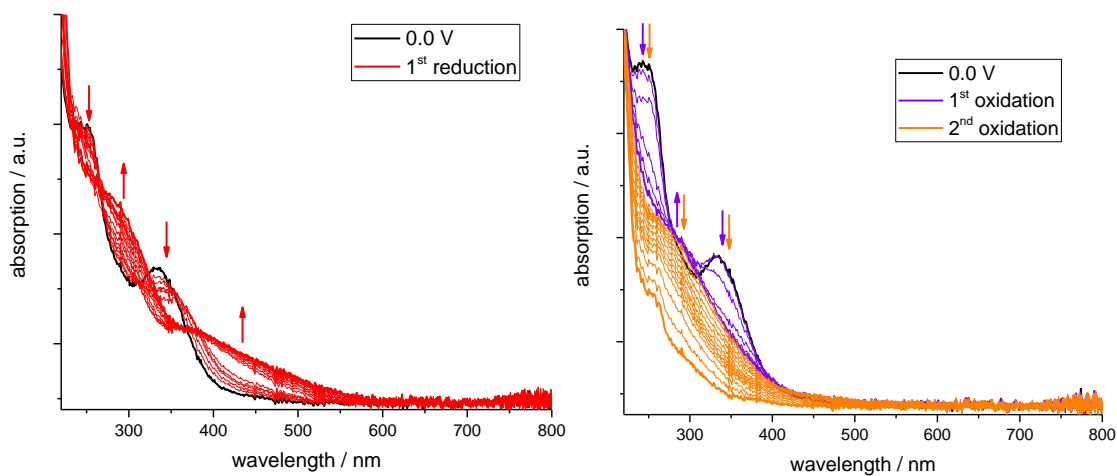


Figure 7.425 Spectroelectrochemical UV/Vis measurements during the reduction (left) and oxidation (right) of [Pd(PPh₃)(bzTSCpBa)Cl] in 0.1 M Bu₄NPF₆ / MeCN with 0.1 V increments.

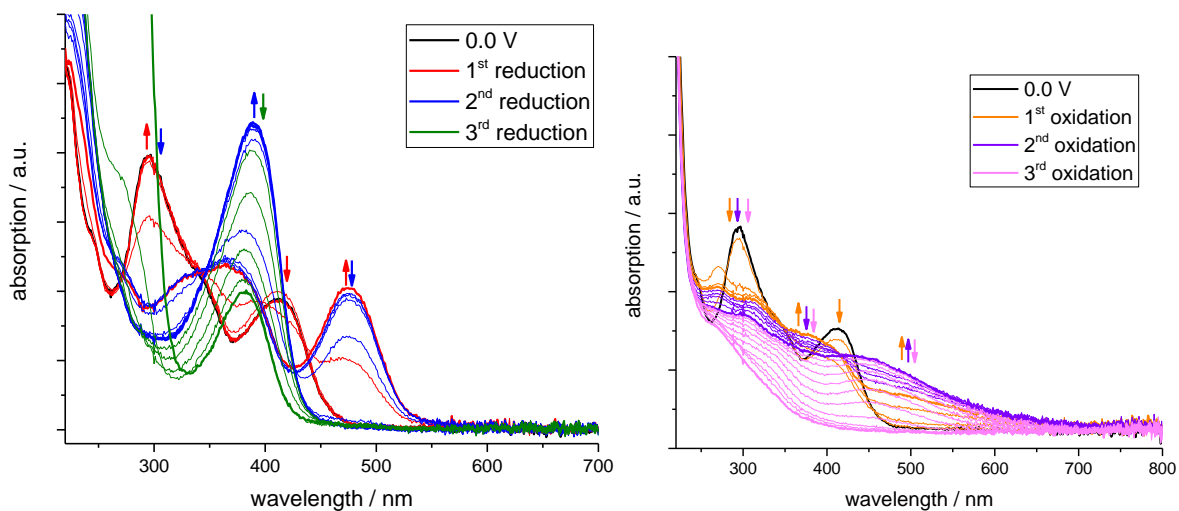


Figure 7.426 Spectroelectrochemical UV/Vis measurements during the reduction (left) and oxidation (right) of [Cu(hphfpyTSCmB)] in 0.1 M Bu₄NPF₆ / MeCN with 0.1 V increments.

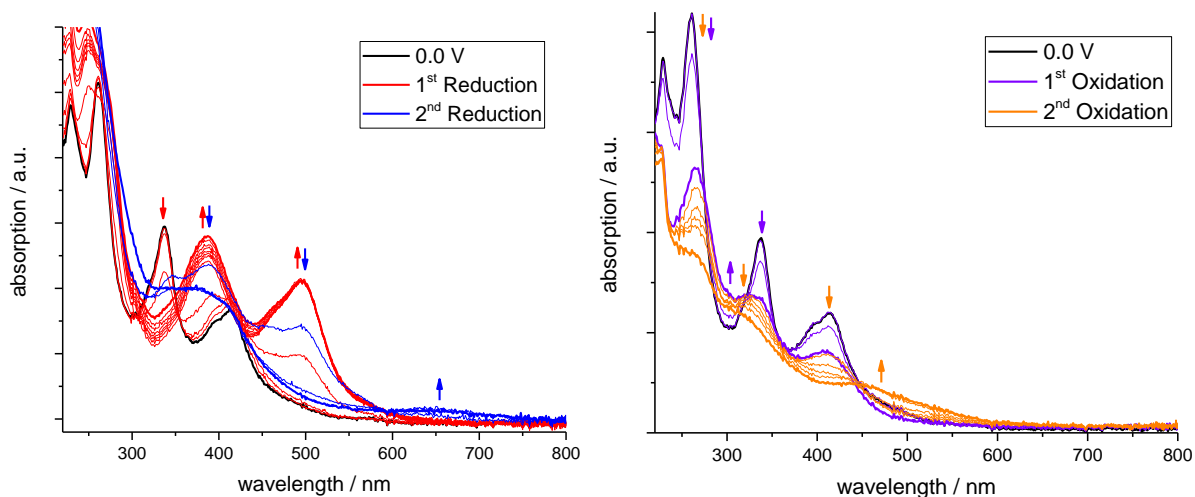


Figure 7.427 Spectroelectrochemical UV/Vis measurements during the reduction (left) and oxidation (right) of [Ni(hphfpyTSCmB)] in 0.1 M Bu₄NPF₆ / MeCN with 0.1 V increments.

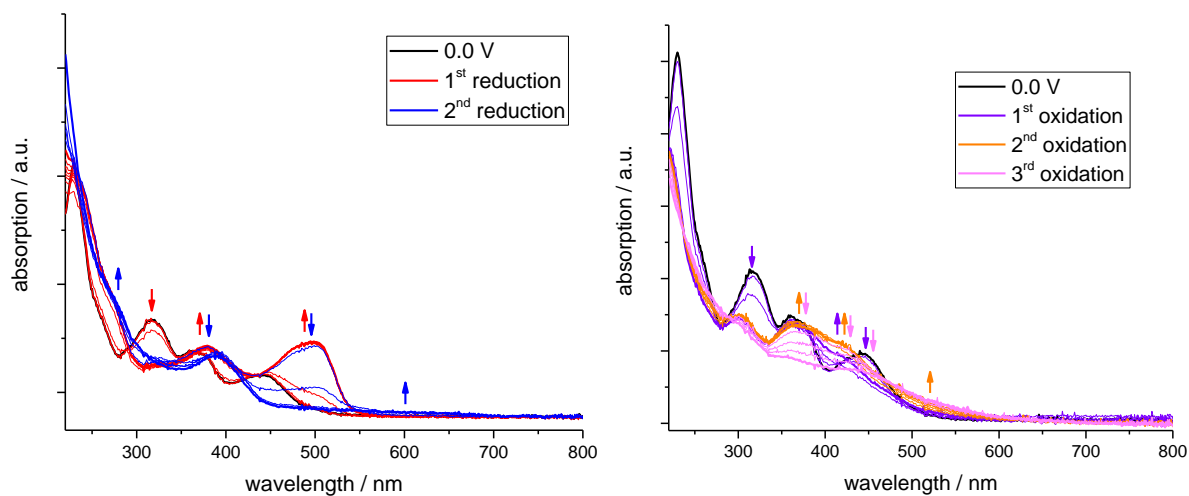


Figure 7.428 Spectroelectrochemical UV/Vis measurements during the reduction (left) and oxidation (right) of [Pd(hphfpyTSCmB)] in 0.1 M Bu₄NPF₆ / MeCN with 0.1 V increments.

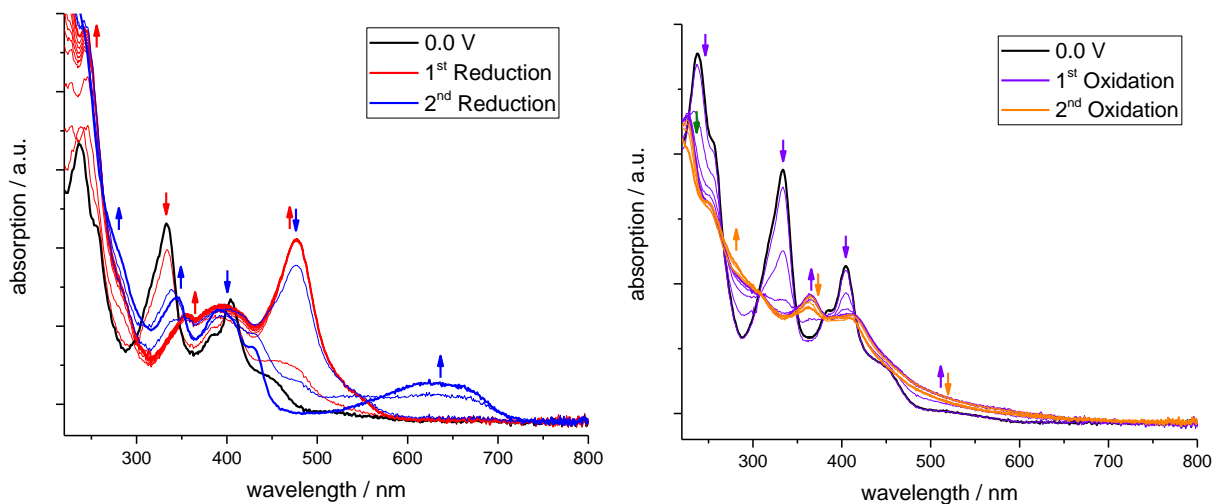


Figure 7.429 Spectroelectrochemical UV/Vis measurements during the reduction (left) and oxidation (right) of [Pt(hphfyTSCmB)] in 0.1 M Bu₄NPF₆ / MeCN with 0.1 V increments.

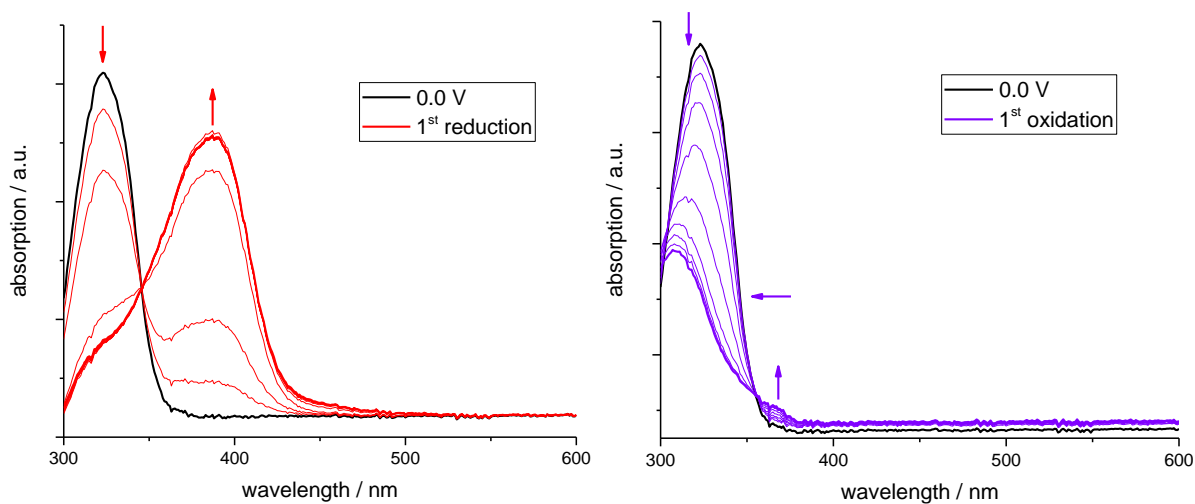


Figure 7.430 Spectroelectrochemical UV/Vis measurements during the reduction (left) and oxidation (right) of [U(bzTSC)₄] in 0.1 M Bu₄NPF₆ / THF with 0.1 V increments.

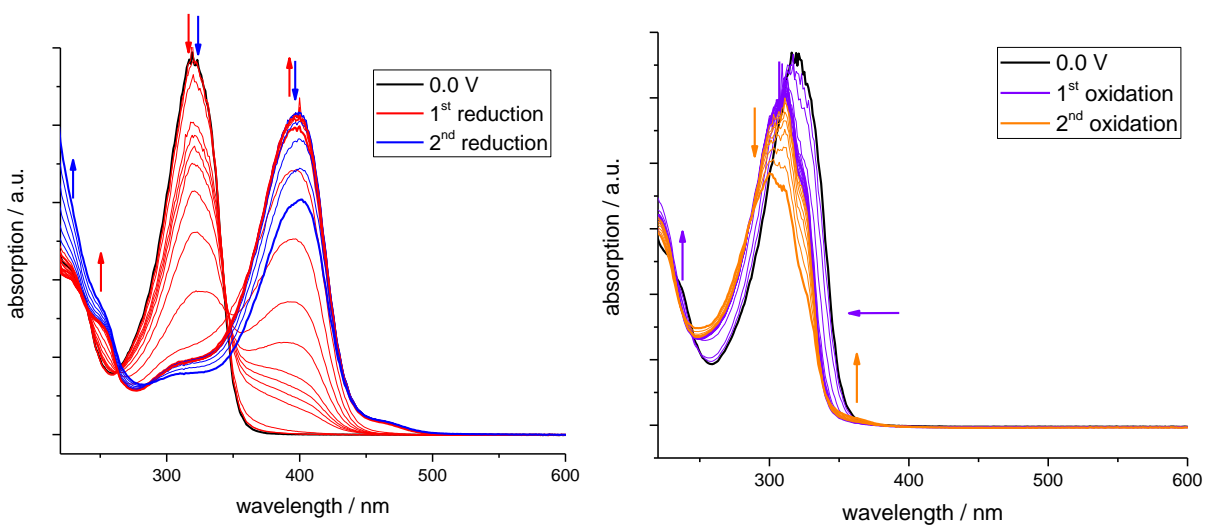


Figure 7.431 Spectroelectrochemical UV/Vis measurements during the reduction (left) and oxidation (right) of [U(bzTSCm)₄] in 0.1 M Bu₄NPF₆ / THF with 0.1 V increments.

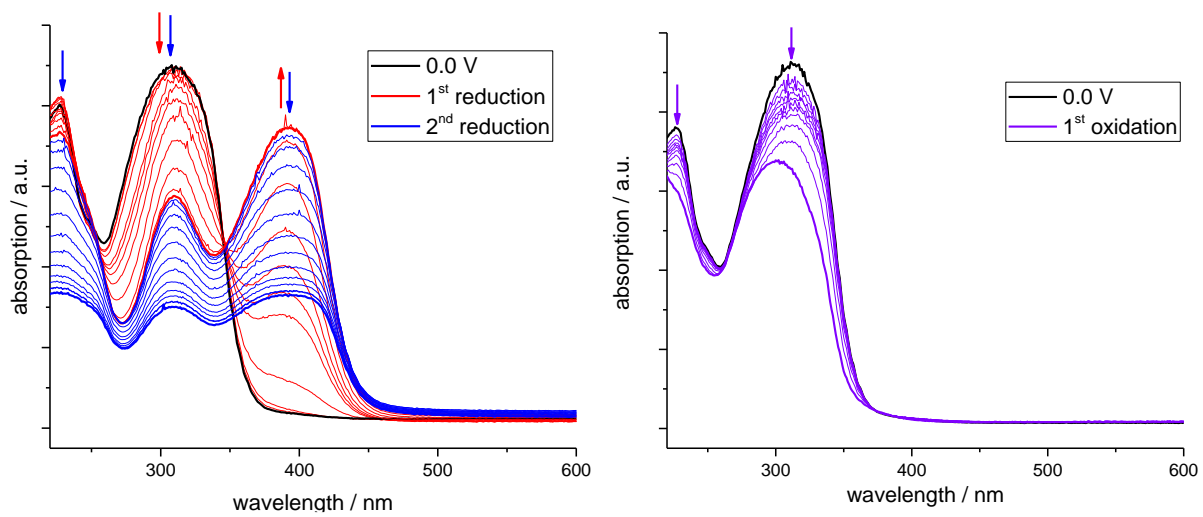


Figure 7.432 Spectroelectrochemical UV/Vis measurements during the reduction (left) and oxidation (right) of [U(bzTSCdm)₄] in 0.1 M Bu₄NPF₆ / THF with 0.1 V increments.

7.11. Crystal data

7.11.1. HfpyTSCmB

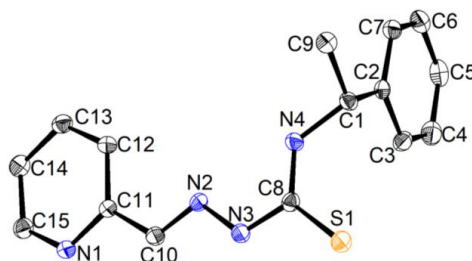


Figure 7.433 Molecular structure of HfpyTSCmB. Atoms are shown with 50 % probability. Hydrogen atoms are omitted for clarity.

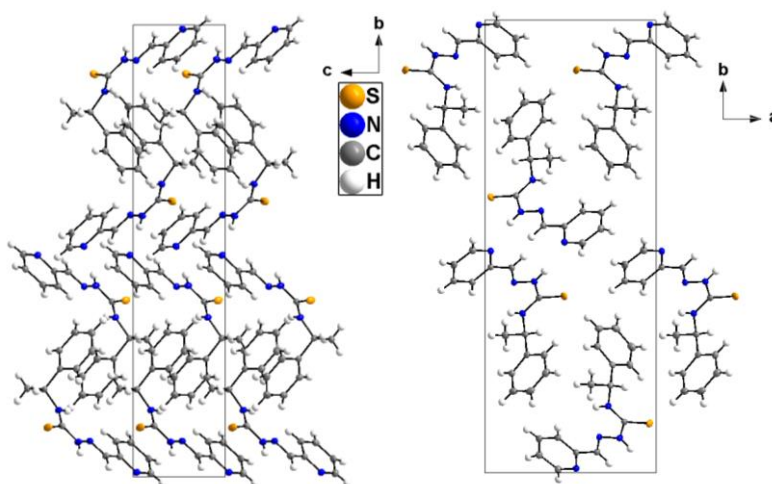


Figure 7.434 Crystal structure of HfpyTSCmB along the crystallographic a-axis (left) and c-axis (right).

Table 7.1 Crystal data and structure refinement for HfpyTSCmB.

empirical formula / formula weight	C ₁₅ H ₁₄ N ₄ S / 284.38 g/mol
temperature / wavelength	100 (1) K / 0.56076 Å
crystal system / space group	orthorhombic / P2 ₁ 2 ₁ 2 ₁
unit cell dimensions	a = 9.994(2) Å; b = 26.463(5) Å; c = 5.3980(11) Å
volume / Z / calculated density	1427.6(5) Å ³ / 16 / 2.316 g/cm ³
absorption coefficient / F(000)	4.328 mm ⁻¹ / 944
theta range for data collection	1.539 to 29.567 deg.
limiting indices	-13<=h<=13, -36<=k<=36, -7<=l<=7
reflections collected / unique	16989 / 3961 [R _{int} = 0.0390]
completeness to theta = 25.242	100.0 %
refinement method	full-matrix least-squares on F ²
data / restraints / parameters	3961 / 0 / 245
goodness-of-fit on F ²	0.741
final R indices [I >= 2σ(I)]	R ₁ = 0.0406, wR ₂ = 0.1124
R indices (all data)	R ₁ = 0.0447, wR ₂ = 0.1173
absolute structure parameter	0.78(3)
largest diff. peak and hole	0.337 and -0.478 e·Å ⁻³

Table 7.2 Atomic coordinates ($\times 10^4$) and equivalent isotropic displacement parameters ($\text{\AA}^2 \times 10^3$) for HfpyTSCmB. $U(\text{eq})$ is defined as one third of the trace of the orthogonalized U_{ij} tensor.

	x	y	z	U(eq)		x	y	z	U(eq)
S(1)	4636(1)	3905(1)	782(1)	24(1)	C(12)	-730(2)	4217(1)	8177(5)	17(1)
N(4)	2214(2)	3524(1)	1913(4)	18(1)	C(14)	-1810(3)	4599(1)	11663(5)	19(1)
N(3)	2886(2)	4227(1)	4042(4)	18(1)	C(15)	-710(3)	4920(1)	11878(5)	20(1)
N(2)	1699(2)	4208(1)	5309(4)	16(1)	C(11)	344(2)	4550(1)	8553(4)	16(1)
N(1)	345(2)	4901(1)	10359(4)	18(1)	C(1)	2352(2)	3066(1)	382(4)	16(1)
C(8)	3165(2)	3872(1)	2279(4)	16(1)	C(9)	1205(3)	3043(1)	-1476(5)	19(1)
C(2)	2466(2)	2610(1)	2096(5)	16(1)	C(10)	1563(2)	4536(1)	7044(5)	18(1)
C(3)	3473(2)	2607(1)	3897(5)	20(1)	C(4)	3583(3)	2212(1)	5571(5)	25(1)
C(13)	-1815(2)	4246(1)	9760(5)	19(1)	C(5)	2665(3)	1813(1)	5502(5)	24(1)
C(7)	1579(3)	2201(1)	1997(5)	18(1)	C(6)	1677(3)	1807(1)	3704(5)	22(1)

Table 7.3 Bond lengths [\AA] and angles [$^\circ$] for HfpyTSCmB.

S(1)-C(8)	1.679(2)	C(14)-C(15)	1.394(3)	C(12)-C(13)-C(14)	119.5(2)
N(4)-C(8)	1.338(3)	C(11)-C(10)	1.466(3)	C(6)-C(7)-C(2)	120.6(2)
N(4)-C(1)	1.473(3)	C(1)-C(9)	1.524(3)	C(13)-C(12)-C(11)	118.3(2)
N(3)-C(8)	1.366(3)	C(4)-C(5)	1.398(4)	C(15)-C(14)-C(13)	118.3(2)
N(3)-N(2)	1.370(3)	C(5)-C(6)	1.384(4)	N(1)-C(15)-C(14)	123.3(2)
N(2)-C(10)	1.285(3)	C(8)-N(4)-C(1)	125.6(2)	N(1)-C(11)-C(12)	122.6(2)
N(1)-C(15)	1.336(3)	C(8)-N(3)-N(2)	119.9(2)	N(1)-C(11)-C(10)	114.8(2)
N(1)-C(11)	1.347(3)	C(10)-N(2)-N(3)	115.5(2)	C(12)-C(11)-C(10)	122.7(2)
C(2)-C(7)	1.400(3)	C(15)-N(1)-C(11)	118.0(2)	N(4)-C(1)-C(9)	109.3(2)
C(2)-C(3)	1.400(3)	N(4)-C(8)-N(3)	115.5(2)	N(4)-C(1)-C(2)	108.5(2)
C(2)-C(1)	1.524(3)	N(4)-C(8)-S(1)	125.8(2)	C(9)-C(1)-C(2)	115.1(2)
C(3)-C(4)	1.387(4)	N(3)-C(8)-S(1)	118.5(2)	N(2)-C(10)-C(11)	120.6(2)
C(13)-C(12)	1.383(3)	C(7)-C(2)-C(3)	118.5(2)	C(3)-C(4)-C(5)	119.9(2)
C(13)-C(14)	1.388(3)	C(7)-C(2)-C(1)	122.8(2)	C(6)-C(5)-C(4)	119.7(2)
C(7)-C(6)	1.395(3)	C(3)-C(2)-C(1)	118.7(2)	C(5)-C(6)-C(7)	120.3(2)
C(12)-C(11)	1.404(3)	C(4)-C(3)-C(2)	121.0(2)		

Table 7.4 Anisotropic displacement parameters ($\text{\AA}^2 \times 10^3$) for HfpyTSCmB. The anisotropic displacement factor exponent takes the form: $-2\pi^2[h^2a^{*2}U_{11}+2hka^*b^*U_{12}+\dots]$.

	U11	U22	U33	U23	U13	U12
S(1)	18(1)	23(1)	30(1)	-4(1)	11(1)	-4(1)
N(4)	15(1)	17(1)	21(1)	-3(1)	5(1)	-1(1)
N(3)	15(1)	17(1)	22(1)	-2(1)	5(1)	-3(1)
N(2)	14(1)	16(1)	18(1)	0(1)	3(1)	0(1)
N(1)	16(1)	17(1)	20(1)	-3(1)	0(1)	-1(1)
C(8)	15(1)	16(1)	18(1)	2(1)	2(1)	1(1)
C(2)	15(1)	16(1)	17(1)	-2(1)	2(1)	1(1)
C(3)	16(1)	23(1)	21(1)	-2(1)	-2(1)	1(1)
C(13)	16(1)	19(1)	23(1)	2(1)	-1(1)	-2(1)
C(7)	18(1)	19(1)	19(1)	-2(1)	0(1)	0(1)
C(12)	16(1)	17(1)	19(1)	-1(1)	0(1)	-1(1)
C(14)	17(1)	24(1)	16(1)	1(1)	4(1)	-1(1)
C(15)	19(1)	22(1)	18(1)	-3(1)	1(1)	0(1)
C(11)	15(1)	16(1)	18(1)	-1(1)	0(1)	0(1)
C(1)	17(1)	16(1)	16(1)	-2(1)	2(1)	-1(1)
C(9)	21(1)	21(1)	16(1)	1(1)	0(1)	0(1)
C(10)	15(1)	17(1)	21(1)	-1(1)	3(1)	-3(1)
C(4)	24(1)	29(1)	21(1)	-1(1)	-2(1)	6(1)
C(5)	31(1)	20(1)	21(1)	2(1)	4(1)	7(1)
C(6)	26(1)	17(1)	23(1)	-1(1)	2(1)	-1(1)

7.11.2. HapyTSCmB

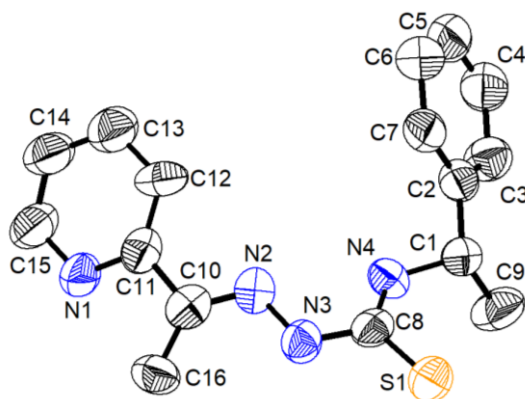


Figure 7.435 Molecular structure of HapyTSCmB. Atoms are shown with 50 % probability. Hydrogen atoms are omitted for clarity.

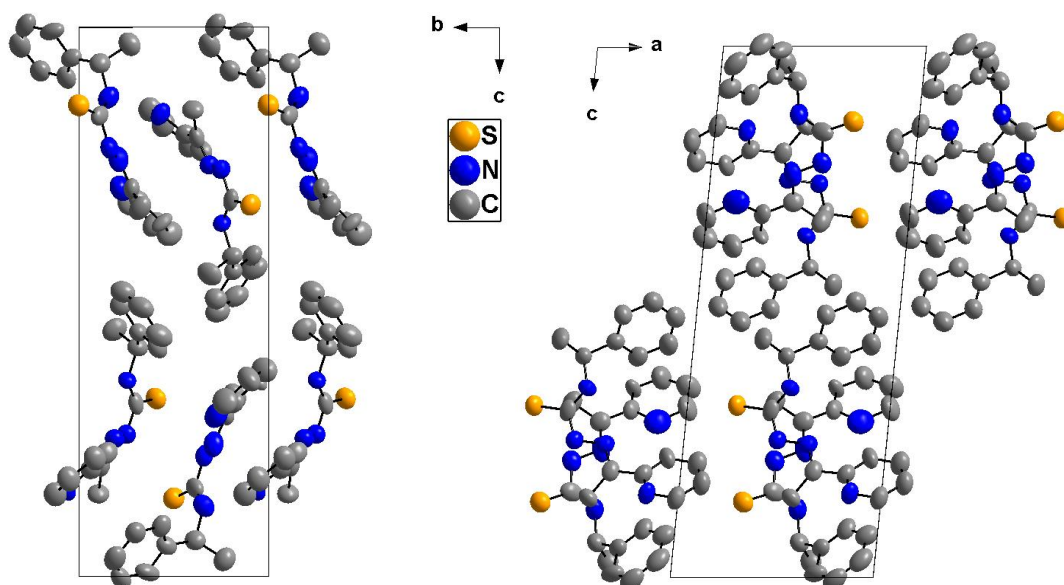


Figure 7.436 Crystal structure of HapyTSCmB along the crystallographic a-axis (left) and b-axis (right).

Table 7.5 Crystal data and structure refinement for HapyTSCmB.

empirical formula / formula weight	C ₁₆ H ₁₈ N ₄ S / 298.41 g/mol
temperature / wavelength	293(2) K / 0.71073 Å
crystal system / space group	orthorhombic / P2 ₁
unit cell dimensions	a = 8.7895(6) Å; b = 7.9268(4) Å; c = 23.0863(19) Å; β = 95.750(6)
Volume / Z / calculated density	1600.39(19) Å ³ / 4 / 1.1631 g/cm ³
absorption coefficient / F(000)	0.178 mm ⁻¹ / 560.7
theta range for data collection	3.54 to 53.64deg.
limiting indices	-11 ≤ h ≤ 11, -10 ≤ k ≤ 8, -29 ≤ l ≤ 29
reflections collected / unique completeness to theta = 25.242	36405 / 6509 [R _{int} = 0.2299]
refinement method	charge flip
data / restraints / parameters	6509 / 1 / 379
goodness-of-fit on F ²	0.796
final R indices [I ≥ 2σ(I)]	R ₁ = 0.0703, wR ₂ = 0.1619
R indices (all data)	R ₁ = 0.2186, wR ₂ = 0.2341
largest diff. peak and hole	0.55 and -0.43 e·Å ⁻³

Table 7.6 Atomic coordinates ($\times 10^4$) and equivalent isotropic displacement parameters ($\text{\AA}^2 \times 10^3$) for HapyTSCmB. U(eq) is defined as one third of the trace of the orthogonalized U_{ij} tensor.

	<i>x</i>	<i>y</i>	<i>z</i>	U(eq)		<i>x</i>	<i>y</i>	<i>z</i>	U(eq)	
S1	-7552(2)	-4047(3)	-3237.5(1)	76.5(7)		C13	766(11)	-825(13)	-2149(5)	94(3)
N2	-3867(8)	-1873(8)	-2508(3)	70.8(19)		C9	-6591(10)	-1880(13)	-4494(4)	92(3)
C8	-5872(9)	-3003(9)	-3147(4)	65(2)		C14	1075(10)	550(13)	-1774(5)	93(3)
N3	-5387(8)	-2490(8)	-2587(3)	66.7(18)		C11	-1844(10)	-613(11)	-1948(4)	73(2)
N4	-5017(7)	-2538(8)	-3568(3)	61.5(17)		C12	-738(10)	-1444(12)	-2247(4)	79(3)
N1	-1566(7)	697(9)	-1583(3)	77(2)		C15	-96(10)	1261(12)	-1495(4)	91(3)
C10	-3464(9)	-1214(10)	-2007(4)	67(2)		C5	-1025(11)	-3268(13)	-4899(5)	96(3)
C1	-5371(9)	-3088(10)	-4169(3)	66(2)		C4	-2198(12)	-2304(13)	-5182(4)	95(3)
C7	-2678(10)	-4132(11)	-4160(4)	77(2)		C16	-4436(10)	-1010(11)	-1501(4)	76(3)
C2	-3857(9)	-3125(10)	-4442(3)	65(2)		C6	-1245(10)	-4233(14)	-4389(5)	103(3)
C3	-3619(10)	-2212(12)	-4945(4)	82(3)						

Table 7.7 Bond lengths [\AA] and angles [deg] for HapyTSCmB.

S1-C8	1.687(8)	C13-C12	1.407(12)	C9-C1-C2	113.2(7)
N2-N3	1.417(9)	C14-C15	1.387(12)	C6-C7-C2	119.8(8)
N2-C10	1.285(9)	C11-C12	1.411(12)	C7-C2-C1	116.6(7)
C8-N3	1.383(10)	C5-C4	1.393(13)	C3-C2-C1	122.7(7)
C8-N4	1.337(10)	C5-C6	1.433(13)	C3-C2-C7	120.7(8)
N4-C1	1.458(9)	C10-N2-N3	115.3(7)	C4-C3-C2	120.3(8)
N1-C11	1.344(10)	N3-C8-S1	116.4(7)	C12-C13-C14	119.4(9)
N1-C15	1.363(10)	N4-C8-S1	126.4(7)	C15-C14-C13	119.7(9)
C10-C11	1.494(11)	N4-C8-N3	117.1(7)	C10-C11-N1	114.6(8)
C10-C16	1.524(11)	C8-N3-N2	114.9(6)	C12-C11-N1	125.2(8)
C1-C2	1.530(10)	C1-N4-C8	121.8(6)	C12-C11-C10	120.2(8)
C1-C9	1.572(11)	C15-N1-C11	117.2(8)	C11-C12-C13	116.2(9)
C7-C2	1.414(11)	C11-C10-N2	112.8(8)	C14-C15-N1	122.3(9)
C7-C6	1.416(12)	C16-C10-N2	127.4(8)	C6-C5-C4	121.6(9)
C2-C3	1.401(11)	C16-C10-C11	119.9(8)	C5-C4-C3	119.1(9)
C3-C4	1.416(12)	C2-C1-N4	106.7(6)	C5-C6-C7	118.4(9)
C13-C14	1.402(13)	C9-C1-N4	110.1(7)		

Table 7.8 Anisotropic displacement parameters ($\text{\AA}^2 \times 10^3$) for HapyTSCmB. The Anisotropic displacement factor exponent takes the form: $-2\pi^2[h^2a^{*2}U_{11}+2hka^*b^*U_{12}+\dots]$.

Atom	U_{11}	U_{22}	U_{33}	U_{12}	U_{13}	U_{23}
S1	66.3(2)	76.6(2)	86.7(2)	-14.4(2)	8.4(11)	-7.5(14)
N2	72(5)	72(5)	66(5)	-4(4)	0(4)	-3(4)
C8	54(5)	44(5)	94(6)	11(4)	-2(5)	-10(5)
N3	64(4)	66(5)	69(5)	-7(4)	4(3)	-3(4)
N4	69(4)	61(4)	56(4)	-2(4)	16(3)	-5(3)
N1	60(4)	73(5)	94(5)	-7(4)	-2(4)	-23(4)
C10	65(5)	47(5)	87(6)	-1(4)	1(5)	11(5)
C1	57(5)	80(6)	61(5)	6(4)	6(4)	-4(4)
C7	77(5)	73(6)	80(6)	12(6)	1(5)	-17(5)
C2	69(5)	64(5)	61(5)	0(4)	6(4)	-5(4)
C3	69(6)	92(7)	85(6)	-2(5)	12(5)	5(6)
C13	74(7)	93(8)	112(8)	12(6)	0(6)	-7(7)
C9	62(5)	113(8)	99(7)	22(5)	1(5)	22(6)
C14	61(6)	99(9)	117(8)	11(6)	4(5)	-9(7)
C11	66(6)	78(6)	72(6)	-1(5)	-8(4)	0(5)

C12	55(5)	93(7)	91(6)	21(5)	21(5)	14(5)
C15	61(6)	99(8)	110(8)	2(5)	-6(5)	-3(6)
C5	77(7)	122(9)	89(7)	-21(6)	13(6)	-25(7)
C4	85(7)	114(9)	87(7)	-10(7)	13(6)	-11(7)
C6	75(6)	132(10)	101(8)	9(7)	11(6)	-26(8)

7.11.3. HdpyTSCmB

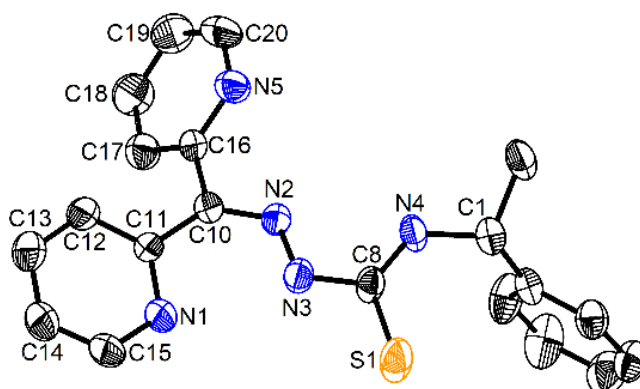


Figure 7.437 Molecular structure of HdpyTSCmB·MeOH. Atoms are shown with 50 % probability. Hydrogen atoms are omitted for clarity.

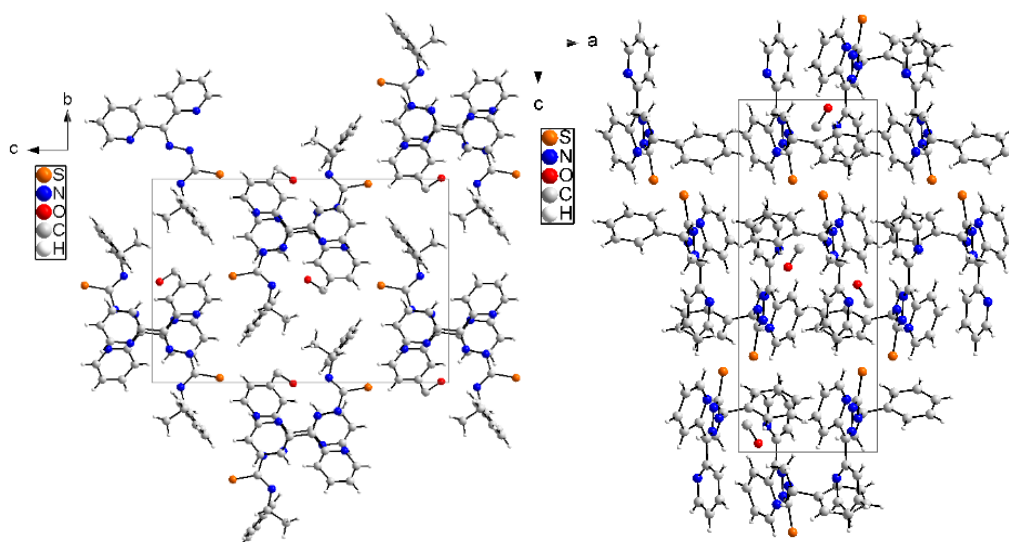


Figure 7.438 Crystal structure of HdpyTSCmB·MeOH along the crystallographic a-axis (left) and b-axis (right).

Table 7.9 Crystal data and structure refinement for HdpyTSCmB·MeOH.

empirical formula / formula weight	C ₂₁ H ₁₇ N ₅ OS / 387.46 g/mol
temperature / wavelength	293(2) K / 0.71073 Å
crystal system / space group	orthorhombic / P2 ₁ 2 ₁ 2 ₁
unit cell dimensions	a = 7.7512(4) Å; b = 13.4952(11) Å; c = 19.6265(11) Å
Volume / Z / calculated density	2053.0(2) Å ³ / 4 / 1.254 g/cm ³
absorption coefficient / F(000)	0.178 mm ⁻¹ / 808
theta range for data collection	1.831 to 26.954 deg.
limiting indices	-9 ≤ h ≤ 8, -17 ≤ k ≤ 17, -24 ≤ l ≤ 24
reflections collected / unique	37979 / 4394 [R _{int} = 0.0910]
completeness to theta = 25.242	100.0 %
refinement method	full-matrix least-squares on F ²
data / restraints / parameters	4394 / 0 / 254
goodness-of-fit on F ²	1.102
final R indices [I ≥ 2σ(I)]	R ₁ = 0.0676, wR ₂ = 0.1614
R indices (all data)	R ₁ = 0.0926, wR ₂ = 0.1729
absolute structure parameter	0.97(5)
largest diff. peak and hole	0.360 and -0.192 e·Å ⁻³

Table 7.10 Atomic coordinates ($\times 10^4$) and equivalent isotropic displacement parameters ($\text{\AA}^2 \times 10^3$) for HdpyTSCmB·MeOH. U(eq) is defined as one third of the trace of the orthogonalized U_{ij} tensor.

	x	y	z	U(eq)		x	y	z	U(eq)
S(1)	3906(3)	4767(1)	2281(1)	69(1)	C(18)	3648(9)	1460(5)	-1354(3)	63(2)
N(4)	3605(6)	5230(3)	961(2)	42(1)	C(12)	1123(7)	900(4)	584(3)	45(1)
N(3)	3227(6)	3595(3)	1258(2)	43(1)	C(17)	3552(7)	1527(4)	-653(3)	47(1)
O(1)	1444(6)	4949(3)	-245(2)	62(1)	C(14)	1224(8)	153(4)	1679(3)	60(2)
N(1)	2762(6)	1649(3)	1488(2)	47(1)	C(3)	7131(8)	6006(4)	956(3)	59(2)
C(10)	2717(6)	2482(3)	390(2)	35(1)	C(6)	7872(8)	7584(4)	1782(3)	53(1)
C(8)	3565(7)	4551(4)	1448(2)	39(1)	C(20)	2162(9)	2977(5)	-1420(3)	61(2)
N(2)	3144(5)	3366(3)	578(2)	35(1)	C(13)	623(8)	145(5)	1016(3)	58(2)
C(16)	2753(7)	2345(3)	-368(2)	36(1)	C(9)	3335(9)	6884(4)	479(3)	61(2)
C(11)	2201(6)	1642(3)	832(2)	35(1)	C(15)	2254(8)	904(4)	1888(3)	53(1)
N(5)	2066(6)	3071(3)	-743(2)	45(1)	C(5)	9184(9)	7066(5)	1480(3)	62(2)
C(2)	5772(7)	6516(3)	1258(2)	38(1)	C(21)	628(11)	5463(5)	-771(4)	80(2)
C(1)	3919(7)	6277(3)	1108(3)	43(1)	C(19)	2925(9)	2188(5)	-1744(3)	64(2)
C(7)	6188(7)	7305(4)	1681(3)	45(1)	C(4)	8809(8)	6275(5)	1067(4)	69(2)

Table 7.11 Bond lengths [\AA] and angles [deg] for HdpyTSCmB·MeOH.

S(1)-C(8)	1.681(5)	C(12)-C(13)	1.381(7)	C(12)-C(11)-C(10)	120.5(4)
N(4)-C(8)	1.324(6)	C(14)-C(15)	1.353(8)	C(16)-N(5)-C(20)	117.1(5)
N(4)-C(1)	1.463(6)	C(14)-C(13)	1.380(8)	C(7)-C(2)-C(3)	117.3(5)
N(3)-C(8)	1.368(6)	C(3)-C(4)	1.368(9)	C(7)-C(2)-C(1)	120.3(4)
N(3)-N(2)	1.372(5)	C(6)-C(5)	1.369(9)	C(3)-C(2)-C(1)	122.3(5)
O(1)-C(21)	1.397(7)	C(20)-C(19)	1.374(8)	N(4)-C(1)-C(2)	113.9(4)
N(1)-C(15)	1.335(6)	C(5)-C(4)	1.373(9)	N(4)-C(1)-C(9)	107.8(4)
N(1)-C(11)	1.358(6)	C(8)-N(4)-C(1)	122.0(4)	C(2)-C(1)-C(9)	108.8(4)
C(10)-N(2)	1.293(6)	C(8)-N(3)-N(2)	119.1(4)	C(6)-C(7)-C(2)	121.2(5)
C(10)-C(11)	1.482(6)	C(15)-N(1)-C(11)	117.3(4)	C(19)-C(18)-C(17)	119.3(6)
C(10)-C(16)	1.500(6)	N(2)-C(10)-C(11)	127.4(4)	C(13)-C(12)-C(11)	119.0(5)
C(16)-N(5)	1.336(6)	N(2)-C(10)-C(16)	113.1(4)	C(18)-C(17)-C(16)	118.6(5)
C(16)-C(17)	1.384(7)	C(11)-C(10)-C(16)	119.5(4)	C(15)-C(14)-C(13)	119.4(5)
C(11)-C(12)	1.393(7)	N(4)-C(8)-N(3)	117.4(4)	C(4)-C(3)-C(2)	121.4(5)
N(5)-C(20)	1.337(7)	N(4)-C(8)-S(1)	125.3(4)	C(5)-C(6)-C(7)	120.3(5)
C(2)-C(7)	1.388(7)	N(3)-C(8)-S(1)	117.3(3)	N(5)-C(20)-C(19)	123.9(5)
C(2)-C(3)	1.392(7)	C(10)-N(2)-N(3)	119.8(4)	C(14)-C(13)-C(12)	118.5(5)
C(2)-C(1)	1.502(8)	N(5)-C(16)-C(17)	122.8(5)	N(1)-C(15)-C(14)	124.0(5)
C(1)-C(9)	1.549(7)	N(5)-C(16)-C(10)	116.6(4)	C(6)-C(5)-C(4)	119.7(6)
C(7)-C(6)	1.373(8)	C(17)-C(16)-C(10)	120.5(4)	C(18)-C(19)-C(20)	118.3(5)
C(18)-C(19)	1.366(9)	N(1)-C(11)-C(12)	121.8(4)	C(3)-C(4)-C(5)	120.2(6)
C(18)-C(17)	1.381(8)	N(1)-C(11)-C(10)	117.6(4)		

Table 7.12 Anisotropic displacement parameters ($\text{\AA}^2 \times 10^3$) for HdpyTSCmB·MeOH. The anisotropic displacement factor exponent takes the form: $-2\pi^2[h^2a^{*2}U_{11}+2hka^*b^*U_{12}+\dots]$.

	U11	U22	U33	U23	U13	U12
S(1)	123(2)	48(1)	35(1)	-4(1)	3(1)	-29(1)
N(4)	51(3)	26(2)	49(2)	3(2)	1(2)	-4(2)
N(3)	58(3)	35(2)	35(2)	-1(2)	-1(2)	-9(2)
O(1)	87(3)	49(2)	51(2)	6(2)	-14(2)	10(2)
N(1)	65(3)	38(2)	37(2)	7(2)	-6(2)	-9(2)
C(10)	39(3)	30(2)	38(2)	0(2)	-3(2)	1(2)
C(8)	44(3)	35(2)	39(2)	-1(2)	5(2)	-12(2)
N(2)	38(2)	32(2)	35(2)	-1(2)	-1(2)	-3(2)
C(16)	40(3)	29(2)	38(2)	3(2)	-3(2)	-5(2)
C(11)	38(3)	31(2)	35(2)	-1(2)	-6(2)	0(2)
N(5)	55(3)	43(2)	36(2)	2(2)	-3(2)	4(2)

C(2)	42(3)	26(2)	45(2)	3(2)	8(2)	1(2)
C(1)	48(3)	31(2)	50(3)	0(2)	2(3)	-1(2)
C(7)	47(3)	36(3)	53(3)	-5(2)	5(2)	4(3)
C(18)	83(5)	59(4)	47(3)	-13(3)	4(3)	11(3)
C(12)	41(3)	45(3)	48(3)	5(2)	-9(2)	-10(2)
C(17)	52(3)	42(3)	46(3)	-2(2)	0(2)	3(3)
C(14)	82(4)	46(3)	52(3)	15(2)	-4(3)	-17(3)
C(3)	53(4)	46(3)	77(4)	-22(3)	17(3)	-5(3)
C(6)	59(4)	42(3)	58(3)	-13(3)	-1(3)	-2(3)
C(20)	81(4)	59(4)	42(3)	11(3)	-15(3)	5(3)
C(13)	59(4)	51(3)	64(3)	8(3)	-6(3)	-21(3)
C(9)	67(4)	35(3)	82(4)	17(3)	-15(3)	-8(3)
C(15)	75(4)	47(3)	36(3)	12(2)	-5(3)	-5(3)
C(5)	47(3)	62(4)	78(4)	-5(3)	-5(3)	-6(3)
C(21)	111(6)	47(4)	81(5)	13(3)	-23(4)	14(4)
C(19)	87(5)	66(4)	39(3)	-6(3)	0(3)	-1(4)
C(4)	44(4)	60(4)	103(5)	-22(4)	20(4)	-2(3)

7.11.4. HbphTSCmB

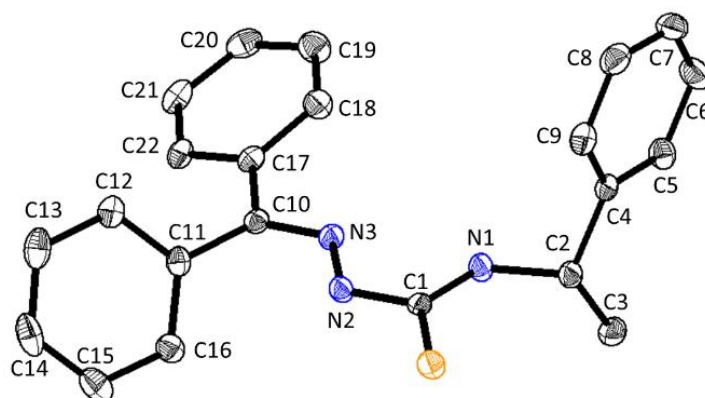


Figure 7.439. Molecular structure of HbphTSCmB. Atoms are shown with 50 % probability. Hydrogen atoms are omitted for clarity.

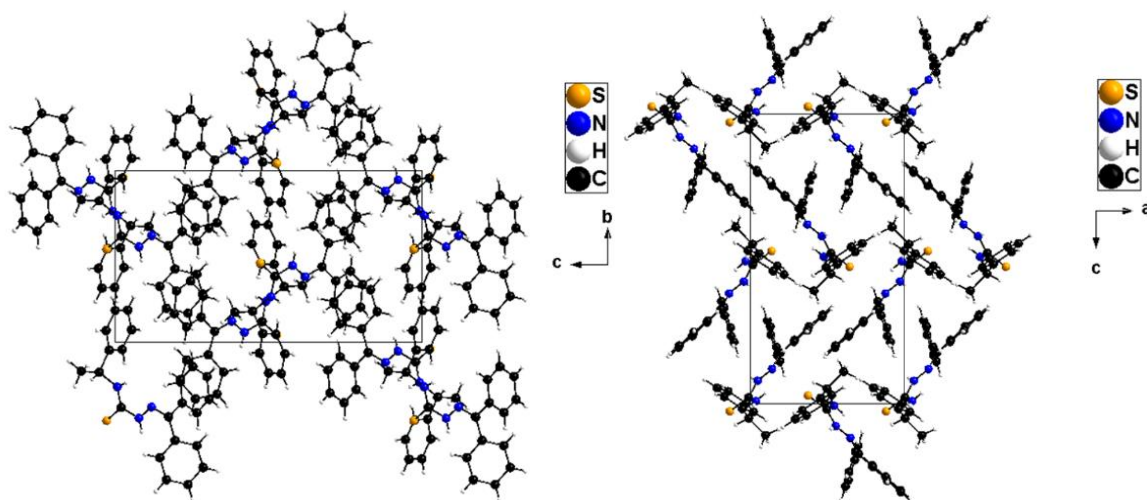


Figure 7.440 Crystal structure of HdpyTSCmB-MeOH along the crystallographic a-axis (left) and b-axis (right).

Table 7.13 Crystal data and structure refinement for HdpyTSCmB·MeOH.

Empirical formula	C ₂₂ H ₂₀ N ₃ S (358.47 g/mol)
Temperature/K	100.0
Crystal system / Space group	Orthorhombic / P2 ₁ 2 ₁ 2 ₁
Unit cell parameters	a = 9.9733(2) Å, b = 10.3024(2) Å, c = 18.4119(4) Å
Volume / Z	1891.80(7) Å ³ /4
ρ _{cal}	1.259 g/cm ³
μ/mm ⁻¹	1.582
F(000)	756.0
Crystal size/mm ³	0.15 × 0.05 × 0.03
Radiation	CuKα (λ = 1.54178 Å)
2θ range for data collection/°	9.606 to 144.062
Index ranges	-12 ≤ h ≤ 10, -12 ≤ k ≤ 12, -22 ≤ l ≤ 22
Reflections collected	25974
Independent reflections	3720 [R _{int} = 0.0679, R _{sigma} = 0.0334]
Data/restraints/parameters	3720/0/244
Goodness-of-fit on F ²	1.105
final R indices [I _o ≥ 2σ(I _o)	R ₁ = 0.0247, wR ₂ = 0.0656
Final R indexes [all data]	R ₁ = 0.0268, wR ₂ = 0.0660
Largest diff. peak/hole / e Å ⁻³	0.18/-0.25
Flack parameter	0.017(5)

Table 7.14 Atomic coordinates (x 10⁴) and equivalent isotropic displacement parameters (Å² × 10³) for HbphTSCmB. U(eq) is defined as one third of the trace of the orthogonalized U_{ij} tensor.

Atom	x	y	z	U(eq)	Atom	x	y	z	U(eq)
S1	6333.6(4)	4599.1(4)	5269.9(2)	20.39(12)	C10	3097.4(17)	4378.4(17)	3252.1(9)	16.1(3)
N1	4673.1(16)	2633.2(15)	4922.2(8)	18.8(3)	C11	3341.6(16)	5754.9(18)	3042.5(10)	17.3(4)
N2	4556.9(14)	4452.0(15)	4217.2(8)	17.3(3)	C12	3749.1(18)	6052.9(19)	2334.9(10)	21.3(4)
N3	3626.2(15)	3803.8(14)	3808.4(8)	16.8(3)	C13	3933.5(19)	7334(2)	2128.3(12)	27.7(4)
C1	5132.5(16)	3826.9(16)	4794.7(10)	16.0(3)	C14	3717(2)	8328.6(19)	2621.3(13)	30.1(5)
C2	5120.5(18)	1779.4(17)	5512.2(10)	18.1(4)	C15	3310.2(18)	8045(2)	3324.7(13)	27.7(4)
C3	4049(2)	1717.4(19)	6100.5(10)	23.1(4)	C16	3122.0(18)	6761.9(18)	3536.4(11)	20.9(4)
C4	5534.2(16)	483.3(17)	5184.4(9)	16.8(3)	C17	2192.2(17)	3564.3(18)	2805.6(9)	16.8(3)
C5	4823.3(17)	-662.5(17)	5289.9(11)	21.2(4)	C18	2234.1(19)	2207.5(19)	2860.8(11)	21.9(4)
C6	5279(2)	-1825.3(19)	4991.3(12)	26.5(4)	C19	1357(2)	1448(2)	2463.8(11)	26.5(4)
C7	6435(2)	-1853.3(19)	4581.0(11)	27.9(4)	C20	427.5(19)	2021(2)	2001.6(11)	25.4(4)
C8	7142(2)	-710(2)	4461.8(11)	27.6(4)	C21	384.1(19)	3357(2)	1934.3(10)	23.4(4)
C9	6693.1(17)	446.8(19)	4761.9(11)	22.5(4)	C22	1265.5(18)	4129.6(18)	2330.6(9)	19.3(4)

Table 7.15 Bond lengths [Å] and angles [deg] for HbphTSCmB.

S1-C1	1.6832(17)	C1-N1-C2	125.37(15)
N1-C1	1.333(2)	N3-N2-C1	118.80(15)
N1-C2	1.467(2)	C10-N3-N2	119.20(15)
N2-N3	1.369(2)	N1-C1-S1	126.09(14)
N2-C1	1.369(2)	N1-C1-N2	115.24(15)
N3-C10	1.295(2)	N2-C1-S1	118.67(13)
C2-C3	1.523(3)	N1-C2-C3	109.78(14)
C2-C4	1.522(2)	N1-C2-C4	108.35(14)
C4-C5	1.391(2)	C4-C2-C3	115.81(15)
C4-C9	1.394(2)	C5-C4-C2	123.44(16)
C5-C6	1.394(3)	C5-C4-C9	118.55(17)

C6-C7	1.379(3)	C9-C4-C2	118.01(16)
C7-C8	1.390(3)	C4-C5-C6	120.52(17)
C8-C9	1.388(3)	C7-C6-C5	120.45(19)
C10-C11	1.490(2)	C6-C7-C8	119.52(18)
C10-C17	1.481(2)	C9-C8-C7	120.09(19)
C11-C12	1.399(3)	C8-C9-C4	120.85(18)
C11-C16	1.397(3)	N3-C10-C11	124.98(16)
C12-C13	1.386(3)	N3-C10-C17	115.36(15)
C13-C14	1.385(3)	C17-C10-C11	119.66(15)
C14-C15	1.388(3)	C12-C11-C10	119.84(16)
C15-C16	1.391(3)	C16-C11-C10	120.85(17)
C17-C18	1.402(3)	C16-C11-C12	119.27(17)
C17-C22	1.399(3)	C13-C12-C11	120.20(19)
C18-C19	1.383(3)	C14-C13-C12	120.25(19)
C19-C20	1.390(3)	C13-C14-C15	120.09(18)
C20-C21	1.382(3)	C14-C15-C16	120.0(2)
C21-C22	1.393(3)	C15-C16-C11	120.16(19)
		C18-C17-C10	120.40(16)
		C22-C17-C10	120.91(17)
		C22-C17-C18	118.68(17)
		C19-C18-C17	120.48(18)
		C18-C19-C20	120.33(19)
		C21-C20-C19	119.91(18)
		C20-C21-C22	120.16(18)
		C21-C22-C17	120.43(18)

Table 7.16 Anisotropic displacement parameters ($\text{\AA}^2 \times 10^3$) for HbphTSCmB. The anisotropic displacement factor exponent takes the form: $-2\pi^2[h^2a^*U_{11}+2hka^*b^*U_{12}+\dots]$.

Atom	U ₁₁	U ₂₂	U ₃₃	U ₂₃	U ₁₃	U ₁₂
S1	21.3(2)	17.83(19)	22.1(2)	-1.03(17)	-5.99(17)	-2.11(16)
N1	21.8(7)	16.6(7)	18.1(8)	1.3(6)	-7.8(6)	-0.9(6)
N2	20.0(7)	14.0(7)	17.9(7)	0.3(6)	-3.9(6)	-0.8(6)
N3	17.4(7)	17.4(7)	15.7(7)	0.2(5)	-1.7(6)	-0.2(6)
C1	17.7(8)	16.2(7)	14.0(8)	-1.2(6)	0.0(7)	4.6(6)
C2	20.7(8)	17.1(8)	16.6(8)	1.3(7)	-4.6(6)	0.9(7)
C3	25.6(9)	25.1(9)	18.6(9)	0.5(7)	-1.2(7)	5.5(8)
C4	18.1(7)	18.4(8)	13.8(7)	1.9(7)	-3.8(6)	1.4(6)
C5	19.5(8)	20.7(8)	23.3(9)	2.9(8)	-3.2(7)	-0.3(7)
C6	29.8(9)	17.0(9)	32.7(10)	-0.8(7)	-6.8(8)	-1.2(8)
C7	35.9(10)	23.9(9)	24(1)	-5.7(7)	-6.3(8)	10.3(8)
C8	28(1)	35.1(11)	19.7(9)	1.9(8)	3.2(7)	8.5(9)
C9	21.5(8)	24.8(9)	21.1(8)	5.1(9)	0.9(7)	-0.5(7)
C10	15.0(7)	18.4(8)	14.8(8)	-0.2(7)	1.6(6)	1.4(6)
C11	13.4(8)	18.9(8)	19.7(8)	3.1(7)	-3.0(6)	0.1(6)
C12	16.9(8)	25.3(9)	21.8(9)	4.9(7)	-0.5(7)	-0.7(7)
C13	20.7(9)	32.7(10)	29.6(10)	13.6(8)	-1.2(8)	-5.2(8)
C14	24.4(9)	21.1(9)	44.7(12)	12.9(8)	-8.6(9)	-5.0(8)
C15	23.8(10)	20.0(9)	39.3(12)	-1.6(9)	-7.3(8)	2.1(8)
C16	19.7(8)	20.1(9)	23.0(9)	-0.4(7)	-2.9(7)	1.4(7)
C17	13.8(8)	21.6(8)	14.9(8)	0.1(7)	1.2(6)	-1.0(7)
C18	21.1(9)	21.8(9)	22.9(9)	-0.1(7)	-2.6(7)	0.0(7)
C19	26.7(9)	23.0(9)	29.8(10)	-1.9(8)	-2.4(9)	-2.7(8)
C20	21.8(9)	33.0(11)	21.2(9)	-6.3(8)	-1.4(7)	-5.9(8)
C21	17.4(8)	36.2(11)	16.6(8)	3.6(8)	-0.6(7)	-3.2(7)
C22	17.5(8)	24.1(8)	16.2(8)	3.9(7)	1.6(7)	-0.9(7)

7.11.5. HFbzTSC

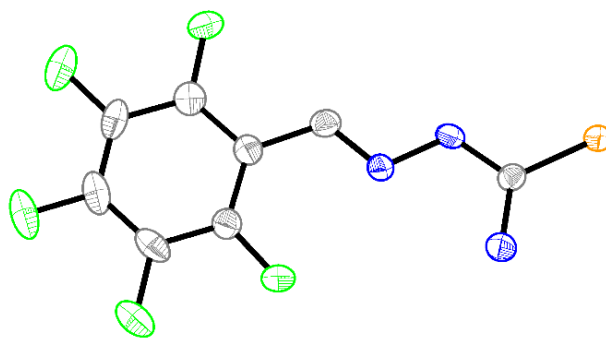


Figure 7.441 Molecular structure of HFbzTSC. Atoms are shown with 50 % probability. Hydrogen atoms are omitted for clarity.

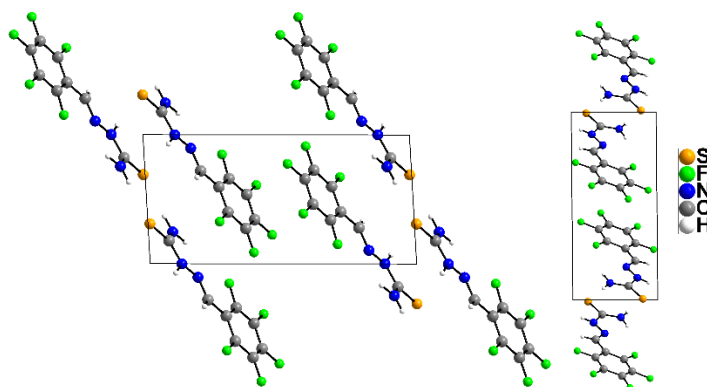


Figure 7.442 Crystal structure of HFbzTSC along the crystallographic a-axis (left) and b-axis (right).

Table 7.17 Crystal data and structure refinement for HFbzTSC.

Empirical formula	C ₈ H ₄ N ₃ F ₃ S (269.20 g/mol)
Temperature/K	150.0
Crystal system / Space group	Triclinic / $P\bar{1}$
a/Å	5.9566(11)
b/Å	6.4362(11)
c/Å	13.043(2)
α /°	86.552(6)
β /°	88.830(6)
γ /°	79.256(5)
Volume / Z	490.35(15) Å ³ / 2
$\rho_{\text{calc}}/\text{cm}^3$	1.8231
μ/mm^{-1}	0.385
F(000)	268.5
Crystal size/mm ³	0.2 × 0.1 × 0.05
Radiation	Mo K α (λ = 0.71073)
2 θ range for data collection/°	6.26 to 56.3
Index ranges	-7 ≤ h ≤ 7, -8 ≤ k ≤ 8, -17 ≤ l ≤ 17
Reflections collected	9448
Independent reflections	2294 [R _{int} = 0.1260, R _{sigma} = 0.1162]
Data/restraints/parameters	2294/0/171
Goodness-of-fit on F ²	1.053

Table 7.18 Atomic coordinates ($\times 10^4$) and equivalent isotropic displacement parameters ($\text{\AA}^2 \times 10^3$) for HFbzTSC. $U(\text{eq})$ is defined as one third of the trace of the orthogonalized U_{ij} tensor.

Atom	<i>x</i>	<i>y</i>	<i>z</i>	<i>U</i> (eq)
S1	1772.246(11)	-3090.615(11)	75.264(11)	31.62(6)
F1	454.902(11)	6731.396(11)	2694.200(11)	35.32(6)
F5	7210.908(11)	1519.382(11)	2923.963(11)	38.21(6)
F4	8990.350(11)	3897.269(11)	4152.175(11)	45.70(6)
F3	6629.560(11)	7752.443(11)	4635.475(11)	52.66(6)
N1	3682.942(11)	1048.056(11)	1764.684(11)	26.10(6)
N2	2397.029(11)	8.545(11)	1190.429(11)	28.17(6)
C8	5943.647(11)	3400.694(11)	3134.732(11)	29.28(6)
C4	2600.371(11)	5997.345(11)	3028.384(11)	32.04(6)
C3	3763.343(11)	4040.164(11)	2744.322(11)	26.74(6)
C7	6883.867(11)	4620.696(11)	3768.223(11)	34.75(6)
C5	3536.933(11)	7257.970(11)	3661.691(11)	34.97(6)
C6	5704.571(11)	6570.485(11)	4017.632(11)	38.66(6)
F2	2327.538(11)	9121.585(11)	3918.471(11)	47.60(6)
N3	5624.170(11)	-2461.650(11)	909.825(11)	30.31(6)
C1	3415.187(11)	-1786.244(11)	754.577(11)	24.41(6)
C2	2630.105(11)	2796.925(11)	2091.300(11)	28.55(6)

Table 7.19 Bond lengths [\AA] and angles [deg] for HFbzTSC.

Atom	Atom	Distance	Atom	Atom	Atom	Angle $^\circ$	Atom	Atom	Atom	Angle $^\circ$
S1	C1	1.6967(2)	C2	N1	N2	115.0874(7)	C6	C7	F4	119.7102(10)
F1	C4	1.3488(2)	C1	N2	N1	119.0455(7)	C6	C7	C8	120.6635(7)
F5	C8	1.34251(19)	C3	C8	F5	121.0139(10)	C6	C5	C4	119.1496(7)
F4	C7	1.3497(2)	C7	C8	F5	117.0117(8)	F2	C5	C4	120.1929(7)
F3	C6	1.33409(16)	C7	C8	C3	121.9568(7)	F2	C5	C6	120.6575(10)
N1	N2	1.36751(16)	C3	C4	F1	119.8703(10)	C7	C6	F3	120.3967(8)
N1	C2	1.27489(18)	C5	C4	F1	117.3319(7)	C5	C6	F3	120.0662(7)
N2	C1	1.35244(18)	C5	C4	C3	122.7935(7)	C5	C6	C7	119.4854(9)
C8	C3	1.3849(2)	C4	C3	C8	115.9066(9)	N2	C1	S1	118.2585(6)
C8	C7	1.36887(16)	C2	C3	C8	124.9030(7)	N3	C1	S1	123.6669(8)
C4	C3	1.3872(2)	C2	C3	C4	119.1753(7)	N3	C1	N2	118.0382(9)
C4	C5	1.38564(16)	C8	C7	F4	119.6263(7)	C3	C2	N1	121.1260(7)
C3	C2	1.45883(17)								
C7	C6	1.3730(2)								
C5	C6	1.3657(2)								
C5	F2	1.33647(19)								
N3	C1	1.3223(2)								

Table 7.20 Anisotropic displacement parameters ($\text{\AA}^2 \times 10^3$) for HFbzTSC. The anisotropic displacement factor exponent takes the form: $-2\pi^2[h2a^*2U_{11}+2hka^*b^*U_{12}+\dots]$.

Atom	U_{11}	U_{22}	U_{33}	U_{12}	U_{13}	U_{23}
S1	24.66(4)	26.31(4)	43.10(17)	-0.10(4)	-9.15(8)	-7.10(9)
F1	30.76(4)	31.73(4)	39.71(18)	3.35(4)	-1.90(8)	0.17(9)
F5	28.33(4)	35.89(4)	47.56(18)	3.29(4)	-9.36(8)	-5.32(9)
F4	38.69(4)	60.08(4)	41.93(18)	-18.68(4)	-13.60(8)	2.26(9)
F3	73.27(4)	55.70(4)	39.65(18)	-35.78(4)	-8.64(8)	-11.57(9)
N1	25.44(4)	22.06(4)	31.32(18)	-5.21(4)	-6.10(8)	-1.41(9)

N2	23.61(4)	25.61(4)	34.99(18)	-3.39(4)	-10.63(8)	0.32(9)
C8	30.18(4)	27.21(4)	31.08(18)	-7.12(4)	-1.02(8)	-0.80(9)
C4	33.68(4)	33.29(4)	29.85(18)	-8.65(4)	2.56(8)	-0.89(9)
C3	29.54(4)	26.40(4)	25.11(18)	-7.89(4)	-1.10(8)	0.63(9)
C7	34.43(4)	47.28(4)	25.81(18)	-17.98(4)	-9.49(8)	7.25(9)
C5	51.86(4)	23.01(4)	32.68(18)	-13.22(4)	9.40(8)	-6.74(9)
C6	53.74(4)	41.87(4)	27.62(18)	-26.43(4)	0.03(8)	-6.04(9)
F2	69.68(4)	29.83(4)	44.16(18)	-9.97(4)	10.23(8)	-10.57(9)
N3	22.92(4)	32.14(4)	35.93(18)	-4.01(4)	-1.86(8)	-5.28(9)
C1	24.05(4)	21.61(4)	27.30(18)	-4.02(4)	0.89(8)	-0.27(9)
C2	27.15(4)	24.74(4)	32.85(18)	-3.50(4)	-3.13(8)	2.52(9)

7.11.6. HFbzTSCm

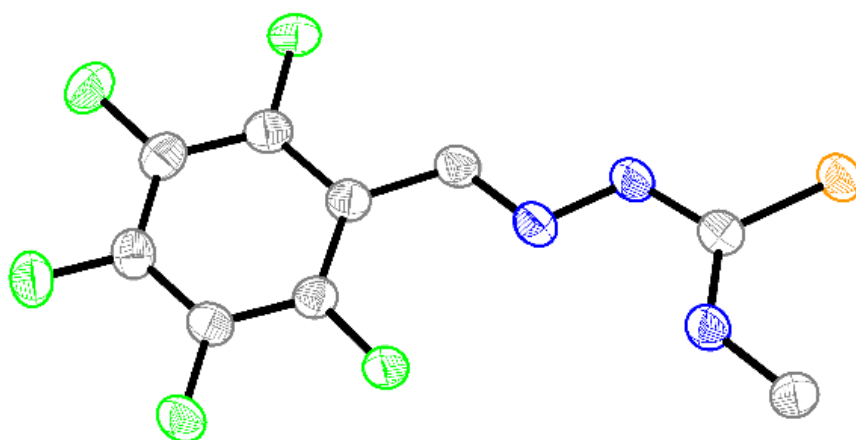


Figure 7.443 Molecular structure of HFbzTSCAd. Atoms are shown with 50 % probability. Hydrogen atoms are omitted for clarity.

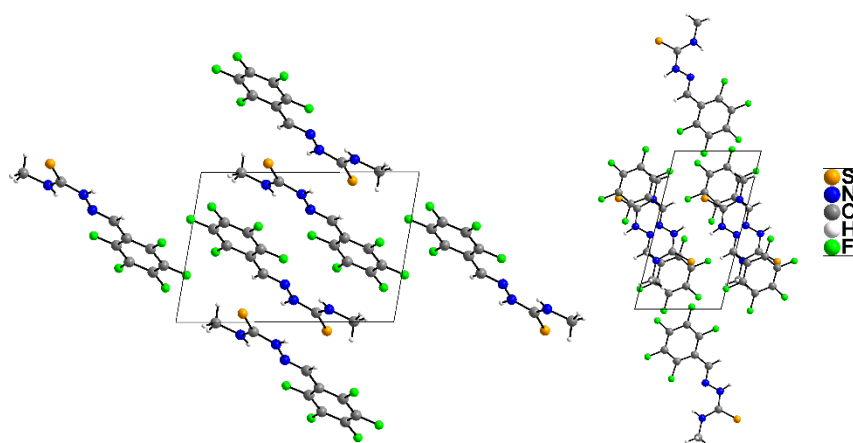


Figure 7.444 Crystal structure of HFbzTSCAd along the crystallographic a-axis (left) and b-axis (right).

Table 7.21 Crystal data and structure refinement for HFbzTSCm.

Empirical formula	C ₉ H ₆ F ₅ N ₃ S (283.23 g/mol)
Temperature/K	100 K
Crystal system / Space group	Triclinic / $P\bar{1}$
a/Å	6.0774(5)
b/Å	7.8697(6)
c/Å	11.6226(10)

$\alpha/^\circ$	99.071(7)
$\beta/^\circ$	103.804(6)
$\gamma/^\circ$	91.774(7)
Volume / Z	531.71(8) Å ³ / 2
ρ_{calc}	1.7689 g/cm ³
μ/mm^{-1}	0.359
F(000)	284.5
Radiation	Mo K α ($\lambda = 0.71073$)
2 Θ range for data collection/ $^\circ$	3.66 to 58.54
Index ranges	-8 $\leq h \leq$ 8, -10 $\leq k \leq$ 10, -15 $\leq l \leq$ 15
Reflections collected	6166
Independent reflections	2797 [R _{int} = 0.0532, R _{sigma} = 0.0486]
Data/restraints/parameters	2797/0/177
Goodness-of-fit on F ²	1.005
Final R indexes [$I_0 \geq 2\sigma(I_0)$]	R ₁ = 0.0431, wR ₂ = 0.1017
Final R indexes [all data]	R ₁ = 0.0594, wR ₂ = 0.1183
Largest diff. peak/hole / e Å ⁻³	0.36/-0.45

Table 7.22 Atomic coordinates ($\times 10^4$) and equivalent isotropic displacement parameters (Å² $\times 10^3$) for HFbzTSCm. U(eq) is defined as one third of the trace of the orthogonalized U_{ij} tensor.

Atom	<i>x</i>	<i>y</i>	<i>z</i>	U(eq)	Atom	<i>x</i>	<i>y</i>	<i>z</i>	U(eq)
S1	5136.9(8)	10579.4(7)	7000.6(5)	36.26(17)	C5	-1730(3)	4890(3)	1731.9(18)	32.6(4)
N3	1059(3)	9159(2)	6934.3(16)	34.4(4)	C7	-5299(3)	3350(3)	1444.1(19)	34.9(4)
N2	2336(3)	8520(2)	5227.0(16)	34.2(4)	C6	-3479(3)	3793(3)	1002.2(17)	34.8(4)
C2	2686(3)	9371(2)	6371.6(18)	31.4(4)	C8	-5321(3)	4032(3)	2610.9(18)	32.1(4)
C1	1177(4)	9957(3)	8163.9(18)	36.9(4)	F4	-7091.4(19)	3611.3(16)	3037.6(11)	38.5(3)
N1	392(3)	7487(2)	4706.1(15)	32.2(3)	F3	-7028(2)	2300.6(18)	745.1(12)	44.9(3)
C3	251(3)	6762(3)	3621.0(18)	31.8(4)	F1	-6(2)	5313.6(17)	1269.1(11)	40.4(3)
C4	-1688(3)	5604(2)	2919.0(16)	29.9(4)	F5	-3683(2)	5774.6(16)	4439.2(11)	38.2(3)
C9	-3555(3)	5133(2)	3326.8(17)	30.1(4)	F2	-3440(2)	3142.7(18)	-123.7(11)	45.2(3)

Table 7.23 Bond lengths [Å] and angles [deg] for HFbzTSCm.

Atom	Atom	Length/Å	Atom	Atom	Atom	Angle/ $^\circ$	Atom	Atom	Atom	Angle/ $^\circ$
S1	C2	1.683(2)	C1	N3	C2	123.97(18)	C6	C5	C4	123.06(18)
N3	C2	1.329(3)	N1	N2	C2	120.18(17)	F1	C5	C4	119.07(17)
N3	C1	1.452(3)	N3	C2	S1	124.15(15)	F1	C5	C6	117.86(17)
N2	C2	1.356(3)	N2	C2	S1	118.90(15)	C8	C7	C6	119.27(18)
N2	N1	1.366(2)	N2	C2	N3	116.93(18)	F3	C7	C6	120.31(18)
N1	C3	1.281(3)	C3	N1	N2	114.35(16)	F3	C7	C8	120.41(19)
C3	C4	1.458(3)	C4	C3	N1	122.40(17)	C7	C6	C5	119.37(18)
C4	C9	1.391(3)	C9	C4	C3	125.43(17)	F2	C6	C5	120.84(19)
C4	C5	1.399(3)	C5	C4	C3	118.82(17)	F2	C6	C7	119.79(18)
C9	C8	1.373(3)	C5	C4	C9	115.75(17)	C7	C8	C9	120.48(18)
C9	F5	1.333(2)	C8	C9	C4	122.06(17)	F4	C8	C9	120.22(17)
C5	C6	1.370(3)	F5	C9	C4	120.00(17)	F4	C8	C7	119.30(18)
C5	F1	1.343(2)	F5	C9	C8	117.94(17)				
C7	C6	1.383(3)								
C7	C8	1.381(3)								
C7	F3	1.332(2)								
C6	F2	1.334(2)								
C8	F4	1.341(2)								

Table 7.24 Anisotropic displacement parameters ($\text{\AA}^2 \times 10^3$) for HFbzTSCm. The anisotropic displacement factor exponent takes the form: $-2\pi^2[h2a^*2U11+2hka^*b^*U12+\dots]$.

Atom	U ₁₁	U ₂₂	U ₃₃	U ₁₂	U ₁₃	U ₂₃
S1	28.1(2)	39.3(3)	39.9(3)	-3.20(18)	9.09(19)	2.4(2)
N3	27.4(8)	38.8(9)	36.7(8)	-0.6(7)	10.2(7)	2.8(7)
N2	28.0(7)	38.0(9)	36.8(9)	-4.9(6)	12.1(7)	2.1(7)
C2	28.2(9)	29.5(9)	37.7(10)	4.6(7)	9.8(7)	6.2(7)
C1	36.7(10)	40.6(11)	35.3(10)	2.9(8)	13.6(8)	4.5(8)
N1	27.3(7)	31.4(8)	37.3(8)	-1.8(6)	8.7(6)	4.2(7)
C3	28.5(8)	34.5(10)	34.4(9)	1.3(7)	12.4(7)	5.2(7)
C4	28.4(8)	31.4(9)	31.5(9)	4.1(7)	10.4(7)	5.0(7)
C9	29.7(9)	32.1(9)	30.4(9)	4.4(7)	11.9(7)	3.9(7)
C5	30.1(9)	36.4(10)	34.7(9)	5.9(7)	13.3(7)	7.1(8)
C7	30.1(9)	35.0(10)	36.9(10)	3.7(7)	5.3(7)	2.4(8)
C6	37.0(10)	37.2(10)	30.3(9)	7.2(8)	9.5(8)	3.6(8)
C8	26.8(8)	34.7(10)	36.6(9)	2.9(7)	10.7(7)	6.9(8)
F4	29.1(6)	43.5(7)	44.4(7)	-2.1(5)	14.1(5)	4.7(5)
F3	37.5(7)	49.3(8)	40.9(7)	-6.3(6)	4.1(5)	-2.8(6)
F1	37.4(6)	50.5(7)	37.9(6)	1.0(5)	19.5(5)	6.6(5)
F5	36.9(6)	45.1(7)	34.0(6)	-5.9(5)	17.6(5)	-1.2(5)
F2	50.0(7)	54.2(8)	30.1(6)	1.5(6)	13.3(5)	-1.4(5)

7.11.7. HFbzTSCdm

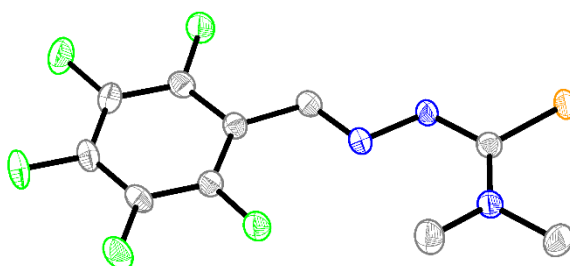


Figure 7.445 Molecular structure of HFbzTSCdm. Atoms are shown with 50 % probability. Hydrogen atoms are omitted for clarity.

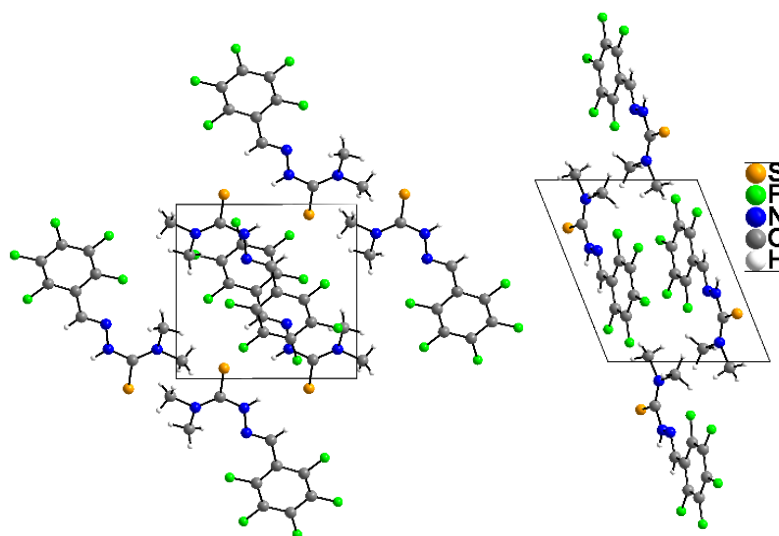


Figure 7.446 Crystal structure of HFbzTSCAd along the crystallographic a-axis (left) and b-axis (right).

Table 7.25 Crystal data and structure refinement for HFbzTSCAd.

Empirical formula	C ₁₀ H ₈ F ₅ N ₃ S (297.25 g/mol)
Temperature/K	150.0
Crystal system / Space group	Triclinic / $P\bar{1}$
a/Å	7.8799(5)
b/Å	8.5657(5)
c/Å	9.3890(6)
α /°	85.627(4)
β /°	67.820(4)
γ /°	78.128(4)
Volume / Z	574.28(6) Å ³ / 2
ρ_{calc}	1.7189 g/cm ³
μ /mm ⁻¹	0.337
F(000)	300.5
Crystal size/mm ³	0.2 × 0.2 × 0.1
Radiation	Mo K α (λ = 0.71073)
2 θ range for data collection/°	4.68 to 50.14
Index ranges	-9 ≤ h ≤ 9, -10 ≤ k ≤ 10, -11 ≤ l ≤ 11
Reflections collected	10614
Independent reflections	2031 [R _{int} = 0.0427, R _{sigma} = 0.0293]
Data/restraints/parameters	2031/0/205
Goodness-of-fit on F ²	1.067
Final R indexes [I _o ≥ 2 σ I _o]	R ₁ = 0.0314, wR ₂ = 0.0760
Final R indexes [all data]	R ₁ = 0.0414, wR ₂ = 0.0808
Largest diff. peak/hole / e Å ⁻³	0.25/-0.23

Table 7.26 Atomic coordinates (x 10⁴) and equivalent isotropic displacement parameters (Å² × 10³) for HFbzTSCAd. U(eq) is defined as one third of the trace of the orthogonalized U_{ij} tensor.

Atom	x	y	z	U(eq)	Atom	x	y	z	U(eq)
S1	9158.8(7)	10581.8(6)	7354.1(6)	29.37(18)	C3	8192(3)	8942(2)	7571(2)	23.2(4)
F3	6236.8(16)	1038.5(13)	3307.1(14)	37.5(3)	C4	8228(3)	6445(2)	4748(2)	24.4(4)
F2	8195.9(17)	2889.7(14)	1045.6(13)	39.6(3)	C5	7773(2)	4978(2)	4438(2)	21.2(4)
F1	9190.1(17)	5429.0(13)	1777.0(12)	34.7(3)	C10	6801(2)	3974(2)	5547(2)	23.0(4)
F5	6243.8(16)	4304.1(13)	7044.1(12)	32.1(3)	C9	6305(3)	2663(2)	5172(2)	25.7(4)
F4	5303.3(16)	1776.9(13)	6271.7(14)	36.2(3)	C8	6772(3)	2287(2)	3655(2)	27.1(4)
N3	7343(2)	8329.1(19)	8941.0(17)	26.9(4)	C6	8237(3)	4534(2)	2921(2)	24.7(4)
N2	8336(2)	8299.3(19)	6236.5(19)	24.9(4)	C7	7747(3)	3235(2)	2518(2)	26.5(4)
N1	7911(2)	6869.4(17)	6109.6(17)	22.2(4)	C2	7371(4)	8982(3)	10322(3)	38.5(6)
C1	6192(4)	7102(3)	9281(3)	40.6(6)					

Table 7.27 Bond lengths [Å] and angles [deg] for HFbzTSCAd.

Atom	Atom	Length/Å	Atom	Atom	Atom	Angle/°	Atom	Atom	Atom	Angle/°
S1	C3	1.6951(19)	C3	N3	C1	127.03(17)	C9	C10	C5	122.48(17)
F3	C8	1.331(2)	C2	N3	C1	112.96(17)	C10	C9	F4	120.41(17)
F2	C7	1.332(2)	C2	N3	C3	119.81(17)	C8	C9	F4	119.25(17)
F1	C6	1.344(2)	C3	N2	N1	125.29(16)	C8	C9	C10	120.28(18)
F5	C10	1.339(2)	C4	N1	N2	115.66(15)	C9	C8	F3	119.70(17)
F4	C9	1.333(2)	N3	C3	S1	122.69(14)	C7	C8	F3	120.91(17)
N3	C1	1.467(3)	N2	C3	S1	115.08(14)	C7	C8	C9	119.36(17)
N3	C3	1.330(2)	N2	C3	N3	122.23(17)	C5	C6	F1	118.96(16)
N3	C2	1.461(3)	C5	C4	N1	121.92(17)	C7	C6	F1	117.49(17)
N2	N1	1.360(2)	C10	C5	C4	125.47(17)	C7	C6	C5	123.54(17)

N2	C3	1.363(2)	C6	C5	C4	119.41(16)	C8	C7	F2	119.93(16)
N1	C4	1.273(2)	C6	C5	C10	115.03(17)	C6	C7	F2	120.79(17)
C4	C5	1.453(3)	C5	C10	F5	120.30(16)	C6	C7	C8	119.28(17)
C5	C10	1.394(3)	C9	C10	F5	117.16(16)				
C5	C6	1.393(3)								
C10	C9	1.372(3)								
C9	C8	1.376(3)								
C8	C7	1.377(3)								
C6	C7	1.371(3)								

Table 7.28 Anisotropic displacement parameters ($\text{\AA}^2 \times 10^3$) for HFbzTSCAd. The anisotropic displacement factor exponent takes the form: $-2\pi^2[h^2a^*2U_{11}+2hka^*b^*U_{12}+\dots]$.

Atom	U ₁₁	U ₂₂	U ₃₃	U ₁₂	U ₁₃	U ₂₃
S1	41.8(3)	24.1(3)	25.3(3)	-15.1(2)	-10.9(2)	-1.93(19)
F3	40.4(7)	28.7(7)	49.5(8)	-16.1(5)	-16.8(6)	-9.8(5)
F2	50.5(8)	43.5(8)	28.4(7)	-17.3(6)	-12.8(6)	-8.8(5)
F1	46.0(7)	34.9(7)	23.6(6)	-20.6(5)	-7.3(5)	3.1(5)
F5	42.7(7)	29.5(6)	23.0(6)	-15.6(5)	-6.8(5)	1.4(5)
F4	40.0(7)	29.9(7)	38.9(7)	-20.4(5)	-8.7(6)	6.2(5)
N3	33.5(9)	25.7(9)	21.1(9)	-10.8(7)	-7.0(7)	0.5(7)
N2	35.2(9)	22.7(9)	19.5(9)	-14.6(7)	-8.8(7)	1.8(7)
N1	22.7(8)	19.0(8)	25.3(9)	-5.7(6)	-8.3(7)	-1.4(6)
C1	51.8(15)	41.3(15)	27.5(12)	-25.3(12)	-4.9(12)	0.9(10)
C3	23.5(10)	21.4(10)	24.5(10)	-3.3(7)	-8.9(8)	-0.5(8)
C4	26.5(10)	23.1(10)	24.9(11)	-10.5(8)	-8.8(8)	3.5(8)
C5	18.9(9)	19.9(9)	25.6(10)	-4.0(7)	-8.8(8)	-0.8(7)
C10	23.1(10)	22.9(10)	22.0(10)	-3.8(7)	-7.5(8)	-1.1(7)
C9	22.5(10)	20.9(10)	32.1(11)	-8.6(8)	-6.9(8)	4.3(8)
C8	25.4(10)	20.9(10)	37.9(12)	-6.8(8)	-12.7(9)	-5.0(8)
C6	24.0(10)	24.1(10)	24.9(10)	-8.0(8)	-6.6(8)	2.6(8)
C7	27.8(11)	28.1(11)	25.0(10)	-5.6(8)	-9.9(8)	-6.6(8)
C2	52.2(16)	42.8(14)	20.7(11)	-16.8(12)	-9.4(11)	-2.4(10)

7.11.8. HFbzTSCAd

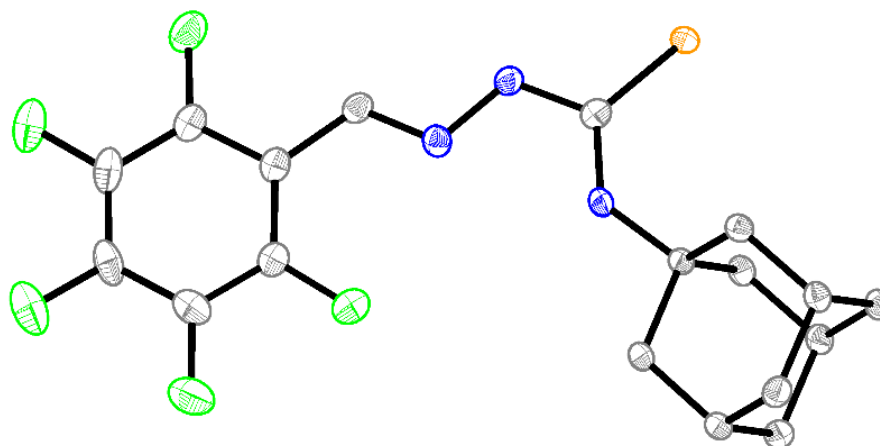


Figure 7.447 Molecular structure of HFbzTSCAd. Atoms are shown with 50 % probability. Hydrogen atoms are omitted for clarity.

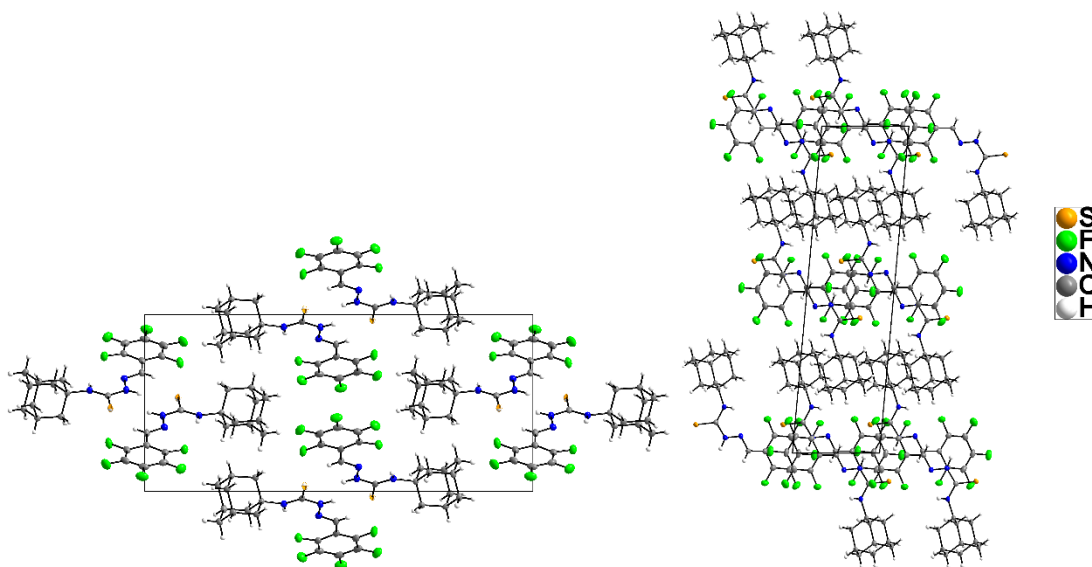


Figure 7.448 Crystal structure of HFbzTSCAd along the crystallographic a-axis (left) and b-axis (right).

Table 7.29 Crystal data and structure refinement for HFbzTSCAd.

Empirical formula	C ₁₈ H ₁₈ F ₅ N ₃ S (403.42 g/mol)
Temperature/K	100.15
Crystal system / Space group	monoclinic / P2 ₁ /n
Unit cell parameters	a = 6.4544(4) Å b = 11.0220(8) Å c = 24.3140(17) Å β = 95.126(3)°
Volume / Z	1722.8(2) Å ³ / 4
ρ _{calc} /cm ³	1.5553
μ/mm ⁻¹	0.248
F(000)	833.0
Crystal size/mm ³	0.1 × 0.1 × 0.04
Radiation	Cu Kα (λ = 1.54178 Å)
2θ range for data collection/°	3.36 to 52.08
Index ranges	-7 ≤ h ≤ 7, -13 ≤ k ≤ 13, -29 ≤ l ≤ 29
Reflections collected	36449
Independent reflections	3381 [R _{int} = 0.0593, R _{sigma} = 0.0262]
Data/restraints/parameters	3381/0/316
Goodness-of-fit on F ²	1.083
Final R indexes [I ≥ 2σ _I]	R ₁ = 0.0452, wR ₂ = 0.1254
Final R indexes [all data]	R ₁ = 0.0491, wR ₂ = 0.1283
Largest diff. peak/hole / e Å ⁻³	0.43/-0.43

Table 7.30 Atomic coordinates (x 10⁴) and equivalent isotropic displacement parameters (Å² × 10³) for HFbzTSCAd. U(eq) is defined as one third of the trace of the orthogonalized U_{ij} tensor.

Atom	x	y	z	U(eq)	Atom	x	y	z	U(eq)
S1	6373.0(8)	285.6(5)	5867.1(2)	18.62(17)	C6	6195(3)	-1299(2)	7103.7(9)	16.8(4)
F1	-1788(2)	-2637.9(14)	6032.8(6)	32.5(4)	C7	-4829(4)	-3252(2)	4508.2(11)	27.7(5)
F2	-2148(2)	-2279.0(16)	4085.4(6)	35.8(4)	C8	5316(3)	859(2)	7759.1(9)	17.0(4)
F5	-5784(3)	-3469.3(16)	4008.8(7)	42.7(4)	C9	-2946(4)	-2652(2)	4551.3(10)	23.5(5)

F3	-5496(3)	-3724.4(16)	5945.0(7)	40.8(4)		C10	3659(3)	338(2)	8108.6(9)	20.3(5)
F4	-7541(2)	-4157.7(15)	4941.1(8)	42.5(4)		C11	4184(3)	-562.8(19)	6984.7(8)	14.9(4)
N2	3308(3)	-705.7(18)	6409.3(8)	17.3(4)		C12	6940(3)	-1203(2)	7719.2(9)	17.6(4)
N4	1093(3)	-1374.3(17)	5516.0(8)	18.8(4)		C13	4566(3)	771.7(19)	7143.0(9)	16.1(4)
N3	2870(3)	-724.1(18)	5468.6(8)	19.5(4)		C14	-5702(3)	-3603(2)	4982.4(11)	27.6(5)
C1	-2757(3)	-2791(2)	5533.6(9)	20.9(5)		C15	5277(3)	-1724(2)	8066.9(9)	20.8(5)
C2	72(3)	-1701(2)	5064.5(9)	19.7(4)		C16	7338(3)	133(2)	7869.9(9)	17.6(4)
C3	4081(3)	-411.5(19)	5938.7(9)	17.4(4)		C17	3253(3)	-996(2)	7953.6(9)	20.0(5)
C4	-1857(3)	-2387(2)	5060.5(9)	19.5(4)		C18	2523(3)	-1080(2)	7337.2(9)	17.9(4)
C5	-4652(4)	-3369(2)	5494.9(11)	25.8(5)						

Table 7.31 Bond lengths [Å] and angles [deg] for HFbzTSCAd.

Atom	Atom	Distance	Atom	Atom	Atom	Angle/°	Atom	Atom	Atom	Angle/°
S1	C3	1.689(2)	C11	N2	C3	130.64(19)	C4	C9	F2	118.7(2)
F1	C1	1.325(3)	C2	N4	N3	116.55(19)	C7	C9	F2	118.8(2)
F2	C9	1.350(3)	C3	N3	N4	118.86(18)	C7	C9	C4	122.5(2)
F5	C7	1.333(3)	C4	C1	F1	120.9(2)	C17	C10	C8	109.51(18)
F3	C5	1.325(3)	C5	C1	F1	117.8(2)	C6	C11	N2	111.67(17)
F4	C14	1.331(3)	C5	C1	C4	121.4(2)	C13	C11	N2	112.38(17)
N2	C3	1.329(3)	C4	C2	N4	121.7(2)	C13	C11	C6	110.18(17)
N2	C11	1.470(3)	N2	C3	S1	126.83(17)	C18	C11	N2	105.21(16)
N4	N3	1.366(3)	N3	C3	S1	117.92(16)	C18	C11	C6	108.53(17)
N4	C2	1.280(3)	N3	C3	N2	115.26(19)	C18	C11	C13	108.64(17)
N3	C3	1.370(3)	C2	C4	C1	125.1(2)	C15	C12	C6	109.71(17)
C1	C4	1.406(3)	C9	C4	C1	116.5(2)	C16	C12	C6	109.34(18)
C1	C5	1.375(3)	C9	C4	C2	118.4(2)	C16	C12	C15	109.75(18)
C2	C4	1.456(3)	C1	C5	F3	120.6(2)	C11	C13	C8	109.52(17)
C4	C9	1.399(3)	C14	C5	F3	118.9(2)	C5	C14	F4	120.9(2)
C5	C14	1.389(4)	C14	C5	C1	120.5(2)	C7	C14	F4	119.5(2)
C6	C11	1.536(3)	C12	C6	C11	109.45(17)	C7	C14	C5	119.6(2)
C6	C12	1.534(3)	C9	C7	F5	119.2(2)	C17	C15	C12	109.33(18)
C7	C9	1.379(3)	C14	C7	F5	121.3(2)	C12	C16	C8	109.68(17)
C7	C14	1.383(4)	C14	C7	C9	119.5(2)	C15	C17	C10	109.41(18)
C8	C10	1.535(3)	C13	C8	C10	110.00(17)	C18	C17	C10	109.21(18)
C8	C13	1.536(3)	C16	C8	C10	109.38(18)	C18	C17	C15	109.01(18)
C8	C16	1.534(3)	C16	C8	C13	109.14(17)	C17	C18	C11	110.68(17)
C10	C17	1.535(3)								
C11	C13	1.535(3)								
C11	C18	1.540(3)								
C12	C15	1.536(3)								
C12	C16	1.533(3)								
C15	C17	1.537(3)								
C17	C18	1.533(3)								

Table 7.32 Anisotropic displacement parameters ($\text{Å}^2 \times 10^3$) for HFbzTSCAd. The anisotropic displacement factor exponent takes the form: $-2\pi^2[h^2a^*2U_{11}+2hka^*b^*U_{12}+\dots]$.

Atom	U ₁₁	U ₂₂	U ₃₃	U ₁₂	U ₁₃	U ₂₃
S1	15.4(3)	25.1(3)	15.8(3)	-2.6(2)	3.77(19)	0.8(2)
F1	34.9(8)	39.1(9)	23.2(7)	-2.5(7)	1.0(6)	2.1(6)
F2	35.0(8)	50.2(10)	21.8(7)	0.3(7)	0.8(6)	-5.4(7)
F5	38.3(9)	46.8(10)	39.9(9)	-0.7(7)	-13.3(7)	-12.8(8)
F3	37.0(9)	42.3(9)	44.6(10)	-4.5(7)	12.1(7)	8.5(8)
F4	24.8(8)	33.9(9)	68.0(12)	-3.4(6)	-0.0(7)	-5.8(8)
N2	12.6(9)	21.5(9)	17.9(9)	-3.1(7)	1.2(7)	-0.7(7)

N4	14.3(8)	21.6(9)	20.6(9)	1.5(7)	2.0(7)	-1.6(7)
N3	17.0(9)	26.1(10)	15.4(9)	-0.7(7)	1.9(7)	0.1(7)
C1	21.4(11)	19.5(11)	21.3(11)	3.9(9)	-0.4(8)	-1.3(9)
C2	18.8(10)	25.4(11)	15.1(10)	3.3(9)	2.1(8)	-1.3(9)
C3	17.2(10)	17.9(10)	17.3(10)	4.8(8)	2.3(8)	-0.5(8)
C4	17.3(10)	20.2(11)	20.5(11)	5.3(8)	0.2(8)	-3.2(8)
C5	22.0(11)	20.0(11)	36.1(13)	2.6(9)	6.9(9)	3.2(10)
C6	13.3(10)	17.3(10)	20.0(10)	0.7(8)	1.9(8)	-1.3(8)
C7	22.7(11)	25.1(12)	33.2(13)	4.7(9)	-8.7(9)	-8.5(10)
C8	15.1(10)	17.0(11)	19.1(11)	-0.8(8)	1.9(8)	-3.0(8)
C9	23.6(11)	24.5(12)	21.9(11)	5.6(9)	-0.9(9)	-3.4(9)
C10	16.0(10)	29.4(12)	15.7(11)	1.3(9)	2.8(8)	-2.4(9)
C11	12.7(9)	17.5(10)	14.8(10)	-0.7(8)	2.4(7)	-0.3(8)
C12	12.4(10)	19.7(11)	20.6(10)	1.7(8)	0.7(8)	1.3(8)
C13	13.0(10)	17.0(10)	18.6(10)	1.9(8)	2.8(8)	0.8(8)
C14	15.4(10)	19.8(11)	46.5(15)	1.3(9)	-2.5(10)	-5.4(10)
C15	19.7(11)	23.2(12)	19.4(11)	-1.9(9)	-0.1(8)	4.6(9)
C16	11.7(9)	22.6(11)	18.3(11)	-0.7(8)	0.3(8)	-0.9(8)
C17	14.4(10)	28.9(12)	17.1(10)	-4.7(9)	3.0(8)	1.6(9)
C18	10.9(9)	24.0(12)	18.8(10)	-2.1(8)	1.8(8)	1.2(8)

7.11.9. HFbzTSCmB

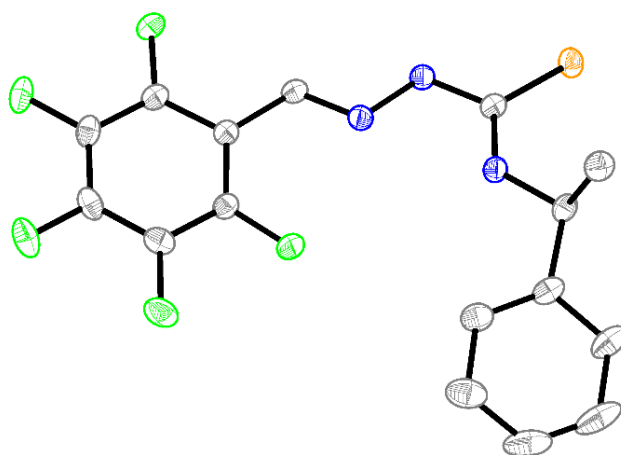


Figure 7.449 Molecular structure of HFbzTSCmB. Atoms are shown with 50 % probability. Hydrogen atoms are omitted for clarity.

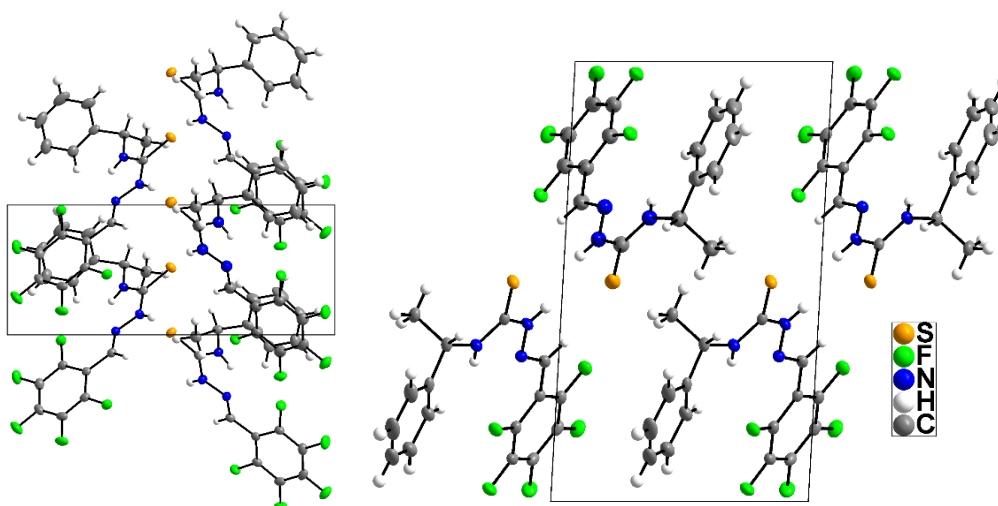


Figure 7.450 Crystal structure of HFbzTSCmB along the crystallographic a-axis (left) and b-axis (right).

Table 7.33 Crystal data and structure refinement for HFbzTSCmB.

Empirical formula	C ₁₆ H ₁₂ F ₅ N ₃ S (373.35 g/mol)
Temperature/K	100.0
Crystal system / Space group	monoclinic / P2 ₁
a/Å	8.8084(3)
b/Å	6.0050(2)
c/Å	15.0956(6)
β/°	93.200(2)
Volume / Z	797.23(5) Å ³ / 2
ρ _{calc} /cm ³	1.5552
μ/mm ⁻¹	2.365
F(000)	382.2
Crystal size/mm ³	0.4 × 0.1 × 0.03
Radiation	Cu Kα (λ = 1.54178)
2θ range for data collection/°	5.86 to 144.06
Index ranges	-10 ≤ h ≤ 10, -7 ≤ k ≤ 6, -18 ≤ l ≤ 18
Reflections collected	25397
Independent reflections	3067 [R _{int} = 0.0448, R _{sigma} = 0.0262]
Data/restraints/parameters	3067/1/236
Goodness-of-fit on F ²	1.082
Final R indexes [I _o ≥ 2σ _{I_o}]	R ₁ = 0.0205, wR ₂ = 0.0524
Final R indexes [all data]	R ₁ = 0.0216, wR ₂ = 0.0525
Largest diff. peak/hole / e Å ⁻³	0.18/-0.17
Flack parameter	0.023(10)

Table 7.34 Atomic coordinates (x 10⁴) and equivalent isotropic displacement parameters (Å² × 10³) for HFbzTSCmB. U(eq) is defined as one third of the trace of the orthogonalized U_{ij} tensor.

Atom	x	y	z	U(eq)	Atom	x	y	z	U(eq)
S1	1929.9(3)	10181.8(5)	4995.6(2)	22.71(9)	C5	-107.2(15)	-1253(2)	1667.9(9)	22.5(3)
F1	-1045.1(9)	-346.4(12)	3036.3(5)	25.42(18)	C6	778.7(16)	-738(2)	967.4(9)	23.9(3)
F2	-893.5(10)	-3162.0(13)	1657.0(6)	29.9(2)	C7	1577.0(15)	1231(2)	978.3(9)	23.5(3)
F3	846.4(10)	-2139.6(14)	280.4(6)	34.4(2)	C8	1513.9(15)	2673(2)	1684.6(9)	19.6(3)
F4	2396.8(10)	1757.4(15)	284.3(5)	32.4(2)	C9	5691.2(15)	9860(2)	4241.2(9)	26.8(3)
F5	2294.2(9)	4578.4(12)	1639.6(5)	25.09(18)	C10	4379.6(14)	10421(2)	3569.9(8)	20.6(3)
N1	1290.9(13)	6573.7(18)	4039.0(7)	19.7(2)	C11	4969.5(14)	10761(2)	2652.8(9)	22.9(3)
N2	1458.7(12)	5281(2)	3303.8(7)	19.2(2)	C12	4945.8(16)	9121(3)	2003.7(10)	28.1(3)
N3	3224.4(12)	8670.4(18)	3552.7(7)	19.7(2)	C13	5579.5(18)	9496(3)	1190.2(11)	37.7(4)
C1	2181.7(14)	8415(2)	4153.5(8)	17.9(3)	C14	6253.4(18)	11516(3)	1024.1(12)	43.2(4)
C2	543.0(15)	3632(2)	3188.9(9)	19.0(3)	C15	6295.0(19)	13146(3)	1656.6(13)	46.0(5)
C3	645.4(15)	2204(2)	2410.4(8)	17.7(3)	C16	5657.1(18)	12788(3)	2473.4(12)	34.3(4)
C4	-168.7(13)	207(2)	2368.2(8)	19.9(2)					

Table 7.35 Bond lengths [Å] and angles [deg] for HFbzTSCmB.

Atom	Atom	Length/Å	Atom	Atom	Atom	Angle/°	Atom	Atom	Atom	Angle/°
S1	C1	1.6802(13)	C1	N1	N2	118.41(10)	C7	C6	C5	119.52(12)
F1	C4	1.3455(14)	C2	N2	N1	116.85(10)	C6	C7	F4	119.34(13)
F2	C5	1.3389(16)	C10	N3	C1	125.10(11)	C8	C7	F4	120.16(13)
F3	C6	1.3394(16)	N1	C1	S1	120.63(9)	C8	C7	C6	120.49(12)
F4	C7	1.3430(16)	N3	C1	S1	124.48(10)	C3	C8	F5	121.11(11)
F5	C8	1.3383(15)	N3	C1	N1	114.88(11)	C7	C8	F5	117.09(11)

N1	N2	1.3689(15)	C3	C2	N2	119.68(11)	C7	C8	C3	121.78(12)
N1	C1	1.3611(16)	C4	C3	C2	119.07(11)	C9	C10	N3	110.61(11)
N2	C2	1.2831(17)	C8	C3	C2	124.90(11)	C11	C10	N3	110.69(10)
N3	C1	1.3352(16)	C8	C3	C4	116.03(11)	C11	C10	C9	110.42(10)
N3	C10	1.4625(16)	C3	C4	F1	119.49(12)	C12	C11	C10	123.75(12)
C2	C3	1.4617(18)	C5	C4	F1	117.85(12)	C16	C11	C10	117.96(13)
C3	C4	1.3969(19)	C5	C4	C3	122.65(11)	C16	C11	C12	118.17(14)
C3	C8	1.3995(18)	C4	C5	F2	120.80(12)	C13	C12	C11	121.05(14)
C4	C5	1.3767(19)	C6	C5	F2	119.69(12)	C14	C13	C12	119.94(17)
C5	C6	1.384(2)	C6	C5	C4	119.51(12)	C15	C14	C13	119.87(15)
C6	C7	1.375(2)	C5	C6	F3	120.18(13)	C16	C15	C14	120.60(16)
C7	C8	1.3773(19)	C7	C6	F3	120.30(13)	C15	C16	C11	120.37(17)
C9	C10	1.5312(17)								
C10	C11	1.5194(18)								
C11	C12	1.388(2)								
C11	C16	1.393(2)								
C12	C13	1.395(2)								
C13	C14	1.380(3)								
C14	C15	1.366(3)								
C15	C16	1.400(2)								

Table 7.36 Anisotropic displacement parameters ($\text{\AA}^2 \times 10^3$) for HFbzTSCmB. The anisotropic displacement factor exponent takes the form: $-2\pi^2[h^2a^{*2}U_{11}+2hka^*b^*U_{12}+\dots]$.

Atom	U_{11}	U_{22}	U_{33}	U_{12}	U_{13}	U_{23}
S1	19.74(14)	23.51(16)	25.29(15)	-1.69(13)	5.01(11)	-6.69(13)
F1	25.5(4)	24.0(4)	27.1(4)	-6.9(3)	4.6(3)	3.1(3)
F2	29.9(4)	18.8(4)	40.2(5)	-5.2(3)	-5.5(4)	-3.8(4)
F3	31.8(5)	37.5(5)	33.5(5)	2.4(4)	-1.0(4)	-18.1(4)
F4	28.0(4)	47.0(5)	22.9(4)	-2.8(4)	8.4(3)	-4.1(4)
F5	25.4(4)	25.4(4)	25.1(4)	-7.2(3)	6.6(3)	1.0(3)
N1	18.5(5)	21.4(6)	19.9(5)	-3.0(4)	6.6(4)	-2.5(4)
N2	19.2(5)	19.6(5)	18.8(5)	-0.2(5)	2.0(4)	-0.6(5)
N3	19.0(5)	19.4(6)	21.1(5)	-2.3(4)	4.7(4)	-2.7(4)
C1	14.3(6)	18.6(6)	20.5(6)	1.2(5)	-0.3(5)	2.8(5)
C2	17.7(6)	19.2(6)	20.4(6)	-0.4(5)	2.8(5)	2.7(5)
C3	15.9(6)	17.6(6)	19.6(6)	1.5(5)	-0.3(5)	1.5(5)
C4	16.7(5)	19.3(6)	23.6(6)	1.2(6)	0.1(4)	4.1(6)
C5	19.2(6)	17.3(6)	30.3(7)	0.3(5)	-5.8(5)	-0.7(5)
C6	20.4(6)	27.4(7)	23.2(7)	5.4(5)	-3.8(5)	-7.9(5)
C7	17.7(6)	32.5(7)	20.4(6)	3.6(5)	2.0(5)	0.1(5)
C8	16.5(6)	19.6(6)	22.7(6)	-0.9(5)	-0.2(5)	2.1(5)
C9	18.4(6)	32.1(8)	29.4(7)	-3.6(6)	-1.6(5)	2.7(6)
C10	15.7(6)	18.6(6)	27.6(6)	-2.0(5)	1.6(5)	0.0(5)
C11	12.9(6)	24.2(7)	31.4(7)	1.4(5)	0.4(5)	9.4(5)
C12	23.6(7)	32.2(8)	29.2(7)	-1.2(6)	7.4(6)	2.4(6)
C13	28.0(8)	55.6(11)	30.1(8)	2.7(7)	7.2(6)	7.0(7)
C14	25.6(8)	65.7(12)	39.1(9)	1.3(8)	8.2(7)	25.6(9)
C15	28.1(8)	46.2(11)	64.3(12)	-7.1(7)	8.4(8)	30.1(10)
C16	25.3(8)	28.9(8)	49.1(9)	-4.3(6)	5.3(6)	12.6(7)

7.11.10. HFbz(m)TSCmB

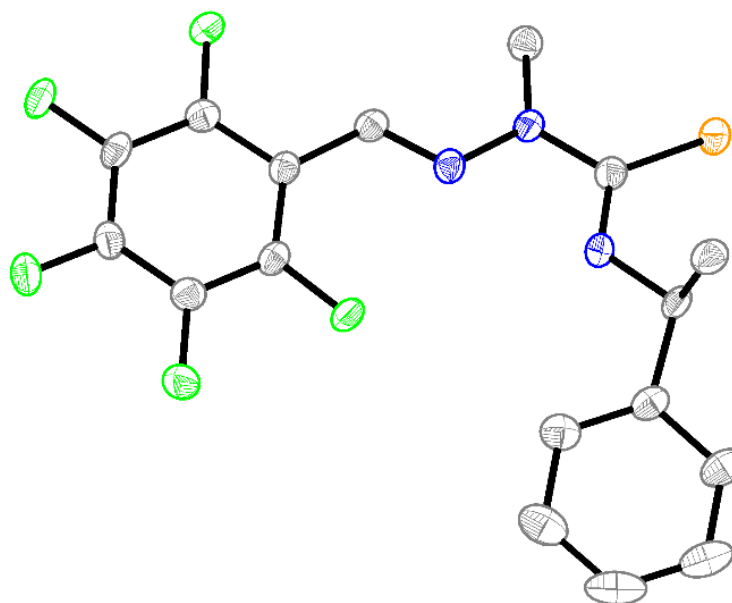


Figure 7.451 Molecular structure of HFbz(m)TSCmB. Atoms are shown with 50 % probability. Hydrogen atoms are omitted for clarity.

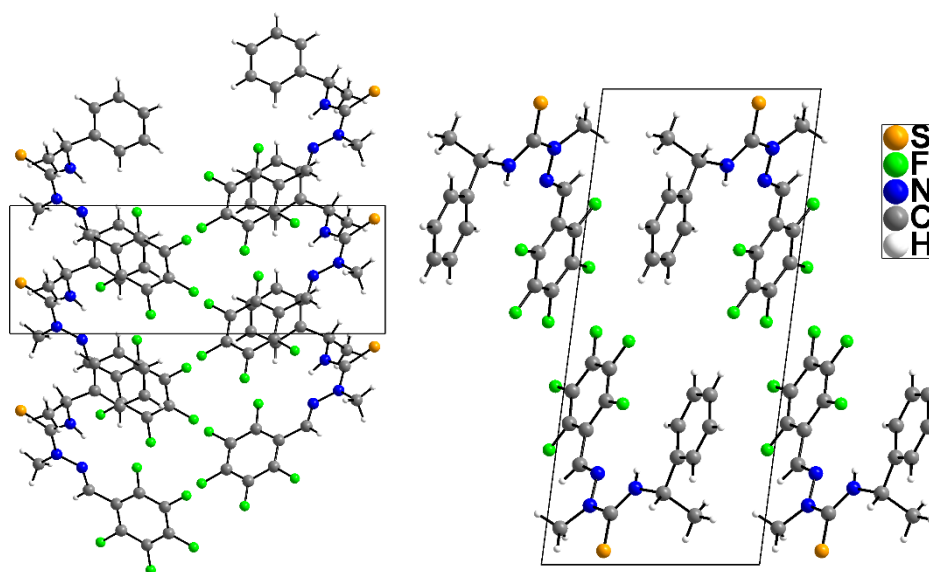


Figure 7.452 Crystal structure of HFbz(m)TSCmB along the crystallographic a-axis (left) and b-axis (right).

Table 7.37 Crystal data and structure refinement for HFbz(m)TSCmB.

Empirical formula	C ₁₇ H ₁₄ F ₅ N ₃ S (387.38g/mol)
Temperature/K	100.0
Crystal system/ Space group	Monoclinic / P2 ₁
a/Å	8.0354(5)
b/Å	5.9755(3)
c/Å	17.6790(11)
β/°	97.368(4)
Volume / Z	841.86(9) Å ³ / 2

$\rho_{\text{calc}}/\text{cm}^3$	1.5281
μ/mm^{-1}	2.261
F(000)	398.2
Crystal size/ mm^3	$0.4 \times 0.04 \times 0.01$
Radiation	Cu $K\alpha$ ($\lambda = 1.54178$)
2Θ range for data collection/ $^\circ$	5.04 to 144.26
Index ranges	$-9 \leq h \leq 9, -7 \leq k \leq 6, -21 \leq l \leq 21$
Reflections collected	26231
Independent reflections	3226 [$R_{\text{int}} = 0.0788, R_{\text{sigma}} = 0.0412$]
Data/restraints/parameters	3226/1/242
Goodness-of-fit on F^2	1.046
Final R indexes [$I \geq 2\sigma(I)$]	$R_1 = 0.0336, wR_2 = 0.0792$
Final R indexes [all data]	$R_1 = 0.0361, wR_2 = 0.0802$
Largest diff. peak/hole / $e \text{ \AA}^{-3}$	0.39/-0.27
Flack parameter	-0.032(17)

Table 7.38 Atomic coordinates ($\times 10^4$) and equivalent isotropic displacement parameters ($\text{\AA}^2 \times 10^3$) for HFbz(m)TSCmB. U(eq) is defined as one third of the trace of the orthogonalized U_{ij} tensor.

Atom	<i>x</i>	<i>y</i>	<i>z</i>	U(eq)	Atom	<i>x</i>	<i>y</i>	<i>z</i>	U(eq)
S1	7229.2(7)	8965.4(9)	291.4(3)	28.24(15)	C5	8839(3)	-637(4)	4231.6(13)	25.1(5)
F1	7215.6(15)	4503.7(19)	3382.6(7)	25.5(3)	C6	9612(3)	-1550(3)	3650.7(13)	23.2(5)
F2	7318.9(18)	2314(2)	4698.9(8)	32.2(3)	C7	9550(3)	-417(4)	2966.8(13)	22.1(5)
F3	8871.6(17)	-1735(2)	4894.1(8)	33.3(3)	C8	7138(3)	7439(4)	1080.7(12)	21.9(5)
F4	10413.0(17)	-3509(2)	3749.9(8)	28.9(3)	C9	4827(3)	9643(4)	1500.9(13)	22.5(5)
F5	10326.7(16)	-1349(2)	2414.4(7)	25.9(3)	C10	4397(3)	10526(4)	2258.6(13)	23.8(5)
N1	8122(2)	5540(3)	1242.6(10)	21.3(4)	C11	4557(3)	9286(4)	2924.6(13)	28.7(5)
N2	7960(2)	4518(3)	1920.2(10)	21.8(4)	C12	4000(3)	10158(5)	3581.2(15)	38.2(6)
N3	6139(2)	7937(3)	1607.5(11)	22.8(4)	C13	3274(3)	12261(5)	3568.1(17)	43.4(7)
C1	8831(3)	2748(4)	2103.4(13)	21.6(4)	C14	3095(3)	13511(4)	2899.9(17)	39.8(7)
C2	8751(3)	1651(4)	2837.2(12)	20.7(4)	C15	3668(3)	12653(4)	2253.6(16)	31.5(6)
C3	8003(3)	2521(4)	3442.5(13)	21.7(5)	C16	3253(3)	8708(4)	1030.4(13)	30.0(5)
C4	8048(3)	1416(4)	4128.4(13)	24.7(5)	C17	9358(3)	4783(4)	767.3(13)	25.0(5)

Table 7.39 Bond lengths [\AA] and angles [deg] for HFbz(m)TSCmB.

Atom	Atom	Length	Atom	Atom	Atom	Angle/ $^\circ$	Atom	Atom	Atom	Angle/ $^\circ$
S1	C8	1.676(2)	C8	N1	N2	115.42(17)	C7	C6	F4	120.4(2)
F1	C3	1.341(2)	C17	N1	N2	121.14(17)	C7	C6	C5	119.3(2)
F2	C4	1.342(3)	C17	N1	C8	123.21(18)	C2	C7	F5	119.54(19)
F3	C5	1.340(3)	C1	N2	N1	118.60(18)	C6	C7	F5	117.69(19)
F4	C6	1.336(2)	C9	N3	C8	123.54(19)	C6	C7	C2	122.8(2)
F5	C7	1.345(3)	C2	C1	N2	120.5(2)	N1	C8	S1	122.02(16)
N1	N2	1.366(2)	C3	C2	C1	125.9(2)	N3	C8	S1	123.52(17)
N1	C8	1.392(3)	C7	C2	C1	118.1(2)	N3	C8	N1	114.45(19)
N1	C17	1.453(3)	C7	C2	C3	115.98(19)	C10	C9	N3	111.73(18)
N2	C1	1.286(3)	C2	C3	F1	121.0(2)	C16	C9	N3	110.39(19)
N3	C8	1.339(3)	C4	C3	F1	116.9(2)	C16	C9	C10	109.95(18)
N3	C9	1.461(3)	C4	C3	C2	122.2(2)	C11	C10	C9	123.9(2)
C1	C2	1.462(3)	C3	C4	F2	120.4(2)	C15	C10	C9	116.9(2)
C2	C3	1.393(3)	C5	C4	F2	119.5(2)	C15	C10	C11	119.0(2)
C2	C7	1.398(3)	C5	C4	C3	120.1(2)	C12	C11	C10	120.2(2)
C3	C4	1.377(3)	C4	C5	F3	120.5(2)	C13	C12	C11	120.2(3)
C4	C5	1.383(3)	C6	C5	F3	119.8(2)	C14	C13	C12	120.0(2)

C5	C6	1.379(3)	C6	C5	C4	119.7(2)	C15	C14	C13	119.6(2)
C6	C7	1.381(3)	C5	C6	F4	120.28(19)	C14	C15	C10	121.0(3)
C9	C10	1.520(3)								
C9	C16	1.528(3)								
C10	C11	1.383(3)								
C10	C15	1.399(3)								
C11	C12	1.397(3)								
C12	C13	1.385(4)								
C13	C14	1.390(4)								
C14	C15	1.384(4)								

Table 7.40 Anisotropic displacement parameters ($\text{\AA}^2 \times 10^3$) for HFbz(m)TSCmB. The anisotropic displacement factor exponent takes the form: $-2\pi^2[h^2a^*2U_{11}+2hka^*b^*U_{12}+\dots]$.

Atom	U ₁₁	U ₂₂	U ₃₃	U ₁₂	U ₁₃	U ₂₃
S1	38.6(3)	19.7(3)	27.2(3)	1.4(2)	7.3(2)	5.2(2)
F1	27.8(6)	18.9(7)	29.5(7)	6.2(5)	2.6(5)	-1.1(5)
F2	35.5(7)	36.5(9)	25.0(7)	8.9(6)	5.5(6)	-0.8(6)
F3	39.2(8)	32.9(9)	27.6(7)	7.0(6)	3.6(6)	10.6(6)
F4	31.8(7)	17.7(7)	35.9(7)	6.1(5)	-0.1(6)	4.4(6)
F5	29.0(6)	20.5(7)	28.3(6)	4.4(5)	3.8(5)	-2.0(5)
N1	24.0(9)	17.6(10)	22.6(9)	1.7(7)	3.6(7)	1.1(7)
N2	24.0(9)	18.0(11)	23.2(9)	-2.0(7)	1.8(7)	2.3(7)
N3	27.2(9)	18.3(10)	22.5(10)	2.3(8)	2.2(7)	3.3(8)
C1	21.2(10)	17.6(12)	25.6(11)	-2.8(8)	0.7(8)	-2.9(8)
C2	20.6(10)	16.8(12)	23.7(11)	-1.5(8)	-1.6(8)	-0.3(8)
C3	18.8(10)	16.9(12)	28.1(11)	-0.2(8)	-2.3(8)	-1.2(9)
C4	23.4(11)	25.6(13)	24.3(11)	0.9(9)	0.6(8)	-2.8(9)
C5	26.3(10)	24.6(13)	23.1(10)	-0.2(9)	-1.5(8)	4.2(9)
C6	22.5(10)	14.2(12)	31.1(11)	-0.6(8)	-3.0(8)	1.0(8)
C7	20.1(10)	21.3(12)	24.7(11)	-2.8(8)	1.6(8)	-2.7(8)
C8	23.4(10)	17.8(12)	23.6(11)	-2.8(8)	-0.5(8)	-0.8(8)
C9	26.8(11)	12.8(12)	27.1(11)	2.1(8)	0.7(9)	0.2(8)
C10	17.7(10)	19.9(12)	32.9(12)	-3.2(8)	0.0(9)	-5.9(9)
C11	23.8(10)	32.6(15)	29.4(11)	-2.2(10)	2.3(9)	-4.2(10)
C12	29.7(13)	55.0(19)	30.1(13)	-8.1(12)	4.5(10)	-6.8(12)
C13	29.3(13)	56(2)	47.5(17)	-10.7(12)	12.8(11)	-28.9(14)
C14	30.0(13)	33.4(18)	57.6(17)	-2.7(10)	11.5(12)	-18.9(13)
C15	25.7(11)	22.2(14)	46.7(15)	-3.5(9)	5.4(10)	-7.1(10)
C16	31.2(12)	25.3(14)	31.5(11)	3.1(10)	-4.3(9)	-5.5(10)
C17	24.0(10)	25.2(12)	25.9(11)	0.9(9)	3.4(8)	0.6(9)

7.11.11. HmphfpyTSC · ½ Et₂O

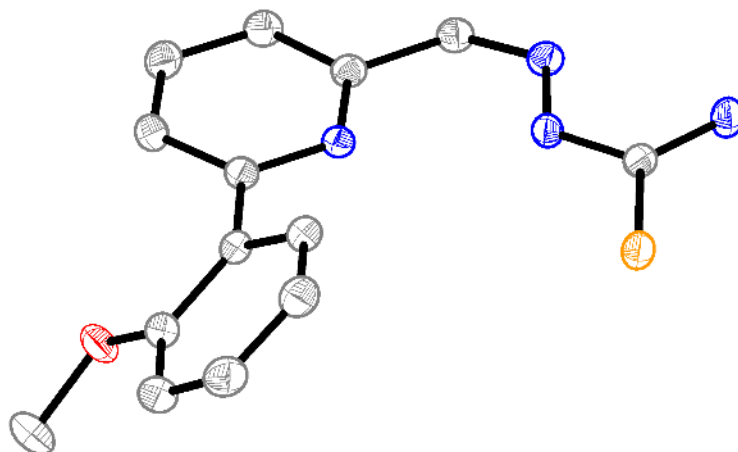


Figure 7.453 Molecular structure of HmphfpyTSC. Atoms are shown with 50% probability. Hydrogen atoms are omitted for clarity.

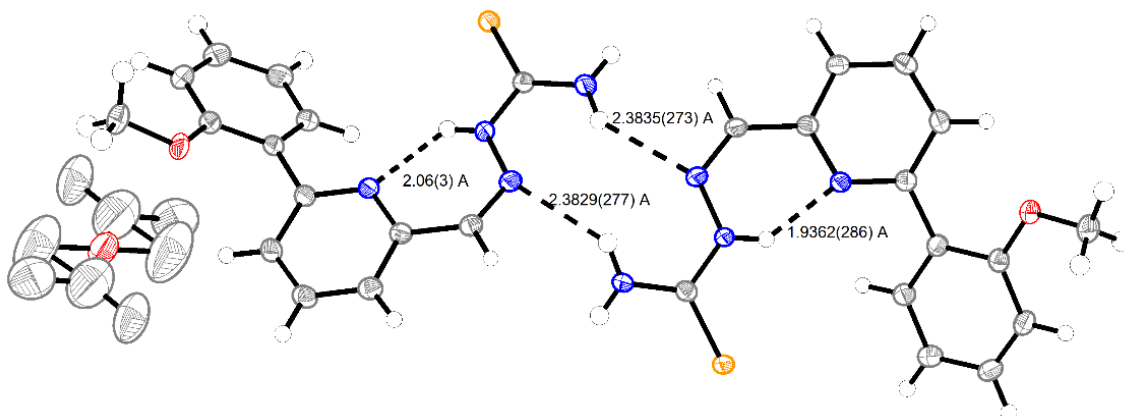


Figure 7.454 Asymmetric unit of HmphfpyTSC · ½ Et₂O. Atoms are shown with 50% probability.

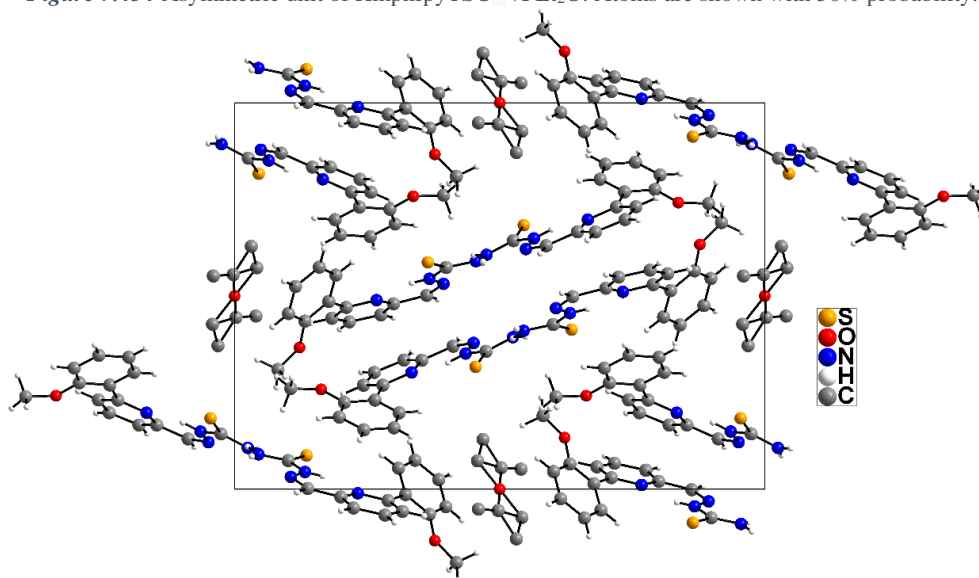


Figure 7.455 Crystal packing along the crystallographic a-axis of HmphfpyTSC · ½ Et₂O.

Table 7.41 Crystal data and structure refinement for HmphfpyTSC · ½ Et₂O.

Empirical formula	C ₃₆ H ₃₈ N ₈ O ₃ S ₂ (646.83 g/mol)
Temperature/K	100.0
Crystal system / Space group	Monoclinic / P2 ₁ /n
a/Å	8.1645(2)
b/Å	16.6339(5)
c/Å	23.1166(7)
β/°	99.6940(10)
Volume / Z	3094.58(15) Å ³ / 4
ρ _{calc} /cm ³	1.3495
μ/mm ⁻¹	1.936
F(000)	1318.4
Crystal size/mm ³	0.13 × 0.04 × 0.02
Radiation	Cu Kα (λ = 1.54178)
2θ range for data collection/°	6.58 to 144.3
Index ranges	-10 ≤ h ≤ 8, -20 ≤ k ≤ 20, -28 ≤ l ≤ 28
Reflections collected	90052
Independent reflections	6081 [R _{int} = 0.0617, R _{sigma} = 0.0227]
Data/restraints/parameters	6081/0/430
Goodness-of-fit on F ²	1.046
Final R indexes [I _o ≥ 2σ(I _o)]	R ₁ = 0.0417, wR ₂ = 0.1212
Final R indexes [all data]	R ₁ = 0.0464, wR ₂ = 0.1260
Largest diff. peak/hole / e Å ⁻³	0.49/-0.82

Table 7.42 Atomic coordinates (x 10⁴) and equivalent isotropic displacement parameters (Å² × 10³) for HmphfpyTSC · ½ Et₂O. U(eq) is defined as one third of the trace of the orthogonalized U_{ij} tensor.

Atom	x	y	z	U(eq)	Atom	x	y	z	U(eq)
S1b	12243.9(5)	6834.3(3)	5454.0(2)	20.54(14)	C11b	13601(2)	8463.5(12)	7561.9(9)	23.8(4)
S1	2032.1(5)	5871.0(3)	3644.1(2)	22.33(14)	C10b	12728(2)	8412.9(12)	6993.8(9)	24.1(4)
O1b	10701.0(17)	7419.2(9)	8368.7(6)	23.4(3)	C9b	11206(2)	8024.9(12)	6896.4(9)	21.3(4)
O1	4066.2(18)	3666.5(9)	1224.2(6)	26.4(3)	C1	4011(2)	5739.0(11)	3989.6(8)	19.0(4)
N1b	8530.0(18)	6978.0(9)	6662.5(7)	17.6(3)	C2	7750(2)	5015.6(11)	3623.0(9)	20.1(4)
N2b	7653.1(19)	6214.1(10)	5493.5(7)	19.8(3)	C3	7477(2)	4797.4(11)	2997.7(8)	19.0(4)
N3b	9252.5(19)	6489.9(10)	5643.5(7)	19.2(3)	C4	8825(2)	4511.3(11)	2756.7(9)	22.4(4)
O2	5000	5000	0	56.4(8)	C5	8573(2)	4329.1(12)	2164.2(9)	24.4(4)
N4b	9806(2)	6068.4(11)	4751.7(7)	23.7(4)	C6	7009(2)	4423.7(11)	1833.2(9)	22.9(4)
N1	5944.5(19)	4892.2(9)	2676.9(7)	18.5(3)	C7	5703(2)	4704.8(11)	2104.8(8)	19.9(4)
N2	6741.8(19)	5316.0(10)	3940.1(7)	19.8(3)	C8	4005(2)	4858.2(12)	1776.0(8)	20.5(4)
N3	5131.9(19)	5444.3(10)	3674.8(7)	19.1(3)	C13	3221(2)	4348.9(12)	1324.3(9)	23.0(4)
N4	4530(2)	5901.3(11)	4550.8(7)	24.2(4)	C12	1656(3)	4546.2(14)	1016.1(9)	28.3(4)
C1b	10331(2)	6431.7(11)	5257.1(8)	18.4(4)	C11	869(3)	5247.5(14)	1149.4(10)	31.1(5)
C2b	6690(2)	6300.8(12)	5878.2(8)	20.0(4)	C10	1610(3)	5746.7(13)	1597.3(10)	28.4(4)
C3b	7016(2)	6661.8(11)	6467.6(8)	18.0(4)	C9	3156(2)	5542.0(12)	1909.5(9)	23.6(4)
C4b	5751(2)	6658.9(11)	6804.6(8)	20.1(4)	C14	3233(3)	3097.9(13)	816.8(10)	33.0(5)
C5b	6092(2)	6979.0(12)	7366.4(8)	21.0(4)	C18	6065(7)	3713(3)	-315(3)	90.0(14)
C6b	7639(2)	7310.0(11)	7568.7(8)	20.4(4)	C16	2583(6)	5518(3)	-401.9(17)	81.6(12)
C7b	8843(2)	7306.8(11)	7202.5(8)	18.0(4)	C14b	11682(3)	7392.9(14)	8941.0(9)	28.8(4)
C8b	10502(2)	7694.1(11)	7353.9(8)	18.9(4)	C15	3828(9)	5555(5)	-27(2)	130(3)
C13b	11401(2)	7755.7(11)	7928.9(8)	19.4(4)	C17	4869(10)	4268(5)	-418(2)	139(3)
C12b	12948(2)	8134.0(11)	8025.6(9)	22.4(4)					

Table 7.43 Bond lengths [Å] and angles [deg] for HmphfpyTSC · ½ Et₂O.

Atom	Atom	Length/Å	Atom	Atom	Atom	Angle/°	Atom	Atom	Atom	Angle/°
S1b	C1b	1.6900(19)	C14b	O1b	C13b	117.52(15)	C9b	C10b	C11b	119.09(19)
S1	C1	1.6919(19)	C14	O1	C13	117.66(16)	C10b	C9b	C8b	122.15(18)
O1b	C13b	1.367(2)	C7b	N1b	C3b	119.20(16)	N3	C1	S1	118.15(14)
O1b	C14b	1.427(2)	C2b	N2b	N3b	116.93(16)	N4	C1	S1	123.99(15)
O1	C13	1.368(2)	C1b	N3b	N2b	120.29(16)	N4	C1	N3	117.86(17)
O1	C14	1.424(2)	C15 ¹	O2	C15	180.0	C3	C2	N2	130.37(17)
N1b	C3b	1.349(2)	C17	O2	C15	123.1(4)	C2	C3	N1	118.94(16)
N1b	C7b	1.347(2)	C17	O2	C15 ¹	56.9(4)	C4	C3	N1	122.62(18)
N2b	N3b	1.372(2)	C17 ¹	O2	C15	56.9(4)	C4	C3	C2	118.44(17)
N2b	C2b	1.291(2)	C17 ¹	O2	C15 ¹	123.1(4)	C5	C4	C3	118.23(18)
N3b	C1b	1.359(2)	C17	O2	C17 ¹	180.0	C6	C5	C4	119.48(18)
O2	C15 ¹	1.323(9)	C7	N1	C3	118.86(16)	C7	C6	C5	119.35(18)
O2	C15	1.323(9)	C2	N2	N3	117.46(16)	C6	C7	N1	121.45(18)
O2	C17 ¹	1.547(8)	C1	N3	N2	120.01(16)	C8	C7	N1	115.72(16)
O2	C17	1.547(8)	N3b	C1b	S1b	117.80(14)	C8	C7	C6	122.74(17)
N4b	C1b	1.321(3)	N4b	C1b	S1b	124.52(14)	C13	C8	C7	122.90(17)
N1	C3	1.352(2)	N4b	C1b	N3b	117.68(17)	C9	C8	C7	118.88(17)
N1	C7	1.341(2)	C3b	C2b	N2b	130.33(17)	C9	C8	C13	118.20(18)
N2	N3	1.370(2)	C2b	C3b	N1b	118.77(16)	C8	C13	O1	116.34(17)
N2	C2	1.292(2)	C4b	C3b	N1b	122.54(17)	C12	C13	O1	123.67(18)
N3	C1	1.353(2)	C4b	C3b	C2b	118.69(16)	C12	C13	C8	119.98(19)
N4	C1	1.323(3)	C5b	C4b	C3b	118.07(17)	C11	C12	C13	120.14(19)
C2b	C3b	1.471(3)	C6b	C5b	C4b	119.78(17)	C10	C11	C12	120.6(2)
C3b	C4b	1.395(3)	C7b	C6b	C5b	119.14(17)	C9	C10	C11	119.1(2)
C4b	C5b	1.388(3)	C6b	C7b	N1b	121.23(17)	C10	C9	C8	121.90(19)
C5b	C6b	1.385(3)	C8b	C7b	N1b	114.62(16)	C17	C18	C15 ¹	59.4(4)
C6b	C7b	1.401(3)	C8b	C7b	C6b	124.06(17)	C18 ¹	C15	O2	125.8(5)
C7b	C8b	1.488(3)	C13b	C8b	C7b	124.20(17)	C16	C15	O2	120.5(7)
C8b	C13b	1.410(3)	C9b	C8b	C7b	117.80(17)	C16	C15	C18 ¹	113.4(8)
C8b	C9b	1.399(3)	C9b	C8b	C13b	117.99(17)	C17 ¹	C15	O2	69.7(6)
C13b	C12b	1.395(3)	C8b	C13b	O1b	117.05(16)	C17 ¹	C15	C18 ¹	56.3(5)
C12b	C11b	1.388(3)	C12b	C13b	O1b	123.10(17)	C17 ¹	C15	C16	169.6(10)
C11b	C10b	1.387(3)	C12b	C13b	C8b	119.84(18)	C18	C17	O2 ¹	117.4(5)
C10b	C9b	1.384(3)	C11b	C12b	C13b	120.62(18)	C15 ¹	C17	O2 ¹	53.3(5)
C2	C3	1.470(3)	C10b	C11b	C12b	120.29(18)	C15 ¹	C17	C18	64.3(6)
C3	C4	1.399(3)								
C4	C5	1.384(3)								
C5	C6	1.383(3)								
C6	C7	1.405(3)								
C7	C8	1.487(3)								
C8	C13	1.412(3)								
C8	C9	1.394(3)								
C13	C12	1.393(3)								
C12	C11	1.391(3)								
C11	C10	1.384(3)								
C10	C9	1.386(3)								
C18	C15 ¹	1.447(9)								
C18	C17	1.336(10)								
C16	C15	1.221(7)								
C15	C17 ¹	1.382(7)								

Table 7.44 Anisotropic displacement parameters ($\text{\AA}^2 \times 10^3$) for HmphpyTSC · ½ Et₂O. The anisotropic displacement factor exponent takes the form: $-2\pi^2[h^2a^*U_{11}+2hka^*b^*U_{12}+\dots]$.

Atom	U ₁₁	U ₂₂	U ₃₃	U ₁₂	U ₁₃	U ₂₃
S1b	14.3(2)	28.6(3)	18.8(2)	-1.51(16)	2.97(17)	-1.06(17)
S1	14.5(2)	35.1(3)	16.9(2)	1.85(17)	1.30(17)	-1.66(18)
O1b	23.4(7)	28.1(7)	17.9(7)	-1.5(6)	1.1(5)	-0.7(5)
O1	28.0(7)	25.3(7)	25.0(7)	-2.2(6)	1.4(6)	-9.9(6)
N1b	15.0(7)	21.1(7)	16.5(7)	0.5(6)	2.2(6)	0.7(6)
N2b	14.8(7)	25.9(8)	18.3(8)	-2.1(6)	1.7(6)	-0.4(6)
N3b	14.0(7)	28.2(8)	15.3(8)	-2.2(6)	2.3(6)	-2.5(6)
O2	51.2(18)	78(2)	37.8(16)	-23.1(17)	-0.2(14)	-4.0(15)
N4b	15.9(8)	36.5(10)	19.5(8)	-4.0(7)	5.7(7)	-5.2(7)
N1	18.5(7)	17.5(7)	19.9(8)	-2.4(6)	4.6(6)	-2.4(6)
N2	15.8(7)	22.8(8)	20.1(8)	0.4(6)	1.2(6)	0.5(6)
N3	14.4(7)	26.4(8)	16.2(8)	-0.1(6)	1.6(6)	-3.4(6)
N4	14.2(8)	40.0(10)	18.2(8)	3.1(7)	1.8(6)	-4.1(7)
C1b	16.5(8)	21.3(9)	17.5(9)	2.9(7)	3.1(7)	2.1(7)
C2b	14.5(8)	26.3(9)	19.1(9)	-2.4(7)	2.4(7)	0.9(7)
C3b	16.0(8)	19.6(8)	18.1(9)	0.4(7)	2.4(7)	2.4(7)
C4b	16.4(8)	22.4(9)	21.5(9)	-1.5(7)	3.3(7)	2.8(7)
C5b	21.2(9)	22.9(9)	20.3(9)	1.5(7)	7.6(7)	3.2(7)
C6b	22.3(9)	21.6(9)	17.6(9)	1.1(7)	4.4(7)	-0.6(7)
C7b	17.3(8)	17.7(8)	18.8(9)	1.5(7)	2.5(7)	1.4(7)
C8b	17.3(8)	18.6(9)	20.6(9)	1.8(7)	2.1(7)	-2.4(7)
C13b	20.6(9)	17.2(8)	20.0(9)	3.0(7)	2.2(7)	-2.0(7)
C12b	20.6(9)	20.8(9)	23.9(10)	1.8(7)	-1.5(7)	-4.8(7)
C11b	16.8(9)	21.7(9)	32.2(11)	-1.3(7)	2.1(8)	-5.2(8)
C10b	20.4(9)	25.2(10)	27.1(10)	-1.5(8)	5.1(8)	0.3(8)
C9b	18.5(9)	24.5(9)	20.8(9)	0.7(7)	2.8(7)	-0.4(7)
C1	17.6(8)	21.5(9)	17.9(9)	-1.6(7)	3.4(7)	0.0(7)
C2	17.3(9)	20.2(9)	22.5(9)	1.0(7)	2.4(7)	0.6(7)
C3	18.9(9)	16.1(8)	22.6(9)	-0.8(7)	4.8(7)	-1.0(7)
C4	19.9(9)	19.0(9)	28.8(10)	1.7(7)	5.2(8)	-1.6(8)
C5	23.6(10)	20.0(9)	32.0(11)	1.3(7)	11.2(8)	-5.2(8)
C6	25.1(10)	20.6(9)	24.3(10)	-1.4(7)	7.8(8)	-6.1(7)
C7	21.7(9)	17.1(8)	21.8(9)	-3.1(7)	6.2(7)	-2.8(7)
C8	20.7(9)	23.6(9)	18.4(9)	-4.4(7)	6.8(7)	-1.8(7)
C13	23.7(9)	25.8(10)	20.2(9)	-4.6(8)	6.1(7)	-2.7(8)
C12	23.9(10)	35.5(11)	24.8(10)	-6.7(8)	2.3(8)	-4.8(9)
C11	19.5(9)	41.4(12)	31.7(11)	-1.6(8)	2.5(8)	-1.6(9)
C10	22.0(10)	31.9(11)	32.7(11)	1.8(8)	8.6(8)	-3.2(9)
C9	21.2(9)	27.2(10)	23.7(10)	-3.3(8)	7.1(8)	-3.8(8)
C14	38.0(12)	28.7(11)	30.0(11)	-5.1(9)	-1.4(9)	-10.6(9)
C18	101(3)	72(3)	102(4)	-28(3)	31(3)	0(3)
C16	106(3)	80(3)	49(2)	-22(2)	-16(2)	6.7(18)
C14b	30.3(10)	35.4(11)	18.4(10)	-0.7(9)	-2.3(8)	0.1(8)
C15	140(5)	177(7)	68(3)	-80(5)	2(4)	22(4)
C17	180(7)	148(6)	72(3)	-87(5)	-26(4)	26(4)

7.11.12. H₂hphfpyTSCmB

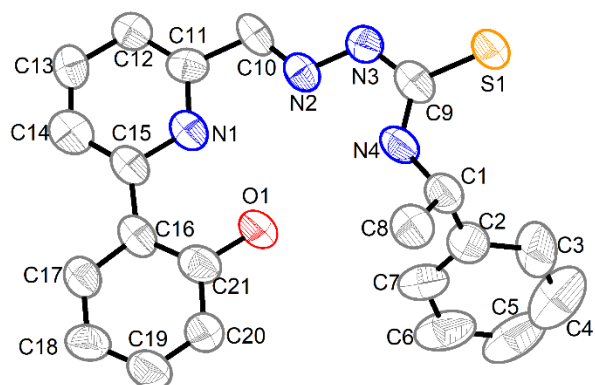


Figure 7.456 Molecular structure of H₂hphfpyTSCmB. Atoms are shown with 50 % probability. Hydrogen atoms are omitted for clarity.

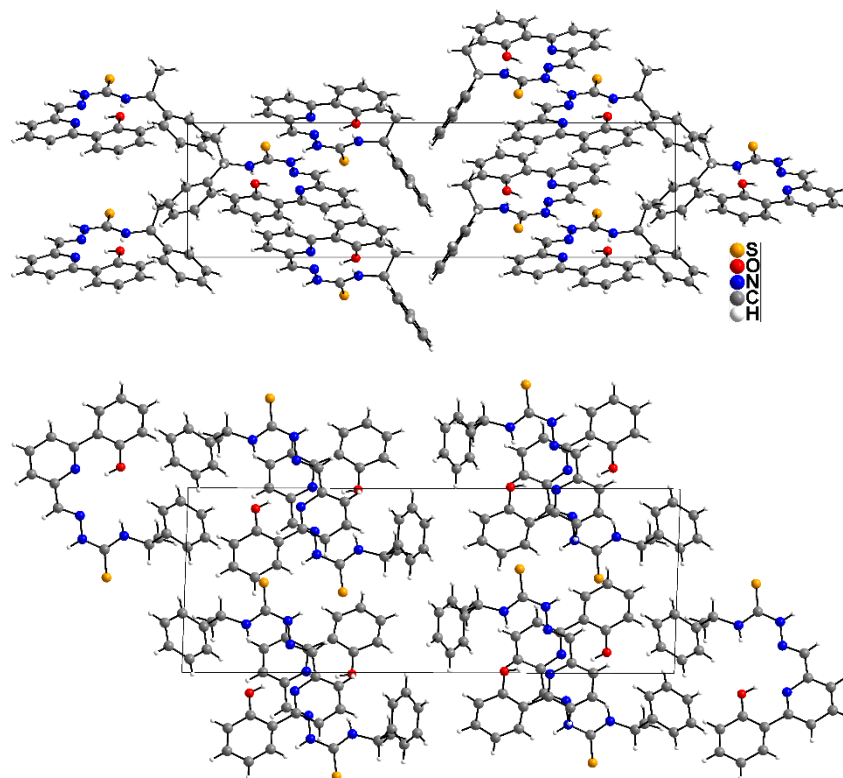


Figure 7.457 Crystal structure of H₂hphfpyTSCmB along the crystallographic a-axis (upper) and b-axis (lower).

Table 7.45 Crystal data and structure refinement for H₂hphfpyTSCmB.

Identification code	H ₂ hphfpyTSCmB
Empirical formula	C ₂₁ H ₂₀ N ₄ OS (376.49 g/mol)
Temperature/K	100
Crystal system /Space group	Monoclinic / P2 ₁
a/Å	9.970(8)
b/Å	7.3255(7)
c/Å	26.683(3)
β/°	91.814(6)
Volume / Z	1947.8(16) Å ³ / 4
ρ _{calc}	1.2837 g/cm ³

μ	1.616 mm ⁻¹
F(000)	795.5
Crystal size/mm ³	0.03 × 0.03 × 0.005
Radiation	Cu K α (λ = 1.54178)
2 Θ range for data collection/°	6.62 to 146.66
Index ranges	-12 ≤ h ≤ 12, -9 ≤ k ≤ 8, -32 ≤ l ≤ 32
Reflections collected	57157
Independent reflections	7558 [R _{int} = 0.2721, R _{sigma} = 0.1492]
Data/restraints/parameters	7558/1/492
Goodness-of-fit on F ²	1.131
Final R indexes [I _o ≥ 2 σ I _o]	R ₁ = 0.1057, wR ₂ = 0.2420
Final R indexes [all data]	R ₁ = 0.1889, wR ₂ = 0.3196
Largest diff. peak/hole / e Å ⁻³	1.02/-0.57
Flack parameter	0.24(7)

Table 7.46 Atomic coordinates ($\times 10^4$) and equivalent isotropic displacement parameters ($\text{\AA}^2 \times 10^3$) for H₂hphfpyTSCmB. U(eq) is defined as one third of the trace of the orthogonalized U_{ij} tensor.

Atom	x	y	z	U(eq)	Atom	x	y	z	U(eq)
S1b	5133(2)	8251(3)	1599.1(10)	63.7(8)	C15b	12211(10)	4199(12)	2346(4)	51(2)
S1	15637(3)	7156(4)	3212.2(11)	70.4(9)	C14	8113(10)	11870(13)	2089(5)	62(3)
O1b	11122(6)	5464(10)	1384(3)	66(2)	C12	9995(9)	10752(13)	1646(4)	53(2)
N1	9944(8)	10420(11)	2525(3)	56(2)	C9	14115(9)	8099(13)	3130(4)	58(3)
N3b	7206(7)	7071(12)	2116(3)	56(2)	C12b	10732(11)	4807(15)	3190(4)	64(3)
N1b	11012(7)	4987(10)	2304(3)	48(2)	C11	10547(9)	10241(13)	2092(4)	53(2)
N4b	7392(8)	6782(11)	1271(3)	53(2)	C13	8711(10)	11610(12)	1649(4)	56(3)
C17	6978(10)	12403(14)	3119(5)	64(3)	C7b	8759(9)	4776(14)	489(4)	59(3)
O1	10084(7)	9932(11)	3452(3)	76(2)	C21	8873(11)	10820(16)	3469(5)	68(3)
N2b	8487(7)	6313(11)	2179(3)	57(2)	C8	13361(11)	10386(16)	4274(5)	74(3)
N4	13336(8)	8624(13)	3504(3)	70(3)	C8b	7261(11)	8878(15)	572(4)	67(3)
C15	8719(9)	11301(13)	2539(4)	51(2)	C13b	11991(10)	4001(16)	3246(4)	65(3)
C10b	8901(9)	6106(13)	2630(4)	52(2)	C18b	14842(10)	2969(18)	1417(4)	75(4)
C21b	12330(9)	4590(13)	1421(4)	52(2)	C1	13689(11)	8587(16)	4034(4)	67(3)
C11b	10228(9)	5285(13)	2717(4)	50(2)	C2	13062(12)	7019(17)	4302(4)	73(3)
C9b	6649(9)	7290(14)	1657(4)	49(2)	C5b	8576(10)	3196(15)	-289(4)	64(3)
C1b	6933(9)	6987(14)	752(4)	57(2)	C19	7174(12)	11992(18)	4000(5)	84(4)
C16b	12906(9)	3991(15)	1873(4)	56(3)	C6b	9276(10)	3529(15)	145(4)	64(3)
C20b	13029(10)	4355(14)	969(4)	58(3)	C19b	14266(9)	3575(14)	973(4)	58(3)
C10	11900(9)	9359(12)	2148(5)	51(3)	C4	13280(30)	4390(20)	4822(7)	128(7)
C14b	12750(9)	3696(16)	2815(4)	66(3)	C2b	7521(9)	5580(13)	412(4)	50(2)
N2	12343(8)	9111(11)	2599(4)	52(2)	C7	11688(13)	6870(18)	4305(4)	80(4)
C17b	14162(9)	3143(16)	1858(4)	66(3)	C3b	6800(11)	5203(15)	-33(4)	67(3)
N3	13599(7)	8307(11)	2658(3)	54.3(19)	C3	13894(16)	5797(17)	4563(5)	96(5)
C18	6482(12)	12656(17)	3586(5)	79(4)	C6	11075(19)	5432(19)	4565(5)	110(5)
C20	8343(12)	11109(17)	3952(5)	76(4)	C4b	7314(11)	3991(17)	-380(5)	75(3)
C16	8170(9)	11465(12)	3042(5)	58(3)	C5	11910(30)	4150(20)	4828(6)	127(7)

Table 7.47. Bond lengths [\AA] and angles [deg] for H₂hphfpyTSCmB.

Atom	Atom	Length/ \AA	Atom	Atom	Atom	Angle/°	Atom	Atom	Atom	Angle/°
S1b	C9b	1.670(10)	C11	N1	C15	119.6(9)	C14b	C15b	N1b	120.7(9)
S1	C9	1.675(10)	C9b	N3b	N2b	120.6(7)	C14b	C15b	C16b	124.4(9)
O1b	C21b	1.364(11)	C15b	N1b	C11b	122.0(9)	C13	C14	C15	121.2(10)

N1	C15	1.384(12)	C1b	N4b	C9b	122.6(8)	C13	C12	C11	117.3(10)
N1	C11	1.327(12)	C16	C17	C18	122.5(12)	N4	C9	S1	124.4(9)
N3b	N2b	1.399(10)	C10b	N2b	N3b	115.4(8)	N3	C9	S1	119.0(7)
N3b	C9b	1.338(12)	C1	N4	C9	126.4(9)	N3	C9	N4	116.6(8)
N1b	C11b	1.388(11)	C16	C15	N1	114.7(10)	C13b	C12b	C11b	120.3(9)
N1b	C15b	1.329(11)	C14	C15	N1	118.4(9)	C10	C11	N1	112.8(9)
N4b	C9b	1.339(11)	C14	C15	C16	126.9(9)	C12	C11	N1	124.0(9)
N4b	C1b	1.453(12)	C11b	C10b	N2b	117.6(8)	C12	C11	C10	123.2(9)
C17	C18	1.368(16)	C16b	C21b	O1b	123.3(9)	C12	C13	C14	119.4(11)
C17	C16	1.394(13)	C20b	C21b	O1b	116.9(9)	C2b	C7b	C6b	121.8(10)
O1	C21	1.374(13)	C20b	C21b	C16b	119.8(9)	C20	C21	O1	116.9(11)
N2b	C10b	1.270(11)	C10b	C11b	N1b	118.0(9)	C16	C21	O1	123.4(9)
N4	C9	1.340(12)	C12b	C11b	N1b	119.0(9)	C16	C21	C20	119.7(10)
N4	C1	1.446(14)	C12b	C11b	C10b	123.0(8)	C12b	C13b	C14b	118.9(10)
C15	C16	1.469(15)	N3b	C9b	S1b	118.8(7)	C19b	C18b	C17b	120.0(10)
C15	C14	1.392(14)	N4b	C9b	S1b	124.6(8)	C8	C1	N4	110.5(9)
C10b	C11b	1.464(13)	N4b	C9b	N3b	116.5(8)	C2	C1	N4	112.8(10)
C21b	C16b	1.392(14)	C8b	C1b	N4b	109.5(9)	C2	C1	C8	111.6(9)
C21b	C20b	1.422(13)	C2b	C1b	N4b	112.8(8)	C7	C2	C1	119.6(11)
C11b	C12b	1.391(14)	C2b	C1b	C8b	110.2(8)	C3	C2	C1	118.7(12)
C1b	C8b	1.505(14)	C17b	C16b	C21b	117.4(9)	C3	C2	C7	121.6(13)
C1b	C2b	1.505(13)	C15b	C16b	C21b	121.3(9)	C4b	C5b	C6b	120.6(10)
C16b	C17b	1.399(13)	C15b	C16b	C17b	121.2(9)	C20	C19	C18	120.5(12)
C16b	C15b	1.467(13)	C19b	C20b	C21b	120.8(10)	C5b	C6b	C7b	119.1(10)
C20b	C19b	1.359(13)	C11	C10	N2	115.9(9)	C18b	C19b	C20b	119.9(9)
C10	N2	1.283(13)	C13b	C14b	C15b	119.2(9)	C5	C4	C3	123.7(18)
C10	C11	1.499(13)	N3	N2	C10	116.7(8)	C7b	C2b	C1b	124.6(10)
C14b	C15b	1.396(14)	C18b	C17b	C16b	121.9(10)	C3b	C2b	C1b	116.7(8)
C14b	C13b	1.415(14)	C9	N3	N2	118.0(8)	C3b	C2b	C7b	118.5(9)
N2	N3	1.388(10)	C19	C18	C17	119.9(11)	C6	C7	C2	120.6(14)
C17b	C18b	1.383(14)	C19	C20	C21	120.5(12)	C4b	C3b	C2b	120.1(10)
N3	C9	1.352(13)	C15	C16	C17	121.3(10)	C4	C3	C2	117.2(16)
C18	C19	1.373(17)	C21	C16	C17	116.9(10)	C5	C6	C7	118.7(17)
C20	C21	1.423(16)	C21	C16	C15	121.6(9)	C3b	C4b	C5b	119.9(11)
C20	C19	1.343(15)	C16b	C15b	N1b	114.9(9)	C6	C5	C4	118.1(17)
C16	C21	1.401(16)								
C14	C13	1.347(15)								
C12	C11	1.349(14)								
C12	C13	1.426(13)								
C12b	C13b	1.391(14)								
C7b	C6b	1.404(14)								
C7b	C2b	1.377(13)								
C8	C1	1.505(16)								
C18b	C19b	1.373(15)								
C1	C2	1.499(17)								
C2	C7	1.375(17)								
C2	C3	1.393(17)								
C5b	C6b	1.355(14)								
C5b	C4b	1.400(15)								
C4	C3	1.39(2)								
C4	C5	1.38(3)								
C2b	C3b	1.396(15)								
C7	C6	1.411(18)								
C3b	C4b	1.392(15)								
C6	C5	1.42(2)								

Table 7.48 Anisotropic displacement parameters ($\text{\AA}^2 \times 10^3$) for $\text{H}_2\text{hphfpyTSCmB}$. The anisotropic displacement factor exponent takes the form: $-2\pi^2[h^2a^*U_{11}+2hka^*b^*U_{12}+\dots]$.

Atom	U_{11}	U_{22}	U_{33}	U_{12}	U_{13}	U_{23}
S1b	51.8(13)	63.9(19)	76.4(17)	15.9(13)	15.5(11)	1.1(15)
S1	60.5(15)	72(2)	78.9(19)	19.0(15)	12.9(13)	3.6(16)
O1b	50(4)	70(5)	79(5)	15(4)	13(3)	12(4)
N1	49(4)	42(5)	78(6)	-2(4)	7(4)	-3(4)
N3b	47(4)	67(6)	55(5)	11(4)	15(3)	0(4)
N1b	35(4)	29(4)	81(6)	7(3)	8(4)	0(4)
N4b	55(4)	41(5)	62(5)	-4(4)	11(4)	0(4)
C17	58(6)	43(6)	93(8)	4(5)	13(5)	17(6)
O1	63(4)	84(6)	82(5)	23(4)	19(4)	7(5)
N2b	48(4)	39(5)	85(6)	6(3)	27(4)	-1(4)
N4	55(4)	91(8)	65(5)	21(5)	11(4)	-12(5)
C15	46(5)	23(5)	84(7)	-7(4)	11(5)	-4(5)
C10b	63(5)	39(6)	55(5)	-4(4)	28(4)	-5(4)
C21b	45(5)	32(6)	80(7)	4(4)	10(5)	9(5)
C11b	51(5)	39(6)	61(6)	3(4)	15(4)	-5(5)
C9b	48(5)	50(6)	49(5)	-3(5)	4(4)	0(5)
C1b	54(5)	50(6)	67(6)	-5(5)	17(4)	4(5)
C16b	52(5)	56(7)	62(6)	-8(5)	1(4)	3(5)
C20b	55(6)	54(7)	65(6)	13(5)	4(5)	-2(5)
C10	33(5)	29(5)	92(9)	-4(4)	5(5)	-12(5)
C14b	54(5)	67(8)	76(7)	17(5)	9(5)	-1(6)
N2	37(4)	45(5)	73(6)	-7(4)	3(4)	-4(4)
C17b	53(5)	62(7)	82(7)	21(5)	7(5)	7(6)
N3	60(4)	36(5)	67(5)	3(4)	11(4)	4(4)
C18	78(7)	78(10)	84(8)	6(7)	32(7)	15(7)
C20	71(7)	81(9)	76(8)	17(6)	14(6)	15(7)
C16	49(5)	24(5)	101(8)	-4(4)	15(5)	6(5)
C15b	69(5)	25(5)	60(6)	-1(4)	12(4)	-3(4)
C14	53(5)	28(6)	105(8)	-31(4)	11(6)	2(6)
C12	54(5)	35(6)	69(7)	-14(4)	9(5)	0(5)
C9	51(5)	27(5)	97(8)	-6(4)	12(5)	-4(5)
C12b	66(7)	65(8)	61(7)	-12(6)	13(5)	-4(6)
C11	58(5)	38(6)	64(6)	-15(4)	16(4)	0(5)
C13	57(6)	26(5)	83(8)	-1(4)	-3(5)	1(5)
C7b	52(5)	47(6)	80(7)	-3(4)	12(5)	-3(5)
C21	68(7)	54(7)	83(8)	3(5)	22(6)	2(6)
C8	70(7)	63(8)	89(8)	-6(6)	6(6)	1(7)
C8b	72(7)	58(7)	72(7)	2(5)	21(5)	8(6)
C13b	57(6)	77(9)	61(7)	3(6)	7(5)	2(6)
C18b	55(6)	97(10)	73(7)	-13(6)	10(5)	-1(7)
C1	61(6)	66(8)	74(8)	11(6)	7(5)	-3(6)
C2	92(8)	65(8)	63(6)	21(7)	7(6)	-16(6)
C5b	63(6)	55(7)	76(7)	3(5)	16(5)	-9(6)
C19	84(8)	76(9)	94(9)	22(7)	33(7)	9(8)
C6b	60(6)	57(7)	74(7)	11(5)	6(5)	-8(6)
C19b	60(5)	51(7)	65(6)	-4(5)	21(5)	-3(5)
C4	230(20)	59(11)	90(12)	1(14)	-24(14)	-7(9)
C2b	45(5)	39(5)	66(6)	5(4)	16(4)	4(5)

C7	98(9)	81(10)	62(7)	-10(7)	25(6)	1(7)
C3b	72(6)	51(7)	78(8)	22(5)	6(6)	-2(6)
C3	126(12)	53(9)	107(10)	44(8)	-10(9)	-17(8)
C6	184(16)	74(11)	75(8)	6(11)	50(9)	-7(8)
C4b	62(7)	77(9)	85(8)	2(6)	11(6)	-7(7)
C5	250(20)	71(12)	58(8)	1(15)	17(12)	-2(8)

7.11.13. [Ni(apyTSCmB)Cl]

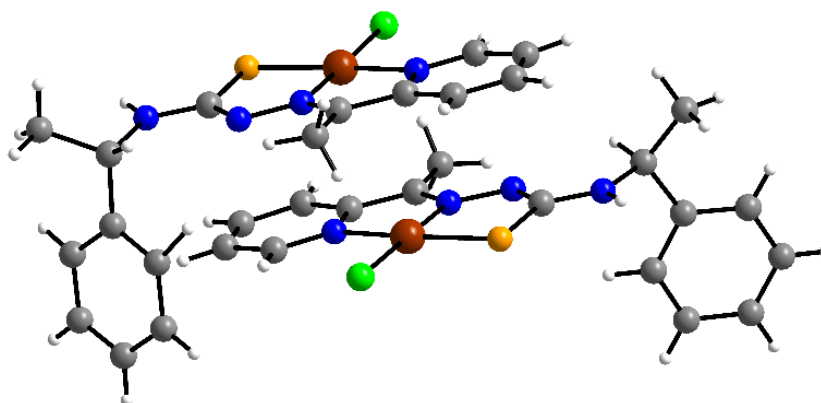


Figure 7.458 Crystal dimeric structure of [Ni(apyTSCmB)Cl] along the crystallographic a-axis (left) and b-axis (right).

Table 7.49 Crystal data and structure refinement for [Ni(apyTSCmB)Cl].

Empirical formula	C ₁₆ H ₁₇ ClN ₄ NiS (391.55 g/mol)
Temperature/K	100.0
Crystal system	Orthorhombic / P2 ₁ 2 ₁ 2 ₁
a/Å	9.8842(11)
b/Å	14.8587(18)
c/Å	22.153(3)
β/°	90.045(6)
Volume / Z	3253.5(7) Å ³ / 8
ρ _{calc} /cm ³	1.5986
μ/mm ⁻¹	1.488
F(000)	1621.4
Radiation	Mo Kα (λ = 0.71073)
2θ range for data collection/°	4.52 to 52.82
Index ranges	-11 ≤ h ≤ 12, -18 ≤ k ≤ 18, -27 ≤ l ≤ 27
Reflections collected	59120
Independent reflections	6687 [R _{int} = 0.4166, R _{sigma} = 0.1949]
Data/restraints/parameters	6687/0/426
Goodness-of-fit on F ²	0.997
Final R indexes [I _o ≥ 2σ _{I_o}]	R ₁ = 0.0957, wR ₂ = 0.1668
Final R indexes [all data]	R ₁ = 0.1535, wR ₂ = 0.1891
Largest diff. peak/hole / e Å ⁻³	3.09/-1.87
Flack parameter	0.02(4)

Table 7.50 Atomic coordinates ($\times 10^4$) and equivalent isotropic displacement parameters ($\text{\AA}^2 \times 10^3$) for $[\text{Ni}(\text{apyTSCmB})\text{Cl}]$. $U(\text{eq})$ is defined as one third of the trace of the orthogonalized U_{ij} tensor.

Atom	<i>x</i>	<i>y</i>	<i>z</i>	<i>U</i> (eq)	Atom	<i>x</i>	<i>y</i>	<i>z</i>	<i>U</i> (eq)
Ni1b	-446.1(14)	5061.6(9)	7112.3(6)	10.4(3)	C11	-386(12)	7511(7)	7061(5)	16(3)
Ni1	-2714.8(14)	6927.1(10)	6501.3(7)	11.6(3)	C12b	-3217(11)	4637(8)	7520(5)	18(3)
S1	-4809(3)	6633.9(19)	6657.2(13)	12.9(6)	C12	17(11)	7305(8)	6041(5)	14(3)
C11	-2884(3)	6688(2)	5540.1(13)	18.6(7)	C1b	2968(10)	5268(7)	5258(5)	12(2)
C11b	-360(3)	5310(2)	8076.6(12)	18.6(7)	C8b	3709(11)	6088(7)	5005(6)	15(3)
N3b	591(9)	4936(7)	5910(4)	15(2)	C6b	5352(12)	3489(9)	4593(5)	22(3)
N4b	2813(9)	5373(6)	5911(4)	13(2)	C5	-4948(14)	3963(9)	9089(6)	28(3)
N2b	-492(9)	4849(6)	6298(4)	13(2)	C1	-5959(10)	6596(7)	8412(5)	9(2)
C9b	1678(11)	5213(7)	6211(5)	13(3)	C7b	4733(13)	4308(8)	4697(5)	20(3)
N4	-5872(9)	6614(6)	7765(4)	13(2)	C7	-6606(11)	4994(8)	8697(5)	18(3)
C9	-4743(10)	6757(7)	7438(5)	10(2)	C16	-1166(11)	7686(9)	8170(5)	18(3)
N1	-834(9)	7277(6)	6504(5)	16(2)	C6	-6238(14)	4127(9)	8901(6)	27(3)
N3	-3636(9)	7024(6)	7728(4)	9(2)	C13b	-4543(13)	4317(8)	7426(5)	21(3)
N2	-2599(9)	7139(6)	7322(4)	13(2)	C2	-5623(12)	5665(7)	8663(5)	13(3)
C11b	-2674(11)	4481(7)	6505(5)	13(2)	C15	919(11)	7833(7)	7150(6)	15(3)
C10b	-1625(11)	4564(7)	6058(5)	11(2)	S1b	1670(3)	5349(2)	6995.8(13)	13.9(7)
C10	-1428(11)	7451(8)	7528(5)	13(3)	C13	1343(13)	7621(9)	6109(6)	21(3)
N1b	-2310(8)	4714(6)	7073(4)	11(2)	C14	1800(12)	7862(7)	6678(6)	16(3)
C14b	-4899(11)	4090(8)	6851(6)	18(3)	C8	-7372(10)	6923(7)	8617(5)	18(3)
C2b	3682(10)	4389(7)	5111(5)	8(2)	C3b	3267(11)	3593(8)	5405(6)	18(3)
C3	-4320(12)	5483(8)	8852(5)	15(3)	C5b	4935(13)	2721(8)	4901(6)	23(3)
C16b	-1844(11)	4369(8)	5417(6)	18(3)	C4b	3895(13)	2778(9)	5313(5)	20(3)
C15b	-3988(10)	4174(7)	6376(5)	12(3)	C4	-3943(14)	4630(10)	9072(6)	29(3)

7.11.14. $[\text{Ni}(\text{apyTSCmB})\text{NCS}]$

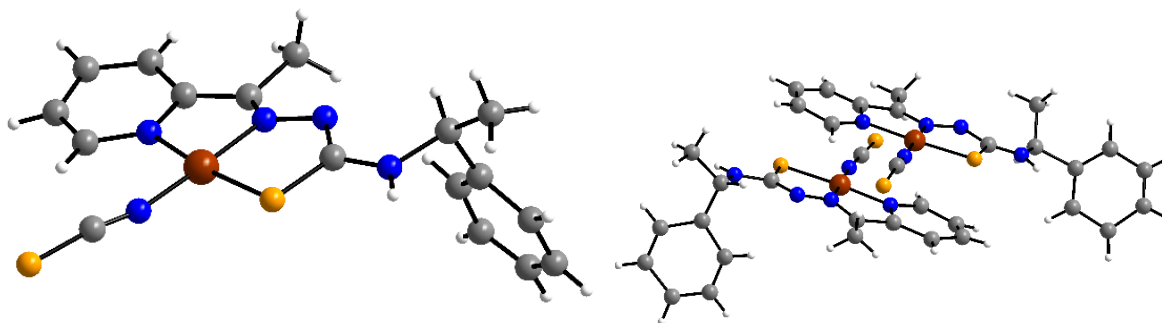


Figure 7.459 Molecular structure of $[\text{Ni}(\text{apyTSCmB})\text{NCS}]$. Atoms are shown with 50 % probability. Hydrogen atoms are omitted for clarity.

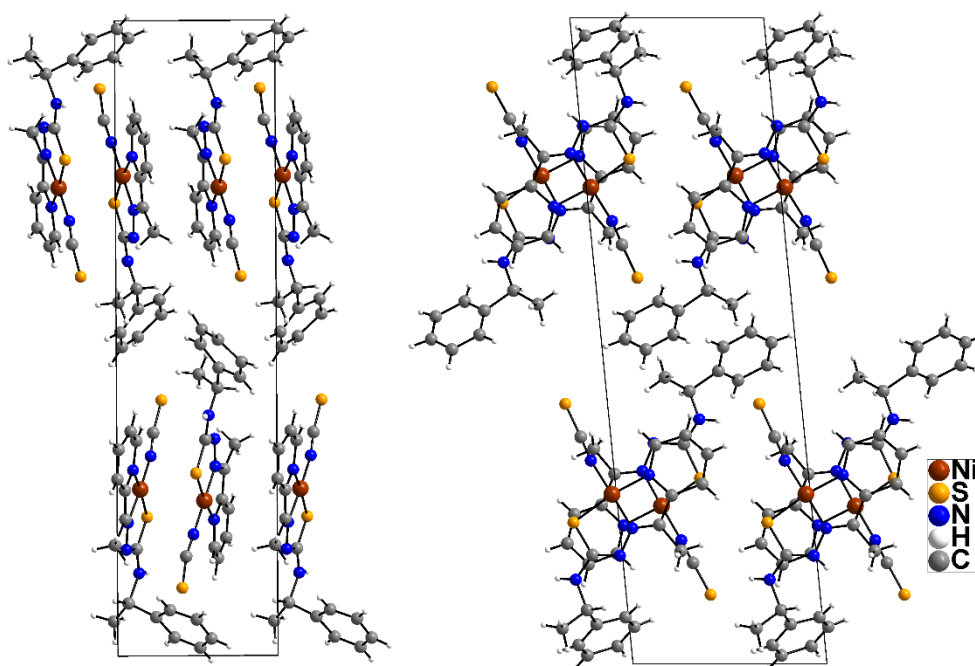


Figure 7.460 Crystal structure of [Ni(apyTSCmB)NCS] along the crystallographic a-axis (left) and b-axis (right).

Table 7.51 Crystal data and structure refinement for [Ni(apyTSCmB)NCS].

Empirical formula	C ₁₇ H ₁₇ N ₅ NiS ₂
Formula weight	414.18
Temperature/K	100 K
Crystal system	monoclinic
Space group	P2 ₁
a/Å	8.6010(17)
b/Å	7.2160(14)
c/Å	28.833(6)
β/°	95.59(3)
Volume / Z	1781.0(6) Å ³ / 4
ρ _{calc}	1.5445 g/cm ³
μ	1.333 mm ⁻¹
F(000)	858.6
Radiation	Synchrotron
2θ range for data collection/°	2.84 to 47.06
Index ranges	-9 ≤ h ≤ 8, -8 ≤ k ≤ 6, -32 ≤ l ≤ 24
Reflections collected	6836
Independent reflections	4251 [R _{int} = 0.0728, R _{sigma} = 0.1185]
Data/restraints/parameters	4251/1/456
Goodness-of-fit on F ²	0.726
Final R indexes [I ≥ 2σ _I]	R ₁ = 0.1100, wR ₂ = 0.2706
Final R indexes [all data]	R ₁ = 0.1329, wR ₂ = 0.2878
Largest diff. peak/hole / e Å ⁻³	1.20/-0.88
Flack parameter	0.26(7)

Table 7.52 Atomic coordinates ($\times 10^4$) and equivalent isotropic displacement parameters ($\text{\AA}^2 \times 10^3$) for [Ni(apyTSCmB)NCS]. U(eq) is defined as one third of the trace of the orthogonalized U_{ij} tensor.

Atom	x	y	z	U(eq)	Atom	x	y	z	U(eq)
Ni1b	2263(3)	453(4)	2441.4(10)	32.6(8)	C6b	8420(30)	2820(30)	4624(8)	46(6)
Ni1	-232(3)	6453(4)	2623.7(11)	41.1(9)	C2b	5880(30)	1390(30)	4533(9)	46(6)
S1	-2359(6)	6867(7)	2186(2)	38.1(15)	C15b	-2270(20)	1950(20)	2313(8)	26(5)
S004	4394(6)	-60(6)	2870(2)	30.7(13)	N4	-2530(30)	6350(40)	1301(7)	71(7)
S2b	4349(8)	-949(11)	1069(2)	60(2)	C16	3040(30)	4850(50)	1746(8)	70(10)
S2	-2177(8)	7799(10)	4024(2)	54.4(19)	C1	-2090(40)	5690(40)	829(8)	72(10)
N1	1769(19)	6008(19)	2924(6)	28(4)	C11	2840(30)	5500(20)	2606(10)	62(8)
N2b	1457(15)	1140(30)	2981(7)	42(6)	C13b	-1790(30)	1280(30)	1539(8)	45(6)
N4b	4648(19)	750(30)	3784(7)	43(5)	C7	-2710(30)	8540(30)	290(9)	53(7)
N1b	215(14)	1045(14)	2141(7)	31(5)	C2	-1680(30)	7410(40)	611(9)	61(8)
N3b	2180(30)	1110(30)	3414(6)	47(6)	C10	2060(30)	5510(30)	2151(7)	46(7)
C12	2250(30)	6226(19)	3388(9)	43(7)	C7b	6850(20)	2710(30)	4391(8)	46(6)
N5	-1150(20)	7110(30)	3145(8)	60(7)	C4b	7750(30)	350(40)	5135(8)	55(7)
C15	4480(20)	5030(20)	2783(9)	36(6)	C5b	8760(30)	1350(40)	4975(9)	58(7)
N5b	3110(20)	-240(20)	1911(6)	43(6)	C16b	-940(30)	2370(40)	3326(10)	63(9)
N2	640(20)	5671(19)	2098(5)	27(4)	C6	-2310(30)	10150(50)	129(10)	78(11)
C17b	3600(20)	-700(20)	1563(8)	28(5)	C17	-1550(30)	7280(40)	3512(11)	63(9)
C4	250(30)	9940(40)	572(8)	53(7)	C11b	-820(20)	1560(40)	2460(8)	49(7)
C13	3860(30)	5870(30)	3536(11)	63(9)	C8	-1540(30)	6210(30)	1684(7)	49(8)
C10b	10(20)	1702(19)	2938(8)	31(6)	C5	-710(50)	10850(50)	272(9)	103(14)
C8b	3730(30)	540(50)	3402(9)	78(10)	C9b	3090(30)	150(30)	4433(7)	50(7)
N3	-134(19)	5560(30)	1673(6)	39(5)	C9	-3460(30)	4770(30)	546(7)	44(7)
C14b	-2780(40)	1810(60)	1862(10)	96(13)	C3	-150(30)	8270(40)	721(10)	66(8)
C14	4895(18)	5122(18)	3250(8)	21(5)	C3b	6250(30)	260(40)	4906(7)	54(7)
C12b	-270(30)	1070(20)	1706(8)	32(6)	C1b	4280(30)	1300(50)	4221(8)	68(10)

7.11.15. [Pd(apyTSCmB)Cl]

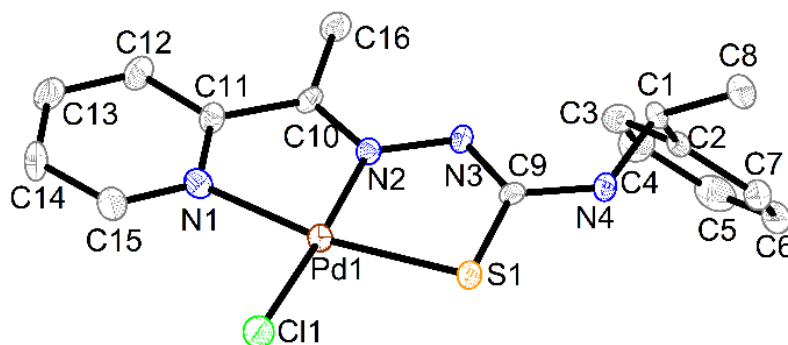


Figure 7.461 Molecular structure of [Pd(apyTSCmB)Cl]. Atoms are shown with 50% probability. Hydrogen atoms are omitted for clarity.

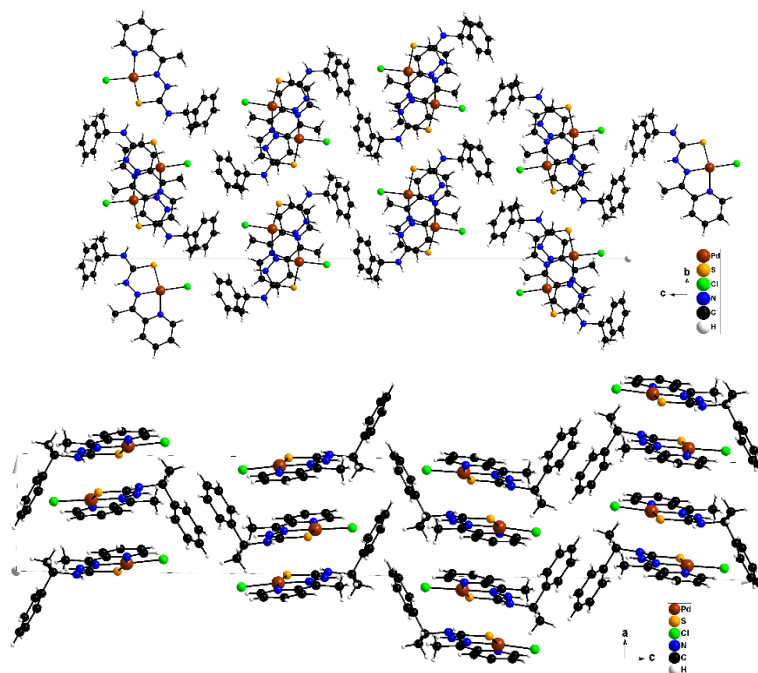


Figure 7.467 Crystal structure of [Pd(apyTSCmB)Cl] along the crystallographic a-axis (upper) and b-axis (lower).

Table 7.53 Crystal data and structure refinement for [Pd(apyTSCmB)Cl].

Empirical formula	C ₁₆ H ₁₈ ClN ₄ PdS (440.28 g/mol)
Temperature	100 K
Crystal system / Space group	Orthorhombic / P2 ₁ 2 ₁ 2 ₁
Unit cell parameters	a = 7.2260(14) Å, b = 10.272(2) Å, c = 45.882(9) Å
Volume / Z	3405.6(12) Å ³ / 8
ρ _{calc}	1.7173 g/cm ³
μ	1.373 mm ⁻¹
F(000)	1754.7
Radiation	Mo Kα (λ = 0.71073 Å)
2θ range for data collection/°	3.56 to 71.32
Index ranges	-11 ≤ h ≤ 11, -16 ≤ k ≤ 16, -74 ≤ l ≤ 73
Reflections collected	46718
Independent reflections	13084 [R _{int} = 0.0437, R _{sigma} = 0.0475]
Data/restraints/parameters	13084/0/420
Goodness-of-fit on F ²	1.048
Final R indices [I _o ≥ 2σ(I _o)]	R ₁ = 0.0554, wR ₂ = 0.1330
Final R indexes [all data]	R ₁ = 0.0622, wR ₂ = 0.1357
Largest diff. peak/hole / e Å ⁻³	1.67/-3.05
Flack parameter	6.786(7)

Table 7.54 Atomic coordinates (x 10⁴) and equivalent isotropic displacement parameters (Å² x 10³) for [Pd(apyTSCmB)Cl]. U(eq) is defined as one third of the trace of the orthogonalized U_{ij} tensor.

Atom	x	y	z	U(eq)	Atom	x	y	z	U(eq)
Pd1b	-6141.7(5)	-4766.4(3)	-5993.34(7)	16.04(8)	C14b	-4778(8)	-8851(5)	-5852.6(13)	23.1(10)
Pd1	-756.7(5)	-7421.5(3)	-6481.38(7)	15.20(7)	C16b	-6099(9)	-6517(5)	-6836.4(11)	23.9(10)
S1b	-6780.3(17)	-2662.1(12)	-6090.2(2)	17.4(2)	C10	-927(6)	-5914(4)	-5972.4(10)	15.7(7)
Cl1	-1144.1(19)	-7754.3(12)	-6974.4(2)	22.9(2)	C16	-977(8)	-5526(5)	-5659.8(10)	20.9(9)
Cl1b	-5965(2)	-4534.4(12)	-5493.5(2)	24.9(2)	C13	-1989(7)	-2847(5)	-6394.4(12)	22.6(10)
S1	-68.2(17)	-9491.6(11)	-6360.5(2)	16.2(2)	C14	-1989(8)	-3372(5)	-6675.0(13)	23.1(10)
N2b	-6310(6)	-5005(4)	-6415.9(8)	16.4(7)	C13b	-4863(8)	-9318(5)	-6132.4(13)	23.1(10)
C9	-19(6)	-9197(4)	-5983.1(10)	13.4(7)	C1	60(7)	-10292(5)	-5493.8(10)	17.8(8)
N3b	-6692(6)	-4010(4)	-6606.7(9)	18.2(8)	C1b	-7571(7)	-1909(5)	-6949.7(10)	17.2(8)

N4b	-7258(6)	-1835(4)	-6632.3(9)	17.7(7)		C7	3159(8)	-10998(6)	-5281.3(12)	24.8(10)
N3	-255(6)	-8053(4)	-5858.2(9)	16.3(7)		C3	2281(8)	-8738(5)	-5259.4(11)	22.9(10)
C9b	-6938(8)	-2860(5)	-6468.8(12)	23.8(10)		C2	1877(8)	-10017(5)	-5342.4(10)	19.6(9)
N1	-1319(6)	-5475(4)	-6484.5(9)	17.0(7)		C8	-792(9)	-11593(5)	-5412.5(12)	25.6(10)
C10b	-6017(7)	-6194(4)	-6521.8(10)	17.9(8)		C2b	-5767(7)	-1980(5)	-7116.7(9)	17.6(8)
N1b	-5522(6)	-6712(4)	-6017.0(9)	17.4(7)		C8b	-8684(8)	-722(6)	-7041.1(11)	24.2(10)
C11	-1309(7)	-4971(4)	-6208.0(10)	16.4(8)		C6b	-2967(8)	-961(6)	-7295.7(12)	24.8(10)
N2	-603(6)	-7092(3)	-6062.6(8)	13.8(7)		C7b	-4549(7)	-928(5)	-7128.3(11)	19.3(9)
C11b	-5584(7)	-7153(5)	-6297.3(11)	17.2(8)		C3b	-5323(8)	-3094(5)	-7275.9(12)	25.1(10)
N4	230(6)	-10261(4)	-5815.1(8)	18.1(7)		C4	3932(10)	-8448(6)	-5116.2(11)	30.2(12)
C12b	-5234(7)	-8451(5)	-6359.6(12)	20.6(9)		C6	4787(9)	-10700(6)	-5134.2(12)	28.4(12)
C15	-1650(7)	-4683(5)	-6709.2(11)	21.4(9)		C5	5202(9)	-9429(7)	-5055.4(12)	31.3(13)
C12	-1645(8)	-3666(5)	-6161.2(12)	21.5(9)		C4b	-3697(10)	-3145(7)	-7441.1(12)	33.2(13)
C15b	-5133(7)	-7535(5)	-5801.6(11)	21.8(9)		C5b	-2535(8)	-2084(7)	-7451.8(11)	30.4(12)

Table 7.55 Bond lengths [\AA] and angles [deg] for $[\text{Pd}(\text{apyTSCmB})\text{Cl}]$.

Atom	Atom	Length/ \AA	Atom	Atom	Atom	Angle/ $^\circ$	Atom	Atom	Atom	Angle/ $^\circ$
Pd1b	S1b	2.2551(14)	C11b	Pd1b	S1b	96.26(5)	C10	N2	Pd1	117.7(3)
Pd1b	Cl1b	2.3067(14)	N2b	Pd1b	S1b	85.01(13)	C10	N2	N3	118.5(4)
Pd1b	N2b	1.957(4)	N2b	Pd1b	Cl1b	178.54(13)	N1b	C11b	C10b	116.8(4)
Pd1b	N1b	2.055(4)	N1b	Pd1b	S1b	165.65(12)	C12b	C11b	C10b	123.1(5)
Pd1	Cl1	2.3039(13)	N1b	Pd1b	Cl1b	97.99(13)	C12b	C11b	N1b	120.1(5)
Pd1	S1	2.2520(13)	N1b	Pd1b	N2b	80.76(17)	C1	N4	C9	125.6(4)
Pd1	N1	2.045(4)	S1	Pd1	Cl1	97.43(5)	C13b	C12b	C11b	119.9(5)
Pd1	N2	1.952(4)	N1	Pd1	Cl1	96.66(13)	C14	C15	N1	122.3(5)
S1b	C9b	1.749(6)	N1	Pd1	S1	165.90(12)	C13	C12	C11	120.0(5)
S1	C9	1.760(5)	N2	Pd1	Cl1	176.06(13)	C14b	C15b	N1b	121.8(5)
N2b	N3b	1.374(6)	N2	Pd1	S1	84.83(12)	C13b	C14b	C15b	119.0(5)
N2b	C10b	1.323(6)	N2	Pd1	N1	81.07(17)	N2	C10	C11	114.8(4)
C9	N3	1.328(6)	C9b	S1b	Pd1b	95.49(19)	C16	C10	C11	121.3(4)
C9	N4	1.348(6)	C9	S1	Pd1	94.98(16)	C16	C10	N2	123.9(4)
N3b	C9b	1.349(7)	N3b	N2b	Pd1b	123.2(3)	C14	C13	C12	118.2(5)
N4b	C9b	1.322(7)	C10b	N2b	Pd1b	118.0(3)	C13	C14	C15	119.3(5)
N4b	C1b	1.472(6)	C10b	N2b	N3b	118.8(4)	C14b	C13b	C12b	119.0(6)
N3	N2	1.383(6)	N3	C9	S1	125.1(4)	C2	C1	N4	112.5(4)
N1	C11	1.368(6)	N4	C9	S1	115.6(3)	C8	C1	N4	107.2(4)
N1	C15	1.340(7)	N4	C9	N3	119.3(4)	C8	C1	C2	114.0(4)
C10b	C11b	1.458(7)	C9b	N3b	N2b	112.4(4)	C2b	C1b	N4b	112.1(4)
C10b	C16b	1.494(7)	C1b	N4b	C9b	123.0(4)	C8b	C1b	N4b	108.2(4)
N1b	C11b	1.368(6)	N2	N3	C9	111.3(4)	C8b	C1b	C2b	111.0(4)
N1b	C15b	1.327(7)	N3b	C9b	S1b	123.9(4)	C6	C7	C2	120.0(6)
C11	C12	1.366(8)	N4b	C9b	S1b	118.7(4)	C4	C3	C2	120.0(6)
C11	C10	1.482(7)	N4b	C9b	N3b	117.3(5)	C7	C2	C1	122.4(5)
N2	C10	1.297(6)	C11	N1	Pd1	111.7(3)	C3	C2	C1	118.7(5)
C11b	C12b	1.378(8)	C15	N1	Pd1	129.2(4)	C3	C2	C7	118.9(5)
N4	C1	1.473(6)	C15	N1	C11	119.0(4)	C7b	C2b	C1b	121.9(5)
C12b	C13b	1.396(8)	C11b	C10b	N2b	113.5(4)	C3b	C2b	C1b	120.3(5)
C15	C14	1.372(8)	C16b	C10b	N2b	123.6(5)	C3b	C2b	C7b	117.7(5)
C12	C13	1.393(8)	C16b	C10b	C11b	123.0(5)	C5b	C6b	C7b	119.6(6)
C15b	C14b	1.393(8)	C11b	N1b	Pd1b	111.0(3)	C6b	C7b	C2b	121.6(5)
C14b	C13b	1.375(8)	C15b	N1b	Pd1b	128.8(4)	C4b	C3b	C2b	121.7(6)
C10	C16	1.491(7)	C15b	N1b	C11b	120.2(5)	C5	C4	C3	121.1(6)
C13	C14	1.396(8)	C12	C11	N1	121.2(5)	C5	C6	C7	121.3(6)
C1	C2	1.512(7)	C10	C11	N1	114.8(4)	C6	C5	C4	118.6(6)

C1	C8	1.512(8)	C10	C11	C12	124.1(5)	C5b	C4b	C3b	118.5(6)
C1b	C2b	1.506(7)	N3	N2	Pd1	123.8(3)	C4b	C5b	C6b	120.9(6)
C1b	C8b	1.525(8)								
C7	C2	1.399(8)								
C7	C6	1.389(9)								
C3	C2	1.395(8)								
C3	C4	1.403(9)								
C2b	C7b	1.394(7)								
C2b	C3b	1.396(8)								
C6b	C7b	1.381(8)								
C6b	C5b	1.388(9)								
C3b	C4b	1.402(9)								
C4	C5	1.377(9)								
C6	C5	1.393(9)								
C4b	C5b	1.386(9)								

Table 7.56 Anisotropic displacement parameters ($\text{\AA}^2 \times 10^3$) for [Pd(apyTSCmB)Cl]. The anisotropic displacement factor exponent takes the form: $-2\pi^2[h2a^*2U11+2hka^*b^*U12+\dots]$.

Atom	U ₁₁	U ₂₂	U ₃₃	U ₁₂	U ₁₃	U ₂₃
Pd1b	17.13(15)	14.38(14)	16.61(13)	-0.24(12)	1.95(12)	0.88(11)
Pd1	16.42(14)	13.72(13)	15.47(13)	0.30(12)	0.15(11)	1.54(11)
S1b	21.4(5)	14.3(5)	16.6(4)	2.6(4)	2.1(4)	0.2(4)
Cl1	29.2(6)	23.8(5)	15.7(4)	4.6(5)	-0.7(4)	0.1(4)
Cl1b	34.3(7)	23.6(5)	16.7(4)	3.8(5)	2.6(5)	0.3(4)
S1	19.8(5)	12.8(5)	16.0(4)	1.5(4)	0.9(4)	0.9(4)
N2b	18.9(17)	13.4(16)	16.9(15)	-0.5(14)	2.1(13)	0.3(12)
C9	9.6(16)	12.8(17)	18.0(17)	1.3(14)	2.5(16)	-0.3(15)
N3b	23(2)	15.5(17)	15.8(17)	-1.9(15)	-2.8(15)	2.3(14)
N4b	23(2)	14.9(17)	15.3(16)	3.2(15)	0.7(15)	2.3(13)
N3	19.4(19)	13.2(16)	16.5(16)	4.5(14)	0.5(14)	2.4(13)
C9b	34(3)	18(2)	19(2)	-5.3(19)	3(2)	2.2(18)
N1	17.7(17)	16.0(16)	17.2(15)	-4.0(14)	0.4(15)	0.2(13)
C10b	14.4(19)	16.9(18)	22(2)	3.4(16)	0.3(17)	-0.5(15)
N1b	18.8(18)	15.1(15)	18.1(16)	1.5(14)	1.9(15)	1.2(14)
C11	15.9(19)	11.9(18)	21.5(19)	-0.9(15)	-1.7(16)	1.1(14)
N2	14.3(16)	11.0(14)	16.1(15)	-1.2(13)	-0.0(13)	0.1(12)
C11b	12.2(18)	15.8(18)	24(2)	-2.1(15)	-0.1(16)	-1.1(15)
N4	25.6(19)	11.9(15)	16.9(16)	4.0(16)	3.2(14)	2.2(13)
C12b	17(2)	19(2)	26(2)	-1.2(17)	0.2(18)	-6.9(18)
C15	21(2)	21(2)	22(2)	-1.0(19)	-1.0(17)	3.3(18)
C12	22(2)	14.0(19)	28(2)	1.1(18)	-1.5(19)	-2.3(17)
C15b	25(2)	17(2)	24(2)	0(2)	2.1(17)	3.6(18)
C14b	23(2)	12.6(19)	33(3)	-0.5(18)	2(2)	7.7(18)
C16b	27(3)	24(2)	20(2)	5(2)	-1(2)	-6.1(17)
C10	11.2(18)	16.3(17)	19.7(18)	5.3(15)	-0.8(17)	0.1(15)
C16	25(2)	20(2)	18.2(18)	5.2(19)	0.6(18)	-2.2(15)
C13	21(2)	13.1(19)	34(3)	-0.2(17)	3.5(19)	-1.5(17)
C14	22(2)	17(2)	30(3)	-1.2(18)	-6(2)	10.0(19)
C13b	20(2)	13.0(19)	36(3)	-3.7(18)	1(2)	1.0(18)
C1	22(2)	15.6(18)	15.5(17)	2.0(18)	5.3(16)	6.4(16)
C1b	16(2)	20(2)	15.1(18)	-0.3(17)	-0.1(16)	2.6(16)
C7	25(2)	24(2)	25(2)	6(2)	6(2)	8.6(19)

C3	27(3)	25(2)	16.3(19)	6(2)	2.7(19)	-1.1(17)
C2	28(2)	18(2)	13.1(17)	7.3(18)	7.0(16)	5.1(14)
C8	31(3)	20(2)	26(2)	-1(2)	6(2)	6.1(18)
C2b	21(2)	19.4(19)	12.3(16)	0.7(18)	-3.0(16)	-0.3(14)
C8b	17(2)	34(3)	22(2)	4(2)	-4.2(18)	5.3(19)
C6b	19(2)	32(3)	23(2)	-3(2)	-3.4(19)	8(2)
C7b	20(2)	17.8(19)	20(2)	3.8(17)	2.0(17)	1.0(16)
C3b	30(3)	23(2)	22(2)	-1(2)	-2(2)	-7.0(18)
C4	42(3)	30(3)	19(2)	6(3)	-4(2)	-3.8(18)
C6	29(3)	35(3)	21(2)	12(2)	4(2)	13(2)
C5	28(3)	49(4)	17(2)	1(3)	-3(2)	3(2)
C4b	38(3)	42(3)	20(2)	4(3)	4(2)	-13(2)
C5b	25(3)	49(4)	17(2)	3(2)	3.7(19)	0(2)

7.11.16. [Pd(dpyTSCmB)Cl]·HCl

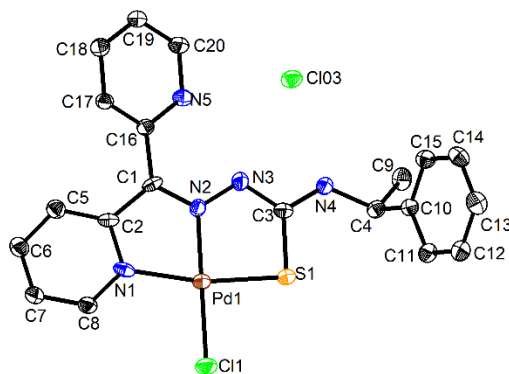


Figure 7.468 Molecular structure of [Pd(dpyTSCmB)Cl]·HCl. Atoms are shown with 50 % probability. Hydrogen atoms are omitted for clarity.

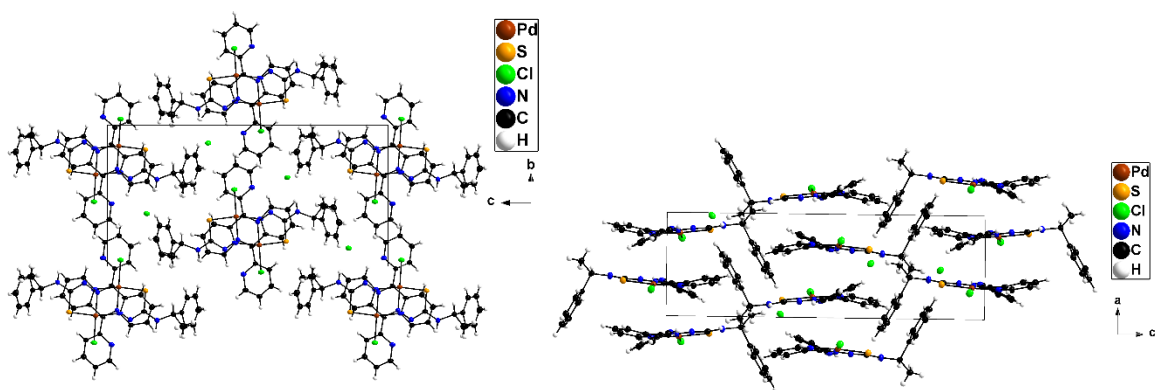


Figure 7.469 Crystal structure of [Pd(dpyTSCmB)Cl]·HCl along the crystallographic a-axis (left) and b-axis (right).

Table 7.57 Crystal data and structure refinement for [Pd(dpyTSCmB)Cl]·HCl.

Empirical formula	C ₂₀ H ₁₈ Cl ₂ N ₅ PdS (537.75 g/mol)
Temperature/	100(2) K
Crystal system	orthorhombic
Space group	P2 ₁ 2 ₁ 2 ₁
Unit cell dimensions	a = 7.5680(15) Å, b = 11.766(2) Å, c = 23.397(5) Å

Volume / Z	2083.4(7) Å ³ / 4
Q _{calc}	1.714 g/cm ³
μ	1.265 mm ⁻¹
F(000)	1076.0
Radiation	synchrotron (λ = 0.71073)
2θ range for data collection/°	3.482 to 78.768
Index ranges	-10 ≤ h ≤ 10, -15 ≤ k ≤ 16, -31 ≤ l ≤ 31
Reflections collected	81969
Independent reflections	8263 [R _{int} = 0.2091, R _{sigma} = 0.1089]
Data/restraints/parameters	8263/0/264
Goodness-of-fit on F ²	1.083
final R indices [I _o ≥ 2σ _{I_o}]	R ₁ = 0.0665, wR ₂ = 0.1526
Final R indexes [all data]	R ₁ = 0.1015, wR ₂ = 0.1685
Largest diff. peak/hole / e Å ⁻³	2.15/-0.91
Flack parameter	-1.34(3)

Table 7.58 Atomic coordinates (x 10⁴) and equivalent isotropic displacement parameters (Å² x 10³) for [Pd(dpyTSCmB)Cl]·HCl. U(eq) is defined as one third of the trace of the orthogonalized U_{ij} tensor.

Atom	x	y	z	U(eq)	Atom	x	y	z	U(eq)
Pd1	1983.1(7)	1487.9(5)	4589.5(3)	18.78(15)	C17	2823(10)	5251(6)	5763(3)	20.1(13)
S1	1650(2)	1736.5(16)	3637.3(9)	21.8(4)	C1	1859(10)	3596(6)	5164(3)	20.2(12)
Cl03	277(3)	6279.7(16)	3593.0(9)	25.9(4)	C8	2081(12)	813(7)	5844(3)	22.8(14)
Cl1	2449(3)	-430.5(17)	4525.8(10)	28.0(4)	C6	1335(11)	2097(8)	6590(4)	25.4(16)
N2	1727(8)	3141(5)	4649(3)	19.2(11)	C16	2056(10)	4821(6)	5269(3)	19.0(13)
N1	2064(8)	1643(5)	5452(3)	20.5(11)	C10	2791(9)	3296(6)	2348(3)	19.2(13)
N5	1579(8)	5574(6)	4850(3)	20.3(12)	C14	5431(11)	4161(8)	1935(4)	25.7(16)
C2	1780(9)	2749(6)	5633(3)	19.0(12)	C3	1478(10)	3219(6)	3688(4)	20.4(14)
N3	1552(9)	3803(6)	4182(3)	23.0(13)	C4	1031(9)	3419(7)	2643(3)	20.3(13)
N4	1211(9)	3848(6)	3229(3)	22.4(13)	C9	-172(12)	4267(8)	2321(4)	28.1(17)
C5	1362(11)	2977(7)	6199(4)	23.9(15)	C12	4975(12)	2138(8)	1862(4)	28.1(17)
C19	2458(11)	7149(7)	5418(4)	26.7(15)	C18	2996(11)	6414(7)	5839(3)	25.3(13)
C20	1761(11)	6706(7)	4921(4)	25.9(16)	C11	3384(10)	2240(7)	2157(4)	24.1(15)
C15	3865(11)	4254(7)	2237(4)	23.2(15)	C7	1738(11)	1007(7)	6420(4)	25.6(16)

Table 7.59 Bond lengths [Å] and angles [deg] for [Pd(dpyTSCmB)Cl]·HCl.

Pd1-S1	2.261(2)	S1-Pd1-Cl1	94.62(8)	C15-C10-C4	121.0(7)
Pd1-Cl1	2.289(2)	N2-Pd1-S1	86.0(2)	C11-C10-C15	117.8(7)
Pd1-N2	1.960(6)	N2-Pd1-Cl1	176.80(19)	C11-C10-C4	121.2(7)
Pd1-N1	2.027(7)	N2-Pd1-N1	81.0(3)	C13-C14-C15	118.9(8)
S1-C3	1.753(8)	N1-Pd1-S1	166.56(16)	N3-C3-S1	124.3(6)
N2-N3	1.349(10)	N1-Pd1-Cl1	98.56(17)	N4-C3-S1	121.0(6)
N2-C1	1.323(10)	C3-S1-Pd1	94.1(3)	N4-C3-N3	114.7(7)
N1-C2	1.385(9)	N3-N2-Pd1	121.7(5)	N4-C4-C10	112.3(6)
N1-C8	1.339(10)	C1-N2-Pd1	117.3(5)	N4-C4-C9	106.7(7)
N5-C20	1.350(10)	C1-N2-N3	120.8(7)	C10-C4-C9	111.1(7)
N5-C16	1.370(10)	C2-N1-Pd1	112.6(5)	C13-C12-C11	119.5(9)
C2-C5	1.388(12)	C8-N1-Pd1	128.0(5)	C19-C18-C17	120.1(8)
C2-C1	1.483(11)	C8-N1-C2	118.5(7)	C12-C11-C10	121.0(8)
N3-C3	1.346(11)	C20-N5-C16	121.5(7)	C6-C7-C8	118.3(8)
N4-C3	1.320(11)	N1-C2-C5	120.6(7)	C12-C13-C14	121.3(8)
N4-C4	1.467(10)	N1-C2-C1	113.5(7)		
C5-C6	1.382(12)	C5-C2-C1	125.8(7)		
C19-C20	1.378(13)	C3-N3-N2	113.9(7)		

C19-C18	1.373(13)	C3-N4-C4	125.6(7)
C15-C10	1.414(11)	C6-C5-C2	119.3(8)
C15-C14	1.385(12)	C18-C19-C20	118.7(7)
C17-C16	1.388(11)	N5-C20-C19	121.1(8)
C17-C18	1.386(11)	C14-C15-C10	121.5(8)
C1-C16	1.470(10)	C18-C17-C16	120.4(7)
C8-C7	1.391(12)	N2-C1-C2	113.5(7)
C6-C7	1.377(12)	N2-C1-C16	123.9(7)
C10-C4	1.507(10)	C16-C1-C2	122.6(6)
C10-C11	1.394(11)	N1-C8-C7	122.8(7)
C14-C13	1.385(13)	C7-C6-C5	120.2(8)
C4-C9	1.546(12)	N5-C16-C17	118.1(7)
C12-C11	1.393(12)	N5-C16-C1	119.1(7)
C12-C13	1.383(13)	C17-C16-C1	122.6(7)

Table 7.60 Anisotropic displacement parameters ($\text{\AA}^2 \times 10^3$) for $[\text{Pd}(\text{dpyTSCmB})\text{Cl}]\cdot\text{HCl}$. The anisotropic displacement factor exponent takes the form: $-2\pi^2[h^2a^*U_{11}+2hka^*b^*U_{12}+\dots]$.

Atom	U_{11}	U_{22}	U_{33}	U_{23}	U_{13}	U_{12}
Pd1	19.3(2)	15.0(2)	22.1(3)	-0.4(2)	-0.2(2)	0.85(17)
S1	26.5(9)	15.8(9)	23.0(9)	-2.0(6)	0.6(6)	0.7(5)
Cl03	30.4(9)	18.4(9)	29.0(10)	-1.4(6)	-5.4(7)	3.9(6)
Cl1	36.4(9)	16.2(8)	31.4(11)	-0.8(7)	-2.8(7)	3.2(6)
N2	21(3)	20(3)	17(3)	-1(2)	0(2)	0.9(19)
N1	17(2)	13(3)	32(3)	5(2)	1(3)	2.0(18)
N5	17(3)	17(3)	27(3)	0(2)	0(2)	2.7(18)
C2	15(3)	12(3)	30(4)	-1(2)	-1(2)	0(2)
N3	28(3)	22(3)	19(3)	0(2)	-1(2)	2(2)
N4	30(3)	20(3)	18(3)	-1(2)	-1(2)	2(2)
C5	24(3)	23(4)	25(4)	1(3)	2(3)	0(3)
C19	37(4)	18(4)	25(4)	0(3)	1(3)	-2(2)
C20	33(4)	17(4)	28(4)	1(2)	-1(3)	1(3)
C15	24(4)	22(4)	24(4)	1(3)	-6(3)	-2(3)
C17	21(4)	17(3)	22(4)	0(2)	1(3)	-2(2)
C1	19(3)	15(3)	27(3)	-9(2)	0(3)	1(3)
C8	27(4)	17(3)	24(4)	2(2)	-2(3)	1(3)
C6	24(4)	27(4)	25(4)	3(3)	1(3)	-3(3)
C16	21(3)	16(3)	20(4)	-1(2)	2(2)	3(2)
C10	18(3)	19(4)	20(3)	0(2)	-3(2)	1(2)
C14	20(3)	28(4)	29(4)	7(3)	-3(3)	-4(3)
C3	20(3)	15(3)	26(4)	0(2)	1(2)	0(2)
C4	19(3)	21(4)	21(3)	-2(3)	-3(2)	0(2)
C9	25(4)	34(5)	25(5)	1(3)	-3(3)	4(3)
C12	32(4)	28(5)	25(5)	-2(3)	2(3)	1(3)
C18	27(3)	24(4)	25(4)	-2(3)	-1(3)	-5(3)
C11	26(4)	25(4)	22(4)	-2(3)	-2(3)	-1(3)
C7	31(4)	21(4)	24(4)	2(3)	0(3)	-6(3)
C13	22(4)	35(5)	31(5)	4(3)	3(3)	2(3)

7.11.17. [Pt(apyTSCmB)Cl]

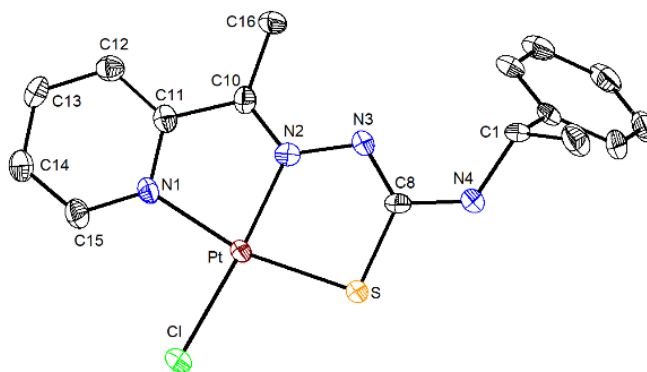


Figure 7.470 Molecular structure of [Pt(apyTSCmB)Cl]. Atoms are shown with 50 % probability. Hydrogen atoms are omitted for clarity.

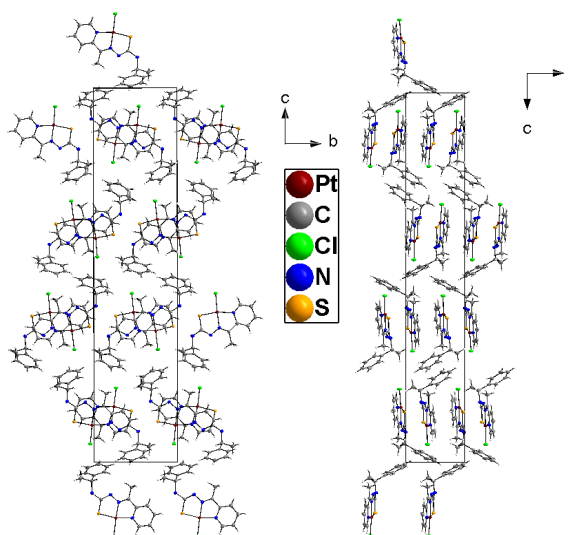


Figure 7.471 Crystal structure of [Pt(apyTSCmB)Cl] along the crystallographic a-axis (left) and b-axis (right).

Table 7.61 Crystal data and structure refinement for [Pt(apyTSCmB)Cl].

empirical formula	C ₁₆ H ₁₆ ClN ₄ PtS / 512.92 g/mol
temperature / wavelength	100(2) K / 1.54178 Å
crystal system, space group	orthorhombic / P2 ₁ 2 ₁ 2 ₁
unit cell dimensions	a = 7.2536(10) Å; b = 10.2592(14) Å; c = 46.003(6) Å
volume / Z / density (calculated)	3423.4(8) Å ³ / 8 / 1.990 g/cm ³
absorption coefficient / F(000)	17.895 mm ⁻¹ / 1952
theta range for data collection	3.843 to 72.411°.
index ranges	-8 ≤ h ≤ 8, -12 ≤ k ≤ 12, -56 ≤ l ≤ 54
reflections collected	35614
independent reflections	6735 [R _{int} = 0.0502]
completeness to theta = 67.679°	100.0 %
refinement method	Full-matrix least-squares on F ²
data / restraints / parameters	6735 / 0 / 419
goodness-of-fit on F ²	1.190
final R indices [I ≥ 2σ _I]	R ₁ = 0.0249, wR ₂ = 0.0621
R indices (all data)	R ₁ = 0.0261, wR ₂ = 0.0621
absolute structure parameter	0.103(4)
largest diff. peak and hole	1.004 and -1.225 e·Å ⁻¹

Table 7.62 Atomic coordinates ($\times 10^4$) and equivalent isotropic displacement parameters ($\text{\AA}^2 \times 10^3$) for [Pt(apyTSCmB)Cl]. U(eq) is defined as one third of the trace of the orthogonalized U_{ij} tensor.

	x	y	z	U(eq)		x	y	z	U(eq)
Pt(1)	1418(1)	4755(1)	4009(1)	18(1)	C(11)	793(10)	7142(7)	3705(2)	22(1)
C(8)	2050(10)	2858(7)	3531(2)	21(1)	C(5)	-2404(13)	2031(10)	2553(2)	37(2)
Cl(1)	1348(3)	4566(2)	4511(1)	28(1)	C(4)	-1969(12)	916(9)	2710(2)	29(2)
C(44)	-1235(15)	3083(9)	2562(2)	40(2)	C(15)	494(11)	7532(8)	4206(2)	27(2)
C(33)	366(13)	3030(8)	2728(2)	31(2)	C(12)	426(11)	8430(7)	3646(2)	26(2)
Cl(2)	6110(3)	7659(2)	3015(1)	27(1)	C(13)	118(11)	9301(7)	3874(2)	27(2)
C(3)	-407(12)	876(8)	2878(2)	26(2)	S(1)	2005(2)	2633(2)	3913(1)	21(1)
C(6)	3737(12)	657(8)	2963(2)	30(2)	S(2)	5268(3)	9478(2)	3631(1)	20(1)
C(14)	151(12)	8831(8)	4154(2)	29(2)	C(16)	1139(13)	6471(7)	3166(2)	27(2)
N(1)	830(9)	6712(6)	3986(1)	22(1)	C(1)	2609(11)	1850(7)	3051(2)	24(2)
N(3)	1797(9)	3973(6)	3395(1)	20(1)	N(4)	2348(10)	1787(6)	3370(1)	23(1)
C(10)	1145(10)	6151(6)	3483(2)	20(1)	N(2)	1458(8)	4998(6)	3585(1)	19(1)
C(2)	814(11)	1926(7)	2889(1)	22(2)					

Table 7.63 Bond lengths [\AA] and angles [deg] for [Pt(apyTSCmB)Cl].

Pt(1)-N(2)	1.966(5)	C(11)-C(12)	1.375(11)	N(2)-C(10)-C(16)	123.7(6)
Pt(1)-N(1)	2.055(6)	C(5)-C(4)	1.391(13)	C(11)-C(10)-C(16)	121.8(6)
Pt(1)-S(1)	2.2623(18)	C(12)-C(13)	1.397(11)	C(33)-C(2)-C(3)	117.4(8)
Pt(1)-Cl(1)	2.3173(16)	C(1)-N(4)	1.481(9)	C(33)-C(2)-C(1)	120.6(7)
C(8)-N(3)	1.317(10)	N(2)-Pt(1)-N(1)	80.2(2)	C(3)-C(2)-C(1)	121.9(7)
C(8)-N(4)	1.341(10)	N(2)-Pt(1)-S(1)	85.75(17)	N(1)-C(11)-C(12)	120.1(7)
C(8)-S(1)	1.775(8)	N(1)-Pt(1)-S(1)	165.82(18)	N(1)-C(11)-C(10)	115.6(6)
C(44)-C(5)	1.373(14)	N(2)-Pt(1)-Cl(1)	177.50(17)	C(12)-C(11)-C(10)	124.3(7)
C(44)-C(33)	1.391(13)	N(1)-Pt(1)-Cl(1)	97.35(18)	C(44)-C(5)-C(4)	119.4(8)
C(33)-C(2)	1.392(11)	S(1)-Pt(1)-Cl(1)	96.75(6)	C(3)-C(4)-C(5)	120.3(8)
C(3)-C(4)	1.372(12)	N(3)-C(8)-N(4)	118.2(6)	N(1)-C(15)-C(14)	120.9(7)
C(3)-C(2)	1.395(11)	N(3)-C(8)-S(1)	125.6(6)	C(11)-C(12)-C(13)	119.8(7)
C(6)-C(1)	1.527(11)	N(4)-C(8)-S(1)	116.2(5)	C(14)-C(13)-C(12)	118.5(7)
C(14)-C(15)	1.376(11)	C(5)-C(44)-C(33)	120.0(8)	C(8)-S(1)-Pt(1)	94.1(2)
C(14)-C(13)	1.376(12)	C(44)-C(33)-C(2)	121.3(8)	N(4)-C(1)-C(2)	112.5(6)
N(1)-C(15)	1.336(9)	C(4)-C(3)-C(2)	121.4(8)	N(4)-C(1)-C(6)	107.2(6)
N(1)-C(11)	1.368(9)	C(15)-C(14)-C(13)	120.2(7)	C(2)-C(1)-C(6)	112.0(6)
N(3)-N(2)	1.391(8)	C(15)-N(1)-C(11)	120.5(6)	C(8)-N(4)-C(1)	122.0(6)
C(10)-N(2)	1.293(9)	C(15)-N(1)-Pt(1)	127.9(5)	C(10)-N(2)-N(3)	119.6(6)
C(10)-C(11)	1.462(10)	C(11)-N(1)-Pt(1)	111.5(5)	C(10)-N(2)-Pt(1)	118.2(5)
C(10)-C(16)	1.496(9)	C(8)-N(3)-N(2)	112.4(6)	N(3)-N(2)-Pt(1)	122.1(4)
C(2)-C(1)	1.502(11)	N(2)-C(10)-C(11)	114.5(6)		

Table 7.64 Anisotropic displacement parameters ($\text{\AA}^2 \times 10^3$) for [Pt(apyTSCmB)Cl]. The anisotropic displacement factor exponent takes the form: $-2\pi^2[h^2a^2U_{11}+2hka*b*U_{12}+\dots]$.

	U11	U22	U33	U23	U13	U12
Pt(1)	23(1)	17(1)	14(1)	-1(1)	-2(1)	0(1)
C(8)	18(3)	25(3)	20(3)	2(3)	-8(3)	3(3)
Cl(1)	43(1)	26(1)	15(1)	0(1)	-2(1)	4(1)
C(44)	45(6)	50(5)	25(4)	14(4)	-6(4)	9(4)
C(33)	41(5)	32(4)	22(4)	7(3)	-1(3)	-3(4)
Cl(2)	39(1)	29(1)	14(1)	0(1)	1(1)	5(1)
C(3)	33(4)	24(4)	20(3)	-2(3)	7(3)	3(3)
C(6)	34(4)	35(4)	21(3)	-7(3)	-1(3)	6(4)
C(14)	31(4)	21(4)	34(4)	-8(3)	-3(3)	1(3)
N(1)	27(3)	20(3)	18(3)	-4(2)	-3(3)	-1(3)

N(3)	24(3)	21(3)	16(3)	-5(2)	0(2)	1(2)
C(10)	18(4)	19(3)	22(3)	4(3)	1(3)	1(3)
C(2)	31(4)	23(3)	11(3)	-2(2)	1(3)	2(3)
C(11)	19(3)	25(3)	22(3)	2(3)	1(3)	-1(3)
C(5)	35(5)	59(6)	17(4)	-3(4)	-5(3)	5(4)
C(4)	30(4)	40(4)	15(3)	-12(3)	4(3)	0(4)
C(15)	33(4)	23(4)	25(4)	-3(3)	-3(3)	-4(3)
C(12)	26(4)	23(4)	27(4)	3(3)	-1(3)	-3(3)
C(13)	25(4)	16(3)	39(4)	0(3)	-4(3)	-2(3)
S(1)	28(1)	18(1)	16(1)	-1(1)	-2(1)	2(1)
S(2)	27(1)	18(1)	16(1)	-1(1)	-2(1)	3(1)
C(16)	39(5)	25(4)	18(3)	5(3)	3(3)	4(4)
C(1)	29(4)	25(4)	19(3)	-2(3)	6(3)	0(3)
N(4)	29(3)	22(3)	19(3)	-2(2)	-1(3)	4(3)
N(2)	17(3)	20(3)	19(3)	2(2)	4(2)	3(2)

7.11.18. [Pt(dpyTSCmB)CN]

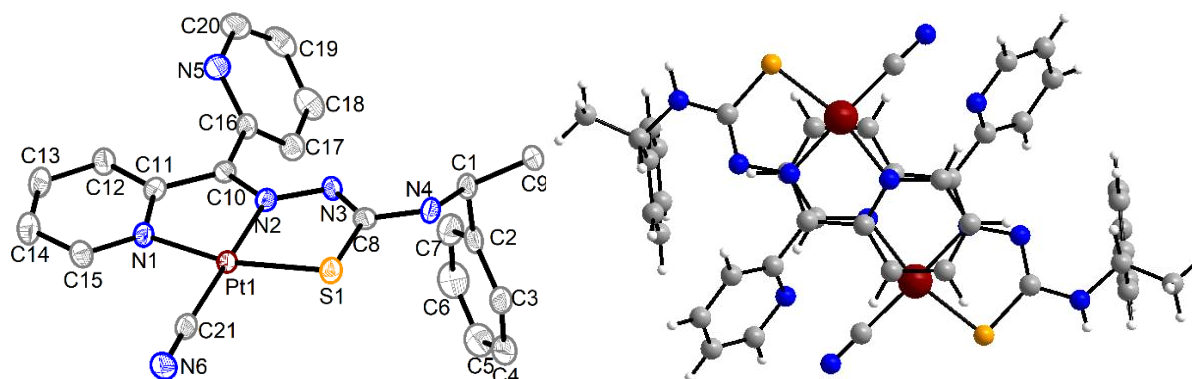


Figure 7.472 Molecular structure of [Pt(dpyTSCmB)CN]. Atoms are shown with 50% probability. H atoms are omitted for clarity. Right: Stacking of the complex in the crystal.

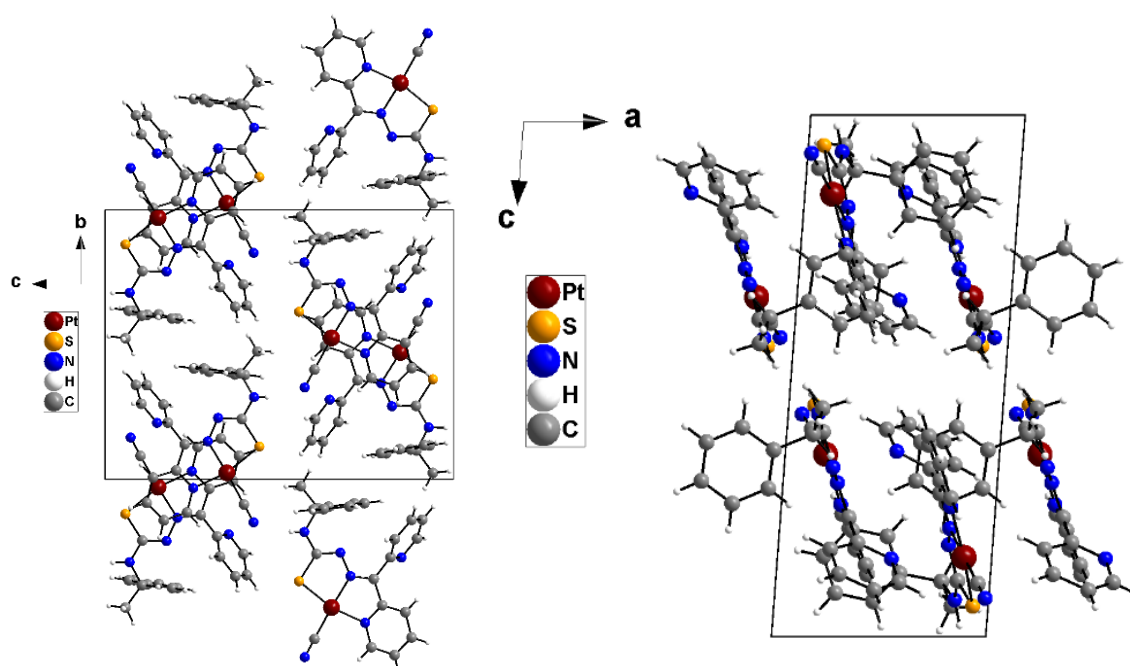


Figure 7.473 Crystal structure of [Pt(dpyTSCmB)CN] along the crystallographic a-axis (left) and b-axis (right).

Table 7.65 Crystal data and structure refinement for [Pt(dpyTSCmB)CN].

Empirical formula / Formula weight	C ₂₁ H ₁₈ N ₆ PtS / 581.56 g/mol
Temperature / Wavelength	150.0 K / 1.54178 Å
Crystal system / Space group	Monoclinic / P2 ₁
Unit Cell Dimensions	a = 7.6316(3) Å b = 14.3698(6) Å / β = 94.3320(10) c = 18.6158(7) Å
Volume / Z	2035.66(14) Å ³ / 4
Q _{calc}	1.8975 g/cm ³
μ	14.011 mm ⁻¹
F(000)	1106.5
Crystal size	0.15 mm × 0.1 mm × 0.02 mm
2θ range for data collection	4.76° to 144.14°
Index ranges	-9 ≤ h ≤ 9, -17 ≤ k ≤ 17, -22 ≤ l ≤ 22
Reflections collected	52088
Independent reflections	7847 [R _{int} = 0.0429, R _{sigma} = 0.0318]
Data/restraints/parameters	7847/1/532
Goodness-of-fit on F ²	1.034
Final R indexes [I _o ≥ 2σ _{I_o}]	R ₁ = 0.0195, wR ₂ = 0.0492
Final R indexes [all data]	R ₁ = 0.0196, wR ₂ = 0.0493
Largest diff. peak/hole	1.01/-1.10 e Å ⁻³
Flack parameter	0.091(7)

Table 7.66 Atomic coordinates (x 10⁴) and equivalent isotropic displacement parameters (Å² × 10³) for [Pt(dpyTSCmB)CN]. U(eq) is defined as one third of the trace of the orthogonalized U_{ij} tensor.

Atom	x	y	z	U(eq)	Atom	x	y	z	U(eq)
Pt1	8115.5(2)	5244.01(3)	3497.38(7)	17.02(4)	C18	7084(8)	8496(3)	1199(3)	32.8(11)
Pt1b	1291.4(2)	4708.89(3)	1521.26(8)	17.41(4)	C17	7569(6)	7778(3)	1676(2)	27.3(9)
S1	8794.5(15)	6219.0(5)	4430.7(6)	22.9(2)	C11	6617(5)	5328(3)	2041(2)	20.0(8)
S1b	721.7(15)	3714.4(5)	585.3(6)	22.9(2)	C15	7128(6)	3771(3)	2353(2)	23.2(9)
N2	7467(5)	6410(2)	2951.1(18)	19.3(7)	C14	6398(7)	3479(3)	1689(3)	29.5(10)
N3	7723(5)	7278(2)	3244.0(18)	20.1(7)	C13	5767(6)	4130(3)	1197(2)	27.9(10)
N4	8597(5)	8050(2)	4278(2)	20.7(7)	C12	5857(6)	5070(3)	1377(2)	24.2(9)
N5	4686(5)	7094(2)	1492.4(19)	27.4(8)	C21	8852(6)	4074(3)	3986(2)	24.3(9)
N1	7237(4)	4677(2)	2531.8(17)	20.3(6)	C10b	2633(6)	3678(3)	2748(2)	19.1(8)
N6	9356(6)	3406(2)	4266(2)	28.4(9)	C8b	1521(5)	2726(3)	1071(2)	18.7(8)
N2b	2056(5)	3572(2)	2074.1(18)	19.6(7)	C1b	2268(5)	1072(2)	1058(2)	20.6(8)
N3b	2061(5)	2713(2)	1763.9(18)	19.3(7)	C9b	1711(6)	238(3)	588(2)	25.7(8)
N4b	1587(5)	1927(2)	706.7(19)	20.8(7)	C2b	4246(5)	1108(2)	1218(2)	19.6(8)
N1b	2086(4)	5295(2)	2490.1(17)	20.3(6)	C7b	4946(6)	969(3)	1924(2)	23.2(8)
N5b	4803(5)	2957(2)	3550(2)	27.0(8)	C6b	6744(7)	971(3)	2079(3)	34.6(11)
N6b	168(6)	6552(2)	735(2)	27.5(9)	C5b	7854(6)	1119(3)	1543(3)	40.8(12)
C10	6815(5)	6302(3)	2285(2)	18.3(8)	C4b	7185(7)	1265(3)	839(3)	34.8(11)
C8	8313(5)	7238(3)	3927(2)	19.9(8)	C3b	5383(6)	1256(3)	678(2)	25.9(9)
C1	8780(6)	8933(2)	3881(2)	22.5(8)	C11b	2686(5)	4654(3)	2994(2)	21.4(8)
C9	8409(6)	9747(3)	4378(2)	28.9(9)	C15b	2120(6)	6202(3)	2660(2)	25.9(9)
C2	10553(6)	8987(2)	3580(2)	24.4(9)	C14b	2746(7)	6518(3)	3326(3)	29.6(10)
C7	10674(7)	9111(3)	2843(2)	32.7(10)	C13b	3361(7)	5875(3)	3846(3)	31.2(10)
C6	12305(8)	9115(3)	2554(3)	40.4(12)	C12b	3329(6)	4938(3)	3677(3)	27.2(10)
C5	13815(7)	8995(3)	2987(3)	38.9(12)	C16b	3187(6)	2883(3)	3219(2)	21.9(9)
C4	13715(7)	8893(3)	3727(3)	36.2(12)	C17b	2071(6)	2134(3)	3299(2)	25.0(9)
C3	12097(6)	8883(3)	4014(3)	26.6(9)	C18b	2653(7)	1409(3)	3739(2)	27.9(10)
C16	6331(6)	7106(3)	1802(2)	20.0(8)	C19b	4341(7)	1451(3)	4072(3)	32.8(11)
C20	4256(7)	7805(3)	1041(2)	33.3(11)	C20b	5346(7)	2233(3)	3972(3)	35.0(11)
C19	5377(8)	8502(3)	889(3)	35.5(12)	C21b	564(6)	5870(3)	1018(2)	25.1(9)

Table 7.67 Anisotropic displacement parameters ($\text{\AA}^2 \times 10^3$) for [Pt(dpyTSCmB)CN]. The anisotropic displacement factor exponent takes the form: $-2\pi^2[h^2a^*U_{11}+2hka^*b^*U_{12}+\dots]$.

Atom	U ₁₁	U ₂₂	U ₃₃	U ₁₂	U ₁₃	U ₂₃
Pt1	19.89(8)	15.40(8)	15.43(8)	-0.62(6)	-0.91(5)	1.02(6)
Pt1b	20.56(8)	14.47(8)	16.99(8)	2.12(6)	-0.03(5)	0.06(6)
S1	31.2(6)	20.1(5)	16.2(5)	0.1(4)	-5.3(4)	0.6(4)
S1b	30.4(6)	18.8(5)	18.5(5)	4.9(4)	-4.9(4)	-1.3(4)
N2	21.1(17)	18.6(17)	17.8(16)	-1.1(14)	-1.0(13)	-1.1(13)
N3	23.7(17)	14.4(16)	21.7(17)	-0.0(13)	-0.8(13)	-1.7(13)
N4	26.8(18)	16.8(17)	17.8(18)	-3.5(14)	-3.5(15)	-1.0(14)
N5	31(2)	27.8(19)	22.6(18)	4.3(16)	-5.8(15)	-0.1(15)
N1	21.3(15)	16.8(15)	22.7(16)	-3.6(15)	1.7(12)	-1.7(16)
N6	37(2)	23(2)	24(2)	4.2(17)	-3.3(17)	4.4(16)
N2b	24.1(18)	16.9(17)	17.3(16)	2.0(14)	-1.9(13)	-1.7(13)
N3b	23.5(17)	14.7(16)	19.4(16)	2.0(13)	-0.5(13)	-3.0(13)
N4b	23.8(17)	19.7(17)	18.1(17)	2.1(14)	-4.5(13)	-2.8(13)
N1b	20.5(15)	19.5(16)	21.1(15)	-3.5(16)	1.8(12)	-1.0(16)
N5b	30(2)	23.6(18)	26.5(19)	-3.3(16)	-5.4(15)	6.7(15)
N6b	40(2)	18.8(19)	22.3(19)	6.2(17)	-4.0(17)	4.8(15)
C10	19.8(19)	20(2)	14.3(18)	1.1(16)	-1.1(15)	1.4(16)
C8	16.5(19)	21(2)	23(2)	-0.3(16)	4.0(15)	-0.6(16)
C1	30(2)	14.1(18)	22.4(19)	-0.6(16)	-7.0(16)	0.5(15)
C9	29(2)	17.5(19)	39(2)	3(2)	-4.9(17)	-7(2)
C2	34(2)	10.6(17)	28(2)	-2.2(16)	-3.3(17)	-1.5(15)
C7	42(3)	26(2)	29(2)	-4(2)	-3.7(19)	3.1(18)
C6	52(3)	36(3)	34(3)	-6(3)	11(2)	4(2)
C5	36(3)	33(3)	50(3)	-7(2)	15(2)	-1(2)
C4	32(3)	22(2)	55(3)	-5(2)	3(2)	-5(2)
C3	30(2)	18(2)	31(2)	-2.6(17)	-1.9(18)	-0.7(17)
C16	28(2)	20(2)	11.3(19)	0.9(17)	-2.3(16)	-2.3(15)
C20	39(3)	36(3)	23(2)	13(2)	-8.6(19)	1.3(19)
C19	54(3)	31(3)	22(2)	17(2)	3(2)	3.9(19)
C18	45(3)	23(2)	31(3)	2(2)	13(2)	7.6(19)
C17	31(2)	26(2)	24(2)	0.4(19)	0.4(18)	-0.6(17)
C11	19.8(18)	21(2)	19.5(19)	-2.4(17)	1.2(14)	-0.7(17)
C15	27(2)	19(2)	25(2)	-2.4(17)	7.4(17)	-0.5(17)
C14	36(3)	24(2)	29(2)	-8.5(19)	7(2)	-4.7(19)
C13	33(2)	30(2)	21(2)	-6(2)	1.5(17)	-8.5(18)
C12	30(2)	21(2)	21.4(19)	-2.0(17)	-0.0(17)	0.2(16)
C21	27(2)	24(2)	21(2)	-1.1(18)	-4.1(17)	-3.6(18)
C10b	21(2)	16.9(19)	19(2)	-0.7(16)	0.8(15)	-0.6(16)
C8b	16.9(19)	17.7(19)	22(2)	1.9(15)	2.4(15)	1.5(15)
C1b	20.9(19)	18.2(19)	22.4(19)	2.4(15)	1.1(15)	-1.1(15)
C9b	28(2)	18.3(19)	30(2)	0(2)	-2.7(16)	-3(2)
C2b	20.9(19)	13.4(17)	24.1(19)	1.8(15)	-0.3(16)	-4.0(14)
C7b	24(2)	21(2)	25(2)	-1.8(16)	3.6(16)	1.5(16)
C6b	25(2)	34(3)	43(3)	2(2)	-9(2)	6(2)
C5b	16(2)	44(3)	62(4)	-1(2)	0(2)	-6(3)
C4b	28(2)	33(3)	45(3)	-5(2)	15(2)	-4(2)
C3b	30(2)	21(2)	28(2)	-1.8(18)	6.5(18)	-3.6(17)

C11b	26(2)	15.3(18)	23(2)	0.0(18)	3.8(15)	0.6(17)
C15b	31(2)	23(2)	24(2)	4.0(18)	5.0(18)	2.0(17)
C14b	40(3)	20(2)	29(2)	-3.4(19)	3(2)	-5.4(19)
C13b	41(3)	27(2)	25(2)	-7(2)	-3.4(19)	-8.7(18)
C12b	34(2)	28(3)	18.6(19)	-1.0(17)	-4.6(17)	-0.5(17)
C16b	28(2)	21(2)	17(2)	-1.2(17)	1.4(16)	-0.9(16)
C17b	26(2)	24(2)	25(2)	-0.3(17)	2.2(17)	1.1(17)
C18b	36(3)	25(2)	23(2)	-3.1(19)	4.7(19)	3.5(17)
C19b	43(3)	24(2)	31(3)	2(2)	-1(2)	9(2)
C20b	35(3)	38(3)	29(2)	3(2)	-12(2)	8(2)
C21b	27(2)	26(2)	22(2)	3.8(19)	-1.0(17)	-6.7(18)

Table 7.68 Bond lengths [Å] and angles [deg] for [Pt(dpyTSCmB)CN].

Pt1-S1	2.2614(9)	C1-C2	1.506(6)	N2-Pt1-S1	84.57(9)	C4-C3-C2	121.3(5)
Pt1-N2	2.003(3)	C2-C7	1.394(6)	N1-Pt1-S1	164.86(10)	C10-C16-N5	115.4(4)
Pt1-N1	2.040(3)	C2-C3	1.385(6)	N1-Pt1-N2	80.48(13)	C17-C16-N5	124.4(4)
Pt1-C21	1.973(4)	C7-C6	1.393(8)	C21-Pt1-S1	97.62(12)	C17-C16-C10	120.1(4)
Pt1b-S1b	2.2700(9)	C6-C5	1.366(8)	C21-Pt1-N2	176.33(17)	C19-C20-N5	124.1(5)
Pt1b-N2b	1.995(3)	C5-C4	1.394(8)	C21-Pt1-N1	97.44(15)	C18-C19-C20	119.6(4)
Pt1b-N1b	2.041(3)	C4-C3	1.381(7)	N2b-Pt1b-S1b	84.95(9)	C17-C18-C19	117.8(4)
Pt1b-C21b	1.973(4)	C16-C17	1.383(6)	N1b-Pt1b-S1b	164.80(9)	C18-C17-C16	118.2(5)
S1-C8	1.763(4)	C20-C19	1.362(7)	N1b-Pt1b-N2b	79.98(13)	C10-C11-N1	115.0(3)
S1b-C8b	1.767(4)	C19-C18	1.385(8)	C21b-Pt1b-S1b	97.86(12)	C12-C11-N1	121.1(4)
N2-N3	1.369(4)	C18-C17	1.393(6)	C21b-Pt1b-N2b	177.19(16)	C12-C11-C10	124.0(4)
N2-C10	1.311(5)	C11-C12	1.377(6)	C21b-Pt1b-N1b	97.21(15)	C14-C15-N1	121.8(4)
N3-C8	1.318(6)	C15-C14	1.382(7)	C8-S1-Pt1	94.57(14)	C13-C14-C15	119.2(4)
N4-C8	1.346(5)	C14-C13	1.372(7)	C8b-S1b-Pt1b	94.25(13)	C12-C13-C14	119.5(4)
N4-C1	1.479(5)	C13-C12	1.391(6)	N3-N2-Pt1	122.5(3)	C13-C12-C11	119.2(4)
N5-C16	1.341(6)	C10b-C11b	1.475(5)	C10-N2-Pt1	116.3(3)	N6-C21-Pt1	177.0(4)
N5-C20	1.348(5)	C10b-C16b	1.483(6)	C10-N2-N3	121.2(3)	C11b-C10b-N2b	114.1(3)
N1-C11	1.367(5)	C1b-C9b	1.525(5)	C8-N3-N2	111.9(3)	C16b-C10b-N2b	122.6(3)
N1-C15	1.345(5)	C1b-C2b	1.517(6)	C1-N4-C8	121.3(3)	C16b-C10b-C11b	123.3(4)
N6-C21	1.145(5)	C2b-C7b	1.395(6)	C20-N5-C16	115.7(4)	N3b-C8b-S1b	125.5(3)
N2b-N3b	1.363(4)	C2b-C3b	1.393(6)	C11-N1-Pt1	112.9(3)	N4b-C8b-S1b	117.1(3)
N2b-C10b	1.306(5)	C7b-C6b	1.381(6)	C15-N1-Pt1	127.9(3)	N4b-C8b-N3b	117.4(3)
N3b-C8b	1.324(5)	C6b-C5b	1.373(8)	C15-N1-C11	119.1(4)	C9b-C1b-N4b	109.1(3)
N4b-C8b	1.337(5)	C5b-C4b	1.385(8)	N3b-N2b-Pt1b	122.2(2)	C2b-C1b-N4b	111.8(3)
N4b-C1b	1.469(5)	C4b-C3b	1.386(7)	C10b-N2b-Pt1b	117.6(3)	C2b-C1b-C9b	111.7(3)
N1b-C11b	1.368(5)	C11b-C12b	1.389(6)	C10b-N2b-N3b	120.1(3)	C7b-C2b-C1b	118.9(4)
N1b-C15b	1.342(5)	C15b-C14b	1.372(7)	C8b-N3b-N2b	112.9(3)	C3b-C2b-C1b	121.9(4)
N5b-C16b	1.341(6)	C14b-C13b	1.392(7)	C1b-N4b-C8b	121.2(3)	C3b-C2b-C7b	119.1(4)
N5b-C20b	1.349(5)	C13b-C12b	1.383(6)	C11b-N1b-Pt1b	112.9(3)	C6b-C7b-C2b	120.0(4)
N6b-C21b	1.142(5)	C16b-C17b	1.388(6)	C15b-N1b-Pt1b	127.5(3)	C5b-C6b-C7b	120.4(5)
C10-C16	1.492(5)	C17b-C18b	1.378(6)	C15b-N1b-C11b	119.5(4)	C4b-C5b-C6b	120.5(5)
C10-C11	1.475(5)	C18b-C19b	1.388(7)	C20b-N5b-C16b	115.9(4)	C3b-C4b-C5b	119.5(4)
C1-C9	1.531(5)	C19b-C20b	1.382(7)	C16-C10-N2	122.5(3)	C4b-C3b-C2b	120.5(4)
				C11-C10-N2	115.2(3)	C10b-C11b-N1b	115.3(4)
				C11-C10-C16	122.3(3)	C12b-C11b-N1b	120.4(4)
				N3-C8-S1	126.2(3)	C12b-C11b-C10b	124.2(4)
				N4-C8-S1	116.3(3)	C14b-C15b-N1b	122.3(4)
				N4-C8-N3	117.5(3)	C13b-C14b-C15b	119.0(4)
				C9-C1-N4	109.0(3)	C12b-C13b-C14b	119.3(4)
				C2-C1-N4	110.6(3)	C13b-C12b-C11b	119.5(4)

C2-C1-C9	113.4(3)	C10b-C16b-N5b	115.0(3)
C7-C2-C1	120.1(4)	C17b-C16b-N5b	124.3(4)
C3-C2-C1	121.7(4)	C17b-C16b-C10b	120.7(4)
C3-C2-C7	118.1(4)	C18b-C17b-C16b	118.5(4)
C6-C7-C2	120.5(5)	C19b-C18b-C17b	118.6(4)
C5-C6-C7	120.7(5)	C20b-C19b-C18b	118.7(4)
C4-C5-C6	119.3(5)	C19b-C20b-N5b	123.9(5)
C3-C4-C5	120.0(5)	N6b-C21b-Pt1b	178.5(4)

7.11.19. $[\{\text{Ir}(\text{PPh}_3)_2\text{Cl}_2\}_2(\mu^2\text{-oxalato-}\kappa^4 \text{O}^1, \text{O}^2:\text{O}^{1'}, \text{O}^{2'})]$.

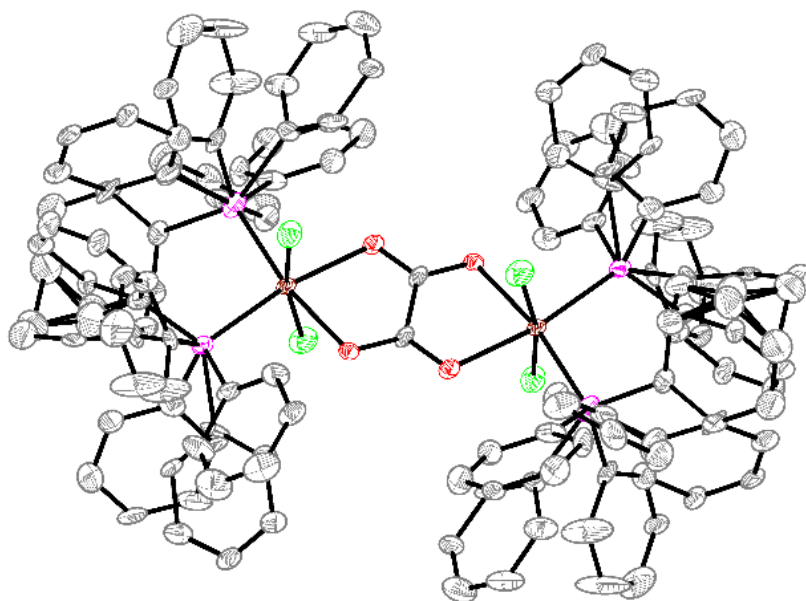


Figure 7.474 Molecular structure of $[\{\text{Ir}(\text{PPh}_3)_2\text{Cl}_2\}_2(\mu^2\text{-oxalato-}\kappa^4 \text{O}^1, \text{O}^2:\text{O}^{1'}, \text{O}^{2'})]$. Atoms are shown with 50% probability. H atoms are omitted for clarity.

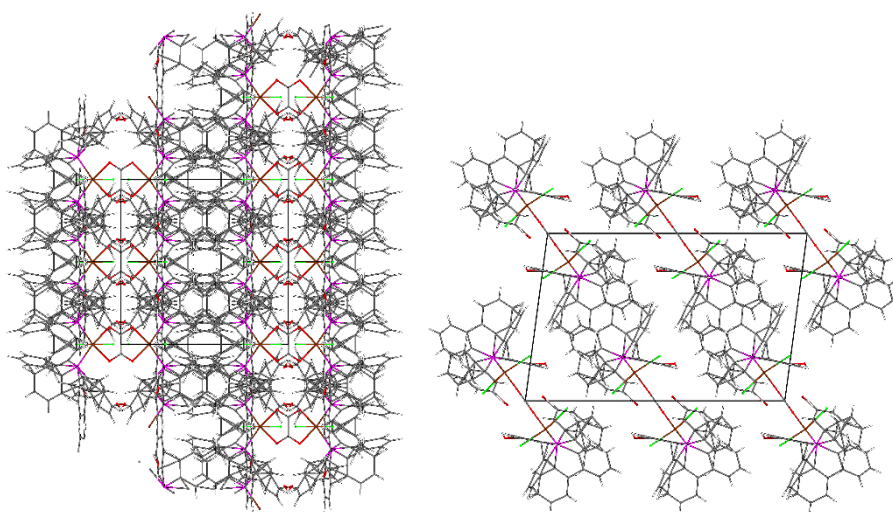


Figure 7.475 Crystal structure of $[\{\text{Ir}(\text{PPh}_3)_2\text{Cl}_2\}_2(\mu^2\text{-oxalato-}\kappa^4 \text{O}^1, \text{O}^2:\text{O}^{1'}, \text{O}^{2'})]$ along the crystallographic a-axis (left) and b-axis (right).

Table 7.69 Crystallographic data of $[\{\text{Ir}(\text{PPh}_3)_2\text{Cl}_2\}_2(\mu^2\text{-oxalato-}\kappa^4 \text{O}^1, \text{O}^2:\text{O}^{1'}, \text{O}^{2'})]$.

Empirical formula	C ₇₄ H ₆₀ Cl ₄ Ir ₂ O ₄ P ₄ (1663.42 g/mol)
Temperature/K	100.0(2)
Crystal system	monoclinic / C2/m
a/Å	20.404(9)
b/Å	12.969(5)
c/Å	13.271(6)
β/°	97.631(14)
Volume / Z	3481(3) Å ³ / 4
ρ _{calc} /cm ³	1.679
μ/mm ⁻¹	4.124
F(000)	1732.0
Radiation	MoKα (λ = 0.71073)
2θ range for data collection/°	4.028 to 51.334
Index ranges	-24 ≤ h ≤ 24, -15 ≤ k ≤ 15, -15 ≤ l ≤ 15
Reflections collected	47285
Independent reflections	3324 [R _{int} = 0.1399, R _{sigma} = 0.0562]
Data/restraints/parameters	3324/15/375
Goodness-of-fit on F ²	1.075
Final R indexes [I _o ≥ 2σ _{I_o}]	R ₁ = 0.0463, wR ₂ = 0.1077
Final R indexes [all data]	R ₁ = 0.0571, wR ₂ = 0.1129
Largest diff. peak/hole / e Å ⁻³	1.86/-2.16

Table 7.70 Atomic coordinates (x 10⁴) and equivalent isotropic displacement parameters (Å² × 10³) for [(Ir(PPh₃)₂Cl₂)₂(μ²-oxalato-κ⁴ O¹, O²:O¹, O²)]. U(eq) is defined as one third of the trace of the orthogonalized U_{ij} tensor.

Atom	x	y	z	U(eq)	Atom	x	y	z	U(eq)
Ir1	5941.3(2)	5000	1689.5(3)	17.61(15)	C18	6298(10)	8745(13)	546(13)	38(4)
Cl1	5060.7(14)	5000	2665(2)	31.6(6)	C19	6198(9)	7862(13)	1101(12)	34(4)
Cl2	6657.6(16)	5000	451(2)	34.4(7)	C20	5824(8)	7510(11)	2446(11)	24(3)
P1	6457.0(13)	6350.7(16)	2590.7(15)	32.0(5)	C21	6098(9)	8502(13)	2535(14)	37(4)
O1	5370(3)	3969(4)	688(4)	24.2(12)	C22	5705(11)	9355(14)	2430(15)	48(5)
C1	5000	4417(8)	0	21(2)	C23	5015(10)	9274(15)	2206(14)	44(5)
C2	7338(7)	5990(11)	3151(11)	24(3)	C24	4743(10)	8327(14)	2100(13)	31(4)
C3	7596(9)	6445(10)	4093(11)	26(4)	C25	5135(8)	7442(12)	2236(11)	27(3)
C4	8252(11)	6213(14)	4508(15)	48(5)	C26	6143(7)	6912(12)	3545(11)	24(3)
C5	8633(10)	5564(16)	4011(16)	49(5)	C27	6014(10)	7968(16)	3534(14)	71(8)
C6	8405(9)	5090(70)	3094(14)	50(9)	C28	5741(13)	8432(16)	4335(17)	76(9)
C7	7744(9)	5354(12)	2639(12)	32(4)	C29	5585(11)	7866(19)	5145(14)	56(6)
C8	7126(8)	6987(11)	2309(13)	29(4)	C30	5708(9)	6812(13)	5149(11)	30(4)
C9	7584(8)	7437(12)	3008(13)	38(4)	C31	5961(4)	6388(6)	4446(6)	30.4(19)
C10	8087(10)	8085(14)	2702(15)	47(5)	C31A	5961(4)	6388(6)	4446(6)	30.4(19)
C11	8122(9)	8245(14)	1669(13)	36(4)	C32	6480(9)	6226(10)	4016(11)	27(4)
C12	7654(10)	7824(14)	953(14)	43(5)	C33	7060(10)	5883(11)	4580(11)	34(4)
C13	7148(10)	7188(12)	1267(12)	36(5)	C34	7098(10)	5692(12)	5625(13)	37(4)
C14	6693(8)	7403(11)	1750(12)	24(3)	C35	6528(9)	5864(13)	6080(11)	29(4)
C15	7311(9)	7858(12)	1858(10)	32(4)	C36	5969(9)	6224(13)	5547(12)	31(4)
C16	7440(10)	8762(13)	1317(13)	37(4)	O3	5666(5)	8613(6)	-239(5)	38(2)
C17	6909(9)	9199(12)	691(11)	28(4)	O2	4428(8)	7778(8)	2233(7)	77(4)

Table 7.71 Bond lengths [Å] and angles [deg] for $[\{\text{Ir}(\text{PPh}_3)_2\text{Cl}_2\}_2(\mu^2\text{-oxalato-}\kappa^4\text{O}^1,\text{O}^2:\text{O}^1',\text{O}^2')]$.

Atom	Atom	Length/Å	Atom	Atom	Atom	Angle/°	Atom	Atom	Atom	Angle/°
Ir1	Cl1	2.350(3)	Cl2	Ir1	Cl1	168.98(10)	C13	C8	P1	116.1(13)
Ir1	Cl2	2.340(3)	P1 ¹	Ir1	Cl1	92.53(8)	C8	C9	C10	120.9(16)
Ir1	P1	2.296(2)	P1	Ir1	Cl1	92.53(8)	C11	C10	C9	120.0(17)
Ir1	P1 ¹	2.296(2)	P1 ¹	Ir1	Cl2	94.59(8)	C12	C11	C10	119.9(17)
Ir1	O1	2.122(5)	P1	Ir1	Cl2	94.59(8)	C11	C12	C13	119.6(16)
Ir1	O1 ¹	2.122(5)	P1	Ir1	P1 ¹	99.45(11)	C8	C13	C12	120.7(16)
P1	C2	1.910(15)	O1	Ir1	Cl1	87.05(16)	C15	C14	P1	123.8(13)
P1	C8	1.679(17)	O1 ¹	Ir1	Cl1	87.05(16)	C19	C14	P1	117.7(12)
P1	C14	1.866(15)	O1 ¹	Ir1	Cl2	84.40(16)	C19	C14	C15	117.7(15)
P1	C20	1.975(15)	O1	Ir1	Cl2	84.40(16)	C14	C15	C16	122.0(16)
P1	C26	1.662(16)	O1 ¹	Ir1	P1 ¹	169.33(14)	C17	C16	C15	117.2(17)
P1	C32	1.893(15)	O1	Ir1	P1 ¹	91.23(15)	C18	C17	C16	121.9(15)
O1	C1	1.248(7)	O1	Ir1	P1	169.33(14)	C17	C18	C19	118.3(17)
C1	C1 ²	1.51(2)	O1 ¹	Ir1	P1	91.23(15)	C17	C18	O3	143.1(15)
C2	C3	1.42(2)	O1 ¹	Ir1	O1	78.1(3)	C19	C18	O3	95.6(13)
C2	C7	1.41(2)	C2	P1	Ir1	111.0(5)	C14	C19	C18	122.8(17)
C3	C4	1.41(3)	C8	P1	Ir1	126.1(5)	C21	C20	P1	116.2(13)
C4	C5	1.37(3)	C8	P1	C20	98.3(7)	C25	C20	P1	126.8(11)
C5	C6	1.38(5)	C8	P1	C32	110.6(7)	C25	C20	C21	117.0(14)
C6	C7	1.44(3)	C14	P1	Ir1	112.6(5)	C22	C21	C20	120.9(18)
C8	C9	1.36(2)	C14	P1	C2	96.2(7)	C21	C22	C23	121.5(18)
C8	C13	1.41(2)	C20	P1	Ir1	106.3(5)	C24	C23	C22	118.5(18)
C9	C10	1.43(3)	C26	P1	Ir1	122.4(5)	C23	C24	C25	121.0(19)
C10	C11	1.40(3)	C26	P1	C2	104.4(7)	C20	C25	C24	121.2(16)
C11	C12	1.37(3)	C26	P1	C14	107.0(7)	C27	C26	P1	120.9(13)
C12	C13	1.43(3)	C32	P1	Ir1	113.8(4)	C27	C26	C31	113.3(14)
C14	C15	1.38(2)	C32	P1	C20	95.2(7)	C31	C26	P1	125.7(11)
C14	C19	1.37(2)	C1	O1	Ir1	113.2(5)	C26	C27	C28	120.5(18)
C15	C16	1.42(2)	O1	C1	O1 ²	124.5(10)	C29	C28	C27	121(2)
C16	C17	1.39(2)	O1	C1	C1 ³	117.8(5)	C28	C29	C30	117.9(18)
C17	C18	1.37(2)	O1 ²	C1	C1 ³	117.8(5)	C31	C30	C29	121.4(16)
C18	C19	1.39(2)	C3	C2	P1	117.4(12)	C30	C31	C26	125.3(12)
C18	O3	1.56(2)	C7	C2	P1	122.7(12)	C32	C31A	C36	121.0(12)
C20	C21	1.40(2)	C7	C2	C3	119.8(15)	C31A	C32	P1	121.2(11)
C20	C25	1.40(2)	C4	C3	C2	118.4(16)	C31A	C32	C33	120.5(14)
C21	C22	1.36(3)	C5	C4	C3	120.8(18)	C33	C32	P1	118.2(13)
C22	C23	1.40(3)	C4	C5	C6	123(3)	C32	C33	C34	121.5(18)
C23	C24	1.35(3)	C5	C6	C7	117(4)	C35	C34	C33	117.3(18)
C24	C25	1.40(2)	C2	C7	C6	121(2)	C36	C35	C34	121.7(15)
C26	C27	1.39(3)	C9	C8	P1	124.4(13)	C35	C36	C31A	118.0(15)
C26	C31	1.466(17)	C9	C8	C13	118.7(16)				
C27	C28	1.40(3)								
C28	C29	1.37(3)								
C29	C30	1.39(3)								
C30	C31	1.251(18)								
C31A	C32	1.285(19)								
C31A	C36	1.474(18)								
C32	C33	1.39(2)								
C33	C34	1.40(2)								
C34	C35	1.40(3)								
C35	C36	1.34(2)								

Table 7.72 Anisotropic displacement parameters ($\text{\AA}^2 \times 10^3$) for $[\{\text{Ir}(\text{PPh}_3)_2\text{Cl}_2\}_2(\mu^2\text{-oxalato-}\kappa^4\text{O}^1,\text{O}^2:\text{O}^1',\text{O}^2')]$. The anisotropic displacement factor exponent takes the form: $-2\pi^2[h^2a^*2U_{11}+2hka^*b^*U_{12}+\dots]$.

Atom	U ₁₁	U ₂₂	U ₃₃	U ₂₃	U ₁₃	U ₁₂
Ir1	31.1(2)	9.7(2)	11.8(2)	0	1.72(14)	0
Cl1	32.8(15)	38.8(17)	23.6(13)	0	5.1(11)	0
Cl2	45.8(18)	37.1(17)	22.6(13)	0	12.8(12)	0
P1	57.7(15)	17.0(10)	18.2(10)	3.1(8)	-6.4(9)	-9.8(10)
O1	40(3)	9(2)	21(3)	0(2)	-5(2)	4(2)
C1	36(6)	21(6)	7(4)	0	1(4)	0
C2	16(7)	26(9)	28(8)	-4(7)	-5(6)	-7(6)
C3	51(10)	2(6)	24(8)	2(6)	-1(7)	-4(7)
C4	67(14)	35(11)	39(11)	1(9)	-5(10)	-3(10)
C5	44(12)	43(12)	57(13)	2(10)	-1(10)	-7(9)
C6	40(8)	60(30)	50(9)	0(20)	1(7)	10(20)
C7	44(10)	24(9)	29(8)	5(6)	8(7)	1(6)
C8	35(9)	16(8)	36(9)	-4(7)	5(7)	3(7)
C9	51(11)	41(11)	21(8)	8(8)	3(8)	-17(9)
C10	59(13)	37(11)	42(11)	-3(9)	-10(9)	-8(10)
C11	46(11)	24(9)	37(10)	19(7)	3(8)	-2(8)
C12	68(14)	25(10)	40(10)	2(8)	23(10)	-15(9)
C13	72(14)	13(8)	21(8)	9(7)	-5(8)	-7(8)
C14	26(8)	12(7)	37(9)	-1(7)	18(7)	-9(6)
C15	49(11)	24(9)	20(8)	13(7)	-8(7)	-6(8)
C16	46(11)	31(10)	36(9)	5(8)	7(8)	-12(8)
C17	47(10)	15(7)	20(7)	1(6)	1(7)	8(7)
C18	52(11)	25(9)	33(9)	7(7)	-4(8)	-7(8)
C19	45(10)	23(9)	32(9)	0(7)	-5(8)	1(8)
C20	38(9)	14(7)	20(7)	4(6)	2(6)	5(7)
C21	41(10)	21(9)	52(11)	-8(8)	12(9)	-5(8)
C22	64(14)	27(11)	56(12)	-14(9)	19(10)	5(9)
C23	54(12)	37(11)	45(11)	3(9)	22(9)	16(9)
C24	51(11)	19(10)	23(9)	1(7)	3(8)	12(8)
C25	42(10)	15(8)	26(8)	-8(6)	12(7)	3(7)
C26	28(8)	23(8)	18(7)	-5(6)	-7(6)	-11(7)
C27	150(30)	30(11)	49(13)	2(10)	67(15)	1(13)
C28	160(30)	17(10)	71(15)	0(10)	74(17)	12(13)
C29	78(16)	70(16)	24(9)	-11(10)	24(10)	1(12)
C30	52(11)	21(9)	15(7)	-2(7)	3(7)	4(8)
C31	38(5)	24(4)	28(4)	6(4)	0(4)	-3(4)
C31A	38(5)	24(4)	28(4)	6(4)	0(4)	-3(4)
C32	49(11)	16(8)	14(7)	-2(6)	3(7)	-1(7)
C33	65(12)	24(9)	9(7)	-6(6)	-6(7)	-12(8)
C34	69(13)	10(8)	30(9)	-2(6)	-5(9)	-4(8)
C35	44(10)	29(9)	14(7)	-8(6)	4(7)	4(8)
C36	45(11)	28(10)	18(8)	-4(7)	-3(7)	3(8)
O3	77(6)	19(4)	17(4)	-3(3)	0(4)	6(4)
O2	179(14)	25(6)	33(5)	19(4)	37(7)	45(7)

7.11.20. **[Ir(PPh₃)₂(bzTSCmB)Cl]**

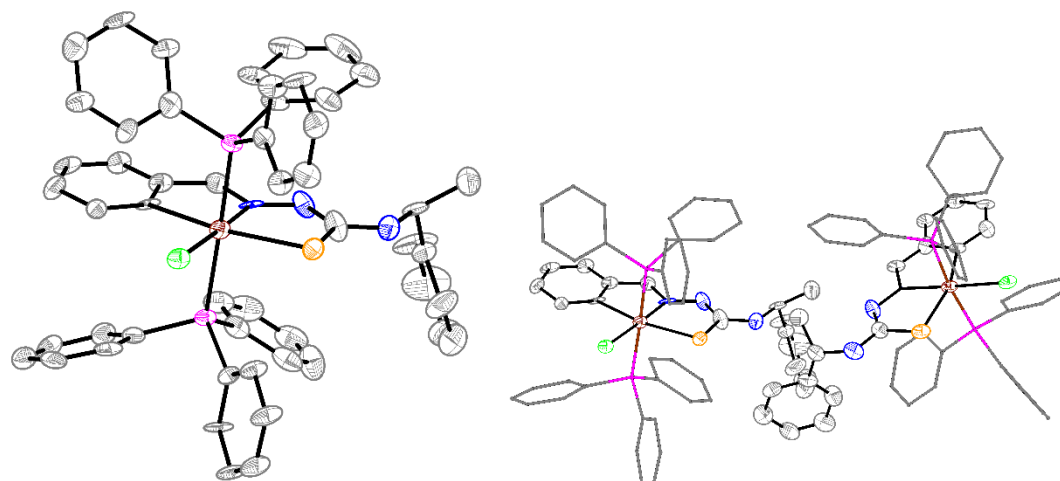


Figure 7.476. left: Molecular structure of [Ir(PPh₃)₂(bzTSCmB)Cl]. Right: asymmetric unit, triphenyl phosphine as wires for clarity. Ellipsoids are shown with 50 % probability. Hydrogen atoms are omitted for clarity.

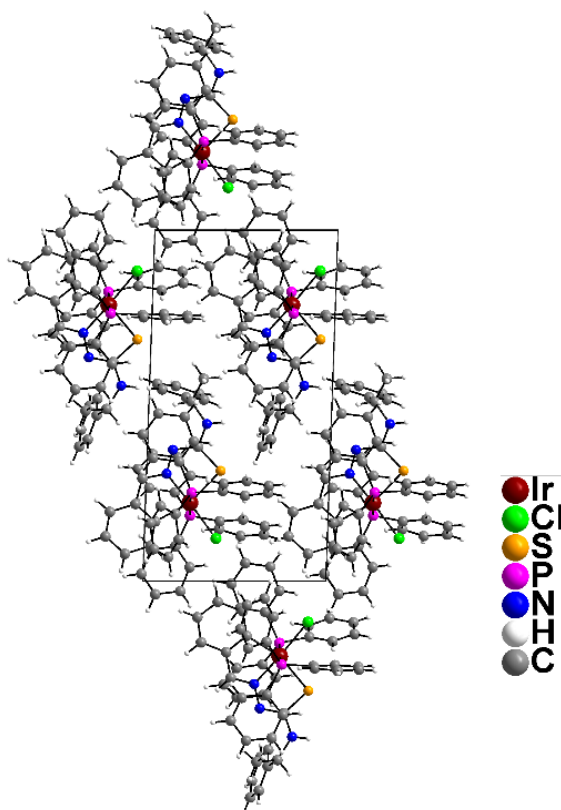


Figure 7.478 Crystal structure of [Ir(PPh₃)₂(bzTSCmB)Cl] along the crystallographic b-axis.

Table 7.73 Crystal data and structure refinement for [Ir(PPh₃)₂(bzTSCmB)Cl].

Empirical formula	C ₅₂ H ₄₅ ClIrN ₃ P ₂ S (1033.64 g/mol)
Temperature/K	100.15
Crystal system	Triclinic / P1
a/Å	9.7457(6)
b/Å	11.8391(8)

c/Å	19.3725(16)
α /°	75.172(5)
β /°	87.674(5)
γ /°	88.402(4)
Volume / Z	2158.6(3) Å ³ / 2
ρ_{calc}	1.5902 g/cm ³
μ	8.023 mm ⁻¹
F(000)	1032.0
Crystal size/mm ³	0.07 × 0.05 × 0.01
Radiation	Cu K α (λ = 1.54178)
2 Θ range for data collection/°	4.72 to 145.3
Index ranges	-12 ≤ h ≤ 12, -14 ≤ k ≤ 14, -23 ≤ l ≤ 23
Reflections collected	82657
Independent reflections	16015 [R _{int} = 0.0935, R _{sigma} = 0.0715]
Data/restraints/parameters	16015/3/1084
Goodness-of-fit on F ²	1.038
Final R indexes [$I_{o} \geq 2\sigma_{I_{o}}$]	R ₁ = 0.0612, wR ₂ = 0.1604
Final R indexes [all data]	R ₁ = 0.0675, wR ₂ = 0.1635
Largest diff. peak/hole / e Å ⁻³	4.11/-3.19
Flack parameter	0.043(13)

Table 7.74 Atomic coordinates ($\times 10^4$) and equivalent isotropic displacement parameters (Å² $\times 10^3$) for [Ir(PPh₃)₂(bzTSCmB)Cl]. U(eq) is defined as one third of the trace of the orthogonalized U_{ij} tensor.

Atom	x	y	z	U(eq)	Atom	x	y	z	U(eq)
Ir1b	7622.04(8)	1880.19(8)	7859.14(8)	26.9(1)	Ir1	2424.72(8)	5020.90(8)	2226.89(8)	24.5(1)
Cl1b	9106.0(15)	1114.3(15)	8834.5(13)	32.3(7)	Cl1	3916.7(15)	5060.1(15)	1209.1(12)	27.3(6)
S1b	9249.6(17)	2654.1(17)	6876.8(14)	35.9(8)	S1	4037.6(17)	4991.5(17)	3139.5(13)	27.9(7)
P2b	7740.7(18)	25.9(18)	7621.5(14)	24.4(7)	P1	2501.0(18)	2962.4(17)	2519.0(1)	24.2(7)
P1b	7577.0(1)	3612.4(1)	8234.7(1)	24.4(7)	P2	2458.9(1)	7075.1(1)	1864.9(1)	22.2(7)
N1b	6282(7)	2512(7)	7064(5)	24(2)	N1	1096(7)	5003(6)	3054(5)	21(2)
N2b	6629(8)	3036(7)	6373(5)	35(3)	N2	1394(8)	4965(7)	3737(5)	33(3)
N3b	8446(8)	3609(8)	5563(6)	41(3)	N3	3198(8)	4939(7)	4473(5)	34(3)
C30b	5289(10)	4791(9)	7523(7)	29(3)	C46	181(11)	7644(10)	2653(8)	45(4)
C15b	3051(10)	1048(10)	8967(7)	38(3)	C17	4193(10)	2211(10)	2571(7)	29(3)
C45b	5065(11)	128(10)	6027(8)	48(4)	C34	834(9)	1279(9)	2137(7)	32(3)
C44b	5947(11)	12(10)	5454(7)	48(4)	C1	2319(10)	4878(9)	5110(7)	31(3)
C26b	5572(10)	3011(10)	10512(8)	37(3)	C19	5497(10)	385(9)	2844(8)	42(4)
C27b	4843(10)	3593(9)	9923(7)	34(4)	C27	1983(11)	1758(10)	4681(7)	47(4)
C28b	5375(10)	3798(9)	9231(7)	32(3)	C3	2993(11)	6917(11)	5163(8)	58(5)
C23b	6747(10)	3453(8)	9119(6)	27(3)	C13	353(9)	5159(8)	1001(6)	23(3)
C29b	6699(10)	4836(8)	7631(7)	27(3)	C25	-273(11)	1895(10)	4178(8)	53(5)
C1b	7686(10)	3972(10)	4901(7)	39(3)	C18	4227(10)	998(10)	2771(7)	39(3)
C48b	5886(10)	-1885(10)	8088(7)	42(4)	C45	-472(11)	8091(10)	3194(8)	51(4)
C52b	7198(10)	-1380(8)	8988(7)	38(4)	C8	2946(10)	4059(10)	5761(7)	47(4)
C12b	5782(9)	1416(8)	8439(6)	23(3)	C48	391(10)	8129(9)	887(7)	35(3)
C25b	6936(10)	2660(9)	10409(6)	33(3)	C51	2062(10)	8003(9)	-291(7)	34(3)
C18b	10477(9)	3767(9)	8283(8)	38(4)	C49	-94(10)	8554(10)	208(7)	36(4)
C4b	6273(10)	6912(10)	3831(8)	48(4)	C50	707(10)	8451(10)	-377(7)	37(4)
C8b	6556(10)	3161(10)	4846(7)	44(4)	C23	1761(10)	2342(8)	3401(7)	30(3)
C43b	7334(11)	-85(8)	5529(7)	41(4)	C9	2757(10)	4989(10)	3825(6)	36(3)
C32b	5352(10)	6705(9)	6695(7)	40(4)	C32	538(10)	1217(10)	907(8)	43(4)
C9b	7970(10)	3148(10)	6237(7)	36(3)	C47	1713(10)	7680(9)	990(6)	29(3)
C33b	6785(11)	6717(8)	6757(7)	38(4)	C36	4068(10)	9055(9)	1475(7)	33(3)

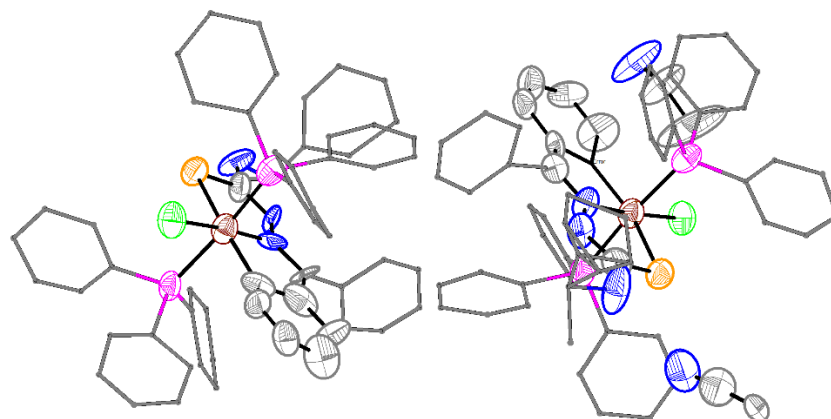


Figure 7.480 Asymmetric unit of $[\text{Ir}(\text{PPh}_3)_2(\text{bphTSCmB})\text{Cl}] \cdot \text{MeCN}$. Ellipsoids are shown with 50 % probability. Hydrogen atoms are omitted, and non-coordinating phenyl rings are depicted as wireframes for clarity.

Table 7.75 Crystal data and structure refinement for $[\text{Ir}(\text{PPh}_3)_2(\text{bphTSCmB})\text{Cl}] \cdot \text{MeCN}$.

Empirical formula	$\text{C}_{120}\text{H}_{100}\text{Cl}_2\text{Ir}_2\text{N}_8\text{P}_4\text{S}_2$ (2300.40 g/mol)
Temperature/K	293(2)
Crystal system	Monoclinic / $P2_1$
$a/\text{\AA}$	18.5194(17)
$b/\text{\AA}$	12.5871(8)
$c/\text{\AA}$	24.119(2)
$\beta/^\circ$	102.739(7)
Volume / Z	5483.9(8) \AA^3 / 2
$\rho_{\text{calc}}/\text{cm}^{-3}$	1.393
μ/mm^{-1}	2.621
$F(000)$	2318.0
Radiation	$\text{MoK}\alpha$ ($\lambda = 0.71073$)
2θ range for data collection/ $^\circ$	3.462 to 53.908
Index ranges	$-22 \leq h \leq 23$, $-16 \leq k \leq 15$, $-30 \leq l \leq 30$
Reflections collected	40533
Independent reflections	21417 [$R_{\text{int}} = 0.1638$, $R_{\text{sigma}} = 0.3155$]
Data/restraints/parameters	21417/9/1248
Goodness-of-fit on F^2	0.823
Final R indexes [$I_o \geq 2\sigma I_o$]	$R_1 = 0.0737$, $wR_2 = 0.1451$
Final R indexes [all data]	$R_1 = 0.2391$, $wR_2 = 0.2139$
Largest diff. peak/hole / $e \text{\AA}^{-3}$	1.31/-1.59
Flack parameter	0.18(2)

Table 7.76 Atomic coordinates ($\times 10^4$) and equivalent isotropic displacement parameters ($\text{\AA}^2 \times 10^3$) for $[\text{Ir}(\text{PPh}_3)_2(\text{bphTSCmB})\text{Cl}] \cdot \text{MeCN}$. $U(\text{eq})$ is defined as one third of the trace of the orthogonalized U_{ij} tensor.

Atom	x	y	z	$U(\text{eq})$	Atom	x	y	z	$U(\text{eq})$
Ir1	-18.6(8)	-4479.33(17)	-3058.3(6)	63.5(5)	C33b	3280(30)	-3010(20)	-1949(19)	99(14)
Ir1b	5164.5(8)	30.14(17)	-1876.6(6)	64.0(5)	C20	-2410(20)	-5540(20)	-1205(19)	83(12)
S1b	4026(5)	-107(4)	-2601(4)	70(2)	C48b	4760(20)	2700(20)	-2776(16)	70(10)
S1	1098(5)	-4449(4)	-2297(4)	64(2)	C53	-618(18)	-2221(19)	-2353(14)	52(8)
P1	223(6)	-6246(4)	-3245(4)	63(3)	C26b	6730(40)	-3350(30)	-350(30)	150(30)
P2b	4897(6)	1837(4)	-1708(4)	65(3)	C55	-510(20)	-2120(20)	-1348(18)	74(11)
P2	-190(6)	-2622(4)	-2957(5)	72(3)	C56	-1200(20)	-1680(20)	-1441(18)	82(12)

P1b	5362(6)	-1812(4)	-1942(4)	66(3)		C6	-40(50)	-3390(30)	220(30)	210(30)
Cl1b	4821(5)	-349(3)	-996(4)	74(3)		C52	1291(18)	-2118(19)	-2980(14)	56(8)
Cl1	401(6)	-4032(3)	-3901(4)	78(3)		C57b	5260(20)	2830(20)	-20(20)	85(13)
N2	-76(13)	-4945(16)	-1857(10)	58(7)		C9b	4454(19)	130(20)	-3119(14)	74(10)
C10	-1189(18)	-5050(20)	-2506(15)	67(9)		C20b	7320(30)	1290(20)	-3780(30)	130(19)
N1b	5567(15)	447(16)	-2561(12)	65(7)		C45b	2760(20)	1590(20)	-1536(17)	86(12)
N2b	5192(15)	401(16)	-3122(11)	68(8)		C3	1080(30)	-3510(20)	-350(20)	112(15)
N3	1048(13)	-5006(15)	-1257(9)	60(6)		C60	4020(20)	-4830(20)	-558(19)	85(19)
C11b	6665(15)	580(20)	-1889(12)	50(7)		C21b	7160(30)	2000(20)	-3460(20)	121(17)
C10b	6265(16)	650(20)	-2490(13)	52(8)		C32b	3230(30)	-3930(20)	-2283(19)	91(13)
C29	1180(20)	-6620(20)	-3230(20)	82(13)		C36b	6540(20)	-2650(20)	-2412(18)	77(11)
C53b	5331(19)	2280(20)	-1032(15)	61(9)		C37	-150(20)	-7370(20)	-4882(19)	79(11)
N3b	4048(17)	14(16)	-3686(12)	85(8)		C34	1410(20)	-7690(20)	-3147(16)	68(10)
C47b	5110(30)	2730(20)	-2210(20)	101(15)		C42b	3670(20)	3160(20)	-1811(16)	67(10)
C12b	6221(18)	290(20)	-1499(14)	66(9)		N4	2670(20)	-4512(18)	-806(16)	116(12)
C9	630(16)	-4843(19)	-1779(12)	55(8)		C19b	7180(30)	220(30)	-3750(30)	140(20)
C16b	7437(17)	806(19)	-1695(13)	58(9)		C35	-180(20)	-6790(20)	-3951(15)	62(9)
C58b	4940(20)	2450(20)	-582(18)	81(12)		C51	1950(20)	-1510(20)	-2823(18)	91(12)
C52b	5642(19)	3640(20)	-2032(16)	67(10)		C56b	6000(30)	3040(20)	50(20)	110(16)
C11	-1547(19)	-4950(20)	-3132(15)	71(9)		C17	-1585(16)	-5280(18)	-2076(13)	52(8)
C25	184(19)	-7920(20)	-1809(16)	66(10)		C39b	5670(30)	-2350(20)	-3540(20)	93(14)
N1	-485(16)	-4872(16)	-2419(13)	78(9)		C57	-1580(20)	-1490(20)	-2001(18)	77(11)
C14	-2138(17)	-4738(19)	-4288(14)	68(10)		C19	-2110(30)	-4650(20)	-1340(30)	133(18)
C13b	6597(18)	235(19)	-926(14)	67(9)		C39	-1310(30)	-7190(20)	-4660(20)	108(16)
C29b	4540(17)	-2639(18)	-2102(13)	49(8)		C37b	6760(20)	-2940(20)	-2914(19)	86(12)
C28b	6650(30)	-2060(20)	-1130(20)	89(14)		C59	3290(20)	-4540(20)	-696(17)	87(11)
C54	-220(20)	-2420(20)	-1790(15)	66(10)		C31b	3870(20)	-4290(20)	-2441(16)	85(11)
C2	595(17)	-4430(20)	-430(13)	59(7)		C28	-610(20)	-7890(20)	-2910(20)	90(13)
C43b	2918(17)	3348(19)	-1746(13)	55(8)		C23b	5930(20)	-2480(20)	-1343(18)	76(11)
C1	725(18)	-5200(20)	-781(14)	68(9)		C50	1930(30)	-550(20)	-2550(20)	109(16)
C8	1250(20)	-6080(20)	-379(18)	90(12)		C38	-890(20)	-7480(20)	-5050(20)	85(13)
C1b	4280(20)	-40(20)	-4184(15)	83(10)		C44	-1650(40)	-1170(20)	-4540(30)	160(20)
C41	-740(20)	-1990(20)	-3595(19)	88(13)		C22	-1800(30)	-6260(20)	-1910(20)	108(15)
C13	-1380(20)	-4520(20)	-4080(15)	81(10)		C48	610(30)	-870(20)	-2530(20)	106(15)
C50b	5360(20)	4210(20)	-3070(20)	98(14)		C18	-1730(30)	-4470(30)	-1770(30)	180(20)
C42	-1460(30)	-2300(20)	-3830(20)	98(14)		C7b	3750(30)	1800(20)	-4450(20)	130(19)
C41b	3920(20)	2130(20)	-1752(17)	69(10)		C4	970(20)	-2690(20)	30(18)	94(12)
C16	-2310(20)	-5060(20)	-3331(15)	77(10)		C49	1290(30)	-210(30)	-2400(30)	150(20)
C32	2610(30)	-7250(20)	-3230(19)	102(14)		C46	-450(40)	-1150(30)	-3830(30)	107(18)
C40b	5370(30)	-2100(20)	-3052(18)	88(13)		C24b	5710(30)	-3100(20)	-1030(30)	130(20)
C18b	6810(20)	40(20)	-3290(20)	98(14)		C5	490(40)	-2550(30)	380(30)	170(20)
C15	-2579(18)	-5020(20)	-3912(13)	68(8)		C2b	4280(30)	1170(20)	-4350(20)	102(14)
C30	1700(18)	-5810(20)	-3298(14)	58(8)		C30b	4480(30)	-3640(20)	-2340(20)	106(15)
C34b	3930(30)	-2260(20)	-1840(20)	121(18)		C22b	6870(30)	1840(20)	-2990(20)	106(16)
C15b	7780(20)	770(20)	-1143(14)	74(10)		C21	-2190(30)	-6440(20)	-1460(30)	120(20)
C46b	3450(20)	1340(20)	-1587(18)	93(13)		C27b	7040(30)	-2620(20)	-560(20)	112(17)
C27	-770(20)	-8740(20)	-2509(19)	86(13)		C47	680(20)	-1790(20)	-2818(19)	84(12)
C14b	7372(16)	510(20)	-742(13)	62(8)		C23	-30(17)	-7306(19)	-2755(14)	50(8)
C33	2070(30)	-8030(20)	-3149(19)	100(14)		C5b	4240(50)	3240(30)	-4840(40)	210(40)
C38b	6390(20)	-2840(20)	-3423(19)	86(12)		C6b	3760(50)	2820(30)	-4650(40)	200(30)
C25b	6060(30)	-3720(20)	-580(20)	109(15)		C7	50(30)	-4380(20)	-190(20)	138(17)
C51b	5790(20)	4240(20)	-2484(17)	76(11)		C8b	3930(20)	-530(20)	-4677(18)	94(13)
C58	-1300(20)	-1770(20)	-2454(17)	73(10)		C59b	1790(40)	-160(30)	-4210(30)	150(20)
C54b	6100(20)	2510(20)	-862(17)	73(11)		C45	-940(40)	-540(30)	-4330(30)	180(30)
N4b	2410(30)	-310(18)	-4074(18)	140(20)		C12	-1067(17)	-4680(20)	-3480(14)	62(9)
C55b	6430(20)	2900(20)	-343(18)	81(12)		C44b	2520(20)	2580(20)	-1599(16)	79(11)

C17b	6670(20)	830(20)	-2960(16)	65(10)		C60b	1020(30)	430(20)	-4480(30)	310(30)
C40	-960(20)	-6870(20)	-4105(18)	76(11)		C31	2410(20)	-6130(20)	-3328(17)	82(11)
C35b	5780(20)	-2200(20)	-2509(15)	67(10)		C26	-390(20)	-8620(20)	-1950(19)	86(12)
C36	190(20)	-6958(19)	-4345(15)	59(9)		C3b	4910(50)	1540(30)	-4490(40)	220(30)
C43	-1950(30)	-1870(20)	-4260(20)	105(15)		C24	390(20)	-7210(20)	-2225(15)	66(10)
C49b	4920(30)	3350(20)	-3190(30)	117(19)		C4b	4930(90)	2800(30)	-4760(60)	370(70)

7.12. TD-DFT calculated transitions for [M(hphfpyTSCmB)]

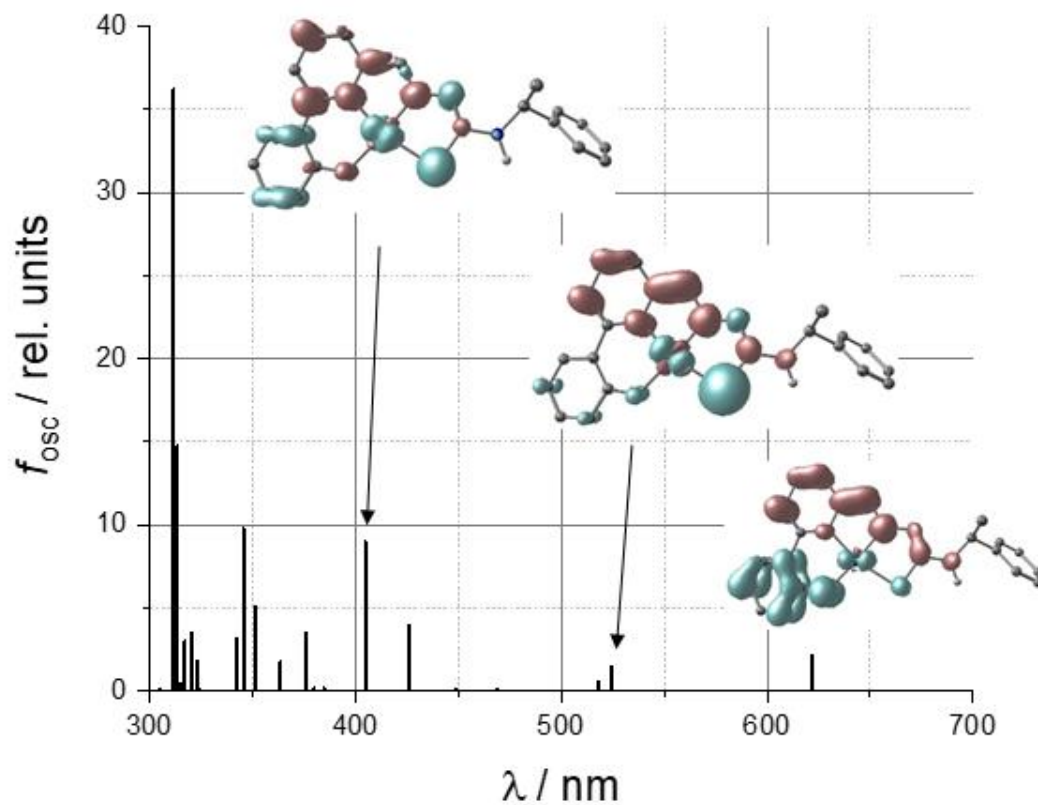


Figure 7.481 TD-DFT calculated optical spectrum of [Pd(hphfpyTSCmB)]; verticals: transitions. Inset: Difference densities of selected transitions.

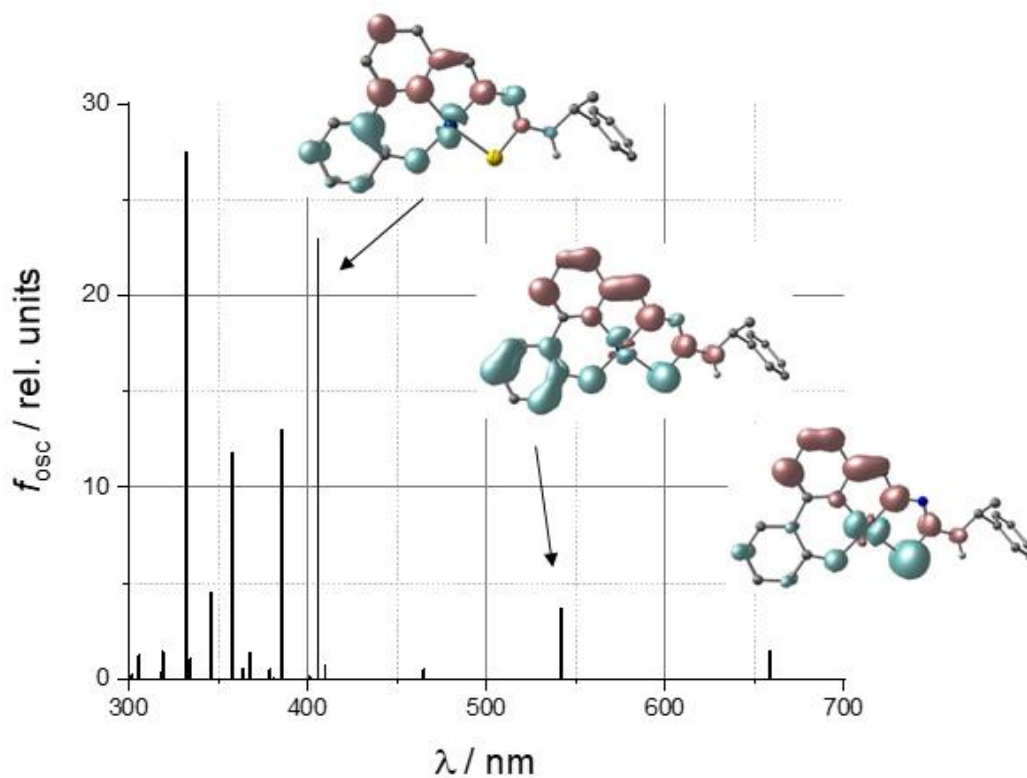


Figure 7.482 TD-DFT calculated optical spectrum of [Pt(hphfpyTSCmB)]; verticals: transitions. Inset: Difference densities of selected transitions.

Table 7.77 TD-DFT calculated absorptions of [Ni(hphfpyTSCmB)] with $f_{osc} > 0.01$; character denotes leading orbital contributions.

transition	ν / cm^{-1}	λ / nm	f_{osc}	character
5	15083.7	663	0.012	H → L (87 %)
11	18639.2	536.5	0.029	H-1 → L (82 %)
16	23089.4	433.1	0.017	H → L+2 (67 %)
20	23561.6	424.4	0.082	H-3 → L (48 %)
27	25785.2	387.8	0.018	H-6 → L+1 (46 %)
31	26858.9	372.3	0.036	H-5 → L (56 %)
33	28047	356.5	0.023	Mixed
34	28405.4	352	0.124	Mixed
35	28539.5	350.4	0.087	Mixed
36	29043.8	344.3	0.053	H-8 → L (68 %)
39	29530.9	338.6	0.021	Mixed
42	30819.5	324.5	0.333	Mixed
47	31203.7	320.5	0.011	H-7 → L+2 (36 %) // H-5 → L+2 (26 %)
49	31516.4	317.3	0.027	H-9 → L (74 %)
59	32989.1	303.1	0.010	H-4 → L+2 (55 %)
64	33693.5	296.8	0.040	H → L+5 (80 %)
70	34876.4	286.7	0.027	mixed

Table 7.78 TD-DFT calculated absorptions of [Pd(hphfpyTSCmB)] with $f_{osc} > 0.01$; character denotes leading orbital contributions.

transition	ν / cm^{-1}	λ / nm	f_{osc}	character
3	16087.5	621.6	0.021	H → L (96 %)
5	19081.4	524.1	0.014	H-1 → L (82 %)
14	23475.9	426	0.039	H → L+2 (67 %)
18	24714	404.6	0.09	H-2 → L (40 %) // H-1 → L+2 (35 %)
24	26619	375.7	0.034	H-3 → L+1 (63 %)
26	27520.5	363.4	0.017	H-4 → L (52 %) // H-1 → L+2 (34 %)
28	28470.1	351.2	0.05	H-6 → L (71 %)
30	28925.9	345.7	0.097	Mixed
32	29203.8	342.4	0.031	H-3 → L+2 (74 %)
41	30992.7	322.7	0.018	H-7 → L (94 %)
42	31236.9	320.1	0.035	H-2 → L+2 (68 %)
44	31558	316.9	0.03	H-9 → L (70 %)
48	31903.3	313.4	0.148	H-8 → L (67 %)
49	32104	311.5	0.362	Mixed

57	33695.6	296.8	0.02	H-1 → L+3 (88 %)
58	33760	296.2	0.109	H-10 → L (48 %)
59	34192.8	292.5	0.035	H → L+5 (50 %)
67	36184.9	276.4	0.035	H-7 → L+1 (88 %)
68	36273.6	275.7	0.044	H-10 → L+1 (62 %)
69	36456.3	274.3	0.075	Mixed
72	36890.4	271.1	0.061	H-6 → L+2 (43 %)
74	37036.9	270	0.017	H-2 → L+3 (96 %)

Table 7.79 TD-DFT calculated absorptions of [Pt(hphfpyTSCmB)] with $f_{osc} > 0.01$; character denotes leading orbital contributions.

transition	ν / cm^{-1}	λ / nm	f_{osc}	character
2	15092.2	662.6	0.015	H → L (92 %)
5	18968.9	527.2	0.034	H-1 → L (87 %)
12	24392.1	410	0.151	H-2 → L (46 %)
18	28003.1	357.1	0.046	H-5 → L (40 %)
20	29085.9	343.8	0.185	Mixed
24	29553.2	338.4	0.082	H-3 → L+1 (40 %)
26	29784.3	335.7	0.092	Mixed
27	29981.5	333.5	0.057	Mixed
28	30023	333.1	0.017	Mixed
30	30643.6	326.3	0.208	Mixed
35	31314.5	319.3	0.033	H-7 → L (90 %)
49	34354.1	291.1	0.034	Mixed
51	34539.9	289.5	0.014	H-1 → L+3 (50 %)
54	35425.4	282.3	0.063	H-6 → L+1 (74 %)
57	36112.9	276.9	0.083	Mixed
59	36277	275.7	0.034	H-2 → L+2 (76 %)
63	37192.5	268.9	0.079	H-3 → L+4 (56 %)
65	37434	267.1	0.017	H-2 → L+4 (50 %)
66	37454	267	0.17	Mixed

7.13. Erklärung

Ich versichere, dass ich die von mir vorgelegte Dissertation selbständig angefertigt, die benutzten Quellen und Hilfsmittel vollständig angegeben und die Stellen der Arbeit – einschließlich Tabellen, Karten und Abbildungen –, die anderen Werken im Wortlaut oder dem Sinn nach entnommen sind, in jedem Einzelfall als Entlehnung kenntlich gemacht habe; dass diese Dissertation noch keiner anderen Fakultät oder Universität zur Prüfung vorgelegen hat; dass sie – abgesehen von unten angegebenen Teilpublikationen – noch nicht veröffentlicht worden ist sowie, dass ich eine solche Veröffentlichung vor Abschluss des Promotionsverfahrens nicht vornehmen werde. Die Bestimmungen der Promotionsordnung sind mir bekannt. Die von mir vorgelegte Dissertation ist von Prof. Dr. Axel Klein betreut worden. Nachfolgend genannte Teilpublikation liegt vor:

A. Haseloer, T. Lützenkirchen, J. P. Strache, I. Neundorf, A. Klein, Building up Pt(II)-thiosemicarbazone-lysine-sC18 conjugates, *ChemBioChem*, **2021**, 22, 694-704. DOI: 10.1002/cbic.202000564.

D. Grödler, **A. Haseloer**, C. Tobeck, Y. Bulut, J.M. Neudörfl, S. Mathur, U. Ruschewitz, A. Klein, M. S. Wickleder and M. Zegke Thiosemicarbazone complexes of uranium(IV), *Eur. J. Inorg. Chem.*, **2021**, 12, 1137-1139. Communication. DOI: 10.1002/ejic.202001118.

A. Haseloer, L. M. Denkler, R. Jordan, M. Reimer, S. Olthof, I. Schmidt, K. Meerholz, G. Hörner and A. Klein, Ni, Pd, and Pt Complexes of a Tetradentate Dianionic Thiosemicarbazone-based O^NN^S Ligand, *Dalton Trans.*, **2021**, 50, 4311-4322. DOI: 10.1039/D1DT00272D.

Ich versichere, dass ich alle Angaben wahrheitsgemäß nach bestem Wissen und Gewissen gemacht habe und verpflichte mich, jedmögliche, die obigen Angaben betreffenden Veränderungen, dem Dekanat unverzüglich mitzuteilen.

Köln, den 20.8.2021

Unterschrift: _____

7.14. Curriculum vitae

Name	Alexander Haseloer
Location and Date of Birth	11.10.1991 in Cologne
Marital status	Unmarried, no children
Citizenship	German
School education	
1998 – 2002	Gemeinschafts Grundschule der Stadt Elsdorf in Berrendorf
2002 – 2011	Silverberg Gymnasium, Bedburg (Abitur, Grade: 2.3)
University education	
2011 – 2015	University of Cologne, Bachelor of Science in Chemistry (Grade: 2.3) Bachelorthesis: "Synthese neuartiger Thiosemicarbazonliganden zur Darstellung zweikerniger Übergangsmetallkomplexe" (AK Klein)
2015 – 2017	University of Cologne, Master of Science in Chemistry (Grade: 1.6) Masterthesis: "Synthesis of Amino Acid Containing Thiosemicarbazones and their Transition Metal Complexes" (AK Klein)
Since 2017	PhD studies in Chemistry at the University of Cologne. Supervised by: Axel Klein
Professional Background	
January 2012 – August 2013	OH-Security
August 2013 – April 2017	Tutor for physics, physical chemistry, and tutorial officer of the students representatives
Since April 2017	Lab Assistant for Inorganic Chemistry (1.&2. Semester, Chemistry) and minor subjects (1. Semester, Biochemistry; 1. Semester Geology)
Cooperation in Societies	
Students Representatives in Chemistry at the University of Cologne	Student Council (January 2013 – January 2016)
Gesellschaft Deutscher Chemiker (GDCh) – Jung Chemiker Forum (JCF)	Regional Spokesman of the JCF (August 2016 – January 2021) Students Representative in the section for nuclear chemistry Founder and Spokesperson of the Junge Wöhler Vereinigung für anorganische Chemie
Verband der Angestellten Akademiker und Führungskräfte in der Chemischen Industrie (VAA)	Students Representative in the universities commission (August 2016 – January 2020)
Planned Conferences	
22 nd Frühjahrssymposium (2020)	Head of Conference
Wöhler Tagung (2020)	Committee member for the Workgroup Klein
JCF - Sustainability Session Achema 2021	Head of Session Management

8. Publications

8.1. Articles

1. H. Barani, M. Khorashadizadeh, **A. Haseloer** and A. Klein, Characterization and Release of a Thiosemicarbazone from Electrospun Polyvinyl Alcohol Core-Shell Nanofibres, *Polymers*, **2020**, *12*(7),1488-1506. DOI: 10.3390/polym12071488.

2. H. Barani, **A. Haseloer**, S. Mathur and A. Klein, Sustained release of a thiosemicarbazone from antibacterial electrospun poly(lactic-co-glycolic acid) fiber mats, *Polym. Adv. Technol.*, **2020**, *31*, 3182-3193. DOI: 10.1002/pat.5043.

3. **A. Haseloer**, T. Lützenkirchen, J. P. Strache, I. Neundorf and A. Klein, Building up Pt(II)-thiosemicarbazone-lysine-sC18 conjugates, *ChemBioChem*, **2021**, *22*, 694-704. DOI: 10.1002/cbic.202000564.

4. D. Grödler, **A. Haseloer**, C. Tobeck, Y. Bulut, J.M. Neudörfl, S. Mathur, U. Ruschewitz, A. Klein, M. S. Wickleder and M. Zegke, Thiosemicarbazone complexes of uranium(IV), *Eur. J. Inorg. Chem.*, **2021**, *12*, 1137-1139. Communication. DOI: 10.1002/ejic.202001118.

5. **A. Haseloer**, L. M. Denkler, R. Jordan, M. Reimer, S. Olthof, I. Schmidt, K. Meerholz, G. Hörner and A. Klein, Ni, Pd, and Pt Complexes of a Tetradentate Dianionic Thiosemicarbazone-based O^NN^NS Ligand, *Dalton Trans.*, **2021**, *50*, 4311-4322. DOI: 10.1039/D1DT00272D.

6. G. Mohammadnezhad, N. Ahfad, S. Meghdadi, H. Farokhpour, S. Schmitz, **A. Haseloer**, A. Buchholz, W. Plass and A. Klein, Dinuclear nickel (II) and copper (II) complexes of 8-(quinoline)1-*H*-pyrazole-3-carboxamide: crystal structure, magnetic properties, and DFT calculations *Eur. J. Inorg. Chem.*, **2021**, *18*, 1786-1795. DOI: 10.1002/ejic.202100142.

7. K. Butsch, **A. Haseloer**, S. Schmitz, I. Ott, J. Schur and A. Klein, Fe(III), Copper and Zinc Complexes of the Rigid 9-Oxido-phenalenone Ligand – Spectroscopy, Electrochemistry and Cytotoxic Properties, *Int. J. Mol. Sci.*, **2021**, *22*, 3976-3994. DOI: 10.3390/ijms22083976.

8.2. Conference presentations

1. „20. Frühjahrssymposium“ 2018 in Konstanz. Poster: “N4 – Functionalization of Thiosemicarbazones for Catalytic and Nuclear Medical Purposes”.
2. „18. Koordinationschemiker Treffen“ 2018 in Heidelberg. Poster:“ N4 – Functionalization of Thiosemicarbazones for Catalytic and Nuclear Medical Purposes”.
3. „2. Ligandendesign Workshop“ 2018 in Köln. **Presentation: “Platin und Iridium Komplexe funktionalisierter Thiosemicarbazone“.**
4. “19. Koordinationschemiker Treffen” 2019 in München. Poster: „N4 funktionalisierte Thiosemicarbazone für nuklearmedizinische Anwendungen“
5. „21. Frühjahrssymposium“ 2019 in Bremen. Poster: “N4 Functionalization of Thiosemicarbazones for Nuclear Medical Purposes”
6. „XXXVII Reunión Bienal De La Real Sociedad Espanola de Química” 2019 in Donostia – San Sebastián. Poster: ”N4 Functionalization of Thiosemicarbazones for Nuclear Medical Purposes”. Travel Grant by the European Younger Chemists Network (EYCN).
7. “Wissenschaftsforum” 2019 in Aachen. **Presentation: “N4 Functionalization of Thiosemicarbazones for Nuclear Medical Purposes”**
8. “20. Koordinationschemiker Treffen” 2020 in Freiburg. **Presentation „Designing Keychains for Therapy – Platinum Thiosemicarbazone Complexes Conjugated to Peptides”.**
9. „23. Frühjahrssymposium“ 2021 in Leipzig (digital conference). **Presentation: „Designing Keychains for Therapy – Platinum Thiosemicarbazone Conjugated to Peptides as Template for Nuclear Medical Theranostics”.**